FINAL REPORT
Contract No.: 87055-11-0562

RSP Project ID (R525.1)

REPORTING DATE – 29 May 2014

PROJECT TITLE: Interfacing Seismological Description of Strong Ground Motion with Engineering Analysis of Soil Structure Interaction for Nuclear Power Plants

REPORT SUBMITTED BY: Structural and Earthquake Engineering Consultants (SEEC) Inc.
855 Arcadia Ave. #E, Arcadia, CA 91007 USA
Contact name: M. D. Trifunac
Phone: (626) 447-9382
Email: trifunac@usc.edu

to

Canadian Nuclear Safety Commission

ATTENTION: Milan Ducic, Nebojsa Orbovic
280 Slater St., Ottawa, Ontario, Canada, K1P 5S9
E-mail: research-recherche@cnsc-ccsn.gc.ca
Nebojsa.Orbovic@cnsc-ccsn.gc.ca

Table of Contents

Executive Summary

As described in the statement of the proposed work the purpose of this contract has been to formulate methodology for seismic wave excitation of numerical models of Nuclear Power Plant (NPP) structures, and specifically to provide detailed input ground motions for computations of seismic soil-structure interaction (SSI) in three dimensions (3D). This is illustrated in Fig. 1. Assuming that the structure, foundation and the surrounding soil are modeled numerically, this task can be accomplished by specifying the components of strong ground motion at a discrete mesh of points in the five surfaces of the "box" ABCD, which represents the boundary and the contact surfaces between the numerical representation of the model inside the box with the elastic, continuum mechanics representation of the site outside the box.

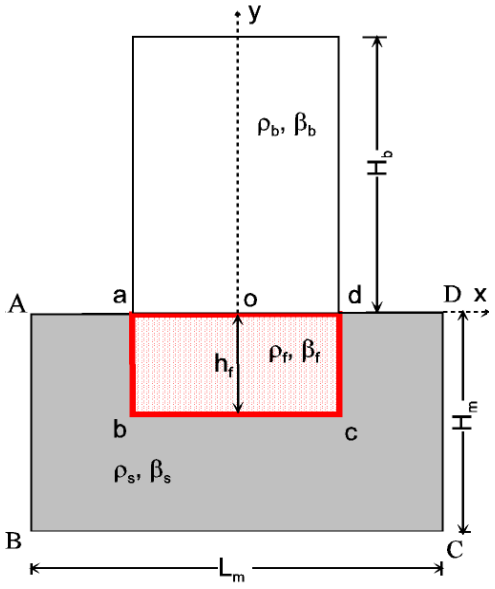

Figure 1. Structure, foundation (abcd), and the surrounding soil (ABCD) for numerical analysis of SSI.

Traditional approach to solving the above problem has been conceptually same as what will be presented in this report, except that it was based on a simplification, which is that the seismic energy arrives to the site as vertically propagating waves (Fig. 2).

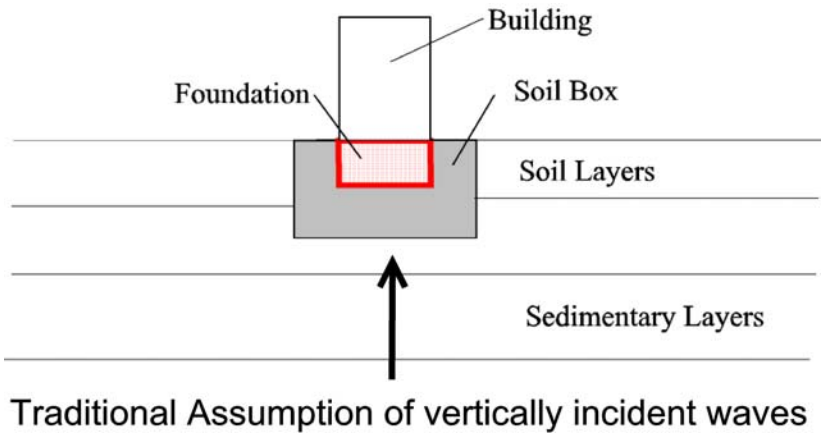

Figure 2. Model in Fig. 1 excited by vertically incident seismic waves

The geological structure near ground surface typically consists of "softer" deposits and therefore the seismic wave velocity decreases as the waves approach the surface. In such media, as a consequence of Snell's Law, the ray path of body waves becomes progressively steeper (progressively closer to the vertical) (see Fig. 3). This fact has been

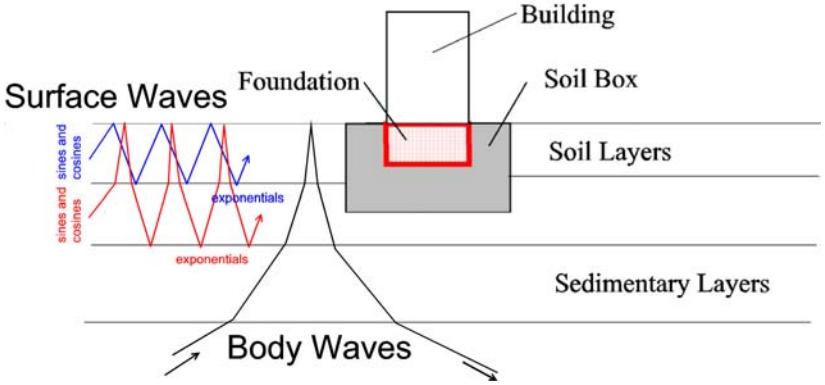

Figure 3. Incident body and surface waves into the parallel, horizontal layers representation of the NPP site.

used to justify the simplified representation of ground shaking at a site in terms of vertically incident waves, and the associated one-dimensional (1D) site representation (Fig. 2).

The wave front of a plane wave with incident angle γ, relative to vertical, will intersect the free surface at A and the vertical axis at B. and as it continues to propagate the points A and B will travel to right and up with phase velocities C_x and C_z (Fig. 4).

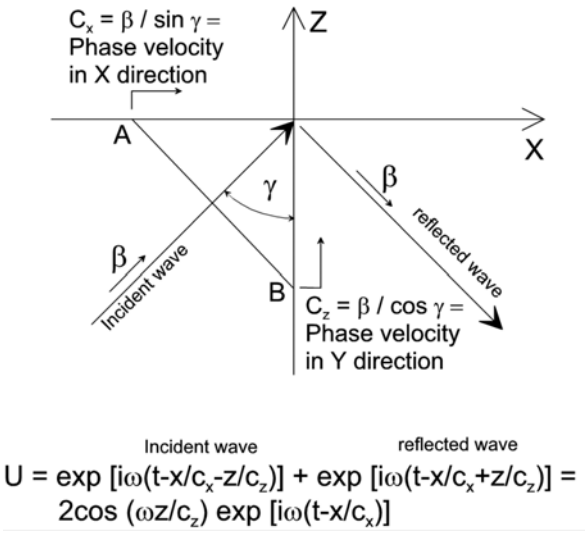

Figure 4. Incident plane wave, horizontal and vertical phase velocities, and particle motion U in the homogeneous half space.

It is seen from Fig. 4, that for γ = 0 the horizontal phase velocity C_x will become infinite (i.e. all points on ground surface will move synchronously) and the model will reduce to 1D representation shown Fig. 2. However, γ is never zero and so the incident plane wave will arrive at the site and excite the structure by propagating horizontally with velocity C_x and with depth dependence described by $\cos(\omega z / C_z)$, as shown in Fig. 4. Therefore, a body wave pulse will move the ground surface as a horizontally propagating wave, as

illustrated in Fig. 5. For nearly vertical wave arrival C_x will be large but the ground motion will still be a horizontally propagating wave.

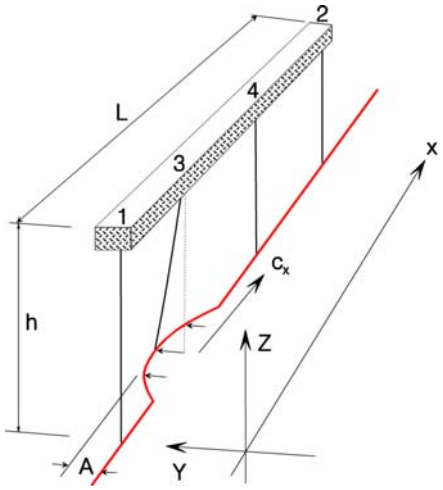

Figure 5. Structure excited by a strong motion pulse propagating with horizontal phase velocity C_x

Soon after the arrival of body waves, surface waves will begin to arrive propagating horizontally through the wave-guide represented by parallel layers (Fig. 6).

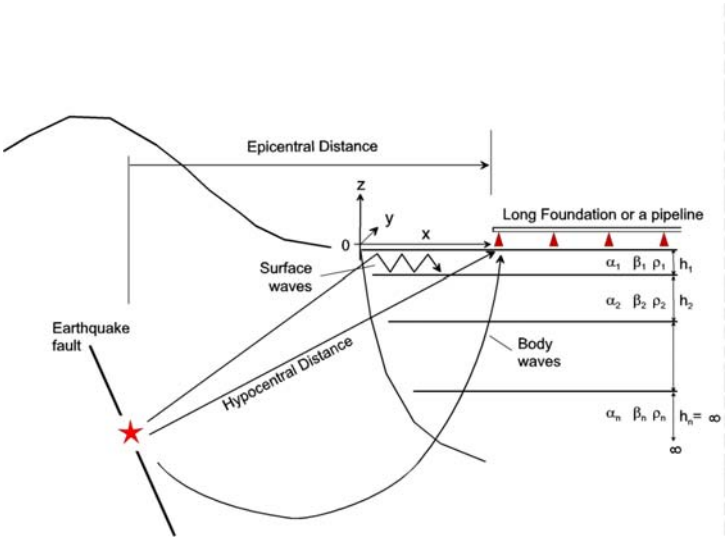

Figure 6. Body and surface waves arriving horizontally, through the layered half space.

Frequency components of surface waves will propagate with different phase velocities, which depend on the frequency of motion and the mode shape number. Those represent

respectively the characteristic values and characteristic functions of the boundary value problem of wave motion in the layered half space. The wave amplitudes (i.e. the wave energy) will propagate with the frequency dependent group velocity. Near ground surface, where C_x is larger than the corresponding material velocity the surface wave mode shapes will have periodic dependence versus depth (sines and cosines), but bellow the depth at which C_x becomes smaller than the material velocities the mode shape amplitudes will decay exponentially with depth (Fig. 3).

Horizontally propagating SH and Love waves will contribute torsional excitation of the foundation in addition to the out-of-plane translations. P, SV and Rayleigh waves, in addition to horizontal and vertical translations, will force the structure to rock in the (x,z) plane. This is illustrated in Fig. 7, which shows the structure excited by incident Rayleigh waves.

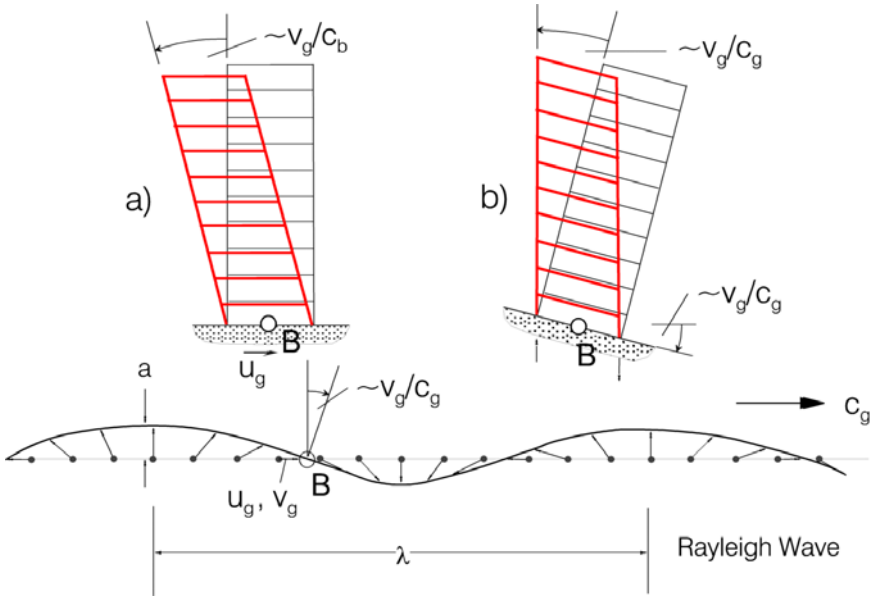

Figure 7. Horizontal, vertical and rocking excitations of a structure by passage of Rayleigh waves. Part (a) shows the drift associated with inertial forces caused by horizontal motion of the base at B. Part (b) illustrates additional drifts caused by rocking of the base.

Strains and curvatures of ground deformation are also necessary for complete description of motions driving the walls of the numerical box ABCD in Fig. 1. Examples of computed strains and curvatures will be shown in Chapter 2.

To accomplish the task of describing the ground motion which consists of body and surface waves, and which can be used to describe the motion at all points bounding the numerical box, it is necessary to formulate algorithms which describe (a) strong ground motion along a HORIZONTAL line extending (radialy) from the earthquake source towards the site of the structure (e.g. along BC in Fig.1), and (b) along a VERTICAL line (e.g. along AB or CD in Fig. 1) in the layered half space. Once these motions have been formulated, the complete motion can be specified at any desired number of points in the five surfaces of the box ABCD.

The algorithms for description of strong earthquake motion along any horizontal line (HL) are described in Chapter 1. The essential feature of the algorithms for describing the motions along HL is the consistent use of phase delays based on the site-specific dispersion of the wave motions through the soil layers described in terms of layered half space.

For description of consistent motions along any vertical line (VL), it is necessary to work with decomposition of wave motion in terms of the frequency dependent mode shapes of body waves and of surface waves, which correspond to the characteristic functions of wave motion in the wave-guide in the layered half space. The mathematical formulation for the algorithms we have developed for the formulation of motions along VL is described in Chapter 2. At the time of this writing this method has been tested, and fully verified in terms of the basic physics of surface wave-guides. However, because it is now available for the first time, it will be necessary to continue to further refine and generalize its output formats, so that it is easily and conveniently consistent with requirements of different numerical models, which will be specified by future users. We will continue to monitor how it is used, by those who work with finite element and with finite difference models, and will further refine its output formats as required.

All of the above has been formulated for the site geology represented by parallel and flat layers. However, in a realistic geological environment, these layers can be quite irregular. Chapter 3 describes the scattering and diffraction of Love surface waves and of body SH waves by layers, which have irregular surface and interfaces. The scattered and diffracted waves, which are caused by irregular layer geometry, will interfere with the input motions and may lead to amplification and deamplification of incident motions, and to concentration of stresses and strains on and below the ground surface.

Chapter 4 extends the results of Chapter 3 for excitation by Rayleigh surface waves and body P and SV waves. These in-plane motions require more complex analyses than what is described in Chapter 3, as there are mode conversions between longitudinal P- and shear SV- wave motions.

Chapter 5 presents a manual describing the computer program SYNAC, which is used to compute the time series representing all components of ground motion (translations, rotations, strains and curvatures) for excitation of the numerical box models for SSI calculations.

Tasks that were to be performed

- Fiscal year 2011/2012:

4.1 Develop software for computation of time series describing three translation components,
4.2 Carry out verification and validation process for 4.1.

- Fiscal year 2012/2013:

4.3 Develop software for computation of time series describing three rotational components of motion,
4.4 Develop software for computation of time series describing all corresponding strains, and
4.5 Develop software for computation of time series describing all components of curvature.
4.6 Carry out verification and validation process for 4.3 to 4.5

- Fiscal year 2013/2014:

4.7 Develop software for computation of time series as in the above 4.1, 4.3, 4.4 and 4.5 for the complete body and surface waves together for all 6 components of motion.
4.8 Carry out verification and validation process for 4.7.

- Fiscal year 2014/2015:

4.9 Develop software for computation of all time series at any point at depth, as in 4.1, 4.3, 4.4 and 4.5 above, but for non-parallel and irregular layers in the half space for all 6 components of motion.
4.10 Carry out verification and validation process for 4.9.

Tasks that have been performed

We completed the work on all of the above tasks in early May of 2014. However, as we started the work it became clear that a better and more efficient sequence of tasks would have been to break up the tasks 4.1 to 4.8 into two groups: (1) For formulation of all motions along an array of surface points, and (2) for the same, but for the array of points along a vertical line down into the layered half space. Consequently our Report I (in Appendix R1) describes the strong motion translations, rotations, strains and curvatures along an array of horizontal points, and Reports II and III (in Appendices R2 and R3) describe the same along an array on a vertical line. The work on Tasks 4.9 and 4.10 is described in Appendices R4-1 and R4-2. Appendix R5 contains a manual on how to use the software for calculation of artificial strong ground motion, including translations, rotations, strains and curvatures versus time.

Chapter 1 Synthetic Earthquake Ground Motions on an Array

I.1 INTRODUCTION

Extended structures are sensitive to differential motion of their supports and their seismic analysis and design require specification of time histories of ground motion at an array of closely spaced points. Because the phase in an accelerogram is not a stable quantity, time histories of ground motion are not predictable directly by empirical scaling models, but can be constructed indirectly, using empirically predicted amplitude spectrum, and some procedure for unfolding the spectrum in time. This chapter presents such a method, which generates synthetic time histories of motion at an array of points. The method is an extension of the SYNACC method, first proposed by Trifunac (1971) and demonstrated for a site in Imperial Valley in Southern California. The method evolved over the years, by inclusion of more current empirical scaling laws for Fourier amplitude spectra of acceleration and frequency dependent duration (Wong and Trifunac 1978, 1979), and extension to prediction of rotational motions (Lee and Trifunac 1985, 1987), strains (Lee 1990) and curvature (Trifunac 1990), all at a point in space (see also review in Lee 2002). This chapterr presents an extension of the SYNACC method to an array of points on the ground surface. It also presents new expressions for the point strains, rotations and curvatures, derived from the new formulation, which differ slightly from the previous expressions.

The method is based on representation of the ground motion by traveling wavelets of surface and body waves, which propagate in space with phase and group velocities that are those of a horizontally layered half-space approximating the soil and geology of the site. The amplitudes of the wavelets are such that the total motion in a narrow frequency band matches a target Fourier amplitude spectrum of acceleration. The methodology has been implemented in a computer program, which has built in a suite of empirical scaling models for prediction of site-specific Fourier amplitude spectra of acceleration, and computes the phase and group velocities specific for the site. A uniform hazard spectrum, or any user specified spectrum can also be used. While the Fourier spectrum determines the overall amplitudes of motion, the layered

structure determines the distribution of the energy in time at a given site, and also the causal relationship between the motions at neighboring points along the supports of the structure. This causal relationship is such that the motions further away from the source are delayed relative to the closer points differently in different frequency bands. Examples are shown of time histories for ground accelerations, velocities and displacements in the radial, transverse and vertical direction, and radial (normal) and transverse (shear) strains, at a point and at an array of points.

This empirical-physical model based method has clear advantages over both the engineering stochastic methods and the seismological physics based methods. The former methods (see recent comprehensive review in Zerva 2009) produce motions with stationary frequency content over the entire duration, in contrast to the nonstataionary nature reveled by the many observations. Further, motions at an array of points are generated using overly simplified coherency function, which is based on a single valued phase velocity, rather than the complete site-specific set for all body waves and surface wave modes. The latter methods involve numerical simulations based on a physical model of the earthquake source and of the wave propagation from the source to the site. They produce motions with correct physical nature, but involve many assumptions and need to be validated with data. Also, due to the lack of detail in the available information about the earthquake source and the wave path, they have difficulties to model high-frequency content of the synthetic motions. The SYNACC method, which is neither stochastic nor purely physics based, does not suffer from these shortcomings. It produces motions with amplitudes that are automatically consistent with observations over a broad frequency range, and does not need calibration. Also, the motions are nonstationary in a physically meaningful sense and consistent with the site soil and geology. In the following we illustrate this method only for translational components of motion. Examples describing strains, rotations and curvatures can be found in Appendix R1

I.2 METHODOLOGY

The geology between the earthquake source and the site can vary considerably, especially for large distances, and different types of waves will arrive at the site via different wave paths, as illustrated in Fig. I.1, showing the earthquake fault, and a segment of a long structure located on sediments. The surface waves (Love and Rayleigh) arrive horizontally through the low velocity layers, with velocities that are frequency dependent, defined by the dispersion in the layers of site soil and geology, while the body waves arrive from depth at an angle, which is close to vertical for soft geology near the surface. Further, the amplitude attenuation is different for body and surface waves, due to different geometric spreading, and for both waves, the attenuation is frequency dependent. The *total* effect can be predicted reliably, in statistical sense, using empirical scaling laws for Fourier amplitude spectra of acceleration. Considering the nature of these processes, in the SYNACC methodology, over the frequency band of interest, 0 to 25 Hz, the empirically predicted Fourier amplitude spectrum is partitioned in N narrow non-overlapping sub-bands, and the energy in each sub-band is partitioned among surface and body waves (Trifunac 1971; Wong and Trifunac 1978, 1979).

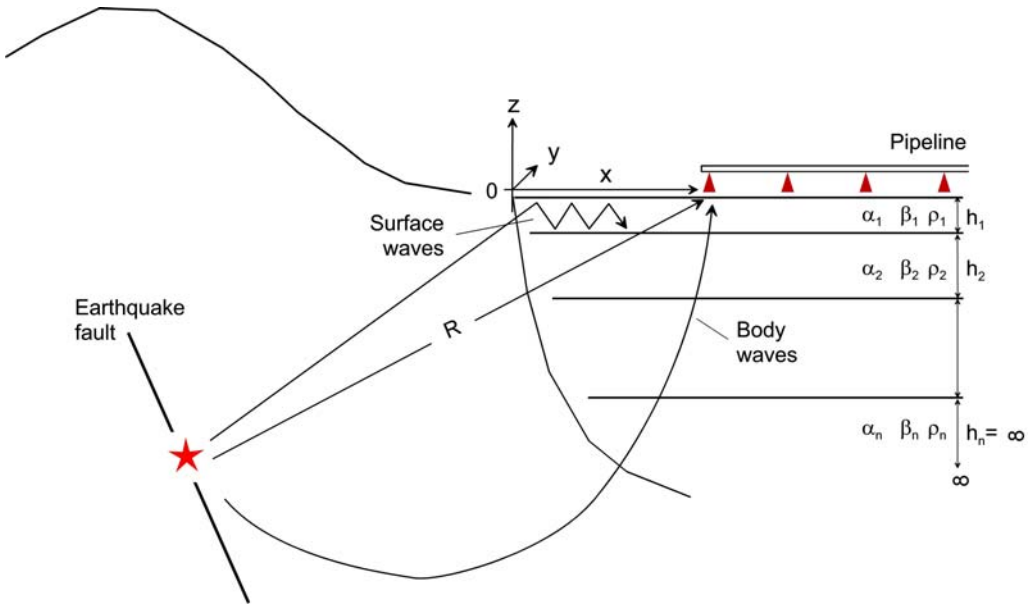

Figure I.1 The Model

Waves in a narrow frequency band propagate as groups, forming wavelet packets, the amplitudes of which are localized in time, and which propagate with their group velocity. The total motion, therefore, can be represented as a superposition of such wavelet packets. In the following, the representation of the surface and body waves that enables generation of related motions at an array of points is presented, highlighting the changes relative to the previous versions for generating motions at a single point.

I.2.1 Representation of Surface Wave Motion at a Site

To expand the surface waves, the soil and geology at the site is locally approximated by a horizontally layered half-space, as shown in Fig. I.2. Let h_i, ρ_i, α_i and β_i be the thickness, mass density and P- and S-wave velocities in the i-th layer, with $i = 1, \ldots, L$, and let the x-axis point in the direction of wave propagation. The layer boundaries define a boundary value problem for the displacement, which has a solution that is a surface wave only for a discrete set of frequency dependent phase velocities $c_m(\omega)$, obtained from the roots of the characteristic equation for the particular problem (Thompson 1950; Haskell 1953) The displacement for an eigenvalue constitutes an eigenfunction (or a mode), and any surface wave motion then can be represented as a linear combination of these eigenfunctions.

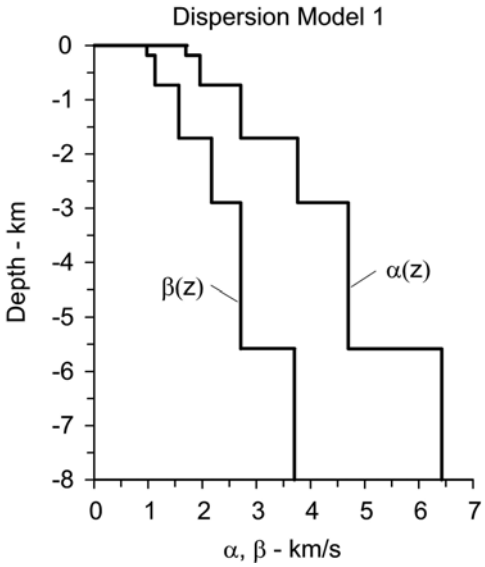

Fig. I.2 Velocity profile for Dispersion Model 1.

Fig. I.2 shows an example of a velocity profile for a site in El Centro in Imperial Valley, California (Trifunac 1971), and Tables I-1a,b,c (in the Appendix A) show the properties of the layers for three variants of this profile, which differ only in the top 180 m. Fig. I.3 shows the phase and group velocities, $c_m(\omega)$ and $U_m(\omega)$ $m = 1,\ldots,5$, for the first five modes of Rayleigh and Love waves, referred to as dispersion curves, for the three variants. The Rayleigh waves are surface waves with in-plane particle motion along an ellipse, which is usually retrograde at the surface, and with vertical to horizontal aspect ratio > 1. The Love waves are surface waves with out of plane particle motion. The group velocity $U_m(\omega) = d\omega / dk_m$, where $k_m(\omega) = \omega / c_m(\omega)$ is the horizontal wave number, is the velocity with which the amplitude envelope of the wavelet packet propagates, and with which the energy is transported. The number of modes is finite for a given frequency, and increases with frequency. The first mode exists at all frequencies, while the higher modes exist only for high enough frequencies. Because the wave velocities in the earth crust are smaller at progressively smaller depths, and because the penetration depth of a mode decreases with frequency, $c_m(\omega)$ decreases with frequency, approaching asymptotically the shear wave velocity of the top layer.

The synthesis is based on dividing the frequency band of interest, 0 to 25 Hz, in N non-overlapping sub-bands, assuming uniform Fourier amplitude within the sub-band, and in each band, representing the surface wave motion as a superposition of the eigenfunctions, evaluated at the central frequency of the sub-band. Let ω_n and $\Delta\omega_n$ be the central frequency and half-bandwidth of the n-the sub-band, $U_{nm} = U_m(\omega_n)$ and $c_{nm} = c_m(\omega_n)$ be the group and phase velocities of the m-th mode in that sub-band, and let $w_{nm}(x;t)$ be the eigenfunction of the m-th mode in the n-th sub-band, at point x on the free surface ($z = 0$), and at time t. Then

$$w_{nm}(x;t) = \mathrm{sinc}\left[\Delta\omega_n\left(t - \frac{x}{U_{nm}}\right)\right]\exp\left[i\left(\omega_n t - k_{nm}x\right)\right] \qquad (1)$$

where

$$k_{nm} = \frac{\omega_n}{c_{nm}}\left(1 - i\frac{1}{2Q}\right) \qquad (2)$$

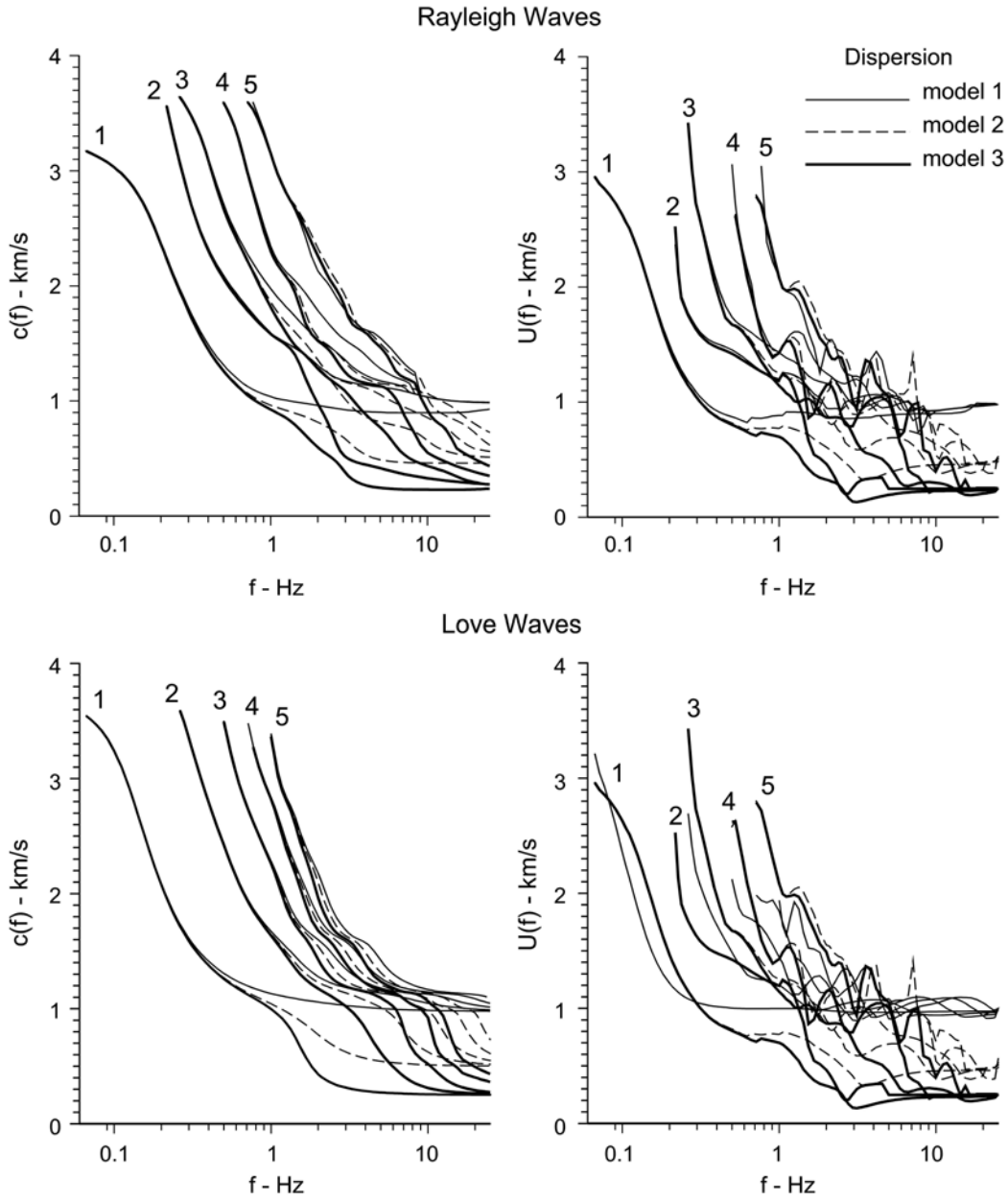

Fig I.3 Phase and Group velocities, for the first five modes of Rayleigh and Love waves.

is the complex horizontal wave number, and Q is the quality factor, assumed to be constant (Trifunac 1994). If no material attenuation is assumed, $1/(2Q) = 0$ and k_{nm} is real. Function $w_{nm}(x;t)$ represents a traveling wavelet, which is a complex exponential of frequency ω_n, amplitude modulated by a sinc function. The amplitude modulation

$$\mathrm{sinc}\left(\Delta\omega_n t\right) = \frac{\sin(\Delta\omega_n t)}{\Delta\omega_n t} \tag{3}$$

is a window in time with half-width $\Delta t_n = \pi / \Delta\omega_n$, which propagates with velocity U_{nm}, while the phase propagates with velocity c_{nm}. Consequently, at a point x, the phase has time lag x / c_{nm}, and the center of the amplitude envelope has time lag x / U_{nm} relative to the reference point, $x = 0$.

Representation (1) is consistent with the following convention of Fourier transform for the pair $f(t)$ and $\hat{f}(\omega)$

$$\begin{aligned} & f(t) \leftrightarrow \hat{f}(\omega) \\ & \hat{f}(\omega) = \int_{-\infty}^{\infty} f(t) e^{-i\omega t} dt \\ & f(t) = \frac{1}{2\pi} \int_{-\infty}^{\infty} \hat{f}(\omega) e^{i\omega t} d\omega \end{aligned} \tag{4}$$

Then, the Fourier transform of the wavelet $w_{nm}(x;t)$ is

$$\hat{w}_{nm}(x;\omega) = \frac{\pi}{\Delta\omega_n} \exp\left[-i\left(\frac{\omega - \omega_n}{U_{nm}} + k_{nm} \right) x \right] p_{\Delta\omega_n}\left(\omega - \omega_n\right) \tag{5}$$

where

$$p_{\Delta\omega_n}\left(\omega - \omega_n\right) = \begin{Bmatrix} 1, & \omega - \Delta\omega_n \le \omega \le \omega_n + \Delta\omega_n \\ 0, & \text{otherwise} \end{Bmatrix} \tag{6}$$

represents a box function with half width $\Delta\omega_n$, centered at frequency ω_n, with amplitude scaled to $\pi / \Delta\omega_n$ and phase shifted by $k_{nm} x$.

According to Eqns. (1) and (5), the energy of the wavelet $w_{nm}(x)$ is localized, in time - around $t = x / U_{nm}$ with spread $\pm\Delta t_n = \pm\pi / \Delta\omega_n$, and, in frequency, around $\omega = \omega_n$ with spread $\pm\Delta\omega_n$, i.e. within a rectangle of constant area $\left(2\Delta t_n\right)\left(2\Delta\omega_n\right) = 2\pi$ in the phase plane. Consequently, finer division of the frequency range (smaller $\Delta\omega_n$) will lead to wider in time

wavelets $w_{nm}(x;t)$, which is a manifestation of the Heisenberg-Gabor uncertainty principle for signals (Gabor 1946, 1953).

Let $u(x,t)$ be the associated analytic signal of a generic component of motion (the specific expansions will be presented in one of the following sections. Because scaling laws for Fourier spectra of acceleration are available, we start with the representation of acceleration in a series of wavelets

$$\ddot{u}(x,t) = \sum_{n=1}^{N} \sum_{m=1}^{M_n} A_{nm}^{*} w_{nm}(x;t) \tag{7}$$

where M_n is the number of modes that exist in the n-th sub-band.

I.2.2 Representation of Velocity, Displacement and Spatial Derivatives

It is convenient to do the synthesis in the frequency domain and then invert to the time domain, because the representations of velocities, displacements, strains, rotations, and curvatures are easily obtainable in the frequency domain by analytical integration and differentiation of the wavelets. The Fourier transforms of acceleration, velocity and displacements are

$$\hat{\ddot{u}}(x,t) = \sum_{n=1}^{N} \sum_{m=1}^{M_n} A_{nm}^{*} \hat{w}_{nm}(x;\omega) \tag{8}$$

$$\hat{\dot{u}}(x;\omega) = \sum_{n=1}^{N} \sum_{m=1}^{M_n} \frac{1}{i\omega_n} A_{nm}^{*} \hat{w}_{nm}(x;\omega) \tag{9}$$

and

$$\hat{u}(x;\omega) = \sum_{n=1}^{N} \sum_{m=1}^{M_n} \frac{-1}{\omega_n^2} A_{nm}^{*} \hat{w}_{nm}(x;\omega) \tag{10}$$

I.2.3 Mode Participation Factors

The coefficients of the expansion A_{nm}^{*} are complex valued and depend on the amplitude of the target spectrum, but, for a given site geology, they are related, as shown in Trifunac (1971)

for a site in Imperial Valley, and their relative amplitude depends on the frequency and mode number (Appendix A). We represent them as

$$A_{nm}^{*} = \alpha_n A_1(m) A_2(\omega_n) \exp\left(i\phi_{nm}^{ran}\right) \tag{11}$$

where ϕ_{nm}^{ran} is a random phase between $-\pi$ and π, describing the randomness in the radiation of energy from the earthquake source and other randomness along the wave path until the arrival to the region near the site, represented by the medium with parallel layers (Fig. I.1). Functions $A_1(m)$ and $A_2(\omega_n)$ are site specific, as in Trifunac (1971), and their product $A_1(m)A_2(\omega_n)$ can be thought of as a site dependent mode participation factor. The coefficients $\alpha_n = \alpha(\omega_n, \Delta\omega_n)$, for given division in sub-bands, depends only on the target spectrum that is to be matched by the synthetics.

The representation (7) differs from that in Trifunac (1971) and Wong and Trifunac (1978, 1979) as follows. In the latter, the phase delay at point x is $\left(\omega_n / U_{mn}\right)t + \phi_{nm}^{ran}$, i.e. the lag of the amplitude modulation plus some random phase shift, while in this chapter, the phase lag is $\left(\omega_n / c_{mn}\right)t$.

In this work, we consider also material attenuation due to Q, which affects the difference between the motions at different points of the array. Minor differences, chosen for convenience in this presentation, are that the random phase is part of the coefficients of expansion, and that the associated analytic signal is expanded.

Another significant difference is in the definition of the reference point $x = 0$. In the latter, $x = 0$ is the epicenter of the earthquake, while, in this work, it is a point between the epicenter and the site, from where the parallel layers geology can be adopted to be representative of the wave path. This point can be referred to as the "the edge of the valley", and $x =$ representative distance from the edge of the valley. Therefore, in this work, x is just the distance over which dispersive wave propagation occurs consistent with the given parallel layers of soil and geology, while the target spectrum to be matched depends on the hypocentral distance R of the site from

the source (Fig. I.1). Such definition of the reference $x = 0$ is more useful for modeling, as the geology can vary considerably between the source and the site. It also helps control the duration of the synthetic motion, and avoid the artifact of unrealistically long duration of the synthetic motion for large source to site distances and softer near surface soil layers. Because the parallel layers structure is an idealization, the "distance from the edge of the valley" is not exact but an abstraction, and can be chosen by trial and error or by iteration, until the duration of the synthetic motion is satisfactory, based on some subjective or objective standard, such as empirical scaling laws.

I.2.4 Expansion of Body Waves

The propagation of body waves is essentially nondispersive, and $c(\omega_n) = U(\omega_n)$. They arrive at the site from depth, often close to vertical due to progressive bending of the rays towards the surface (Fig. I.1), and consequently propagate horizontally with larger phase velocities $c(\omega_n)$ than the surface waves. Further, their amplitude at a given frequency reflects the interference characteristics of the layers, which depends on incident angle. In the SYNACC synthesis, the body waves are treated as two additional "surface wave modes", one for P- and the other one for S-waves, with large phase and group velocities, and contributing respectively to the in-plane and out of plane motions, and with mode participation factor same as those for the Love modes, i.e. not reflecting the site interference characteristics, but with the flexibility to increase or decrease their participation, relative to that of the surface waves. Site-specific interference features could be included by appropriate frequency dependent mode participation factors, derived e.g. using the propagator matrix of the medium (Trampert et al.1993; Mehta et al. 2007).

I.*2.5 Determination of the Expansion Coefficients for a Site*

The site-specific mode participation factors, $A_1(m)A_2(\omega_n)$, can be determined by analysis of recorded motion in the region, as in Trifunac (1971), for example. In this chapter, for illustration purposes, the same functions as in Trifunac (1971) are used, included in Appendix A (of Appendix R1) for completeness of this presentation. The coefficients α_n are determined from the requirement that some representative value of $\left|\hat{\ddot{u}}(x;\omega)\right|$ over the n-th sub-band matches a

target value. For example, such representative value can be obtained by averaging $\log_{10}\left|\hat{\ddot{u}}(x;\omega)\right|$ and converting back to linear scale. Let $FS^{tar}(\omega_n)$ be the amplitude spectrum to be matched by the (real valued) synthetic acceleration. Then

$$\alpha_n = \frac{2FS^{tar}(\omega_n)}{10^{\frac{1}{2\Delta\omega_n}\int_{\omega_n-\Delta\omega_n}^{\omega_n+\Delta\omega_n}\log_{10}\left|\sum_{m=1}^{M_n+2}A_1(m)A_2(\omega_n)\exp\left(i\phi_{nm}^{ran}\right)\hat{w}_{nm}(x;\omega)\right|d\omega}} \tag{12}$$

where M_n+2 is the total number of surface and body waves contributing to the particular component of motion. The factor of 2 multiplying $FS^{tar}(\omega_n)$ is because $\hat{\ddot{u}}(x;\omega)$ is the Fourier transform of the associated analytic signal, which, for $\omega>0$, has amplitudes twice of those of its real part. The expression for the α_n in Eqn. (12) differs from Trifunac (1971) and Wong and Trifunac (1978, 1979) in the averaging.

I.2.6 Motion at an Array of Sites

The sites where related motions are needed for analysis of extended structures are typically at distances greater than few tens of meters. For such distances, it is assumed that the motion differs only because of deterministic propagation and attenuation due to Q, while the randomness in phase and mode participation factors, included in coefficients A_{nm}^{*}, is the same. For such an array of sites, the motion at one representative site, at $x=x_0$, is first synthesized by matching the target spectrum, which gives the coefficients $A_{nm}^{*}(x_0)$, and the motion at another sites, at $x=x_0+\Delta x$, is then computed as

$$\hat{\ddot{u}}(x_0+\Delta x,\omega)=\sum_{n=1}^{N}\sum_{m=1}^{M_n}A_{nm}^{*}(x_0)\hat{w}_{nm}(x_0+\Delta x;\omega) \tag{13}$$

I.2.7 Trigger Time Adjustment

The above equations correspond to reference time, which is such that, at $x = 0$, the amplitude envelopes of all the wavelets are centered at $t = 0$. The wavelets, however, have energy also for time $t < 0$, as the main lobes of the sinc functions extend over the interval $[-\Delta t_n, +\Delta t_n]$, where $\Delta t_n = \pi / \Delta\omega_n$. For small x, x / U_{nm} may be considerably smaller than Δt_n, in which case the entire pulse does not contribute to the synthetic accelerogram, if its starting time (which would be the trigger time of an imaginary instrument that has recorded the motion) is set even to $t = 0$. This can be avoided by time shifting the synthetic time history, which is conveniently done in the frequency domain. For example, for time shift t_0, $\hat{w}_{nm}(x;\omega)$ needs to be multiplied by $\exp(-i\omega t_0)$.

I.2.8 Cartesian Components of Linear Motions

Having presented the analytical developments for a generic component of motion, we now proceed with the specific expansions for the Cartesian $x - y - z$ coordinate system shown in Fig. I.1. Let $u_x(x;t)$, $u_y(x;t)$ and $u_z(x;t)$ be the displacement components along the three coordinate axes, which have specific expansions

$$\hat{\ddot{u}}_x(x,t) = \sum_{n=1}^{N} \sum_{m=1}^{M_n} A_{nm}^{*x} \hat{w}_{nm}^{x}(x;\omega) \tag{14}$$

$$\hat{\ddot{u}}_y(x,t) = \sum_{n=1}^{N} \sum_{m=1}^{M_n} A_{nm}^{*y} \hat{w}_{nm}^{y}(x;\omega) \tag{15}$$

and

$$\hat{\ddot{u}}_z(x,t) = \sum_{n=1}^{N} \sum_{m=1}^{M_n} A_{nm}^{*z} \hat{w}_{nm}^{z}(x;\omega) \tag{16}$$

Because $u_x(x;t)$ and $u_z(x;t)$ are expanded in Rayleigh modes, the expansion wavelets $\hat{w}_{nm}^{x}(x;\omega)$ are as in Eqn. (5) with group and phase velocities U_{nm}^{R} and c_{nm}^{R} specific for the

corresponding Rayleigh mode, and $\hat{w}^z_{nm}(x;\omega) = V_{nm}\hat{w}^x_{nm}(x;\omega)$ where $V_{nm} = V_m(\omega_n)$ is the complex ratio of vertical to horizontal amplitude of the elliptic particle motion at the surface for the mode. Similarly, $u_y(x;t)$ is expanded in Love modes, and $\hat{w}^y_{nm}(x;\omega)$ are as in Eqn. (5) with group and phase velocities U^L_{nm} and c^L_{nm} specific for the corresponding Love mode.

I.2.9 Generation of Target Spectrum

Site specific target Fourier amplitude spectra for a *scenario* earthquake can be generated using an empirical scaling model, for given earthquake magnitude, hypocentral distance, site conditions, and probability of being exceeded, which reflects the uncertainty in the scaling law. The uncertainty in the earthquake size, location and occurrence rate can also be included by specifying as a target spectrum a uniform hazard Fourier spectrum, which has amplitudes with equal probability of being exceeded from any earthquake considered.

SYNACC has built in the Fourier amplitude scaling models developed by Trifunac and Lee (1985, 1989a), in addition to the earlier models (Trifunac 1976, 1979.1989b), and can also use uniform hazard spectrum generated by the program NEQRISK (Lee and Trifunac 1985), which has built in the same suite of scaling models as those built in SYNACC for a scenario earthquake, or any user provided Fourier amplitude spectrum. The built in scaling models differ in the input parameters, and a particular model can be chosen depending on the details of the information available about the site. For example, the earthquake magnitude and hypocentral distance can be provided or, alternatively, the Modified Mercalli site intensity. The local site conditions are described in terms of two scales – geologic one, which samples the geology up to the depths of the order of kilometers, and local soil one, which samples soil properties near the surface up to depths of two hundred meters. The classification based on geology can be described in two ways, by a categorical variable, such as the *geologic site condition* parameter s, which can take values 0 (sediments), 2 (rock), and 1 (intermediate site conditions), or by a numeric variable, such as the depth of sediments h. The local soil classification is described by the categorical variable - local soil condition parameter s_L, which can take on the values 0 (“rock” soil), 1 (stiff soil) and 2 (deep soil).

I.3 RESULTS

The methodology is illustrated for a scenario earthquake. A suite of synthetic motions and strains are presented for different earthquake sizes, hypocentral distances, and dispersion models, at a site and an array of sites. The target Fourier spectra were computed using the MMI-SITE-SOIL model (Trifunac and Lee 1985), with $s = 0$ (sediments) and $s_L = 2$ (deep soil). Synthetic motions were computed at 4096 points in time with time step 0.02 s, i.e. with total length of about 82 s. Unless mentioned otherwise, the trigger time was adjusted by adding a 5 s shift. The number of sub-bands is 73.

I.3.1 Synthetic Motions at a Point

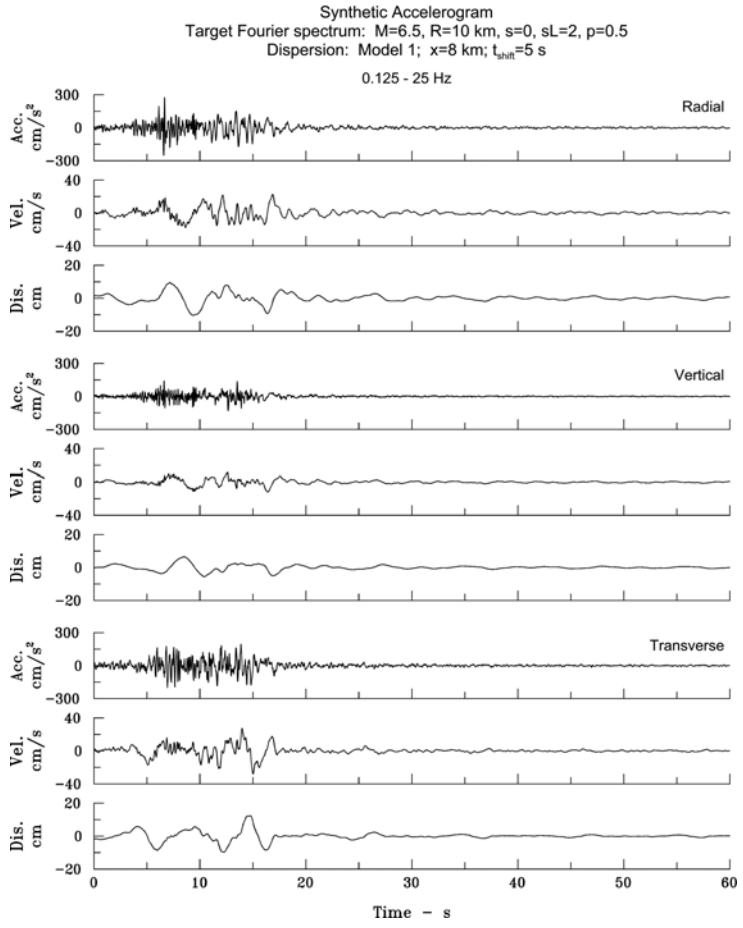

Fig. I.4 Artificial acceleration, velocity and displacement that match the target Fourier spectrum of acceleration of M6.5 earthquake, at hypocentral distance $R = 10$ km, and for a site on sediments ($s = 2$) and deep soil ($s_L = 2$), unfolded with dispersion model 1.

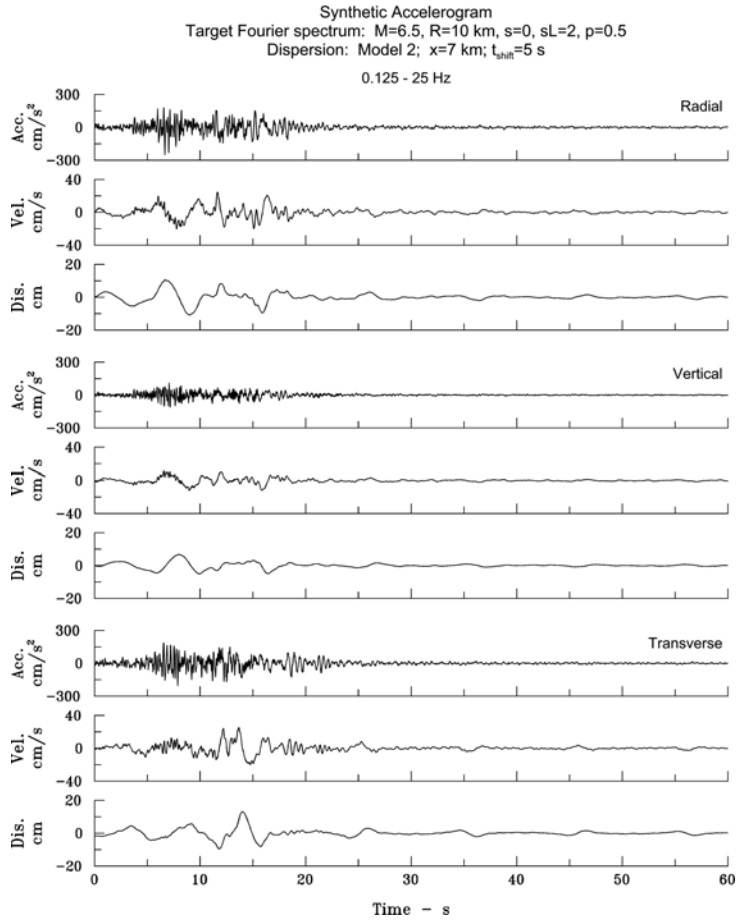

Fig. I.5 Artificial acceleration, velocity and displacement that match the target Fourier spectrum of acceleration of M6.5 earthquake, at hypocentral distance $R = 10$ km, and for a site on sediments ($s = 2$) and deep soil ($s_L = 2$), unfolded with dispersion model 2.

Figs. I.4, I.5 and I.6 show the three component synthetic motions (accelerations, velocities and displacements) from a moderate and near earthquake ($M = 6.5$ and $R = 10$ km), respectively for dispersion models 1, 2 and 3, discussed in the Model section of this chapter (Fig. I.2 and I.3).

Model 1 is the same as the benchmark model in Trifunac (1971) and in Wong and Trifunac (1978, 1979), which corresponds to a site in El Centro in Imperial Valley, southern California, and the other two models are its variants that are "softer" in the top 180 m. The "distance from the edge of the valley" was chosen to be $x = 8$ km, 7 km and 6 km for the three models. It can be

seen that the amplitudes of motion are similar for the three dispersion models, as they have been generated for the same target spectrum. The time histories, however, differ in that late arrivals of high frequency waves are seen in the records for dispersion model 3, which has the softest top layer.

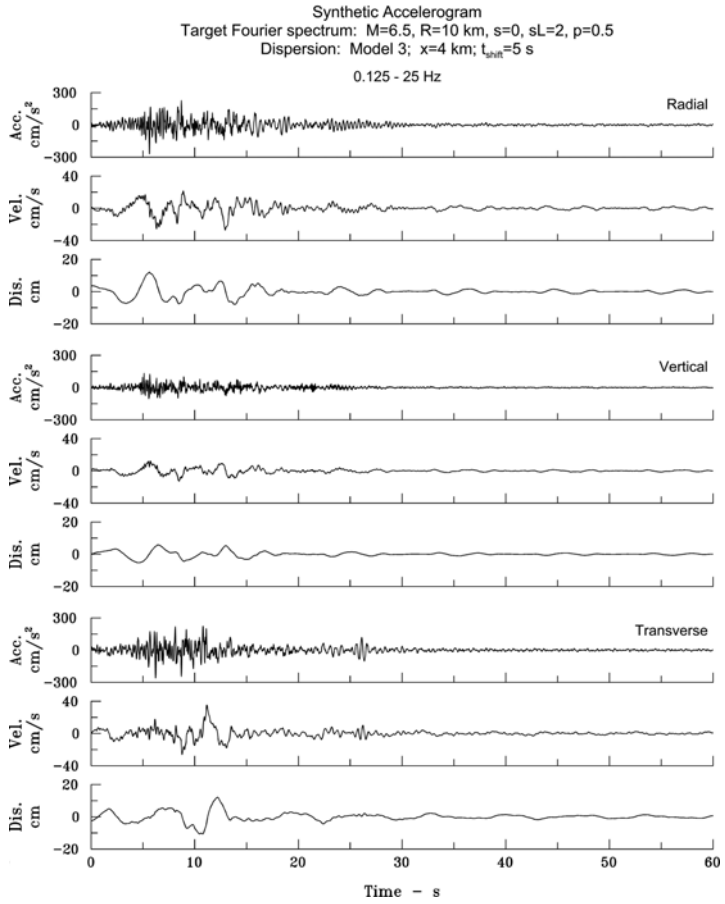

Fig. I.6 Artificial acceleration, velocity and displacement that match the target Fourier spectrum of acceleration of M6.5 earthquake, at hypocentral distance $R = 10$ km, and for a site on sediments ($s = 2$) and deep soil ($s_L = 2$), unfolded with dispersion model 3.

Finally, Fig. I.7 shows the agreement between the Fourier amplitude spectra of the synthetic motions and the target spectra, for all the cases for the $M = 6.5$ earthquake.

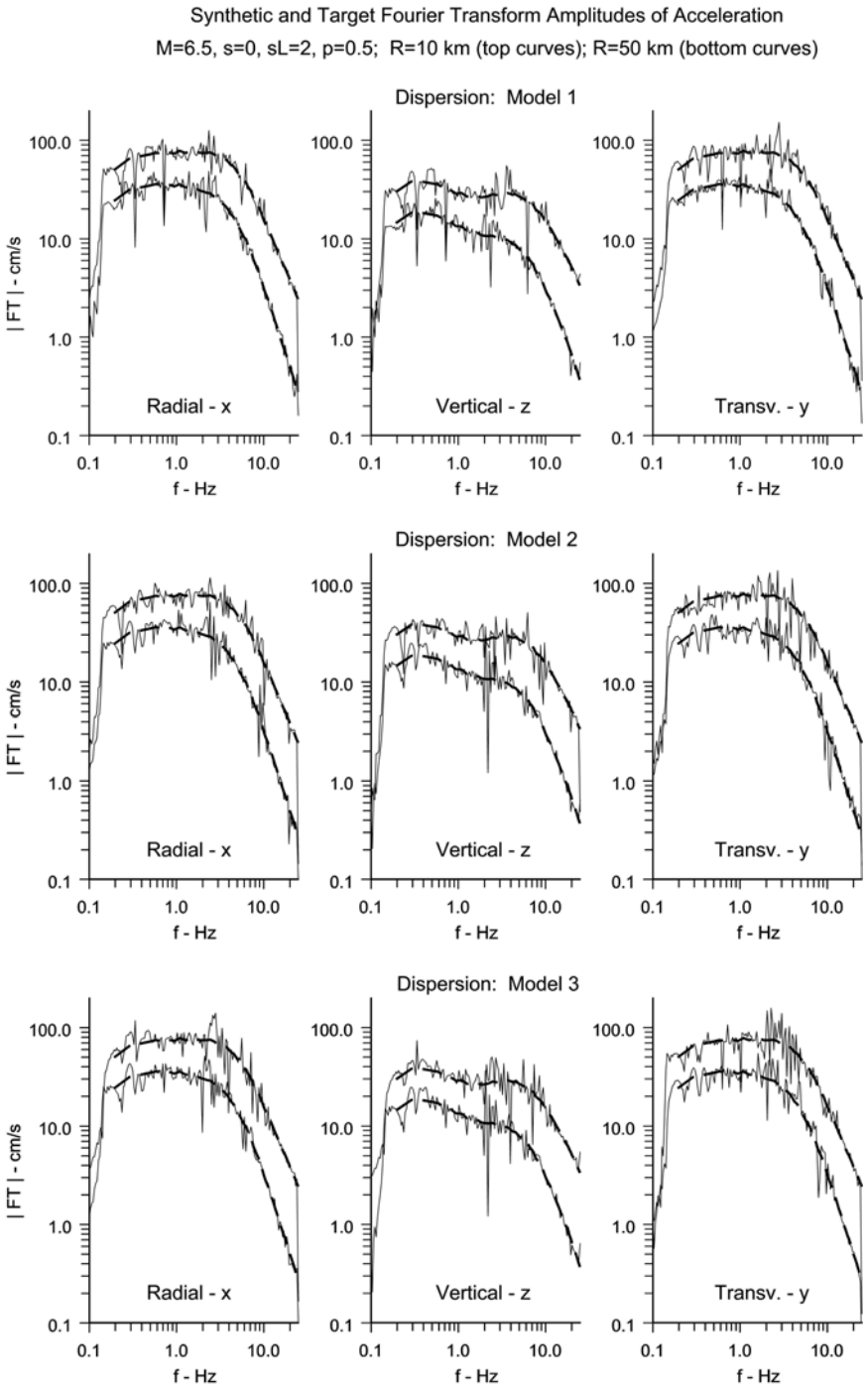

Fig. I.7 Fourier Transform amplitudes of synthetic accelerations for M6.5 earthquake, unfolded by dispersion models 1 (top), 2 (middle) and 3 (bottom), for radial (left), vertical (center) and transverse (right) motions.

I.3.2 Motions at an Array of Points

Figs I.8, I.9 and I.10 show snapshots of synthetic accelerations at six sites, 100 m apart in the radial direction, with the closest site being at $R = 10$ km distance from a M6.5 earthquake. The figures show respectively the radial, vertical and transverse components, all unfolded in time with dispersion model 3, and with $x = 4$ km. These figures show noticeable differences in the acceleration time histories even though the sites are very close to each other. The differences, created by a purely deterministic physical model of wave propagation, are more complex than single phase shift and some small amplitude decay.

The displacements, having more energy in the lower frequency part of the spectrum, differ much less at such small distances, because the lower frequency energy propagates with much longer wavelengths.

They exhibit a high degree of similarity of the waveforms even at distances several kilometers away, as it can be seen in Figs. I.11, I.12 and I.13, which illustrate radial, vertical and transverse synthetic displacements at sites 1 km apart in the radial direction.

I.4 DISCUSSION AND CONCLUSIONS

A method for generating synthetic time histories of earthquake ground motion at an array of points along the ground surface was presented, which is an extension of the SYNACC methodology, originally developed for a single site. Such motions are needed for design of long structures, pipelines and bridges (Kojić and Trifunac 1988; Todorovska and Trifunac 1990a,b; Jalali and Trifunac 2007, 2009, 2011; Kashefi and Trifunac 1986), and in particular for nonlinear analyses, which need to be performed in the time domain. The methodology combines empirical scaling laws for Fourier amplitude spectra of acceleration with a physical model of wave propagation in a horizontally layered half-space. Consequently, the amplitudes of the synthetic motions are consistent in statistical sense with observations, while the phase and local differences between points of the array are consistent with local characteristics of wave propagation. The presented examples for ground accelerations, velocities and displacements

(and for strains, rotations and curvatures in Appendix R1) generated by the method showed that the method produces realistic and physically meaningful time histories.

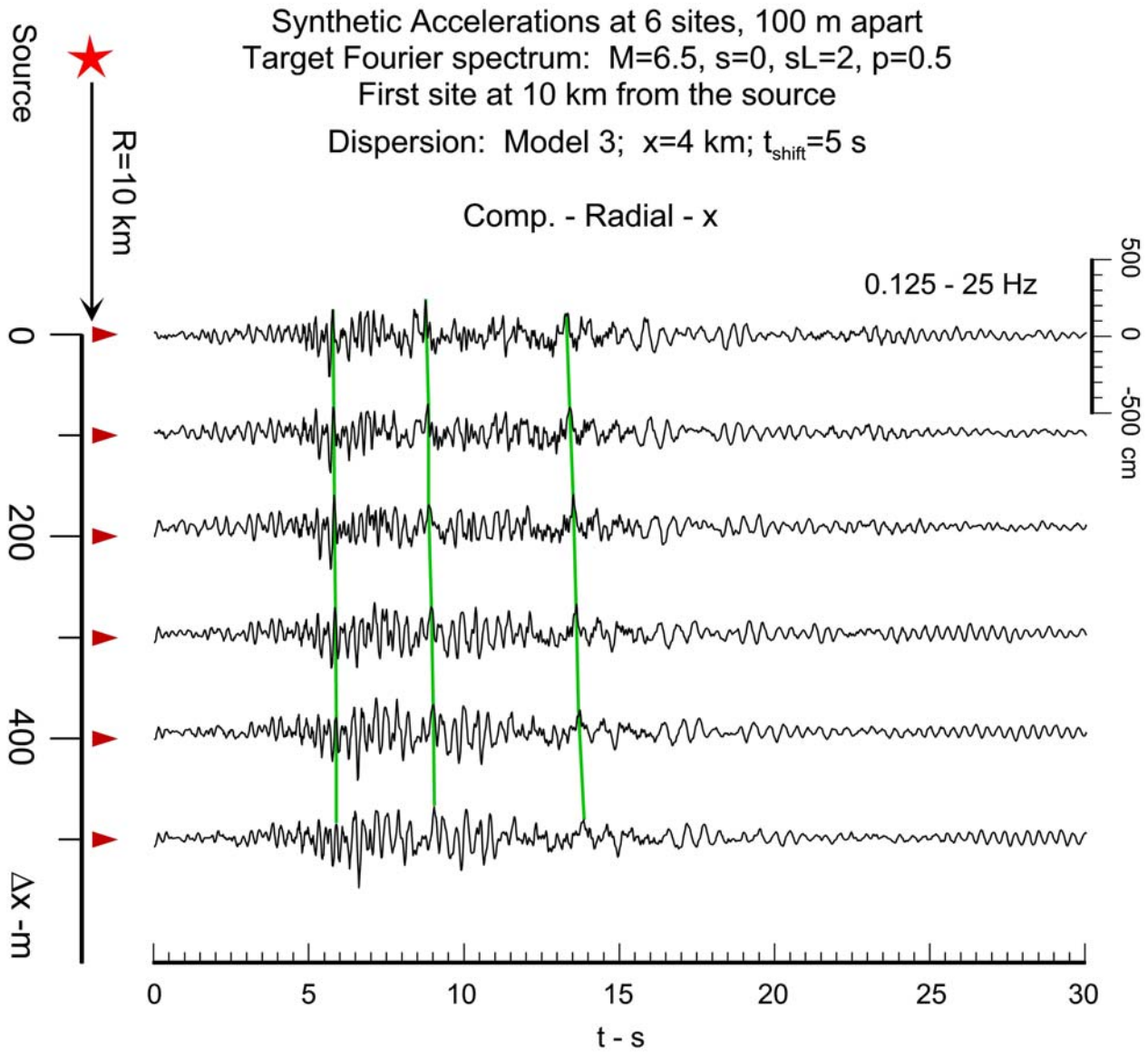

Fig. I.8 Snapshots of synthetic acceleration - radial component - at six sites, 100 m apart in the radial direction. The target spectrum is that of M6.5 earthquake, at hypocentral distance $R = 10$ km (the closest site), for site condition - sediments ($s = 2$) and deep soil ($s_L = 2$), unfolded with dispersion model 3.

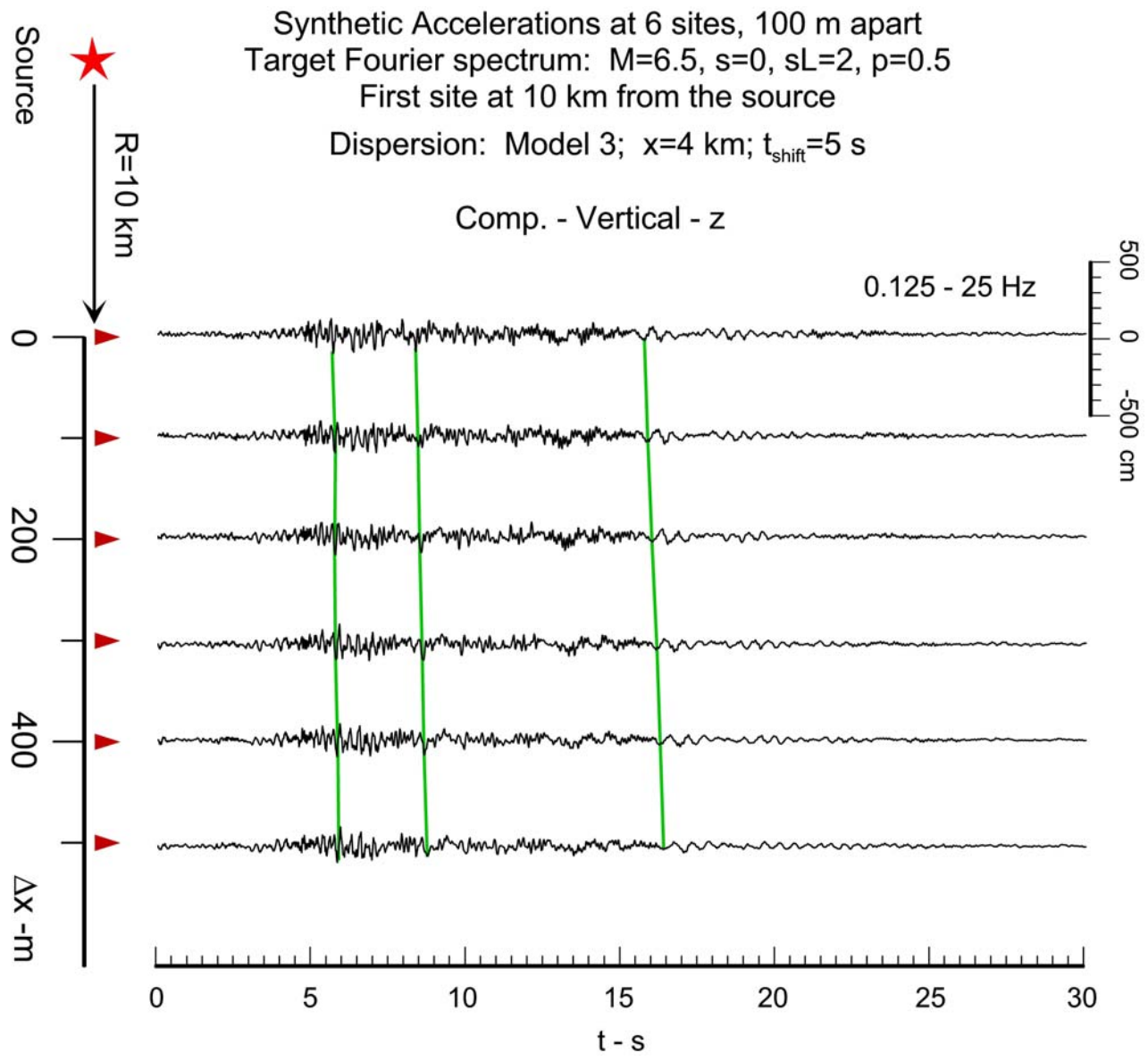

Fig. I.9 Snapshots of synthetic acceleration - vertical component - at six sites, 100 m apart in the radial direction. The target spectrum is that of M6.5 earthquake, at hypocentral distance $R = 10$ km (the closest site), for site condition - sediments ($s = 2$) and deep soil ($s_L = 2$), unfolded with dispersion model 3.

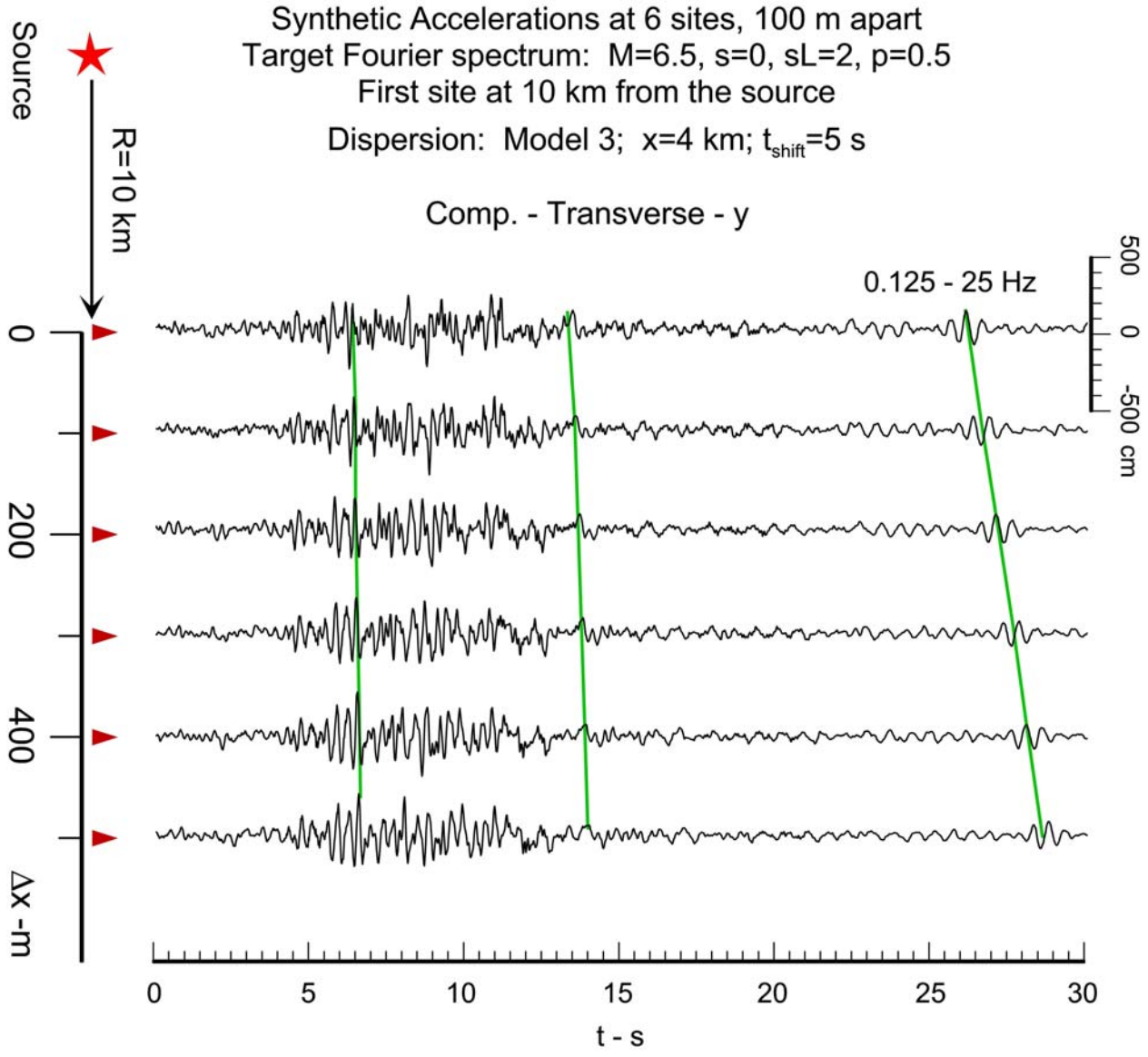

Fig. I.10 Snapshots of synthetic acceleration - transverse component - at six sites, 100 m apart in the radial direction. The target spectrum is that of M6.5 earthquake, at hypocentral distance $R = 10$ km (the closest site), for site condition - sediments ($s = 2$) and deep soil ($s_L = 2$), unfolded with dispersion model 3.

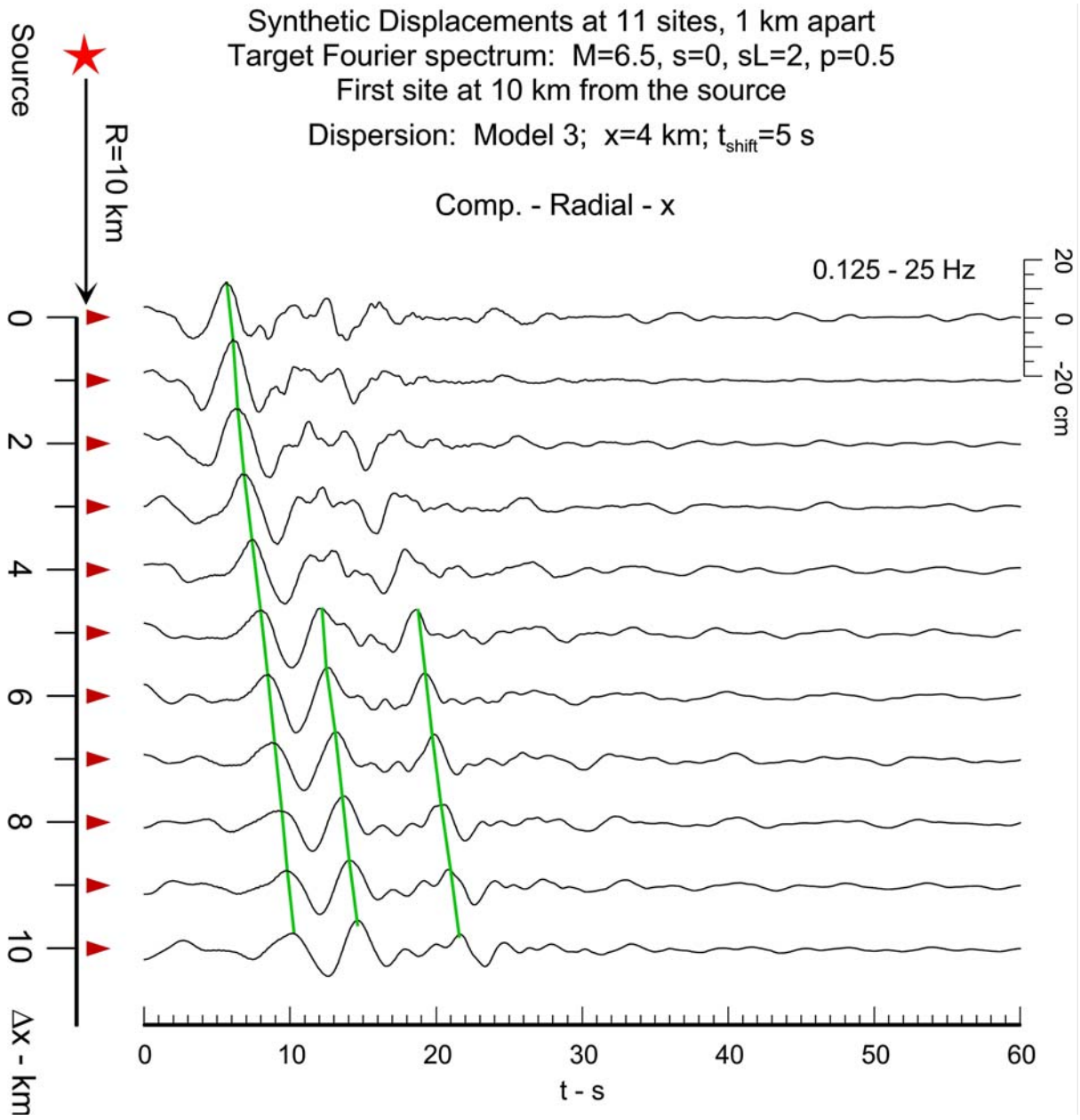

Fig. I.11 Snapshots of synthetic displacement - radial component - at eleven sites, 1 km apart in the radial direction. The target spectrum is that of M6.5 earthquake, at hypocentral distance $R = 10$ km (the closest site), for site condition - sediments ($s = 2$) and deep soil ($s_L = 2$), unfolded with dispersion model

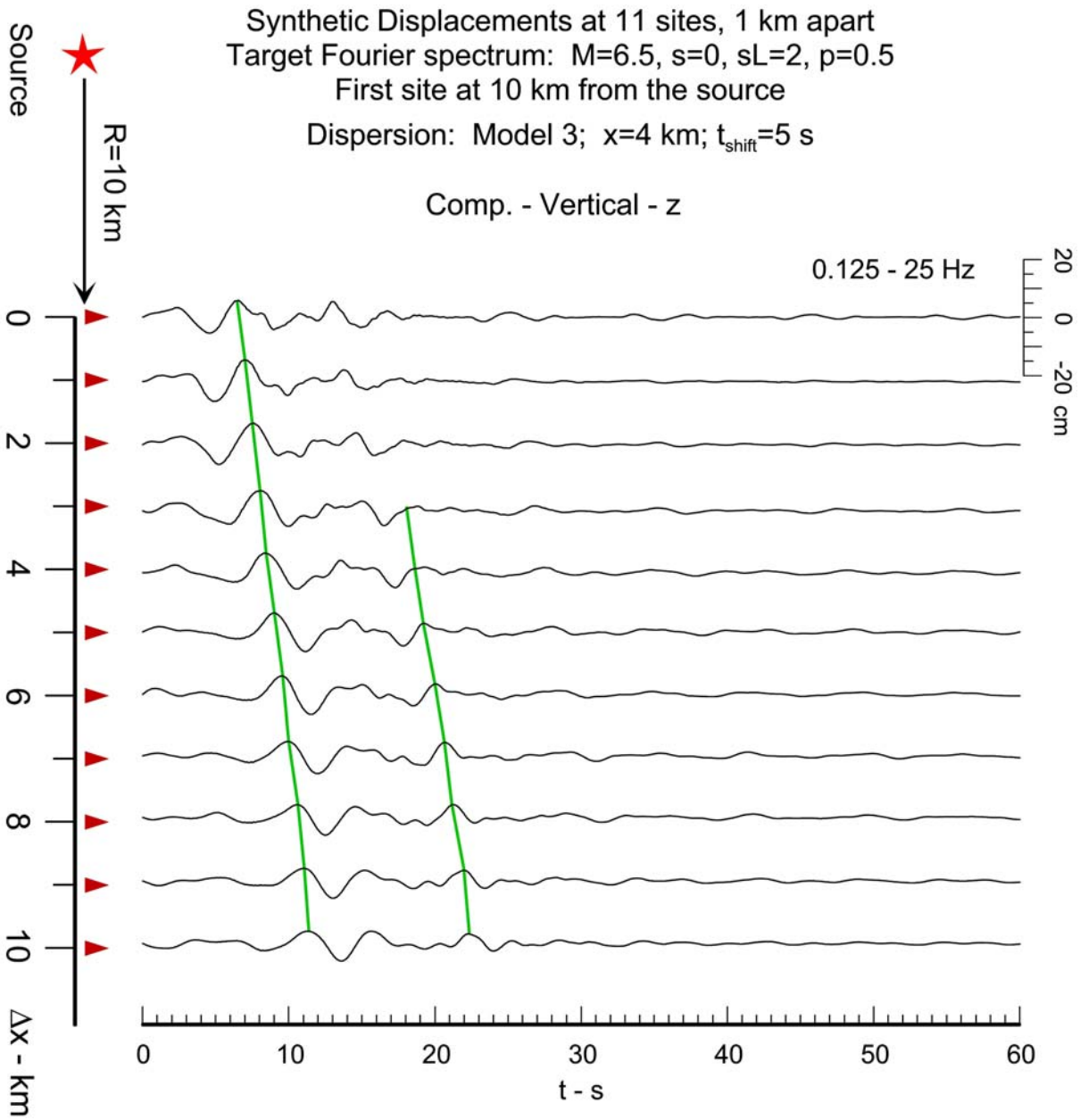

Fig. I.12 Snapshots of synthetic displacement - vertical component - at eleven sites, 1 km apart in the radial direction. The target spectrum is that of M6.5 earthquake, at hypocentral distance $R = 10$ km (the closest site), for site condition - sediments ($s = 2$) and deep soil ($s_L = 2$), unfolded with dispersion model 3.

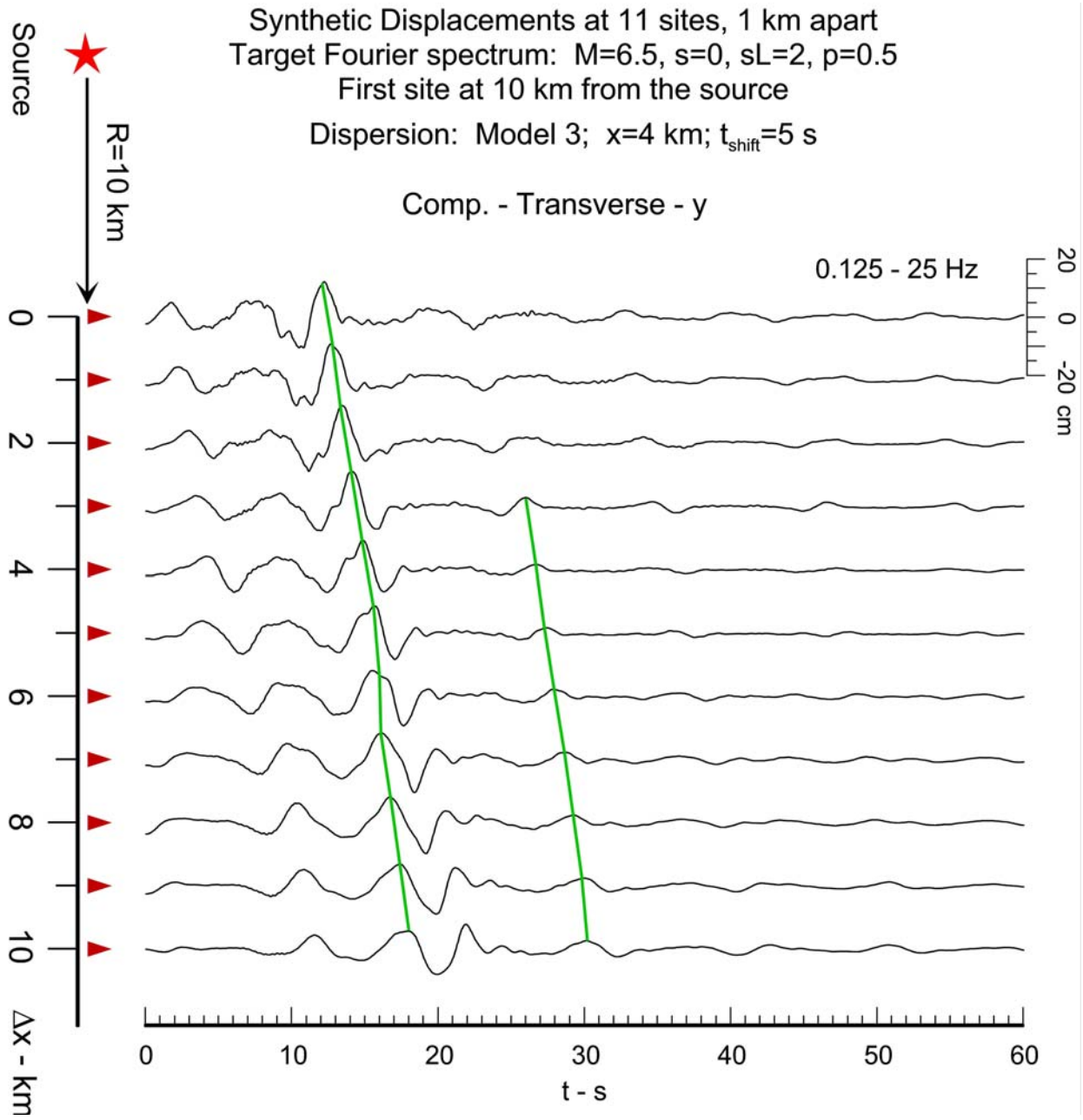

Fig. I.13 Snapshots of synthetic displacement - transverse component - at eleven sites, 1 km apart in the radial direction. The target spectrum is that of M6.5 earthquake, at hypocentral distance $R = 10$ km (the closest site), for site condition - sediments ($s = 2$) and deep soil ($s_L = 2$), unfolded with dispersion model 3.

REFERENCES

1. Trifunac MD (1971). A method for synthesizing realistic strong ground motion, *Bull. Seism. Soc. Amer.*, **61**:1739-1753.
2. Wong HL, Trifunac MD (1978). Synthesizing realistic strong motion accelerograms, *Report No. 78-07*, Dept. of Civil Engrg., U. of So. California, Los Angeles, California.
3. Wong HL, Trifunac MD (1979). Generation of artificial strong motion accelerograms, *Int. J. Earthquake Eng. Struct. Dynamics*, **7**, 509-527.
4. Lee VW, Trifunac MD (1985). Torsional accelerograms, *Int. J. Soil Dyn. Earthq. Eng.*, **4**(3), 132-139.
5. Lee VW, Trifunac MD (1987). Rocking strong earthquake accelerations, *Int. J. Soil Dyn. Earthq. Eng.*, **6**(2):75-89.
6. Lee VW (1990). Surface strains associated with strong earthquake shaking, *Proc. J.S.C.E., 422(n* I-14), 187-194.
7. Trifunac MD (1990). Curvograms of strong ground motion, *ASCE, EMD*, 116(6), 1426-1432.
8. Lee VW (2002). Empirical scaling of strong earthquake ground motion - Part III: Synthetic Strong Motion, *ISET J. of Earthquake Technology*, Paper No. 427, **39**(4), 273-310.
9. Zerva A. (2009). Spatial variation of seismic ground motions: modeling and engineering applications. CRC Press, Taylor and Francis Group, Boca Raton, Florida.
10. Thompson WT. (1950). Transmission of elastic waves through a stratified solid, *J. of Applied Physics*, **21**, 89-93.
11. Haskell NA. (1953). The dispersion of surface waves in multilayered media, *Bull. Seism. Soc. Am.* **43,** 17-34.
12. Trifunac MD. (1994). Q and high frequency strong motion spectra, *Soil Dyn. Earthq. Eng.*, **13**(3), 149-161.
13. Gabor D. (1946). Theory of communications, *J. of the Institute of Electrical Engineers - Part III: Radio and Communication Engineering*, **93**(26), 429-457.
14. Gabor D. (1953). Communication theory and physics, *Institute of Radio Engineers, Professional Group on Information Theory,* **1**(1), 48-59.
15. Trampert J, Cara M, Frogneux M. (1993). SH propagator matrix and Q_S estimates from borehole- and surface-recorded earthquake data, *Geophys. J. Int.*; **112**:290-299.
16. Mehta K, Snieder R, Graizer V. (2007). Extraction of near-surface properties for a lossy layered medium using the propagator matrix, *Geophys. J. Int.*;**169**, 271-280.
17. Trifunac MD, Lee VW (1985). Preliminary empirical model for scaling Fourier amplitude spectra of strong ground acceleration in terms of earthquake magnitude, source to station distance, site intensity and recording site conditions, *Report CE 85-03*, Dept. of Civil Eng., U. So. California, Los Angeles, California.
18. Trifunac MD. (1989a). Dependence of Fourier spectrum amplitudes of recorded strong earthquake accelerations on magnitude, local soil conditions and on depth of sediments, *Earthq. Eng Struct. Dyn.*, **18**(7):999-1016.

19. Trifunac MD. (1989b). Empirical Scaling of Fourier Spectrum Amplitudes of Recorded Strong Earthquake Accelerations in Terms of Magnitude and Local Soil and Geologic Conditions, *Earthq. Eng Eng Vib*., **9**(2), 23-44.

20. Trifunac, MD. (1976). Preliminary empirical model for scaling Fourier amplitude spectra of strong ground acceleration in terms of earthquake magnitude, source to station distance and recording site conditions, *Bull. Seism. Soc. Amer*., **66**, 1343-1373.

21. Trifunac, MD. (1979). Preliminary empirical model for scaling Fourier amplitude spectra of strong motion acceleration in terms of Modified Mercalli Intensity and geologic site conditions, Earthqu. Engng Struct. Dynam., **7**, 63-74.

22. Lee VW, Trifunac MD (1985). Uniform risk spectra of strong earthquake ground motion. *Report No. 85-05*, Dept. of Civil Engrg., U. So. California, Los Angeles, California.

23. Kojić, S. and Trifunac, M.D. 1988). Transient Pressures in Hydrotechnical Tunnels During Earthquakes *Int. J. Struct. Dyn.Earthq. Eng.* 16(3), 523-539.

24. Todorovska, MI, Trifunac, MD. (1990a). Propagation of Earthquake Waves in Buildings With Soft First Floor, *ASCE, EMD*, 116(4), 892-900.

25. Todorovska, MI, Trifunac, MD. (1990b). Note on Excitation of Long Structures by Ground Waves, *ASCE, EMD*, 116(4), 952-964.

26. Jalali RS, Trifunac MD. (2007). Strength-Reduction Factors for Structures Subjected to Differential Near-Source Ground Motion, *Indian Society of Earthq. Techn. J.* , **44**(1), 285-304.

27. Jalali RS, Trifunac MD. (2009). Response Spectra for Near-source, Differential and Rotational Strong Motion, *Bull. Seism. Soc. Amer.*, 99(2B), 1404-1415, See also Erratum: *Bull. Seism. Soc. Amer.*, 99(5), 3094-3095.

28. Jalali RS, Trifunac MD. (2011). A note on the wave-passage effects in out-of-plane response of long structures to strong earthquake pulses, *Soil Dyn. Earthq. Eng.*, **31**(4), 640-647.

29. Kashefi I, Trifunac MD. (1986). Investigation of Earthquake Response of Simple Bridge Structures, *Report No. CE 86-02*, Dept. of Civil Engrg., U. So. California, Los Angeles, California.

Appendix A: Coefficients $A_1(m)$ and $A_2(\omega_n)$

Trifunac [1] suggested the following empirical equations for $A_1(m)$ and $A_2(\omega_n)$

$$A_1(m) = \left| \exp\left(-(m - m_0)^2 / 2C_0^2 \right) + C_R X_m \right|$$

and

$$A_2(\omega_n) = \left| B_0 \exp\left(-(\omega_n - \omega_p)^2 / 2\omega_B^2 \right) + B_R X_n \right|$$

with X_m and X_n being random numbers between -1 and 1, and the values of other constants are suggested in Table A1.

Table A1: Empirical Scaling Coefficients for Equations (5) and (6) (from [1])

Mode	C_0	m_o	C_R	B_0	ω_p	ω_B	B_R
1	3	5	0.2	1.5	10	5	0.1
2	3	5	0.2	1.5	10	5	0.1
3	3	5	0.2	1.5	10	5	0.1
4	3	5	0.2	2.0	25	15	0.1
5	3	5	0.2	2.0	25	15	0.1
6	3	6	0.2	3.0	30	10	0.3
7	3	7	0.2	1.5	30	5	0.25

Table I-1a Profile for dispersion model 1

No.	**Error! Objects cannot be created from editing field codes.** - [km]	**Error! Objects cannot be created from editing field codes.**- [km/s]	**Error! Objects cannot be created from editing field codes.**- [km/s]	**Error! Objects cannot be created from editing field codes.**- [gm/cm^3]
1	0.18	1.70	0.98	1.28
2	0.55	1.96	1.13	1.36
3	0.98	2.71	1.57	1.59
4	1.19	3.76	2.17	1.91
5	2.68	4.69	2.71	2.19
6	∞	6.40	3.70	2.71

Table I-1b Profile for dispersion model 2

No.	**Error! Objects cannot be created from editing field codes.** - [km]	**Error! Objects cannot be created from editing field codes.**- [km/s]	**Error! Objects cannot be created from editing field codes.**- [km/s]	**Error! Objects cannot be created from editing field codes.**- [gm/cm^3]
1a	0.06	0.867	0.50	1.2
1b	0.12	1.70	0.98	1.28
2	0.55	1.96	1.13	1.36
3	0.98	2.71	1.57	1.59
4	1.19	3.76	2.17	1.91
5	2.68	4.69	2.71	2.19
6	∞	6.40	3.70	2.71

Table I-1c Profile for dispersion model 3

No.	**Error! Objects cannot be created from editing field codes.** - [km]	**Error! Objects cannot be created from editing field codes.**- [km/s]	**Error! Objects cannot be created from editing field codes.**- [km/s]	**Error! Objects cannot be created from editing field codes.**- [gm/cm^3]
1a	0 .03	0.4335	0.25	1.20
1b	0.03	0.867	0.50	1.2
1c	0.12	1.70	0.98	1.28
2	0.55	1.96	1.13	1.36
3	0.98	2.71	1.57	1.59
4	1.19	3.76	2.17	1.91
5	2.68	4.69	2.71	2.19
6	∞	6.40	3.70	2.71

Chapter 2 Synthetic Translational Motions of Surface and Body Waves in Elastic Layered Medium over Half-Space

Summary

The following is a brief description of the results presented in the Reports I (Appendix R1) and II (Appendix R2), which includes the theory and verification examples of how to extend the synthesis of strong ground motion along a vertical array of points, into the depth of a layered half space. Together Reports I and II describe the complete methodology for computing all components of strong ground motion at any point on the surface or at arbitrary point at some depth in the layered half space. The verification of this methodology has been performed by detailed analysis of the nature of synthesized motions at depth, and by verifying that the motions satisfy all known seismological properties and principles of body and surface wave propagation in layered half space. It was found that the synthesized motions meet all known properties of strong earthquake ground motion, and constitute realistic representation of strong earthquake waves in a set of parallel layers overlying the half space.

II.1 Synthetic Translational Motions of Surface Waves in a Layered Medium at Points on the Half-Space Surface – a Review

The synthetic translational components of acceleration are constructed to have a required Fourier amplitude spectrum, $\boldsymbol{FS(\omega)}$, and a given duration, $\boldsymbol{D(\omega)}$, at the site. A complete review of the method first proposed by Trifunac (1971), and later refined by Wong and Trifunac (1978, 1979), for the generation of synthetic accelerograms, can also be found in the review paper by Lee (2002) and Todorovska et al (2013). The following is needed to construct synthetic motions:

1.1 Wave Dispersion Curves at a Site

1.2 Arrival Times of body waves and of each mode and frequency band of Surface Waves

1.3 Contribution of the Modes at a Given Frequency Band

1.4 Determination of Relative Amplitudes and Phrases of all body and Surface Waves.

1.5 The Total Accelerogram is then a Superposition of time-histories of all the contributing waves.

Reports I and II outline the details of the above procedures and therefore not all of those will not be repeated here. The complete process will be referred to as the "SYNACC *algorithm"*. It applies to the translational (out of plane) horizontal component of surface *Love waves* and body *SH waves*, as well as to both the horizontal and vertical translational components of surface *Rayleigh waves* and body *P and SV waves*. Report II has presented also how the time and space derivatives of translational motions can be used to construct rotational components of strong motion (rocking and torsional accelerograms, velocities and displacements), all components of curvature and all components of strain, associated with passage of strong translational components of motion. To emphasize the essential parts of the physical nature of this problem we will focus our attention here mainly on the translational components of motion, and refer the reader to the material in Report II for further details and examples about the associated rotational, curvature and strain components of motion.

Figure II.1 shows an example of dispersion curves at a site in El Centro Area in Imperial Valley, California (model 1 refers to the properties of parallel layers; see Todorovska et al 2013). The site is a 6-layered medium, and has been used in many of our previous studies (Lee, 2002) to illustrate various synthetic components of strong ground motion. This figure shows the phase velocities of Love and Rayleigh waves at the site, which can be employed to generate the synthetic accelerations at the site. Figure II.2 is an example of one such synthetic translational accelerogram.

II-2 Synthetic Translational Motions of Love and Body SH Waves On and Below Surface of a Layered Medium

Let $c = c(\omega)$ be the wave speed of a mode of Love waves in the half-space with n elastic layers over half space. c is the (horizontal) phase velocity of the waves in each layer of the elastic media above the half space,

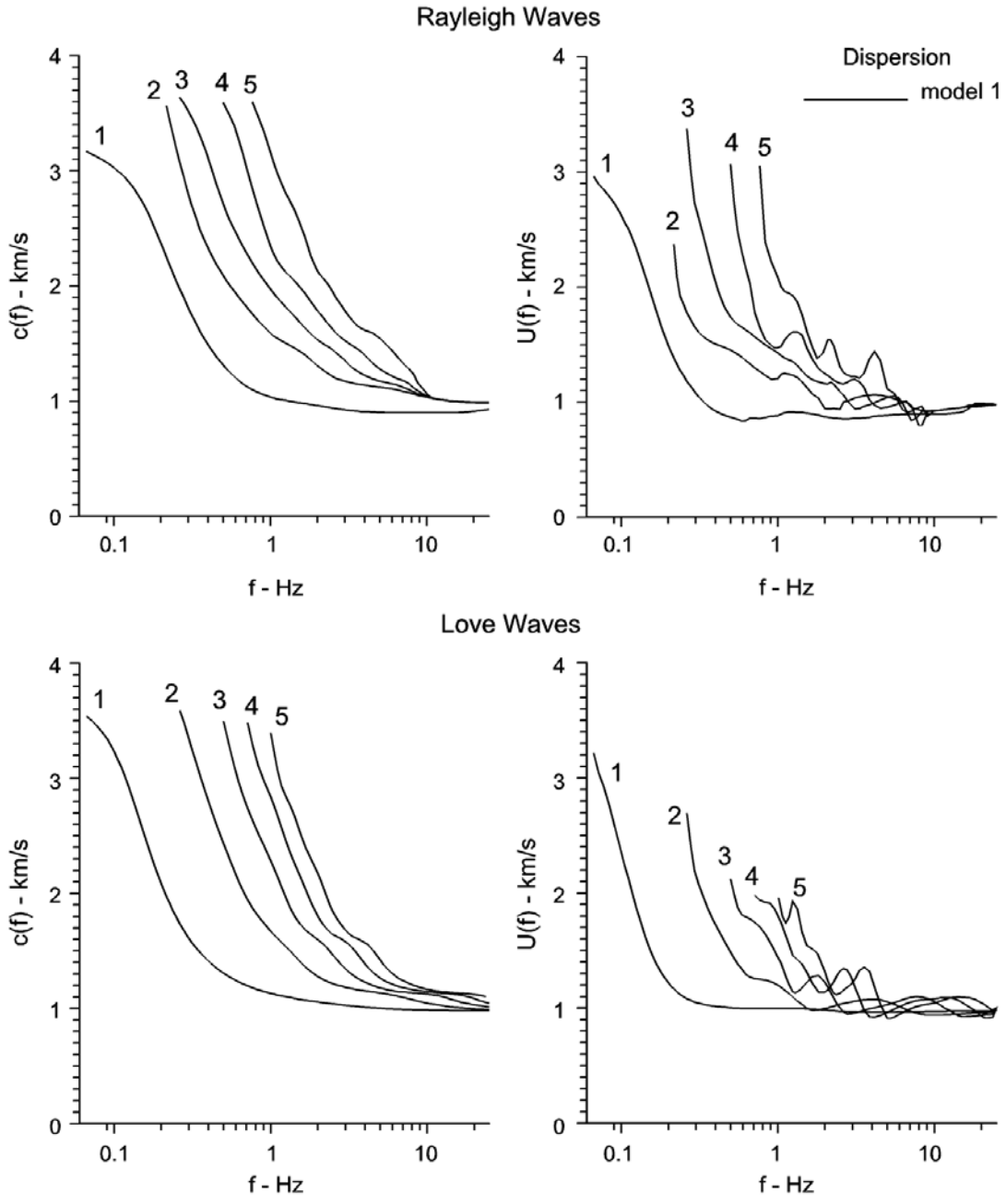

Figure II.1 Phase Velocities (left) and Group velocities (right) for Love & Rayleigh Waves

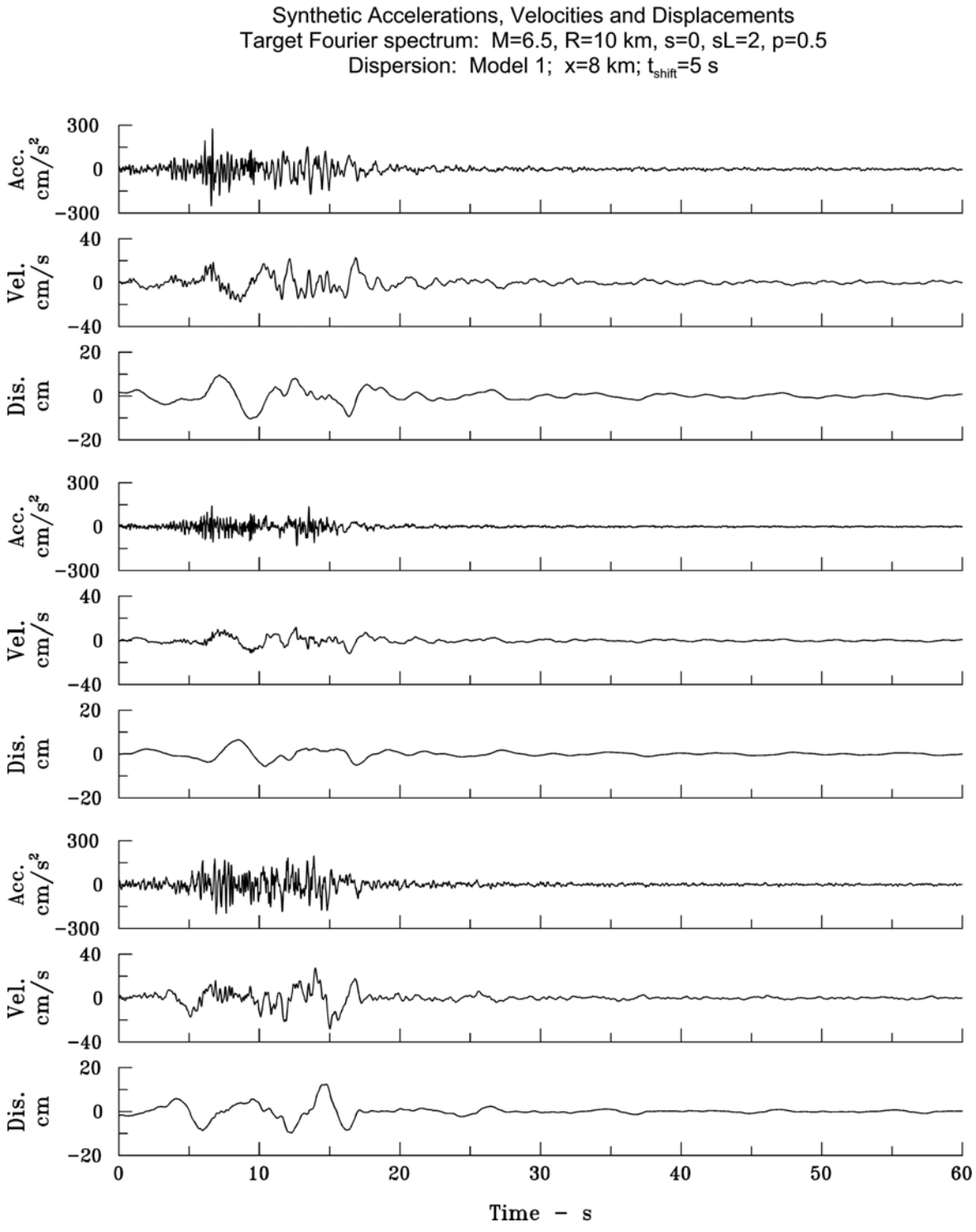

Figure II.2 Synthetic Translational Accelerogration Time Histories.

II-2 Synthetic Translational Motions of Love and Body SH Waves On and Below Surface of a Layered Medium

Let $c = c(\omega)$ be the wave speed of a mode of Love waves in the half-space with n elastic layers over half space. c is also the (horizontal) phase velocity of the waves in each layer of the elastic media above the half space.

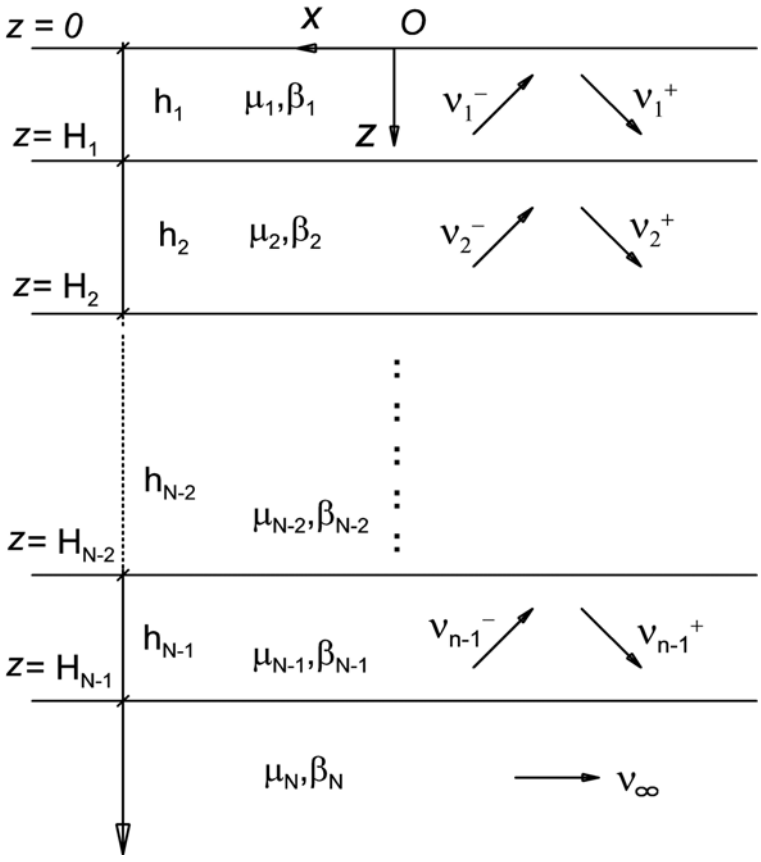

Figure II.3. N-layered half-space with Love waves.

For each layer l, with $l = 1, \ldots, N$, the displacement of the Waves in the layer takes the form (in the anti-plane, y- direction):

$$v_l^-, v_l^+ : \qquad v_l^- = C_l^- e^{ik(x-\gamma_l z)} \qquad v_l^+ = C_l^+ e^{ik(x+\gamma_l z)} \tag{II.1}$$

There are the upward and downward propagating rays of Love waves present in the l^{th} layer. Here $k = k(\omega) = \omega / c(\omega)$ is the horizontal wave number of the waves at frequency ω, and with phase velocity $c = c(\omega)$. The term e^{ikx}, which is same in all layers, together with the time harmonic term $e^{i\omega t}$, corresponds to the waves propagating in the **–ve** *x* direction. The terms $e^{\mp ik\gamma_l y}$ are the vertical components of the waves with the negative term propagating upwards (**–ve** *y*) and the positive term propagating downwards (*y*). Here $\gamma_l = \gamma_l(\beta_l)$ is given by

$$\gamma_l = \frac{\left(k_{\beta_l}^2 - k^2\right)^{1/2}}{k} = \left(\left(k_{\beta_l}/k\right)^2 - 1\right)^{1/2} = \left(\left(c/\beta_l\right)^2 - 1\right)^{1/2} \qquad \text{(II.2)}$$

so that $k\gamma_l$ is the vertical wave number of the waves in the l^{th} layer of the medium with shear wave velocity β_l. In general, the wave velocities increase as one moves down through the layers, so that $\beta_1 < \beta_2 < \ldots < \beta_n < \beta$, with the semi-infinite half-space layer at the bottom having the highest shear wave speed β. The motion associated with Love waves in the semi-infinite layer, $l = N$, is given by

$$v_\infty = C_\infty e^{ik(x - \gamma z)} = C_\infty e^{ikx - k\bar{\gamma} z} \qquad \text{(II.3)}$$

where $$\bar{\gamma} = \frac{\left(k^2 - k_\beta^2\right)^{1/2}}{k} = \left(1 - \left(k_\beta/k\right)^2\right)^{1/2} = \left(1 - \left(c/\beta\right)^2\right)^{1/2} \qquad \text{(II.4)}$$

$\bar{\gamma}$ is the complement of γ and is real, so that the term $e^{ikx - k\bar{\gamma} y}$ in v_∞ corresponds to a motion whose amplitude is exponentially decaying with depth below the surface.

The coefficients C_l^-, C_l^+, respectively of the waves, v_l^-, v_l^+, in each of the layers *l*, for *l* = **1** to **n**, are all related by the stress and displacement boundary conditions. In the topmost layer, the zero-stress boundary condition at the half-space surface is

$$\tau_{zy}\Big|_{z=0} = \mu_1 \frac{\partial v_1}{\partial z}\Big|_{z=0} = 0 \qquad \text{(II.5)}$$

for waves $v_1 = v_1^+ + v_1^-$ in the top layer $l = 1$. This gives

$$\mu_1 \left.\frac{\partial v_1}{\partial z}\right|_{z=0} = \mu_1 \left.\left(\frac{\partial v_1^+}{\partial z} + \frac{\partial v_1^-}{\partial z}\right)\right|_{z=0} = 0, \qquad \text{or}$$

$$\mu_1 \left.\left(C_1^+ e^{ik(x+\gamma_1 z)} - C_1^- e^{ik(x-\gamma_1 z)}\right)\right|_{z=0} = 0, \quad \text{for all } x, \tag{II.6}$$

so that $C_1^+ - C_1^- = 0$ or $C_1^+ = C_1^-$

Starting from $l = 1$, it can be shown by induction that if the waves in the l^{th} layer are known, then the waves in the $(l+1)^{th}$ layer can also be known, including the bottom semi-infinite layer.

One can start with the l^{th} layer, where the waves are given by:

v_l^-, v_l^+ :

$$v_l^- = C_l^- e^{ik(x-\gamma_l z)} = C_l^- e^{-ik\gamma_l z} e^{ikx}$$
$$v_l^+ = C_l^+ e^{ik(x+\gamma_l z)} = C_l^+ e^{+ik\gamma_l z} e^{ikx}$$

Equation (II.1) above

with known (complex) coefficients C_l^-, C_l^+. The waves in the $(l+1)^{th}$ layer below, are of the form:

v_{l+1}^-, v_{l+1}^+ :

$$v_{l+1}^- = C_{l+1}^- e^{ik(x-\gamma_{l+1} z)} = C_l^- e^{-ik\gamma_{l+1} z} e^{ikx}$$
$$v_{l+1}^+ = C_{l+1}^+ e^{ik(x+\gamma_{l+1} z)} = C_l^+ e^{+ik\gamma_{l+1} z} e^{ikx} \tag{II.7}$$

with coefficients , C_{l+1}^-, C_{l+1}^+ to be evaluated. At the common interface between the l^{th} layer and $(l+1)^{th}$ layer, where $z = H_l$, the continuity of displacement and of stress at the interface between the 2 layers gives:

At the interface of the l^{th} & $(l+1)^{th}$ medium, $z = H_l$:

$$v_l^+ + v_l^- = v_{l+1}^+ + v_{l+1}^-$$
$$\mu_l \frac{\partial}{\partial z}\left(v_l^+ + v_l^-\right) = \mu_{l+1} \frac{\partial}{\partial z}\left(v_{l+1}^+ + v_{l+1}^-\right) \tag{II.8}$$

or

$$\begin{bmatrix} 1 & 1 \\ \mu_l\gamma_l & -\mu_l\gamma_l \end{bmatrix}\begin{pmatrix} C_l^+ e^{+ik\gamma_l H_l} \\ C_l^- e^{-ik\gamma_l H_l} \end{pmatrix} = \begin{bmatrix} 1 & 1 \\ \mu_{l+1}\gamma_{l+1} & -\mu_{l+1}\gamma_{l+1} \end{bmatrix}\begin{pmatrix} C_{l+1}^+ e^{+ik\gamma_{l+1} H_l} \\ C_{l+1}^- e^{-ik\gamma_{l+1} H_l} \end{pmatrix} \qquad \text{(II.9)}$$

giving C_{l+1}^-, C_{l+1}^+ in terms of C_l^-, C_l^+ .

This means that once the complex Fourier coefficient at a given frequency of one mode of surface Love waves is given at a point of a site on the half-space surface, the complex Fourier coefficients of the same mode on and below the surface are known.

The procedure for body SH waves incident from the semi-infinite layer is the same, with the one component of surface Love waves replaced by two components of body SH waves, one propagating upward and the other propagating downwards.

II-3 Synthetic Translational Motions of Rayleigh and Body P and SV Waves On or Below the surface of Layered Half Space

Let $c = c(\omega)$ be the phase velocity of a mode of Rayleigh waves in the half-space with N elastic layers. c is the (horizontal) phase velocity of both the P- and SV-waves in each layer of the elastic media above the half space such that $c < \beta_{\max} = \beta_N$, the shear wave speed in the semi-infinite N^{th} layer (Figure II.4)

For each layer l, with $l = 1, \ldots, N$, the P- and SV-Waves in the layer take the form:

$$\varphi_l^-, \varphi_l^+, \psi_l^-, \psi_l^+ : \qquad \begin{aligned} \varphi_l^- &= A_l^- e^{ik(x - a_l z)} \\ \varphi_l^+ &= A_l^+ e^{ik(x + a_l z)} \\ \psi_l^- &= B_l^- e^{ik(x - b_l z)} \\ \psi_l^+ &= B_l^+ e^{ik(x + b_l z)} \end{aligned} \qquad \text{(II.10)}$$

Those are the upward and downward propagating waves in the l^{th} layer, where $k = k(\omega) = \omega / c(\omega)$ is the horizontal wave number of the P- and SV-waves at frequency ω and phase velocity $c = c(\omega)$. The terms $e^{\mp ika_l z}$ for the P-waves and $e^{\mp ikb_l z}$ for the

SV-waves are the phases for vertical components of the waves. The ones with the ***–ve*** exponent are propagating upwards (***–ve*** y) and those with the ***+ve*** exponent are propagating downwards (***+ve*** y). Here $\boldsymbol{a_l = a_l(\alpha_l, c)}$ and $\boldsymbol{b_l = b_l(\beta_l, c)}$ are given by

$$\begin{aligned} a_l &= \frac{\left(k_{\alpha_l}^2 - k^2\right)^{1/2}}{k} = \left(\left(k_{\alpha_l}/k\right)^2 - 1\right)^{1/2} = \left(\left(c/\alpha_l\right)^2 - 1\right)^{1/2} \\ b_l &= \frac{\left(k_{\beta_l}^2 - k^2\right)^{1/2}}{k} = \left(\left(k_{\beta_l}/k\right)^2 - 1\right)^{1/2} = \left(\left(c/\beta_l\right)^2 - 1\right)^{1/2} \end{aligned} \qquad \text{(II.11)}$$

so that $\boldsymbol{ka_l}$ and $\boldsymbol{kb_l}$ are the vertical wave numbers of the ***P***- and ***SV***-waves in the $\boldsymbol{l^{th}}$ layer of the medium with longitudinal wave speed α_l and shear wave velocity β_l.

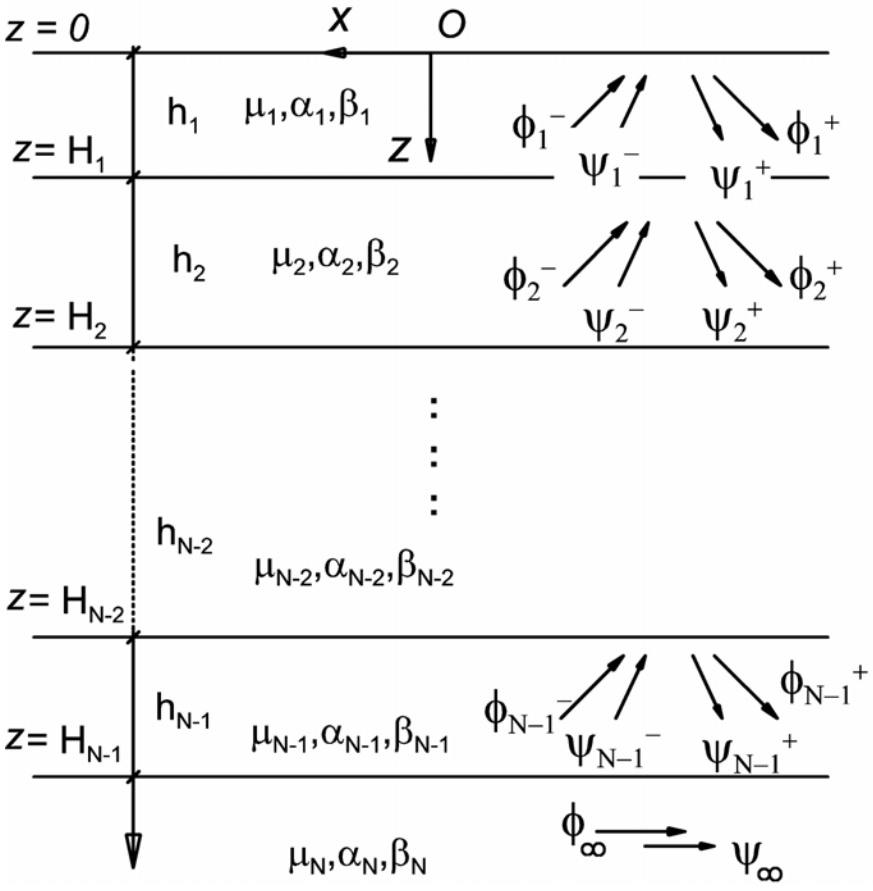

Figure II.4 N-layered half-space with Rayleigh waves

The surface waves in the semi-infinite layer at the bottom take the form:

$$\begin{aligned} \varphi_\infty &= A_\infty e^{ik(x-az)} = A_\infty e^{ikx-k\bar{a}z} \\ \psi_\infty &= B_\infty e^{ik(x-bz)} = B_\infty e^{ikx-k\bar{b}z} \end{aligned} \tag{II.12}$$

where

$$\begin{aligned} \bar{a} &= \frac{\left(k^2-k_\alpha^2\right)^{1/2}}{k} = \left(1-\left(k_\alpha/k\right)^2\right)^{1/2} = \left(1-\left(c/\alpha\right)^2\right)^{1/2} \\ \bar{b} &= \frac{\left(k^2-k_\beta^2\right)^{1/2}}{k} = \left(1-\left(k_\beta/k\right)^2\right)^{1/2} = \left(1-\left(c/\beta\right)^2\right)^{1/2} \end{aligned} \tag{II.13}$$

and $\bar{a}$, $\bar{b}$ are the complements of a, b and both are real, so that the terms $e^{-k\bar{a}z}$ in φ_∞ and $e^{-k\bar{b}z}$ in ψ_∞ both correspond to surface wave terms with amplitudes that are exponentially decaying with depth.

The coefficients A_l^-, A_l^+, of the *P*-wave potentials, φ_l^-, φ_l^+, and B_l^-, B_l^+, of the *SV*-wave potentials, ψ_l^-, ψ_l^+, in each of the layers l, for l = 1 to N, are all related by the stress and displacement boundary conditions. In the topmost layer, the zero-stress boundary conditions at the half-space surface is

$$\sigma_z\big|_{z=0} = \tau_{zx}\big|_{z=0} \tag{II.14}$$

for *P*- and *SV*-wave potentials. Let U_0, W_0 be the horizontal and vertical (complex) displacements at the origin, the reference point at the free surface. Then stress boundary conditions at the half-space surface ($z = 0$) and the displacement on the half-space surface at the origin **(0., 0.)** take the form:

$$\begin{bmatrix} 1 & 1 & b_1 & -b_1 \\ a_1 & -a_1 & -1 & -1 \\ 1-b_1^2 & 1-b_1^2 & -2b_1 & 2b_1 \\ 2a_1 & -2a_1 & 1-b_1^2 & 1-b_1^2 \end{bmatrix} \begin{pmatrix} A_1^+ \\ A_1^- \\ B_1^+ \\ B_1^- \end{pmatrix} = \frac{1}{ik} \begin{pmatrix} U_0 \\ V_0 \\ 0 \\ 0 \end{pmatrix} \tag{II.15}$$

We start with the l^{th} layer, where the wave potentials are given by:

$\varphi_l^-,\ \varphi_l^+,\ \psi_l^-,\ \psi_l^+$:

$$\begin{aligned}\varphi_l^- &= A_l^- e^{ik\left(x-a_l z\right)}\\ \varphi_l^+ &= A_l^+ e^{ik\left(x+a_l z\right)}\\ \psi_l^- &= B_l^- e^{ik\left(x-b_l z\right)}\\ \psi_l^+ &= B_l^+ e^{ik\left(x+b_l z\right)}\end{aligned}$$

Equation (II.10) above

with known (complex) coefficients $A_l^-,\ A_l^+$ for the ***P***-wave and $B_l^-,\ B_l^+$ for the ***SV***-wave potentials. The waves in the $(l+1)^{th}$ layer are of the form, with $(l+1)$ replacing l everywhere in Equation (3.1):

$\varphi_{l+1}^-,\ \varphi_{l+1}^+,\ \psi_{l+1}^-,\ \psi_{l+1}^+$:

$$\begin{aligned}\varphi_{l+1}^- &= A_{l+1}^- e^{ik\left(x-a_{l+1}z\right)}\\ \varphi_{l+1}^+ &= A_{l+1}^+ e^{ik\left(x+a_{l+1}z\right)}\\ \psi_{l+1}^- &= B_{l+1}^- e^{ik\left(x-b_{l+1}z\right)}\\ \psi_{l+1}^+ &= B_{l+1}^+ e^{ik\left(x+b_{l+1}z\right)}\end{aligned} \qquad \text{(II.15)}$$

with the coefficients $A_{l+1}^-,\ A_{l+1}^+$ for the ***P***-wave and $B_{l+1}^-,\ B_{l+1}^+$ for the ***SV***-wave potentials, next to be evaluated. At the interface between the l^{th} layer and $(l+1)^{th}$ layer, where $z = H_l$, the continuity of (***x***- and ***z***- components of) displacements and (normal and shear) stresses at the interface gives:

$$\begin{bmatrix}1 & 0 & 0 & 0\\ 0 & 1 & 0 & 0\\ 0 & 0 & \mu_{l+1} & 0\\ 0 & 0 & 0 & \mu_{l+1}\end{bmatrix}\begin{bmatrix}1 & 1 & b_{l+1} & -b_{l+1}\\ a_{l+1} & -a_{l+1} & -1 & -1\\ 1-b_{l+1}^2 & 1-b_{l+1}^2 & -2b_{l+1} & 2b_{l+1}\\ 2a_{l+1} & -2a_{l+1} & 1-b_{l+1}^2 & 1-b_{l+1}^2\end{bmatrix}\begin{pmatrix}A_{l+1}^+ e^{ika_{l+1}H_l}\\ A_{l+1}^- e^{-ika_{l+1}H_l}\\ B_{l+1}^+ e^{ikb_{l+1}H_l}\\ B_{l+1}^- e^{-ikb_{l+1}H_l}\end{pmatrix} =$$

$$\begin{bmatrix}1 & 0 & 0 & 0\\ 0 & 1 & 0 & 0\\ 0 & 0 & \mu_l & 0\\ 0 & 0 & 0 & \mu_l\end{bmatrix}\begin{bmatrix}1 & 1 & b_l & -b_l\\ a_l & -a_l & -1 & -1\\ 1-b_l^2 & 1-b_l^2 & -2b_l & 2b_l\\ 2a_l & -2a_l & 1-b_l^2 & 1-b_l^2\end{bmatrix}\begin{pmatrix}A_l^+ e^{ika_l H_l}\\ A_l^- e^{-ika_l H_l}\\ B_l^+ e^{ikb_l H_l}\\ B_l^- e^{-ikb_l H_l}\end{pmatrix} \qquad \text{(II.16)}$$

Equation (II.16) can be written in the form, at $z = H_l$:

$$\left[\boldsymbol{M}_{l+1}\left(\boldsymbol{H}_l\right)\right]\begin{pmatrix}\boldsymbol{A}_{l+1}^{+}\\ \boldsymbol{A}_{l+1}^{-}\\ \boldsymbol{B}_{l+1}^{+}\\ \boldsymbol{B}_{l+1}^{-}\end{pmatrix}=\left[\boldsymbol{M}_{l}\left(\boldsymbol{H}_l\right)\right]\begin{pmatrix}\boldsymbol{A}_{l}^{+}\\ \boldsymbol{A}_{l}^{-}\\ \boldsymbol{B}_{l}^{+}\\ \boldsymbol{B}_{l}^{-}\end{pmatrix} \quad \textbf{or} \quad \begin{pmatrix}\boldsymbol{A}_{l+1}^{+}\\ \boldsymbol{A}_{l+1}^{-}\\ \boldsymbol{B}_{l+1}^{+}\\ \boldsymbol{B}_{l+1}^{-}\end{pmatrix}=\left[\boldsymbol{N}_{l}\left(\boldsymbol{H}_l\right)\right]\begin{pmatrix}\boldsymbol{A}_{l}^{+}\\ \boldsymbol{A}_{l}^{-}\\ \boldsymbol{B}_{l}^{+}\\ \boldsymbol{B}_{l}^{-}\end{pmatrix} \tag{II.17}$$

with $\left[\boldsymbol{N}_{l}\left(\boldsymbol{H}_l\right)\right]=\left[\boldsymbol{M}_{l+1}\left(\boldsymbol{H}_l\right)\right]^{-1}\left[\boldsymbol{M}_{l}\left(\boldsymbol{H}_l\right)\right]$, both $\left[\boldsymbol{M}_{l}\left(\boldsymbol{H}_l\right)\right]=\left[\boldsymbol{M}_{l}\left(\mu_l,a_l,b_l,\boldsymbol{H}_l\right)\right]$ and $\left[\boldsymbol{M}_{l}\left(\boldsymbol{H}_l\right)\right]=\left[\boldsymbol{M}_{l}\left(\mu_l,a_l,b_l,\boldsymbol{H}_l\right)\right]$ matrices defined from Equation (II.16). Note that at the last semi-infinite layer, $\boldsymbol{l}=\boldsymbol{N}$, the Rayleigh surface waves have only one component of longitudinal *P*- and shear *SV*- waves. The cases of body P- and SV-waves are similar, except that the one component of Rayleigh *P*- and *SV*- surface waves at the semi-infinite medium is replaced each by two components of corresponding body *P*- and body *SV*-waves, one propagating upwards and one propagating downwards.

In summary, this means that once the complex Fourier coefficient at a given frequency of one mode of surface Rayleigh and body P and SV waves is given at one point of a site at the half-space surface, the complex Fourier coefficients of the same mode of surface and body P and SV waves at any point on and below the surface, in any of the elastic layers, is also known.

Numerical implementation of the above boundary-valued problem to study the propagation of elastic waves in a layered media was first presented and formulated in the pioneering works by Thomson (1950) and Haskell (1953). Thomson (1950) first set up the theoretical groundwork to be extended later by Haskell (1953). A brief summary of the historical review and development of the Thomson-Haskell's transfer (Propagating) Matrix method for both Love and Rayleigh surface waves is given in the Report II (in Appendix R2), and will not be repeated here.

Here we adopt the method proposed by Liu (2010) to implement the improved Thomson-Haskell Propagating matrix method to successfully avoid numerical underflow and overflow problems encountered in the numerical implementation.

II-4 Love and SH Body Wave Mode Shapes - The Synthetic Transverse Translational Motions

Next we describe the mode shapes of Love waves and of body SH waves in the 6-layered site at Imperial Valley, in El Centro, California. With the modified Thomson-Haskell propagator matrix as stated in the previous section, the relative amplitudes can now be computed for each mode of the Love (and Rayleigh) waves at all points on or below the half-space surface, for each frequency where the waves exist. At this intermediate stage of the synthesis of motions the displacement amplitude for all modes will be normalized to be one at the half-space surface.

A complete set of graphs of mode shapes for all the periods of all five modes of Love waves and body SH waves of a selected incident angle are given in the Report II in Appendix R2. A few of these modes at selected frequencies are shown here for illustration only.

Mode #1 has phase velocities for all 91 periods in the range from 15 sec down to 0.04 sec. The Thomson-Haskell computation gives the mode shapes of the Mode#1 Love waves in the same wide period range. Fig. II.5 **s**hows the plots of this Love wave mode shape at four selected periods: $\boldsymbol{T = 5,\ 1.0,\ 0.5,\ \text{and } 0.1\ s}$. As expected for Mode #1, all mode amplitudes that start with unit amplitude at the surface, stay positive all the way, and finally decay to zero at depth. The waves at long periods (small frequencies) decay slower than the waves at short periods (high frequencies).

Fig. II.6 below illustrates the Mode#3 at $\boldsymbol{T = 2, 0.75, 0.2}$ and **0.075** sec.

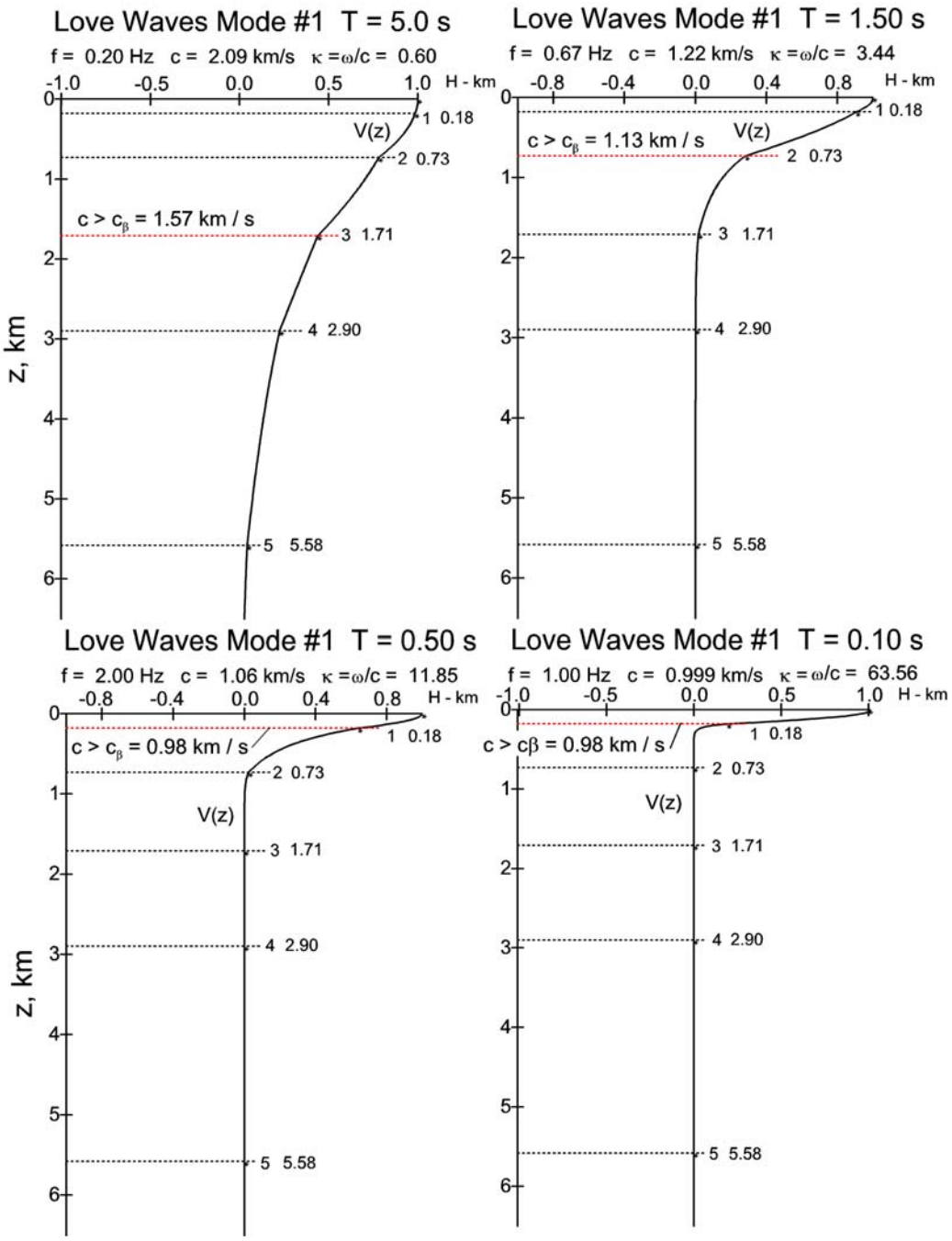

Fig. II.5 Mode#1 Love Wave Mode Shapes at $T = 5,\ 1.0,\ 0.5,$ and $0.1\ s$

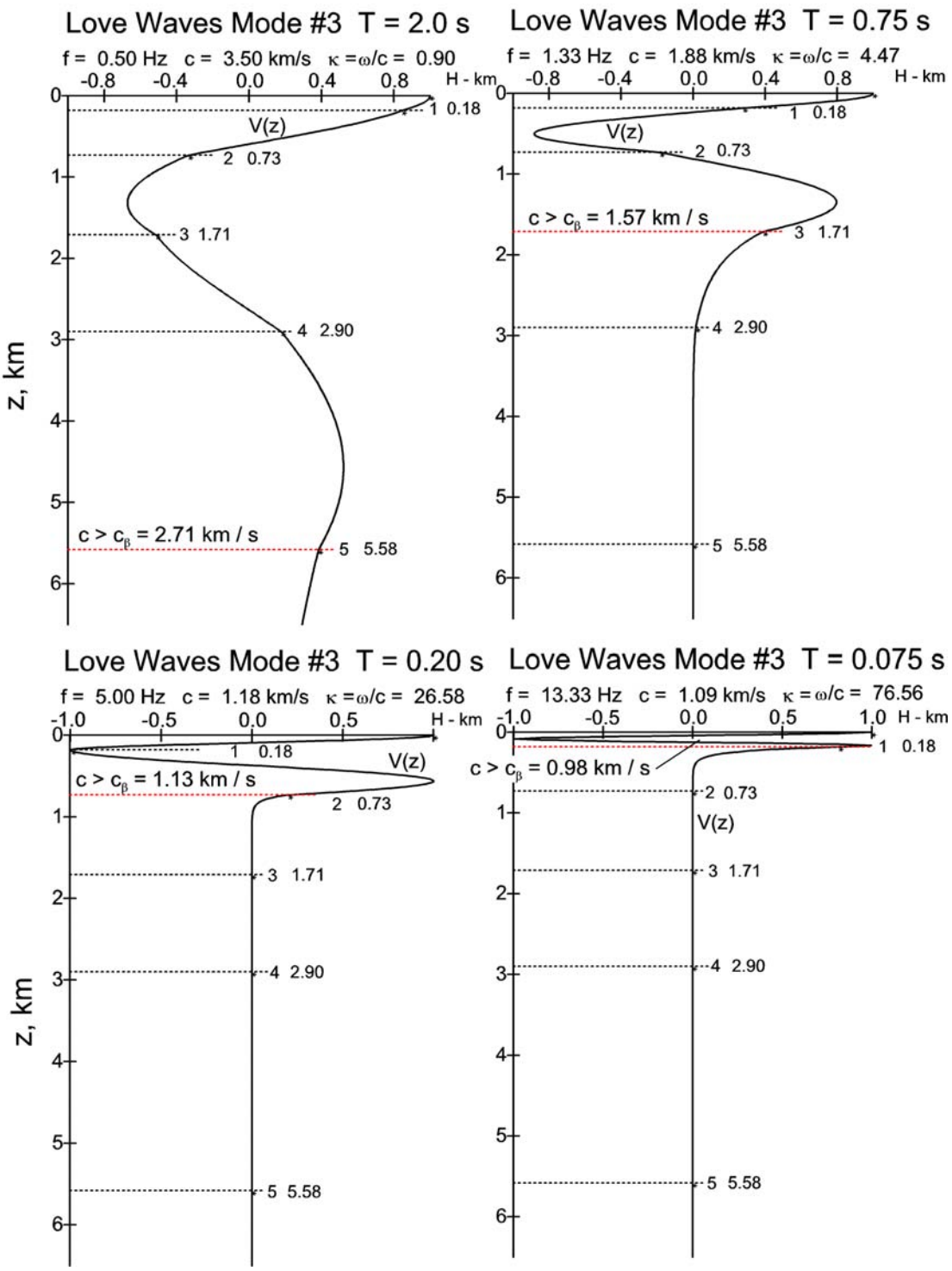

Fig. II.6 Mode#3 Love wave at T = **2, 0.75, 0.2** and **0.075** s.

Fig. II.7 illustrates synthetic accelerations calculated for the El Centro cite, with six-layers, at 100 depths equally spaced from the surface to a depth of almost 6 km below, for epicentral distance of $\boldsymbol{R = 8.0\ km}$ from an earthquake of magnitude 6.5, focal depth $\boldsymbol{H = 6.0\ km}$, or a hypocentral distance of $\boldsymbol{D = 10.0\ km.}$ The geological condition of $s = \mathbf{0}$ (alluvium) and soil condition of $s_L = \mathbf{2}$ (deep soil) are assumed. The SYNACC program determines that the appropriate duration of the record should be just above 40 seconds. The depth of each accelerogram is labeled at intervals 0.6 km apart. Of the 100 accelerogration time histories, six are plotted green, and labeled 0 to 5. The one labeled 0 is the accelerogram at the ground surface $\boldsymbol{z = 0}$, while the ones labeled 1 to 5 are those at depths closest to the interfaces between adjacent layers. The actual time scale of the above time histories has been shifted to have a common time scale, where $\boldsymbol{T = 0}$ **sec** is defined by SYNACC to be the time $\boldsymbol{D/c_{max}}$, where $\boldsymbol{c_{max}}$ is the maximum phase velocity of all the waves arriving at the site.

The figure shows that, at the short distance of $\boldsymbol{D = 10.0\ km}$, both the Love waves and body waves arrive within a few seconds of each other. The direct arrival time of the SH body waves is $\boldsymbol{T = 4.49\ s}$. The arrival times for Love waves will be different for different modes, and for waves at different periods, since the phase velocities $\boldsymbol{c = c(T)}$, depend on the period of the waves, as shown by the dispersion curves in Figure I.1. The acceleration time histories show that the strong-motions arrives at about $\boldsymbol{T = 5.0\ s}$, which follows soon after the direct arrival time of body waves at $\boldsymbol{T = 4.49\ s}$.

Figure II.8 shows the corresponding displacements calculated at the same site. The depth of each displacement is again labeled at intervals 0.6 km apart. Of the 100 displacement time histories, six are again plotted green, and labeled 0 to 5, as in the case for acceleration. The new SYNACC computer program computes the displacement at all depths from the corresponding acceleration time histories.

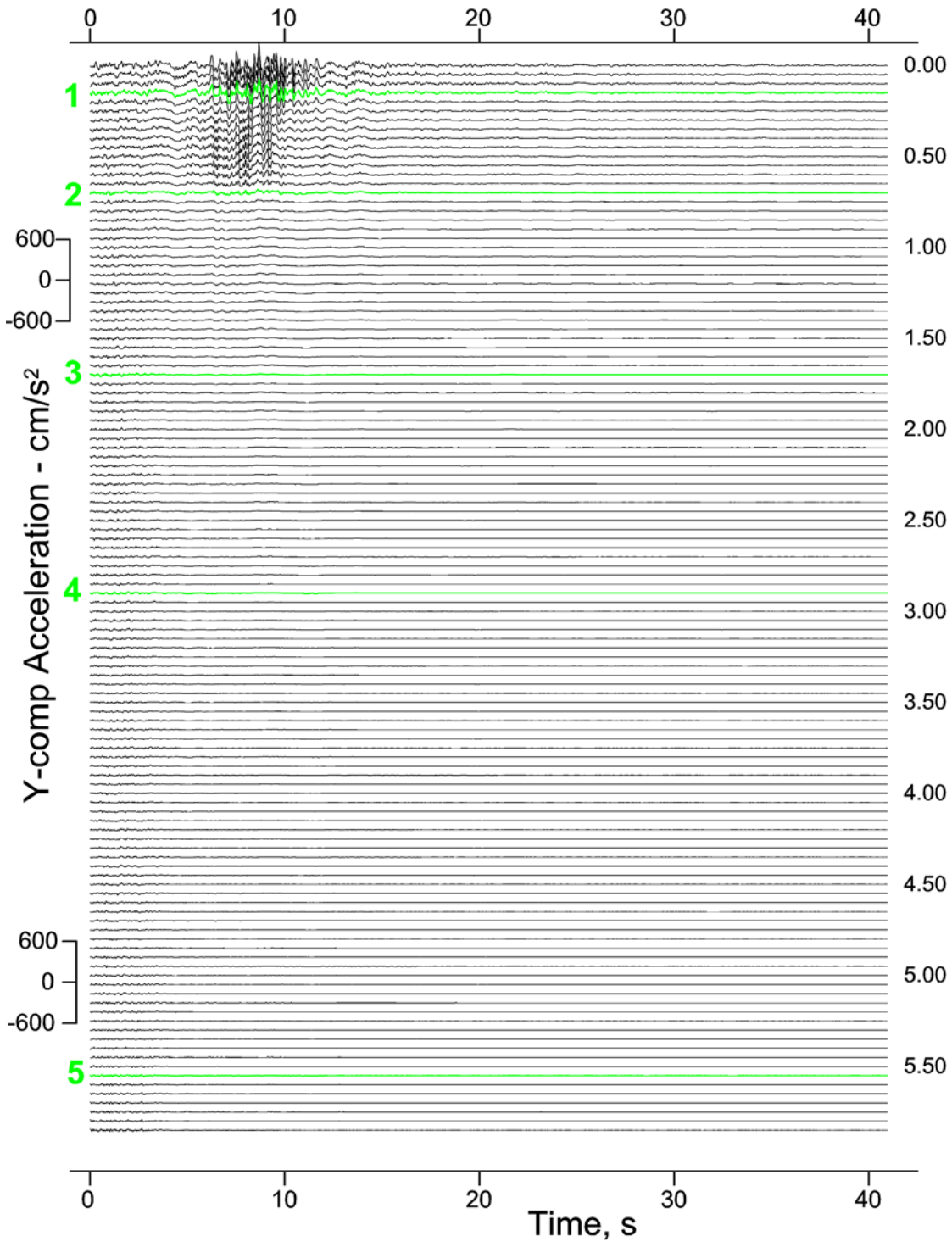

Fig. II.7 Synthetic Acceleration: $M = 6.5,\ R = 8.0\ km,\ H = 6.0\ km,\ s = 0,\ s_L = 2$

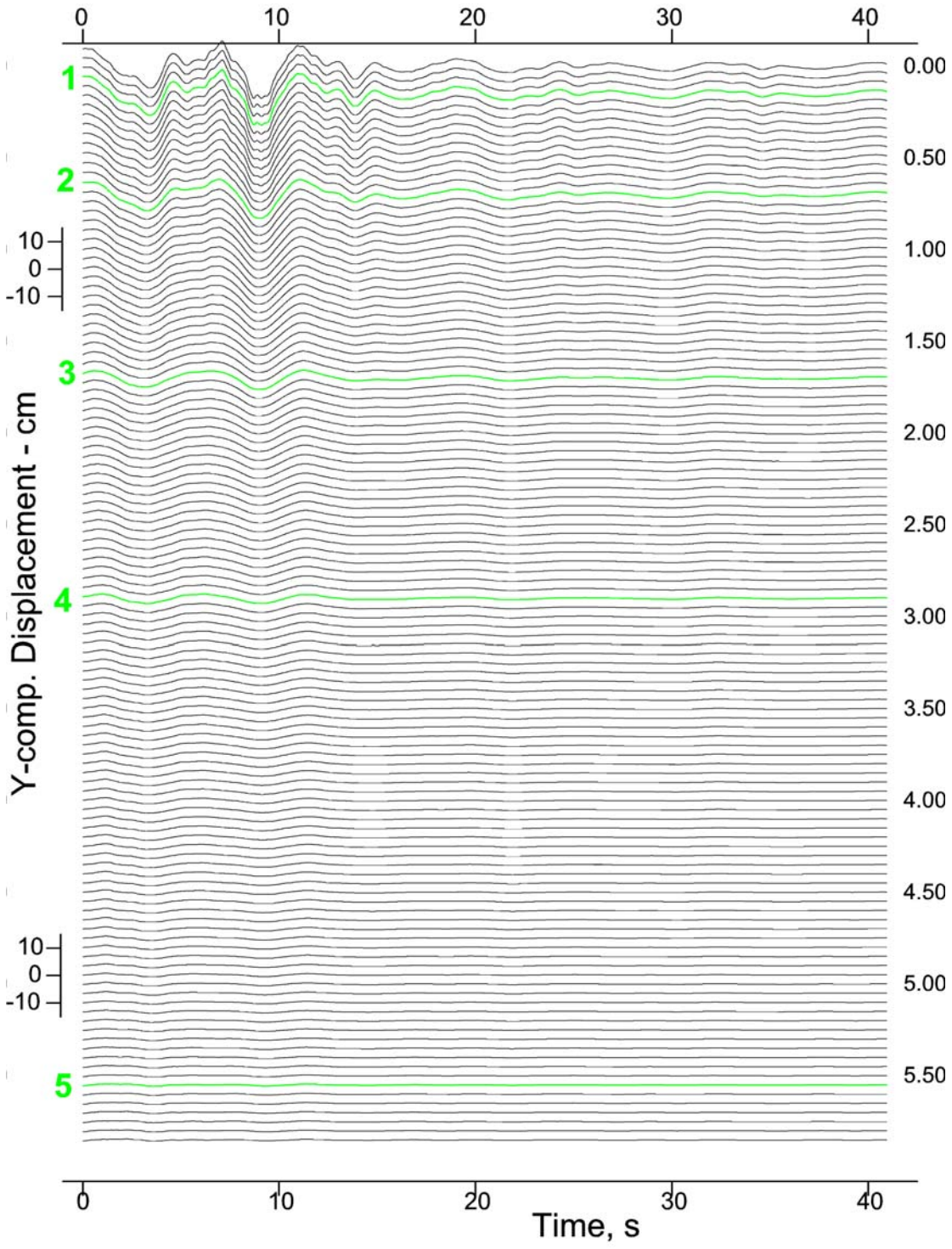

Fig. II.8 Synthetic Displacement: $\boldsymbol{M = 6.5,\ R = 8.0\ km,\ H = 6.0\ km,\ s = 0,\ s_L = 2}$

II-5 Rayleigh and P, SV Body Wave Mode Shapes - The Synthetic Radial and Vertical Translational Motions

With the modified Thomson-Haskell propagator matrix as stated in the first section, the relative amplitudes can be computed for each mode of the Rayleigh waves at all points on or below the half-space surface, for each frequency where the waves exist and in each layer of the layered half-space. The output synthetic acceleration will now have the horizontal (radial) and vertical components of motion. The vertical displacement amplitude for all modes will be normalized to be one at the half-space surface.

Fig. II.9 shows plots of two components (*x*- and *z*-) of Rayleigh wave mode amplitudes at four selected periods: $\boldsymbol{T = 5,\ 1.0,\ 0.5,\ \text{and}\ 0.1\ s}$. The mode #1 of Rayleigh waves has phase velocities at all 91 periods from 15 sec down to 0.04 sec. The Thomson-Haskell computation gives the mode shapes of the mode#1 of Rayleigh waves in the same wide period range at every specified point below the surface. Each graph shows two components of mode shape amplitudes versus the depth *z*, measured in kilometers below the surface. Note that at the half-space surface, with the *z*-component motion $\boldsymbol{W(z)\big|_{z=0} = 1}$, the *x*-component of motion, $\boldsymbol{U(z)\big|_{z=0} = i\gamma W(z)\big|_{z=0} = i\gamma}$, is an imaginary number, where $\boldsymbol{\gamma}$ is a ratio computed from the Haskell algorithm for estimating phase velocities of Rayleigh waves. With this normalization, $\boldsymbol{W(z)}$ will stay real, while $\boldsymbol{U(z)}$ will stay imaginary for all z. Without loss of generality, only the imaginary part of $\boldsymbol{U(z)}$ is plotted here.

Mode #2 of Rayleigh waves has phase velocities for 74 periods in the range from 4.6 sec down to 0.04 sec. The Thomson-Haskell computation gives the mode shapes of the Mode#2 in the same period range. Fig. II.10 illustrates the plots of both components of Rayleigh wave mode shape amplitudes at four selected periods: $\boldsymbol{T = 3.0,\ 1.0,\ 0.3,\ \text{and}\ 0.1\ s}$.

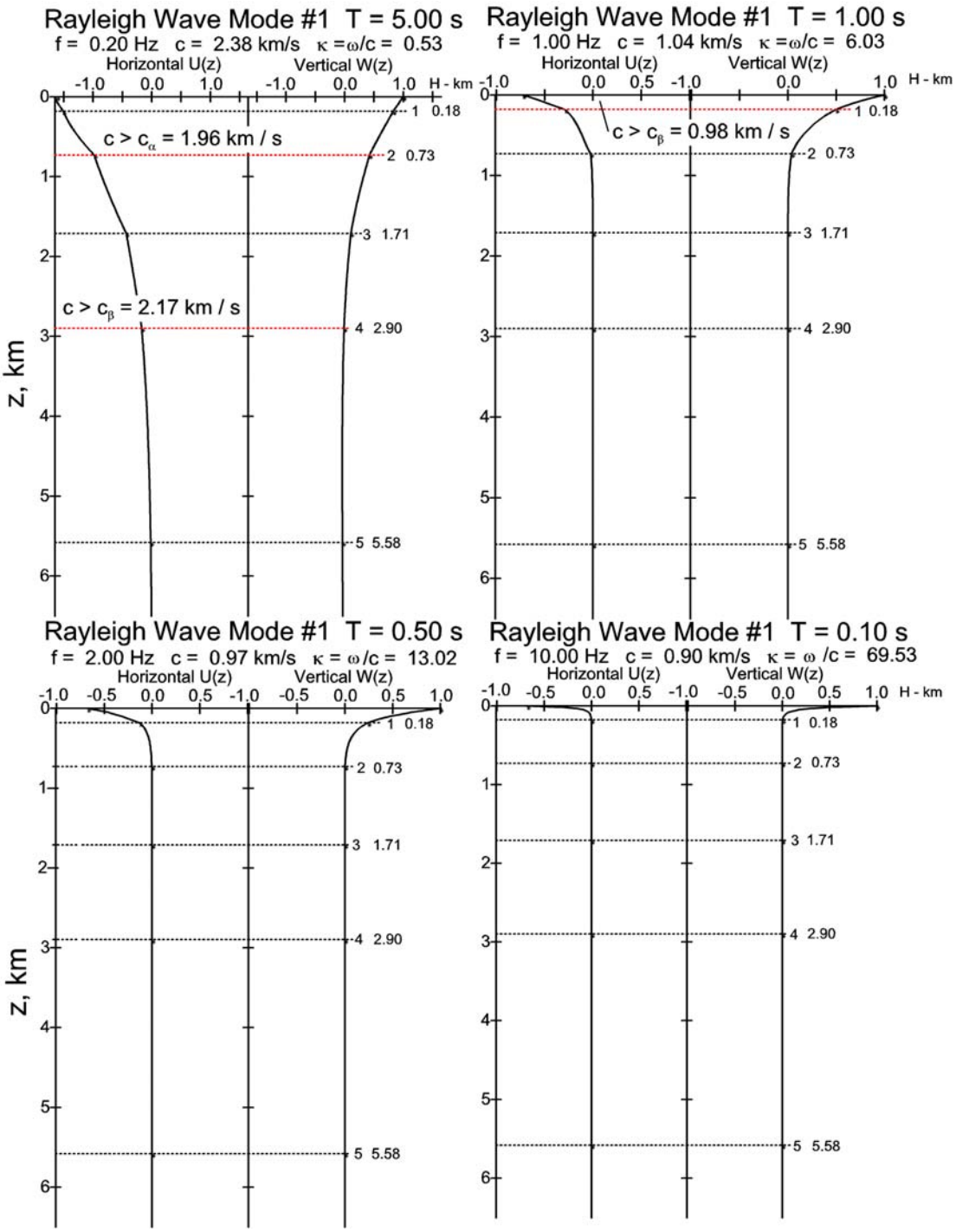

Fig. II.9 Mode#1: *x*- and *z*- Rayleigh Wave Mode Shapes at $\boldsymbol{T = 5,\ 1.0,\ 0.5,\ \text{and}\ 0.1\ s}$

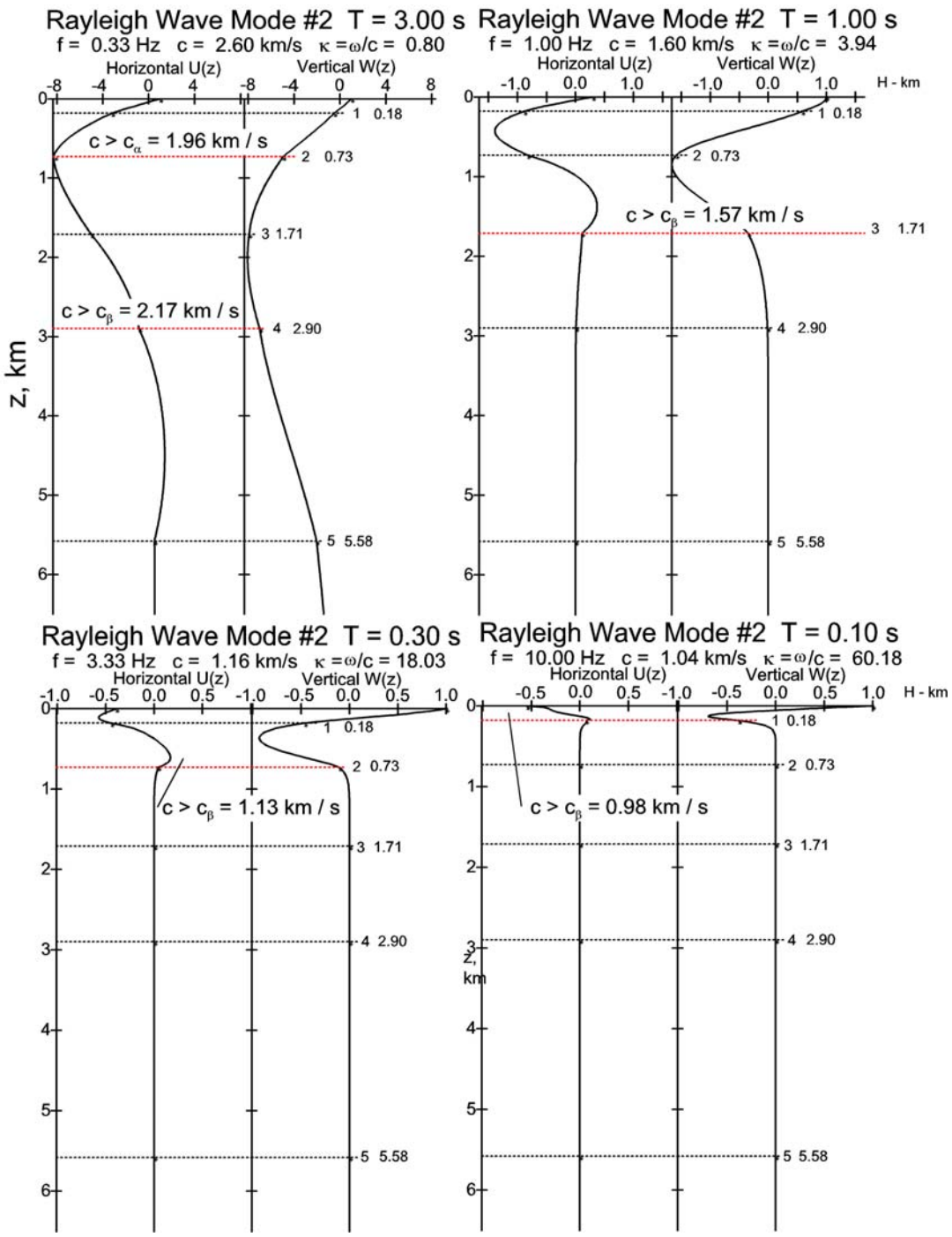

Fig. II.10 Mode#2: *x*-and *z*- Rayleigh Wave Mode Shapes at $\boldsymbol{T = 3,\ 1,\ 0.3,}$ **and 0.1** $\boldsymbol{s}$

Unlike Mode #1, the Mode #2 mode shapes will change sign and cross the zero line before decaying to zero at some depth. The waves at long periods (low frequencies) decay slower with depth than the waves at short periods (high frequencies). Note that at some periods, the mode amplitudes go below -1.0, resulting in larger amplitudes of motions below the surface than at the surface.

The mode shapes for other periods and for Modes #1 to Modes #5 of Rayleigh waves can be perused in the Appendix R2 with Report II.

Fig. II.11 and II.12 illustrate synthetic accelerations for both the horizontal $\boldsymbol{U(z)}$ and vertical $\boldsymbol{W(z)}$ components of motion, calculated for the same El Centro six-layered site model, at 100 depths equally spaced from the surface to almost 6 km below the surface, and for the same earthquake at the same hypocentral distance of $\boldsymbol{D = 10.0\ km}$ and at the same geological and local soil site conditions as for the Love waves described above. The depth of each accelerogram is again labeled at 0.6 km spacing. Six of them are plotted green, and labeled 0 to 5. The one labeled 0 is the accelerogram at the top surface, while the ones labeled 1 to 5 are at depths at or closest to the interfaces between adjacent layers.

For the horizontal (radial) component, the strong-motions are seen at the depths of the first two top layers, up to $\boldsymbol{z \sim 0.7\ km}$. Smaller horizontal motions are observed in the 3rd layer up to $\boldsymbol{z \sim 1.7\ km}$, beyond which depth the motions become small. For the vertical motions, the strong motions are observed in the first three top layers up to $\boldsymbol{z \sim 1.7\ km}$, and the maximum motions are taking place in the 3rd layer from the top. For the transverse component, the motions below the surface in our examples are smaller than those at the surface. For the radial and vertical components in the example considered here, it is seen that the motions for the six-layered model in El Centro, can be larger at depth than at the surface.

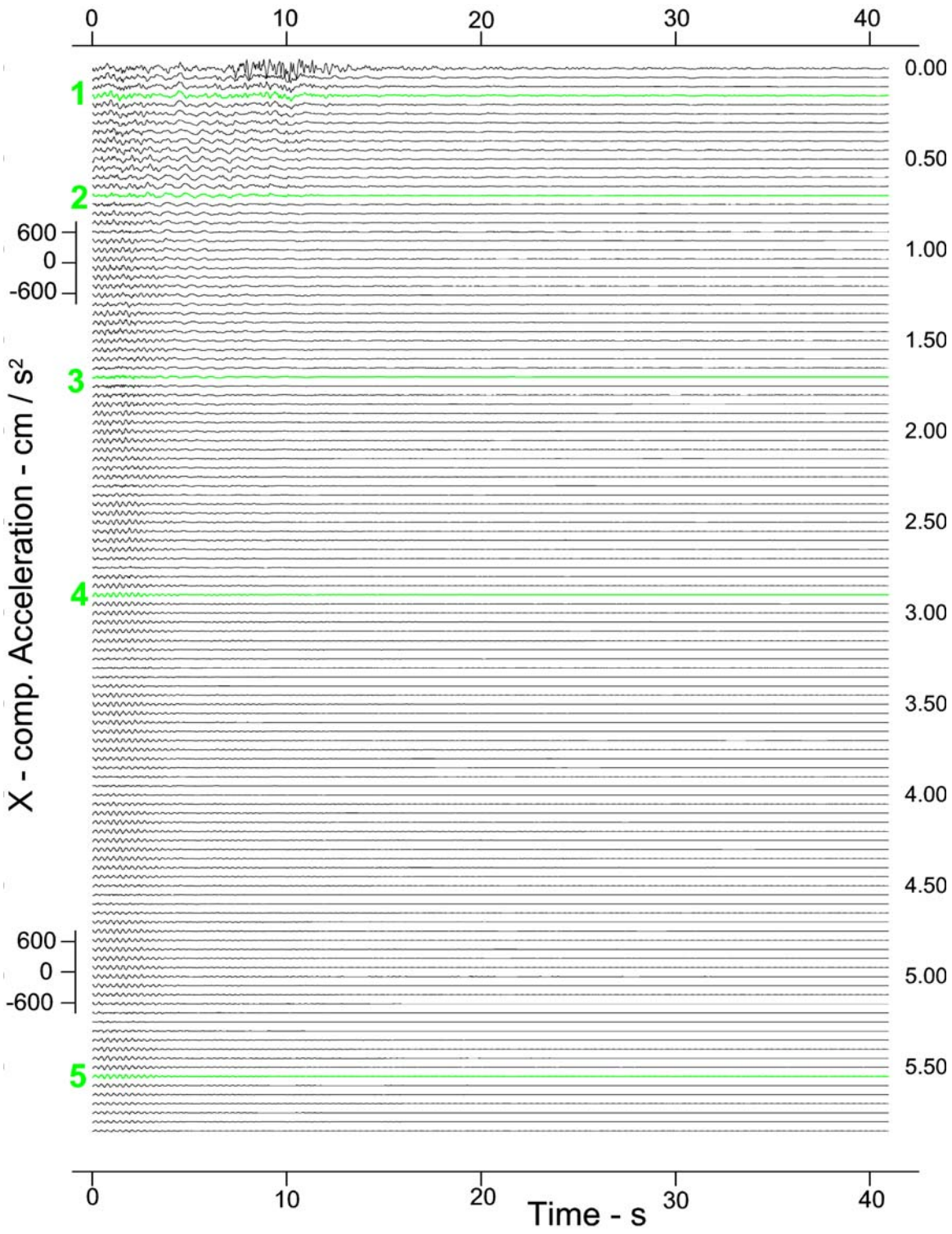

Fig. II.11 Synthetic Acceleration: **M**=6.5, **R**=8.0 km, **H**=6.0 km, **s**=0, **soil**=2
Horizontal (radial) Motions

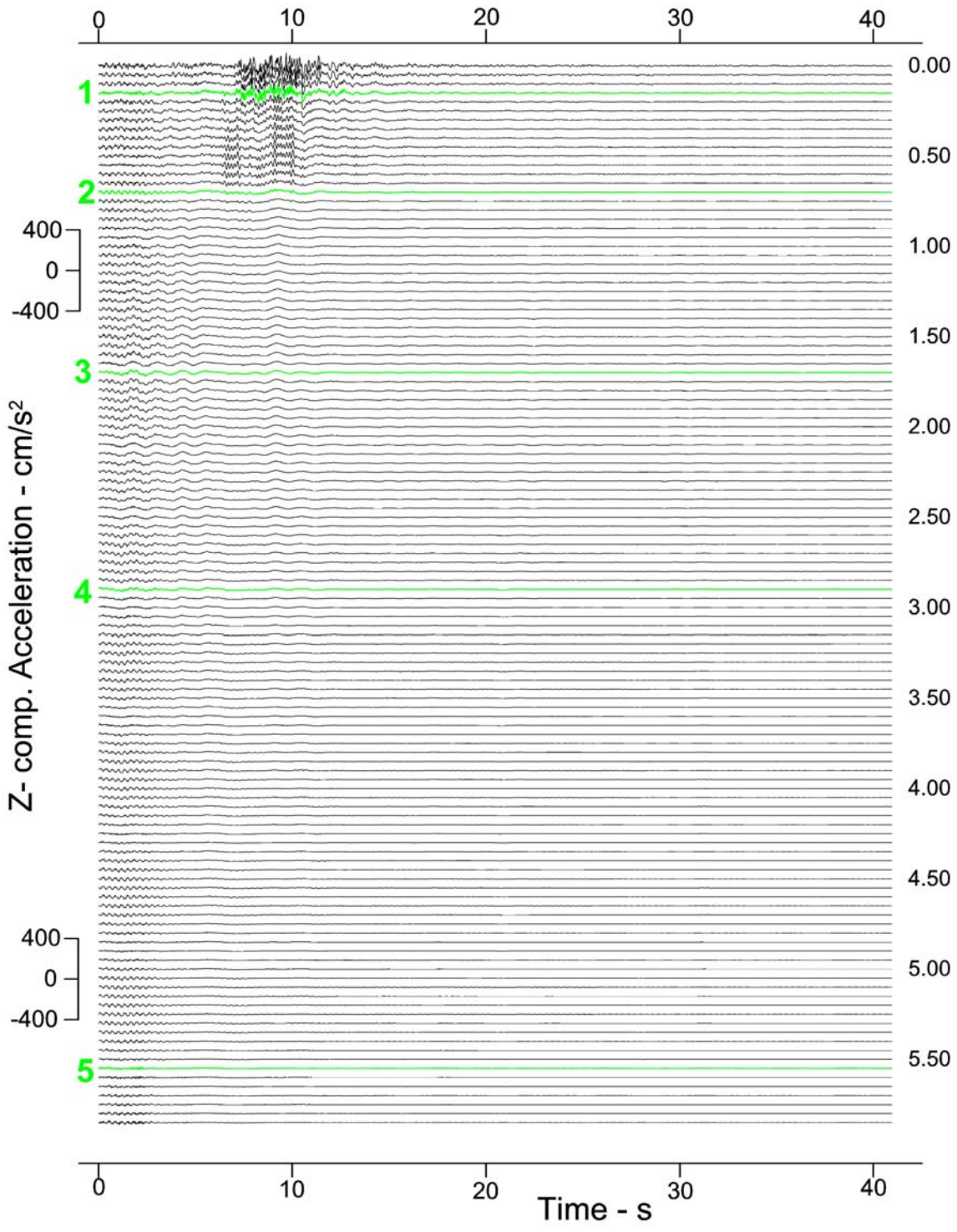

Fig. II.12 Synthetic Acceleration: **M**=6.5, **R**=8.0 km, **H**=6.0 km, **s**=0, **soil**=2
Vertical Motions

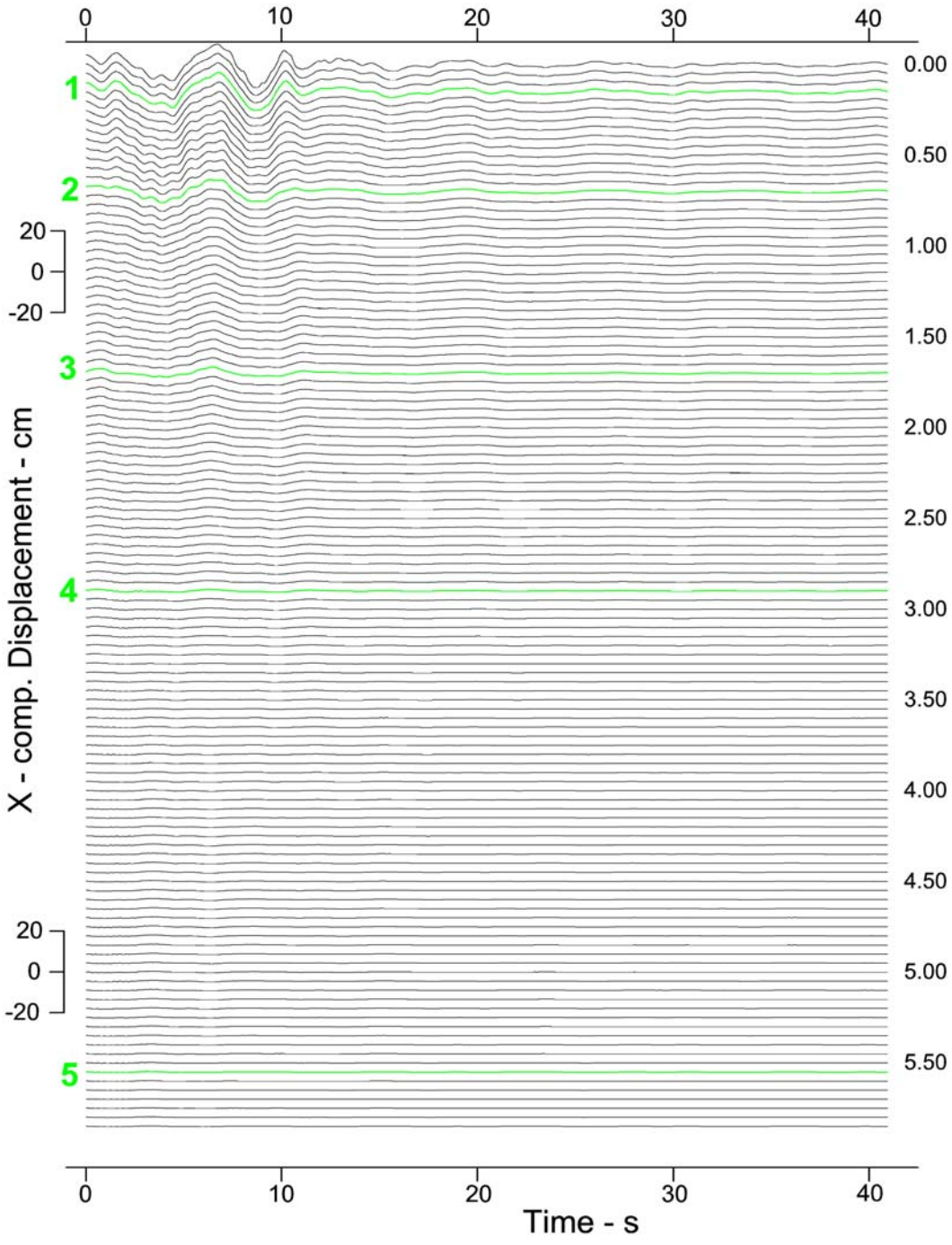

Fig. II.13 Synthetic Displacement: **M**=6.5, **R**=8.0 km, **H**=6.0 km, **s**=0, **soil**=2 Horizontal (radial) Motions.

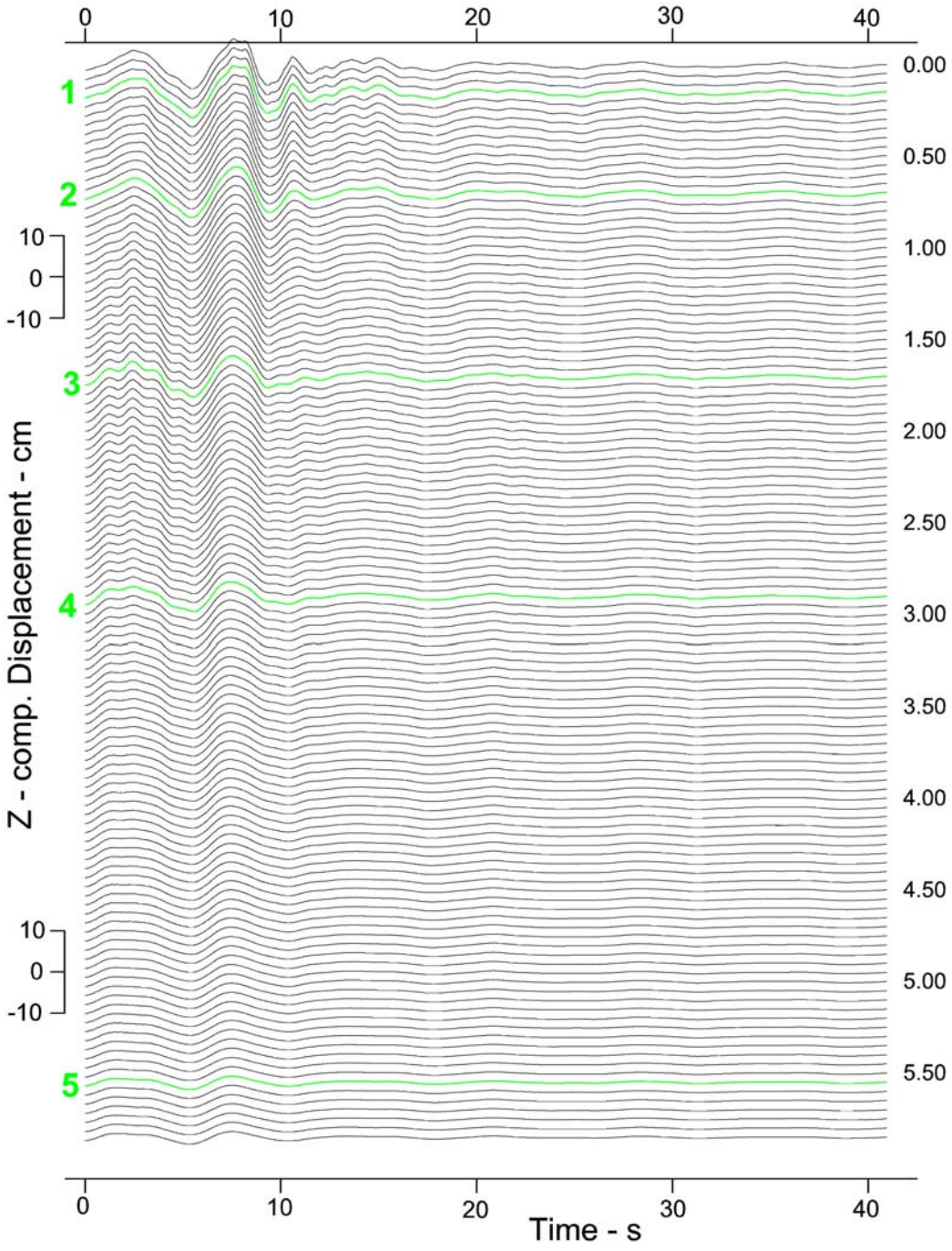

Fig. II.14 Synthetic Displacements: at **M**=6.5, **R**=8.0 km, **H**=6.0 km, **s**=0, **soil**=2
Vertical Motions

This is consistent with the mode shapes of Rayleigh waves in Report II (Appendix R2), where it is found that, for all modes of Rayleigh waves, at this site, at moderate periods, large motions occur in the first three top layers, and then begin to die down at greater depths. The decay of amplitudes with depth is even faster for waves with higher frequencies. For the horizontal component, it is noted that the maximum motions are observed in the 2nd layer, for most periods. For the vertical component, the maximum motions are observed in the 3rd layer.

Fig. II.13 and II.14 show the plots of the corresponding synthetic displacements of the two components of motions. The depth for all displacements is again labeled at intervals of 0.6 km apart. Six are plotted green, and labeled 0 to 5. The one, which is labeled 0 is the displacement at the top surface $\boldsymbol{z = 0}$, while the ones labeled 1 to 5 are those at depths corresponding to or closest to the interfaces between adjacent layers. The new SYNACC program computes the displacements at all depths from the corresponding acceleration time histories in the frequency domain to get the displacement spectra, and then taking the inverse Fourier transform.

The same observations for displacement time histories can be made as for accelerations, namely, the strong-motions dominate in the first three layers of the site model, up to $\boldsymbol{z = 1.7\ km}$. Unlike accelerations, the displacements, especially for the vertical components, do not completely die down even at large depths.

II-6 Synthetic Rotational Motions of Surface and Body Waves On and Below a Layered Media

Starting from the translational component of motions, $\tilde{U} = (U, V, W)$, the rotational components of motion are defined as (Appendix R3):

$$\tilde{\Omega} = \tfrac{1}{2}\tilde{\nabla} \times \tilde{U} = \tfrac{1}{2}\begin{vmatrix} i & j & k \\ \partial/\partial x & \partial/\partial y & \partial/\partial z \\ U & V & W \end{vmatrix} = \tfrac{1}{2}\begin{vmatrix} i & j & k \\ \partial/\partial x & 0 & \partial/\partial z \\ U & V & W \end{vmatrix} \qquad \text{(II.`8)}$$

Since $U = U(x,z)$, $V = V(x,z)$ and $W = W(x,z)$, i.e. all components of motions are dependent only on x and z, with $\partial/\partial y(\ ) = 0$. It then follows that

Rotational Motions are given by: $$\tilde{\Omega} = \begin{pmatrix} \Omega_x \\ \Omega_y \\ \Omega_z \end{pmatrix} = \tfrac{1}{2}\begin{pmatrix} -\partial V/\partial z \\ \partial U/\partial z - \partial W/\partial x \\ \partial V/\partial x \end{pmatrix} \qquad \text{(II.19)}$$

with

$\Omega_x = -\tfrac{1}{2}\partial V/\partial z$ = **Out-of--plane Rocking** component of the Love and body ***SH*** waves propagating in the x-direction,

$\Omega_y = \tfrac{1}{2}\left(\partial U/\partial z - \partial W/\partial x\right)$ = **In-plane Rocking** component of the Rayleigh and body ***P, SV*** waves in the ***x-z*** plane,

$\Omega_z = \tfrac{1}{2}\partial V/\partial x$ = **Out-of--plane Torsional** rotation about z-axis, caused by the Love and body ***SH*** waves

As for the Torsional and Rocking accelerograms (Lee and Trifunac, 1985,87, Todorovska et al, 2013) at the half-space surface, we can now also compute the 1st and 2nd time derivatives of the **Torsional** and **Rocking** motions to obtain the Torsional and Rocking velocities and acceleration time-histories at points below the half-space surface in the layered medium.

Torsional and **Rocking Velocities:**

$$\frac{\partial \Omega}{\partial t} = \begin{pmatrix} \dot{\Omega}_x \\ \dot{\Omega}_y \\ \dot{\Omega}_z \end{pmatrix} = \frac{1}{2} \begin{pmatrix} -\partial \dot{V} / \partial z \\ \partial \dot{U} / \partial z - \partial \dot{W} / \partial x \\ \partial \dot{V} / \partial x \end{pmatrix} \tag{II.20}$$

Torsional and **Rocking Accelerations:**

$$\frac{\partial^2 \Omega}{\partial t^2} = \begin{pmatrix} \ddot{\Omega}_x \\ \ddot{\Omega}_y \\ \ddot{\Omega}_z \end{pmatrix} = \frac{1}{2} \begin{pmatrix} -\partial \ddot{V} / \partial z \\ \partial \ddot{U} / \partial z - \partial \ddot{W} / \partial x \\ \partial \ddot{V} / \partial x \end{pmatrix} \tag{II.21}$$

The computation of the 1st and 2nd time derivatives of the Torsional and Rocking motions is not difficult. This is because, as for Torsional and Rocking (Lee and Trifunac, 1985,87; Todorovska et al, 2013) accelerograms at the half-space surface, the Torsional and Rocking accelerations can be computed, in the frequency domain, directly, as d/dx and d/dz derivatives, from the corresponding translational acceleration components, as described in Report III (Appendix R3), and from which the Torsional and Rocking velocity, and Torsional and Rocking displacements can then also be computed in the frequency domain.

Similarly the strain components of motions are given by the symmetric matrix:

$$[\varepsilon] = \begin{bmatrix} \varepsilon_x & \varepsilon_{xy} & \varepsilon_{xz} \\ \varepsilon_{yx} & \varepsilon_y & \varepsilon_{yz} \\ \varepsilon_{zx} & \varepsilon_{zy} & \varepsilon_z \end{bmatrix} = \begin{bmatrix} \partial U/\partial x & \frac{1}{2}\left(\cancel{\partial U/\partial y} + \partial V/\partial x\right) & \frac{1}{2}\left(\partial U/\partial z + \partial W/\partial x\right) \\ \varepsilon_{yx} & \cancel{\partial V/\partial y} & \frac{1}{2}\left(\partial V/\partial z + \cancel{\partial W/\partial y}\right) \\ \varepsilon_{zx} & \varepsilon_{zy} & \partial W/\partial z \end{bmatrix} \tag{II.22}$$

again with all components of motion being dependent only on x and z, and with $\partial/\partial y(\ ) = 0$. Thus

$$[\varepsilon]=\begin{bmatrix}\varepsilon_x & \varepsilon_{xy} & \varepsilon_{xz}\\ \varepsilon_{yx} & \varepsilon_y & \varepsilon_{yz}\\ \varepsilon_{zx} & \varepsilon_{zy} & \varepsilon_z\end{bmatrix}=\begin{bmatrix}\partial U/\partial x & \frac{1}{2}\partial V/\partial x & \frac{1}{2}\left(\partial U/\partial z+\partial W/\partial x\right)\\ \varepsilon_{yx} & 0 & \frac{1}{2}\partial V/\partial z\\ \varepsilon_{zx} & \varepsilon_{zy} & \partial W/\partial z\end{bmatrix} \qquad \text{(II.23)}$$

Taking symmetry into account, five out of six components of the strain matrix exist, with the only component of strain that vanishes everywhere being ε_y, the normal strain in the anti-plane *y*- direction. Note that, when strain is calculated at the half-space surface (Lee, 1990), the shear strain $\varepsilon_{xz}=0$, since the corresponding shear stress $\tau_{xz}=2\mu\varepsilon_{xz}=0$ at the half-space surface.

In exactly the same way as the computation of the Torsional and Rocking accelerograms in Equations (II.20) and (II.21) above, one can also compute the first and second time derivatives of the strain matrix to obtain the strain acceleration time histories at points below the half-space surface inside the layered medium:

Strain velocities:

$$\frac{d}{dt}[\varepsilon]=[\dot{\varepsilon}]=\begin{bmatrix}\dot{\varepsilon}_x & \dot{\varepsilon}_{xy} & \dot{\varepsilon}_{xz}\\ \dot{\varepsilon}_{yx} & \dot{\varepsilon}_y & \dot{\varepsilon}_{yz}\\ \dot{\varepsilon}_{zx} & \dot{\varepsilon}_{zy} & \dot{\varepsilon}_z\end{bmatrix}=\begin{bmatrix}\partial \dot{U}/\partial x & \frac{1}{2}\partial \dot{V}/\partial x & \frac{1}{2}\left(\partial \dot{U}/\partial z+\partial \dot{W}/\partial x\right)\\ \dot{\varepsilon}_{yx} & 0 & \frac{1}{2}\partial \dot{V}/\partial z\\ \dot{\varepsilon}_{zx} & \dot{\varepsilon}_{zy} & \partial \dot{W}/\partial z\end{bmatrix} \qquad \text{(II.24)}$$

and **Strain accelerations:**

$$\frac{d^2}{dt^2}[\varepsilon]=[\ddot{\varepsilon}]=\begin{bmatrix}\ddot{\varepsilon}_x & \ddot{\varepsilon}_{xy} & \ddot{\varepsilon}_{xz}\\ \ddot{\varepsilon}_{yx} & \ddot{\varepsilon}_y & \ddot{\varepsilon}_{yz}\\ \ddot{\varepsilon}_{zx} & \ddot{\varepsilon}_{zy} & \ddot{\varepsilon}_z\end{bmatrix}=\begin{bmatrix}\partial \ddot{U}/\partial x & \frac{1}{2}\partial \ddot{V}/\partial x & \frac{1}{2}\left(\partial \ddot{U}/\partial z+\partial \ddot{W}/\partial x\right)\\ \ddot{\varepsilon}_{yx} & 0 & \frac{1}{2}\partial \ddot{V}/\partial z\\ \ddot{\varepsilon}_{zx} & \ddot{\varepsilon}_{zy} & \partial \ddot{W}/\partial z\end{bmatrix} \qquad \text{(II.25)}$$

The computation of the 1st and 2nd time derivatives of the strain motions is not difficult. This is because, as in the case of Torsional and Rocking (Lee and Trifunac, 1985,87; Todorovska et al, 2013) accelerograms and the strains (Lee 1990) at the half-space surface, the strain accelerations can again first computed, in the frequency domain,

directly, as d/dx and d/dz derivatives, from the corresponding translational acceleration components, as given in Report III (in Appendix R3), and from which the strain velocity, and strain displacement motions can then also be computed in the frequency domain.

Finally, as in Trifunac (1990), the curvatures in the vertical, transverse and radial directions are respectively given by:

Vertical:
$$k_2(t) = \frac{\partial^2 u_2 / \partial x_1^2}{\left[1 + \left(\partial u_2 / \partial x_1\right)^2\right]^{3/2}} \approx \partial^2 u_2 / \partial x_1^2 = \frac{\ddot{u}_2}{c^2} \qquad \text{(II.26)}$$

Transverse:
$$k_3(t) \approx \partial^2 u_3 / \partial x_1^2 = \frac{\ddot{u}_3}{c^2} \qquad \text{(II.27)}$$

and

Radial:
$$k_1(t) \approx \partial^2 u_1 / \partial x_1^2 = \frac{\ddot{u}_1}{c^2} \qquad \text{(II.28)}$$

Those are all computed directly from the translational components, the numerical implementation of which is summarized in the next section.

The numerical procedure for computing the d/dx and d/dz derivatives of the corresponding translational motions will follow much along the same line as that of the corresponding translational motions described above. This allows the mode shapes of the rotational, strain and curvature components of both Rayleigh and Love surface waves, and of the body P, SV and SH waves, to be computed, as for the translational components.

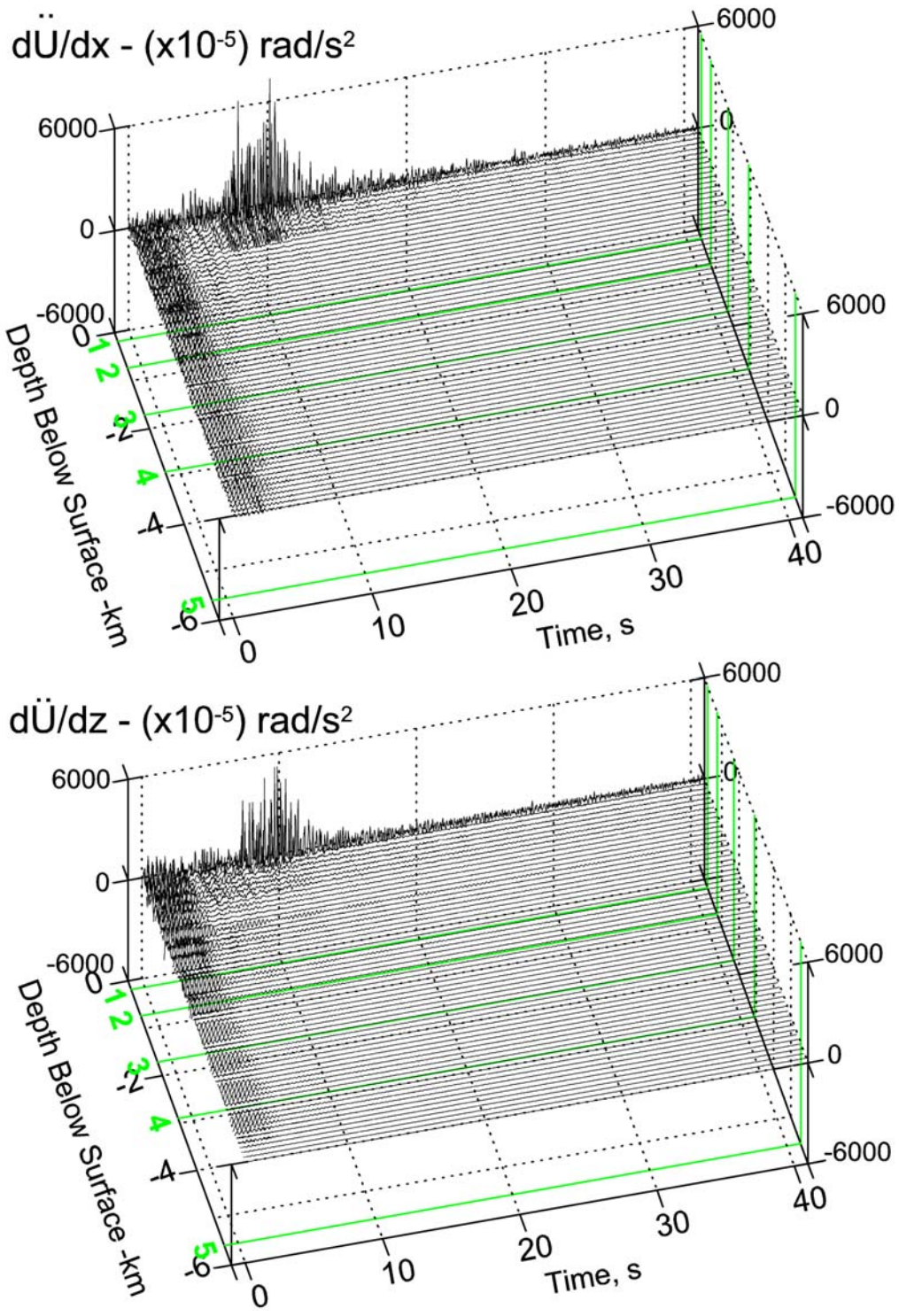

Fig. 15a. Synthetic Rotational Acceleration: $\boldsymbol{M = 6.5,\ R = 8.0\ km,\ H = 6.0\ km,\ s = 0,\ s_L = 2}$

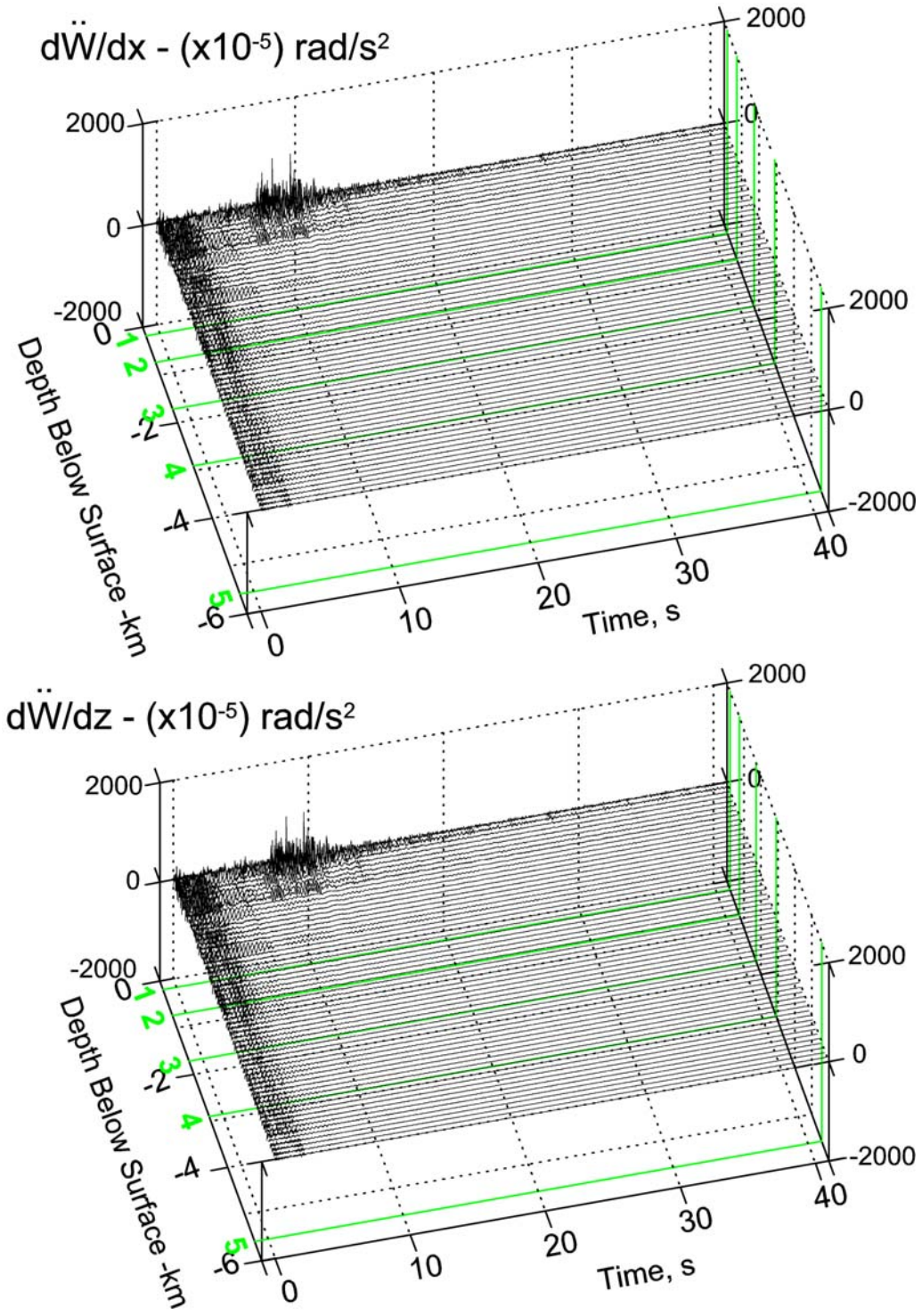

Fig. 15b.Synthetic Rotational Acceleration: $\boldsymbol{M = 6.5,\ R = 8.0\ km,\ H = 6.0\ km,\ s = 0,\ s_L = 2}$

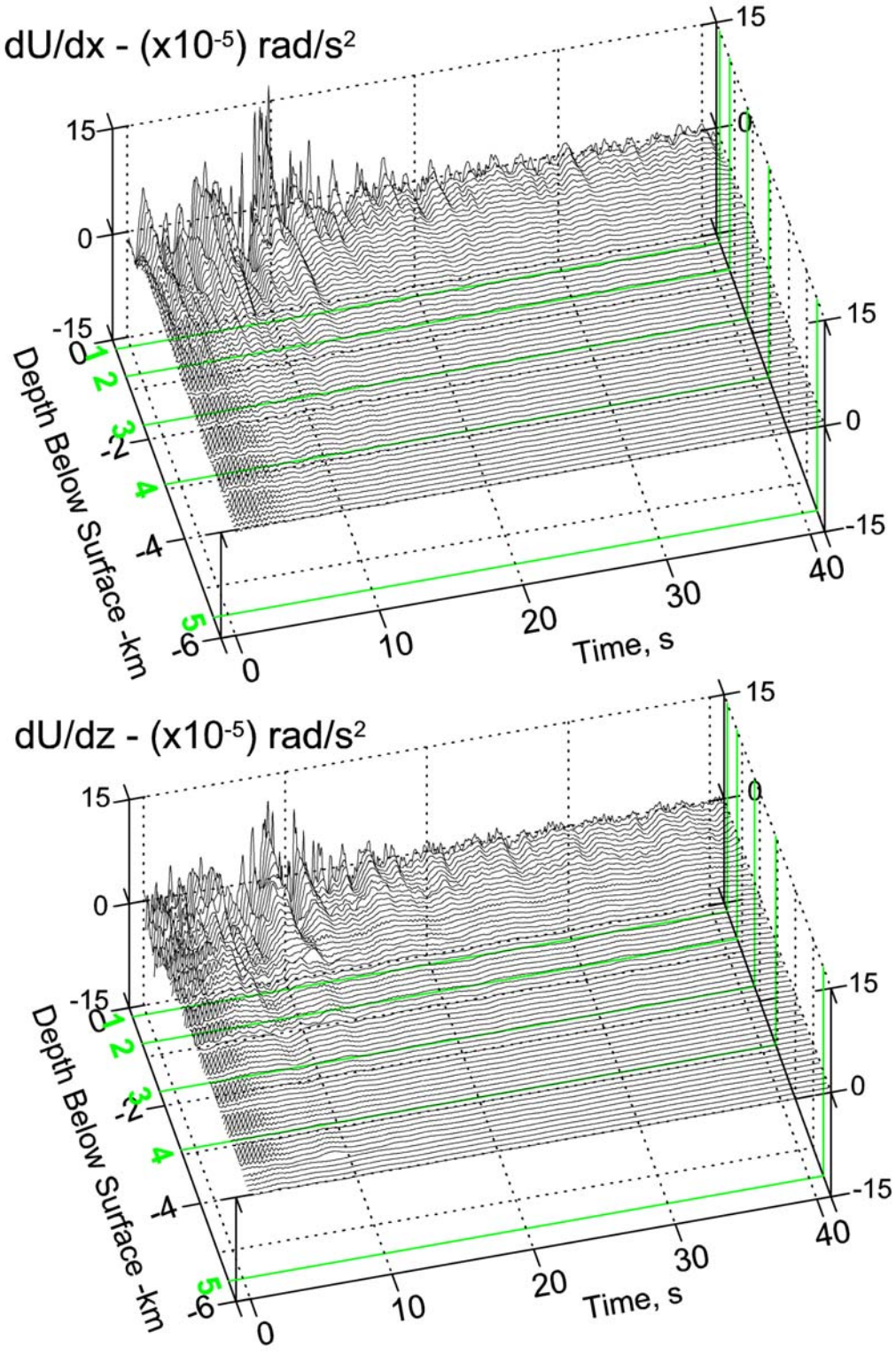

Fig. 16a. Synthetic Rotational Displacement: $\boldsymbol{M = 6.5,\ R = 8.0\ km,\ H = 6.0\ km,\ s = 0,\ s_L = 2}$

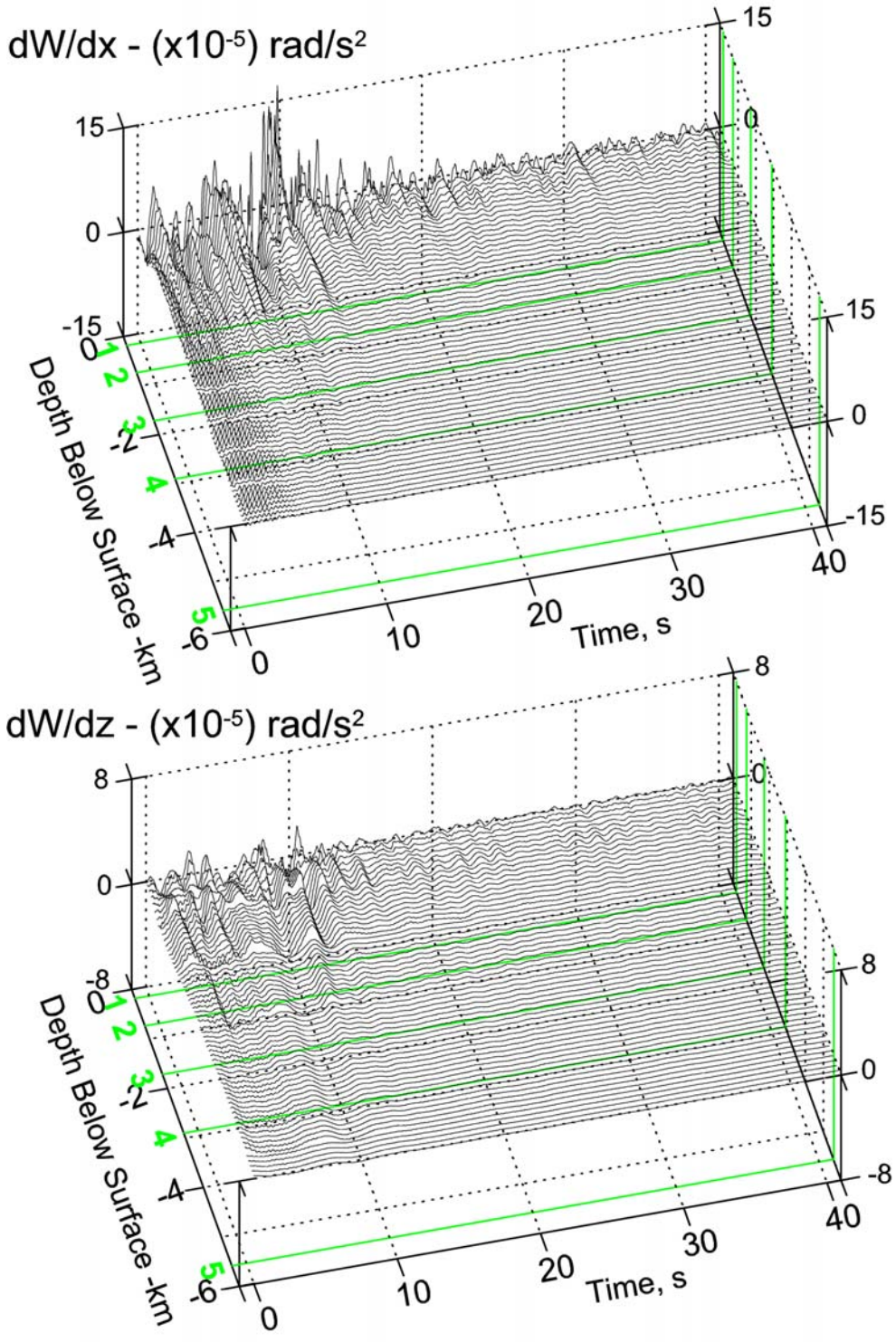

Fig. 16b Synthetic Rotational Displacement: $\boldsymbol{M = 6.5,\ R = 8.0\ km\ \&\ H = 6.0\ km,\ s = 0,\ s_L = 2}$

Figures II.15a and b show the 3-D plots of synthetic rotational accelerations of the horizontal (radial) and vertical components of motion for the same 120 acceleration translational time histories corresponding to the 2-D representations in Figure II.11 and 12. Figures II.16a and b show the 3-D views of the rotational displacement respectively for the horizontal and vertical components corresponding to the 2-D plots of the translational components of motion in Figures II.13 and II.14.

For the radial and vertical rotational components in the example considered here, it is observed that for the six-layered model in Imperial Valley at El Centro site, large rotational motions are observed only on and near the surface. This is consistent with the rotational mode shape of Rayleigh waves in the last chapter, where it is found that, for all modes of Rayleigh waves, at moderate periods, large motions occur in the first two top layers, and then began to die down at greater depths. The decay of amplitudes with depth is even faster for waves with higher frequencies. The same is true of the transverse rotational motions.

References

Haskell, N.A. (1953). The Disperson of Surface waves on Multilayered Media, *Bull Seismol. Soc. Am., 43, 17-34.*

Lee, V.W. (2002). Empirical Scaling of Strong Earthquake Ground Motion: Part I: Attenuation and Scaling of Response Spectra, *ISET J. Earthquake Technology, 39(4), 219–254*.

Liu, T. (2010). Efficient Reformulation of the Thomson-Haskell Method for Computation of Surface Waves in Layered Half-Space, *Short Note, Bull Seismol. Soc. Am.,* 100(5A), *2310-2316.*

Thomson, W.T. (1950) Transmission of Elastic Waves Through a Stratified Solid Media, *J. Appl. Phys. 21, 89-93.*

Todorovska, M.I., Trifunac, M.D. Lee, V.W. and Orbović, N. (2013). Synthetic Earthquake Ground Motions on an Array, *Soil Dynamics and Earthquake Engineering, 48,* 234-251.

Trifunac, M.D. (1971). A Method for Synthesizing Realistic Strong Ground Motion, *Bull. Seism. Soc. Amer., 61, 1755-1770*.

Wong, H.L. and Trifunac, M.D. (1978). Synthesizing Realistic Strong Motion

Accelerograms, *Report **CE** 78-07, Dept. of Civil Eng.,* Univ. of Southern California, Los Angeles, California, U.S.A.

Wong, H.L. and Trifunac, M.D. (1979). Generation of Artificial Strong Motion Accelerograms, *Earthquake Engineering Structural Dynamics, **7**, 509-527.*

Chapter 3 Scattering and Diffraction of Earthquake Motions in Irregular Elastic Layers, I: Love and SH Waves

Summary

We describe the wave propagation through an irregularly layered, elastic medium for incoming body (SH) and surface (Love) waves. As a result of irregular geometry, each layer generates additional waves by scattering and diffraction. These additional waves modify the input motions and locally may lead to larger motions and concentrations of stresses, strains, and rotations on or below the ground surface. For engineering design, and in particular for analyses of soil-structure interaction, it is important to understand the nature and the consequences of such motions.

The scattering and diffraction of Love and SH waves by irregular layers will be investigated by the weighted-residuals method. The scattered and diffracted mode shapes and spectral amplification characteristics at different frequencies will be examined and discussed.

I. Introduction

I.1 General Introduction

Two-dimensional site response to incident earthquake waves in irregularly layered stratum can be evaluated by numerical models based on finite elements or finite differences, but the response calculated by analytical methods combined with the weighted-residues method provides a valuable baseline reference to validate the results from the numerical approach (Vai et al., 1999). Finite numerical models have boundaries that require special attention in which the waves propagate inside and outside of the modeled space without significant changes, so that the comparison with the analytical solution becomes a valuable verification tool.

In this chapter, we study the elastic, layered medium for incidence of out-of-plane surface (Love) and body (SH) waves. We will study the motions at points on and below the half-space surface, in the vicinity of the irregularly shaped elastic layers.

I.2 Ground Motion On and Below a Site With Irregular Topography and Irregular Layer Thickness

The seismic ground motion of a layered medium with irregular topography has been studied in both seismology and earthquake engineering. Aki and Larner (1970) applied analytical methods to evaluate the site response of an irregular, layered medium for incident plane SH waves, and Kohketsu (1987a,b) extended the study to a multi-layered medium. Chen (1990, 1993, 1995), and Kohketsu et al. (1991) used the Aki-Larner method to generate synthetic seismograms for seismological study of regional topography effects. Chen (1999) investigated the modal solutions and excitation of Love waves in multi-layered media with irregular interfaces. Lee & Wu (1994a,b) used the weighted-residual method to study motions near an irregular canyon.

II. Love Surface and Body SH Waves On and Below the Surface of an Elastic, Layered Medium

Elastic-wave motion in *N*-Layered half space can be formulated in terms of the approach proposed by Thomson (1950) and Haskel (1953). For the waves incident from the left, consider the model shown in Fig. III.1 below.

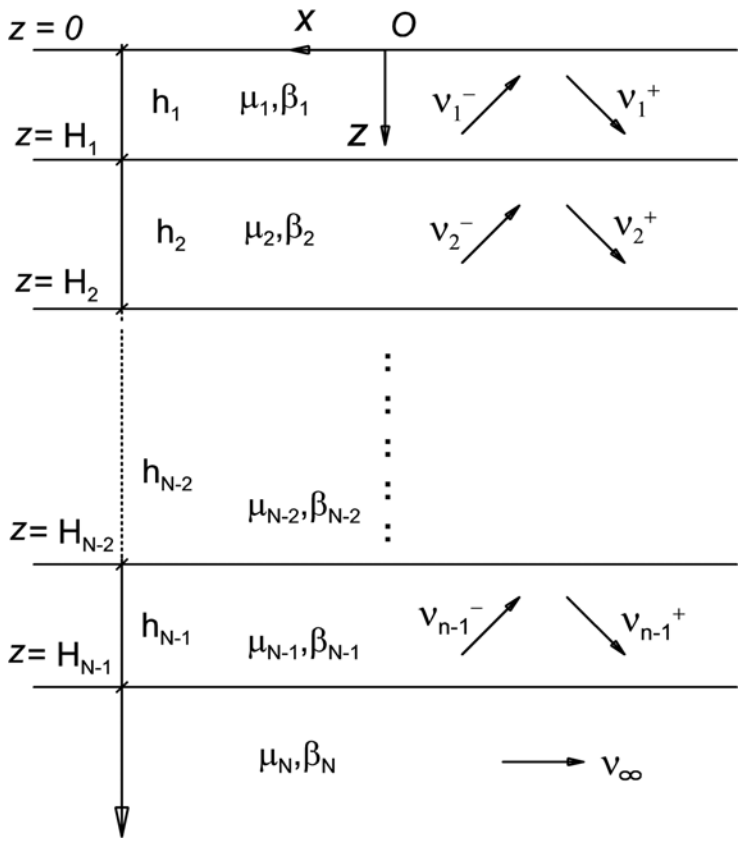

Fig. III.1. N-layered half space with Love waves.

For each of these l regular layers, with $l = 1, \ldots, N$, the displacement of the Love surface waves at each frequency ω takes the following form (in the anti-plane, y-component direction):

$$v_1^-,\ v_1^+ : \qquad \begin{aligned} v_l^- &= C_l^- e^{ik\left(x-\gamma_l z\right)} e^{-i\omega t} \\ v_l^+ &= C_l^+ e^{ik\left(x+\gamma_l z\right)} e^{-i\omega t} \end{aligned} \quad . \tag{III.1}$$

The harmonic term $e^{-i\omega t}$ is present in all of the wave terms, and it will be understood and omitted in all subsequent equations.

Those are, respectively, the upward- and downward-propagating waves in the l^{th} layer, where $k = k(\omega) = \omega / c(\omega)$ is the horizontal wave number at frequency ω and phase velocity $c = c(\omega)$. The term e^{ikx}, which is also the same in each layer, is the horizontal component of the waves, which together with the time-harmonic term $e^{i\omega t}$ corresponds to the waves propagating in

the **–ve** x direction. The terms $e^{\mp ik\gamma_l y}$ are the vertical components of the waves with the negative term propagating upward (**–ve** y) and the positive term propagating downward (y). We define $\gamma_l = \gamma_l(\beta_l)$ by

$$\gamma_l = \frac{\left(k_{\beta_l}^2 - k^2\right)^{1/2}}{k} = \left(\left(k_{\beta_l}/k\right)^2 - 1\right)^{1/2} = \left(\left(c/\beta_l\right)^2 - 1\right)^{1/2}, \tag{III.2}$$

so that $k\gamma_l$ is then the vertical wave number of the waves in the l^{th} layer of the medium with shear wave velocity β_l. In most cases, the wave velocities increase as one moves down through the layers, so that $\beta_1 < \beta_2 < \ldots < \beta_n < \beta$, with the semi-infinite half-space layer at the bottom having the highest shear-wave speed β. With $c = c(\omega)$, the wave speeds of the surface Love waves, $c < \beta$, and the surface waves take the form

$$v_\infty = C_\infty e^{ik(x - \gamma z)} = C_\infty e^{ikx - k\bar{\gamma} z}, \tag{III.3}$$

where

$$\bar{\gamma} = \frac{\left(k^2 - k_\beta^2\right)^{1/2}}{k} = \left(1 - \left(k_\beta/k\right)^2\right)^{1/2} = \left(1 - \left(c/\beta\right)^2\right)^{1/2}, \tag{III.4}$$

where $\bar{\gamma}$ is the complement of γ and is real, which means that the term $e^{ikx - k\bar{\gamma} y}$ corresponds to a surface wave with an amplitude that is exponentially decaying with depth (in y). With β_l, the shear-wave speed in the l^{th} layer, and $c = c(\omega)$, the Love-wave speed and also the (horizontal) phase velocity of the waves in each layer above the half space (Fig. III.1), we can have $c \geq \beta_l$ or $c < \beta_l$. If $c \geq \beta_l$, the term $\gamma_l = \gamma_l(\beta_l)$ in Eq. (III.2) is real, and both waves v_l^+ and v_l^- in Eq. (1) will correspond to harmonic plane waves. If, however, $c < \beta_l$, then from Eq. (III.2) we have the following:

$\gamma_l = \left(\left(c/\beta_l\right)^2 - 1\right)^{1/2}$ is imaginary, and $\bar{\gamma}_l = \left(1 - \left(c/\beta_l\right)^2\right)^{1/2}$ is real. (III.5)

III. Love and Body SH Waves Incident to Irregularly Layered, Elastic Medium

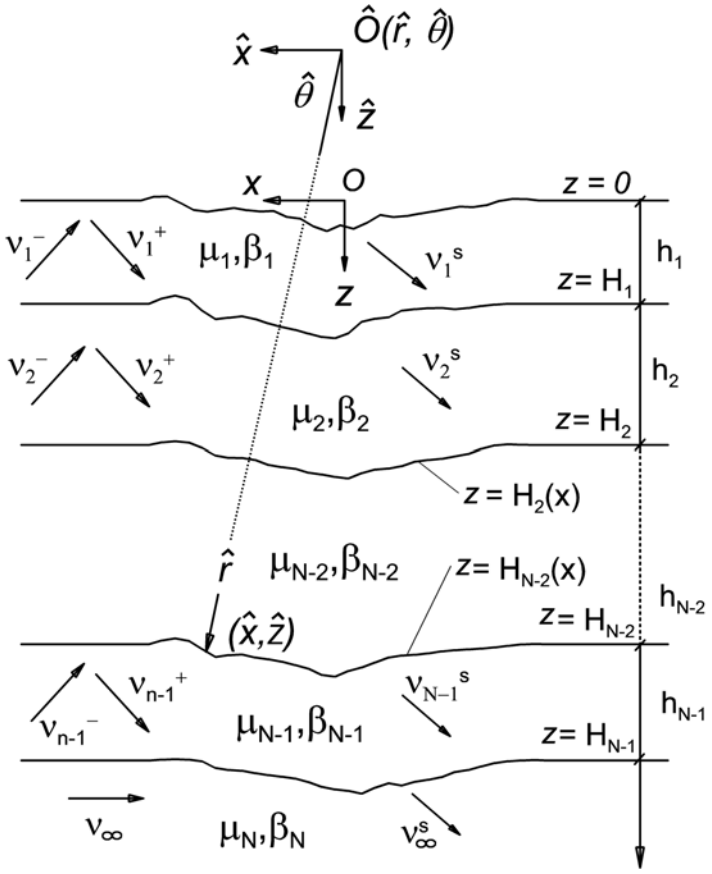

Fig. III.2. Irregularly-shaped, N-layered half space with Love waves.

The previous section described out-of-plane Love waves propagating along an *N*-layered half space, where the layers are perfectly flat and parallel. Consider next the case in which this is not so. Figure III.2 shows a model in which the parallel layers are not flat in some finite region but are flat elsewhere. Chen (1990) applied a method for seismogram synthesis in multi-layered media with irregular topography over a half space for waves incident from an arbitrary source. Later, a method called "global generalized reflection/transmission matrices method" (GGRTM) was developed for two-dimensional SH waves (Chen 1990, 1995) and two-dimensional P and SV waves, and for studying these waves in detail to get an alternative version for the classical theory of Love waves in a laterally homogeneous, multi-layered medium (Chen 1999).

A boundary-integral formulation was applied in the analysis of the two-dimensional, irregularly layered, elastic media by Sanchez-Sesma and Campillo (1991). Further applications to alluvial valleys for incident P, SV, and Rayleigh waves were presented by Sanchez-Sesma and Campillo (1993), and the methodology called the "indirect-boundary-element method" (IBEM) to simulate the elastic wave propagation in two-dimensional, irregularly layered media was presented by Vai et al. (1999).

Turning back to Fig. III.2, without loss of generality we will assume that each of these irregular surfaces at each interface between the l^{th} and $(l+1)^{th}$ layers, which extends from $x=-\infty$ to $x=+\infty$, can be represented by a curve $z=H_l(x)$ along the interface. We assume that this curve will be the flat surface $z=H_l$ almost everywhere but that it will deviate from the flat surface within some finite region in which it is defined numerically by a set of points (x_i, z_i). The same curve can also be represented in polar coordinates $(\hat{r},\hat{\theta})$, with $\hat{r}=\hat{r}(\hat{\theta})$ in a common coordinate system $(\hat{x},\hat{z})$ with origin at some point $\hat{O}$, above the half space in this example, as shown in Fig. III.2.

With the surface Love waves v_l^-, v_l^+ or body SH waves at each layer l incident to these irregular surfaces, additional scattered waves will be generated, which can be represented by

$$v_l^s=\sum_{n=0}^{\infty}\left(A_{l,n}^{(1)}H_n^{(1)}(k_l\hat{r})+A_{l,n}^{(2)}H_n^{(2)}(k_l\hat{r})\right)\cos n\theta\ , \qquad \text{(III.6a)}$$

with both outgoing and incoming waves (relative to $\hat{O}$ for each layer $l=1,2,\ldots,N-1$, except for the last semi-infinite layer. For this layer, $l=N$, and the scattered wave, $v_\infty^s=v_N^s$ takes the form

$$v_\infty^s=v_N^s=\sum_{n=0}^{\infty}A_{\infty,n}H_n^{(1)}(k\hat{r})\cos n\theta\ , \qquad \text{(III.6b)}$$

with only outgoing waves satisfying Somerfield's radiation condition at infinity. Here, the wave terms in the scattered waves in all layers use only the cosine functions, as the range of θ in each layer is the half range from 0 to π, where the sine and cosine functions are not orthogonal and only the cosine functions are enough to form an orthogonal set of functions (Lee & Liu 2014).

The scattered waves, together with the free-field surface Love waves, form the complete motion in the layered media. Writing $\boldsymbol{v}_l^{ff} = \boldsymbol{v}_l^{+} + \boldsymbol{v}_l^{-}$ as the free-field surface Love or Body SH waves in the l^{th} medium, the resultant wave in the same medium is $\boldsymbol{v}_l = \boldsymbol{v}_l^{ff} + \boldsymbol{v}_l^{s}$, which, together, must satisfy the following set of boundary conditions (Lee and Wu, 1994a):

1) On the half-space surface, $\boldsymbol{z = H_0(x)}$, so the resultant waves in the top layer $\boldsymbol{(l = 1)}$ must together satisfy the half-space surface free-field stress condition:

$$\tau_{nt} = \mu_1 \frac{\partial v_1}{\partial \hat{n}} = \mu_1 \frac{\partial \left(v_1^{ff} + v_1^{s} \right)}{\partial \hat{n}} = 0, \tag{III.7a}$$

or

$$\frac{\partial v_1^{s}}{\partial \hat{n}} = -\frac{\partial v_1^{ff}}{\partial \hat{n}} \ . \tag{III.7b}$$

2) For $\boldsymbol{l = 1, 2, \ldots, N-1}$, at the interface between the $\boldsymbol{l^{th}}$ layer and the $\boldsymbol{(l+1)^{th}}$ layer below, and $\boldsymbol{z = H_l(x)}$, so the resultant waves in these two layers must satisfy the continuity of displacement and stress at the interface as follows:

$$\boldsymbol{v_l = v_l^{ff} + v_l^{s} = v_{l+1}^{ff} + v_{l+1}^{s} = v_{l+1}} \tag{III.8a}$$

or

$$\boldsymbol{v_l^{s} - v_{l+1}^{s} = -\left(v_l^{ff} - v_{l+1}^{ff} \right)} \tag{III.8b}$$

$$\begin{aligned} \mu_l \frac{\partial v_l}{\partial \hat{n}} &= \mu_{l+1} \frac{\partial v_{l+1}}{\partial \hat{n}} \\ \mu_l \frac{\partial \left(v_l^{ff} + v_l^{s} \right)}{\partial \hat{n}} &= \mu_{l+1} \frac{\partial \left(v_{l+1}^{ff} + v_{l+1}^{s} \right)}{\partial \hat{n}} \\ \text{or} \qquad \mu_l \frac{\partial v_l^{s}}{\partial \hat{n}} - \mu_{l+1} \frac{\partial v_{l+1}^{s}}{\partial \hat{n}} &= -\left(\mu_l \frac{\partial v_l^{ff}}{\partial \hat{n}} - \mu_{l+1} \frac{\partial v_{l+1}^{ff}}{\partial \hat{n}} \right), \end{aligned} \tag{III.9}$$

with the unknown wave functions on the left-hand side and the known functions on the right-hand side. Here, in Eqs. (III.3) and (III.5), $\hat{\boldsymbol{n}}$ is the normal at a boundary point (x, z), where $\boldsymbol{z = H_l(x)}$, and $\frac{\partial}{\partial \hat{n}}(\ )$ is the corresponding normal derivative of the wave functions given by

$$\frac{\partial}{\partial \hat{n}}(\ ) = \tilde{\nabla}(\ ) \cdot \hat{n} = \cos\alpha \frac{\partial}{\partial r}(\ ) + \frac{\sin\alpha}{r} \frac{\partial}{\partial \theta}(\ ), \tag{III.10a}$$

where α is the angle that the normal $\hat{n}$ makes with the radial vector, as shown in Fig. III.3 (Lee & Wu 1994a,b). For the free-field waves, which are available in rectangular coordinates, Eq. (10a) can also be expressed as shown in Fig. III.3:

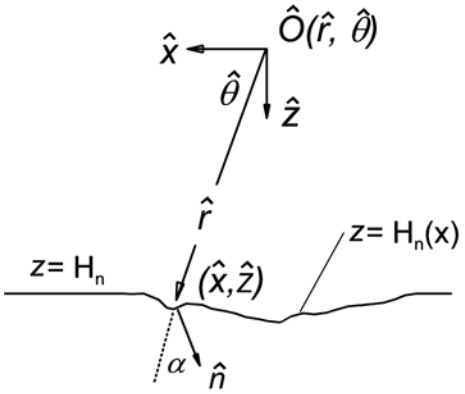

Fig. III.3. Angle α between radial vector and normal at a point

$$\frac{\partial}{\partial \hat{n}}(\ ) = \tilde{\nabla}(\ ) \cdot \hat{n} = n_x \frac{\partial}{\partial x}(\ ) + n_z \frac{\partial}{\partial z}(\ ), \tag{III.10b}$$

where the normal $\hat{n}$ is expressed in rectangular coordinates as $\hat{n} = n_x \hat{e}_x + n_z \hat{e}_z$, and $\hat{e}_x$, $\hat{e}_z$ are, respectively, the unit vectors in the *x*- and *z*- directions.

On the flat part of the interface between the l^{th} and $(l+1)^{th}$ layers, on the left and right parts of the curve $z = H_l(x)$, where it is flat, the Love waves in between the layers already satisfy the continuity of displacement and stress at the interface. This means that only the scattered waves will appear in the continuity equations at those points. More precisely, Eqs. (III.3b), (III.4b), and (III.5b) can be written as

$$\frac{\partial v_1^s}{\partial \hat{n}} = -\tau_1^{ff} = \begin{cases} -\dfrac{\partial v_1^{ff}}{\partial \hat{n}} & \text{at irregular surface point of } z = H_0(x), \\ 0 & \text{on flat surface point of } z = H_0(x) = 0 \end{cases}, \tag{III.11a}$$

$$v_l^s - v_{l+1}^s = -\delta v_l^{ff} = \begin{cases} -\left(v_l^{ff} - v_{l+1}^{ff}\right) & \text{at irregular surface point of } z = H_l(x), \\ 0 & \text{on flat surface point of } z = H_l(x) = \mathrm{H}_l \end{cases}, \tag{III.11b}$$

and $$\mu_l \frac{\partial v_l^s}{\partial n} - \mu_{l+1} \frac{\partial v_{l+1}^s}{\partial n} = -\delta\tau_l^{ff}$$

$$= \begin{cases} -\left(\mu_l \dfrac{\partial v_l^{ff}}{\partial n} - \mu_{l+1} \dfrac{\partial v_{l+1}^{ff}}{\partial n} \right) & \text{at irregular surface point of } z = H_l(x), \\ 0 & \text{on a flat surface point of } z = H_l(x) = \mathrm{H}_l \end{cases} \quad \text{(III.11c)}$$

To solve this boundary-valued problem, one would have to find a wave function, v_l, as given in Eq. (III.6a) for each layer $l = 1, 2 \ldots, N-1$, and as given in Eq. (III.6b) for the bottom semi-infinite layer $l = N$.

IV. The Weighted-Residues (Moment) Method

IV.1 Methodology

For completeness of this presentation, we briefly summarize the method described by Lee and Wu (1994a,b). It is seen from the above sections that the wave functions at each layer together have to satisfy the set of boundary conditions numerically at every point on the interfaces as given in Eqs. (III.7), (III.8), and (III.9). Since these surfaces are not flat, a numerical procedure has to be applied.

Harrington (1967), in his classic paper, "Matrix Methods for Field Problems," presented a well-defined, unified treatment of most of the existing numerical methods for the above boundary-valued problems, which he called the "moment methods," and applied the method to electromagnetic wave problems. Soon afterward, Fenlon (1969) applied the same method to acoustic-wave problems, and Lee and Wu (1994a,b) applied the method to elastic-wave problems in arbitrarily shaped canyons in elastic half space. Another common name for the special case of the moment method used here is the weighted-residues method. We will summarize the method, following Lee and Wu (1994a,b).

Assume that a general equation to be satisfied is of the form

$$\mathcal{L} f = g \ , \quad \text{(III.12)}$$

where $\mathcal{L}$ is a linear operator, f is an unknown function to be solved, and g is a given known function. The boundary conditions in Eqs. (III.11a,b,c) and (III.12) above are all of this form, with $\mathcal{L}$ being a linear combination of the identity and the derivative operators, f being a sum or difference of the unknown wave functions and their derivatives in adjacent media, and g being the corresponding sum or difference of the known free-field Love-wave functions and their derivatives in adjacent media. All of the unknown wave functions f are here represented as a series of basis functions $\ldots, f_0, f_1, \ldots, f_n, \ldots$:

$$f = \sum_n c_n f_n \,, \tag{III.13}$$

with c_n as a sequence of unknown coefficients to be determined. The range of the indices of the functions can either be infinite ($-\infty$ to ∞) or semi-infinite (0 to ∞). Since $\mathcal{L}$ is a linear operator, Eq. (10) takes the form, in terms of residues, ε, to be set to zero:

$$\varepsilon = \sum_n c_n \mathcal{L} f_n - g = 0 \,. \tag{III.14}$$

Next, we choose a scalar inner product $\langle f, g \rangle$ to be defined on any pair of functions in the domain of $\mathcal{L}$ and a set of weight functions $\ldots, w_0, w_1, \ldots, w_n, \ldots$ in the domain. We take the inner product of the residues with each weight function and equate it to zero as follows:

$$\begin{aligned} \langle \varepsilon, w_m \rangle &= \left\langle \sum_n c_n \mathcal{L} f_n - g, w_m \right\rangle \\ &= \sum_n c_n \langle \mathcal{L} f_n, w_m \rangle - \langle g, w_m \rangle = 0 \\ \text{so} \quad & \sum_n \langle \mathcal{L} f_n, w_m \rangle \, c_n = \langle g, w_m \rangle \end{aligned} \tag{III.15a}$$

or in matrix form:

$$\left[A_{mn}\right] \{c_n\} = \{g_m\} \,, \tag{III.15b}$$

with $\left[A_{mn}\right] = \langle \mathcal{L} f_n, w_m \rangle$ being a matrix of infinite order, and $\{g_m\} = \langle g, w_m \rangle$ being a known vector computed from the free-field surface Love waves or body SH waves. The matrix is composed of a ***(2N - 1)*** set of boundary conditions in Eqs. (11a,b,c) and for the set of ***(2N - 1)*** coefficients from the ***(2N - 1)*** wave functions in Eqs. (6a,b) for the ***N***-Layered media.

Depending upon the choice of the weight functions, they can also be considered as a set of basis functions, orthogonal with respect to the inner product, and here the residues are expanded in

terms of these basis functions using the inner product. We set each term of the expansion here to be zero.

Using the weighted residue method, the boundary conditions at each layer take the following form:

(1) Starting in the top layer, the half-space surface, from Eq. (7), is as follows:

$$\sum_{n=0}^{\infty}\sum_{j=1,2}\left\langle \frac{\partial}{\partial \hat{\boldsymbol{n}}}\left(\boldsymbol{H}_n^{(j)}(\boldsymbol{k}_1\hat{\boldsymbol{r}})\cos n\theta\right), \boldsymbol{w}_m\right\rangle \boldsymbol{A}_{1,n}^{(j)} \;=\; -\left\langle \frac{\partial \boldsymbol{v}_1^{ff}}{\partial \hat{\boldsymbol{n}}}, \boldsymbol{w}_m\right\rangle, \tag{III.16a}$$

or in matrix form, at the top surface of the 1st layer (surface of the half space):

$$\sum_{n=0}^{\infty}\left[\left\langle \frac{\partial}{\partial \hat{\boldsymbol{n}}}\left(\boldsymbol{H}_n^{(1)}(\boldsymbol{k}_1\hat{\boldsymbol{r}})\cos n\theta\right), \boldsymbol{w}_m\right\rangle \quad \left\langle \frac{\partial}{\partial \hat{\boldsymbol{n}}}\left(\boldsymbol{H}_n^{(2)}(\boldsymbol{k}_1\hat{\boldsymbol{r}})\cos n\theta\right), \boldsymbol{w}_m\right\rangle\right]\begin{Bmatrix}\boldsymbol{A}_{1,n}^{(1)}\\ \boldsymbol{A}_{1,n}^{(2)}\end{Bmatrix} = -\left\langle \frac{\partial \boldsymbol{v}_1^{ff}}{\partial \hat{\boldsymbol{n}}}, \boldsymbol{w}_m\right\rangle \tag{III.16b}$$

(2) For the interface between the $\boldsymbol{l}^{th}$ and $(\boldsymbol{l}+1)^{th}$ layers, for $\boldsymbol{l}=1,2,3\ldots$ from Eq. (11):

$$\begin{aligned}\sum_{n=0}^{\infty}\sum_{j=1,2}&\left\langle \boldsymbol{H}_n^{(j)}(\boldsymbol{k}_l\hat{\boldsymbol{r}})\cos n\theta, \boldsymbol{w}_m\right\rangle \boldsymbol{A}_{l,n}^{(j)} \;-\; \left\langle \boldsymbol{H}_n^{(j)}(\boldsymbol{k}_{l+1}\hat{\boldsymbol{r}})\cos n\theta, \boldsymbol{w}_m\right\rangle \boldsymbol{A}_{l+1,n}^{(j)}\\ &= -\left\langle \boldsymbol{v}_l^{ff} - \boldsymbol{v}_{l+1}^{ff}\;,\; \boldsymbol{w}_m\right\rangle\end{aligned} \tag{III.17a}$$

$$\begin{aligned}\sum_{n=0}^{\infty}\sum_{j=1,2}&\mu_l\left\langle \frac{\partial}{\partial \hat{\boldsymbol{n}}}\left(\boldsymbol{H}_n^{(j)}(\boldsymbol{k}_l\hat{\boldsymbol{r}})\cos n\theta\right), \boldsymbol{w}_m\right\rangle \boldsymbol{A}_{l,n}^{(j)} \;-\; \mu_{l+1}\left\langle \frac{\partial}{\partial \hat{\boldsymbol{n}}}\left(\boldsymbol{H}_n^{(j)}(\boldsymbol{k}_{l+1}\hat{\boldsymbol{r}})\cos n\theta\right), \boldsymbol{w}_m\right\rangle \boldsymbol{A}_{l+1,n}^{(j)}\\ &= -\left\langle \mu_l\frac{\partial \boldsymbol{v}_l^{ff}}{\partial \hat{\boldsymbol{n}}} - \mu_{l+1}\frac{\partial \boldsymbol{v}_{l+1}^{ff}}{\partial \hat{\boldsymbol{n}}}\;,\; \boldsymbol{w}_m\right\rangle\end{aligned} \tag{III.17b}$$

or in matrix form, at each interface between the $\boldsymbol{l}^{th}$ and $(\boldsymbol{l}+1)^{th}$ layers, for $\boldsymbol{l}=1,2,3\ldots$

$$\begin{aligned}\sum_{n=0}^{\infty}\sum_{j=1,2}&\begin{bmatrix}\left\langle \boldsymbol{H}_n^{(j)}(\boldsymbol{k}_l\hat{\boldsymbol{r}})\cos n\theta, \boldsymbol{w}_m\right\rangle & -\left\langle \boldsymbol{H}_n^{(j)}(\boldsymbol{k}_{l+1}\hat{\boldsymbol{r}})\cos n\theta, \boldsymbol{w}_m\right\rangle\\ \mu_l\left\langle \frac{\partial}{\partial \hat{\boldsymbol{n}}}\left(\boldsymbol{H}_n^{(j)}(\boldsymbol{k}_l\hat{\boldsymbol{r}})\cos n\theta\right), \boldsymbol{w}_m\right\rangle & -\mu_{l+1}\left\langle \frac{\partial}{\partial \hat{\boldsymbol{n}}}\left(\boldsymbol{H}_n^{(j)}(\boldsymbol{k}_{l+1}\hat{\boldsymbol{r}})\cos n\theta\right), \boldsymbol{w}_m\right\rangle\end{bmatrix}\begin{Bmatrix}\boldsymbol{A}_{l,n}^{(j)}\\ \boldsymbol{A}_{l+1,n}^{(j)}\end{Bmatrix}\\ &= -\begin{Bmatrix}\left\langle \boldsymbol{v}_l^{ff} - \boldsymbol{v}_{l+1}^{ff}\;,\; \boldsymbol{w}_m\right\rangle\\ \left\langle \mu_l\frac{\partial \boldsymbol{v}_l^{ff}}{\partial \hat{\boldsymbol{n}}} - \mu_{l+1}\frac{\partial \boldsymbol{v}_{l+1}^{ff}}{\partial \hat{\boldsymbol{n}}}\;,\; \boldsymbol{w}_m\right\rangle\end{Bmatrix}\end{aligned} \tag{III.17c}$$

Note that for the interface between layer $N-1$ and the bottom (last) semi-infinite layer N, Eqs. (III.17a) and (III.17b) will have only the outgoing wave terms $A^{(1)}_{N,n}$, $n = 0,1,2\ldots$, without the incoming wave terms $A^{(2)}_{N,n}$, $n = 0,1,2\ldots$

IV.2 Numerical Implementation

In this section, we summarize the numerical procedure for solving the system of complex equations derived in the previous section. It can be observed that for an elastic half space with N (≥ 1) layers there are $(N-1)$ interfaces between the layers, plus the topmost half space with no elastic medium above. With Hankel functions of both the 1st and 2nd kind present (except in the bottom semi-infinite layer), this gives a total set of $2(N-1)+1 = 2N-1$ waves for a $2N-1$ set of boundary conditions from all of the layers.

Since each set of equations at each interface involves only waves at each side of the interface, a simple, elegant numerical algorithm can be derived to allow each set of wave coefficients at each medium to be solved separately, making the problem simple numerically. In other words, we are solving, for each layer, *M* complex equations with *M* unknowns separately at each step. The following is a brief summary of the numerical procedure.

Starting from the top surface, where $z = 0$, we have the matrix equation for the zero-stress boundary condition along the whole (regular and irregular) surface of the half-space, in the following form:

$$\left[E_1\right]\left\{\tilde{A}_1^{(1)}\right\} + \left[E_1^*\right]\left\{\tilde{A}_1^{(2)}\right\} + \left\{\tilde{e}_1\right\}\Big|_{z=0} = \mathbf{0}\ , \qquad \text{(III.18)}$$

from which $\left\{\tilde{A}_1^{(2)}\right\}$ can be expressed in terms of $\left\{\tilde{A}_1^{(1)}\right\}$ and $\left\{\tilde{e}_1\right\}$. Next, the displacement and stress continuity equations at the interface between layers *l* and *l + 1*, as in Eq. (III.17c) above, at the interface $z = h_l$ can be written in the following form:

$$\left[M_l(h_l)\right]\begin{Bmatrix}\tilde{A}_l^{(1)}\\ \tilde{A}_l^{(2)}\end{Bmatrix} + \left\{\tilde{e}_l(h_l)\right\} = \left[M_{l+1}(h_l)\right]\begin{Bmatrix}\tilde{A}_{l+1}^{(1)}\\ \tilde{A}_{l+1}^{(2)}\end{Bmatrix} + \left\{\tilde{e}_{l+1}(h_l)\right\}$$

or in the form : $$\begin{Bmatrix}\tilde{A}_{l+1}^{(1)}\\ \tilde{A}_{l+1}^{(2)}\end{Bmatrix} = \left[M_l(h_l)\right]\begin{Bmatrix}\tilde{A}_l^{(1)}\\ \tilde{A}_l^{(2)}\end{Bmatrix} + \left\{\tilde{m}_l(h_l)\right\} \qquad \text{(III.19)}$$

for some matrices $\left[M_l(h_l)\right]$ and vectors $\left\{\tilde{m}_l(h_l)\right\}$. Equation (III.19) shows that the coefficients in layer *l +1* can be expressed in terms of those of layer *l* above. Iteratively this can be successively applied from layer to layer backward. In other words, the coefficients of every layer can be expressed in terms of those of the top, first layer. In the top layer, Eq. (III.18) shows that $\left\{\tilde{A}_1^{(2)}\right\}$ can be expressed in terms of $\left\{\tilde{A}_1^{(1)}\right\}$, which means that the coefficients of each layer can all be expressed in terms of $\left\{\tilde{A}_1^{(1)}\right\}$, as follows:

$$\begin{Bmatrix}\tilde{A}_l^{(1)}\\ \tilde{A}_l^{(2)}\end{Bmatrix} = \left(\begin{bmatrix}T_{l1}(h_l)\\ T_{l2}(h_l)\end{bmatrix}\left\{\tilde{A}_1^{(1)}\right\} + \begin{Bmatrix}\tilde{t}_{l1}(h_l)\\ \tilde{t}_{l2}(h_l)\end{Bmatrix}\right) \qquad \text{(III.20)}$$

for some transformation matrices $T_{l1}(h_l)$ and $T_{l2}(h_l)$ and for vectors $\tilde{t}_{l1}(h_l)$ and $\tilde{t}_{l2}(h_l)$. Note that at the bottom semi-infinite layer, *l* = *N*, only outgoing waves (to infinity) exist, and $\left\{\tilde{A}_N^{(2)}\right\} = \left\{\tilde{0}\right\}$.

The reason we selected to have the coefficients of all waves in each layer expressed in terms of a set of coefficients of waves in the top layer is because we know that for surface waves, and most of the time for body waves, the waves in the top layer are more dominant. With the coefficients $\left\{\tilde{A}_1^{(1)}\right\}$ evaluated, the coefficients of the waves in all layers can be found from Eq. (III.20).

V. The Scattered and Diffracted Mode Shapes of Love and SH Waves

V.1 The Input Free-Field Waves

In the following, we illustrate examples for Love waves and body SH waves incident from the left via a regular parallel-layered medium. We will consider the five lowest mode shapes of Love waves in the frequency range 0.07 Hz–25 Hz. To those, we will add body SH waves as the

"6^{th} mode" of waves in the parallel-layered medium (Trifunac 1971; Wong and Trifunac 1979; Lee and Trifunac 1985, 1987; Todorovska et al. 2013). Each of these six mode shapes at each period (frequency) will be used as the free-field input wave into the irregularly layered medium. In the example that follows, we will take a simple two-layered medium to illustrate the process. The following parameters will be used for this two-layered model (Figure III.4):

Table 1

Two-Layered Velocity Model				
Layer	Thickness (km)	P-wave Speed (α, km/s)	S-Wave Speed (β, km/s)	Density, ρ (gm/cc)
1	1.38	1.70	0 98	1.28
2	∞	6.40	3.`70	2.71

Those are the same first and last layers of the six-layered model described in Todorvska et al. (2013), except that the top layer is now taken to be 1.38 km thick. The computer program "Haskel.exe" (Todorocka et al. 2013) has been used to calculate the phase velocities of each mode of Love waves in the range from 14.0–0.04 s, and for a total of 91 discrete period values.

V.2 -The Scattered and Diffracted Mode Shapes

We next consider the case of an irregularly shaped, layered medium superimposed on the parallel two-layered medium. For this example, we select a shallow, "almost-flat" ellipse with a ratio of the vertical axis to the horizontal axis of 0.1 at both the half-space surface and the interface of the two layers. The half width or radius of the horizontal major axis is taken to be 1.0 km long for both. Thus, the half-width or radius of the minor axis is 0.1 km deep.

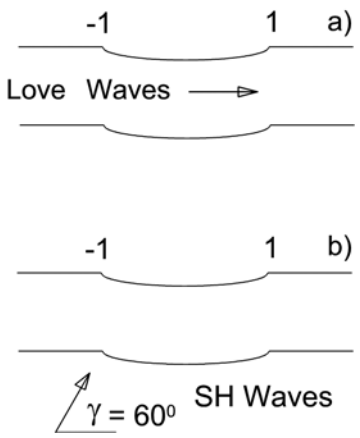

Fig. III.4. Irregular, two-layered medium with incident Love waves (a) and SH body waves (b).

Figure III.5 illustrates the scattered and diffracted mode shapes for Mode #3 of Love Waves in the two-layered medium (shown in Fig. III.4). The mode shapes are illustrated at four selected frequencies—f = 13.33, 18.18, 20.0, and 25.0 Hz—which are the frequencies below the period of 0.1 s (or frequencies beyond 10 Hz). It was found that since the irregular parts of the layer we chose for this example are almost flat, the long-period waves do not "see" the irregularities, and the scattered and diffracted waves at those long periods are small. As the frequencies of the incident-mode shapes increase from 15.0 to 25.0 Hz, and especially for the frequencies f = 18.18, 20.0, and 25.0 Hz, the Love waves experience some scattering and diffraction in the top layer, and most noticeably in the 18.18-Hz mode shape, which is shown in the lower left corner of Fig. III.5. Further examples of the scattered mode shapes can be found in Appendix R4-1 (Report IV-1).

With the irregular, almost-flat elliptic surfaces from $x = -1.0$ km to $x = +1.0$ km at both the half-space surface and at the surface with the half space, the scattered and diffracted mode shapes are plotted at equally spaced intervals along the *x*-axis from $x = -2.0$ km to $x = +2.0$ km at 0.1 km apart. The dashed line at the left side of each graph represents the input free-field mode shape propagating along the parallel-layered medium from left to right, arriving at the irregular surfaces at $x = -1.0$ km. As the mode number increases, the mode shapes of both the input free-field motion and the signs of the scattered and diffracted Love waves change sign *(M - 1)* times as they go down vertically from the top surface, where *"M"* is the mode number. The scattering and diffraction will become more complex as the mode number increases (Appendix R4-1).

VI. The Synthetic Scattered and Diffracted Time Histories

The scattered and diffracted Love waves and SH body-wave mode shapes can next be used to generate the synthetic out-of-plane transverse (***y***-) components of accelerations at all points on and below the ground surface in the vicinity of the irregular layers. The input Love and body SH waves to these diffracted waves are the out-of-plane waves generated in the regular layered media of elastic half space. The complete description of this procedure is given in Todorovska et al. (2013).

We will use the following parameters to generate the example time histories:

	$M = 6.5,\ R = 8.0km,\ H = 6.0km,\ s = 0,\ s_L = 2$
where	M = earthquake magnitude R = epicentral distance H = focal depth of earthquake s = geologic site condition of the recording site, where s = 0, alluvial site, s = 1, intermediate site, and s = 2, rock site s_L = soil condition of the recording site, where s_L = 0, rock soil, s_L =1, intermediate soil, and s_L =2, soft soil type.

VI.1 Time Histories

The time history of the transverse out-of-plane motions at the top surface $z = 0$ has been generated by the SYNACC method (Trifunac 1971; Wong and Trifunac 1979; Lee and Trifunac 1985, 1987; Todorovska et al. 2013). The time histories at points $z > 0$, below the half-space surface, have been generated by the recently generalized SYNACC program, which uses the mode shapes below the half-space surface to construct the motions at depth. Because of the scattering and diffraction, these out-of-plane mode shapes are now space dependent, and the acceleration-time histories are different at every point on the half-space surface and at depth.

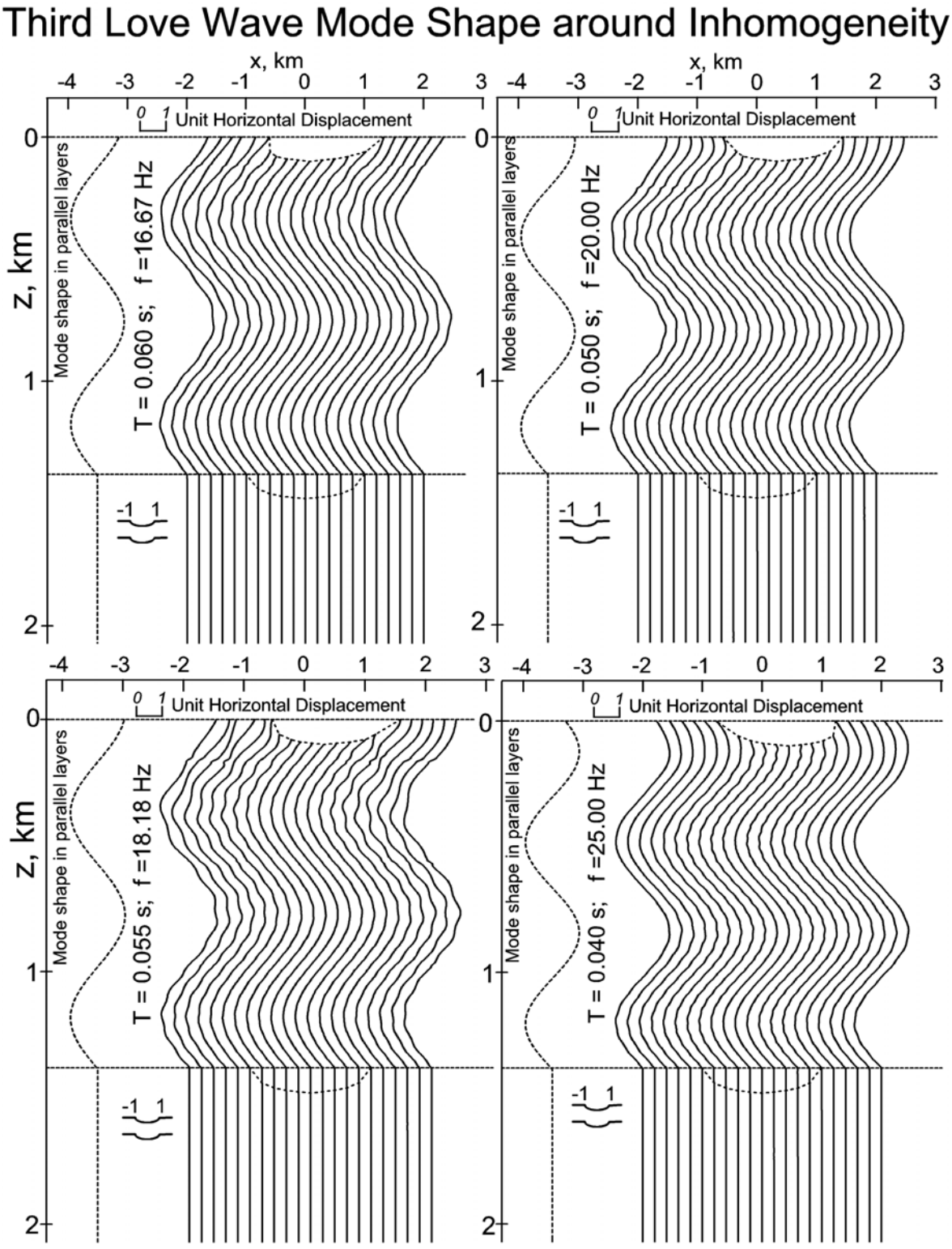

Fig. III.5. Mode #3: Scattered and diffracted mode shapes at f = 13.33, 18.18, 20.0, & 25.0 Hz.

Figure III.6 shows three synthetic displacement-time histories calculated in the two-layered medium at 101 depths equally spaced from the layered half-space top surface ($z = 0$) to a depth of $z = 2$ km, below the first layer which extends to a depth of $z = 1.38$ km. The time histories are at three vertical sets of points along the half-space surface, at $x = -2.0$ km, (1.0 km to the left of the left rim of the canyon), $x = 0.0$ km (the center of the canyon), and $x = +2.0$ km (1.0 km to the right of the right rim of the canyon). The time histories at the left and right rims of the canyon are all plotted at $z = 0$ km, the layered half-space surface, while the time histories at the middle of the canyon start at $z = 0.1$ km, the bottom of the canyon.

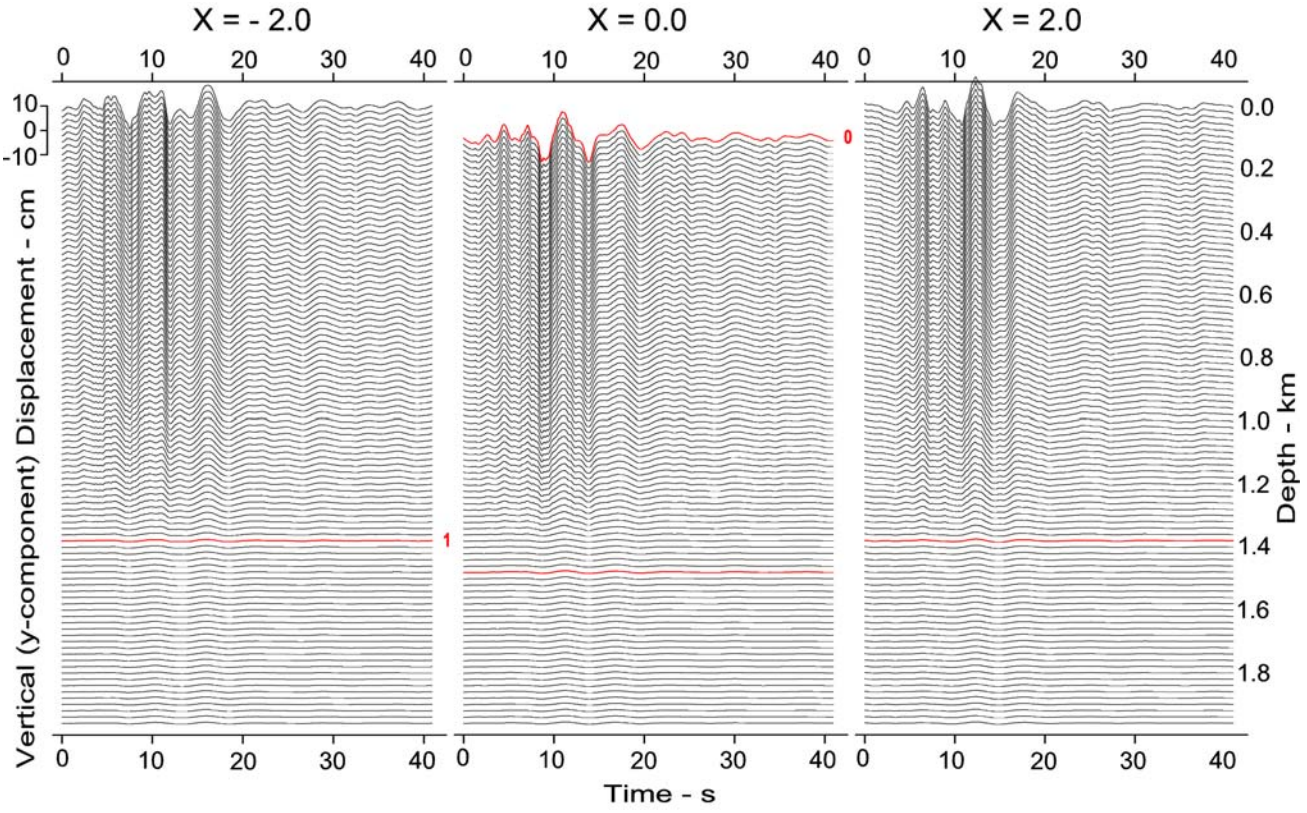

Fig. III.6. Horizontal, out-of-plane, synthetic displacements at x = -2, 0, and 2 km.

The origin at the center of the canyon on the half-space surface is situated at an epicentral distance of $R = 8.0\ km$ from the earthquake source of focal depth $H = 6.0$ km, which would

correspond to a hypocentral distance of $D = \left(R^2 + H^2\right)^{1/2}$, or $D = 10.0$ km. The time history of displacement at the half-space surface, $z = 0$ km, on the left at $x = -2.0$ km, is thus at an epicentral distance of $R = 6.0\ km$ and a hypocentral distance of D □ **8.5** km, **1.5** km closer. Similarly, the time history of displacement at the half-space surface, $z = 0$ km, on the right at $x = +2.0$ km is thus at an epicentral distance of $R = 10.0\ km$ and a hypocentral distance of D □ **11.7** km, **1.7** km further away. The new SYNACC program determines that the appropriate duration of the displacement record should be just above 40 s. The depths of the time histories in the figure are at intervals of 0.20 km apart. Of the 101 displacement-time histories, a few are plotted red, and those are the time histories at the interface. In the middle graph, the top red curve is at the bottom of the canyon, while the one below is at the elliptical interface.

It can be seen that the waves arrive earlier on the left side of the canyon compared with the waves below the center of the canyon, while the waves on the right side of the canyon arrive later, with each side differing by a few seconds. The amplitudes of the waves are similar but different because of the scattering and diffraction. In all of the graphs, the strong motions are seen only in the top layer, down to z = **1.38** km, which is the interface with half space. This is consistent with the fact that the Love-wave mode-shape amplitudes diminish exponentially in the half space.

VI.2 The Fourier and Response Spectral Amplitudes

The time histories above show that the motions, because of scattering and diffraction, can differ from point to point at points on or below the half-space surface in the vicinity of the irregularly layered media. To further illustrate these differences, we will show the spectral amplitudes of the motions at different points.

Figure III.7 shows the response as well as the Fourier spectral amplitudes at four surface points on the Layered media. This is a typical Volume 3 plot, as in “routine digitization and data processing” (Lee and Trifunac 1979) of strong-motion accelerograms, which we use to describe spectral content in the strong ground motions in the form that is used in engineering design.

These spectral amplitudes show similar trends and yet are all different. They are spectral plots for only four points of the irregularly layered media. Each point on top and below the layered media, to the left and to the right of the irregular surface and interface, will all have its own spectral amplitude. The pseudo relative velocity (PSV) spectra are shown for damping values of 0.0 and 0.20 of the critical value. The spectra for no damping are characterized by rapid oscillations because the oscillator has no memory (Udwadia and Trifunac 1974; Gupta and Trifunac 1988). The spectra for 20% damping are smooth because of the considerable memory of the oscillator with large damping. These spectra show the clear differences in response at different surface stations.

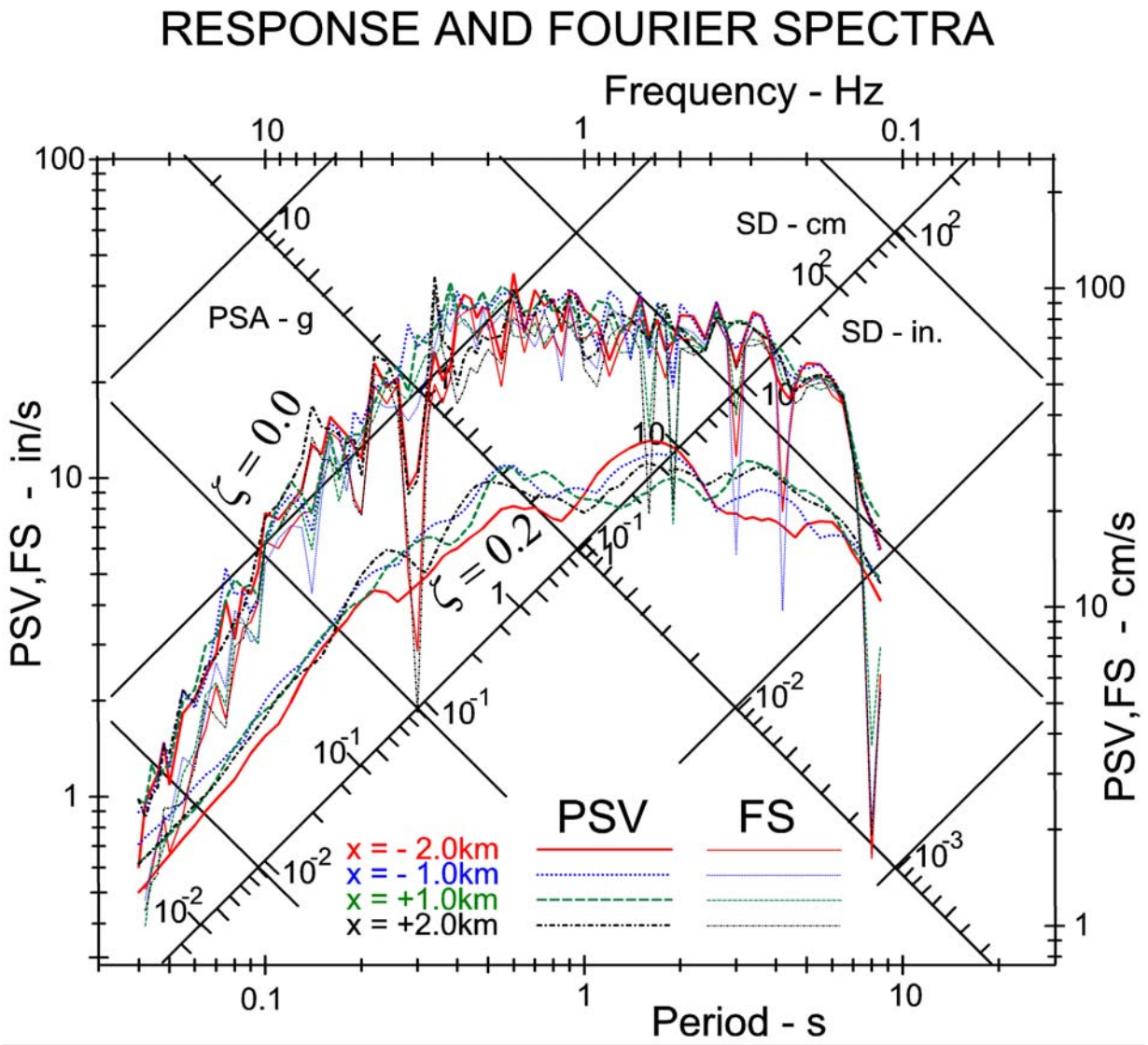

Fig. III.7. Response- and Fourier-amplitude spectra of surface motions at x = -2, -1, 1, and 2.

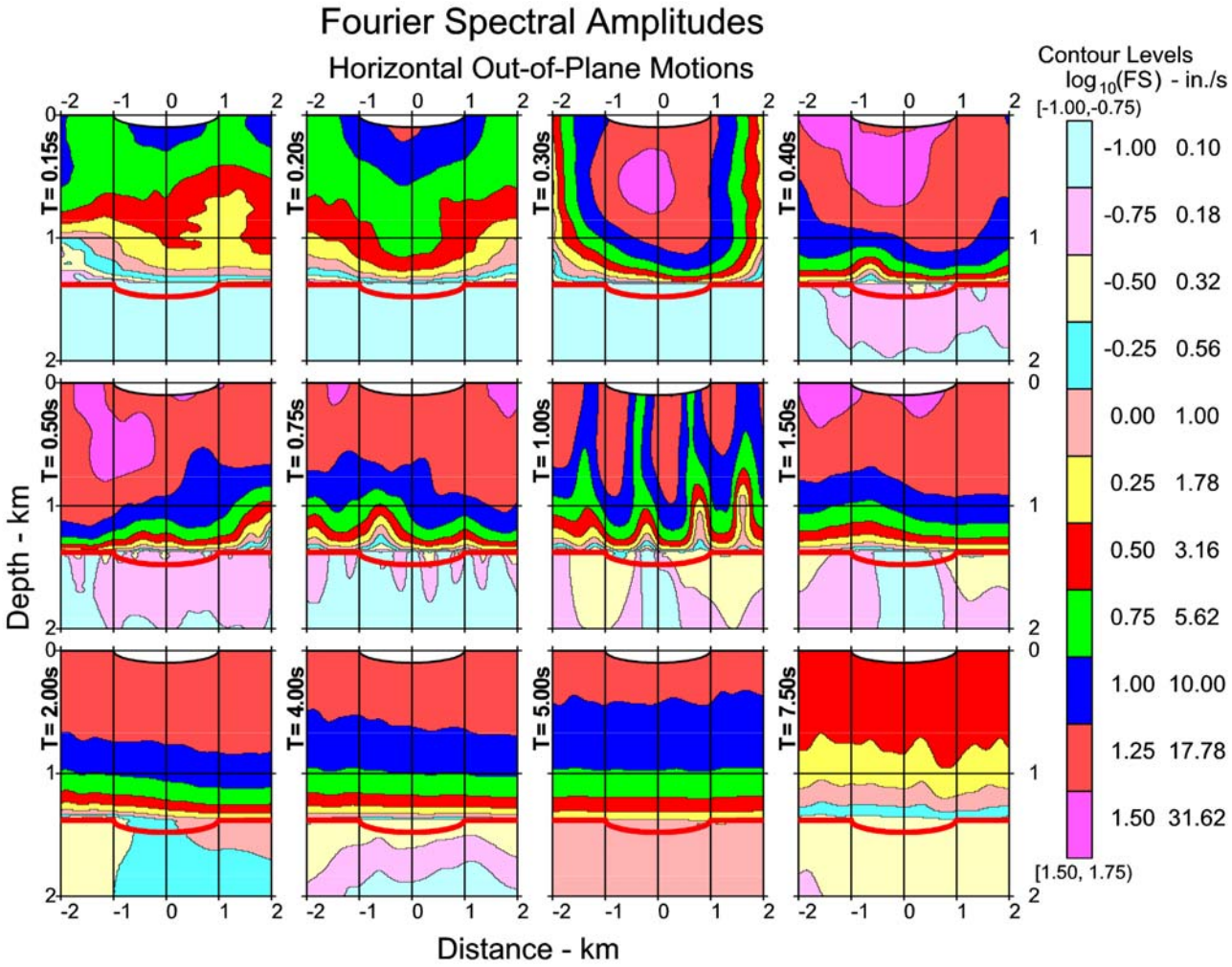

Fig. III.8. Contours of Fourier amplitude spectra (FS) in the area surrounding the inhomogeneus layer ($-2 < x < 2$ km and $0 < depth < 2$ km) at 12 periods: T = 0.15, 0.20, 0.30, 0.40, 0.50, 0.75. 1.00, 1.50, 2.00, 4.00, 5.00, and 7.50 s.

The simplest way to show the variations of Fourier spectral (FS) amplitudes is to plot their contours at selected periods. Figure III.8 shows such contours in units of *in./s*, at 12 selected periods: T = 0.15, 0.20, 0.30, 0.40, 0.50, 0.75, 1.00, 1.50, 2.00, 4.00, 5.00, and 7.50 s. The contour levels are for the Fourier spectra in logarithmic scale**,** *log FS*, in the range -1.0 to 1.75 in steps of 0.25, so that the corresponding Fourier amplitudes in linear scale are in the range 0.10 in./s to over 56 in./s. As can be seen from the figure, the Fourier amplitudes are larger near the top medium of the layer, with amplitudes varying from point to point in the range of around 0.1 in./s to above 56 in./s. Below the top layer**,** $\mathbf{z} >$ 1.38 km, the motions are all below 1 in./s.

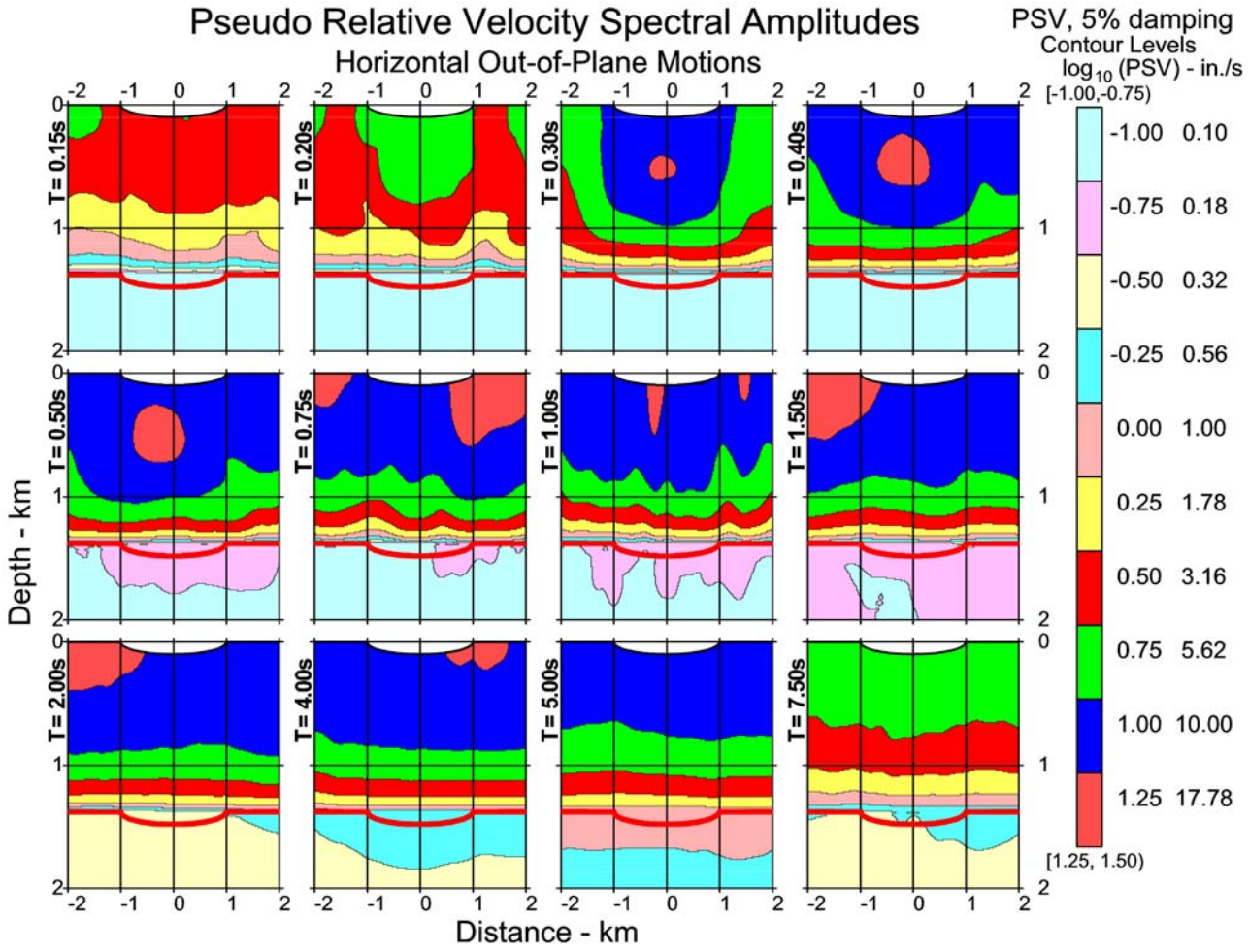

Fig. III.9. Contours of pseudo-relative velocity spectra (PSV) in the area surrounding the inhomogeneus layer ($-2 < x < 2$ km and $0 < depth < 2$ km), at 12 periods—T = 0.15, 0.20, 0.30, 0.40, 0.50, 0.75. 1.00, 1.50, 2.00, 4.00, 5.00, and 7.50 s—and for 5% of critical damping.

Figure III.9 shows the corresponding contour plots of the PSV response spectral amplitudes at 5% damping in units of *in./s*. Those contours show trends and ranges of amplitudes similar to the Fourier-spectrum amplitudes in Fig. III.8.

V. Summary

In this chapter we illustrated the wave propagation in and near an irregularly layered medium for the out-of-plane transverse component of earthquake ground motions corresponding to the incoming Love surface waves and body SH waves. Additional waves were generated at each layer as a result of scattering and diffraction at the irregular half-space surface and irregular interfaces between the layers. The out-of-plane scattered and diffracted shear waves were computed using the

weighted-residues method to satisfy the (out-of-plane shear) zero-stress boundary condition on the top half-space surface and the continuity of (out-of-plane) stress and displacement at the interface surfaces between adjacent layers.

The contour plots of the Fourier and response spectra illustrate how the motions vary from point to point at or below the half-space surface and for different periods of motions. These waves generated by scattering and diffraction will result in amplification and de-amplification at various points on the layered medium depending upon the different irregular geometries.

In this chapter, we illustrated the amplification of motions near inhomogeneity only for translational components of motion. With spatial differentiation, it is now also possible to calculate the amplification of rotational components of motion on ground surfaces and anywhere inside the layers (Trifunac 2009). However, it will be necessary to study many different layer geometries to identify the general trends for both translational and rotational components of strong motion. These studies are beyond the scope of this work and will be presented in our future papers.

Previous work on the scattering and diffraction of elastic waves by surface and subsurface topographies in a homogeneous, elastic half space can now be extended to an irregularly layered, elastic half space. The method presented in this work will be useful because more realistic geometries can be modeled, which will permit synthesis of artificial earthquake motions for use in design that are more realistic than the frequently used elastic half space, with or without the uniformly parallel layers. The methodology presented here can also be extended to the cases of irregularly layered poroelastic media.

The method we presented here can be further generalized to cases in which the geometry of the surface topography and of the interface surfaces for one or several layers has to be represented by different convex or concave surfaces. Such cases generate wave-scattered and -diffracted motions, and they need to be approximated by the Hankel functions with different origins. This is illustrated in Fig. III.10, in which the bottom interface of layer 2 is convex upward, thus creating a "hill-interface" within the layer. The waves in such layers will best be represented in terms of their own coordinate systems, such as (x_2, z_2) in Fig. III. 10. In general, the waves in all layers can then each be represented by their own coordinate systems and the addition theorem can be used to apply the

boundary conditions at all interfaces. Conceptually, the method of solution to such problems will be same as the one presented in this paper, except that more model-specific modeling will be required to solve each problem. We will show examples of such modeling in our future work.

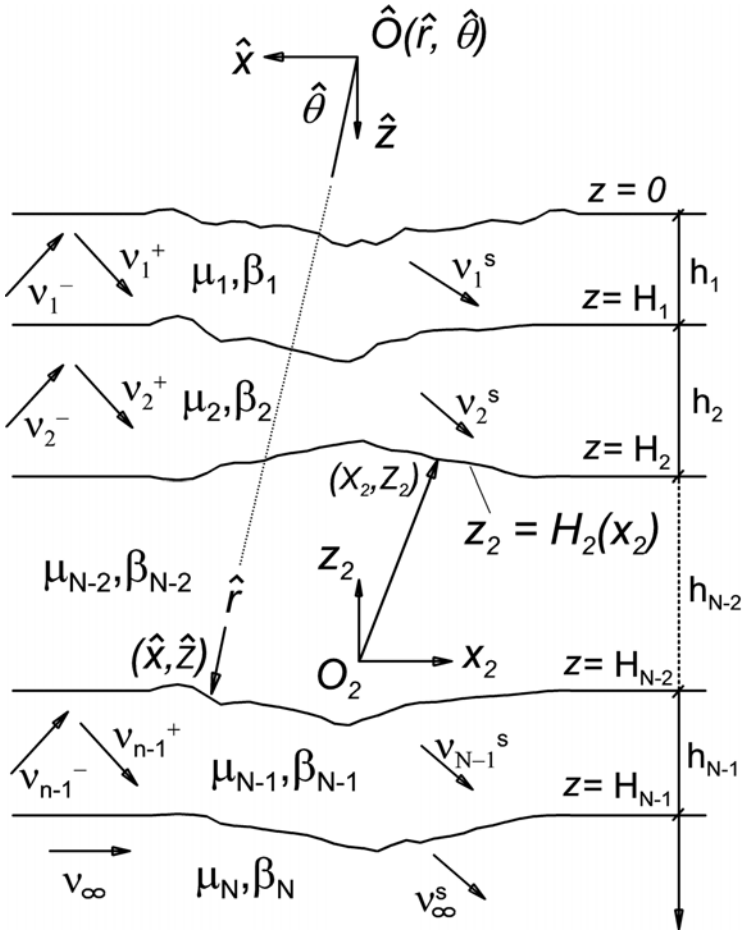

Fig. III.10. Irregularly layered media with multiple coordinate systems.

The method developed in this work now enables us to compute analytical representations of seismic-wave motions in irregular media, which can in general be modeled only numerically. This will be particularly useful for verification and testing of the accuracy with which transmitting boundaries in numerical algorithms are able to transmit the waves without spurious reflections.

References

Aki, K. & Larner, K.L. (1970). Surface motion of a layered medium having an irregular interface due to incident plane SH-waves, *J. Geophys. Res.* 75, 1921-1941.

Chen, X.F. (1990). Seismogram synthesis for multi-layered media with irregular interfaces by using global Reflection/Transmission matrices method. I. Theory for 2D SH case, *Bull, Soc. Am, **80**, 1694-1724.*

Chen, X.F. (1993). A systematic and efficient method of computing normal mod for multi-layered half-space, *Geophys. J. Int. **115**, 391-409.*

Chen, X.F. (1995). Seismogram synthesis for multi-layered media with irregular interfaces by using global Reflection/Transmission matrices method. II. Numerical test and application for 2D SH case, *Bull, Soc. Am, **85**, 1094-1106.*

Chen, X.F. (1999). Love Waves in Multi-layered Media with Irregular interfaces, I. Modal solution and Excitation formulation, *Bull. Seismo. Soc. Am.*, 89, 1519-1534.

Fenlon, F. H. (1969). Calculation of the acoustic radiation field at the surface of a finite cylinder by the method of weighted residuals, *Proc. IEEE,* 57(3), 291-306.

Gupta, I.D. and Trifunac. M.D. (1988). Order-Statistics of Peaks in Earthquake Response, J. of Eng. Mechanics – ASCE, 114(10), 1605-1627.

Harrington. R. F. (1967). Matrix methods for field problems, *Proc. IEEE, 1967, 55*. 136-149.

Haskell, N.A. (1953). The Dispersion of Surface waves on Multi-layered Media, *Bull Seismol. Soc. Am.* 43 *17-34.*

Kohketsu, K. (1987a). 2-D reflectivity method and synthetic seismograms in irregularly layered structures. I, SH-wave generation, *Geophys. J. Astr. Soc.* 89, 821-831.

Kohketsu, K. (1987b). Synthetic seismograms in realistic media: a wave theoretical approach, *Bull. Earthquake Res. Inst. Univ. Tokyo* 62, 201-245.

Kohketsu, K., B. L. N. Kennett & H. Takenaka (1991). 2-D reflectivity method and synthetic seismograms for irregularly layered structures. II, Invariant embedding approach, *Geophys. J. Int.* 105, 119-130.

Lee, V.W. & M.D. Trifunac (1979) . Automatic Digitization and Data Processing of Strong-Motion Accelerograms , Part II: Computer Processing of Accelerograms, *Civil Eng. Report CE 79-15 II,* Univ. of Southern Cal., Los Angeles, California.

Lee, V.W. & M.D. Trifunac (1985). Torsional Accelerograms, *Int. J. Soil Dynamics & Earth quake Eng., 4(3), 132-13.*.

Lee, V.W. & M.D. Trifunac (1987). Rocking Strong Earthquake Accelerations, *Int. J. Soil Dynamics & Earthquake Eng., 6(2),* 75-89.

Lee, V.W. & X.Y. Wu (1994a). Application of the Weighted Residual Method to Diffraction by 2-D Canyons of Arbitrary Shape, I: Incident SH Waves, *Int. J. Soil Dynamics & Earthquake Eng., 13(5),* 1994, 355-364.

Lee, V.W. & X.Y. Wu (1994b). Application of the Weighted Residual Method to Diffraction by 2-D Canyons of Arbitrary Shape, II: Incident P, SV & Rayleigh Waves, *Int. J. Soil Dynamics & Earthquake Eng., 13(5),* 1994, 365-373.

Lee, V.W. & W.Y. Liu (2014). Two-Dimensional Diffraction of P- and SV-Waves Around a Semi-Circular Canyon in an Elastic Half-Space: An Analytic Solution via a Stress-Free Wave Function, *Int. J. Soil Dynamics and Earthquake Engineering, 63, 110-119*.

Sanchez-Sesma, F.J. & Campillo, M. (1991). Diffraction of P, SV, and Rayleigh waves by topographic features: a boundary integral formulation, *Bull. Seism. Soc. Am.*, 81, 2234-2253.

Sanchez-Sesma, F.J. & Campillo, M. (1993). Topography effects for incident P, SV, and Rayleigh waves, *Tectonophysics,* 218, 113-125.

Thomson, W.T. (1950). Transmission of Elastic Waves Through a Stratified Solid Media, *J. Appl. Phys. 21, 89-93.*

Todorovska, M.I., Trifunac, M.D. Lee, V.W. and Orbović, N. (2013). Synthetic Earthquake Ground Motions on an Array, *Soil Dynamics and Earthquake Engineering, 48,* 234-251.

Trifunac, M.D. (1971). A Method for Synthesizing Realistic Strong Ground Motion, *Bull. Seism. Soc. Amer., 61(6),* 1739-1753.

Trifunac, M.D. & V.W. Lee (1979). Automatic Digitization and Data Processing of Strong-Motion Accelerograms, Part I: Automatic Digitization, *Civil Eng. Report CE 79-15 I,* Univ. of Southern Cal., Los Angeles, California.

Trifunac, M.D. (2009). The role of Strong Motion Rotations in the Response of Structures near Earthquake Faults, *Soil Dynamics and Earthquake Engineering*, 29(2) 382-393.

Udwadia, F.E. and Trifunac, M.D. (1974). Characterization of Response Spectra through Statistics of Oscillator Response, *Bull Seismological Soc. of America,* 64(1), 205-219.

Vai R., J.M. Castillo-Covarrubias, F.J. Sanchez-Sesma, D. Komatistsch, & J.P. Vilotte (1999). Elastic wave propagation in an irregularly layered medium, *Soil Dynamics & Earthquake Engineering*, 18, 11-18.

Wong. H.L. and Trifunac, M.D. (1979). Generation of Artificial Strong Motion Accelerograms, *Int. J. Earthquake Engineering Struct. Dynamics*, 7(6), 509-527.

Chapter 4 Scattering and Diffraction of Earthquake Motions in Irregular, Elastic Layers, II: Rayleigh and Body P and SV Waves

Summary

We present our analysis of the wave propagation in an irregularly layered, elastic wave-guide excited by incoming Rayleigh surface waves and P and SV body waves. Our aim is to show examples of applying a method that will make it possible to analyze the distribution and amplification of displacements, rotations, curvatures, strains, and stresses on or below the ground surface during passage of strong earthquake ground motion. We employ the weighted-residuals method,, which makes it possible to calculate the scattered and diffracted waves, and then we illustrate the amplification of motions in the vicinity of inhomogeneity.

IV.1 Introduction

In this chapter, we describe a method for the computation of scattered and diffracted waves for in-plane Rayleigh surface waves and body P and SV waves around a local irregularity in a layered medium. The method used and the nature of the model, in the work presented here follows closely the related analysis in which we examined the scattering and diffraction of Love surface waves and body SH waves (Chapter 3).

A brief review of the related studies and of the weighted–residues method were presented in chapter 3, and will not be repeated here. Instead, we will proceed straight to the presentation of the present work, introducing additional references as we go along and as they are required by the specific stages of the analysis.

IV.2 Rayleigh and Body P and SV Waves Incident on an Irregularly Layered Media

As in Chapter III, we consider the case of an ***N***-layered half space with Rayleigh and body P and SV waves incident from the left. An approach for solving this problem

was first formulated by Thomson (1950) and Haskell (1953) in a manner that is useful for the present study. For each regular, flat layer $\boldsymbol{l}$, with $\boldsymbol{l = 1, \ldots, N}$, the P- and SV-wave potentials, respectively, take the forms shown in Fig. IV.1:

$$\varphi_l^-,\ \varphi_l^+,\ \psi_l^-,\ \psi_l^+ : \qquad \begin{aligned} \varphi_l^- &= A_l^- e^{ik\left(x - a_l z\right)} \\ \varphi_l^+ &= A_l^+ e^{ik\left(x + a_l z\right)} \\ \psi_l^- &= B_l^- e^{ik\left(x - b_l z\right)} \\ \psi_l^+ &= B_l^+ e^{ik\left(x + b_l z\right)} \end{aligned} \qquad \text{(IV.1a)}$$

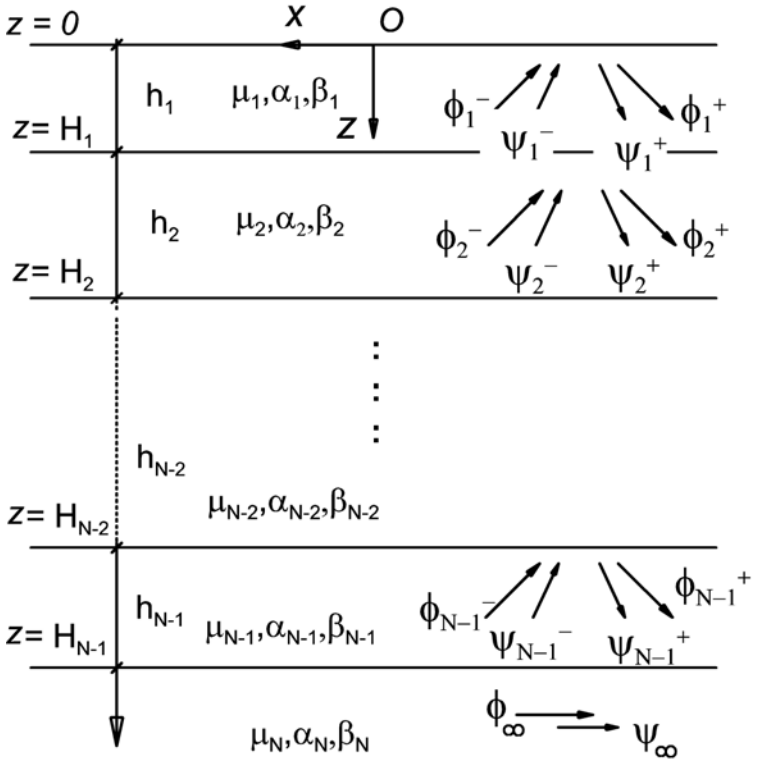

Fig. IV.1. N-layered half space with Rayleigh waves.

Those potentials represent respectively the upward and downward propagating waves in $\boldsymbol{l^{th}}$ layer, $\boldsymbol{k = k(\omega) = \omega / c(\omega)}$ is the horizontal wave number of the ***P***- and ***SV***-waves at frequency $\boldsymbol{\omega}$ and phase velocity $\boldsymbol{c = c(\omega)}$. The term $\boldsymbol{e^{ikx}}$, which is same in all layers,

describes the horizontal propagation of the waves, which together with the time-harmonic term $e^{i\omega t}$ corresponds to waves propagating in the –*ve x* direction. The terms $e^{\mp ika_l z}$ for the P waves and $e^{\mp ikb_l z}$ for the SV waves are, respectively, the corresponding vertical components of the waves. The ones with the **–*ve*** exponent are propagating upward (**–*ve*** *y*), and those with the **+*ve*** exponent are propagating downward (**+*ve*** *y*). Here, $a_l = a_l(\alpha_l, c)$ and $b_l = b_l(\beta_l, c)$ are respectively defined by

$$\begin{aligned} a_l &= \frac{\left(k_{\alpha_l}^2 - k^2\right)^{1/2}}{k} = \left(\left(k_{\alpha_l}/k\right)^2 - 1\right)^{1/2} = \left(\left(c/\alpha_l\right)^2 - 1\right)^{1/2} \\ b_l &= \frac{\left(k_{\beta_l}^2 - k^2\right)^{1/2}}{k} = \left(\left(k_{\beta_l}/k\right)^2 - 1\right)^{1/2} = \left(\left(c/\beta_l\right)^2 - 1\right)^{1/2} \end{aligned}, \qquad \text{(IV.1b)}$$

so that ka_l and kb_l are the vertical wave numbers of the P and SV waves in the l^{th} layer of the medium with longitudinal wave speed α_l and shear-wave velocity β_l. In general, the wave speeds increase as one moves down into the layers, so that $\beta_1 < \beta_2 < \ldots < \beta_N < \beta$, with the semi-infinite half-space layer at the bottom having the highest shear-wave speed β. The same can be said about the longitudinal wave speeds, which means that $\alpha_1 < \alpha_2 < \ldots < \alpha_N < \alpha$, with α the longitudinal wave speed of the semi-infinite medium being the largest. With $c = c(\omega)$, the wave speeds of the surface Rayleigh waves, $c < \beta < \alpha$, and the surface waves take the forms:

$$\begin{aligned} \varphi_\infty &= A_\infty e^{ik(x - az)} = A_\infty e^{ikx - k\bar{a}z} \\ \psi_\infty &= B_\infty e^{ik(x - bz)} = B_\infty e^{ikx - k\bar{b}z} \end{aligned} \qquad \text{(IV.2a)}$$

where

$$\begin{aligned} \bar{a} &= \frac{\left(k^2 - k_\alpha^2\right)^{1/2}}{k} = \left(1 - \left(k_\alpha/k\right)^2\right)^{1/2} = \left(1 - \left(c/\alpha\right)^2\right)^{1/2} \\ \bar{b} &= \frac{\left(k^2 - k_\beta^2\right)^{1/2}}{k} = \left(1 - \left(k_\beta/k\right)^2\right)^{1/2} = \left(1 - \left(c/\beta\right)^2\right)^{1/2} \end{aligned}, \qquad \text{(IV.2b)}$$

and $\bar{a}$, $\bar{b}$ are, respectively, the complements of a, b, and both are real, so that the terms $e^{-k\bar{a}z}$ in φ_∞ and $e^{-k\bar{b}z}$ in ψ_∞ both correspond to surface-wave terms with amplitudes that exponentially decay with depth.

With β_l, the shear-wave speed in the l^{th} layer of the medium, and $c = c(\omega)$, the Rayleigh wave speeds and the (horizontal) phase velocities of the waves in each layer of the elastic media above the half space (Fig. 1), we can have $c \geq \beta_l$ or $c < \beta_l$.

Next, we will consider the case in which the layers are not perfectly flat.

IV.3 Rayleigh and Body P and SV Waves Incident to Irregular Layers

IV.3.1 The Model

Figure IV.2 shows a model in which the layers are not perfectly flat in some finite region but are flat beyond this region. We assume that each of these irregular surfaces, at each of the interfaces between the l^{th} and the $(l+1)^{th}$ layers—which outside this region extend from $x = -\infty$ to $x = +\infty$ —can be represented by a curve $z = h_l(x)$ at the interface. We further assume that this curve will be the flat surface $z = H_l$ almost everywhere but will be irregular within some finite region, where it can be defined by a set of points (x_i, z_i). The same curve can also be represented in polar coordinates $(\hat{r}, \hat{\theta})$, with $\hat{r} = \hat{r}(\hat{\theta})$ in a common coordinate system $(\hat{x}, \hat{z})$, with origin at some point $\hat{O}$ above the half space as follows:

As in the case of surface Love waves (chapter 3), with surface Rayleigh-wave potentials or body P- or SV-wave potentials—φ_l^-, φ_l^+ for P waves and ψ_l^-, ψ_l^+ for SV waves—at each layer l incident to these irregular surfaces, additional scattered-wave potentials are generated, which can be represented by

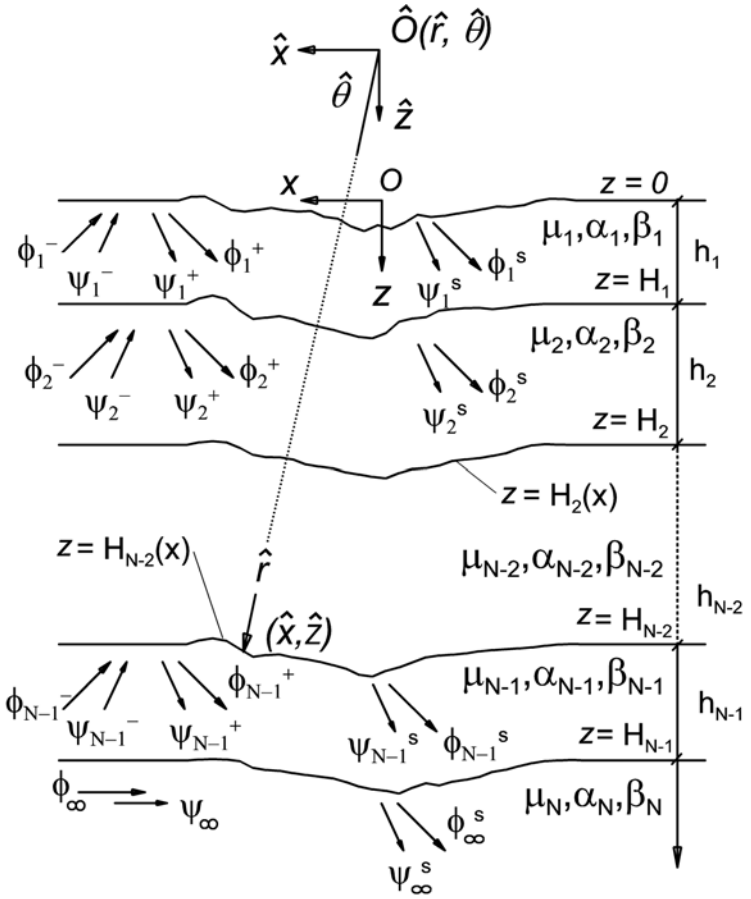

Figure IV.2. Irregularly shaped, N-layered half space with Rayleigh waves.

$$\begin{aligned}\varphi_l^s &= \sum_{n=0}^{\infty}\left(A_{l,n}^{(1)}H_n^{(1)}(k_{\alpha_l}\hat{r}) + A_{l,n}^{(2)}H_n^{(2)}(k_{\alpha_l}\hat{r})\right)\ \cos n\theta \\ \psi_l^s &= \sum_{n=0}^{\infty}\left(B_{l,n}^{(1)}H_n^{(1)}(k_{\beta_l}\hat{r}) + B_{l,n}^{(2)}H_n^{(2)}(k_{\beta_l}\hat{r})\right)\ \cos n\theta\end{aligned}, \tag{IV.3}$$

with both outgoing and incoming waves for each layer $l = 1, 2, \ldots, N-1$, except for the last semi-infinite layer. For this layer, $l = N$, the scattered waves, $\varphi_\infty^s = \varphi_N^s$ and $\psi_\infty^s = \psi_N^s$, respectively, the P- and SV- potentials, take the forms

$$\begin{aligned}\varphi_\infty^s = \varphi_N^s &= \sum_{n=0}^{\infty} A_{\infty,n}H_n^{(1)}(k_{\alpha_l}\hat{r})\ \cos n\theta \\ \psi_\infty^s = \psi_N^s &= \sum_{n=0}^{\infty} B_{\infty,n}H_n^{(1)}(k_{\beta_l}\hat{r})\ \cos n\theta\end{aligned}, \tag{IV.4}$$

with only outgoing waves satisfying Somerfield's radiation condition at infinity.

The scattered waves, together with the free-filed surface Rayleigh or body P and SV waves, form the resultant waves in the layered medium. Writing $\varphi_l^{ff} = \varphi_l^+ + \varphi_l^-$ and $\psi_l^{ff} = \psi_l^+ + \psi_l^-$ as the free-field surface Rayleigh or body P and SV waves in the l^{th} layer, the resultant waves in the same layer are $\varphi_l = \varphi_l^{ff} + \varphi_l^s$ and $\psi_l = \psi_l^{ff} + \psi_l^s$, respectively, for the P and SV wave potentials. Together, these waves must satisfy the following set of boundary conditions (Lee and Wu, 1994b):

1. On the half-space surface, $z = H_0(x)$, the resultant waves in the top layer $(l = 1)$ must together satisfy the half-space surface-traction (stress)-free boundary condition, as follows:

$$\tilde{T} = T_r \hat{e}_r + T_\theta \hat{e}_\theta = 0 \quad \text{at} \quad z = H_0(x); \tag{IV.5a}$$

separating the contribution of traction due to the free-field and scattered waves, we have:

$$\tilde{T} = \tilde{T}^{ff} + \tilde{T}^s, \tag{IV.5b}$$

which gives, at $z = H_0(x)$:

$$\begin{aligned} T_r^s &= -T_r^{ff} \\ T_\theta^s &= -T_\theta^{ff} \end{aligned}. \tag{IV.5c}$$

2. For $l = 1, 2, \ldots, N-1$, at the interface between the l^{th} layer and the $(l+1)^{th}$ layer below, $z = H_l(x)$, the resultant waves in these two layers must satisfy the continuity of displacement and stress at the interface, at $z = H_l(x)$:

$$\begin{aligned} \tilde{U}_l &= \tilde{U}_{l+1} \\ \tilde{T}_l &= \tilde{T}_{l+1} \end{aligned}; \tag{IV.6a}$$

with U_l, $\tilde{T}_l$, respectively, the displacement and traction vectors in layer l, and U_{l+1}, $\tilde{T}_{l+1}$ the corresponding ones in layer $l+1$. Separating the contribution of the displacement and traction due to the free-field and scattered waves, we have:

$$\begin{aligned} \tilde{\boldsymbol{U}}_l &= \tilde{\boldsymbol{U}}_l^{ff} + \tilde{\boldsymbol{U}}_l^{s} \\ \tilde{\boldsymbol{T}}_l &= \tilde{\boldsymbol{T}}_l^{ff} + \tilde{\boldsymbol{T}}_l^{s} \end{aligned}, \tag{IV.6b}$$

which gives, at $\boldsymbol{z} = \boldsymbol{H}_l(\boldsymbol{x})$:

$$\begin{aligned} \tilde{\boldsymbol{U}}_l^{s} - \tilde{\boldsymbol{U}}_{l+1}^{s} &= -\left(\tilde{\boldsymbol{U}}_l^{ff} - \tilde{\boldsymbol{U}}_{l+1}^{ff}\right) \\ \tilde{\boldsymbol{T}}_l^{s} - \tilde{\boldsymbol{T}}_{l+1}^{s} &= -\left(\tilde{\boldsymbol{T}}_l^{ff} - \tilde{\boldsymbol{T}}_{l+1}^{ff}\right) \end{aligned}, \tag{IV.6c}$$

where the unknown wave functions are on the left-hand side and the known functions are on the right-hand side. As in Eq. (IV.3) above, both the displacement and traction vectors at each layer can be expressed in the radial and tangential components, as follows:

$$\begin{aligned} \tilde{\boldsymbol{U}}_l &= \left(\boldsymbol{U}_l\right)_r \hat{\boldsymbol{e}}_r + \left(\boldsymbol{U}_l\right)_\theta \hat{\boldsymbol{e}}_\theta \\ \tilde{\boldsymbol{T}}_l &= \left(\boldsymbol{T}_l\right)_r \hat{\boldsymbol{e}}_r + \left(\boldsymbol{T}_l\right)_\theta \hat{\boldsymbol{e}}_\theta \end{aligned}, \tag{IV.7}$$

so that the displacement and traction vectors in Eq. (IV.6b) can be separated into component forms, at $\boldsymbol{z} = \boldsymbol{H}_l(\boldsymbol{x})$:

$$\begin{aligned} \left(\boldsymbol{U}_{l+1}^{s}\right)_r - \left(\boldsymbol{U}_l^{s}\right)_r &= -\left(\left(\boldsymbol{U}_{l+1}^{ff}\right)_r - \left(\boldsymbol{U}_l^{ff}\right)_r\right) \\ \left(\boldsymbol{U}_{l+1}^{s}\right)_\theta - \left(\boldsymbol{U}_l^{s}\right)_\theta &= -\left(\left(\boldsymbol{U}_{l+1}^{ff}\right)_\theta - \left(\boldsymbol{U}_l^{ff}\right)_\theta\right) \end{aligned} \tag{IV.8a}$$

and

$$\begin{aligned} \left(\boldsymbol{T}_{l+1}^{s}\right)_r - \left(\boldsymbol{T}_l^{s}\right)_r &= -\left(\left(\boldsymbol{T}_{l+1}^{ff}\right)_r - \left(\boldsymbol{T}_l^{ff}\right)_r\right) \\ \left(\boldsymbol{T}_{l+1}^{s}\right)_\theta - \left(\boldsymbol{T}_l^{s}\right)_\theta &= -\left(\left(\boldsymbol{T}_{l+1}^{ff}\right)_\theta - \left(\boldsymbol{T}_l^{ff}\right)_\theta\right) \end{aligned}. \tag{IV. 8b}$$

Here, the radial and tangential components of traction, $\boldsymbol{T}_r$ and $\boldsymbol{T}_\theta$, can be expressed in terms of the various components of stresses in cylindrical coordinates (Lee and Wu, 1994b):

$$\begin{aligned} \boldsymbol{T}_r &= \sigma_r \cos\alpha + \tau_{r\theta} \sin\alpha \\ \boldsymbol{T}_\theta &= \sigma_\theta \sin\alpha + \tau_{r\theta} \cos\alpha \end{aligned}, \tag{IV.9}$$

where α is the angle that the normal $\hat{\boldsymbol{n}} = \boldsymbol{n}_r \hat{\boldsymbol{e}}_r + \boldsymbol{n}_\theta \hat{\boldsymbol{e}}_\theta = \cos\alpha\, \hat{\boldsymbol{e}}_r + \sin\alpha\, \hat{\boldsymbol{e}}_\theta$ makes with the radial vector, as shown in Fig. IV.3 (Lee and Wu, 1994a,b):

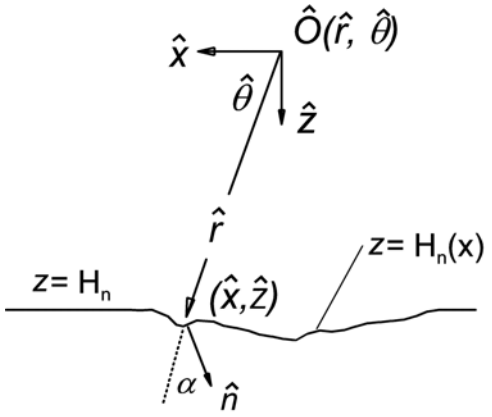

Fig. IV.3. Angle α between radial vector and normal at a point (Lee and Wu, 1994a,b).

Expressions for the radial and angular components of the displacement vectors and stresses can be expressed in terms of the corresponding wave potentials (Pao and Mow, 1973). For the scattered wave potentials, at a point $\left(\hat{r},\hat{\theta}\right)=\left(\hat{r}(\theta),\hat{\theta}\right)$ on the irregular surface (or at any point anywhere) they will take the following form:

$$\begin{aligned}\left(U_l^s\right)_r &= \sum_n{}_{j=1,2}\, A_{l,n}^{(j)} D_{r1}^{(j)}(n, k_{\alpha_l}\hat{r},\hat{\theta}) + B_{l,n}^{(j)} D_{r2}^{(j)}(n, k_{\beta_l}\hat{r},\hat{\theta}) \\ \left(U_l^s\right)_\theta &= \sum_n{}_{j=1,2}\, A_{l,n}^{(j)} D_{\theta 1}^{(j)}(n, k_{\alpha_l}\hat{r},\hat{\theta}) + B_{l,n}^{(j)} D_{\theta 2}^{(j)}(n, k_{\beta_l}\hat{r},\hat{\theta})\end{aligned}, \tag{IV.10}$$

where $D_{r1}^{(j)}(n, k_{\alpha_l}\hat{r},\hat{\theta})$ and $D_{r2}^{(j)}(n, k_{\beta_l}\hat{r},\hat{\theta})$ are the corresponding radial displacements from the P and SV scattered-wave potentials, and $D_{\theta 1}^{(j)}(n, k_{\alpha_l}\hat{r},\hat{\theta})$ and $D_{\theta 2}^{(j)}(n, k_{\beta_l}\hat{r},\hat{\theta})$ are their corresponding angular displacements.

Similarly, the traction components at a point on the irregular surface $\left(\hat{r},\hat{\theta}\right)=\left(\hat{r}(\theta),\hat{\theta}\right)$ with normal $\hat{n}=n_r\hat{e}_r+\ n_\theta\,\hat{e}_\theta=\cos\alpha\,\hat{e}_r+\ \sin\alpha\,\hat{e}_\theta$ take the form:

$$\left(T_l^s\right)_r = \sum_n \sum_{j=1,2} A_{l,n}^{(j)} \mathcal{T}_{r1}^{(j)}(n, k_{\alpha_l}\hat{r}, \hat{\theta}, \hat{n}) + B_{l,n}^{(j)} \mathcal{T}_{r2}^{(j)}(n, k_{\beta_l}\hat{r}, \hat{\theta}, \hat{n})$$
$$\left(T_l^s\right)_\theta = \sum_n \sum_{j=1,2} A_{l,n}^{(j)} \mathcal{T}_{\theta 1}^{(j)}(n, k_{\alpha_l}\hat{r}, \hat{\theta}, \hat{n}) + B_{l,n}^{(j)} \mathcal{T}_{\theta 2}^{(j)}(n, k_{\beta_l}\hat{r}, \hat{\theta}, \hat{n}) \quad , \tag{IV.11}$$

where $\mathcal{T}_{r1}^{(j)} = \mathcal{T}_{r1}^{(j)}(n, k_{\alpha_l}\hat{r}, \hat{\theta}, \hat{n})$ and $\mathcal{T}_{r2}^{(j)} = \mathcal{T}_{r2}^{(j)}(n, k_{\beta_l}\hat{r}, \hat{\theta}, \hat{n})$ are the corresponding radial components of traction from the P and SV scattered-wave potentials. Similarly, $\mathcal{T}_{\theta 1}^{(j)} = \mathcal{T}_{\theta 1}^{(j)}(n, k_{\alpha_l}\hat{r}, \hat{\theta}, \hat{n})$, $\mathcal{T}_{\theta 2}^{(j)} = \mathcal{T}_{\theta 2}^{(j)}(n, k_{\alpha_l}\hat{r}, \hat{\theta}, \hat{n})$ are the corresponding stresses.

Using the weighted-residue method, as in the case of the out-of-plane Love waves in chapter 3, from Harrington (1967) for electromagnetic waves and Lee and Wu (1994a,b) for elastic waves, the boundary conditions at each layer take the form:

1. Starting from the top layer, the half-space surface, from Eqs. (IV.4b):

$$\sum_{n=0}^{\infty} \sum_{j=1,2} \left\langle \mathcal{T}_{r1}^{(j)}(n, k_{\alpha_1}\hat{r}, \hat{\theta}, \hat{n}), w_m \right\rangle A_{1,n}^{(j)} + \left\langle \mathcal{T}_{r2}^{(j)}(n, k_{\beta_1}\hat{r}, \hat{\theta}, \hat{n}), w_m \right\rangle B_{1,n}^{(j)} = -\left\langle \left(T_1^{ff}\right)_r, w_m \right\rangle$$
$$\sum_{n=0}^{\infty} \sum_{j=1,2} \left\langle \mathcal{T}_{\theta 1}^{(j)}(n, k_{\alpha_1}\hat{r}, \hat{\theta}, \hat{n}), w_m \right\rangle A_{1,n}^{(j)} + \left\langle \mathcal{T}_{\theta 2}^{(j)}(n, k_{\beta_1}\hat{r}, \hat{\theta}, \hat{n}), w_m \right\rangle B_{1,n}^{(j)} = -\left\langle \left(T_1^{ff}\right)_\theta, w_m \right\rangle . \tag{IV.12}$$

2) For the interface between the l^{th} and $(l+1)^{th}$ layers, for $l = 1, 2, 3\ldots$ from Eq. (IV.8a) for displacements:

$$\sum_{n=0}^{\infty} \sum_{j=1,2} \Big[\left\langle D_{r1}^{(j)}(n, k_{\alpha_l}\hat{r}, \hat{\theta}), w_m \right\rangle A_{l,n}^{(j)} + \left\langle D_{r2}^{(j)}(n, k_{\beta_l}\hat{r}, \hat{\theta}), w_m \right\rangle B_{l,n}^{(j)} \tag{IV.13a}$$
$$- \left\langle D_{r1}^{(j)}(n, k_{\alpha_{l+1}}\hat{r}, \hat{\theta}), w_m \right\rangle A_{l+1,n}^{(j)} - \left\langle D_{r2}^{(j)}(n, k_{\beta_{l+1}}\hat{r}, \hat{\theta}), w_m \right\rangle B_{l+1,n}^{(j)} \Big] = -\left\langle \left(U_l^{ff}\right)_r - \left(U_{l+1}^{ff}\right)_r , w_m \right\rangle \tag{IV.13b}$$

$$\sum_{n=0}^{\infty} \sum_{j=1,2} \Big[\left\langle D_{\theta 1}^{(j)}(n, k_{\alpha_l}\hat{r}, \hat{\theta}), w_m \right\rangle A_{l,n}^{(j)} + \left\langle D_{\theta 2}^{(j)}(n, k_{\beta_l}\hat{r}, \hat{\theta}), w_m \right\rangle B_{l,n}^{(j)}$$

$$- \left\langle D_{\theta 1}^{(j)}(n,k_{\alpha_{l+1}}\hat{r},\hat{\theta}),w_m \right\rangle A_{l+1,n}^{(j)} - \left\langle D_{\theta 2}^{(j)}(n,k_{\beta_{l+1}}\hat{r},\hat{\theta}),w_m \right\rangle B_{l+1,n}^{(j)} \Big] = -\left\langle \left(U_l^{ff}\right)_\theta - \left(U_{l+1}^{ff}\right)_\theta , w_m \right\rangle$$

and from Eq. (8b) for stresses:

$$\sum_{n=0}^{\infty} \sum_{j=1,2} \Big[\left\langle T_{r1}^{(j)}(n,k_{\alpha_l}\hat{r},\hat{\theta},\hat{n}) , w_m \right\rangle A_{l,n}^{(j)} + \left\langle T_{r2}^{(j)}(n,k_{\beta_l}\hat{r},\hat{\theta},\hat{n}) , w_m \right\rangle B_{l,n}^{(j)} \tag{IV.14a}$$

$$- \left\langle T_{r1}^{(j)}(n,k_{\alpha_{l+1}}\hat{r},\hat{\theta},\hat{n}) , w_m \right\rangle A_{l+1,n}^{(j)} - \left\langle T_{r2}^{(j)}(n,k_{\beta_{l+1}}\hat{r},\hat{\theta},\hat{n}) , w_m \right\rangle B_{l+1,n}^{(j)} \Big] = -\left\langle \left(T_l^{ff}\right)_r - \left(T_{l+1}^{ff}\right)_r , w_m \right\rangle$$

$$\sum_{n=0}^{\infty} \sum_{j=1,2} \Big[\left\langle T_{\theta 1}^{(j)}(n,k_{\alpha_l}\hat{r},\hat{\theta},\hat{n}) , w_m \right\rangle A_{l,n}^{(j)} + \left\langle T_{\theta 2}^{(j)}(n,k_{\beta_l}\hat{r},\hat{\theta},\hat{n}) , w_m \right\rangle B_{l,n}^{(j)} \tag{IV.14b}$$

$$- \left\langle T_{\theta 1}^{(j)}(n,k_{\alpha_{l+1}}\hat{r},\hat{\theta},\hat{n}) , w_m \right\rangle A_{l+1,n}^{(j)} - \left\langle T_{\theta 2}^{(j)}(n,k_{\beta_{l+1}}\hat{r},\hat{\theta},\hat{n}) , w_m \right\rangle B_{l+1,n}^{(j)} \Big] = -\left\langle \left(T_l^{ff}\right)_\theta - \left(T_{l+1}^{ff}\right)_\theta , w_m \right\rangle .$$

In matrix form, Eqns. (IV.13a,b) and (IV.14a,b) take the form:

$$\sum_{n=0}^{\infty} \sum_{j=1,2} \begin{bmatrix} D_{r1}^{(j)}(l,m,n) & D_{r2}^{(j)}(l,m,n) & -D_{r1}^{(j)}(l+1,m,n) & -D_{r2}^{(j)}(l+1,m,n) \\ D_{\theta 1}^{(j)}(l,m,n) & D_{\theta 2}^{(j)}(l,m,n) & -D_{\theta 2}^{(j)}(l+1,m,n) & -D_{\theta 2}^{(j)}(l+1,m,n) \\ T_{r1}^{(j)}(l,m,n) & T_{r2}^{(j)}(l,m,n) & -T_{r1}^{(j)}(l+1,m,n) & -T_{r2}^{(j)}(l+1,m,n) \\ T_{\theta 1}^{(j)}(l,m,n) & T_{\theta 2}^{(j)}(l,m,n) & -T_{\theta 1}^{(j)}(l+1,m,n) & -T_{\theta 2}^{(j)}(l+1,m,n) \end{bmatrix} \begin{Bmatrix} A_{l,n}^{(j)} \\ B_{l,n}^{(j)} \\ A_{l+1,n}^{(j)} \\ B_{l+1,n}^{(j)} \end{Bmatrix}$$

$$= -\begin{Bmatrix} \left\langle \left(U_l^{ff}\right)_r - \left(U_{l+1}^{ff}\right)_r , w_m \right\rangle \\ \left\langle \left(U_l^{ff}\right)_\theta - \left(U_{l+1}^{ff}\right)_\theta , w_m \right\rangle \\ \left\langle \left(T_l^{ff}\right)_r - \left(T_{l+1}^{ff}\right)_r , w_m \right\rangle \\ \left\langle \left(T_l^{ff}\right)_\theta - \left(T_{l+1}^{ff}\right)_\theta , w_m \right\rangle \end{Bmatrix} \tag{IV.14c}$$

with properly defined matrix elements $D_{r1}^{(j)}(l,m,n)$,… and $T_{r1}^{(j)}(l,m,n)$,… etc.

Note that for the interface between layer $N-1$ and the (last) semi-infinite layer N , Eqs. (13a,b) and (14a,b) will have only the outgoing wave terms $A_{N,n}^{(1)}$, $B_{N,n}^{(1)}$, $n = 0,1,2\ldots$ and without the incoming wave terms $A_{N,n}^{(2)}$, $B_{N,n}^{(2)}$, $n = 0,1,2\ldots$

IV.3.2 Numerical Implementation

For the completeness of this presentation, we include here a brief summary of the numerical procedure used to apply the system of complex equations derived in the last section for in-plane Rayleigh and body P and SV waves. Mathematically, this is the same procedure that we used in chapter 3 for out-of-plane Love waves and body SH waves.

For elastic half-space with N (≥ 1) layers, there are $(N-1)$ interfaces between the layers, plus the topmost half space with no elastic medium above. With Hankel functions of both the 1st and 2nd kind of both longitudinal P and shear SV waves present (except in the bottom semi-infinite layer), this gives a total of $2(N-1)+1=2N-1$ pairs of waves for 2N-1 pairs of (normal and shear) boundary conditions from all of the layers.

Since each set of equations at each interface involves only waves at each side of the interface, a simple, elegant numerical algorithm can be derived to allow each set of wave coefficients at each medium to be solved separately, making the problem simple numerically. This was already shown for Love waves in chapter 3. In other words, we are solving, for each layer, *M* complex equations in *M* unknowns separately at each step. The following is a detailed description of the numerical procedure.

Starting from the top surface, where $z=0$, we have the matrix equation for the zero-stress boundary condition along the whole (regular and irregular) surface of the half space, in the form:

$$\left[E_1\right]\left\{\tilde{C}_1^{(1)}\right\} + \left[E_1^*\right]\left\{\tilde{C}_1^{(2)}\right\} + \left\{\tilde{e}_1\right\}\Big|_{z=0} = \mathbf{0}, \qquad \text{(IV.15)}$$

where $\left\{\tilde{C}_1^{(1)}\right\}$ and $\left\{\tilde{C}_1^{(2)}\right\}$ are the two vectors $\left\{A_{10}^{(1)}, B_{10}^{(1)}, A_{11}^{(1)}, B_{11}^{(1)}, A_{12}^{(1)}, B_{12}^{(1)}, \ldots\right\}^T$ and $\left\{A_{10}^{(2)}, B_{10}^{(2)}, A_{11}^{(2)}, B_{11}^{(2)}, A_{12}^{(2)}, B_{12}^{(2)}, \ldots\right\}^T$, respectively, in the top layer. As in the case of Love and SH body waves in chapter 3, $\left\{\tilde{C}_1^{(2)}\right\}$ can be expressed in terms of $\left\{\tilde{C}_1^{(1)}\right\}$ and $\left\{\tilde{e}_1\right\}$.

Next, the displacement and stress-continuity equations at the interface between layers *l* and *l+1*, as in Eq. (IV.14c) above, at the interface, $z = h_l$ can be written in the form:

$$\left[\boldsymbol{M}_l(h_l)\right]\begin{Bmatrix}\tilde{C}_l^{(1)}\\ \tilde{C}_l^{(2)}\end{Bmatrix} + \left\{\tilde{e}_l(h_l)\right\} = \left[\boldsymbol{M}_{l+1}(h_l)\right]\begin{Bmatrix}\tilde{C}_{l+1}^{(1)}\\ \tilde{C}_{l+1}^{(2)}\end{Bmatrix} + \left\{\tilde{e}_{l+1}(h_l)\right\} \tag{IV.16}$$

$$\text{or in the form: } \begin{Bmatrix}\tilde{C}_{l+1}^{(1)}\\ \tilde{C}_{l+1}^{(2)}\end{Bmatrix} = \left[\boldsymbol{M}_l(h_l)\right]\begin{Bmatrix}\tilde{C}_l^{(1)}\\ \tilde{C}_l^{(2)}\end{Bmatrix} + \left\{\tilde{m}_l(h_l)\right\}$$

for some matrix $\left[\boldsymbol{M}_l(h_l)\right]$ and vector $\left\{\tilde{m}_l(h_l)\right\}$. Equation (IV.16) shows that the wave coefficients in layer *l+1* can be expressed in terms of those of layer *l* above, as in chapter 3. Iteratively, this can successively be applied from layer to layer backward. In other words, the coefficients in every layer can be expressed in terms of those in the top, first layer. Since in the top layer, Eq. (IV.15) shows that $\left\{\tilde{C}_1^{(2)}\right\}$ can be expressed in terms of $\left\{\tilde{C}_1^{(1)}\right\}$, the coefficients of each layer can all be expressed in terms of $\left\{\tilde{C}_1^{(1)}\right\}$, as follows:

$$\begin{Bmatrix}\tilde{C}_l^{(1)}\\ \tilde{C}_l^{(2)}\end{Bmatrix} = \left(\begin{bmatrix}T_{l1}(h_l)\\ T_{l2}(h_l)\end{bmatrix}\left\{\tilde{C}_1^{(1)}\right\} + \begin{Bmatrix}\tilde{t}_{l1}(h_l)\\ \tilde{t}_{l2}(h_l)\end{Bmatrix}\right) \tag{IV.17}$$

for some transformation matrices $T_{l1}(h_l)$ and $T_{l2}(h_l)$ and vectors $\tilde{t}_{l1}(h_l)$ and $\tilde{t}_{l2}(h_l)$. Note that at the bottom, semi-infinite layer, $l = N$, only outgoing waves (to infinity) exist, and $\left\{\tilde{C}_N^{(2)}\right\} = \left\{\tilde{0}\right\}$.

As in the case of Love waves in chapter 3, the reason why we decided to have the coefficients of all waves in each layer expressed in terms of the coefficients of waves in the top layer is that we know, for surface waves and for body waves, that the top-layer waves are more dominant.

IV.4 The Diffracted Mode Shapes of Rayleigh Waves and P and SV Body Waves

IV.4.1 The Input Free-Field Waves

We can calculate and plot the displacement mode shapes of in-plane Rayleigh surface waves for a selected range of periods starting from 15 s down to 0.04 s (0.07–25 Hz). We then do the same for the mode shapes resulting from in-plane body P and SV waves for a given incidence angle. We consider the body P and SV waves here as the "11^{th} and 12^{th} modes" of waves in the parallel, layered medium (Trifunac 1971; Wong and Trifunac 1979; Lee and Trifunac 1985, 1987; Todorovska et al. 2013). We are now able to extend this procedure to generate the mode shapes at every point on and below the surface of the layered medium (Lee et al. 2014).

Each of these mode shapes, at each period (frequency), will be used as the free-field input wave into the irregularly layered medium studied here. In what follows, we will take a rather simple two-layered medium to illustrate the process, as we did previously in the case of Love and body SH waves. The following parameters in Table IV.1 are used for this two-layered model.

Table IV.1. Two-Layered Velocity Model

Layer	Thickness, km	P-wave Speed, α, km/s	S-wave Speed, β, km/s	Density, ρ gm/cc
1	1.38000	1.70000	0.98000	1.28000
2	∞	6.40000	3.70000	2.71000

These are the same top and bottom layers of the six-layered model considered in many of our previous studies (e.g., Todorovska et al. 2013), except that the top layer is now 1.38 km thick. The computer program Haskel.exe is again used to calculate the phase velocities of each mode of Love waves, as in chapter 3, in the period 14.0 –0.04 s, for a total of 91 discrete period values.

IV.4.2 Scattered and Diffracted Mode Shapes

For this chapter, we select the same irregularly layered model as that used for Love surface waves and body SH waves in chapter 3. It is a shallow, "almost-flat" ellipse with a ratio of vertical minor axis / horizontal major axis = 0.1 at both the half-space surface and the interface of the two layers. The half width or radius of the horizontal major axis is taken to be 1.0 km long for both, or in other words the major diameter is 2.0 km long. Figure IV.4 shows a sketch of this model for excitation by incident Rayleigh surface waves and incident body P or SV waves.

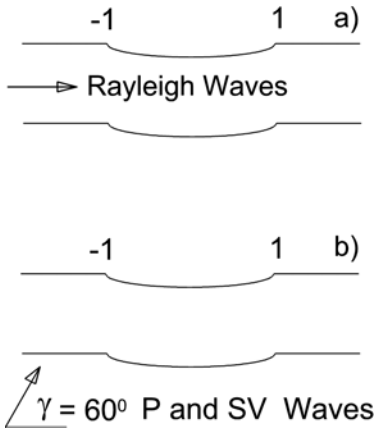

Fig. IV.4. The 2-layered model with (a) incident Rayleigh and (b) P and SV waves.

Figures IV.5a and IV.5b illustrate the scattered and diffracted mode shapes, respectively, for the horizontal (x-component) and vertical (z-component) motions of mode #3 of Rayleigh waves at four selected frequencies: f = 1.0, 2.0, 3.33, and 6.67 Hz. With the irregular, almost-flat, elliptic surfaces from $x = -1.0$ km to $x = +1.0$ km on both the half-space surface $(z = 0\,\text{km})$ and the surface of the interface of the two media $(z = 1.38\,\text{km})$, the diffracted mode shapes are plotted at equally spaced intervals along x from $x = -2.0$ km to $x = +2.0$ km, at 0.1 km apart. The dashed line on the left side of each graph represents the input free-field mode shapes propagating in the parallel-layered medium from the left and arriving at the irregular zone. The shapes of the elliptical canyons on the top and at the interface are also plotted with dashed lines, showing how they have deformed from the regular elliptical shape.

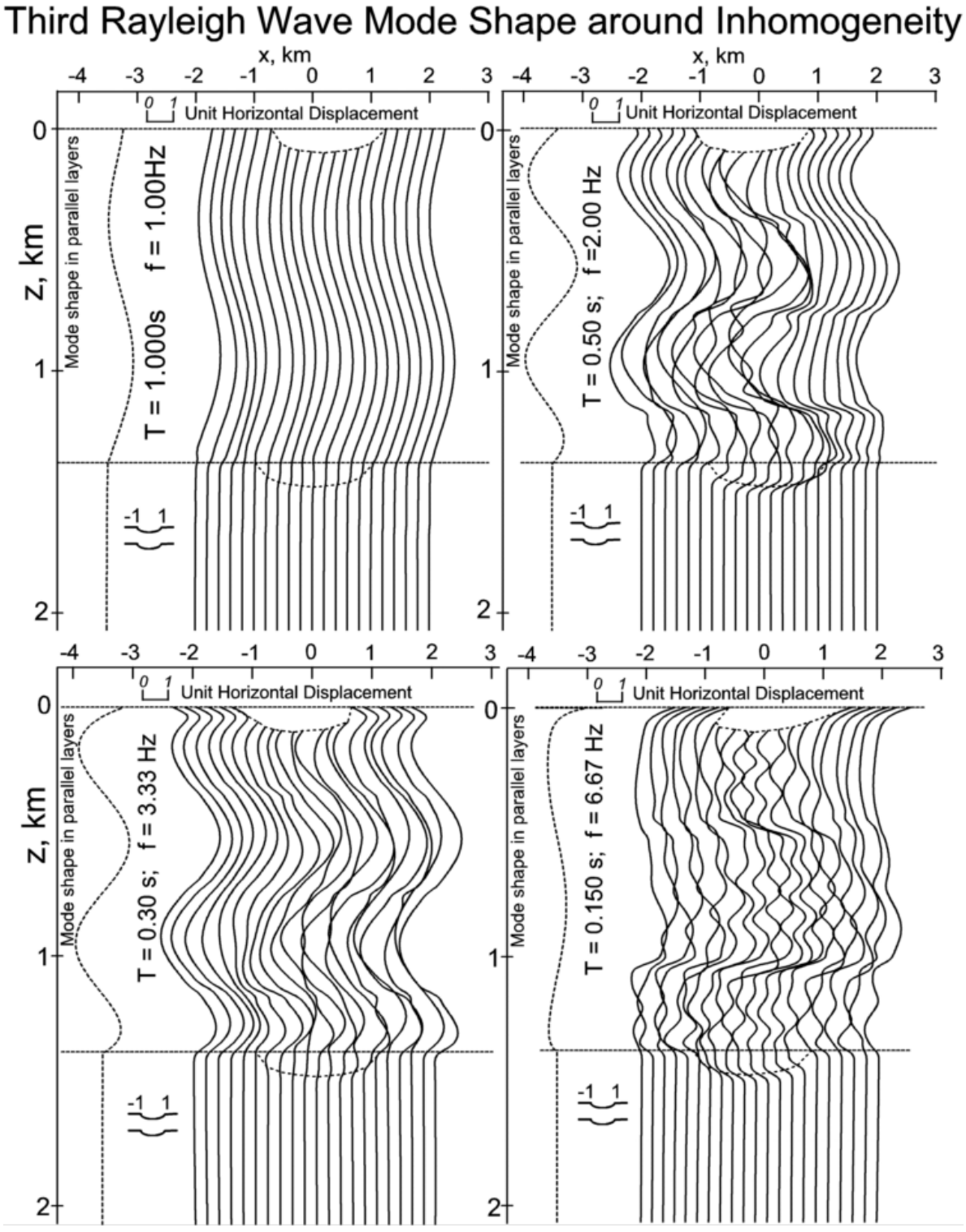

Fig. IV.5a. The third Rayleigh mode shape, horizontal (x-axis) component, with scattered and diffracted mode shapes at f = 1.0, 2.0, 3.33, and 6.67 Hz**.**

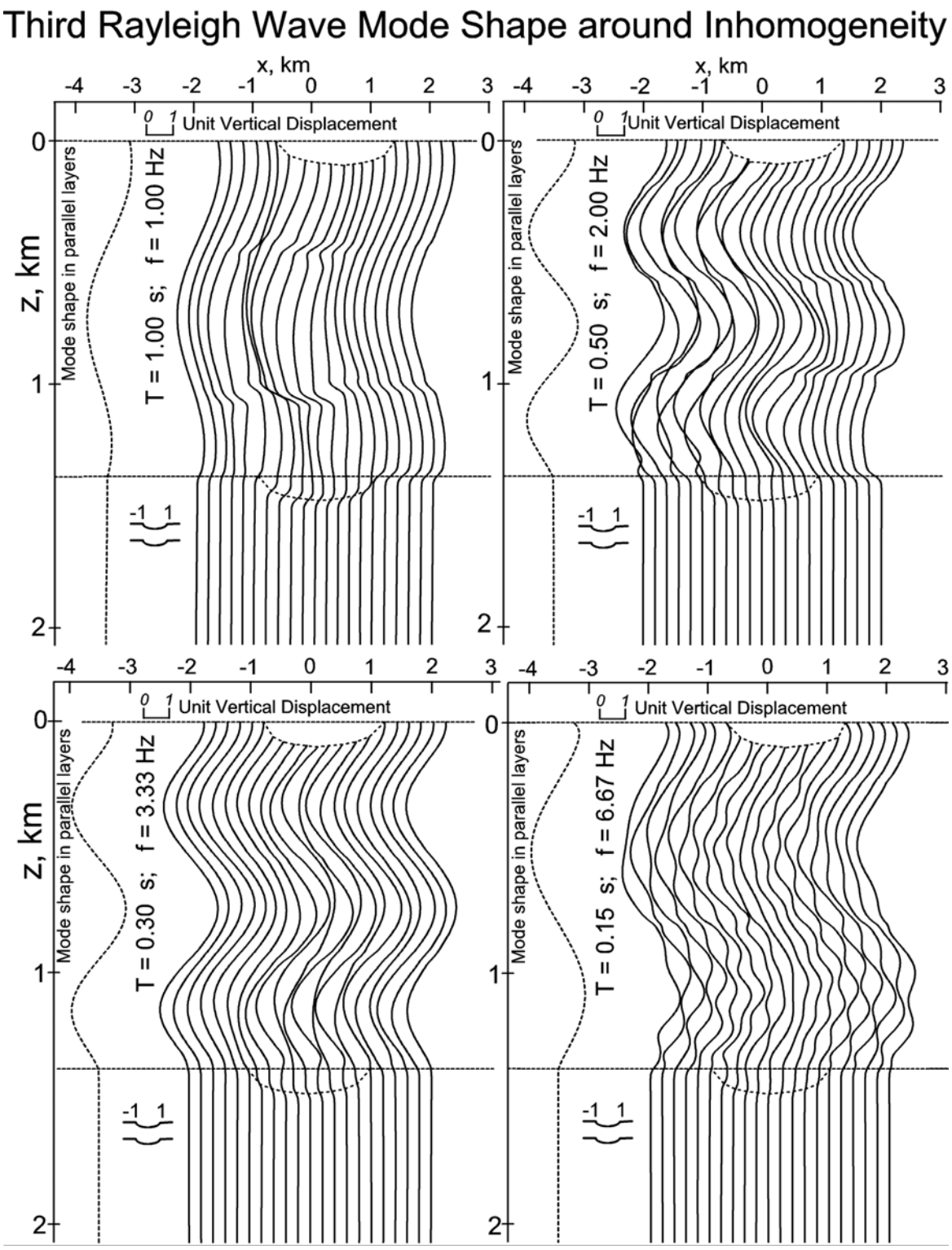

Fig. IV.5b. Third Rayleigh mode shape, vertical (z-axis) component, with scattered and diffracted mode shapes at f = 1.0, 2.0, 3.33, and 6.67 Hz.

For all frequencies below 1.0 Hz (or all periods above 1 s.), the waves are not much affected by the almost-flat, irregular surfaces. The higher-mode Rayleigh waves are more oscillatory in the layer before decaying to almost zero at the interface with the half space. As the mode number increases, both the mode shapes of the input free field and those of the diffracted Rayleigh waves go through *M-1* sign changes as they go down vertically from the top surface, where *"M"* is the mode number. Thus, the scattered and diffracted mode shapes are also more oscillatory in the layer. This behavior increases with increasing frequency. Further, such diffraction behavior also becomes more complex, for both the horizontal x- and vertical z-components of motion, as the mode number increases (Appendix R4-2).

At present, we are able to do the calculations of the scattered and diffracted waves for the Rayleigh waves up to f ~ 6.67 Hz (period #61, T = 0.15s). Calculations for higher frequencies, up to the frequency of f = 25.0 Hz (period #91, T = 0.04s), will need more work on the numerical procedures to ensure convergence of the computed results. This will be considered and described in our future papers.

IV.5 Synthetic, Scattered and Diffracted, In-Plane Time Histories

The scattered and diffracted, in-plane Rayleigh and body P and SV wave mode shapes can next be used to generate the synthetic, scattered and diffracted, in-plane radial (x-) and vertical (z-) components of accelerations at all points on and below the surface in the vicinity of the irregularly layered medium. The input Rayleigh and body P and SV waves to these diffracted waves are the in-plane waves generated in the regularly layered media of elastic half space. The complete description of the procedures for generation of these time histories is given in Todorovska et al. (2013). As in chapter 3, we will use the following parameters in Table IV.2 to generate the time-histories.

Table IV.2: Time-History Parameters

Case 1:	$\boldsymbol{M = 6.5,\ R = 8.0km,\ H = 6.0km,\ s = 0,\ s_L = 2}$
where	$\boldsymbol{M}$ = earthquake magnitude

	$\boldsymbol{R}$ = epicentral distance $\boldsymbol{H}$ = focal depth of earthquake $\boldsymbol{s}$ = geologic site condition of the recording site, where s = 0, alluvial site; s = 1, intermediate site; and s = 2, rock site $\boldsymbol{s_L}$ = soil condition of the recording site, where $\boldsymbol{s_L}$ = 0, rock soil; $\boldsymbol{s_L}$ =1, intermediate soil; and $\boldsymbol{s_L}$ =2, soft-soil type.

IV.5.1 Synthetic Time Histories

The time history of the radial and vertical in-plane motions at the top surface $\boldsymbol{z = 0}$ has been generated by the SYNACC method (Trifunac 1971; Wong and Trifunac 1979; Lee and Trifunac 1985, 1987; Todorovska et al. 2013). The time histories at points $\boldsymbol{z > 0}$, below the half-space surface, have been generated by the updated SYNACC program, which uses the mode shapes below the half-space surface to construct the motions at depth. Because of the scattering and diffraction, these in-plane mode shapes

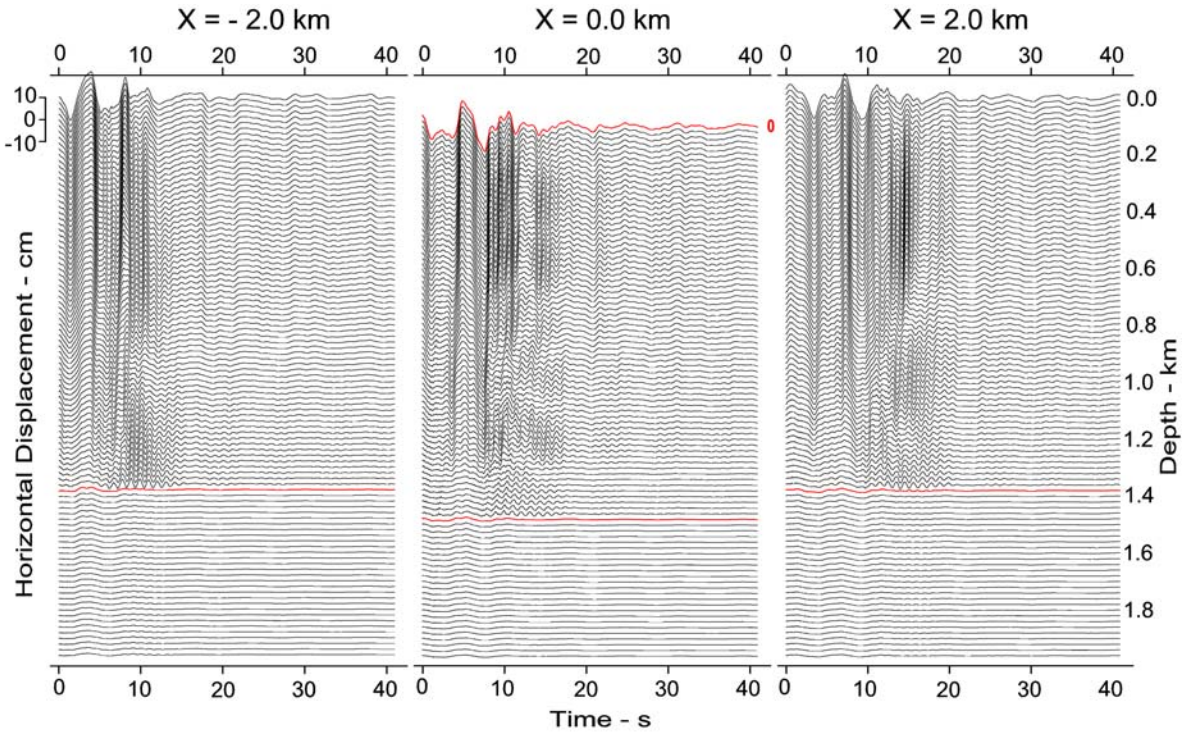

Fig. IV.6a. Horizontal, in-plane, synthetic displacements at x = -2.0, 0.0, and 2.0 km.

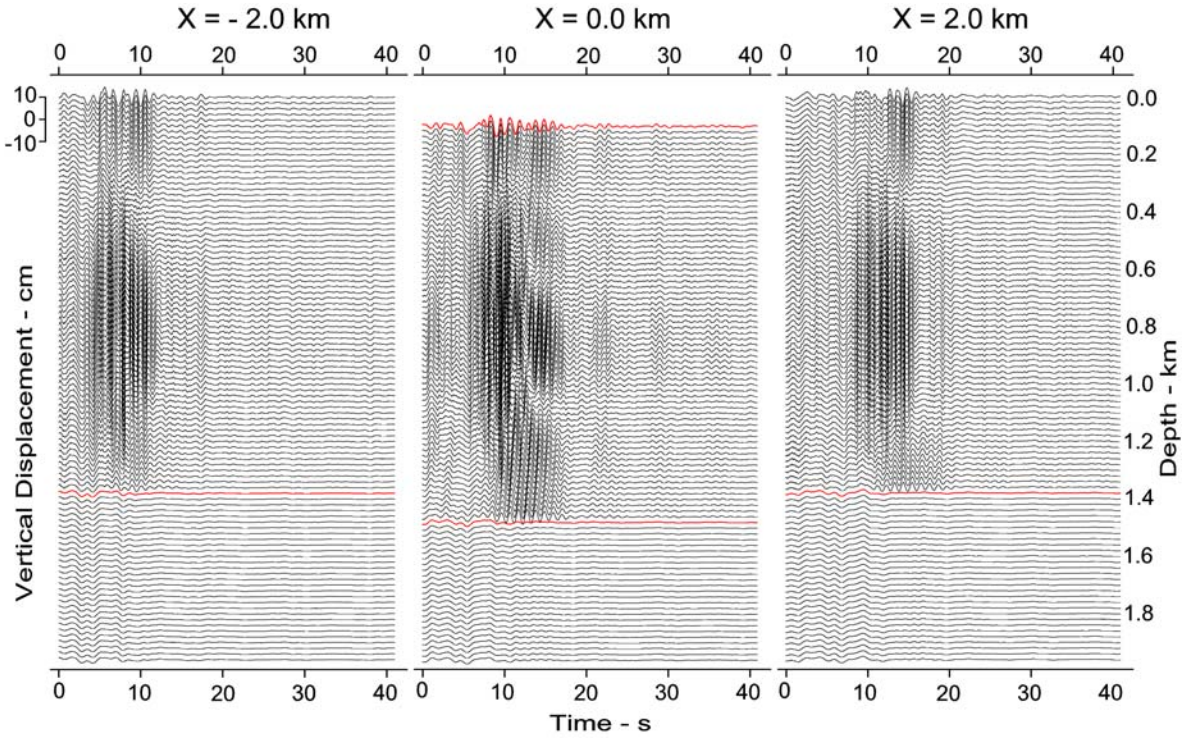

Fig. IV.6b. Vertical, in-plane, synthetic displacements at x = -2.0, 0.0, and 2.0 km.

are now space dependent, and therefore the acceleration time histories are different at every point on the half-space surface and at depth.

Figures IV.6a and IV.6b show the horizontal (radial; x- component) and vertical (z- component) motions for synthetic-displacement time histories calculated in the two-layered model at 101 depths equally spaced from the half-space surface ($\boldsymbol{z = 0}$) to a depth of $\boldsymbol{z = 2}$ km below the first layer up to a depth of $\boldsymbol{z = 1.38}$ km. The time histories are plotted as three vertical lines, at $\boldsymbol{x = -2.0}$ km (on the left), $\boldsymbol{x = 0.0}$ km (in the center), and $\boldsymbol{x = +2.0}$ km (on the right) of the center of the canyon. The time histories on the left and right sides of the canyon are all plotted from $\boldsymbol{z = 0}$ km, which is the layered half-space surface, while the time histories in the middle of the canyon start at $\boldsymbol{z = 0.1}$ km, which is the bottom of the canyon.

The origin at the center of the canyon on the half-space surface is situated at the epicentral distance of $R = 8.0\ km$ from an earthquake source at focal depth $H = 6.0$ km, so that the hypocentral distance is $D = 10.0$ km**.** The time history at the top and on the left is at $x = -2.0$ km, and thus it is at the epicentral distance of $R = 6.0\ km$ and a hypocentral distance of D □ **8.5** km, **1.5** km closer. Similarly, the time history at top right is at $x = +2.0$ km, and thus it is at an epicentral distance of $R = 10.0\ km$ and a hypocentral distance of D □ **11.7** km, or **1.7** km further away.

In all of the figures, the strong motions are seen mainly in the top layer, at depths of up to 1.38 km. Further, in all of the figures, whether it is the radial x- component or the vertical z- component, and whether it is the acceleration, velocity, or displacement motion, it can be seen that the waves arrive earlier on the left side and later on the right side.

IV.5.2 Fourier- and Response-Spectral Amplitudes

The time histories in Fig. IV.6a,b show that the motions can differ appreciably from point to point in the vicinity of the irregularly layered medium. To illustrate the variations of these motions from an earthquake-engineering viewpoint, we will next show the pseudo relative velocity (PSV) and Fourier (FS) spectral amplitudes at selected points.

Figures IV.7a and IV.7b show the plots of the PSV spectral amplitudes at several surface points on the layered medium. The format of the plots we use is a typical "Volume 3" plot, which we use in the routine digitization (Trifunac and Lee 1979) and data processing (Lee and Trifunac 1979) of strong-motion accelerograms to describe the spectral content in the strong ground motions.

Overall, these spectral amplitudes are very similar, but their details are all different. The spectra are plotted at four points on the irregularly layered media. Each point on top and below the layered media, and to the left and right of the irregular surface and interface, will have its own spectral amplitudes.

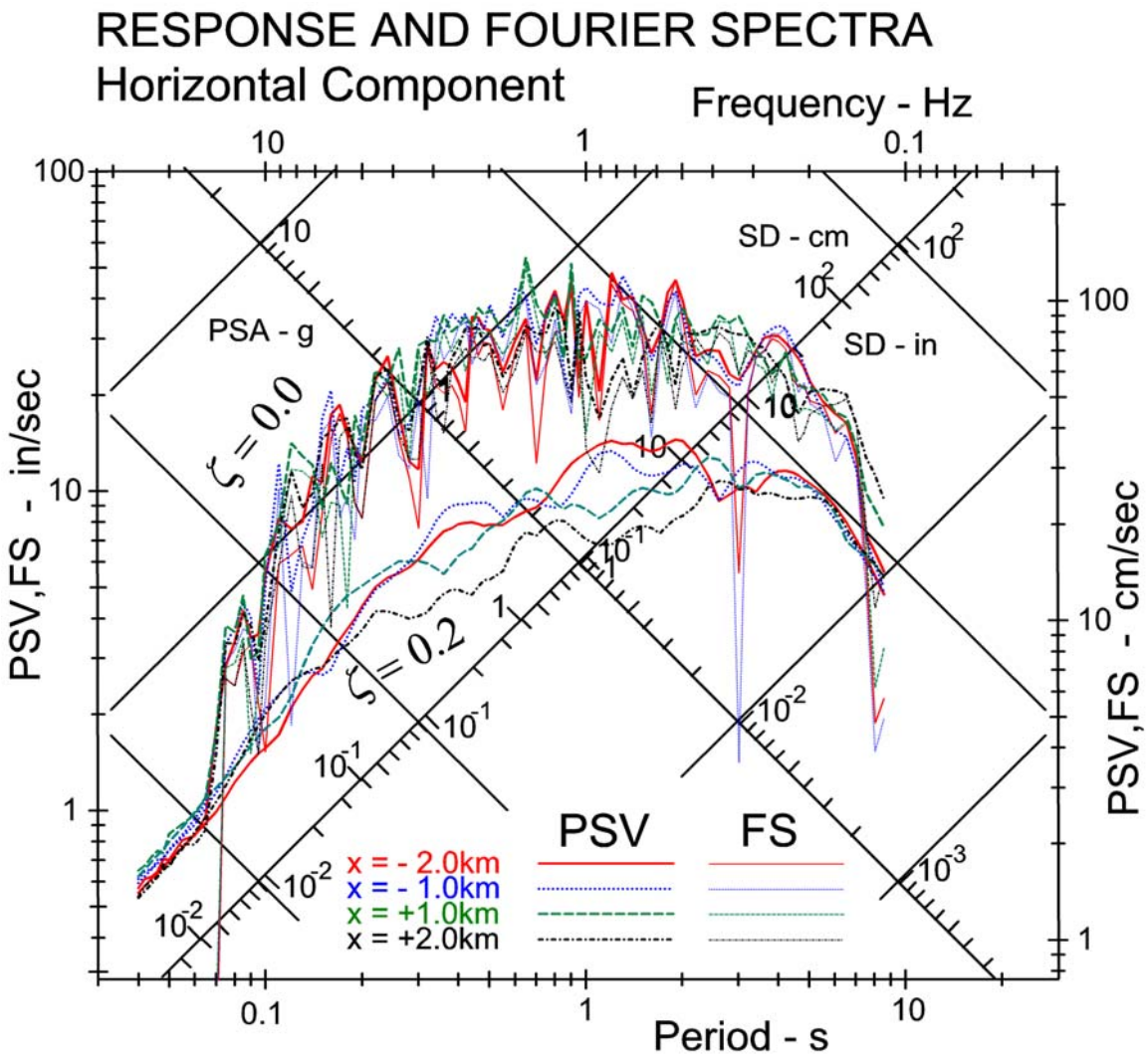

Fig. IV.7a. Response- and Fourier-amplitude spectra—horizontal components.

Illustrating how the Fourier- and response-spectral amplitudes change from point to point from left to right and from top to bottom in the vicinity of inhomogeneity would take too many pages of plots to show the amplitudes at many different points. However, a simple and convenient way to accomplish this is to plot the contours of the Fourier- and response-spectral amplitudes at a sufficient number of selected periods inside the medium. Figures IV.8a and IV.8b are plots of this type, which show the radial (x-) and vertical (z-) contour plots of the Fourier-spectral amplitudes in units of in./s at 12 selected periods:

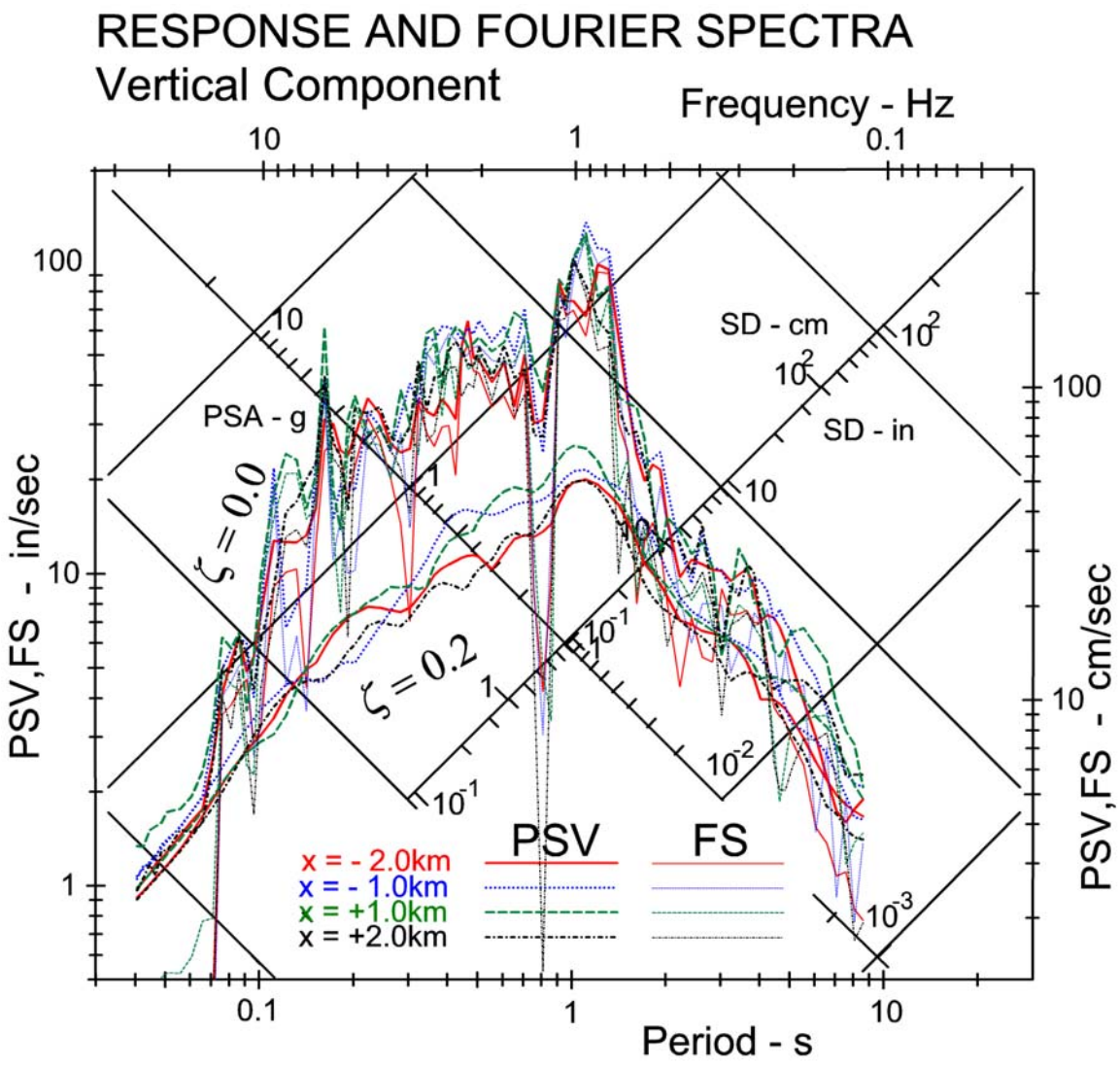

Fig. IV.7b Response- and Fourier-amplitude spectra—vertical components.

T = 0.15, 0.20, 0.30, 0.40, 0.50, 0.75, 1.00, 1.50, 2.00, 4.00, 5.00, and 7.50 s, at the corresponding frequencies: f = 6.67, 5.00, 3.33, 2.50, 2.00, 1.33, 1.00, 0.67, 0.50, 0.25, 0.20, and 0.133 Hz.

The contours are plotted with the logarithms of the Fourier amplitudes, so that the contour levels are also in log scale, with log (FS) ranging from -1.0 to 2.25 in steps of 0.25, and the Fourier amplitudes in the linear scale ranging from 0.10 in./s to over 315 in./s. It can be seen that for all of the 12 periods shown the Fourier amplitudes are larger

in the top layer, with amplitudes varying from point to point in the range from around 1 in./s to above 100 in./s**.** Below the top layer**,** z > 1.38 km, and the motions are typically smaller than 1 in./s.

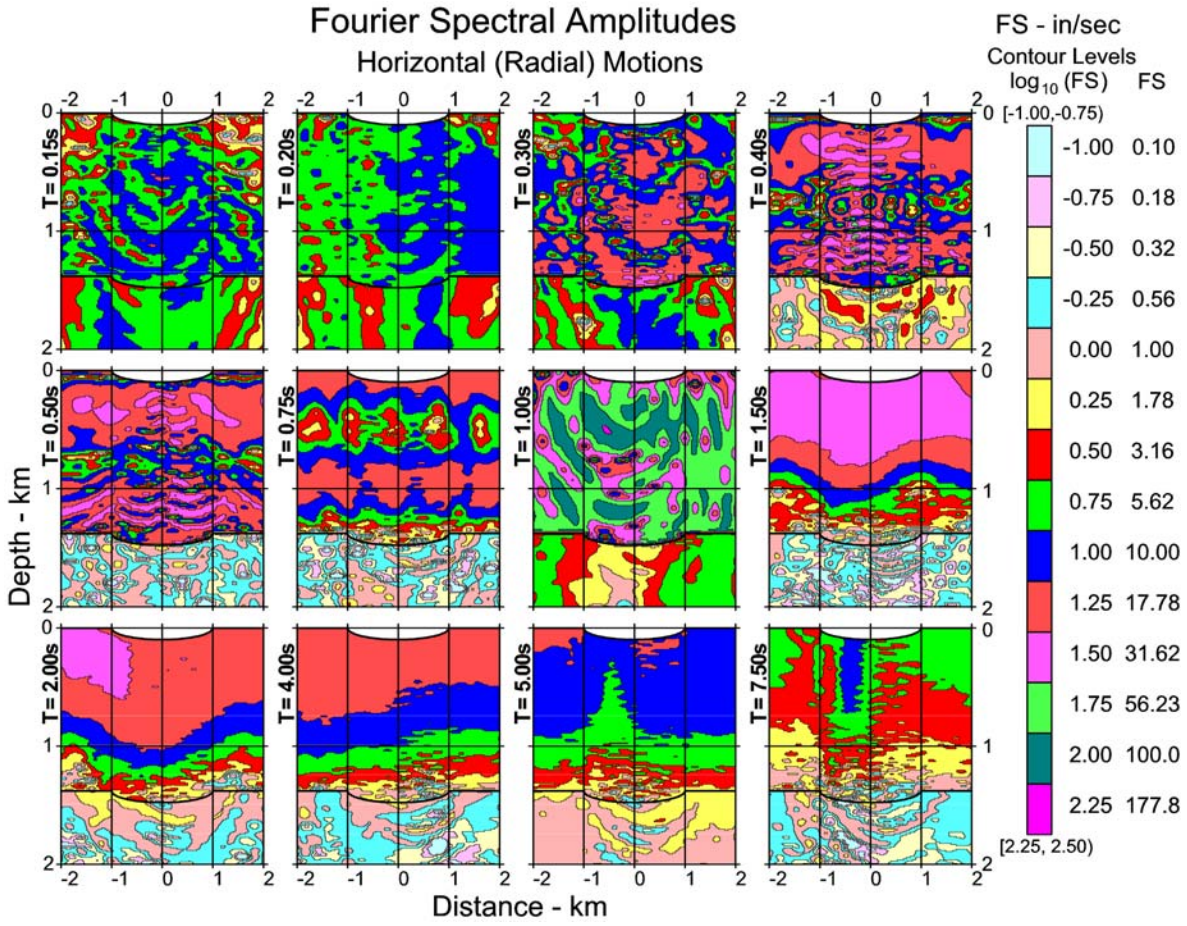

Fig. IV.8a Fourier-spectral amplitudes—horizontal components.

There is one noticeable difference between Figs IV.8a and **IV.**8b, on the one hand, for the in-plane, radial- and vertical-component Fourier amplitudes here, and the corresponding amplitudes in Fig. III.8, on the other hand, for the out-of-plane, transverse-component Fourier amplitudes in chapter 3**.** Comparing the figures here and in chapter 3, it can be seen that in each of the 12 periods plotted, the Fourier amplitude contours vary much more and are more oscillatory inside the layer. Physically, the out-of-plane, transverse motions in chapter 3 are of only one component and one type of motion—namely, the horizontal transverse component of motion, which does not lead to mode

conversion anywhere in the model. In contrast, the in-plane radial and vertical motions here are of two components and of two types of motions—namely, the horizontal and vertical in-plane motions on the one hand, and the longitudinal and shear-wave motions of different wave speeds on the other. Thus, the mode conversions, which are present for all motions studied in this chapter lead to more complicated contour plots, as illustrated in Figs. IV.8a and IV.8b.

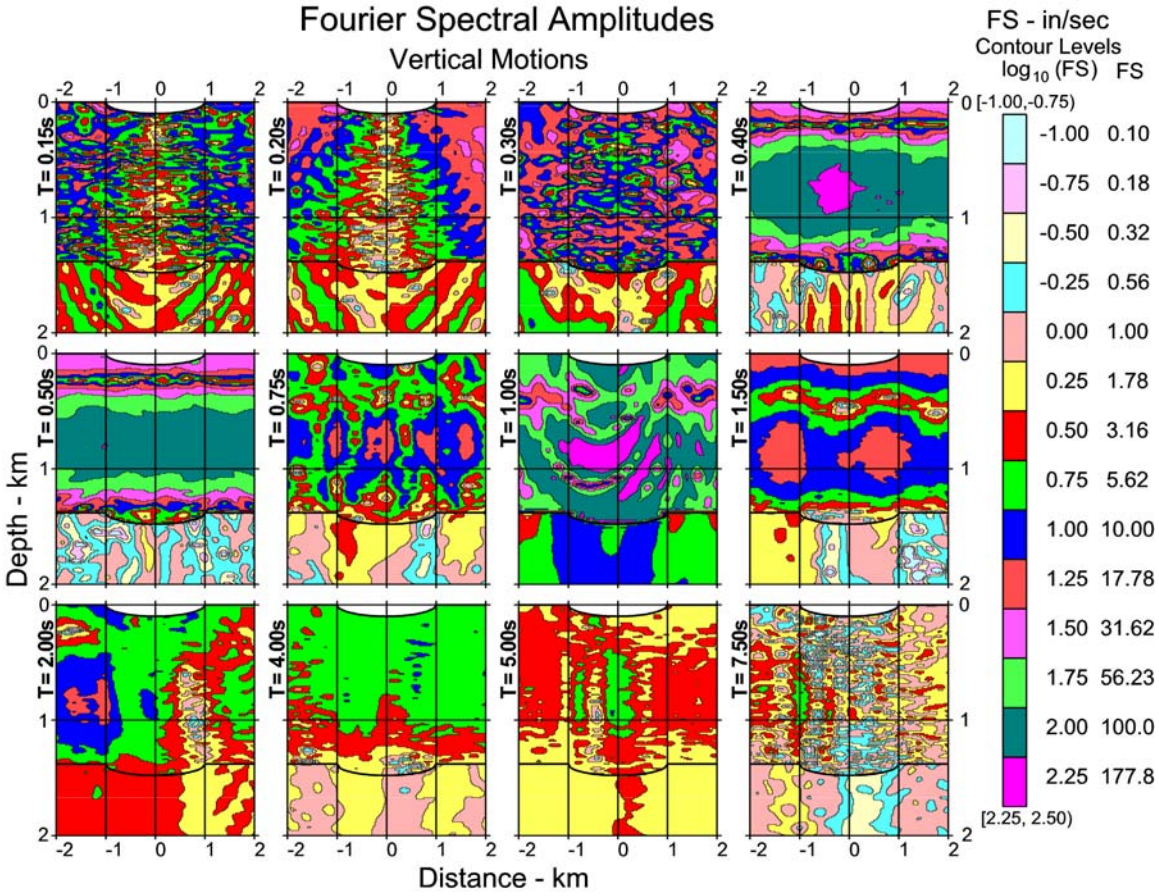

Fig. IV.8b. Fourier-spectral amplitudes—vertical component.

Figures IV.9a and IV.9b show the contour plots of in-plane radial and vertical components of the PSV response-spectral amplitudes at 5% damping in units of in./s These plots show the same trends and ranges of amplitudes as the Fourier amplitudes in Figs. IV.8a and IV.8b. Again, comparing with the corresponding figures in chapter 3, for the out-of-plane, transverse component 5% PSV amplitudes**,** while the contour levels there and here are of comparable amplitudes, at each of the 12 periods shown, the contour values here change more and faster from point to point.

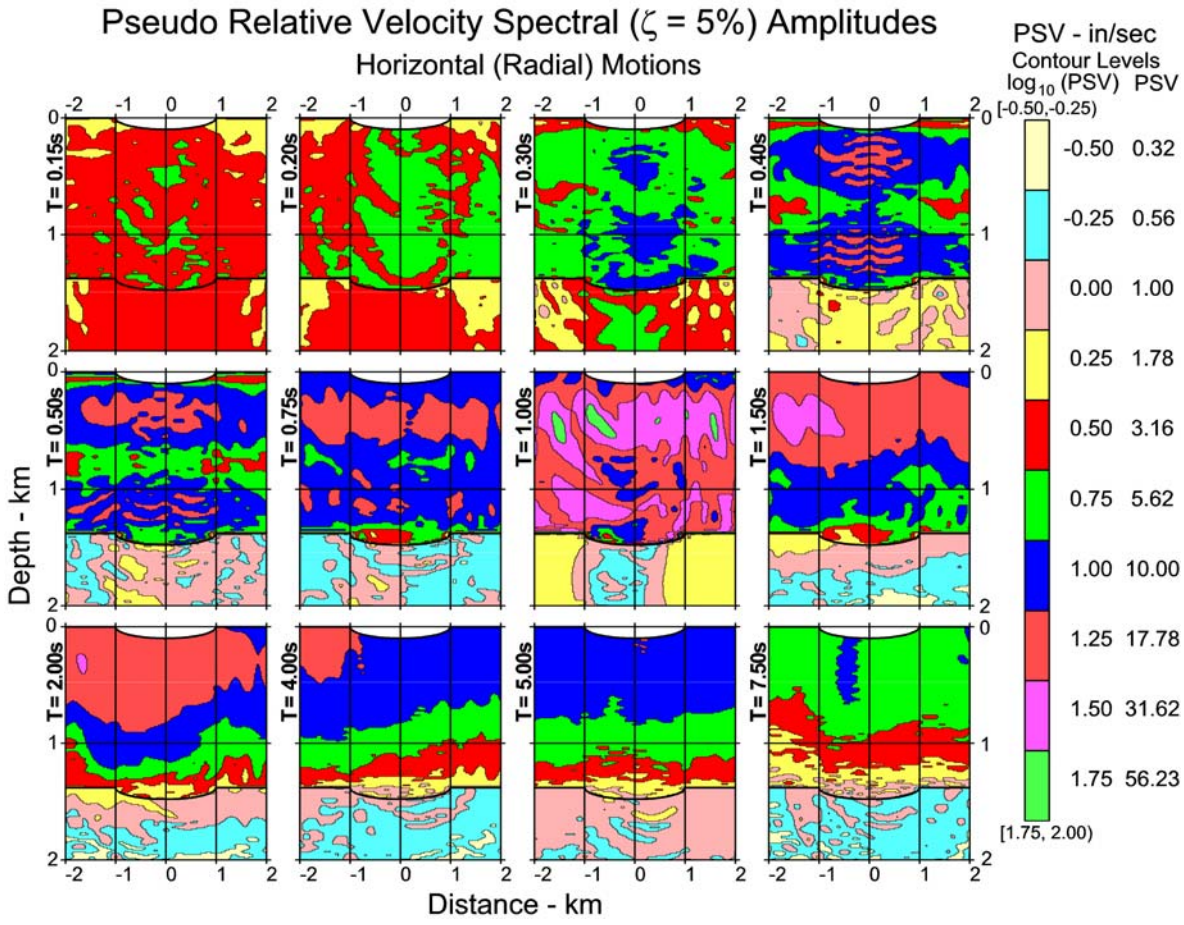

Fig. IV.9a. PSV-spectral amplitudes—horizontal component, for 5% damping.

VI. Summary

In this chapter, we analyzed the wave propagation in an irregularly layered medium for the in-plane radial and vertical components of motion. With the incoming Rayleigh surface waves and body P and SV waves, additional scattered and diffracted waves are generated by irregular interfaces between the layers. The scattered and diffracted waves are computed using the weighted-residues method to satisfy (1) the (in-plane) coupled, normal, and shear zero-stress boundary conditions on the top half-space surface; and (2) the continuity of (in-plane) coupled stress and displacement at the layer interface surfaces.

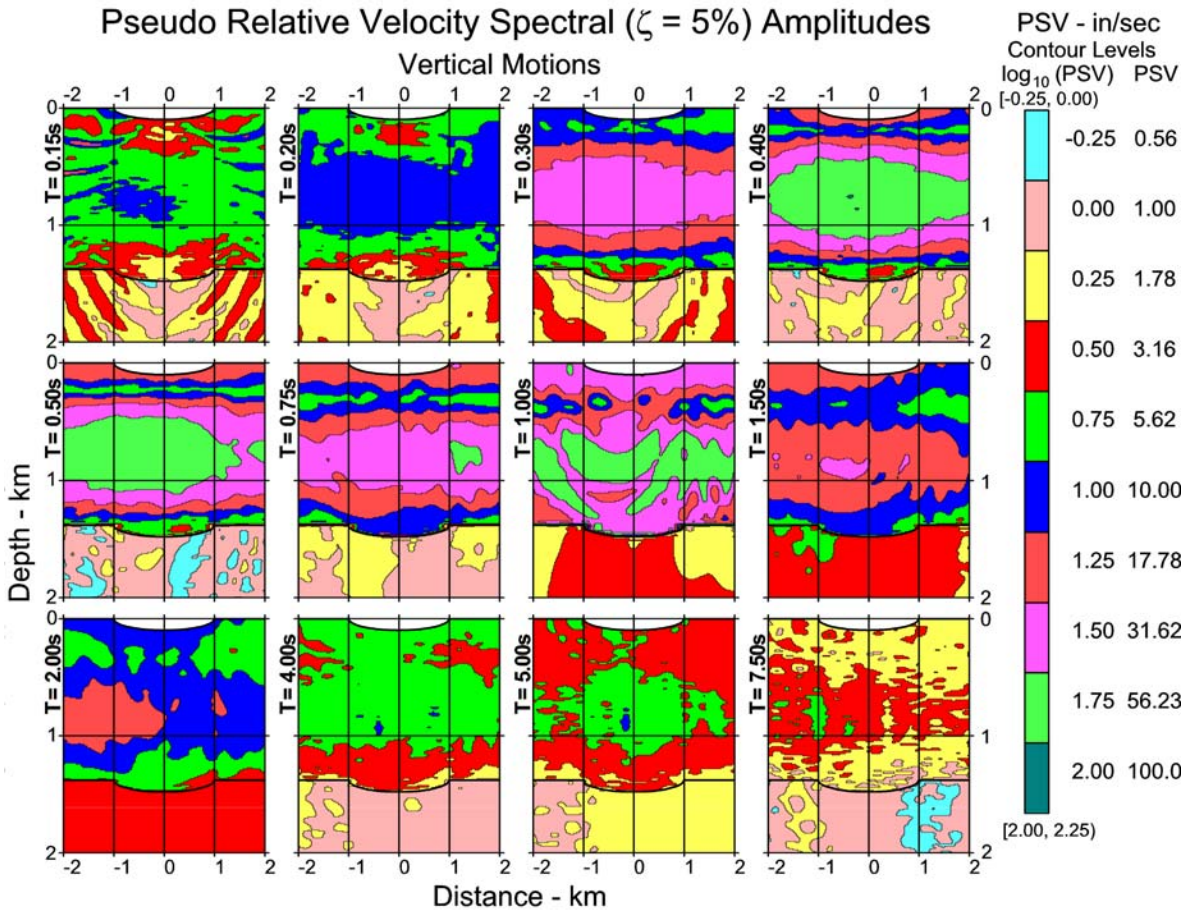

Fig. IV.9b. PSV-spectral amplitudes—vertical component, for 5% damping.

The contour plots in Figs. IV.8 and IV.9 show that the Fourier- and response-spectral amplitudes vary quite rapidly from point to point at and below the half-space surface and also vary from period to period of motions. The scattered and diffracted waves may result in amplification and de-amplification at various points on the layered medium.

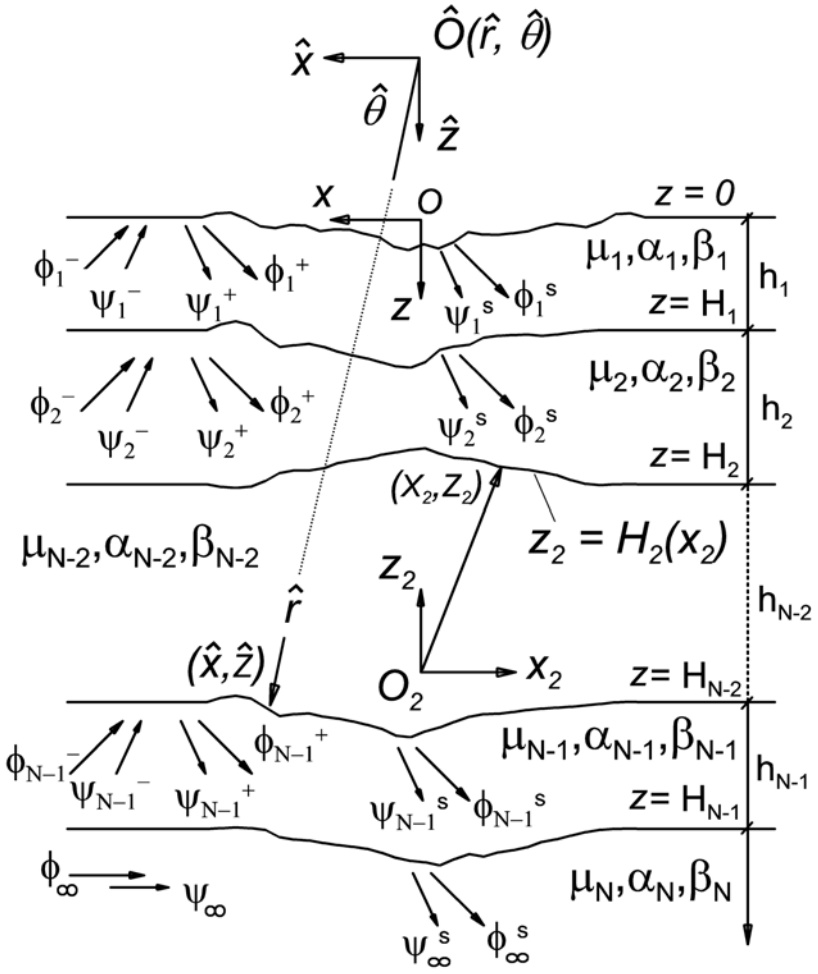

Figure IV.10. Irregularly layered medium with multiple coordinate systems.

The work on the scattering and diffraction of elastic waves by surface and subsurface topographies in a homogeneous, elastic half space for both out-of-plane Love (chapter 3) and in-plane Rayleigh (this Chapter) surface waves can further be extended to more irregularly layered, elastic half spaces than illustrated here. This will enable

engineering calculations of site-specific strong ground motion to be evaluated for more general and realistic models than those based on elastic, uniform, parallel-layered media, as considered in the past. The methodology presented in this chapter can also be extended to cases of irregularly layered, poroelastic media, in which the boundary conditions can be much more complicated.

As in chapter 3, the present results can be further generalized to cases in which the geometries of surface topography and of interfaces between the layers have to be represented by additional origins of cylindrical coordinates. This is illustrated in Fig. IV.10, where it can be seen that the bottom interface of layer 2 is convex upward, which is a case of a "hill interface." It is then more appropriate to associate it with its own coordinate system (x_2, z_2) to describe the interface surface. The waves in the layers may then all be represented by their own coordinate systems, and the addition theorem can be used to apply the boundary conditions at the interfaces.

References

1. Aki, K. & Larner, K.L. (1970). Surface motion of a layered medium having an irregular interface due to incident plane SH-waves, *J. Geophys. Res.* 75, 1921-1941.

2. X. Chen (1990). Seismogram synthesis for multi-layered media with irregular interfaces by using global Reflection/Transmission matrices method. I. Theory for 2D SH case, *Bull, Soc. Am,* 80*,* 1694-1724.

3. X. Chen (1993). A systematic and efficient method of computing normal mod for multi-layered half-space, *Geophys. J. Int.* 115*, 391-409.*

4. X. Chen (1995). Seismogram synthesis for multi-layered media with irregular interfaces by using global Reflection/Transmission matrices method. II. Numerical test and application for 2D SH case, *Bull, Soc. Am,* 85, 1094-1106.

5. Chen, X.F. (1999). Love Waves in Multi-layered Media with Irregular interfaces, I. Modal solution and Excitation formulation, *Bull. Seismo. Soc. Am.*, 89, 1519-1534.

6. N. A. Haskell (1953). The Dispersion of Surface waves on Multilayered Media, *Bull Seismol. Soc. Am.* 43, 17-34.

7. Kohketsu, K. (1987a). 2-D reflectivity method and synthetic seismograms in irregularly layered structures. I, SH-wave generation, *Geophys. J. Astr. Soc.* 89, 821-831.

8. Kohketsu, K. (1987b). Synthetic seismograms in realistic media: a wave theoretical approach, *Bull. Earthquake Res. Inst. Univ. Tokyo* 62, 201-245.

9. Kohketsu, K., B. L. N. Kennett & H. Takenaka (1991). 2-D reflectivity method and synthetic seismograms for irregularly layered structures. II, Invariant embedding approach, *Geophys. J. Int.* 105, 119-130.

10. Lee, V. W. & M.D. Trifunac (1979). Automatic Digitization and Data Processing of Strong-Motion Accelerograms, Part II: Computer Processing of Accelerograms, Civil Eng. Report CE 79-15 II Univ. of Southern Cal., Los Angeles, CA

11. Lee, V.W. & M.D. Trifunac (1985). Torsional Accelerograms, *Int. J. Soil Dynamics & Earth quake Eng.,* 4(3), 132-139.

12. Lee, V.W. & M.D. Trifunac (1987). Rocking Strong Earthquake Accelerations, *Int. J. Soil Dynamics & Earthquake Eng., 6(2),* 75-89.

13. Lee, V.W. & X. Y. Wu (1994a). Application of the Weighted Residual Method to Diffraction by 2-D Canyons of Arbitrary Shape, I: Incident SH Waves, *Int. J. Soil Dynamics & Earthquake Eng., 13(5),* 1994, 355-364.

14. Lee, V.W. & X. Y. Wu (1994b). Application of the Weighted Residual Method to Diffraction by 2-D Canyons of Arbitrary Shape, II: Incident P, SV & Rayleigh Waves, *Int. J. Soil Dynamics & Earthquake Eng.,* 13(5), 365-373.

15. V. W. Lee, W. Y. Liu, M.D. Trifunac, and N. Orbović (2014). Scattering and Diffraction of Earthquake Motions in Irregular Elastic Layers, I: Love and SH Waves *(in preparation).*

16. Pao, Y.-H. and C.-C. Mow (1973). Diffraction of Elastic Waves and Dynamic Stress Concentrations, *Crane, Russak & Company Inc., New York, New York.*

17. Sanchez-Sesma, F.J. & Campillo, M. (1991). Diffraction of P, SV, and Rayleigh waves by topographic features: a boundary integral formulation, *Bull. Seism. Soc. Am.*, 81, 2234-2253.

18. Sanchez-Sesma, F.J. & Campillo, M. (1993). Topography effects for incident P, SV, and Rayleigh waves, *Tectonophysics,* 218, 113-125.

19. Thomson, W.T. (1950). Transmission of Elastic Waves Through a Stratified Solid Media, *J. Appl. Phys. 21, 89-93.*

20. Todorovska, M.I., Trifunac, M.D. Lee, V.W. and Orbović, N. (2013). Synthetic Earthquake Ground Motions on an Array, *Soil Dynamics and Earthquake Engineering, 48,* 234-251.

21. Trifunac, M.D. (1971). A Method for Synthesizing Realistic Strong Ground Motion, *Bull. Seism. Soc. Amer.,* 61(6), 1739-1753.

22. Trifunac, M.D. & V.W. Lee (1979). Automatic Digitization and Data Processing of Strong-Motion Accelerograms, Part I: Automatic Digitization, *Civil Eng. Report CE 79-15 I Univ. of Southern Cal., Los Angeles, CA*

23. Vai R., J.M. Castillo-Covarrubias, F.J. Sanchez-Sesma, D. Komatistsch, & J.P. Vilotte (1999). Elastic wave propagation in an irregularly layered medium, *Soil Dynamics & Earthquake Engineering*, 18, 11-18.

24. Wong. H.L. and Trifunac, M.D. (1979). Generation of Artificial Strong Motion Accelerograms, *Int. J. Earthquake Engineering Struct. Dynamics*, 7(6), 509-527.

Chapter 5 Manual to Execute EQSYNACC to generate Synthetic Accelerogram for Points on or Below the Half-space

V.I The Original Synthetic Accelerogram Program for Points on Half-space: SYNACC

The synthetic translational and rotational components of acceleration are constructed to have a required Fourier amplitude spectrum, $\boldsymbol{FS(\omega)}$, and a given duration, $\boldsymbol{D(\omega)}$, at the half-space surface of a given site. A complete review of the method first proposed by Trifunac (1971b), and later refined by Wong and Trifunac (1978, 1979), for the generation of synthetic accelerograms, can also be found in the review paper by Lee (2002) and Todorovska et al (2013)**.** In short, the following files and information are needed to construct synthetic motions:

1. **Period.dat**: the Data file of the Periods of waves
2. **HskWav.dat**: Wave Dispersion Data at a Site
3. **InSyn.dat: Input data file for SYNACC.EXE**
4. **Option** to be used for constructing the Fourier Amplitudes in the given Frequency Band

V.I.1 Period.dat

The data file is listed as follows, to be read in by the program:

0.040	0.042	0.044	0.046	0.048	0.050
0.055	0.060	0.065	0.070	0.075	0.080
0.085	0.090	0.095	0.10	0.11	0.12
0.13	0.14	0.15	0.16	0.17	0.18
0.19	0.20	0.22	0.24	0.26	0.28
0.30	0.32	0.34	0.36	0.38	0.40
0.42	0.44	0.46	0.48	0.50	0.55
0.60	0.65	0.70	0.75	0.80	0.85
0.90	0.95	1.00	1.10	1.20	1.30
1.40	1.50	1.60	1.70	1.80	1.90
2.00	2.20	2.40	2.60	2.80	3.00
3.20	3.40	3.60	3.80	4.00	4.20
4.40	4.60	4.80	5.00	5.50	6.00
6.50	7.00	7.50	8.00	8.50	9.00
9.50	10.00	11.00	12.00	13.00	14.00
15.00					

There is a total of 91 periods from 0.040 s to 15.00 s. In terms of frequency this corresponds to the frequency range of 0.07 Hz to 25 Hz.

V.I.2 Hskwav.dat: The Original Haskel Program - HASKEL.EXE

This section will describe the input needed to generate the wave dispersion data at a site: Hskwav.dat

V.I.2.1 Input: The Layered Media Elastic Properties

Following Trifunac (1971), Wong and Trifunac (1978), at a given site, we first select an approximate geological profile to be represented by the equivalent parallel layers. A model can have N layers. For each layer l, with l = 1 to N, the parameters h_l, α_l, β_l and ρ_l must be specified, where

h_l = layer thickness,

α_l = P −wave velocity,

β_l = S −wave velocity, and

ρ_l = density of the l^{th} layer,

with the bottom $l = N$ medium having infinite thickness.

The file HskLin.dat here is an example of such a file used in Report I (see Appendix R1):

Hsklin.dat:

6 LAYER Imperial Valley VELOCITY MODEL			
0.18	1.70	0.98	1.28
0.55	1.96	1.13	1.36
0.98	2.71	1.57	1.59
1.19	3.76	2.17	1.91
2.68	4.69	2.71	2.19
.00	6.40	3.70	2.71
15, 0.1,1.0,10,0			

The 1st line is the number of elastic layers, *N*, followed by a name identifying the medium. This is then followed by *N* lines with four column each specifying the elastic properties in each layer. The first column is the thickness of each layer in km. The second column is the P-wave velocity in km/s. The third column is the shear wave velocity in km/s. The fourth and last column is the mass density in gr/c³. Those are followed by a line with 5 numbers: 15., 0.1, 1.0, 10, 0, which respectively are:

i) TST = 15 sec = Starting longest period to start iterations,
ii) TMIN = 0.1 sec = Down to minimum period,
iii) DTS = 1.0 sec = Spacing of periods to start iterations,
iv) Nsmx = 10 = Recommended number of iterations in search of the roots.
v) NMCL = 0, Number of Modes of Rayleigh and Love waves (set to default of 5)

V.I.2.2 Output: Wave Dispersion Data of the Site

With the input file **Hsklin.dat**, the program **Haskel.exe** is first executed. It will compute, for both the Rayleigh and Love surface waves their group and phase velocities, each between the starting period $\boldsymbol{T = 15\,sec}$ down to $\boldsymbol{T \sim 0.1\,sec}$ or in a frequency range from $\boldsymbol{f = 0.07\,Hz}$ to $\boldsymbol{f \sim 10\,Hz}$. This will give, for $\boldsymbol{m = 1}$ to $\boldsymbol{5}$ modes of Rayleigh and Love waves, $\boldsymbol{C_m(\omega_n)}$ and $\boldsymbol{U_m(\omega_n)}$, respectively representing their phase and group velocities, at a set of discrete frequencies $\boldsymbol{\omega_n}$. For Rayleigh waves, **HASKEL.EXE** also gives the ratios of the vertical to horizontal displacement amplitudes at the half-space surface. The output data will be the file **Hskout.dat**. The set of discrete frequencies $\boldsymbol{\omega_n}$ is usually a set of non-uniform frequencies within the frequency range. The program then interpolate to the frequencies corresponding to the 91 discrete periods of the data file **Period.dat** above, and outputs the data in **Hskwav.dat**, which will be the input file for **SYNACC.EXE**.

With the calculations of group and phase velocities, in the late 70's, no actual travel time data were used for the corresponding body P, SV and SH waves. An equivalent "mode" of body

waves was created for both the longitudinal P- and shear S- waves. The P-wave "mod" was created using the range from α_{min} to α_{max}, from short period to long period, where α_{min} and α_{max} are the minimum and maximum P-wave velocities in the layered half space model of the site. Similarly, the equivalent S-wave "mode" was created using the range from β_{min} to β_{max}, where β_{min} and β_{max} are the minimum and maximum S-wave velocity is the layered model of the site. This old approach has been replaced at present by the P, SV and SH body wave modes calculated analytically from body waves incident from below.

Figure II.1 in Chapter II is an example of one such plot of the phase velocities for five modes of Rayleigh waves and five modes of Love waves for the 6-layered El Centro Imperial Valley site for which the layer properties are those given in the file **Hsklin.dat** above. The Rayleigh waves are plotted as solid lines and the Love waves as dashed lines. The horizontal axis for period is plotted in logarithmic scale from around $\boldsymbol{T = 0.04\,s}$ to $\boldsymbol{T = 15\,s}$.

On the left side of the figure between $\boldsymbol{T = 0.10\,s}$ and $\boldsymbol{T = 0.40\,s}$ are two graphs, one solid and one dashed. The solid graph is a smooth step function going from α_{min} to α_{max} representing the body P-wave, while the dashed graph is the corresponding step function from β_{min} to β_{max} representing the body S-wave. These curves were used in the older versions of the program. As shown in the later sections, calculations are now available for P, SV and SH Body waves incident into the layers from half-space.

V.I.3 Insyn.dat: Input data for SYNACC.EXE

SYNACC will next open the file **InSyn.dat** in unit NU1 and read input from:

```
OPEN(NU1,FILE='InsynS.dat',STATUS='OLD')
```

1) **Input 1:** IWRT: Output Mode

   IWRT =0: Output ALL input read in
   =1: Simplified Output

```
Write(*,1111)
1111  FORMAT(' INPUT IWRT = ')
READ(NU1,*)IWRT
```

2) **Input 2:** Date and Time of the Synthetic Earthquake

```
Write(*,*)' INPUT MONTH,DAY,YEAR,HOUR,MIN& SEC.:'
READ(NU1,*)IMON,IDAY,IYEAR,IHOUR,IMIN,ISEC
```

3) **Input 3:** ICHOIC - Options to be used for constructing the Fourier Amplitudes in the given Frequency Band

```
Write(*,*)' OPTIONS: (0)QUIT,'
Write(*,*)' (1)MAG-SITE,(2)MMI-SITE,(3)MAG-DEPTH,(4)MMI-DEPTH,'
Write(*,*)' (5)INPUT FS,(6)MAG-DEPTH-SOIL,(7)MAG-SITE-SOIL,'
Write(*,*)' (8)MMI-DEPTH-SOIL, OR (9)MMI-SITE-SOIL MODEL?'
Write(*,1)
READ(NU1,*)ICHOIC
```

   This part of the input will be described in more detail in (the next) Section I.4

4) **Input 4:** INMAX, PDURN

   INMAX= number of times allowed to double the duration to allow for late arrival waves

```
Write(*,*) ' INMAX (2,4,8,16...),PDURN = '
READ(NU1,*)INMAX,PDURN
```

5) **Input 5: IGYZBE**

   IGYZBE= Initial random number to be used to generate the synthetic accelorgram

```
Write(*,3)
READ(NU1,*)IGYZBE
```

6) **Input 6:** Synthetic Record Reference name of

It is of the form XXNNN, where 'XX' are alphabetic characters and 'NNN' are numeric digits.

```
Write(*,21)' INPUT SYNTHETIC RECORD REFERENCE # (XXNNN): ')
READ(NU1,22)(IREF(I),I=1,3)
22    FORMAT(40A2)
```

7) **Input 7:** Synthetic Record log number

```
Write(*,*)' INPUT SYNTHETIC RECORD LOG # (80.01.12): '
READ(NU1,22)(IREF(I),I=4,7)
```

8) **Input 8:** IFDUR, duration parameter

IFDUR	=0	do not impose the empirical scaling to get duration. Instead, duration is computed from the epicentral distance and dispersion curves,
	=1	Impose the empirical scaling to calculate duration

```
Write(*,2)' INPUT DURATION PARAMETER(0/1): '
READ(NU1,*)IFDUR
```

9) **Input 9:**IPR, probability level

IPR is a number between 1 and 9 corresponding to the probability level of 0.1 to 0.9

```
Write(*,*)' INPUT PROBABILITY LEVEL #, (1 TO 9, FOR .1 TO .9): '
READ(NU1,*)IPR
```

10) **Input 10:** Earthquake parameters depending on ICHOIC of Input 3

Depending of the option ICHOIC, earthquake parameters like magnitude or intensity, epicentral distance,… are input here. This part of the input will be described in more detail in (the next) Section I.4

11) **Input 11:** NWAVE, total number of dispersed waves

```
Write(*,*)' INPUT THE TOTAL # OF DISPERSION MODES, NWAVE(10)
= '
READ(NU1,*) NWAVE
```

12) **Input 12:** Output Haskell velocity data Filename

```
Write(*,*)' THIS PROGRAM READS IN RAYLEIGH & LOVE WAVE
DATA,'
Write(*,*)' FROM OUTPUT OF HASKEL & HSKFIX PROGRAMS,'
Write(*,*)' HASKEL VEL. DATA Filename(A20)
Read(nu1,9001)INFILE                    !12/2/12 char*30 infile
```

13) **Input 13:** Yes/No for 1st arrival time at T=0

```
Write(*,6201)' MIN. ARRIVAL TIME AS T=0? (0)Y(1)N (0/1): '
READ(NU1,*)ITMIN
```

14) **Input 14:** Mode participation factor

```
MPFCTR=1
Write(*,*)'  MODE PARTICIPATING METHOD? (1/2): ')
READ(NU1,*)MPFCTR
```

V.I.4 Options to be used for constructing the Fourier Amplitudes in the given Frequency Band

Currently **SYNACC** has a total of ***nine*** options to construct the Fourier amplitudes in the given frequency band. All except one are constructed from empirical regression equations.

V.I.4.1 The Original and Current Regression Equations

Programmed into the original synthetic accelerogram program **SYNACC.EXE** are ***nine*** options by which the Fourier amplitudes for the synthetic acceleorgrams at the half-space surface can be generated. All except the ***5th*** option are regression equations developed from the 1970s, through the 1990s for the generation of Fourier and Response spectral amplitudes and for the duration of strong-motion.

The first 4 options constitute the original set of regression equations developed in the 1970's and 1980's for the *Magnitude* or *MMI* models with local site geology specified by site geological site conditions *(s = 0,1,2 respectively for rock, intermediate and soft sites)* or depth of alluvium, *h, in km*. The ***5th*** option allows the users to input their own Fourier amplitudes. The 6th to 9th options were added in the early 90's for the *Mag-Site-Soil,MMI-Site-Soil, Mag-Depth-Soil* and *MMI-Depth-Soil* models, where the soil condition, s_L is added as an additional parameter in the regression.

These are the format statements in **SYNACC.EXE,** used to inform the user what to input, depending on the options just described:

```
CC-----------------------------------------------------------------------
1       FORMAT(' INPUT CHOICE PARAMETER(0 TO 9): ')
2       FORMAT(' INPUT DURATION PARAMETER(0/1): ')
3       FORMAT(' INITIAL RANDOM INTEGER <OR 0 FOR SAME AS LAST RUN>: ')
4       FORMAT(' INPUT EPICENTRAL DISTANCE (KM): ')
5       FORMAT(' INPUT MAGNITUDE SCALE: ')
6       FORMAT(' INPUT PROBABILITY LEVEL #, (1 TO 9, FOR .1 TO .9): ')
7       FORMAT(' INPUT SITE CONDITION (0/1/2): ')
8       FORMAT(' INPUT COMPONENT SPECIFICATION (0:HORZ,1:VERT): ')
9       FORMAT(' INPUT M.M.I. SCALE: ')
10      FORMAT(' INPUT DEPTH OF ALLUVIUM (KM): ')
11      FORMAT(' CHOICE OPTION NUMBER = ',I2)
12      FORMAT(' DURATION PARAMETER = ',I2)
13      FORMAT(' INITIAL RANDOM # [=0 IF READ FROM SYNRAN.DAT]: ',I9)
14      FORMAT(' EPICENTRAL DISTANCE (KM) = ',F10.3)
15      FORMAT(' MAGNITUDE SCALE = ',F5.2)
16      FORMAT(' PROBABILITY LEVEL, P(.1<P<.9): ',F3.1)
17      FORMAT(' SITE CONDITION = ',I1)
18      FORMAT
    1(' COMPONENT(0:RAD,1:TRAN,2:VERT,3:TORSION,4:ROCKING) = ',I1)
19      FORMAT(' M.M.I. SCALE = ',I2)
20      FORMAT(' DEPTH OF ALLUVIUM (KM) = ',F10.1)
```

SYNACC will first request from the user the option (ICHOIC):

```
        WRITE(*,*)' OPTIONS: (0)QUIT,'
        WRITE(*,*)' (1)MAG-SITE,(2)MMI-SITE,(3)MAG-DEPTH,(4)MMI-DEPTH,'
        WRITE(*,*)' (5)INPUT FS,(6)MAG-DEPTH-SOIL,(7)MAG-SITE-SOIL,'
        WRITE(*,*)' (8)MAG-DEPTH-SOIL, OR (9)MMI-SITE-SOIL MODEL?'
        WRITE(*,1)
        READ(NU1,*)ICHOIC
```

1) Option 1: Magnitude-Site Model (Trifunac, 1976, Trifunac and Lee, 1985)

```
        CC-----------------------------------------------------------------
        CC    ICHOIC=1: INPUT DISTANCE, MAGNITUDE,
        CC              SITE CONDITIONS:       MAG-SITE MODEL
        CC-----------------------------------------------------------------
```

```
            WRITE(*,4)
            READ(NU1,*)DIST
            WRITE(*,5)
            READ(NU1,*)AM
            WRITE(*,7)
            READ(NU1,*)IS
```

2) Option 2: Intensity-Site Model (Trifunac, 1979, Trifunac and Lee, CE 1985-04)

```
      CC-----------------------------------------------------------------------
      CC    ICHOIC=2: INPUT DISTANCE, MM INTENSITY, CONFIDENCE LEVEL,
      CC    SITE CONDITION:   MMI-SITE MODEL
      CC-----------------------------------------------------------------------
            WRITE(*,4)
            READ(NU1,*)DIST
            WRITE(*,9)
            READ(NU1,*)MMI
            WRITE(*,7)
            READ(NU1,*)IS
```

3) Option 3: Magnitude-Depth Model (Trifunac and Lee, 1978, 1989, Westermo and Trfiunac, 1978))

```
      CC-----------------------------------------------------------------------
      CC    ICHOIC=3: INPUT DISTANCE, MAGNITUDE, CONFIDENCE LEVEL,
      CC     DEPTH:         MAG-DEPTH MODEL
      CC-------------------------------------------------------------
            WRITE(*,4)
            READ(NU1,*)DIST
            WRITE(*,5)
            READ(NU1,*)AM
            WRITE(*,10)
            READ(NU1,*)DEPTH
      CC             ALLLUV. DEPTH NOW READ IN UNITS OF KM
```

4) Option 4: Intensity-Depth Model (Trifunac and Lee, 1985)

```
      CC-----------------------------------------------------------------------
      CC    ICHOIC=4: INPUT DISTANCE, MM INTENSITY, CONFIDENCE LEVEL,
      CC       DEPTH:       MMI-DEPTH MODEL
      CC-------------------------------------------------------------
            WRITE(*,4)
            READ(NU1,*)DIST
            WRITE(*,9)
            READ(NU1,*)MMI
            WRITE(*,10)
            READ(NU1,*)DEPTH
      CC             ALLLUV. DEPTH NOW READ IN UNITS OF KM
```

5) Option 5: Use Input FS data

```
      CC-----------------------------------------------------------------------
      CC    ICHOIC=5: INPUT USER'S FOURIER SPECTRUM, TOTAL OF NTAB
POINTS.
      CC-----------------------------------------------------------------------
                        NTAB=91
            WRITE(*,4)
```

```
      READ(NU1,*)DIST
      WRITE(*,321)DIST
321         FORMAT('20D=',F5.1,',USER INPUT FS AMPS AT 91 PERIODS.')
      WRITE(*,*)' FOR THE 91 PERIODS:'
      WRITE(*,'(1X,13F6.2)')(PRD(I),I=1,91)
      WRITE(*,*)' INPUT 91 HORZ RADIAL FS AMP IN UNITS OF IN/SEC:'
      READ(NU1,*) (AU(IJ,1),IJ=1,NTAB)
      WRITE(*,*)' INPUT 91 HORZ TRANSVERSE FS AMP IN UNITS OF
IN/SEC:'
      READ(NU1,*) (AU(IJ,3),IJ=1,NTAB)
      WRITE(*,*)' INPUT 91 VERT FS AMP IN UNITS OF IN/SEC:'
      READ(NU1,*) (AU(IJ,2),IJ=1,NTAB)
```

6) Option 6: Magnitude-Site-Soil Model

```
CC-----------------------------------------------------------------------
CC    ICHOIC=6      MAG-SITE-SOIL MODEL
CC-----------------------------------------------------------------------
WRITE(*,*)' INPUT HYPO DIST(KM),MAG,SITE(0/1/2),SOIL(0/1/2):'
READ(NU1,*) Disti, AM, IS, ISOIL
```

7) Option 7: Intensity-Site-Soil Model (Trifunac, 1991)

```
CC-----------------------------------------------------------------------
CC    ICHOIC=7      MMI-SITE-SOIL MODEL
CC-----------------------------------------------------------------------
WRITE(*,*)' INPUT HYPO DIST(KM),MMI,SITE(0/1/2),SOIL(0/1/2):'
READ(NU1,*)DIST,MMI,IS,ISOIL
```

8) Option 8: Magnitude-Depth-Soil Model (Trifunac and Lee, 1987, 1989)

```
CC-----------------------------------------------------------------------
CC    ICHOIC=8      MAG-DEPTH-SOIL MODEL
CC-----------------------------------------------------------------------
WRITE(*,*)' INPUT HYPO DIST(KM),MAG,DEPTH(km),SOIL(0/1/2):'
READ(NU1,*) Disti, AM, DEPTH, ISOIL
```

9) Option 9: Intensity-Depth-Soil Model (Lee, 1990)

```
CC-----------------------------------------------------------------------
CC    ICHOIC=9      MMI-DEPTH-SOIL MODEL
CC-----------------------------------------------------------------------
WRITE(*,*)' INPUT HYPO DIST(KM),MMI,DEPTH(km),,SOIL(0/1/2):'
READ(NU1,*)DIST,MMI,DEPTH,ISOIL
```

Example 1:

Here is an example of the **SYNACC** input file **InSyn.DAT** for **option #6, ICHOIC=6**:

InSynDat:

```
1                       IWRT
01,01,13,12,00,00       CURRENTDATE (Mo-Da-Yr) &TIME (00:00:00)
6                       ICHOIC,MODEL#
```

```
2,.875                  INMAX, PDURN
12345                   INITIALRANDOM # between <-32767,32767>
LA003                   RECORDREFERENCE NAME
89.03.01                RECORDLOG #
1                       DURNATION PARAMETER (0/1)
5                       PROB LEVEL (1 TO 9)
1.5, 6.5, 0, 2          HYPOCENTRAL DIST,MAG/MMI,SITE/DEPTH,SOIL
10                      # OF WAVE MODES
HSKWAV.DAT
0                       T=0 At Dist/Cmax
2                       MODE PARTICIPATION FACTOR
```

Example 2:

Here is another example of the **SYNACC** input file **InSyn.DAT** for **option #5, ICHOIC=5**, where the user inputs the 3 components (Radial, Transverse and Vertical) of Fourier amplitude data:

InSyn.dat:

```
1                       IWRT
01,01,13,12,00,00       CURRENTDATE (Mo-Da-Yr) &TIME (00:00:00)
5                       ICHOIC,MODEL#
2,.875                  INMAX, PDURN
12345                   INITIALRANDOM # between <-32767,32767>
LA003                   RECORDREFERENCE NAME
89.03.01                RECORDLOG #
1                       DURNATION PARAMETER (0/1)
5                       PROB LEVEL (1 TO 9)
 1.00000E-10  1.00000E-10  3.94577E-01  3.94800E-01
 2.05194E-01  3.25239E-01  3.93269E-01  3.76363E-01
 2.49990E-01  2.54802E-01  6.85321E-01  3.63371E-01
 6.42797E-01  7.00448E-01  5.24887E-01  1.02113E+00
1.34502E+00  1.65811E+00  3.05650E+00  2.81909E+00
4.49047E+00  3.65102E+00  6.02187E+00  5.33620E+00
3.33898E+00  6.96100E+00  1.03893E+01  1.24187E+01
1.43819E+01  1.90009E+01  6.81712E+00  2.48083E+01
2.16060E+01  1.89132E+01  2.10551E+01  2.55125E+01
1.66354E+01  9.61588E+00  1.30416E+01  9.97679E+00
1.78276E+01  2.11354E+01  1.93958E+01  1.22380E+01
2.02096E+01  1.35959E+01  9.66726E+00  1.38484E+01
```

2.19153E+01 1.98801E+01 2.78279E+01 3.55078E+01
2.10803E+01 2.55126E+01 2.44259E+01 1.99576E+01
1.21552E+01 1.59339E+01 1.06934E+01 1.20950E+01
1.27204E+01 1.34753E+01 1.44391E+01 2.07096E+01
3.57730E+01 4.53028E+01 4.99574E+01 4.13284E+01
3.36581E+01 2.80684E+01 2.30985E+01 1.86020E+01
1.67221E+01 1.51307E+01 1.36718E+01 1.23297E+01
1.07276E+01 9.53787E+00 8.96607E+00 9.17404E+00
9.35428E+00 9.51199E+00 9.40564E+00 8.05007E+00
6.83720E+00 5.74562E+00 3.86015E+00 2.28893E+00
1.52479E+00 1.77728E+00 1.99610E+00 End of FS Radial Comp.
1.00000E-10 1.00000E-10 2.31009E-01 1.94537E-01
3.19194E-01 3.83051E-01 3.76469E-01 3.32717E-01
4.43216E-01 5.09405E-01 4.04593E-01 5.44001E-01
4.89834E-01 3.01687E-01 7.09059E-01 1.37829E+00
1.27044E+00 2.21121E+00 2.04364E+00 4.62448E+00
4.79836E+00 2.79309E+00 5.69368E+00 6.53701E+00
8.06265E+00 3.63794E+00 1.13821E+01 1.01337E+01
5.93430E+00 2.41781E+01 1.72239E+01 1.99994E+01
1.20149E+01 2.22880E+01 1.37573E+01 1.24219E+01
1.64474E+01 1.27367E+01 1.83200E+01 2.73839E+01
2.88879E+01 2.37006E+01 2.61794E+01 2.06856E+01
2.95908E+01 1.02047E+01 1.51625E+01 1.86747E+01
2.17198E+01 2.72379E+01 3.20074E+01 1.73098E+01
1.86640E+01 1.29285E+01 2.74345E+01 2.43018E+01
1.83995E+01 1.11270E+01 1.50910E+01 1.54509E+01
1.50808E+01 1.37118E+01 1.86422E+01 2.99603E+01
4.27058E+01 4.49779E+01 4.38568E+01 3.28721E+01
2.31079E+01 2.08690E+01 1.91644E+01 1.76222E+01
1.57691E+01 1.40516E+01 1.24772E+01 1.10288E+01
1.14860E+01 1.22635E+01 1.24978E+01 1.20185E+01
1.16030E+01 1.12395E+01 1.07896E+01 9.72566E+00
8.77375E+00 7.91703E+00 6.43724E+00 5.20409E+00
4.39439E+00 4.07555E+00 3.79923E+00 End of FS Transverse Comp.
1.00000E-10 1.00000E-10 4.59384E-01 3.17400E-01
4.38541E-01 3.33765E-01 3.86963E-01 1.17292E+00
6.97446E-01 1.03180E+00 9.03084E-01 1.78482E+00
5.54601E-01 9.67074E-01 1.27816E+00 1.41444E+00
3.90060E+00 4.10452E+00 3.13484E+00 1.95386E+00
4.53177E+00 1.18723E+00 5.14047E+00 5.65238E+00
6.60988E+00 2.85910E+00 3.17751E+00 3.52807E+00
8.17153E+00 9.91231E+00 1.27238E+01 4.76816E+00
7.27592E+00 2.97489E+00 5.21361E+00 5.07673E+00

```
4.32826E+00    9.07128E+00    2.04633E+00    1.24525E+01
1.01732E+01    5.53326E+00    6.02687E+00    1.14904E+01
9.38652E+00    9.88448E+00    1.13447E+01    6.72983E+00
1.17014E+01    7.19098E+00    6.32351E+00    9.26453E+00
8.32524E+00    5.78888E+00    6.38161E+00    8.23842E+00
8.39110E+00    1.05250E+01    1.17266E+01    1.08374E+01
8.69151E+00    5.03464E+00    6.84980E+00    1.09076E+01
1.42376E+01    1.04890E+01    7.56431E+00    7.11810E+00
6.72146E+00    6.49314E+00    6.29370E+00    6.11326E+00
5.35652E+00    4.63204E+00    3.96794E+00    3.35696E+00
4.28392E+00    5.30411E+00    5.57428E+00    4.85386E+00
4.22950E+00    3.68318E+00    3.26290E+00    3.20659E+00
3.15620E+00    3.11086E+00    3.03253E+00    2.96726E+00
2.82022E+00    2.54681E+00    2.30987E+00                    End of FS Vertical Comp.
10                        # OF WAVE MODES
HSKWAV.DAT
0                         T=0 At Dist/Cmax
2                         MODE PARTICIPATION FACTOR
```

V.I.5 The SYNACC Output Files

With the input files of SYNACC all read in, SYNACC will

1) Use each mode of the Wave Dispersion Data at the site and their arrival times at each frequency band to assemble the contribution of each mode of surface and Body waves.

2) Determine the Relative Amplitudes and Phrases of all body and modes of Surface Waves, Sum up all the modes of waves in the frequency domain and by inverse Fourier Transform, create the (Volume 2, Corrected) time-histories of Total Accelerogram.

3) The above process is performed for the following components of motions:

i) The **Radial**, **Transverse** and **Vertical** (Trifunac, 1971; Wong and Trifunac, 1978, 1979) components of **Translational** motions, with respective output files: **V2X01.DAT, V2Y01.DAT and V2Z01.DAT**.

ii) The **Torsion** (Lee and Trifaunc, 1985) and **Rocking** (Lee and Trifunac, 1987) components of **Rotational** Motions, with respective output files: **V2T01.DAT** and **V2R01.DAT**.

iii) The **Radial Normal, Horizontal Shear** and **Vertical Normal** components of **Strain**

(Lee, 1990) time history, all in one output file**: V2E01.DAT**.

iv) The **Radial, Tranverse** and **Vertical** components of **Curvature** (Trifunac, 1990) time histories (**Curvograms**), all in one output file**: V2E01.DAT**.

Figure II.2 in Chapter 2 is an example of one such plot of the translational accelerogram time history at the El Centro Imperial Valley layered media generated by an earthquake of magnitude $\boldsymbol{M = 6.5}$ at hypocentral distance of $\boldsymbol{10\,km}$. This is generated from the original synthetic accelerogram program **SYNACC.EXE** and represents one component of the translational motions at the half-space surface at the site. The input option of **Option 1** above is used for **Option 1: Magnitude-Site Model (Trifunac, 1976, Trifunac and Lee, 1985)** for a site condition of $\boldsymbol{s = 0}$, which is the site condition for an alluvial site. A peak ground acceleration of $\left|\boldsymbol{a}_{\max}\right| \sim \boldsymbol{450\,cm/s^2}$ or almost $\boldsymbol{0.5\ g}$ is attained, which is similar to the data recorded in the 1940 Imperial Valley Earthquake, in El Centro, California.

V.II The Updated Synthetic Accelerogram Program for Points on or Below Half-space Surface: EQSYNACC

The updated Synthetic Accelerogram Program here is created to include the developments described in the following two reports:

1. Synthetic Translational Motions of Surface Waves on and below the surface of layered medium**,** Report II in Appendix R2.

2. Synthetic Rotational Motions of Surface Waves in and below the surface of layered Medium**,** Report III in Appendix R3.

V.II.1 The Updated Haskel Program

In **Chapter 2: Synthetic Translational Motions of Surface and body waves on or below the surface of layered medium,** starting with the wave dispersion file **Hskwav.dat**, we constructed the synthetic translational motions of Love and body SH waves for points on and below the surface in the half-space layered model. In Section III of the same report, we constructed the synthetic translational motions of Rayleigh and body P and SV waves. Here the translational components are the Radial, Transverse and Vertical components of motion, namely, acceleration $\left(\ddot{U},\ddot{V},\ddot{W}\right)^T$, velocity $\left(\dot{U},\dot{V},\dot{W}\right)$ and displacement $\left(U,V,W\right)$ time histories. The numerical calculations for each mode at each frequency are described in Section IV of Report I, in Appendix R1.

Figure II.5 in chapter 2, section II-5 is an example of one such plot of the transverse (***y***-) component Love wave mode shape amplitudes at four periods: $\boldsymbol{T = 5,\ 1.0,\ 0.5,\ \text{and}\ 0.1\ s}$. The amplitude of each mode shape is normalized to be one at the surface of the half-space, and so it becomes the scaling factors or transfer function for the wave amplitudes along the depth. Each graph shows the mode shape amplitudes versus the *z*, which is the depth in kilometers below the half-space surface.

In the next section, Section II-6 of **Chapter 2: Synthetic Rotational Motions of Surface and Body Waves on or below the surface in Layered Medium,** we extended the analysis and results of Section II-5, Chapter 2, to construct the synthetic rotational motions of Love and body SH waves, and Rayleigh and body P and SV waves. The computation of the Rotational components of motions: Torsion, Rocking and Strain time histories all involve either or both of the $\partial/\partial x$ and $\partial/\partial z$ derivatives of the corresponding translational accelerations $\left(\ddot{U},\ddot{V},\ddot{W}\right)^T$, velocities $\left(\dot{U},\dot{V},\dot{W}\right)$ and displacements $\left(U,V,W\right)$.

V.II.2 The Input and Output Files for New HskzdzModes.EXE

With the available data for each frequency of each mode of surface Rayleigh and Love waves, and body P, SV and SH waves, an identical file as Hskwav.dat for the wave dispersion data at the site can now be constructed at any given point on or below the half-space surface. The procedure is as follows:

1) A data file Zxcoord.dat is created, which consists of the specified *z*- and *x*-coordinates of the points on or below the site. The lines below is an example of a part of such a file consisting of 120 points on or vertically below the site.
The first line specifies the number of points and the exponent factor used to make the data in units of km. The '0' here means the data are in units of km. If the data are given in meters, then it would be '-3', i.e. $\mathbf{10^{-3}}$ km. Starting from the 2nd line, the 1st column has the z-coordinates and the 2nd column the x-coordinates, which are all 0's here. This 2nd column is of no use here, but will be needed later to generate the synthetic acceleration data at any specified point with ***(z, x)*** coordinates at the site.

Example 1: Zxcoord.dat for points vertically below a given site:

```
 120        0    # of points, 10^exponent of km
0.05     0.00
0.10     0.00
```

```
0.15      0.00
0.20      0.00
0.25      0.00
0.30      0.00
0.35      0.00
0.40      0.00
0.45      0.00
0.50      0.00
0.55      0.00
0.60      0.00
  :         :    (Lines from z=0.65down to z=5.60 skipped…)
5.65      0.00
5.70      0.00
5.75      0.00
5.80      0.00
5.85      0.00
5.90      0.00
5.95      0.00
6.00      0.00
```

The ***z***-coordinates are specified here from $z = 0.05$ (below the surface) to $z = 6.0$ ***km*** (further down) and are equally spaced at **0.05** ***km*** apart. The point $z = 0.0$ ***km*** on the half-space surface will by a default and will be included.

Example 2: Zxcoord.dat for points at a fixed depth varying in the horizontal direction (left to right):

```
                          # of points, 10^exponent of
  140          -3         km
192.97         1.5
192.97         3.0
192.97         4.5
192.97         6.0
192.97         7.5
192.97         9.0
192.97        10.5
192.97        12.0
192.97        13.5
192.97        15.0
192.97        16.5
192.97        18.0
```

```
      192.97      19.5
:           :          (Lines from x=21.0 to x=196.5 skipped…)
      192.97     198.0
      192.97     199.5
      192.97     201.0
      192.97     202.5
      192.97     204.0
      192.97     205.5
      192.97     207.0
      192.97     208.5
      192.97     210.0
```

Here the 140 points of ***(z, x)*** coordinates are input in units of $\mathbf{10^{-3}}$ ***km***, i.e. in units of meters. They are all at a depth of $z = 192.97 \times 10^{-3}\, km$ or $192.97m$ with the ***x***-coordinates ranging from $x = 1.5\, m$ to $x = 210\, m$ in steps of $1.5\, m$. The point $x = 0.0\ km$ at the depth of $z = 192.97m$ will be included by default.

2) This file, together with the dispersion file **Hskwav.dat** output from **HASKEL.EXE** in the previous section, are now the input files for the program **NewHSKzDzModes.EXE.** The file **Hskwav.dat** has the phase and group velocities for each mode of surface Rayleigh and Love waves, at each period, at the point $z = 0.0$ on the half-space surface.

This program reads the data in the file Hskwav.dat, and using the modified Haskell-Thompson propagator matrices created in Section IV.3 of Report II (Appendix R2) and Section IV.3 of Report III (Appendix R3), produces the internal propagator matrix files, **RYLGMTRX.DAT** and **LOVEMTRX.DAT**, for both the translational and rotational components of motion for the Rayleigh and Love surface wave modes and also the new representation of body P, SV and SH wave modes for given angles of incidences from the bottom semi-infinite medium. As an example, for the 6 layered example, we use angles of incidence of 83^o and 84.5^o (with respect to horizontal) for the examples of synthetic accelerograms at hypocentral distances of 10 and $40\ km$.

3) This program will at each z-coordinate in the file Zxcoord.dat (starting at $z = 0.0\ km$ on the half-space surface), produce an updated wave dispersion file, **HSKwav.___,** where **'.___'** in the file extension is the index number of the ***z***-coordinate in the file **Zxcoord.dat**. For the example file **Zxcoord.dat** above, this would range from ***'000'*** ($z = 0.0\ km$) at the surface to ***'120'*** ($z = 6.0\ km$) at the very bottom of the medium. The program will produce, for each file **Hskwav.___,** 5 modes of Rayleigh and 5 modes of Love surface waves. For each mode, at each period, **NewHSKzDzModes.EXE,** as the name suggests, will write the following at each period of each mode of Rayleigh waves:

T, Period of the Rayleigh wave in second,

i) ***c,*** Phase velocity of the Rayleigh wave in km/s,

ii) ***u,*** Group velocity of the Rayleigh wave in km/s,

iii) W/U Ratio of vertical to horizontal wave displacement amplitudes,

iv) U , the relative ***x***-component Rayleigh wave translational motion, which is

v) available as an imaginary number (See Report II),

vi) W , the ***z***-component Rayleigh wave translational motion, which is a real number (See Report II in Appendix R2), and normalized to be =1 at the half-space surface,

vii) $dU/dz\left(\times 10^{-5}\right)$, the ***z***-derivative of the ***x***-component of Rayleigh wave motion,

viii) $dW/dz\left(\times 10^{-5}\right)$, the ***z***-derivative of the ***z***-component of Rayleigh wave motion,

$dU/dx\left(\times 10^{-5}\right)$, the ***x***-derivative of the ***x***-component of Rayleigh wave motion,

$dW/dx\left(\times 10^{-5}\right)$, the ***x***-derivative of the ***z***-component of Rayleigh wave motion.

And similarly at each period of each mode of Love waves (transverse direction):

i) ***T,*** Period of the Love wave in second,

ii) ***c,*** Phase velocity of the Love wave in km/s,

iii) ***u,*** Group velocity of the Love wave in km/s,

iv) Ratio =0.0 since this doesn't apply to Love waves

v) V , the ***y***-component wave translational motion, which is available as a real number (See Report II, in Appendix R2), and normalized to be =1 at the half-space surface

$dV/dz\left(\times 10^{-5}\right)$, the ***z***-derivative of the ***y***-component of Love wave motion

vi) $dV/dz\left(\times 10^{-5}\right)$, the ***z***-derivative of the ***y***-component of Love wave motion,

vii) $dV/dz\left(\times 10^{-5}\right)$, the ***z***-derivative of the ***y***-component of Love wave motion,

4) In exactly the same way as for the five modes of Rayleigh waves and five modes of Love waves, additional modes corresponding to waves from incident body P-, SV and SH- waves, respectively mode# 11, 12 and 13 at a specified angle of incidence are created, written in files **BodyW___.___,** where **'W___'**in the file name specifies the angle of incidence of the body waves. For example, **'W845'**would correspond to body waves at incident angle of **84.5**^{o} . **'.___'** in the file extension is again the index number of the ***z***-coordinate.

Appendix V-1 gives for **Mode 1 of Rayleigh waves** mode shapes in the output file **Hskwav.000** of the Program **"NewHSKzDzModes.EXE"**

Appendix V-2 gives for **Mode 1 of Love waves** the corresponding output in **Hskwav.000.**

Appendix V-3 gives for **Mode 11 body P- Waves** the mode shapes in the file **BodyW845.000.**

V.II.3 The Updated Synthetic Accelerogram Program for Points On and Below the Half-Space Surface: EQSYNACC.EXE

With the dispersion data of the Rayleigh and Love surface waves and the body P, SV and SH waves computed at points on and below the half-space surface, the synthetic translational and rotational components of the acceleration, velocity and displacement time histories of every point on or below the half-space surface will next be constructed. Each such point will have a designated Fourier amplitude spectra and a designated duration.

Here is the structure of the Working Folder:

Working

1) **Batch files**: **SynA<u>nnn</u>.BAT**

Example of **SynA<u>nnn</u>.BAT, with '<u>nnn</u>' = '025'**:

SynA025.BAT

```
MD z025
CD z025
COPY ..\1ZFolder\*.* *.*
COPY ..\InsynS\InSynS.025 InSynS.dat
CALLAccSynS
CD ..\
```

2) **Data files:** **Period.dat, Zxcoord.dat**

3) **Subfolders:** **Working\Programs**
Working\1ZFolder
Working\InSynS
Working\HskWav
Working\BodyW__ (Example: **Working\BodyW830\)**

The following set of files and the information are needed to construct the synthetic motions at all the points:

1 **Period.dat**: the Data file of the Periods of waves. This is the same data file as given in **Section I.1** above for the original SYNACC program.

2. **Zxcoord.dat:** the same data file of the ***z***- and ***x***- coordinates of the points as given in Section II.2 above.

3. **..\HskWav\HskWav.___:** Wave Dispersion Data of the Rayleigh and Love surface waves at every point on or below the half-space surface at the given site. Here the file extension **".___"** is again the index number of the (***z, x)***-coordinate in the file **Zxcoord.dat.** Since there are now many such files, one for each point in the file **Zxcoord.dat,** they are all placed in the sub-folder **..\HskWav**\inside the working directory (folder).

4. **..\BodyW___\BodyW___.___:**the file of additional modes corresponding to waves from incident **P-, SV- and SH- body waves**, respectively modes # 11, 12 and 13 for a specified angle of incidence, as described in **Section II.2** above. As in the case of the Haskel files, there is one file for each point in the file **Zxcoord.dat.** Those are also all placed in the subfolder **..\BodyW___**\inside the working directory (folder), where **'W___'** in the name of the folder specifies the angle of incidence of the body waves, as for all the body wave files in the subfolder.

5. **..\InSynS\InSyn.___:** These are the input files for the updated program **EQSYNACC.EXE.** They are the same input file as **InSyn.dat** for the original **SYNACC.EXE** program as described in **Section I.3** above. The difference now is that there are many such files, one for each point in the file **Zxcoord.dat.** Those are all placed in the subfolder **..\InSynS** inside the working directory (folder). There are also now additional lines of input, to identify the coordinates

of the point on or below the site where the synthetic accelerogram data are to be generated. Here is a brief description of the file, with emphasis on where the additional inputs are, in addition to those for **InSyn.dat** described in **Section I.3** above:

1) **Input 1:** IWRT: Output Mode
2) **Input 2:** Date and Time of the Synthetic Earthquake
3) **Input 3:** ICHOIC– Options to be used for constructing the Fourier Amplitudes in the given frequency band
4) **Input 4:** INMAX, PDURN
5) **Input 5: IGYZBE**
6) **Input 6:** Synthetic Record Reference name
7) **Input 7:** Synthetic Record log number
8) **Input 8:** IFDUR, duration parameter
9) **Input 9:** IPR, probability level
10) **Input 10:** Earthquake parameters depending on ICHOIC of Input 3

Inputs #1 to #10 are identical to those used in the original 'SYNACC.EXE" program. As described in Section I.3 above. The following ***(NEW) inputs*** are modified for the **Updated 'EQSYNACC.EXE' Program:**

11) **Input 11:** NWAVE, total number of dispersion waves
12) **Input 12:** Output Haskel surface wave velocity data filename

Here there is one Haskel velocity data file for each **(z, x)** coordinates given in the file **Zxcoord.dat**, and those are of the form **..\Hskwav\Hskwav.___**, where the file extension **'.___'** is the index number of the **(*z, x)*** coordinate in the file **Zxcoord.dat.** The files are all in a separate subfolder **HskWav**\ inside the EQSYNACC working folder **Working\ .**

13) **Input 13:** ***(z, x)*** coordinate location on or below the site, 10^exp in km

This is the same input as used in the file **Zxcoord.dat**.

```
write(*,*)' at (z,x)E__ (+/-exp) ='                    !!!New
read(NU1,*,err=6101)zLoc,xLoc,kexp                      !!!New
```

14) **Input 14:** Output body wave velocity data filename

```
!8/4       Read in Body wave filename
write(*,*)' Body Wave Mode Shape Filename(a20): '
read(nu1,9001)BodyFile          !12/2/12 now 30 chars long
write(*,9001)' ',BodyFile
```

Here there's one Body wave velocity data file for each **(z, x)** coordinates given in the file **Zxcoord.dat**, and those are of the form **..\Bodywave\BodyW___.___**, where the file extension **'.___'** is the index number of the (***z, x)*** coordinate in the file **Zxcoord.dat.** The files are all in a separate subfolder **BodyW___** inside the EQSYNACC working folder **Working\ .**

15) **Input 15:** Yes/No for 1st arrival time at T=0

16) **Input 16:** Mode participation factor

Input #15 and 16 are identical to **Inputs #13 and 14** of the input file for the **Original "SYNACC.EXE' program.**

The following file **InSyn.025** is an example of such an input file:

InSyn.025:

```
1                           IWRT
01,01,13,12,00,00           CURRENT DATE (Mo-Da-Yr) & TIME (00:00:00)
6                           ICHOIC, MODEL#
2,.875                      INMAX, PDURN
12345                       INITIAL RANDOM # <-32767,32767>
LA003                       RECORD REF NAME
1208.025                    RECORD LOG #
1                           DURNATION PARAMETER (0/1)
5                           PROB LEVEL (1 TO 9)
4125, 6.5, 0, 2             HYPO. DIST, MAG/MMI,SITE/DEPTH,SOIL
10                          # OF WAVE MODES
..\HSKWAV\HSKWAV.025
```

1.250, .000 0	**z, x Location, 10^exp km**
..\BodyW840\BodyW840.025	
0	**T=0 At Dist/Cmax**
2	**MODE PARTICIPATION FACTOR**

V.II.4 The EQSYNACC Output Files

With the input files of **EQSYNACC** all read in, execution of **EQSYNACC** will do the following:

1) Create, for each point of ***(z, x)*** coordinate in the file Zxcoord.dat, a subfolder inside the working folder **\Working** of some generic name **\Working\zx___,** where '___' in the subfolder name is index number of the (***z, x)*** coordinate in the file **Zxcoord.dat.**

2) At each such subfolder, the program **EQSYNACC.EXE** will use the same algorithm and procedure as the original program **SYNACC.EXE** to generate each mode of synthetic accelerogration data, as described in **Section I.5** above, namely, use each mode of the wave dispersion data at the site and their arrival times at each frequency band to assemble the contribution of each mode of surface and body waves. Currently, there are five modes of Rayleigh waves (Mode#1 to 5), five modes of Love waves (Mode#6 to 10), one mode for each of the Incident body P, SV and SH waves (Modes #11 to 13)

3) At each point ***(z, x)*** on or below the half-space surface at the site, the relative amplitudes and phrases of each mode of Rayleigh and Love surface waves are determined relative to that at the surface point where $z = 0$ using the mode shape data files in the folder **..\Hskwav**. Similarly, the relative amplitudes and phases of each mode of body P, SV and SH waves are determined relative to that at the surface, using the mode shape data files in the folder **..\BodyW___,** where **'W___'** in the name of the folder specifies the angle of incidence of the body waves used. All modes of the waves at each point are then summed up in the frequency domain.

4) At the surface point ***(z, x) = (0, 0),*** the translational components of the Fourier

amplitudes of acceleration are scaled to be the same as that calculated by the regression equations specified by the parameter **'ICHOIC'** in **Input#3**. The Fourier amplitudes of all points of ***(z, x)*** below are then scaled relative to the surface point as in the previous step 3). By inverse Fourier Transform (using FFT), the Volume 2, corrected time-histories of total accelerogram are calculated.

5) The above process was performed for the following components of translational motions:

The **Radial**, **Transverse** and **Vertical** (Trifunac, 1971; Wong and Trifunac, 1978, 1979) components of **Translational** motions (the **U-, V-, W-** components), respectively

The Translational files:

V2X01.DAT

V2Y01.DAT

V2Z01.DAT.

These are the same output files as in the original SYNACC, which are now extended for all defined points below the half-space surface.

Figures II.7, II.11 and II.13 of Chapter 2 are examples of synthetic acceleration time histories of the transverse, radial and vertical components of motions at a given site where the strong-motion earthquake and site parameters are specified as:

$$M = 6.5,\ R = 8.0km,\ \ H = 6.0km,\ s = 0,\ s_L = 2$$

See Chapter 2 for further explanation of these parameters. The examples are calculated for the El Centro six-layered site model, at 100 depths equally spaced from the surface to almost 6 km below the surface, and at hypocentral distance of $D = 10.0km$,

Figures II.8, II.12 and II.14 of Chapter 2 show examples of the synthetic displacement time histories of the transverse, radial and vertical components of motions at the same site.

6) Unlike the Original **SYNACC.EXE** program, which will output the **Torsion** and

Rocking components of **Rotational** Motions, and the **Strain** motions, the **NEW EQSYNACC.EXE** program will output the **d/dx-** and **d/dz-** derivatives of the **U-(Radial), V-(Transverse) and W-(Vertical)** translational components, as follows:

The **d/dx- derivative files:**

V2DUDX.DAT

V2DVDX.DAT

V2DWDX.DAT

and **the d/dz- derivative files:**

V2DUDZ.DAT

V2DVDZ.DAT

V2DWDZ.DAT

from which the **Rocking, Torsion** and **Strain** component time histories can be defined. For example, The synthetic motion, $\partial U/\partial x$ is the synthetic ***normal strain***, ε_x Similarly, $\partial W/\partial z$ is the synthetic ***normal strain***, ε_z. As for the two derivative components $\partial U/\partial z$ and $\partial W/\partial x$, those can be used to compute, $\Omega_y = \frac{1}{2}\left(\partial U/\partial z - \partial W/\partial x\right)$, the in-plane ***Rocking*** component of the Rayleigh and body ***P, SV*** waves in the ***x-z*** plane, or the y- direction rotation, while $\varepsilon_{xz} = \frac{1}{2}\left(\partial U/\partial z + \partial W/\partial x\right)$ is the ***Shear Strain*** the ***x-z*** plane.

Figures II.15a and b of Chapter 2 show r the synthetic rotational accelerations for the horizontal Motions: $d\ddot{U}/dx$, $d\ddot{U}/dz$ and vertical motions: , $d\ddot{W}/dx$, $d\ddot{W}/dz$. Finally Figures II.16a and b of Chapter 2 show the synthetic rotational displacement time histories of the same motions.

7) The **Radial, Transverse** and **Vertical** components of **Curvature** (Trifunac, 1990) time histories (Curvograms), are all in one output file**: V2K01.DAT**. This is the same as in the case of the original **SYNACC.EXE** program.

8) The New **EQSYNACC.EXE** program currently has a new option which, at the request of the user, outputs the above files separately for each mode of motions. These files are named as follows:

	The Translational files:		
Mode#	**Radial**	**Transverse**	**Vertical**
1	**V2X01.M01**	**V2Y01.M01**	**V2Z01.M01**
2	**V2X01.M02**	**V2Y01.M02**	**V2Z01.M02**
3	**V2X01.M03**	**V2Y01.M03**	**V2Z01.M03**
⋮	⋮	⋮	⋮
11	**V2X01.M11**	**V2Y01.M11**	**V2Z01.M11**
12	**V2X01.M12**	**V2Y01.M12**	**V2Z01.M12**
13	**V2X01.M13**	**V2Y01.M13**	**V2Z01.M13**

where the extension **'.M__'** indicates the **Mode#** of the data in the file. Here **M01** through **M05** are the 5 modes of **Rayleigh** waves, M06 through M10 are the 5 modes of Love waves. **M11** through **M13** are respectively for incident body **P-, SV- and SH-** waves. Similarly for the **d/dx** and **d/dz** derivative files:

	The d/dx and d/dz derivatives files:		
Mode#	**Radial d/d/x, d/dz**	**Trans. d/d/x, d/dz**	**Vertical d/d/x, d/dz**
1	**V2DUD(X,Z).M01**	**V2DVD(X,Z).M01**	**V2DWD(X,Z).M01**
2	**V2DUD(X,Z).M02**	**V2DVD(X,Z).M02**	**V2DWD(X,Z).M02**
3	**V2DUD(X,Z).M03**	**V2DVD(X,Z).M03**	**V2DWD(X,Z).M03**
⋮	⋮	⋮	⋮
11	**V2DUD(X,Z).M11**	**V2DVD(X,Z).M11**	**V2DWD(X,Z).M11**
12	**V2DUD(X,Z).M12**	**V2DVD(X,Z).M12**	**V2DWD(X,Z).M12**
13	**V2DUD(X,Z).M13**	**V2DVD(X,Z).M13**	**V2DWD(X,Z).M13**

References

1. **V. W. Lee (1990)** Surface Strains Associated with Strong Earthquake Shaking, *Proc. J.S. C.E., 422(n* I-14), 187-194.

2. **V.W. Lee (2002).** Empirical Scaling of Strong Earthquake Ground Motion: Part III: Synthetic Strong Motion, *ISET J.Earthquake Technology, 39(4), 273-310.*

3. **V. W. Lee & M.D. Trifunac (1985)** Torsional Accelerograms, *Int. J. Soil Dynamics & Earth quake Eng., 4(3), 132-139.*

4. **V. W. Lee & M.D. Trifunac (1987)** Rocking Strong Earthquake Accelerations, *Int. J. Soil Dynamics & Earthquake Eng., 6(2),* 75-89.

5. **M. D. Trifunac (1971**) A Method for Synthesizing Realistic Strong Ground Motion, *Bull. Seism. Soc. Amer., 61(6),* 1739-1753.

6. **M. D. Trifunac (1976)** Preliminary Empirical Model for Scaling Fourier Amplitude Spectra of Strong Ground Acceleration in Terms of Earthquake Magnitude, Source to Station Distance and Recording Site Conditions, *Bull. Seism. Soc. Amer., 66(4),* 1343-1373.

7. **M. D. Trifunac (1990)** Curvograms of Strong Ground Motion, ASCE, EMD, 116(6), 1426-1432.

8. **M. D. Trifunac (1991)** Empirical Scaling of Fourier Spectrum Amplitudes of Recorded Strong Earthquake Accelerations in Terms of Modified Mercalli Intensity, Local Soil Conditions and Depth of Sediments, *Int. J. Soil Dynamics and Earthquake Eng.,* 10(1), 65-72.

9. **Todorovska, M.I., Trifunac, M.D. Lee, V.W. and Orbović, N. (2013).** Synthetic Earthquake Ground Motions on an Array, *Soil Dynamics and Earthquake Engineering, 48,* 234-251.

10. **M.D. Trifunac & V. W. Lee (1978)** Dependence of the Fourier Amplitude Spectra of Strong-Motion Accelerograms on Depths of Sedimentary Deposits, *Civil Eng. Report CE 78-14, Univ. of Southern Cal., Los Angeles.*

11. **M.D. Trifunac & V. W. Lee (1985)** Preliminary Empirical Model for Scaling Fourier Amplitude Spectra of Strong Ground Acceleration in Terms of Earthquake Magnitude, Source to Station Distance, Site Intensity and Recording Site

Conditions, *Civil Eng. Report CE 85-03, Univ. of Southern Cal., Los Angeles.*

12. **M.D. Trifunac &V. W. Lee (1989)** Empirical Model for Scaling Fourier Amplitude Spectra of Strong Earthquake Ground Acceleration in Terms of Earthquake Magnitude, Source to Station Distance, Site Intensity and Recording Site Conditions, *Int. J. Soil Dynamics & Earthquake Eng..8(3),* 110-125.

13. **B.D. Westermo & M.D. Trifunac (1978)** Correlations of the Frequency Dependent Duration of Strong Earthquake Ground Motion with the Magnitude, Epicentral Distance and the Depth of Sediments at the Recording Site, *Department of Civil Engineering, Report CE 78-12*, Univ. of Southern Calif., Los Angeles, California.

14. **H.L. Wong & M.D. Trifunac (1978)** Synthesizing Realistic Strong Motion Accelerograms, *Department of Civil Engineering, Report CE 78-07*, University of Southern Calif., Los Angeles, California.

15. **H.L. Wong & M.D. Trifunac (1979)** Generation of Artificial Strong Motion Accelerograms, *Int. J. Earthquake Engineering Struct. Dynamics, 7(6),* 509-527.

Appendix V.1

Mode 1 Rayleigh Waves in Hskwav.000:

6 LAYER Velocity Model				
Imperial Valley VELOCITY MODEL				
Thickness, km	alpha, km/s	beta, km/s	density	Depth from top, km
0.18	1.70	0.98	1.28	0.18
0.55	1.96	1.13	1.36	0.73
0.98	2.71	1.57	1.59	1.71
1.19	3.76	2.17	1.91	2.90
2.68	4.69	2.71	2.19	5.58
.00	6.40	3.70	2.71	5.58

RAYLEIGH WAVE DISPERSION
LAYER VELOCITY MODEL FOR

PERIOD	C	U	RATIO	Imag[U(z)]	Real[W(z)]	dU/dz(^-5)	dW/dz(^-5)	dU/dx(^-5)	dW/dx(^-5)
Rayleigh Wave Mode# 1 U,W(z) at z= .000E-3 km									
15.00	3.17131	2.96209	1.32144	1.32144E+00	1.00000E+00	-1.32084E-01	5.85346E-02	-1.74541E-01	1.32084E-01
14.00	3.15297	2.89729	1.36955	1.37000E+00	1.00000E+00	-1.42342E-01	6.53771E-02	-1.94944E-01	1.42342E-01
13.00	3.13177	2.85438	1.42305	1.42000E+00	1.00000E+00	-1.54329E-01	7.36517E-02	-2.19618E-01	1.54329E-01
12.00	3.10639	2.79749	1.483	1.48000E+00	1.00000E+00	-1.68555E-01	8.38300E-02	-2.49968E-01	1.68555E-01
11.00	3.07499	2.72319	1.54973	1.55000E+00	1.00000E+00	-1.85756E-01	9.65417E-02	-2.87872E-01	1.85756E-01
10.00	3.03486	2.62693	1.62225	1.62000E+00	1.00000E+00	-2.07034E-01	1.12635E-01	-3.35861E-01	2.07034E-01

9.50	3.00841	2.56712	1.65985	1.66000E+00	1.00000E+00	-2.19846E-01	1.22378E-01	-3.64912E-01	2.19846E-01
9.00	2.98196	2.50730	1.69744	1.70000E+00	1.00000E+00	-2.34118E-01	1.33274E-01	-3.97402E-01	2.34118E-01
8.50	2.94606	2.42245	1.73263	1.73000E+00	1.00000E+00	-2.50911E-01	1.45794E-01	-4.34736E-01	2.50911E-01
8.00	2.90741	2.33224	1.76601	1.77000E+00	1.00000E+00	-2.70137E-01	1.59990E-01	-4.77064E-01	2.70137E-01
7.50	2.85779	2.22061	1.79214	1.79000E+00	1.00000E+00	-2.93149E-01	1.76188E-01	-5.25364E-01	2.93149E-01
7.00	2.79710	2.09476	1.80778	1.81000E+00	1.00000E+00	-3.20903E-01	1.94552E-01	-5.80122E-01	3.20903E-01
6.50	2.72535	1.95668	1.81232	1.81000E+00	1.00000E+00	-3.54686E-01	2.15573E-01	-6.42805E-01	3.54686E-01
6.00	2.63182	1.80471	1.79182	1.79000E+00	1.00000E+00	-3.97899E-01	2.39102E-01	-7.12963E-01	3.97899E-01
5.50	2.51546	1.64997	1.74071	1.74000E+00	1.00000E+00	-4.54151E-01	2.65120E-01	-7.90544E-01	4.54151E-01
5.00	2.37800	1.49917	1.65672	1.66000E+00	1.00000E+00	-5.28443E-01	2.93605E-01	-8.75482E-01	5.28443E-01
4.80	2.31929	1.43994	1.61705	1.62000E+00	1.00000E+00	-5.64396E-01	3.06071E-01	-9.12656E-01	5.64396E-01
4.60	2.25468	1.38552	1.56468	1.56000E+00	1.00000E+00	-6.05811E-01	3.17891E-01	-9.47900E-01	6.05811E-01
4.40	2.18951	1.33155	1.51113	1.51000E+00	1.00000E+00	-6.52199E-01	3.30520E-01	-9.85557E-01	6.52199E-01
4.20	2.12237	1.28024	1.45259	1.45000E+00	1.00000E+00	-7.04871E-01	3.43375E-01	-1.02389E+00	7.04871E-01
4.00	2.05344	1.23135	1.38951	1.39000E+00	1.00000E+00	-7.64958E-01	3.56464E-01	-1.06292E+00	7.64958E-01
3.80	1.98326	1.18361	1.3245	1.32000E+00	1.00000E+00	-8.33713E-01	3.70326E-01	-1.10425E+00	8.33713E-01
3.60	1.91099	1.13780	1.25623	1.26000E+00	1.00000E+00	-9.13312E-01	3.84772E-01	-1.14733E+00	9.13312E-01

3.40	1.83720	1.09297	1.18768	1.19000E+00	1.00000E+00	-1.00588E+00	-4.00645E-01	-1.19466E+00	-1.00588E+00
3.20	1.76143	1.04942	1.11876	1.12000E+00	1.00000E+00	-1.11472E+00	-4.18232E-01	-1.24710E+00	-1.11472E+00
3.00	1.68433	1.00883	1.05289	1.05000E+00	1.00000E+00	-1.24346E+00	-4.39066E-01	-1.30923E+00	-1.24346E+00
2.80	1.60677	0.97045	0.98941	9.89000E-01	1.00000E+00	-1.39659E+00	-4.63404E-01	-1.38180E+00	-1.39659E+00
2.60	1.53024	0.93858	0.93324	9.33000E-01	1.00000E+00	-1.57924E+00	-4.94261E-01	-1.47381E+00	-1.57924E+00
2.40	1.45624	0.91263	0.88377	8.84000E-01	1.00000E+00	-1.79778E+00	-5.32832E-01	-1.58882E+00	-1.79778E+00
2.20	1.38512	0.89147	0.8408	8.41000E-01	1.00000E+00	-2.06191E+00	-5.81404E-01	-1.73365E+00	-2.06191E+00
2.00	1.31735	0.87300	0.80482	8.05000E-01	1.00000E+00	-2.38478E+00	-6.43670E-01	-1.91932E+00	-2.38478E+00
1.90	1.28465	0.86338	0.7894	7.89000E-01	1.00000E+00	-2.57420E+00	-6.81482E-01	-2.03207E+00	-2.57420E+00
1.80	1.25236	0.85104	0.77549	7.75000E-01	1.00000E+00	-2.78727E+00	-7.24886E-01	-2.16150E+00	-2.78727E+00
1.70	1.22044	0.83627	0.76291	7.63000E-01	1.00000E+00	-3.02841E+00	-7.74825E-01	-2.31040E+00	-3.02841E+00
1.60	1.18814	0.82400	0.75132	7.51000E-01	1.00000E+00	-3.30516E+00	-8.32785E-01	-2.48323E+00	-3.30516E+00
1.50	1.15573	0.86507	0.74028	7.40000E-01	1.00000E+00	-3.62437E+00	-8.99796E-01	-2.68305E+00	-3.62437E+00
1.40	1.12973	0.85971	0.73718	7.37000E-01	1.00000E+00	-3.97262E+00	-9.82124E-01	-2.92854E+00	-3.97262E+00
1.30	1.10444	0.85923	0.73439	7.34000E-01	1.00000E+00	-4.37617E+00	-1.07780E+00	-3.21382E+00	-4.37617E+00
1.20	1.08090	0.86756	0.73182	7.32000E-01	1.00000E+00	-4.84410E+00	-1.18887E+00	-3.54501E+00	-4.84410E+00
1.10	1.06005	0.87857	0.72876	7.29000E-01	1.00000E+00	-5.38841E+00	-1.31693E+00	-3.92686E+00	-5.38841E+00

1.00	1.04122	0.88427	0.7247	7.25000E-01	1.00000E+00	-6.03445E+00	-1.46660E+00	-4.37316E+00	-6.03445E+00
0.95	1.03223	0.88435	0.72223	7.22000E-01	1.00000E+00	-6.40737E+00	-1.55193E+00	-4.62759E+00	-6.40737E+00
0.90	1.02334	0.91565	0.71956	7.20000E-01	1.00000E+00	-6.82209E+00	-1.64627E+00	-4.90890E+00	-6.82209E+00
0.85	1.01663	0.91437	0.71505	7.15000E-01	1.00000E+00	-7.27107E+00	-1.74361E+00	-5.19917E+00	-7.27107E+00
0.80	1.00994	0.91369	0.71007	7.10000E-01	1.00000E+00	-7.77668E+00	-1.85187E+00	-5.52199E+00	-7.77668E+00
0.75	1.00334	0.91325	0.7045	7.05000E-01	1.00000E+00	-8.34969E+00	-1.97273E+00	-5.88236E+00	-8.34969E+00
0.70	0.99671	0.91058	0.69829	6.98000E-01	1.00000E+00	-9.00561E+00	-2.10894E+00	-6.28853E+00	-9.00561E+00
0.65	0.98985	0.90540	0.69171	6.92000E-01	1.00000E+00	-9.76556E+00	-2.26536E+00	-6.75494E+00	-9.76556E+00
0.60	0.98254	0.89800	0.68498	6.85000E-01	1.00000E+00	-1.06581E+01	-2.44834E+00	-7.30056E+00	-1.06581E+01
0.55	0.97440	0.89036	0.67817	6.78000E-01	1.00000E+00	-1.17241E+01	-2.66645E+00	-7.95094E+00	-1.17241E+01
0.50	0.96526	0.87532	0.67237	6.72000E-01	1.00000E+00	-1.30186E+01	-2.93555E+00	-8.75334E+00	-1.30186E+01
0.48	0.9612	0.87101	0.67066	6.71000E-01	1.00000E+00	-1.36184E+01	-3.06297E+00	-9.13328E+00	-1.36184E+01
0.46	0.95696	0.86681	0.66921	6.69000E-01	1.00000E+00	-1.42734E+01	-3.20337E+00	-9.55193E+00	-1.42734E+01
0.44	0.95254	0.86303	0.66811	6.68000E-01	1.00000E+00	-1.49915E+01	-3.35898E+00	-1.00160E+01	-1.49915E+01
0.42	0.94797	0.85995	0.66738	6.67000E-01	1.00000E+00	-1.57811E+01	-3.53203E+00	-1.05320E+01	-1.57811E+01
0.40	0.94328	0.85777	0.66706	6.67000E-01	1.00000E+00	-1.66525E+01	-3.72529E+00	-1.11082E+01	-1.66525E+01
0.38	0.93855	0.85663	0.66713	6.67000E-01	1.00000E+00	-1.76173E+01	-3.94153E+00	-1.17530E+01	-1.76173E+01

0.36	0.93382	0.85662	0.66758	6.68000E-01	1.00000E+00	-1.86902E+01	4.18440E+00	-1.24772E+01	1.86902E+01
0.34	0.92918	0.85779	0.66837	6.68000E-01	1.00000E+00	-1.98885E+01	4.45793E+00	-1.32929E+01	1.98885E+01
0.32	0.92470	0.86004	0.66946	6.69000E-01	1.00000E+00	-2.12339E+01	4.76727E+00	-1.42152E+01	2.12339E+01
0.30	0.92047	0.86303	0.67078	6.71000E-01	1.00000E+00	-2.27536E+01	5.11852E+00	-1.52626E+01	2.27536E+01
0.28	0.91653	0.86572	0.67225	6.72000E-01	1.00000E+00	-2.44836E+01	5.51978E+00	-1.64591E+01	2.44836E+01
0.26	0.9128	0.86674	0.67384	6.74000E-01	1.00000E+00	-2.64747E+01	5.98278E+00	-1.78397E+01	2.64747E+01
0.24	0.90933	0.88049	0.67547	6.75000E-01	1.00000E+00	-2.87904E+01	6.52182E+00	-1.94470E+01	2.87904E+01
0.22	0.90692	0.88286	0.67687	6.77000E-01	1.00000E+00	-3.14911E+01	7.14840E+00	-2.13154E+01	3.14911E+01
0.20	0.9049	0.88761	0.67811	6.78000E-01	9.99999E-01	-3.47175E+01	7.89524E+00	-2.35424E+01	3.47175E+01
0.19	0.90409	0.88996	0.67864	6.79000E-01	1.00000E+00	-3.65775E+01	8.32472E+00	-2.48230E+01	3.65775E+01
0.18	0.90339	0.89213	0.6791	6.79000E-01	1.00000E+00	-3.86395E+01	8.79997E+00	-2.62401E+01	3.86395E+01
0.17	0.90282	0.89409	0.6795	6.79000E-01	1.00000E+00	-4.09383E+01	9.32899E+00	-2.78176E+01	4.09383E+01
0.16	0.90235	0.89581	0.67983	6.80000E-01	1.00000E+00	-4.35196E+01	9.92203E+00	-2.95859E+01	4.35196E+01
0.15	0.90199	0.89727	0.68009	6.80000E-01	1.00000E+00	-4.64394E+01	1.05918E+01	-3.15830E+01	4.64394E+01
0.14	0.90172	0.89853	0.68029	6.80000E-01	1.00000E+00	-4.97714E+01	1.13551E+01	-3.38590E+01	4.97714E+01
0.13	0.90154	0.90017	0.68044	6.80000E-01	1.00000E+00	-5.36107E+01	1.22337E+01	-3.64789E+01	5.36107E+01
0.12	0.90153	0.90405	0.68054	6.81000E-01	1.00000E+00	-5.80789E+01	1.32552E+01	-3.95250E+01	5.80789E+01

0.11	0.90201	0.91301	0.68061	6.81000E-01	9.99999E-01	-6.33250E+01	-1.44541E+01	-4.30997E+01	-6.33250E+01
0.10	0.90363	0.94321	0.68064	6.81000E-01	1.00000E+00	-6.95327E+01	-1.58717E+01	-4.73268E+01	-6.95327E+01
0.095	0.90496	0.97596	0.68065	6.81000E-01	1.00000E+00	-7.30848E+01	-1.66827E+01	-4.97452E+01	-7.30848E+01
0.090	0.90868	0.98358	0.68065	6.81000E-01	1.00000E+00	-7.68292E+01	-1.75374E+01	-5.22938E+01	-7.68292E+01
0.085	0.91313	0.98336	0.68065	6.81000E-01	1.00000E+00	-8.09521E+01	-1.84785E+01	-5.51001E+01	-8.09521E+01
0.080	0.91759	0.98313	0.68066	6.81000E-01	1.00000E+00	-8.55935E+01	-1.95383E+01	-5.82602E+01	-8.55935E+01
0.075	0.92205	0.98291	0.68066	6.81000E-01	1.00000E+00	-9.08582E+01	-2.07401E+01	-6.18435E+01	-9.08582E+01
0.070	0.92651	0.98269	0.68066	6.81000E-01	1.00000E+00	-9.68795E+01	-2.21145E+01	-6.59420E+01	-9.68795E+01
0.065	0.93097	0.98246	0.68066	6.81000E-01	1.00000E+00	-1.03832E+02	-2.37016E+01	-7.06743E+01	-1.03832E+02
0.060	0.93542	0.98224	0.68066	6.81000E-01	1.00000E+00	-1.11949E+02	-2.55545E+01	-7.61995E+01	-1.11949E+02
0.055	0.93988	0.98202	0.68066	6.81000E-01	1.00000E+00	-1.21547E+02	-2.77454E+01	-8.27323E+01	-1.21547E+02
0.050	0.94434	0.98179	0.68067	6.81000E-01	9.99999E-01	-1.33070E+02	-3.03762E+01	-9.05771E+01	-1.33070E+02
0.048	0.94612	0.9817	0.68067	6.81000E-01	1.00000E+00	-1.38354E+02	-3.15824E+01	-9.41736E+01	-1.38354E+02
0.046	0.94790	0.98161	0.68067	6.81000E-01	1.00000E+00	-1.44099E+02	-3.28936E+01	-9.80835E+01	-1.44099E+02
0.044	0.94969	0.98152	0.68067	6.81000E-01	1.00000E+00	-1.50365E+02	-3.43239E+01	-1.02349E+02	-1.50365E+02
0.042	0.95147	0.98143	0.68067	6.81000E-01	1.00000E+00	-1.57230E+02	-3.58912E+01	-1.07022E+02	-1.57230E+02
0.040	0.95325	0.97955	0.68067	6.81000E-01	1.00000E+00	-1.64783E+02	-3.76154E+01	-1.12163E+02	-1.64783E+02

Appendix V.2

Mode 1 Love waves in Hskwav.000:

LOVE WAVE DISPERSION
LAYER VELOCITY MODELFOR

PERIOD	c, km/s	u, km/s	n/a	Real[V(z)]	dV/dz(^-5)	dV/dx(^-5)
Love WaveMode# 1V(z) atz= .000E-3 km						
15.00	3.53897	3.21717	0	1.00000E+00	0.00000E+00	1.18362E-01
14.00	3.50616	3.04785	0	1.00000E+00	0.00000E+00	1.28003E-01
13.00	3.46498	2.93077	0	1.00000E+00	0.00000E+00	1.39488E-01
12.00	3.41070	2.77435	0	1.00000E+00	0.00000E+00	1.53517E-01
11.00	3.33717	2.58106	0	1.00000E+00	0.00000E+00	1.71163E-01
10.00	3.23653	2.35901	0	1.00000E+00	0.00000E+00	1.94133E-01
9.50	3.16800	2.24421	0	1.00000E+00	0.00000E+00	2.08771E-01
9.00	3.09946	2.12942	0	1.00000E+00	0.00000E+00	2.25243E-01
8.50	3.00846	2.00112	0	1.00000E+00	0.00000E+00	2.45707E-01
8.00	2.91278	1.87267	0	1.00000E+00	0.00000E+00	2.69639E-01
7.50	2.79834	1.74359	0	1.00000E+00	0.00000E+00	2.99377E-01
7.00	2.67256	1.61918	0	1.00000E+00	0.00000E+00	3.35857E-01
6.50	2.53706	1.49991	0	1.00000E+00	0.00000E+00	3.81010E-01
6.00	2.39071	1.39319	0	1.00000E+00	0.00000E+00	4.38028E-01
5.50	2.24004	1.30007	0	1.00000E+00	0.00000E+00	5.09990E-01
5.00	2.08823	1.22022	0	1.00000E+00	0.00000E+00	6.01771E-01

4.80	2.02748	1.19065	0	1.00000E+00	0.00000E+00	6.45628E-01
4.60	1.96792	1.16619	0	1.00000E+00	0.00000E+00	6.94088E-01
4.40	1.90847	1.14221	0	1.00000E+00	0.00000E+00	7.48242E-01
4.20	1.85022	1.12080	0	1.00000E+00	0.00000E+00	8.08551E-01
4.00	1.79305	1.10172	0	1.00000E+00	0.00000E+00	8.76047E-01
3.80	1.73695	1.08425	0	1.00000E+00	0.00000E+00	9.51939E-01
3.60	1.68268	1.06951	0	1.00000E+00	0.00000E+00	1.03723E+00
3.40	1.62975	1.05634	0	1.00000E+00	0.00000E+00	1.13391E+00
3.20	1.57859	1.04521	0	1.00000E+00	0.00000E+00	1.24383E+00
3.00	1.52953	1.03594	0	1.00000E+00	0.00000E+00	1.36931E+00
2.80	1.48174	1.02771	0	1.00000E+00	0.00000E+00	1.51443E+00
2.60	1.43635	1.02101	0	1.00000E+00	0.00000E+00	1.68247E+00
2.40	1.39266	1.01508	0	1.00000E+00	0.00000E+00	1.87985E+00
2.20	1.35054	1.00983	0	1.00000E+00	0.00000E+00	2.11471E+00
2.00	1.31009	1.00528	0	1.00000E+00	0.00000E+00	2.39800E+00
1.90	1.29049	1.00331	0	1.00000E+00	0.00000E+00	2.56255E+00
1.80	1.27131	1.00163	0	1.00000E+00	0.00000E+00	2.74572E+00
1.70	1.25252	1.00021	0	1.00000E+00	0.00000E+00	2.95084E+00
1.60	1.23424	0.99925	0	1.00000E+00	0.00000E+00	3.18171E+00
1.50	1.21622	0.99851	0	1.00000E+00	0.00000E+00	3.44411E+00
1.40	1.19894	0.99845	0	1.00000E+00	0.00000E+00	3.74330E+00
1.30	1.18203	0.99869	0	1.00000E+00	0.00000E+00	4.08891E+00
1.20	1.16559	0.99925	0	1.00000E+00	0.00000E+00	4.49214E+00
1.10	1.14972	1.00008	0	1.00000E+00	0.00000E+00	4.96815E+00
1.00	1.13442	1.00081	0	1.00000E+00	0.00000E+00	5.53868E+00
0.95	1.12696	1.00098	0	1.00000E+00	0.00000E+00	5.86878E+00
0.90	1.11957	1.00106	0	1.00000E+00	0.00000E+00	6.23571E+00
0.85	1.11229	1.00074	0	1.00000E+00	0.00000E+00	6.64573E+00

0.80	1.10505	1.00027	0	1.00000E+00	0.00000E+00	7.10735E+00
0.75	1.09785	0.99908	0	1.00000E+00	0.00000E+00	7.63090E+00
0.70	1.09063	0.99753	0	1.00000E+00	0.00000E+00	8.23009E+00
0.65	1.08337	0.99539	0	1.00000E+00	0.00000E+00	8.92257E+00
0.60	1.07591	0.99237	0	1.00000E+00	0.00000E+00	9.73313E+00
0.55	1.06824	0.98873	0	1.00000E+00	0.00000E+00	1.06942E+01
0.50	1.06026	0.98450	0	1.00000E+00	0.00000E+00	1.18522E+01
0.48	1.05699	0.98268	0	1.00000E+00	0.00000E+00	1.23842E+01
0.46	1.05361	0.98081	0	1.00000E+00	0.00000E+00	1.29641E+01
0.44	1.05015	0.97890	0	1.00000E+00	0.00000E+00	1.35980E+01
0.42	1.04666	0.97701	0	1.00000E+00	0.00000E+00	1.42931E+01
0.40	1.04302	0.97518	0	1.00000E+00	0.00000E+00	1.50601E+01
0.38	1.03937	0.97337	0	1.00000E+00	0.00000E+00	1.59084E+01
0.36	1.03558	0.97178	0	1.00000E+00	0.00000E+00	1.68536E+01
0.34	1.03177	0.97026	0	1.00000E+00	0.00000E+00	1.79109E+01
0.32	1.02787	0.96905	0	1.00000E+00	0.00000E+00	1.91026E+01
0.30	1.02393	0.96804	0	1.00000E+00	0.00000E+00	2.04545E+01
0.28	1.01996	0.96727	0	1.00000E+00	0.00000E+00	2.20008E+01
0.26	1.01598	0.96692	0	1.00000E+00	0.00000E+00	2.37860E+01
0.24	1.01202	0.96684	0	1.00000E+00	0.00000E+00	2.58690E+01
0.22	1.00809	0.96708	0	1.00000E+00	0.00000E+00	2.83307E+01
0.20	1.00424	0.96766	0	1.00000E+00	0.00000E+00	3.12833E+01
0.19	1.00237	0.96809	0	1.00000E+00	0.00000E+00	3.29912E+01
0.18	1.00051	0.96855	0	1.00000E+00	0.00000E+00	3.48888E+01
0.17	0.99870	0.96912	0	1.00000E+00	0.00000E+00	3.70080E+01
0.16	0.99693	0.96976	0	1.00000E+00	0.00000E+00	3.93908E+01
0.15	0.99520	0.97048	0	1.00000E+00	0.00000E+00	4.20899E+01
0.14	0.99356	0.97147	0	1.00000E+00	0.00000E+00	4.51708E+01

0.13	0.99198	0.97281	0	1.00000E+00	0.00000E+00	4.87230E+01
0.12	0.99051	0.97473	0	1.00000E+00	0.00000E+00	5.28615E+01
0.11	0.98932	0.97814	0	1.00000E+00	0.00000E+00	5.77365E+01
0.10	0.98851	0.97922	0	1.00000E+00	0.00000E+00	6.35622E+01
0.095	0.98811	0.97935	0	1.00000E+00	0.00000E+00	6.69347E+01
0.090	0.98763	0.97939	0	1.00000E+00	0.00000E+00	7.06876E+01
0.085	0.98716	0.97943	0	1.00000E+00	0.00000E+00	7.48813E+01
0.080	0.98668	0.97947	0	1.00000E+00	0.00000E+00	7.96001E+01
0.075	0.98620	0.97950	0	1.00000E+00	0.00000E+00	8.49481E+01
0.070	0.98572	0.97954	0	1.00000E+00	0.00000E+00	9.10601E+01
0.065	0.98525	0.97958	0	1.00000E+00	0.00000E+00	9.81115E+01
0.060	0.98477	0.97962	0	1.00000E+00	0.00000E+00	1.06339E+02
0.055	0.98429	0.97966	0	1.00000E+00	0.00000E+00	1.16063E+02
0.050	0.98382	0.97969	0	1.00000E+00	0.00000E+00	1.27730E+02
0.048	0.98363	0.97971	0	1.00000E+00	0.00000E+00	1.33078E+02
0.046	0.98343	0.97973	0	1.00000E+00	0.00000E+00	1.38892E+02
0.044	0.98324	0.97974	0	1.00000E+00	0.00000E+00	1.45234E+02
0.042	0.98305	0.97976	0	1.00000E+00	0.00000E+00	1.52179E+02
0.040	0.98286	0.98008	0	1.00000E+00	0.00000E+00	1.59819E+02

Appendix V.3

Mode 11 Body P- Waves in BodyW845.000:

6 LAYER Velocity Model				
Imperial Valley VELOCITY MODEL				
Thickness, km	alpha, km/s	beta, km/s	density	Depth from top, km
0.18	1.70	0.98	1.28	0.18
0.55	1.96	1.13	1.36	0.73
0.98	2.71	1.57	1.59	1.71
1.19	3.76	2.17	1.91	2.90
2.68	4.69	2.71	2.19	5.58
.00	6.40	3.70	2.71	5.58

BODY WAVE DISPERSION
LAYER VELOCITY MODEL FOR

PERIOD	c, km/s	(n/a)	(n/a)	Imag[U(z)]	Real[W(z)]	dU/dz(^-5)	dW/dz(^-5)	dU/dx(^-5)	dW/dx(^-5)
Body P- Wave Mode# 11 U,W(z) at z= .000E-3 km									
15.00	6.45000	0	0	-1.80906E+00	1.00000E+00	-6.49620E-02	-3.94119E-02	1.17520E-01	6.49620E-02
14.00	6.45000	0	0	-1.85095E+00	1.00000E+00	-6.96021E-02	-4.32049E-02	1.28830E-01	6.96022E-02
13.00	6.45000	0	0	-1.89027E+00	1.00000E+00	-7.49561E-02	-4.75168E-02	1.41688E-01	7.49562E-02
12.00	6.45000	0	0	-1.92613E+00	1.00000E+00	-8.12025E-02	-5.24530E-02	1.56407E-01	8.12026E-02
11.00	6.45000	0	0	-1.95777E+00	1.00000E+00	-8.85845E-02	-5.81615E-02	1.73429E-01	8.85846E-02

10.00	6.45000	0	0	-1.98495E+00	1.00000E+00	-9.74430E-02	-6.48658E-02	1.93420E-01	9.74431E-02
9.50	6.45000	0	0	-1.99703E+00	1.00000E+00	-1.02572E-01	-6.86954E-02	2.04839E-01	1.02572E-01
9.00	6.45000	0	0	-2.00834E+00	1.00000E+00	-1.08270E-01	-7.29224E-02	2.17443E-01	1.08270E-01
8.50	6.45000	0	0	-2.01907E+00	1.00000E+00	-1.14639E-01	-7.76244E-02	2.31464E-01	1.14639E-01
8.00	6.45000	0	0	-2.02915E+00	1.00000E+00	-1.21804E-01	-8.28879E-02	2.47159E-01	1.21804E-01
7.50	6.45000	0	0	-2.03753E+00	1.00000E+00	-1.29924E-01	-8.87788E-02	2.64725E-01	1.29924E-01
7.00	6.45000	0	0	-2.04009E+00	1.00000E+00	-1.39204E-01	-9.52396E-02	2.83989E-01	1.39204E-01
6.50	6.45000	0	0	-2.02453E+00	1.00000E+00	-1.49912E-01	-1.01783E-01	3.03502E-01	1.49912E-01
6.00	6.45000	0	0	-1.96026E+00	1.00000E+00	-1.62405E-01	-1.06765E-01	3.18356E-01	1.62405E-01
5.50	6.45000	0	0	-1.79231E+00	1.00000E+00	-1.77169E-01	-1.06492E-01	3.17542E-01	1.77169E-01
5.00	6.45000	0	0	-1.48654E+00	1.00000E+00	-1.94886E-01	-9.71564E-02	2.89705E-01	1.94886E-01
4.80	6.45000	0	0	-1.34018E+00	1.00000E+00	-2.03006E-01	-9.12409E-02	2.72066E-01	2.03006E-01
4.60	6.45000	0	0	-1.19448E+00	1.00000E+00	-2.11833E-01	-8.48570E-02	2.53030E-01	2.11833E-01
4.40	6.45000	0	0	-1.05752E+00	1.00000E+00	-2.21461E-01	-7.85423E-02	2.34201E-01	2.21462E-01
4.20	6.45000	0	0	-9.31259E-01	1.00000E+00	-2.32007E-01	-7.24582E-02	2.16059E-01	2.32007E-01
4.00	6.45000	0	0	-8.03692E-01	1.00000E+00	2.51353E-01	-8.49203E-02	1.95786E-01	2.43608E-01
3.80	6.45000	0	0	-5.73926E-01	1.00000E+00	6.49222E-01	-1.90320E-01	1.47171E-01	2.56429E-01
3.60	6.45000	0	0	-1.21849E+00	1.00000E+00	-	2.74417E-01	3.29814E-01	2.70675E-01

3.40	6.45000	0	0	-8.37301E-01	1.00000E+00	1.10328E+00 -2.86597E-01	-8.04764E-02	2.39968E-01	2.86597E-01
3.20	6.45000	0	0	-7.20895E-01	1.00000E+00	-3.04509E-01	-7.36187E-02	2.19519E-01	3.04509E-01
3.00	6.45000	0	0	-5.93310E-01	1.00000E+00	-3.24810E-01	-6.46289E-02	1.92713E-01	3.24810E-01
2.80	6.45000	0	0	-4.04105E-01	1.00000E+00	-3.48011E-01	-4.71631E-02	1.40633E-01	3.48011E-01
2.60	6.45000	0	0	-1.96669E-01	1.00000E+00	-3.74781E-01	-2.47189E-02	7.37079E-02	3.74781E-01
2.40	6.45000	0	0	-7.44285E-02	1.00000E+00	-4.06012E-01	-1.01343E-02	3.02189E-02	4.06013E-01
2.20	6.45000	0	0	-4.72817E-02	1.00000E+00	-4.42923E-01	8.67461E-03	2.09421E-02	4.42923E-01
2.00	6.45000	0	0	-1.28314E-01	1.00000E+00	-4.87215E-01	2.83372E-02	6.25166E-02	4.87215E-01
1.90	6.45000	0	0	-2.62172E-01	1.00000E+00	-5.12858E-01	-4.50919E-02	1.34457E-01	5.12858E-01
1.80	6.45000	0	0	-4.62670E-01	1.00000E+00	8.88796E-01	-8.39972E-02	2.50466E-01	5.41350E-01
1.70	6.45000	0	0	1.08812E-01	1.00000E+00	-1.29557E+00	5.99271E-02	-6.23703E-02	5.73194E-01
1.60	6.45000	0	0	8.61284E-02	1.00000E+00	-6.09019E-01	1.80184E-02	-5.24538E-02	6.09019E-01
1.50	6.45000	0	0	1.75171E-01	1.00000E+00	-6.49620E-01	5.11451E-02	-1.13794E-01	6.49620E-01
1.40	6.45000	0	0	9.34311E-03	1.00000E+00	-6.96021E-01	1.20801E-01	-6.50301E-03	6.96022E-01
1.30	6.45000	0	0	-3.76042E-01	1.00000E+00	-7.49561E-01	-9.45278E-02	2.81867E-01	7.49562E-01
1.20	6.45000	0	0	-2.11961E-01	1.00000E+00	-8.12025E-01	-5.77219E-02	1.72118E-01	8.12025E-01
1.10	6.45000	0	0	2.11456E+00	1.00000E+00	-	-6.30851E-01	-	8.85846E-01

						8.50732E+00		1.87317E+00	
1.00	6.45000	0	0	-1.07758E-01	1.00000E+00	-9.74430E-01	2.31645E-01	1.05003E-01	9.74431E-01
0.95	6.45000	0	0	-4.06482E-01	1.00000E+00	-1.02572E+00	1.51760E-01	4.16935E-01	1.02572E+00
0.90	6.45000	0	0	-5.00290E-01	1.00000E+00	-1.08270E+00	-1.81654E-01	5.41664E-01	1.08270E+00
0.85	6.45000	0	0	-2.12769E-01	1.00000E+00	-1.14639E+00	-8.18005E-02	2.43916E-01	1.14639E+00
0.80	6.45000	0	0	2.03166E-01	1.00000E+00	-1.51744E+00	-8.56182E-02	-2.47463E-01	1.21804E+00
0.75	6.45000	0	0	6.25002E-01	1.00000E+00	-1.29924E+00	2.72324E-01	-8.12028E-01	1.29924E+00
0.70	6.45000	0	0	5.26729E-01	1.00000E+00	-1.39204E+00	5.62471E-01	-7.33230E-01	1.39204E+00
0.65	6.45000	0	0	-1.54140E+00	1.00000E+00	-1.49912E+00	-7.74941E-01	2.31075E+00	1.49912E+00
0.60	6.45000	0	0	-2.89206E-01	1.00000E+00	-1.62405E+00	-4.59319E-01	4.69685E-01	1.62405E+00
0.55	6.45000	0	0	9.70465E-03	1.00000E+00	-1.77169E+00	-2.83281E-02	-1.71937E-02	1.77169E+00
0.50	6.45000	0	0	2.55393E+00	1.00000E+00	-2.59862E+01	-2.28896E+00	-4.97726E+00	1.94886E+00
0.48	6.45000	0	0	3.82539E-01	1.00000E+00	-2.03006E+00	2.60436E-01	-7.76577E-01	2.03006E+00
0.46	6.45000	0	0	5.26907E-03	1.00000E+00	-2.11833E+00	6.37821E-01	-1.11616E-02	2.11833E+00
0.44	6.45000	0	0	-6.62124E-01	1.00000E+00	-2.21461E+00	-4.91759E-01	1.46635E+00	2.21462E+00
0.42	6.45000	0	0	3.15404E-01	1.00000E+00	-1.51427E+02	-1.00947E+00	-7.31761E-01	2.32007E+00
0.40	6.45000	0	0	-5.09269E-01	1.00000E+00	-2.43608E+00	-4.16057E-01	1.24062E+00	2.43608E+00

0.38	6.45000	0	0	1.36556E-01	1.00000E+00	2.56429E+00	-5.39895E-01	-3.50168E-01	2.56429E+00
0.36	6.45000	0	0	8.34954E-02	1.00000E+00	3.47495E+00	-7.77881E-01	-2.26001E-01	2.70675E+00
0.34	6.45000	0	0	1.61742E-01	1.00000E+00	2.86597E+00	1.59213E+00	-4.63548E-01	2.86597E+00
0.32	6.45000	0	0	-7.83054E-01	1.00000E+00	9.90475E+00	-7.99664E-01	2.38447E+00	3.04510E+00
0.30	6.45000	0	0	3.57629E-02	1.00000E+00	3.58843E+00	2.52771E-01	-1.16162E-01	3.24810E+00
0.28	6.45000	0	0	3.46575E-01	1.00000E+00	3.48011E+00	1.34672E+00	-1.20612E+00	3.48011E+00
0.26	6.45000	0	0	-2.46652E+00	1.00000E+00	1.53945E+01	5.48702E+00	-9.24403E+00	3.74781E+00
0.24	6.45000	0	0	1.75647E+00	1.00000E+00	1.21399E+01	-3.69668E+00	-7.13148E+00	4.06013E+00
0.22	6.45000	0	0	-1.00638E+00	1.00000E+00	1.35494E+01	1.49488E+00	-4.45749E+00	4.42923E+00
0.20	6.45000	0	0	1.71676E-01	1.00000E+00	4.87215E+00	-1.00635E+00	-8.36430E-01	4.87215E+00
0.19	6.45000	0	0	-1.42609E+00	1.00000E+00	2.84408E+01	6.57357E+00	-7.31384E+00	5.12858E+00
0.18	6.45000	0	0	5.53923E-01	1.00000E+00	1.88426E+01	-2.05407E+00	-2.99866E+00	5.41350E+00
0.17	6.45000	0	0	-4.42545E-01	1.00000E+00	1.01859E+01	2.08252E+00	-2.53664E+00	5.73194E+00
0.16	6.45000	0	0	-1.10177E+00	1.00000E+00	2.80501E+01	-4.94037E+00	-6.71000E+00	6.09019E+00
0.15	6.45000	0	0	-3.65427E+00	1.00000E+00	2.87556E+01	8.17365E+00	-2.37389E+01	6.49620E+00
0.14	6.45000	0	0	9.48046E-01	1.00000E+00	1.38859E+01	-2.21293E+00	-6.59861E+00	6.96022E+00
0.13	6.45000	0	0	-3.64750E+00	1.00000E+00	3.03608E+01	-1.00898E+01	-2.73403E+01	7.49562E+00
0.12	6.45000	0	0	1.24707E-01	1.00000E+00	8.12025E+00	3.39607E-01	-1.01266E+00	8.12026E+00

0.11	6.45000	0	0	-7.95266E+00	1.00000E+00	1.37413E+02	-2.36257E+01	7.04483E+01	8.85845E+00
0.10	6.45000	0	0	-5.27639E-01	1.00000E+00	-1.04044E+01	1.93421E+00	5.14147E+00	9.74430E+00
0.095	6.45000	0	0	-1.63671E+00	1.00000E+00	1.69910E+01	-5.63007E+00	1.67880E+01	1.02572E+01
0.090	6.45000	0	0	-4.02834E-03	1.00000E+00	-1.08270E+01	7.97454E-01	4.36148E-02	1.08270E+01
0.085	6.45000	0	0	3.95053E-01	1.00000E+00	-1.15267E+01	1.51881E+00	-4.52884E+00	1.14639E+01
0.080	6.45000	0	0	2.26467E-01	1.00000E+00	-1.22488E+01	1.19878E+00	-2.75845E+00	1.21804E+01
0.075	6.45000	0	0	6.69894E-01	1.00000E+00	-1.29924E+01	2.91885E+00	-8.70354E+00	1.29924E+01
0.070	6.45000	0	0	3.30943E+00	1.00000E+00	-4.18887E+01	1.54497E+01	-4.60687E+01	1.39204E+01
0.065	6.45000	0	0	1.41389E-01	1.00000E+00	2.56898E+01	-4.61849E+00	2.11959E+00	1.49912E+01
0.060	6.45000	0	0	-1.28346E-01	1.00000E+00	-1.62405E+01	7.75379E-01	2.08440E+00	1.62405E+01
0.055	6.45000	0	0	-9.08622E-01	1.00000E+00	5.69378E+01	-6.55676E+00	1.60980E+01	1.77169E+01
0.050	6.45000	0	0	3.95032E+01	1.00000E+00	5.63086E+02	2.58183E+02	-7.69862E+02	1.94886E+01
0.048	6.45000	0	0	2.49486E+00	1.00000E+00	-3.07547E+01	1.69852E+01	-5.06472E+01	2.03006E+01
0.046	6.45000	0	0	-4.14021E-01	1.00000E+00	2.11833E+01	-2.94124E+00	8.77032E+00	2.11833E+01
0.044	6.45000	0	0	6.90904E-02	1.00000E+00	-2.21461E+01	1.08889E+00	-1.53009E+00	2.21462E+01
0.042	6.45000	0	0	1.21869E+00	1.00000E+00	2.32007E+01	-9.48222E+00	2.82745E+01	2.32007E+01
0.040	6.45000	0	0	-2.84811E-01	1.00000E+00	-2.43608E+01	2.32682E+00	-6.93822E+00	2.43608E+01

APPENDIX R1
(Reporting Date 21 May 2012)

REPORT No. I
Contract No.: 87055-11-0562
RSP Project ID (R525.1)

REPORTING DATE – 21 May 2012

PROJECT TITLE; Interfacing Seismological Description of Strong Ground Motion with Engineering Analysis of Soil Structure Interaction for Nuclear Power Plants

REPORT SUBMITTED BY: Structural and Earthquake Engineering Consultants (SEEC) Inc.
855 Arcadia Ave. #E, Arcadia, CA 91007 USA
Contact name: M. D. Trifunac
Phone: (626) 447-9382
Email: trifunac@usc.edu

to

Canadian Nuclear Safety Commission

ATTENTION: Nanci Laroche, Nebojsa Orbovic
280 Slater St., , Ottawa, Ontario, Canada, K1P 5S9
E-mail: research-recherche@cnsc-ccsn.gc.ca
Nebojsa.Orbovic@cnsc-ccsn.gc.ca

INTRODUCTION

As described in the statement of the proposed work the purpose of this contract is to formulate a comprehensive regulatory approach for seismic wave excitation of NPP structures, and specifically to provide detailed procedures for computations of overall response associated with seismic soil-structure interaction in 3D. This is illustrated in Fig. 1. Assuming that the structure, foundation and the surrounding soil are modeled numerically, this task can be accomplished by specifying components of strong ground motion at a discrete mesh of points in the five surfaces of the "box" ABCD, which represents the boundary and the contact surfaces between the numerical representation of the model inside the box with the elastic, continuum mechanics representation of the site outside the box.

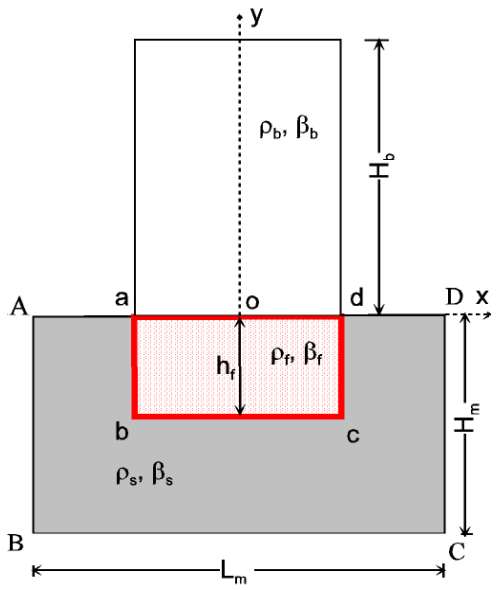

Figure 1. Structure, foundation (abcd), and the surrounding soil (ABCD) for numerical analysis of SSI.

To accomplish this task it is necessary to formulate algorithms which describe (a) strong ground motion along a HORIZONTAL line radialy extending from the earthquake source towards the site of the structure (e.g. along BC in Fig.1), and (b) along a VERTICAL line (e.g. along AB or CD in Fig. 1) in the layered half space. Once these algorithms have been formulated, the complete motion can be specified at any desired number of points in the five surfaces of the box ABCD..

The algorithms for description of strong earthquake motion along any horizontal line

(HL) have been completed and tested, and are described in detail in Appendix I. The essential feature of the algorithms for describing the motions along HL is the consistent use of phase delays based on the site specific dispersion of the wave motions through the foundation soil described in terms of layered half space. For description of consistent motions along any vertical line (VL), it is necessary to work with decomposition of wave motion in terms of the frequency dependent mode shapes, which correspond to the characteristic functions of the surface waves in the layered half space. The mathematical formulation for the algorithms we are developing for the formulation of motions along VL is described in Appendix II. At the time of this writing this method has been developed, but needs to be tested and verified.

APPENDIX I

Synthetic Earthquake Ground Motions on an Array

INTRODUCTION

Extended structures, such as pipelines and bridges, for example, are sensitive to differential motion of their supports and their seismic analysis and design require specification of time histories of ground motion at an array of closely spaced points. Because the phase in an accelerogram is not a stable quantity, time histories of ground motion are not predictable directly by empirical scaling models, but can be constructed indirectly, using empirically predicted amplitude spectrum, and some procedure for unfolding the spectrum in time. This paper presents such a method, which generates synthetic time histories of motion at an array of points. The method is an extension of the SYNACC method, first proposed by Trifunac [1] and demonstrated for a site in Imperial Valley in Southern California. The method evolved over the years, by inclusion of more current empirical scaling laws for Fourier amplitude spectra of acceleration and frequency dependent duration [2,3], and extension to prediction of rotational motions [4,5], strains [6] and curvature [7], all at a point in space (see also review in [8]). This paper presents an extension of the SYNACC method to an array of points on the ground surface. It also presents new expressions for the point strains, rotations and curvatures, derived from the new formulation, which differ slightly from the previous expressions. In what follows, for brevity, we will use “pipeline” to mean any long structure supported by many separate foundations.

The method is based on representation of the ground motion by traveling wavelets of surface and body waves, which propagate in space with phase and group velocities that are those of a horizontally layered half-space approximating the soil and geology of the site. The amplitudes of the wavelets are such that the total motion in a narrow frequency band matches a target Fourier amplitude spectrum of acceleration. The methodology has been implemented in a computer program, which has built in a suite of empirical scaling models for prediction of site specific Fourier amplitude spectra of acceleration, and computes the phase and group velocities specific for the site. A uniform hazard spectrum, or any user specified spectrum can also be used. While the Fourier spectrum determines the overall amplitudes of motion, the layered structure determines the distribution of the energy in time at a given site, and also the causal relationship between the motions at neighboring points along the supports of the structure. This causal relationship is such that the motions further away from the source are delayed relative to the closer points differently in different frequency bands. Examples are shown of time histories for ground accelerations, velocities and displacements in the radial, transverse and vertical direction, and radial (normal) and transverse (shear) strains, at a point and at an array of points.

This empirical-physical model based method has clear advantages over both the engineering stochastic methods and the seismological physics based methods. The former methods (see recent comprehensive review in [9]) produce motions with stationary frequency content over the entire duration, in contrast to the nonstataionary nature reveled by the many observations. Further, motions at an array of points are generated using overly simplified coherency function, which is based on a single valued

phase velocity, rather than the complete site-specific set for all body waves and surface wave modes. The latter methods involve numerical simulations based on a physical model of the earthquake source and of the wave propagation from the source to the site. They produce motions with correct physical nature, but involve many assumptions and need to be validated with data. Also, due to the lack of detail in the available information about the earthquake source and the wave path, they have difficulties to model high-frequency content of the synthetic motions. The SYNACC method, which is neither stochastic nor purely physics based, does not suffer from these shortcomings. It produces motions with amplitudes that are automatically consistent with observations over a broad frequency range, and does not need calibration. Also, the motions are nonstationary in a physically meaningful sense and consistent with the site soil and geology.

METHODOLOGY

The geology between the earthquake source and the site can vary considerably, especially for large distances, and different types of waves will arrive at the site via different wave paths, as illustrated in Fig. 1, showing the earthquake fault, and a segment of a pipeline located on sediments. The surface waves (Love and Rayleigh) arrive horizontally through the low velocity layers, with velocities that are frequency dependent, defined by the dispersion in the layers of site soil and geology, while the body waves arrive from depth at an angle, which is close to vertical for soft geology near the surface. Further, the amplitude attenuation is different for body and surface waves, due to different geometric spreading, and for both waves, the attenuation is frequency dependent. The *total* effect can be predicted reliably, in statistical sense, using empirical scaling laws for Fourier amplitude spectra of acceleration. Considering the nature of

these processes, in the SYNACC methodology, over the frequency band of interest, 0 to 25 Hz, the empirically predicted Fourier amplitude spectrum is partitioned in N narrow non-overlapping subbands, and the energy in each subband is partitioned among surface and body waves [1,2,3]. Waves in a narrow frequency band propagate as groups, forming wavelet packets, the amplitudes of which are localized in time, and which propagate with their group velocity. The total motion, therefore, can be represented as a superposition of such wavelet packets. In the following, the representation of the surface and body waves that enables generation of related motions at an array of points is presented, highlighting the changes relative to the previous versions for generating motions at a single point [1,2,3,6].

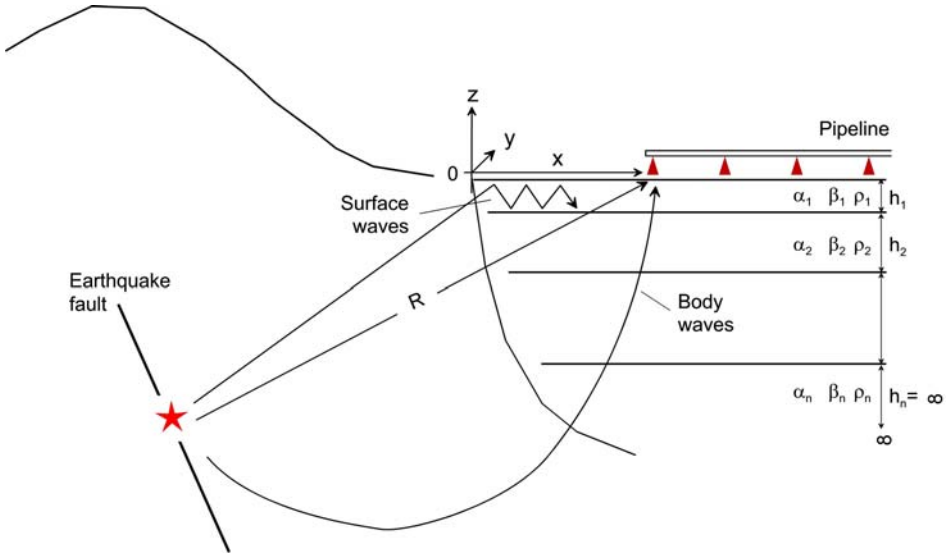

Fig. 1 Model.

Representation of Surface Wave Motion at a Site

To expand the surface waves, the soil and geology at the site is locally approximated by a horizontally layered half-space, as shown in Fig. 1. Let h_i, ρ_i, α_i and β_i be the thickness, mass density and P- and S-wave velocities in the i-th layer, with $i = 1, \ldots, L$,

and let the x-axis point in the direction of wave propagation. The layer boundaries define a boundary value problem for the displacement, which has a solution that is a surface wave only for a discrete set of frequency dependent phase velocities $c_m(\omega)$, obtained from the roots of the characteristic equation for the particular problem [10,11]. The displacement for an eigenvalue constitutes an eigenfunction (or a mode), and any surface wave motion then can be represented as a linear combination of these eigenfunctions.

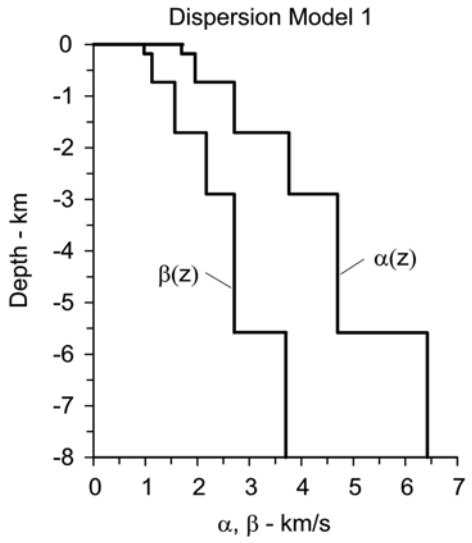

Fig. 2 Velocity profile for Dispersion Model 1.

Fig. 2 shows an example of a velocity profile for a site in El Centro in Imperial Valley, California [1], and Tables 1a,b,c show the properties of the layers for three variants of this profile, which differ only in the top 180 m. Fig. 3 shows the phase and group velocities, $c_m(\omega)$ and $U_m(\omega)$ $m = 1,\ldots,5$, for the first five modes of Rayleigh

Table 1a Profile for dispersion model 1

No.	h - [km]	α - [km/s]	β - [km/s]	ρ -[gm/cm^3]
1	0.18	1.70	0.98	1.28
2	0.55	1.96	1.13	1.36
3	0.98	2.71	1.57	1.59
4	1.19	3.76	2.17	1.91
5	2.68	4.69	2.71	2.19
6	∞	6.40	3.70	2.71

Table 1b Profile for dispersion model 2

No.	h - [km]	α - [km/s]	β - [km/s]	ρ -[gm/cm^3]
1a	0.06	0.867	0.50	1.2
1b	0.12	1.70	0.98	1.28
2	0.55	1.96	1.13	1.36
3	0.98	2.71	1.57	1.59
4	1.19	3.76	2.17	1.91
5	2.68	4.69	2.71	2.19
6	∞	6.40	3.70	2.71

Table 1c Profile for dispersion model 3

No.	h - [km]	α - [km/s]	β - [km/s]	ρ -[gm/cm^3]
1a	0 .03	0.4335	0.25	1.20
1b	0.03	0.867	0.50	1.2
1c	0.12	1.70	0.98	1.28
2	0.55	1.96	1.13	1.36
3	0.98	2.71	1.57	1.59
4	1.19	3.76	2.17	1.91
5	2.68	4.69	2.71	2.19
6	∞	6.40	3.70	2.71

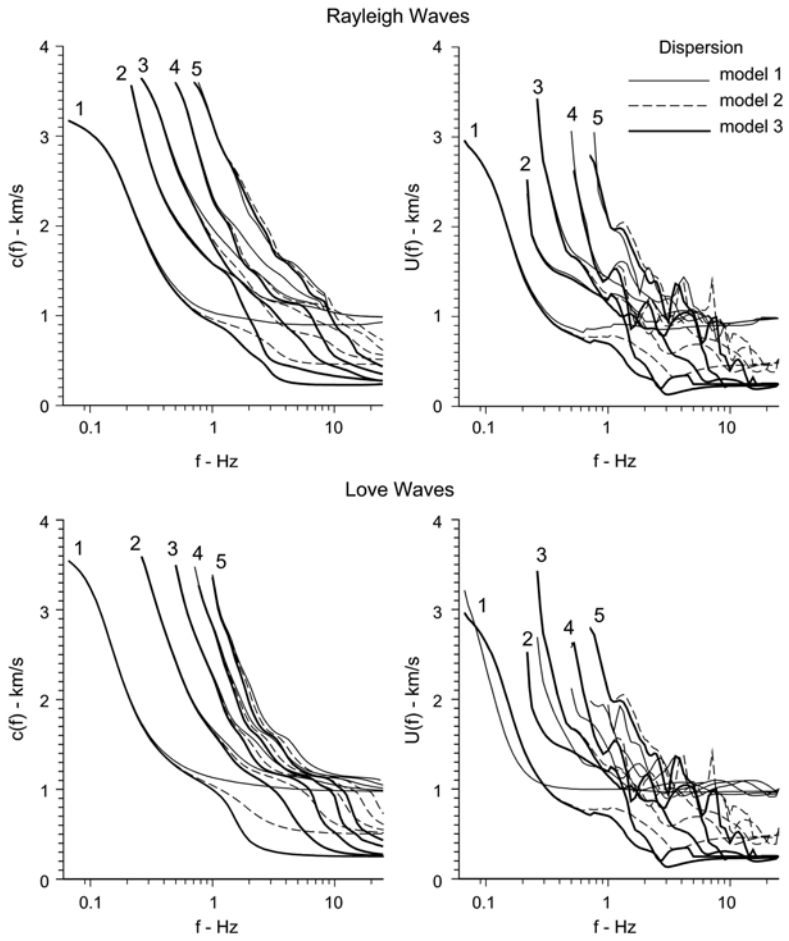

Fig. 3 Phase velocities $c(f)$ (left) and group velocities $U(f)$ (right) as functions of frequency f for Rayleigh waves (top) and Love waves (bottom), for the first five modes. The three types of curves correspond to the different dispersion models. It can be seen that, for the three models, which differ only in the top 180 m, at low frequencies, the phase and group velocities do not depend on the model but only on the mode. In contrast, at high frequencies, they depend less on the mode and strongly on the model, all approaching the velocity in the top layer for the model.

and Love waves, referred to as dispersion curves, for the three variants. The Rayleigh waves are surface waves with in-plane particle motion along an ellipse, which is usually retrograde at the surface, and with vertical to horizontal aspect ratio > 1. The Love waves are surface waves with out of plane particle motion. The group velocity $U_m(\omega) \triangleq d\omega / dk_m$, where $k_m(\omega) \triangleq \omega / c_m(\omega)$ is the horizontal wave number, is the

velocity with which the amplitude envelope of the wavelet packet propagates, and with which the energy is transported. The number of modes is finite for a given frequency, and increases with frequency. The first mode exists at all frequencies, while the higher modes exist only for high enough frequencies. Because the wave velocities in the earth crust are smaller at progressively smaller depths, and because the penetration depth of a mode decreases with frequency, $c_m(\omega)$ decreases with frequency, approaching asymptotically the shear wave velocity of the top layer.

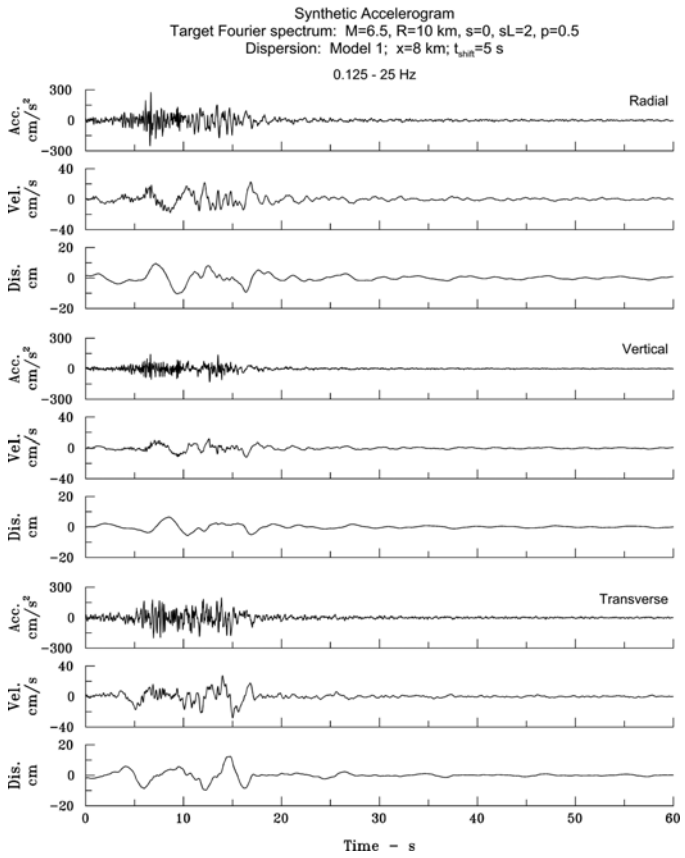

Fig. 4 Artificial acceleration, velocity and displacement that matchthe target Fourier spectrum of acceleration of M6.5 earthquake, at hypocentral distance $R = 10$ km, and for a site on sediments ($s = 2$) and deep soil ($s_L = 2$), unfolded with dispersion model 1.

As mentioned earlier, the synthesis is based on dividing the frequency band of interest, 0 to 25 Hz, in N non-overlapping subbands, assuming uniform Fourier amplitude within the subband, and in each band, representing the surface wave motion as a superposition of the eigenfunctions, evaluated at the central frequency of the subband. Let ω_n and $\Delta\omega_n$ be the central frequency and half-bandwidth of the n-the subband, $U_{nm} = U_m(\omega_n)$ and $c_{nm} = c_m(\omega_n)$ be the group and phase velocities of the m-th mode in that subband, and let $w_{nm}(x;t)$ be the eigenfunction of the m-th mode in the n-th subband, at point x on the free surface ($z = 0$), and at time t. Then

$$w_{nm}(x;t) = \mathrm{sinc}\left[\Delta\omega_n\left(t - \frac{x}{U_{nm}}\right)\right]\exp\left[i\left(\omega_n t - k_{nm}x\right)\right] \qquad (1)$$

where

$$k_{nm} = \frac{\omega_n}{c_{nm}}\left(1 - i\frac{1}{2Q}\right) \qquad (2)$$

is the complex horizontal wave number, and Q is the quality factor, assumed to be constant [12]. If no material attenuation is assumed, $1/(2Q) = 0$ and k_{nm} is real. Function $w_{nm}(x;t)$ represents a traveling wavelet, which is a complex exponential of frequency ω_n, amplitude modulated by a sinc function. The amplitude modulation

$$\mathrm{sinc}\left(\Delta\omega_n t\right) = \frac{\sin(\Delta\omega_n t)}{\Delta\omega_n t} \qquad (3)$$

is a window in time with half-width $\Delta t_n = \pi / \Delta\omega_n$, which propagates with velocity U_{nm}, while the phase propagates with velocity c_{nm}. Consequently, at a point x, the phase has

time lag x / c_{nm}, and the center of the amplitude envelope has time lag x / U_{nm} relative to the reference point, $x = 0$.

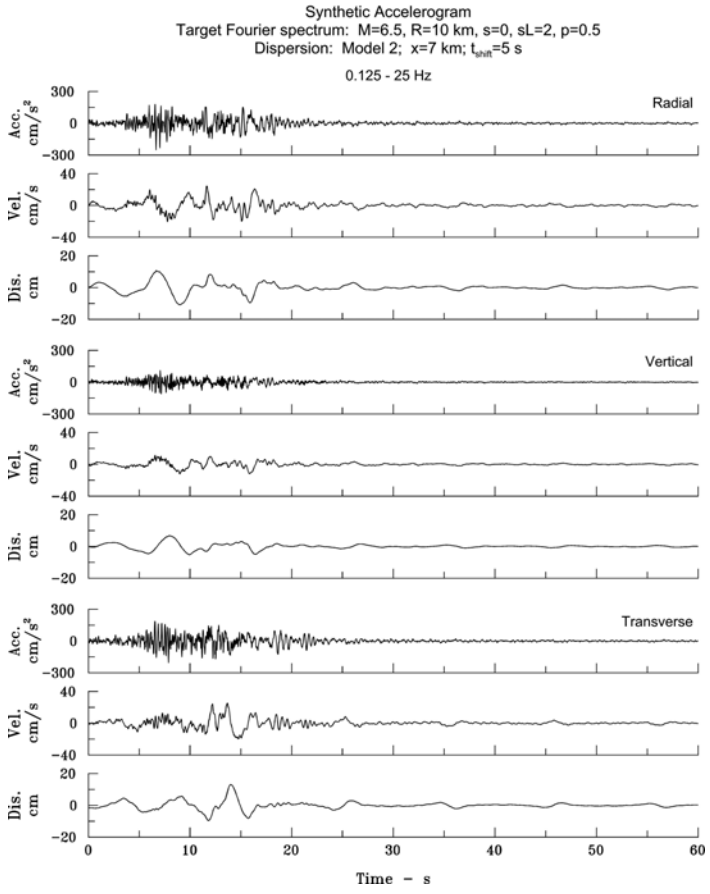

Fig. 5 Artificial acceleration, velocity and displacement that match the target Fourier spectrum of acceleration of M6.5 earthquake, at hypocentral distance $R = 10$ km, and for a site on sediments ($s = 2$) and deep soil ($s_L = 2$), unfolded with dispersion model 2.

Representation (1) is consistent with the following convention of Fourier transform for the pair $f(t)$ and $\hat{f}(\omega)$

$$f(t) \leftrightarrow \hat{f}(\omega)$$
$$\hat{f}(\omega) = \int_{-\infty}^{\infty} f(t) e^{-i\omega t} dt \qquad (4)$$
$$f(t) = \frac{1}{2\pi} \int_{-\infty}^{\infty} \hat{f}(\omega) e^{i\omega t} d\omega$$

Then, the Fourier transform of the wavelet $w_{nm}(x;t)$ is

$$\hat{w}_{nm}(x;\omega) = \frac{\pi}{\Delta\omega_n} \exp\left[-i\left(\frac{\omega - \omega_n}{U_{nm}} + k_{nm} \right) x \right] p_{\Delta\omega_n}(\omega - \omega_n) \qquad (5)$$

where

$$p_{\Delta\omega_n}(\omega - \omega_n) = \begin{cases} 1, & \omega - \Delta\omega_n \le \omega \le \omega_n + \Delta\omega_n \\ 0, & \text{otherwise} \end{cases} \qquad (6)$$

represents a box function with half width $\Delta\omega_n$, centered at frequency ω_n, with amplitude scaled to $\pi / \Delta\omega_n$ and phase shifted by $k_{nm}x$.

According to Eqns (1) and (5), the energy of the wavelet $w_{nm}(x)$ is localized, in time - around $t = x / U_{nm}$ with spread $\pm\Delta t_n = \pm\pi / \Delta\omega_n$, and, in frequency, around $\omega = \omega_n$ with spread $\pm\Delta\omega_n$, i.e. within a rectangle of constant area $(2\Delta t_n)(2\Delta\omega_n) = 2\pi$ in the phase plane. Consequently, finer division of the frequency range (smaller $\Delta\omega_n$) will lead to wider in time wavelets $w_{nm}(x;t)$, which is a manifestation of the Heisenberg-Gabor uncertainty principle for signals [13,14].

Let $u(x,t)$ be the associated analytic signal of a generic component of motion (the specific expansions will be presented in one of the following sections. Because scaling

laws for Fourier spectra of acceleration are available, we start with the representation of acceleration in a series of wavelets

$$\ddot{u}(x,t) = \sum_{n=1}^{N} \sum_{m=1}^{M_n} A_{nm}^{*} w_{nm}(x;t) \qquad (7)$$

where M_n is the number of modes that exist in the n-th subband.

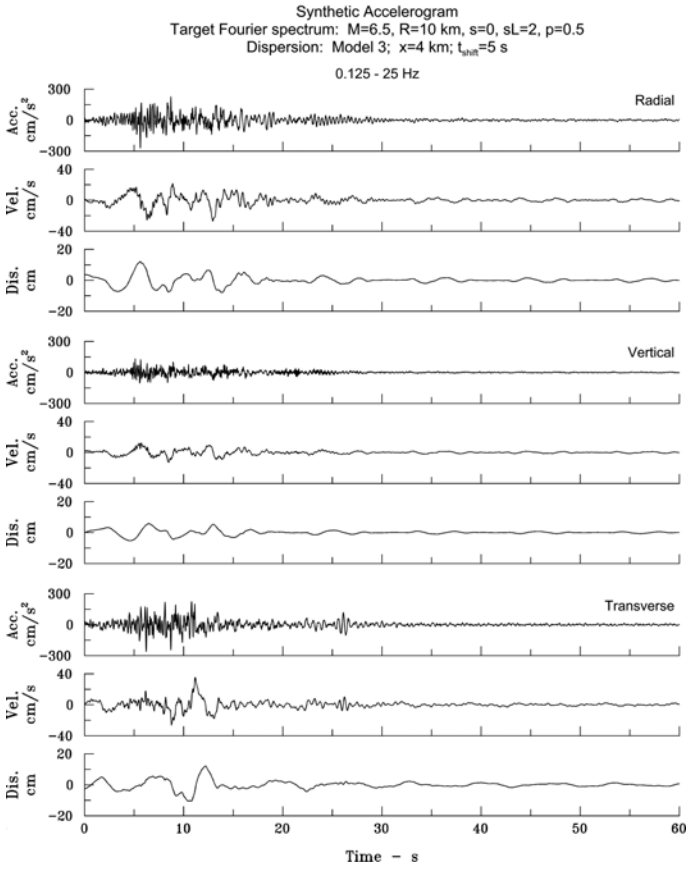

Fig. 6 Artificial acceleration, velocity and displacement that match the target Fourier spectrum of acceleration of M6.5 earthquake, at hypocentral distance $R = 10$ km, and for a site on sediments ($s = 2$) and deep soil ($s_L = 2$), unfolded with dispersion model 3.

Representation of Velocity, Displacement and Spatial Derivatives

It is convenient to do the synthesis in the frequency domain and then invert to the time domain, because the representations of velocities, displacements, strains, rotations, and curvatures are easily obtainable in the frequency domain by analytical integration and differentiation of the wavelets. The Fourier transforms of acceleration, velocity and displacements are

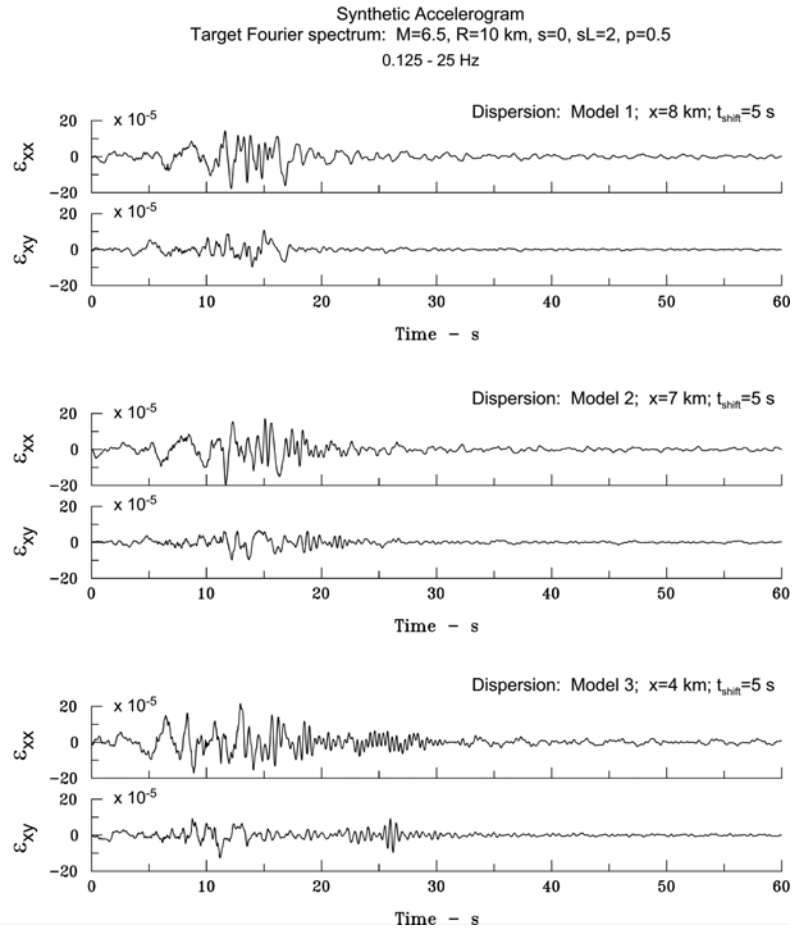

Fig. 7 Artificial axial and shear strain, ε_{xx} and ε_{xy}, for target corresponding to M6.5 earthquake, at hypocentral distance $R = 10$ km, and for a site on sediments ($s = 2$) and deep soil ($s_L = 2$), unfolded with dispersion models 1 (top), 2 (middle) and 3 (bottom).

$$\hat{\ddot{u}}(x,t) = \sum_{n=1}^{N} \sum_{m=1}^{M_n} A_{nm}^{*} \hat{w}_{nm}(x;\omega) \tag{8}$$

$$\hat{\dot{u}}(x;\omega) = \sum_{n=1}^{N} \sum_{m=1}^{M_n} \frac{1}{i\omega_n} A_{nm}^{*} \hat{w}_{nm}(x;\omega) \tag{9}$$

and

$$\hat{u}(x;\omega) = \sum_{n=1}^{N} \sum_{m=1}^{M_n} \frac{-1}{\omega_n^2} A_{nm}^{*} \hat{w}_{nm}(x;\omega) \tag{10}$$

Further, the first and second derivatives of $\hat{w}_{nm}(x;\omega)$ are

$$\frac{\partial}{\partial x} \hat{w}_{nm}(x;\omega) = -i\left(\frac{\omega - \omega_n}{U_{nm}} + k_{nm} \right) \hat{w}_{nm}(x;\omega) \tag{11}$$

and

$$\frac{\partial^2}{\partial x^2} \hat{w}_{nm}(x;\omega) = \left[-i\left(\frac{\omega - \omega_n}{U_{nm}} + k_{nm} \right) \right]^2 \hat{w}_{nm}(x;\omega) \tag{12}$$

which gives for the corresponding derivatives of displacements

$$\frac{\partial}{\partial x} \hat{u}(x;\omega) = \sum_{n=1}^{N} \sum_{m=1}^{M_n} \frac{i}{\omega_n^2} \left(\frac{\omega - \omega_n}{U_{nm}} + k_{nm} \right) A_{nm}^{*} \hat{w}_{nm}(x;\omega) \tag{13}$$

and

$$\frac{\partial^2}{\partial x^2} \hat{u}(x;\omega) = \sum_{n=1}^{N} \sum_{m=1}^{M_n} \frac{1}{\omega_n^2} \left(\frac{\omega - \omega_n}{U_{nm}} + k_{nm} \right)^2 A_{nm}^{*} \hat{w}_{nm}(x;\omega) \tag{14}$$

Mode Participation Factors

The coefficients of the expansion A_{nm}^{*} are complex valued and depend on the amplitude of the target spectrum, but, for a given site geology, they are related, as shown in [1] for a site in Imperial Valley, and their relative amplitude depends on the frequency and mode number. We represent them as

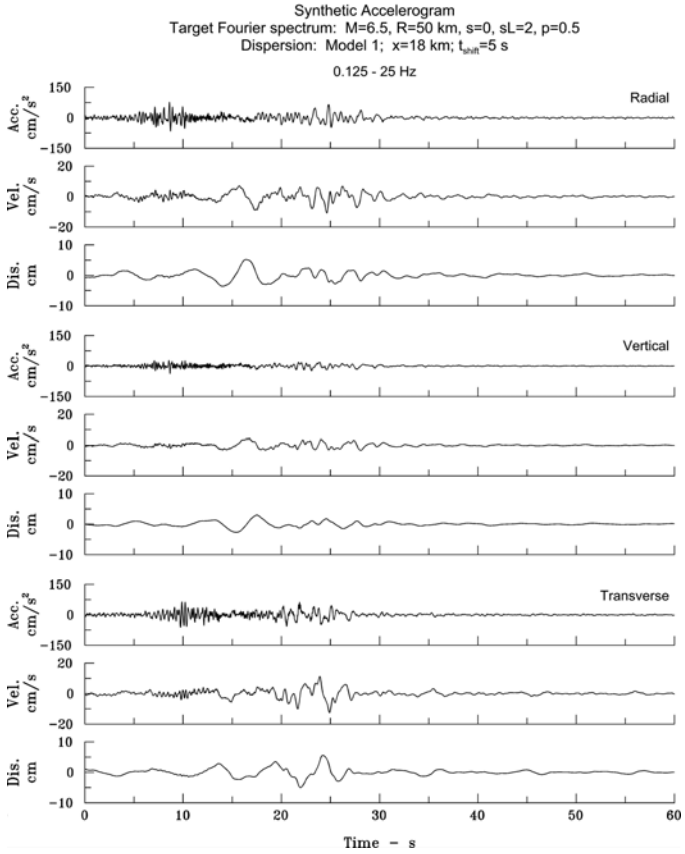

Fig. 8 Artificial acceleration, velocity and displacement that match the target Fourier spectrum of acceleration of M6.5 earthquake, at hypocentral distance $R = 50$ km, and for a site on sediments ($s = 2$) and deep soil ($s_L = 2$), unfolded with dispersion model 1.

$$A_{nm}^{*} = \alpha_n A_1(m) A_2(\omega_n) \exp\left(i\phi_{nm}^{ran}\right) \qquad (15)$$

where ϕ_{nm}^{ran} is a random phase between $-\pi$ and π, describing the randomness in the radiation of energy from the earthquake source and other randomness along the wave path until the arrival to the region near the site, represented by the medium with parallel layers (Fig. 1). Functions $A_1(m)$ and $A_2(\omega_n)$ are site specific, as in [1], and their product $A_1(m)A_2(\omega_n)$ can be thought of as a site dependent mode participation factor. The coefficients $\alpha_n = \alpha(\omega_n, \Delta\omega_n)$, for given division in subbands, depends only on the target spectrum that is to be matched by the synthetics.

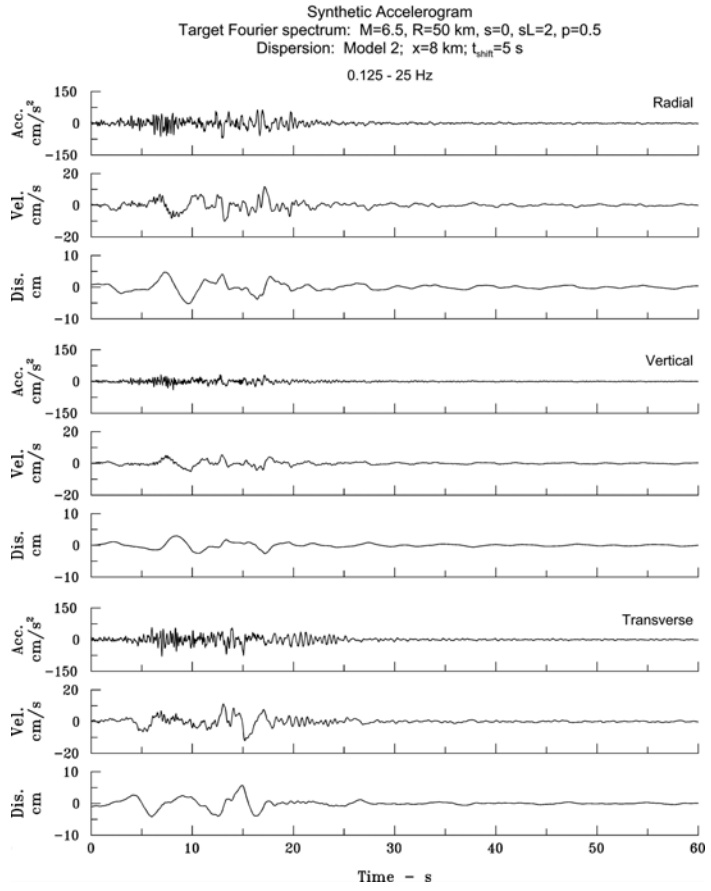

Fig. 9 Artificial acceleration, velocity and displacement that match the target Fourier spectrum of acceleration of M6.5 earthquake, at hypocentral distance $R = 50$ km, and for a site on sediments ($s = 2$) and deep soil ($s_L = 2$), unfolded with dispersion model 2.

The representation (7) differs from that in [1,2,3] as follows. In the latter, the phase delay at point x is $(\omega_n / U_{mn})t + \phi_{nm}^{ran}$, i.e. the lag of the amplitude modulation plus some random phase shift, while in this paper, the phase lag is $(\omega_n / c_{mn})t$. In this paper, we consider also material attenuation due to Q, which affects the difference between the

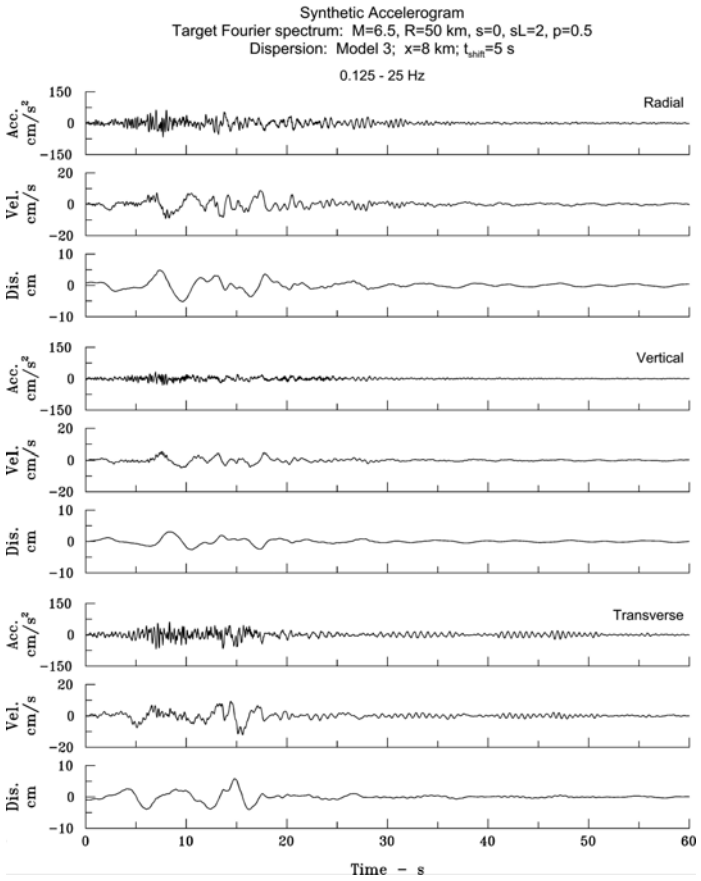

Fig. 10 Artificial acceleration, velocity and displacement that match the target Fourier spectrum of acceleration of M6.5 earthquake, at hypocentral distance $R = 50$ km, and for a site on sediments ($s = 2$) and deep soil ($s_L = 2$), unfolded with dispersion model 3.

motion at different points of the array. Minor differences, chosen for convenience in this paper, are that the random phase is part of the coefficients of expansion, and that the associated analytic signal is expanded. Another significant difference is in the definition

of the reference point $x = 0$. In the latter, $x = 0$ is the epicenter of the earthquake, while, in this work, it is a point between the epicenter and the site, from where the parallel layers geology can be adopted to be representative of the wave path. This point can be

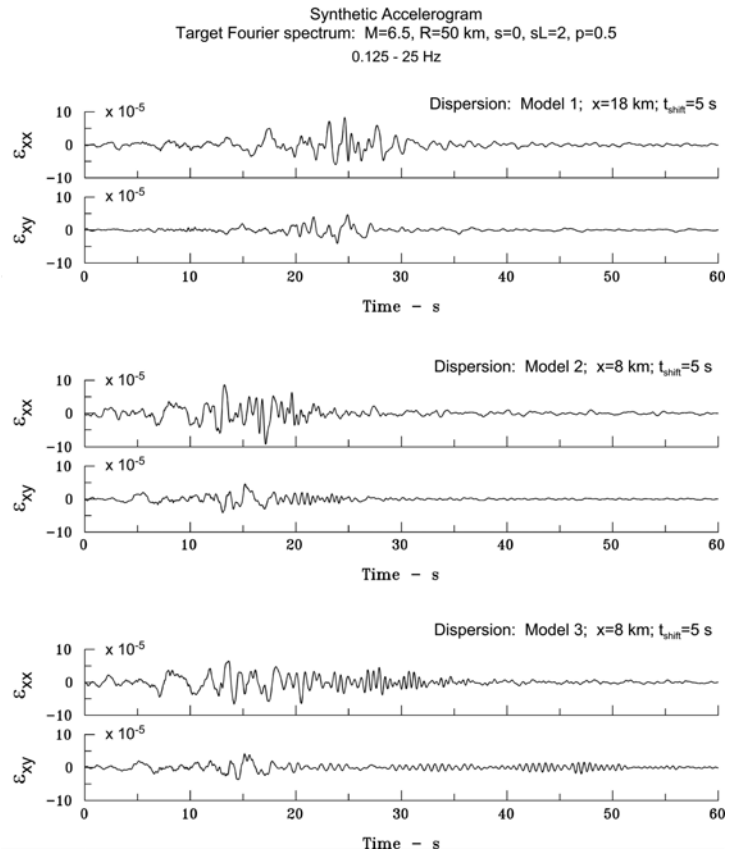

Fig. 11 Artificial axial and shear strain, ε_{xx} and ε_{xy}, for target corresponding to M6.5 earthquake, at hypocentral distance $R = 50$ km, and for a site on sediments ($s = 2$) and deep soil ($s_L = 2$), unfolded with dispersion models 1 (top), 2 (middle) and 3 (bottom).

referred to as the "the edge of the valley", and $x =$ representative distance from the edge of the valley. Therefore, in this paper, x is just the distance over which dispersive wave propagation occurs consistent with the given parallel layers of soil and geology, while the target spectrum to be matched depends on the hypocentral distance R of the site from the source (Fig. 1). Such definition of the reference $x = 0$ is more useful for modeling, as the

geology can vary considerably between the source and the site. It also helps control the duration of the synthetic motion, and avoid the artifact of unrealistically long duration of

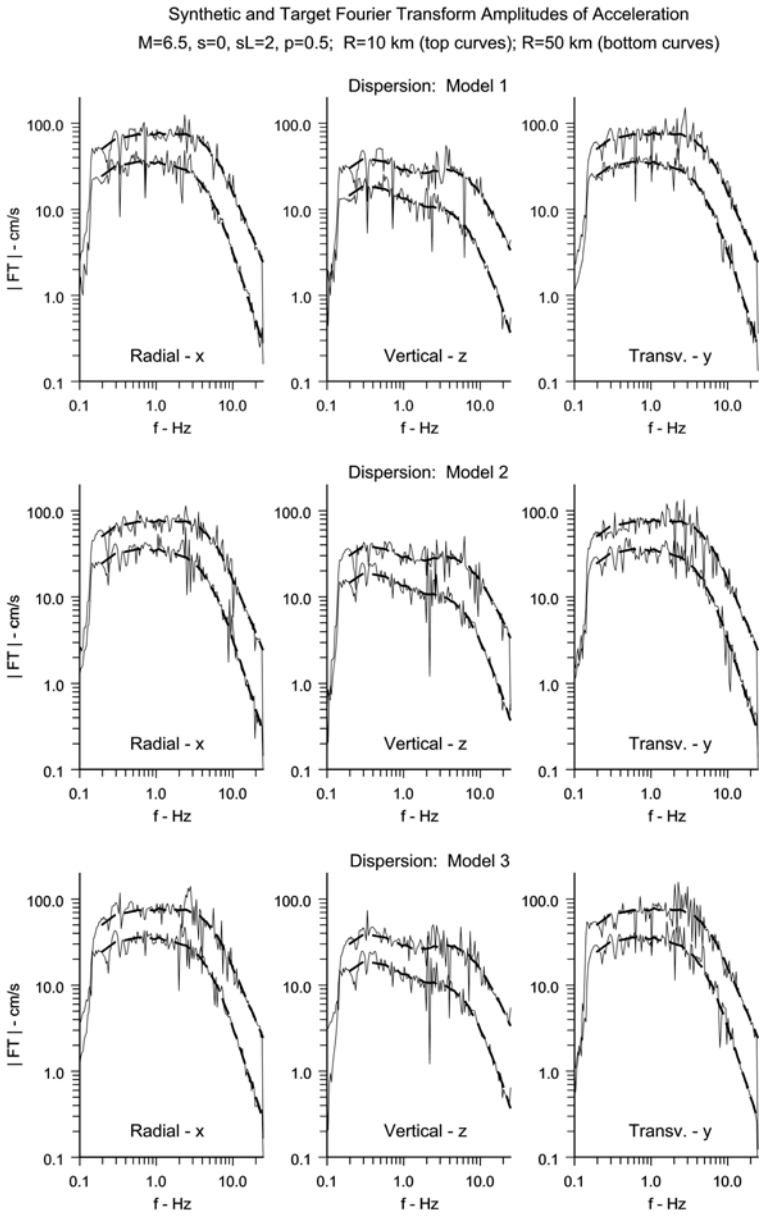

Fig. 12 Fourier Transform amplitudes of synthetic accelerations for M6.5 earthquake, unfolded by dispersion models 1 (top), 2 (middle) and 3 (bottom), for radial (left), vertical (center) and transverse (right) motions.

the synthetic motion for large source to site distances and softer near surface soil layers. Because the parallel layers structure is an idealization, the "distance from the edge of the valley" is not exact but an abstraction, and can be chosen by trial and error or by iteration, until the duration of the synthetic motion is satisfactory, based on some subjective or objective standard, such as empirical scaling laws [1].

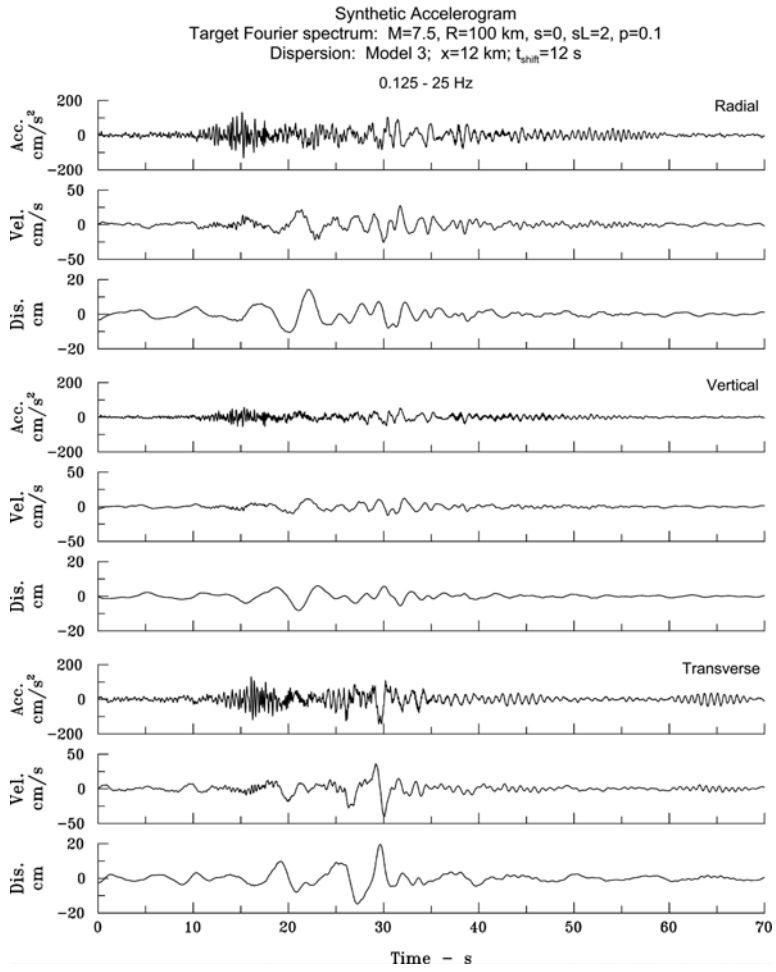

Fig. 13 Artificial acceleration, velocity and displacement that match the target Fourier spectrum of acceleration of M7.5 earthquake, at hypocentral distance $R = 100$ km, for a site on sediments ($s = 2$) and deep soil ($s_L = 2$),and probability of being exceeded $p = 0.1$, unfolded with dispersion model 3.

Expansion of Body Waves

The propagation of body waves is essentially nondispersive, and $c(\omega_n) = U(\omega_n)$. They arrive at the site from depth, often close to vertical due to progressive bending of the rays towards the surface (Fig. 1), and consequently propagate horizontally with larger

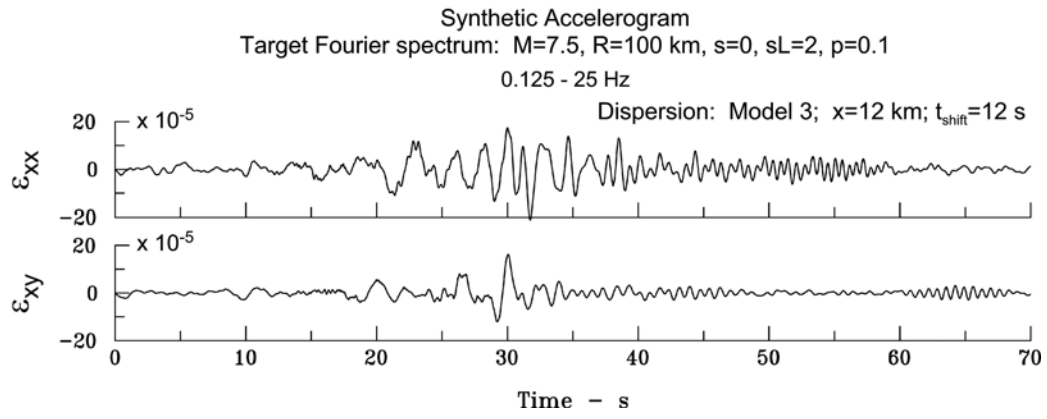

Fig. 14 Artificial axial and shear strain, ε_{xx} and ε_{xy}, for target corresponding to M7.5 earthquake, at hypocentral distance $R = 100$ km, for a site on sediments ($s = 2$) and deep soil ($s_L = 2$), and probability of being exceeded $p = 0.1$, unfolded with dispersion model 3.

phase velocities $c(\omega_n)$ than the surface waves. Further, their amplitude at a given frequency reflects the interference characteristics of the layers, which depends on incident angle. In the SYNACC synthesis, the body waves are treated as two additional "surface wave modes", one for P- and the other one for S-waves, with large phase/group velocities, and contributing respectively to the in-plane and out of plane motions, and with mode participation factor same as those for the Love modes, i.e. not reflecting the site interference characteristics, but with the flexibility to increase or decrease their participation, relative to that of the surface waves. Site specific interference features could be included by appropriate frequency dependent mode participation factors,

derived e.g. using the propagator matrix of the medium [15,15]. Pipelines, however, are light, long and flexible structures, hence more sensitive to strains and differential motions, which are caused largely by the surface waves, and including the site interference (resonances) is not essential.

Determination of the Expansion Coefficients for a Site

The site specific mode participation factors, $A_1(m)A_2(\omega_n)$, can be determined by analysis of recorded motion in the region, as in [1], for example. In this paper, for illustration purposes, the same functions as in [1] are used, included in Appendix A for completeness of this paper. The coefficients α_n are determined from the requirement that some representative value of $\left|\hat{\ddot{u}}(x;\omega)\right|$ over the n-th subband matches a target value. For example, such representative value can be obtained by averaging $\log_{10}\left|\hat{\ddot{u}}(x;\omega)\right|$ and converting back to linear scale. Let $FS^{tar}(\omega_n)$ be the amplitude spectrum to be matched by the (real valued) synthetic acceleration. Then

$$\alpha_n = \frac{2FS^{tar}(\omega_n)}{10^{\frac{1}{2\Delta\omega_n}\int_{\omega_n-\Delta\omega_n}^{\omega_n+\Delta\omega_n}\log_{10}\left|\sum_{m=1}^{M_n+2}A_1(m)A_2(\omega_n)\exp\left(i\phi_{nm}^{ran}\right)\hat{w}_{nm}(x;\omega)\right|d\omega}} \tag{16}$$

where M_n+2 is the total number of surface and body waves contributing to the particular component of motion. The factor of 2 multiplying $FS^{tar}(\omega_n)$ is because $\hat{\ddot{u}}(x;\omega)$ is the Fourier transform of the associated analytic signal, which, for $\omega>0$, has amplitudes twice of those of its real part. The expression for the α_n in Eqn. (16) differs from [1] and [2,3] in the averaging.

Motion at an Array of Sites

The sites where related motions are needed for analysis of extended structures are typically at distances from few tens of meters to few kilometers. For such distances, it is assumed that the motion differs only because of deterministic propagation and attenuation due to Q, while the randomness in phase and mode participation factors, included in coefficients A_{nm}^{*}, is the same. For such an array of sites, the motion at one representative site, at $x = x_0$, is first synthesized by matching the target spectrum, which gives the coefficients $A_{nm}^{*}(x_0)$, and the motion at another sites, at $x = x_0 + \Delta x$, is then computed as

$$\hat{\ddot{u}}(x_0 + \Delta x, \omega) = \sum_{n=1}^{N} \sum_{m=1}^{M_n} A_{nm}^{*}(x_0) \hat{w}_{nm}(x_0 + \Delta x; \omega) \tag{17}$$

Trigger Time Adjustment

The above equations correspond to reference time, which is such that, at $x = 0$, the amplitude envelopes of all the wavelets are centered at $t = 0$. The wavelets, however, have energy also for time $t < 0$, as the main lobes of the sinc functions extend over the interval $[-\Delta t_n, +\Delta t_n]$, where $\Delta t_n = \pi / \Delta\omega_n$. For small x, x / U_{nm} may be considerably smaller than Δt_n, in which case the entire pulse does not contribute to the synthetic accelerogram, if its starting time (which would be the trigger time of an imaginary instrument that has recorded the motion) is set even to $t = 0$. This can be avoided by time shifting the synthetic time history, which is conveniently done in the frequency

domain. For example, for time shift t_0, $\hat{w}_{nm}(x;\omega)$ needs to be multiplied by $\exp(-i\omega t_0)$.

Cartesian Components of Linear Motions, Strains, Rotations and Curvatures

Having presented the analytical developments for a generic component of motion, we now proceed with the specific expansions for the Cartesian $x-y-z$ coordinate system shown in Fig. 1. Let $u_x(x;t)$, $u_y(x;t)$ and $u_z(x;t)$ be the displacement components along the three coordinate axes, which have specific expansions

$$\hat{\ddot{u}}_x(x,t) = \sum_{n=1}^{N}\sum_{m=1}^{M_n} A_{nm}^{*x}\hat{w}_{nm}^{x}(x;\omega) \qquad (18)$$

$$\hat{\ddot{u}}_y(x,t) = \sum_{n=1}^{N}\sum_{m=1}^{M_n} A_{nm}^{*y}\hat{w}_{nm}^{y}(x;\omega) \qquad (19)$$

and

$$\hat{\ddot{u}}_z(x,t) = \sum_{n=1}^{N}\sum_{m=1}^{M_n} A_{nm}^{*z}\hat{w}_{nm}^{z}(x;\omega) \qquad (20)$$

Because $u_x(x;t)$ and $u_z(x;t)$ are expanded in Rayleigh modes, the expansion wavelets $\hat{w}_{nm}^{x}(x;\omega)$ are as in Eqn. (5) with group and phase velocities U_{nm}^{R} and c_{nm}^{R} specific for the corresponding Rayleigh mode, and $\hat{w}_{nm}^{z}(x;\omega) = V_{nm}\hat{w}_{nm}^{x}(x;\omega)$ where $V_{nm} = V_m(\omega_n)$ is the complex ratio of vertical to horizontal amplitude of the elliptic particle motion at the surface for the mode. Similarly, $u_y(x;t)$ is expanded in Love modes, and $\hat{w}_{nm}^{y}(x;\omega)$ are as in Eqn. (5) with group and phase velocities U_{nm}^{L} and c_{nm}^{L} specific for the corresponding Love mode.

The point strains, (stains on an infinitesimal volume at the point on ground surface), can be obtained from the spatial derivatives of the synthetic displacements. The compressional strain is

$$\hat{\varepsilon}_{xx}(x;\omega) = \frac{\partial}{\partial x}\hat{u}_x(x;\omega) \tag{21}$$

and the shear strain is

$$\begin{aligned}\hat{\varepsilon}_{xy}(x;\omega) &= \frac{1}{2}\left[\frac{\partial}{\partial x}\hat{u}_y(x;\omega) + \frac{\partial}{\partial y}\hat{u}_x(x;\omega)\right] \\ &= \frac{1}{2}\frac{\partial}{\partial x}\hat{u}_y(x;\omega)\end{aligned} \tag{22}$$

with the displacement derivatives as in Eqn. (13). The expression in Eqn. (21) and (22) differs from [6] in that it is exact, and includes also the variation of the amplitude envelope with x, through the term $\frac{\omega-\omega_n}{U_{nm}}$ in Eqn. (13). For small $\Delta\omega_n$, the difference is small.

The point rotations, (rotations of an infinitesimal volume at the point on the ground surface), can be obtained by applying the curl operator on the displacement vector

$$\begin{aligned}\vec{\psi}(x;\omega) &= \nabla \times \vec{u}(x;\omega) \\ &= \begin{vmatrix} \vec{i} & \vec{j} & \vec{k} \\ \frac{\partial}{\partial x} & \frac{\partial}{\partial y} & \frac{\partial}{\partial z} \\ u_x & u_y & u_z \end{vmatrix}\end{aligned} \tag{23}$$

where $\vec{i}$, $\vec{j}$ and $\vec{k}$ are unit vectors in the x, y and z directions. The nonzero rotations are the torsion $\psi_z(x;\omega)\vec{k}$

$$\psi_z(x;\omega)\vec{k} = \frac{\partial u_z(x;\omega)}{\partial x}\vec{k} \qquad (24)$$

and rocking $\psi_y(x;\omega)\vec{j}$

$$\psi_y(x;\omega)\vec{j} = -\frac{\partial u_y(x;\omega)}{\partial x}\vec{j} \qquad (25)$$

with the displacement derivatives as in Eqn. (13).

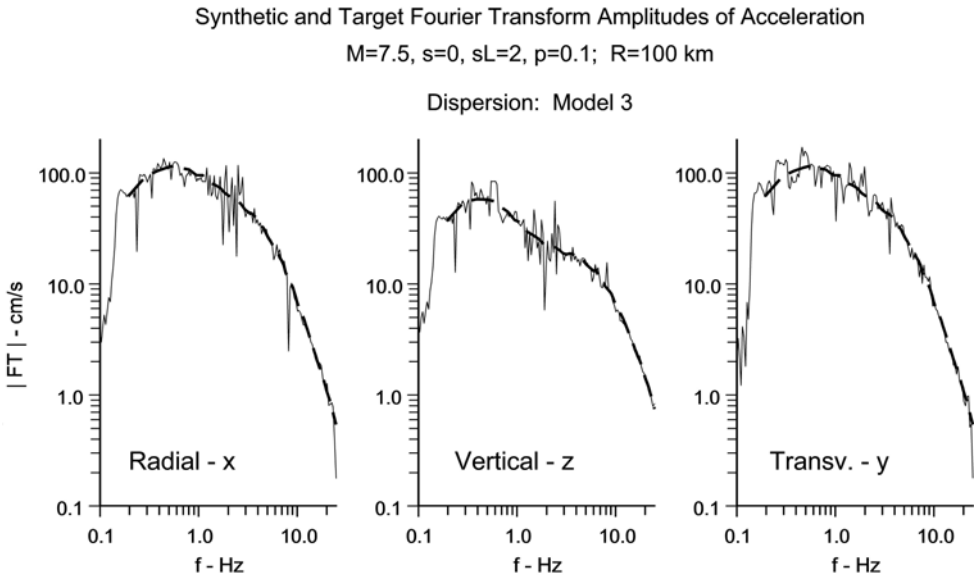

Fig. 15 Fourier Transform amplitudes of synthetic accelerations for to M7.5 earthquake, at hypocentral distance $R = 100$ km, for a site on sediments ($s = 2$) and deep soil ($s_L = 2$), and probability of being exceeded $p = 0.1$, unfolded with dispersion model 3, for radial (left), vertical (center) and transverse (right) motions.

The curvature of ground motion, for small deformations, can be approximated by the second spatial derivative of displacement. The curvatures in the $x-y$ and $x-z$ planes are

$$\kappa_{yx}(x;\omega)=\frac{\partial^2 u_y(x;\omega)}{\partial x^2} \tag{26}$$

and

$$\kappa_{zx}(x;\omega)=\frac{\partial^2 u_z(x;\omega)}{\partial x^2} \tag{27}$$

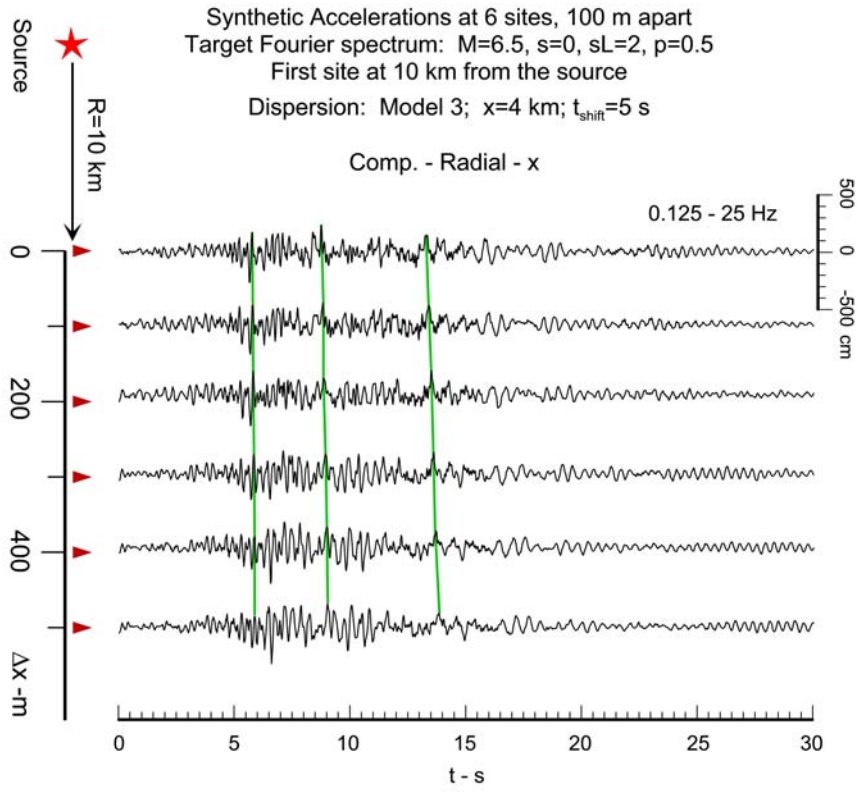

Fig. 16 Snapshots of synthetic acceleration - radial component - at six sites, 100 m apart in the radial direction. The target spectrum is that of M6.5 earthquake, at hypocentral distance $R=10$ km (the closest site), for site condition - sediments ($s=2$) and deep soil ($s_L=2$), unfolded with dispersion model 3.

with the second derivatives of displacement as in Eqn. (14), and with positive and negative curvatures corresponding respectively to convex and concave shapes.

Generation of Target Spectrum

Site specific target Fourier amplitude spectra for a *scenario* earthquake can be generated using an empirical scaling model, for given earthquake magnitude, hypocentral distance, site conditions, and probability of being exceeded, which reflects the uncertainty in the scaling law. The uncertainty in the earthquake size, location and occurrence rate can also be included by specifying as a target spectrum a uniform hazard Fourier spectrum, which has amplitudes with equal probability of being exceeded from any earthquake considered.

SYNACC has built in the Fourier amplitude scaling models developed by [16,17], in addition to the earlier models developed [19,20], and can also use uniform hazard spectrum generated by the program NEQRISK [22], which has built in the same suite of scaling models as those built in SYNACC for a scenario earthquake, or any user provided Fourier amplitude spectrum. The built in scaling models differ in the input parameters, and a particular model can be chosen depending on the details of the information available about the site. For example, the earthquake magnitude and hypocentral distance can be provided or, alternatively, the Modified Mercalli site intensity. The local site conditions are described on two scales – geologic one, which samples the geology up to the depths of the order of kilometers, and local soil one, which samples soil properties near the surface up to depths of two hundred meters. The classification based on geology can be described in two ways, by a categorical variable, such as the *geologic site condition* parameter s, which can take values 0 (sediments), 2 (rock), and 1 (intermediate

site conditions), or by a numeric variable, such as the depth of sediments h. The local soil classification is described by the categorical variable - local soil condition parameter s_L, which can take on the values 0 ("rock" soil), 1 (stiff soil) and 2 (deep soil).

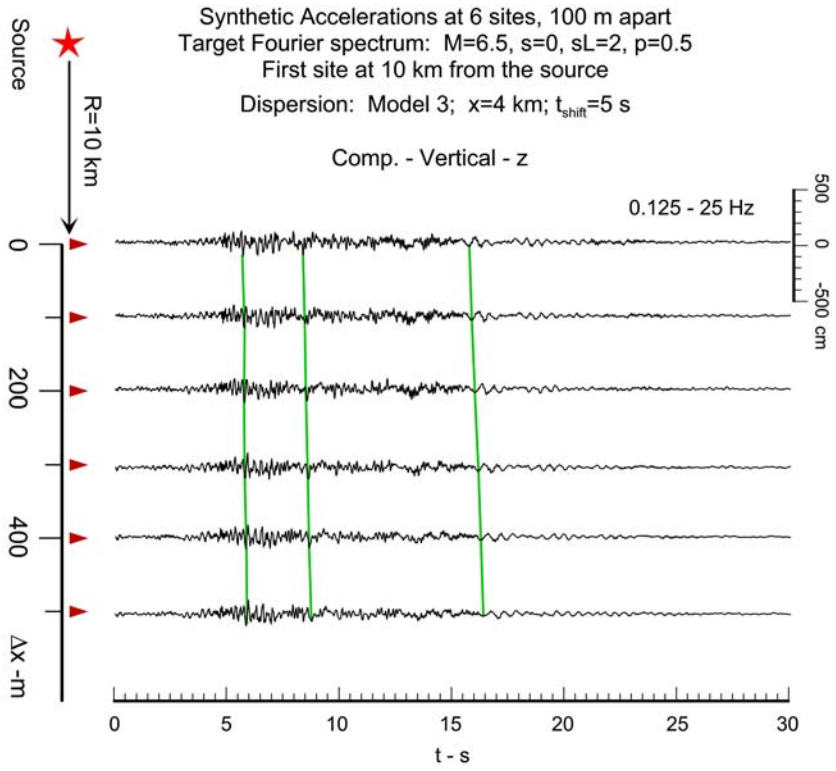

Fig. 17 Snapshots of synthetic acceleration - vertical component - at six sites, 100 m apart in the radial direction. The target spectrum is that of M6.5 earthquake, at hypocentral distance $R = 10$ km (the closest site), for site condition - sediments ($s = 2$) and deep soil ($s_L = 2$), unfolded with dispersion model 3.

RESULTS

The methodology is illustrated for a scenario earthquake. A suite of synthetic motions and strains are presented for different earthquake sizes, hypocentral distances, and dispersion models, at a site and an array of sites. The target Fourier spectra were

computed using the MMI-SITE-SOIL model [16], with $s = 0$ (sediments) and $s_L = 2$ (deep soil). Synthetic motions were computed at 4096 points in time with time step 0.02 s, i.e. with total length of about 82 s. Unless mentioned otherwise, the trigger time was adjusted by adding a 5 s shift. The number of subbands is 73.

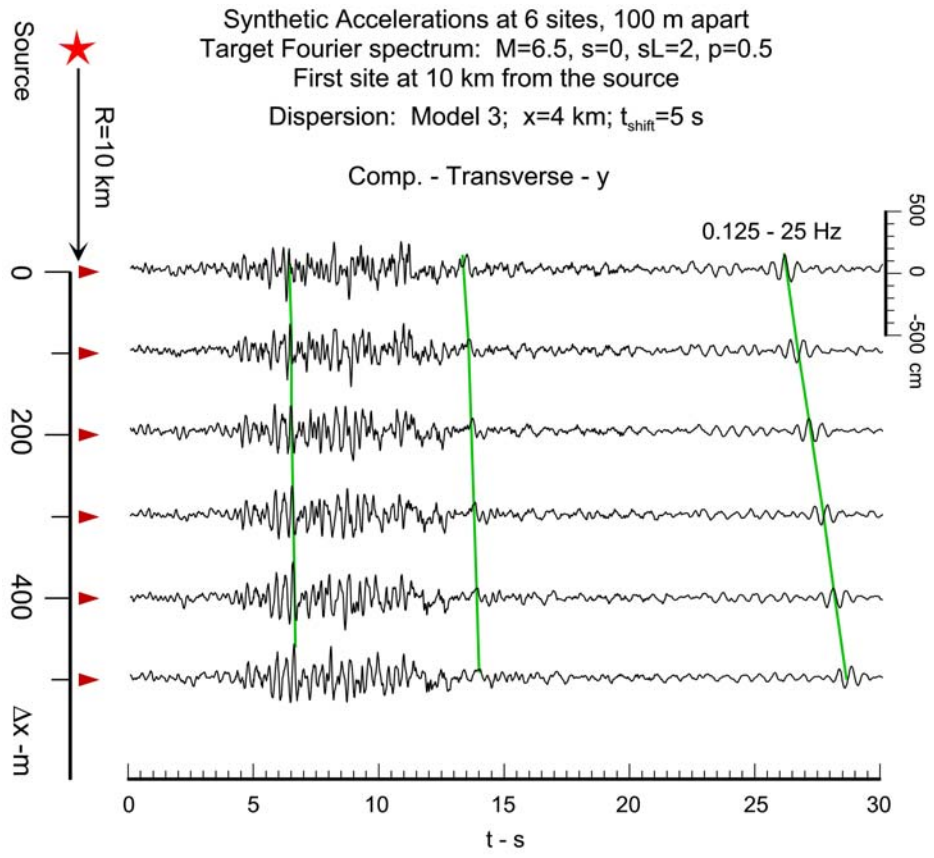

Fig. 18 Snapshots of synthetic acceleration - transverse component - at six sites, 100 m apart in the radial direction. The target spectrum is that of M6.5 earthquake, at hypocentral distance $R = 10$ km (the closest site), for site condition - sediments ($s = 2$) and deep soil ($s_L = 2$), unfolded with dispersion model 3.

Synthetic Motions at a Point

Figs. 4, 5 and 6 show tree component synthetic motions (accelerations, velocities and displacements) from a moderate and near earthquake ($M = 6.5$ and $R = 10$ km), respectively for dispersion models 1, 2 and 3, discussed in the Model section of this paper

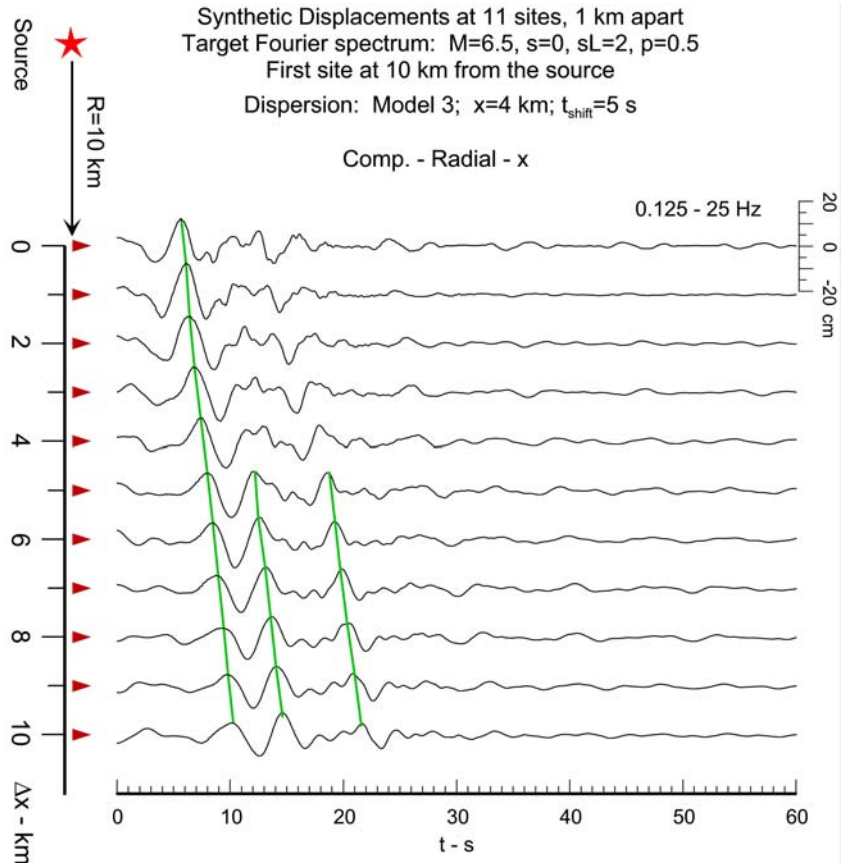

Fig. 19 Snapshots of synthetic displacement - radial component - at eleven sites, 1 km apart in the radial direction. The target spectrum is that of M6.5 earthquake, at hypocentral distance $R = 10$ km (the closest site), for site condition - sediments ($s = 2$) and deep soil ($s_L = 2$), unfolded with dispersion model 3.

(Tables 1a,b,c; Fig. 2 and 3). Model 1 is the same as the benchmark model in [1,2,3], which corresponds to a site in El Centro in Imperial Valley, southern California, and the other two models are its variants that are "softer" in the top 180 m. The "distance from the edge of the valley" $x = 8$ km, 7 km and 6 km for the three models.

Fig. 7 shows the strain time historiesFigs. 8 – 11 show similar results for $R = 50$ km, with "distance from the edge of the valley" $x = 18$ km, 8 km and 8 km for the three models. Figs. 11 show the strain time histories. It can be seen that the amplitudes of motion are similar for the three dispersion models, as they have been generated for the same target spectrum. The time histories, however, differ in that late arrivals of high frequency waves are seen in the records for dispersion model 3, which has the softest top layer. . The peak radial and shear strains (see definition in Eqs. (21) and (22)), for the sites at $R = 10$ km are about 0.02% and 0.01% for all three models, and are the largest for model 3, which is the softest at the top. For the sites at $R = 50$ km, the peak radial and shear strains are about 0.01% and 0.005%, and are the largest for model 2. They are not the largest for model 3, because of the smaller peak amplitudes, due to the longer duration (for the same Fourier spectrum), relative to the other two models. Finally, Fig. 12 shows the agreement between the Fourier amplitude spectra of the synthetic motions and the target spectra, for all the cases for the $M = 6.5$ earthquake.

Figures 13, 14 and 15 show similar results (synthetic motions, strains and Fourier spectra) for a larger but more distant earthquake ($M = 7.5$ and $R = 100$ km), and only for dispersion model 3 with $x = 12$ km, and trigger time adjustment by a 12 s shift. These

records have longer duration than the previous ones, which is physically meaningful due to both larger magnitude and source to site distance. The peak radial and shear strains are 0.021% and 0.016%.

Motions at an Array of Points

Figs 16, 17 and 18 show snapshots of synthetic accelerations at six sites, 100 m apart in the radial direction, with the closest site being at $R = 10$ km distance from a M6.5 earthquake. The figures show respectively the radial, vertical and transverse components,

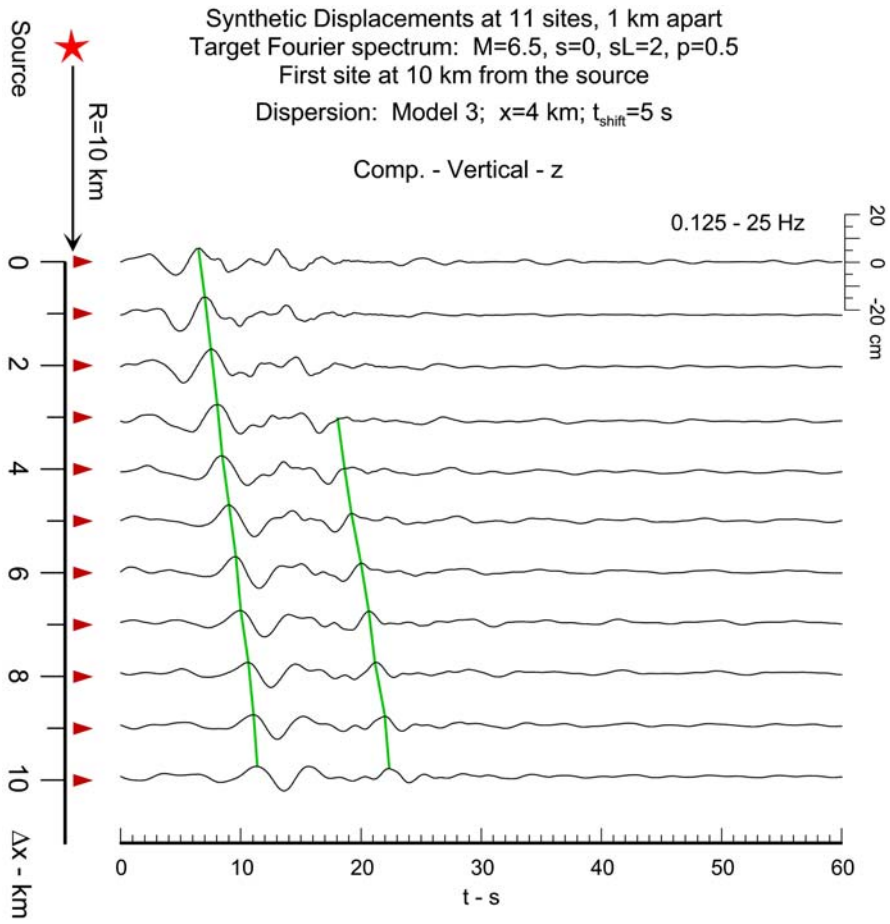

Fig. 20 Snapshots of synthetic displacement - vertical component - at eleven sites, 1 km apart in the radial direction. The target spectrum is that of M6.5 earthquake, at hypocentral

distance $R = 10$ km (the closest site), for site condition - sediments ($s = 2$) and deep soil ($s_L = 2$), unfolded with dispersion model 3.

all unfolded in time with dispersion model 3, and with $x = 4$ km. These figures show noticeable differences in the acceleration time histories even though the sites are very close to each other. The differences, created by a purely deterministic physical model of wave propagation, are more complex than single phase shift and some small amplitude decay.

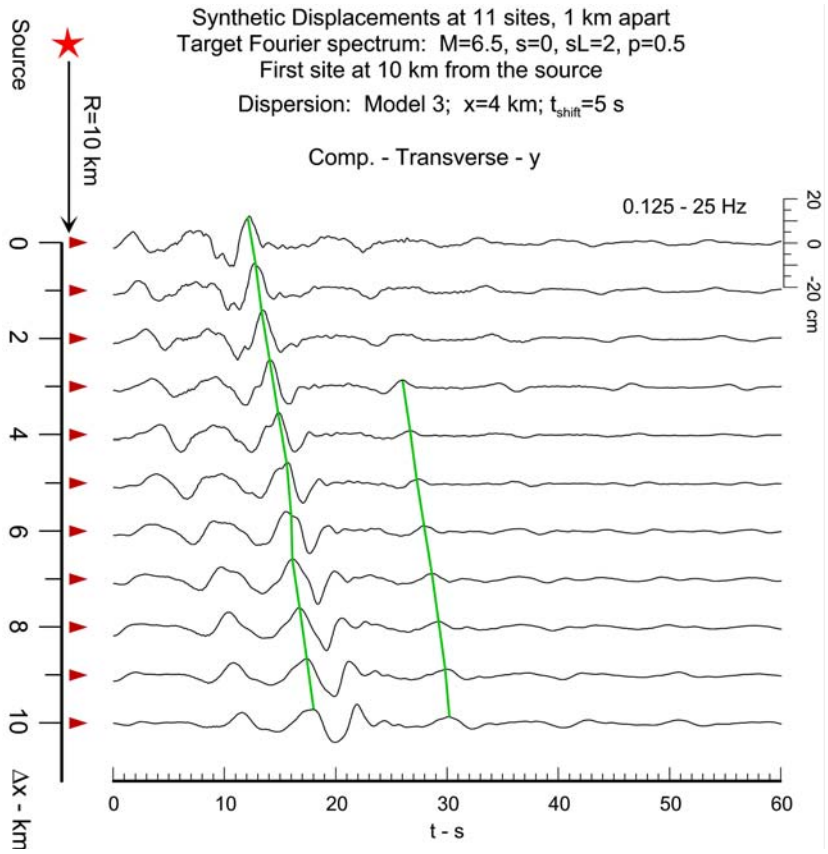

Fig. 21 Snapshots of synthetic displacement - transverse component - at eleven sites, 1 km apart in the radial direction. The target spectrum is that of M6.5 earthquake, at hypocentral distance $R = 10$ km (the closest site), for site condition - sediments ($s = 2$) and deep soil ($s_L = 2$), unfolded with dispersion model 3.

The displacements, having more energy in the lower frequency part of the spectrum, differ much less at such small distances, because the lower frequency energy propagates with much larger velocities $U(\omega)$. They exhibit a high degree of similarity of the waveforms even at distances several kilometers away, as it can be seen in Figs. 19, 20 and 21, which illustrate radial, vertical and transverse synthetic displacements at sites 1 km apart in the radial direction.

DISCUSSION AND CONCLUSIONS

A method for generating synthetic time histories of earthquake ground motion at an array of points along the ground surface was presented, which is an extension of the SYNACC methodology, originally developed for a single site. Such motions are needed for design of long structures, pipelines and bridges [23-29], and in particular for nonlinear analyses, which need to be performed in the time domain. The methodology combines empirical scaling laws for Fourier amplitude spectra of acceleration with a physical model of wave propagation in a horizontally layered half-space. Consequently, the amplitudes of the synthetic motions are consistent in statistical sense with observations, while the phase and local differences between points of the array are consistent with local characteristics of wave propagation. The presented examples for ground accelerations, velocities, displacements and strains generated by the method showed that the method produces realistic and physically meaningful time histories.

REFERENCES

1. Trifunac MD (1971). A method for synthesizing realistic strong ground motion, *Bull. Seism. Soc. Amer.*, **61**:1739-1753.
2. Wong HL, Trifunac MD (1978). Synthesizing realistic strong motion accelerograms, *Report No. 78-07*, Dept. of Civil Engrg., U. of So. California, Los Angeles, California.
3. Wong HL, Trifunac MD (1979). Generation of artificial strong motion accelerograms, *Int. J. Earthquake Eng. Struct. Dynamics*, **7**:509-527.
4. Lee VW, Trifunac MD (1985). Torsional accelerograms, *Int. J. Soil Dyn. Earthq. Eng.*, **4**(3):132-139.
5. Lee VW, Trifunac MD (1987). Rocking strong earthquake accelerations, *Int. J. Soil Dyn. Earthq. Eng.*, **6**(2):75-89.
6. Lee VW (1990). Surface strains associated with strong earthquake shaking, *Proc. J.S.C.E., 422(n* I-14), 187-194.
7. Trifunac MD (1990). Curvograms of strong ground motion, *ASCE, EMD*, 116(6), 1426-1432.
8. Lee VW (2002). Empirical scaling of strong earthquake ground motion - Part III: Synthetic Strong Motion, *ISET J. of Earthquake Technology*, Paper No. 427, **39**(4):273-310.
9. Zerva A. (2009). Spatial variation of seismic ground motions: modeling and engineering applications. CRC Press, Taylor and Francis Group, Boca Raton, Florida.
10. Thompson WT. (1950). Transmission of elastic waves through a stratified solid, *J. of Applied Physics*, **21**:89-93.
11. Haskell NA. (1953). The dispersion of surface waves in multilayered media, *Bull. Seism. Soc. Am.* **43**:17-34.
12. Trifunac MD. (1994). Q and high frequency strong motion spectra, *Soil Dyn. Earthq. Eng.*, **13**(3):149-161.
13. Gabor D. (1946). Theory of communications, *J. of the Institute of Electrical Engineers - Part III: Radio and Communication Engineering*, **93**(26):429-457.
14. Gabor D. (1953). Communication theory and physics, *Institute of Radio Engineers, Professional Group on Information Theory,* **1**(1):48-59.
15. Trampert J, Cara M, Frogneux M. (1993). SH propagator matrix and Q_S estimates from borehole- and surface-recorded earthquake data, *Geophys. J. Int.*; **112**:290-299.
16. Mehta K, Snieder R, Graizer V. (2007). Extraction of near-surface properties for a lossylayered medium using the propagator matrix, *Geophys. J. Int.*;**169**:271-280.
17. Trifunac MD, Lee VW (1985). Preliminary empirical model for scaling Fourier amplitude spectra of strong ground acceleration in terms of earthquake magnitude, source to station distance, site intensity and recording site conditions, *Report CE 85-03*, Dept. of Civil Eng., U. So. California, Los Angeles, California.
18. Trifunac MD. (1989a). Dependence of Fourier spectrum amplitudes of recorded strong earthquake accelerations on magnitude, local soil conditions and on depth of sediments, *Earthq. Eng Struct. Dyn.*, **18**(7):999-1016.

19. Trifunac MD. (1989b). Empirical Scaling of Fourier Spectrum Amplitudes of Recorded Strong Earthquake Accelerations in Terms of Magnitude and Local Soil and Geologic Conditions, *Earthq. Eng Eng Vib*., **9**(2):23-44.

20. Trifunac, MD. (1976). Preliminary empirical model for scaling Fourier amplitude spectra of strong ground acceleration in terms of earthquake magnitude, source to station distance and recording site conditions, *Bull. Seism. Soc. Amer*., **66**:1343-1373.

21. Trifunac, MD. (1979). Preliminary empirical model for scaling Fourier amplitude spectra of strong motion acceleration in terms of Modified Mercalli Intensity and geologic site conditions, Earthqu. Engng Struct. Dynam., **7**:63-74.

22. Lee VW, Trifunac MD (1985). Uniform risk spectra of strong earthquake ground motion. *Report No. 85-05*, Dept. of Civil Engrg., U. So. California, Los Angeles, California.

23. Kojić, S. and Trifunac, M.D. 1988). Transient Pressures in Hydrotechnical Tunnels During Earthquakes *Int. J. Struct. Dyn.Earthq. Eng.* 16(3), 523-539.

24. Todorovska, MI, Trifunac, MD. (1990). Propagation of Earthquake Waves in Buildings With Soft First Floor, *ASCE, EMD*, 116(4), 892-900.

25. Todorovska, MI, Trifunac, MD. (1990). Note on Excitation of Long Structures by Ground Waves, *ASCE, EMD*, 116(4), 952-964.

26. Jalali RS, Trifunac MD. (2007). Strength-Reduction Factors for Structures Subjected to Differential Near-Source Ground Motion, *Indian Society of Earthq. Techn. J.* , **44**(1):285-304.

27. Jalali RS, Trifunac MD. (2009). Response Spectra for Near-source, Differential and Rotational Strong Motion, *Bull. Seism. Soc. Amer.*, 99(2B), 1404-1415, See also Erratum: *Bull. Seism. Soc. Amer.*, 99(5), 3094-3095.

28. Jalali RS, Trifunac MD. (2011). A note on the wave-passage effects in out-of-plane response of long structures to strong earthquake pulses, *Soil Dyn. Earthq. Eng.*, **31**(4):640-647.

29. Kashefi I, Trifunac MD. (1986). Investigation of Earthquake Response of Simple Bridge Structures, *Report No. CE 86-02*, Dept. of Civil Engrg., U. So. California, Los Angeles, California.

Appendix A: Coefficients $A_1(m)$ and $A_2(\omega_n)$

Trifunac [1] suggested the following empirical equations for $A_1(m)$ and $A_2(\omega_n)$

$$A_1(m) = \left| \exp\left(-(m - m_0)^2 / 2C_0^2 \right) + C_R X_m \right|$$

and

$$A_2(\omega_n) = \left| B_0 \exp\left(-(\omega_n - \omega_p)^2 / 2\omega_B^2 \right) + B_R X_n \right|$$

with X_m and X_n being random numbers between -1 and 1, and the values of other constants are suggested in Table A1.

Table A1: Empirical Scaling Coefficients for Equations (5) and (6) (from [1])

Mode	C_0	m_o	C_R	B_0	ω_p	ω_B	B_R
1	3	5	0.2	1.5	10	5	0.1
2	3	5	0.2	1.5	10	5	0.1
3	3	5	0.2	1.5	10	5	0.1
4	3	5	0.2	2.0	25	15	0.1
5	3	5	0.2	2.0	25	15	0.1
6	3	6	0.2	3.0	30	10	0.3
7	3	7	0.2	1.5	30	5	0.25

APPENDIX II

Part A: Synthetic Translational Motions of Love Waves In or Below a Layered Media

Given $c = c(\omega)$, the wave speed of a mode of Love waves in the half-space with n elastic layered elastic media on top. c is also the (horizontal) phase velocity of the waves in each layer of the elastic media above the half space (Figure 1)

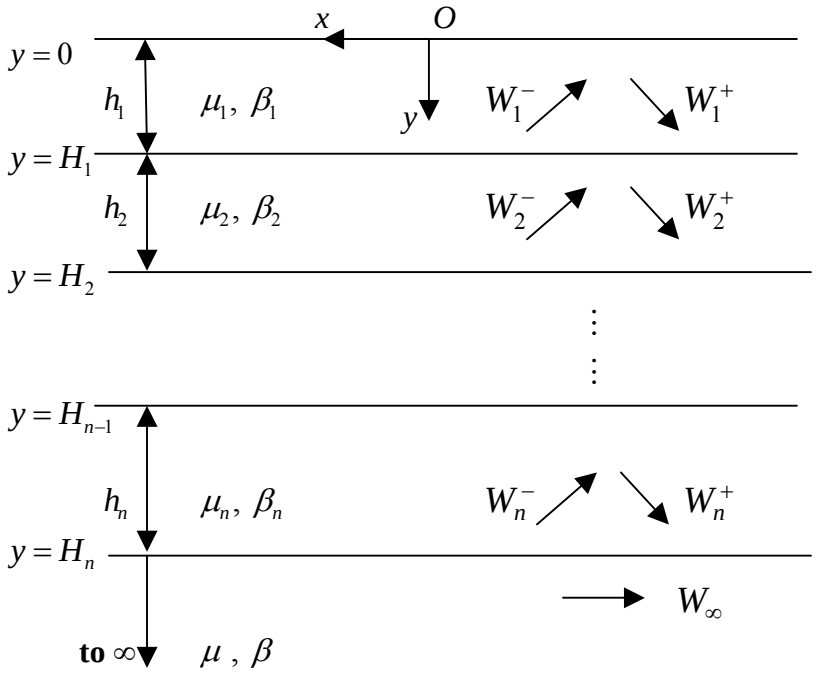

Figure 1 n-layered half-space with Love waves

For each layer l, with $l = 1, \ldots, n$, the Waves in the layer take the form W_l^-, W_l^+ :

$$\begin{aligned} W_l^- &= C_l^- e^{ik(x-\gamma_l y)} \\ W_l^+ &= C_l^+ e^{ik(x+\gamma_l y)} \end{aligned} \qquad (1)$$

They are respectively the upward and downward propagating Loves waves present in the *i-th* layer and $k = k(\omega) = \omega / c(\omega)$ is the horizontal wave number of the waves at

frequency ω and phase velocity $c = c(\omega)$. The term e^{ikx}, which is also the same in each layer, is the horizontal component of the waves, which together with the time harmonic term $e^{i\omega t}$, corresponds to waves propagating in the –*ve x* direction. The terms $e^{\mp ik\gamma_l y}$ are the vertical components of the waves with the –*ve* term propagating upwards (–*ve y*) and the +*ve* term propagating downwards (+*ve y*). Here $\gamma_l = \gamma_l(\beta_l)$ is given by

$$\gamma_l = \frac{\left(k_{\beta_l}^2 - k^2\right)^{1/2}}{k} = \left(\left(k_{\beta_l}/k\right)^2 - 1\right)^{1/2} = \left(\left(c/\beta_l\right)^2 - 1\right)^{1/2} \tag{2}$$

so that $k\gamma_l$ is the vertical wave number of the waves in the l-th layer of the medium with shear wave velocity β_l. In general, the wave velocities increase in going down the layers, so that $\beta_1 < \beta_2 < \ldots < \beta_n < \beta$, with the semi-infinite half-space at the bottom having the highest shear wave speed β. With $c = c(\omega)$ the wave speed of the surface Love waves, $c < \beta$, and the surface waves take the form:

$$W_\infty = C_\infty e^{ik(x - \gamma y)} = C_\infty e^{ikx - k\bar{\gamma} y} \tag{3}$$

where

$$\bar{\gamma} = \frac{\left(k^2 - k_\beta^2\right)^{1/2}}{k} = \left(1 - \left(k_\beta/k\right)^2\right)^{1/2} = \left(1 - \left(c/\beta\right)^2\right)^{1/2} \tag{4}$$

$\bar{\gamma}$ is the complement of γ and is real, so that the term $e^{ikx - k\bar{\gamma} y}$ in W_∞ correspond to a surface wave term whose amplitude is exponentially decaying with depth (in y) below the surface. With β_l the shear wave speed in the l-th layer of the medium, and $c = c(\omega)$, the Love wave speed and also the (horizontal) phase velocity of the waves in all layers of the elastic media above the half space (Fig.1), we can have $c \geq \beta_l$ or $c < \beta_l$. If $c \geq \beta_l$, the term $\gamma_l = \gamma_l(\beta_l)$ in Equation (2) is real and both waves W_l^+ and W_l^- in Equation (1) will correspond to harmonic plane waves. If, however, $c < \beta_l$ then, as from Equation (2):

$$\gamma_l = \left(\left(c/\beta_l\right)^2 - 1\right)^{1/2} \text{ is imaginary and } \bar{\gamma}_l = \left(1 - \left(c/\beta_l\right)^2\right)^{1/2} \text{ is real} \tag{5}$$

so that, from Equation (1):

$W_l^-,\ W_l^+$:

$$W_l^- = C_l^- e^{ik\left(x-\gamma_l y\right)} = C_l^- e^{ikx} e^{+k\bar{\gamma}_l y}$$
$$W_l^+ = C_l^+ e^{ik\left(x+\gamma_l y\right)} = C_l^+ e^{ikx} e^{-k\bar{\gamma}_l y} \qquad (6)$$

meaning that the waves W_l^+ will be exponentially decaying , while the waves W_l^- will be exponentially growing in the l-th layer.

The coefficients $C_l^-,\ C_l^+$, respectively of the waves, $W_l^-,\ W_l^+$, in each of the layers l, for $l = 1$ to **n**, are all related by the stress and displacement boundary conditions. In the topmost layer, the zero-stress boundary condition at the half-space surface,

$$\tau_{yz}\Big|_{y=0} = \mu_1 \frac{\partial W_1}{\partial y}\Big|_{y=0} = 0 \qquad (7)$$

for waves $W_1 = W_1^+ + W_1^-$ at the top layer $l = 1$. This gives

$$\mu_1 \frac{\partial W_1}{\partial y}\Big|_{y=0} = \mu_1 \left(\frac{\partial W_1^+}{\partial y} + \frac{\partial W_1^-}{\partial y} \right)\Big|_{y=0} = 0, \qquad \text{or}$$
$$\mu_1 \left(C_1^+ e^{ik\left(x+\gamma_1 y\right)} - C_1^- e^{ik\left(x-\gamma_1 y\right)} \right)\Big|_{y=0} = 0, \quad \text{for all } x, \qquad (8)$$

so that $C_1^+ - C_1^- = 0$ or $C_1^+ = C_1^-$

Recall from above that we have shown that at a given site on the half-space surface, one can use the **"SYNACC *algorithm*"** to define the complex Fourier components of acceleration of each mode *m* of surface Love (and Rayleigh) waves at each frequency ω within the n-th frequency band $\left[\omega_n - \delta\omega_n, \omega_n + \delta\omega_n\right]$ of the whole spectrum. We'll take the site to be at the origin $O\left((x, y) = (0., 0.)\right)$ in Figure 1 above. Since the Fourier Transform of displacement $D(\omega)$ and acceleration $A(\omega)$ are related at frequency ω by

$$A(\omega) = -\omega^2 D(\omega) \qquad (9)$$

So the waves for acceleration and displacement at frequency ω are related the same way. Let $C_0 = C_{0,mn} = {-A_{nm}(\omega)}/{\omega^2}$ be such complex Fourier components of displacement of

the ***m**-th* mode of surface Love waves at frequency ω within the ***n***-th frequency band $\left[\omega_n - \delta\omega_n, \omega_n + \delta\omega_n\right]$ at the site ***O(0.,0.)*** in the top layer $(l = 1)$. Then

$$C_0 = W_1\big|_{(x,y)=(0,0)} = W_1^+ + W_1^-\big|_{(x,y)=(0,0)} = \left(C_1^+ e^{ik\left(x+\gamma_1 y\right)} + C_1^- e^{ik\left(x-\gamma_1 y\right)}\right)\Big|_{(x,y)=(0,0)} \qquad (10)$$

or $\quad C_0 = C_1^+ + C_1^-$

Equation (8) and Equation (10) together give $C_1^+ = C_1^- = C_0/2$, or the waves in the 1st layer be given by:

$$\begin{aligned} W_1 = W_1(x,y) &= W_1^+ + W_1^- = C_0/2\left(e^{ik\left(x+\gamma_1 y\right)} + e^{ik\left(x-\gamma_1 y\right)}\right) \\ &= C_0 e^{ikx}\cos\gamma_1 y \end{aligned} \qquad (11)$$

Recall that $C_0 = C_{0,mn}$ is the complex Fourier components of displacement of the *m-th* mode of surface Love waves at frequency ω within the *n*-th frequency band $\left[\omega_n - \delta\omega_n, \omega_n + \delta\omega_n\right]$ at the site ***O*(0.,0.)** in the top layer $(l = 1)$.

In summary, this means that once the complex Fourier coefficient at a given frequency of one mode of surface Love waves is given at one point of a site at the half-space surface, the complex Fourier coefficient of the same mode of waves at any point on and below the surface, in the top layer, is known.

The next step is to extend this to evaluate the complex Fourier coefficients at a given frequency of one mode of surface Love waves at any point of any elastic layers below the surface. Starting from $l = 1$, we will show by induction that if the waves at the l^{th} layer are known, then the waves at the $(l+1)^{th}$ layer can also be known, including the bottom semi-infinite layer,

Start with the l^{th} layer, where the waves are given by:

$W_l^-,\ W_l^+$ **:**

$$\begin{aligned} W_l^- &= C_l^- e^{ik\left(x-\gamma_l y\right)} = C_l^- e^{-ik\gamma_l y} e^{ikx} \\ W_l^+ &= C_l^+ e^{ik\left(x+\gamma_l y\right)} = C_l^+ e^{+ik\gamma_l y} e^{ikx} \end{aligned}$$

Equation (6) above

with known (complex) coefficients $C_l^-,\ C_l^+$. The waves in the $(l+1)^{th}$ layer below, of the form:

$W_{l+1}^-,\ W_{l+1}^+$:

$$\begin{aligned} W_{l+1}^- &= C_{l+1}^- e^{ik\left(x-\gamma_{l+1}y\right)} = C_l^- e^{-ik\gamma_{l+1}y} e^{ikx} \\ W_{l+1}^+ &= C_{l+1}^+ e^{ik\left(x+\gamma_{l+1}y\right)} = C_l^+ e^{+ik\gamma_{l+1}y} e^{ikx} \end{aligned} \qquad (12)$$

with coefficients , $C_{l+1}^-,\ C_{l+1}^+$ can next be evaluated. At the common interface between the l^{th} layer and $(l+1)^{th}$ layer, where $y = H_l$, the continuity of displacement and stress at the interface between the 2 layers gives:

At $y = H_l$:

$$\begin{aligned} W_l^+ + W_l^- &= W_{l+1}^+ + W_{l+1}^- \\ \mu_l \frac{\partial}{\partial y}\left(W_l^+ + W_l^-\right) &= \mu_{l+1} \frac{\partial}{\partial y}\left(W_{l+1}^+ + W_{l+1}^-\right) \end{aligned} \qquad (13)$$

or

$$\begin{bmatrix} 1 & 1 \\ \mu_l\gamma_l & -\mu_l\gamma_l \end{bmatrix} \begin{pmatrix} C_l^+ e^{+ik\gamma_l H_l} \\ C_l^- e^{-ik\gamma_l H_l} \end{pmatrix} = \begin{bmatrix} 1 & 1 \\ \mu_{l+1}\gamma_{l+1} & -\mu_{l+1}\gamma_{l+1} \end{bmatrix} \begin{pmatrix} C_{l+1}^+ e^{+ik\gamma_{l+1} H_l} \\ C_{l+1}^- e^{-ik\gamma_{l+1} H_l} \end{pmatrix} \qquad (14)$$

giving $C_{l+1}^-,\ C_{l+1}^+$ in terms of $C_l^-,\ C_l^+$.

Starting from the top layer, with the (complex) coefficients of the waves $C_1^+ = C_1^- = C_0/2$, expressed in terms of $C_0 = C_{0,mn}$, that of the waves at the origin, Equation (14) gives an iterative step to compute the wave coefficients $C_l^-,\ C_l^+$ of each elastic layer *l*, for $l = 1, \ldots, n$. At the bottom of the last n^{th} layer, at $y = H_n$, the interface is now between it and the semi-infinite medium below, which has a mode of surface Love waves given by:

$$W_\infty = C_\infty e^{ik\left(x-\gamma y\right)} = C_\infty e^{ikx - k\bar{\gamma} y} \qquad \text{Equation (3) above}$$

and the continuity equations now take the form, with μ the shear modulus of the semi-infinite half-space below:

At $y = H_n$:

$$\begin{aligned} W_n^+ + W_n^- &= W_\infty \\ \mu_n \frac{\partial}{\partial y}\left(W_n^+ + W_n^-\right) &= \mu \frac{\partial W_\infty}{\partial y} \end{aligned} \qquad (13)$$

or

$$\begin{bmatrix} 1 & 1 \\ i\mu_n\gamma_n & -i\mu_n\gamma_n \end{bmatrix} \begin{pmatrix} C_n^+ e^{+ik\gamma_n H_n} \\ C_n^- e^{-ik\gamma_n H_n} \end{pmatrix} = \begin{pmatrix} 1 \\ -\mu\,\bar{\gamma} \end{pmatrix} C_\infty e^{-k\bar{\gamma} H_n} \qquad (14)$$

The solution $c = c(\omega)$ of that mode of Love surface waves will guarantee that both equations are satisfied by the surface wave coefficients in the semi-infinite half-space. This completes the derivation.

In summary, this means that once the complex Fourier coefficient at a given frequency of one mode of surface Love waves is given at one point of a site at the half-space surface, the complex Fourier coefficient of the same mode of surface waves at any point on and below the surface, at any of the elastic layers down below, is also known.

Part B: Synthetic Translational Motions of Rayleigh Waves In or Below a Layered Media

Given $c = c(\omega)$, the wave speed of a mode of Rayleigh waves in the half-space with n elastic layered media on top. c is also the (horizontal) phase velocity of both the P- and SV-waves in each layer of the elastic media above the half space (Fig. 1)

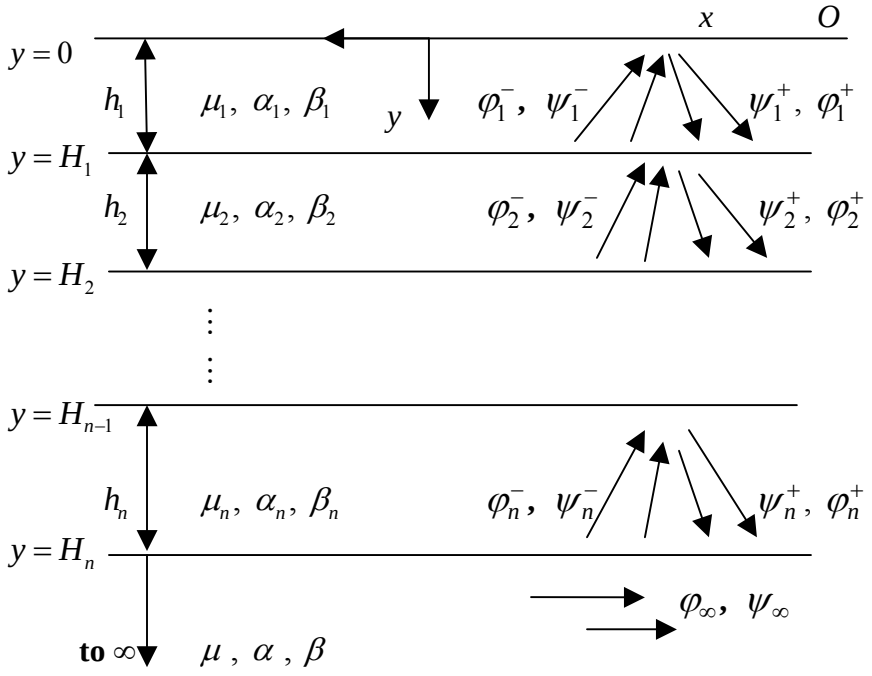

Figure 1 n-layered half-space with Rayleigh waves

For each layer l, with $l = 1, \ldots, n$, the P- and SV-Waves in the layer respectively take the form:

$$\varphi_l^- : \quad \begin{aligned} \varphi_l^- &= A_l^- e^{ik\left(x-\gamma_{\alpha,l}y\right)} \\ \varphi_l^+ &= A_l^+ e^{ik\left(x+\gamma_{\alpha,l}y\right)} \\ \psi_l^- &= B_l^- e^{ik\left(x-\gamma_{\beta,l}y\right)} \\ \psi_l^+ &= B_l^+ e^{ik\left(x+\gamma_{\beta,l}y\right)} \end{aligned} \qquad (1)$$

They are respectively the upward and downward propagating waves with $k = k(\omega) = \omega / c(\omega)$ being the horizontal wave number of the P- and SV-waves in *i-th* layer, at frequency ω and with phase velocity $c = c(\omega)$ The term e^{ikx}, which is also the same in all layers, is the horizontal component of the waves, which together with the time harmonic term $e^{i\omega t}$, correspond to waves propagating in the *–ve x* direction, which is to the right. The term $e^{\mp ik\gamma_{\alpha,l}y}$, for the P-waves and $e^{\mp ik\gamma_{\beta,l}y}$ for the SV-waves are respectively the vertical arguments for the same waves. The ones with the ***–ve*** *exponent* terms are propagating upwards (***–ve*** *y*) and those with the ***+ve*** *exponent* terms are propagating downwards (***+ve*** *y*). Here $\gamma_{\alpha,l} = \gamma_{\alpha,l}(\alpha_l)$ and $\gamma_{\beta,l} = \gamma_{\beta,l}(\alpha_l)$ are respectively given by

$$\begin{aligned} \gamma_{\alpha,l} &= \frac{\left(k_{\alpha_l}^2 - k^2\right)^{1/2}}{k} = \left(\left(k_{\alpha_l}/k\right)^2 - 1\right)^{1/2} = \left(\left(c/\alpha_l\right)^2 - 1\right)^{1/2} \\ \gamma_{\beta,l} &= \frac{\left(k_{\beta_l}^2 - k^2\right)^{1/2}}{k} = \left(\left(k_{\beta_l}/k\right)^2 - 1\right)^{1/2} = \left(\left(c/\beta_l\right)^2 - 1\right)^{1/2} \end{aligned} \qquad (2)$$

so that $k\gamma_{\alpha,l}$ and $k\gamma_{\beta,l}$ are the vertical wave numbers of respectively the ***P***- and ***SV***-waves in the l-th layer of the medium with longitudinal wave speed α_l and shear wave velocity β_l. In general, the wave speeds increase as one goes down into the deeper layers, so that $\beta_1 < \beta_2 < \ldots < \beta_n < \beta$, with the semi-infinite half-space layer at the bottom having the highest shear wave speed β. The same can be said about the

longitudinal wave speeds, so that $\alpha_1 < \alpha_2 < \ldots < \alpha_n < \alpha$, with α the longitudinal wave speed of the semi-infinite medium furthest below being the highest. With $c = c(\omega)$ the wave speed of the surface Rayleigh waves there, $c < \beta < \alpha$, and the surface waves take the form:

$$\begin{aligned} \varphi_\infty &= A_\infty e^{ik(x-\gamma_\alpha y)} = A_\infty e^{ikx-k\bar{\gamma}_\alpha y} \\ \psi_\infty &= B_\infty e^{ik(x-\gamma_\beta y)} = B_\infty e^{ikx-k\bar{\gamma}_\beta y} \end{aligned} \tag{3}$$

where

$$\begin{aligned} \bar{\gamma}_\alpha &= \frac{\left(k^2 - k_\alpha^2\right)^{1/2}}{k} = \left(1 - \left(k_\alpha / k\right)^2\right)^{1/2} = \left(1 - \left(c/\alpha\right)^2\right)^{1/2} \\ \bar{\gamma}_\beta &= \frac{\left(k^2 - k_\beta^2\right)^{1/2}}{k} = \left(1 - \left(k_\beta / k\right)^2\right)^{1/2} = \left(1 - \left(c/\beta\right)^2\right)^{1/2} \end{aligned} \tag{4}$$

$\bar{\gamma}_\alpha$, $\bar{\gamma}_\beta$ are respectively the complements of γ_α, γ_β and both are real, so that the terms $e^{-k\bar{\gamma}_\alpha y}$ in φ_∞ and $e^{-k\bar{\gamma}_\beta y}$ in ψ_∞ both correspond to surface wave terms with amplitudes that are exponentially decaying with depth into the half space.

With β_l the shear wave speed in the ***l-th*** layer of the medium, and $c = c(\omega)$, the Rayleigh wave speed and also the (horizontal) phase velocity of the waves in all layers of the elastic media above the half space (Figure.1), we can have $c \geq \beta_l$ or $c < \beta_l$.

If $c \geq \beta_l$, the term $\gamma_{\beta,l} = \gamma_{\beta,l}(\beta_l)$ in Equation (2) is real and both the ***SV***- waves W_l^+ and W_l^- in Equation (1) will correspond to harmonic plane waves. If, however, $c < \beta_l$ then, as from Equation (2):

$$\gamma_{\beta,l} = \left(\left(c/\beta_l\right)^2 - 1\right)^{1/2} \text{ is imaginary and } \bar{\gamma}_{\beta,l} = \left(1 - \left(c/\beta_l\right)^2\right)^{1/2} \text{ is real} \tag{5}$$

so that, from Equation (1):

$\psi_l^-,\ \psi_l^+$:

$$\psi_l^- = B_l^- e^{ik\left(x-\gamma_{\beta,l}y\right)} = B_l^- e^{ikx} e^{+k\bar{\gamma}_{\beta,l}y}$$
$$\psi_l^+ = B_l^+ e^{ik\left(x+\gamma_{l\beta,l}y\right)} = B_l^+ e^{ikx} e^{-k\bar{\gamma}_{\beta,l}y} \tag{6}$$

meaning that the waves ψ_l^+ will be exponentially decaying, while the waves ψ_l^- are exponentially growing in the ***l***-th layer.

The same observations can be made of the cases for $c \geq \alpha_l$ or $c < \alpha_l$, in regards to the ***P***-wave potentials $\varphi_l^-,\ \varphi_l^+$ in the ***l***-th layer.

The coefficients A_l^-, A_l^+, respectively of the ***P***-wave potentials, $\varphi_l^-,\ \varphi_l^+$, and $B_l^-,\ B_l^+$, respectively of the ***SV***-wave potentials, $\psi_l^-,\ \psi_l^+$, in each of the layers ***l***, for ***l*** = 1 to ***n***, are all related by the stress and displacement boundary conditions. In the topmost layer, the zero-stress boundary conditions at the half-space surface is

$$\sigma_y\big|_{y=0} = \tau_{yz}\big|_{y=0} \tag{7}$$

for P- and SV-wave potentials. Let $U_0,\ V_0$ respectively be the *horizontal* and *vertical* (complex) displacements at the origin, the reference point at the free surface. Then stress boundary conditions at the half-space surface ($y = 0$) and the displacement specification on the half-space surface at the origin **(0., 0.)** take the form:

$$\begin{bmatrix} 1 & 1 & \gamma_{\beta,1} & -\gamma_{\beta,1} \\ \gamma_{\alpha,1} & -\gamma_{\alpha,1} & -1 & -1 \\ 1-\gamma_{\beta,1}^2 & 1-\gamma_{\beta,1}^2 & -2\gamma_{\beta,1} & 2\gamma_{\beta,1} \\ 2\gamma_{\alpha,1} & -2\gamma_{\alpha,1} & 1-\gamma_{\beta,1}^2 & 1-\gamma_{\beta,1}^2 \end{bmatrix} \begin{pmatrix} A_1^+ \\ A_1^- \\ B_1^+ \\ B_1^- \end{pmatrix} = \frac{1}{ik} \begin{pmatrix} U_0 \\ V_0 \\ 0 \\ 0 \end{pmatrix} \tag{8}$$

Recall from above that we have shown that at a given site on the surface, one can use the **"SYNACC *algorithm***" to define the complex Fourier components of acceleration of each mode ***m*** of surface Rayleigh waves at each frequency ω within the ***n-th*** frequency band $\left[\omega_n - \delta\omega_n, \omega_n + \delta\omega_n\right]$ of the whole spectrum. We will take the site to be at the origin $O\big((x,y)=(0.,0.)\big)$ in Figure 1 above. Since the Fourier Transform of displacement $D(\omega)$ and acceleration $A(\omega)$ are related at frequency ω by

$$A(\omega) = -\omega^2 D(\omega) \tag{9}$$

so the waves for acceleration and displacement at frequency ω are related the same way. Let $U_0 = A_{0,mn}$, $V_0 = B_{0,mn}$, respectively be such complex Fourier (in-plane) horizontal and vertical components of displacement of the *m-th* mode of surface Rayleigh waves at frequency ω within the **n-th** frequency band $\left[\omega_n - \delta\omega_n, \omega_n + \delta\omega_n\right]$ at the site **O(0.,0.)** in the top layer $(l = 1)$.

From Equation (8), it is seen that, given the complex Fourier components of displacement, U_0, V_0, of the m-th mode of surface Rayleigh waves at frequency ω, at a site on the half-space surface, as estimated by the **"SYNACC *algorithm*"** described above, one can solve for the complex coefficients A_1^-, A_1^+ and B_1^-, B_1^+ respectively of the ***P***- and ***SV***-wave potentials associated with the waves in the 1^{st} media on top. With the waves in the top layer defined, it can be used to compute the displacement everywhere in the top layer.

In summary, this means that once the complex Fourier coefficient at a given frequency of any mode of surface Rayleigh waves is given at one point of a site at the half-space surface, the complex Fourier coefficient of the same mode of waves at any point on and below the surface, in the top layer, is known.

The next step is to extend this to evaluate the complex Fourier coefficients at a given frequency of each mode of surface Rayleigh waves at any point of all the elastic layers below the surface. Starting from $l = 1$, we will show by induction that if the waves at the l^{th} layer are known, then the waves at the $(l+1)^{th}$ layer can also be known, including the bottom, semi-infinite layer,

We start with the l^{th} layer, where the wave potentials are given by:

$\varphi_l^-,\ \varphi_l^+,\ \psi_l^-,\ \psi_l^+$:

$$\begin{aligned}\varphi_l^- &= A_l^- e^{ik\left(x-\gamma_{\alpha,l}y\right)}\\ \varphi_l^+ &= A_l^+ e^{ik\left(x+\gamma_{\alpha,l}y\right)}\\ \psi_l^- &= B_l^- e^{ik\left(x-\gamma_{\beta,l}y\right)}\\ \psi_l^+ &= B_l^+ e^{ik\left(x+\gamma_{\beta,l}y\right)}\end{aligned}$$

Equation (1) above

with known (complex) coefficients $A_l^-,\ A_l^+$ for the ***P***-wave and $B_l^-,\ B_l^+$ for the ***SV***-wave potentials . The waves in the $(l+1)^{th}$ layer below, of the form, with ***(l+1)*** replacing ***l*** everywhere in Equation (1):

$\varphi_{l+1}^-,\ \varphi_{l+1}^+,\ \psi_{l+1}^-,\ \psi_{l+1}^+$:

$$\begin{aligned}\varphi_{l+1}^- &= A_{l+1}^- e^{ik\left(x-\gamma_{\alpha,l+1}y\right)}\\ \varphi_{l+1}^+ &= A_{l+1}^+ e^{ik\left(x+\gamma_{\alpha,l+1}y\right)}\\ \psi_{l+1}^- &= B_{l+1}^- e^{ik\left(x-\gamma_{\beta,l+1}y\right)}\\ \psi_{l+1}^+ &= B_{l+1}^+ e^{ik\left(x+\gamma_{\beta,l+1}y\right)}\end{aligned} \qquad (10)$$

with coefficients $A_{l+1}^-,\ A_{l+1}^+$ for the ***P***-wave and $B_{l+1}^-,\ B_{l+1}^+$ for the ***SV***-wave potentials are next to be evaluated. At the common interface between the l^{th} layer and $(l+1)^{th}$ layer, where $y = H_l$, the continuity of (***x***- and ***y***- components) of displacements and (normal and shear) stresses at the interface between the 2 layers gives, at $y = H_l$ are

$$\begin{bmatrix}1 & 0 & 0 & 0\\ 0 & 1 & 0 & 0\\ 0 & 0 & \mu_{l+1} & 0\\ 0 & 0 & 0 & \mu_{l+1}\end{bmatrix}\begin{bmatrix}1 & 1 & \gamma_{\beta,l+1} & -\gamma_{\beta,l+1}\\ \gamma_{\alpha,l+1} & -\gamma_{\alpha,l+1} & -1 & -1\\ 1-\gamma_{\beta,l+1}^2 & 1-\gamma_{\beta,l+1}^2 & -2\gamma_{\beta,l+1} & 2\gamma_{\beta,l+1}\\ 2\gamma_{\alpha,l+1} & -2\gamma_{\alpha,l+1} & 1-\gamma_{\beta,l+1}^2 & 1-\gamma_{\beta,l+1}^2\end{bmatrix}\begin{pmatrix}A_{l+1}^+ e^{ik\gamma_{\alpha,l+1}H_l}\\ A_{l+1}^- e^{-ik\gamma_{\alpha,l+1}H_l}\\ B_{l+1}^+ e^{ik\gamma_{\beta,l+1}H_l}\\ B_{l+1}^- e^{-ik\gamma_{\beta,l+1}H_l}\end{pmatrix} =$$

$$\begin{bmatrix}1 & 0 & 0 & 0\\ 0 & 1 & 0 & 0\\ 0 & 0 & \mu_l & 0\\ 0 & 0 & 0 & \mu_l\end{bmatrix}\begin{bmatrix}1 & 1 & \gamma_{\beta,l} & -\gamma_{\beta,l}\\ \gamma_{\alpha,l} & -\gamma_{\alpha,l} & -1 & -1\\ 1-\gamma_{\beta,l}^2 & 1-\gamma_{\beta,l}^2 & -2\gamma_{\beta,l} & 2\gamma_{\beta,l}\\ 2\gamma_{\alpha,l} & -2\gamma_{\alpha,l} & 1-\gamma_{\beta,l}^2 & 1-\gamma_{\beta,l}^2\end{bmatrix}\begin{pmatrix}A_l^+ e^{ik\gamma_{\alpha,l}H_l}\\ A_l^- e^{-ik\gamma_{\alpha,l}H_l}\\ B_l^+ e^{ik\gamma_{\beta,l}H_l}\\ B_l^- e^{-ik\gamma_{\beta,l}H_l}\end{pmatrix} \qquad (11)$$

Equation (11) can be written in the form, at $y = H_l$:

$$\left[M_{l+1}(H_l)\right]\begin{pmatrix} A_{l+1}^{+} \\ A_{l+1}^{-} \\ B_{l+1}^{+} \\ B_{l+1}^{-} \end{pmatrix} = \left[M_{l}(H_l)\right]\begin{pmatrix} A_{l}^{+} \\ A_{l}^{-} \\ B_{l}^{+} \\ B_{l}^{-} \end{pmatrix} \quad \textbf{or} \quad \begin{pmatrix} A_{l+1}^{+} \\ A_{l+1}^{-} \\ B_{l+1}^{+} \\ B_{l+1}^{-} \end{pmatrix} = \left[N_{l}(H_l)\right]\begin{pmatrix} A_{l}^{+} \\ A_{l}^{-} \\ B_{l}^{+} \\ B_{l}^{-} \end{pmatrix} \qquad (12)$$

with $\left[N_{l}(H_l)\right] = \left[M_{l+1}(H_l)\right]^{-1}\left[M_{l}(H_l)\right]$, both $\left[M_{l}(H_l)\right] = \left[M_{l}(\mu_l, \gamma_{\alpha,l}, \gamma_{\beta,l}, H_l)\right]$ and $\left[M_{l}(H_l)\right] = \left[M_{l}(\mu_l, \gamma_{\alpha,l}, \gamma_{\beta,l}, H_l)\right]$ matrices defined from Equation (11).

Starting from the top layer, with the (complex) coefficients of the waves A_1^-, A_1^+ and B_1^-, B_1^+ expressed in terms of, $U_0 = U_{0,mn}$ and $V_0 = V_{0,mn}$ respectively the Fourier component of the waves in the horizontal and vertical directions at the origin, Equation (12) gives an iterative steps to compute the wave coefficients A_l^-, A_l^+ and B_l^-, B_l^+ of each elastic layer l, for $l = 1, \ldots, n$. At the bottom of the last n^{th} layer, at $y = H_n$, the interface is now between it and the semi-infinite medium below, which has a mode of surface Rayleigh waves given by:

$$\begin{aligned} \varphi_\infty &= A_\infty e^{ik(x-\gamma_\alpha y)} = A_\infty e^{ikx - k\bar{\gamma}_\alpha y} \\ \psi_\infty &= B_\infty e^{ik(x-\gamma_\beta y)} = B_\infty e^{ikx - k\bar{\gamma}_\beta y} \end{aligned} \qquad \text{Equation (3) above}$$

The continuity of displacements and stress between the waves at $y = H_n$ gives

$$\begin{bmatrix} 1 & 0 & 0 & 0 \\ 0 & 1 & 0 & 0 \\ 0 & 0 & \mu & 0 \\ 0 & 0 & 0 & \mu \end{bmatrix}\begin{bmatrix} 1 & i\bar{\gamma}_\beta \\ \bar{\gamma}_\alpha & -1 \\ 1+\bar{\gamma}_\beta^2 & -i2\bar{\gamma}_\beta \\ 2i\bar{\gamma}_\alpha & 1+\bar{\gamma}_\beta^2 \end{bmatrix}\begin{pmatrix} A_\infty e^{-k\bar{\gamma}_\alpha H_n} \\ B_\infty e^{-k\bar{\gamma}_\beta H_n} \end{pmatrix} = \left[M_{n}(H_n)\right]\begin{pmatrix} A_n^{+} \\ A_n^{-} \\ B_n^{+} \\ B_n^{-} \end{pmatrix} \qquad (13)$$

where, from Equation (11) and Equation (12), the matrix $\left[M_{n}(H_n)\right]$ in the right-hand side can be written in full as:

$$\left[M_{n}(H_n)\right] = \qquad (14)$$

$$\begin{bmatrix} 1 & 0 & 0 & 0 \\ 0 & 1 & 0 & 0 \\ 0 & 0 & \mu_n & 0 \\ 0 & 0 & 0 & \mu_n \end{bmatrix}\begin{bmatrix} 1 & 1 & \gamma_{\beta,n} & -\gamma_{\beta,n} \\ \gamma_{\alpha,n} & -\gamma_{\alpha,n} & -1 & -1 \\ 1-\gamma_{\beta,n}^2 & 1-\gamma_{\beta,n}^2 & -2\gamma_{\beta,n} & 2\gamma_{\beta,n} \\ 2\gamma_{\alpha,n} & -2\gamma_{\alpha,n} & 1-\gamma_{\beta,n}^2 & 1-\gamma_{\beta,n}^2 \end{bmatrix}\begin{bmatrix} e^{ik\gamma_{\alpha,n} H_n} & 0 & 0 & 0 \\ 0 & e^{-ik\gamma_{\alpha,n} H_n} & 0 & 0 \\ 0 & 0 & e^{ik\gamma_{\beta,n} H_n} & 0 \\ 0 & 0 & 0 & e^{-ik\gamma_{\beta,n} H_n} \end{bmatrix}$$

The solution $c = c(\omega)$ for that mode of Rayleigh surface waves will guarantee that Equation (13) is satisfied by the surface wave coefficients in the semi-infinite half-space. This completes the derivation.

In summary, this means that once the complex Fourier coefficient at a given frequency of one mode of surface Rayleigh waves is given at one point of a site at the half-space surface, the complex Fourier coefficient of the same mode of surface waves at any point on and below the surface, at any of the elastic layers down below, is also known.

APPENDIX R2

(Reporting Date 12 September 2012)

REPORT No. II

Contract No.: 87055-11-0562
RSP Project ID (R525.1)

REPORTING DATE – 12 September 2012

PROJECT TITLE: Interfacing Seismological Description of Strong Ground Motion with Engineering Analysis of Soil Structure Interaction for Nuclear Power Plants

REPORT SUBMITTED BY: Structural and Earthquake Engineering Consultants (SEEC) Inc.
855 Arcadia Ave. #E, Arcadia, CA 91007 USA
Contact name: M. D. Trifunac
Phone: (626) 447-9382
Email: trifunac@usc.edu, misha.trifunac@gmail.com

to

Canadian Nuclear Safety Commission

ATTENTION: Nanci Laroche, Nebojsa Orbovic
280 Slater St., Ottawa, Ontario, Canada, K1P 5S9
E-mail: research-recherche@cnsc-ccsn.gc.ca
Nebojsa.Orbovic@cnsc-ccsn.gc.ca

Synthetic Translational Motions of Surface and Body Waves On or Below an Elastic Layered Half-Space

Abstract

This, second report, Report #2, is a continuation of the Report #1 (submitted 21 May 2012). In Report #1 we presented the theory and verification examples of computing synthetic strong earthquake ground motion for an array of points on the surface of the layered half space. This Report #2 presents, theory and varification examples of how to extend the synthesizing of strong ground motion along a vertical array of points, into the depth of the layered half space. Together Reports #1 and #2 constitute the complete methodology for computing translational components of strong ground motion at any point on the surface or at arbitrary depth in the layered half space. With these tools it is now possible to calculate translational components of strong motion as input into a finite element or finite difference numerical "box", which can be used in time computations of earthquake response of complex linear and nonlinear soil structure interaction problems. In the Report #1 we showed how the synthesized motions can be verified by comparison of the Fourier amplitude spectra of synthesized motions with the empirical scaling equations for the Fourier spectra corresponding to the same earthquake and site conditions. In this Report #2 the verification has been performed by detailed analysis of the nature of synthesized motions at depth, by verifying that the motions satisfy all known seismological properties and principles of body and surface wave propagation in layered half space. By examining the properties of the plots of this motion within the layered half space, as will be seen from the body of this report, we find that the synthesized motions meet all known properties of strong motion, and constitute realistic representation of strong motion in the set of parallel layers overlying the half space.

I. Synthetic Translational Motions of Surface Waves of a Layered Media at Points on the Half-Space Surface – Review

Observational studies of strong ground motion in the 1970's showed that a typical strong motion record consists of near-field, intermediate-field, body and surface waves contributing different amounts to the total result, depending on the earthquake source mechanism and on the wave path (Trifunac, 1971a, 1971b; Trifunac, 1972a, 1972b; Trifunac, 1973). Empirical studies of spectral characteristics (Trifunac, 1976, 1979a, 1979b, 1993, 1994, 1995a, 1995b; Trifunac and Anderson, 1977; Trifunac and Lee, 1978, 1985) and frequency-dependent duration (Trifunac and Westermo, 1976a, 1976b; Trifunac and Novikova, 1994, 1995) have further shown the nature of the dependence of strong motion on the geologic environment of the recording station. Consequently, realistic artificial accelerograms must have nonstationary frequency, amplitude and duration characteristics that agree with the trends present in the recorded accelerograms.

In choosing a suitable accelerogram for a particular analysis, many factors must be taken into account, for example, the distance between the source and the site, the size of the earthquake, and the geology surrounding the site. The recorded accelerograms cannot be modified in a simple way to satisfy the engineering design requirements at all sites (Lee and Trifunac, 1989), and thus, site-dependent artificial synthetic accelerograms are needed.

The synthetic translational components of acceleration are constructed to have a required Fourier amplitude spectrum, $\boldsymbol{FS(\omega)}$, and a given duration, $\boldsymbol{D(\omega)}$, at the site. A complete review of the method first proposed by **Trifunac (1971b)**, and later refined by **Wong and Trifunac (1978, 1979)**, for the generation of synthetic accelerograms, can also be found in the review paper by **Lee (2002).** In short, the following items are needed to construct synthetic motions:

1.1 Wave Dispersion Curves at a Site

1.2 Arrival Times of body waves and of each mode and frequency band of Waves

1.3 Contribution of the Modes at a Given Frequency Band

1.4 Determination of Relative Amplitudes and Phrases of all body and modes of Surface Waves.

1.5 The Total Accelerogram as a Superposition of time-histories of all the contributing waves.

The rest of this section is a brief summary of the above procedures, as summarized in Lee (2002). It will be referred to as the **"SYNACC *algorithm*"**. It applies to the translational (out 0f plane) horizontal component of surface *Love waves* and body *SH waves*, as well as to both the horizontal and vertical translational components of surface *Rayleigh waves* and body *P and SV waves*.

1.1 Wave Dispersion Curves at a Site

Figure I.1 Phase Velocities for

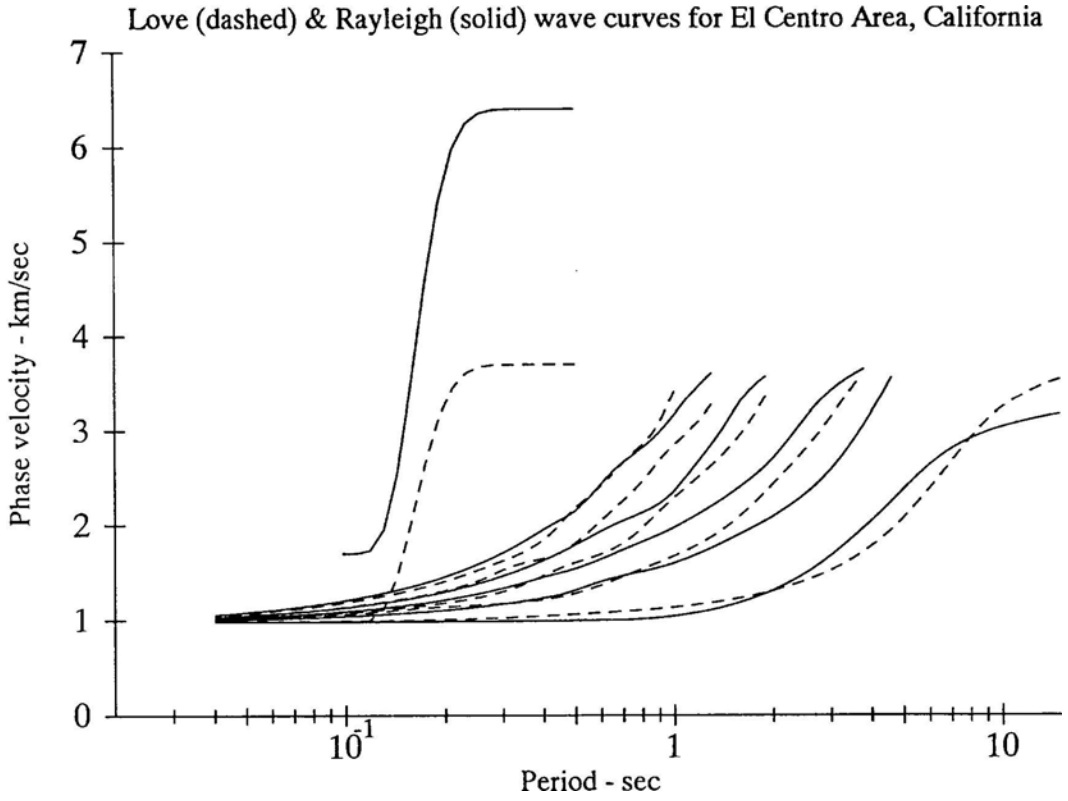

For a given site, a geological profile with equivalent layered medium must first be

selected. A model can have $N = n + 1$ layers. For each layer l with l = 1 to N the parameters h_l, α_l, β_l and ρ_l must be specified, where

h_l = layer thickness,

α_l = P −wave velocity,

β_l = S −wave velocity, and

ρ_l = mass density of l^{th} layer,

with the bottom $l = N$ medium of infinite thickness.

In such a medium, surface waves will travel in a dispersive manner, and this will depend on (1) the material properties of the medium, (2) the frequency of the wave motion, and on (3) the thicknesses of different layers.

Through calculation for the group and phase velocities of the Rayleigh and Love surface waves, the dispersion curves can be evaluated. The results will be given for each mode (for $m = 1, 2, \ldots, M$) of Rayleigh and Love surface waves separately, and will consist of both the phase and group velocities, $C_m(\omega_n)$ and $U_m(\omega_n)$, for a given set of selected frequencies, ω_n, $n = 1, 2, \ldots, N$. Figure **I.1** is an example of such dispersion velocities for a site at El Centro Area in Imperial Valley, California.

1.2 Arrival Times of each mode and frequency bands of Waves

Once the dispersion curves have been computed, the arrival time of the $m-th$ mode at frequency ω_n can be written as

$$t^*_{nm}(R) = R / U_m(\omega_n) \tag{1.1}$$

where R is the epicentral distance from the source to the site. For computational efficiency, Equation (1.1) will be assumed to hold not only at frequency, ω_n, but at all frequencies within the band, which is narrow enough for $U_m(\omega_n)$ to be assumed constant.

1.3 Contribution of the Modes at a Given Frequency Band, $\omega_n \pm \Delta\omega_n$

Within the frequency band $\omega_n \pm \Delta\omega_n$, the $m-th$ mode of surface waves is assumed to have a Fourier transform

$$A_{nm}(\omega) = \begin{cases} \frac{\pi}{2} \mathbf{A_{nm}} e^{-i\left[(\omega-\omega_n)t^*_{nm}+\phi_n\right]} & |\omega-\omega_n| \le \Delta\omega_n \\ 0 & \textbf{otherwise} \end{cases} \qquad (1.2)$$

$$A_{nm}(-\omega) = A^*_{nm}(\omega)$$

where ϕ_n is the phase. It is introduced to model the source randomness and other effects along the path. t^*_{nm} is the arrival time of the $m-th$ mode given in Equation (1.1). $\mathbf{A_{nm}}$ is the relative amplitude of the $m-th$ mode. The phase ϕ_n will be assumed to be a random number in the interval $[-\pi, \pi]$. The relative amplitude $\mathbf{A_{nm}}$ will be described in the next sub-section.

The inverse transform of equation (1.2) is given by

$$a_{nm}(t) = \frac{1}{2\pi} \int_{-\infty}^{\infty} A_{nm}(\omega) e^{i\omega t} d\omega \qquad (1,3a)$$

which can be calculated to be

$$a_{nm}(t) = \mathbf{A_{nm}} \frac{\sin \Delta\omega_n \left(t - t^*_{nm}\right)}{\left(t - t^*_{nm}\right)} \cos\left(\omega_n t + \phi_n\right) \qquad (1.3b)$$

This represents the contribution of the $m-th$ mode at the given frequency band. The total contribution of all the modes at the same frequency band is then given by

$$a_n(t) = \sum_{m=1}^{M} \delta_n a_{nm}(t) = \sum_{m=1}^{M} \delta_n \mathbf{A_{nm}} \frac{\sin \Delta\omega_n \left(t - t^*_{nm}\right)}{\left(t - t^*_{nm}\right)} \cos\left(\omega_n t + \phi_n\right) \qquad (1.3c)$$

where M is the total number of wave modes, and δ_n is the scaling factor used to determine the final amplitude of $FS(\omega_n)$, as described in the next sub-section.

1.4 Determination of $\mathbf{A_{nm}}$ and δ_n

The relative amplitudes of different modes of surface waves, $\mathbf{A_{nm}}$, depend on the earthquake source mechanism and the propagation path, and will be different in each case. Hence, it is useful to estimate these amplitudes empirically on the basis of previous acceleration recordings. The following empirical equations for $\mathbf{A_{nm}}$ have been proposed and used by Tribunac (1971b):

$$A^*_{nm}(\omega_n) = A_1(m)A_2(\omega_n) \tag{1.4a}$$

where
$$A_1(m) = \left| \exp\left[-(m-m_0)^2 \Big/ 2C_0^2 \right] + C_R X_m \right| \tag{1.4b}$$

and
$$A_2(\omega_n) = \left| B_0 \exp\left[-(\omega_n - \omega_p)^2 \Big/ 2\omega_B^2 \right] + B_R X_n \right| \tag{1.4c}$$

with X_m and X_n being random numbers in the interval $[-1., 1.]$, and the values of other constants are given in Table 1 below:

Table 1: Empirical Scaling Coefficients for Equations (1.4b) and (1.4c)

(Trifunac, 1971a, 1971b)

Mode	C_0	m_0	C_R	B_0	ω_P	ω_B	B_R
1	3	5	0.2	1.5	10	5	0.1
2	3	5	0.2	1.5	10	5	0.1
3	3	5	0.2	1.5	10	5	0.1
4	3	5	0.2	2.0	25	15	0.1
5	3	5	0.2	2.0	25	15	0.1
6	3	6	0.2	3.0	30	10	0.3
7	3	7	0.2	1.5	30	5	0.25

The scaling factor δ_n is next determined, by using the empirically determined Fourier amplitudes. The Fourier amplitude of $a_n(t)$ in Equation (1.3c) is given by

$$|A_n(\omega)| = \begin{cases} \left| \sum_{m=1}^{M} \frac{\pi}{2} \delta_n \mathbf{A_{nm}} e^{-i\left[(\omega-\omega_n)t^*_{nm}+\phi_n\right]} \right| & |\omega-\omega_n| \le \Delta\omega_n \\ \mathbf{0} & \mathbf{otherwise} \end{cases} \quad (1.5a)$$

for $\mathbf{0} \le \omega < \infty$, and $|A_{nm}(-\omega)| = |A^*_{nm}(\omega)| = |A_{nm}(\omega)|$.

It is seen that the amplitude $|A_n(\omega)|$ is defined only over the narrow band of width $2\Delta\omega_n$. Its average amplitude over this band is given by

$$\overline{|A_n(\omega)|} = \frac{1}{2\Delta\omega_n} \int_{\omega_n-\Delta\omega_n}^{\omega_n+\Delta\omega_n} |A_n(\omega)| \, d\omega \quad (1.5b)$$

which should agree with the empirically estimated Fourier amplitude $\widehat{FS}(\omega_n)$,

$$\overline{|A_n(\omega)|} = \widehat{FS}(\omega_n) \quad (1.5c)$$

Combining Equations (1.5a), (1.5b) and (1.5c), δ_n becomes

$$\delta_n = \frac{2\Delta\omega_n \widehat{FS}(\omega_n)}{\frac{\pi}{2} \int_{\omega_n-\Delta\omega_n}^{\omega_n+\Delta\omega_n} \left| \sum_{m=1}^{M} \frac{\pi}{2} \mathbf{A_{nm}} e^{-i\left[(\omega-\omega_n)t^*_{nm}+\phi_n\right]} \right| d\omega} \quad (1.5d)$$

The Fourier amplitude $\widehat{FS}(\omega_n)$ at frequency ω_n may be estimated from empirical scaling equations, by using the earthquake parameters specified at the site. These parameters may include a suitable combination of the following:

M = local magnitude M_L or surface wave magnitude M_S (Richter, 1958),

R = epicentral distance,

MMI = modified Mercalli intensity at the site,

s = geological site classification (**s** = 0, 1 or 2),

$\mathbf{S_L}$ = soil site classification (0, 1 or 2),

h = depth of sediments, and

v = component direction (**v** =0: horizontal; **v** =1: vertical).

1.5 The Total Accelerogram

The total accelerogram can be expressed as

$$a(t) = \sum_{n=1}^{N} a_n(t) \tag{1.6}$$

where N is the total number of frequency bands. From Equations (1.3c) and (1.6) this becomes

$$a(t) = \sum_{n=1}^{N}\left(\sum_{m=1}^{M} \delta_n \mathrm{A}_{\mathrm{nm}} \frac{\sin \Delta\omega_n \left(t - t^*_{nm}\right)}{\left(t - t^*_{nm}\right)} \cos\left(\omega_n t + \phi_n\right) \right) \tag{1.7}$$

One final property, the ***Duration or 'time length', $D(\omega)$***, of the accelerogram time history, $a(t)$, will be determined by using the empirical results on ***Strong-Motion Duration*** (Trifunac and Brady, 1975; Trifunac and Novikova, 1994) and the first and last arrival times of the waves. This completes the review and description of the **"SYNACC *algorithm*"**. Figure **I.2** is an example of one such synthetic translational accelerogram.

Figure I.2 Synthetic Translational Accelerogram Time Histories

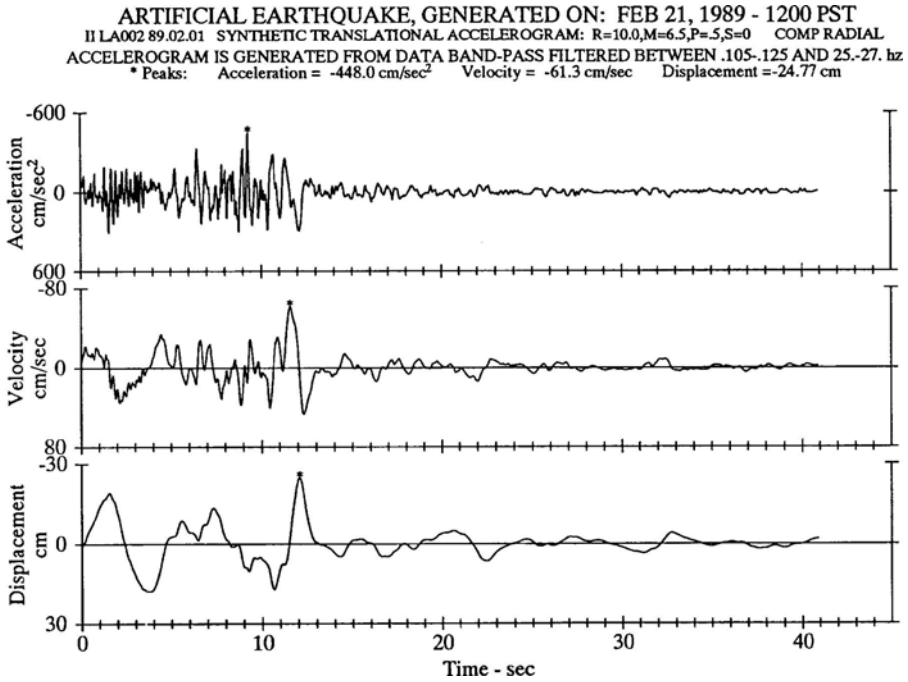

II. Synthetic Translational Motions of Love and Body SH Waves On and Below Surface of a Layered Media

Let $c = c(\omega)$ be the wave speed of a mode of Love waves in the half-space with n elastic layers over half space. c is also the (horizontal) phase velocity of the waves in each layer of the elastic media above the half space (Figure **II.1**)

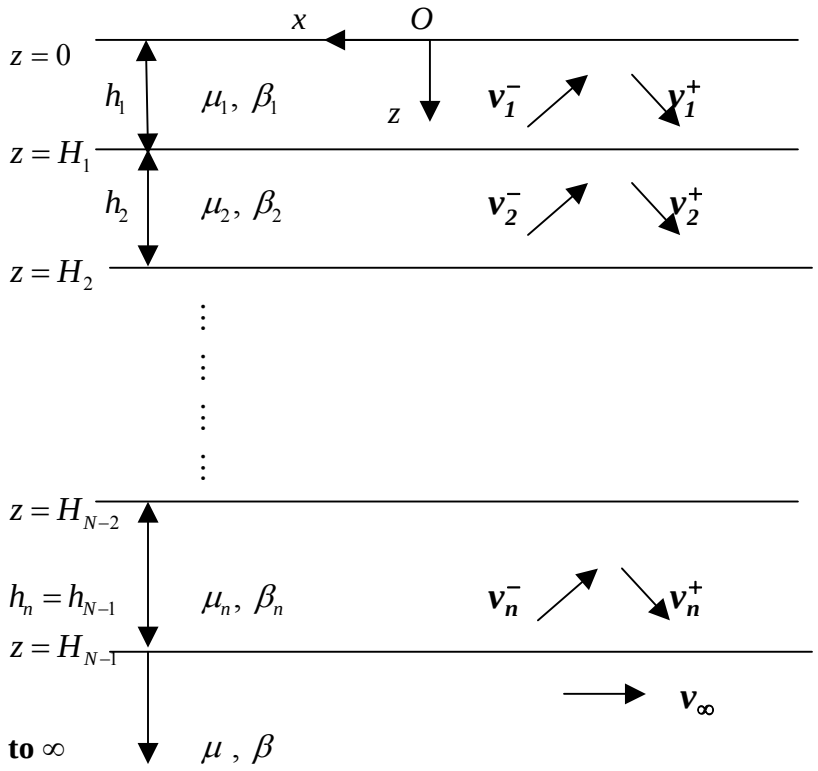

Figure II.1 n-layered half-space with Love waves

For each layer l, with $l = 1, \ldots, n$, the displacement of the Waves in the layer takes the form (in the anti-plane, y- direction):

$$v_1^-, v_1^+ : \qquad \begin{aligned} v_l^- &= C_l^- e^{ik(x-\gamma_l z)} \\ v_l^+ &= C_l^+ e^{ik(x+\gamma_l z)} \end{aligned} \tag{2.1}$$

There are the upward and downward propagating rays of Love waves present in the l^{th} layer. Here $k = k(\omega) = \omega / c(\omega)$ is the horizontal wave number of the waves at frequency ω and phase velocity $c = c(\omega)$. The term e^{ikx}, which is also same in each layer, is the horizontal component of the waves, which together with the time harmonic term $e^{i\omega t}$, corresponds to the waves propagating in the ***–ve*** *x* direction. The terms $e^{\mp ik\gamma_l y}$ are the vertical components of the waves with the ***negative*** term propagating upwards (***–ve*** *y*) and the ***positive*** term propagating downwards (*y*). Here $\gamma_l = \gamma_l(\beta_l)$ is given by

$$\gamma_l = \frac{\left(k_{\beta_l}^2 - k^2\right)^{1/2}}{k} = \left(\left(k_{\beta_l}/k\right)^2 - 1\right)^{1/2} = \left(\left(c/\beta_l\right)^2 - 1\right)^{1/2} \tag{2.2}$$

so that $k\gamma_l$ is the vertical wave number of the waves in the l^{th} layer of the medium with shear wave velocity β_l. In general, the wave velocities increase as one moves down through the layers, so that $\beta_1 < \beta_2 < \ldots < \beta_n < \beta$, with the semi-infinite half-space layer at the bottom having the highest shear wave speed β. With $c = c(\omega)$ the wave speed of the surface Love waves there, $c < \beta$, and the surface waves take the form:

$$v_\infty = C_\infty e^{ik(x - \gamma z)} = C_\infty e^{ikx - k\bar{\gamma} z} \tag{2.3}$$

where $$\bar{\gamma} = \frac{\left(k^2 - k_\beta^2\right)^{1/2}}{k} = \left(1 - \left(k_\beta/k\right)^2\right)^{1/2} = \left(1 - \left(c/\beta\right)^2\right)^{1/2} \tag{2.4}$$

$\bar{\gamma}$ is the complement of γ and is real, so that the term $e^{ikx - k\bar{\gamma} y}$ in W_∞ corresponds to a surface wave term whose amplitude is exponentially decaying with depth (in ***y***) below the surface. With β_l the shear wave speed in the l^{th} layer of the medium, and $c = c(\omega)$, the Love wave speed and also the (horizontal) phase velocity of the waves in each layer of the elastic media above the half space (Fig.1), we can have $c \geq \beta_l$ or $c < \beta_l$. If $c \geq \beta_l$, the term $\gamma_l = \gamma_l(\beta_l)$ in Equation (2.2) is real and both waves v_l^+ and v_l^- in Equation (1) will correspond to harmonic plane waves. If, however, $c < \beta_l$ then, as from Equation (2.2):

$$\gamma_l = \left(\left(c/\beta_l \right)^2 - 1 \right)^{1/2} \text{ is imaginary and } \bar{\gamma}_l = \left(1 - \left(c/\beta_l \right)^2 \right)^{1/2} \text{ is real} \tag{2.5}$$

so that, from Equation (2.1)

$$\begin{aligned} v_l^- &= C_l^- e^{ik\left(x - \gamma_l z\right)} = C_l^- e^{ikx} e^{+k\bar{\gamma}_l z} \\ v_l^+ &= C_l^+ e^{ik\left(x + \gamma_l z\right)} = C_l^+ e^{ikx} e^{-k\bar{\gamma}_l z} \end{aligned} \tag{2.6}$$

$v_l^-,\ v_l^+$:

This means that the waves v_l^+ will be exponentially decaying, while the waves v_l^- are exponentially growing in the l^{th} layer.

The coefficients $C_l^-,\ C_l^+$, respectively of the waves, $w_l^-,\ w_l^+$, in each of the layers l, for $l = 1$ to **n**, are all related by the stress and displacement boundary conditions. In the topmost layer, the zero-stress boundary condition at the half-space surface is

$$\tau_{zy}\Big|_{z=0} = \mu_1 \frac{\partial v_1}{\partial z}\Big|_{z=0} = 0 \tag{2.7}$$

for waves $v_1 = v_1^+ + v_1^-$ at the top layer $l = 1$. This gives

$$\begin{aligned} &\mu_1 \frac{\partial v_1}{\partial z}\Big|_{z=0} = \mu_1 \left(\frac{\partial v_1^+}{\partial z} + \frac{\partial v_1^-}{\partial z} \right)\Big|_{z=0} = 0, \qquad \text{or} \\ &\mu_1 \left(C_1^+ e^{ik\left(x + \gamma_1 z\right)} - C_1^- e^{ik\left(x - \gamma_1 z\right)} \right)\Big|_{z=0} = 0, \quad \text{for all } x, \end{aligned} \tag{2.8}$$

so that $C_1^+ - C_1^- = 0$ or $C_1^+ = C_1^-$

Recall from above that we have stated that at a given site on the half-space surface, one can use the **"SYNACC *algorithm*"** to define the complex Fourier components of acceleration of each mode *m* of surface Love (and Rayleigh) waves at each frequency ω within the n-th frequency band $\left[\omega_n - \delta\omega_n, \omega_n + \delta\omega_n\right]$ of the whole spectrum. We will take the site to be at the origin O $\left((x, y) = (0., 0.)\right)$ in Figure **II.1** above. Since the Fourier Transforms of displacement $D(\omega)$ and acceleration $A(\omega)$ are related at frequency ω by

$$A(\omega) = -\omega^2 D(\omega) \tag{2.9}$$

the waves for acceleration and displacement at frequency ω are related the same way. Let $C_0 = C_{0,mn}(\omega) = -A_{nm}(\omega)/\omega^2$ be such complex Fourier components of displacement of the m^{th} mode of surface Love waves at frequency ω within the n^{th} frequency band $[\omega_n - \delta\omega_n, \omega_n + \delta\omega_n]$ at the site **O(0.,0.)** in the top layer $(l = 1)$. Then

$$C_0 = v_1|_{(x,z)=(0,0)} = v_1^+ + v_1^-|_{(x,z)=(0,0)} = \left(C_1^+ e^{ik(x+\gamma_1 z)} + C_1^- e^{ik(x-\gamma_1 z)} \right)\Big|_{(x,z)=(0,0)} \qquad (2.10)$$

or $\quad C_0 = C_1^+ + C_1^-$

Equations (2.8) and (2.10) together give $C_1^+ = C_1^- = C_0/2$, or the waves in the 1st layer are given by:

$$\begin{aligned} v_1 = v_1(x,z) &= v_1^+ + v_1^- = C_0/2 \left(e^{ik(x+\gamma_1 z)} + e^{ik(x-\gamma_1 z)} \right) \\ &= C_0 e^{ikx} \cos \gamma_1 z \end{aligned} \qquad (2.11)$$

Recall that $C_0 = C_{0,mn}$ is the complex Fourier component of displacement of the *m-th* mode of surface Love waves at frequency ω within the *n*-th frequency band $[\omega_n - \delta\omega_n, \omega_n + \delta\omega_n]$ at the site **O(0.,0.)** in the top layer $(l = 1)$.

In summary, this means that once the complex Fourier coefficient at a given frequency of one mode of surface Love waves is given at one point of a site at the half-space surface, the complex Fourier coefficient of the same mode of waves at any point on and below the surface, in the top layer, is known.

The next step is to continue this to evaluate the complex Fourier coefficients at a given frequency of one mode of surface Love waves at any point of any elastic layer below the surface. Starting from $l = 1$, we will show by induction that if the waves at the l^{th} layer are known, then the waves at the $(l+1)^{th}$ layer can also be known, including the bottom semi-infinite layer,

Start with the l^{th} layer, where the waves are given by:

v_l^-, v_l^+ :

$$\begin{aligned} v_l^- &= C_l^- e^{ik(x-\gamma_l z)} = C_l^- e^{-ik\gamma_l z} e^{ikx} \\ v_l^+ &= C_l^+ e^{ik(x+\gamma_l z)} = C_l^+ e^{+ik\gamma_l z} e^{ikx} \end{aligned}$$

Equation (2.6) above

with known (complex) coefficients C_l^-, C_l^+. The waves in the $(l+1)^{th}$ layer below, of the form:

v_{l+1}^-, v_{l+1}^+ :

$$\begin{aligned} v_{l+1}^- &= C_{l+1}^- e^{ik\left(x-\gamma_{l+1}z\right)} = C_l^- e^{-ik\gamma_{l+1}z} e^{ikx} \\ v_{l+1}^+ &= C_{l+1}^+ e^{ik\left(x+\gamma_{l+1}z\right)} = C_l^+ e^{+ik\gamma_{l+1}z} e^{ikx} \end{aligned} \tag{2.12}$$

with coefficients , C_{l+1}^-, C_{l+1}^+ can next be evaluated. At the common interface between the l^{th} layer and $(l+1)^{th}$ layer, where $z = H_l$, the continuity of displacement and stress at the interface between the 2 layers gives:

At the interface of the l^{th} & $(l+1)^{th}$ medium, $z = H_l$:

$$\begin{aligned} v_l^+ + v_l^- &= v_{l+1}^+ + v_{l+1}^- \\ \mu_l \frac{\partial}{\partial z}\left(v_l^+ + v_l^-\right) &= \mu_{l+1} \frac{\partial}{\partial z}\left(v_{l+1}^+ + v_{l+1}^-\right) \end{aligned} \tag{2.13}$$

or

$$\begin{bmatrix} 1 & 1 \\ \mu_l\gamma_l & -\mu_l\gamma_l \end{bmatrix} \begin{pmatrix} C_l^+ e^{+ik\gamma_l H_l} \\ C_l^- e^{-ik\gamma_l H_l} \end{pmatrix} = \begin{bmatrix} 1 & 1 \\ \mu_{l+1}\gamma_{l+1} & -\mu_{l+1}\gamma_{l+1} \end{bmatrix} \begin{pmatrix} C_{l+1}^+ e^{+ik\gamma_{l+1} H_l} \\ C_{l+1}^- e^{-ik\gamma_{l+1} H_l} \end{pmatrix} \tag{2.14}$$

giving C_{l+1}^-, C_{l+1}^+ in terms of C_l^-, C_l^+ .

Starting from the top layer, with the (complex) coefficients of the waves $C_1^+ = C_1^- = C_0/2$, expressed in terms of $C_0 = C_{0,mn}$, that of the waves at the origin, Equation (2.14) gives an iterative step to compute the wave coefficients C_l^-, C_l^+ of each elastic layer *l*, for $l = 1, \ldots, n$. At the bottom of the last $n^{th} = (N-1)^{th}$ layer, at $z = H_n = H_{N-1}$, the interface is now between it and the semi-infinite medium below, which has a mode of surface Love waves given by:

$$v_N = v_\infty = C_\infty e^{ik\left(x-\gamma z\right)} = C_\infty e^{ikx - k\bar{\gamma}z} \qquad \text{Equation (2.3) above}$$

and the continuity equations now take the form, with μ the shear modulus of the semi-infinite half-space below:

At $y = H_n = H_{N-1}$:

$$\begin{aligned} v_n^+ + v_n^- &= v_\infty \\ \mu_n \frac{\partial}{\partial z}\left(v_n^+ + v_n^-\right) &= \mu \frac{\partial v_\infty}{\partial z} \end{aligned} \tag{2.13}$$

or

$$\begin{bmatrix} 1 & 1 \\ i\mu_n\gamma_n & -i\mu_n\gamma_n \end{bmatrix} \begin{pmatrix} C_n^+ e^{+ik\gamma_n H_n} \\ C_n^- e^{-ik\gamma_n H_n} \end{pmatrix} = \begin{pmatrix} 1 \\ -\mu\,\bar{\gamma} \end{pmatrix} C_\infty e^{-k\bar{\gamma}H_n} \tag{2.14}$$

The solution $c = c(\omega)$ of that mode of Love surface waves will guarantee that both equations are satisfied by the surface wave coefficients in the semi-infinite half-space. This completes the derivation.

For the case of body SH waves incident from the semi-infinite medium at the bottom, we will consider the model in Figure II.2. It is the same N-layered media model as in Figure II.1, for the case of Love surface waves, but now the waves in all layers are body waves.

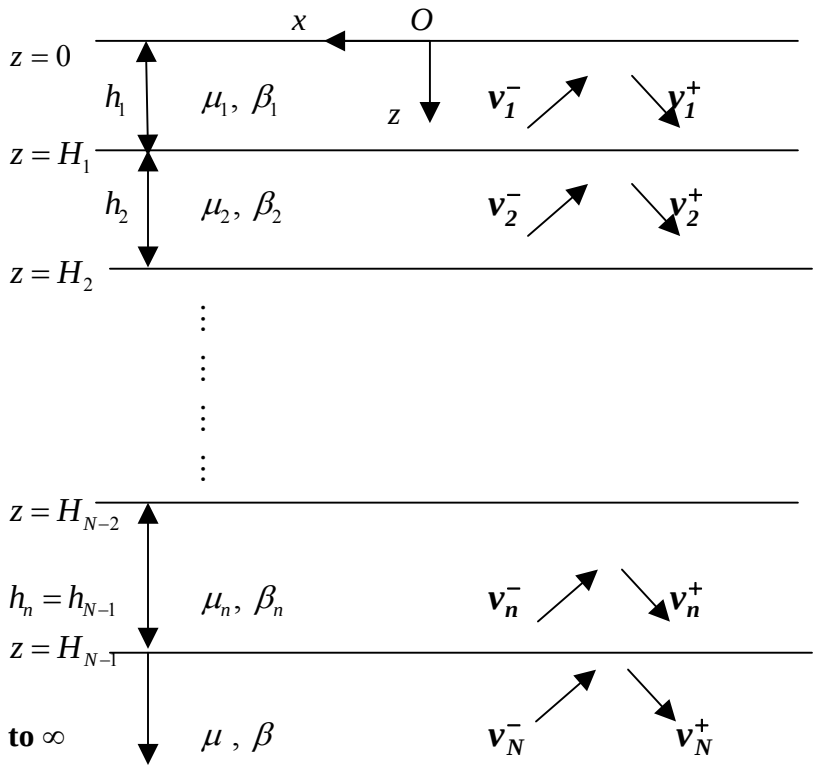

Figure II.2 n-layered half-space with incident body SH waves

The body waves in all layers have a common constant phase velocity c, now independent of frequency ω, and dependent only on the incident angle of the incident body SH waves. It is higher than $\beta_{max} = \beta_N$, the shear wave speed at the bottom semi-infinite N^{th} layer.

The wave $v_N = v_\infty$ at the bottom semi-infinite layer will also be replaced by the waves v_N^- and v_N^+, respectively the incident and reflected body SH waves:

$v_N^-,\ v_N^+$:

$$v_N^- = C_N^- e^{ik\left(x-\gamma_N z\right)} = C_N^- e^{-ik\gamma_N z} e^{ikx}$$
$$v_N^+ = C_N^+ e^{ik\left(x+\gamma_N z\right)} = C_N^+ e^{+ik\gamma_N z} e^{ikx} \qquad (2.15)$$

as in all the other layers $l = 1,\ 2,\ \ldots,\ N-1$, in Equation (2.6) above. At the interface with the layer above, instead of Equation (2.13), the continuity equations are:

At $y = H_n = H_{N-1}$:

$$v_n^+ + v_n^- = v_N$$
$$\mu_n \frac{\partial}{\partial z}\left(v_n^+ + v_n^-\right) = \mu \left(\frac{\partial v_N^+}{\partial z} + \frac{\partial v_N^-}{\partial z}\right) \qquad (2.16)$$

In summary, this means that once the complex Fourier coefficient at a given frequency of one mode of surface Love waves or body waves is given at one point of a site at the half-space surface, the complex Fourier coefficient of the same mode of surface or body waves at any point on and below the surface, at any of the elastic layers down below, is also known.

The above method will be referred in what follows as the reflection-transmission (R-T) coefficient matrix method for Love and body SH waves.

III. Synthetic Translational Motions of Rayleigh and Body P and SV Waves On or Below the surface of Layered Half Space

Let $c = c(\omega)$ be the phase velocity of a mode of Rayleigh waves in the half-space with N elastic layers. c is also the (horizontal) phase velocity of both the P- and SV-waves in each layer of the elastic media above the half space such that $c < \beta_{max} = \beta_N$, the shear wave speed at the bottom semi-infinite N^{th} layer (Fig.III.1).

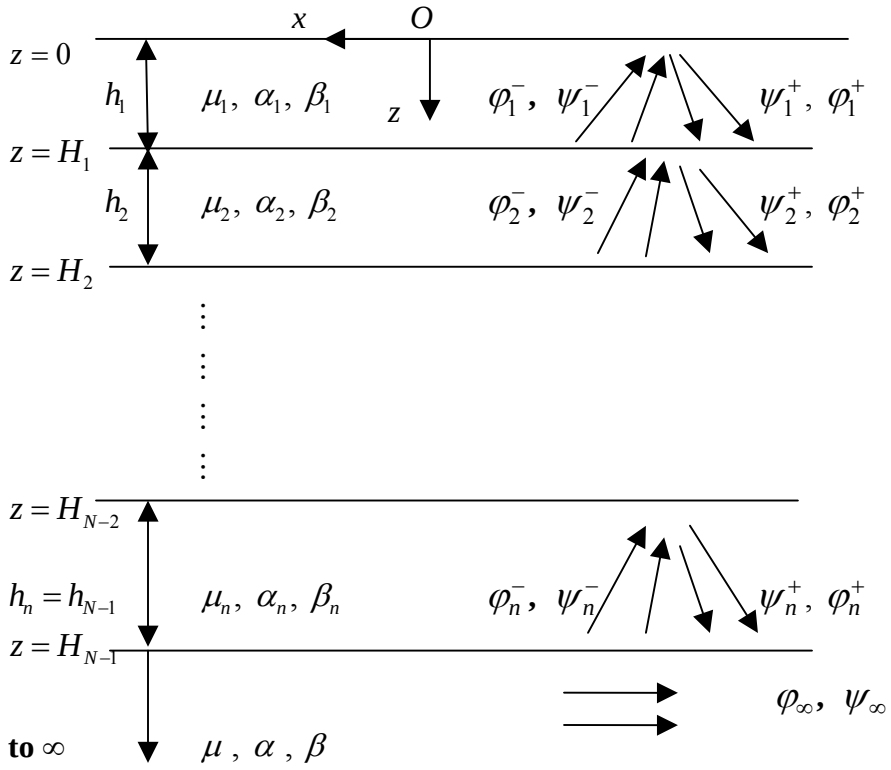

Figure III.1 n-layered half-space with Rayleigh waves

For each layer l, with $l = 1, \ldots, N$, the P- and SV-Waves in the layer respectively take the form:

$$\varphi_l^-,\ \varphi_l^+,\ \psi_l^-,\ \psi_l^+ :\qquad \begin{aligned} \varphi_l^- &= A_l^- e^{ik\left(x-a_l z\right)} \\ \varphi_l^+ &= A_l^+ e^{ik\left(x+a_l z\right)} \\ \psi_l^- &= B_l^- e^{ik\left(x-b_l z\right)} \\ \psi_l^+ &= B_l^+ e^{ik\left(x+b_l z\right)} \end{aligned} \tag{3.1}$$

They are respectively the upward and downward propagating waves present in the l^{th} layer. $k = k(\omega) = \omega / c(\omega)$ is the horizontal wave number of the P- and SV-waves at frequency ω and phase velocity $c = c(\omega)$. The term e^{ikx}, which is also the same in each layer, is the horizontal component of the waves, which together with the time harmonic term $e^{i\omega t}$, corresponds to waves propagating in the *–ve x* direction. The terms $e^{\mp ika_l z}$ for the P-waves and $e^{\mp ikb_l z}$ for the SV-waves are respectively the vertical components of the waves. The ones with the ***–ve*** *exponent* are propagating upwards (***–ve*** *y*) and those with the ***+ve*** *exponent* are propagating downwards (***+ve*** *y*). Here $a_l = a_l(\alpha_l, c)$ and $b_l = b_l(\beta_l, c)$ are respectively given by

$$\begin{aligned} a_l &= \frac{\left(k_{\alpha_l}^2 - k^2\right)^{1/2}}{k} = \left(\left(k_{\alpha_l} / k\right)^2 - 1\right)^{1/2} = \left(\left(c / \alpha_l\right)^2 - 1\right)^{1/2} \\ b_l &= \frac{\left(k_{\beta_l}^2 - k^2\right)^{1/2}}{k} = \left(\left(k_{\beta_l} / k\right)^2 - 1\right)^{1/2} = \left(\left(c / \beta_l\right)^2 - 1\right)^{1/2} \end{aligned} \tag{3.2}$$

so that ka_l and kb_l are the vertical wave numbers of the ***P***- and ***SV***-waves in the l^{th} layer of the medium with longitudinal wave speed α_l and shear wave velocity β_l. In general, the wave speeds increase as one goes down into the layers, so that $\beta_1 < \beta_2 < \ldots < \beta_N < \beta$, with the semi-infinite half-space layer at the bottom having the highest shear wave speed β. The same can be said about the longitudinal wave speeds, so that $\alpha_1 < \alpha_2 < \ldots < \alpha_N < \alpha$, with α the longitudinal wave speed of the semi-infinite medium furthest below being the highest. With $c = c(\omega)$ the wave speed of the surface Rayleigh waves, $c < \beta < \alpha$, and the surface waves take the form:

$$\begin{aligned} \varphi_\infty &= A_\infty e^{ik(x-az)} = A_\infty e^{ikx-k\bar{a}z} \\ \psi_\infty &= B_\infty e^{ik(x-bz)} = B_\infty e^{ikx-k\bar{b}z} \end{aligned} \tag{3.3}$$

where

$$\begin{aligned} \bar{a} &= \frac{\left(k^2-k_\alpha^2\right)^{1/2}}{k} = \left(1-\left(k_\alpha/k\right)^2\right)^{1/2} = \left(1-\left(c/\alpha\right)^2\right)^{1/2} \\ \bar{b} &= \frac{\left(k^2-k_\beta^2\right)^{1/2}}{k} = \left(1-\left(k_\beta/k\right)^2\right)^{1/2} = \left(1-\left(c/\beta\right)^2\right)^{1/2} \end{aligned} \tag{3.4}$$

and $\bar{a}$, $\bar{b}$ are respectively the complements of a, b and both are real, so that the terms $e^{-k\bar{a}z}$ in φ_∞ and $e^{-k\bar{b}z}$ in ψ_∞ both correspond to surface wave terms with amplitudes that are exponentially decaying with depth below the surface.

With β_l the shear wave speed in the l^{th} layer of the medium, and $c = c(\omega)$, the Rayleigh wave speed and also the (horizontal) phase velocity of the waves in each layer of the elastic media above the half space (Figure **III.1**), we can have $c \geq \beta_l$ or $c < \beta_l$.

If, in the l^{th} layer, $c \geq \beta_l$, the term $b_l = b_l(\beta_l, c)$ in Equation (3.2) is real, both the ***SV***-waves W_l^+ and W_l^- in Equation (3.1) will correspond to harmonic plane waves. If, however, $c < \beta_l$ then, as from Equation (3.2):

$$b_l = \left(\left(c/\beta_l\right)^2 - 1\right)^{1/2} \text{ is imaginary and } \bar{b}_l = \left(1-\left(c/\beta_l\right)^2\right)^{1/2} \text{ is real} \tag{3.5}$$

so that, from Equation (3.1):

ψ_l^-, ψ_l^+ :

$$\begin{aligned} \psi_l^- &= B_l^- e^{ik(x-b_l z)} = B_l^- e^{ikx} e^{+k\bar{b}_l z} \\ \psi_l^+ &= B_l^+ e^{ik(x+b_l z)} = B_l^+ e^{ikx} e^{-k\bar{b}_l z} \end{aligned} \tag{3.6}$$

meaning that the waves ψ_l^+ will be exponentially decaying in z, while the waves ψ_l^- are exponentially growing in the l^{th} layer.

The same observations can be made of the cases for $c \geq \alpha_l$ or $c < \alpha_l$, in regards to the ***P***-wave potentials φ_l^-, φ_l^+ in the l^{th} layer.

The coefficients A_l^-, A_l^+, respectively of the ***P***-wave potentials, φ_l^-, φ_l^+, and B_l^-, B_l^+, respectively of the ***SV***-wave potentials, ψ_l^-, ψ_l^+, in each of the layers l, for l = 1 to N, are all related by the stress and displacement boundary conditions. In the topmost layer, the zero-stress boundary conditions at the half-space surface,

$$\sigma_z\big|_{z=0} = \tau_{zx}\big|_{z=0} \tag{3.7}$$

for *P*- and *SV*-wave potentials. Let U_0, W_0 respectively be the *horizontal* and *vertical* (complex) displacements at the origin, the reference point at the free surface. Then stress boundary conditions at the half-space surface ($z = 0$) and the displacement specification on the half-space surface at the origin **(0., 0.)** take the form:

$$\begin{bmatrix} 1 & 1 & b_1 & -b_1 \\ a_1 & -a_1 & -1 & -1 \\ 1-b_1^2 & 1-b_1^2 & -2b_1 & 2b_1 \\ 2a_1 & -2a_1 & 1-b_1^2 & 1-b_1^2 \end{bmatrix} \begin{pmatrix} A_1^+ \\ A_1^- \\ B_1^+ \\ B_1^- \end{pmatrix} = \frac{1}{ik} \begin{pmatrix} U_0 \\ V_0 \\ 0 \\ 0 \end{pmatrix} \tag{3.8}$$

Recall from above that we have shown that at a given site on the surface, one can use the **"SYNACC *algorithm***" to define the complex Fourier components of acceleration of each mode m of surface Rayleigh waves at each frequency ω within the n^{th} frequency band $\left[\omega_n - \delta\omega_n, \omega_n + \delta\omega_n\right]$ of the whole spectrum. We will take the site to be at the origin $O\big((x,y) = (0.,0.)\big)$ in Figure **III.1** above. Since the Fourier Transforms of displacement $D(\omega)$ and acceleration $A(\omega)$ are related at frequency ω by

$$A(\omega) = -\omega^2 D(\omega) \tag{3.9}$$

so the waves for acceleration and displacement at frequency ω are related the same way. Let $U_0 = A_{0,mn}$, $V_0 = B_{0,mn}$, respectively be such complex Fourier (in-plane) horizontal and vertical component of displacement of the m^{th} mode of surface Rayleigh waves at frequency ω within the n^{th} frequency band $\left[\omega_n - \delta\omega_n, \omega_n + \delta\omega_n\right]$ at the site **O(0.,0.)** in the top layer $(l = 1)$.

From Equation (3.8), it is seen that, given the complex Fourier components of displacement, U_0, V_0, of the m-th mode of surface Rayleigh waves at frequency ω, at a site on the half-space surface, as estimated by the **"SYNACC *algorithm*"**, one can solve for the complex coefficients $\boldsymbol{A_1^-}$, $\boldsymbol{A_1^+}$ and $\boldsymbol{B_1^-}$, $\boldsymbol{B_1^+}$ respectively of the ***P***- and ***SV***-wave potentials associated with the waves in the $\boldsymbol{1^{st}}$ media on top. With the waves on the top layer defined, those can be used to compute the displacements everywhere in the top layer.

In summary, this means that once the complex Fourier coefficient at a given frequency of one mode of surface Rayleigh waves is given at one point of a site at the half-space surface, the complex Fourier coefficient of the same mode of waves at any point on and below the surface, in the top layer, is known.

The next step is to extend this to evaluate the complex Fourier coefficients at a given frequency of each mode of surface Rayleigh waves at any point of all the elastic layers below the surface. Starting from $\boldsymbol{l=1}$, we will show by induction that if the waves at the $\boldsymbol{l^{th}}$ layer are known, then the waves at the $\boldsymbol{(l+1)^{th}}$ layer can also be known, including the bottom semi-infinite layer.

Start with the $\boldsymbol{l^{th}}$ layer, where the wave potentials are given by:

$\boldsymbol{\varphi_l^-}$, $\boldsymbol{\varphi_l^+}$, $\boldsymbol{\psi_l^-}$, $\boldsymbol{\psi_l^+}$ **:**

$$\begin{aligned} \boldsymbol{\varphi_l^-} &= \boldsymbol{A_l^- e^{ik(x-a_l z)}} \\ \boldsymbol{\varphi_l^+} &= \boldsymbol{A_l^+ e^{ik(x+a_l z)}} \\ \boldsymbol{\psi_l^-} &= \boldsymbol{B_l^- e^{ik(x-b_l z)}} \\ \boldsymbol{\psi_l^+} &= \boldsymbol{B_l^+ e^{ik(x+b_l z)}} \end{aligned}$$

Equation (3.1) above

with known (complex) coefficients $\boldsymbol{A_l^-}$, $\boldsymbol{A_l^+}$ for the ***P***-wave and $\boldsymbol{B_l^-}$, $\boldsymbol{B_l^+}$ for the ***SV***-wave potentials. The waves in the $\boldsymbol{(l+1)^{th}}$ layer below, of the form, with $\boldsymbol{(l+1)}$ replacing $\boldsymbol{l}$ everywhere in Equation (3.1):

$$\varphi_{l+1}^{-},\ \varphi_{l+1}^{+},\ \psi_{l+1}^{-},\ \psi_{l+1}^{+}:\qquad \begin{aligned}\varphi_{l+1}^{-} &= A_{l+1}^{-}e^{ik\left(x-a_{l+1}z\right)}\\ \varphi_{l+1}^{+} &= A_{l+1}^{+}e^{ik\left(x+a_{l+1}z\right)}\\ \psi_{l+1}^{-} &= B_{l+1}^{-}e^{ik\left(x-b_{l+1}z\right)}\\ \psi_{l+1}^{+} &= B_{l+1}^{+}e^{ik\left(x+b_{l+1}z\right)}\end{aligned} \tag{3.10}$$

with the coefficients $A_{l+1}^{-},\ A_{l+1}^{+}$ for the ***P***-wave and $B_{l+1}^{-},\ B_{l+1}^{+}$ for the ***SV***-wave potentials next to be evaluated. At the common interface between the l^{th} layer and $\left(l+1\right)^{th}$ layer, where $y=H_l$, the continuity of (***x***- and ***y***- components of) displacements and (normal and shear) stresses at the interface between the 2 layers gives, at $y=H_l$:

$$\begin{bmatrix}1 & 0 & 0 & 0\\ 0 & 1 & 0 & 0\\ 0 & 0 & \mu_{l+1} & 0\\ 0 & 0 & 0 & \mu_{l+1}\end{bmatrix}\begin{bmatrix}1 & 1 & b_{l+1} & -b_{l+1}\\ a_{l+1} & -a_{l+1} & -1 & -1\\ 1-b_{l+1}^2 & 1-b_{l+1}^2 & -2b_{l+1} & 2b_{l+1}\\ 2a_{l+1} & -2a_{l+1} & 1-b_{l+1}^2 & 1-b_{l+1}^2\end{bmatrix}\begin{pmatrix}A_{l+1}^{+}e^{ika_{l+1}H_l}\\ A_{l+1}^{-}e^{-ika_{l+1}H_l}\\ B_{l+1}^{+}e^{ikb_{l+1}H_l}\\ B_{l+1}^{-}e^{-ikb_{l+1}H_l}\end{pmatrix} =$$
$$\begin{bmatrix}1 & 0 & 0 & 0\\ 0 & 1 & 0 & 0\\ 0 & 0 & \mu_l & 0\\ 0 & 0 & 0 & \mu_l\end{bmatrix}\begin{bmatrix}1 & 1 & b_l & -b_l\\ a_l & -a_l & -1 & -1\\ 1-b_l^2 & 1-b_l^2 & -2b_l & 2b_l\\ 2a_l & -2a_l & 1-b_l^2 & 1-b_l^2\end{bmatrix}\begin{pmatrix}A_l^{+}e^{ika_l H_l}\\ A_l^{-}e^{-ika_l H_l}\\ B_l^{+}e^{ikb_l H_l}\\ B_l^{-}e^{-ikb_l H_l}\end{pmatrix} \tag{3.11}$$

Equation (3.11) can be written in the form, at $y=H_l$:

$$\left[M_{l+1}\left(H_l\right)\right]\begin{pmatrix}A_{l+1}^{+}\\ A_{l+1}^{-}\\ B_{l+1}^{+}\\ B_{l+1}^{-}\end{pmatrix}=\left[M_l\left(H_l\right)\right]\begin{pmatrix}A_l^{+}\\ A_l^{-}\\ B_l^{+}\\ B_l^{-}\end{pmatrix}\quad\textbf{or}\quad\begin{pmatrix}A_{l+1}^{+}\\ A_{l+1}^{-}\\ B_{l+1}^{+}\\ B_{l+1}^{-}\end{pmatrix}=\left[N_l\left(H_l\right)\right]\begin{pmatrix}A_l^{+}\\ A_l^{-}\\ B_l^{+}\\ B_l^{-}\end{pmatrix} \tag{3.12}$$

with $\left[N_l\left(H_l\right)\right]=\left[M_{l+1}\left(H_l\right)\right]^{-1}\left[M_l\left(H_l\right)\right]$, both $\left[M_l\left(H_l\right)\right]=\left[M_l\left(\mu_l,a_l,b_l,H_l\right)\right]$ and $\left[M_l\left(H_l\right)\right]=\left[M_l\left(\mu_l,a_l,b_l,H_l\right)\right]$ matrices defined from Equation (3.11).

Starting from the top layer, with the (complex) coefficients of the waves $A_1^{-},\ A_1^{+}$ and $B_1^{-},\ B_1^{+}$ expressed in terms of, $U_0=U_{0,mn}$ and $V_0=V_{0,mn}$ respectively the Fourier components of the waves in the horizontal and vertical directions at the origin, Equation (3.12) gives an iterative

step to compute the wave coefficients A_l^-, A_l^+ and B_l^-, B_l^+ of each elastic layer l, for $l = 1, \ldots, n = N-1$. At the bottom of the last n^{th} layer, at $y = H_n = H_{N-1}$, the interface is now between it and the semi-infinite medium below, which has a mode of surface Rayleigh waves given by:

$$\varphi_N = \varphi_\infty = A_\infty e^{ik(x-az)} = A_\infty e^{ikx-k\bar{a}z}$$
$$\psi_N = \psi_\infty = B_\infty e^{ik(x-bz)} = B_\infty e^{ikx-k\bar{b}z}$$

Equation (3.3) above

The continuity of displacement and stress between the layers at $y = H_n$ gives

$$\begin{bmatrix} 1 & 0 & 0 & 0 \\ 0 & 1 & 0 & 0 \\ 0 & 0 & \mu & 0 \\ 0 & 0 & 0 & \mu \end{bmatrix} \begin{bmatrix} 1 & i\bar{b} \\ \bar{a} & -1 \\ 1+\bar{b}^2 & -i2\bar{b} \\ 2i\bar{a} & 1+\bar{b}^2 \end{bmatrix} \begin{pmatrix} A_\infty e^{-k\bar{a}H_n} \\ B_\infty e^{-k\bar{b}H_n} \end{pmatrix} = \left[M_n(H_n)\right] \begin{pmatrix} A_n^+ \\ A_n^- \\ B_n^+ \\ B_n^- \end{pmatrix} \tag{3.13}$$

where, from Equation (3.11) and Equation (3.12), the matrix $\left[M_n(H_n)\right]$ in the right-hand side can be written in full as:

$$\left[M_n(H_n)\right] = \tag{3.14}$$
$$\begin{bmatrix} 1 & 0 & 0 & 0 \\ 0 & 1 & 0 & 0 \\ 0 & 0 & \mu_n & 0 \\ 0 & 0 & 0 & \mu_n \end{bmatrix} \begin{bmatrix} 1 & 1 & b_n & -b_n \\ a_n & -a_n & -1 & -1 \\ 1-b_n^2 & 1-b_n^2 & -2b_n & 2b_n \\ 2a_n & -2a_n & 1-b_n^2 & 1-b_n^2 \end{bmatrix} \begin{bmatrix} e^{ika_n H_n} & 0 & 0 & 0 \\ 0 & e^{-ika_n H_n} & 0 & 0 \\ 0 & 0 & e^{ikb_n H_n} & 0 \\ 0 & 0 & 0 & e^{-ikb_n H_n} \end{bmatrix}$$

The solution $c = c(\omega)$ of that mode of Rayleigh surface waves will guarantee that Equation (3.13) is satisfied by the surface wave coefficients in the semi-infinite half-space. This completes the derivation.

For the case of body *P* or SV waves incident from the semi-infinite medium at the bottom, we will consider the model in Figure III.2. It is the same *N*-layered model as in Figure III.1, for the case of Rayleigh surface waves, but now the *P* and *SV* waves in all layers are body waves. The body waves in all layers have a common constant horizontal phase velocity c, now independent of frequency ω, and dependent only on the incident angle of *P* or *SV* waves. For incident *P* waves, $\psi_N^- = 0$, and c is higher than $\alpha_{\max} = \alpha_N$, the longitudinal *P* wave speed at the

bottom semi-infinite N^{th} layer. For incident *SV* waves, $\varphi_N^- = \mathbf{0}$, and the phase velocity $\boldsymbol{c}$ is higher than $\beta_{\max} = \beta_N$, the shear *SV* wave speed at the bottom semi-infinite N^{th} layer. (Figure III.2).

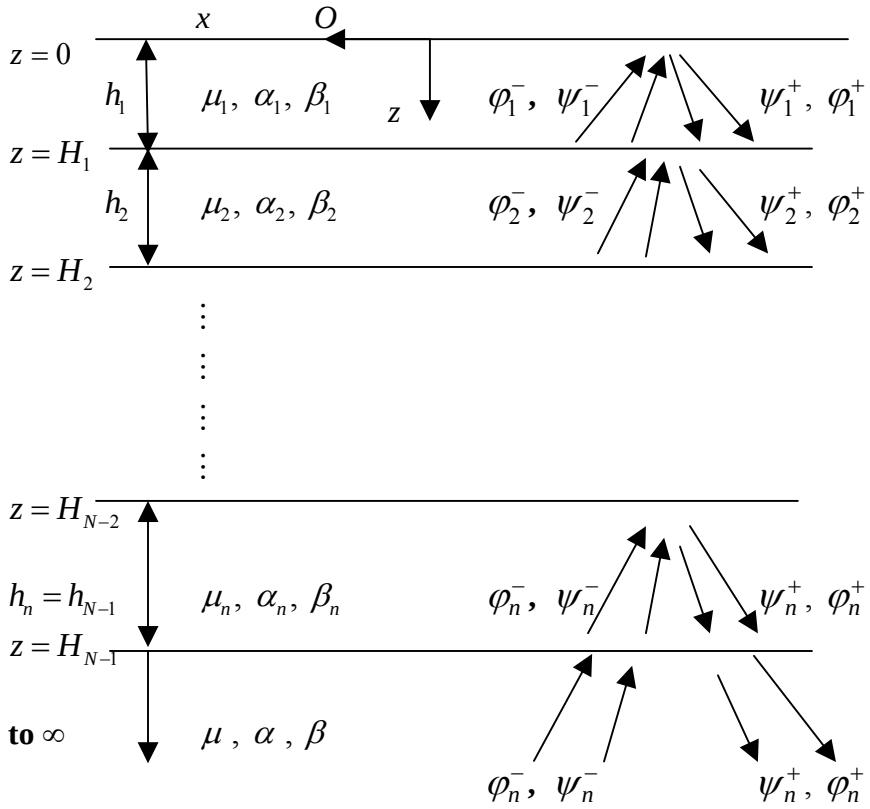

Figure III.2 n-layered half-space with Body P and SV waves

The Rayleigh waves $\varphi_N = \varphi_\infty$ and $\psi_N = \psi_\infty$ in the bottom semi-infinite layer will now be replaced by the body *P* waves φ_N^- and φ_N^+, and *SV* waves ψ_N^- and ψ_N^+ respectively, the incident and reflected body *P* and *SV* waves:

$$\varphi_N^-,\ \varphi_N^+,\ \psi_N^-,\ \psi_N^+ : \qquad \begin{aligned} \varphi_N^- &= A_N^- e^{ik\left(x - a_N z\right)} \\ \varphi_N^+ &= A_N^+ e^{ik\left(x + a_N z\right)} \\ \psi_N^- &= B_N^- e^{ik\left(x - b_N z\right)} \\ \psi_N^+ &= B_N^+ e^{ik\left(x + b_N z\right)} \end{aligned} \tag{3.15}$$

as in all the other layers $l = 1,\ 2,\ \ldots,\ N-1$, in Equation (3.1) above. At the interface with the layer above, the interface between the $n^{th} = (N\text{-}1)^{th}$ layer and the N^{th} layer, instead of Equation

(3.13), the continuity equations are the continuity of displacement and stress between the two layers. They are, as in Equation (3.11), with $l = n = (N-1)$ and $l+1 = N$:

$$\begin{bmatrix} 1 & 0 & 0 & 0 \\ 0 & 1 & 0 & 0 \\ 0 & 0 & \mu_N & 0 \\ 0 & 0 & 0 & \mu_N \end{bmatrix} \begin{bmatrix} 1 & 1 & b_N & -b_N \\ a_N & -a_N & -1 & -1 \\ 1-b_N^2 & 1-b_N^2 & -2b_N & 2b_N \\ 2a_N & -2a_N & 1-b_N^2 & 1-b_N^2 \end{bmatrix} \begin{pmatrix} A_N^+ e^{ika_N H_N} \\ A_{l+1}^- e^{-ika_N H_N} \\ B_N^+ e^{ikb_N H_N} \\ B_N^- e^{-ikb_N H_N} \end{pmatrix} =$$

$$\begin{bmatrix} 1 & 0 & 0 & 0 \\ 0 & 1 & 0 & 0 \\ 0 & 0 & \mu_l & 0 \\ 0 & 0 & 0 & \mu_l \end{bmatrix} \begin{bmatrix} 1 & 1 & b_l & -b_l \\ a_l & -a_l & -1 & -1 \\ 1-b_l^2 & 1-b_l^2 & -2b_l & 2b_l \\ 2a_l & -2a_l & 1-b_l^2 & 1-b_l^2 \end{bmatrix} \begin{pmatrix} A_l^+ e^{ika_l H_l} \\ A_l^- e^{-ika_l H_l} \\ B_l^+ e^{ikb_l H_l} \\ B_l^- e^{-ikb_l H_l} \end{pmatrix} \qquad (3.16)$$

In summary, this means that once the complex Fourier coefficient at a given frequency of one mode of surface Rayleigh and body P and SV waves is given at one point of a site at the half-space surface, the complex Fourier coefficient of the same mode of surface and body P and SV waves at any point on and below the surface, at any of the elastic layers down below, is also known.

The above method will be referred in what follows as the reflection-transmission (R-T) coefficient matrix method for Rayleigh, and body P and SV waves.

IV. The Numerical Implementation

Numerical implementation of the above boundary-valued problem to study the propagation of elastic waves in a layered media was first presented and formulated in the pioneering work by Thomson (1950) and Haskell (1953). Thomson (1950) first set up the theoretical groundwork to be extended later by Haskell (1953)

The following section is a brief summary of Thomson-Haskell method.

IV.1 The Original Thomson-Haskell's Transfer Matrix Method

The objective here is to use the equations developed in the above two sections to evaluate the displacement and stress at every point of every medium in the half-space. In what follows we will follow the approach of Thomson (1950) and Haskell (1953). We will first present the (simpler) case of Love and SH waves, and then follow with the (more complicated) case of Rayleigh, P and SV waves.

(1) Love Waves

There the displacement-stress state vector $[v_l, \tau_l]^T$ of the l^{th} layer is to be expressed in terms of the coefficients of the wave functions of the l^{th} layer in matrix form. Further, instead of a global coordinate system for all the media, each layer has its own local *z*-vertical coordinate system, so that in the l^{th} layer, we have $\boldsymbol{z = 0}$ at the top and $\boldsymbol{z = h_l}$ at the bottom of the layer. Using the above equations, this takes the form:

$$\begin{aligned} \boldsymbol{v_l(x,z)} &= \left(\boldsymbol{C_l^+ e^{+ik\gamma_l z} + C_l^- e^{-ik\gamma_l z}}\right)\boldsymbol{e^{ikx}} \\ \tau_l(x,z) &= \mu_l \frac{\partial \boldsymbol{v_l}}{\partial \boldsymbol{z}} = \boldsymbol{i}\mu_l \boldsymbol{k}\gamma_l \left(\boldsymbol{C_l^+ e^{+ik\gamma_l z} - C_l^- e^{-ik\gamma_l z}}\right)\boldsymbol{e^{ikx}} \end{aligned} \tag{4.1}$$

or, in matrix form

$$\begin{pmatrix} v_l(x,z) \\ \tau_l(x,z) \end{pmatrix} = \begin{bmatrix} 1 & 1 \\ i\mu_l k\gamma_l & -i\mu_l k\gamma_l \end{bmatrix} \begin{bmatrix} e^{i\mu_l k\gamma_l z} & 0 \\ 0 & e^{-i\mu_l k\gamma_l z} \end{bmatrix} \begin{pmatrix} C_l^+ \\ C_l^- \end{pmatrix} e^{ikx} \qquad (4.2a)$$
$$= \quad [T_l][E_l(z)]\left(\tilde{C}_l\right)e^{ikx}$$

Equation (4.2a) allows the displacement-stress state vector at any point of the l^{th} layer to be evaluated in terms of the coefficients of the wave functions there, and vice versa. In other words, if the displacement-state vector is known at one point of the l^{th} layer, the displacement-stress state vector will be known at every point of the l^{th} layer. Here note that $[T_l]$ is a constant matrix in the l^{th} layer, and the exponential matrix $[E_l(z)]$ is a diagonal matrix dependent on the vertical depth z, but independent of the horizontal distance x. $\left(\tilde{C}_l\right)$ is the coefficient vector of the waves in the l^{th} layer. This means that the only x-dependence in the above equation for the l^{th} layer is in the term e^{ikx}. Without loss of generality, we will set $x = 0$ for now, so that $e^{ikx} = 1$, and will be omitted from the above equation. Omitting x, we will write the state vector as

$$\begin{pmatrix} v_l(z) \\ \tau_l(z) \end{pmatrix} = \begin{pmatrix} v_l(x,z) \\ \tau_l(x,z) \end{pmatrix}\Big|_{x=0} = \begin{bmatrix} 1 & 1 \\ i\mu_l k\gamma_l & -i\mu_l k\gamma_l \end{bmatrix} \begin{bmatrix} e^{i\mu_l k\gamma_l z} & 0 \\ 0 & e^{-i\mu_l k\gamma_l z} \end{bmatrix} \begin{pmatrix} C_l^+ \\ C_l^- \end{pmatrix} \qquad (4.2b)$$
$$= \quad [T_l][E_l(z)]\left(\tilde{C}_l\right)$$

Further, at the top of the l^{th} layer, where $z = 0$ in the l^{th} local coordinate system, we have

$$\begin{pmatrix} v_l(0) \\ \tau_l(0) \end{pmatrix} = \begin{bmatrix} 1 & 1 \\ i\mu_l k\gamma_l & -i\mu_l k\gamma_l \end{bmatrix} \begin{pmatrix} C_l^+ \\ C_l^- \end{pmatrix} = [T_l]\left(\tilde{C}_l\right) \qquad (4.3)$$

since $[E_l(z)] = [E_l(0)] = [I]$, the identity matrix at $z = 0$. Eliminating the coefficient vector $\left(\tilde{C}_l\right)$ in Equations (4.2b) and (4.3) gives

$$\begin{pmatrix} v_l(z) \\ \tau_l(z) \end{pmatrix} = \begin{bmatrix} 1 & 1 \\ i\mu_l k\gamma_l & -i\mu_l k\gamma_l \end{bmatrix} \begin{bmatrix} e^{i\mu_l k\gamma_l z} & 0 \\ 0 & e^{-i\mu_l k\gamma_l z} \end{bmatrix} \begin{bmatrix} 1 & 1 \\ i\mu_l k\gamma_l & -i\mu_l k\gamma_l \end{bmatrix}^{-1} \begin{pmatrix} v_l(0) \\ \tau_l(0) \end{pmatrix} \qquad (4.4)$$

or
$$\begin{pmatrix} v_l(z) \\ \tau_l(z) \end{pmatrix} = [T_l][E_l(z)][T_l]^{-1} \begin{pmatrix} v_l(0) \\ \tau_l(0) \end{pmatrix}$$

for $\mathbf{0 \le z \le h_l}$, at any point in the l^{th} layer. In particular, at the bottom point of the l^{th} layer, where $\mathbf{z = h_l}$, Equation (4.4) becomes:

$$\begin{pmatrix} \boldsymbol{v_l(h_l)} \\ \boldsymbol{\tau_l(h_l)} \end{pmatrix} = \boldsymbol{[T_l][E_l(h_l)][T_l]^{-1}} \begin{pmatrix} \boldsymbol{v_l(0)} \\ \boldsymbol{\tau_l(0)} \end{pmatrix}$$
$$\begin{pmatrix} \boldsymbol{v_l(h_l)} \\ \boldsymbol{\tau_l(h_l)} \end{pmatrix} = \boldsymbol{[\mathcal{H}_l]} \begin{pmatrix} \boldsymbol{v_l(0)} \\ \boldsymbol{\tau_l(0)} \end{pmatrix} \tag{4.5}$$

where $\boldsymbol{[\mathcal{H}_l] = [T_l][E_l(h_l)][T_l]^{-1}}$ is the Haskell propagator matrix that expresses the displacement-stress state vector at the bottom of the l^{th} layer in terms of that at the top of the layer.

Define a set of displacement-stress state vectors, for $\boldsymbol{l = 1, 2, \ldots, N}$:

$$\begin{pmatrix} \boldsymbol{V_l} \\ \mathbf{T}_l \end{pmatrix} = \left. \begin{pmatrix} \boldsymbol{v_l(z)} \\ \boldsymbol{\tau_l(z)} \end{pmatrix} \right|_{z=0} \tag{4.6}$$

which correspond to the state vector at the top of each layer. Since the stress-displacement state vectors are continuous across the interface from one medium to the one below,
one can write Equation (4.5) as

$$\boldsymbol{l = 1,\ 2,\ \ldots,\ N-1} \quad \begin{pmatrix} \boldsymbol{V_{l+1}} \\ \mathbf{T}_{l+1} \end{pmatrix} = \boldsymbol{[T_l][E_l(h_l)][T_l]^{-1}} \begin{pmatrix} \boldsymbol{V_l} \\ \mathbf{T}_l \end{pmatrix} = \boldsymbol{[\mathcal{H}_l]} \begin{pmatrix} \boldsymbol{V_l} \\ \mathbf{T}_l \end{pmatrix} \tag{4.7a}$$

In the reverse order, we also have

$$\begin{pmatrix} \boldsymbol{V_l} \\ \mathbf{T}_l \end{pmatrix} = \boldsymbol{[T_l][E_l(h_l)]^{-1}\ [T_l]^{-1}} \begin{pmatrix} \boldsymbol{V_{l+1}} \\ \mathbf{T}_{l+1} \end{pmatrix} = \boldsymbol{[\mathcal{H}_l]^{-1}} \begin{pmatrix} \boldsymbol{V_{l+1}} \\ \mathbf{T}_{l+1} \end{pmatrix} \tag{4.7b}$$

The displacement-stress vector at the top of the last (semi-infinite) layer can then be expressed in terms of that at the top of the 1st surface layer:

$$\begin{pmatrix} \boldsymbol{V_N} \\ \mathbf{T}_N \end{pmatrix} = \boldsymbol{[\mathcal{H}_{N-1}][\mathcal{H}_{N-2}]\ldots[\mathcal{H}_1]} \begin{pmatrix} \boldsymbol{V_1} \\ \mathbf{T}_1 \end{pmatrix} \tag{4.8a}$$

or in the reverse order

$$\begin{pmatrix} \boldsymbol{V_1} \\ \mathbf{T}_1 \end{pmatrix} = \boldsymbol{[\mathcal{H}_1]^{-1} \ldots [\mathcal{H}_{N-2}]^{-1}[\mathcal{H}_{N-1}]^{-1}} \begin{pmatrix} \boldsymbol{V_N} \\ \mathbf{T}_N \end{pmatrix} \tag{4.8b}$$

Equations (4.4) through (4.8) allow the displacement-stress vector to be calculated at every point of every layer in the layered half space.

(2) Rayleigh Waves

The case of Rayleigh, P and SV waves will next be considered. Start again with the l^{th} layer, $l = 1, 2, \ldots, N$ (Figure **III.1**):

$$\varphi_l = \varphi_l^+ + \varphi_l^- = \left(A_l^+ e^{+ika_l z} + A_l^- e^{-ika_l z} \right) e^{ikx}$$
$$\psi_l = \psi_l^+ + \psi_l^- = \left(B_l^+ e^{+ikb_l z} + B_l^- e^{-ikb_l z} \right) e^{ikx} \qquad \text{Eqn. (3.1,2) above}$$

With a_l, b_l defined in Equation (3.2), the displacement components at each point of the l^{th} layer, $l = 1, 2, \ldots, N$, are then given by:

$$u_l = \frac{\partial \varphi_l}{\partial x} - \frac{\partial \psi_l}{\partial z}, \qquad w_l = \frac{\partial \varphi_l}{\partial z} + \frac{\partial \psi_l}{\partial x} \tag{4.9}$$

In terms of the potentials in Equation (3.1), they take the form:

$$u_l / ik = \left[\left(A_l^+ e^{+ika_j z} + A_l^- e^{-ika_l z} \right) - b_l \left(B_l^+ e^{+ikb_l z} - B_l^- e^{-ikb_l z} \right) \right] e^{ikx}$$
$$w_l / ik = \left[a_l \left(A_l^+ e^{+ika_j z} - A_l^- e^{-ika_l z} \right) + \left(B_l^+ e^{+ikb_l z} + B_l^- e^{-ikb_l z} \right) \right] e^{ikx} \tag{4.10}$$

Next, the stress components $(\tau_{zx})_l$ and $(\sigma_z)_l$ at each point of the l^{th} layer, $l = 1, 2, \ldots, N$, are then given by:

$$\begin{pmatrix} (\sigma_z)_l \\ (\tau_{zx})_l \end{pmatrix} = \begin{pmatrix} \lambda_l \nabla^2 \varphi_l + 2\mu_l \varepsilon_z \\ 2\mu_l \varepsilon_{zx} \end{pmatrix} = \begin{pmatrix} -\lambda_l k_{\alpha_l}^2 \varphi_l + \mu_l \dfrac{\partial w_l}{\partial z} \\ \mu_l \left(\dfrac{\partial u_l}{\partial z} + \dfrac{\partial w_l}{\partial x} \right) \end{pmatrix} \tag{4.11}$$

In terms of the potentials in Equation (3.1), they take the form:

$$\begin{pmatrix} (\sigma_z)_l \\ (\tau_{zx})_l \end{pmatrix} = \begin{pmatrix} (\sigma_z(x,z))_l \\ (\tau_{zx}(x,z))_l \end{pmatrix}$$
$$\mu_l k^2 \left(\begin{bmatrix} 1-b_l^2 & -2b_l \\ -2a_l & -(1-b_l^2) \end{bmatrix} \begin{pmatrix} A_l^+ e^{+ika_l z} \\ B_l^+ e^{+ikb_l z} \end{pmatrix} + \begin{bmatrix} 1-b_l^2 & 2b_l \\ 2a_l & -(1-b_l^2) \end{bmatrix} \begin{pmatrix} A_l^- e^{-ika_l z} \\ B_l^- e^{-ikb_l z} \end{pmatrix} \right) e^{ikx} \tag{4.12}$$

Writing $\mu_l = \rho_l c_{\beta_l}^2$ for the shear modulus of the l^{th} layer, $l = 1, 2, \ldots, N$, and normalizing the stresses in Equation (4.12), the stresses $\begin{pmatrix} (\sigma_z)_l \\ (\tau_{zx})_l \end{pmatrix}$ take the form:

$$\begin{pmatrix} (\sigma_z)_l / (kc)^2 & (\tau_{zx})_l / (kc)^2 \end{pmatrix}^T =$$
$$\rho_l \left(c_{\beta_l}^2 / c^2 \right) \left(\begin{bmatrix} 1-b_l^2 & -2b_l \\ -2a_l & -(1-b_l^2) \end{bmatrix} \begin{pmatrix} A_l^+ e^{+ika_l z} \\ B_l^+ e^{+ikb_l z} \end{pmatrix} + \begin{bmatrix} 1-b_l^2 & 2b_l \\ 2a_l & -(1-b_l^2) \end{bmatrix} \begin{pmatrix} A_l^- e^{-ika_l z} \\ B_l^- e^{-ikb_l z} \end{pmatrix} \right) e^{ikx} \tag{4.13}$$

Defining $\gamma_l = 2\left(\beta_l / c\right)^2$, and from Equation (3.2),

$$\left(\beta_l^2 / c^2\right)\left(1-b_l^2\right) = \left(\beta_l^2 / c^2\right)\left(2 - \left(c^2 / \beta_l^2\right)\right) = \left(\gamma_l - 1\right) \tag{4.14}$$

equation (4.13) becomes

$$\begin{pmatrix} (\sigma_z)_l / (kc)^2 \\ (\tau_{zx})_l / (kc)^2 \end{pmatrix} = \rho_l \left(\begin{bmatrix} \gamma_l - 1 & -\gamma_l b_l \\ -\gamma_l a_j & 1-\gamma_l \end{bmatrix} \begin{pmatrix} A_l^+ e^{+ika_l z} \\ B_l^+ e^{+ikb_l z} \end{pmatrix} + \begin{bmatrix} \gamma_l - 1 & \gamma_l b_l \\ \gamma_l a_l & 1-\gamma_l \end{bmatrix} \begin{pmatrix} A_l^- e^{-ika_l z} \\ B_l^- e^{-ikb_l z} \end{pmatrix} \right) e^{ikx} \tag{4.15a}$$

which will be switched in the order of x to z:

$$\begin{pmatrix} (\tau_{zx})_l / (kc)^2 \\ (\sigma_z)_l / (kc)^2 \end{pmatrix} = \rho_j \left(\begin{bmatrix} -\gamma_j a_j & 1-\gamma_j \\ \gamma_j - 1 & -\gamma_j b_j \end{bmatrix} \begin{pmatrix} A_j^+ e^{+ika_j z} \\ B_j^+ e^{+ikb_j z} \end{pmatrix} + \begin{bmatrix} \gamma_j a_j & 1-\gamma_j \\ \gamma_j - 1 & \gamma_j b_j \end{bmatrix} \begin{pmatrix} A_j^- e^{-ika_j z} \\ B_j^- e^{-ikb_j z} \end{pmatrix} \right) e^{ikx} \tag{4.15b}$$

In summary, the displacement and stress vector in the l^{th} layer can be put into a matrix form as (Dunkin, 1965; Liu, 2010):

$$\begin{pmatrix} \tilde{u}_l(x,z) \\ \tilde{\sigma}_l(x,z) \end{pmatrix} = \begin{bmatrix} T_l^1 & T_l^2 \\ T_l^3 & T_l^4 \end{bmatrix} \begin{bmatrix} E_l^+(z) & 0 \\ 0 & E_l^-(z) \end{bmatrix} \begin{pmatrix} \tilde{C}_l^+ \\ \tilde{C}_l^- \end{pmatrix} e^{ikx} \tag{4.16}$$

where

1) $\tilde{u}_l(z)$ and $\tilde{\sigma}_l(z)$ are respectively the (normalized) displacement and stress vectors:

$$\tilde{u}_l(x,z) = \begin{pmatrix} u_l(x,z)/ik \\ w_l(x,z)/ik \end{pmatrix} \qquad \tilde{\sigma}_l(z) = \begin{pmatrix} \left(\tau_{zx}(x,z)\right)_l \,/(kc)^2 \\ \left(\sigma_z(x,z)\right)_l/(kc)^2 \end{pmatrix} \tag{4.17}$$

2) T_l^1, T_l^2, T_l^3 and T_l^4 are all 2 x 2 matrices, so that $\left[T_l\right] = \begin{bmatrix} T_l^1 & T_l^2 \\ T_l^3 & T_l^4 \end{bmatrix}$ is a 4 x 4 matrix given by,

$$[T_l] = \begin{bmatrix} 1 & -b_l & 1 & b_l \\ a_l & 1 & -a_l & 1 \\ -\rho_l\gamma_l a_l & \rho_l(1-\gamma_l) & \rho_l\gamma_l a_l & \rho_l(1-\gamma_l) \\ \rho_l(\gamma_l-1) & -\rho_l\gamma_l b_l & \rho_l(\gamma_l-1) & \rho_l\gamma_l b_l \end{bmatrix} \tag{4.18}$$

Note that the 4 x 4 matrix $\left[T_l\right] = \begin{bmatrix} T_l^1 & T_l^2 \\ T_l^3 & T_l^4 \end{bmatrix}$ is constant in the l^{th} medium.

3) $E_l^+(z)$ and $E_l^-(z)$ are respectively diagonal elements of the 4 x 4 diagonal matrix:

$$E_l^+(z) = \begin{bmatrix} e^{+ika_l z} & 0 \\ 0 & e^{+ikb_l z} \end{bmatrix} \quad \text{and} \quad E_l^-(z) = \begin{bmatrix} e^{-ika_l z} & 0 \\ 0 & e^{-ikb_l z} \end{bmatrix} \tag{4.19}$$

Note that in each layer the exponents in these terms can either be real or imaginary. Take for example a case when $c < \beta_l < \alpha_l$, then both a_l and b_l (Equation (3.2)) will be imaginary, and so $e^{+ika_l z}$ and $e^{+ikb_l z}$ are exponentials decaying in z, while $e^{-ika_l z}$ and $e^{-ikb_l z}$ are exponentials increasing in z.

4) $\tilde{C}_j^+$ and $\tilde{C}_j^-$ are respectively 2 x 1 column vectors of the P and SV potentials:

$$\tilde{C}_j^+ = \begin{pmatrix} A_j^+ \\ B_j^+ \end{pmatrix} \quad \text{and} \quad \tilde{C}_j^- = \begin{pmatrix} A_j^- \\ B_j^- \end{pmatrix} \tag{4.20}$$

As shown in Equation (4.16), the only x-dependence in the above equation for the l^{th} layer is, as with Love waves, again only in the term e^{ikx}. Without loss of generality, we will set

$x = 0$ for now, so that $e^{ikx} = 1$ and will be omitted from the above equation. Omitting x, we will write the state vector in Equation (4.16) as

$$\begin{pmatrix} \tilde{u}_l(z) \\ \tilde{\sigma}_l(z) \end{pmatrix} = \begin{pmatrix} \tilde{u}_l(x,z) \\ \tilde{\sigma}_l(x,z) \end{pmatrix}\Big|_{x=0} = \begin{bmatrix} T_l^1 & T_l^2 \\ T_l^3 & T_l^4 \end{bmatrix} \begin{bmatrix} E_l^+(z) & 0 \\ 0 & E_l^-(z) \end{bmatrix} \begin{pmatrix} \tilde{C}_l^+ \\ \tilde{C}_l^- \end{pmatrix}$$
$$= \quad [T_l][E_l(z)]\left(\tilde{C}_l\right) \tag{4.21}$$

Further, at the top of the l^{th} layer, where $z = 0$ in the l^{th} local coordinate, we have

$$\begin{pmatrix} \tilde{u}_l(0) \\ \tilde{\sigma}_l(0) \end{pmatrix} = \begin{bmatrix} T_l^1 & T_l^2 \\ T_l^3 & T_l^4 \end{bmatrix} \begin{pmatrix} \tilde{C}_l^+ \\ \tilde{C}_l^- \end{pmatrix} = [T_l]\left(\tilde{C}_l\right) \tag{4.22}$$

Since $[E_l(z)] = [E_l(0)] = [I]$, becomes identity matrix at $z = 0$. Eliminating the coefficient vector $\left(\tilde{C}_l\right)$ in Equations (4.21) and (4.22) gives, at each of the l^{th} layers, $l = 1, 2, \ldots, N$

$$\begin{pmatrix} \tilde{u}_l(z) \\ \tilde{\sigma}_l(z) \end{pmatrix} = \begin{bmatrix} T_l^1 & T_l^2 \\ T_l^3 & T_l^4 \end{bmatrix} \begin{bmatrix} E_l^+(z) & 0 \\ 0 & E_l^-(z) \end{bmatrix} \begin{bmatrix} T_l^1 & T_l^2 \\ T_l^3 & T_l^4 \end{bmatrix}^{-1} \begin{pmatrix} \tilde{u}_l(0) \\ \tilde{\sigma}_l(0) \end{pmatrix}$$
or
$$\begin{pmatrix} \tilde{u}_l(z) \\ \tilde{\sigma}_l(z) \end{pmatrix} = [T_l][E_l(z)][T_l]^{-1} \begin{pmatrix} \tilde{u}_l(0) \\ \tilde{\sigma}_l(0) \end{pmatrix} \tag{4.23}$$

for $0 \le z \le h_l$, at any point in the l^{th} layer below. In particular, at the bottom point of the l^{th} layer, where $z = h_l$, Equation (4.23) becomes:

$$\begin{pmatrix} \tilde{u}_l(h_l) \\ \tilde{\sigma}_l(h_l) \end{pmatrix} = [T_l][E_l(h_l)][T_l]^{-1} \begin{pmatrix} \tilde{u}_l(0) \\ \tilde{\sigma}_l(0) \end{pmatrix}$$
$$\begin{pmatrix} \tilde{u}_l(h_l) \\ \tilde{\sigma}_l(h_l) \end{pmatrix} = [\mathcal{H}_l] \begin{pmatrix} \tilde{u}_l(0) \\ \tilde{\sigma}_l(0) \end{pmatrix} \tag{4.24}$$

where $[\mathcal{H}_l] = [T_l][E_l(h_l)][T_l]^{-1}$ is again the Haskell propagator matrix for Rayleigh waves, which expresses the displacement-stress state vector at the bottom of the l^{th} layer in terms of that at the top of the layer.

As for the case of Love waves, we define a set of displacement-stress state vectors, for $l = 1, 2, \ldots, N$, one for each layer, as:

$$\begin{pmatrix} \tilde{U}_l \\ \tilde{\Sigma}_l \end{pmatrix} = \begin{pmatrix} \tilde{u}_l(z) \\ \tilde{\sigma}_l(0) \end{pmatrix}\Big|_{z=0} = \begin{pmatrix} \tilde{u}_l(0) \\ \tilde{\sigma}_l(0) \end{pmatrix} \tag{4.25}$$

which corresponds to the state vector at the top of each layer. Since the stress-displacement state vectors are continuous across the interface from one layered medium to the one below, one can write Equation (4.24) as:

$$l = 1,\ 2,\ \ldots,\ N-1 \qquad \begin{pmatrix} \tilde{U}_{l+1} \\ \tilde{\Sigma}_{l+1} \end{pmatrix} = [T_l]\,[E_l(h_l)]\,[T_l]^{-1} = [\mathcal{H}_l] \begin{pmatrix} \tilde{U}_l \\ \tilde{\Sigma}_l \end{pmatrix} \tag{4.26a}$$

In the reverse order, we also have

$$\begin{pmatrix} \tilde{U}_l \\ \tilde{\Sigma}_l \end{pmatrix} = [T_l]\,[E_l(h_l)]^{-1}[T_l]^{-1} \begin{pmatrix} \tilde{U}_{l+1} \\ \tilde{\Sigma}_{l+1} \end{pmatrix} = [\mathcal{H}_l]^{-1} \begin{pmatrix} \tilde{U}_{l+1} \\ \tilde{\Sigma}_{l+1} \end{pmatrix} \tag{4.26b}$$

The displacement-stress vector at the top of the last (semi-infinite) layer can then be expressed in terms of that at the top of the 1st surface layer:

$$\begin{pmatrix} \tilde{U}_N \\ \tilde{\Sigma}_N \end{pmatrix} = [\mathcal{H}_{N-1}][\mathcal{H}_{N-2}]\cdots[\mathcal{H}_1] \begin{pmatrix} \tilde{U}_1 \\ \tilde{\Sigma}_1 \end{pmatrix} \tag{4.27a}$$

or in the reverse order $\begin{pmatrix} V_1 \\ \tilde{\Sigma}_1 \end{pmatrix} = [\mathcal{H}_1]^{-1} \cdots [\mathcal{H}_{N-2}]^{-1}[\mathcal{H}_{N-1}]^{-1} \begin{pmatrix} V_N \\ \tilde{\Sigma}_N \end{pmatrix}$ (4.28b)

Equations (4.24) through (4.28) allow the displacement-stress vector to be calculated at every point of every layer in the half space from top to bottom.

In summary, this section gives a detailed step-by-step derivation of how the application of the continuity of stress and displacement boundary conditions between layers, as given in Section III above, leads to the above matrix equation, relating the state vector of stress and displacement at each layer to the coefficient vectors of *SH* displacements and the *P* and *SV* wave potentials

IV.2 The Improved Matrix Propagator Algorithm

The Thomson-Haskell propagator matrices derived above are based on the use of matrix multiplication in the frequency-wave number domain. In theory and in principle, this provides the tool for the computation of harmonic elastic waves in a layered, elastic media. It has been used to calculate the roots of the zero-determinant of the propagation matrices to determine the phase velocities of the Rayleigh and Love surface waves. Here, in our context, it can also be used to find the mode shapes of the displacement responses of the layered media in the vertical direction. Since its development in the 50's, the study of wave propagation in a layered elastic media has generated much attention and widespread applications.

In the 60's and 70's, high-speed computations using mainframe computers become available. Computer programs were developed to perform the calculations of these matrices, as reported by Dorman et al (1960) and Press et al (1961). As seen from above, for the case of Love and SH waves, the matrices in each layer are of order two. For the cases of Rayleigh and P and SV waves, these matrices in each layer are of order four. For a N-layer media, these matrices are thus of order $2N$ for Love, SH (scalar) elastic waves and of order $4N$ for Rayleigh, P and SV (vector) waves. When the number of layers N becomes moderately large, it is thus seen that these calculations become cumbersome. Further, it is found from experience then that when the wave frequencies are large, the matrix components are very large and the exponential wave functions approach both overflow and underflow ranges numerically, making it impossible to obtain the roots and mode shapes accurately. Such numerical instabilities exist even at moderate wave frequencies for larger layer thickness. This problem is more noticeable in layers where the phase velocity is less than the wave speed, so that both waves that are exponentially increasing and decreasing in the vertical z-direction exist in the layer. The problem is more significant for vector (Rayleigh, P and SV) waves than scalar (Love and SH) waves.

Knopoff (1964) reported on such numerical problem, first calling attention to the long-standing difficulty in the solution experienced by many workers and researchers in this subject area. Knopoff proposed an alternate matrix formulation to try to avoid the above-mentioned

numerical difficulties. Duncan (1965), at the same time, after reading a preprint of Knopoff's paper, proposed another matrix formulation similar to that of Knopoff (1964).

Here is a brief summary of various proposed modifications of the solution methods for the direct Reflection-Transmission matrix method and the Thomson-Haskell propagator matrix method, to avoid the inherent numerical instability. This covers the period from the 1960s to 2010. The published methods are developed mostly for the troublesome Rayleigh, P and SV vector waves, but the procedures can also be applied to the Love and SH scalar waves.

Knopoff (1964), Duncan (1965), and Thrower (1965) replaced the original Thomson-Haskell propagator matrix with its second-order minor matrices. Both Thrower (1965) and Randall (1967) reported success using the alternate formulation. Further modification of the method was proposed by Watson (1970).

Later Kennet (1974) revisited the Reflection-Transmission (R-T) matrix method and derived a new recursive algorithm for generating the generalized reflection-transmission coefficients of the wave potentials to avoid the numerical instabilities. Those were subsequently updated in Kennet and Kerry (1979, Luco and Apsel (1983), Kennet (1983, 2001) and Chapman (2003). Those are now referred to as the generalized R-T coefficient method.

Chapman and Phinney (1972) adopted the same Gram-Schmidt orthogonalization inner-product method for radio waves developed by Pitteway (1965) to elastic waves, which claimed to improve the numerical stability of the propagator algorithm, under some imposed restrictions in the propagation step. Wang (1999) also proposed such othogonalization and normalization procedures in the propagation step.

Recently, an efficient and elegant method which combines the second-order minor method of Knopoff (1965) and others with the Langer block-diagonal decomposition has been presented by Chapman (2003) in the paper titled, " Yet another elastic Plane-wave Layer-matrix algorithm". Ma et al (2012) just recently proposed another such method in formulating the

Thomson-Haskell propagator matrix, also using the orthonormalization and the Langer block-diagonal decomposition methods.

With so many "efficient" and "elegant" methods for layered-media matrix calculations presented, it would be tedious and time consuming to study all of them, and implement them to evaluate which is the preferred method to be used. As pointed out by Ma et al (2012), the three methods above, namely,

1) recursive reflection-transmission matrix method,
2) orthonormalization method, and
3) minor matrix method

are, as stated in their paper: "… all somewhat related and solve the numerical instability in the original Thomson-Haskell propagator matrix method equally well …" This makes a lot of sense since they are all numerical method implemented to solve the same boundary-valued problem with identical physics.

The numerical scheme used in this work is an improved modification of the Thomson-Haskell transfer matrix method using the above methodology proposed recently by Liu (2010). The same method has successfully been generalized from layered elastic media to that of layered azimuthally anisotropic media (Liu et al, 2012). Instead of directly multiplying the Thomson-Haskell propagator matrix, this method defines for each layer an intermediate stiffness matrix and state vector and performs the propagation through an intermediate step at each layer. This modified scheme keeps the simplicity of the original propagator method with the intermediate step able to efficiently avoid and exclude the exponential growth terms. Here is a brief summary of the scheme for Rayleigh waves as in Liu (2010). It is then modified to cover the case of incident P and SV body waves.

IV.3 The Improved Numerical Implementation for Rayleigh Waves

Start with the Thomson-Haskell Propagator matrix, for $l = 1,\ 2,\ \ldots,\ N-1$

$$\begin{pmatrix} \tilde{U}_{l+1} \\ \tilde{\Sigma}_{l+1} \end{pmatrix} = \left[T_l\right]\left[E_l(h_l)\right]\left[T_l\right]^{-1} = \left[\mathcal{H}_l\right]\begin{pmatrix} \tilde{U}_l \\ \tilde{\Sigma}_l \end{pmatrix} \qquad \text{Equation (4.16) above}$$

with the matrices $\left[T_l\right]$ and $\left[E_l(h_l)\right]$ given in Equations (4.18) and (4.19). Following Kausel and Roesset (1981), express first the stress vector in terms of the displacement vector at each layer $l,\ l = 1,\ \ldots,\ N$ by one involving a layered stiffness matrix S_l, namely, $\left(\tilde{\Sigma}_l\right) = \left[S_l\right]\left(\tilde{U}_l\right)$, so that the displacement-stress state vector takes the form

$$\begin{pmatrix} \tilde{U}_l \\ \tilde{\Sigma}_l \end{pmatrix} = \begin{bmatrix} I \\ S_l \end{bmatrix}\tilde{U}_l \tag{4.28}$$

and the propagating Equation (4.16) becomes, for $l = 1,\ 2,\ 3,\ \ldots,\ N-2,\ N-1$:

$$\begin{bmatrix} I \\ S_{l+1} \end{bmatrix}\tilde{U}_{l+1} = \left[T_l\right]\left[E_l(h_l)\right]\left[T_l\right]^{-1}\begin{bmatrix} I \\ S_l \end{bmatrix}\tilde{U}_l = \left[\mathcal{H}_l\right]\begin{bmatrix} I \\ S_l \end{bmatrix}\tilde{U}_l \tag{4.29a}$$

or, in reverse order, for $l = N-1,\ N-2,\ \ldots,\ 3,\ 2,\ 1$:

$$\begin{bmatrix} I \\ S_l \end{bmatrix}\tilde{U}_l = \left[T_l\right]\left[E_l(h_l)\right]^{-1}\left[T_l\right]^{-1}\begin{bmatrix} I \\ S_{l+1} \end{bmatrix}\tilde{U}_{l+1} = \left[\mathcal{H}_l\right]^{-1}\begin{bmatrix} I \\ S_{l+1} \end{bmatrix}\tilde{U}_{l+1} \tag{4.29b}$$

with the 4 x 4 diagonal matrices $\left[E_l(h_l)\right] = \begin{bmatrix} \mathcal{E}_l^{+} & 0 \\ 0 & \mathcal{E}_l^{-} \end{bmatrix}$ and $\left[E_l(h_l)\right]^{-1} = \begin{bmatrix} \mathcal{E}_l^{-} & 0 \\ 0 & \mathcal{E}_l^{+} \end{bmatrix}$. Here $\mathcal{E}_l^{+} = E_l^{+}(h_l)$ and $\mathcal{E}_l^{-} = E_l^{-}(h_l)$ are both 2 x 2 diagonal matrices given in Equation (4.19) above.

Equation (4.29b) will be used to define the stiffness matrix sequentially, starting from the bottom semi-infinite layer, where $l = N$. For Rayleigh waves, the waves are surface waves with exponentially decaying amplitudes, and thus $C_N^{-} = 0$. Applying Equation (4.28), with $l = N$:

$$\begin{bmatrix} \boldsymbol{I} \\ \boldsymbol{S}_N \end{bmatrix} \tilde{\boldsymbol{U}}_N = \begin{pmatrix} \tilde{\boldsymbol{U}}_N \\ \tilde{\boldsymbol{\Sigma}}_N \end{pmatrix} = \begin{pmatrix} \boldsymbol{v}_N(\boldsymbol{0}) \\ \tau_N(\boldsymbol{0}) \end{pmatrix} = \begin{bmatrix} \boldsymbol{T}_N^1 & \boldsymbol{T}_N^2 \\ \boldsymbol{T}_N^3 & \boldsymbol{T}_N^4 \end{bmatrix} \begin{pmatrix} \boldsymbol{C}_N^+ \\ \boldsymbol{0} \end{pmatrix} \tag{4.30}$$

gives $\left[\boldsymbol{S}_N\right] = \left[\boldsymbol{T}_N^3\right]\left[\boldsymbol{T}_N^1\right]^{-1}$, the stiffness of the semi-infinite bottom layer, the half-space. Using Equation (4.29b), with $\boldsymbol{l = N-1}$, the stiffness matrix for the layer right above would be computed directly from the Thomson-Haskell Propagator matrix equation:

$$\begin{bmatrix} \boldsymbol{I} \\ \boldsymbol{S}_l \end{bmatrix} \tilde{\boldsymbol{U}}_l = \left[\boldsymbol{T}_l\right] \begin{bmatrix} \boldsymbol{\mathcal{E}}_l^- & \boldsymbol{0} \\ \boldsymbol{0} & \boldsymbol{\mathcal{E}}_l^+ \end{bmatrix} \left[\boldsymbol{T}_l\right]^{-1} \begin{bmatrix} \boldsymbol{I} \\ \boldsymbol{S}_{l+1} \end{bmatrix} \tilde{\boldsymbol{U}}_{l+1} \tag{4.31}$$

Direct substitution in the calculation would involve adding and subtracting expressions involving the exponential terms in $\boldsymbol{\mathcal{E}}_l^-$ and $\boldsymbol{\mathcal{E}}_l^+$. As noted above for Equation (4.19), when $\boldsymbol{c < \alpha_l}$ or $\boldsymbol{c < \beta_l}$, or both, one or all of the exponents in the terms $\boldsymbol{\mathcal{E}}_l^-$ and $\boldsymbol{\mathcal{E}}_l^+$ would be real, making them respectively exponentially increasing and decreasing. It is the additions and subtractions of these exponentially increasing and exponentially decreasing terms together that makes the terms numerically unstable, with possible overflow and underflow, especially when the frequency is high and/or the layer is thick.

Liu (2010) proposed a step to avoid such numerical problem. From Equations (4.22), (4.25) and (4.28)

$$\begin{bmatrix} \boldsymbol{I} \\ \boldsymbol{S}_l \end{bmatrix} \tilde{\boldsymbol{U}}_l = \begin{pmatrix} \tilde{\boldsymbol{U}}_l \\ \tilde{\boldsymbol{\Sigma}}_l \end{pmatrix} = \begin{pmatrix} \tilde{\boldsymbol{u}}_l(\boldsymbol{0}) \\ \tilde{\boldsymbol{\sigma}}_l(\boldsymbol{0}) \end{pmatrix} = \left[\boldsymbol{T}_l\right] \begin{pmatrix} \tilde{\boldsymbol{C}}_l^+ \\ \tilde{\boldsymbol{C}}_l^- \end{pmatrix} \tag{4.32a}$$

Rewrite it in terms of an intermediate 'auxiliary' stiffness matrix $\left[\bar{\boldsymbol{S}}_l\right]$, and call $\bar{\boldsymbol{U}}_l = \tilde{\boldsymbol{C}}_l^+$:

$$\begin{bmatrix} \boldsymbol{I} \\ \boldsymbol{S}_l \end{bmatrix} \tilde{\boldsymbol{U}}_l = \left[\boldsymbol{T}_l\right] \begin{bmatrix} \boldsymbol{I} \\ \bar{\boldsymbol{S}}_l \end{bmatrix} \bar{\boldsymbol{U}}_l \ , \tag{4.32b}$$

where from (4.31)

$$\begin{bmatrix} \boldsymbol{I} \\ \bar{\boldsymbol{S}}_l \end{bmatrix} \bar{\boldsymbol{U}}_l = \begin{bmatrix} \boldsymbol{\mathcal{E}}_l^- & \boldsymbol{0} \\ \boldsymbol{0} & \boldsymbol{\mathcal{E}}_l^+ \end{bmatrix} \underbrace{\left[\boldsymbol{T}_l\right]^{-1} \begin{bmatrix} \boldsymbol{I} \\ \boldsymbol{S}_{l+1} \end{bmatrix}} \tilde{\boldsymbol{U}}_{l+1}$$

to be rewritten as

$$= \begin{bmatrix} \boldsymbol{\mathcal{E}}_l^- & \boldsymbol{0} \\ \boldsymbol{0} & \boldsymbol{\mathcal{E}}_l^+ \end{bmatrix} \begin{bmatrix} \boldsymbol{P}_l^1 \\ \boldsymbol{P}_l^2 \end{bmatrix} \tilde{\boldsymbol{U}}_{l+1} = \begin{bmatrix} \boldsymbol{\mathcal{E}}_l^- \boldsymbol{P}_l^1 \\ \boldsymbol{\mathcal{E}}_l^+ \boldsymbol{P}_l^2 \end{bmatrix} \tilde{\boldsymbol{U}}_{l+1} \tag{4.33}$$

where

$$\left[\boldsymbol{P}_l\right] = \begin{bmatrix} \boldsymbol{P}_l^1 \\ \boldsymbol{P}_l^2 \end{bmatrix} = \left[\boldsymbol{T}_l\right]^{-1} \begin{bmatrix} \boldsymbol{I} \\ \boldsymbol{S}_{l+1} \end{bmatrix} \tag{4.34}$$

so that the intermediate Stiffness matrix is defined in terms of $\left[\boldsymbol{S}_{l+1}\right]$, the Stiffness matrix of the layer below. Solving for $\bar{\boldsymbol{S}}_l$ gives (Liu, 2010):

$$\bar{\boldsymbol{S}}_l = \left[\boldsymbol{E}_l^+\right]\left[\boldsymbol{P}_l^2\right]\left[\boldsymbol{P}_l^1\right]^{-1}\left[\boldsymbol{E}_l^+\right] \tag{4.35}$$

Note that the intermediate stiffness matrix $\bar{\boldsymbol{S}}_l$ involves only the diagonal matrix term $\left[\boldsymbol{E}_l^+\right]$ and not $\left[\boldsymbol{E}_l^-\right]$. This has the numerical advantage that should the waves in the layer be surface-wave type and non-harmonic $\left(\boldsymbol{c} < \boldsymbol{\alpha} \text{ or } \boldsymbol{c} < \boldsymbol{\beta}\right)$, the terms in $\left[\boldsymbol{E}_l^+\right]$ would be exponentially decaying, and hence would tend to zero, especially when the layer thickness or the wave frequency is large.

With this intermediate step, the intermediate stiffness matrix $\left[\bar{\boldsymbol{S}}_{N-1}\right]$ can be found from Equation (4.35), without any numerical problem. Using equation (4.32), this in turn gives the stiffness matrix $\left[\boldsymbol{S}_{N-1}\right]$ in the same layer. This procedure can be repeated until the top layer is reached.

At the top layer, Liu (2010) pointed out that by imposing $\left|\boldsymbol{S}_1\right| = \boldsymbol{det}\left[\boldsymbol{S}_1\right] = \boldsymbol{0}$, this becomes a new efficient procedure to estimate the root of the phase velocity of the Rayleigh waves. Also, with the stiffness matrix known here, one can also assume a displacement value of $\boldsymbol{W}_0 = \boldsymbol{W}(\boldsymbol{z})\big|_{z=0} = \boldsymbol{1}$ (to be scaled later). The zero-determinant equation $\left|\boldsymbol{S}_1\right| = \boldsymbol{det}\left[\boldsymbol{S}_1\right] = \boldsymbol{0}$ also gives the ratio $\boldsymbol{U}_0/\boldsymbol{W}_0$, so that the horizontal motion $\boldsymbol{U}_0$ at the surface is also known. One can then proceed down the layer to get the displacement state vector, Equation (4.28), at each layer. The motions everywhere are thus computed.

The case of Love surface waves proceeds the same way, except the matrices are half the size, namely 2 x 2 instead of 4 x 4, and scalar instead of 2 x 2 matrices.

In summary, the use of the intermediate stiffness matrix avoided the numerical problem encountered by the original Thomson-Haskell propagator matrix for Rayleigh waves.

IV.4 The New Numerical Implementation for P and SV Body Waves

The procedure for P and SV body waves follows the same concept, but is applied in a different order. It is different from Rayleigh waves because, instead of surface waves at the bottom semi-infinite layer, we now have incident P or SV body waves coming from the layers below. We thus will not be able to start by writing down the stiffness matrix $\left[\boldsymbol{S}_N\right]$ of the bottom layer, as in the case of Rayleigh waves. Instead, we will start from the top layer.

At each layer $\boldsymbol{l = 1,\ 2,\ \ldots,\ N}$, from Equation (4.21) above:

$$\begin{pmatrix}\tilde{u}_l(z)\\ \tilde{\sigma}_l(z)\end{pmatrix}=\begin{pmatrix}\tilde{u}_l(x,z)\\ \tilde{\sigma}_l(x,z)\end{pmatrix}\Bigg|_{x=0}=\begin{bmatrix}T_l^1 & T_l^2\\ T_l^3 & T_l^4\end{bmatrix}\begin{bmatrix}E_l^+(z) & 0\\ 0 & E_l^-(z)\end{bmatrix}\begin{pmatrix}\tilde{C}_l^+\\ \tilde{C}_l^-\end{pmatrix} \qquad \text{(4.21) above}$$

$$= \left[T_l\right]\left[E_l(z)\right]\left(\tilde{C}_l\right)$$

Rewrite it as:

$$\begin{pmatrix}\tilde{u}_l(z)\\ \tilde{\sigma}_l(z)\end{pmatrix}=\begin{bmatrix}\Gamma_l^1 & \Gamma_l^2\\ \Gamma_l^3 & \Gamma_l^4\end{bmatrix}\begin{bmatrix}E_l^-(z) & 0\\ 0 & E_l^+(z)\end{bmatrix}\begin{pmatrix}\tilde{C}_l^-\\ \tilde{C}_l^+\end{pmatrix} \qquad (4.35a)$$

$$=\left[\Gamma_l\right]\left[E_l(z)\right]^{-1}\left(\tilde{C}_l^{\mp}\right)$$

where $\left(\tilde{C}_l^{\mp}\right)=\begin{pmatrix}\tilde{C}_l^-\\ \tilde{C}_l^+\end{pmatrix}$ is obtained by switching the order of the terms $\tilde{C}_l^+$ and $\tilde{C}_l^-$ in the coefficient matrix, so that the 2 x 2 sub-matrix $\boldsymbol{E_l^+(z)}$ and $\boldsymbol{E_l^-(z)}$ are also switched in the middle matrix $\left[\boldsymbol{E_l(z)}\right]$, and $\left[\Gamma_l\right]$ is the new transformation matrix given by

$$\left[\Gamma_l\right]=\begin{bmatrix}\Gamma_l^1 & \Gamma_l^2\\ \Gamma_l^3 & \Gamma_l^4\end{bmatrix}=\begin{bmatrix}T_l^2 & T_l^1\\ T_l^4 & T_l^3\end{bmatrix} \qquad (4.35b)$$

obtained by switching the 3^{rd} and 4^{th} columns with the 1^{st} and 2^{nd} columns in the $\left[\boldsymbol{T_l}\right]$ matrix. With this new matrix, $\left[\Gamma_l\right]$, the displacement-stress state vector at the top $\boldsymbol{(z=0)}$ and bottom $\boldsymbol{(z=h_l)}$ of the $\boldsymbol{l^{th}}$ layer is given by:

$$\begin{pmatrix}\tilde{u}_l(0)\\ \tilde{\sigma}_l(0)\end{pmatrix}=\left[\Gamma_l\right]\left[E_l(z)\right]^{-1}\Big|_{z=0}\left(\tilde{C}_l^{\mp}\right)=\left[\Gamma_l\right]\left(\tilde{C}_l^{\mp}\right) \qquad (4.36a)$$

$$\begin{pmatrix}\tilde{u}_l(h_l)\\ \tilde{\sigma}_l(h_l)\end{pmatrix}=\left[\Gamma_l\right]\left[E_l(h_l)\right]^{-1}\left(\tilde{C}_l^{\mp}\right)$$

so that
$$\begin{pmatrix} \tilde{u}_l(h_l) \\ \tilde{\sigma}_l(h_l) \end{pmatrix} = \left[\Gamma_l\right]\left[E_l(h_l)\right]^{-1}\left[\Gamma_l\right]^{-1}\begin{pmatrix} \tilde{u}_l(0) \\ \tilde{\sigma}_l(0) \end{pmatrix} \tag{4.36b}$$

or, in terms of the state vectors defined at each layer in Equation (4.25) above:

$$\begin{pmatrix} \tilde{U}_{l+1} \\ \tilde{\Sigma}_{l+1} \end{pmatrix} = \left[\Gamma_l\right]\begin{bmatrix} \mathcal{E}_l^- & 0 \\ 0 & \mathcal{E}_l^+ \end{bmatrix}\left[\Gamma_l\right]^{-1}\begin{pmatrix} \tilde{U}_l \\ \tilde{\Sigma}_l \end{pmatrix} \tag{4.37a}$$

where, with $\left[E_l(h_l)\right] = \begin{bmatrix} \mathcal{E}_l^+ & 0 \\ 0 & \mathcal{E}_l^- \end{bmatrix}$, it follows that $\left[E_l(h_l)\right]^{-1} = \begin{bmatrix} \mathcal{E}_l^- & 0 \\ 0 & \mathcal{E}_l^+ \end{bmatrix}$. Here $\mathcal{E}_l^+ = E_l^+(h_l)$ and $\mathcal{E}_l^- = E_l^-(h_l)$ are both 2 x 2 matrices given in Equation (4.19) above.

In terms of the stiffness matrix S_l, namely, from Equation (4.28), $\left(\tilde{\Sigma}_l\right) = \left[S_l\right]\left(\tilde{U}_l\right)$:

$$\begin{bmatrix} I \\ S_{l+1} \end{bmatrix}\tilde{U}_{l+1} = \left[\Gamma_l\right]\begin{bmatrix} \mathcal{E}_l^- & 0 \\ 0 & \mathcal{E}_l^+ \end{bmatrix}\left[\Gamma_l\right]^{-1}\begin{bmatrix} I \\ S_l \end{bmatrix}\tilde{U}_l \tag{4.37b}$$

Equation (4.37b) is in the same form as Equation (4.29b) for Rayleigh waves, which goes from bottom up, expressing $\tilde{U}_l$ in terms of $\tilde{U}_{l+1}$, except we are now in the opposite order, going from top down, expressing $\tilde{U}_{l+1}$ in terms of $\tilde{U}_l$.

Equation (4.37b) will be used to define the stiffness matrix starting from the surface of the top layer. As in the case of Equation (4.29b) for Rayleigh waves, introduce in Equation (4.37b) a new (different) intermediate 'auxiliary' stiffness matrix $\left[\underline{S}_l\right]$, and a new auxiliary displacement vector $\underline{U}_l$ can be defined as:

$$\begin{bmatrix} I \\ S_{l+1} \end{bmatrix}\tilde{U}_{l+1} = \left[\Gamma_l\right]\begin{bmatrix} I \\ \underline{S}_l \end{bmatrix}\underline{U}_l \ , \tag{4.38}$$

where
$$\begin{bmatrix} I \\ \underline{S}_l \end{bmatrix}\underline{U}_l = \begin{bmatrix} \mathcal{E}_l^- & 0 \\ 0 & \mathcal{E}_l^+ \end{bmatrix}\underbrace{\left[\Gamma_l\right]^{-1}\begin{bmatrix} I \\ S_l \end{bmatrix}}\tilde{U}_l$$

to be rewritten as
$$= \begin{bmatrix} \mathcal{E}_l^- & 0 \\ 0 & \mathcal{E}_l^+ \end{bmatrix}\begin{bmatrix} Q_l^1 \\ Q_l^2 \end{bmatrix}\tilde{U}_l = \begin{bmatrix} \mathcal{E}_l^- Q_l^1 \\ \mathcal{E}_l^+ Q_l^2 \end{bmatrix}\tilde{U}_l \tag{4.39}$$

where $$\left[\boldsymbol{Q}_l\right]=\begin{bmatrix}\boldsymbol{Q}_l^1\\ \boldsymbol{Q}_l^2\end{bmatrix}=\left[\boldsymbol{\Gamma}_l\right]^{-1}\begin{bmatrix}\boldsymbol{I}\\ \boldsymbol{S}_l\end{bmatrix} \tag{4.40}$$

The intermediate stiffness matrix $\left[\underline{\boldsymbol{S}}_l\right]$ is thus written in terms of the stiffness matrix $\left[\boldsymbol{S}_l\right]$ of the same layer. Solving for $\underline{\boldsymbol{S}}_l$ gives, as in Equation (4.35) for the case of Rayleigh waves:

$$\underline{\boldsymbol{S}}_l=\left[\boldsymbol{\mathcal{E}}_l^+\right]\left[\boldsymbol{Q}_l^2\right]\left[\boldsymbol{Q}_l^1\right]^{-1}\left[\boldsymbol{\mathcal{E}}_l^+\right] \tag{4.41}$$

Note that again the intermediate stiffness matrix $\underline{\boldsymbol{S}}_l$ involves only the matrix term $\left[\boldsymbol{\mathcal{E}}_l^+\right]$ and not $\left[\boldsymbol{\mathcal{E}}_l^-\right]$. As stated above, the terms in $\left[\boldsymbol{\mathcal{E}}_l^+\right]$ would only be harmonic, or be exponentially decaying, which would tend to zero, especially when the layer thickness or the wave frequency is large. Using equation (4.38), this in turn gives the stiffness matrix $\left[\boldsymbol{S}_{l+1}\right]$ in the layer. This procedure can be repeated until the bottom semi-infinite layer is reached.

The case of incident SH body waves proceeds the same way, except the matrices are half the size, namely 2 x 2 instead of 4 x 4, and scalar instead of 2 x 2 matrices.

In summary, the use of the intermediate stiffness matrix avoids the numerical problem encountered by the original Thomson-Haskell propagator matrix for P and SV body waves.

V. Love and SH Body Wave Mode Shapes

Figure I.1 in section I above shows the computed phase velocities for 5 modes of Love waves (dashed lines) and 5 modes of Rayleigh waves (solid lines) at the Imperial Valley El Centro 6-layered media. With the modified Thomson-Haskell propagator matrix defined in Section IV above, the relative amplitudes can now be computed for each mode of the Love waves for each frequency where the waves exist at each layer of the half-space. Assuming the displacement amplitude to be one at the half-space surface.

The next sub-section will be a description of the Love Waves mode #1 to mode #5, the five modes for which the calculations were made to obtain the phase velocities $\boldsymbol{c = c(T)}$ for a range of periods starting from 15sec down to 0.04sec.This is followed by another sub-section of the mode shapes resulting from body SH waves for a given incident angle. This will be taken to be a "6^{th} mode" of waves to be included in the generation of synthetic translational motions in the (anti-plane, SH) transverse direction.

A complete set of graphs of mode shapes for all the periods of all five modes of Love waves and body SH waves for a selected incident angle are given in Appendix A at the end of this report.

V.1 Love Waves Mode #1 to Mode #5

Mode #1 has phase velocities for all 91 periods in the range from 15 sec down to 0.04 sec. The Thomson-Haskell computation gives the mode shapes of the Mode#1 Love waves in the same wide period range. Figure V.1 shows the plots of such Love wave mode shape amplitudes at four selected periods: $\boldsymbol{T = 5,\ 1.0,\ 0.5,\ \text{and}\ 0.1\ s}$.

As stated above, the amplitude of the mode shape is normalized to be one at the surface of the half-space, so that the mode shape values are the scaling factors or transfer function values of the waves along different depths from the half-space surface for mode #1 waves. Each graph shows the mode shape amplitudes versus the distance *z*, which is the depth in kilometers below the half-space surface.

As expected for Mode #1 mode shapes, all curves that started with unit amplitude at $\boldsymbol{z = 0}$, at the surface, stay positive all the way, and finally decay to zero down below. The waves at long periods (short frequencies) decay slower than the waves at short periods (high frequencies). Note that the amplitudes stay below unity all the way.

As an example, the mode shape for the waves at $\boldsymbol{T = 5\text{sec}\ \left(0.2hz\right)}$ period in the top-left graph decays slowly and stays above zero all the way down to $\boldsymbol{z = 6km}$, which is just inside the semi-infinite half-space medium, the 6th layer in the model, where $\boldsymbol{z > 5.58km}$. The mode shape for the waves at $\boldsymbol{T = 1\text{sec}\ \left(1.0hz\right)}$ period in the top-right graph decays a bit faster and stays above zero only down to $\boldsymbol{z \sim 1.5km}$, which is just inside the 3rd layer in the model, where $\boldsymbol{0.73 \le z \le 1.71km}$. The mode shape for the waves at $\boldsymbol{T = 0.5\text{sec}\ \left(2.0hz\right)}$ period in the bottom-left graph now decays much faster and stays above zero only down to $\boldsymbol{z \sim 0.7km}$, which is close to the bottom of the 2nd layer in the model, where $\boldsymbol{0.18 \le z \le 0.73km}$. Finally, the mode shape for the waves at $\boldsymbol{T = 0.1\text{sec}\ \left(10.0hz\right)}$ period in the bottom-left graph now decays so fast that it stays above zero only down to $\boldsymbol{z \sim 0.2km}$, which is just inside the 2nd layer in the model, with the 1st layer in the range $\boldsymbol{0.0 \le z \le 0.18km}$.

Figure V.1 Mode#1 Love Waves Mode Shapes at $T = 5,\ 1.0,\ 0.5,$ and $0.1\ s$

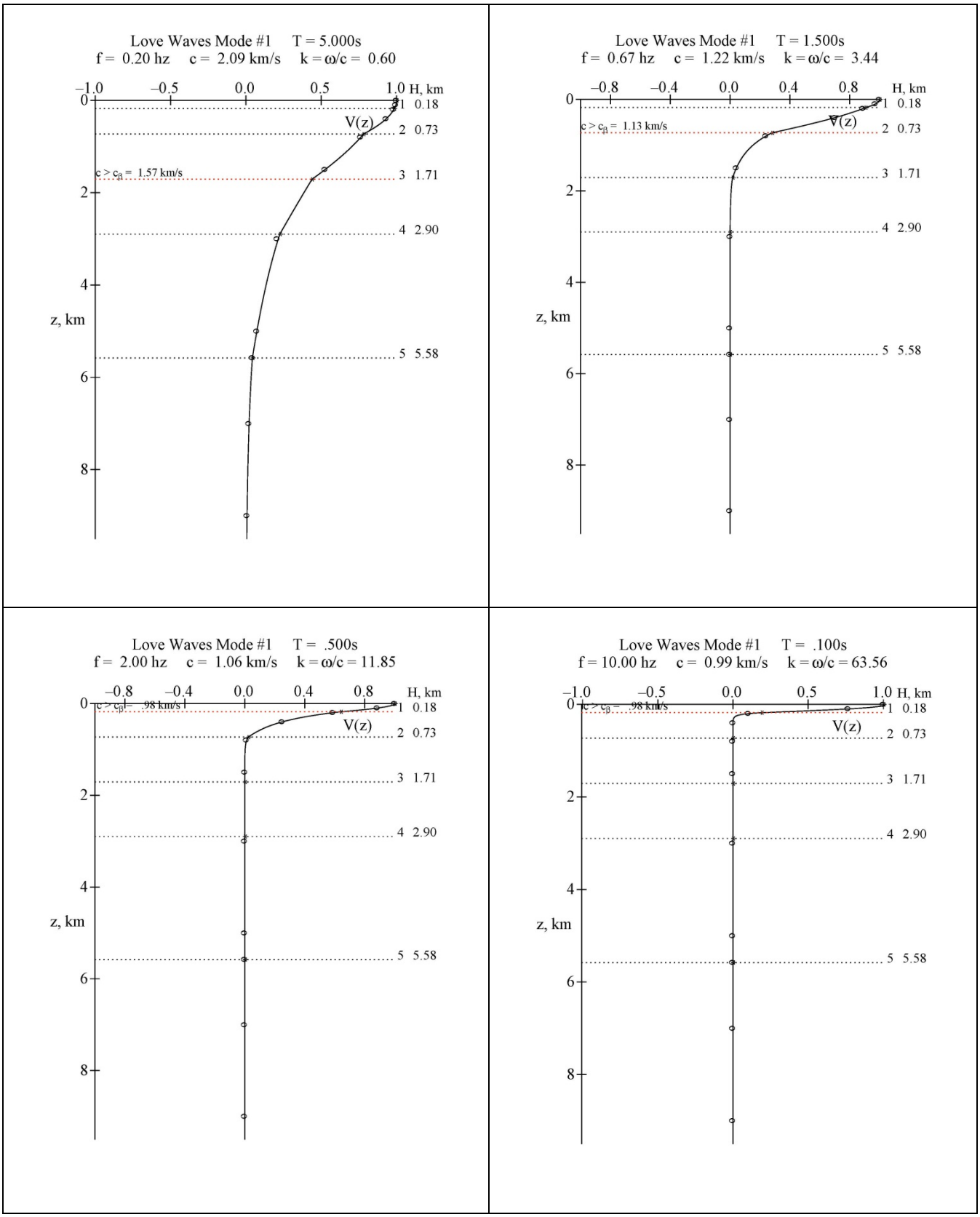

The mode shapes for all 91 periods of Mode #1 of Love Waves can be found in Appendix A-1.

Mode #2 has phase velocities for all 70 periods in the range from 3.8 sec down to 0.04 sec. The Thomson-Haskell computation thus gives the mode shapes of the Mode#2 Love waves in the same wide period range. Figure V.2 shows the plots of such Love wave mode shape amplitudes at four selected periods: $\boldsymbol{T = 3.8,\ 1.0,\ 0.3,\ \text{and } 0.1\ s}$.

Again, as for Mode #1, the amplitude of the mode shape is normalized to one at the surface of the half-space, so that the mode shape values are again the scaling factors of transfer function values of the waves along the depth for mode #2 waves. Each graph shows the mode shape amplitudes versus the distance z, measured as depth in kilometers below the half-space surface.

The mode #2 mode shape starts with unit amplitude at $\boldsymbol{z = 0}$ on the surface. Unlike Mode #1, which started positive and stayed positive before decaying to zero, the mode #2 will decay to negative values at some depth and stay negative before decaying to zero. The shape at long periods (short frequencies) decays slower than the shape at short periods (high frequencies). Note that at some periods, the mode shape amplitudes can go below -1.0 in the negative range, *resulting in larger amplitudes of motion below the surface.* As an example, the mode shape for the waves at $\boldsymbol{T = 3.6\,\text{sec}\ \left(0.28hz\right)}$ period in the top-left graph decays slowly, turns negative in the 3rd layer, $\boldsymbol{0.73 \le z \le 1.71km}$, at around $\boldsymbol{z \sim 1.5km}$, reaching a negative minimum (no more than -0.5) in the 4th layer around $\boldsymbol{z \sim 3km}$. It stays negative all the way down beyond $\boldsymbol{z = 10km}$, outside the range of the plots, way below in the half-space medium, the 6thlayer in the model, where $\boldsymbol{z > 5.58km}$.

Figure V.2 Mode#2 Love Waves Mode Shapes at ***T* = 3.6, 1.0, 0.3, and 0.1 *s***

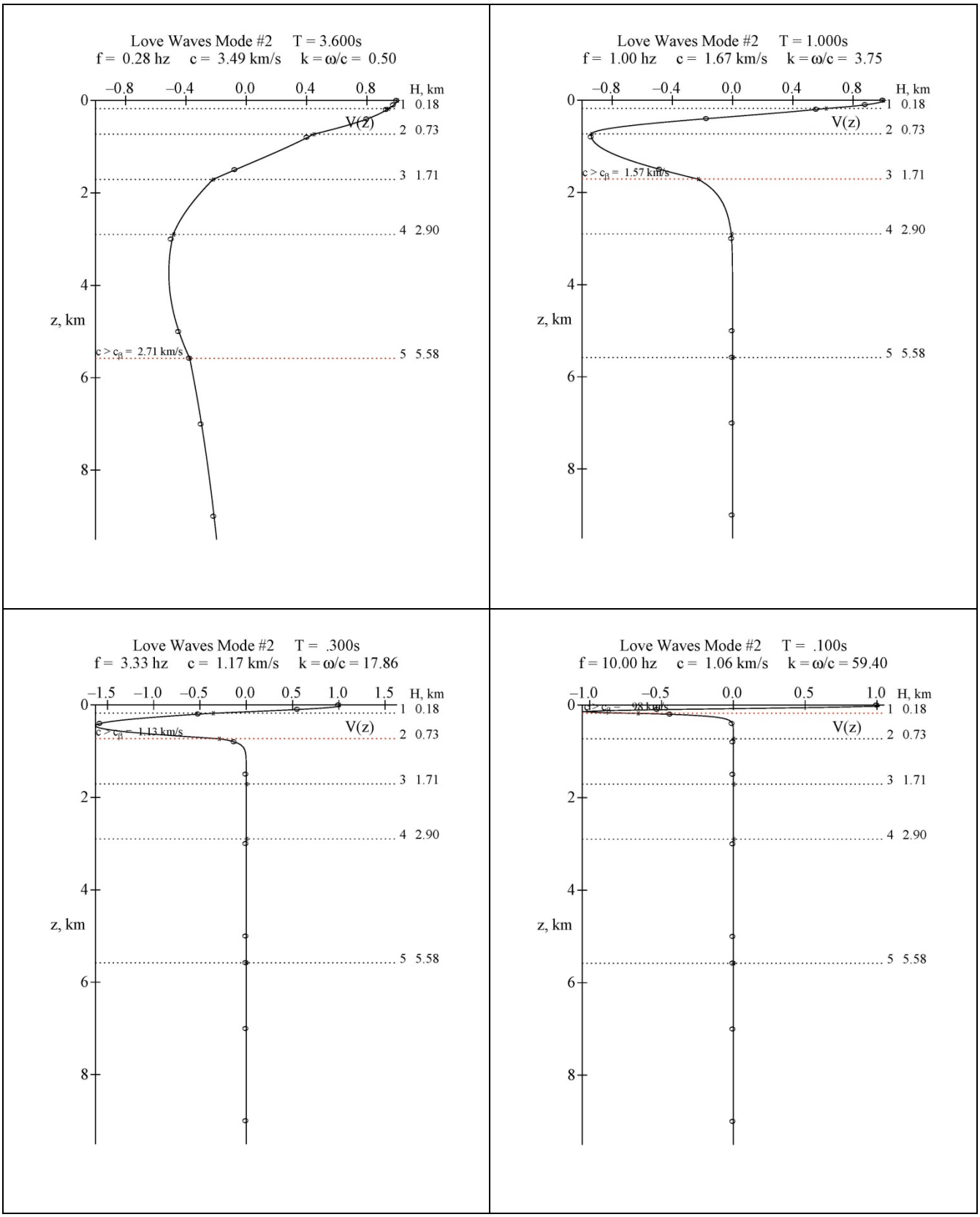

The mode shape for the waves at $\boldsymbol{T = 1\text{sec}\ \ (1.0hz)}$ period, in the top-right graph, decays a bit faster to negative values around $\boldsymbol{z \sim 0.5km}$, in the 2nd layer, $\boldsymbol{0.18 \le z \le 0.73km}$. It stays negative, with the negative minimum (close to -1.0) right at the start of the 3rd layer at $\boldsymbol{z = 0.73km}$, then decays to zero right at the interface of the 4th and 5th layer at $\boldsymbol{z = 2.90km}$.

The mode shape for the waves at $\boldsymbol{T = 0.3\text{sec}\ \ (3.33hz)}$ period, shown in the bottom-left graph, now decays much faster to negative values around $\boldsymbol{z \sim 0.15km}$ in the top 1stlayer $\boldsymbol{0.0 \le z \le 0.18km}$. It stays negative, reaching a negative minimum below -1.5, around $\boldsymbol{z \sim 0.5km}$ in the 2nd layer, $\boldsymbol{0.18 \le z \le 0.73km}$. It then decays to zero right at the start of the 3rd layer, $\boldsymbol{0.73 \le z \le 1.71km}$, before $\boldsymbol{z \sim 0.8km}$.

Finally, the mode shape for the waves at $\boldsymbol{T = 0.1\text{sec}\ \ (10.0hz)}$ period in the bottom-right graph decays so fast that it goes negative right in the top 1st layer, $\boldsymbol{0.0 \le z \le 0.18km}$, reaches its negative minimum close to the interface of the 1st and 2nd layers at $\boldsymbol{z = 0.8km}$ and immediately, decays to zero in the same 2nd layer. The mode shapes for all 70 periods of Mode#2 of Love waves can be found in Appendix A-2.

Mode #3 has phase velocities for all 61 periods in the range from 2.0 sec down to 0.04 sec. The Thomson-Haskell computation gives the mode shapes of the Mode#3 of Love waves in the same period range. Figure V.3 shows the plots of mode shape amplitudes at four selected periods: $\boldsymbol{T = 2.0,\ 0.75,\ 0.2,\ \text{and}\ 0.075\ s}$. The mode shapes have the right feature expected for the 3rd mode, namely, all graphs cross the zero line twice before decaying to zero at some depth. The mode shapes for all 61 periods of Mode #3 Love Waves are found in Appendix A-3. Finally the mode shapes for all available periods of Mode #4 and Mode #5 are respectively plotted in Appendices A-4 and A-5.

Figure V.3 Mode#3 Love Waves Mode Shapes at $T = 2.0,\ 0.75,\ 0.2,$ and $0.075\ s$

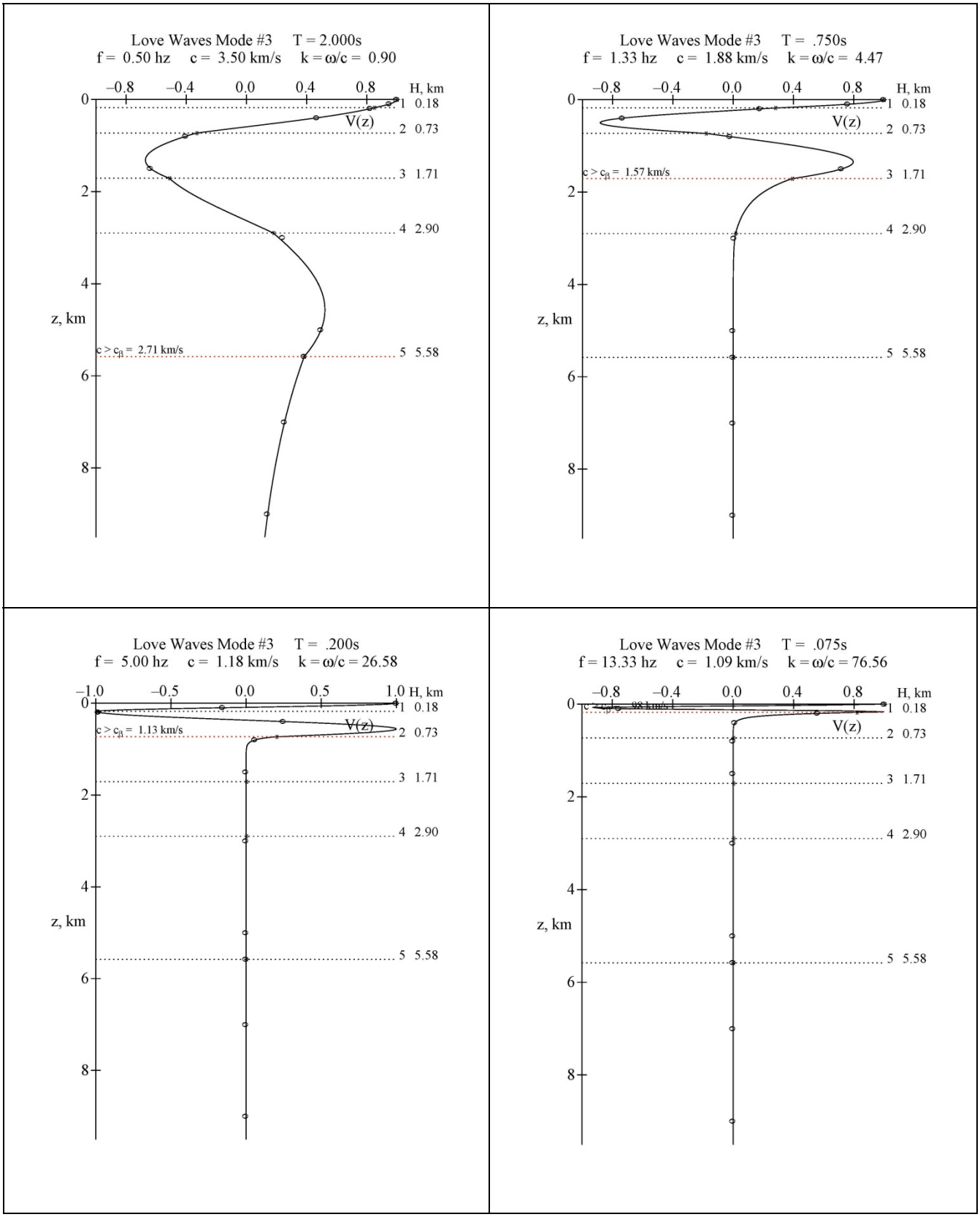

V.2 Body SH Waves with a Given Incident Angle

Figure V.4 shows the plots of SH body wave mode shape amplitudes at four selected periods: $T = 5.0,\ 1.5,\ 0.50,\ \text{and}\ 0.15\ s$, assuming a given angle of incidence of body SH waves at $\gamma = 85^o$ with respect to the vertical direction from the bottom semi-infinite 6th layer. Such mode shapes can be computed at all 91 periods in the range from $T = 15.0\ s$ down to $T = 0.04\ s$.

This corresponds to an almost horizontal angle of incidence. The actual angle of incidence will be different in each case, and will depend on

1) the actual location and focal depth of the earthquake source,
2) the actual location of the recording site and its epicentral distance from the source.

The next two sections will illustrate two cases where either

1) the site is in the near-field of the source, with hypocentral distance $D \approx 10km$, or
2) the site is in the far-field from the source, with hypocentral distance $D \approx 40km$.

In each case, a ray path is traced so that the ray will take the shortest time to travel from the source to the site, and as the next section shows, each ray will have an angle of incidence different, but close to the angle of incidence of body SH waves at $\gamma = 85^o$, selected for this example.

In each case, the mode shapes are normalized to have amplitude one at the half-space surface of $z = 0$. At depth, the body SH waves will then all have amplitudes that oscillate. Unlike the surface Love waves, these are body waves and hence the mode shape amplitudes will not decay to zero.

The mode shapes for all available periods of body waves from incident SH-waves are plotted in Appendix A-6.

Figure V.4 SH Body Waves at T = 5.0, 1.5, 0.50, and 0.15 s

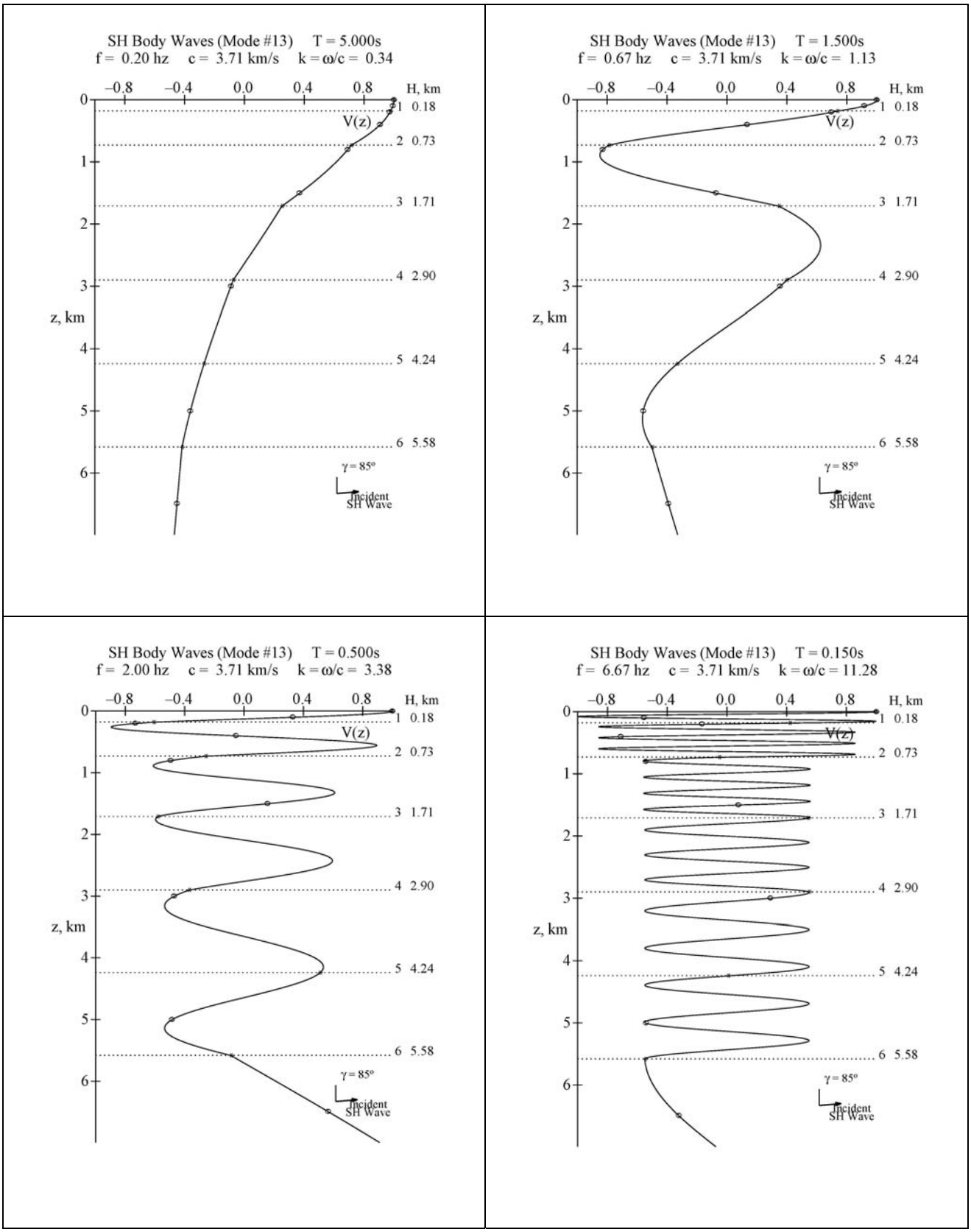

VI. Rayleigh and P and SV Body Wave Mode Shapes

Next we illustrate the mode shapes for the five modes of Rayleigh surface waves. As in the case of Love waves, with the modified Thomson-Haskell propagator matrix defined in Section IV above, the relative amplitudes can now be computed for each mode of the Rayleigh waves for each frequency where the waves exist and in each layer of the half-space. There will now be 2 components of in-plane motions, the horizontal *x*-component and the vertical *z*-component. We will normalize the displacement amplitude of both components with respect to the vertical z-component of motion at the half-space surface.

The next sub-sections will describe the Rayleigh waves mode #1 to mode #5, for the phase velocities $\boldsymbol{c = c(T)}$, in the range of periods starting from 15sec down to 0.04sec. This will be followed by a sub-section of the mode shapes of body P and SV waves for a given incident angle. This will be taken to be the "6^{th} and 7^{th} modes" of waves to be included in the generation of synthetic translational motions in the (in-plane, P and SV) radial and vertical directions. A complete set of figures of mode shapes for all the periods of all five modes of Rayleigh waves and body P and SV waves for a selected incident angle are given in Appendix B at the end of this report.

VI.1 Rayleigh Waves Mode #1 to Mode #5

The mode #1 of Rayleigh waves has phase velocities for all 91 periods from 15 sec down to 0.04 sec. The Thomson-Haskell computation gives the mode shapes of the mode#1 of Rayleigh waves in the same wide period range at every specified point below the surface. Figure VI.1 shows the plots of two components (*x*- and *z*-) of such Rayleigh wave mode amplitudes at four selected periods: $\boldsymbol{T = 5,\ 1.0,\ 0.5,\ \text{and}\ 0.1\ s}$.

The amplitudes of the mode shapes of both components are normalized with respect to the vertical component of motion at the surface of the layered half-space, so that the mode shape values are the scaling factors or transfer function values of the waves at different depths from the half-space surface. Each graph has two components of plots of the mode shape amplitudes versus the distance *z*, measured in kilometers below the half-space surface. Note that at the half-space surface, with the *z*-component of motion $\boldsymbol{W(z)\big|_{z=0} = 1}$, the *x*-component of motion, $\boldsymbol{U(z)\big|_{z=0} = i\gamma W(z)\big|_{z=0} = i\gamma}$, is an imaginary number, where $\boldsymbol{\gamma}$ is a ratio computed from the Haskell algorithm for estimating phase velocities of Rayleigh waves. With this normalization, $\boldsymbol{W(z)}$ will stay real, while $\boldsymbol{U(z)}$ will stay imaginary for all z. Without loss of generality, only the imaginary part of $\boldsymbol{U(z)}$ will be plotted here.

As expected for Mode #1 mode shape, all amplitudes start at $\boldsymbol{z = 0}$, on the surface, maintain the same sign without crossing the zero line, and decay to zero at some depth below the surface. The waves at long periods (short frequencies) decay slower than the waves at short periods (high frequencies).

As an example, the *z*-component of the mode shape for the waves at $\boldsymbol{T = 5\,\text{sec}\ \ (0.2hz)}$ period is shown in the top-left graph of Fig. **VI.1**. It starts with unit amplitude on the surface, decays slowly and stays above zero all the way down to $\boldsymbol{z \sim 3km}$, which is just inside the 5th layer. The (imaginary part of) *x*-component of the mode shape, on the other hand, starts at $\boldsymbol{\sim -1.6}$, and stays negative before decaying to zero around $\boldsymbol{z \sim 5km}$, near the bottom of the 5th layer.

Figure VI.1 Mode#1 of Rayleigh Waves. *x*- and *z*- Mode Shapes at $T = 5,\ 1.0,\ 0.5,$ and $0.1\ s$

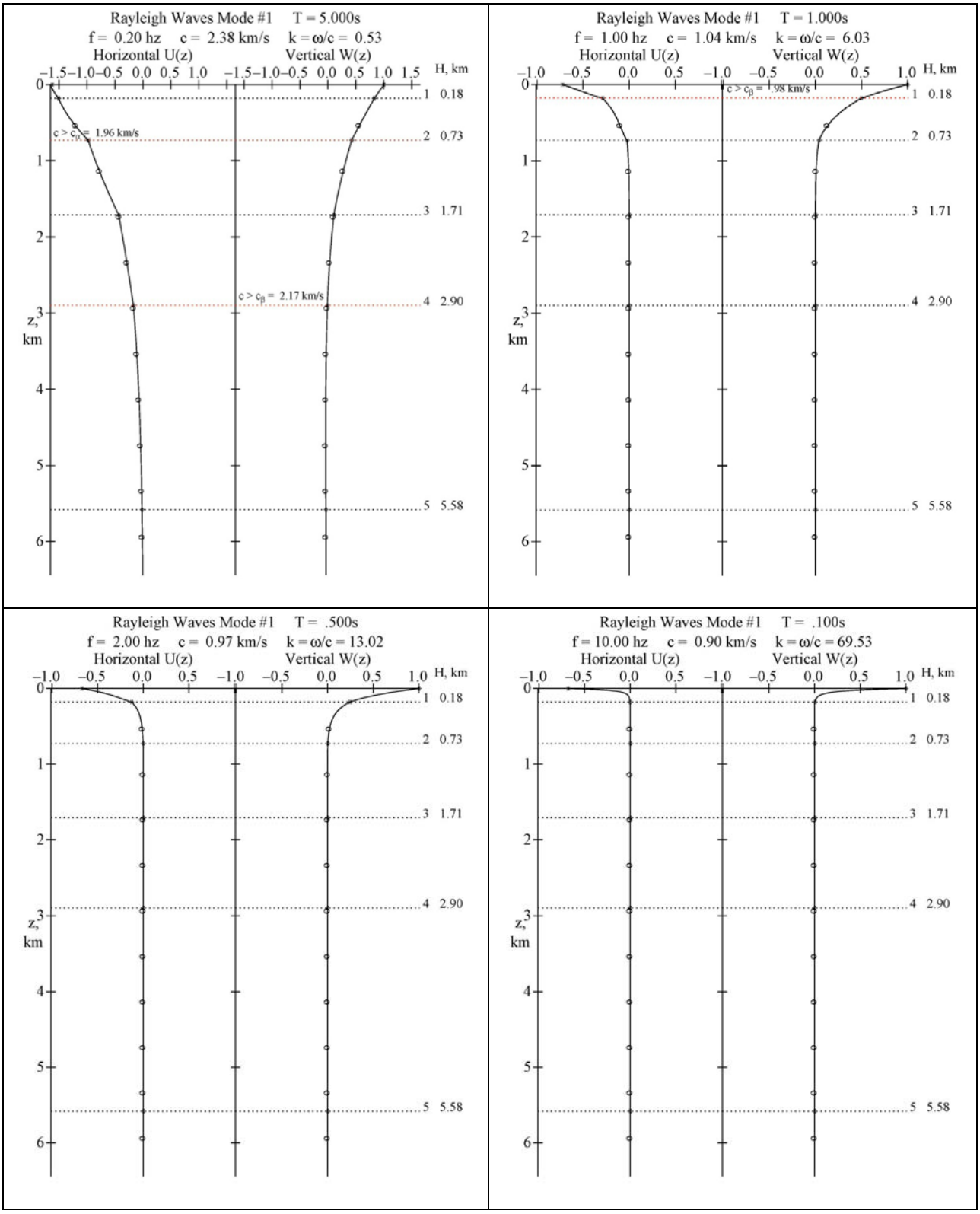

The mode shapes for both components at $T = 1\,\text{sec}$ period $(1.0hz)$ in the top-right graph decay a bit faster to zero around $z \sim 0.75km$, which is just inside the 3rd layer in the model, where $0.73 \le z \le 1.71km$. The mode shapes for the waves at $T = 0.5\,\text{sec}$ $(2.0hz)$ period in the bottom-left graph decay much faster and stay above zero only down to $z \sim 0.5km$, inside the 2nd layer, where $0.18 \le z \le 0.73km$. Finally, the mode shapes for the waves at $T = 0.1\,\text{sec}$ $(10.0hz)$ period, in the bottom-right graph decay so fast that they both decay to zero before $z \sim 0.15km$, which is inside the 1st layer of the model, $0.0 \le z \le 0.18km$.

One interesting difference between this and the Love wave mode shapes is that the amplification factor (normalized mode shape amplitude) can be above one for one or both of the components of motion. The mode shapes for all 91 periods of Mode #1 of Rayleigh Waves can be found in Appendix B-1.

Mode #2 of Rayleigh waves has phase velocities for all 74 periods in the range from 4.6 sec down to 0.04 sec. The Thomson-Haskell computation gives the mode shapes of the Mode#2 in the same wide period range. Figure VI.2 illustrates the plots of both components of Rayleigh wave mode shape amplitudes at four selected periods: $T = 3.0,\ 1.0,\ 0.3,\ \text{and}\ 0.1\ s$. The *z*-component mode shape amplitude is normalized to one at the surface of the half-space, so that the mode shape values again become the scaling factors or transfer function values of the waves along the depth for mode #2 waves. Each graph shows plots of the mode shape amplitudes for both components versus depth in kilometers.

Unlike the Mode #1 mode shapes, the mode #2 shapes will change sign and cross the zero line before decaying to zero at some depth below. The waves at long periods (low frequencies) decay slower than the waves at low periods (high frequencies). Note again that at some periods, the mode shapes go below -1.0 in the negative range, *resulting in higher amplitudes of motion below the surface than at the surface.*

The mode shape for both x- and z- components at $T = 3.0\,\text{sec}$ $(0.33hz)$, shown in the top-left graph, decays slowly. The horizontal x-component starts positive at the top surface, turns negative down below, and reaches a negative maximum amplitude of almost **-8** at or close to the start of the 3rd layer around $z = 0.73km$. The negative z- component starts at the normalized

Figure VI.2 Mode#2 of Rayleigh Waves. *x*- and *z*- Mode Shapes at $T = 3,\ 1,\ 0.3,$ and $0.1\ s$

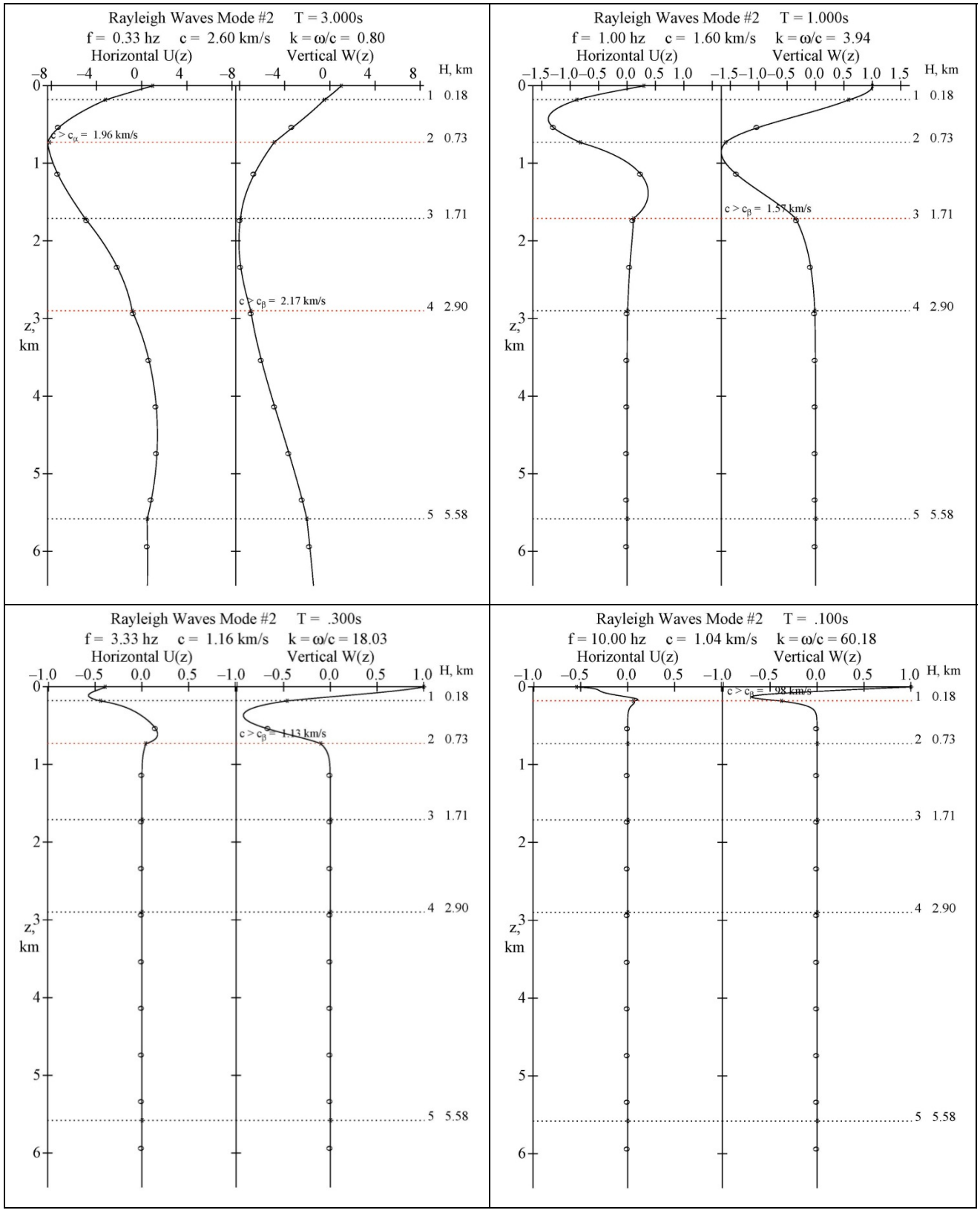

amplitude of 1.0, turns negative in the 1st layer before $z = 0.18km$, and reaches a negative minimum amplitude of almost **-8** right after the start of the 4th layer, beyond $z = 1.71km$. After the negative maxima, both components then gradually oscillate and cross the zero line one more time before decaying to zero right after the start of the bottom of 6th semi-infinite layer, where $z > 5.58km$. Thus mode #2 has amplitudes with magnitudes much greater than one, the normalized amplitude for the z- component at the surface. This can occur for all the modes of Rayleigh waves beyond mode #1.

The mode shapes for all available periods of Modes #2 to Modes #5 of Rayleigh Waves are found respectively in Appendix B-2 through B-5.

VI.2 Body P and SV Waves of a Given Incident Angle

Figure VI.3 shows the plots of P and SV body wave mode shapes at four selected periods: $T = 5.0,\ 1.5,\ 0.50,\ \text{and}\ 0.15\ s$, assuming a given angle of incidence for P- waves at $\gamma = 85^o$ with respect to the vertical direction from the bottom semi-infinite 6th layer. Such mode shapes are available at all 91 periods in the range from $T = 15.0\ s$ down to $T = 0.04\ s$.

As for the body SH- waves, this corresponds to an almost horizontal angle of incidence. The actual angle of incidence used will be different for each case, and will dependent on

3) the actual location and focal depth of the earthquake source,
4) the actual location of the recording site and its epicentral distance from the source.

The next two sections will illustrate two cases where either

3) the site is in the near-field of the source, with hypocentral distance $D \approx 10km$, or
4) the site is in the far-field from the source, with hypocentral distance $D \approx 40km$.

In each case, a ray path is traced so that the ray will take the shortest travel time from source to the site, and as the next section will show, they each will have an angle of incidence close to the angle of incidence of body P waves at $\gamma = 85^o$ selected for this example.

Figure V.3 P and SV Body Wave modes for Incident P Waves at $T = 5.0,\ 1.5,\ 0.50,$ and $0.15\ s$

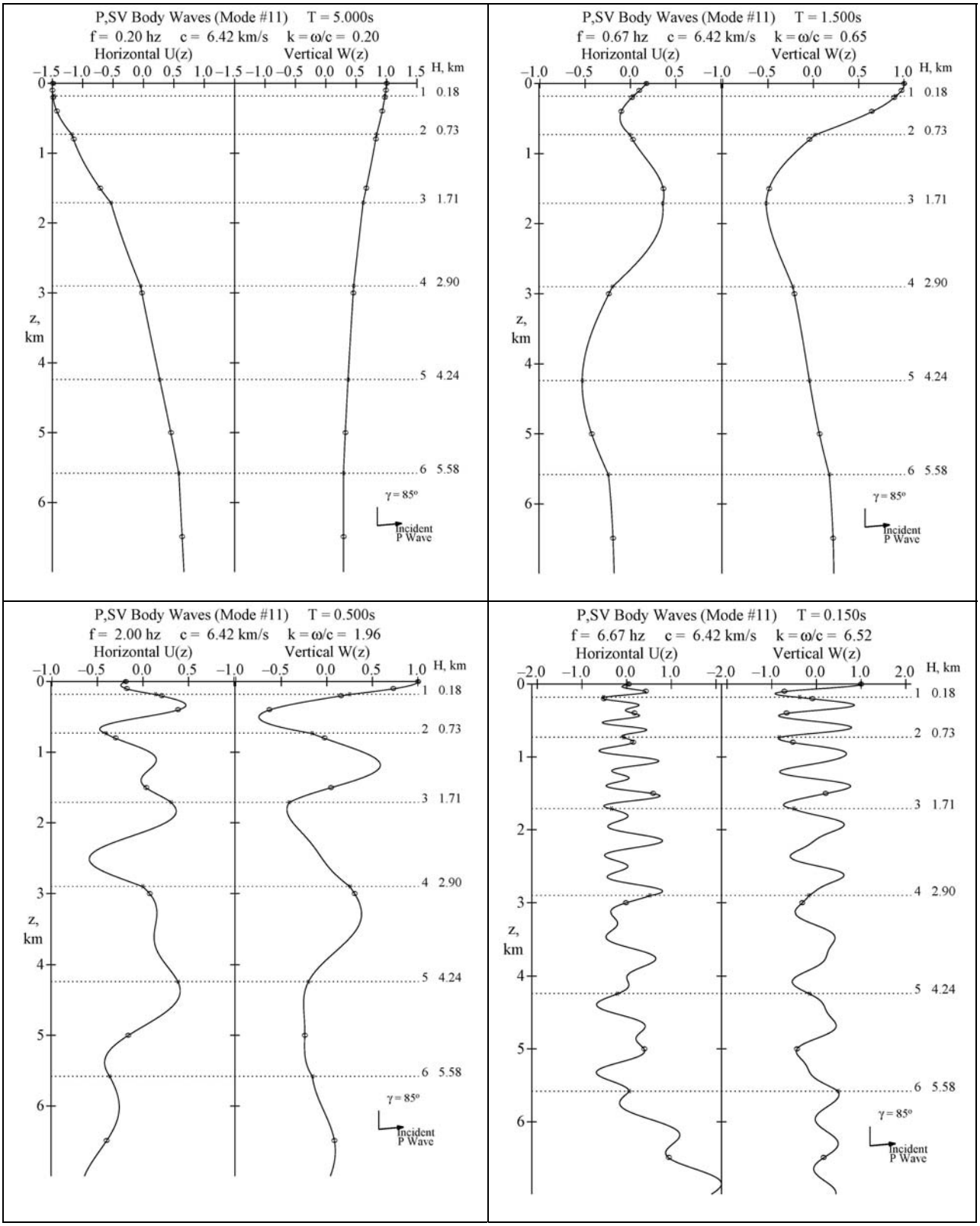

Figure V.4 P and SV Body Wave modes for Incident SV-Waves at $T = 5.0,\ 1.5,\ 0.50,$ and $0.15\ s$

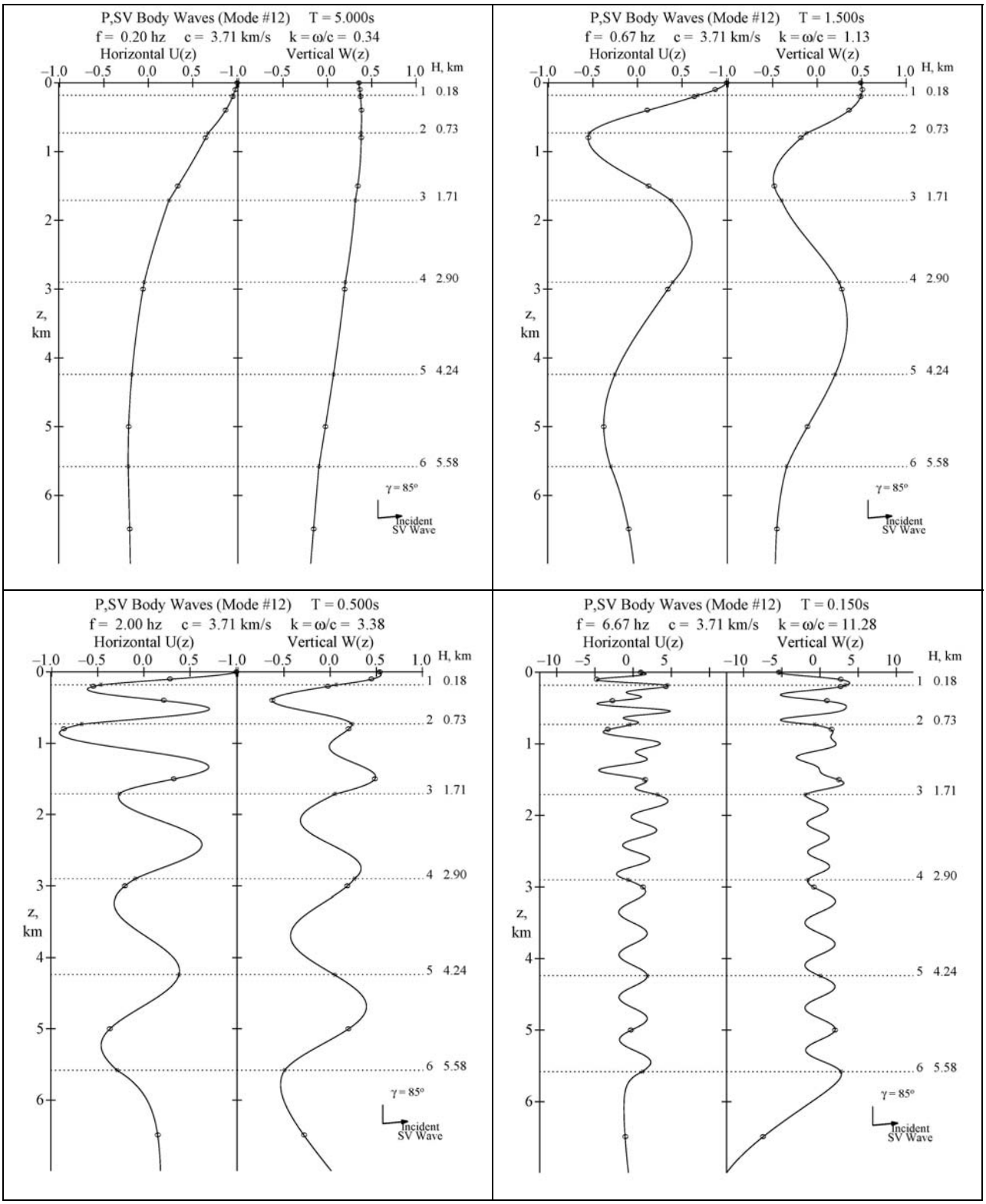

VII. The Synthetic Transverse Translational Motions

With the mode shapes and Transfer functions available for the 5 modes of Love waves and 1 "mode" of Body SH waves, the procedures of Section II are now ready to generate the synthetic transverse components of acceleration at all depths z below the surface. We will pick the same El Centro 6-Layered elastic model and select the following two cases of parameters for the earthquake source and site characteristics:

1) Case 1: $\boldsymbol{M = 6.5,\ R = 8.0km,\ H = 6.0km,\ s = 0,\ s_L = 2}$

2) Case 2: $\boldsymbol{M = 6.5,\ R = 40.0km,\ H = 9.0km,\ s = 0,\ s_L = 2}$

where

$\boldsymbol{M}$ = earthquake magnitude

$\boldsymbol{R}$ = epicentral distance

$\boldsymbol{H}$ = focal depth of earthquake

$\boldsymbol{s}$ = geologic site condition of the recording site, where

s = 0, alluvial site, s = 1, intermediate site and s = 2, rock site

$\boldsymbol{s_L}$ = soil condition of the recording site, where

$\boldsymbol{s_L}$ = 0, rock soil, $\boldsymbol{s_L}$ =1, stiff soil and $\boldsymbol{s_L}$ =2, deep soil

The two cases are on the same site, with the same geological and soil site conditions, and are subjected to an earthquake of the same magnitude. They differ only in the epicentral distances and the earthquake focal depths. Case 1 illustrates near-field motions with small epicentral distance and shallow focal depth. Case 2 has larger epicentral distance and slightly deeper source.

VII.1 Case 1: $\boldsymbol{M = 6.5,\ R = 8.0km}$ & $\boldsymbol{H = 6.0km\ \left(D = 10.0km\right),\ s = 0,\ s_L = 2}$

As described in the above sections, the time history at the top surface $\boldsymbol{z = 0}$ will be generated by the SYNACC method (**Trifunac, 1971b; Wong and Trifunac, 1978, 1979**; **Lee and Trifunac, 1985, 1987**), using the currently developed SYNACC algorithm, which includes a

mode of SH body waves. Figure VII.1 is a plot of the ray path taken by the SH body waves from the earthquake source to arrive at the recording site.

Figure VII.1 SH Body Waves Ray Path from Source

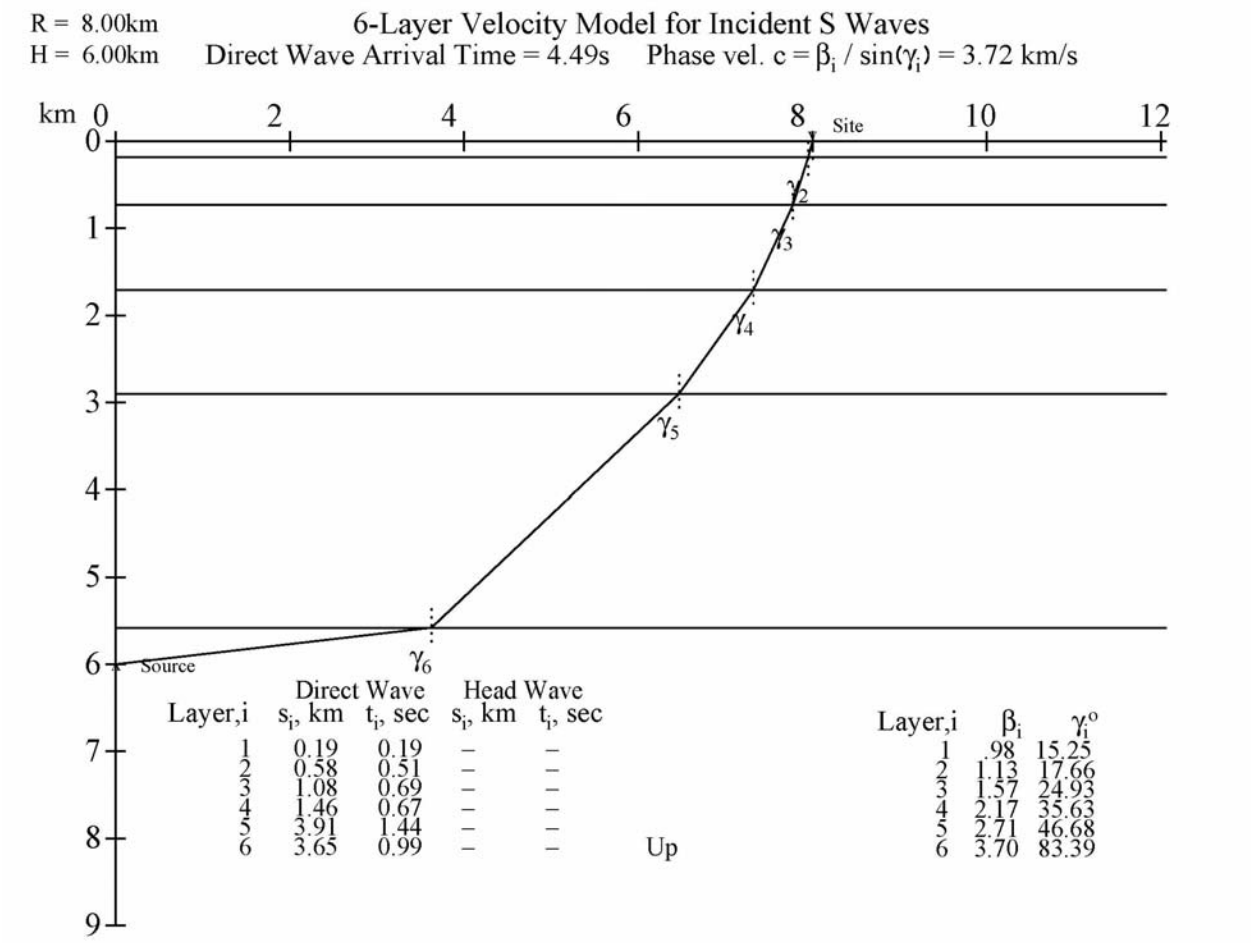

The ray path is chosen so that the phase velocities at each layer of the 6-layered media is the same, or that the angles of the ray travel are determined so that Snell's Law is satisfied at each interface, namely, for each layer $\boldsymbol{i = 1,\ 2,\ \ldots,\ 6}$:

$$\boldsymbol{c = \beta_i \,/ \sin(\gamma_i) = \ 3.72 \text{ km/s, a constant}} \qquad \text{(VII.1)}$$

where $\boldsymbol{\beta_i}$ = shear wave speed, and $\boldsymbol{\gamma_i}$ = angle the ray makes with respect to the vertical direction at the $\boldsymbol{i^{th}}$ layer. It shows that the ray will start at an angle of $\boldsymbol{\gamma_6 \sim 83.4^o}$ with respect to vertical, with almost horizontal path, and bend up into the layered media so that it arives at the site with $\boldsymbol{\gamma_1 \sim 15.3^o}$, with respect to the vertical.

Figure VII.2 SH Body Waves at T = 3.6, 1.5, 0.36, and 0.15 s

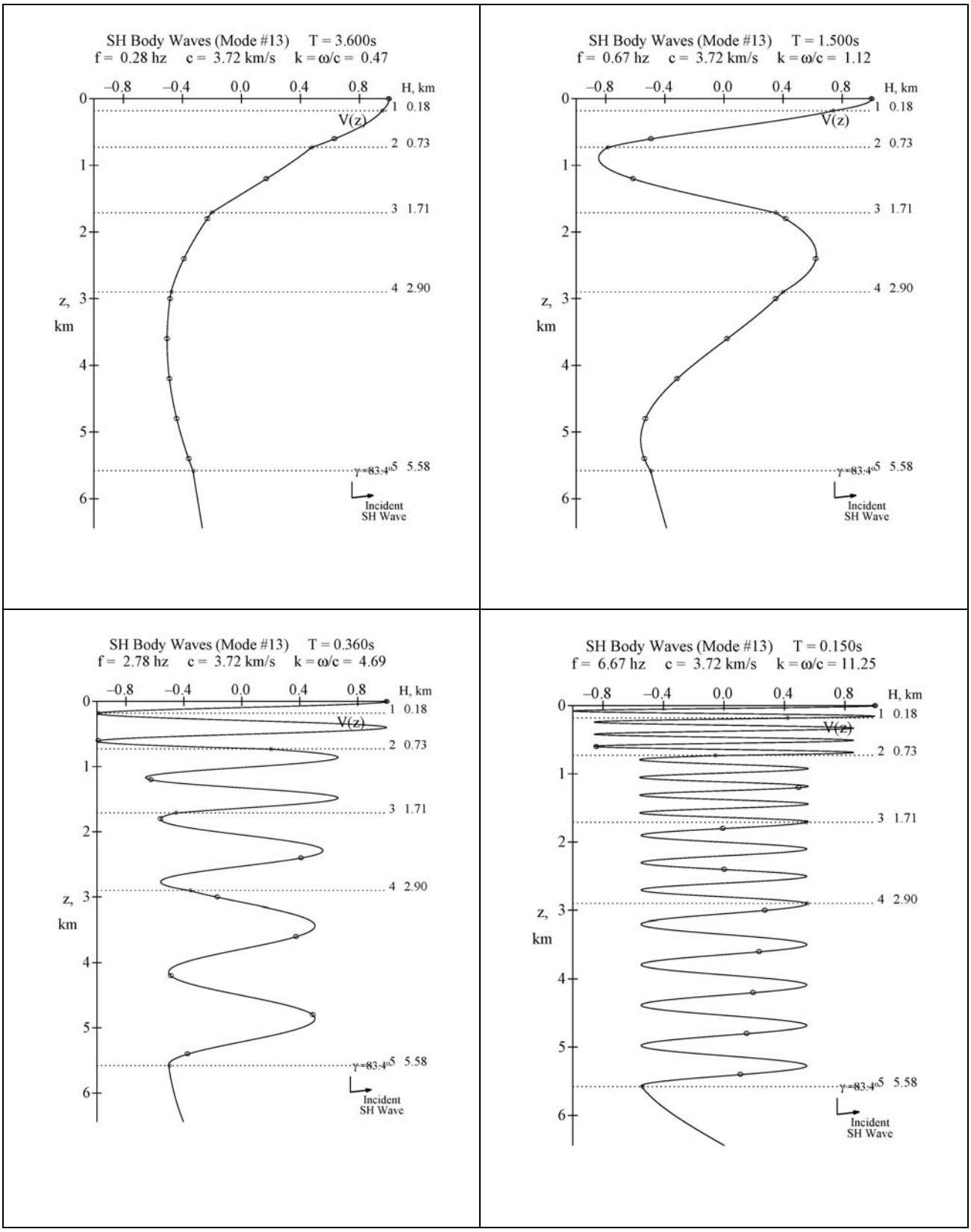

Figure VII.2 shows the SH body wave mode shapes at four selected periods: $T = 3.6,\ 1.5,\ 0.36,\ \text{and}\ 0.15\ s$. Such mode shapes are available at all 91 periods in the range from $T = 15.0\ s$ down to $T = 0.04\ s$. This allows us to generate "an extra mode of body SH waves", which together with the 5 modes of Love waves, can be used to generate the transverse components of synthetic translational motions at all depths on and below the surface.

Figure VII.3 shows a synthetic acceleration calculated at the El Centro cite, with six-layers, at 100 points equally spaced from the surface to a depth of almost 6km below. At an epicentral distance of $R = 8.0km$ from an earthquake source of focal depth $H = 6.0km$, which corresponds to the hypocentral distance of $D = \left(R^2 + H^2\right)^{1/2} = \left(8.0^2 + 6.0^2\right)^{1/2} = 10.0km.$ The **SYNACC** program determines that the appropriate duration of the accelerogram record should be just above 40 seconds. The depth of each accelerogram is labeled at intervals 0.6 km apart. Of the 100 acceleration time histories, six are plotted green, and labeled 0 to 5. The one labeled 0 is the accelerogram at the top surface $z = 0$, while the ones labeled 1 to 5 are those at depths, which are closest to the interfaces between adjacent layered media.

Note that the actual time scale of the above time histories has been shifted to have a common time scale, where $T = 0\ \ \text{sec}$ is defined by SYNACC to be the time $D/c_{\max}$, where D is the hypocentral distance and $c_{\max}$ is the maximum phase velocity of the waves.

Perusal of Figure VII.3 shows that, at such a short distance, $D = 10.0km$, both the Love waves and body waves arrive within a few seconds. The SH body waves have the same phase velocity at all periods and the figure shows that the direct arrival time of the SH body waves is $T = 4.49s$. The arrival times for Love waves will be different for different modes, and for waves at different periods, since the phase velocities $c = c(T)$, depend on the period of the waves, as shown by the dispersion curves in Figure I.1. The acceleration time histories show that the strong-motions arrives by about $T = 5.0s$, which follows the direct arrival time of body waves at $T = 4.49s$.

Figure VII.3 Synthetic Acceleration: $M = 6.5$, $R = 8.0km$, $H = 6.0km$, $s = 0$, and $s_L = 2$

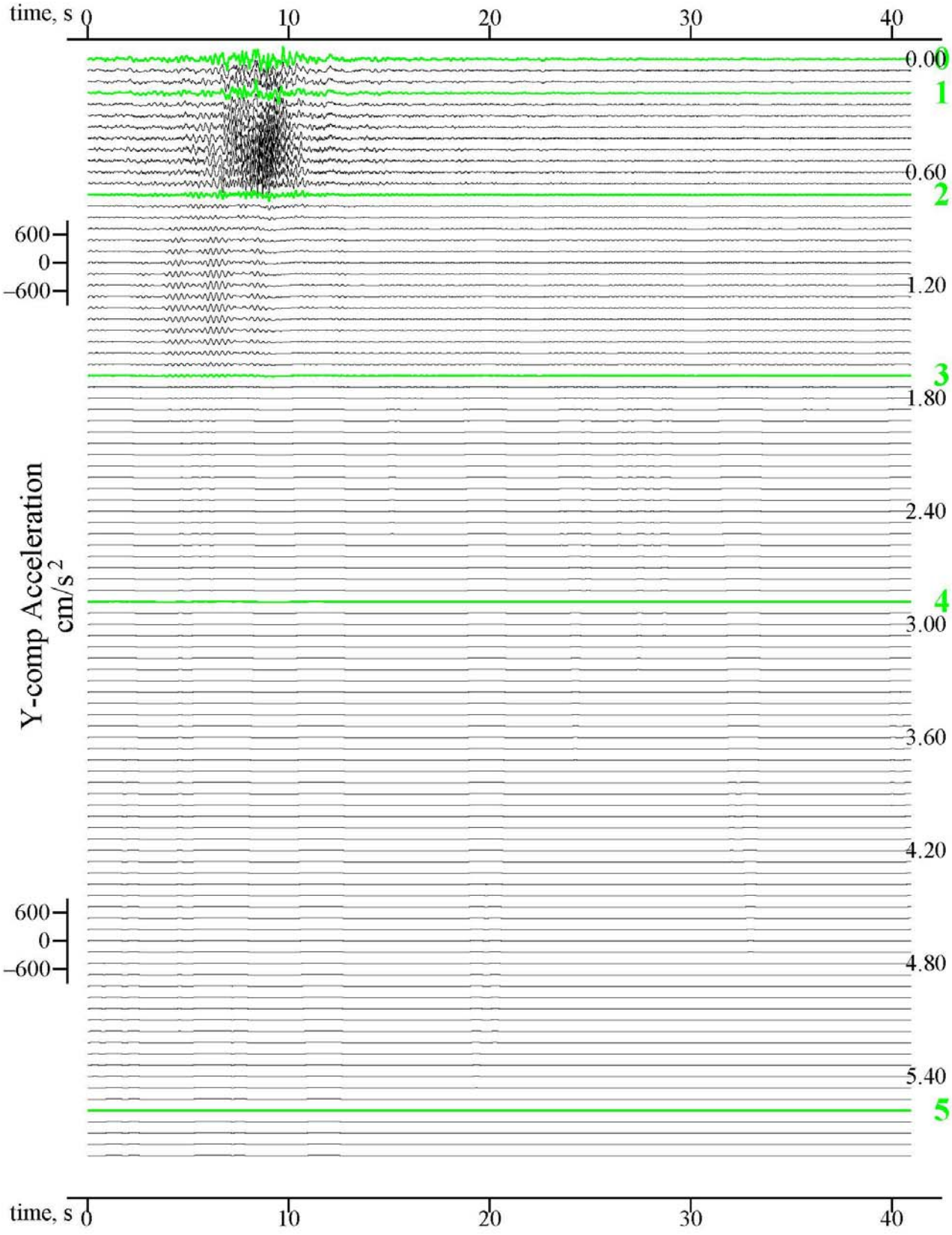

The strong-motion is observed at depths in the first two top layers, up to $z \sim 0.7km$. Smaller motions are in the 3rd layer up to $z \sim 1.7km$, beyond which the motions become small. This is consistent with the mode shape amplitudes of Love waves (Section V), where it was found that, for all modes, at moderate periods, the motions stay close to, but are always less than those at the top surface, in the first two layers, and then began to die down further below. The attenuation is faster for the waves at higher frequencies.

Figure VII.4 shows the corresponding synthetic velocity. The actual depth of each velocity time function is labeled at each 0.6 km apart. Of the 100 velocity time histories, six of them are plotted green, and labeled 0 to 5. The one labeled 0 is the velocity at the top surface $z = 0$, while the ones labeled 1 to 5 are those time histories at depths on or closest to the interfaces between adjacent layered media.

The new SYNACC program computes the velocity at all depths from the corresponding acceleration time histories from the Fourier transform in the frequency domain to get the velocity spectra, and then taking its inverse Fourier transform.

Figure VII.5 shows the corresponding displacements calculated at the same El Centro site. The actual depth of each displacement is again labeled at depths 0.6 km apart. Of the 100 displacement time histories, six of them are again plotted green, and labeled 0 to 5. The one labeled 0 is the displacement at the top surface $z = 0$, while the ones labeled 1 to 5 are again those at depths on or closest to the interfaces between adjacent layered media. The new SYNACC program computes the displacement at all depths from the corresponding acceleration time histories in the frequency domain to get the displacement spectra, and then taking its inverse Fourier transform.

Figure VII.4 Synthetic Velocity: $M = 6.5,\ R = 8.0km,\ H = 6.0km,\ s = 0,$ and $s_L = 2$

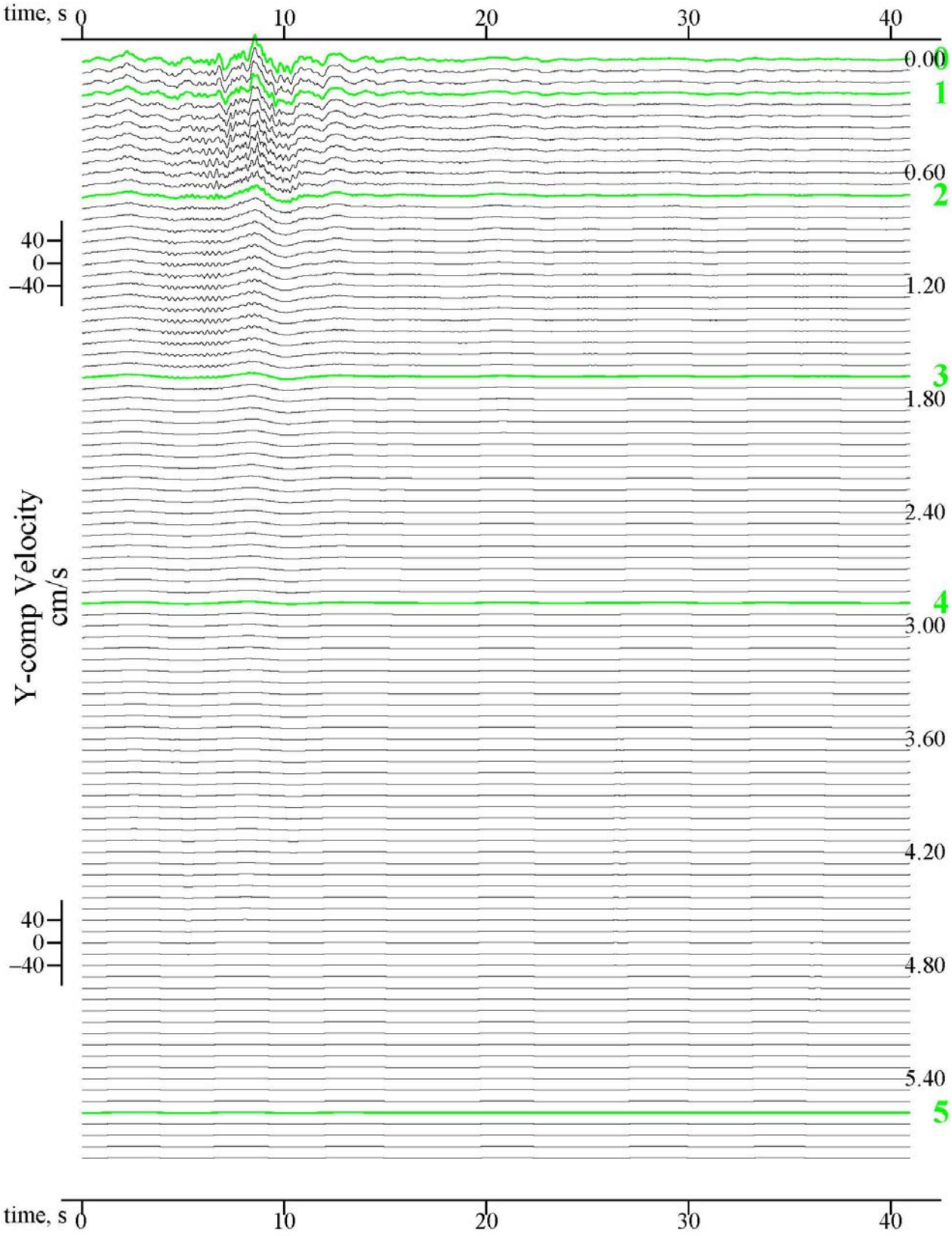

Figure VII.5 Synthetic Displacement: $M = 6.5,\ R = 8.0km,\ H = 6.0km,\ s = 0,$ and $s_L = 2$

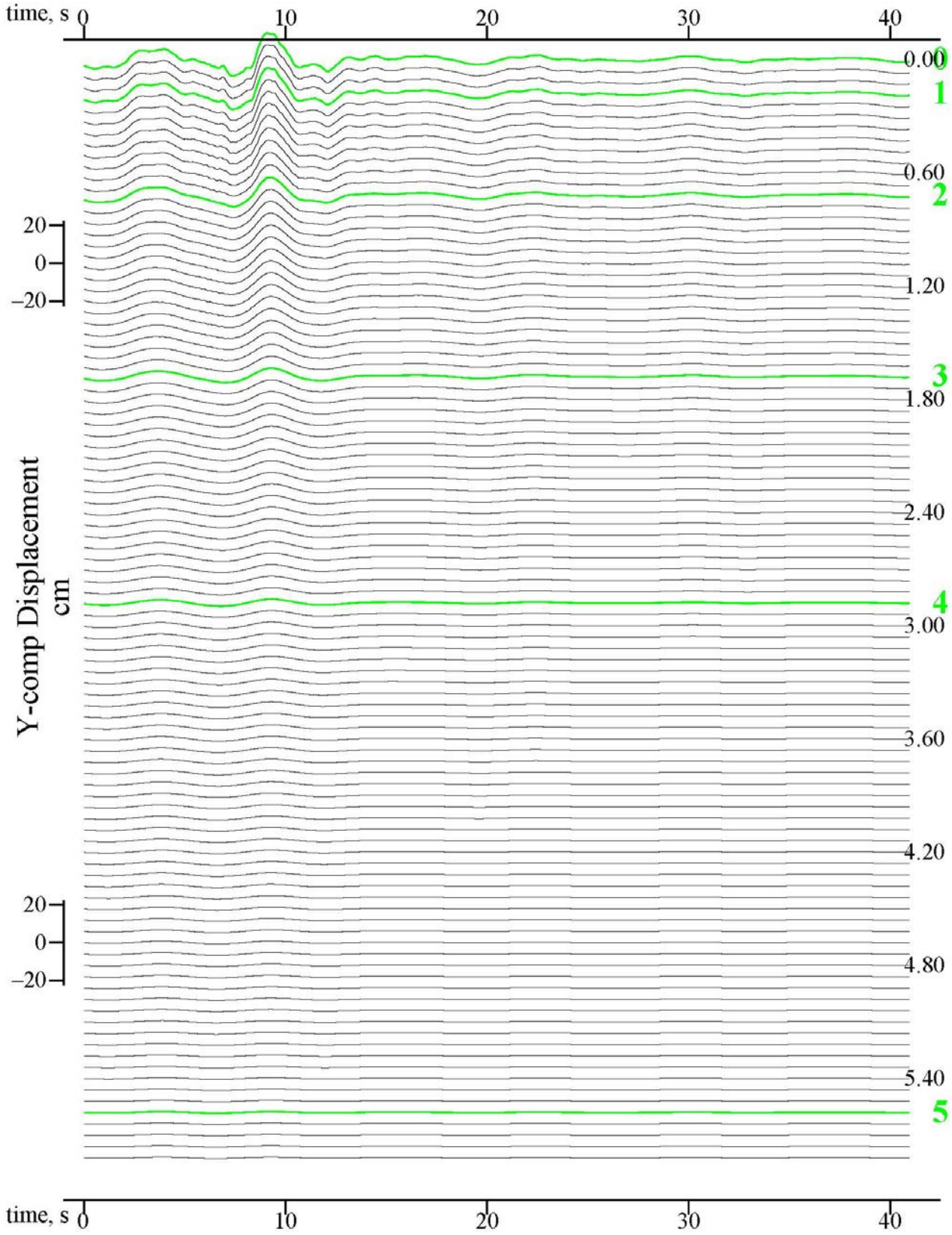

It is instructive to plot the above two-dimensional (2-D) time histories of acceleration, velocity and displacement in Figures VII.3, 4 and 5, as three-dimensional (3-D) figures.

Figure VII.6 in the next page is the 3-D plot of the translational motions of the same 100 accelerations corresponding to Figure VII.3. The two horizontal longitudinal and transverse coordinate axes are now correspondingly the **time** axis and the **depth** below surface. The vertical axis shows the amplitude of **acceleration** in cm/s^2. The five green lines, labeled 0 to 5, again correspond to the positions where the layers meet.

Figures VII.7 and VII.8 in the two pages following show the 3-D representation of synthetic velocities and displacements corresponding to the 2-D plots of Figures VII.4 and VII.5

Figure VII.6 Synthetic Acceleration for $M = 6.5,\ R = 8.0km,\ H = 6.0km,\ s = 0,$ and $s_L = 2$

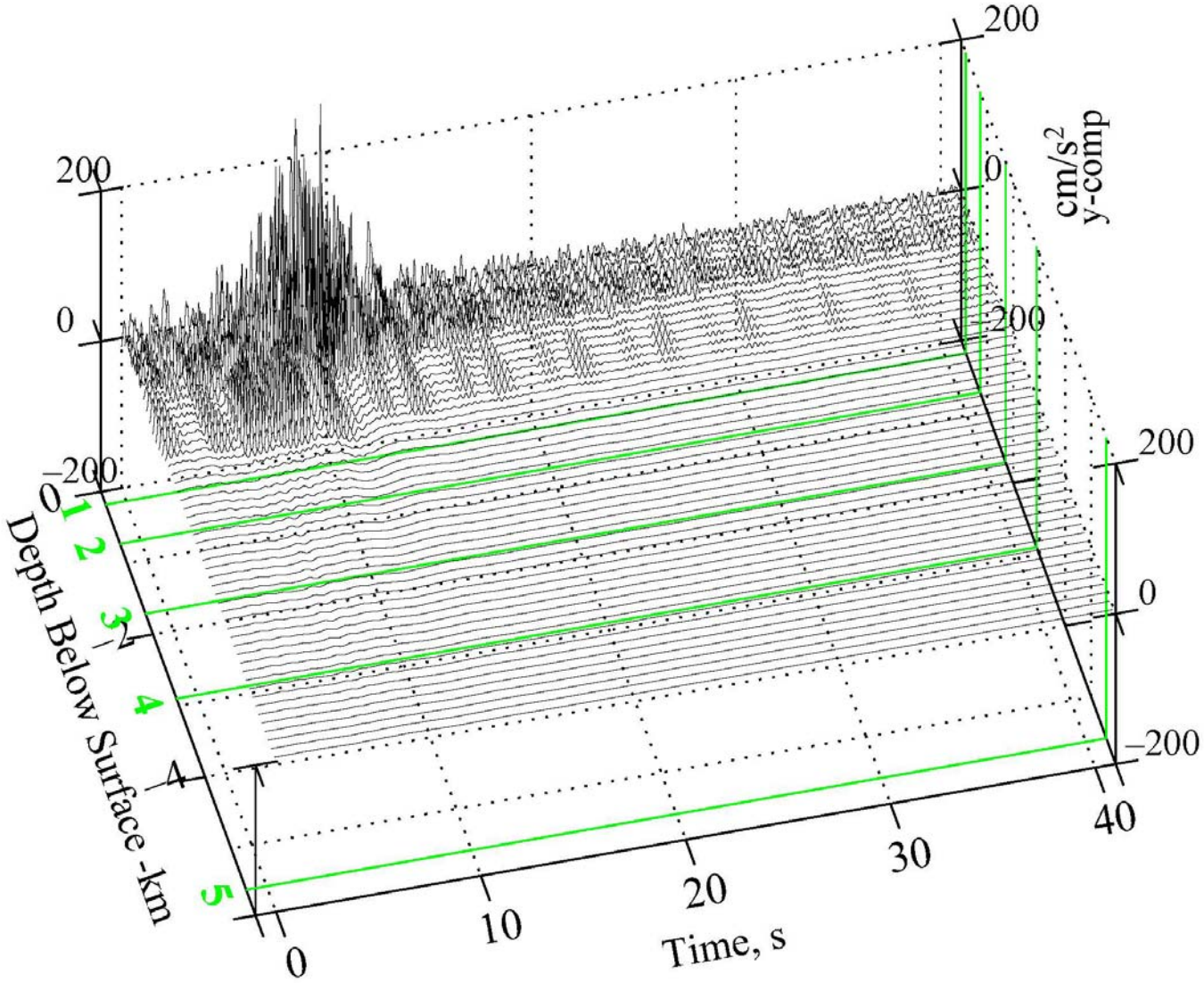

Figure VII.7 Synthetic Velocity for $M = 6.5$, $R = 8.0km$, $H = 6.0km$, $s = 0$, and $s_L = 2$

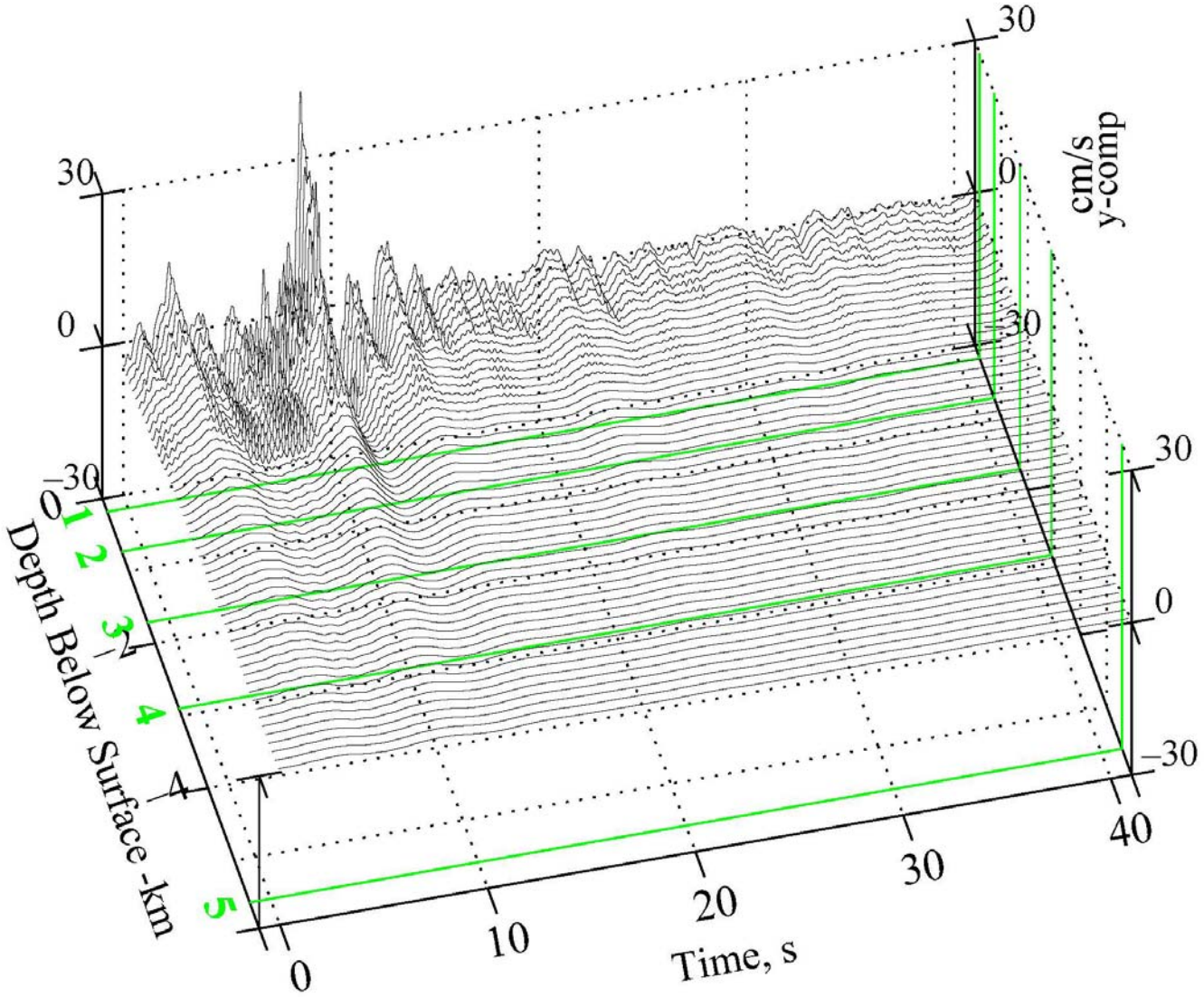

Figure VII.8 Synthetic Displacement for $M = 6.5$, $R = 8.0km$, $H = 6.0km$, $s = 0$, and $s_L = 2$

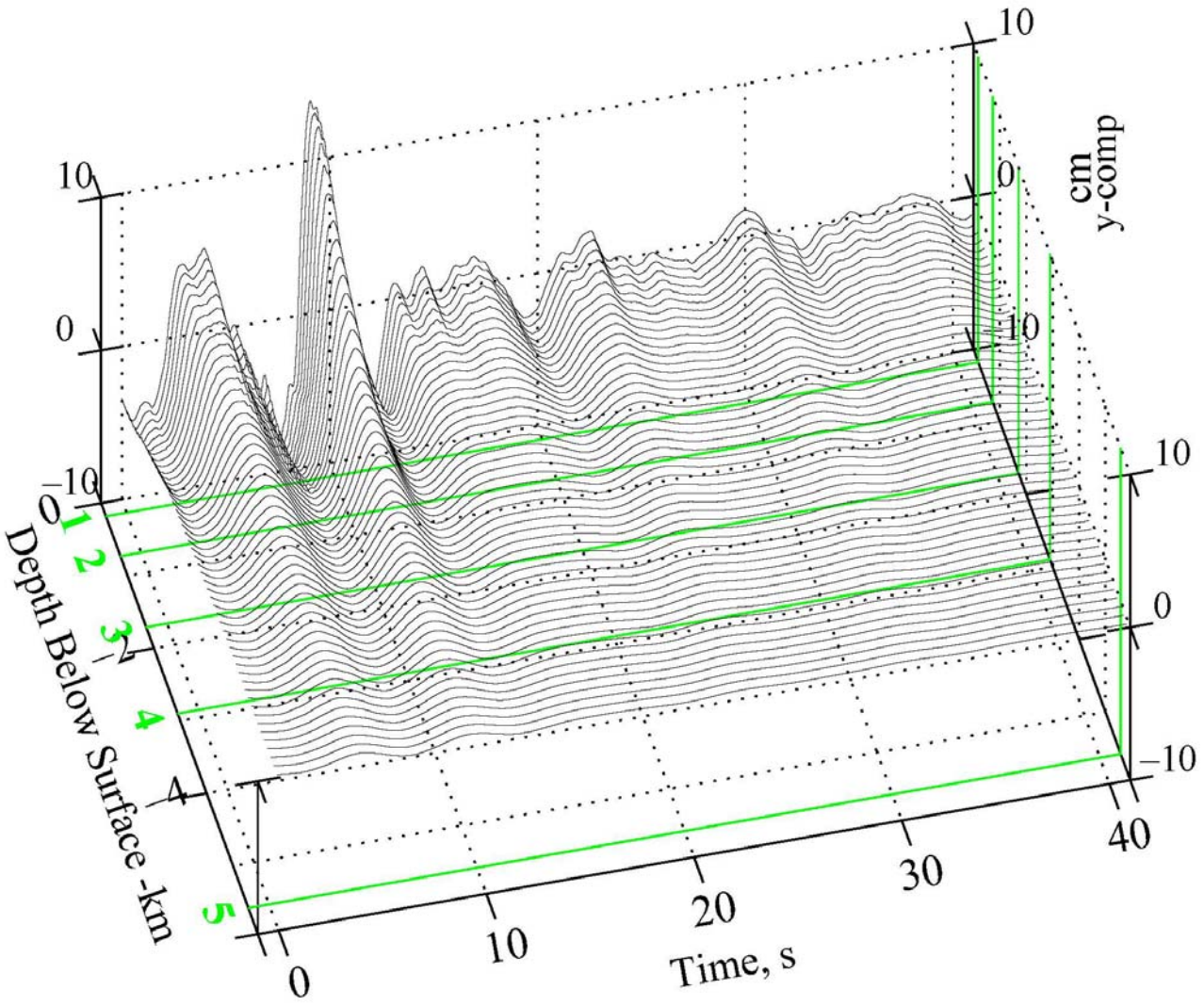

VII.2 Case 2: $M = 6.5,\ R = 40.0km,\ H = 9.0km\ \left(D = 41.0km\right),\ s = 0,$ and $s_L = 2$

We now consider an example of far field motion, for epicentral distance $\boldsymbol{R = 40.0\ km}$ and an earthquake source at a focal depth of $\boldsymbol{H = 9.0\ km}$. This corresponds to a hypocentral distance of $\boldsymbol{D = \left(R^2 + H^2\right)^{1/2} = \left(40.0^2 + 9.0^2\right)^{1/2} = 41\ km}$. Figure VII.9 shows a plot of the path taken by the SH body waves from the earthquake source to the recording site. As before, the path is chosen so that the phase velocities in each layer is the same, or that the angles the ray travels are determined so that Snell's Law is satisfied at each interface (Equation VII.1).

Figure VII.9 SH Body Waves Ray Path from Source to Site

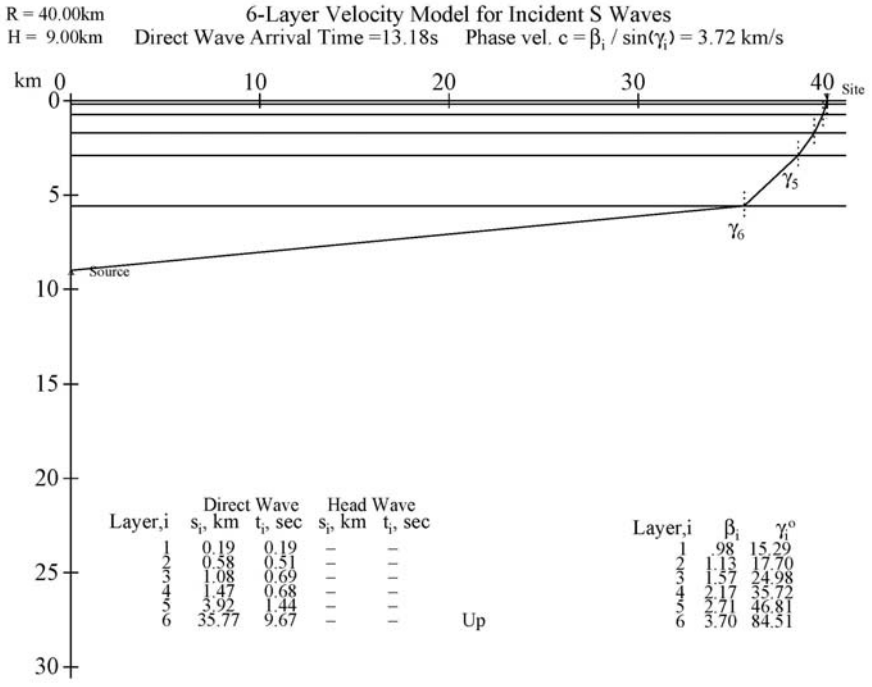

This results in the ray starting with an angle of $\boldsymbol{\gamma_6 \sim 84.5^o}$ with respect to vertical, and incident at the site with $\boldsymbol{\gamma_1 \sim 15.3^o}$. Figure VII.10 shows the SH body wave mode shapes at four selected periods: $\boldsymbol{T = 5.0,\ 1.5,\ 0.50,\ and\ 0.15\ s}$. As in Case 1, this allows us to generate an extra mode of body SH waves, which, together with the 5 modes of Love waves, can be used to generate the transverse components of synthetic translational motions at all depths at and below the surface.

Figure VII.10 SH Body Waves at $T = 5.0,\ 1.5,\ 0.50,$ and $0.15\ s$

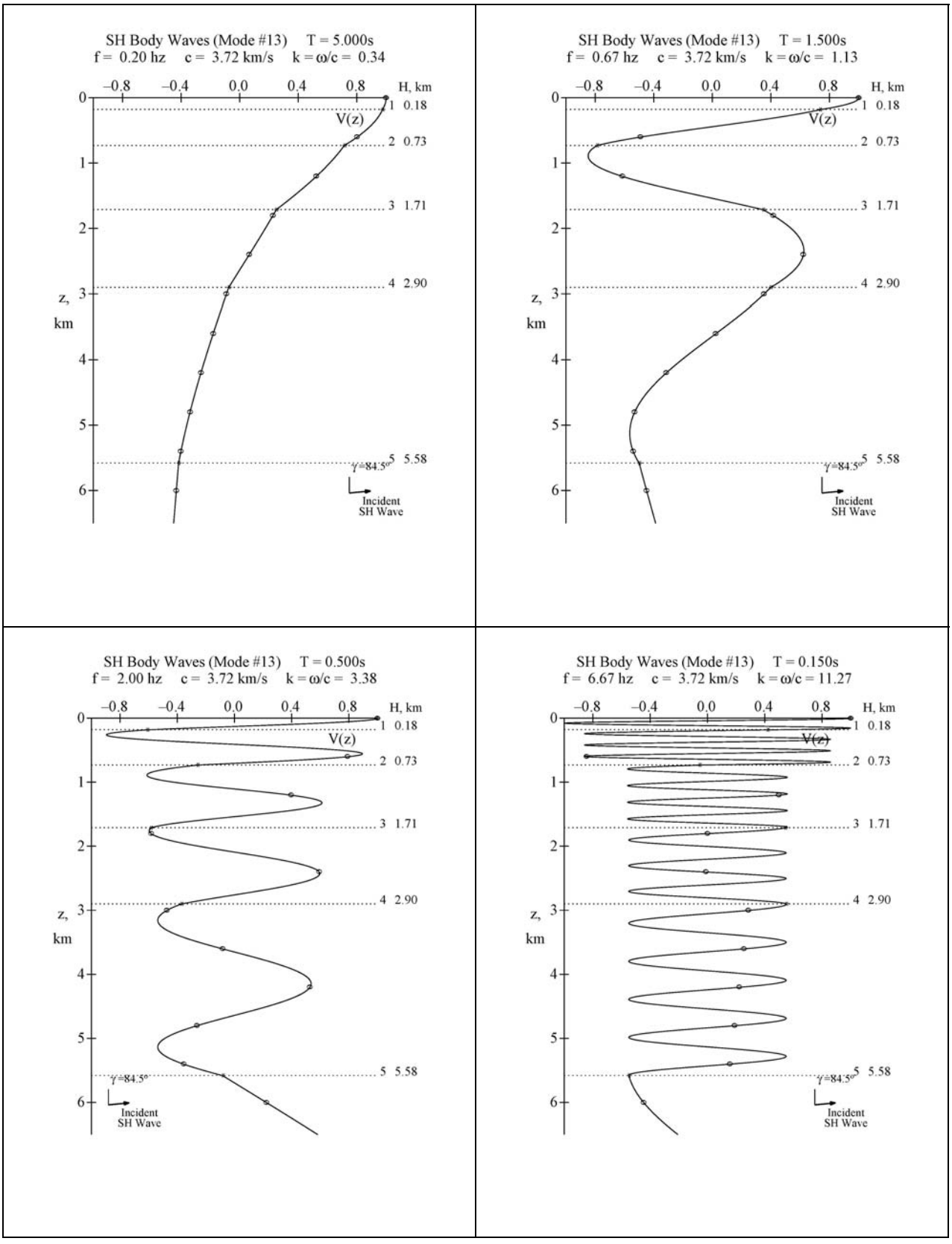

In the following we present only 3-D plots for this case. Figure VII.11 shows the synthetic acceleration calculated at the El Centro site for case 2 earthquake parameters. Again the SYNACC computer program determined that the appropriate duration of the accelerogram record should be just above 40 seconds. As in case 1, the two horizontal longitudinal and transverse coordinate axes are correspondingly the **time** axis and to the **depth** in **km** below the surface. The vertical axis gives the amplitudes of **acceleration**in in $\boldsymbol{cm/s^2}$. The five green lines, labeled 1 to 5, again correspond to the positions where the layers meet. Recall that the actual time scale of the time histories has all been shifted to have a common time scale, where $\boldsymbol{T = 0}$ **sec** is defined by SYNACC to be the time $\boldsymbol{D/c_{max}}$, where $\boldsymbol{D}$ is the hypocentral distance and $\boldsymbol{c_{max}}$ is the maximum phase velocity of the waves.

Perusal of Figure VII.11 shows that, in far-field at distance $\boldsymbol{D = 41.0km}$, the Love surface waves and body SH waves arrive at different times. The SH body waves have the same phase velocity at all periods and Figure VII.9 shows that the direct arrival time of the body SH waves is $\boldsymbol{T = 13.18s}$. The arrival times for the Love waves will be different for the different modes, and for waves at different periods, as shown by the dispersion curve in Figure I.1. The acceleration curves show that the noticeable surface waves did not arrive until after 20s from the start of the earthquake.

The strong-motion surface waves, beyond the 20sec, are observed at depths of the first three top layers, up to $\boldsymbol{z \sim 1.7km}$. The first two layers have stronger motions than the 3rd layer, with negligible motions observed beneath the 3rd layer. This is consistent with the mode shapes of Section V. The decrease of motions is even faster for waves at higher frequencies. *However, the body SH waves before 20sec are noticeable at all depths, consistent with Figure VII.10.*

Figures VII.12 and VII.13 show the 3-D plots of the corresponding synthetic velocity and displacement, computed from the synthetic acceleration, same way as in case 1. Strong motions are again observed, as in acceleration, in the 1st 3 top layers, and body waves arrive much earlier than the surface waves.

Figure VII.11 Synthetic Acceleration for $M = 6.5,\ R = 40.km,\ H = 9.km,\ s = 0,$ and $s_L = 2$

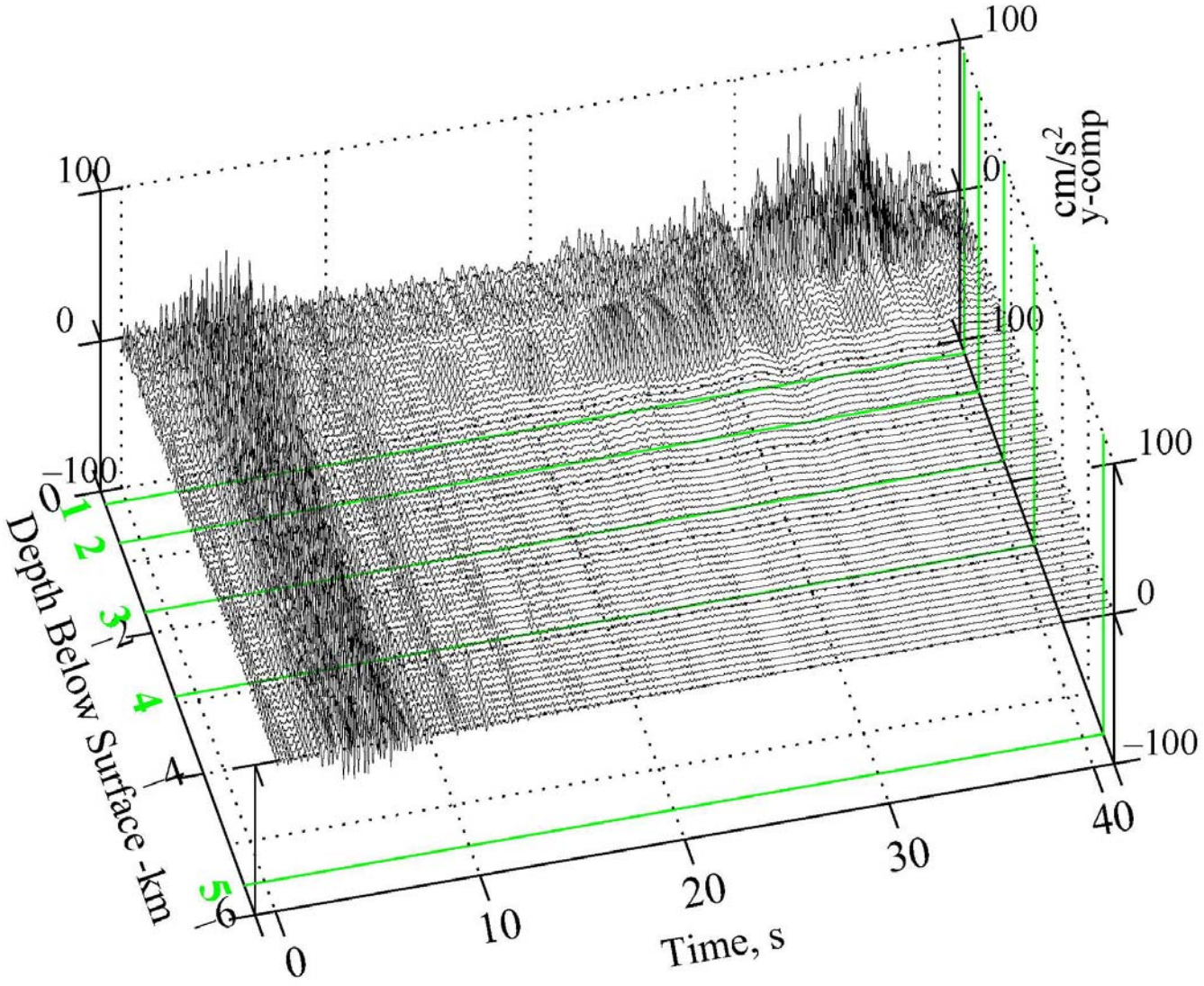

Figure VII.12 SyntheticVelocity for $M = 6.5,\ R = 40.km,\ H = 9.km,\ s = 0,$ and $s_L = 2$

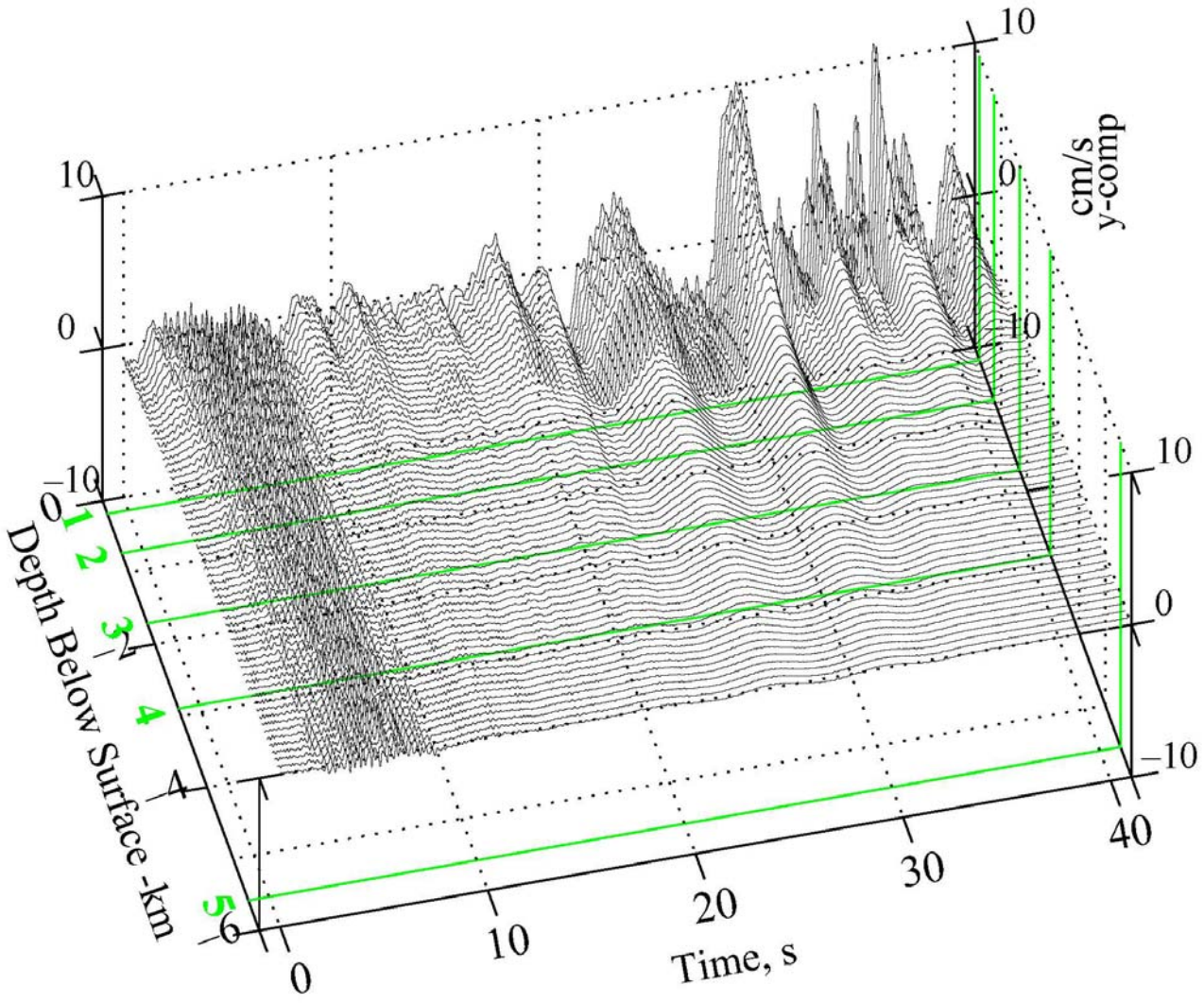

Figure VII.13 Synthetic Displacements for $M = 6.5,\ R = 40.km,\ H = 9.km,\ s = 0,$ and $s_L = 2$

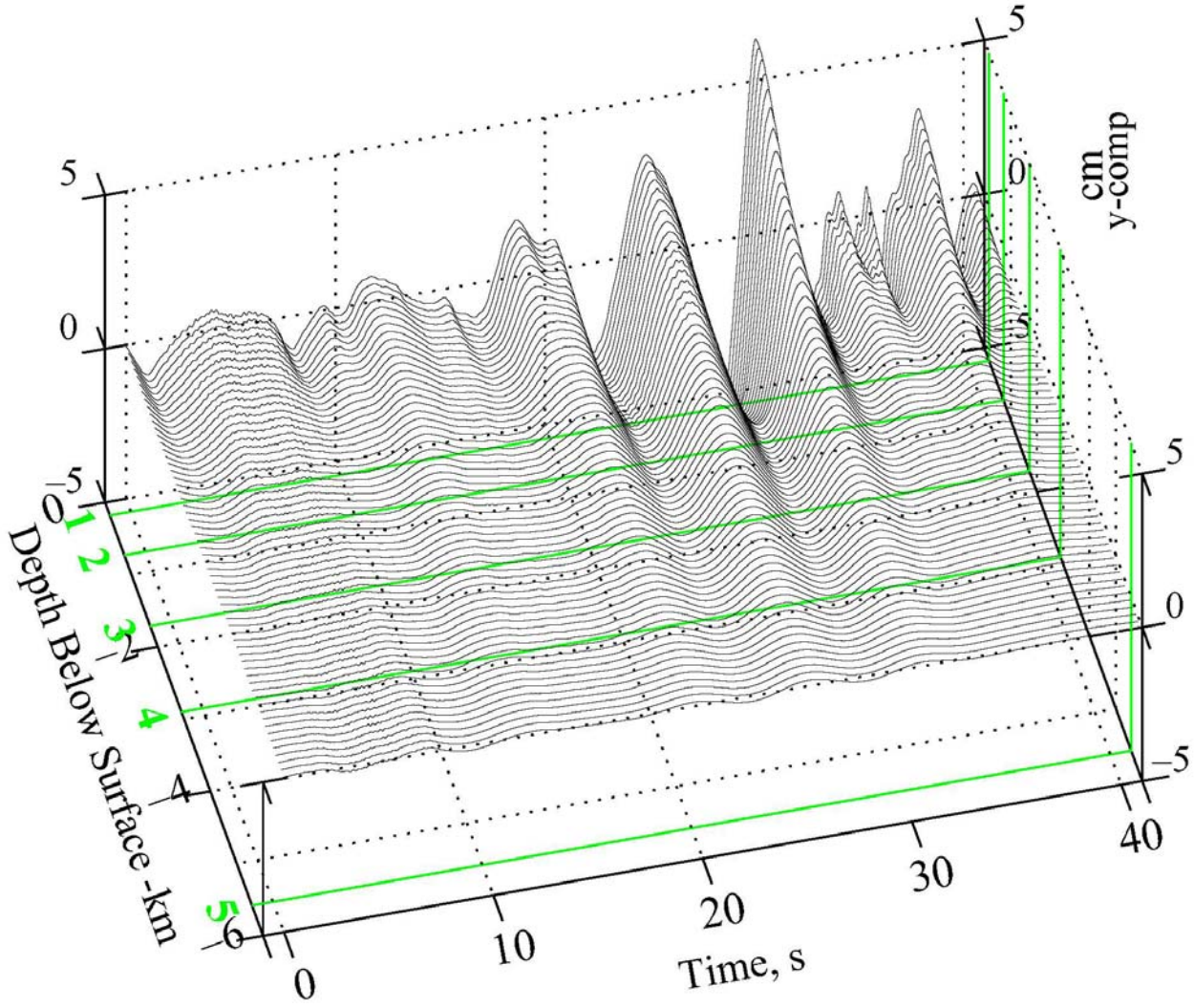

The contributions of the synthetic motions from body waves and surface waves are easier visualized by plotting them separately, as in Figures VII.14, VII.15, VII.16, in the next three pages, for synthetic acceleration, velocity and displacement.

The two 3-D graphs in Figure VII.14 represent the acceleration time histories of the body waves and of surface waves. The body wave time histories on the left show that the waves arrive at the beginning and dominate the motions at all depths within the first 10+ seconds. The body wave motions are also seen at all depths below the surface. The surface wave time histories on the right show the motions, which arrive later, at about 20 seconds after the earthquake. In this example the body wave peak acceleration has a smaller maximum compared with that of the surface waves. This results from the fact that the weights assigned to the five modes of surface Love waves are higher than the weight assigned to the mode #6 of body waves. Combining the motions of the body waves and of surface waves results in the complete acceleration time histories, which are shown in Figure VII.11.

The two 3-D graphs in Figure VII.15 represent the velocity time histories of the body waves and the surface waves. As for the acceleration time histories, the body wave velocity time histories on the left display noticeable motions only during the first 10 seconds, after which the motions die out. These motions are clearly noticeable at all depths. The surface wave velocity time histories on the right show strong motions only in the top 3 layers and the maximum motions occur there after about 20 seconds from the earthquake origin time.

The two 3-D graphs in Figure VII.16 represent the displacement time histories of the body waves and of the surface waves. Unlike the acceleration time histories, the body wave displacement time histories (on the left) show only few noticeable motions at all depths, even during the first 10 seconds. The surface wave displacement time histories on the right are more dominant, especially in the top 3 layers and the maximum motions again occur there beyond the 20 seconds after the earthquake origin time.

Figure VII.14 Contributions of Body and Surface Waves to Total Synthetic Acceleration

Body Waves **Surface Waves**

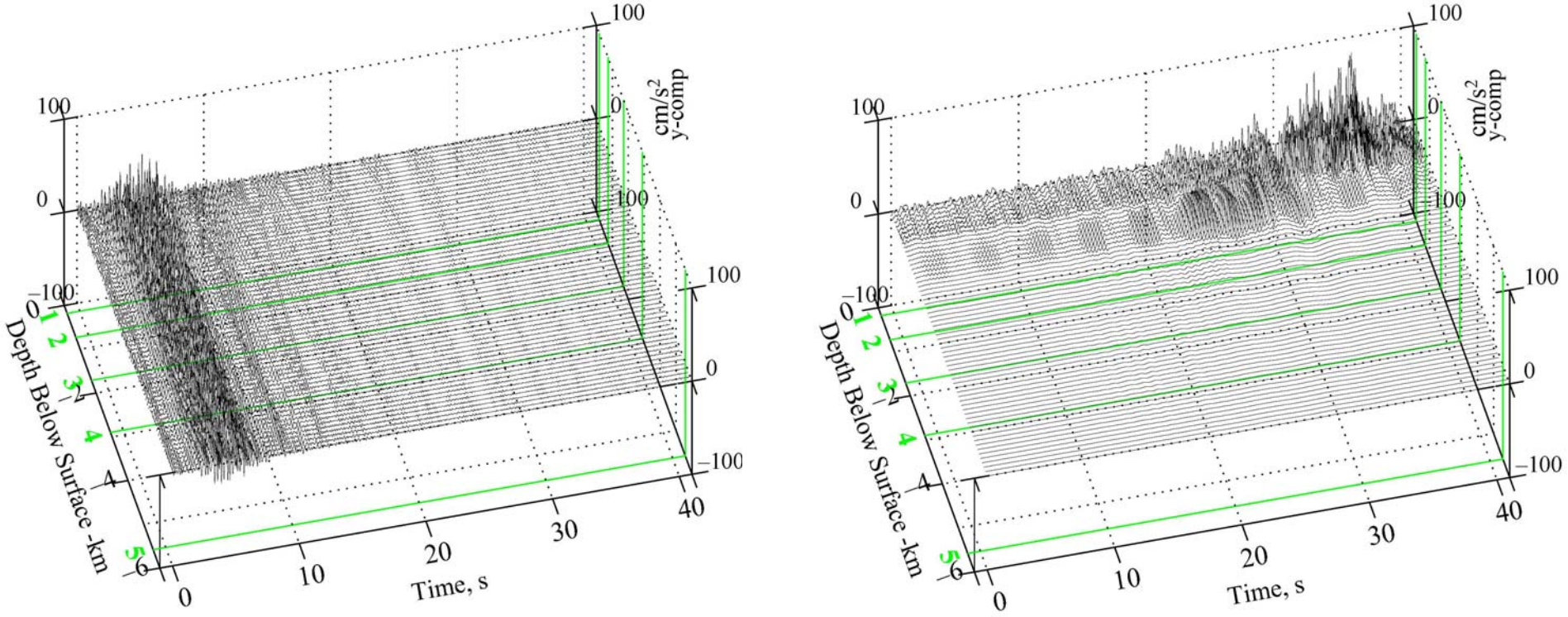

Figure VII.15 Contributions of Body and Surface Waves to Total Synthetic Velocity

Body Waves **Surface Waves**

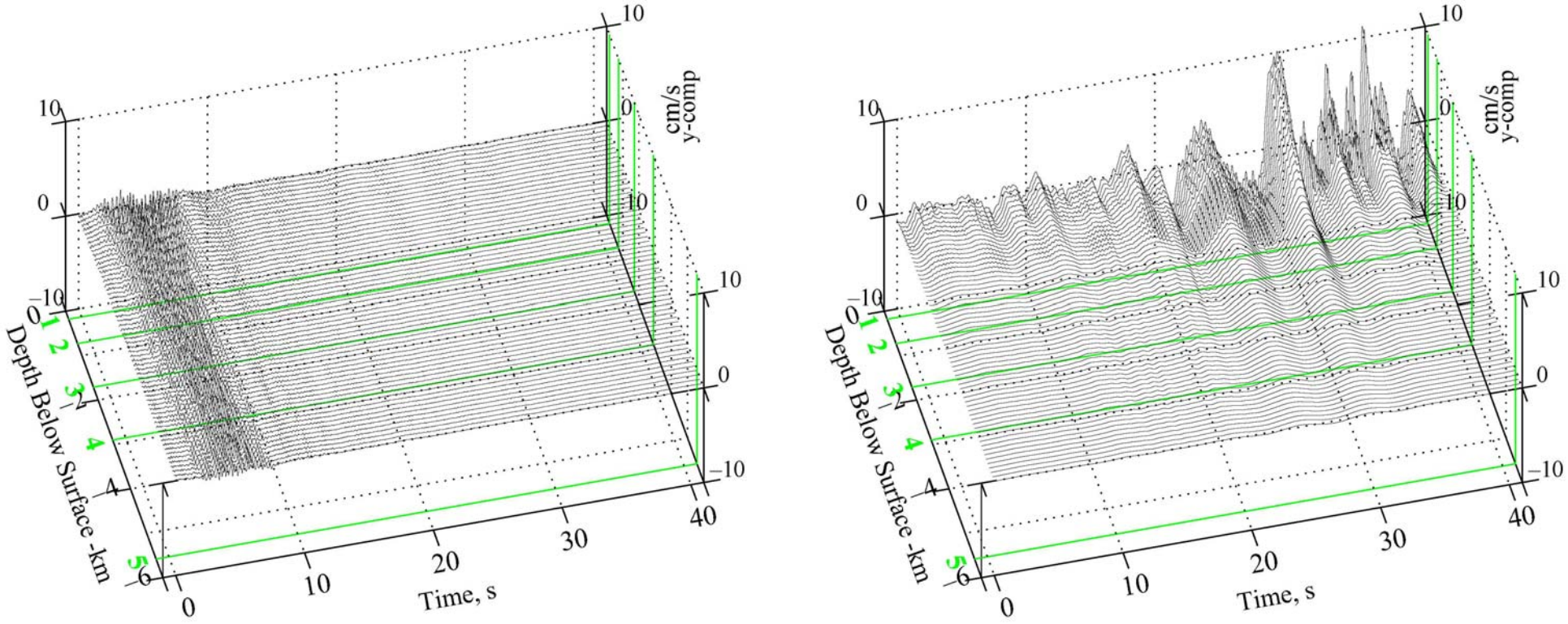

Figure VII.16 Contributions of Body and Surface Waves to Total Synthetic Displacement

Body Waves **Surface Waves**

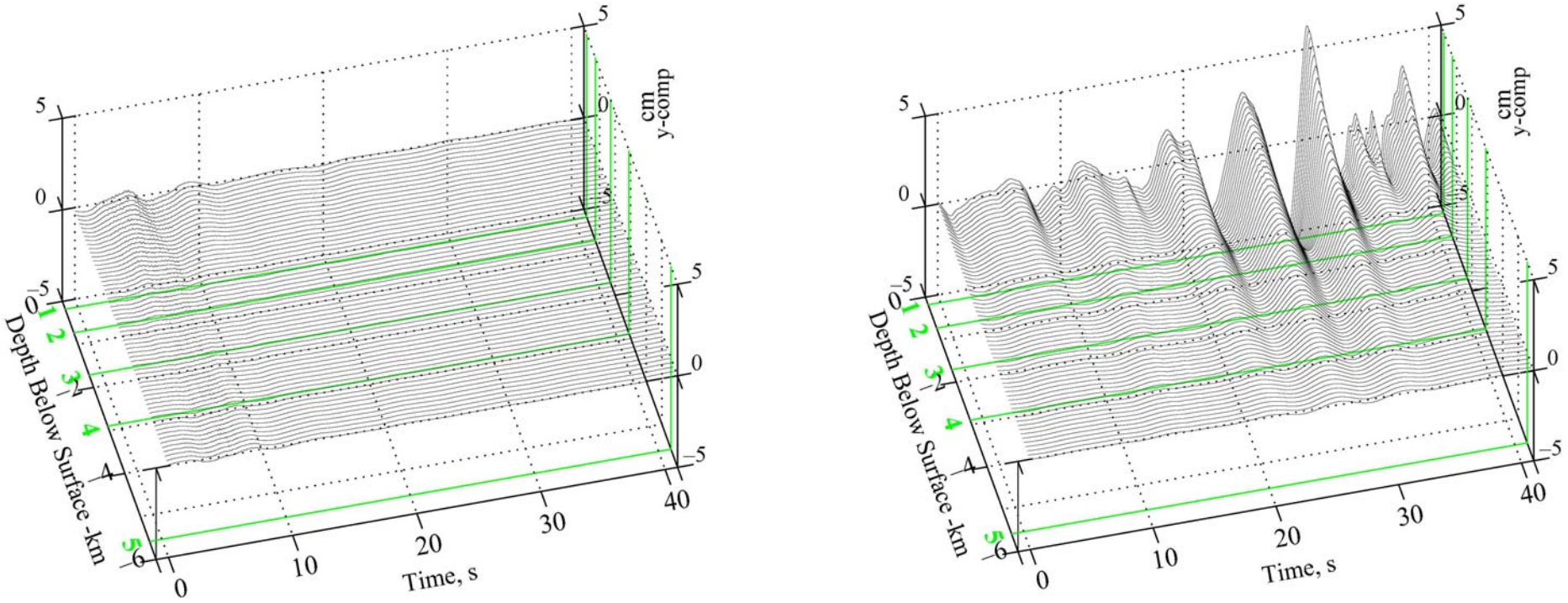

VIII. The Synthetic Radial and Vertical Translational Motions

We will select again the same El Centro 6-Layered elastic model for a site and will consider the following two cases of earthquake source and site characteristics:

1) Case 1: $\boldsymbol{M = 6.5,\ R = 8.0km,\ H = 6.0km,\ s = 0,\ s_L = 2}$

2) Case 2: $\boldsymbol{M = 6.5,\ R = 40.0km,\ H = 9.0km,\ s = 0,\ s_L = 2}$

where the earthquake parameters $\boldsymbol{M, R, H, s, s_L}$ are defined as in Section VII for Synthetic Transverse Translational motions. The two cases differ only in the epicentral distances and the earthquake focal depths. Case 1 is the case of near-field motions, while case 2 is the case of motions further away.

VIII.1 Case 1: $\boldsymbol{M = 6.5,\ R = 8.0km,\ H = 6.0km\ \left(D = 10.0km\right),\ s = 0,}$ and $\boldsymbol{s_L = 2}$

As before, the time histories at the top surface $\boldsymbol{z = 0}$ are generated by the existing SYNACC method, and the current SYNACC algorithm is used to include the modes of longitudinal, P waves (mode #6) and shear, SV waves (mode #7).

Figure VIII.1a shows the ray path taken by the P-waves from the earthquake source to the recording site. The ray path is chosen so that the phase velocities at each layer of the 6-layered media are the same, or that the angles the ray travels are determined so that Snell's Law is satisfied at each interface, for the layers $\boldsymbol{i = 1,\ 2,\ \ldots,\ 6}$:

$$\boldsymbol{c = \alpha_i \,/ \sin\left(\gamma_i\right) = \ 6.44 \text{ km/s, a constant}} \qquad \text{(VIII.1)}$$

where α_i = are the compressional wave speeds, and γ_i = angles the ray makes with respect to the vertical direction at the $\boldsymbol{i^{th}}$ layer. It shows the ray starting at an angle of $\gamma_6 \sim \boldsymbol{83.4^o}$ with respect to the vertical, and progressing up the layered media and ariving at the site with $\gamma_1 \sim \boldsymbol{15.3^o}$.

Figure VIII.1a P- Body Waves Ray Path from Source to Site

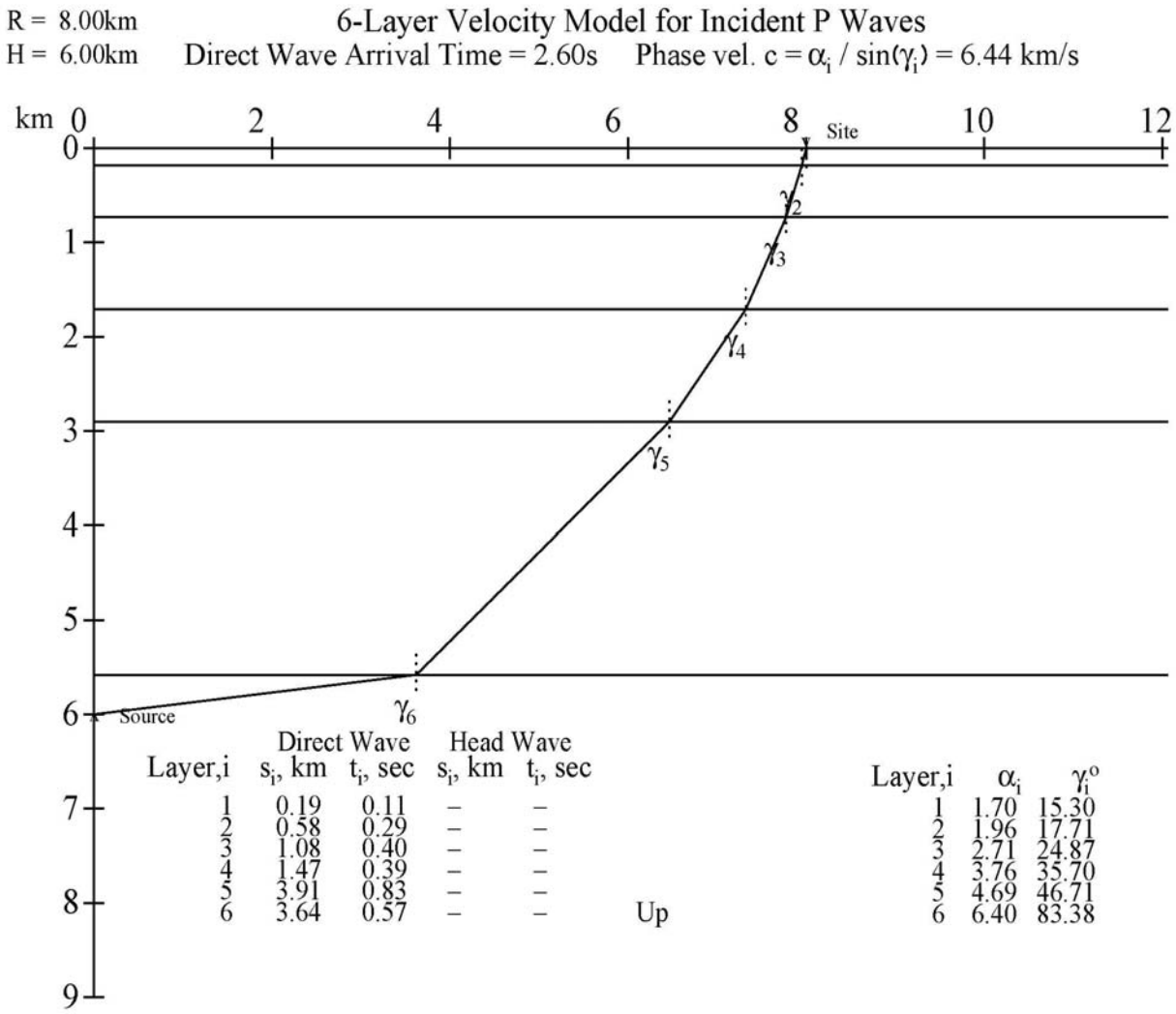

Figure VIII.1b shows the ray path taken by the (slower) SV body waves. The ray path is again chosen so that the phase velocities in each layer of the 6-layered media are the same (Equation VII.1 of Section VII). It shows that the ray will start with an angle $\gamma_6 \sim$ **83.4°** with respect to vertical, and then progress up the layered media arriving at the site with $\gamma_1 \sim$ **15.3°** Note that P-waves have almost the same starting angle at the source and ending angle at the site.

Figure VIII.1b SV- Body Waves Ray Path from Source to Site

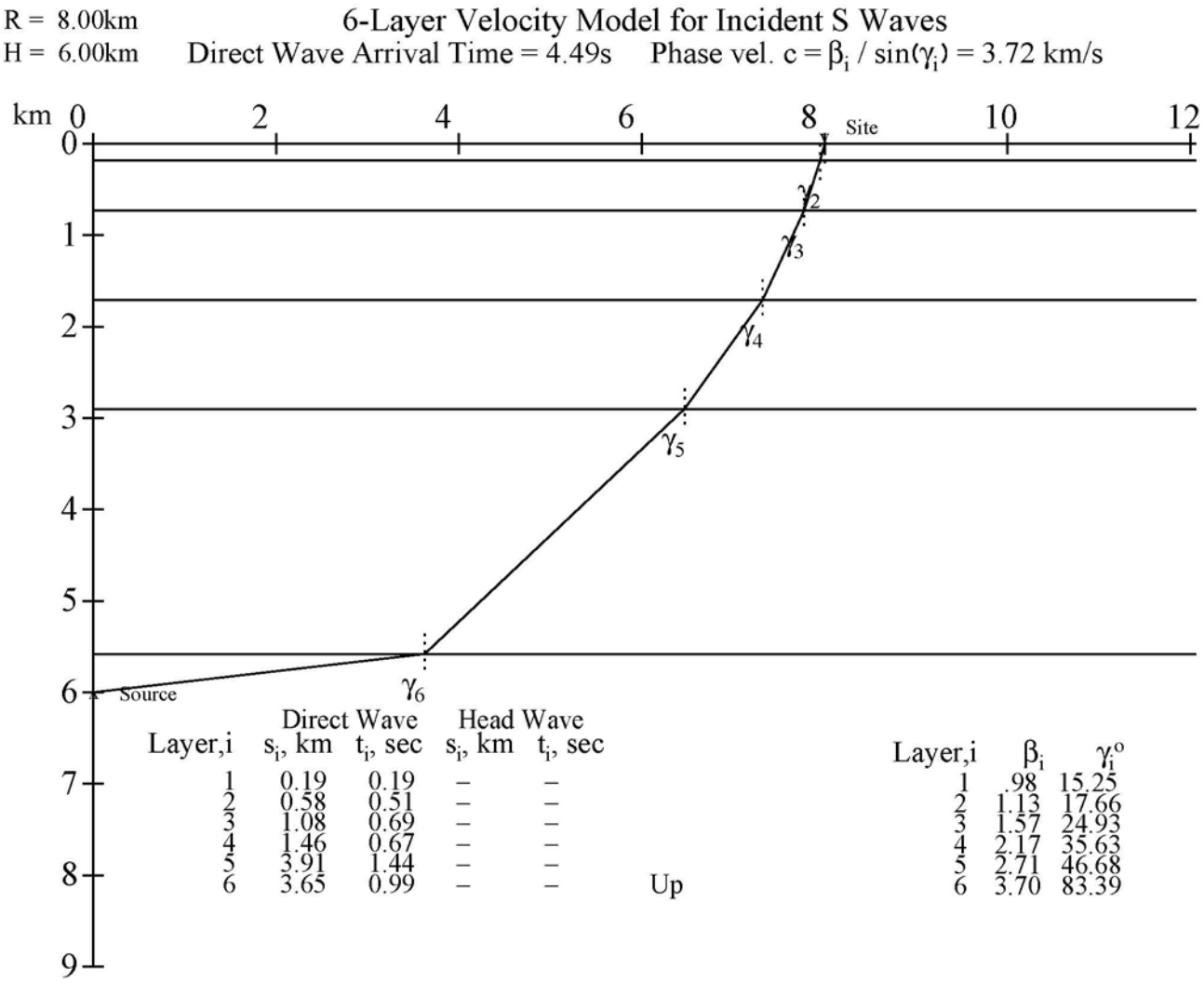

Figure VIII.2a shows the displacement mode shapes from incident P-waves at four selected periods: $\boldsymbol{T = 3.6,\ 1.5,\ 0.36,\ \text{and}\ 0.15\ s}$. Such mode shapes are available at all 91 periods in the range from $\boldsymbol{T = 15.0\ s}$ down to $\boldsymbol{T = 0.04\ s}$. This allows us to generate the mode#6 for incident P-waves to be used in generation of the transverse components of synthetic translational motions at all depths at and below the surface.

Note that for $\boldsymbol{T = 0.36\ s}$, with the vertical component $\boldsymbol{W(z)}$ normalized to have unit amplitude at the half-space surface, the corresponding horizontal $\boldsymbol{U(z)}$ has the corresponding starting amplitude of over 7.0 at the surface.

Figure VIII.2a Incident P-Waves at T = 3.6, 1.5, 0.36, and 0.15 s

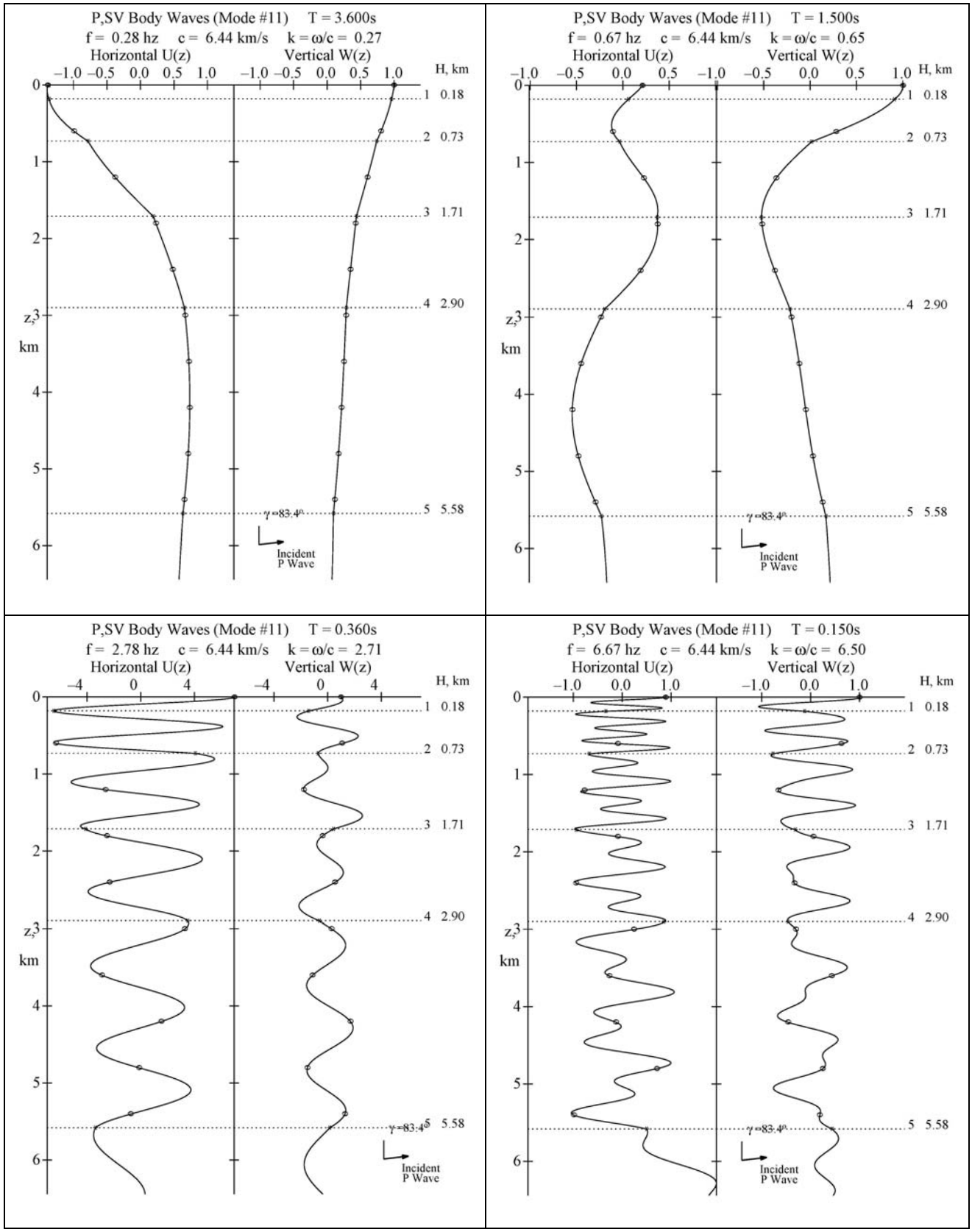

Figure VIII.2b Incident SV-waves at $T = 3.6,\ 1.5,\ 0.36,$ and $0.15\ s$

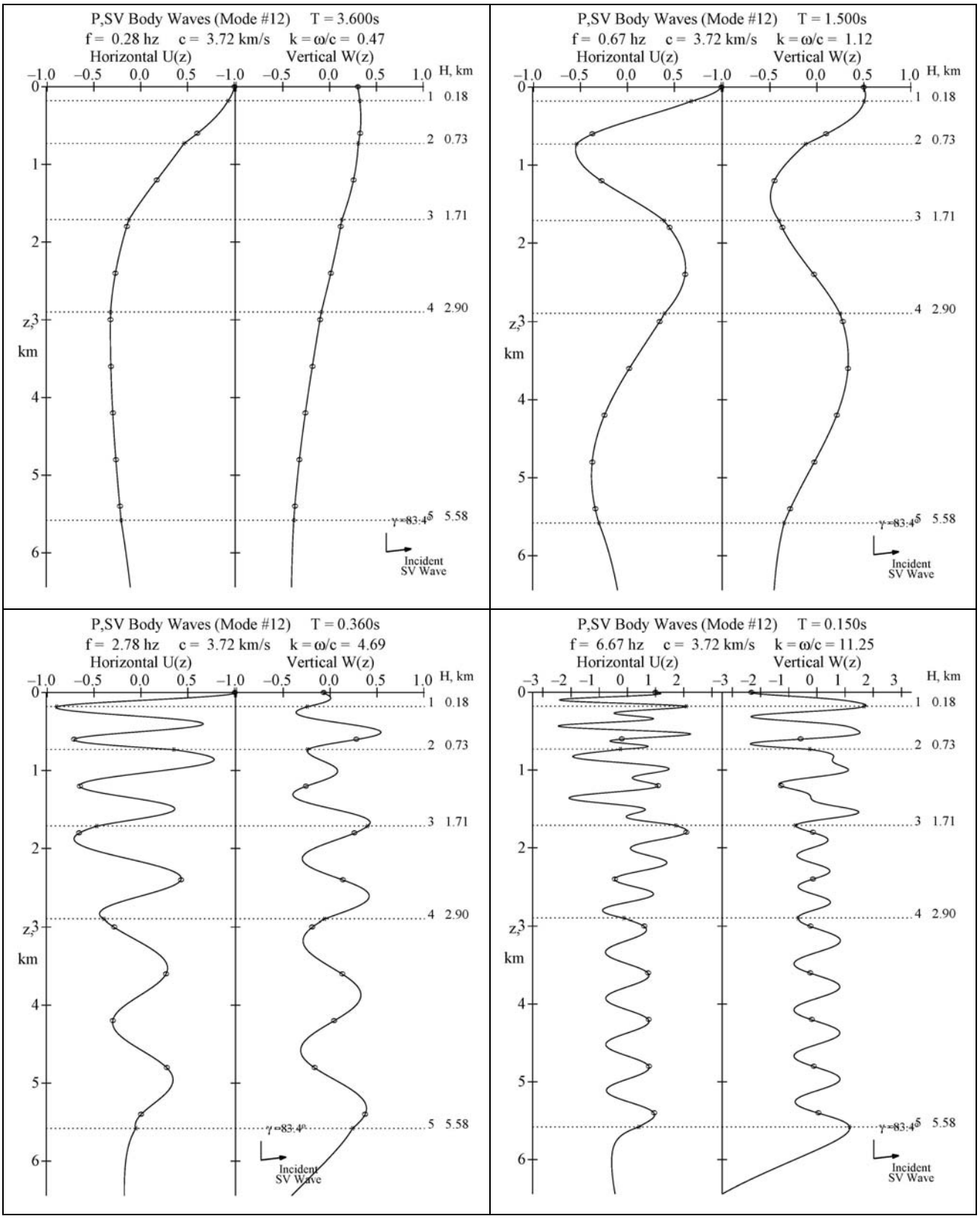

Figure VIII.2b shows the mode shapes for incident SV- waves at four selected periods: $\boldsymbol{T = 3.6,\ 1.5,\ 0.36,\ and\ 0.15\ s}$. Such mode shapes are again available at all 91 periods in the range from $\boldsymbol{T = 15.0\ s}$ down to $\boldsymbol{T = 0.04\ s}$. This allows us to generate the mode shape for incident SV- waves to be used as mode #7 in generation of the transverse components of synthetic translational motions at all depths. In the graphs the x-component $\boldsymbol{U(z)}$ for incident body SV waves is now normalized to have unit amplitude at $\boldsymbol{z = 0}$. Note that for $\boldsymbol{T = 0.15\ s}$, with the horizontal component $\boldsymbol{U(z)}$ normalized to have unit amplitude at the half-space surface, the corresponding horizontal $\boldsymbol{U(z)}$ and vertical $\boldsymbol{W(z)}$ motions both have maximum amplitude of over 2.0 in the top two layers.

With both the P- and SV- waves generating an extra mode in the layered media, together with the five modes of Rayleigh waves, can now be used to generate the radial and vertical components of synthetic translational motions at all depths on and below the surface.

Figures VIII.3a and b are plots of such synthetic accelerations respectively for both the horizontal $\boldsymbol{U(z)}$ and vertical $\boldsymbol{W(z)}$ components, calculated for the El Centro six-layered site model, at 100 depths equally spaced from the surface to almost 6 km below the surface, and for Case 1. At the hypocentral distance of $\boldsymbol{D = 10.0km}$, the **SYNACC** computer program determines that the appropriate duration of the accelerogram record should be just above 40 seconds.

As in the examples of the transverse components of motion, in Section VII, the depth of each accelerogram is labeled at 0.6 km spacing. Of the 100 acceleration time histories, six of them are plotted green, and labeled 0 to 5. The one labeled 0 is the accelerogram at the top surface $\boldsymbol{z = 0}$, while the ones labeled 1 to 5 are at depths at or closest to the interfaces between adjacent layered media.

Figure VIII.3a Synthetic Acceleration for **M**=6.5, **R**=8.0km, **H**=6.0km, **s**=0, and **soil**=2
Horizontal, Radial Motions

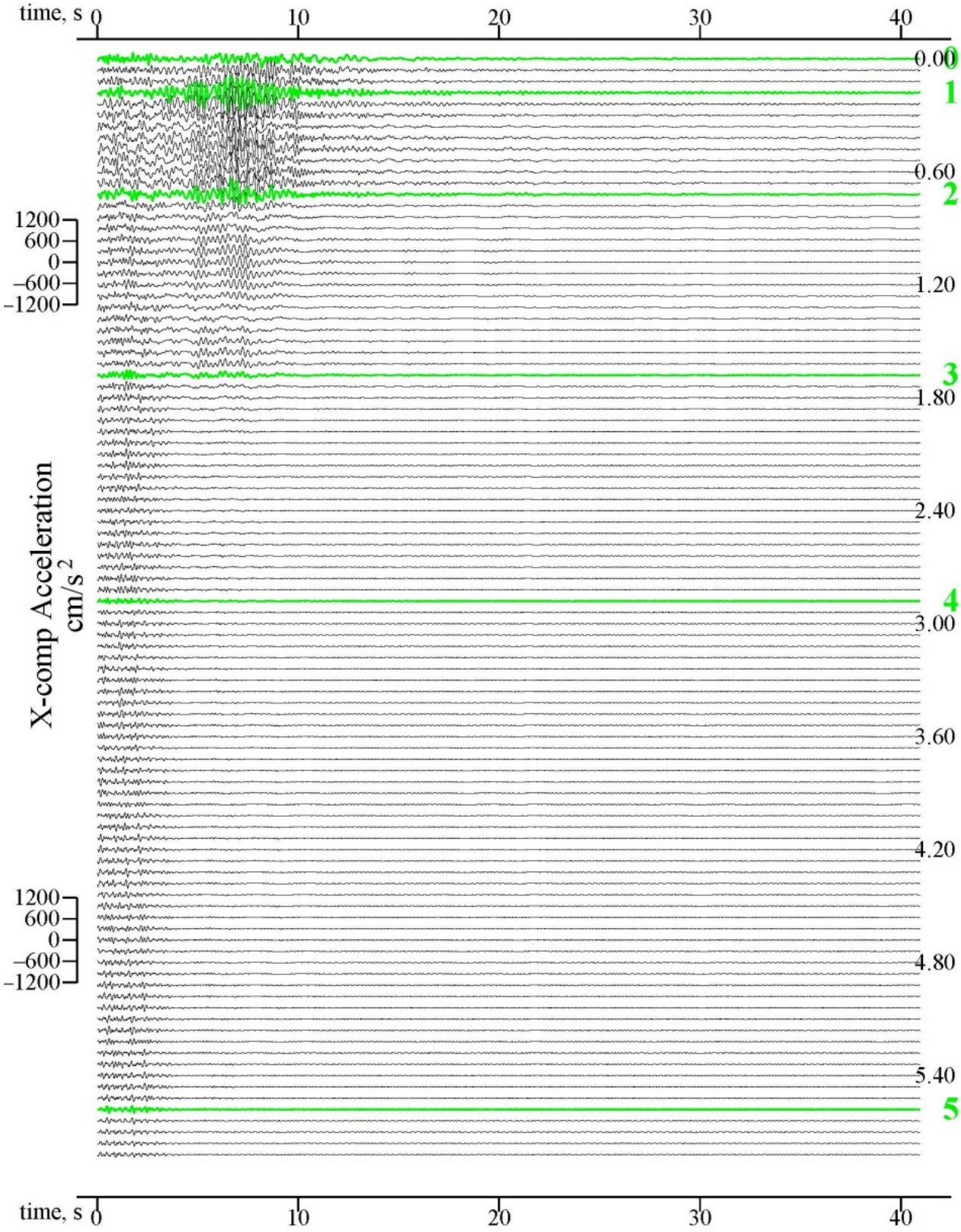

Figure VIII.3b Synthetic Acceleration for **M**=6.5, **R**=8.0km, **H**=6.0km, **s**=0, and **soil**=2
Vertical Motions

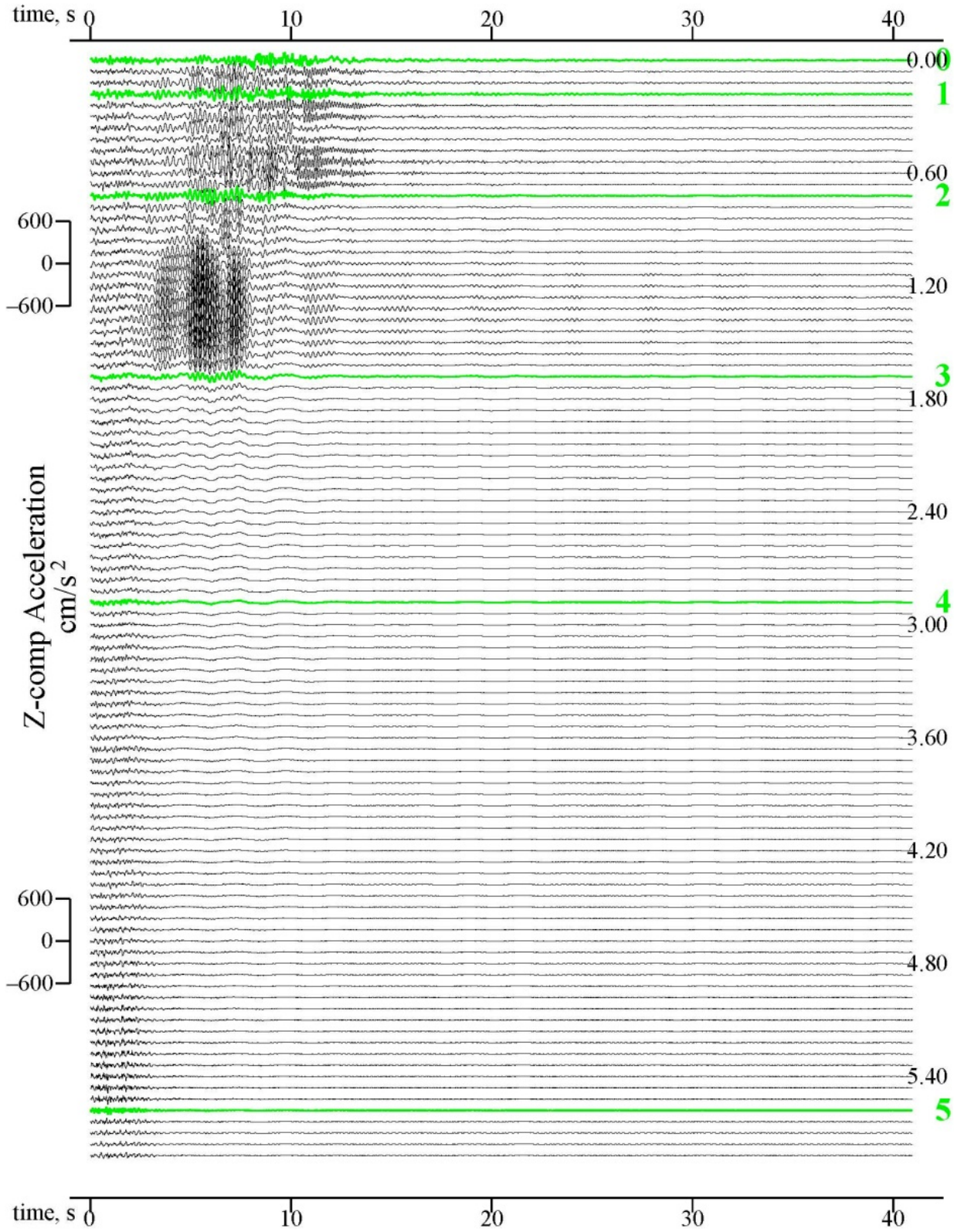

Recall that the time scale of the time histories has been shifted to have a common time origin, where $T = 0$ **sec** is defined by SYNACC to be the time D/c_{max}, where D is the hypocentral distance and c_{max} is the maximum phase velocity of the waves. Perusal of Figures VIII.3a and b will show that, for near filed distance with $D = 10.0km$, both the Rayleigh waves and incident and reflected P- and SV-body waves arrive within a few seconds of the start of the earthquake. The body waves have the same phase velocity at all periods and the direct arrival time of the P-waves (Figure VIII.1a) is $T = 2.60s$, while the arrival time for the SV- waves (Figure VIII.1b) is $T = 4.49s$. The arrival times for the Rayleigh waves will be different for different modes, and for different periods, since the phase velocities $c = c(T)$, depend on the periods, as shown by the dispersion curves in Figure I.1. The plots of acceleration curves do show that the strong-motions are all within the first 10 seconds from the start of the earthquakes.

Another point to note is that, for the horizontal component, the strong-motions are seen at the depths of the first two top layers, up to $z \sim 0.7km$. Smaller horizontal motions are observed in the 3rd layer up to $z \sim 1.7km$, beyond which the motions become small. For the vertical motions, the strong motions are observed in the first three top layers up to $z \sim 1.7km$, and the maximum motions are taking place in the 3rd layer from the top.

For the transverse component in Section VI, the motions below the surface are never higher than those at the surface. For the radial and vertical components in the example considered here, it is observed that the motions for the six-layered model at El Centro site can be much higher at depths than those at the surface.

This is consistent with the mode shape curves of Rayleigh waves in Section VI and in Appendix B, where it is found that, for all modes of Rayleigh waves, at moderate periods, large motions occur in the first three top layers, and then began to die down at greater depths. The decay of amplitudes with depth is even faster for waves with higher frequencies. For the horizontal component, it is noted that the maximum motions are observed in the 2nd layer from top for most periods. For the vertical component, the maximum motions are observed in the 3rd layer from top.

Figure VIII.4a Synthetic Velocity for **M**=6.5, **R**=8.0km, **H**=6.0km, **s**=0, and **soil**=2

Horizontal, Radial Motions

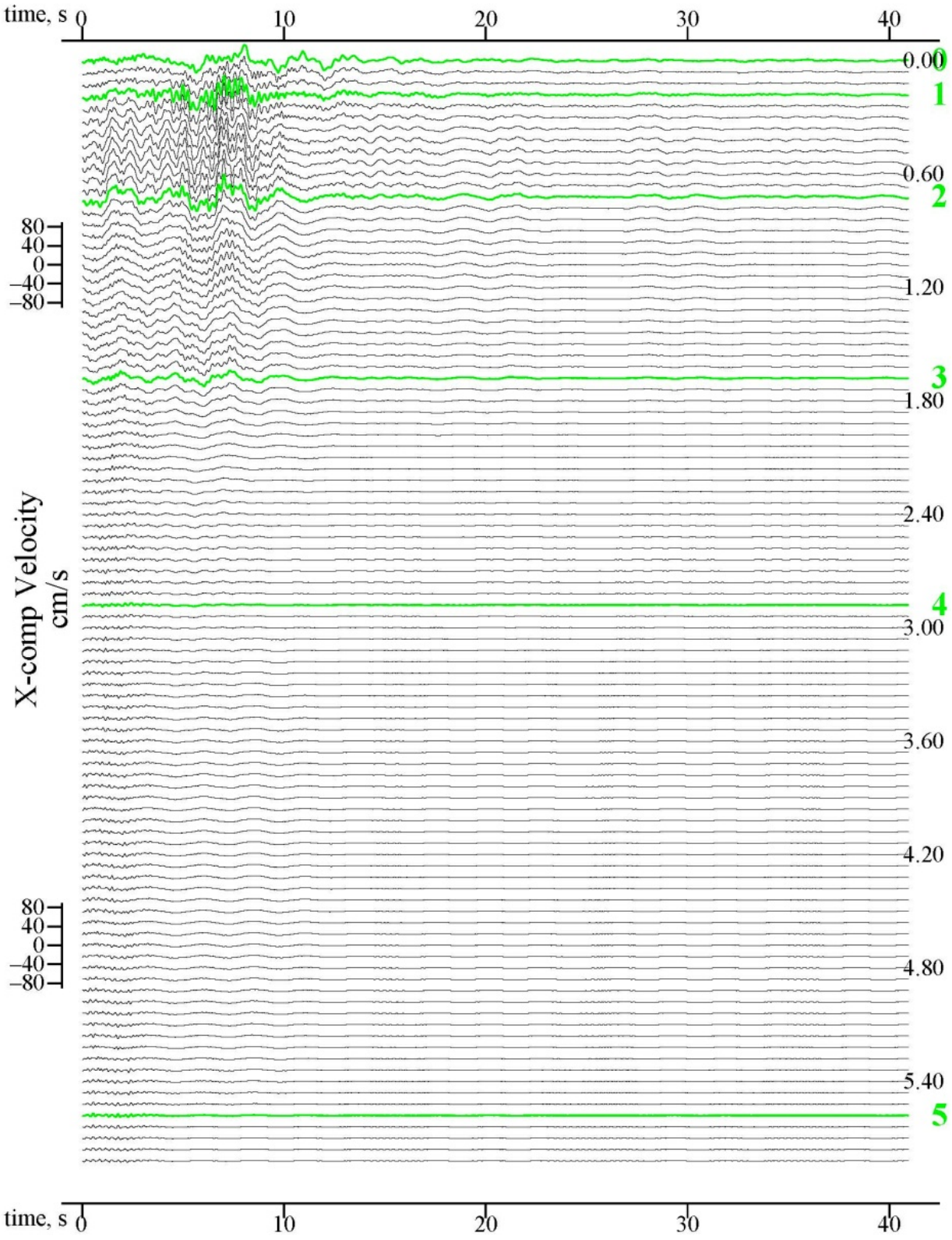

Figure VIII.4b Synthetic Velocity for **M**=6.5, **R**=8.0km, **H**=6.0km, **s**=0, and **soil**=2

Vertical Motions

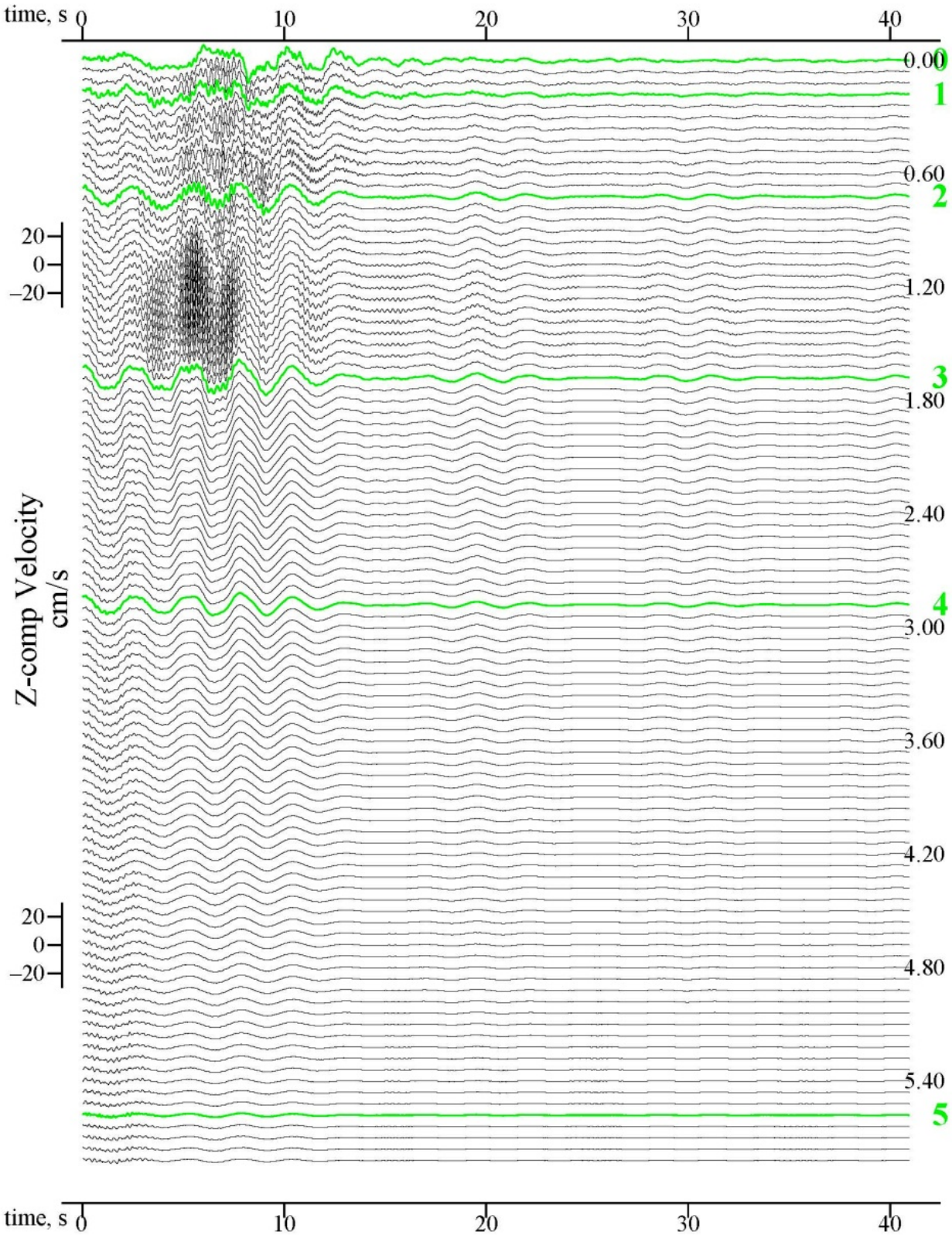

Figures VIII.4a and b show the synthetic velocity calculated for the El Centro six-layered site model for both horizontal $\boldsymbol{U(z)}$ and vertical $\boldsymbol{W(z)}$ components of motion. The depth of each velocity trace is labeled at points 0.6 km apart. Of the 100 velocity time histories, six are plotted green, and labeled 0 to 5. The one labeled 0 is the velocity at the top surface $\boldsymbol{z = 0}$, while the ones labeled 1 to 5 are at depths at or closest to the interfaces between adjacent layers. The new SYNACC program computes the velocity at all depths from the corresponding acceleration time histories from the Fourier transform in the frequency domain, to get the velocity spectra, and then taking its inverse Fourier transform.

The same observations for velocity can be made as for accelerations, namely, the strong-motions are again observed in the first two layers of this site, up to $\boldsymbol{z = 0.7km}$. Unlike acceleration, the velocity motions, especially for the vertical component, do not completely die down even at larger depths.

Figures VIII.5a and b show the plots of the corresponding synthetic displacement of the 2 components of motions. The depth for all displacements is again labeled at intervals of 0.6 km apart. Of the 100 displacement time histories, six are plotted green, and labeled 0 to 5. The one, which is labeled 0 is the displacement at the top surface $\boldsymbol{z = 0}$, while the ones labeled 1 to 5 are those at depths corresponding to or closest to the interfaces between adjacent layers. The new SYNACC program computes the displacement at all depths from the corresponding acceleration time histories in the frequency domain to get the displacement spectra, and then taking its inverse Fourier transform.

The same observations for displacement time histories can be made as for accelerations, namely, the strong-motions are observed in the first three layers of the site model, up to $\boldsymbol{z = 1.7km}$. Unlike accelerations, the displacements, especially for the vertical components, do not completely die down even at large depths.

Figure VIII.5a Synthetic Displacement for **M**=6.5, **R**=8.0km, **H**=6.0km, **s**=0, and **soil**=2

Horizontal, Radial Motions

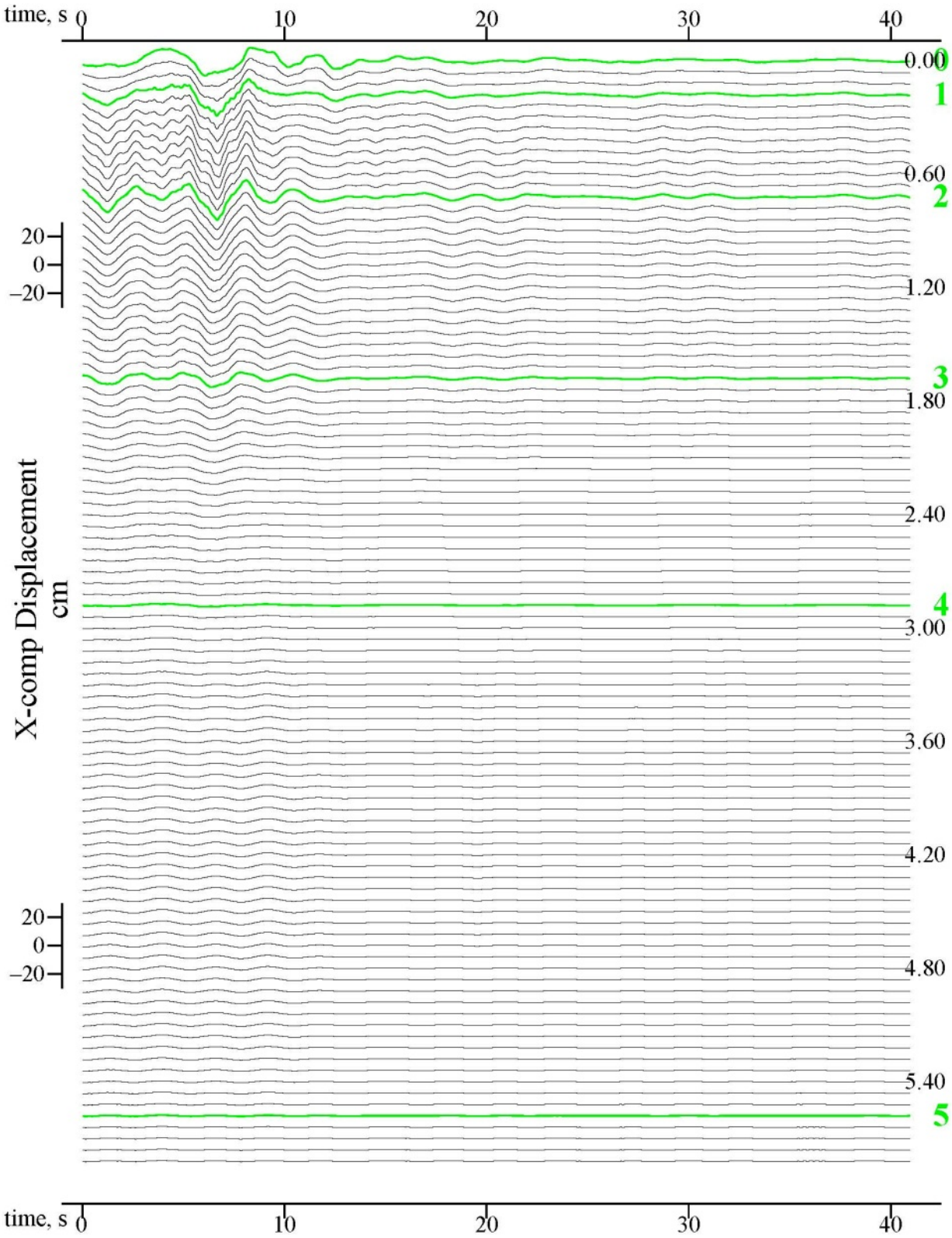

Figure VIII.5b Synthetic Displacement for **M**=6.5, **R**=8.0km, **H**=6.0km, **s**=0, and **soil**=2

Vertical Motions

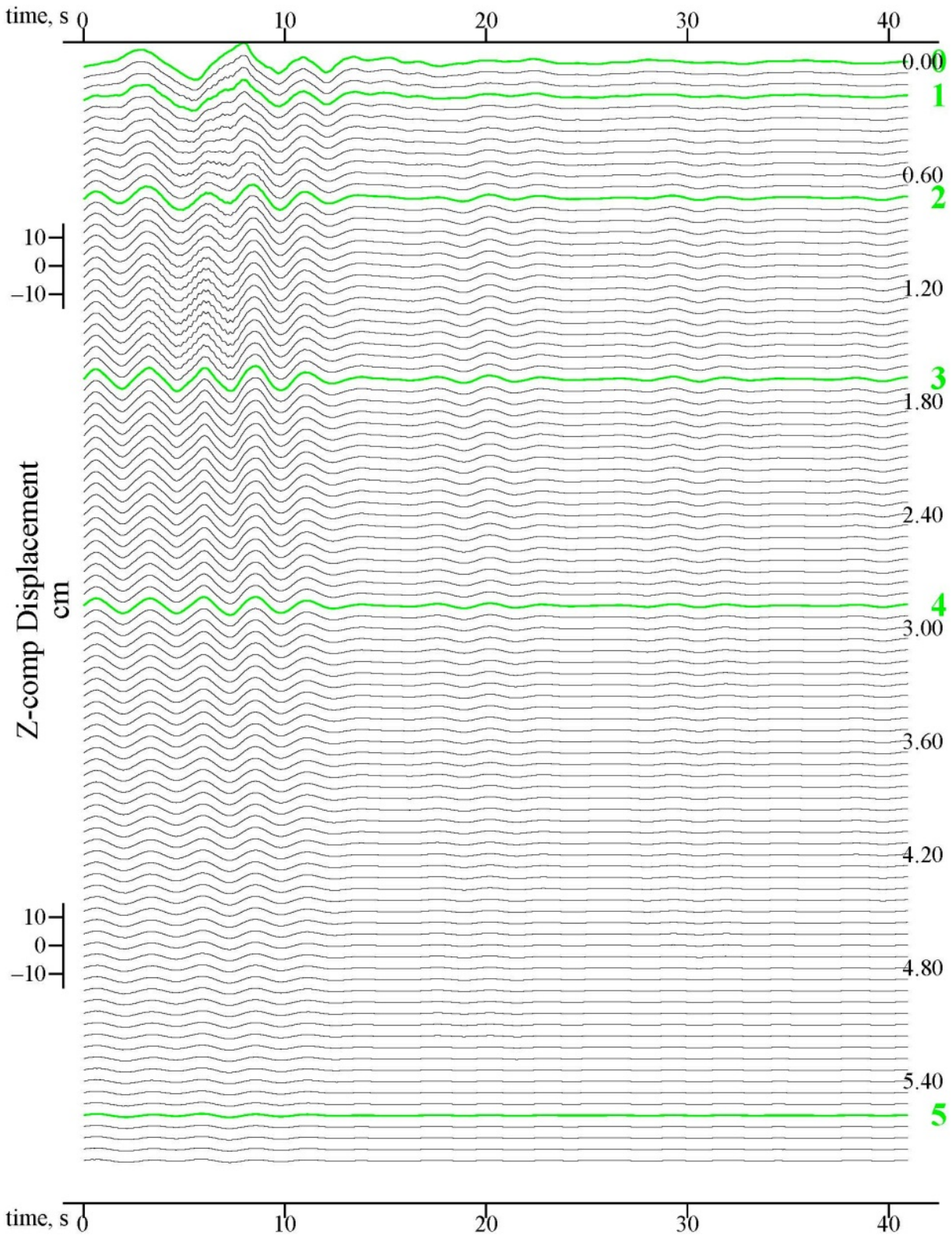

As for the transverse components in Section VII, the same time histories of synthetic acceleration, velocity and displacement motions, from Figures VIII.3, 4 and 5, will now be presented as three-dimensional (3-D) figures.

Figures VIII.6a and b are the 3-D plots of synthetic translational motions respectively of the horizontal radial and vertical components for the same 100 acceleration time histories corresponding to Figure VIII.3.

Figure VIII.6a Synthetic Acceleration for **M**=6.5, **R**=8.0km, **H**=6.0km, **s**=0, and **soil**=2
Horizontal, Radial Motions

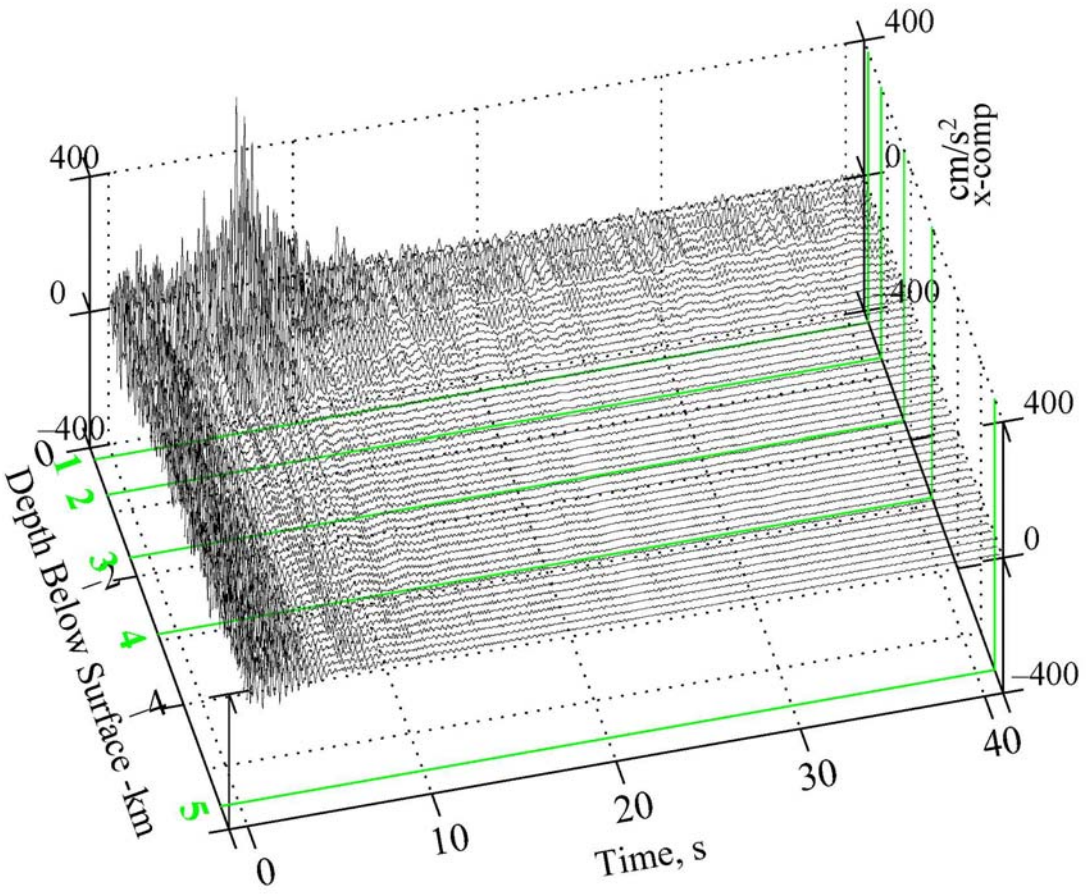

Figure VIII.6b Synthetic Acceleration for **M**=6.5, **R**=8.0km, **H**=6.0km, **s**=0, and **soil**=2

Vertical Motions

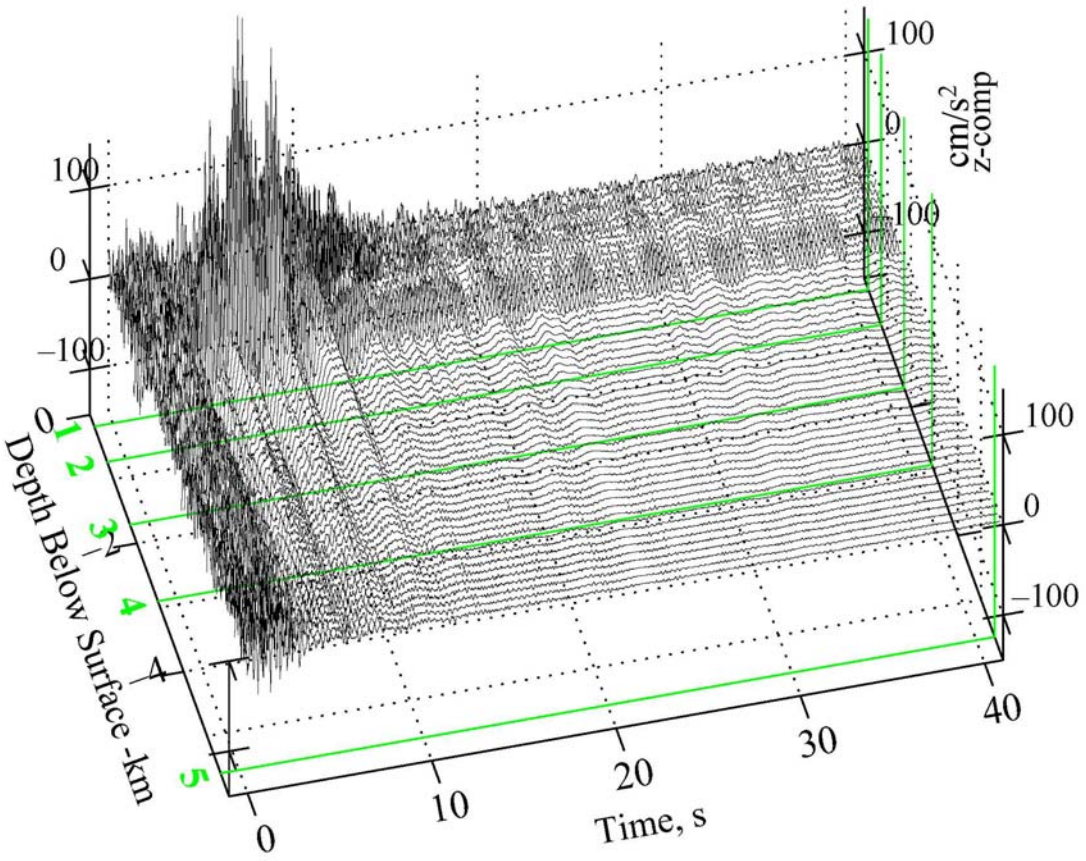

Figures VIII.7a and b show the 3-D views of velocity respectively for the horizontal and vertical components corresponding to the 2-D plots in Figures VIII.4a and b.

Figure VIII.7 Synthetic Velocity for $M = 6.5$, $R = 8.0km$, $H = 6.0km$, $s = 0$, and $s_L = 2$

(a) Horizontal, Radial Motions **(b) Vertical Motions**

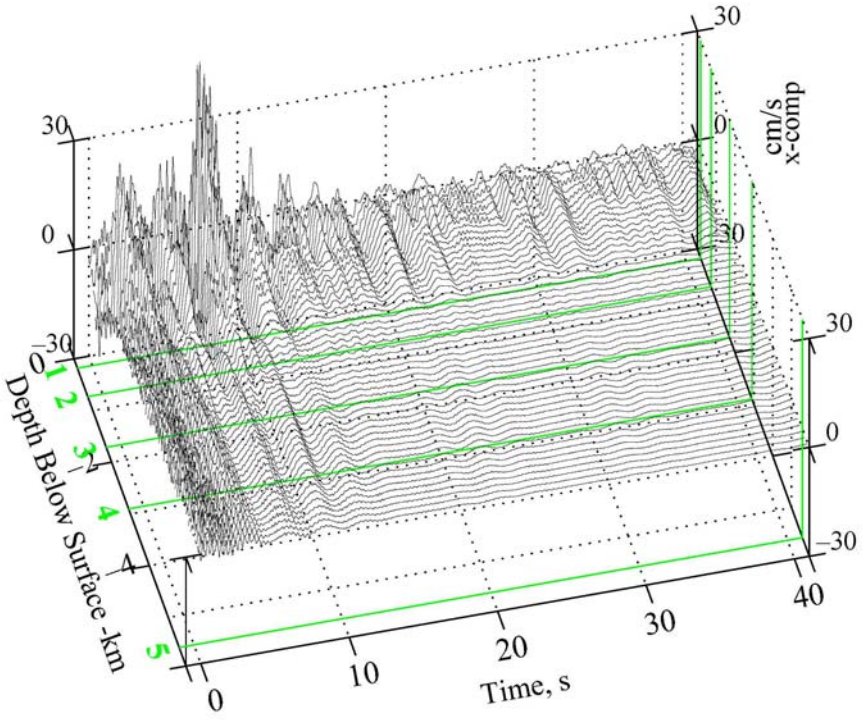

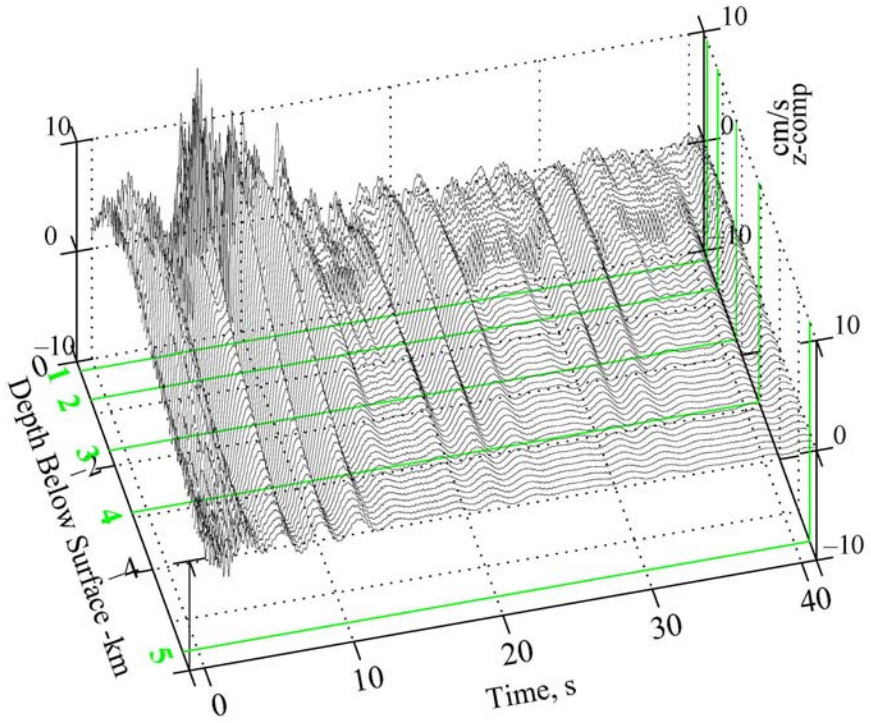

Figures VIII.8a and b show the 3-D views of displacement respectively for the horizontal and vertical components corresponding to the 2-D plots in Figures VIII.5a and b.

Figure VIII.8 Synthetic Displacement for $M = 6.5$, $R = 8.0km$, $H = 6.0km$, $s = 0$, and $s_L = 2$

(a) Horizontal, Radial Motions **(b) Vertical Motions**

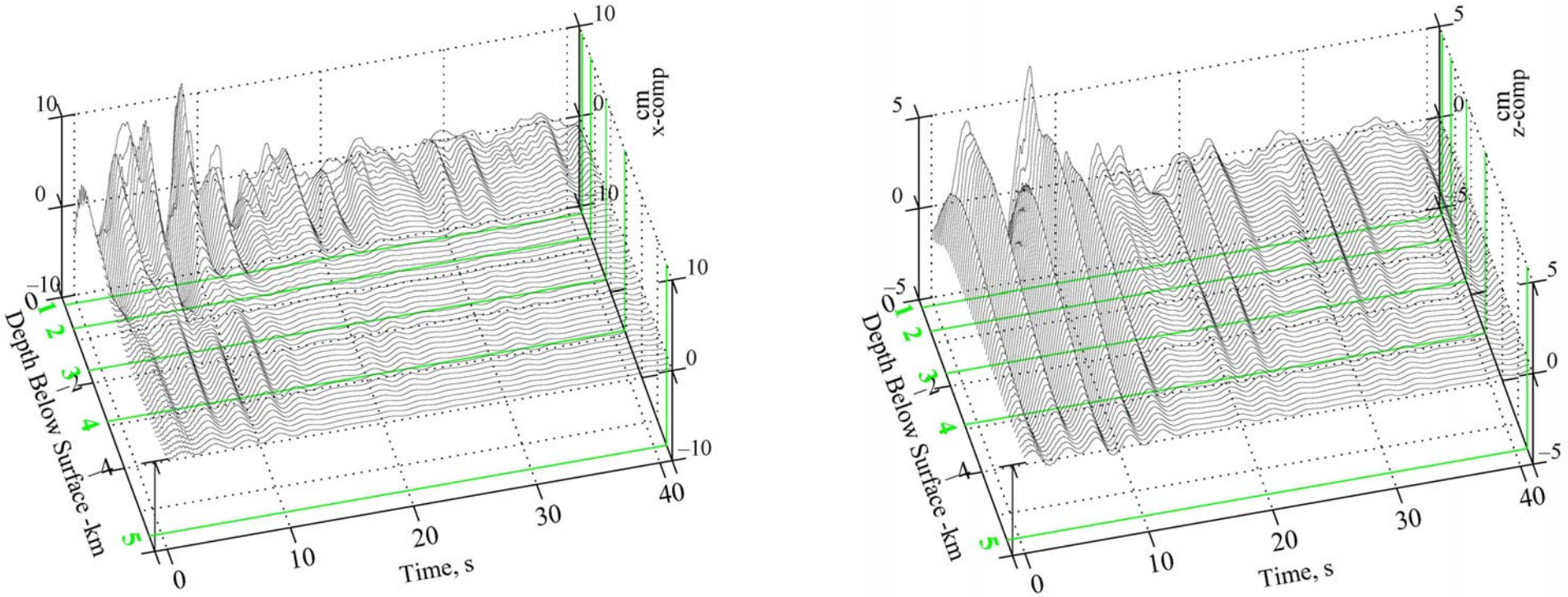

VIII.2 Case 2: $M = 6.5,\ R = 40.0km,\ H = 9.0km\ \left(D = 41.0km\right),\ s = 0,$ and $s_L = 2$

We now consider the far field motions, with epicentral distance of $\boldsymbol{R = 40.0km}$ and an earthquake source at a focal depth of $\boldsymbol{H = 9.0km}$. This corresponds to a hypocentral distance of $\boldsymbol{D = \left(R^2 + H^2\right)^{1/2} = \left(40.0^2 + 9.0^2\right)^{1/2} = 41\ km}$.

Figure VIII.9a P Waves Ray Path from Source to Site

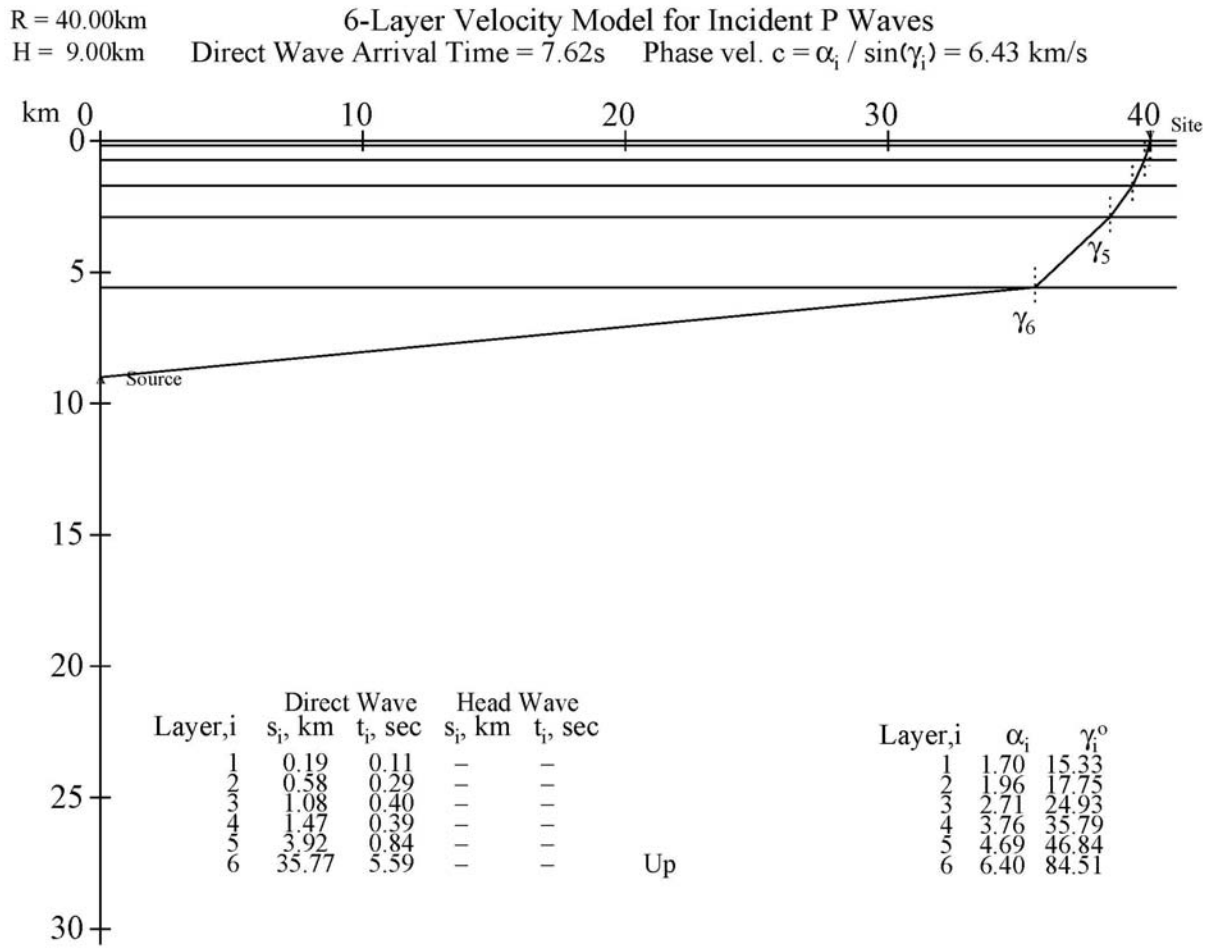

Layer,i	Direct Wave s_i, km	Direct Wave t_i, sec	Head Wave s_i, km	Head Wave t_i, sec
1	0.19	0.11	–	–
2	0.58	0.29	–	–
3	1.08	0.40	–	–
4	1.47	0.39	–	–
5	3.92	0.84	–	–
6	35.77	5.59	–	–

Layer,i	α_i	γ_i^o
1	1.70	15.33
2	1.96	17.75
3	2.71	24.93
4	3.76	35.79
5	4.69	46.84
6	6.40	84.51

Figure VIII.9a shows a plot of the ray path taken by the (faster) P waves, from the earthquake source to the recording site. As before, the ray path is chosen so that the phase velocities at each layer of the 6-layered media are the same.

$$\boldsymbol{c = \alpha_i \,/\sin\left(\gamma_i\right) = \ 6.43\ km/s,\ a\ constant} \qquad \text{(VIII.2)}$$

where α_i = P wave speed, and γ_i = angle the ray makes with respect to the vertical direction at the i^{th} layer. The ray will start with an angle $\gamma_6 \sim 84.5^o$ with respect to vertical direction, and progress up the layered media arriving at the site with $\gamma_1 \sim 15.3^o$. The phase velocity at all layers is the same, $c = 6.43 km/s$.

Figure VIII.9b shows the ray path taken by the (slower) SV waves from the earthquake source to the recording site.

Figure VIII.9b Ray Path of SV Waves from Source to Site

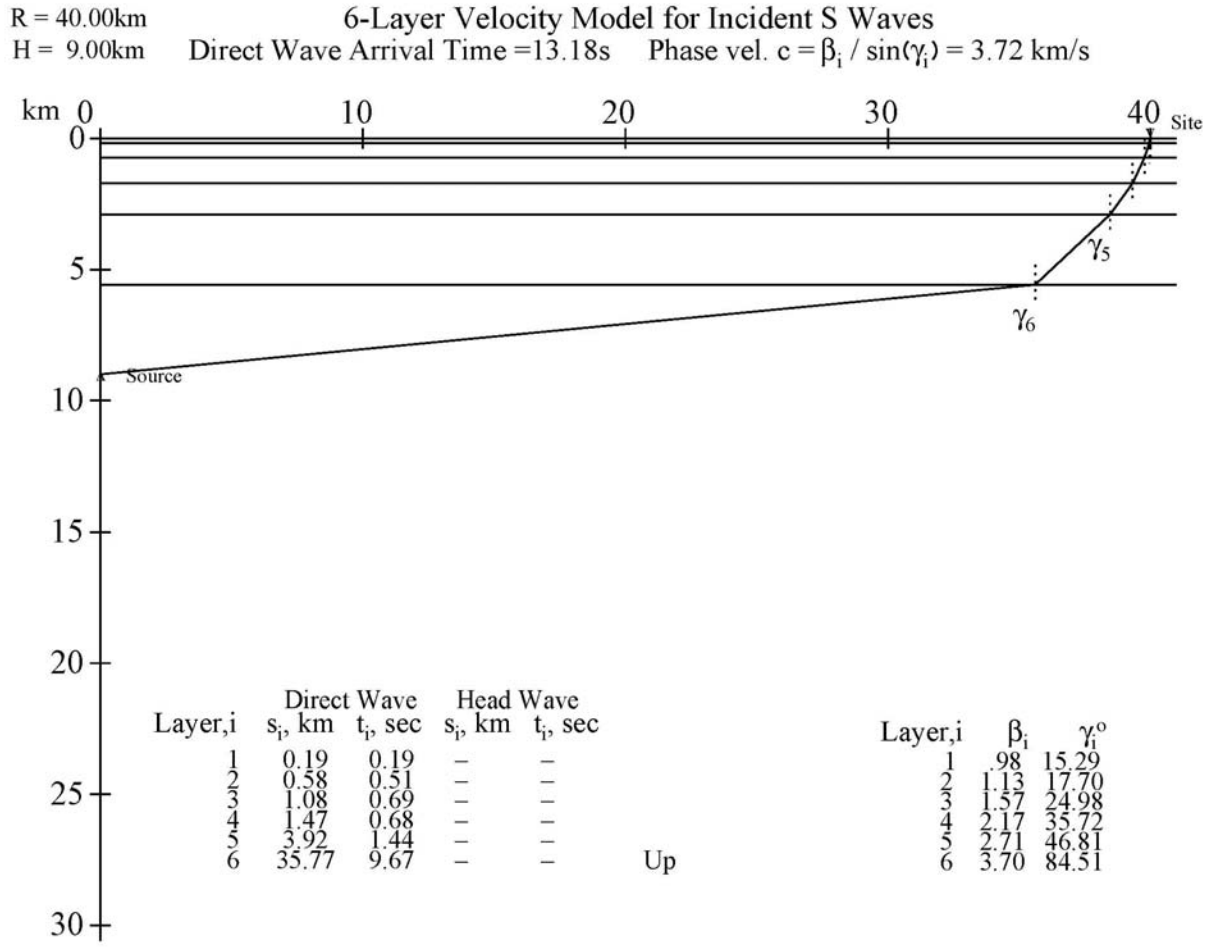

Layer,i	Direct Wave s_i, km	Direct Wave t_i, sec	Head Wave s_i, km	Head Wave t_i, sec
1	0.19	0.19	–	–
2	0.58	0.51	–	–
3	1.08	0.69	–	–
4	1.47	0.68	–	–
5	3.92	1.44	–	–
6	35.77	9.67	–	–

Layer,i	β_i	γ_i^o
1	.98	15.29
2	1.13	17.70
3	1.57	24.98
4	2.17	35.72
5	2.71	46.81
6	3.70	84.51

This results in the ray starting with an angle of $\gamma_6 \sim 84.5^o$ with respect to vertical, and progressing up the layered media and arriving at the site with $\gamma_1 \sim 15.3^o$. These are practically

the same angles as for the incident P-waves, even though the phase velocity is slower: $\boldsymbol{c = 3.72 km / s}$.

Figure VIII.10a shows the typical plots of mode shape amplitudes for incident P-waves at four selected periods: $\boldsymbol{T = 5.0,\ 1.5,\ 0.50,\ and\ 0.15\ s}$. Such mode shapes are available at all 91 periods in the range from $\boldsymbol{T = 15.0\ s}$ down to $\boldsymbol{T = 0.04\ s}$. They are similar to the mode shapes of incident body P-waves in Figure VIII.2a of Case 1, the only difference being that the incident angle, from Figure VIII.9a, is now $\boldsymbol{84.5^o}$ with respect to the vertical from the bottom semi-infinite layer #6. As in Case 1, this allows us now to generate an extra mode for incident P-waves, which together with the 5 modes of Rayleigh waves, can be used to generate the horizontal radial and vertical components of synthetic translational motions at all depths on and below the surface.

Figure VII.10b presents the typical plots of such mode shape amplitudes for incident SV-waves at four selected periods: $\boldsymbol{T = 5.0,\ 1.5,\ 0.50,\ and\ 0.15\ s}$. Such mode shapes are again available at all 91 periods in the range from $\boldsymbol{T = 15.0\ s}$ down to $\boldsymbol{T = 0.04\ s}$. As in Case 1, this allows us how to generate the mode for incident SV-waves, which together with the 5 modes of Rayleigh waves, can be used to generate the horizontal radial and vertical components of synthetic translational motions at all depths at and below the surface.

Figure VIII.10a Incident P- Waves at $T = 5.0,\ 1.5,\ 0.50,$ and $0.15\ s$

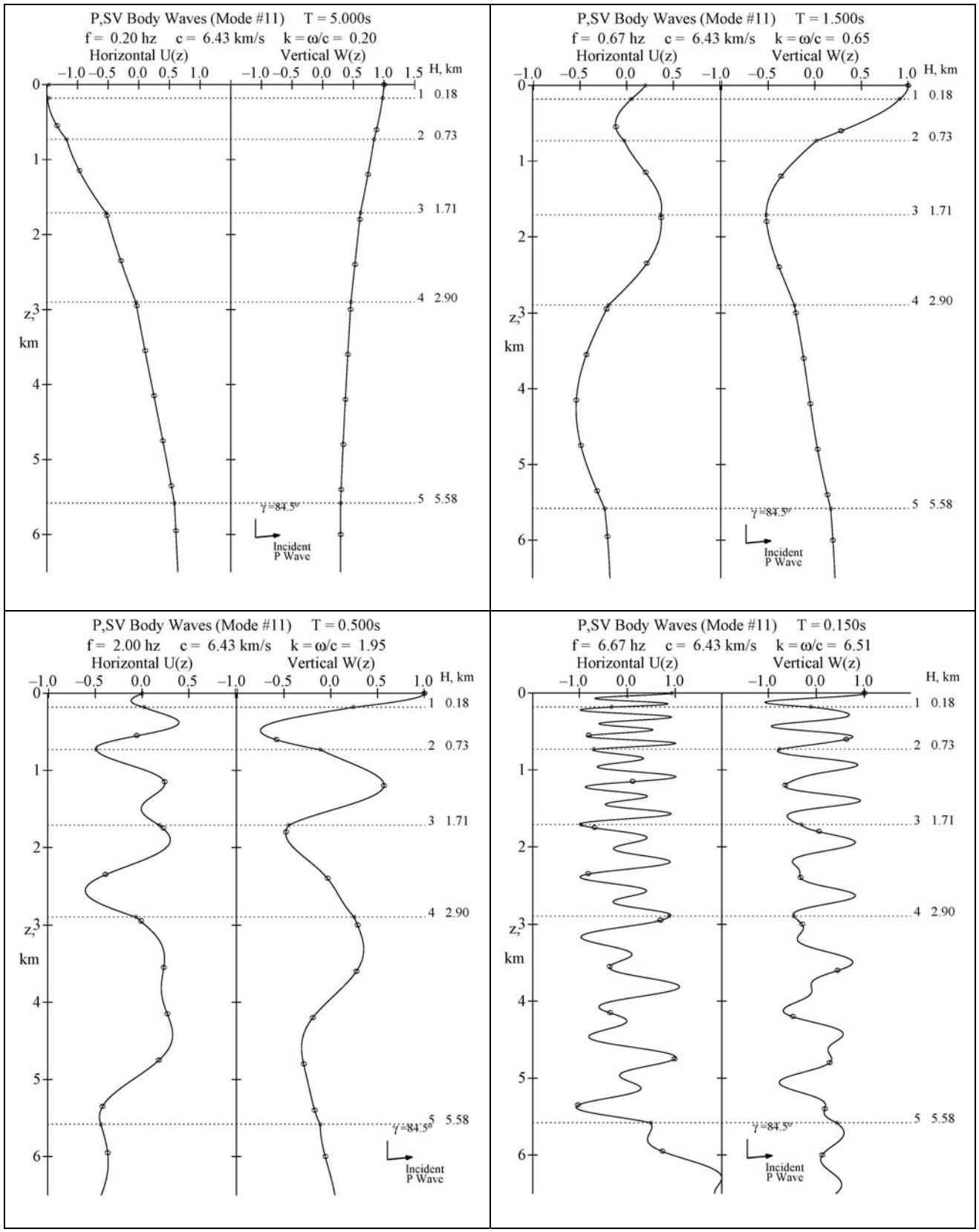

Figure VIII.10b Incident SV- Waves at T = 5.0, 1.5, 0.50, and 0.15 *s*

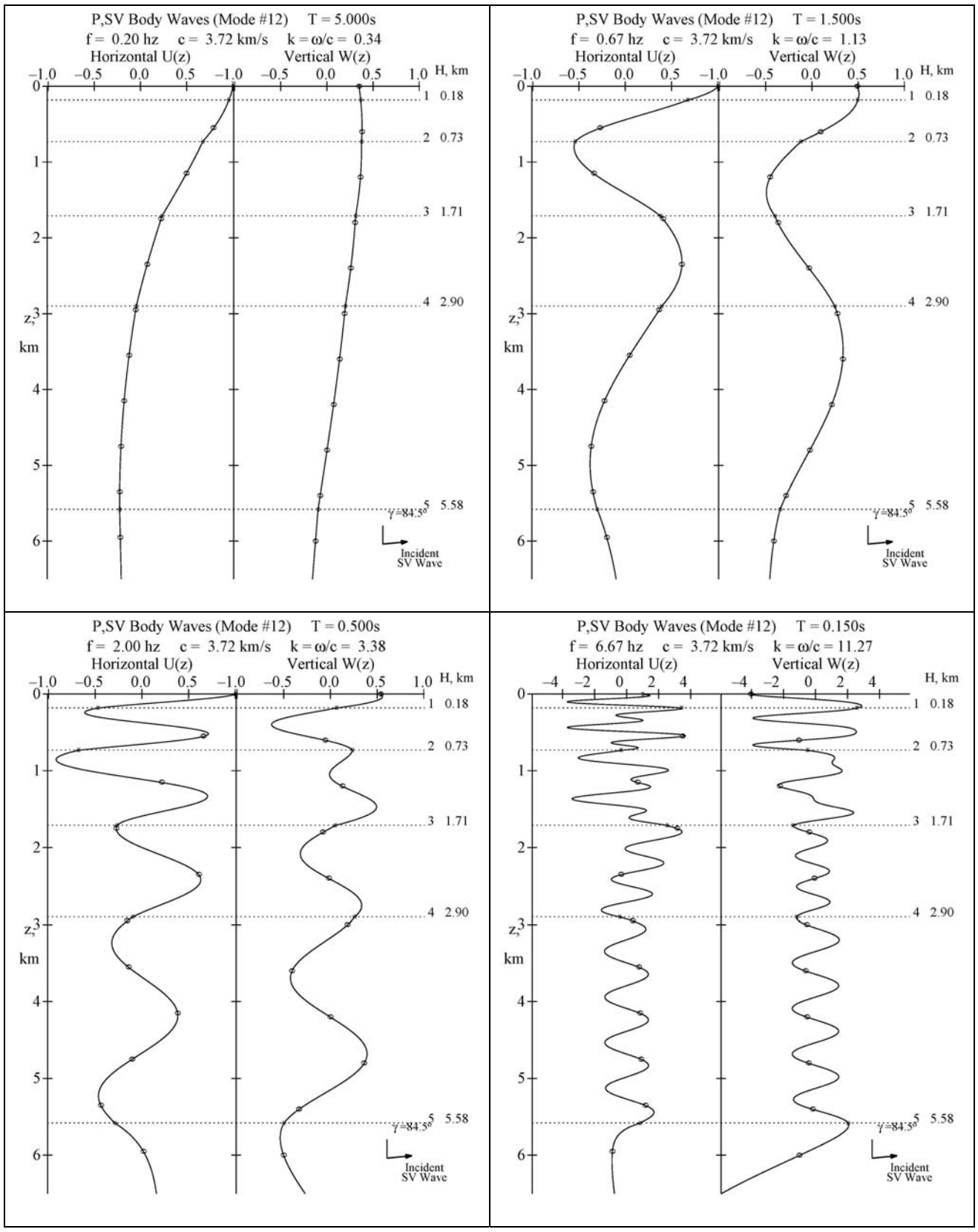

Figures VIII.11a and b are the 3-D plots of the synthetic translational motions of the horizontal radial and vertical components calculated for the El Centro six-layered site for case 2 earthquake parameters. Again the SYNACC program determines that the appropriate duration of the accelerogram record should be above 40 seconds. The 3-D plot has the two horizontal longitudinal and transverse coordinate axes correspond to the **time** and to the **depth** in **km** below the surface. The vertical axis is the **acceleration** in cm/s^2. The five green lines, labeled 1 to 5, correspond to the positions of the boundaries between the layers.

Figure VIII.11a Synthetic Acceleration for **M**=6.5, **R**=40.km, **H**=9.km, **s**=0, and **soil**=2
Horizontal, Radial Motions

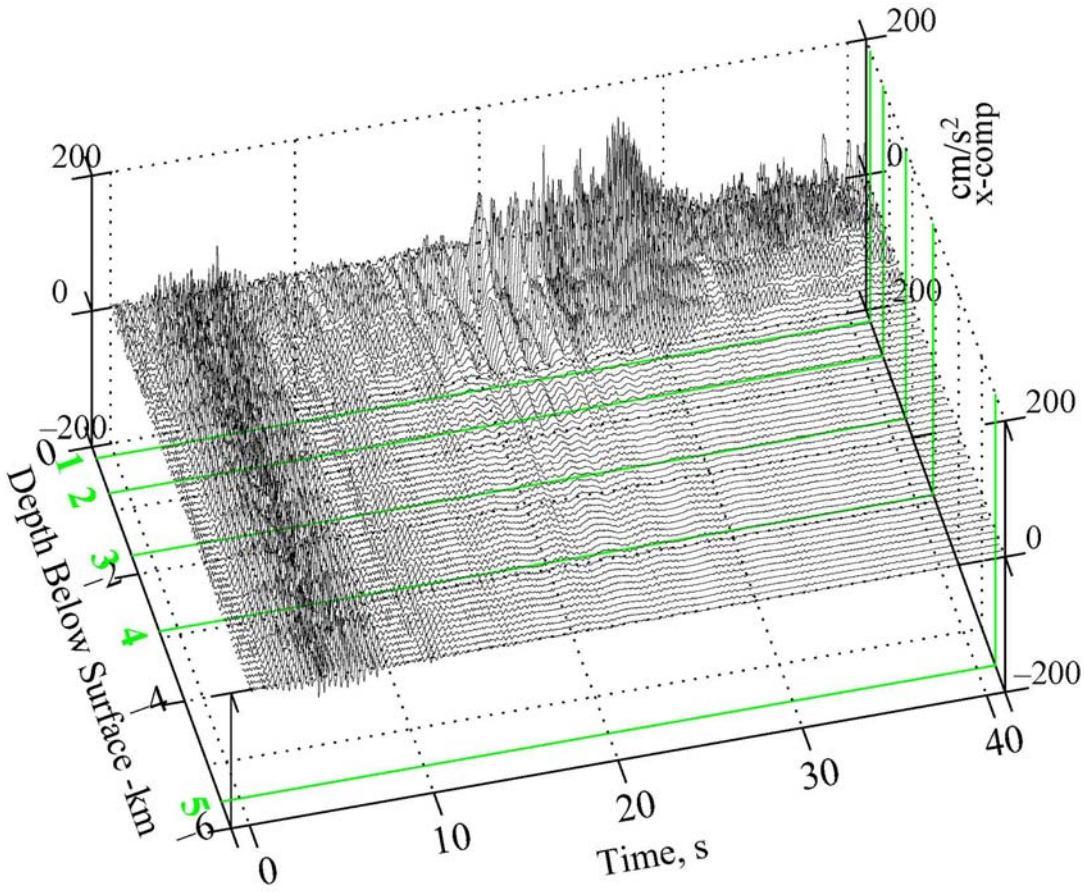

Figure VIII.11b Synthetic Acceleration for **M**=6.5, **R**=40.km, **H**=9.km, **s**=0, and **soil**=2
Vertical Motions

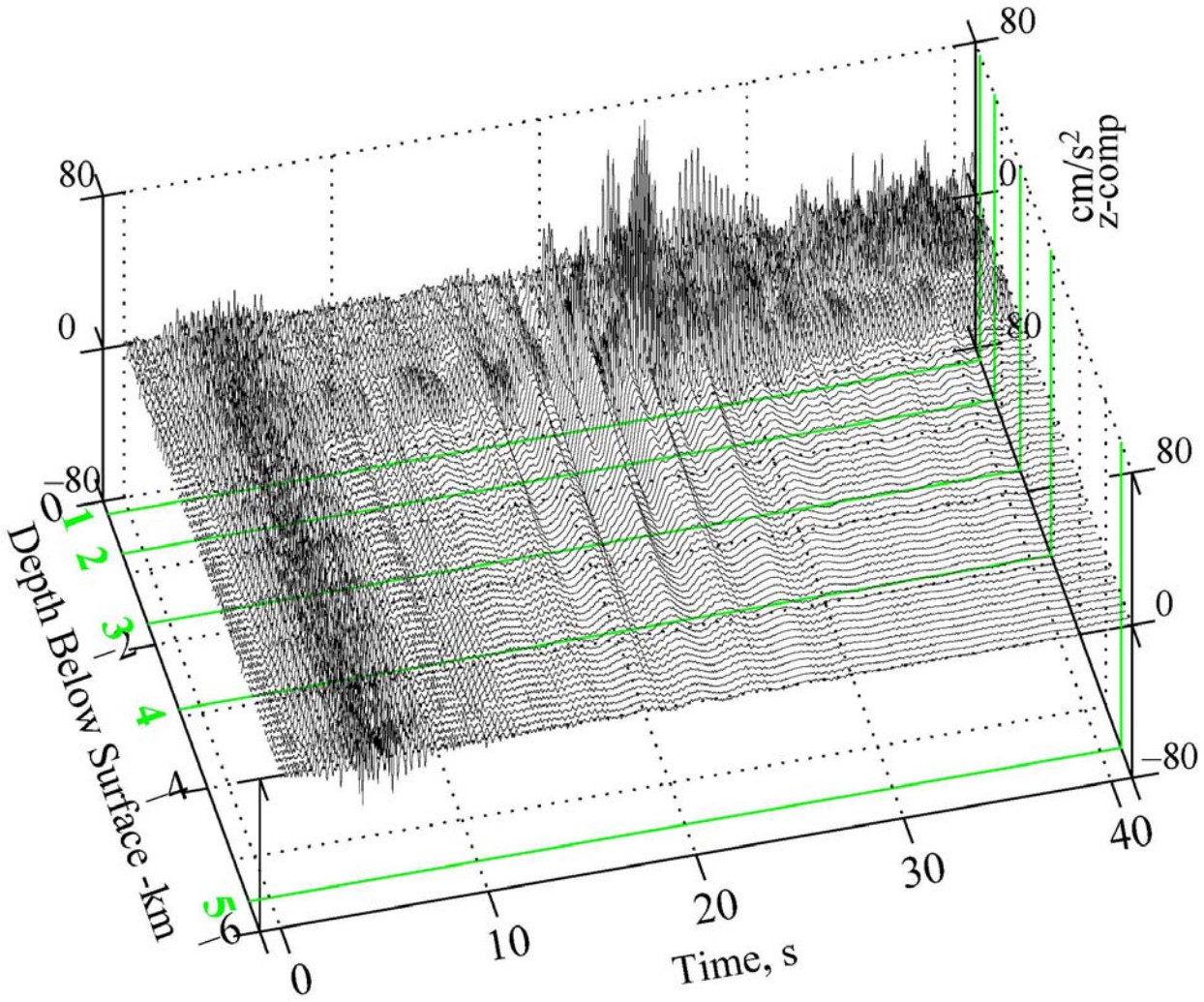

Perusal of Figures VIII.11a and b will show that, at far-field distance, here $\boldsymbol{D = 41.0km}$, the Rayleigh surface waves and body P and SV waves arrive at different times from the earthquake origin time. The P waves have the same phase velocity at all periods and Figure

VIII.9a shows that the arrival time of the P waves is $T = 7.62s$, while the arrival time for the SV waves, from Figure VIII.9b, is $T = 13.18s$. Recall that the actual time scale of the time histories has been shifted to have a common time scale, where $T = 0$ **sec** is defined by SYNACC to be the time D/c_{max}, where D is the hypocentral distance and c_{max} is the maximum phase velocity of the waves.

The arrival times for the Rayleigh waves will be different for the different modes, and for waves at different periods, since the phase velocities $c = c(T)$, depend on the period, as shown by the dispersion curves in Figure I.1. The accelerations show that the noticeable surface waves do not arrive until after 20s from the start of the earthquake.

The strong-motion surface waves beyond the 20sec, are observed at depths of the first three top layers, up to $z \sim 1.7km$. The first two layers contain stronger motions than the 3rd layer, with negligible motions being observed deeper than the 3rd layer. As in Case 1, *for the radial and vertical components here, it is observed that the motions can be larger at depths than at the surface.*

As in Case 1, this is consistent with the nature of mode shapes of Rayleigh waves of Section VI and Appendix B, where it is found that, for all modes of Rayleigh waves, at moderate periods, large motions can occur in the layers near top surface, before the amplitudes begin to die down with depth. The decay of amplitudes with depth is even faster for waves at higher frequencies. For the horizontal component, and the example site presented here, it is noted that the maximum motions occur in the 2nd layer from top, for most periods. For the vertical component, the maximum motions are observed in the 3rd layer from top.

Figures VIII.12a and b show the 3-D synthetic motions of the horizontal radial and vertical components of the velocity time histories. They are computed by SYNACC, from synthetic accelerations, the same way as in Case 1.

The velocity time histories show that the body waves and surface waves arrive at different times. The body waves are present in the first 10 seconds of the record, while the

surface waves appear after 20 seconds. For both velocity and displacement, the body waves are significant at all depths, while the surface waves are more noticeable only on the top 3 layers, up to $z = 1.7km$.

Figure VIII.12a **Synthetic Velocity for M**=6.5, **R**=40.km, **H**=9. km, **s**=0, and **soil**=2
Horizontal, Radial Motions

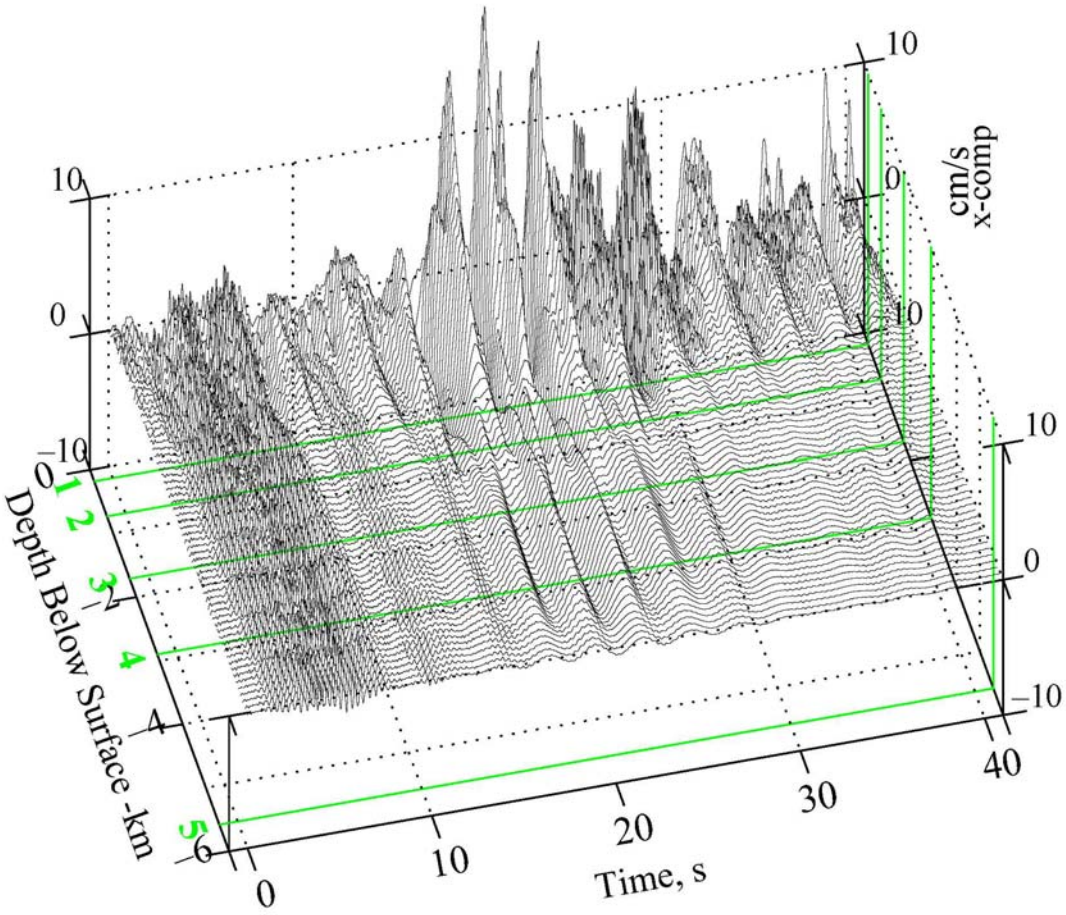

Figure VIII.12b **Synthetic Velocity for M**=6.5, **R**=40.km, **H**=9. km, **s**=0, and **soil**=2

Vertical Motions

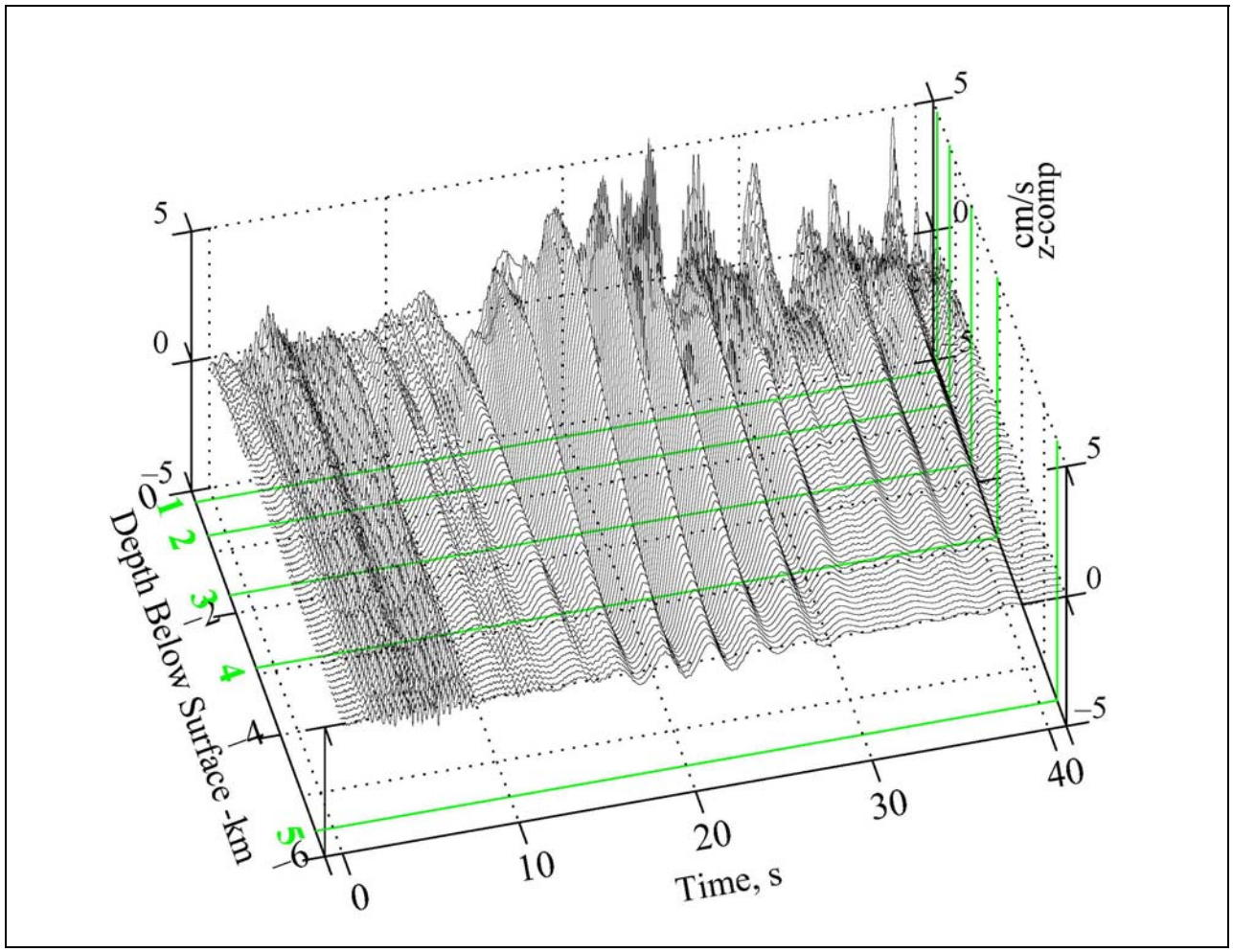

Figures VIII.13a and b show the 3-D synthetic motions of the horizontal radial and vertical components of displacement time histories. They are computed by SYNACC, from synthetic accelerations, the same way as in Case 1.

Figure VIII.13 Synthetic Displacement for M=6.5, **R**=40.km, **H**=9. km, **s**=0, and **soil**=2

(a) Horizontal, Radial Motions

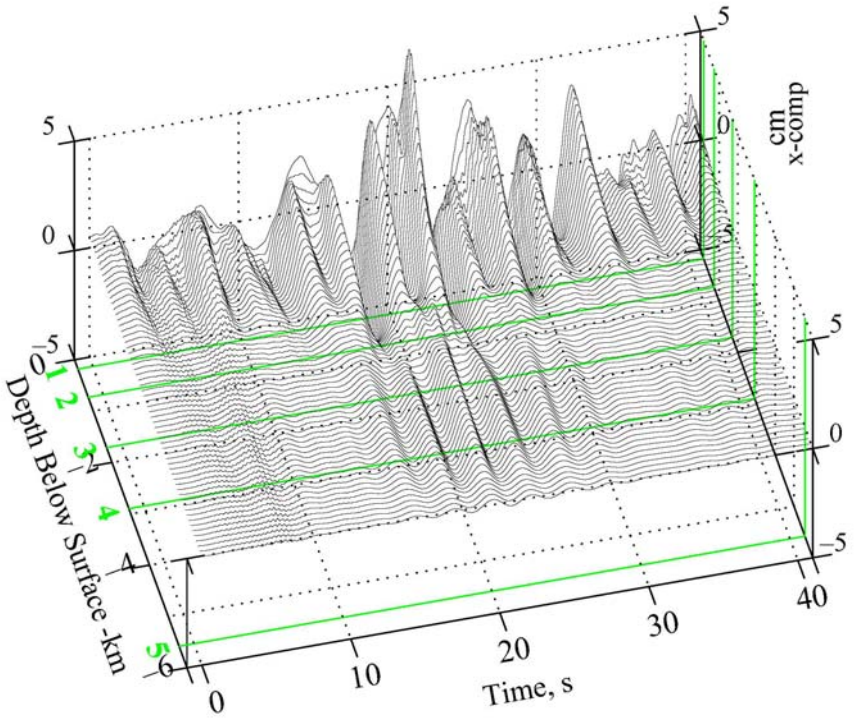

(b) Vertical Motions

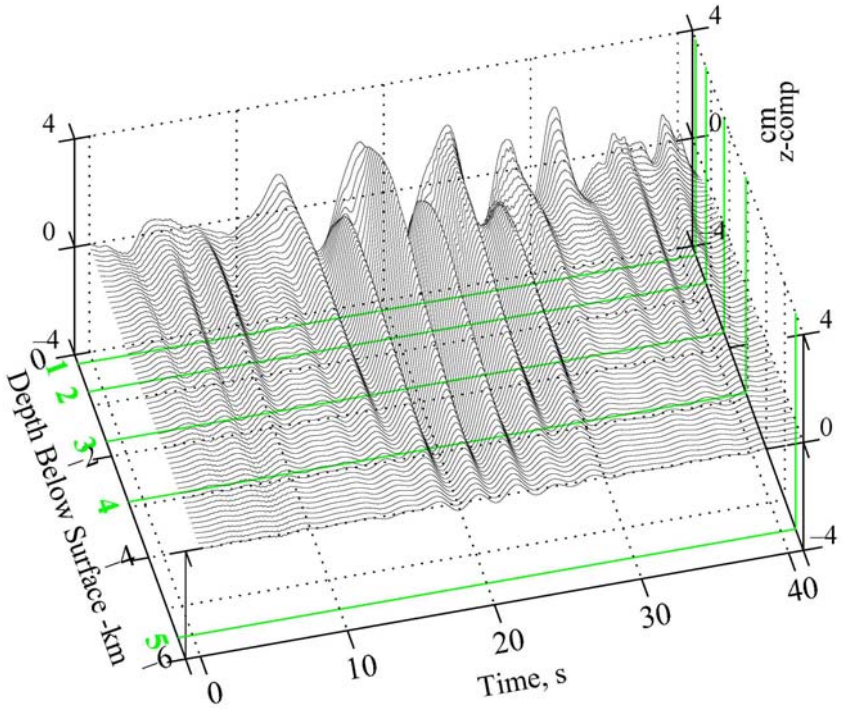

The contributions of the synthetic motions from body waves and surface waves can be better visualized by plotting them separately, as in Figures VII.14, 15 and 16a and b below.

Figure VIII.14a shows the horizontal, radial *x*-component acceleration, velocity and displacement time-histories of both the body waves and surface waves, plotted in separate graphs. Figure VIII.14b shows the corresponding plots for the vertical z- component of motion.

In both figures, Figures VIII.14a (x-comp) and 14b (z-comp), the two 3-D graphs represent the acceleration time histories of the body waves and of surface waves. The body waves (at the left) arrive at the very beginning and dominate the motions at all depths within the first 10+ seconds. The surface waves (on the right) arrive later, with the motions not seen until 20 seconds after the record starts. Combining the motions of the body waves and surface waves results in the acceleration time histories of the total x-component synthetic motions as shown in Figure VIII.11, where the two types of motions are clearly distinguishable.

The two 3-D graphs of Figures VIII.15a (x-comp) and VIII.15b (z-comp) represent the velocity time histories of the body waves and of surface waves. The trend of the velocity time histories is as in that of the accelerations. The surface wave velocity time histories (on the right) have strong motions only at the top 3 layers of the media and the maxima occur there beyond the 20 seconds after the earthquake starts.

The two 3-D graphs in Figures VIII.16a (x-comp) and VIII.16b (z-comp) show the displacement time histories of the body waves and of surface waves. Unlike the acceleration time histories, the displacement time histories of body wave (on the left) have small motions at all depths, even during the first 10 seconds. The surface wave displacement time histories (on the right) are more dominant, especially in the top 3 layers, and the maxima occur there beyond the 20 seconds after the earthquake starts.

Figure VIII.14a Contributions of Body and Surface Waves to x-Comp. of Acceleration

Body Waves

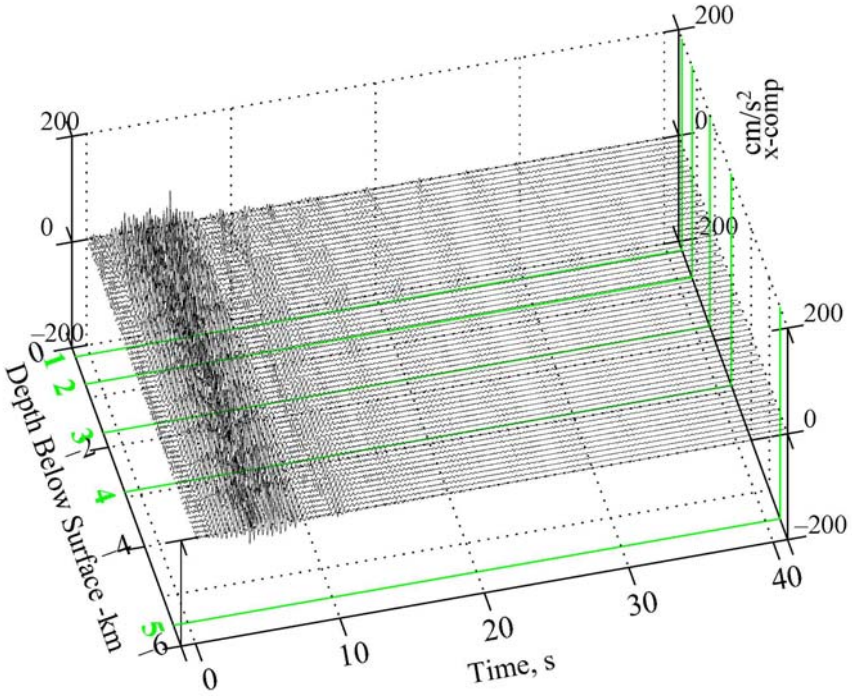

Surface Waves

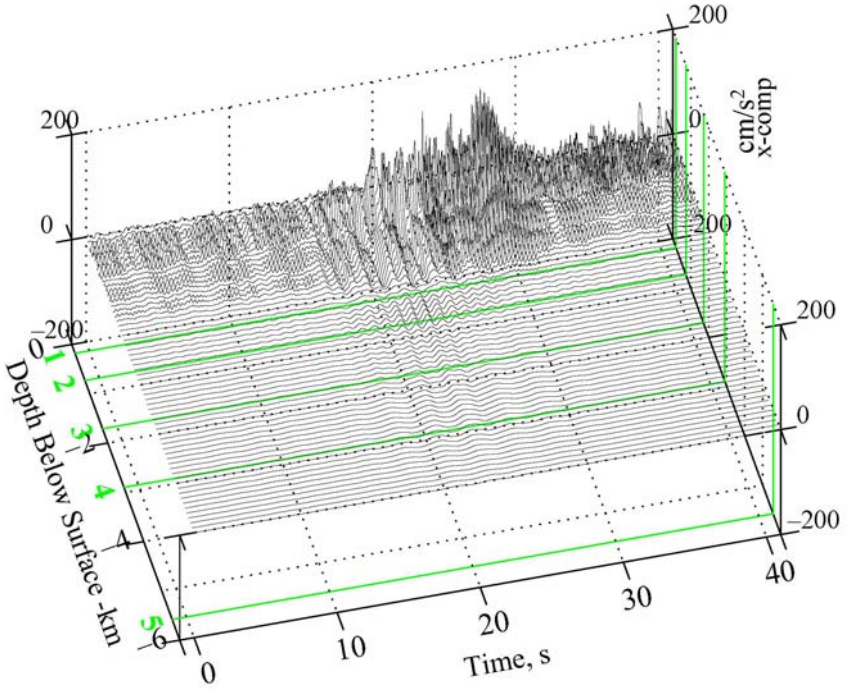

Figure VIII.14b Contributions of Body and Surface Waves to z-Comp. of Acceleration

Body Waves

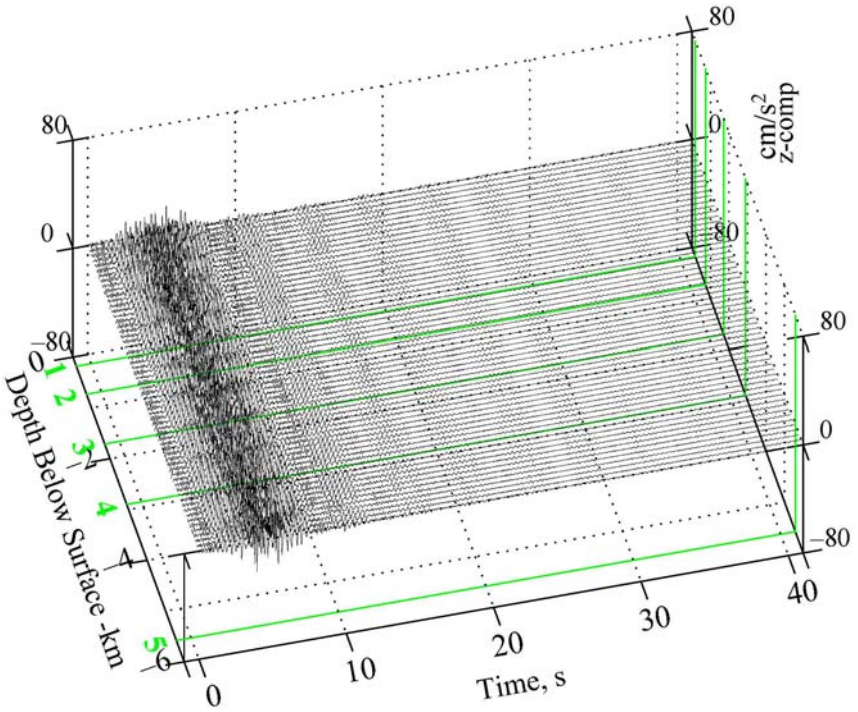

Surface Waves

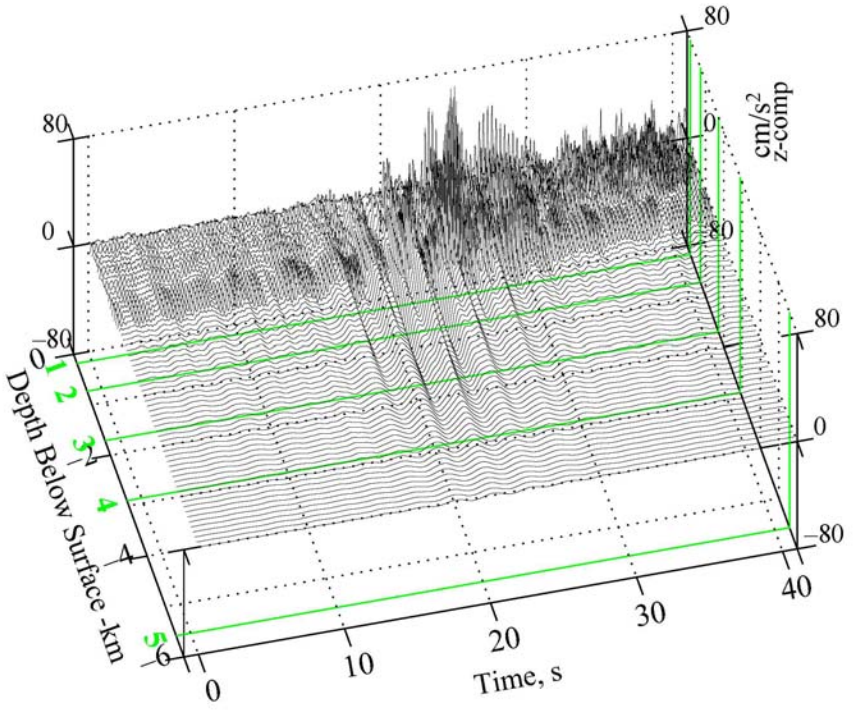

Figure VIII.15a Contributions of Body and Surface Waves to x-Comp. of Velocity

Body Waves

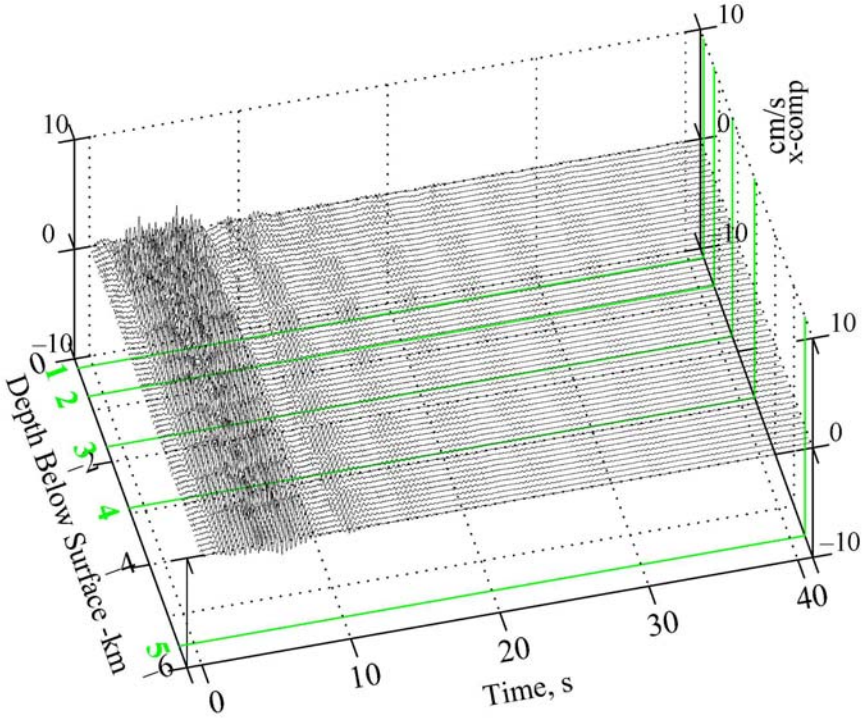

Surface Waves

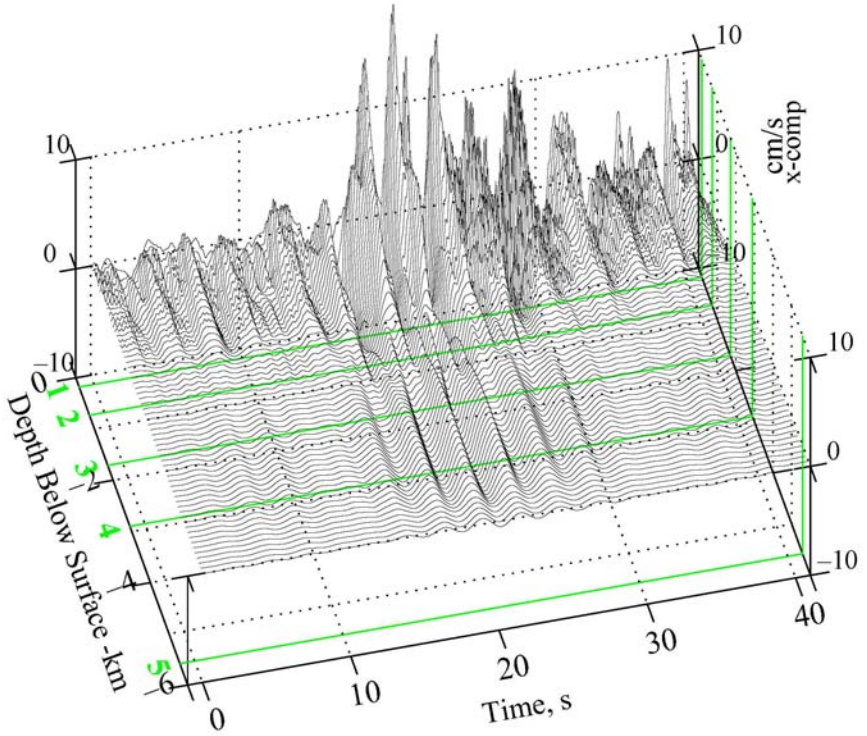

Figure VIII.15b Contributions of Body and Surface Waves to z-Comp. of Velocity

Body Waves

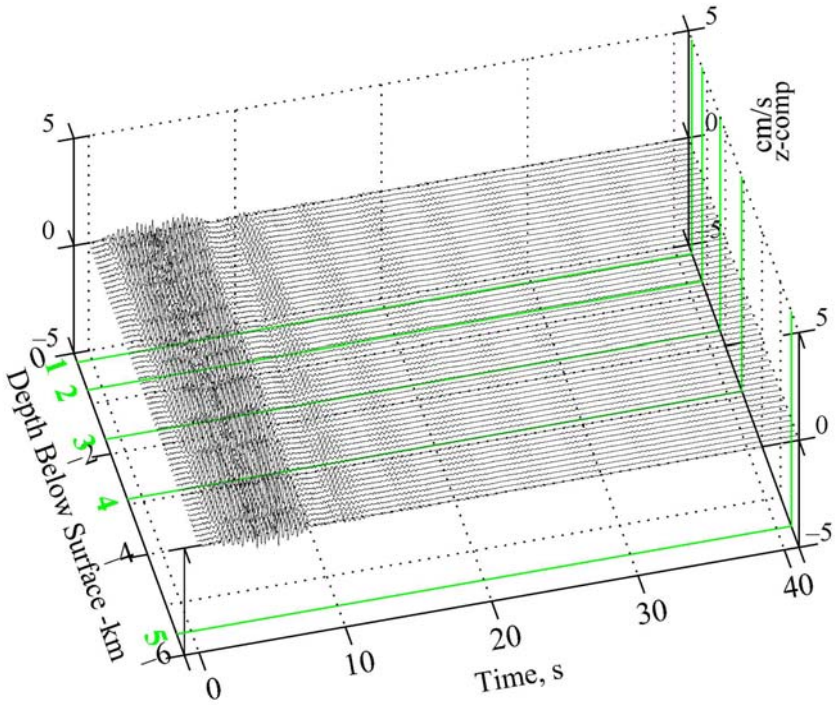

Surface Waves

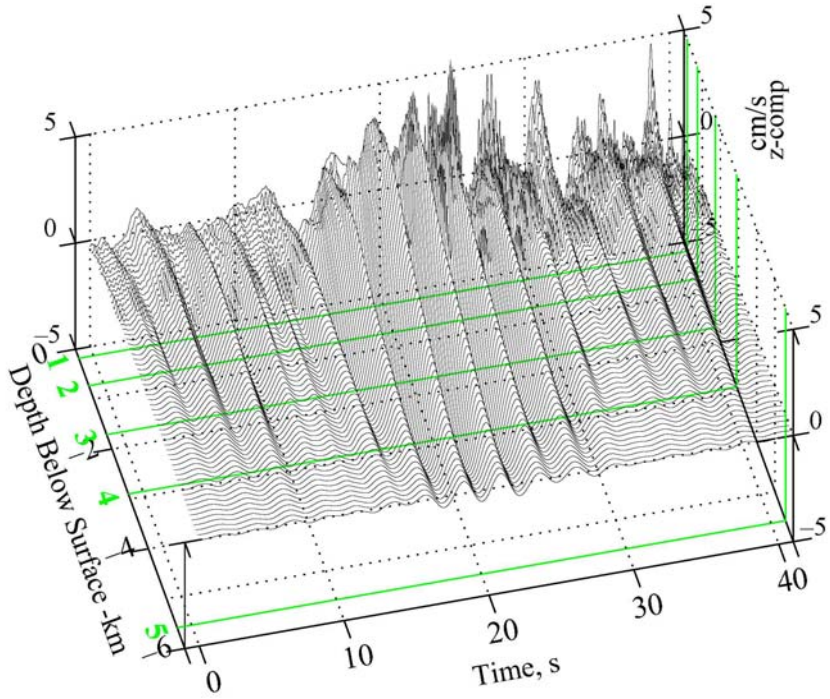

Figure VIII.16a Contributions of Body and Surface Waves to x-Comp. of Displacement

Body Waves

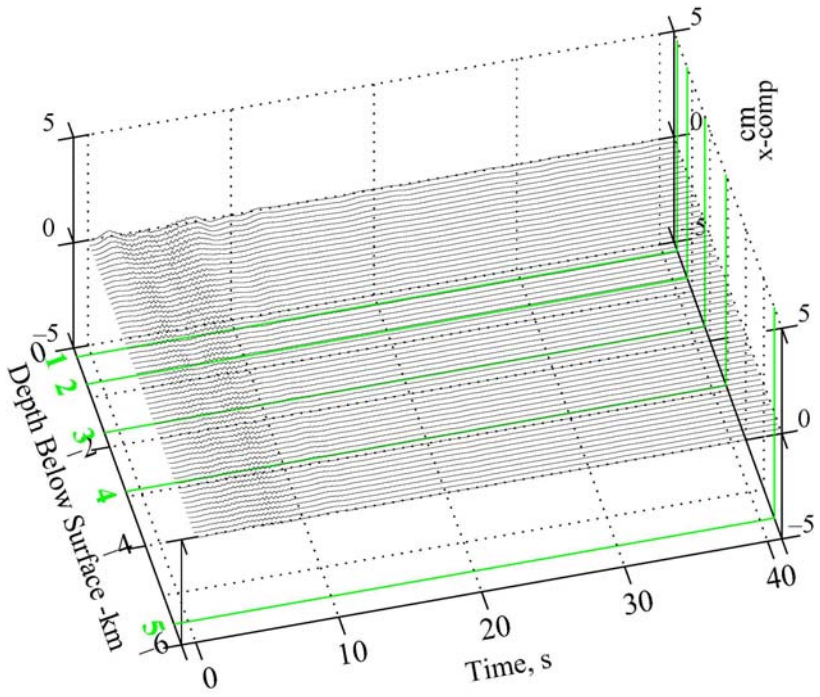

Surface Waves

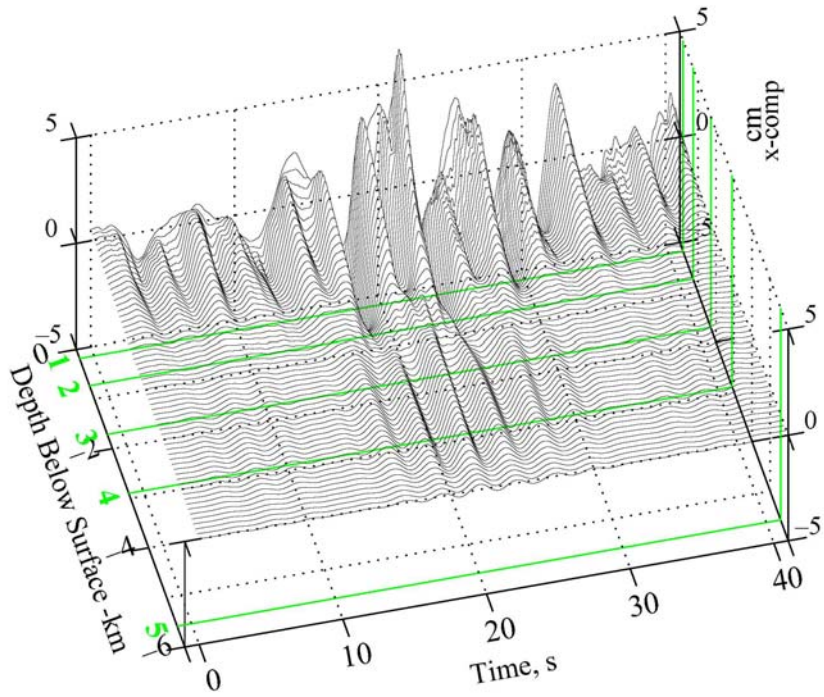

Figure VIII.16b Contributions of Body and Surface Waves to z-Comp. of Displacement

Body Waves

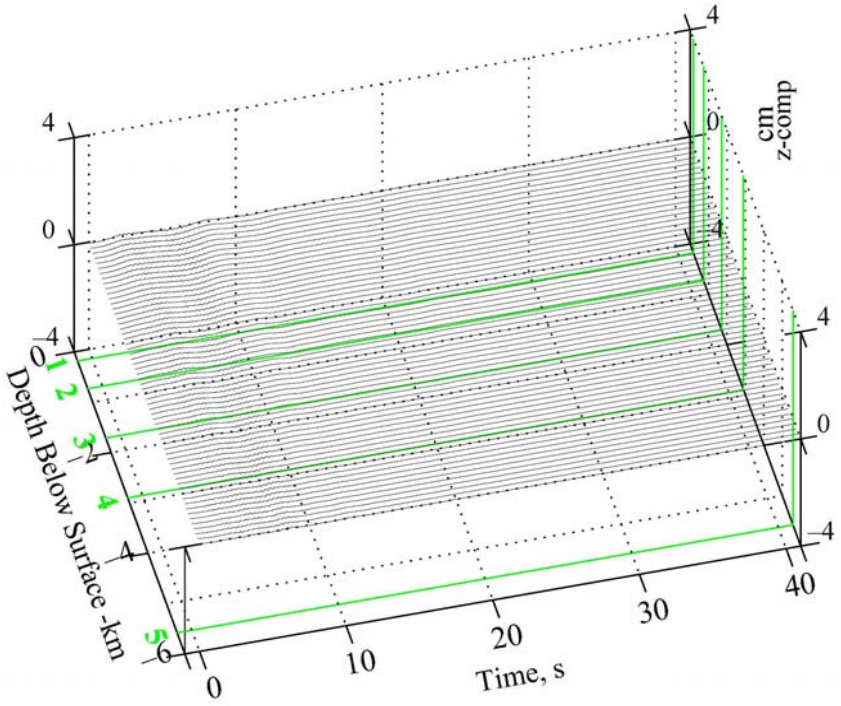

Surface Waves

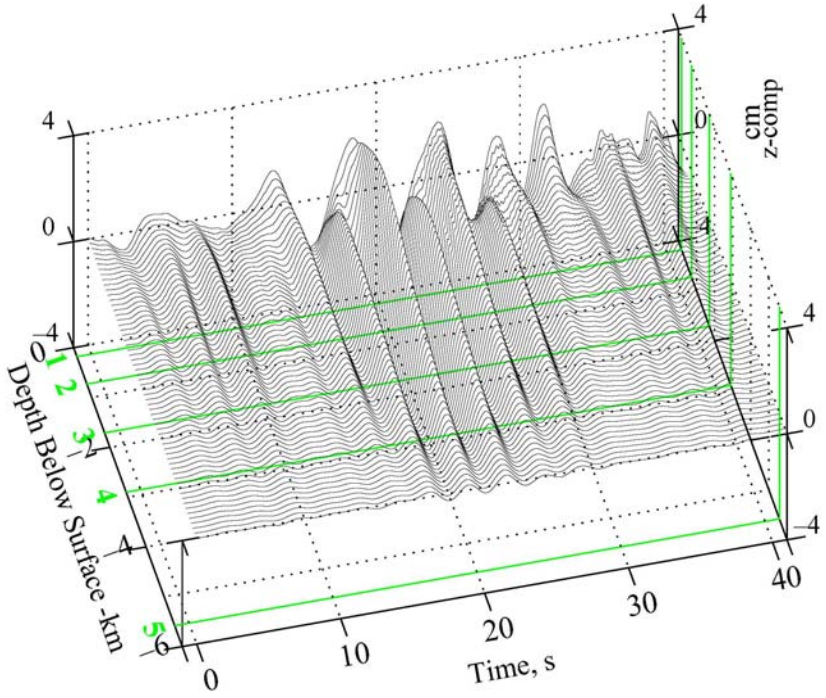

References

1. Buchen, P.W. and R. Ben-Hador (1996). Free mode surface-wave computations, *Geophys. J. Int.* ***124****, 869-887.*

2. Chapman , C.H. (2003) Yet another Elastic Plane- Wave Layer-Matrix algorithm, *Geophys. J. Int.* ***154****, 212-223.*

3. Chapman , C.H. and R.A. Phinney (1972). Diffracted Seismic Signals and their Numerical Solution, *Math. Comp .Phys.,* ***12****, 165-230.*

4. Dorman, J.M., M. Ewing and J. Oliver (1960). Study of Shear Velocity Distribution by Mantle Rayleigh Waves, *Bull Seismol. Soc. Am.,* ***50****, 87-115.*

5. Dunkin J.W. (1965). Computations of modal solutions in layered elastic media at high frequencies, *Bull Seismol. Soc. Am.,* ***55(2)****, 335-358.*

6. Haskell, N.A. (1953). The Dispersion of Surface waves on Multilayered Media, *Bull Seismol. Soc. Am.,* ***43****, 17-34.*

7. Kennett , B.L.N. (1974). Reflection, Rays and Reverberations, *Geophys. J. Int.* ***64****, 1685-1696.*

8. Kennett , B.L.N. (1983). Seismic Wave Propagation in a stratified Media. *Cambridge University Press, New York, 342pp.*

9. Kennett, B.L.N. (2001) The Seismic Wave field Vol. I: Introduction and Theoretical Development, *Cambridge University Press, 370 pp.*

10. Kennett, B. L. N. (2003). The Seismic Wave field. Volume II: Interpretation of Seismograms on Regional and Global Scales, *Cambridge University Press, 534 pp.*

11. Kennett , B.L.N and N.J. Kerry (1979). Seismic Waves in a stratified Half-Space, *Geophys. J. R. Astr. Soc.* ***57****, 557-583*.

12. Knopoff, L. (1964). A Matrix Method for Elastic Wave Problems, *Bull Seismol. Soc. Am.,* ***45****, 431-438.*

13. Lee, V.W. (2002). Empirical Scaling of Strong Earthquake Ground Motion: Part I: Attenuation and Scaling of Response Spectra, *ISET J. Earthquake Technology*, **39(4)**, 219–254.

14. Lee, V.W. and Trifunac, M.D. (1989). A Note on Filtering Strong Motion Accelerograms to Produce Response Spectra of Specified Shape and Amplitude, *Europ. Earthqu. Engng,* ***VIII(2),*** *38-45.*

15. Liu, T. (2010). Efficient Reformulation of the Thomson-Haskell Method for Computation of Surface Waves in Layered Half-Space, *Short Note, Bull Seismol. Soc. Am.,* ***100(5A)****, 2310-2316.*

16. Liu, T., C. Zhao and Y. Duan (2012). Generalized Transfer Matrix Method for Propagation of Surface Waves in Layered azimuthally Anisotropic Half-Space, *Geophys. J. Int.* ***190****, 1204-1212*

17. Luco, J.E. and R.J. Apsel (1983). On the Green's function for a Layered Half-Space, Part I, *Bull Seismol. Soc. Am.,* ***73****, 909-929.*

18. Ma, Y., R. Wang and H. Zhoul (2012). A Note on the equivalence of the Three Major Propagator Algorithms for Computational Stability and Efficiency, *Earthq. Sci.,* ***25****, 55-64.*

19. Pitteway, M.L.V. (1965). The Numerical Calculation of Wave-Fields, Reflection Coefficients and Polarization for Long Radio Waves in the Lower Ionosphere I, *Phil. Trans. R. Soc. London,* ***A 257,*** *219-241.*

20. Press, F., D. Harkrider and C.A. Seafeldt (1961). A Fast, Convenient Program for Computation of Surface Wave Dsipersion curves on multilayered media, *Bull. Seismol. Soc. Am.,* ***51****, 495-502.*

21. Randall, M.J. (1967). Fast Programs for Layered Half-Space Problems, *Bull Seismol. Soc. Am.,* ***57****, 1299-1316.*

22. Thomson, W.T. (1950). Transmission of Elastic Waves Through a Stratified Solid Media, *J. Appl. Phys. 21, 89-93.*

23. Thrower, E.N. (1965). The Computation of Dispersion of Elastic Waves in Layered Media, *J. Sound Vib.,* ***2****, 210-226.*

24. Trifunac, M.D. (1971a). Response Envelope Spectrum and Interpretation of Strong Earthquake Ground Motion, *Bull. Seism. Soc. Amer.,* ***61****, 343-356.*

25. Trifunac, M.D. (1971b). A Method for Synthesizing Realistic Strong Ground Motion, *Bull. Seism. Soc. Amer.,* ***61****, 1755-1770.*

26. Trifunac, M.D. (1972a). Stress Estimates for San Fernando, California, Earthquake of 9 February 1971: Main Event and Thirteen Aftershocks", *Bull. Seism. Soc. Amer.,* ***62****, 721-750.*

27. Trifunac, M.D. (1972b). Tectonic Stress and Source Mechanism of the Imperial Valley, California, Earthquake of 1940, *Bull. Seism. Soc. Amer.,* ***62****, 1283-1302.*

28. Trifunac, M.D. (1973). Analysis of Strong Earthquake Ground Motion for Prediction of Response Spectra, *Earthqu. Engng Struct. Dynam.,* ***2(1)****, 59-69.*

29. Trifunac, M.D. (1976). Preliminary Empirical Model for Scaling Fourier Amplitude Spectra of Strong Ground Acceleration in Terms of Earthquake Magnitude, Source to Station Distance and Recording Site Conditions*, Bull. Seism. Soc. Amer.,* ***66****, 1343-1373.*

30. Trifunac, M.D. (1979a). Preliminary Empirical Model for Scaling Fourier Amplitude Spectra of Strong Motion Acceleration in Terms of Modified Mercalli Intensity and Geologic Site Conditions, *Earthqu. Engng Struct. Dynam., **7**, 63-74*.

31. Trifunac, M.D. (1979b). A Note on Surface Strains Associated with Incident Body Waves, *Bull. EAEE, **5**, pp. 5-95*.

32. Trifunac, M.D. (1993). Long Period Fourier Amplitude Spectra of Strong Motion Acceleration, *Soil Dynam. Earthqu. Engng, **12(6)**, 363-382*.

33. Trifunac, M.D. (1994). Q and High Frequency Strong Motion Spectra, *Soil Dynam. Earthqu. Engng, **13(3)**, 149-161.*

34. Trifunac, M.D. (1995a). Pseudo Relative Velocity Spectra of Earthquake Ground Motion at Long Periods, *Soil Dynam. Earthqu. Engng, **14(5)**, 331-346.*

35. Trifunac, M.D. (1995b). Pseudo Relative Velocity Spectra of Earthquake Ground Motion at High Frequencies, *Earthqu. Engng Struct. Dynam., **24(8)**, 1113-1130.*

36. Trifunac, M.D. and Anderson, J.G. (1977). Preliminary Empirical Models for Scaling Absolute Acceleration Spectra, *Report **CE 76-03**, Dept. of Civil Eng., Univ. of Southern California, Los Angeles, California, U.S.A.*

37. Trifunac, M.D. and Brady, A.G. (1975). A Study on the Duration of Strong Earthquake Ground Motion, *Bull. Seism. Soc. Amer., **65**, 581-626*.

38. Trifunac, M.D. and Lee, V.W. (1978). Dependence of the Fourier Amplitude Spectra of Strong Motion Acceleration on the Depth of Sedimentary Deposits, *Report **CE 78-14**, Dept. of Civil Eng., Univ. of Southern California, Los Angeles, California, U.S.A.*

39. Trifunac, M.D. and Lee, V.W. (1985). Preliminary Empirical Model for Scaling Fourier Amplitude Spectra of Strong Ground Acceleration in Terms of Earthquake Magnitude, Source to Station Distance, Site Intensity and Recording Site Conditions, *Report **CE 85-03**, Dept. of Civil Eng., Univ. of Southern California, Los Angeles, California, U.S.A*.

40. Trifunac, M.D. and Westermo, B.D. (1976a). Dependence of Duration of Strong Earthquake Ground Motion on Magnitude, Epicentral Distance, Geologic Conditions at the Recording Station and Frequency of Motion, *Report **CE 76-02**, Dept. of Civil Eng., Univ. of Southern California, Los Angeles, California, U.S.A.*

41. Trifunac, M.D. and Westermo, B.D. (1976b). Correlations of Frequency Dependent Duration of Strong Earthquake Ground Motion with the Modified Mercalli Intensity and the Geologic Conditions at the Recording Stations, *Report **CE 77-03**, Dept. of Civil Eng., Univ. of Southern California, Los Angeles, California, U.S.A*.

42. Trifunac, M.D. and Novikova, E.I. (1994). State of the Art Review on Strong Motion Duration, *10th Europ. Conf. Earthqu. Engng, Vienna, Austria. **1**, 131-140*.

43. Trifunac, M.D. and Novikova, E.I. (1995). Duration of Earthquake Fault Motion in California, *Earthqu. Engng Struct. Dynam., **24(6)**, 781-799.*

44. Wang, R. (1999). A Simple Orthonormalization Method for Stable and Efficient Computation of Green's Functions, *Bull Seismol. Soc. Am., **89**, 733-741.*

45. Watson, T.H. (1970). A Note on Fast Computation of Rayleigh Wave Dsipersion in the Multi-Layered Half-Space, *Bull Seismol. Soc. Am., **60**, 161-166.*

46. Wong, H.L. and Trifunac, M.D. (1978). Synthesizing Realistic Strong Motion Accelerograms, *Report **CE 78-07**, Dept. of Civil Eng., Univ. of Southern California, Los Angeles, California, U.S.A.*

47. Wong, H.L. and Trifunac, M.D. (1979). Generation of Artificial Strong Motion Accelerograms, *Earthquake Engineering Structural Dynamics, **7**, 509-527.*

Appendix A – Love and SH Body Waves Mode Shapes

Appendix A-1 – Mode #1 Love Waves Mode Shapes

Fig. A-1.1 Love Wave Mode #1, Page 1 of 11 T=15.0-8.5 s

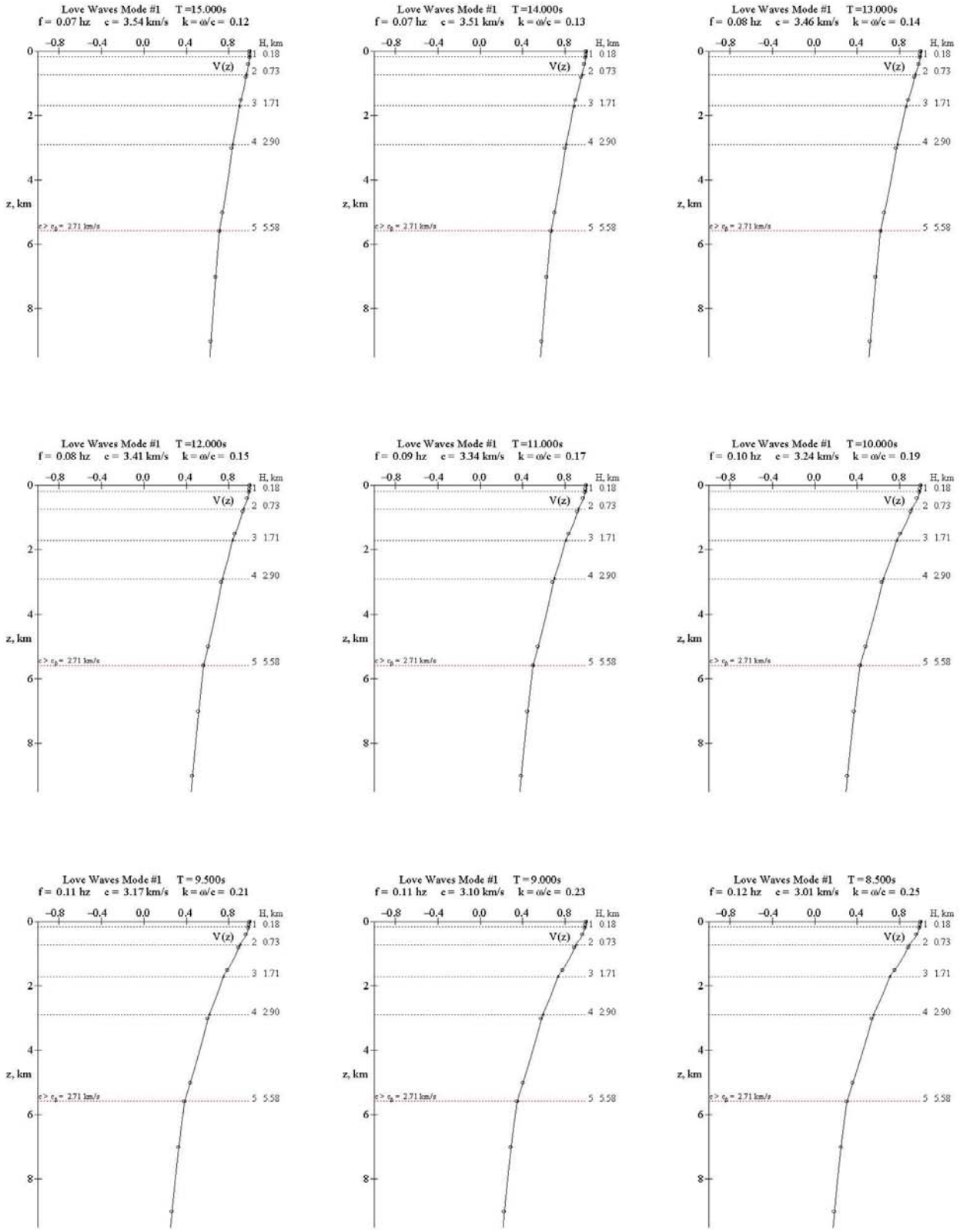

Fig. A-1.2 Love Wave Mode #1, Page 2 of 11 T=8.0-4.6s

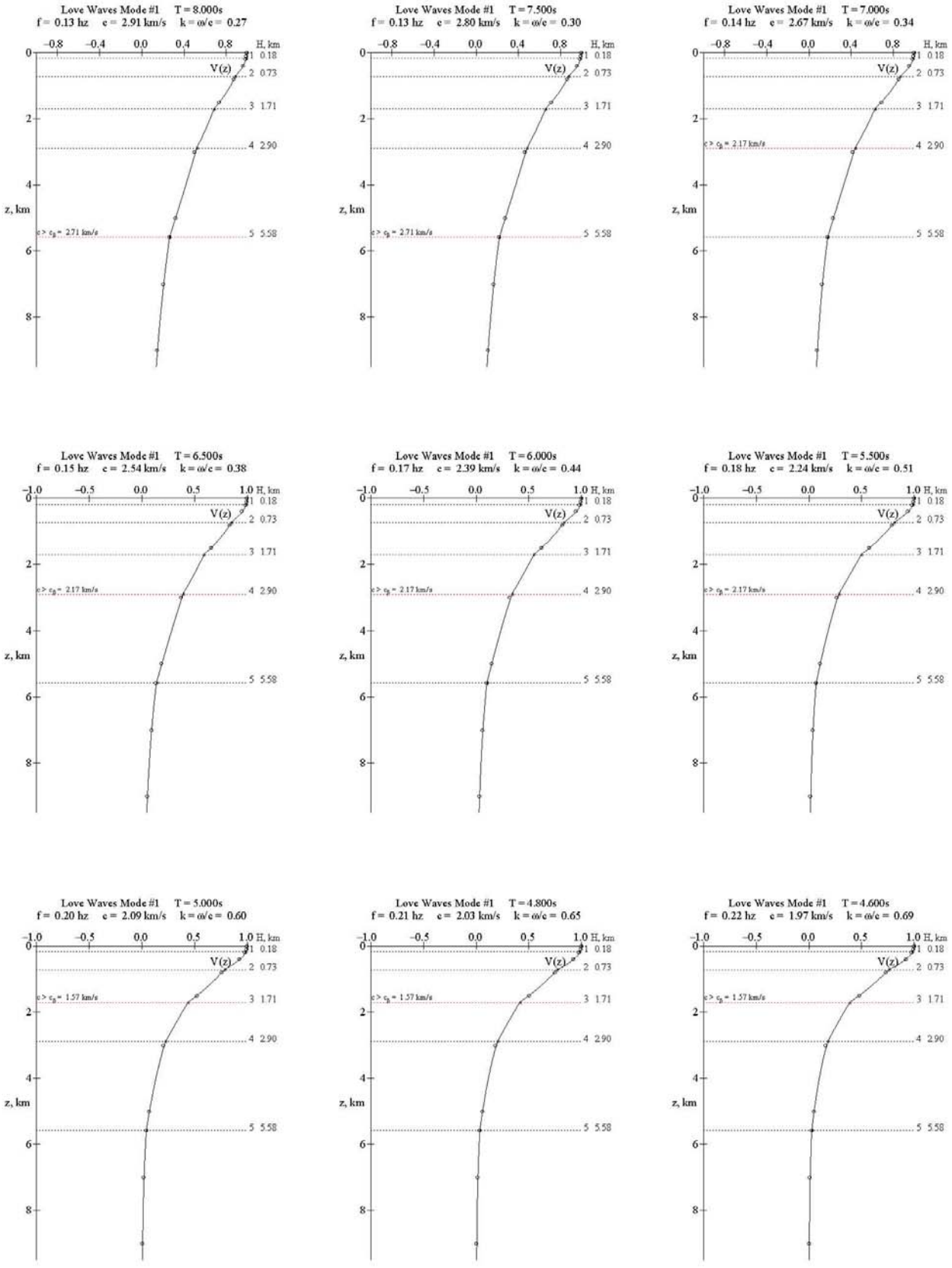

Fig. A-1.3 Love Wave Mode #1, Page 3 of 11 T=4.4-2.8s

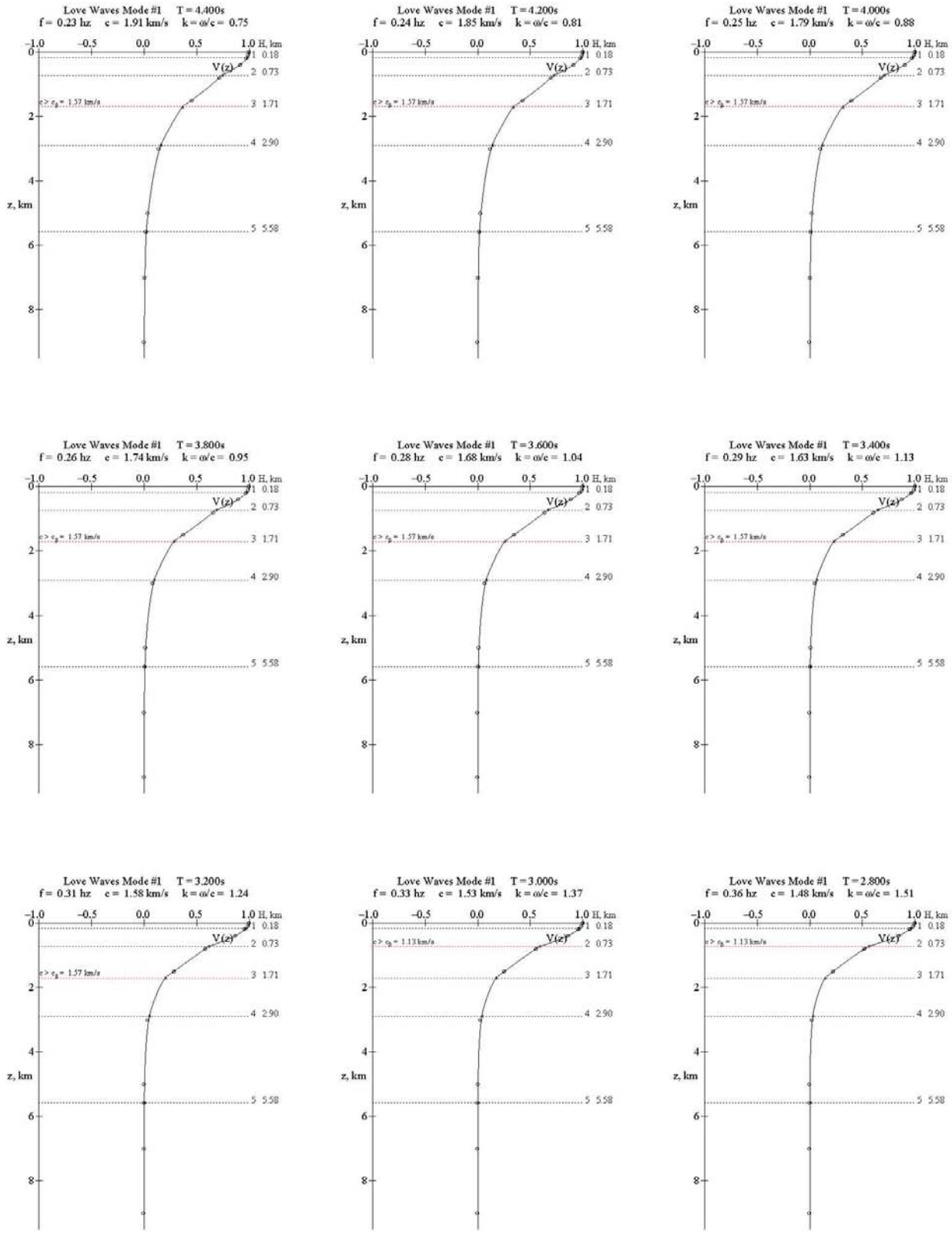

Fig. A-1.4 Love Wave Mode #1, Page 4 of 11 T=2.6-1.5s

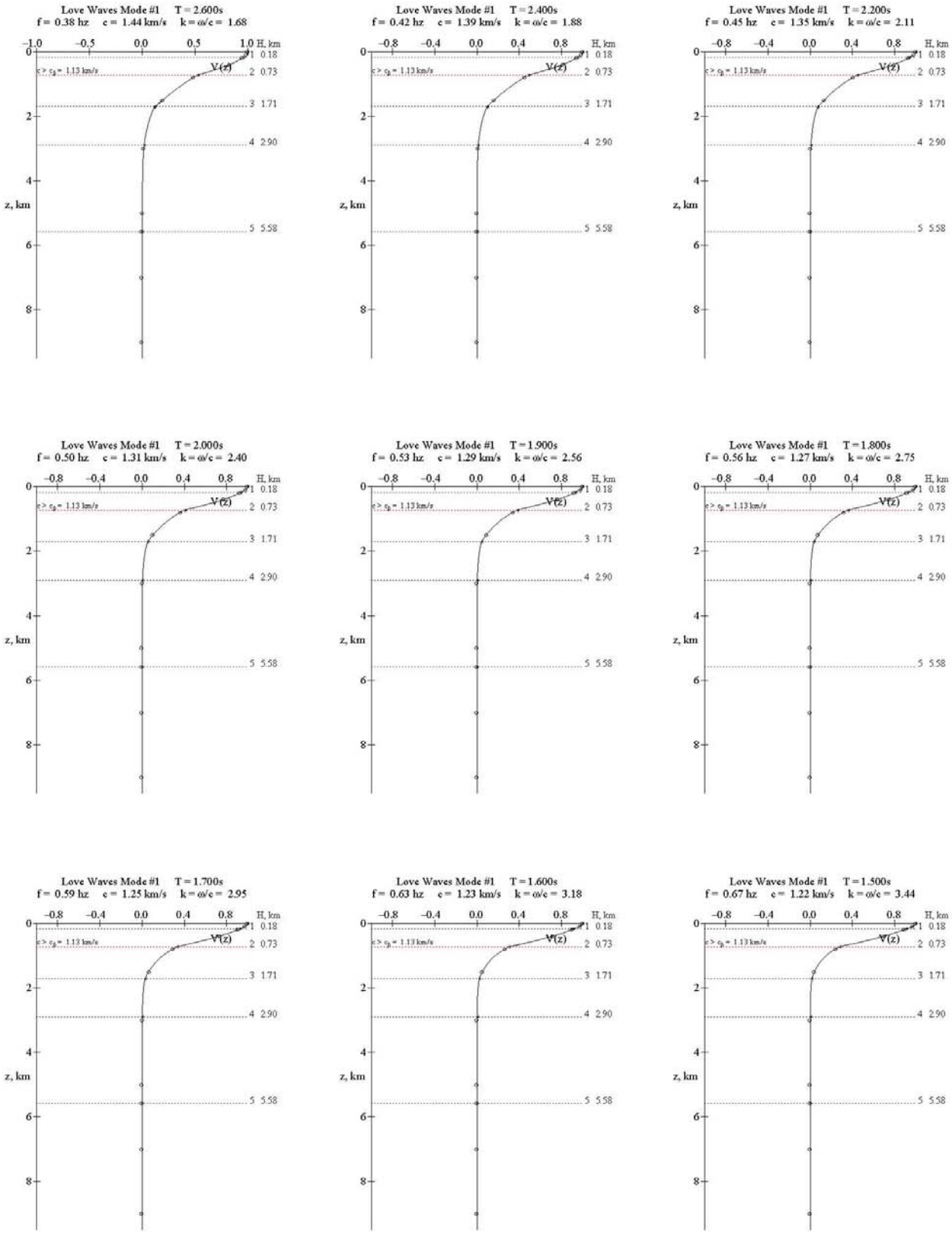

Fig. A-1.5 Love Wave Mode #1, Page 5 of 11 T=1.4-0.8s

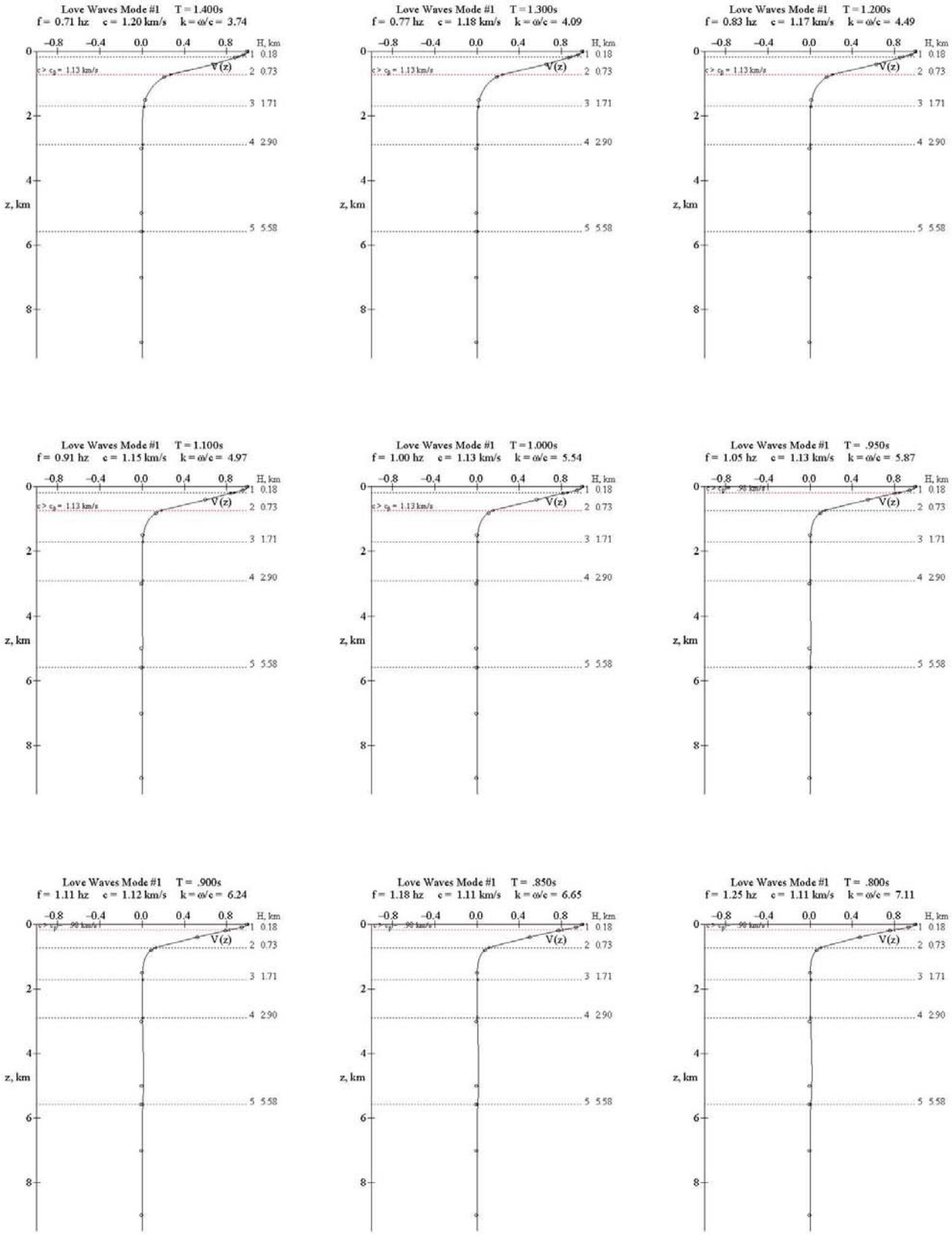

Fig. A-1.6 Love Wave Mode #1, Page 6 of 11 T=0.75-0.44s

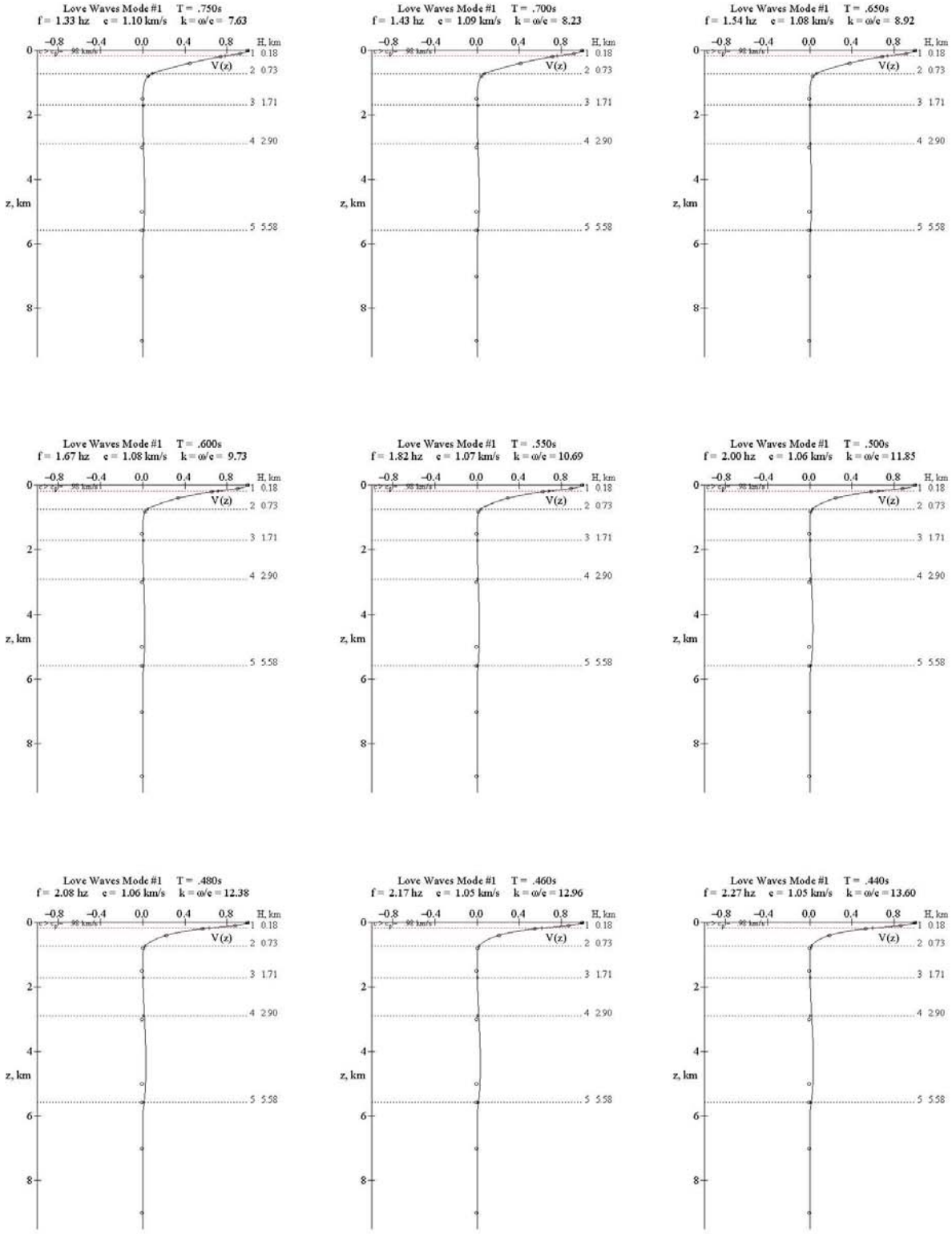

Fig. A-1.7 Love Wave Mode #1, Page 7 of 11 T=0.42-0.26s

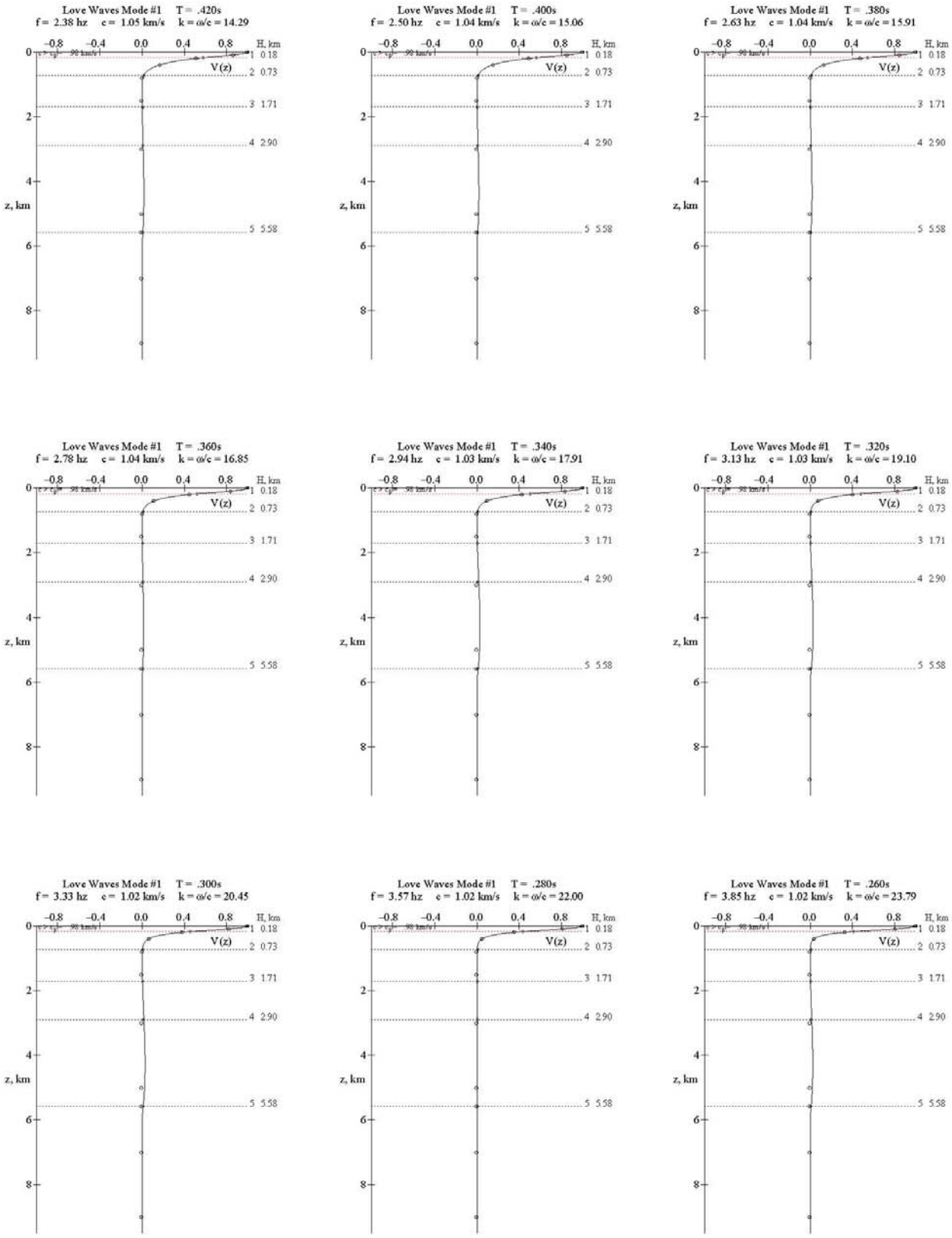

Fig. A-1.8 Love Wave Mode #1, Page 8 of 11 T=0.24-0.14s

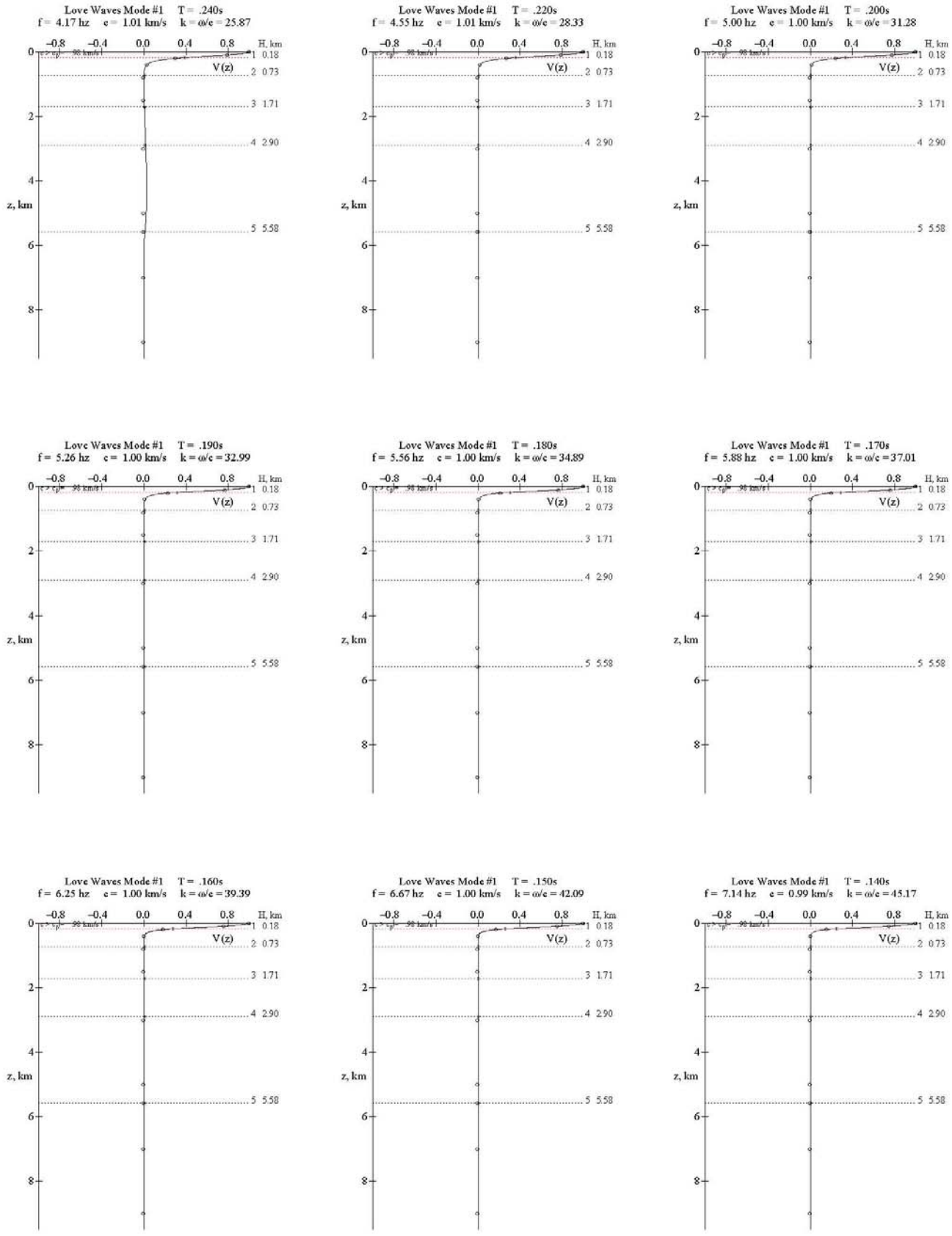

Fig. A-1.9 Love Wave Mode #1, Page 9 of 11 T=0.130-0.075s

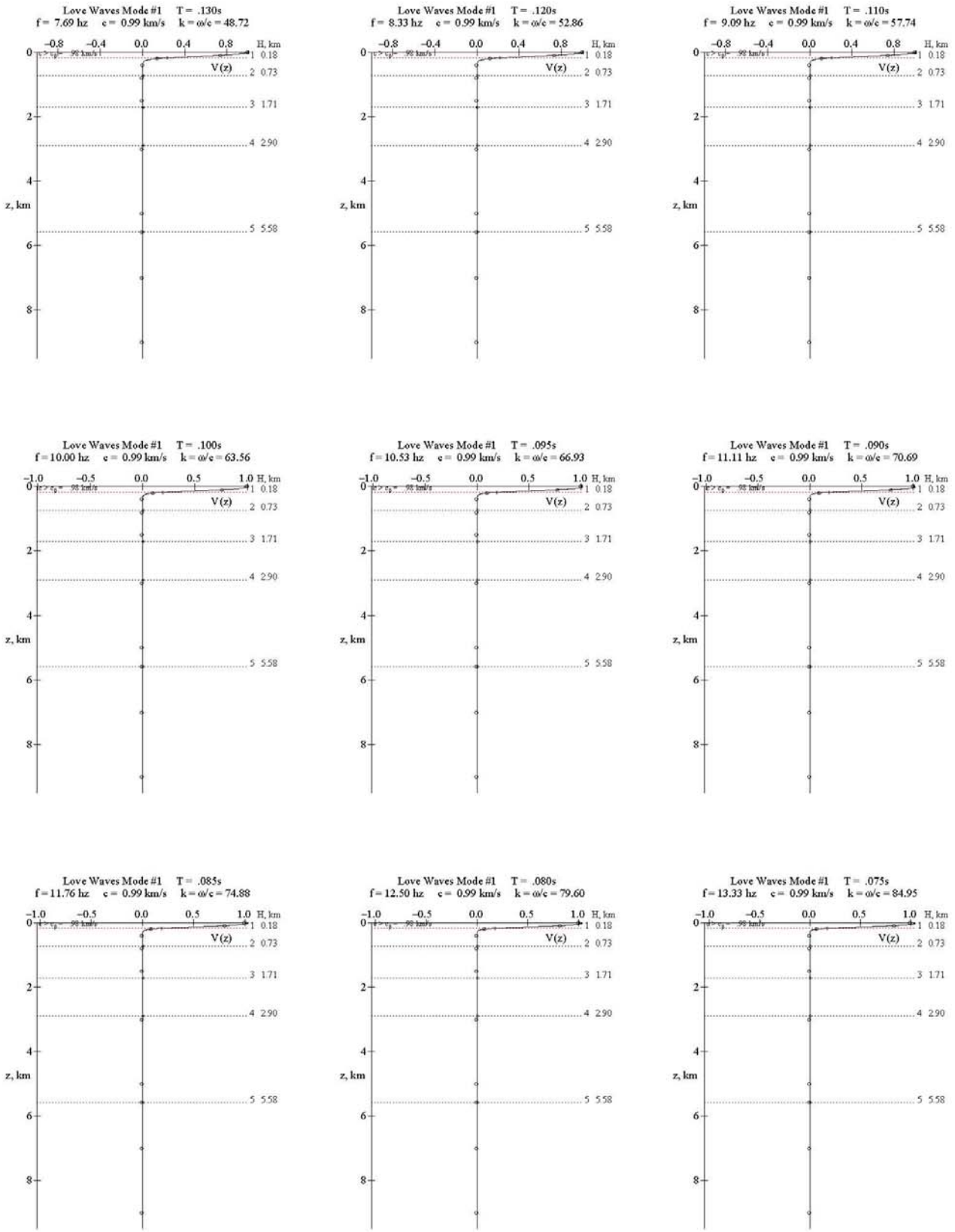

Fig. A-1.10 Love Wave Mode #1, Page 10 of 11 T=0.070-0.042s

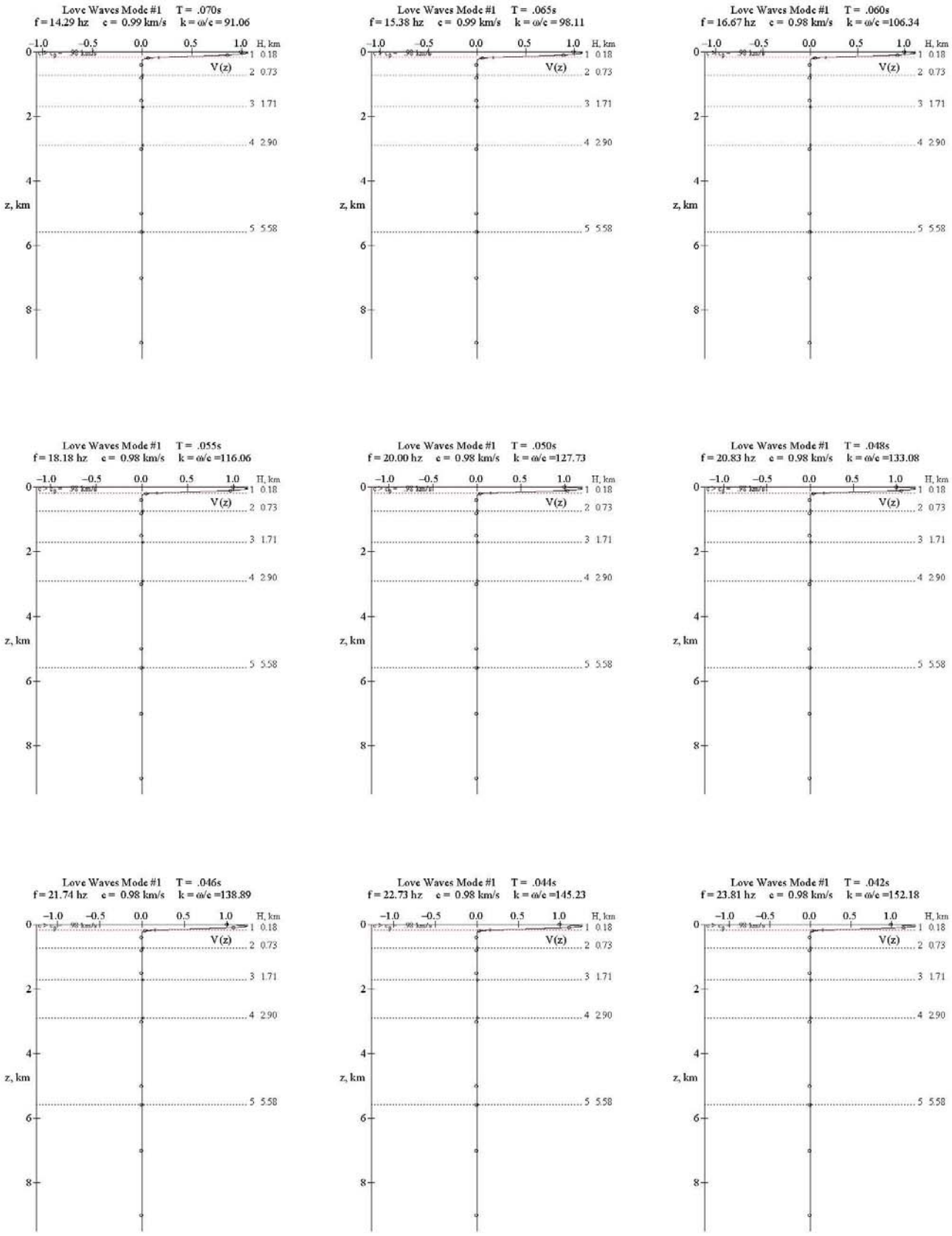

Fig. A-1.11 Love Wave Mode #1, Page 11 of 11 T=0.040s

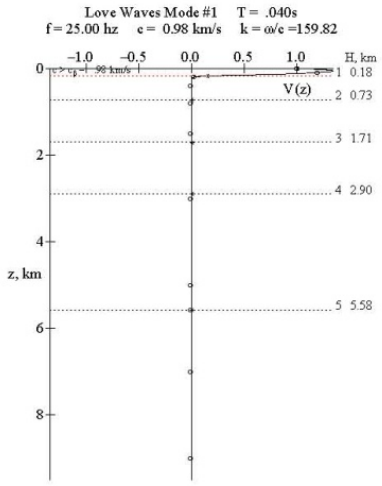

Appendix A-2 – Mode #2 Love Waves Mode Shapes

Fig. A-2.1 Love Wave Mode #2, Page 1 of 8 T=3.8-2.2s

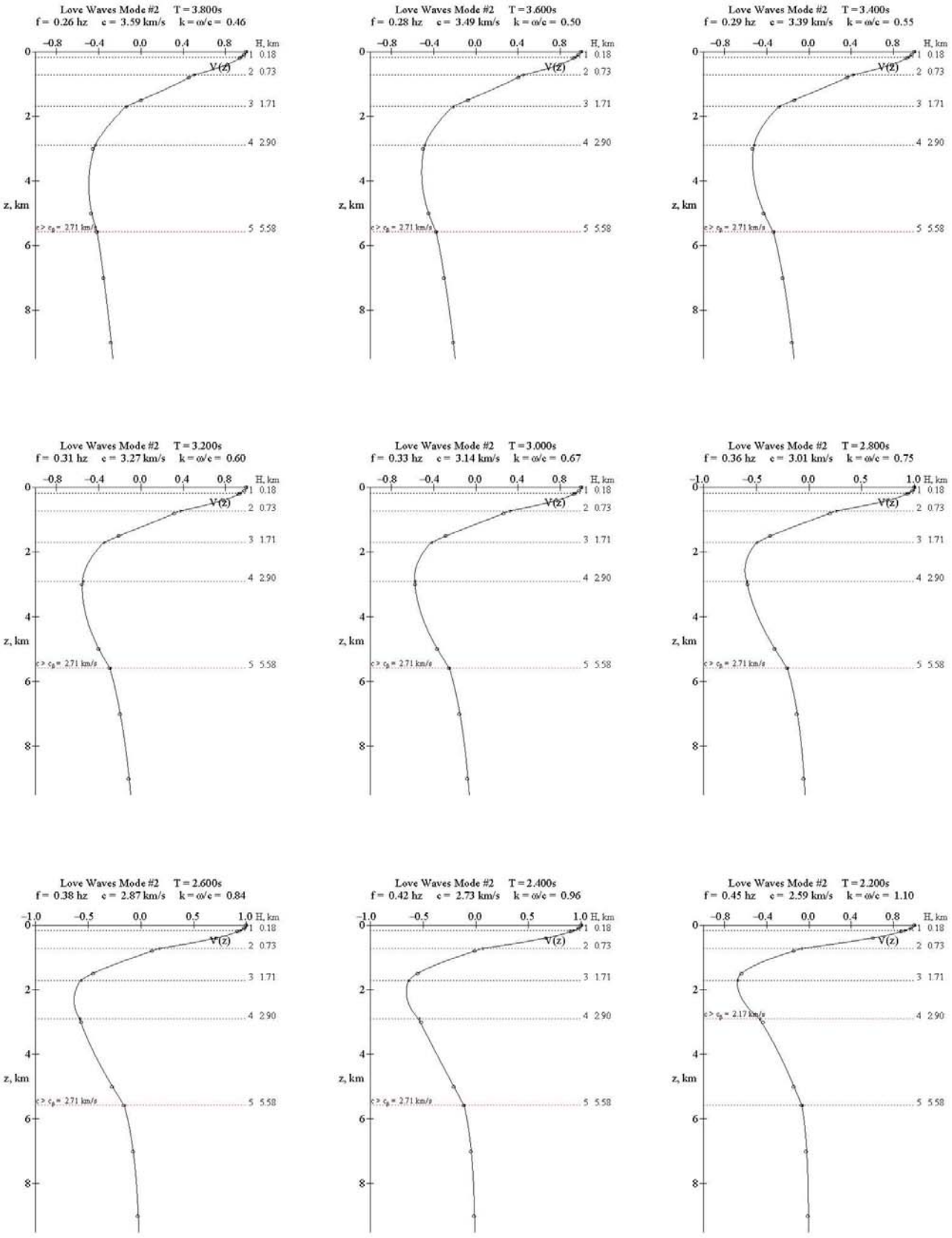

Fig. A-2.2 Love Wave Mode #2, Page 2 of 8 T=2.0-1.2s

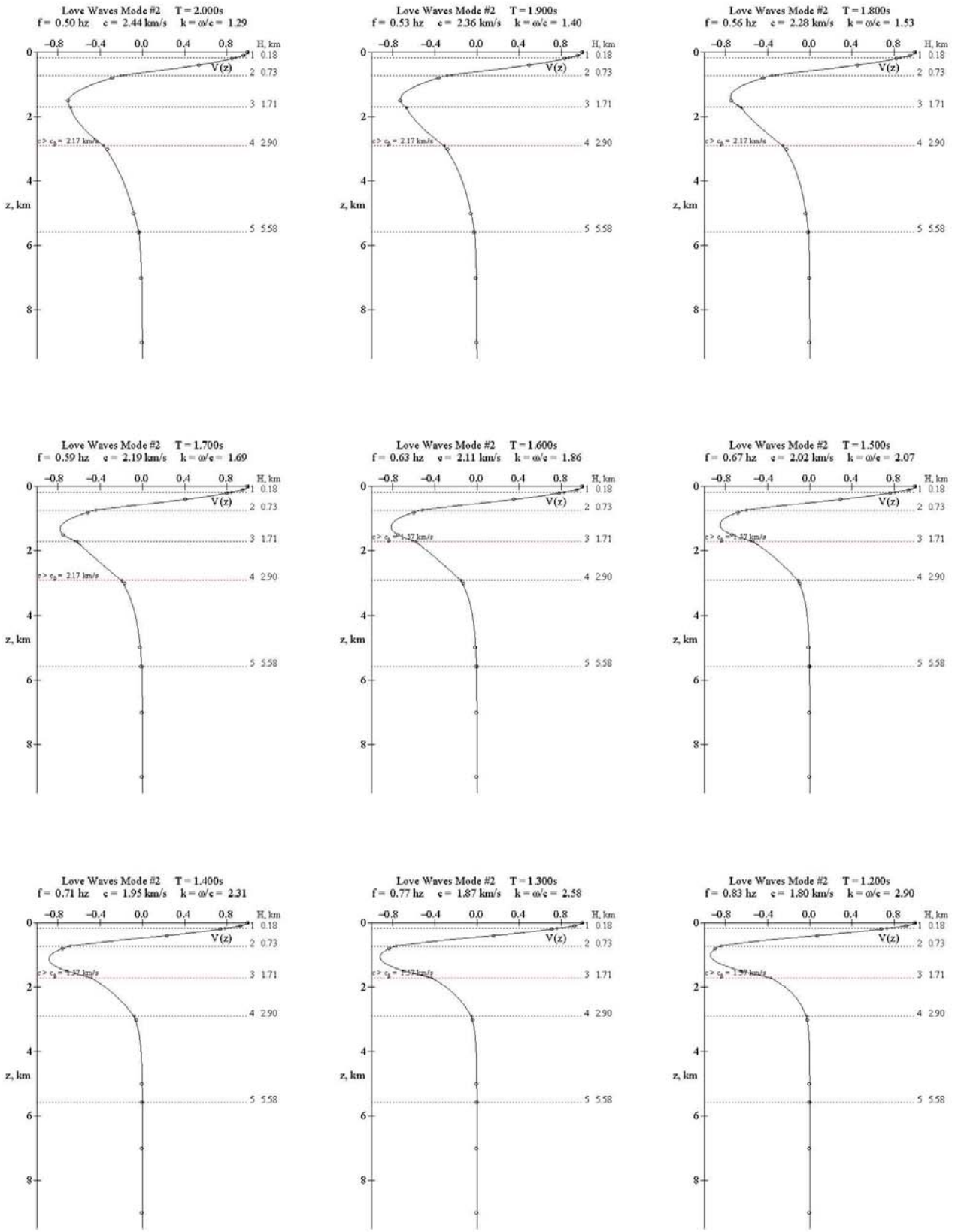

Fig. A-2.3 Love Wave Mode #2, Page 3 of 8 T=1.1-0.65s

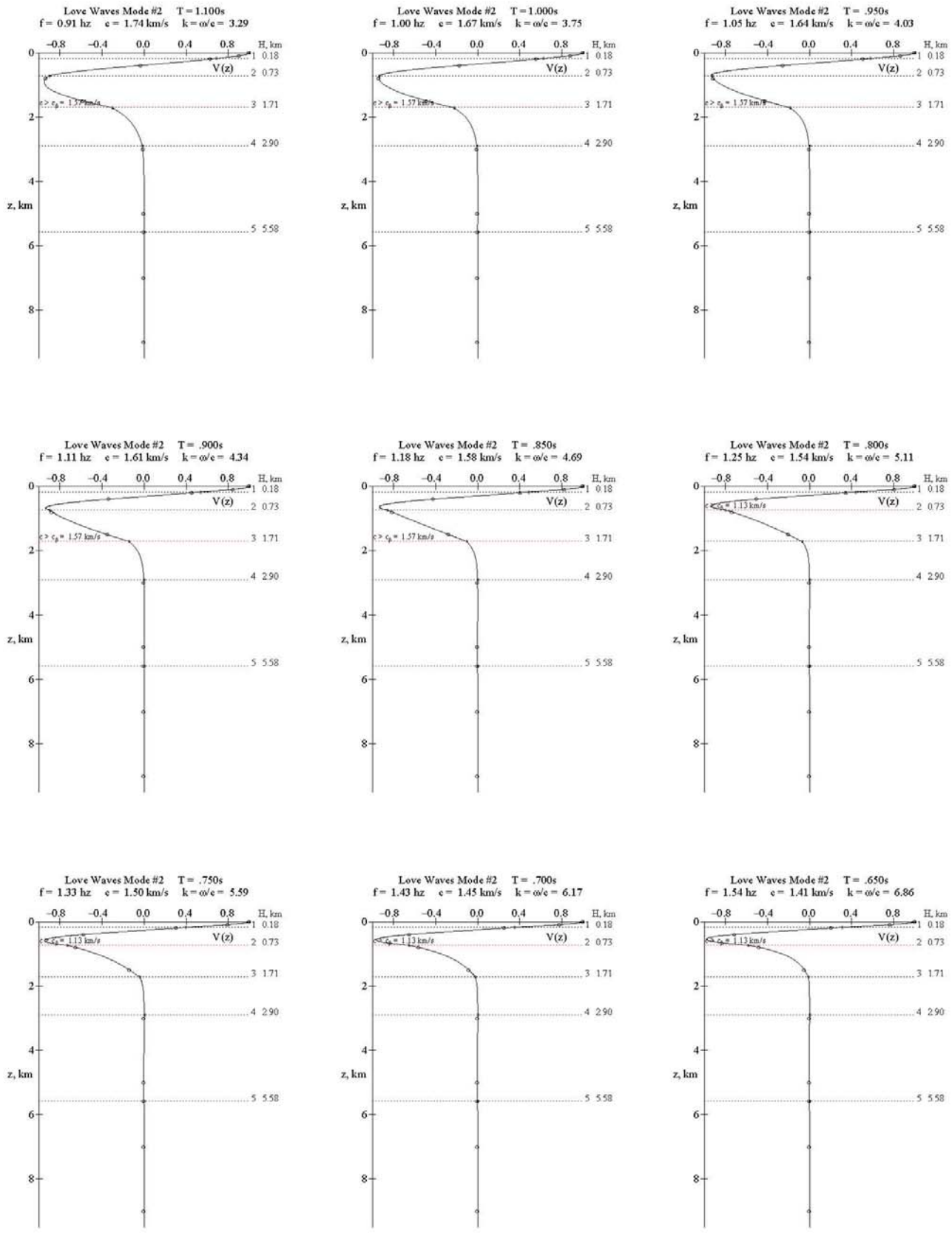

Fig. A-2.4 Love Wave Mode #2, Page 4 of 8 T=0.60-0.38s

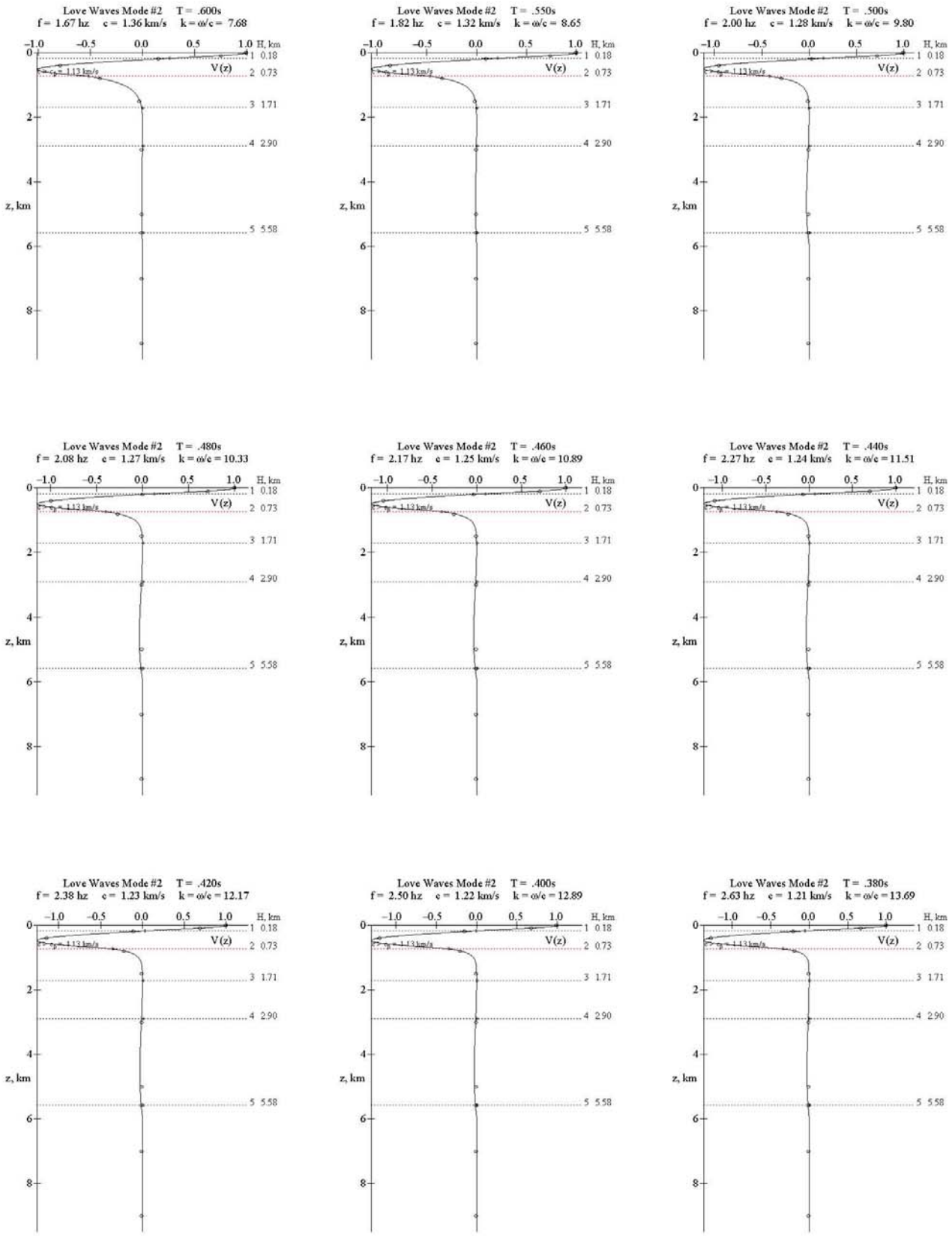

Fig. A-2.5 Love Wave Mode #2, Page 5 of 8 T=0.36-0.20s

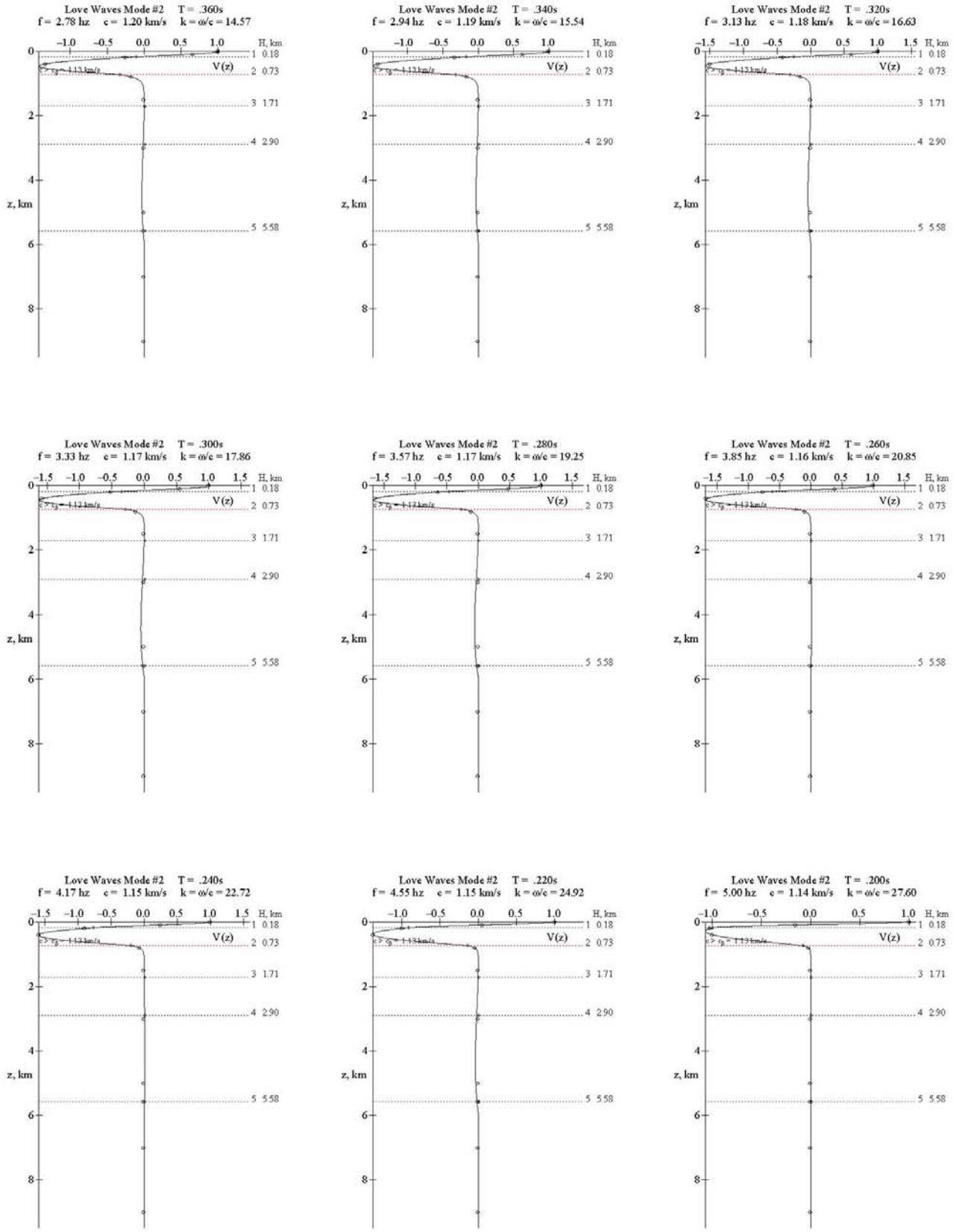

Fig. A-2.6 Love Wave Mode #2, Page 6 of 8 T=0.19-0.11s

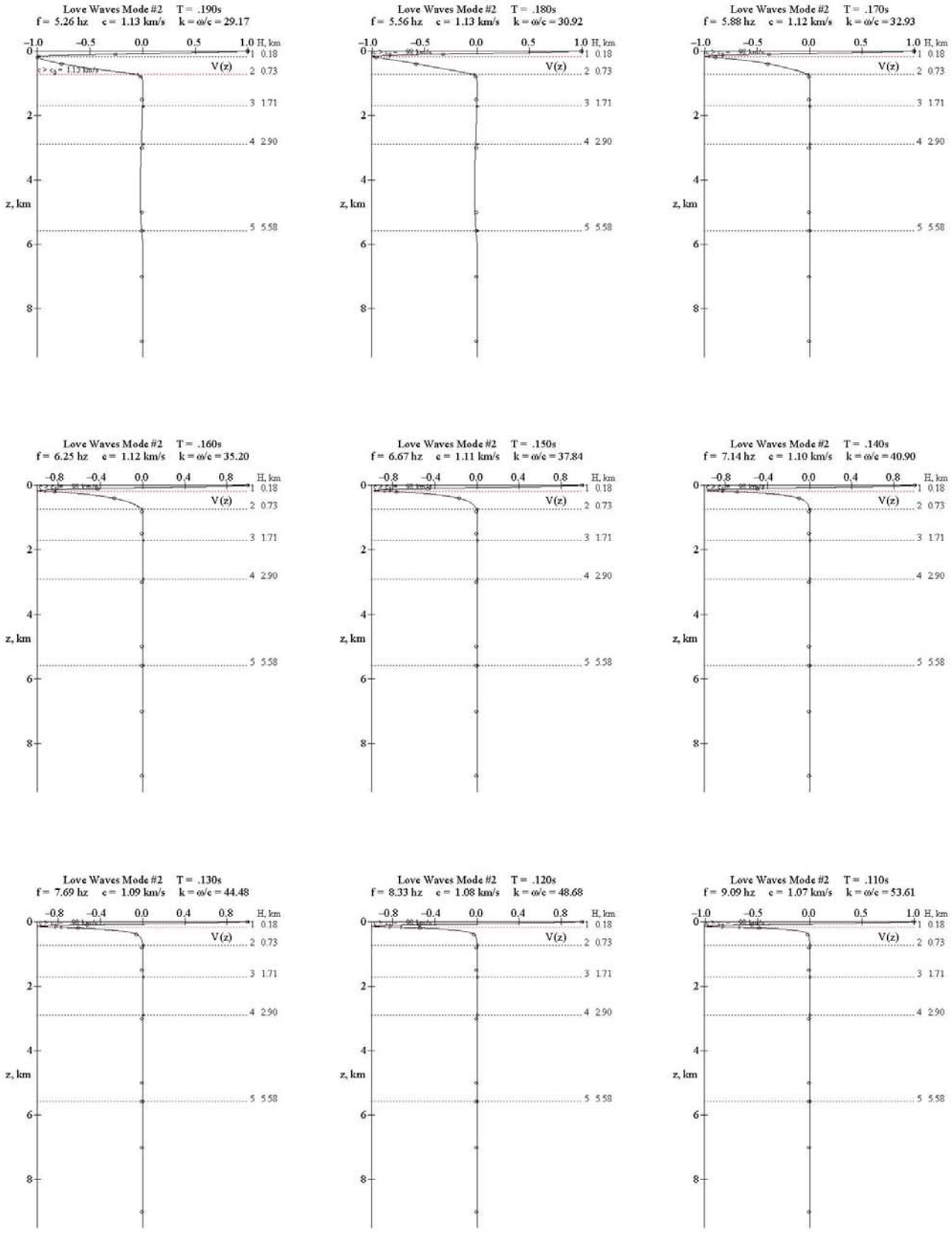

Fig. A-2.7 Love Wave Mode #2, Page 7 of 8 T=0.10-0.06s

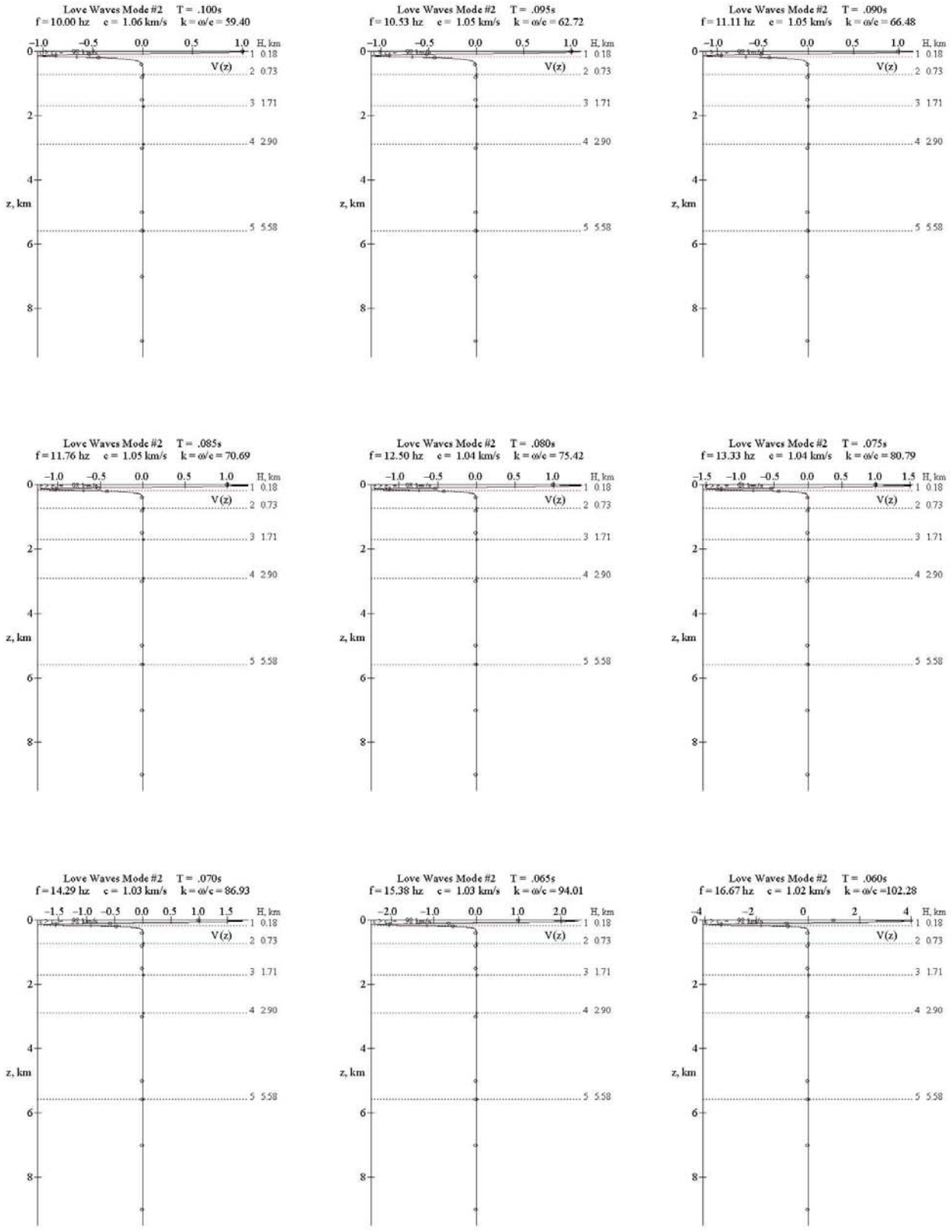

Fig. A-2.8 Love Wave Mode #2, Page 8 of 8 T=0.055-0.040s

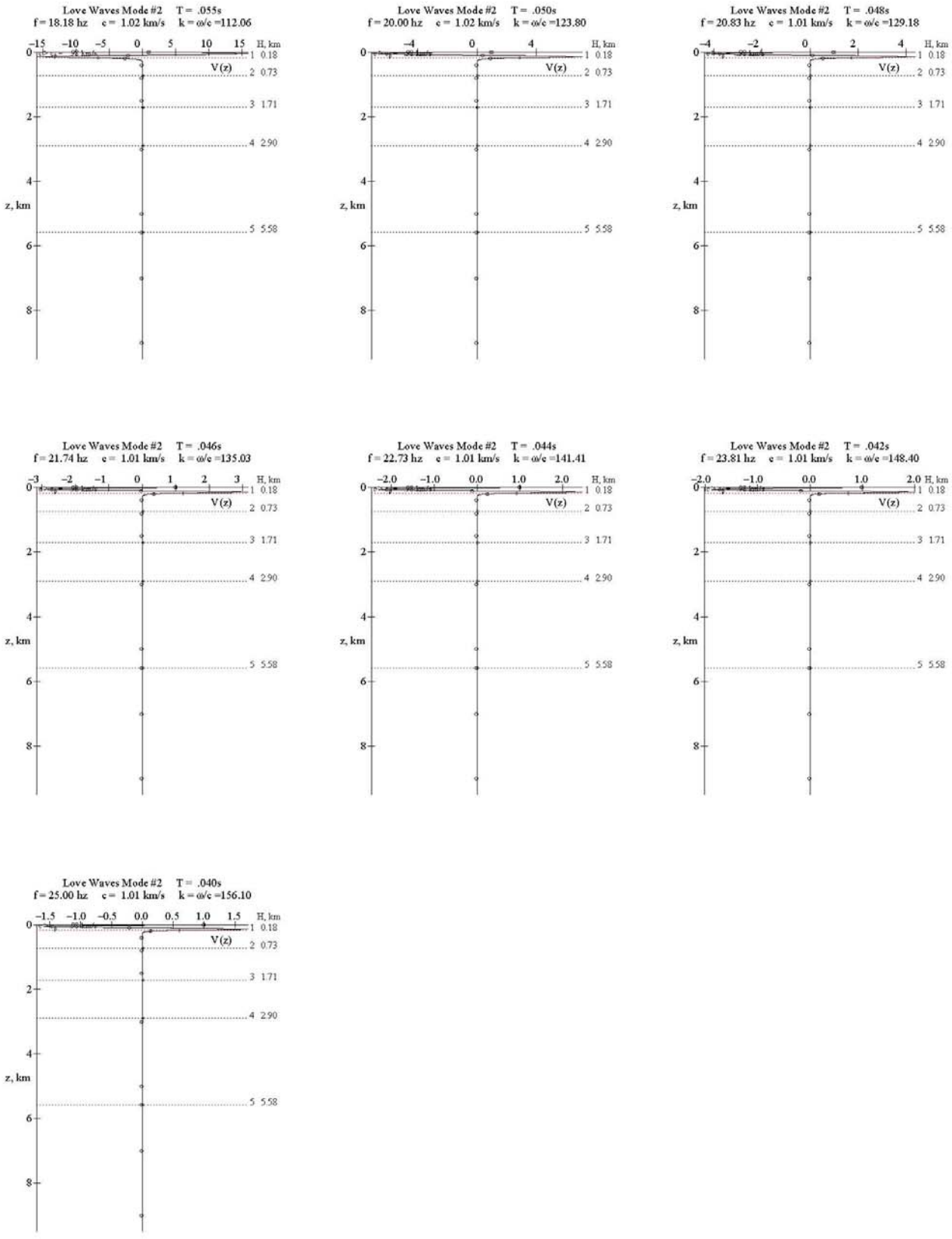

Appendix A-3 – Mode #3 Love Waves Mode Shapes

Fig. A-3.1 Love Wave Mode #3, Page 1 of 7 T=2.0-1.2s

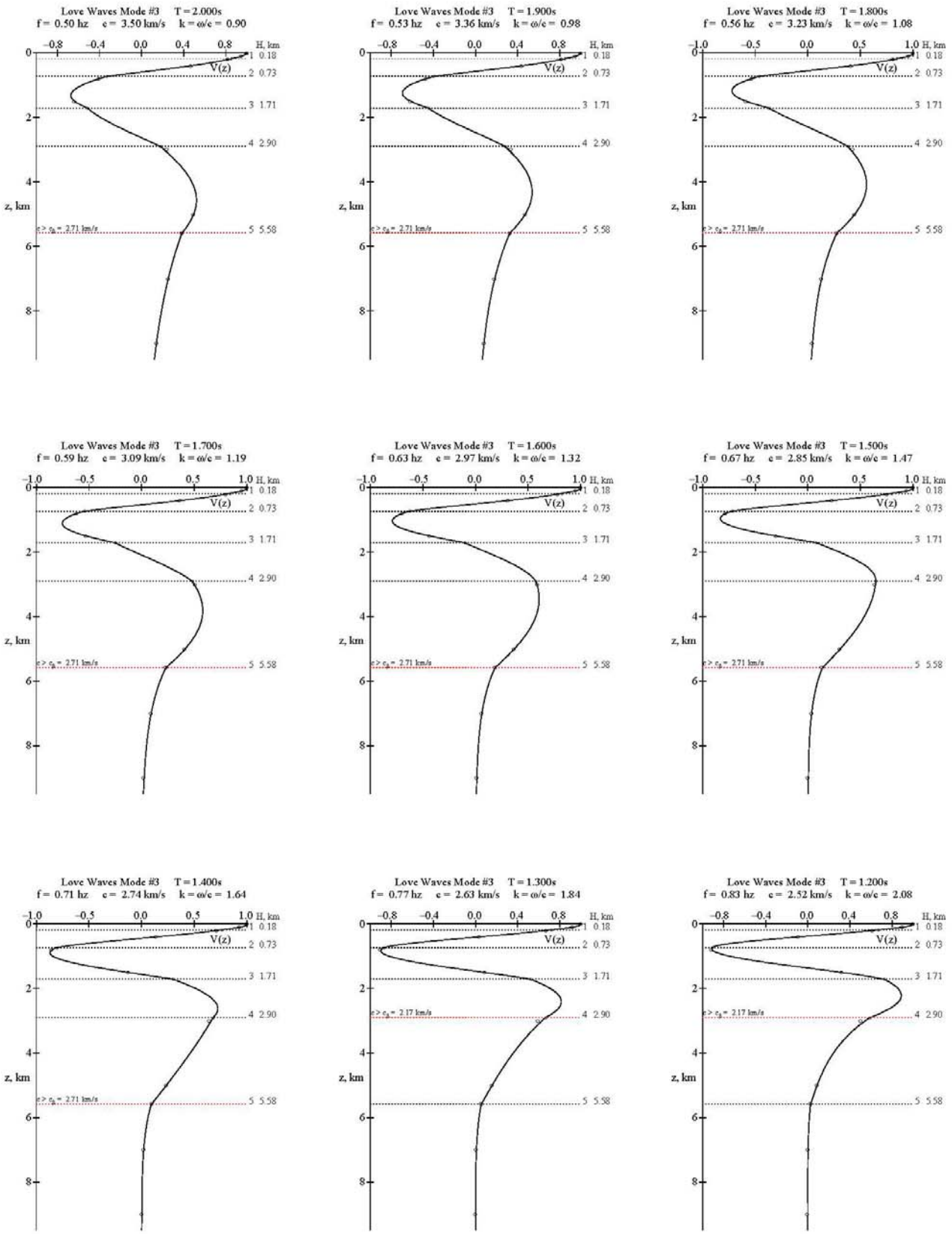

Fig. A-3.2 Love Wave Mode #3, Page 2 of 7 T=1.1-0.65s

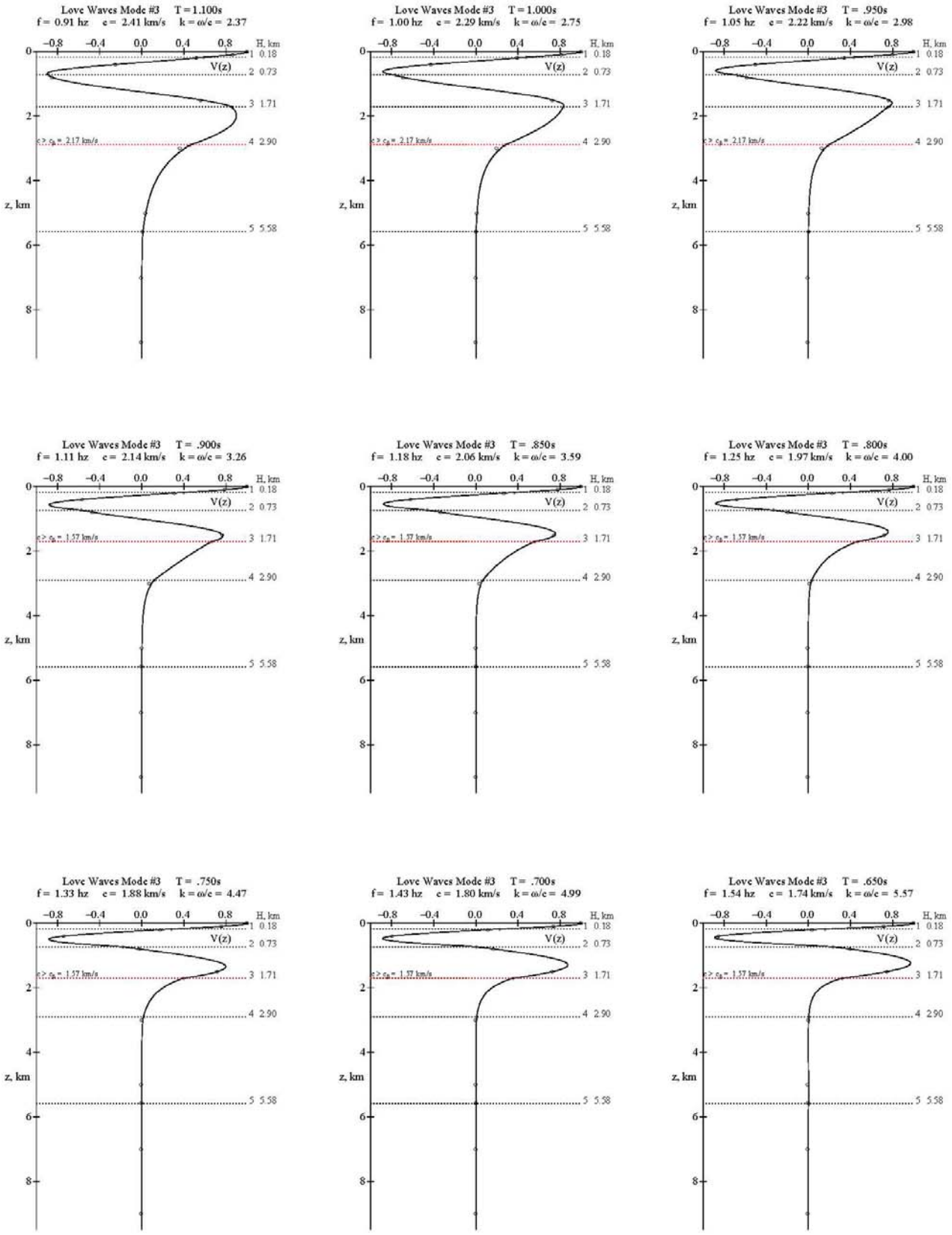

Fig. A-3.3 Love Wave Mode #3, Page 3 of 7 T=0.60-0.38s

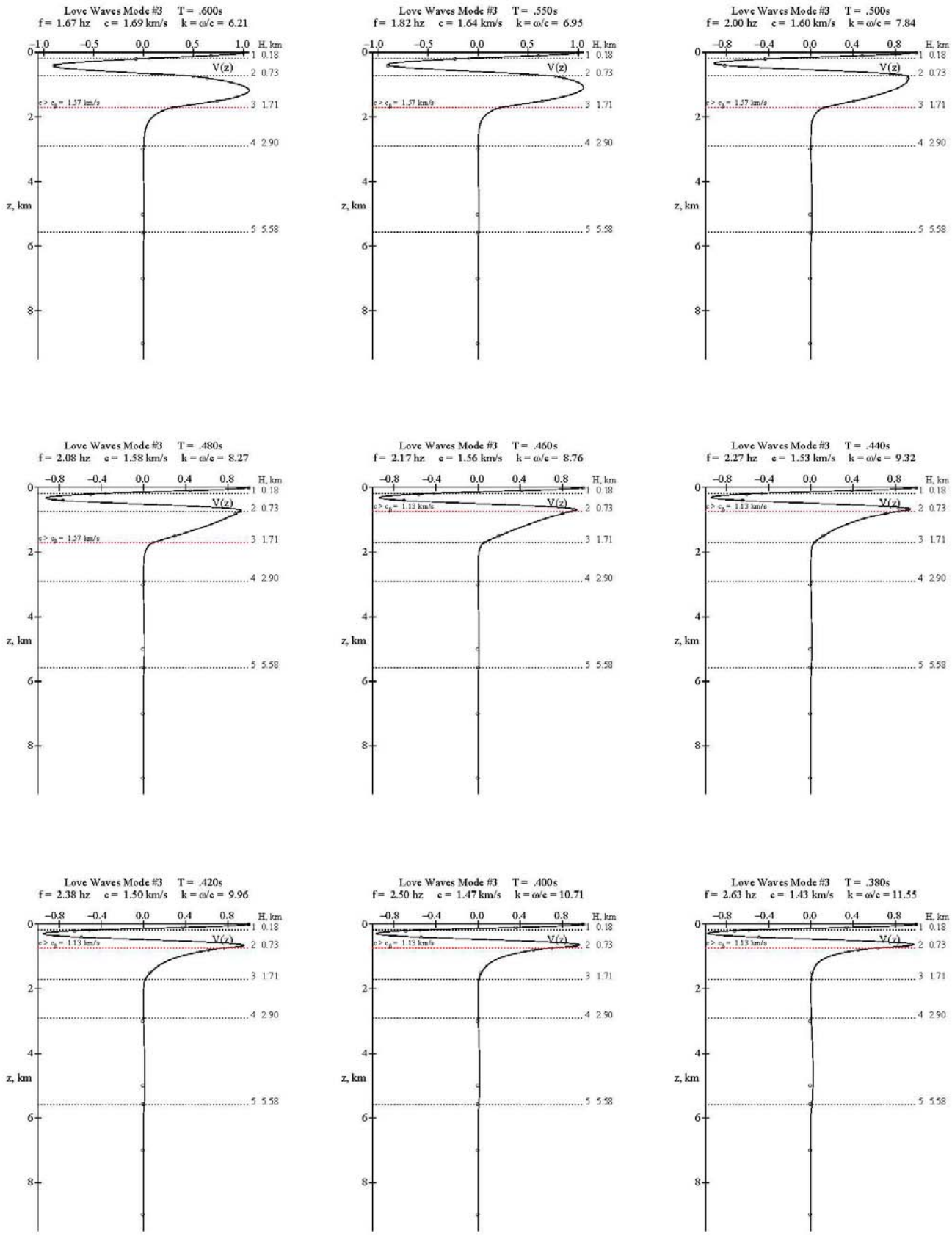

Fig. A-3.4 Love Wave Mode #3, Page 4 of 7 T=0.36-0.20s

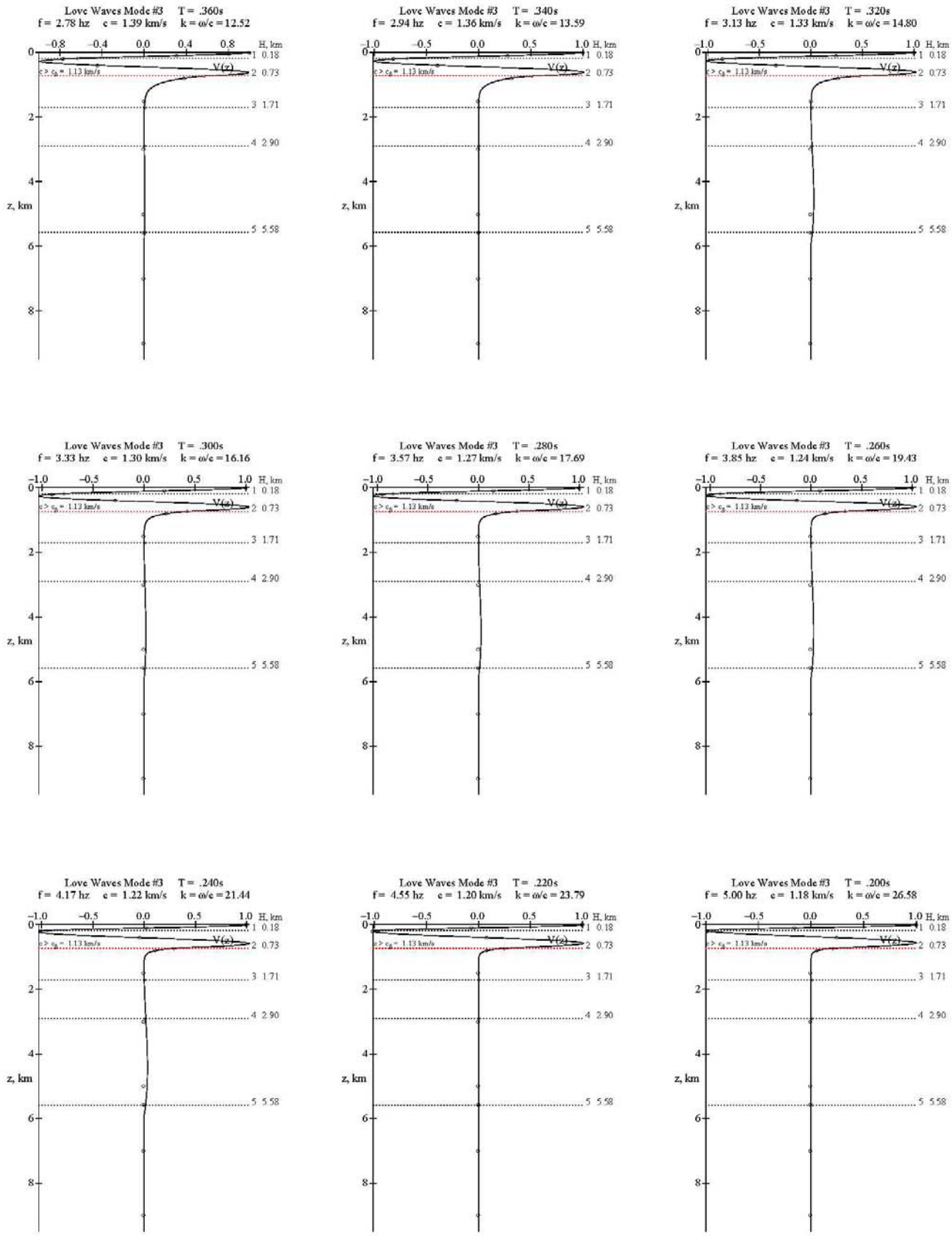

Fig. A-3.5 Love Wave Mode #3, Page 5 of 7 T=0.19-0.11s

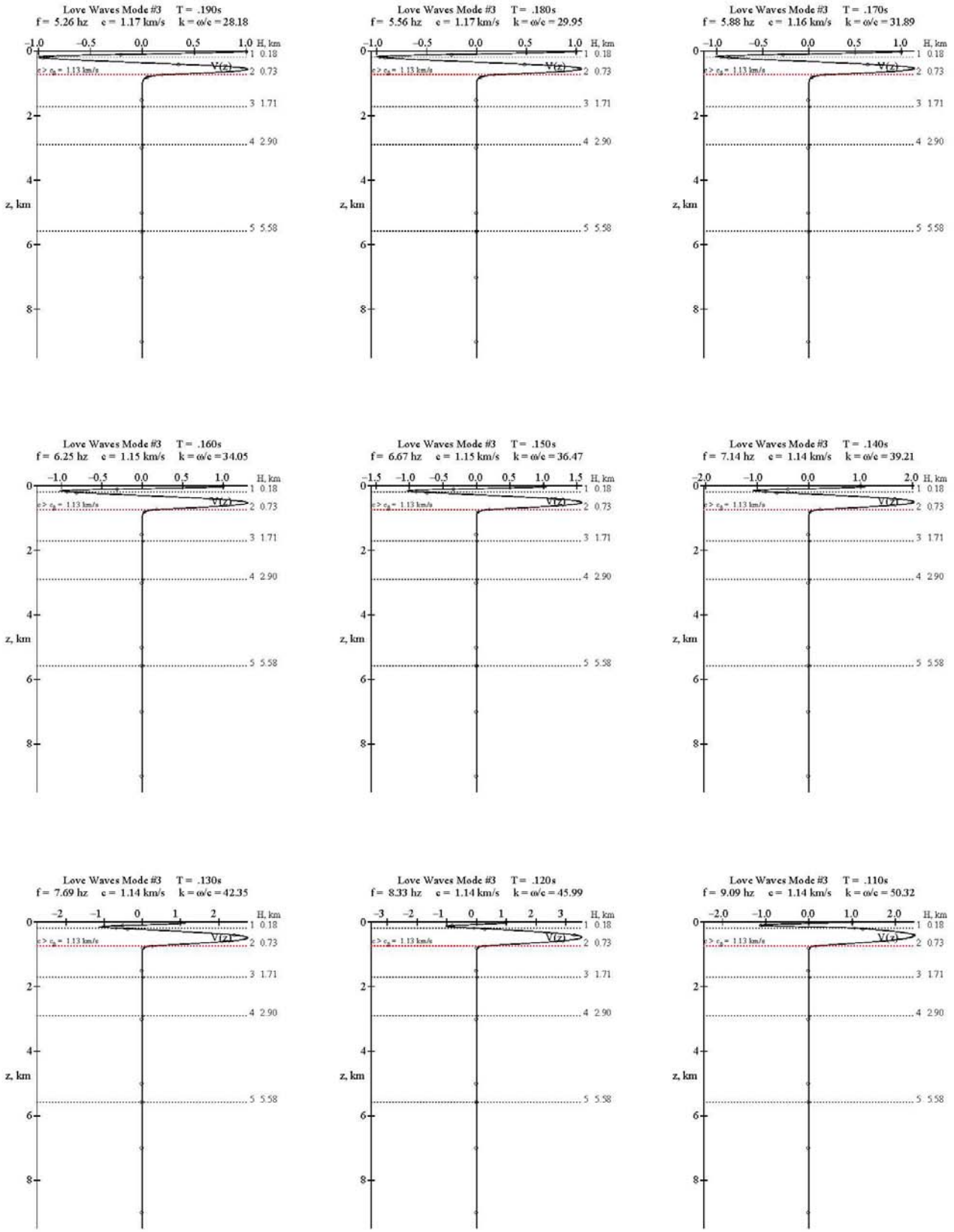

Fig. A-3.6 Love Wave Mode #3, Page 6 of 7 T=0.10-0.06s

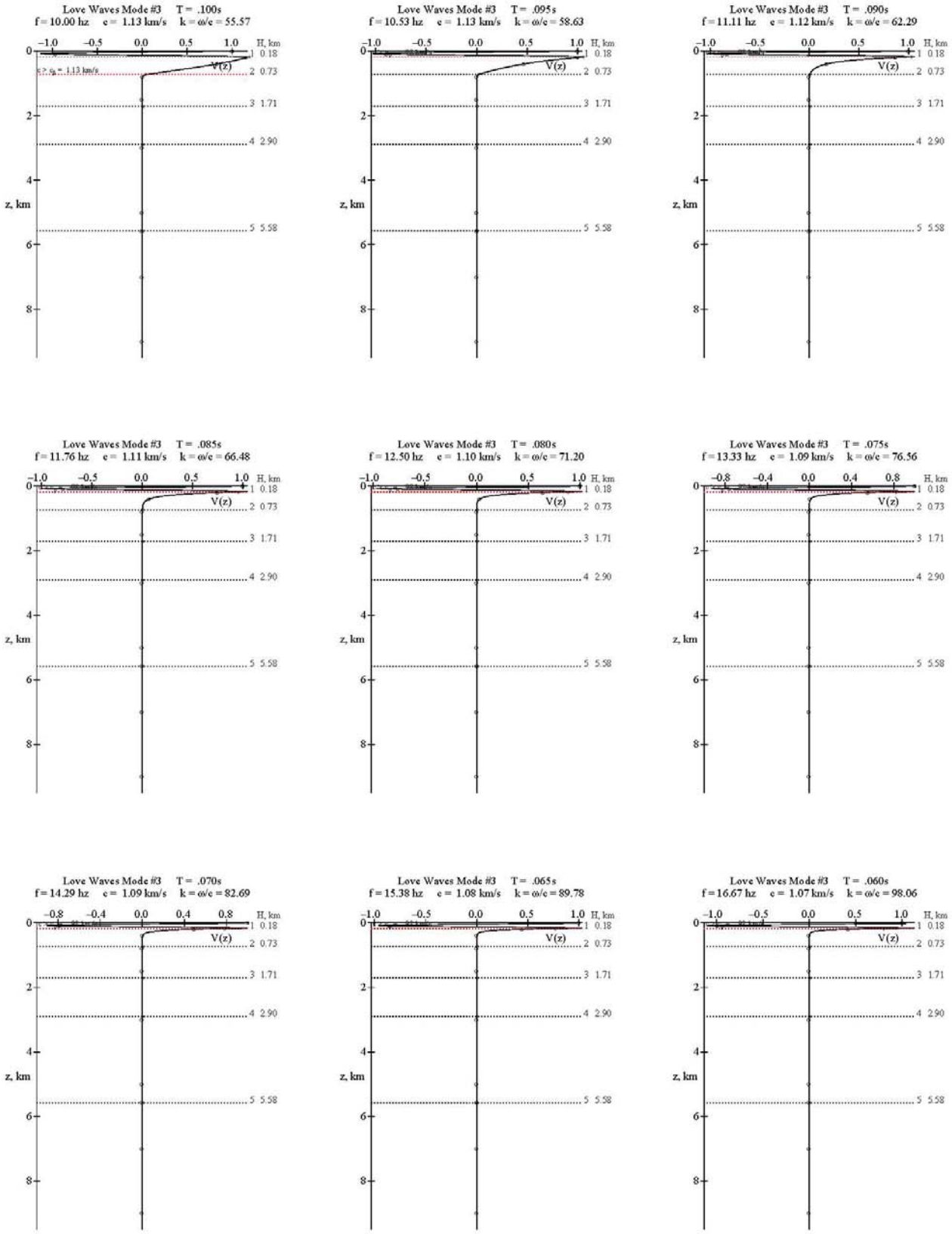

Fig. A-3.7 Love Wave Mode #3, Page 7 of 7 T=0.055-0.040s

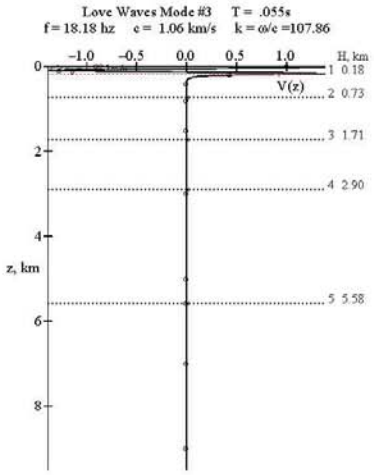

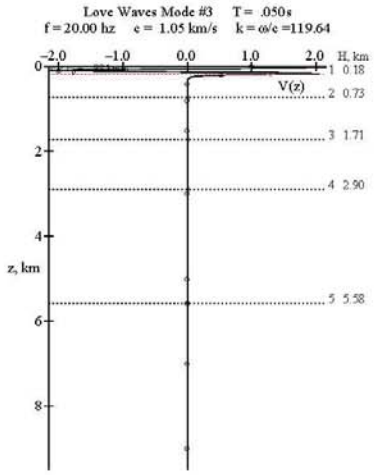

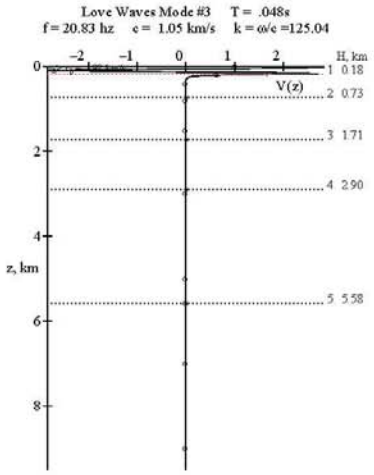

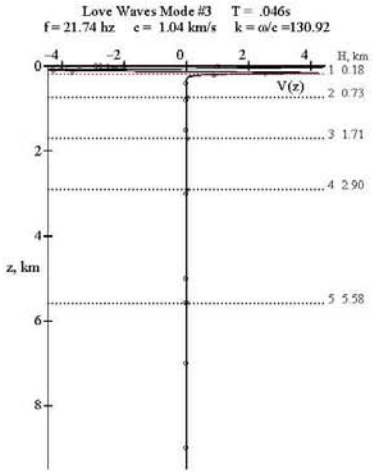

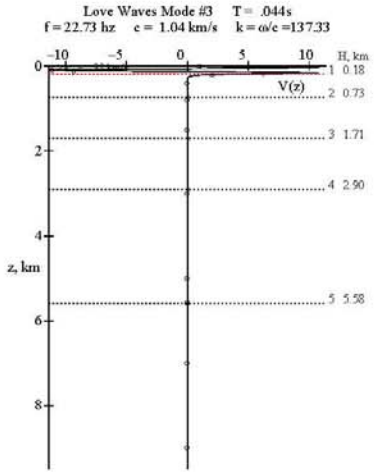

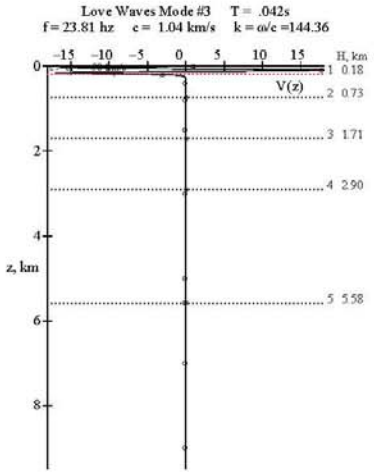

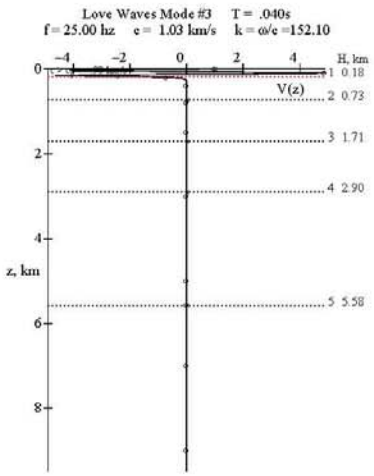

Appendix A-4 – Mode #4 Love Waves Mode Shapes

Fig. A-4.1 Love Wave Mode #4, Page 1 of 7 T=1.40-0.80s

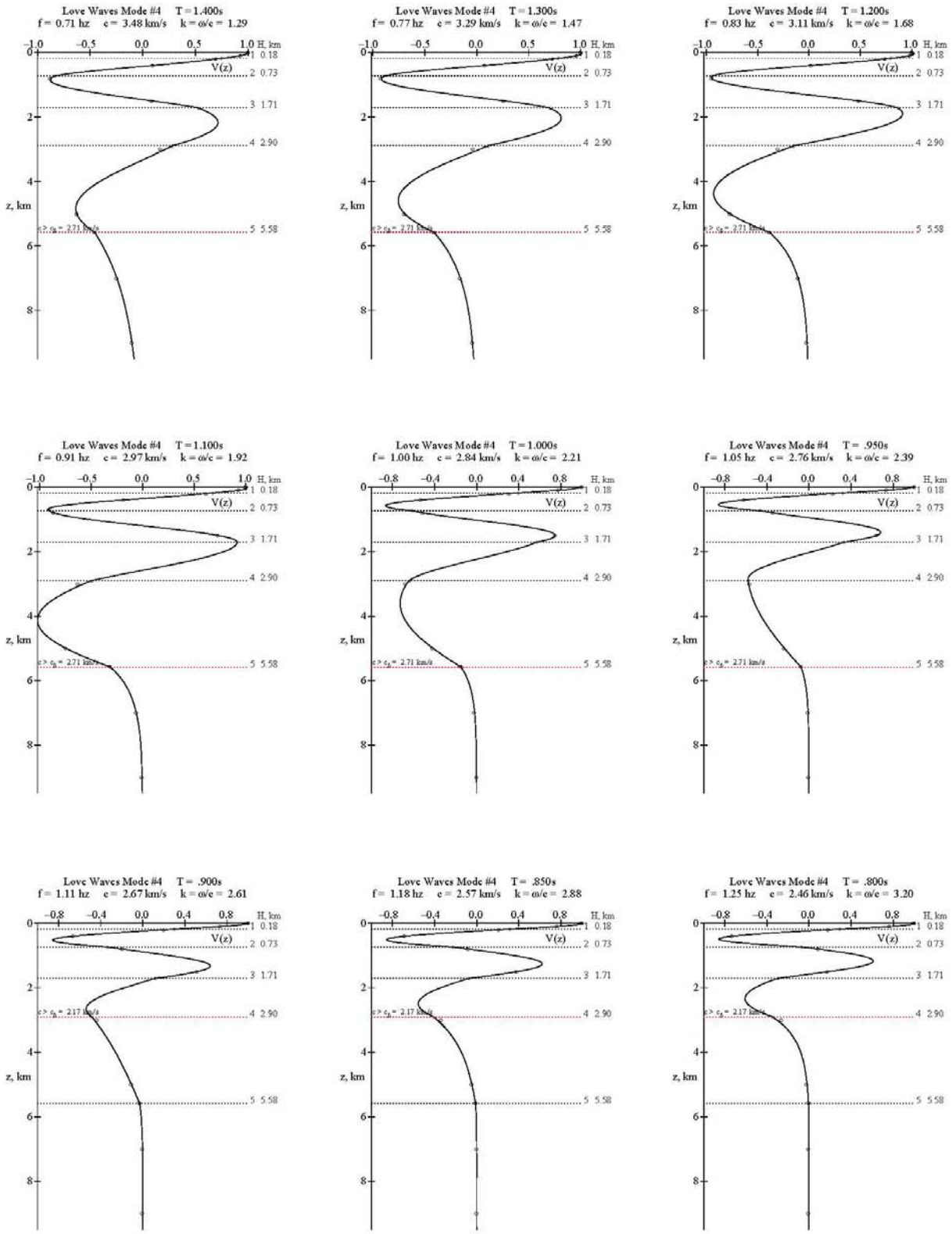

Fig. A-4.2 Love Wave Mode #4, Page 2 of 7 T=0.75-0.44s

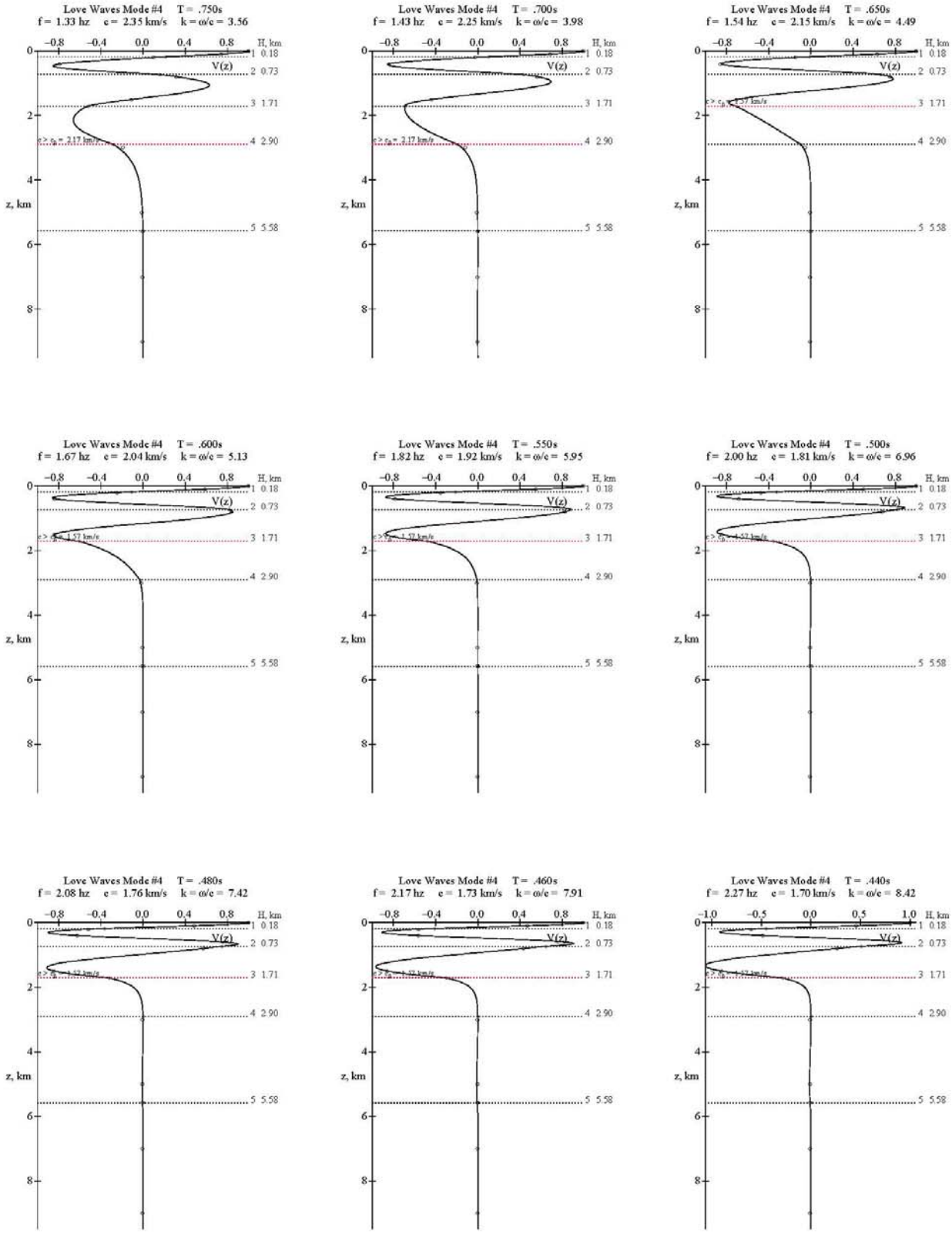

Fig. A-4.3 Love Wave Mode #4, Page 3 of 7 T=0.42-0.26s

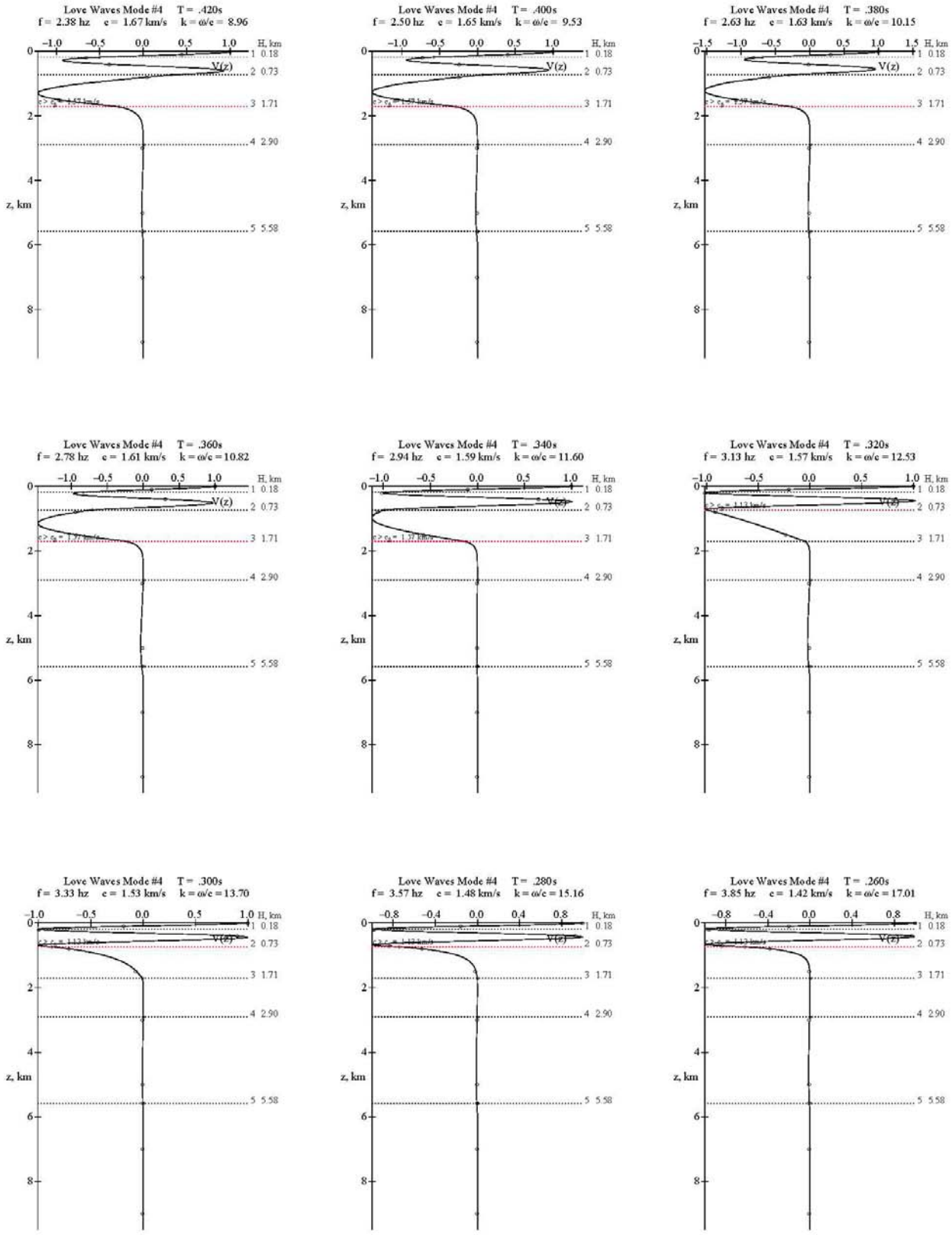

Fig. A-4.4 Love Wave Mode #4, Page 4 of 7 T=0.24-0.14s

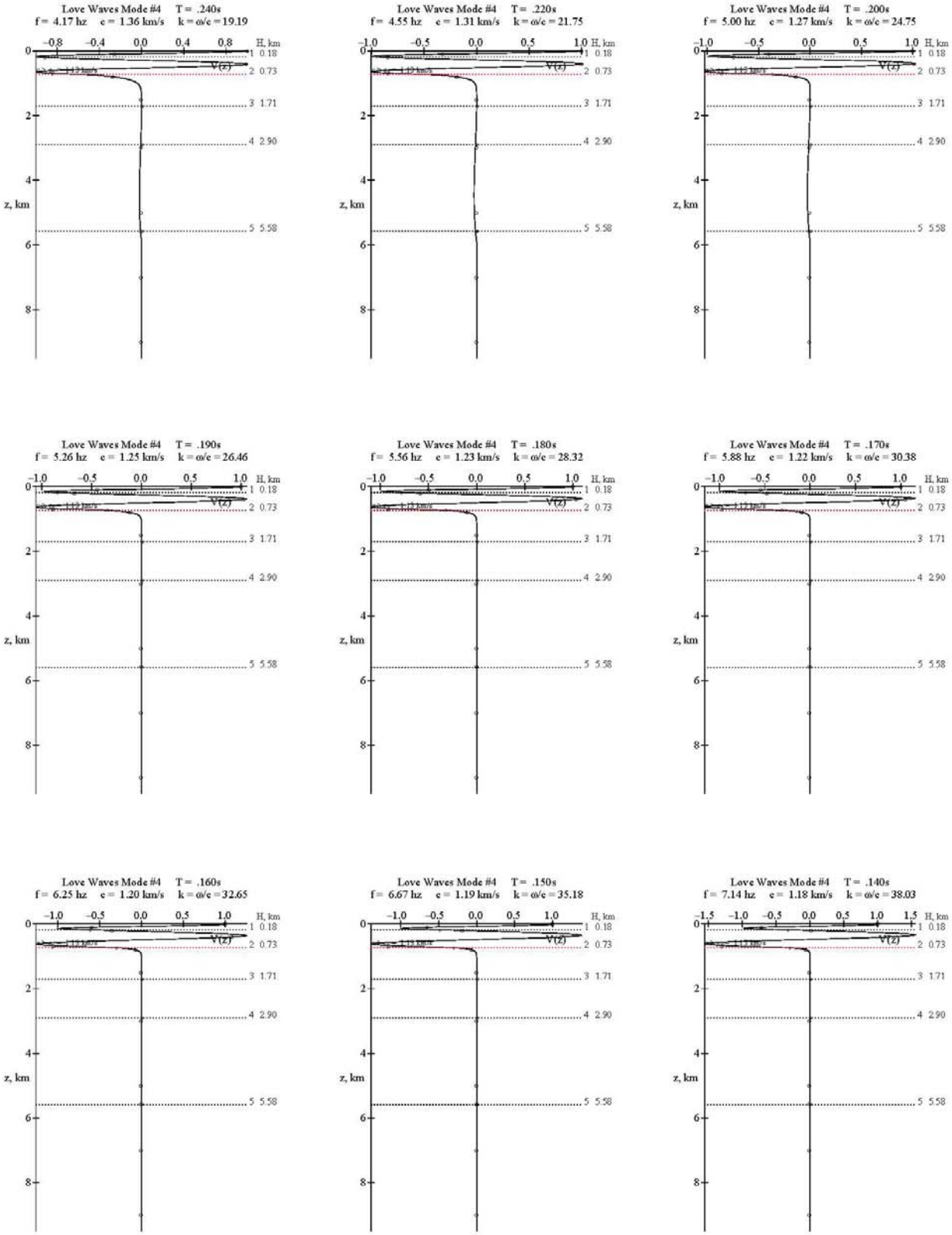

Fig. A-4.5 Love Wave Mode #4, Page 5 of 7 T=0.130-0.075s

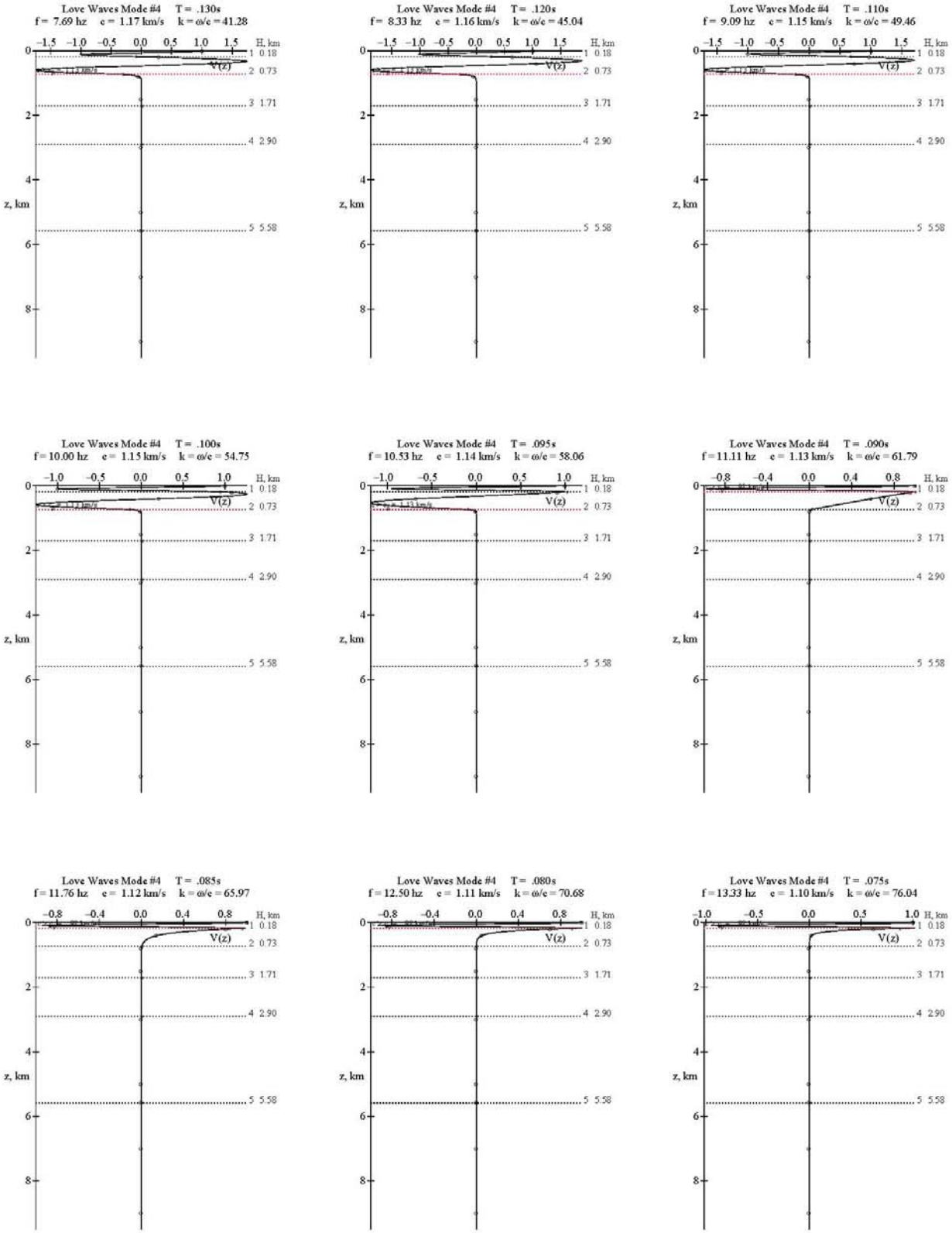

Fig. A-4.6 Love Wave Mode #4, Page 6 of 7 T=0.070-0.042s

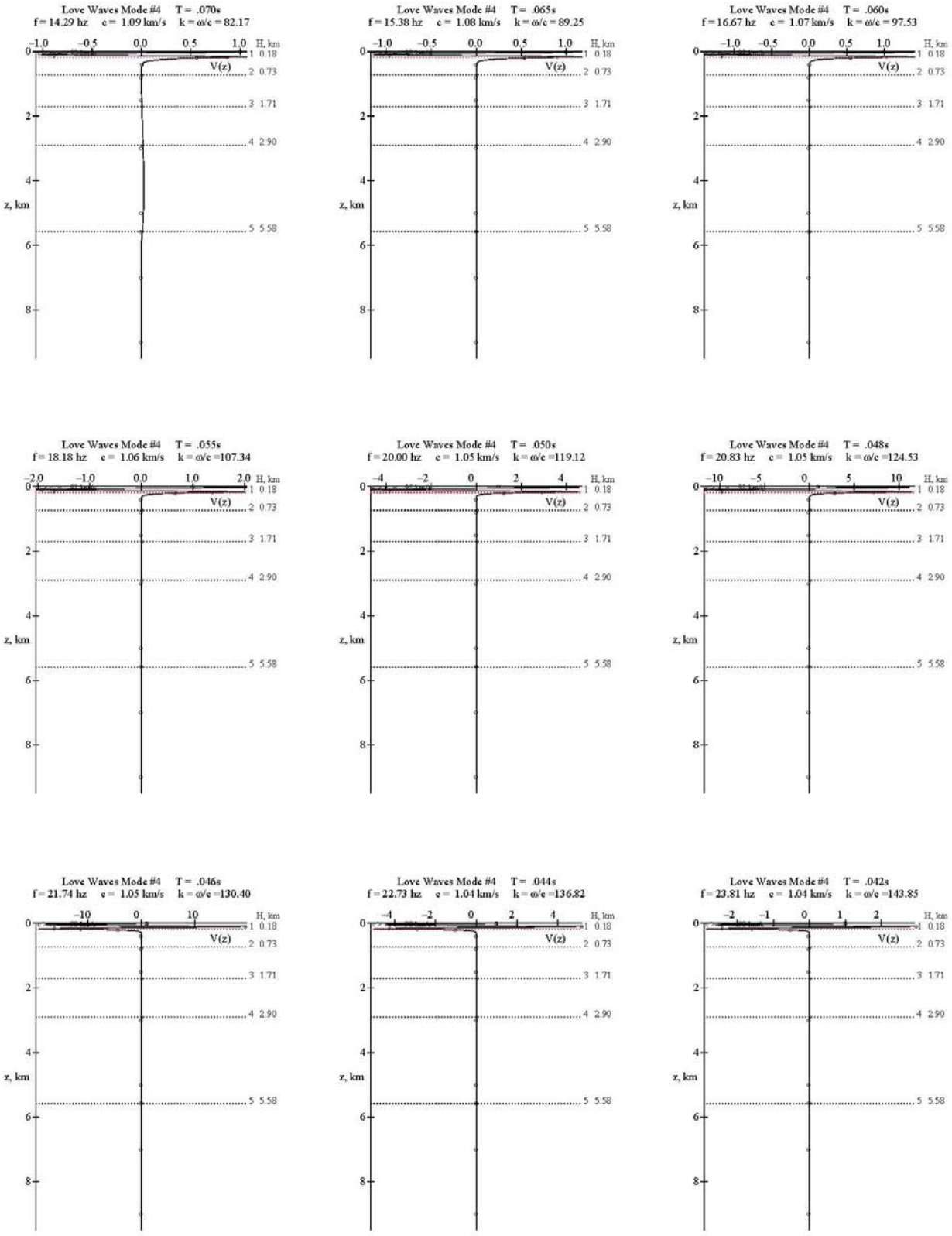

Fig. A-4.7 Love Wave Mode #4, Page 7 of 7 T=0.040s

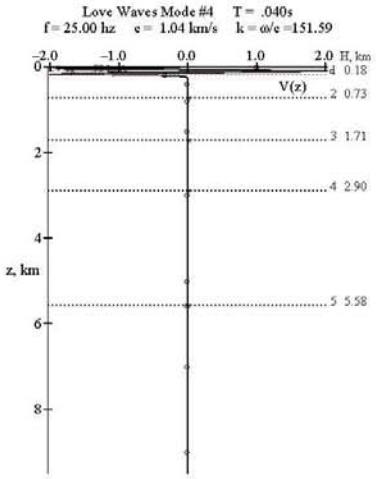

Appendix A-5 – Mode #5 Love Waves Mode Shapes

Fig. A-5.1 Love Wave Mode #5, Page 1 of 5 T=1.00-0.60s

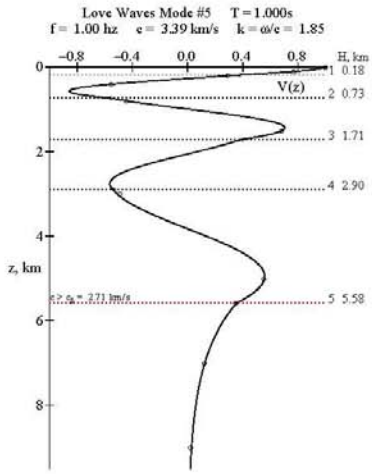

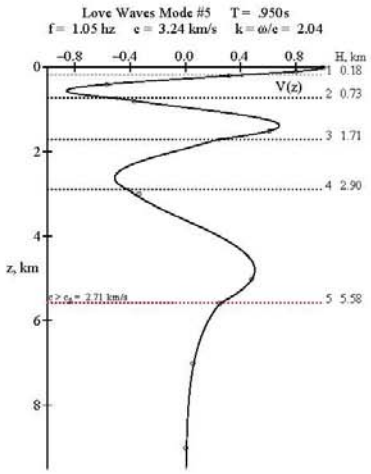

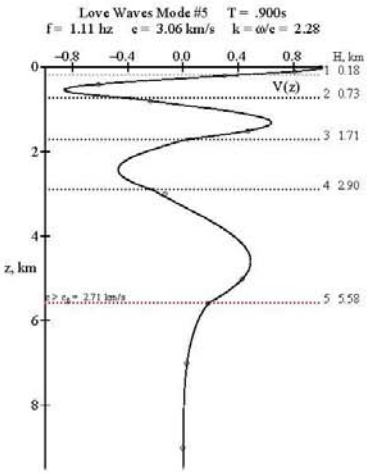

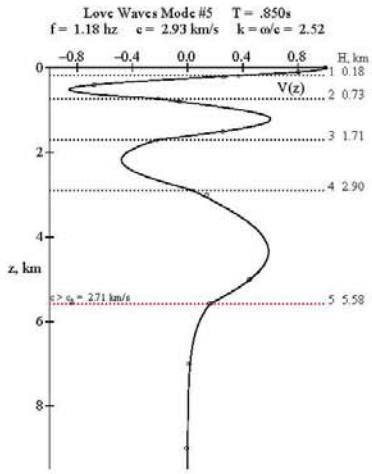

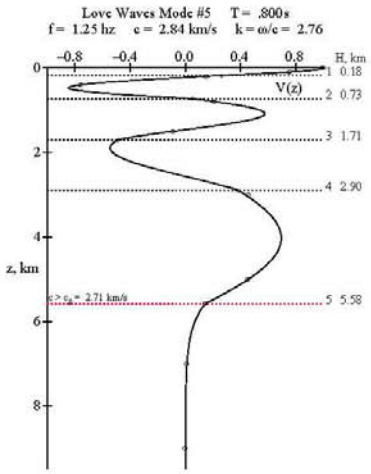

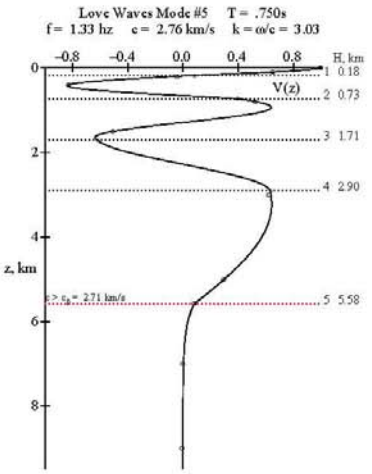

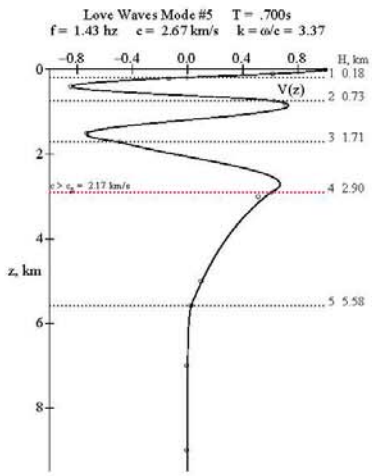

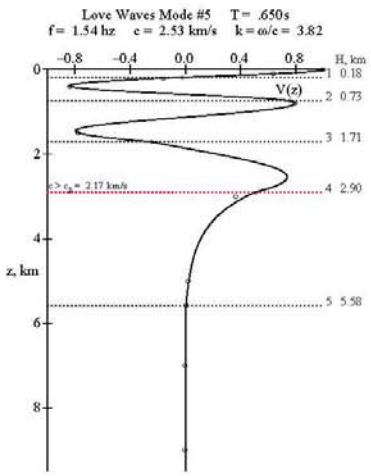

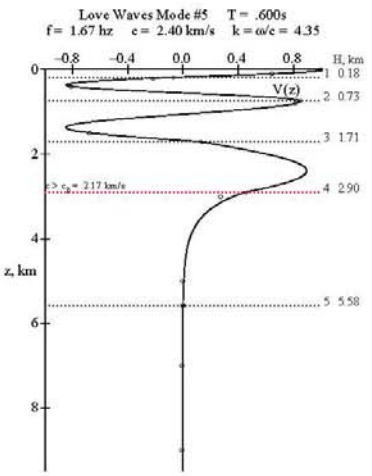

Fig. A-5.2 Love Wave Mode #5, Page 2 of 6 T=0.55-0.36s

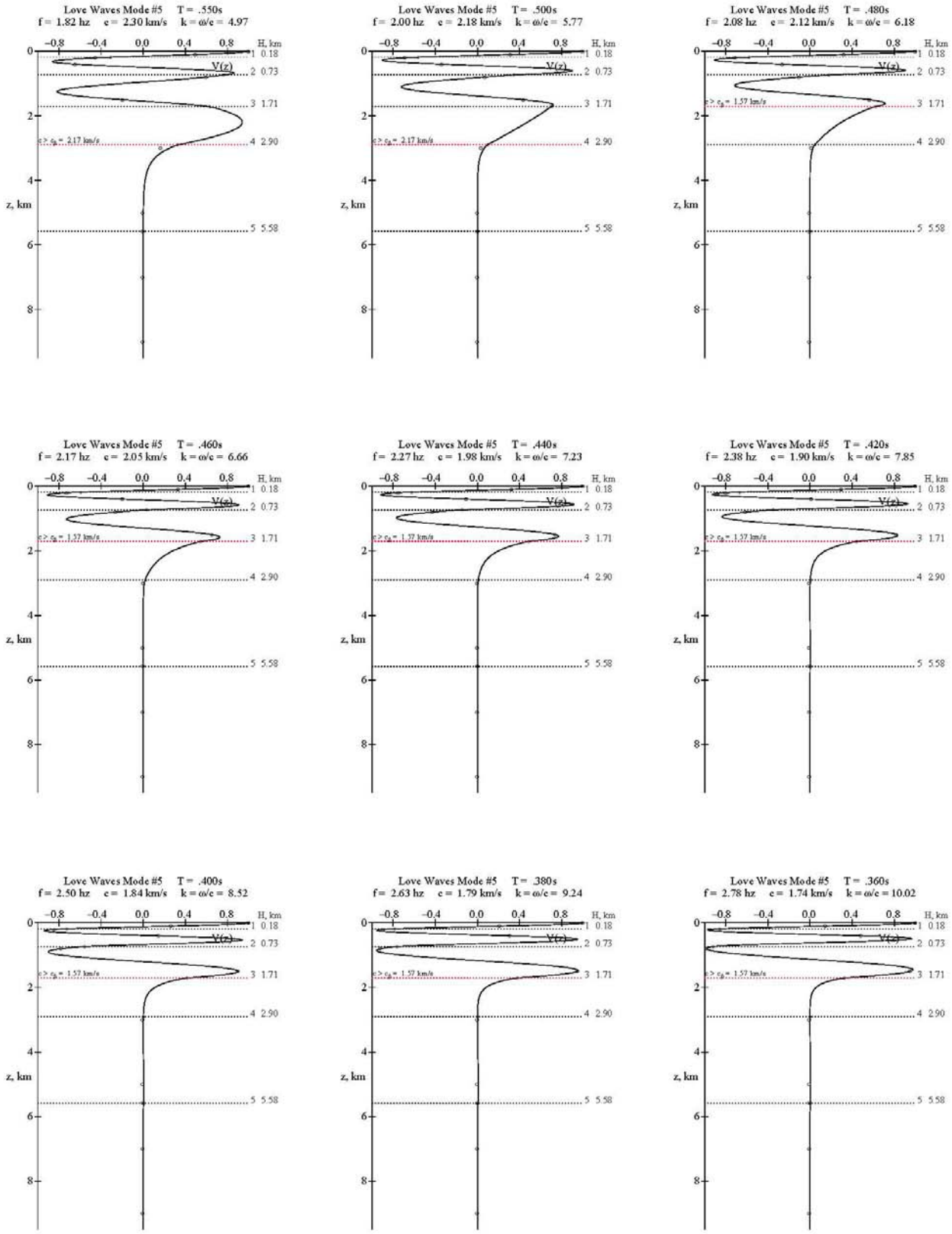

Fig. A-5.3 Love Wave Mode #5, Page 3 of 6 T=0.34-0.19s

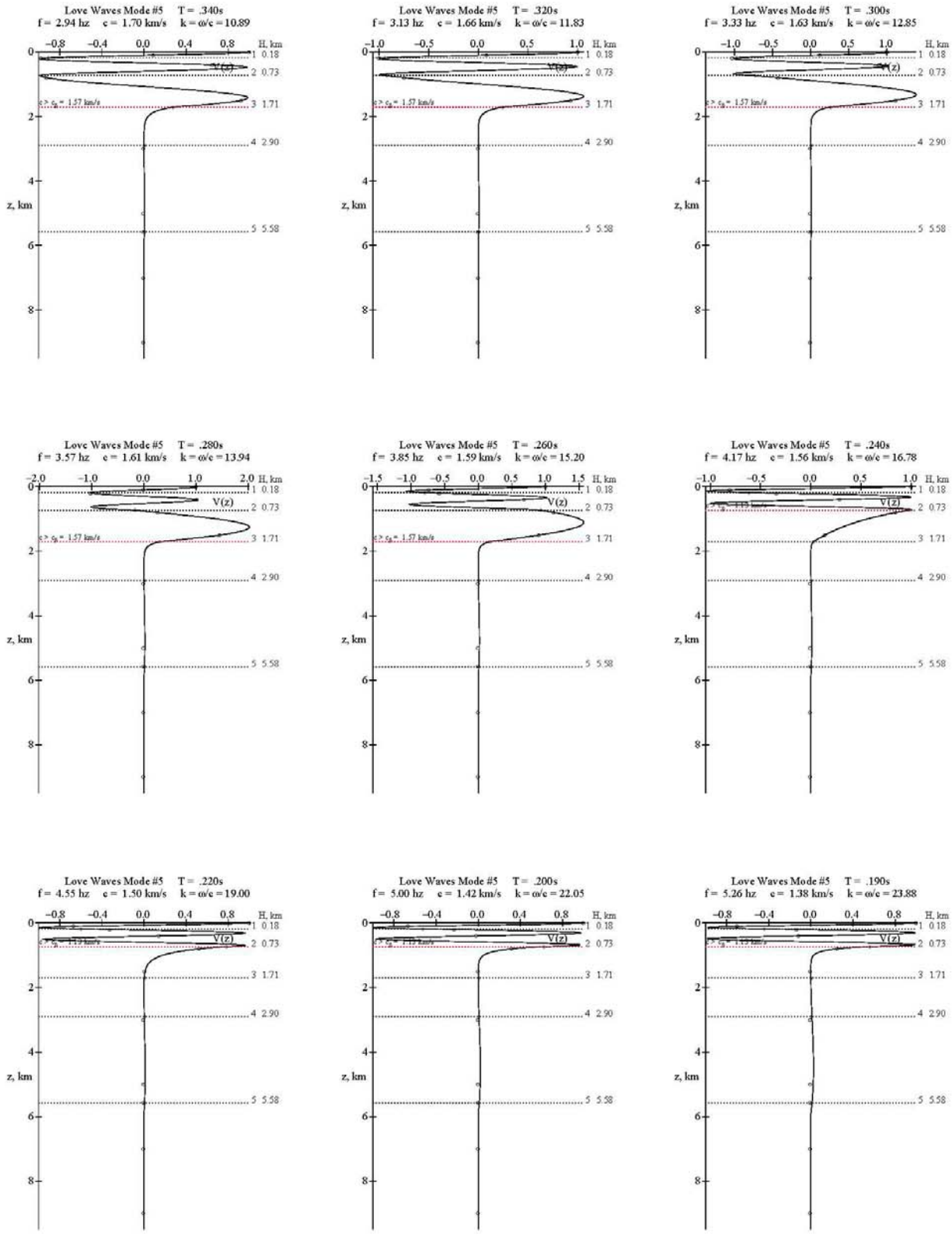

Fig. A-5.4 Love Wave Mode #5, Page 4 of 6 T=0.18-0.10s

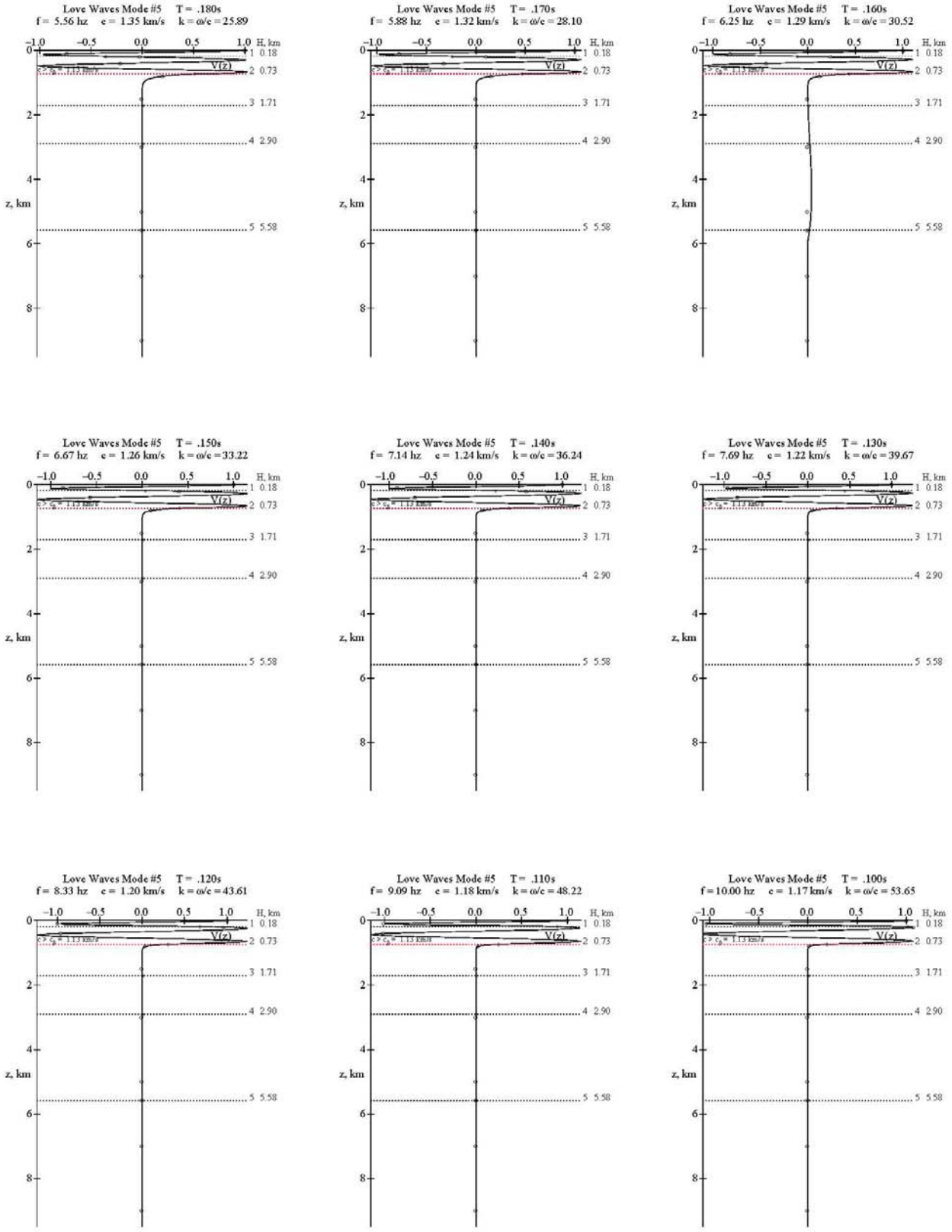

Fig. A-5.5 Love Wave Mode #5, Page 5 of 6 T=0.095-0.055s

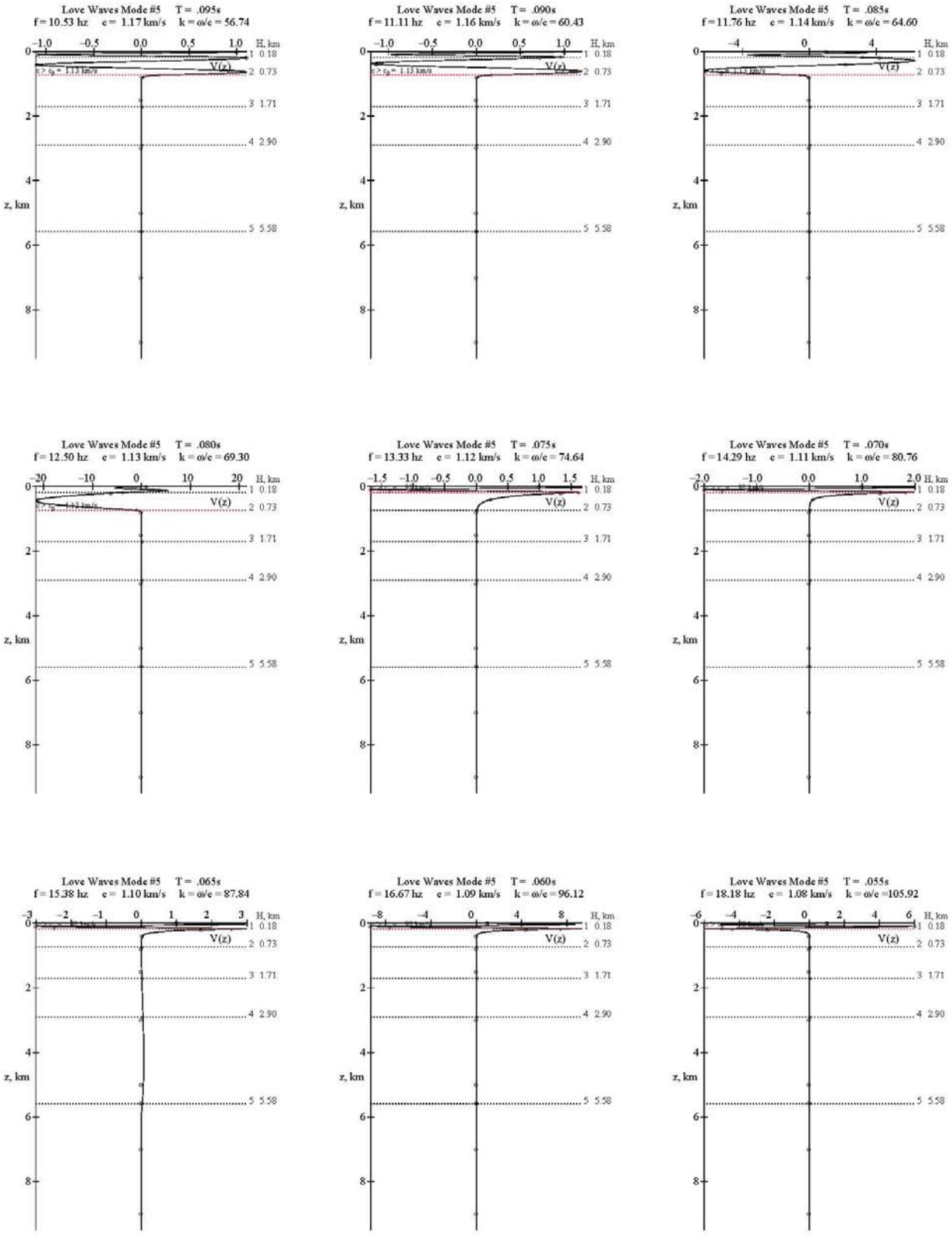

Fig. A-5.6 Love Wave Mode #5, Page 6 of 6 T=0.050-0.040s

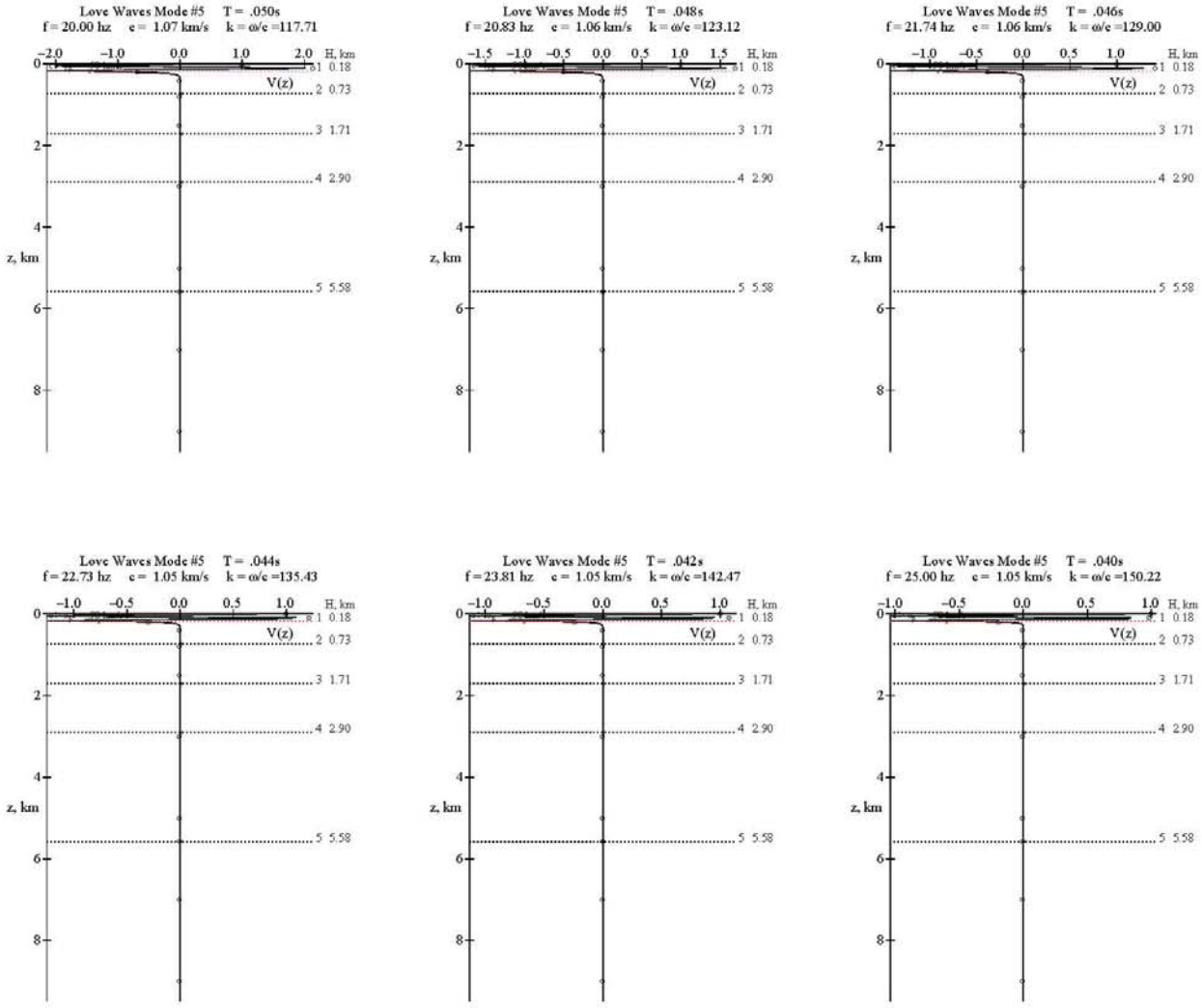

Appendix A-6 – Body SH Waves Mode Shapes: $\gamma = 85^o$

Fig. A-6.1 Body SH Waves (Mode#6), Page 1 of 11 T=15.0-8.5s

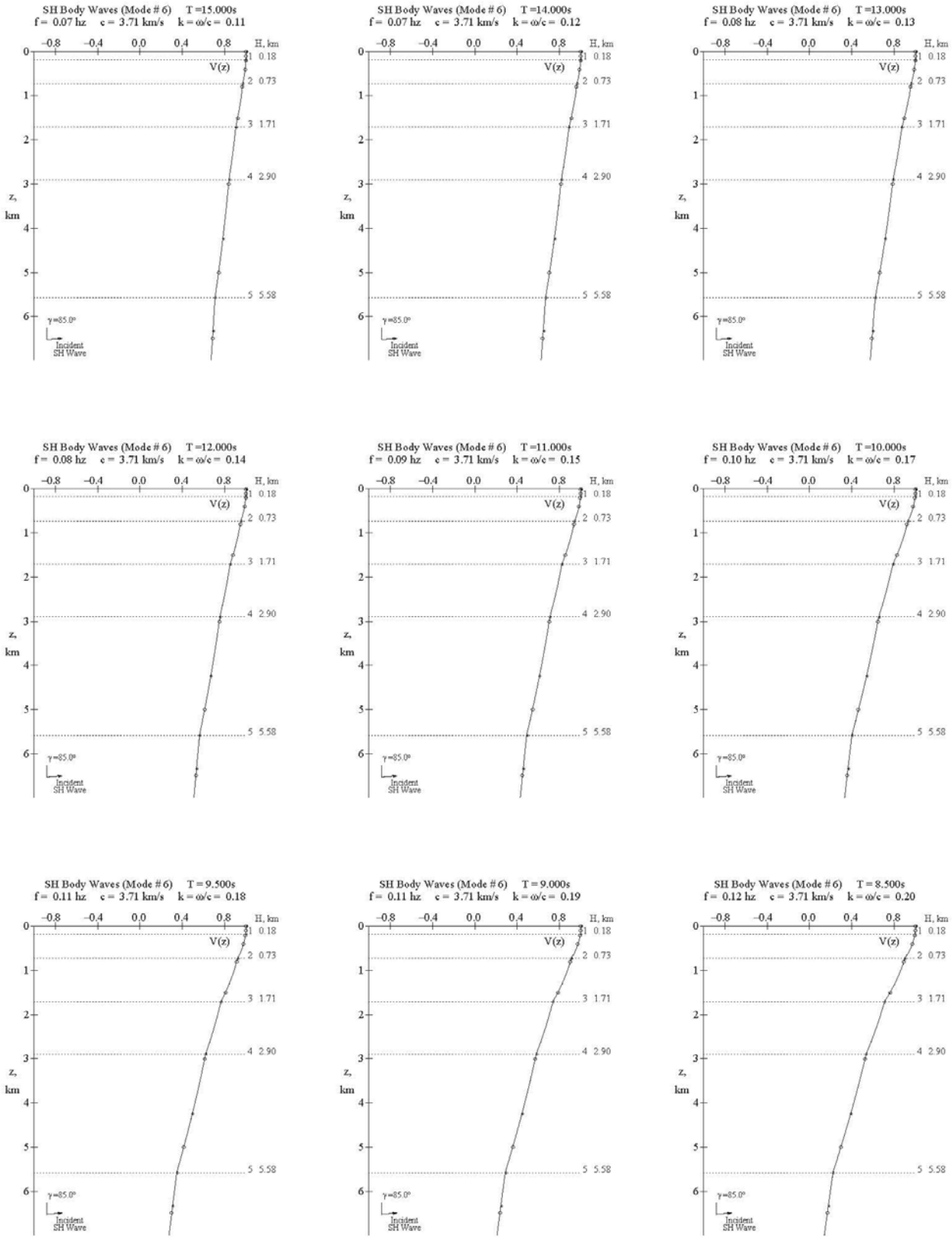

Fig. A-6.2 Body SH Waves (Mode#6), Page 2 of 11 T=8.0-4.6s

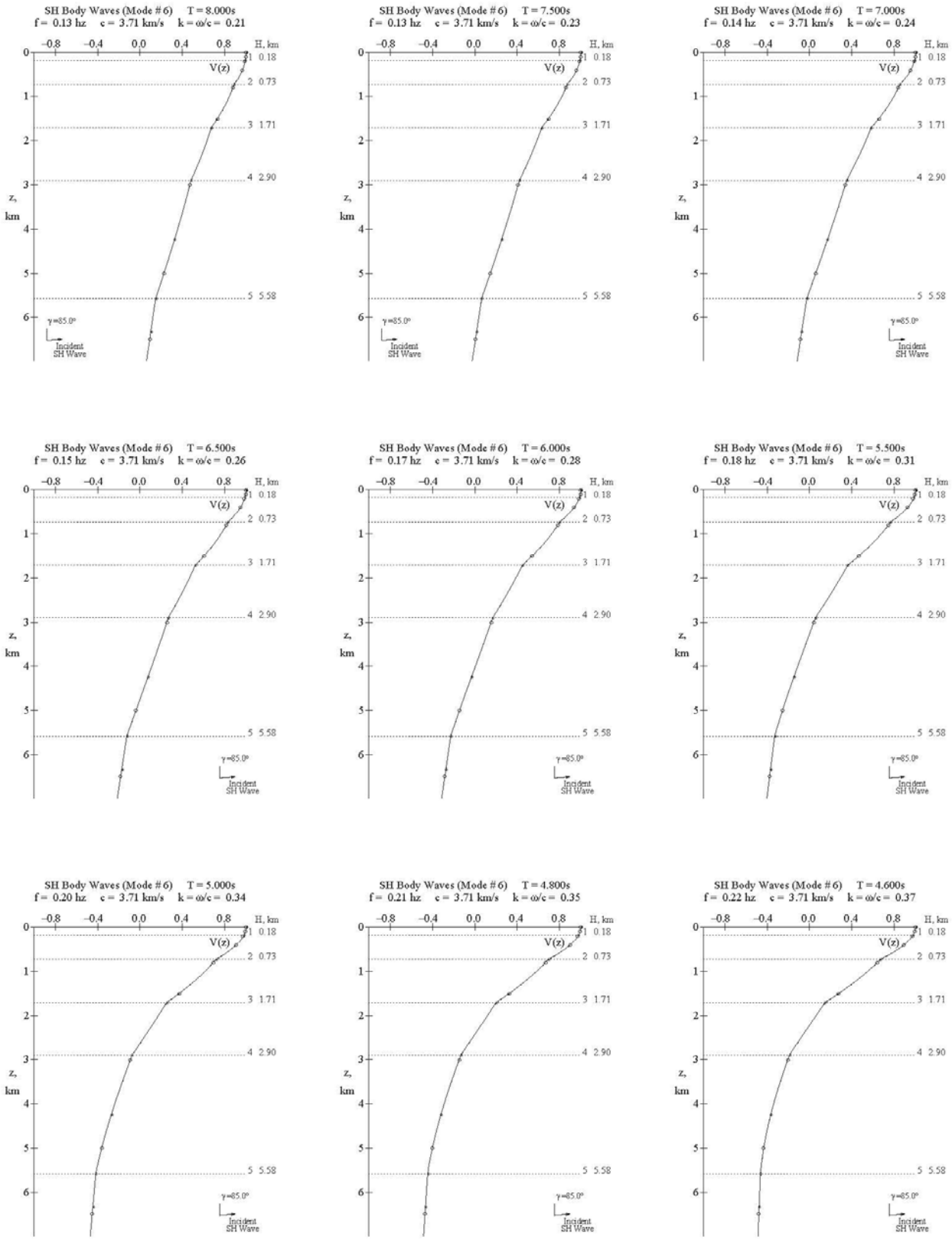

Fig. A-6.3 Body SH Waves (Mode#6), Page 3 of 11 T=4.4-2.8s

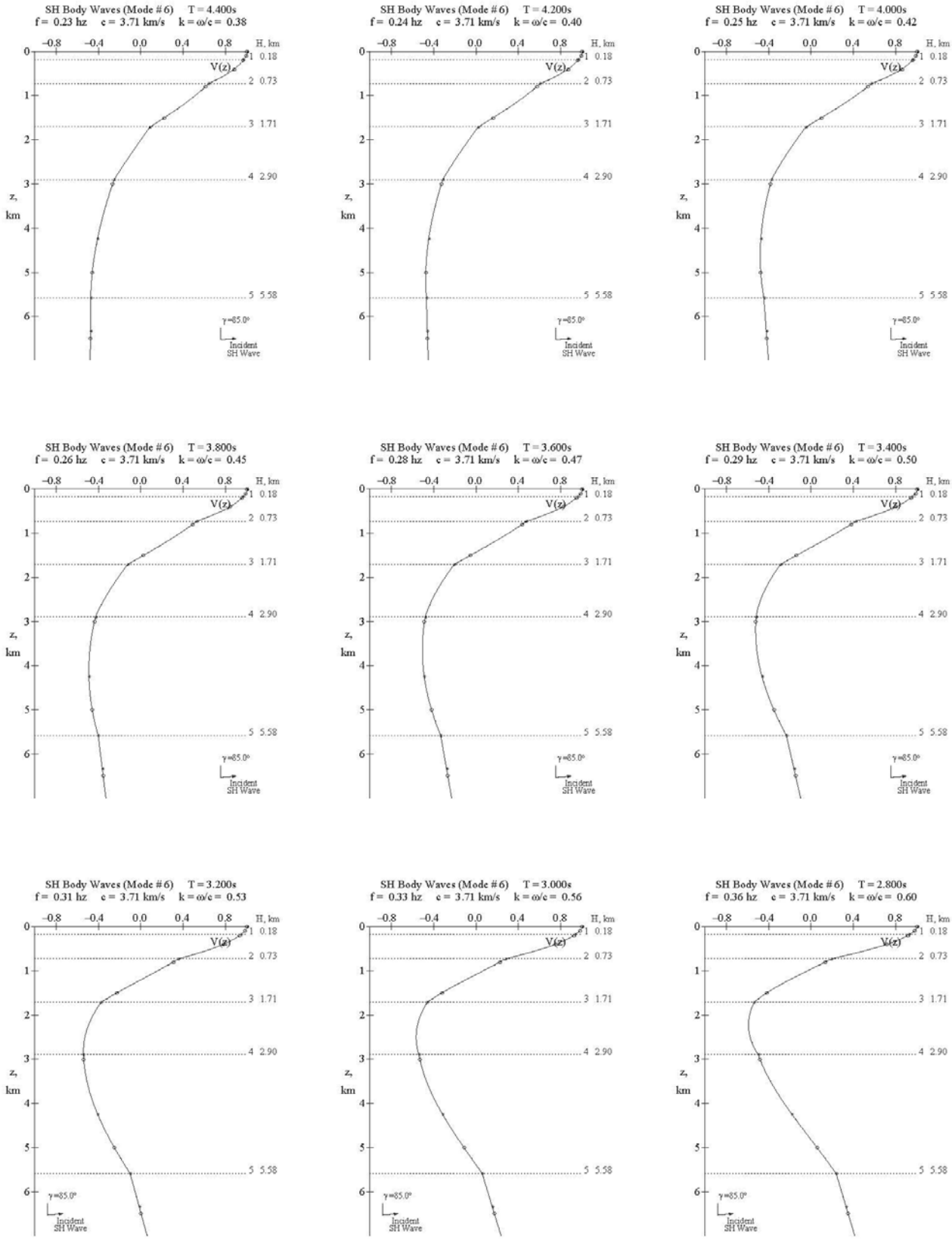

Fig. A-6.4 Body SH Waves (Mode#6), Page 4 of 11 T=2.6-1.5s

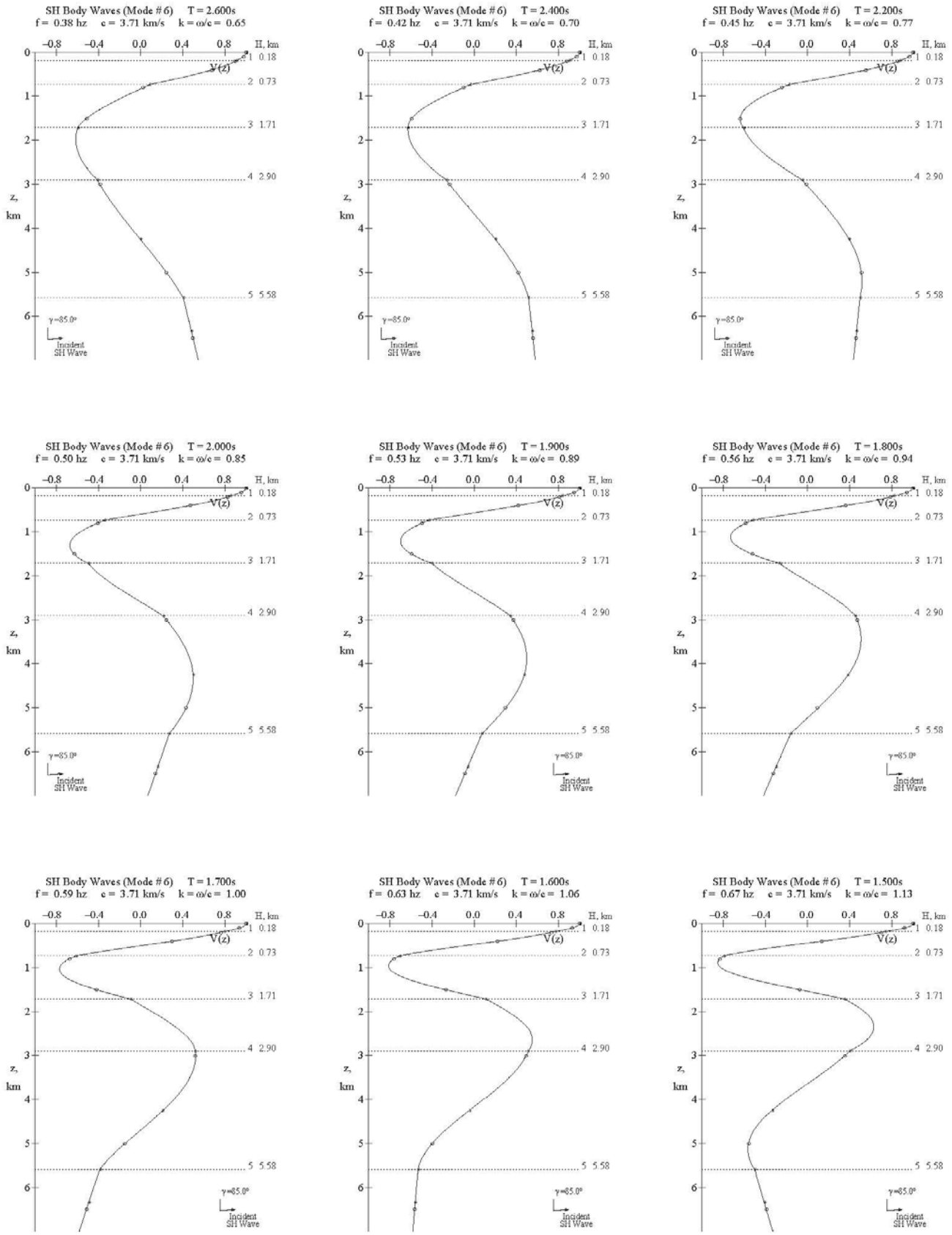

Fig. A-6.5 Body SH Waves (Mode#6), Page 5 of 11 T=1.40-0.80s

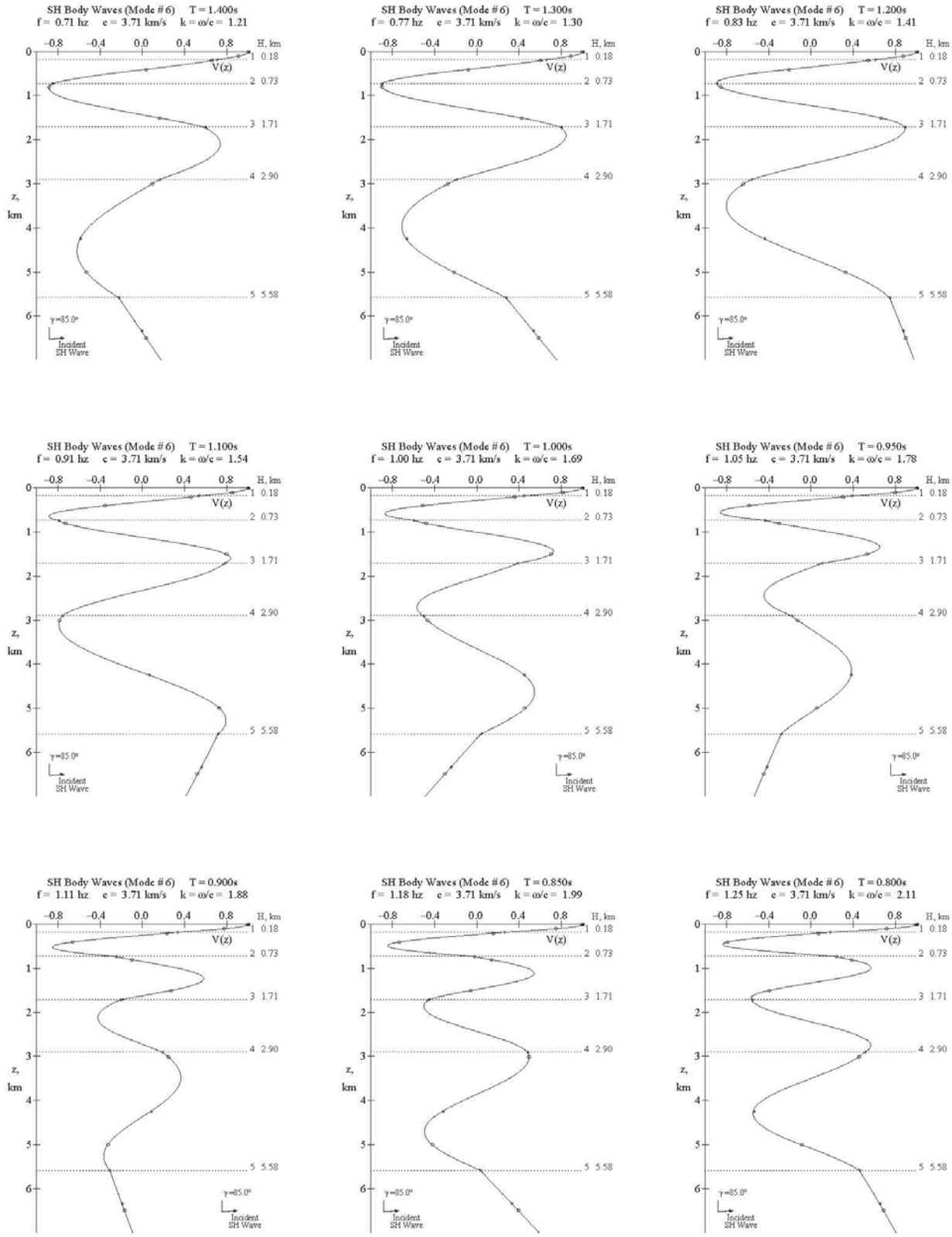

Fig. A-6.6 Body SH Waves (Mode#6), Page 6 of 11 T=0.75-0.44s

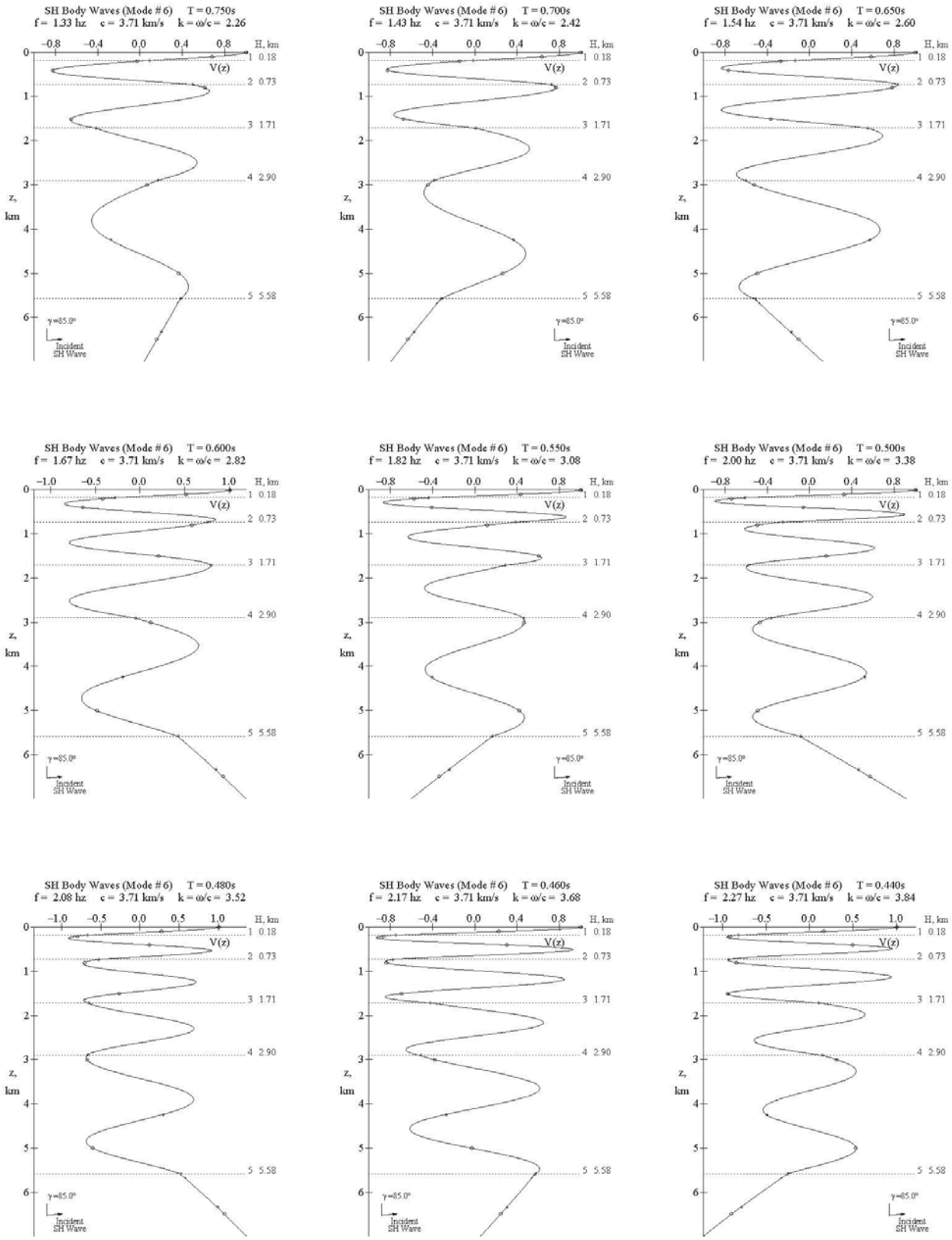

Fig. A-6.7 Body SH Waves (Mode#6), Page 7 of 11 T=0.42-0.26s

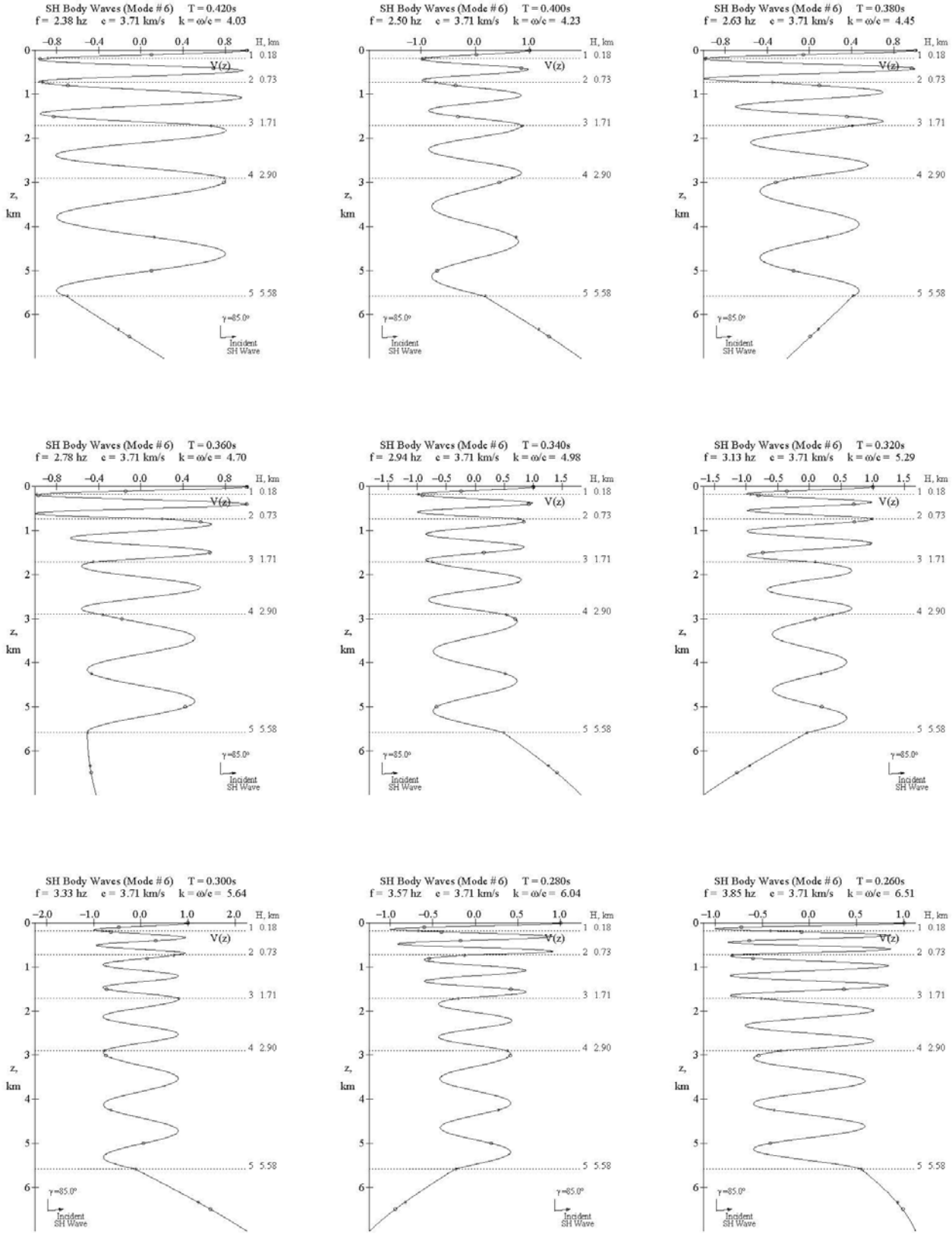

Fig. A-6.8 Body SH Waves (Mode#6), Page 8 of 11 T=0.24-0.14s

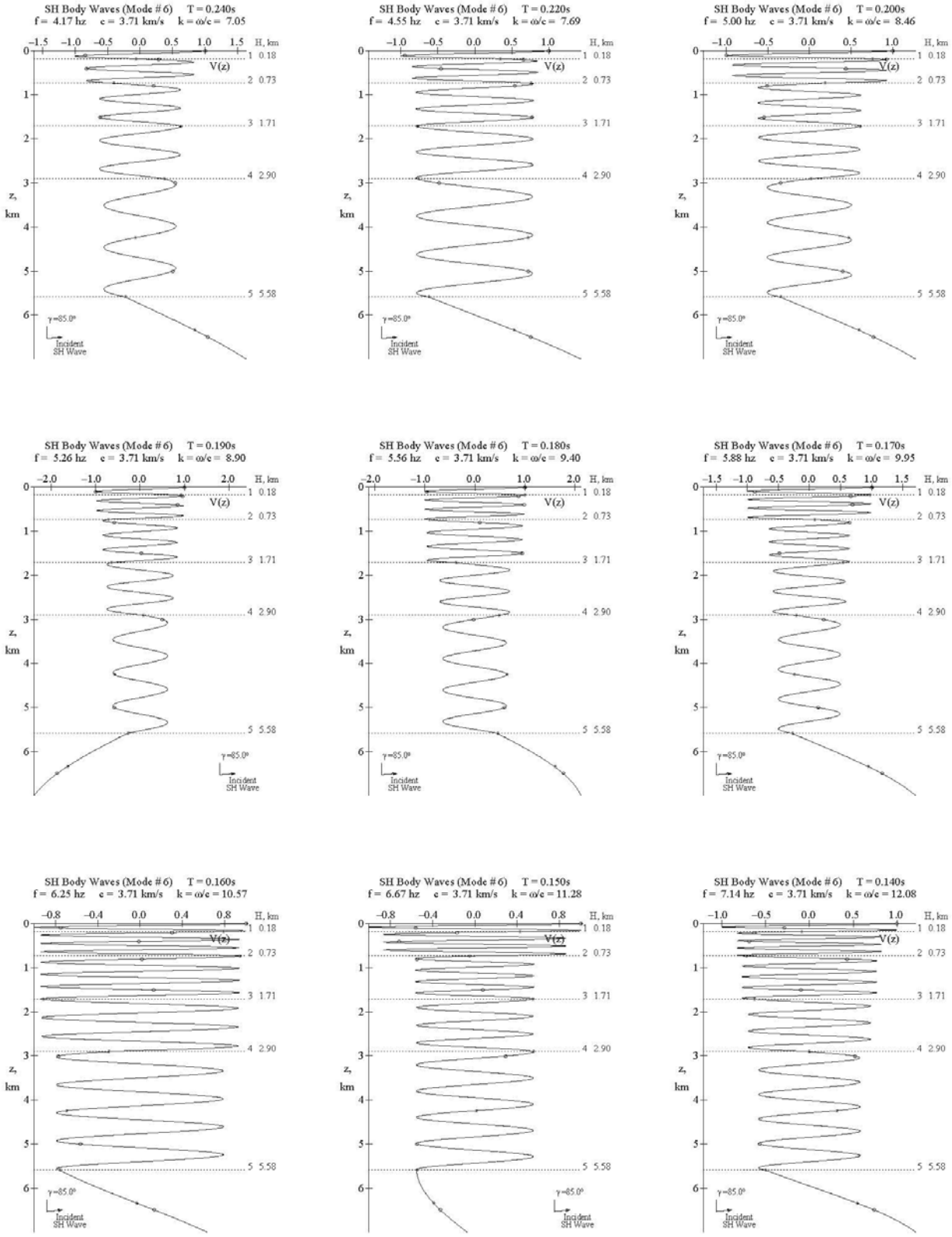

Fig. A-6.9 Body SH Waves (Mode#6), Page 9 of 11 T=0.130-0.075s

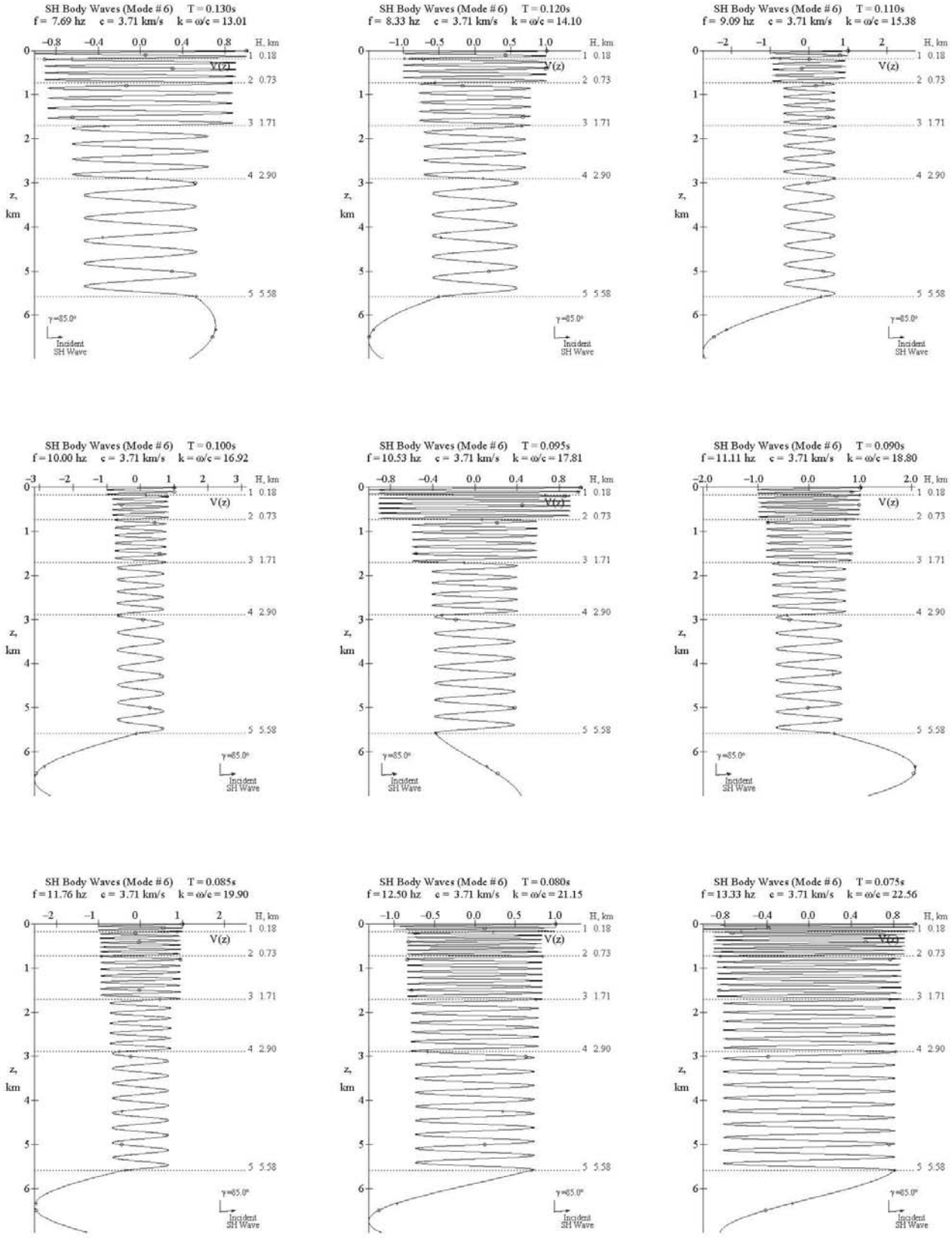

Fig. A-6.10 Body SH Waves (Mode#6), Page 10 of 11 T=0.070-0.042s

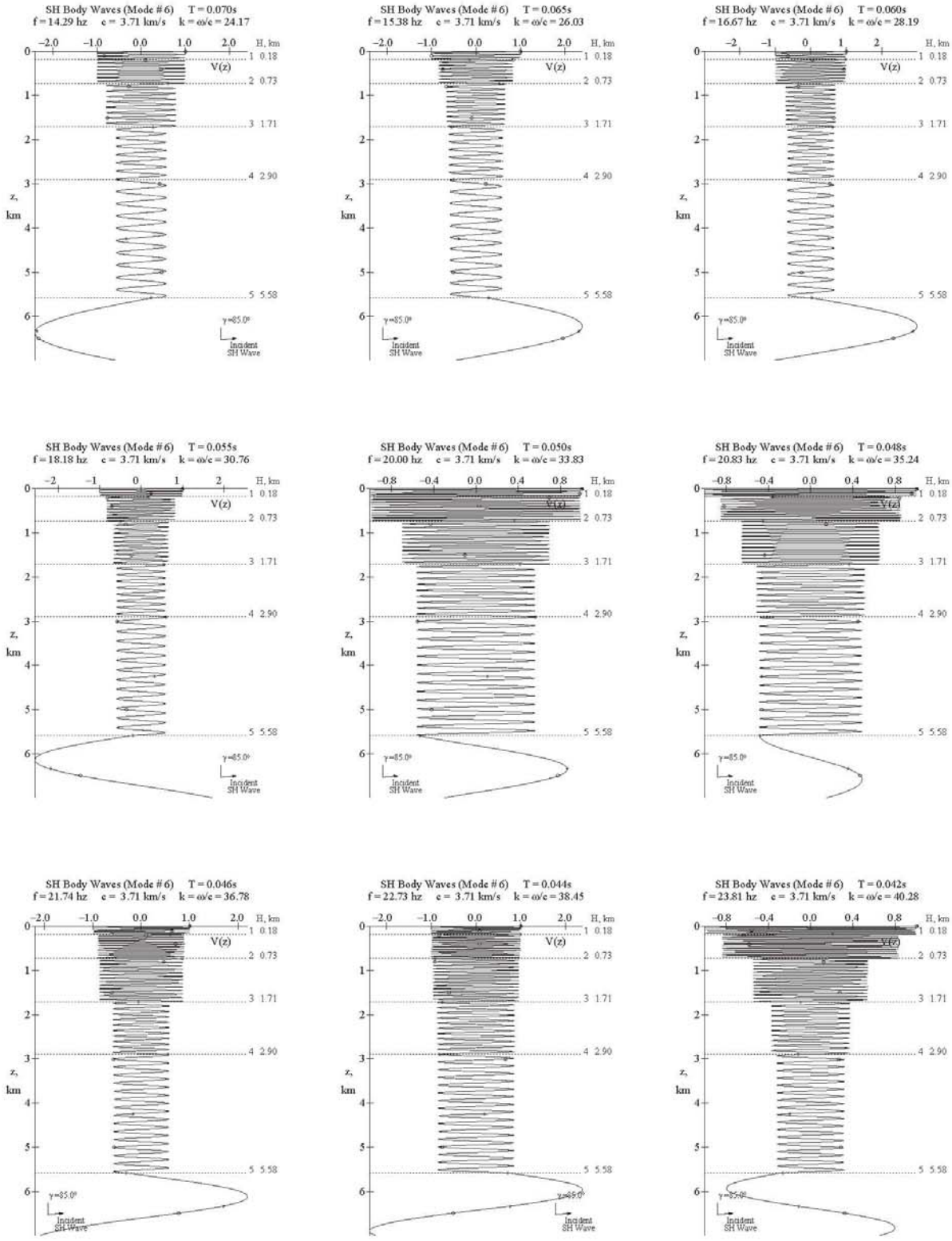

Fig. A-6.11 Body SH Waves (Mode#6), Page 11 of 11 T=0.040s

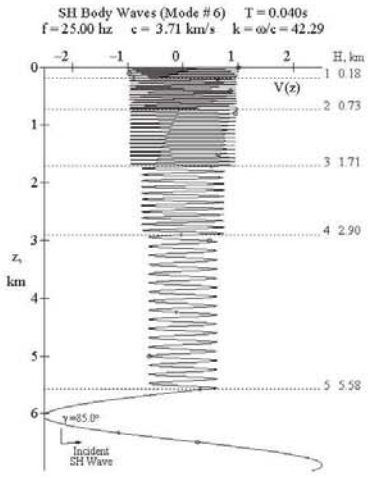

Appendix B – Rayleigh and P, SV Body Waves Mode Shapes

Appendix B-1 Mode #1 Rayleigh Waves

Fig. B-1.1 Rayleigh Wave Mode #1, Page 1 of 11 T=15.0-8.5s

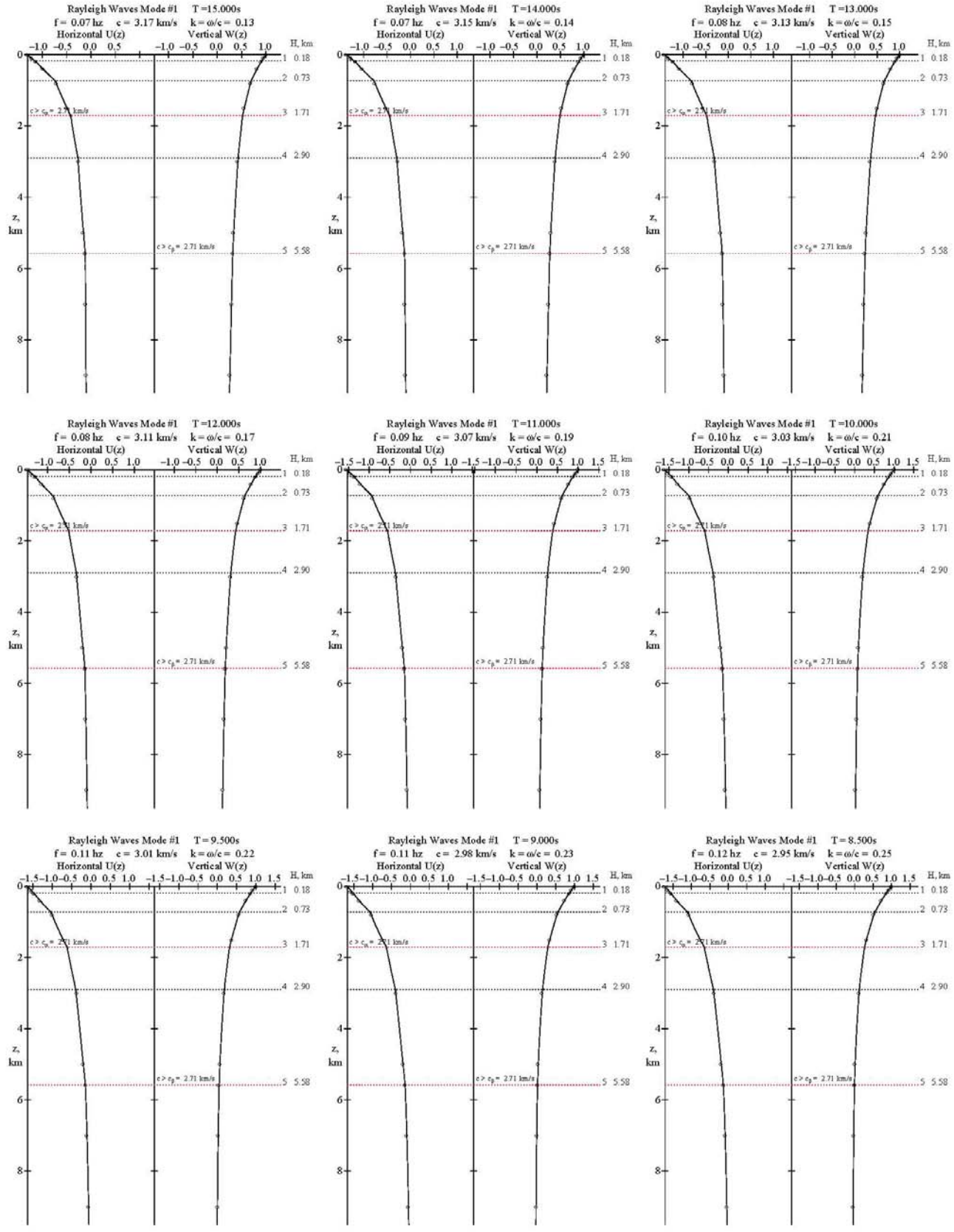

Fig. B-1.2 Rayleigh Wave Mode #1, Page 2 of 11 T=8.0-4.6s

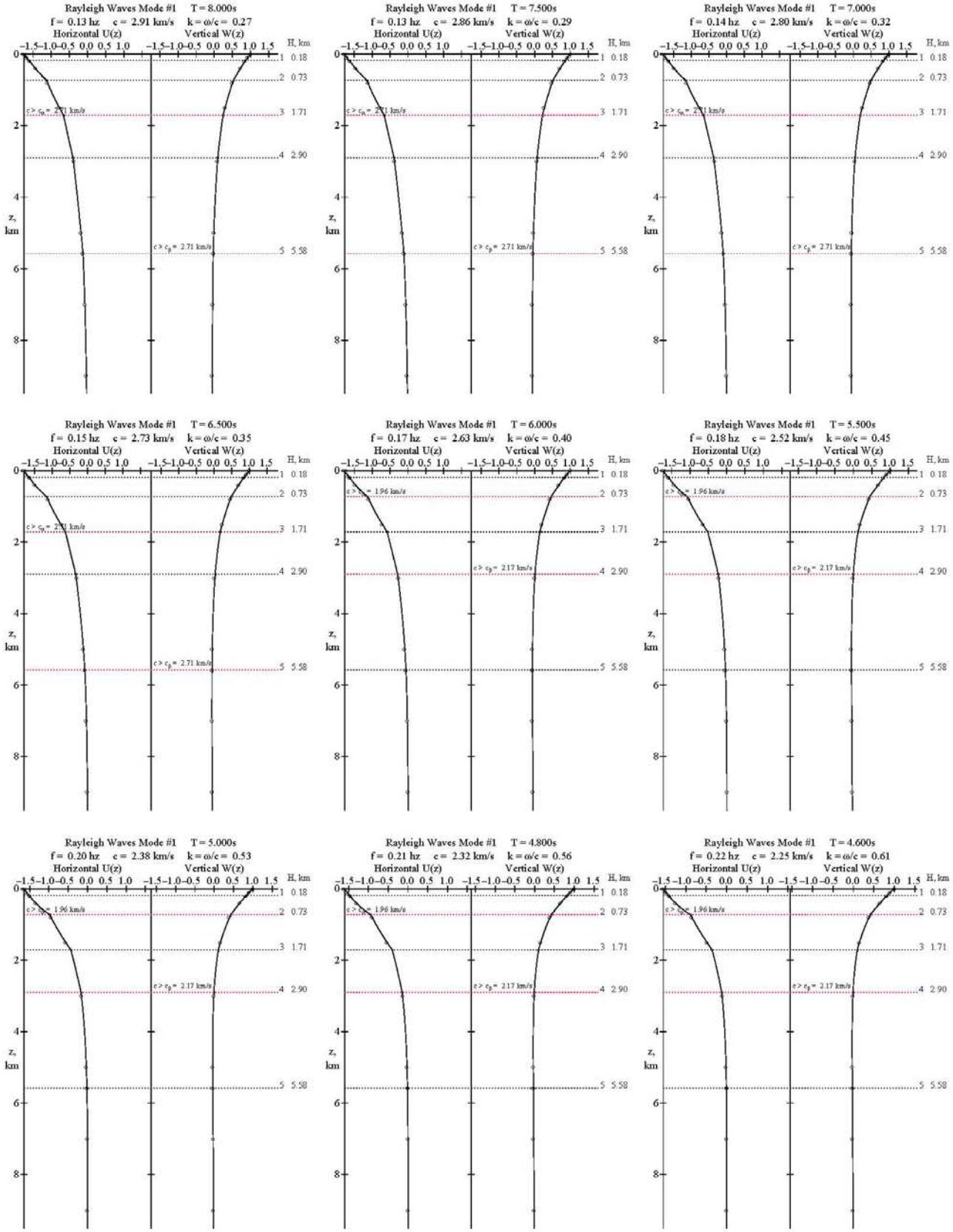

Fig. B-1.3 Rayleigh Wave Mode #1, Page 3 of 11 T=4.4-2.8s

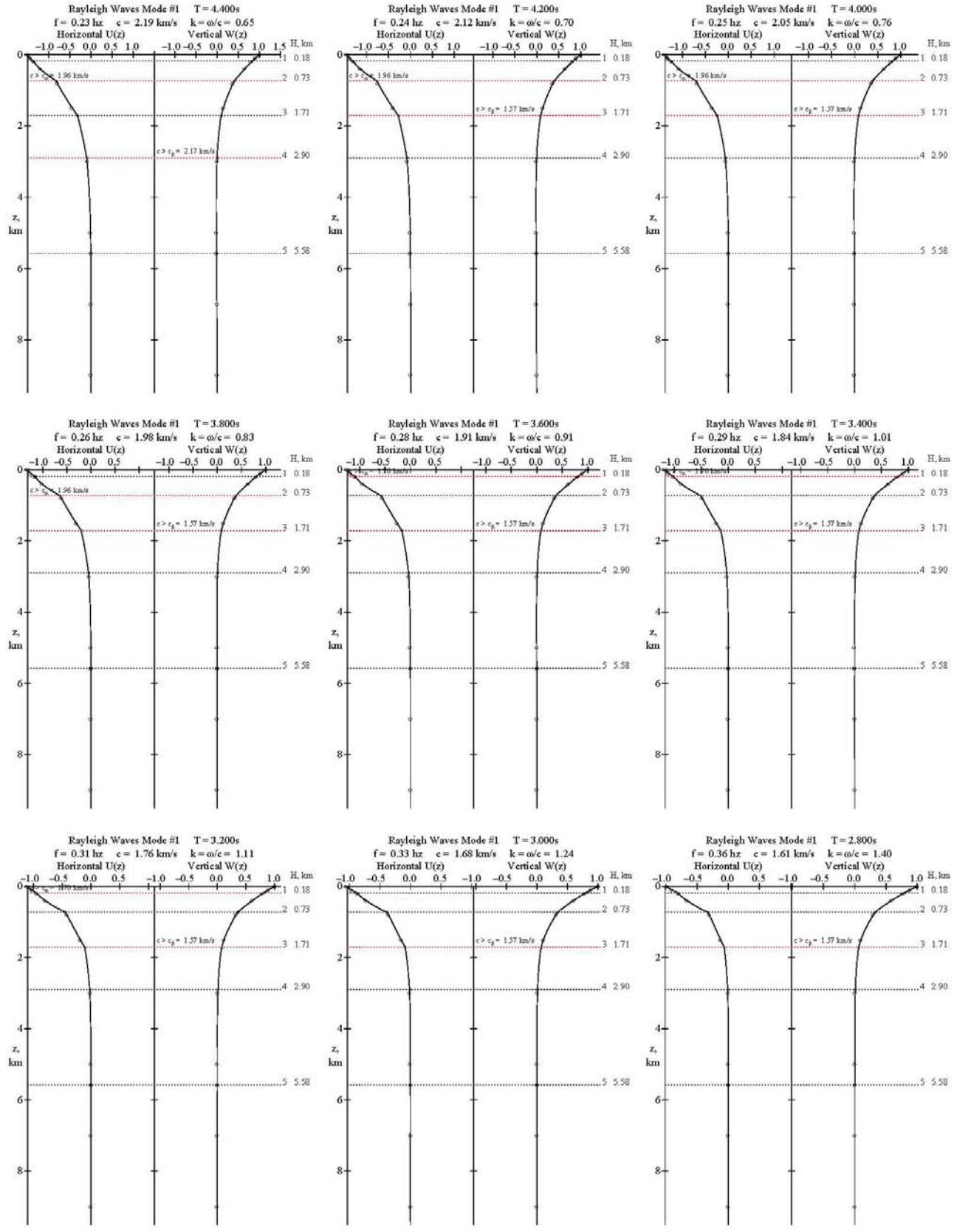

Fig. B-1.4 Rayleigh Wave Mode #1, Page 4 of 11 T=2.6-1.5s

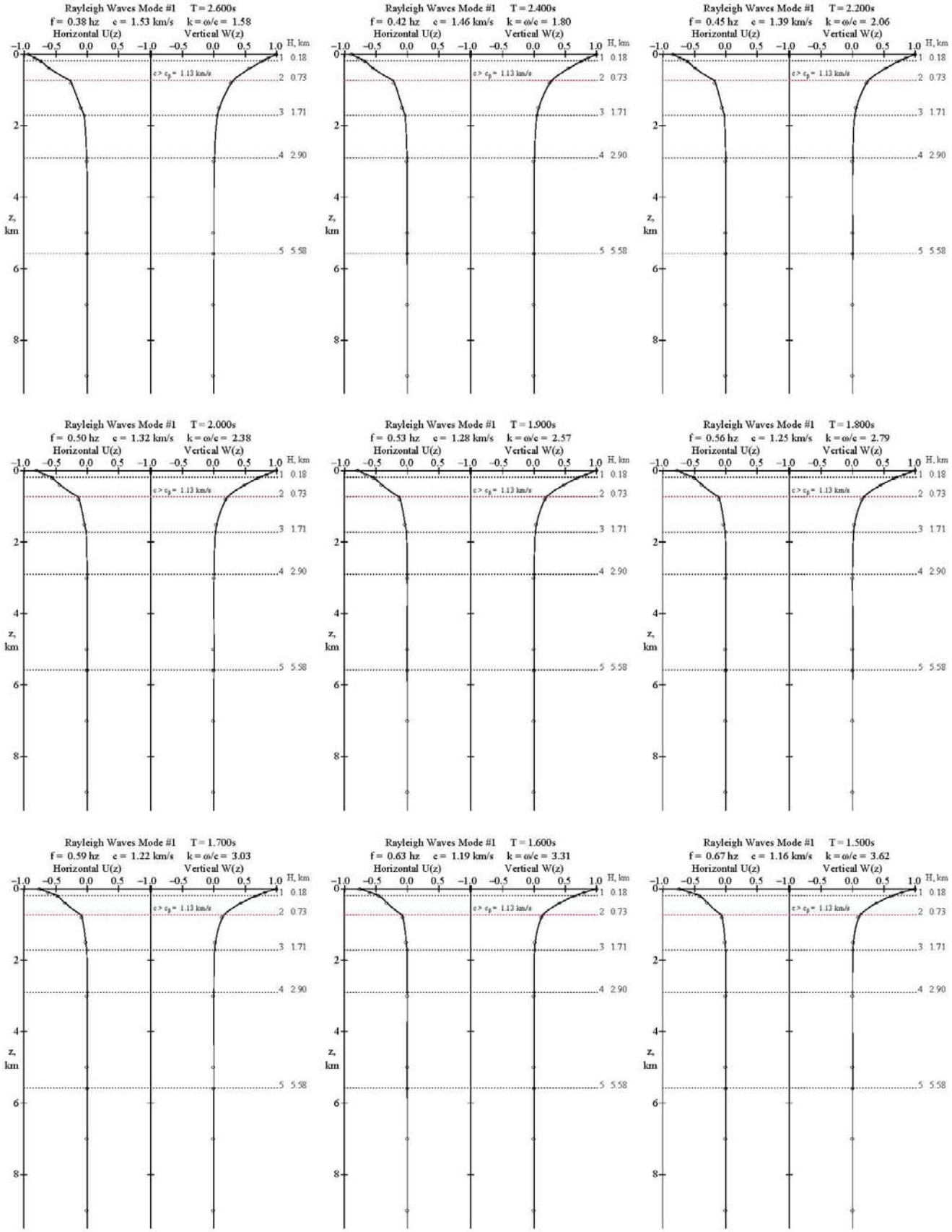

Fig. B-1.5 Rayleigh Wave Mode #1, Page 5 of 11 T=1.4-0.8s

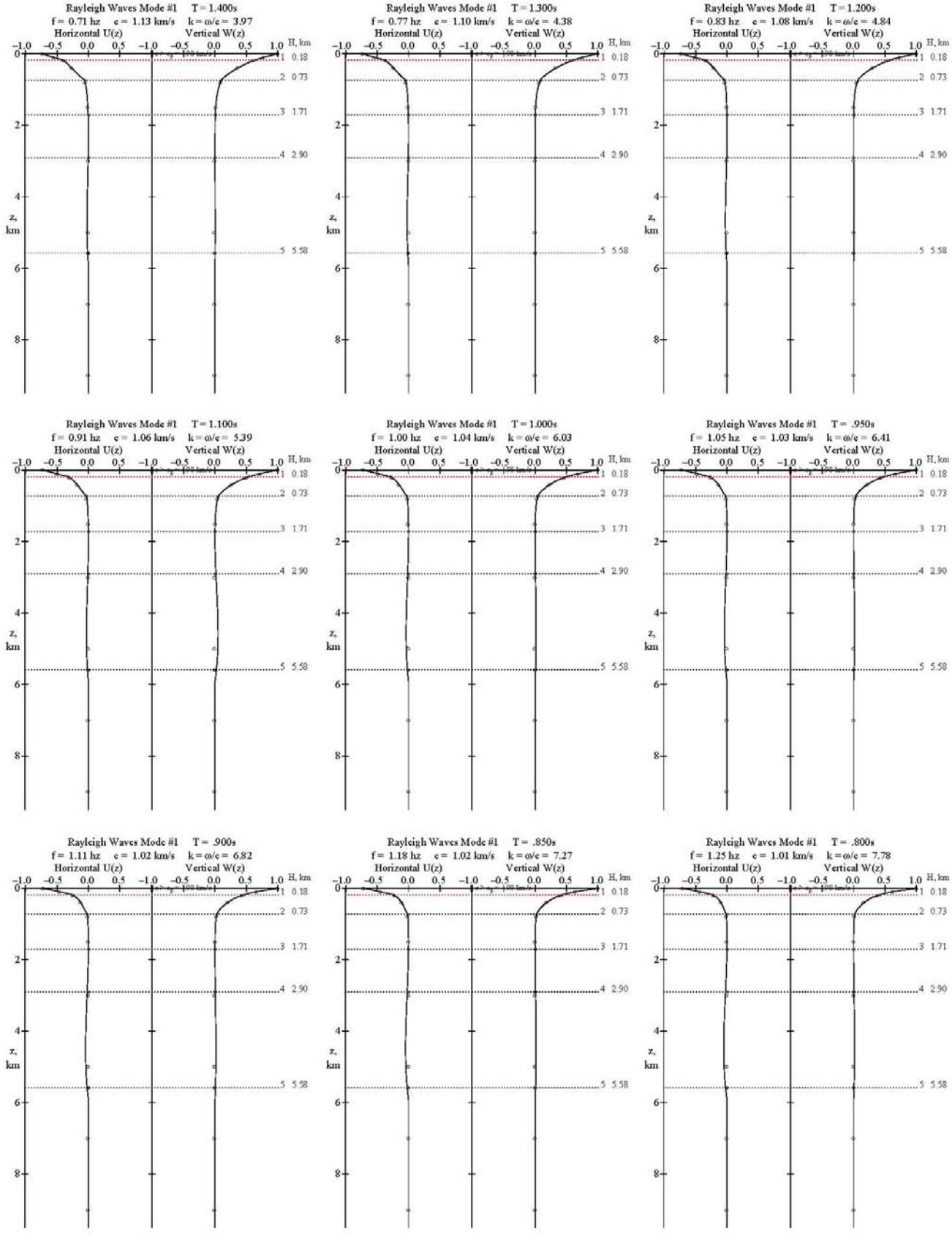

Fig. B-1.6 Rayleigh Wave Mode #1, Page 6 of 11 T=0.75-0.44s

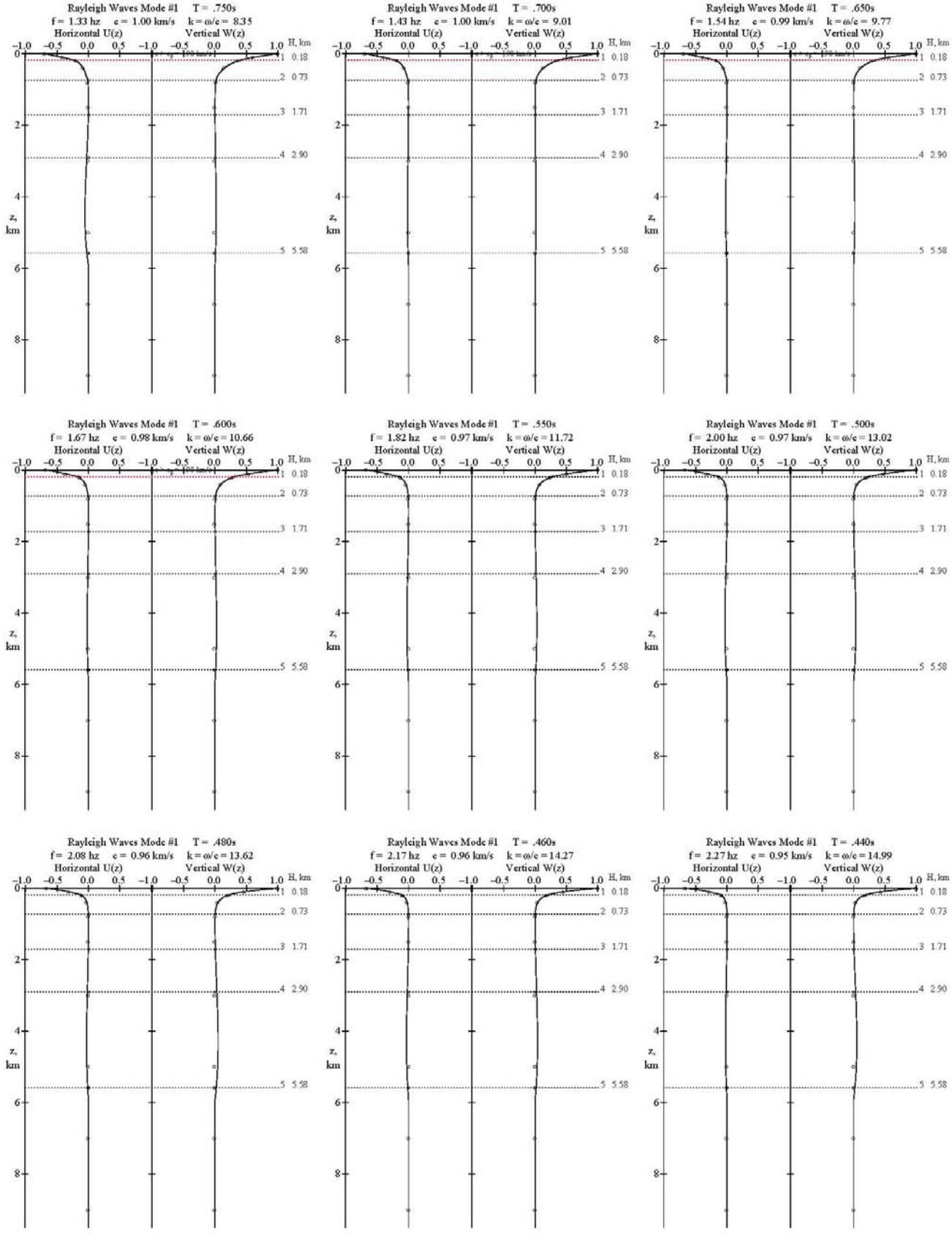

Fig. B-1.7 Rayleigh Wave Mode #1, Page 7 of 11 T=0.42-0.26s

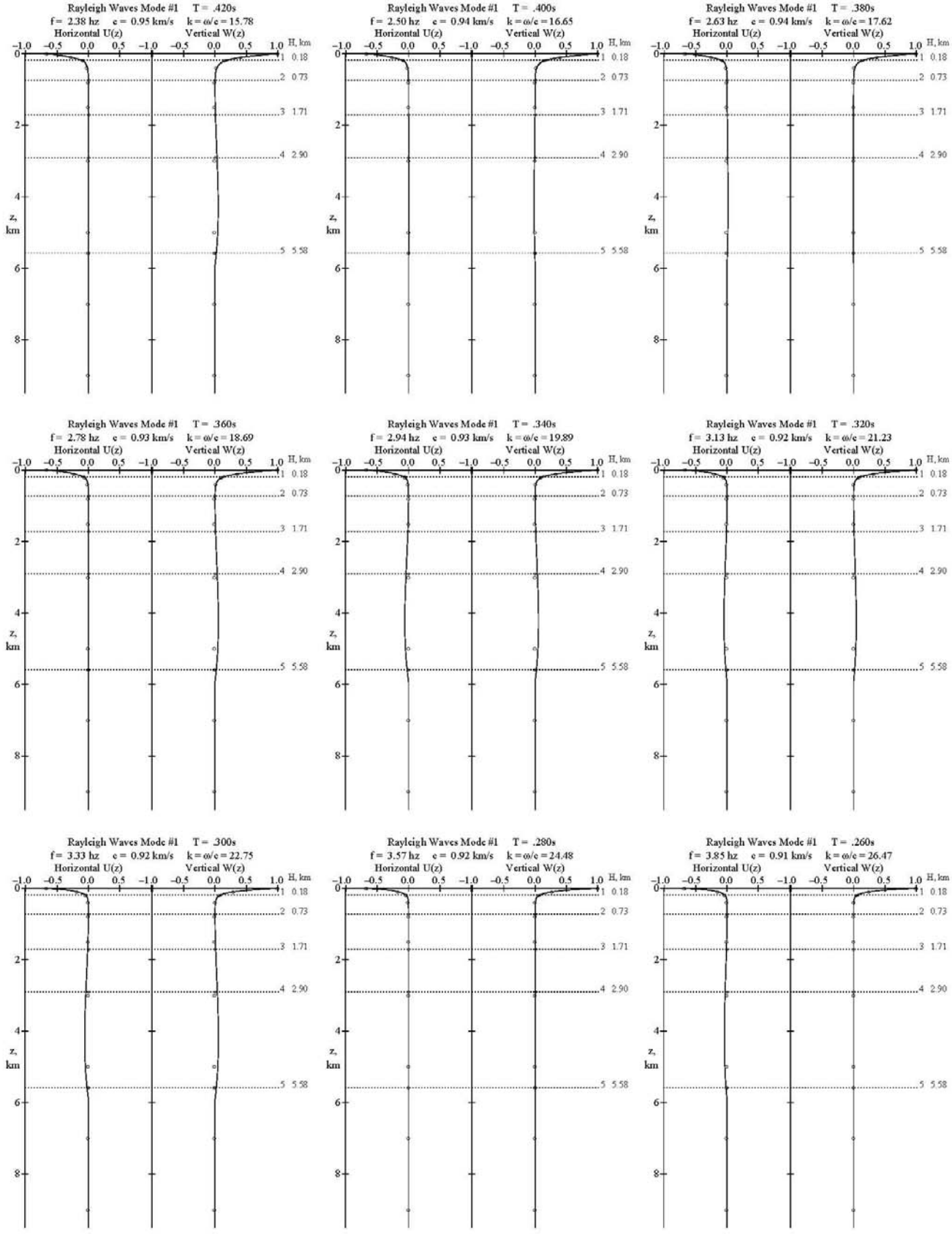

Fig. B-1.8 Rayleigh Wave Mode #1, Page 8 of 11 T=0.24-0.14s

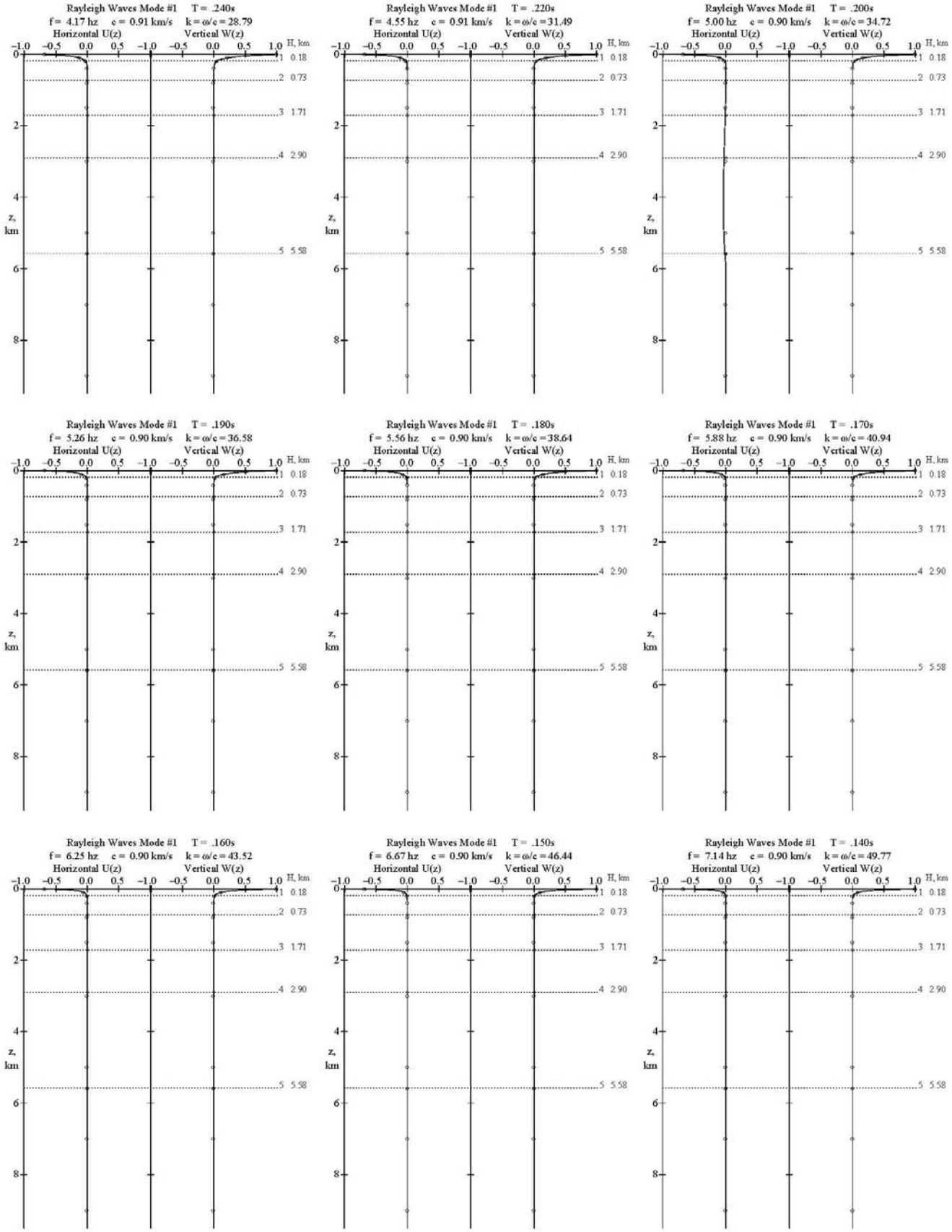

Fig. B-1.9 Rayleigh Wave Mode #1, Page 9 of 11 T=0.130-0.075s

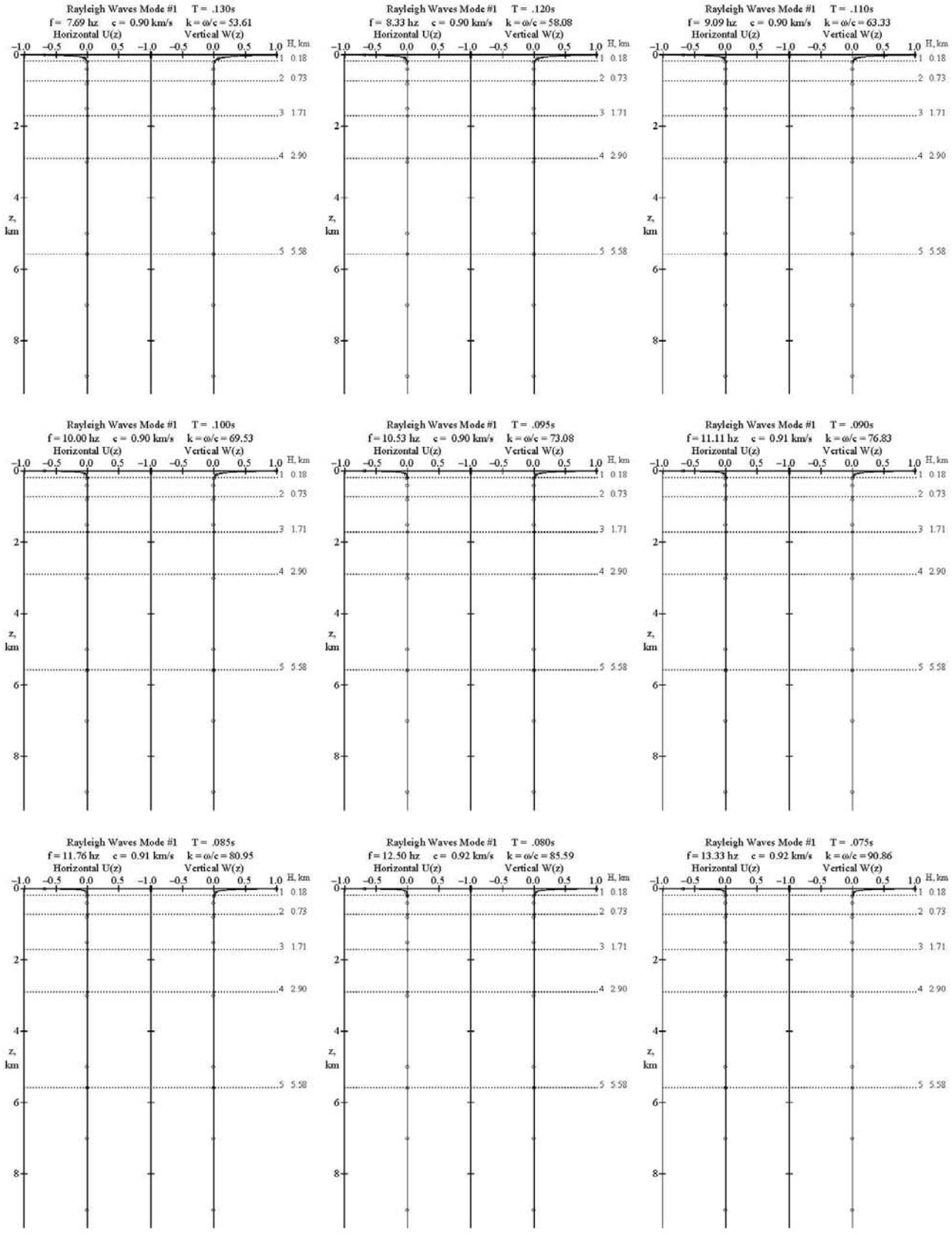

Fig. B-1.10 Rayleigh Wave Mode #1, Page 10 of 11 T=0.070-0.042s

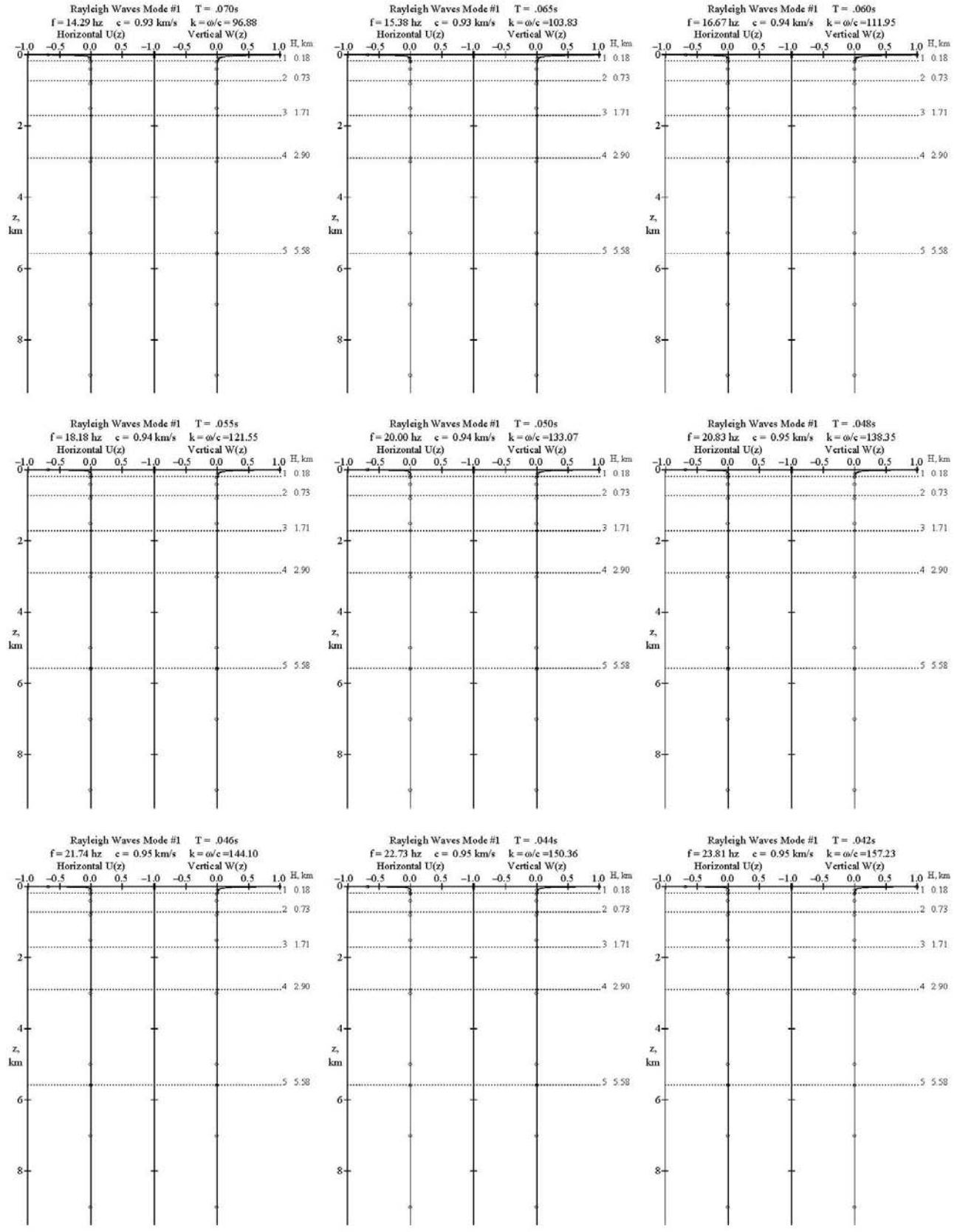

Fig. B-1.11 Rayleigh Wave Mode #1, Page 11 of 11 T=0.040s

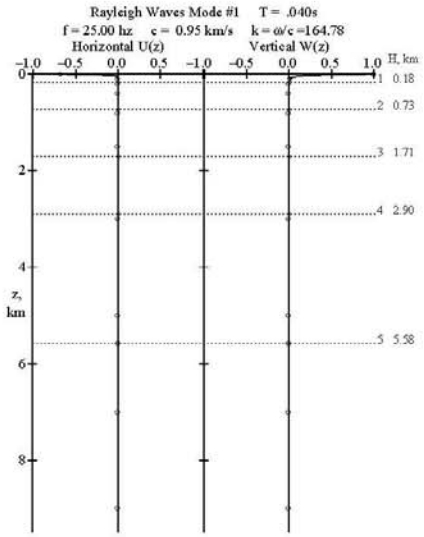

Appendix B-2 – Mode #2 Rayleigh Waves Mode Shapes

Fig. B-2.1 Rayleigh Wave Mode #2, Page 1 of 9 T=4.6-3.0S

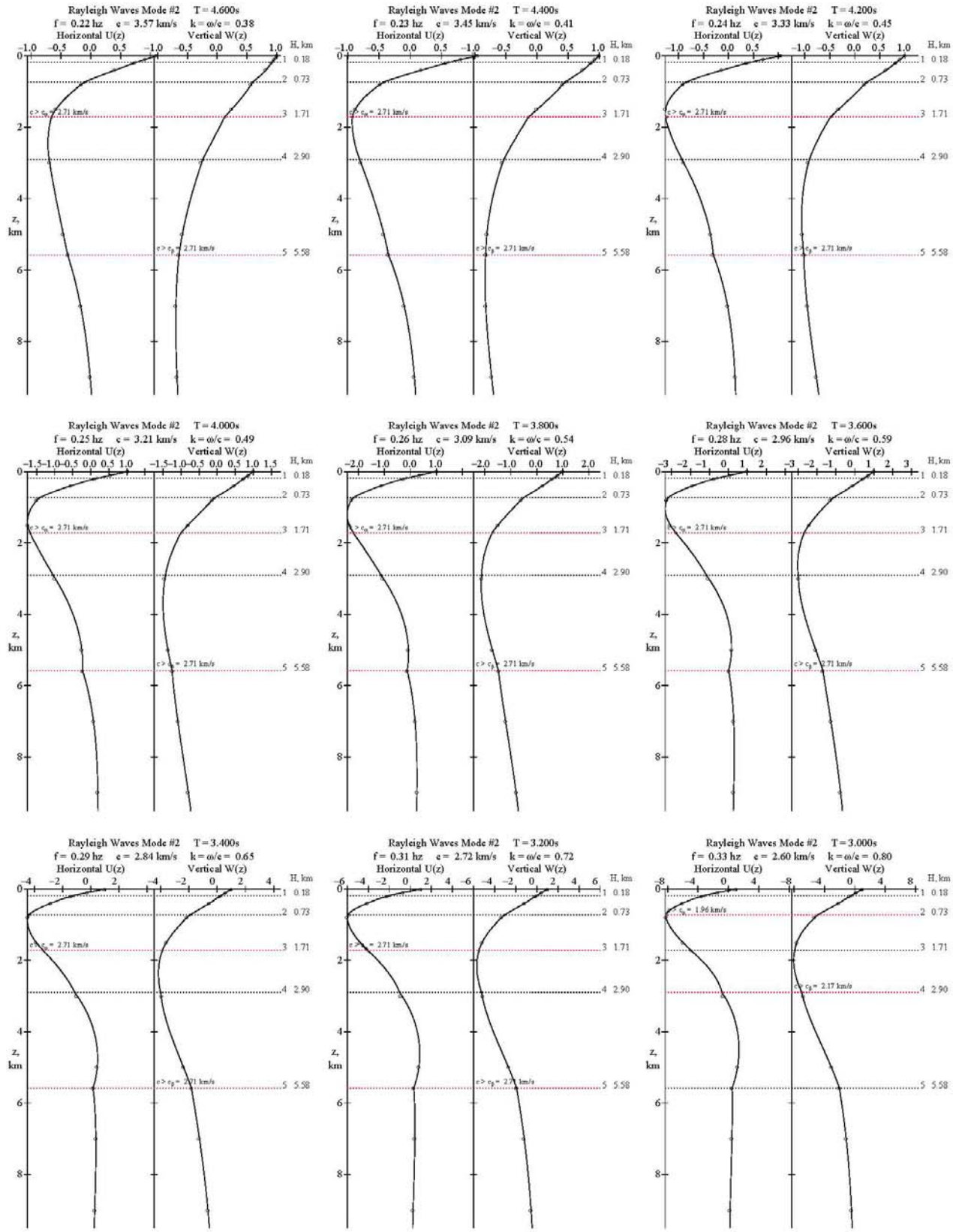

Fig. B-2.2 Rayleigh Wave Mode #2, Page 2 of 9 T=2.8-1.6s

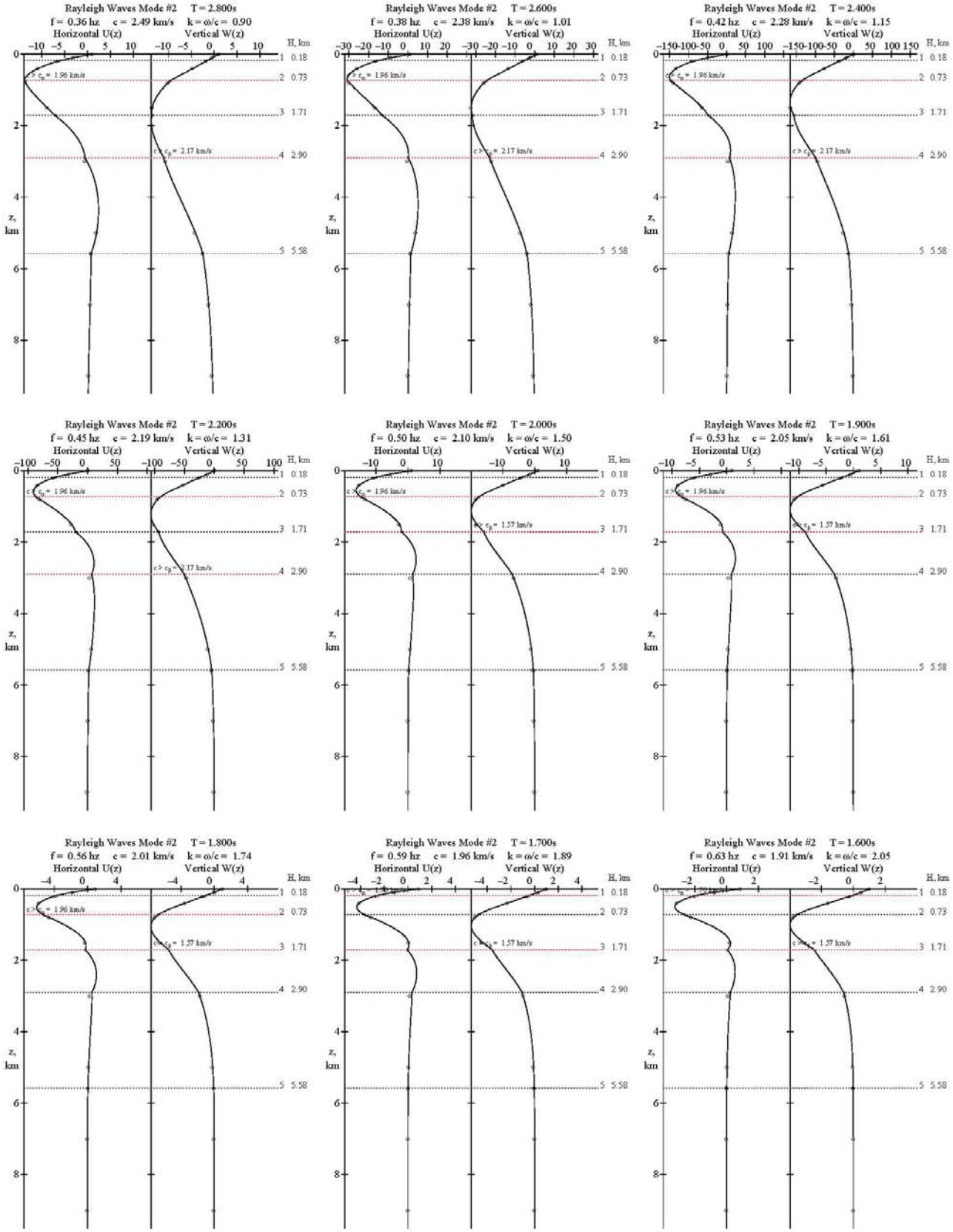

Fig. B-2.3 Rayleigh Wave Mode #2, Page 3 of 9 T=1.5-0.85s

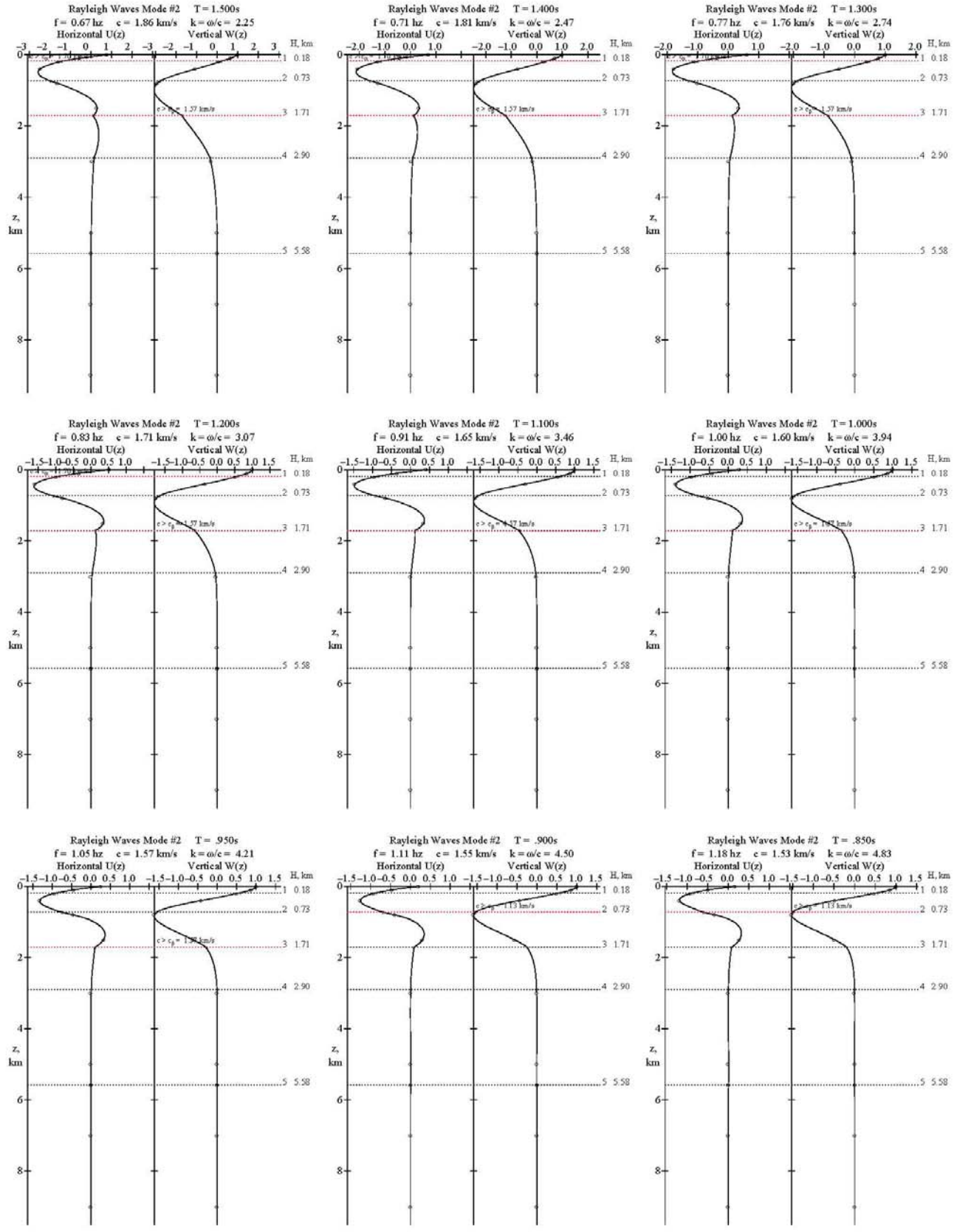

Fig. B-2.4 Rayleigh Wave Mode #2, Page 4 of 9 T=0.80-0.46s

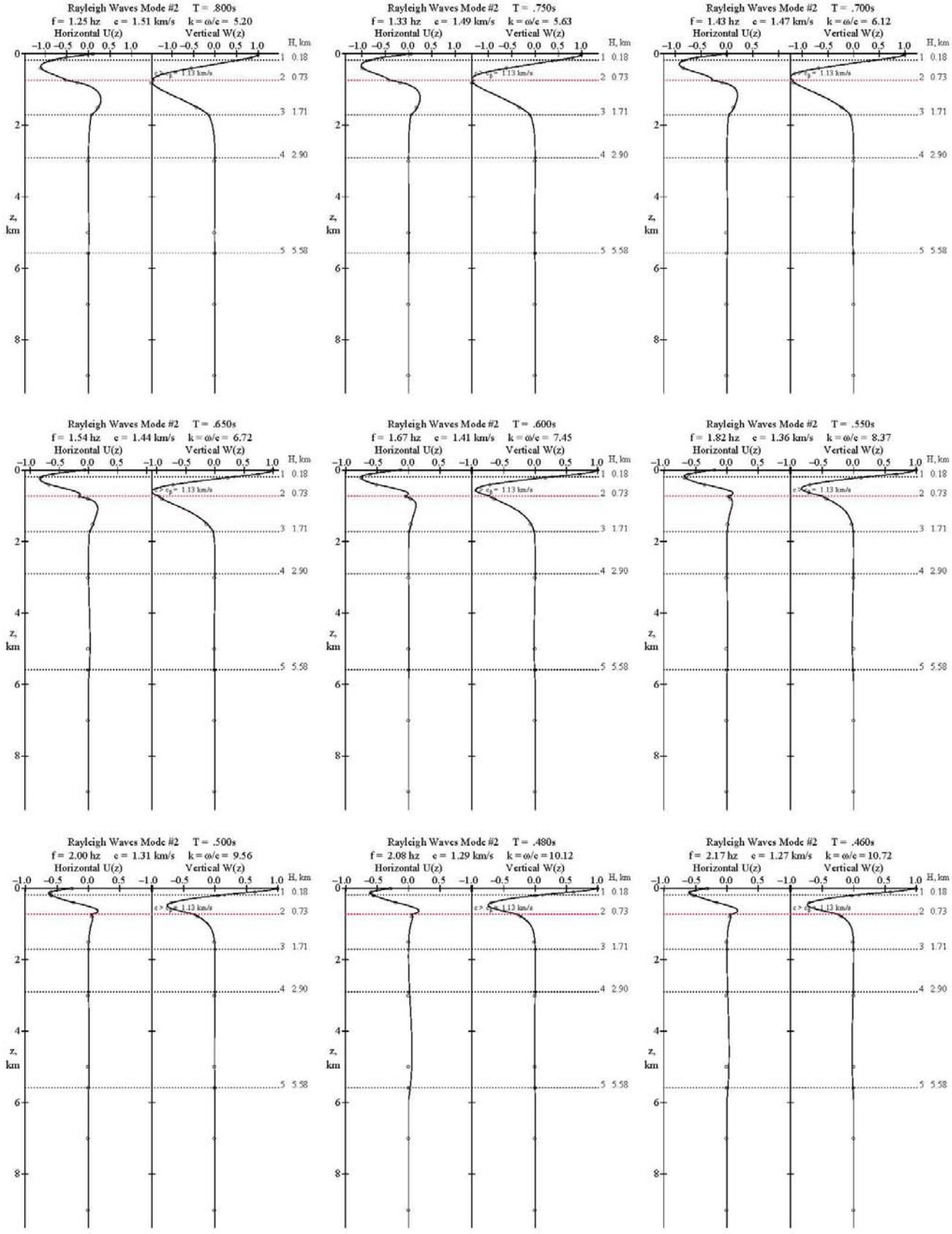

Fig. B-2.5 Rayleigh Wave Mode #2, Page 5 of 9 T=0.44-0.28s

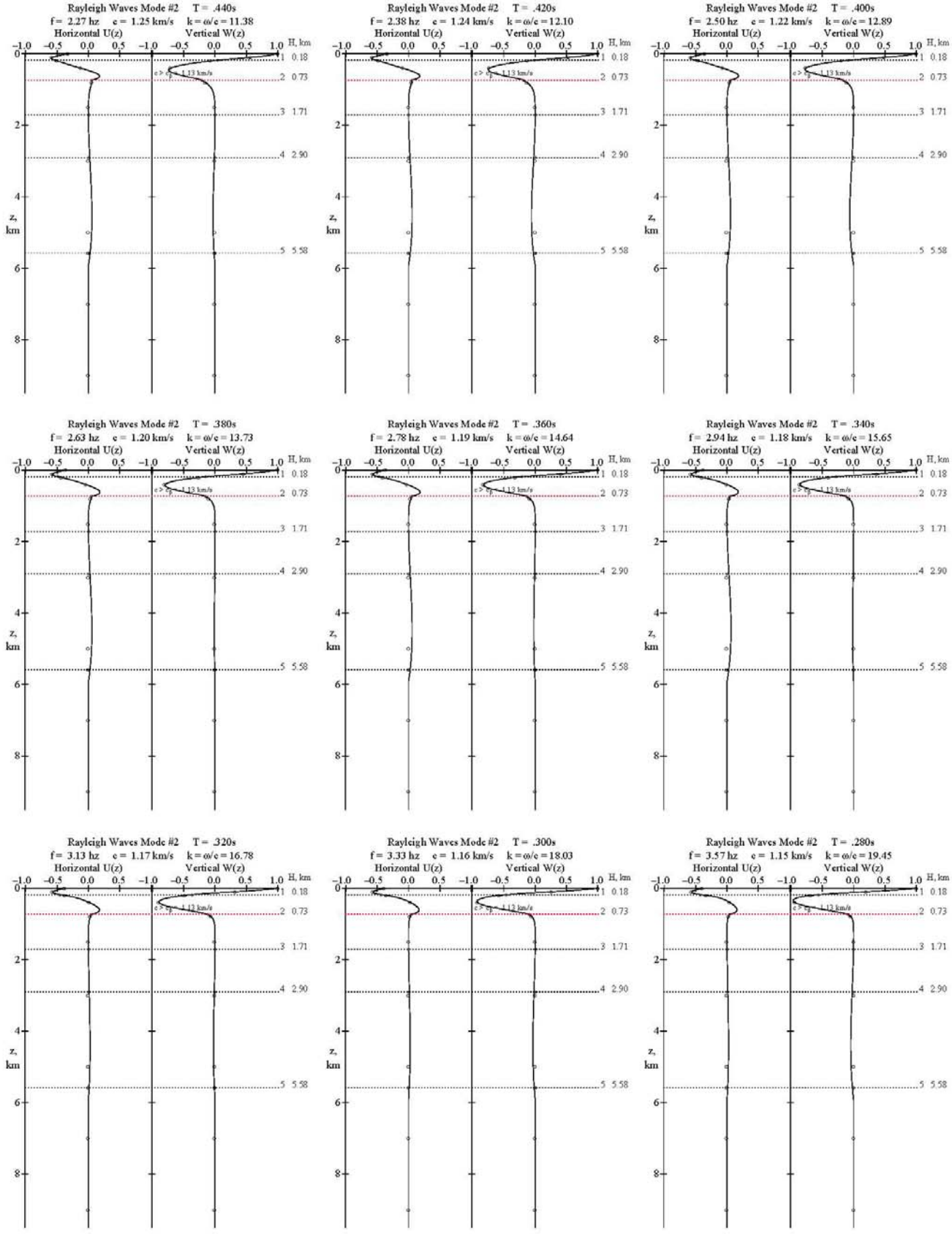

Fig. B-2.6 Rayleigh Wave Mode #2, Page 6 of 9 T=0.26-0.15s

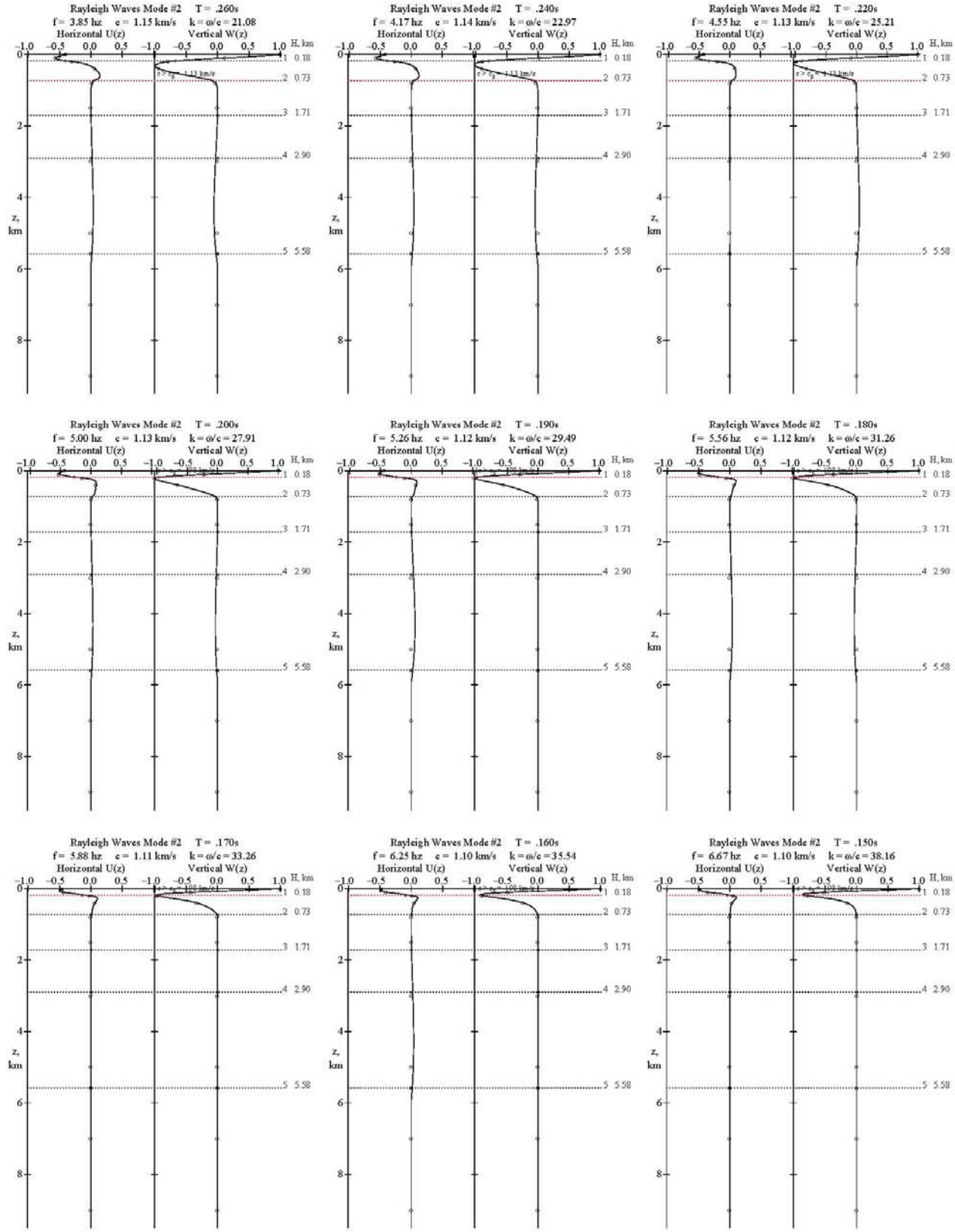

Fig. B-2.7 Rayleigh Wave Mode #2, Page 7 of 9 T=0.140-0.080s

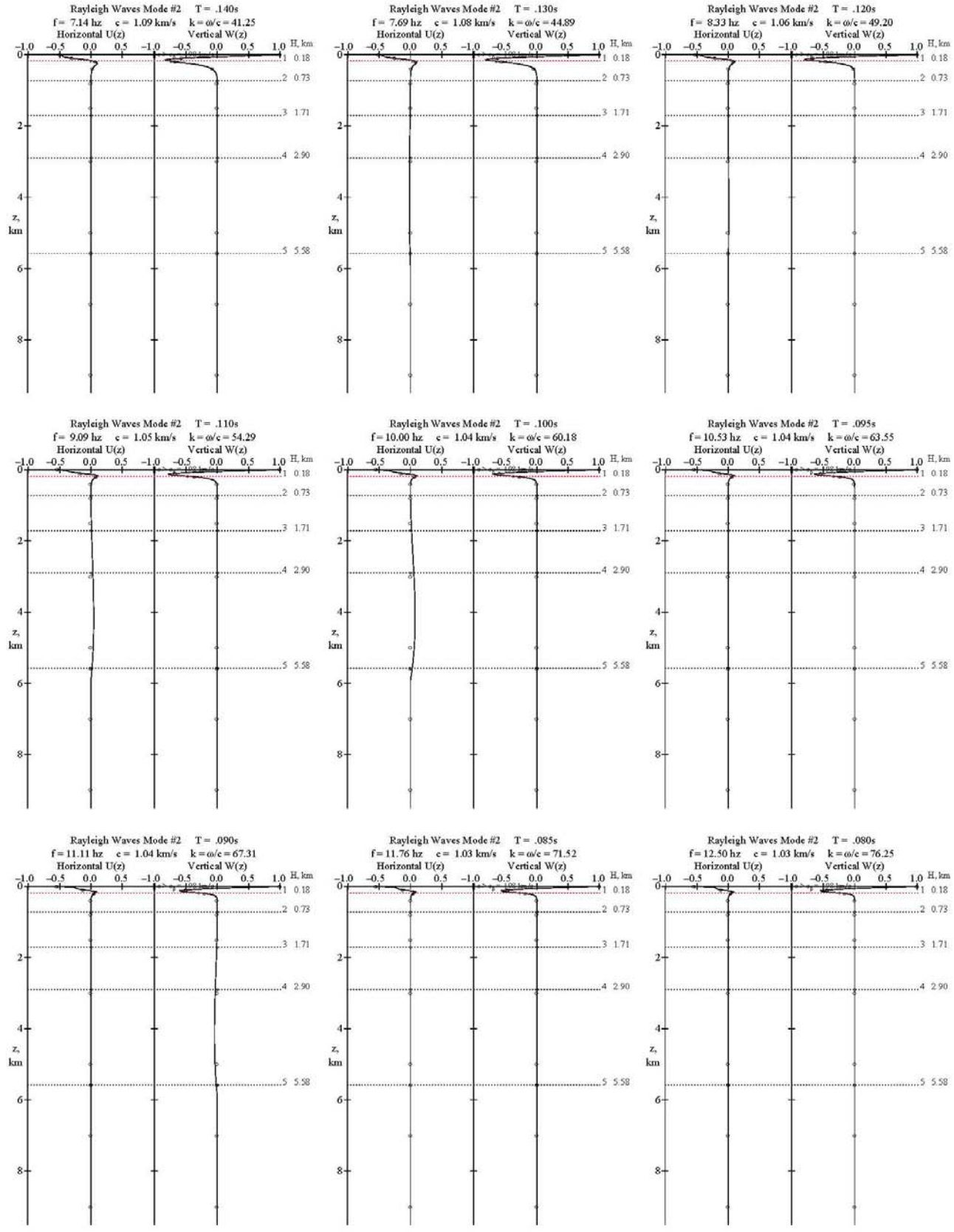

Fig. B-2.8 Rayleigh Wave Mode #2, Page 8 of 9 T=0.075-0.044s

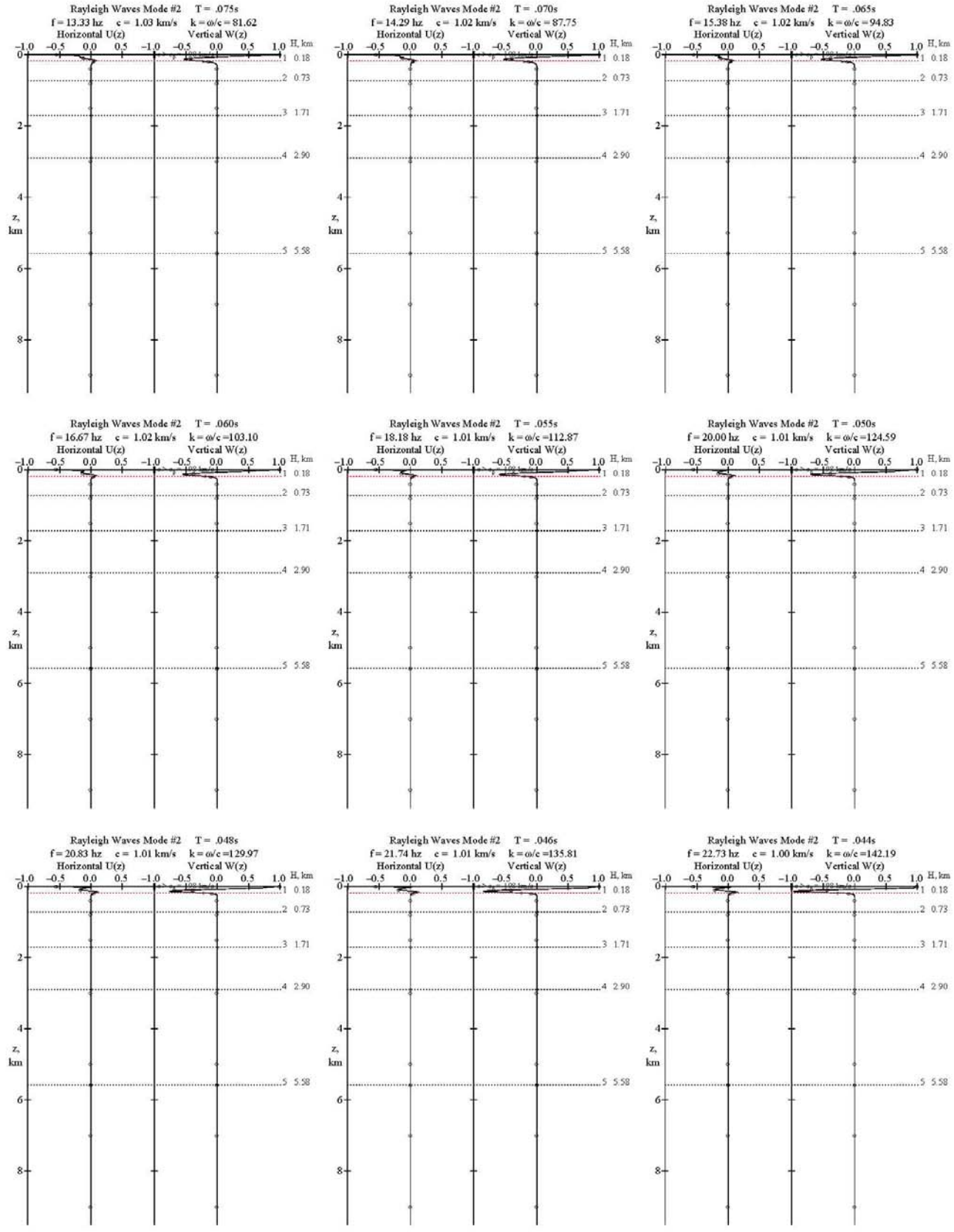

Fig. B-2.9 Rayleigh Wave Mode #2, Page 9 of 9 T=0.042-0.040s

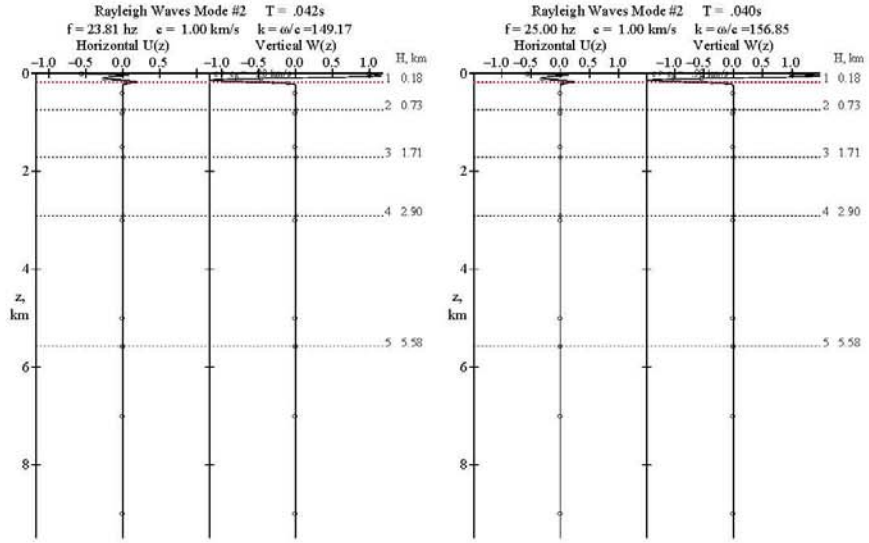

Appendix B-3 – Mode #3 Rayleigh Waves Mode Shapes

Fig. B-3.1 Rayleigh Wave Mode #3, Page 1 of 8 T=3.8-2.2s

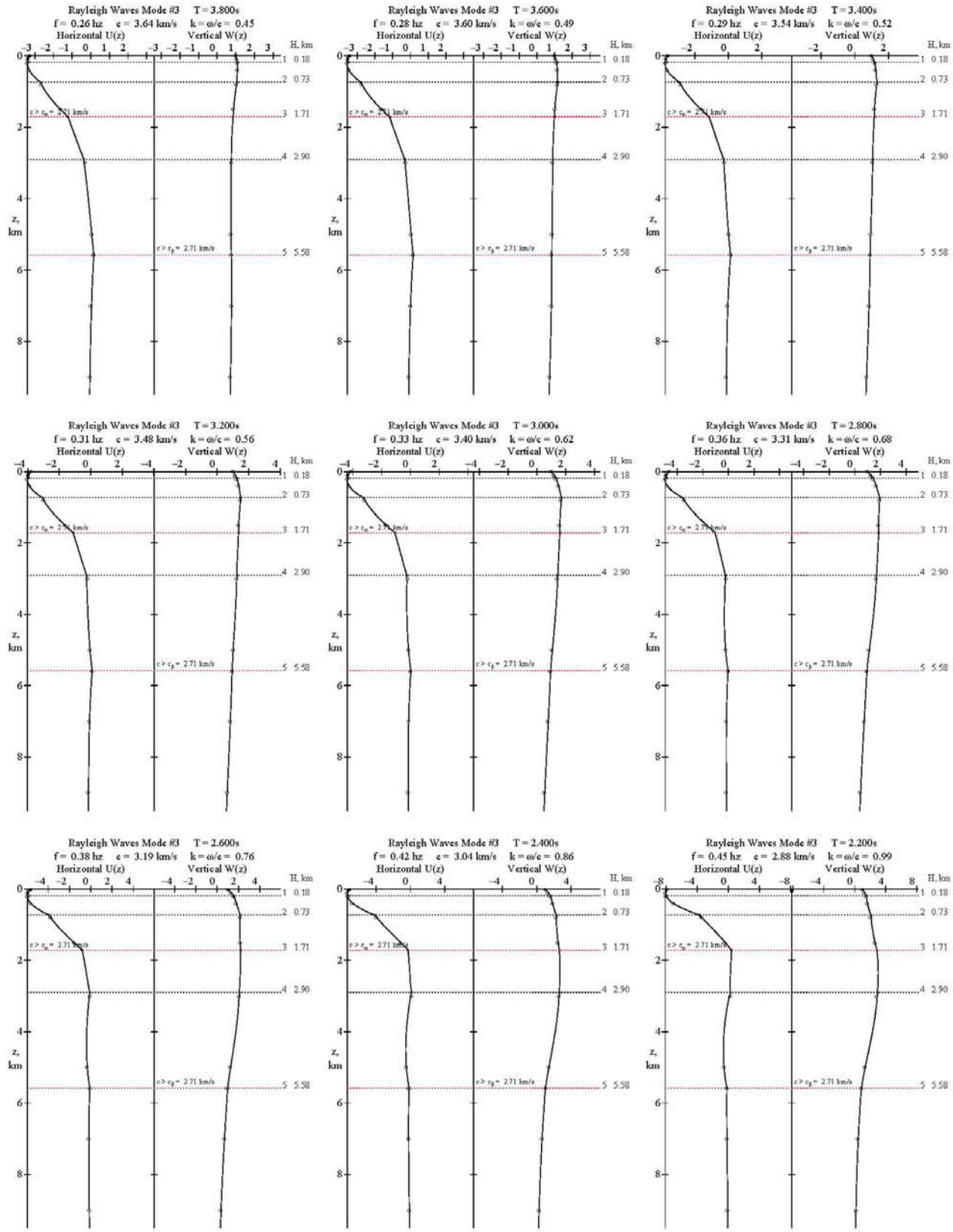

Fig. B-3.2 Rayleigh Wave Mode #3, Page 2 of 8 T=2.0-1.2s

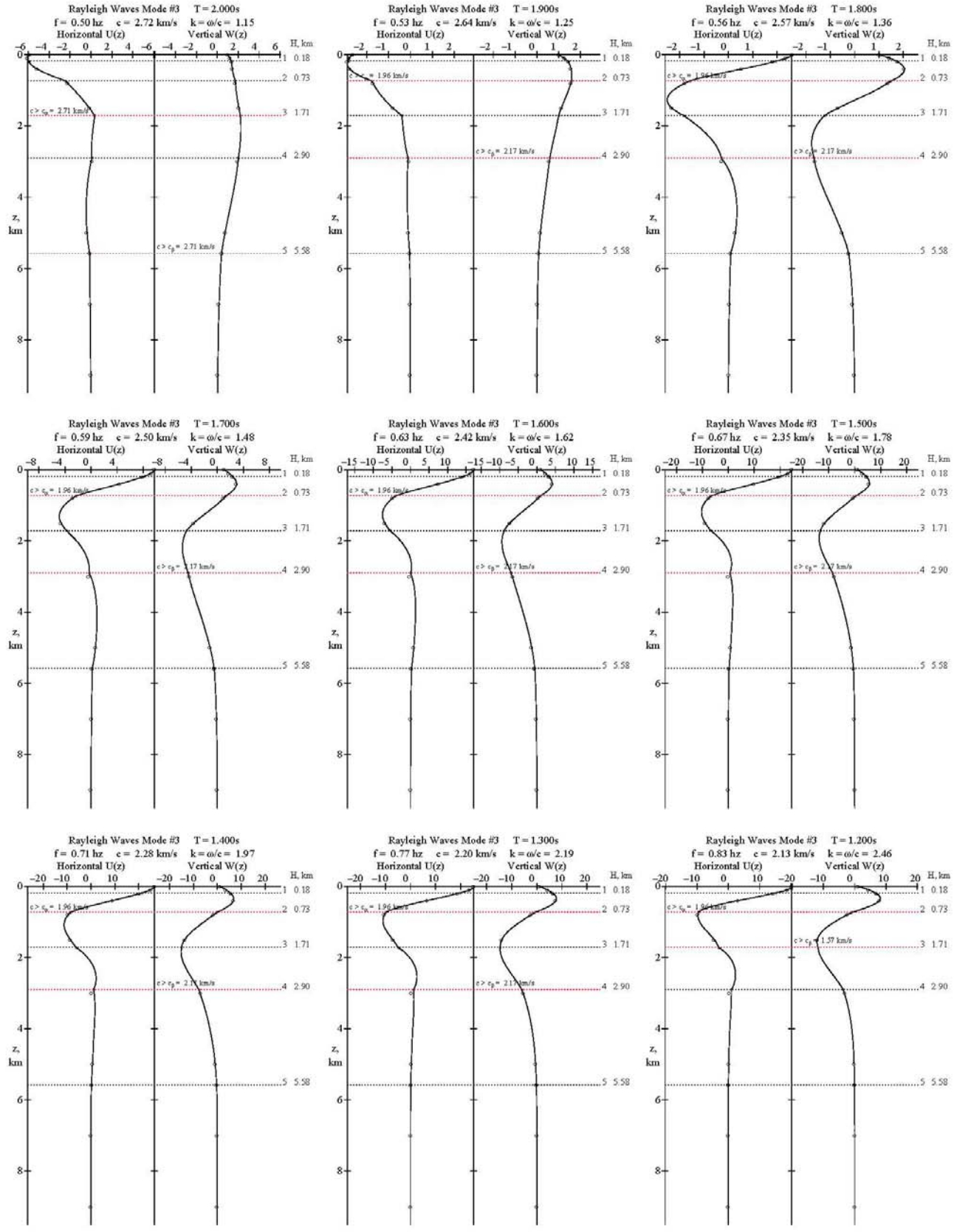

Fig. B-3.3 Rayleigh Wave Mode #3, Page 3 of 8 T=1.1-0.65s

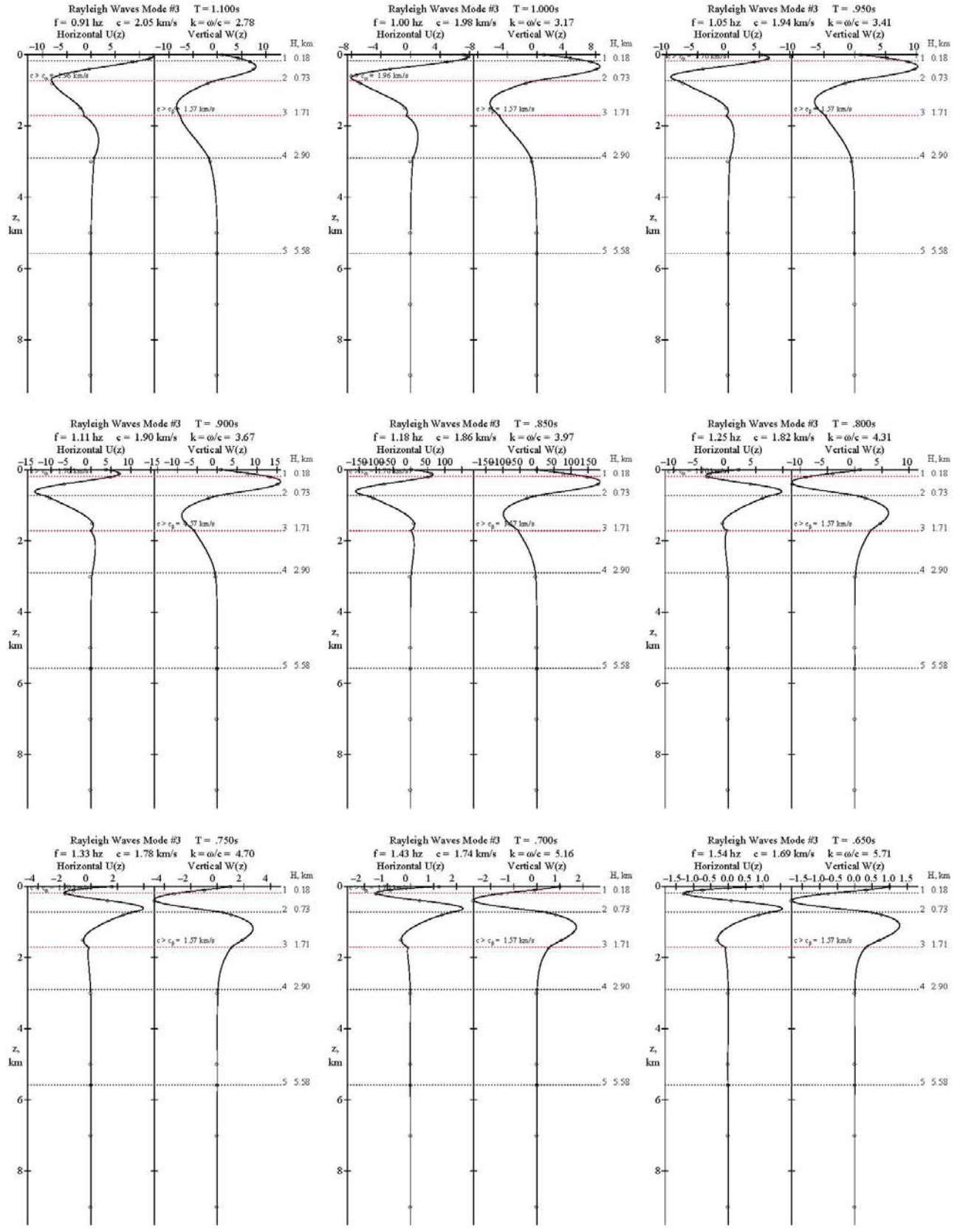

Fig. B-3.4 Rayleigh Wave Mode #3, Page 4 of 8 T=0.60-0.38s

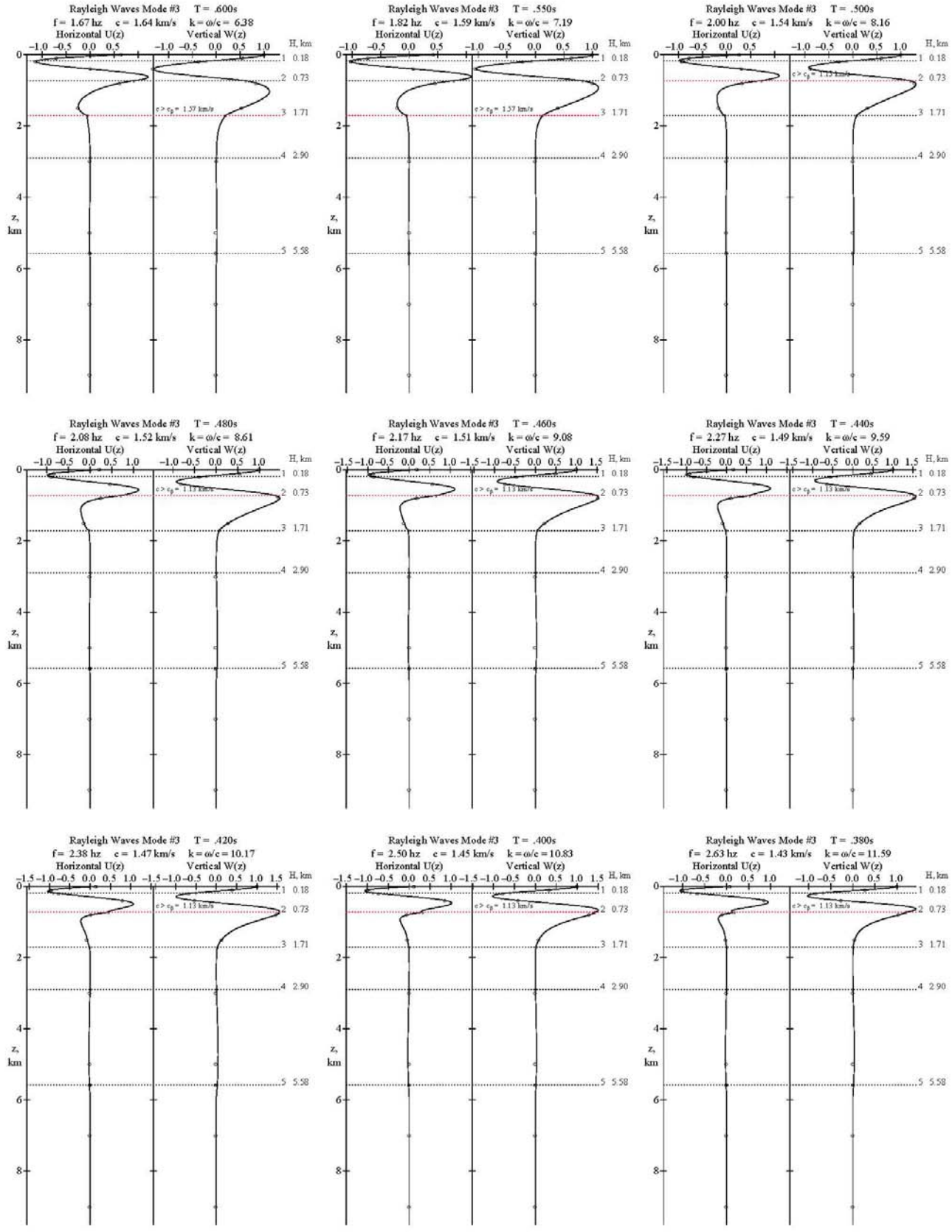

Fig. B-3.5 Rayleigh Wave Mode #3, Page 5 of 8 T=0.36-0.20s

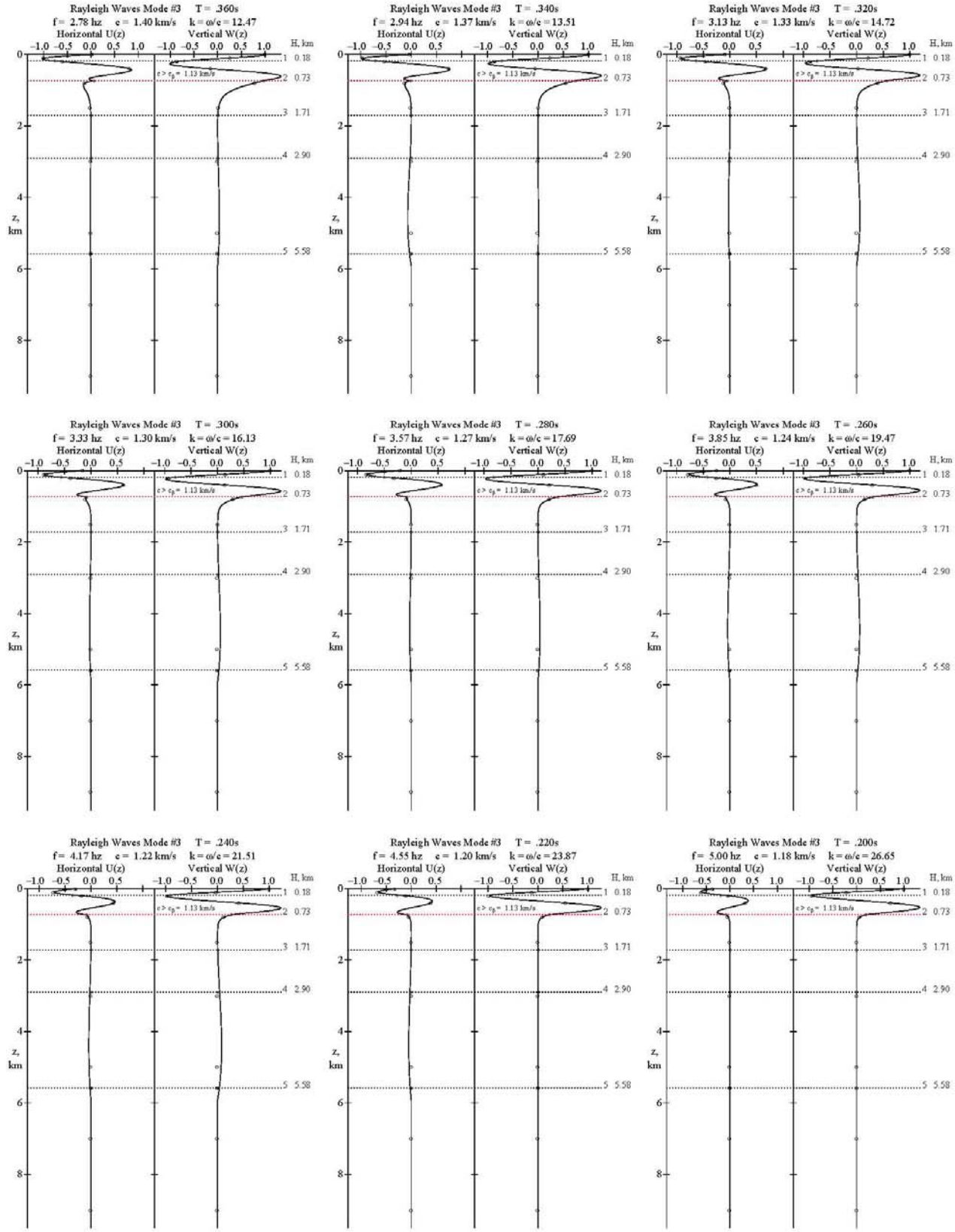

Fig. B-3.6 Rayleigh Wave Mode #3, Page 6 of 8 T=0.19-0.11s

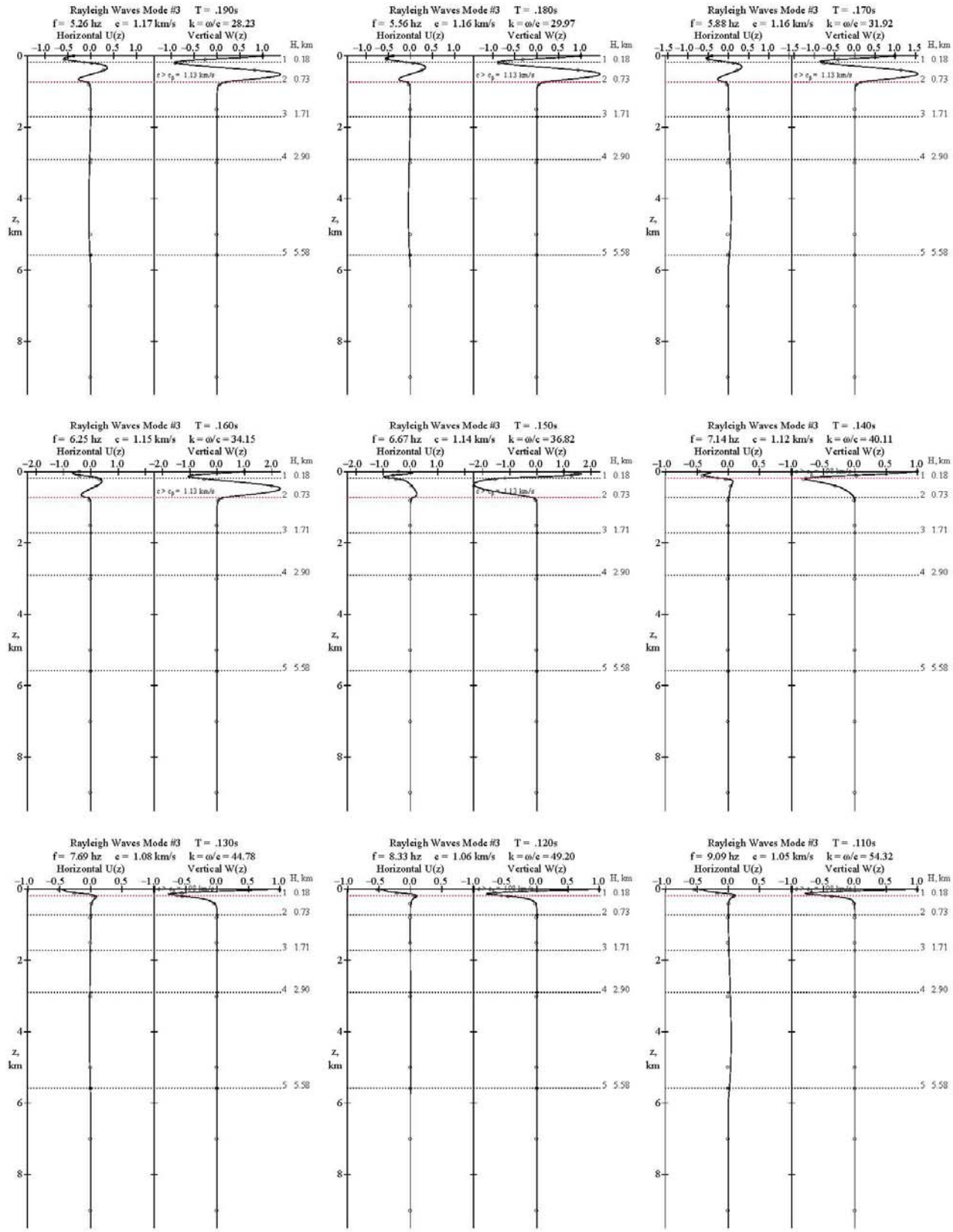

Fig. B-3.7 Rayleigh Wave Mode #3, Page 7 of 8 T=0.10-0.06s

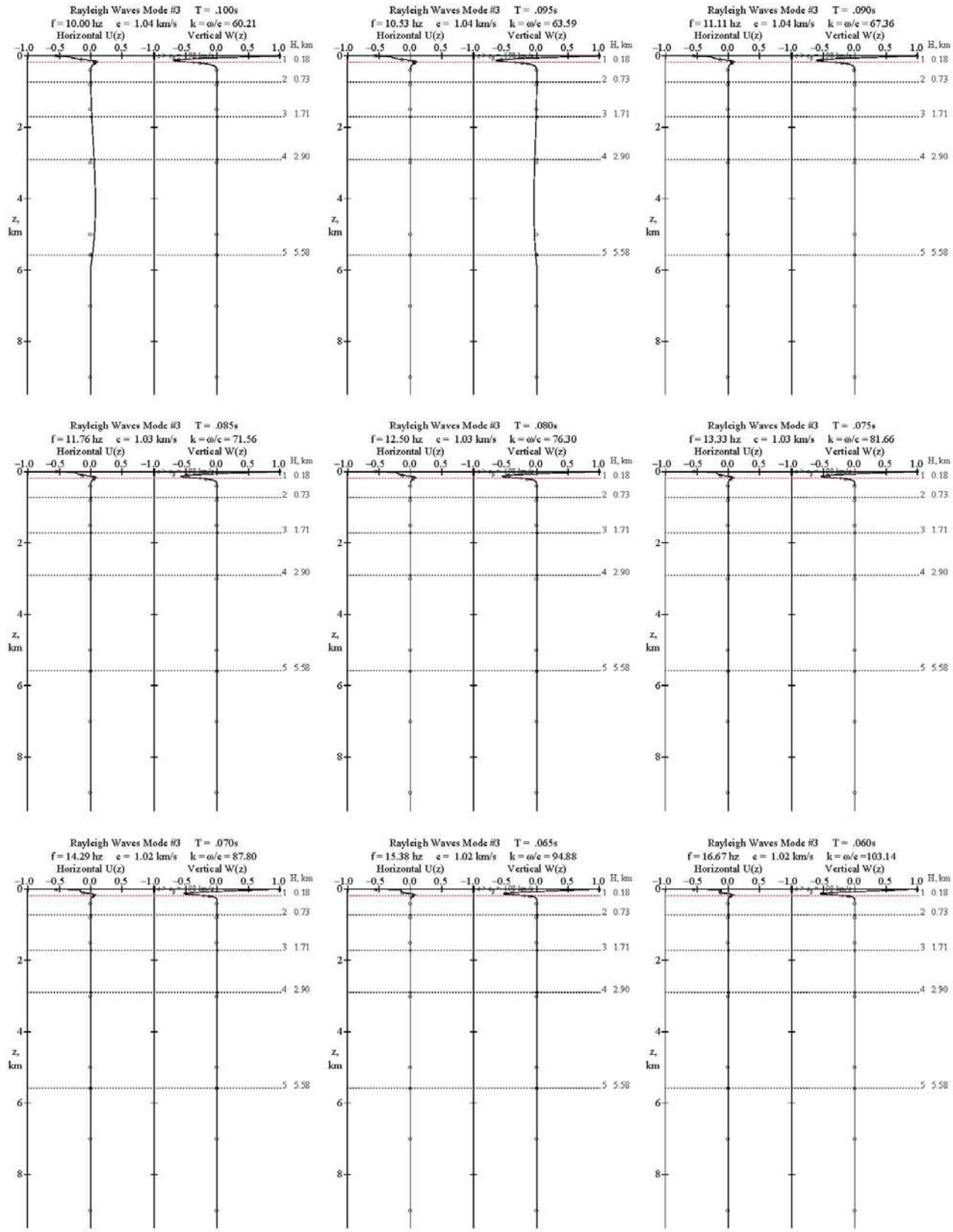

Fig. B-3.8 Rayleigh Wave Mode #3, Page 8 of 8 T=0.055-0.040s

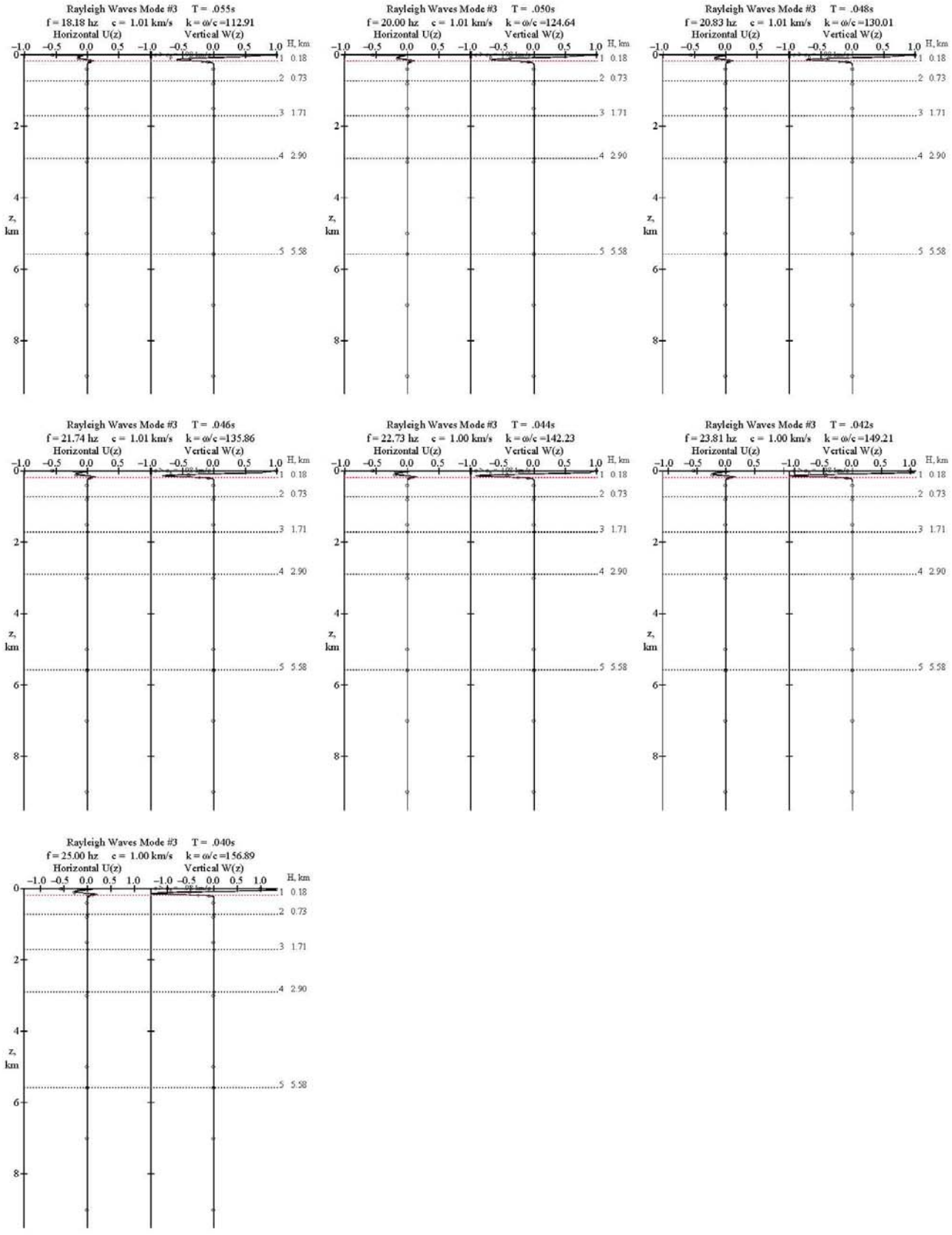

Appendix B-4 – Mode #4 Rayleigh Waves Mode Shapes

Fig. B-4.1 Rayleigh Wave Mode #4, Page 1 of 7 T=2.0-1.2s

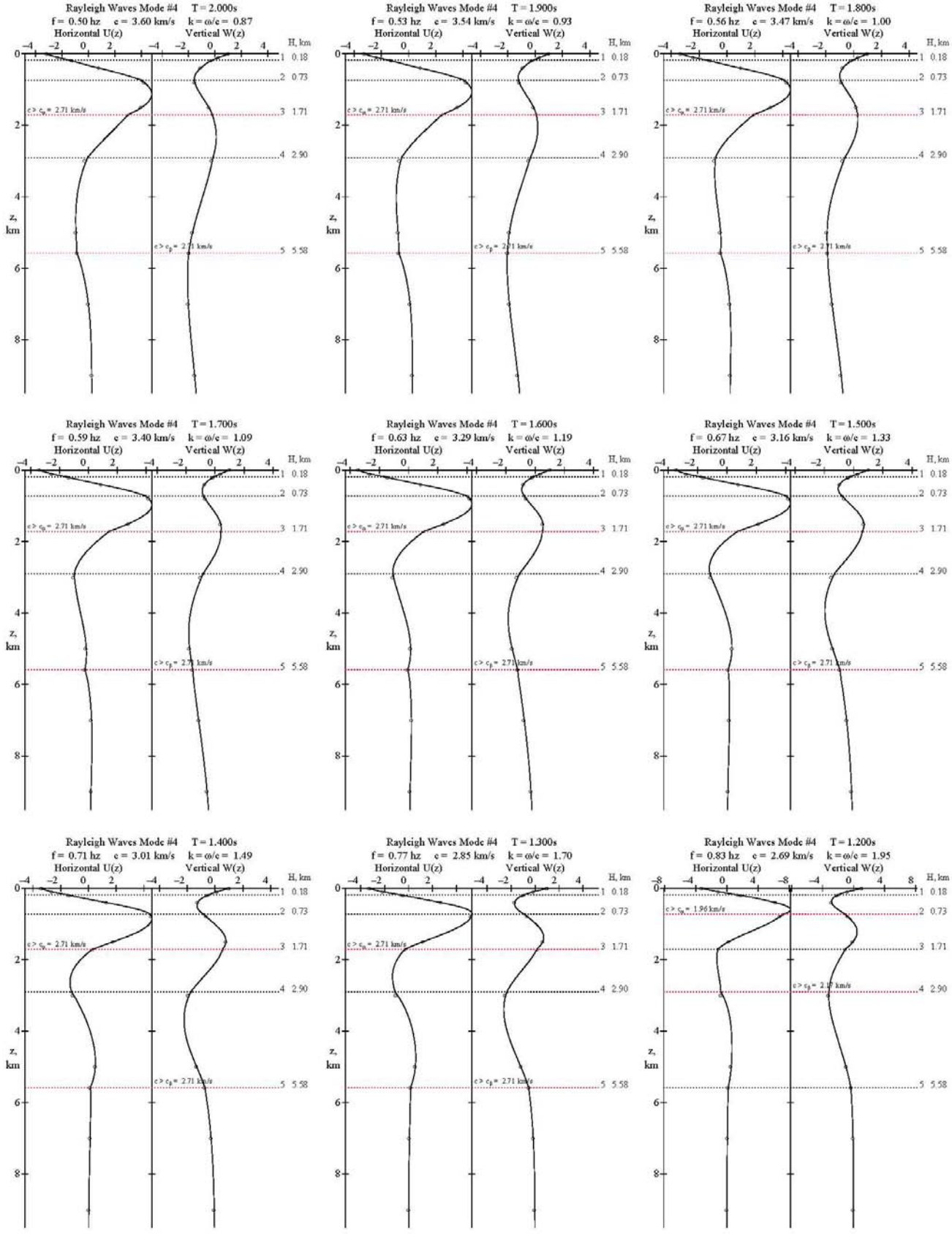

Fig. B-4.2 Rayleigh Wave Mode #4, Page 2 of 7 T=1.1-0.65s

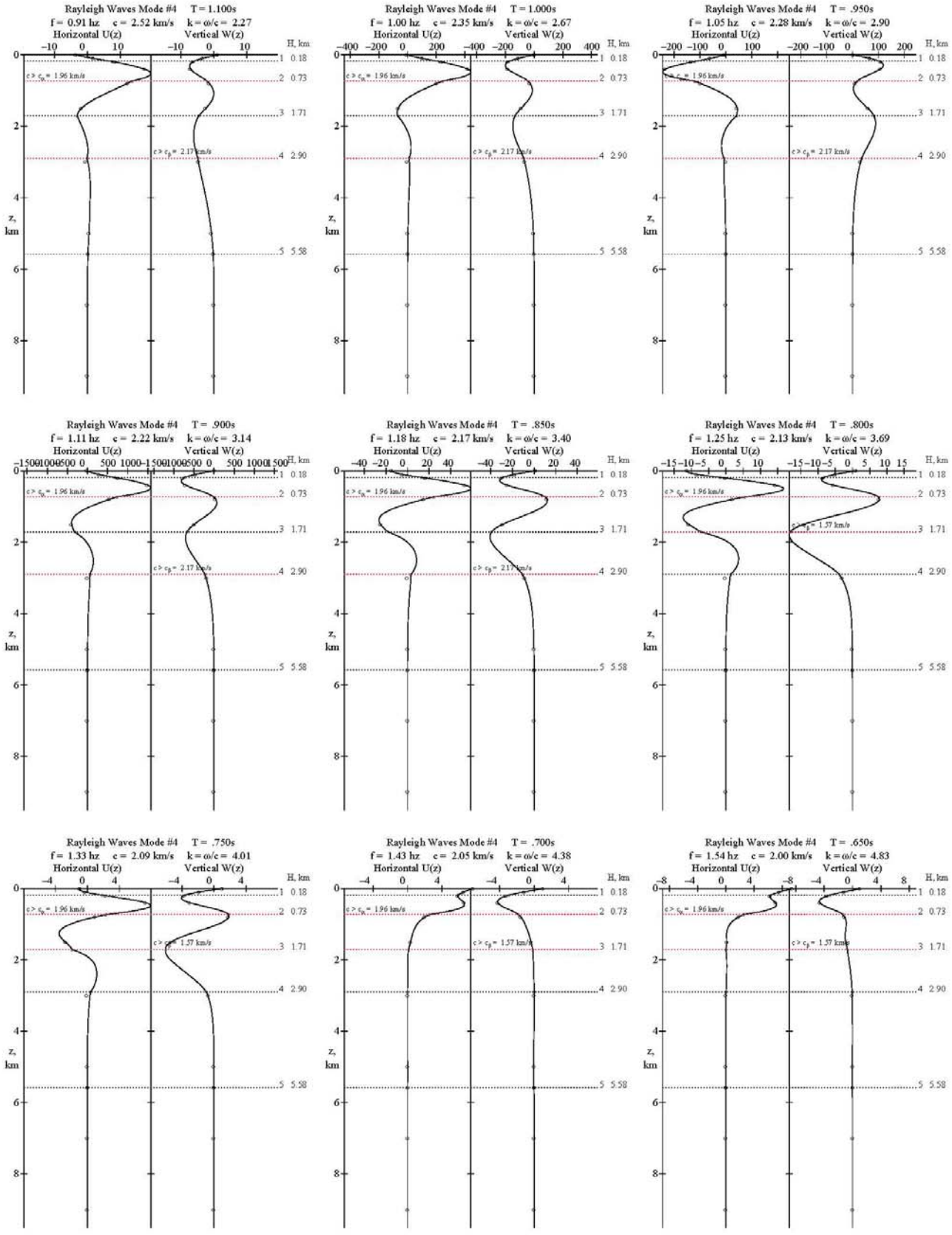

Fig. B-4.3 Rayleigh Wave Mode #4, Page 3 of 7 T=0.60-0.38s

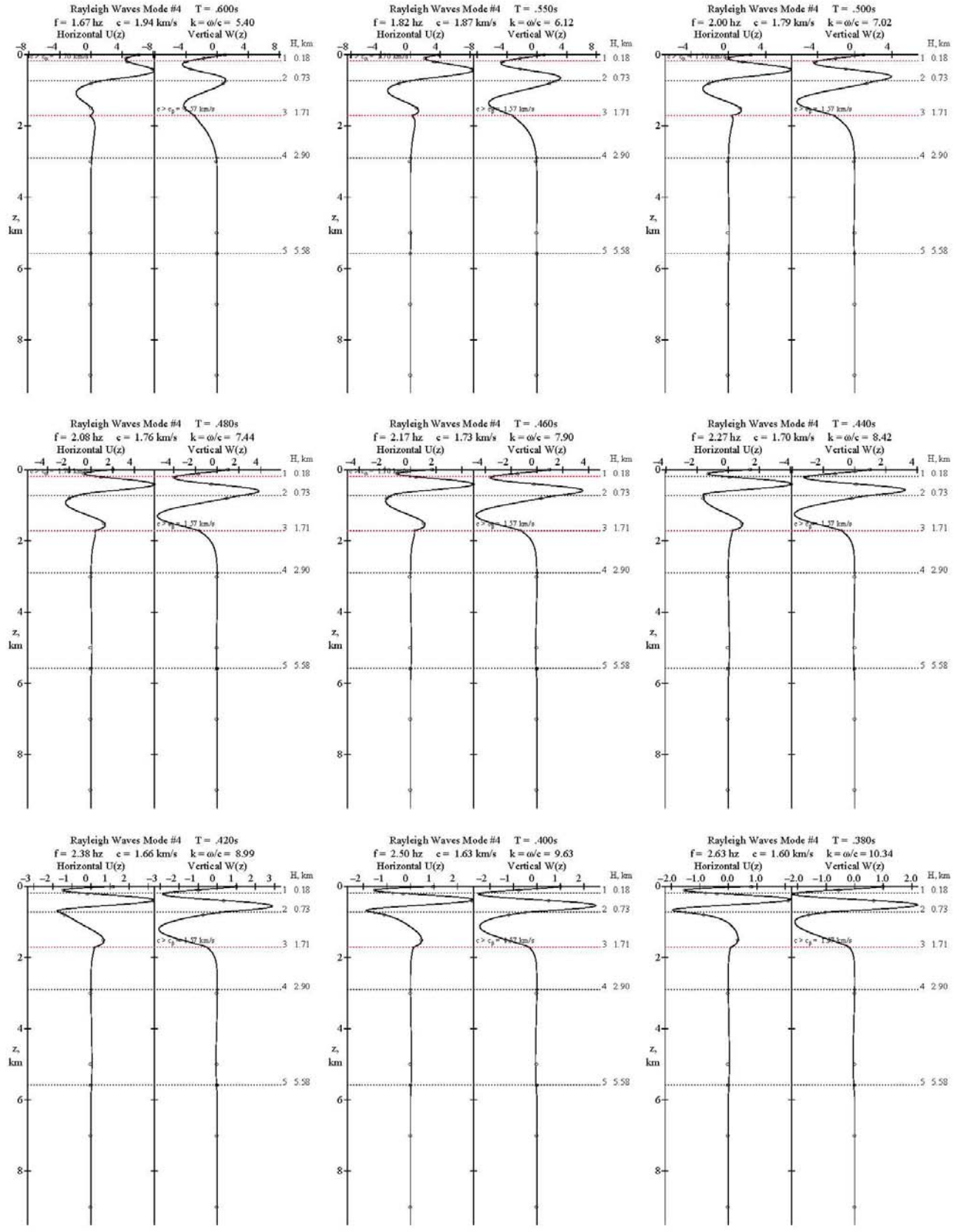

Fig. B-4.4 Rayleigh Wave Mode #4, Page 4 of 7 T=0.36-0.20s

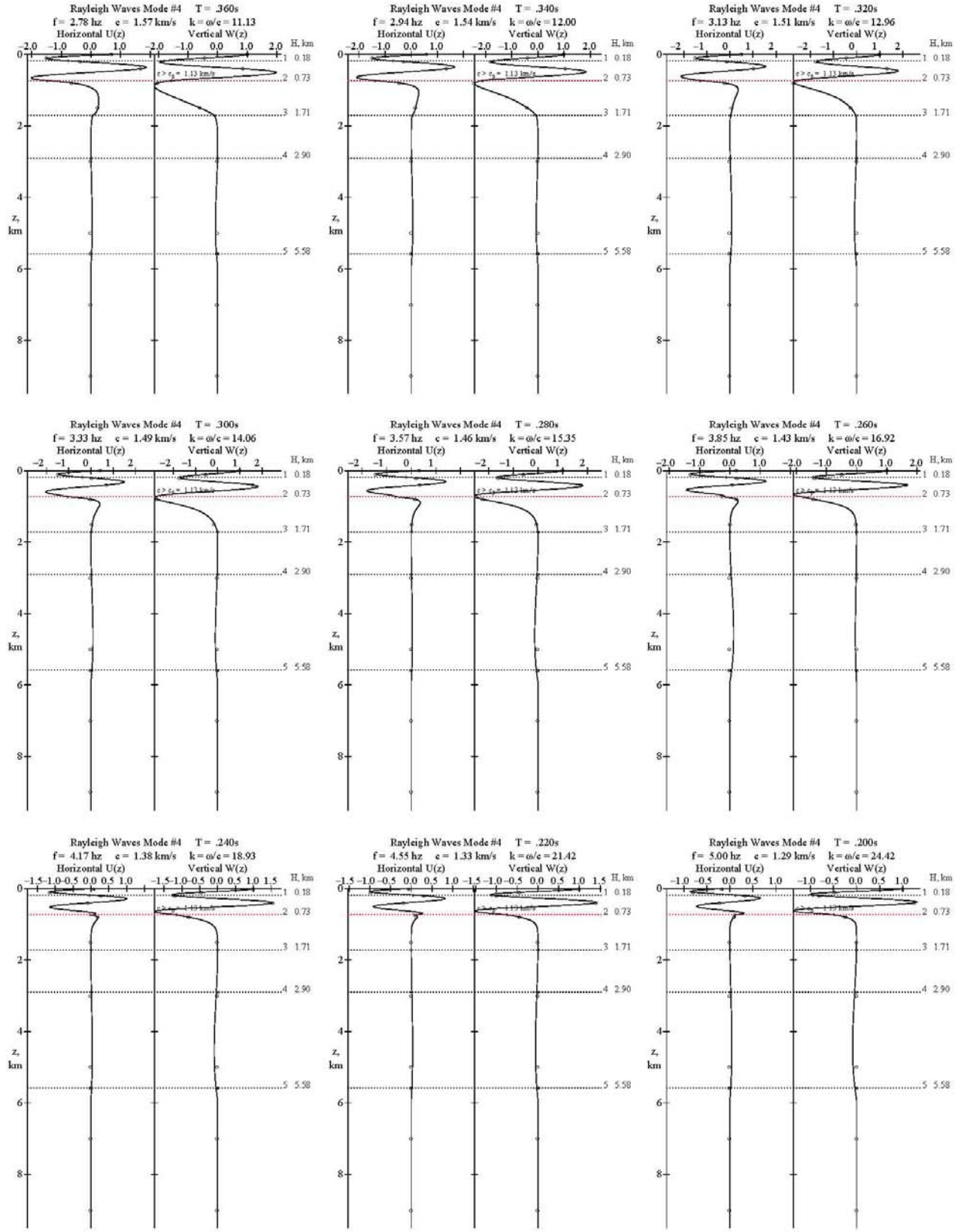

Fig. B-4.5 Rayleigh Wave Mode #4, Page 5 of 7 T=0.19-0.11s

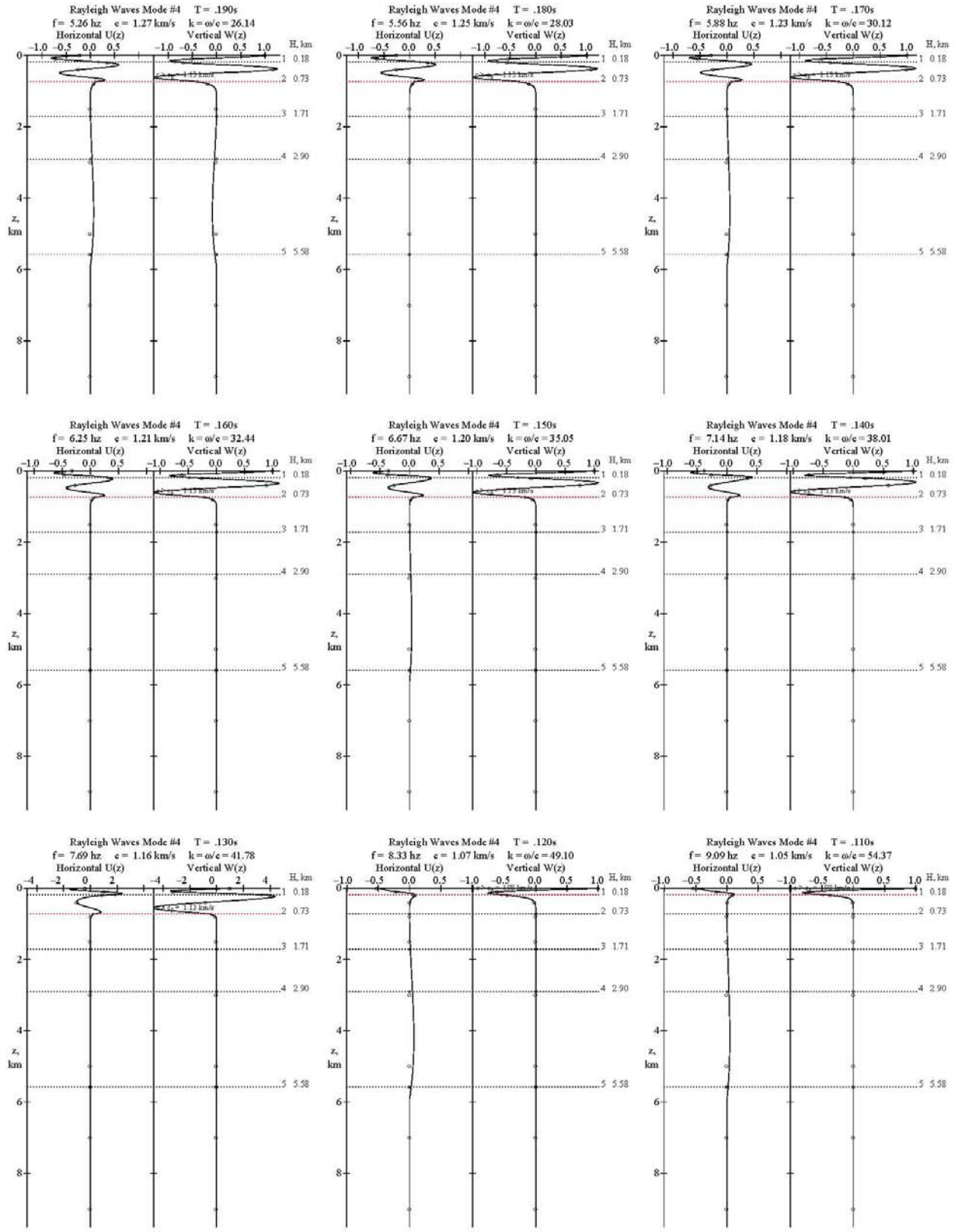

Fig. B-4.6 Rayleigh Wave Mode #4, Page 6 of 7 T=0.10-0.06s

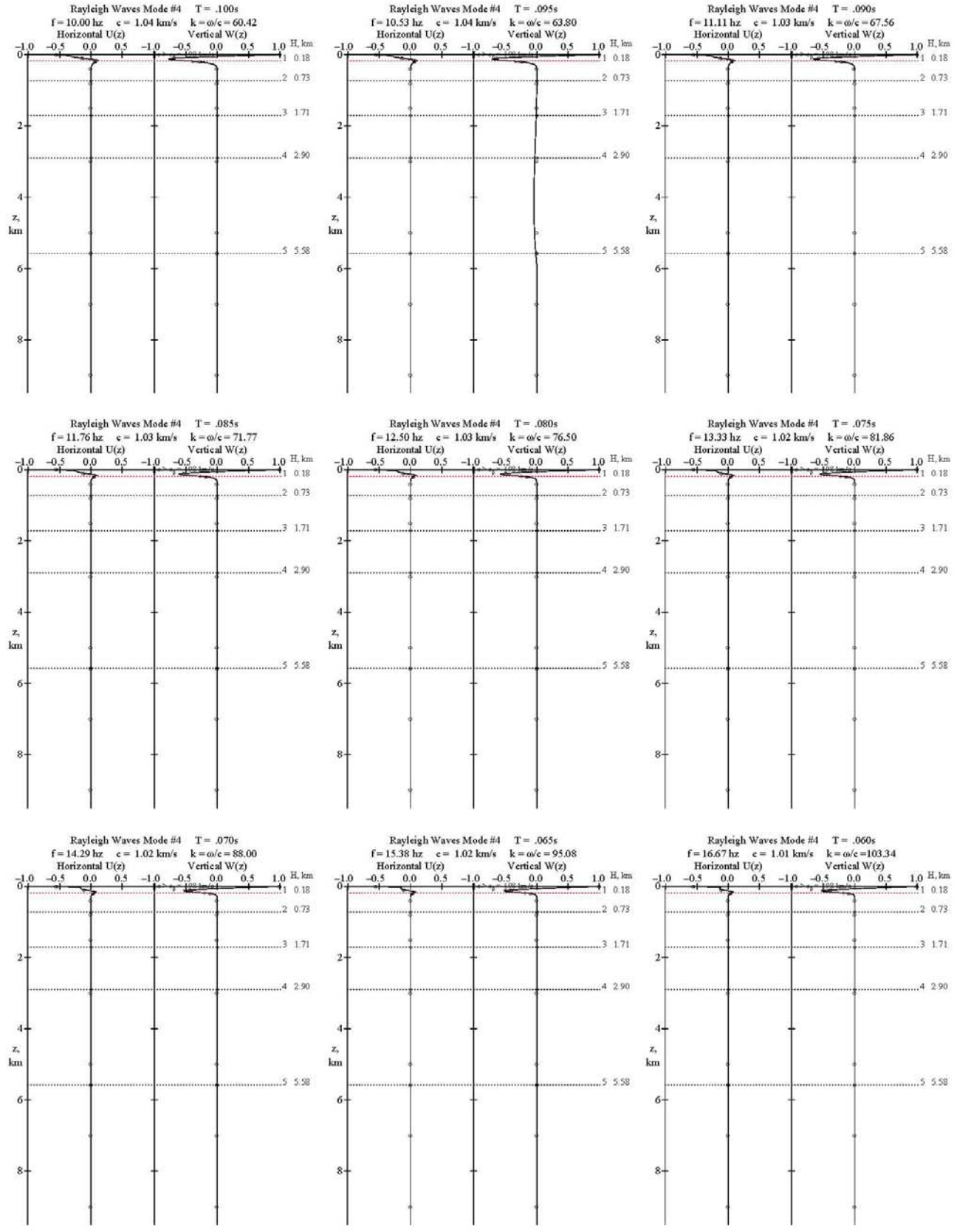

Fig. B-4.7 Rayleigh Wave Mode #4, Page 7 of 7 T=0.055-0.040s

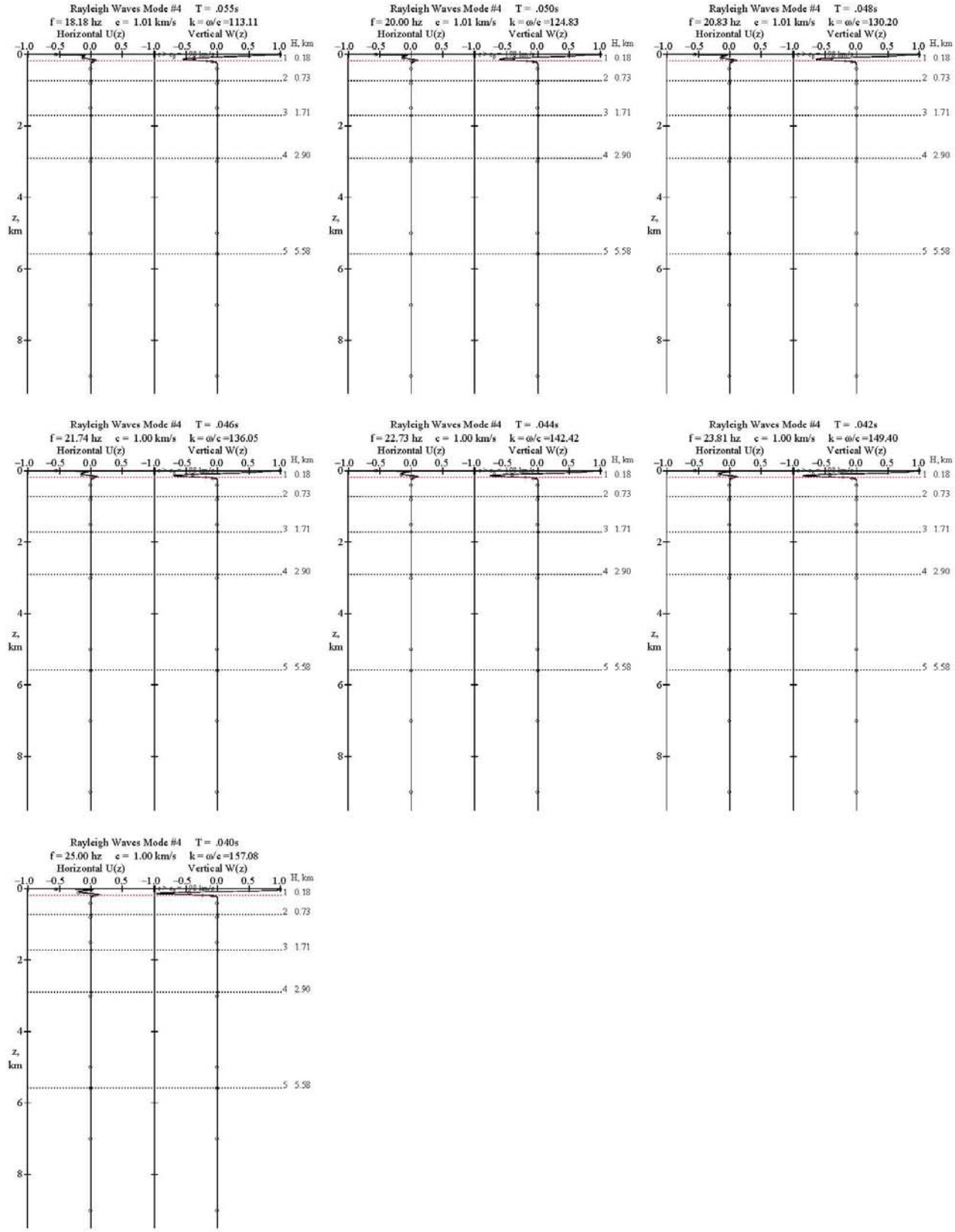

Appendix B-5 – Mode #5 Rayleigh Waves Mode Shapes

Fig. B-5.1 Rayleigh Wave Mode #5, Page 1 of 6 T=1.30-0.75s

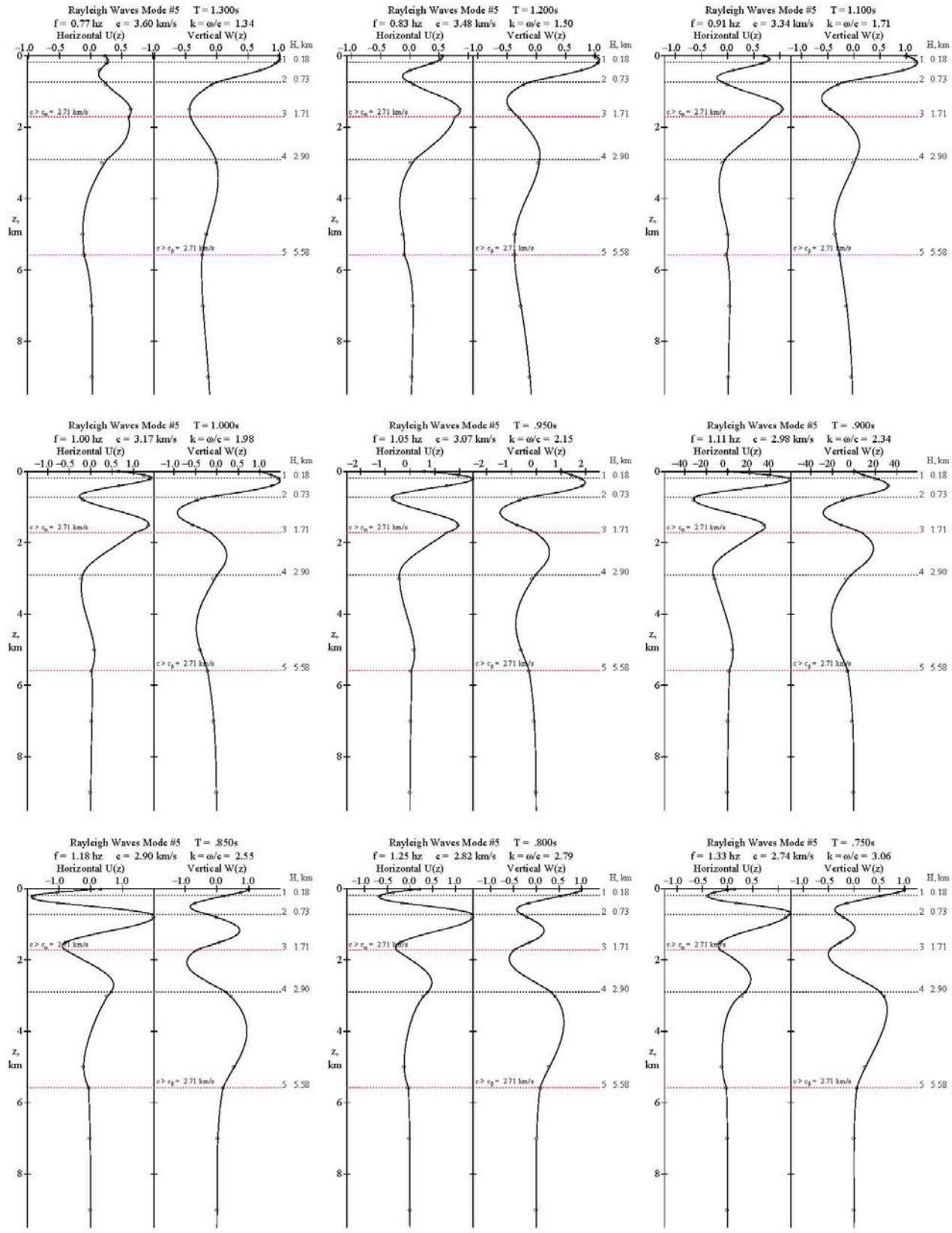

Fig. B-5.2 Rayleigh Wave Mode #5, Page 2 of 6 T=0.70-0.42s

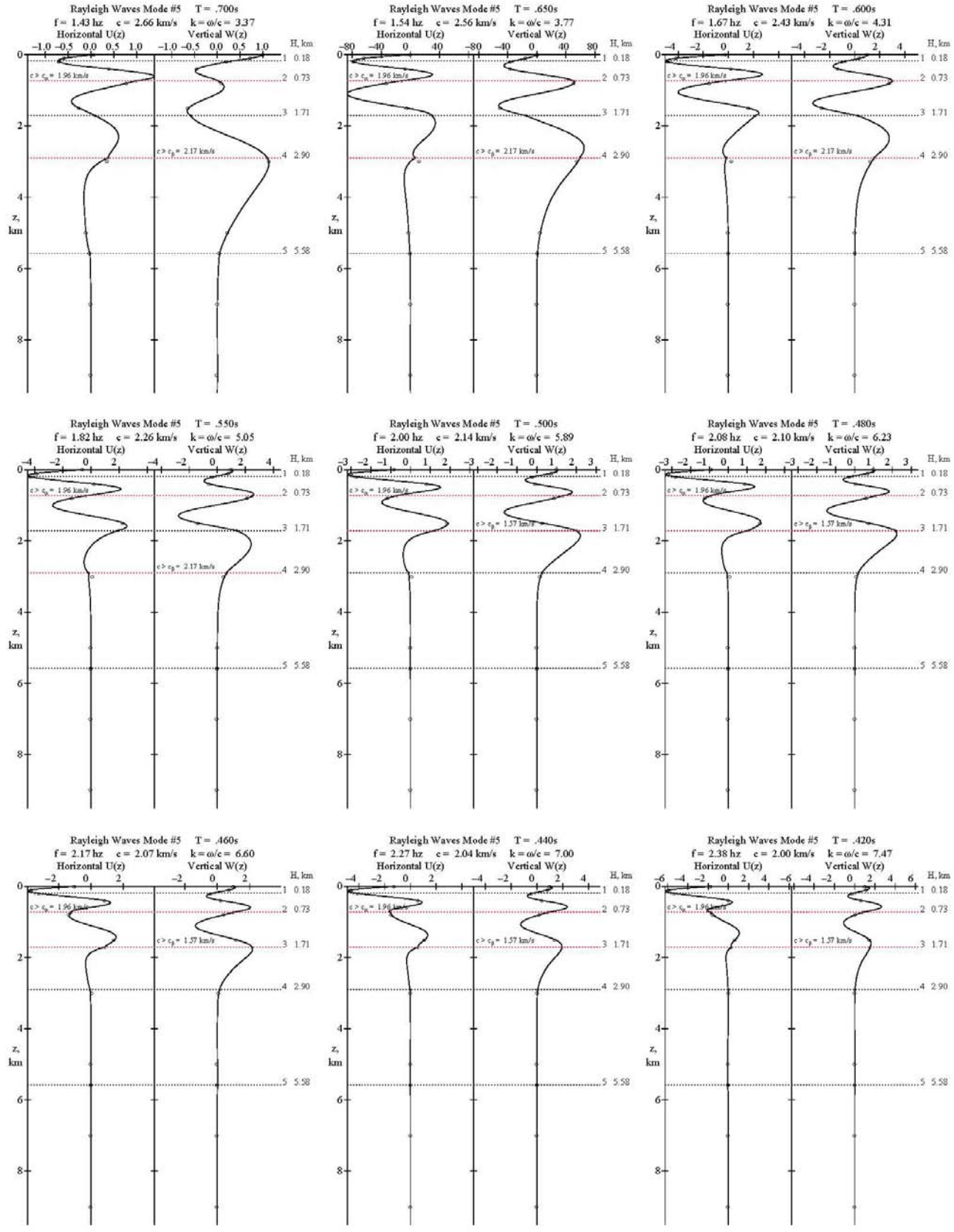

Fig. B-5.3 Rayleigh Wave Mode #5, Page 3 of 6 T=0.40-0.24s

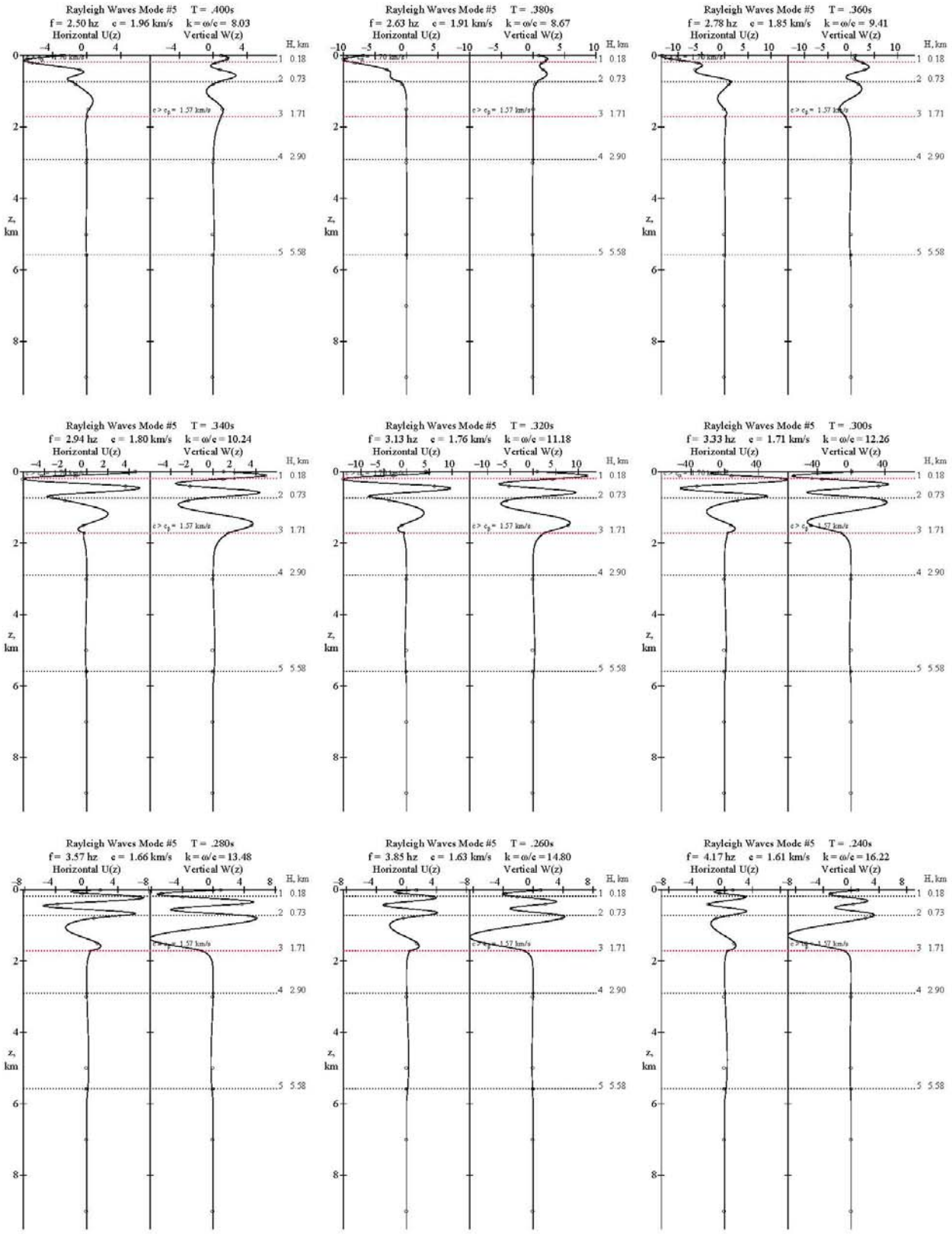

Fig. B-5.4 Rayleigh Wave Mode #5, Page 4 of 6 T=0.22-0.13s

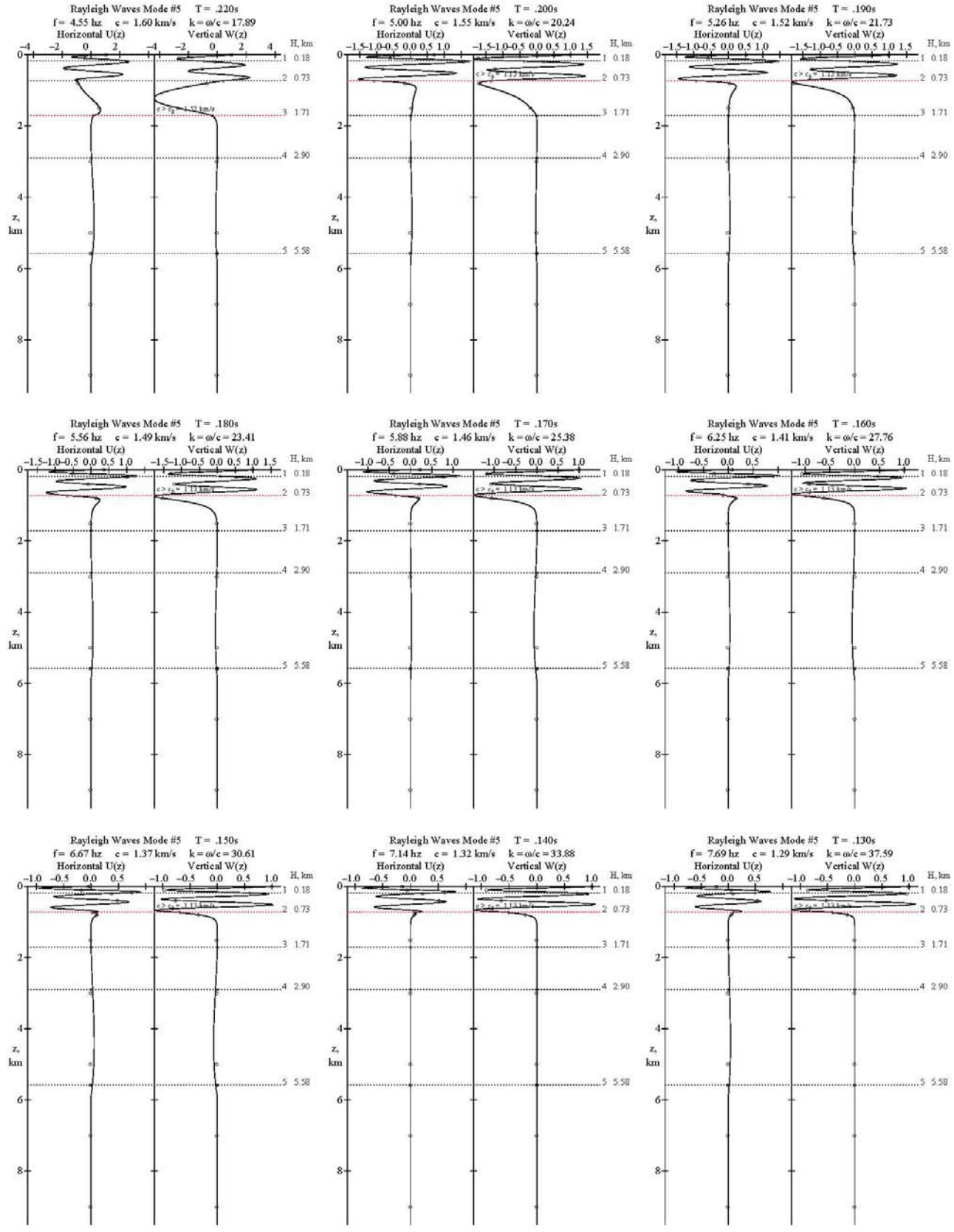

Fig. B-5.5 Rayleigh Wave Mode #5, Page 5 of 6 T=0.120-0.070s

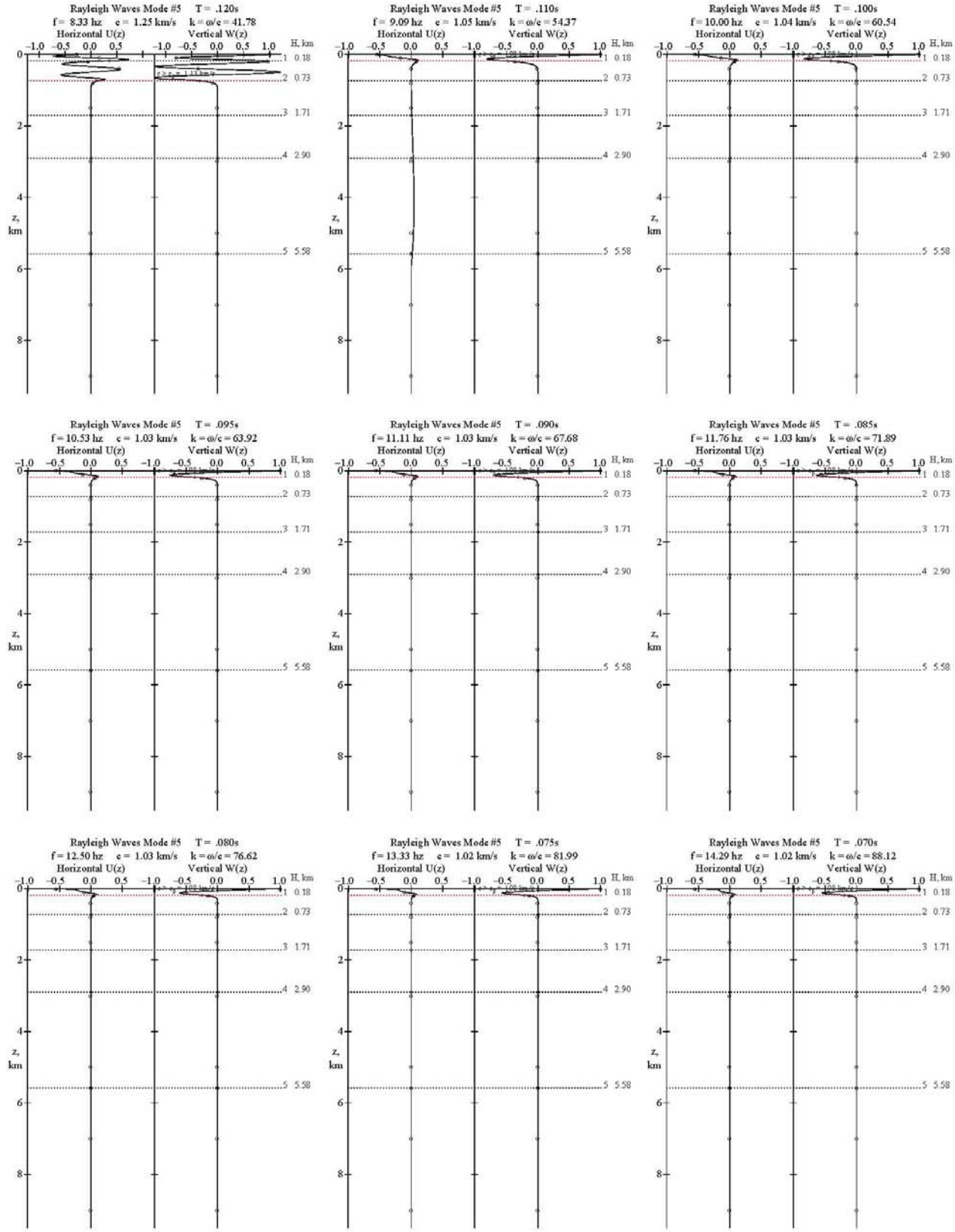

Fig. B-5.6 Rayleigh Wave Mode #5, Page 6 of 6 T=0.065-0.040s

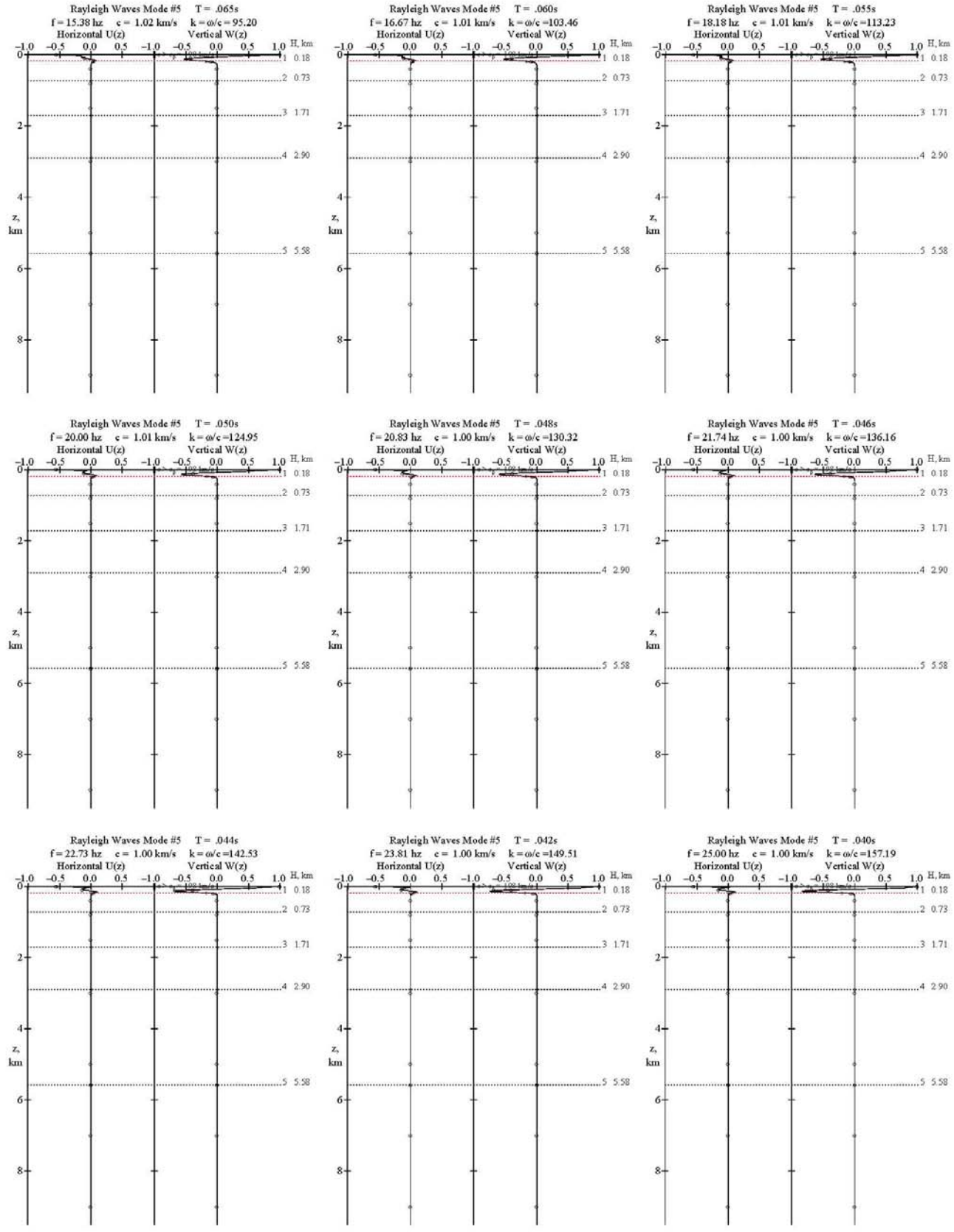

Appendix B-6 Body P, SV Waves (Mode#6), P-Wave Incident @ $\gamma = 85^o$

Fig. B-6.1 Body P, SV Waves (Mode#6), Page 1 of 11 T=15.0-8.5s

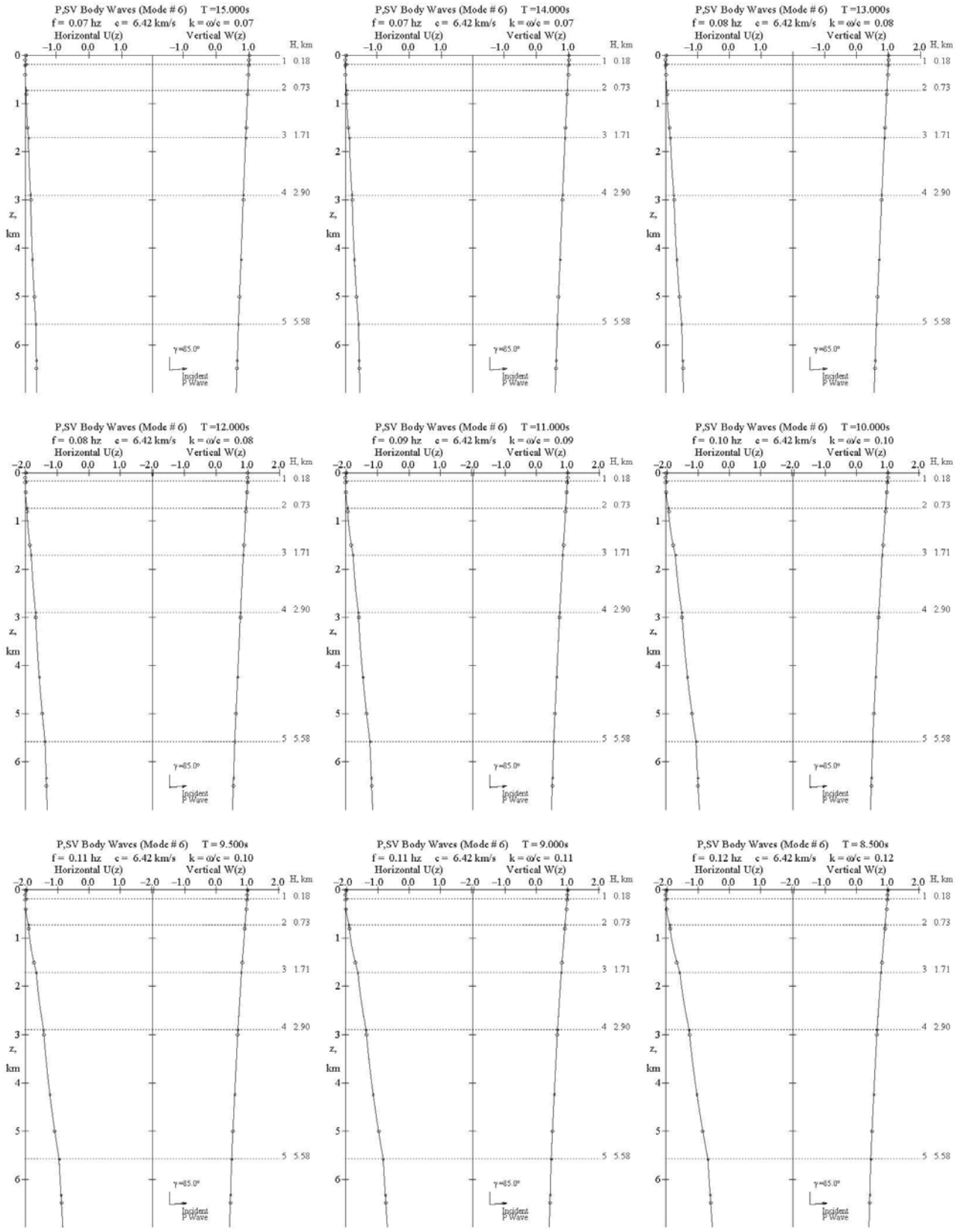

Fig. B-6.2 Body P, SV Waves (Mode#6), Page 2 of 11 T=8.0-4.6s

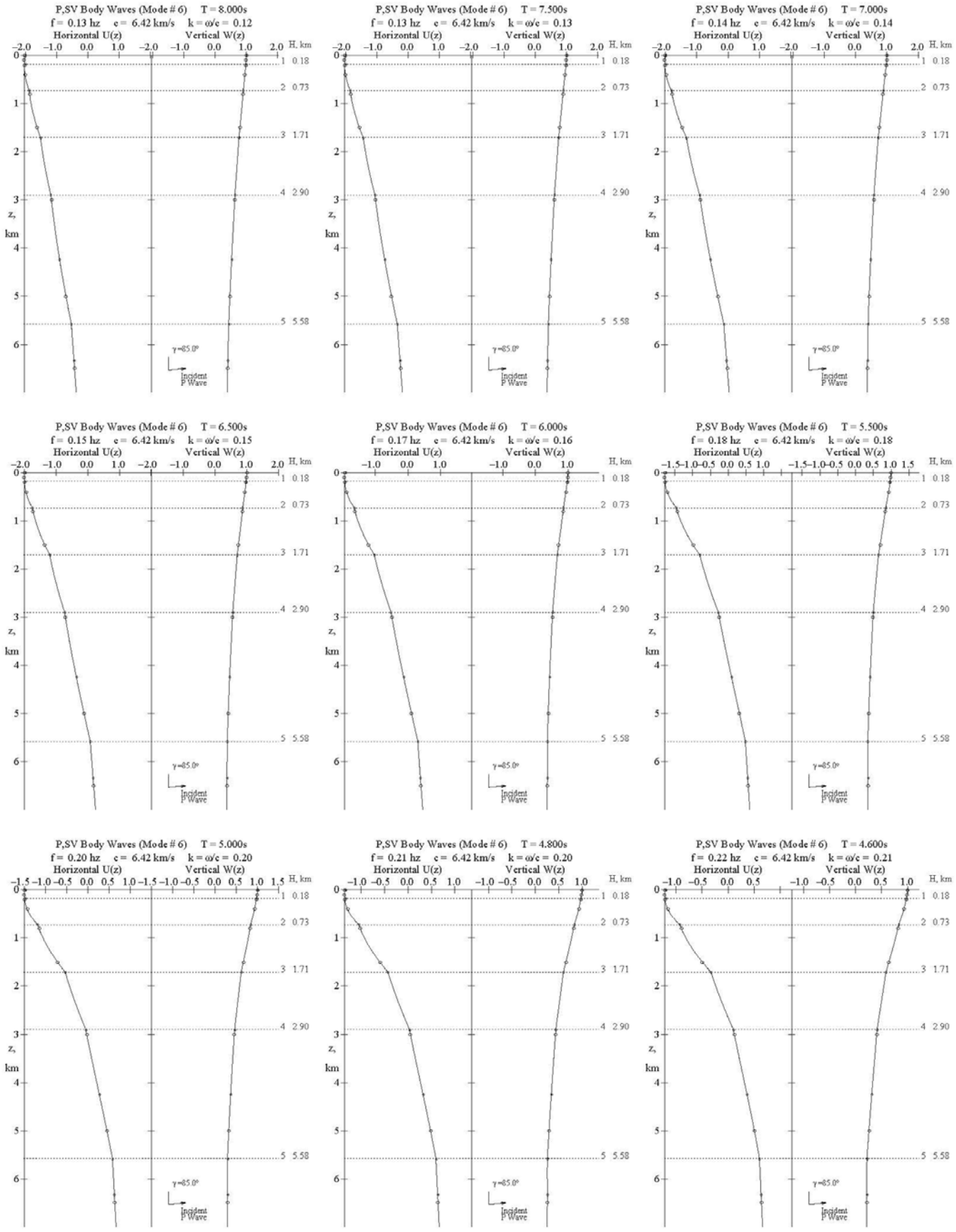

Fig. B-6.3 Body P, SV Waves (Mode#6), Page 3 of 11 T=4.4-2.8s

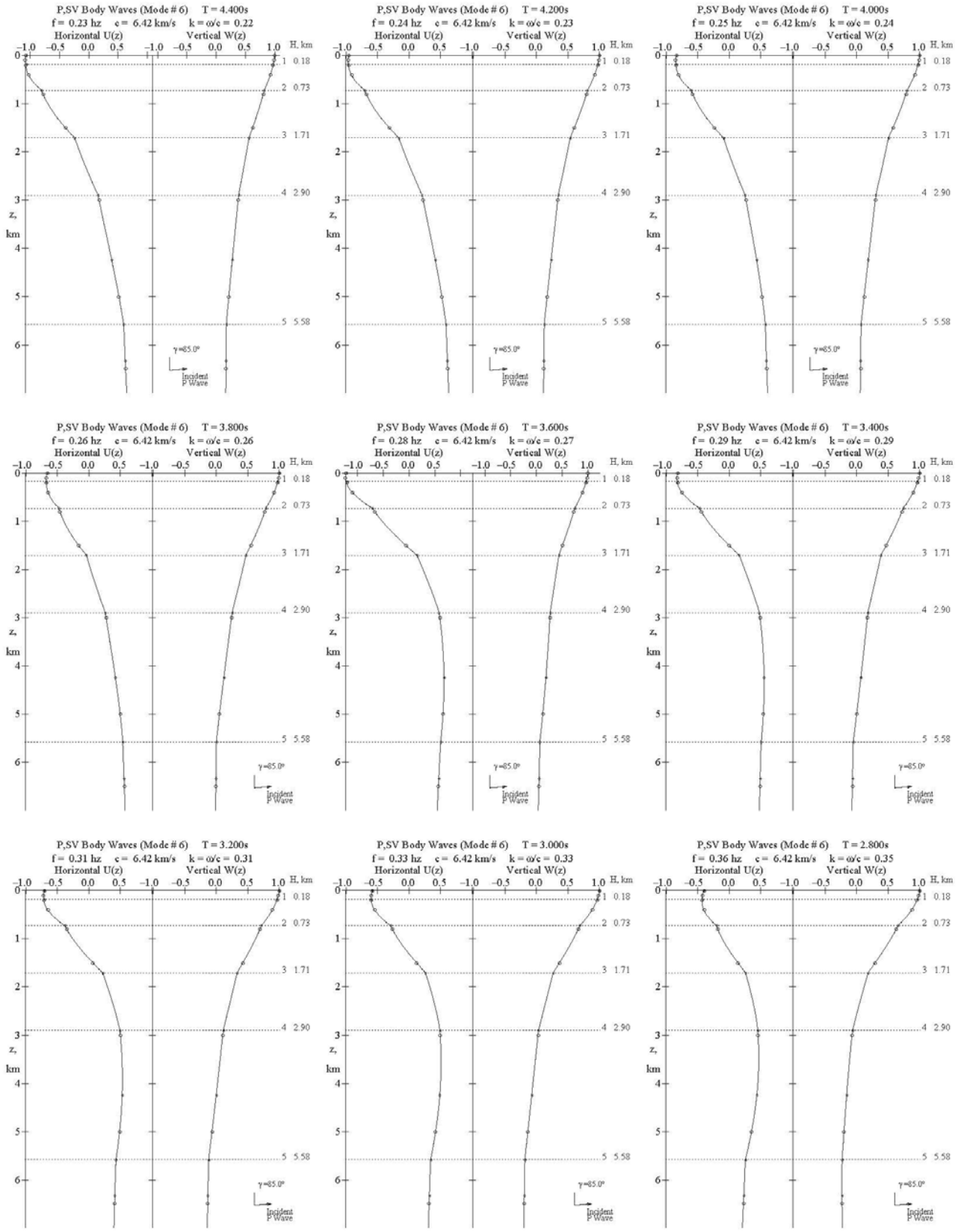

Fig. B-6.4 Body P, SV Waves (Mode#6), Page 4 of 11 T=2.6-1.5s

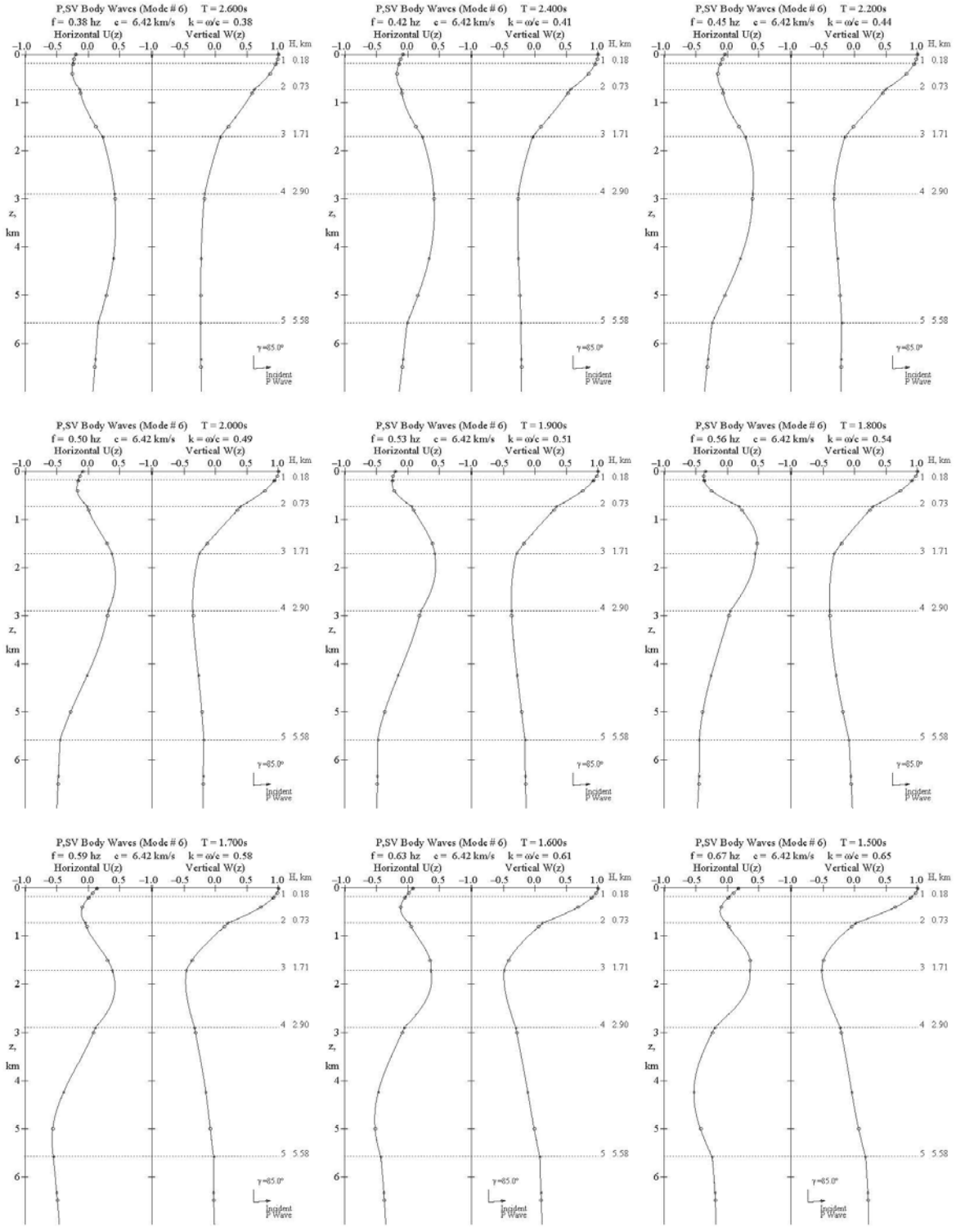

Fig. B-6.5 Body P, SV Waves (Mode#6), Page 5 of 11 T=1.4-0.8s

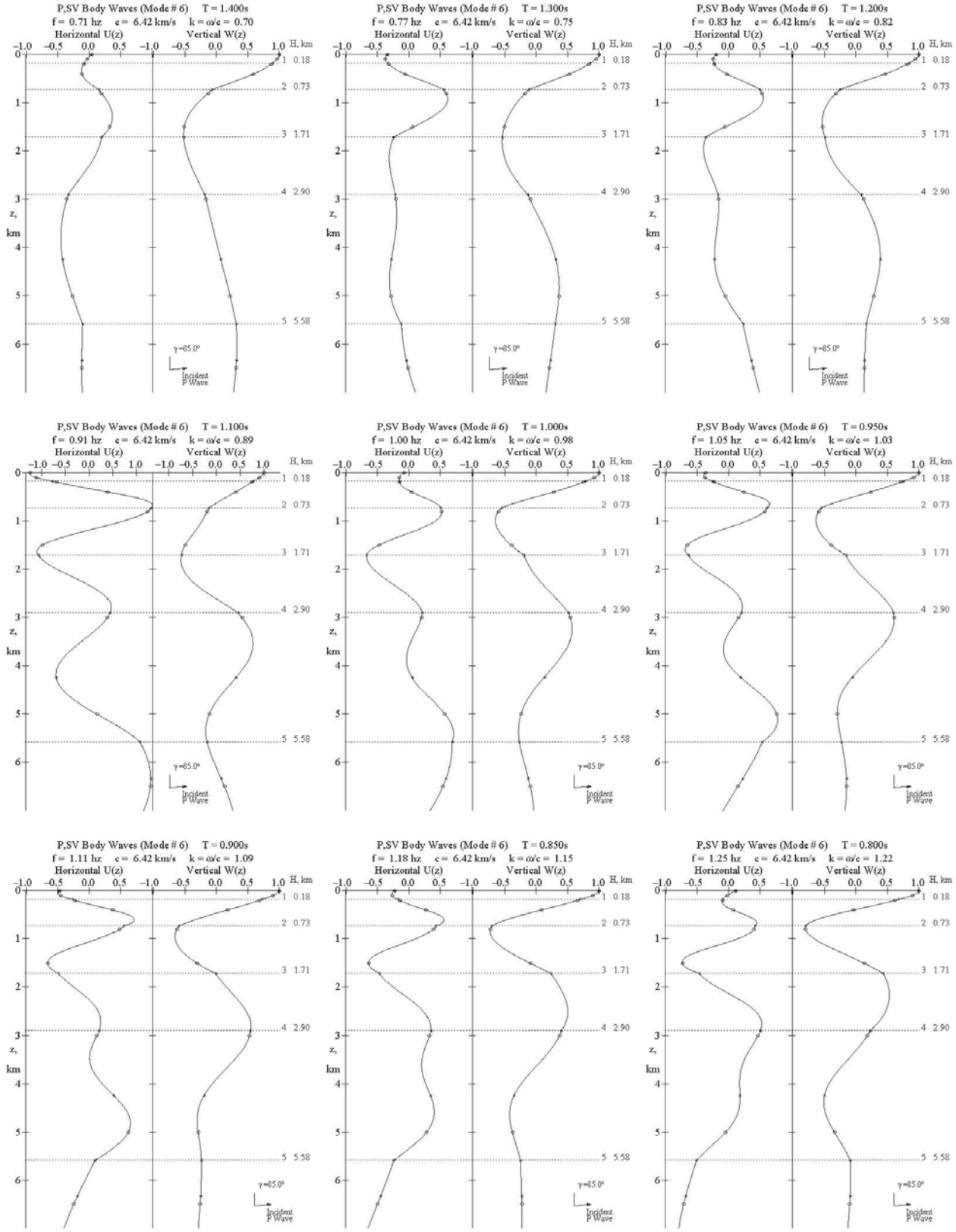

Fig. B-6.6 Body P, SV Waves (Mode#6), Page 6 of 11 T=0.75-0.44s

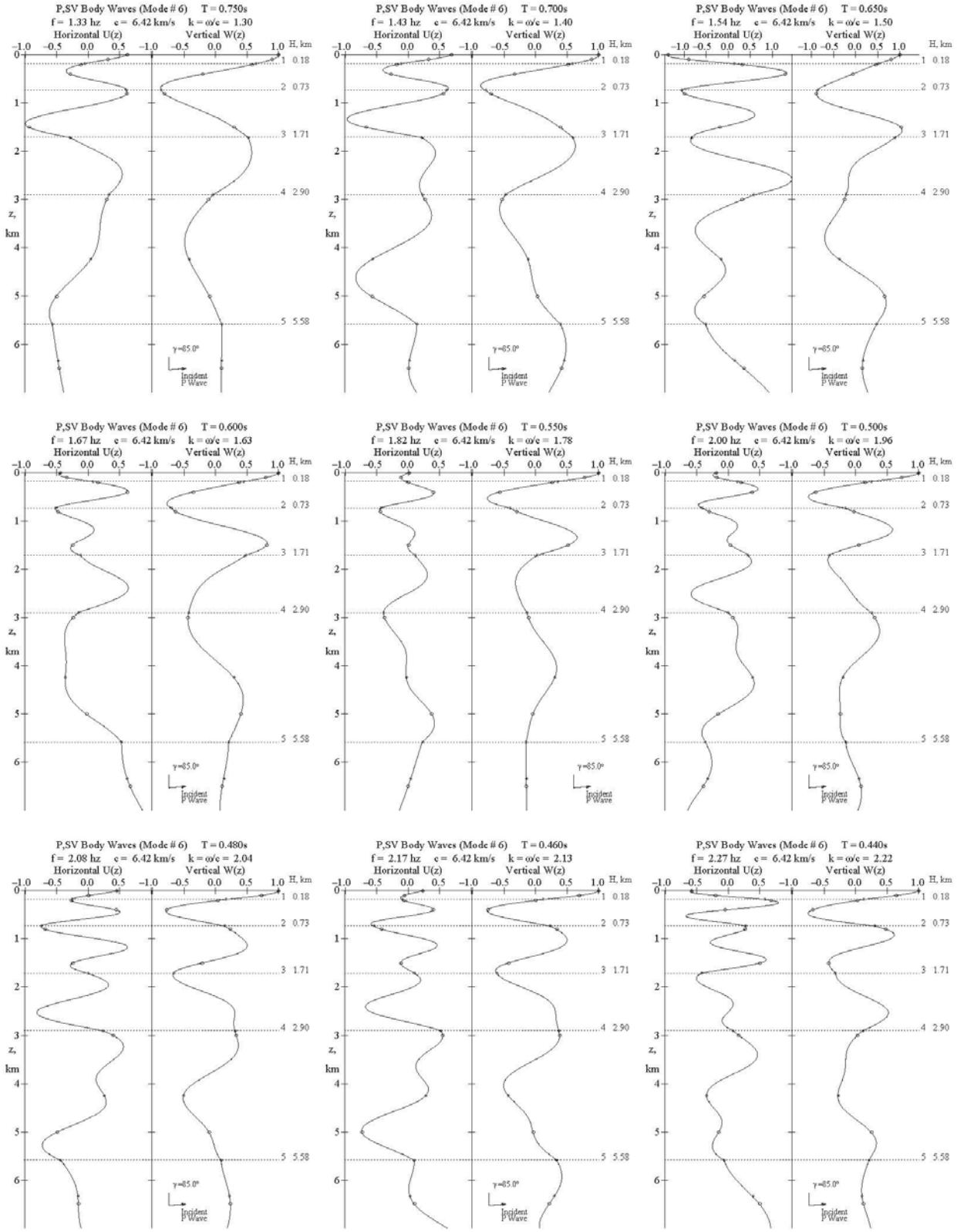

Fig. B-6.7 Body P, SV Waves (Mode#6), Page 7 of 11 T=0.42-0.26s

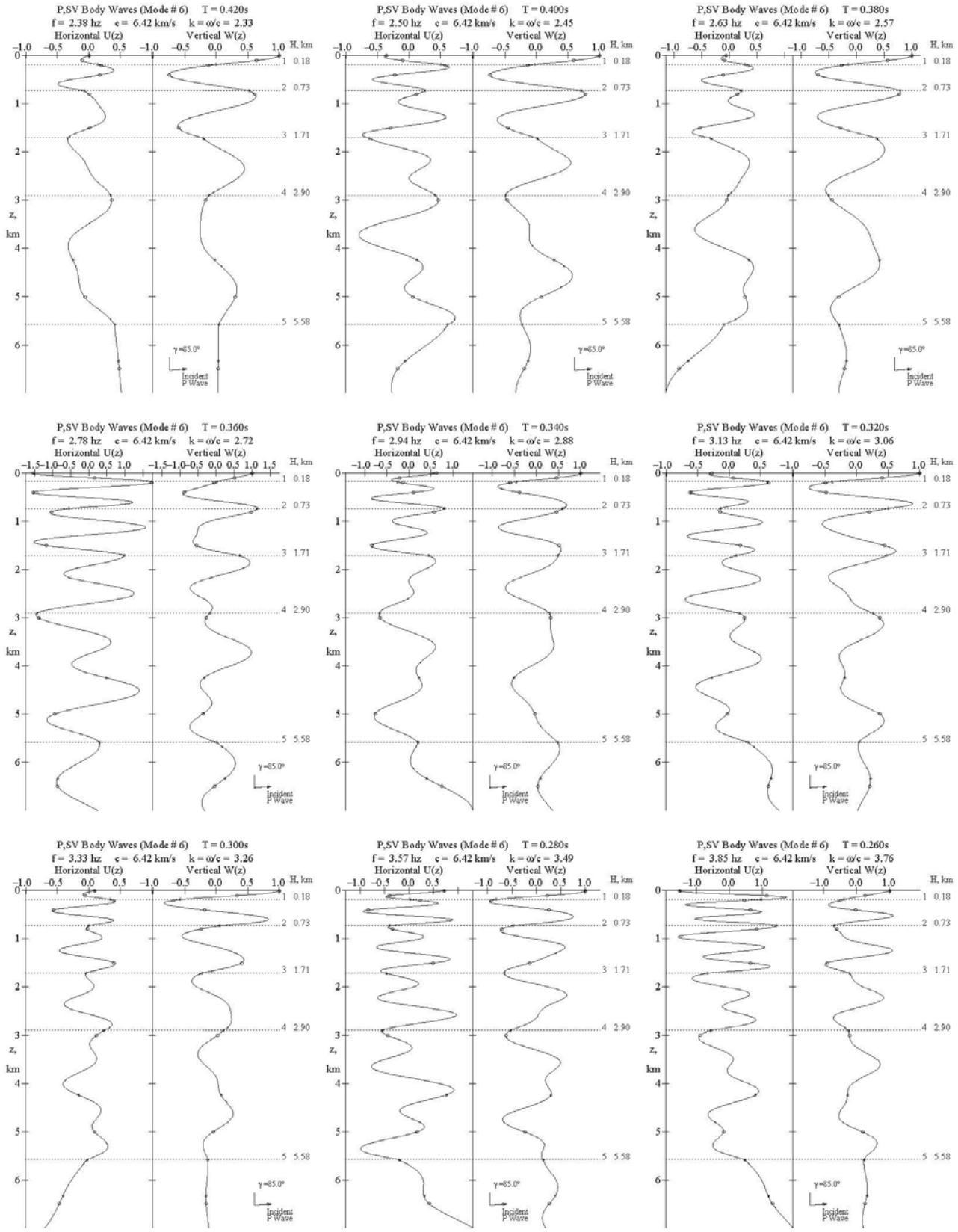

Fig. B-6.8 Body P, SV Waves (Mode#6), Page 8 of 11 T=0.24-0.14s

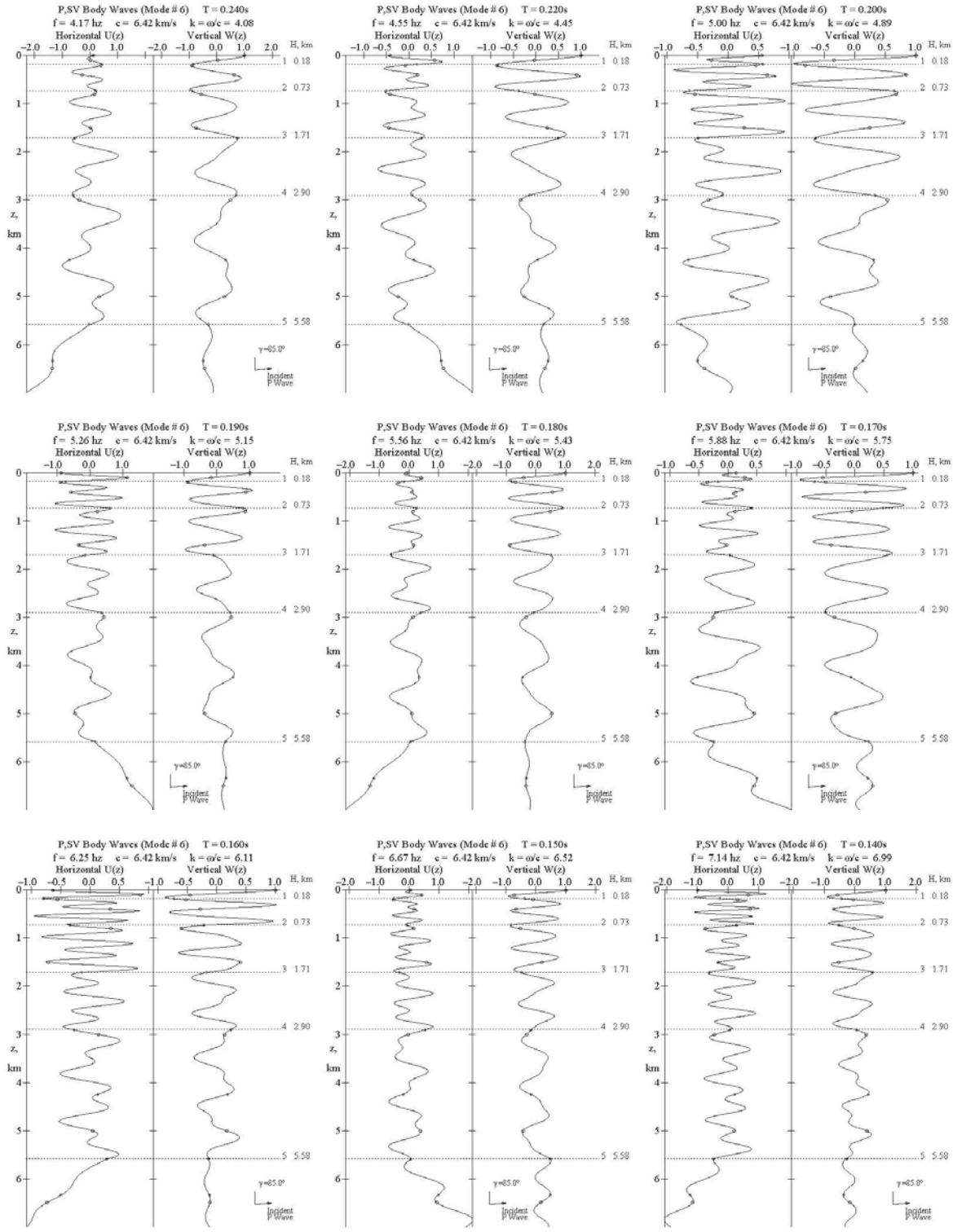

Fig. B-6.9 Body P, SV Waves (Mode#6), Page 9 of 11 T=0.130-0.075s

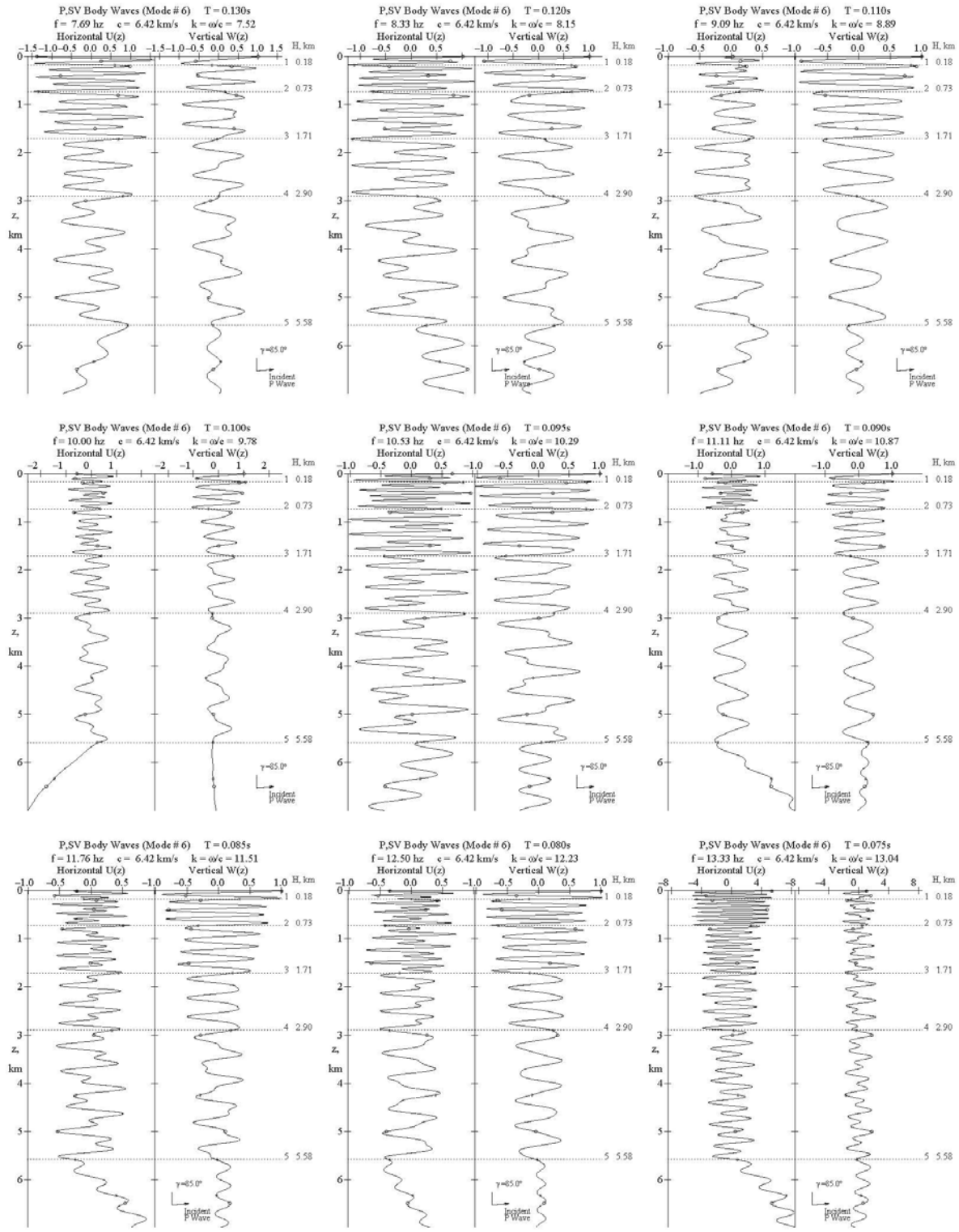

Fig. B-6.10 Body P, SV Waves (Mode#6), Page 10 of 11 T=0.070-0.042s

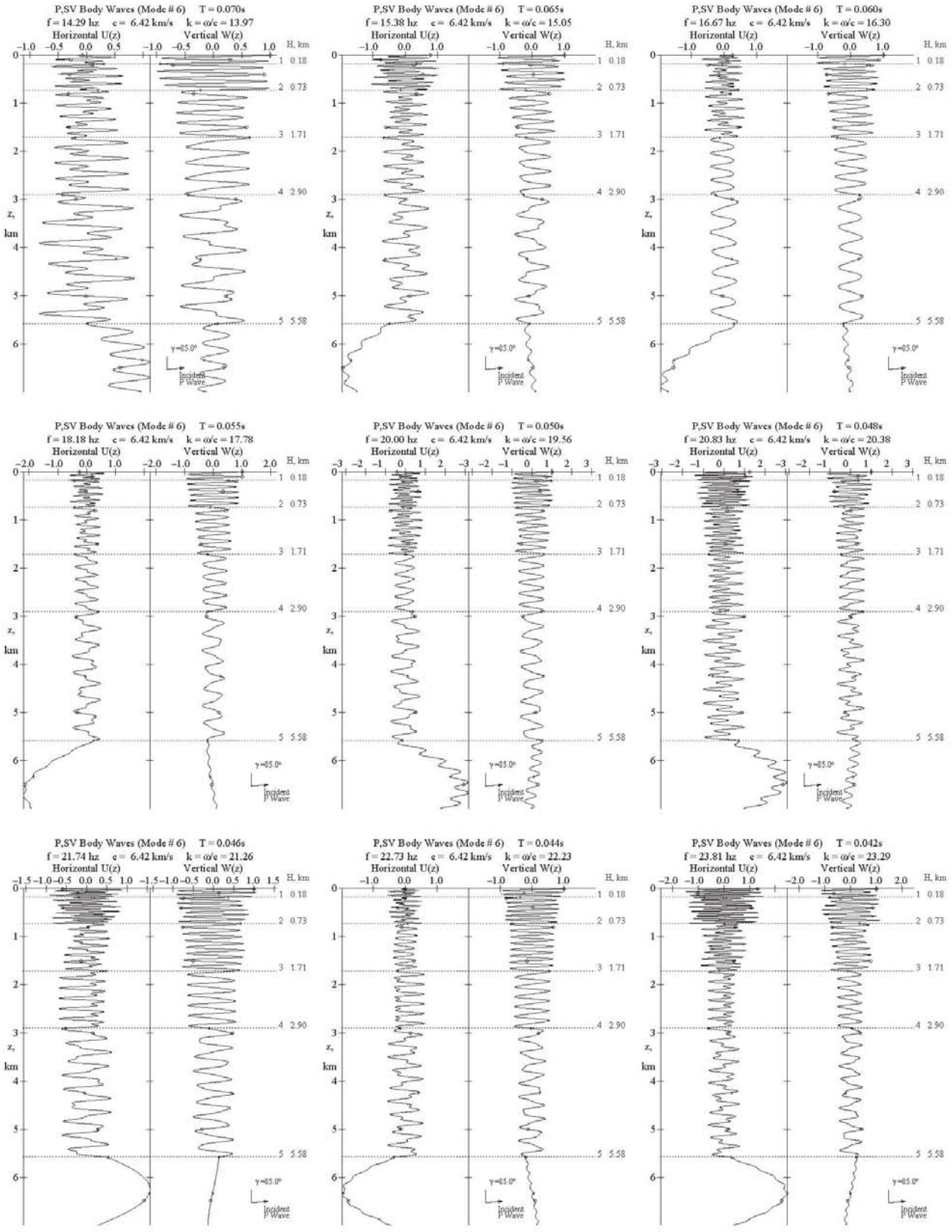

Fig. B-6.11 Body P, SV Waves (Mode#6), Page 11 of 11 T=0.040s

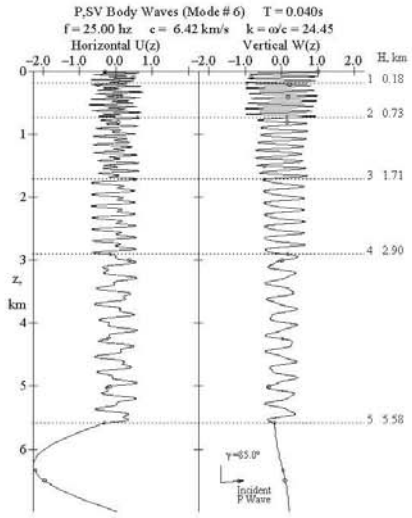

Appendix B-7 Body P, SV Waves (Mode#7), SV-Wave Incident @ $\gamma = 85^o$

Fig. B-7.1 Body P, SV Waves (Mode#7), Page 1 of 11 T=15.0-8.5s

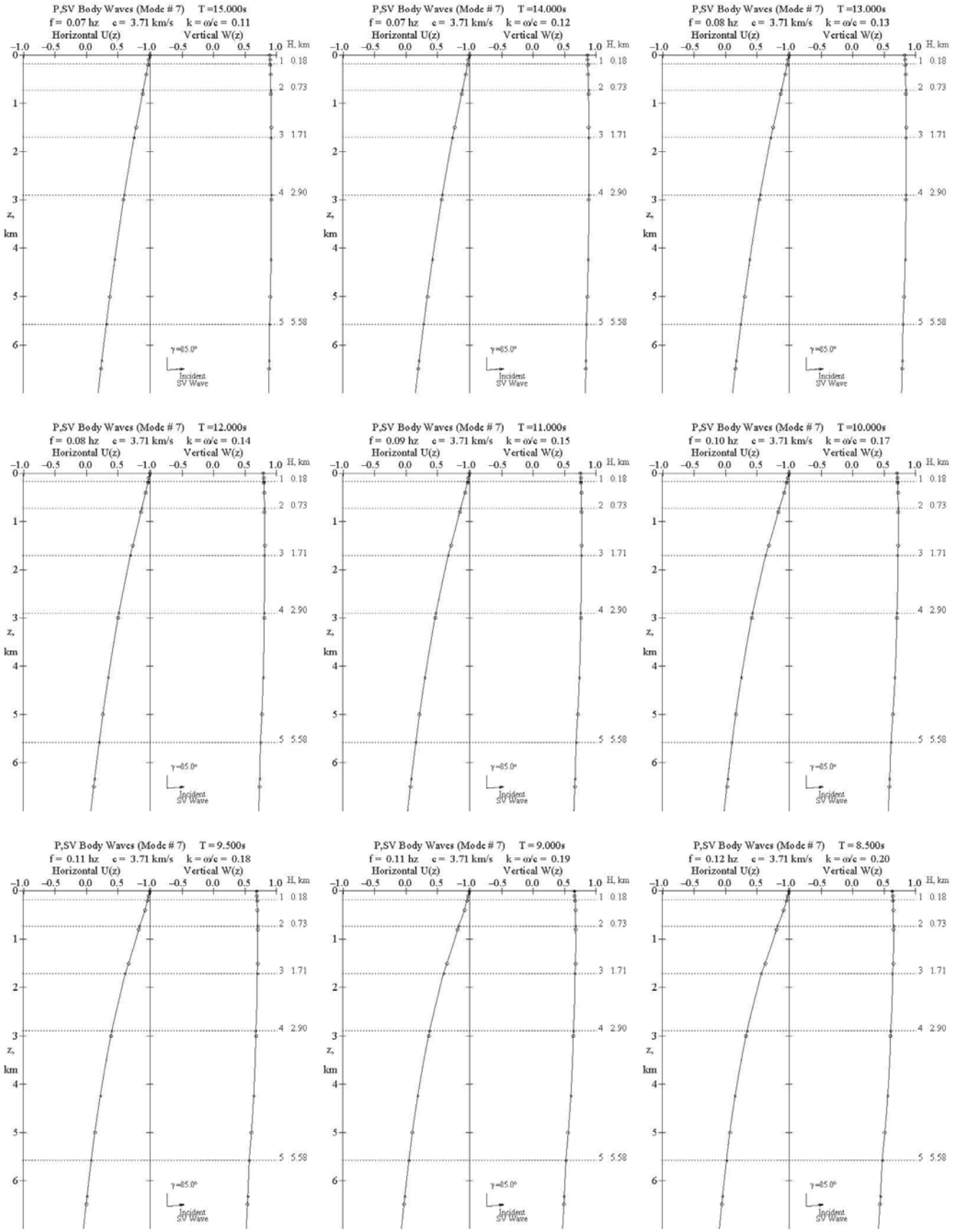

Fig. B-7.2 Body P, SV Waves (Mode#7), Page 2 of 11 T=8.0-4.6s

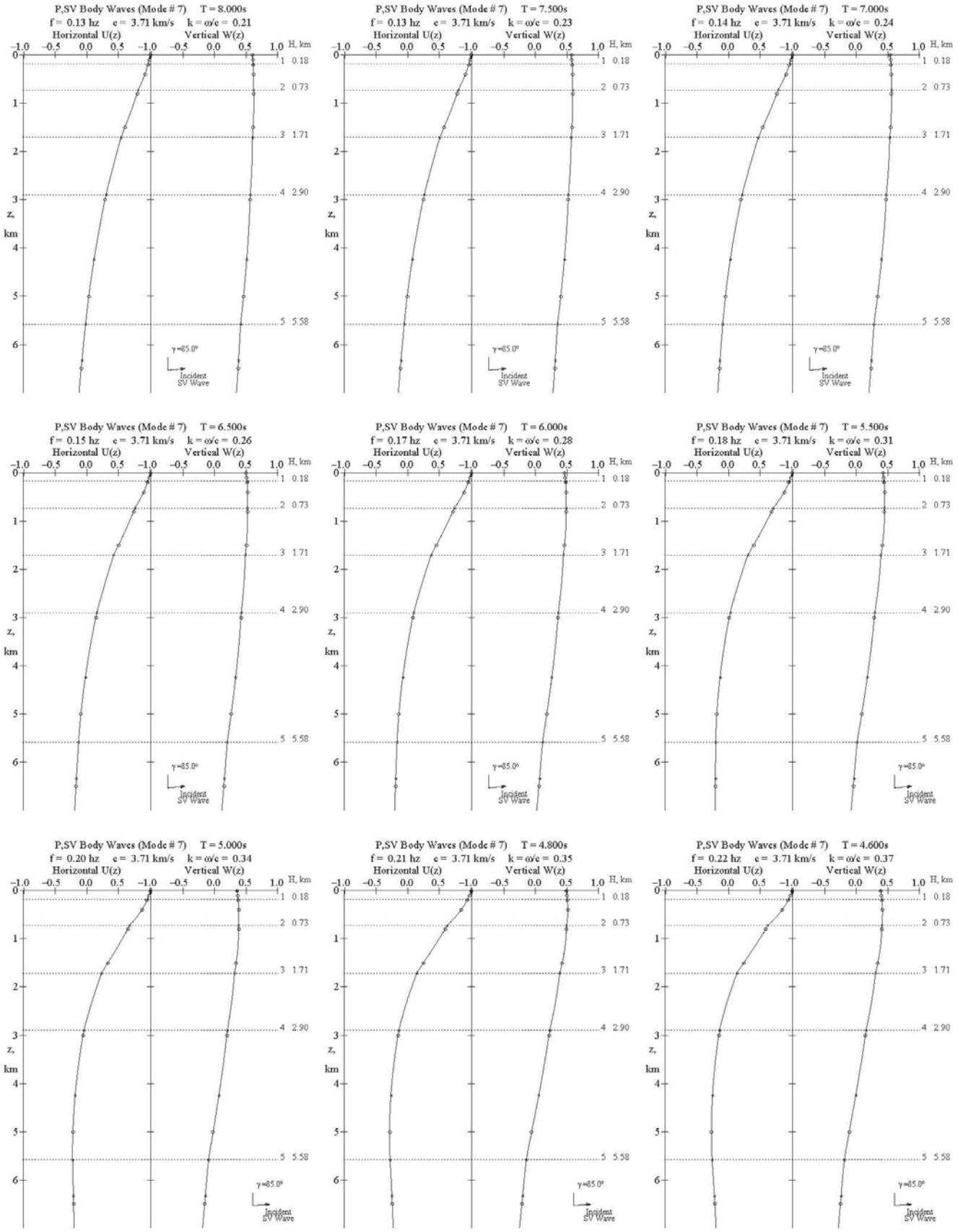

Fig. B-7.3 Body P, SV Waves (Mode#7), Page 3 of 11 T=4.4-2.8s

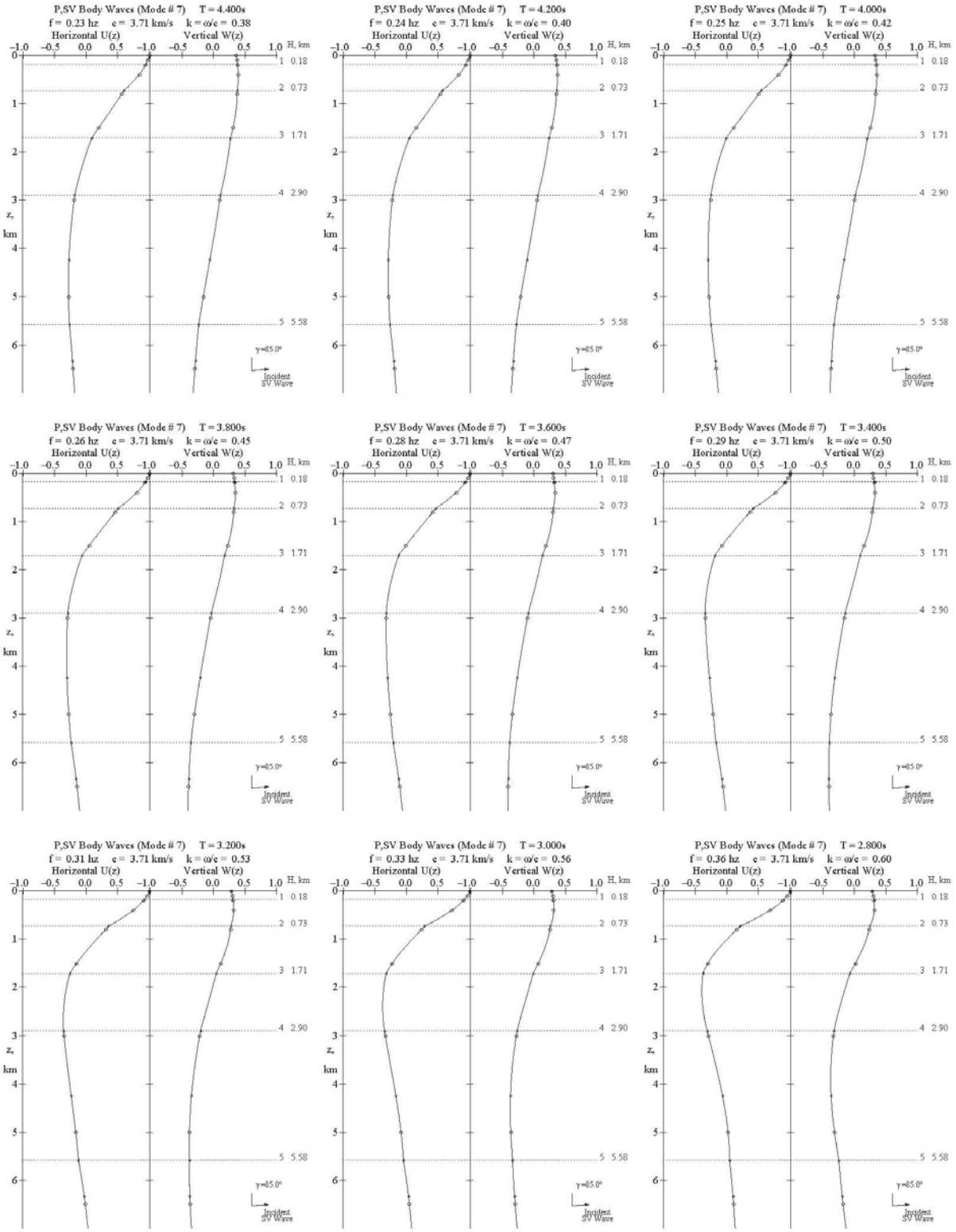

Fig. B-7.4 Body P, SV Waves (Mode#7), Page 4 of 11 T=2.6-1.5s

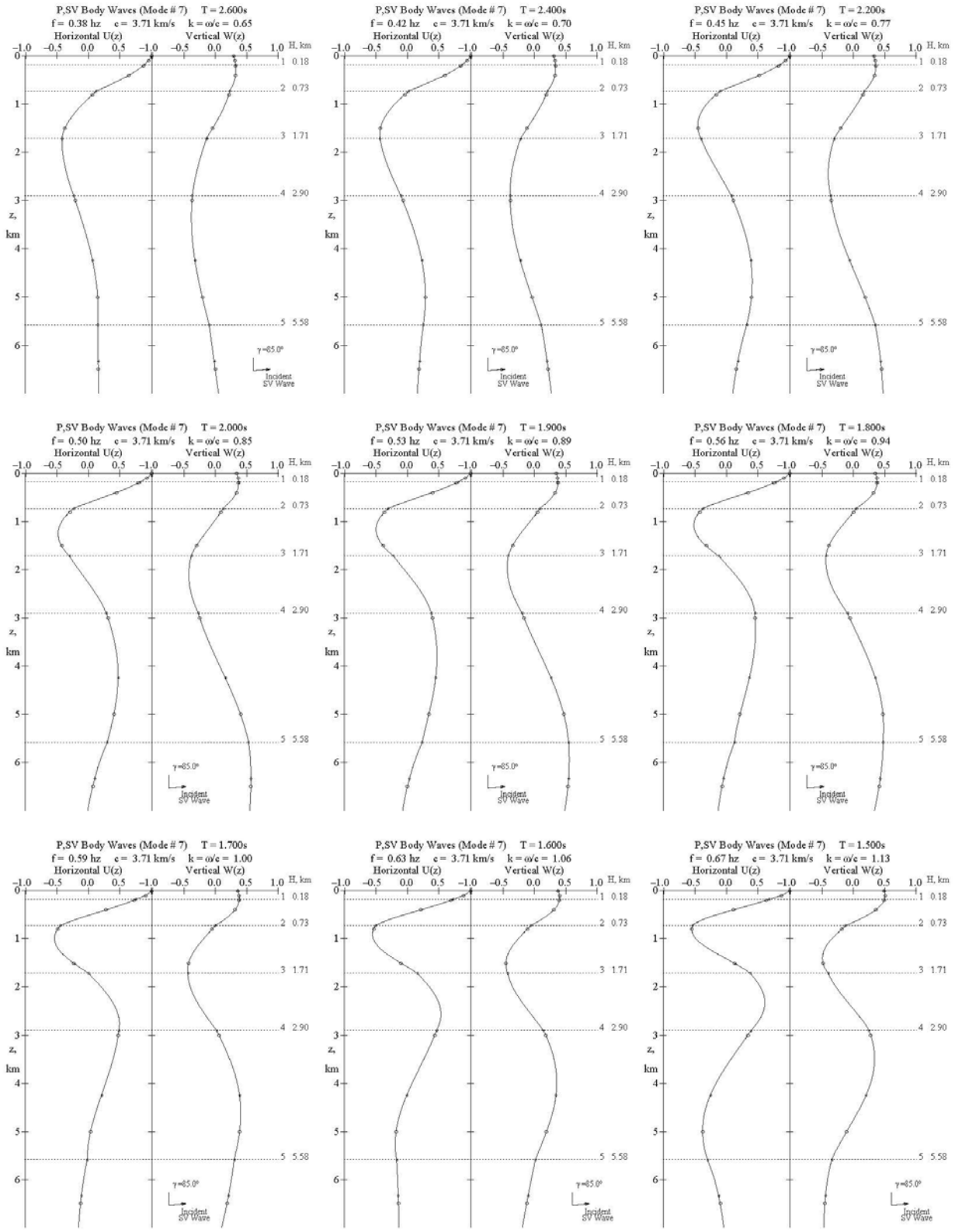

Fig. B-7.5 Body P, SV Waves (Mode#7), Page 5 of 11 T=1.4-0.8s

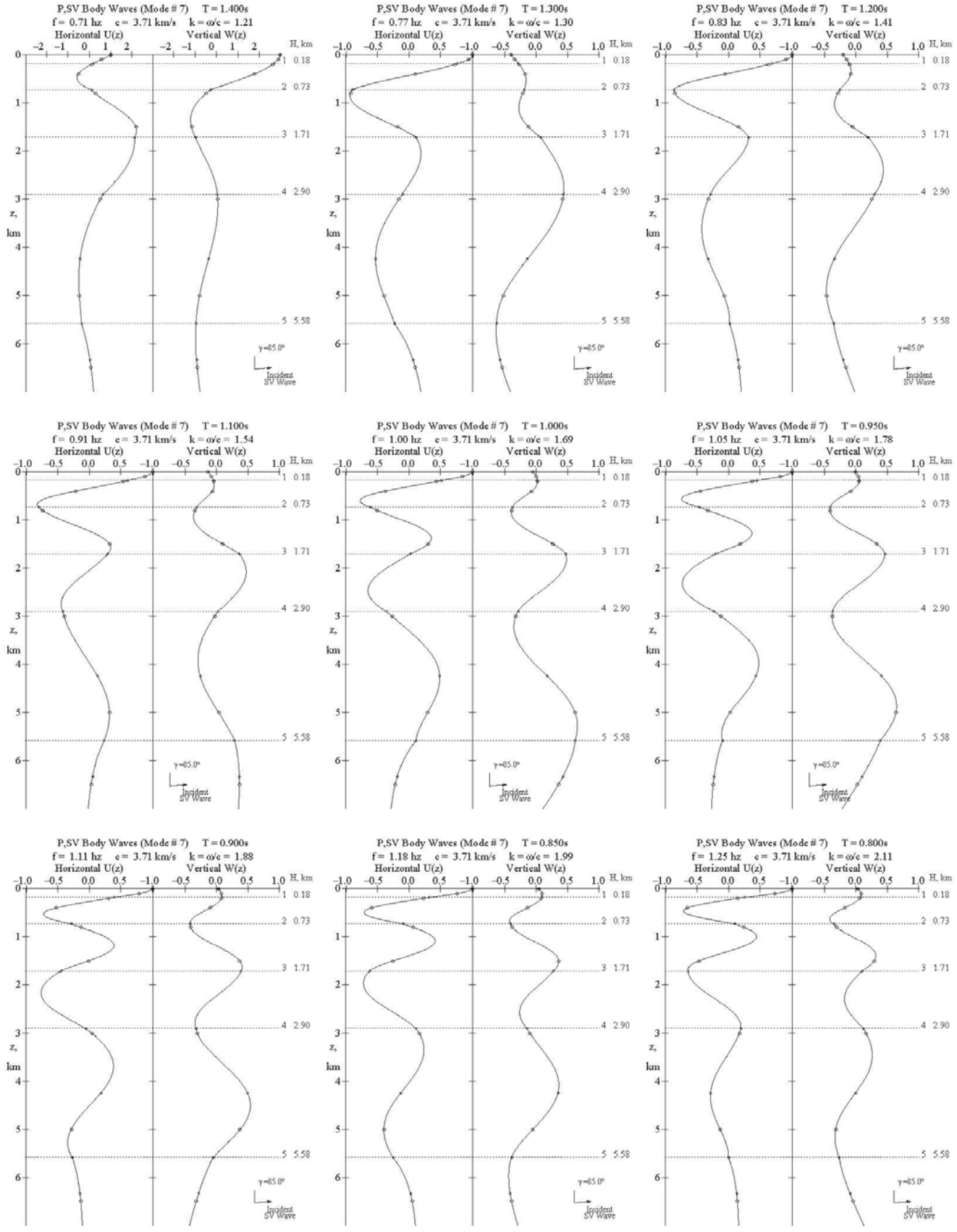

Fig. B-7.6 Body P, SV Waves (Mode#7), Page 6 of 11 T=0.75-0.44s

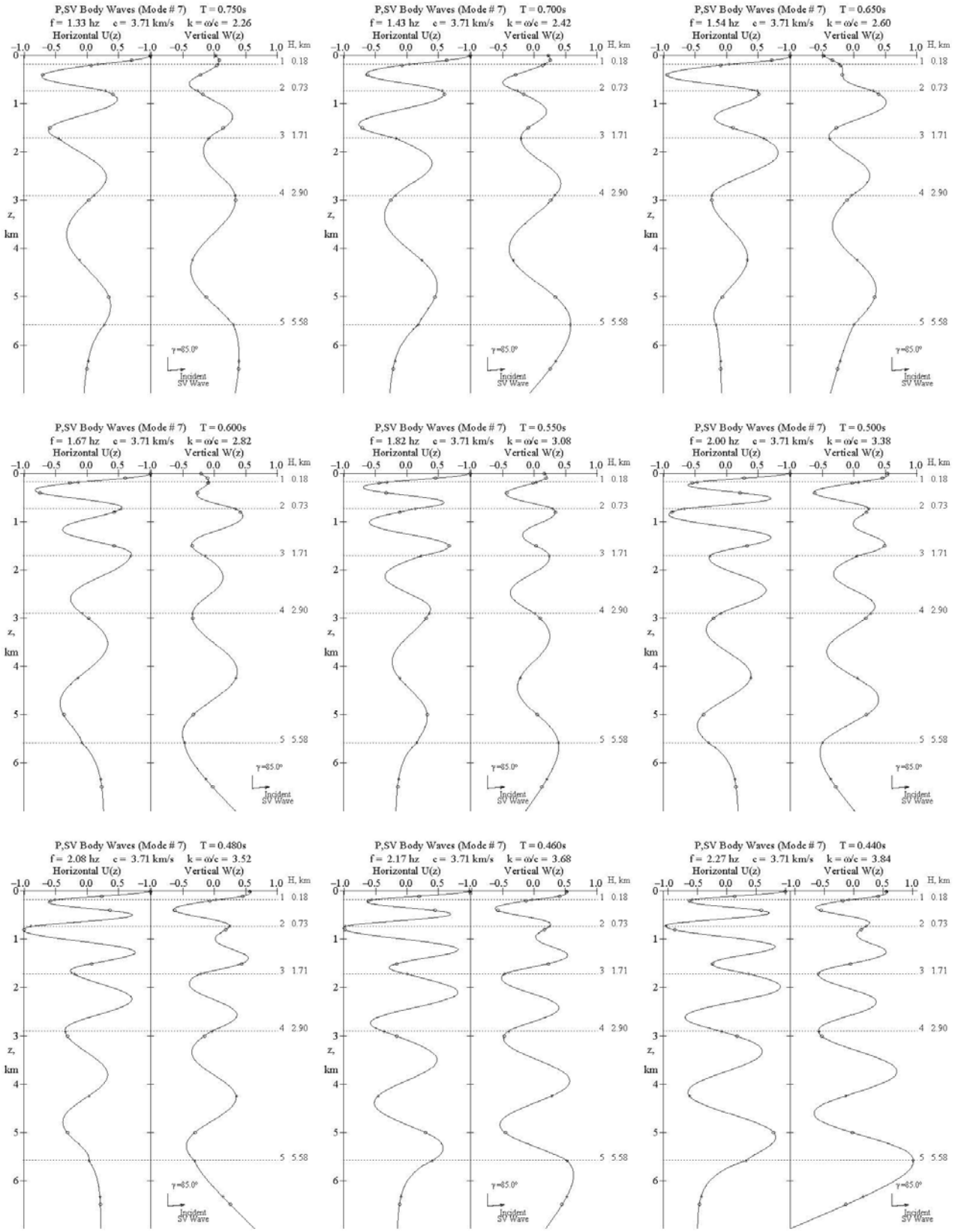

Fig. B-7.7 Body P, SV Waves (Mode#7), Page 7 of 11 T=0.42-0.26s

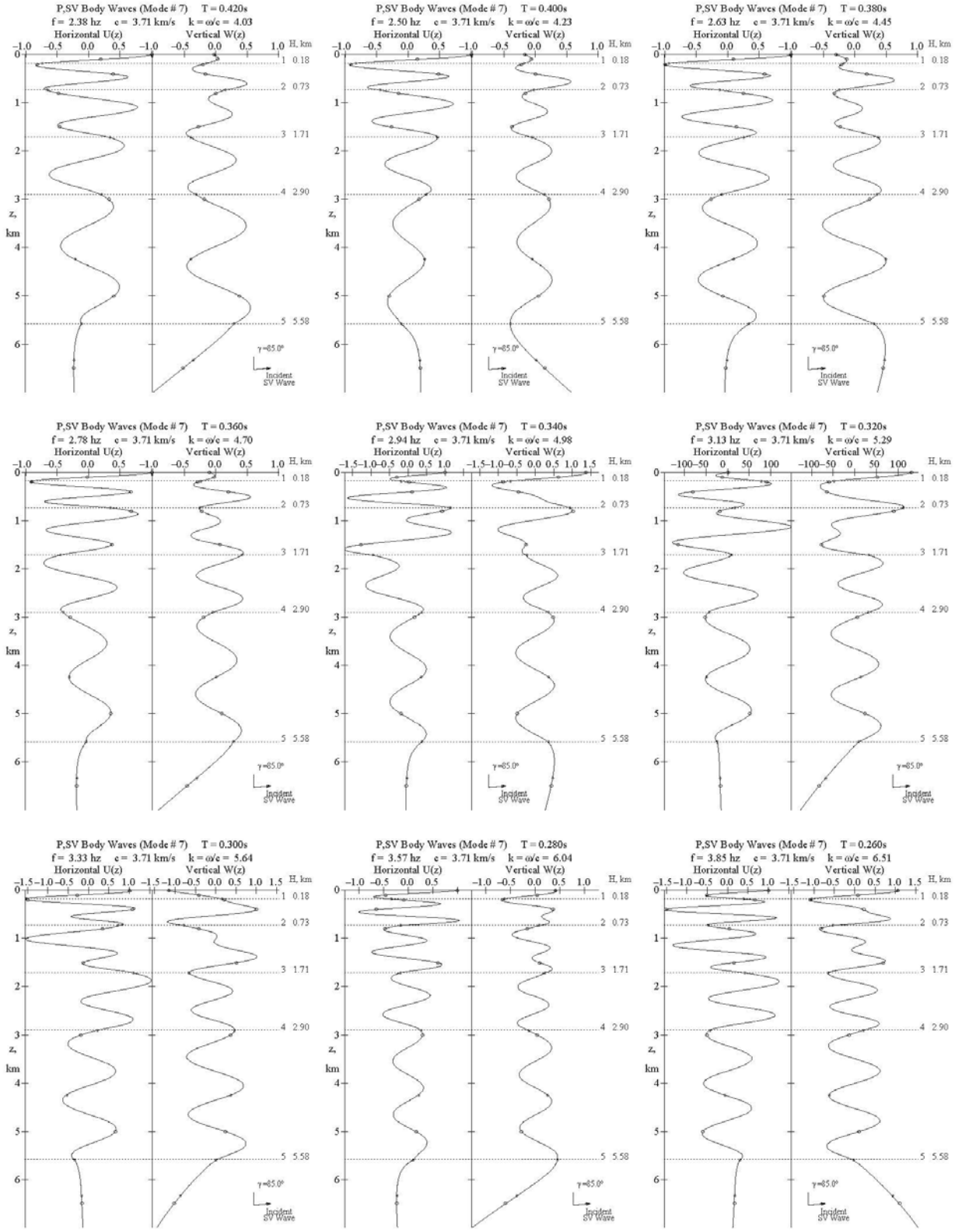

Fig. B-7.8 Body P, SV Waves (Mode#7), Page 8 of 11 T=0.24-0.14s

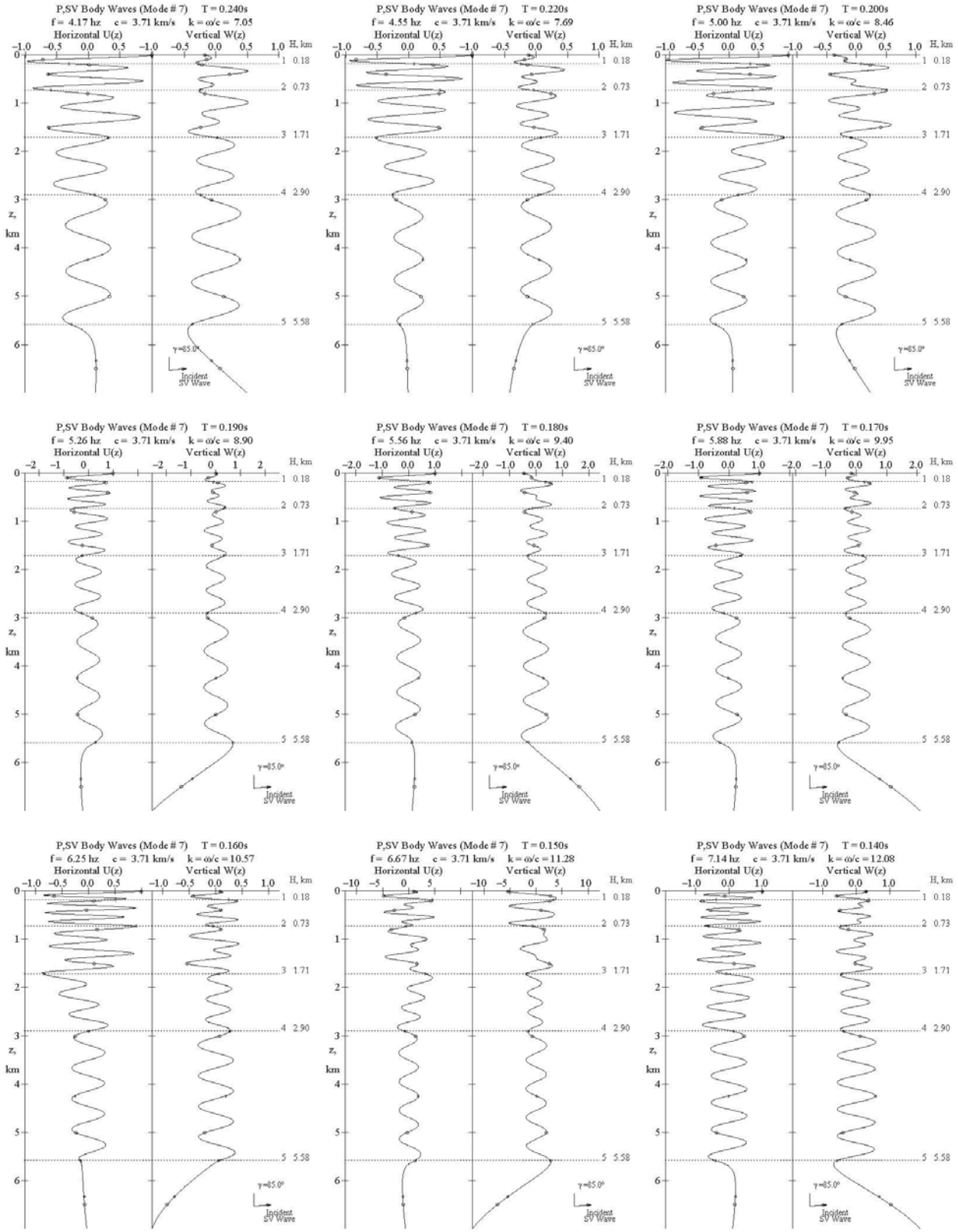

Fig. B-7.9 Body P, SV Waves (Mode#7), Page 9 of 11 T=0.130-0.075s

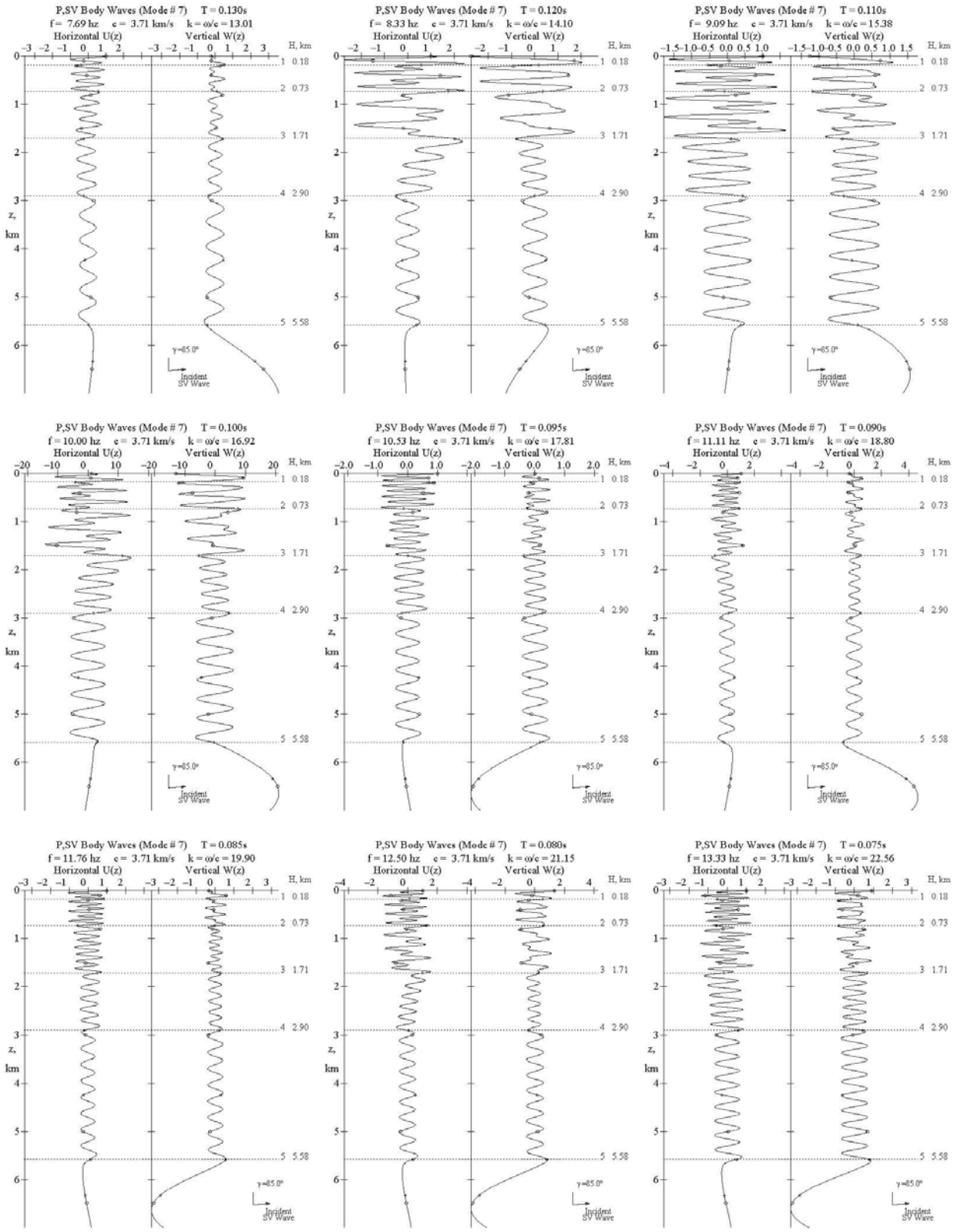

Fig. B-7.10 Body P, SV Waves (Mode#7), Page 10 of 11 T=0.070-0.042s

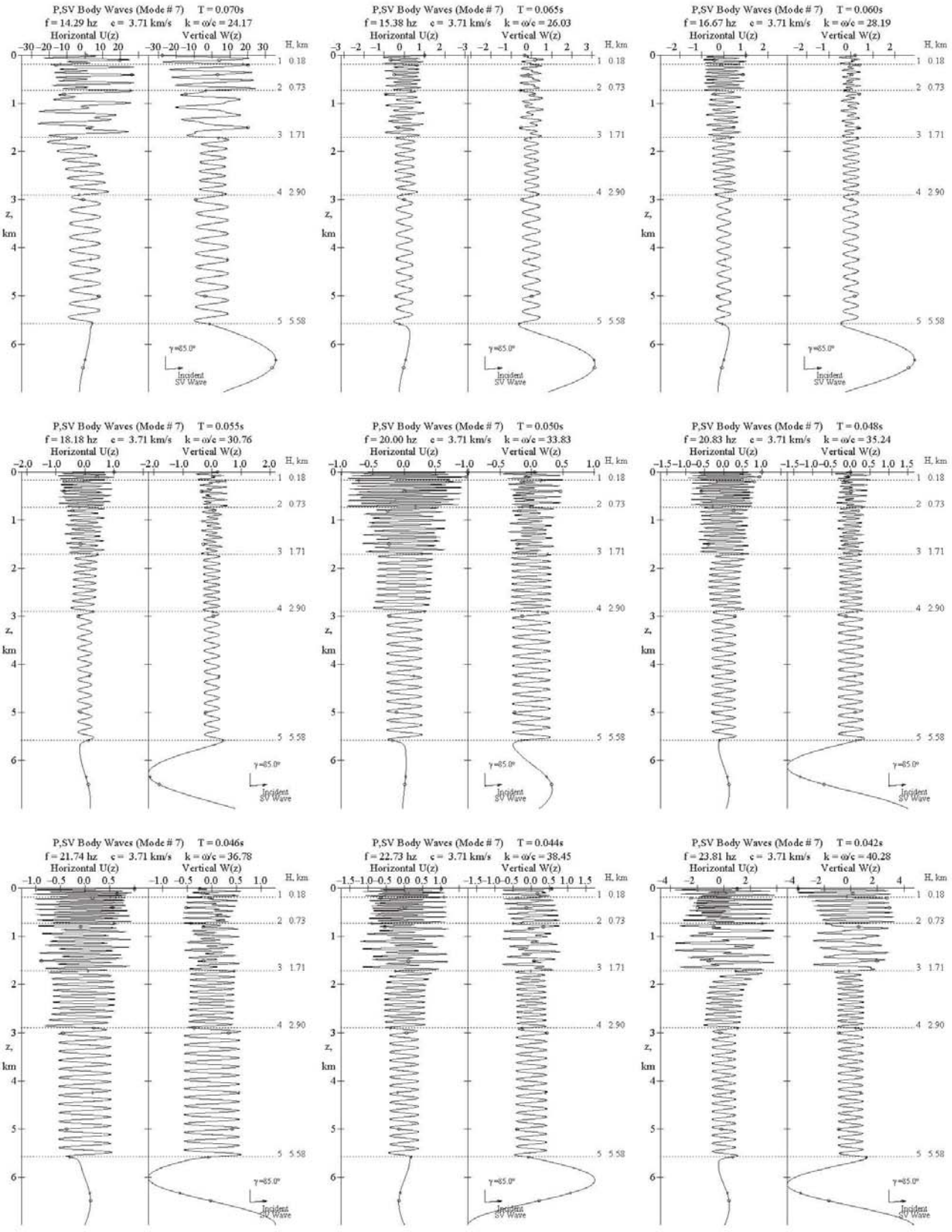

Fig. B-7.11 Body P, SV Waves (Mode#7), Page 11 of 11 T=0.040s

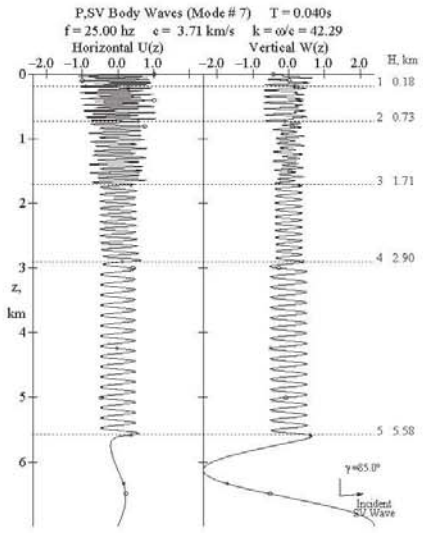

APPENDIX R3

(Reporting Date 12 February 2013)

REPORT No. III

Contract No.: 87055-11-0562
RSP Project ID (R525.1)

REPORTING DATE – 12 February 2013

PROJECT TITLE: Interfacing Seismological Description of Strong Ground Motion with Engineering Analysis of Soil Structure Interaction for Nuclear Power Plants

REPORT SUBMITTED BY: Structural and Earthquake Engineering Consultants (SEEC) Inc.
855 Arcadia Ave. #E, Arcadia, CA 91007 USA
Contact name: M. D. Trifunac
Phone: (626) 447-9382
Email: trifunac@usc.edu, misha.trifunac@gmail.com

to

Canadian Nuclear Safety Commission

ATTENTION: Nanci Laroche, Nebojsa Orbovic
280 Slater St., Ottawa, Ontario, Canada, K1P 5S9
E-mail: research-recherche@cnsc-ccsn.gc.ca
Nebojsa.Orbovic@cnsc-ccsn.gc.ca

Synthetic Rotational Motions of Surface and Body Waves On or Below an Elastic Layered Half-Space

Abstract

This, third report, Report #3, is a continuation of the Reports #1 and #2 (submitted 21 May and 12 September 2012 respectively). In Report #1 we presented the theory and verification examples of computing synthetic strong earthquake ground motion for an array of points on the surface of the layered half space. The Report #2 presented, theory and verification examples of how to extend the synthesizing of translational strong ground motion along a vertical array of points, into the depth of the layered half space. This Report #3 complements and completes the results of Report #2 by including formulation and methodology for computing rotational, strain and curvature components of motion. With these tools it is now possible to calculate all components of strong motion as input into a finite element or finite difference numerical "box", which can be used in time computations of earthquake response of complex linear and nonlinear soil structure interaction problems.

Collectively Reports #1, 2 and 3 present all results, which were planed for proposed tasks 4.1 through 4.7. The verification task 4.8 will be carried out interactively with the development of the work on tasks 4.9 and 4.10. It is necessary to run numerical simulations in the soil box to test and to refine further the details of the computed input motions. This work will be carried out during the remainder of 2013.

I. Synthetic Rotational Motions of Surface Waves in Layered Media at Points on the Half-Space Surface – A Review

I.1 Introduction

Observational and theoretical studies of strong ground motion in the late 1960's and 1970's showed that a typical strong motion record consists of near-field, intermediate-field, body and surface waves contributing different amounts to the total result, depending on the earthquake source mechanism and on the wave path (Trifunac, 1971a, 1971b; Trifunac, 1972a, 1972b; Trifunac, 1973). Empirical studies of spectral characteristics (Trifunac, 1976, 1979a, 1979b, 1993, 1994, 1995a, 1995b; Trifunac and Anderson, 1977; Trifunac and Lee, 1978, 1985) and frequency-dependent duration (Trifunac and Westermo, 1976a, 1976b; Trifunac and Novikova, 1994, 1995) have shown the nature of the dependence of strong motion on the geologic environment of the recording station. Consequently, realistic artificial accelerograms must have nonstationary frequency, amplitude and duration characteristics that agree with the trends present in the recorded accelerograms.

In choosing a suitable accelerogram for a particular engineering analysis, many factors must be taken into account, for example, the distance between the source and the site, the size of the earthquake, and the geology surrounding the site. The recorded accelerograms cannot be modified in a simple way to satisfy the requirements at all sites (Lee and Trifunac, 1989), and thus, site-dependent artificial synthetic accelerograms are needed.

Since the first strong-motion recording of the 1933 Long Beach Earthquake, during the following 80 years of strong motion observation, over several thousands of significant strong motion accelerograms have been recorded, processed and analyzed, in the US and in the rest of the world. This data represents invaluable collection of strong-motion records, and serves as a library for strong earthquake ground motion studies and research, but does not cover all cases of different recording conditions. For many engineering applications, it is often necessary to estimate future shaking at a site, with site conditions that are outside the range of parameters in

the available library of recorded data (Trifunac and Lee, 1987). This happens, in particular in those parts of the world where recorded data is limited or is not yet processed. This situation is common even today, after many years of strong motion observation (Lee and Trifunac, 2012).

Our previous report (Report 2, Lee and Trifunac, 2012) has shown how it is possible to estimate the strong-motion recordings at a site, not just at the ground surface, but also at points below the ground surface, as long as the site geology, and the physical properties of the layers bellow the site surface are known. The present report is a continuation, and extension of the previous report (Report 2, Lee and Trifunac, 2012), which described synthetic translational motions at and below the ground surface. This report deals with the rotational (torsion and rocking), strain and curvature components of strong ground motions at and below the ground surface. Those are constructed in conjunction with the synthetic translational motions. Further details of the theory and steps for the construction of the synthetic translational motions at depth in the layered half space can be found in the previous report ((Report 2, Lee and Trifunac, 2012), *which will subsequently in all following chapters be referred to as Report 2.*

I.2 The Total Translational Accelerogram

Recall that the total tranlsational accelerogram in Report 2 (Lee and Trifunac, 2012) is derived from the corresponding Fourier Transform of the translational motions, where, within the frequency band $\omega_n \pm \Delta\omega_n$, the $m-th$ mode of surface waves, it is assumed to have a Fourier transform

$$A_{nm}(\omega) = \begin{cases} \frac{\pi}{2} \mathbf{A}_{\mathbf{nm}} e^{-i\left[(\omega-\omega_n)t^*_{nm}+\phi_n\right]} & |\omega-\omega_n| \le \Delta\omega_n \\ \mathbf{0} & \mathbf{otherwise} \end{cases} \qquad \text{Report 2 (1.2)}$$

$$A_{nm}(-\omega) = A^*_{nm}(\omega)$$

where the phase ϕ_n is assumed to be a random number in the interval $[-\pi, \pi]$, and $t^*_{nm}(R) = R/U_m(\omega_n)$ is the arrival time of the $m-th$ mode at frequency ω_n, with R the epicentral distance from the source to site, and $U_m(\omega_n)$ is the group velocity of the $m-th$ mode of surface waves (for $m = 1$ to 10), or the corresponding wave speed of the body waves (for

$m = 11$ to 13). The $\mathbf{A}_{nm}$ is the relative amplitude of each mode at each band contributing to the total waves, as given by Equation (1.4) in Report 2.

From Report I , Lee and Trifunac, 2012: Figure I.2

Figure 1 Synthetic Translational Accelerogram Time Histories

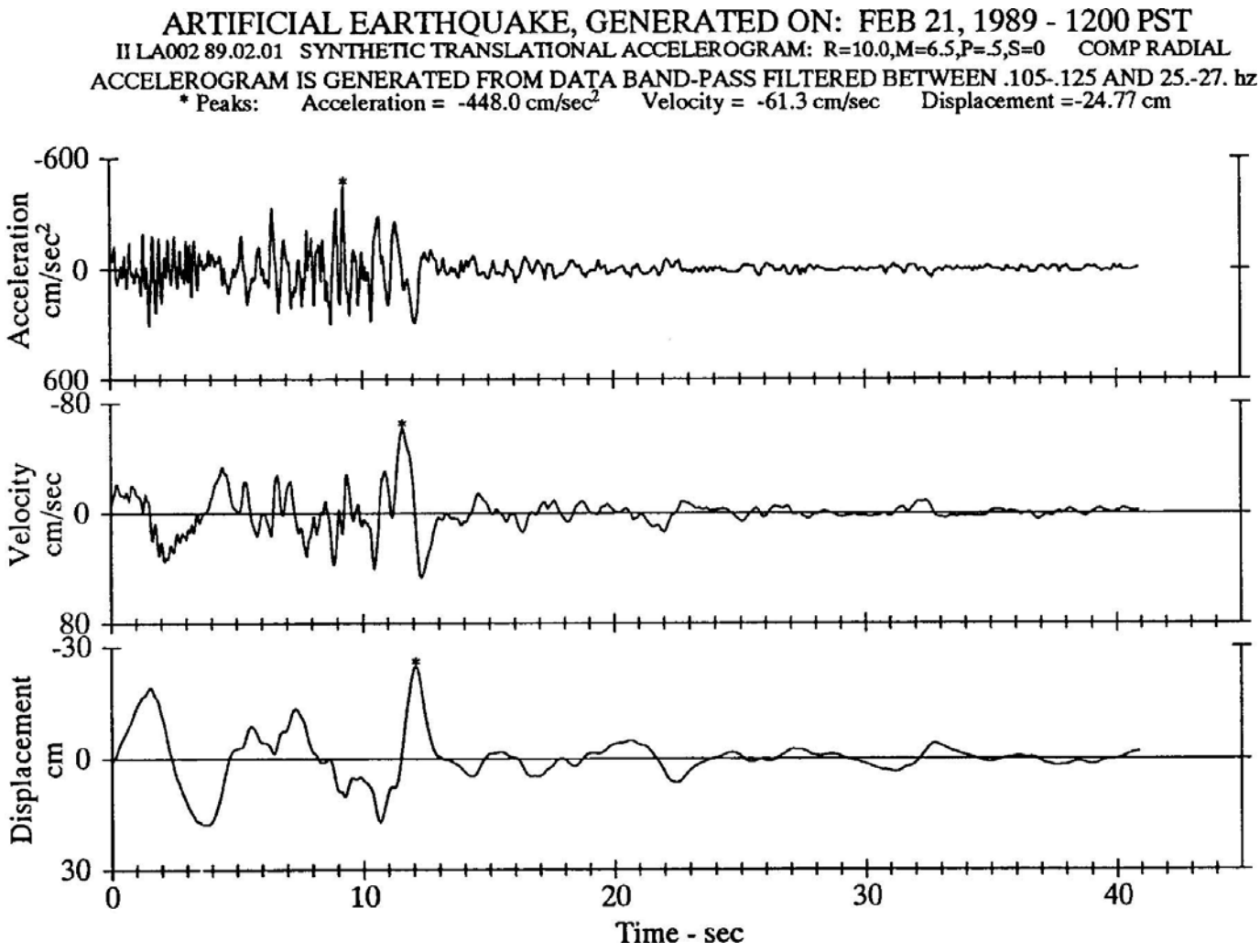

The inverse transform of Report 2 equation (1.2) is given by

$$a_{nm}(t) = \frac{1}{2\pi}\int_{-\infty}^{\infty} A_{nm}(\omega) e^{i\omega t} d\omega \qquad \text{Report 2 (1.3a)}$$

which can be calculated to be

$$a_{nm}(t) = \mathrm{A_{nm}} \frac{\sin \Delta\omega_n \left(t - t^*_{nm}\right)}{\left(t - t^*_{nm}\right)} \cos\left(\omega_n t + \phi_n\right) \qquad \text{Report 2 (1.3b)}$$

From this the total translational accelerogram is expressed as

$$a(t) = \sum_{n=1}^{N} a_n(t) = \sum_{n=1}^{N} \delta_n \sum\nolimits_{m=1}^{M} a_{nm}(t) \qquad \text{Report 2 (1.6)}$$

where N is the total number of frequency bands, with frequencies within $\omega_n \pm \Delta\omega_n$ at each band. δ_n is the scaling factor used to determine the final amplitude of the waves at each of the frequency bands. Equation (1.6) can further be written as

$$a(t) = \sum_{n=1}^{N} \delta_n \left(\sum_{m=1}^{M} \mathrm{A_{nm}} \frac{\sin \Delta\omega_n \left(t - t^*_{nm}\right)}{\left(t - t^*_{nm}\right)} \cos\left(\omega_n t + \phi_n\right) \right) \qquad \text{Report 2 (1.7)}$$

Figure 1 above (from Figure **I.2 of Report 2)** is an example of one such synthetic translational accelerogram, taken to represent an earthquake from the El Centro in Imperial Valley of magnitude $M = 6.5$, at a site with site condition $S = 0$ and an epicicentral distance of $R = 10km$.

I.3 The Torsional and Rocking Accelerorams

The importance of torsional and rocking excitations has been shown by the studies of Dravinski and Trifunac (1979, 1980), Kobori and Shinozaki (1975), Luco (1976), Bielak (1978), Lee (1979), Gupta and Trifunac (1987, 1988, 1990a, 1990b, 1990c, 1991), Todorovska and Lee (1989), and Todorovska and Trifunac (1989, 1990a, 1990b, 1992, 1993). With the slow development of strong-motion instruments that record rotational components of strong motions (Hudson, 1983a.b; Trifunac and Todorovska, 2001), it became necessary to explore the possibility of estimating those in terms of the corresponding translational components of strong shaking.

By considering the horizontal propagation of plane waves with constant velocity C, Newmark (1969) estimated the contribution to the displacements of a building foundation,

resulting from torsional earthquake ground motions. Tso and Hsu (1978) used a similar approach, in addition to assuming that the motions also included plane non-dispersive waves. Nathan and MacKenzie (1975) discussed the possible averaging effects of foundation sizes on the resulting torsional excitations of buildings. These investigations, however, failed to consider the dependence of the phase velocity on the frequencies of the incoming Love waves. Their assumption that the incoming waves are of constant phase velocity at all frequencies makes their results useless. Lee and Trifunac (1985) included the effects of wave dispersion and transient arrivals in the estimation of torsional accelerograms in an elastic layered half-space. The earlier work of Trifunac (1982) in calculating the torsional component of incident plane SH-waves was extended to enable the calculation of torsion from surface Love waves. With this, Lee and Trifunac (1985) included the effects of wave dispersion and transient arrivals in the estimation of torsional accelerograms in an elastic layered half-space.

For the m-th mode of the surface Love waves at frequency ω, within the frequency band $\omega_n \pm \Delta\omega_n$, the Fourier transform of the torsional motion, $\Psi_{nm}(\omega)$, is related to that of the horizontal translational (anti-plane) motion of Love waves, $H_{nm}(\omega)$, by the ratio (Lee and Trifunac, 1985):

$$\frac{\Psi_{nm}(\omega)}{H_{nm}(\omega)} = \frac{-i\omega}{2c_{nm}} \tag{1}$$

where $c_{nm} = c_m(\omega_n)$ is the Love-wave phase velocity of the m-th mode at frequency $\omega = \omega_n$.

With the Foruier transform of torsion defined, its time histories can next be calculated. **Figure 2** is a plot of the Torsional acceleration, velocity and displacement at the same site as the corresponding translational motions in Figure 1. The units of Torsional acceleration, velocity and displacement are respectively

$$rad/sec^2,\ rad/sec \text{ and } rad \text{ all } \times 10^{-5}$$

In exactly the same way, for the m-th mode of the surface Love waves at frequency ω within the frequency band $\omega_n \pm \Delta\omega_n$, the Fourier transform of the rocking motion, $\Phi_{nm}(\omega)$, is related to that of the vertical motions of Rayleigh Loves, $V_{nm}(\omega)$, by the ratio (Lee and Trifunac, 1987):

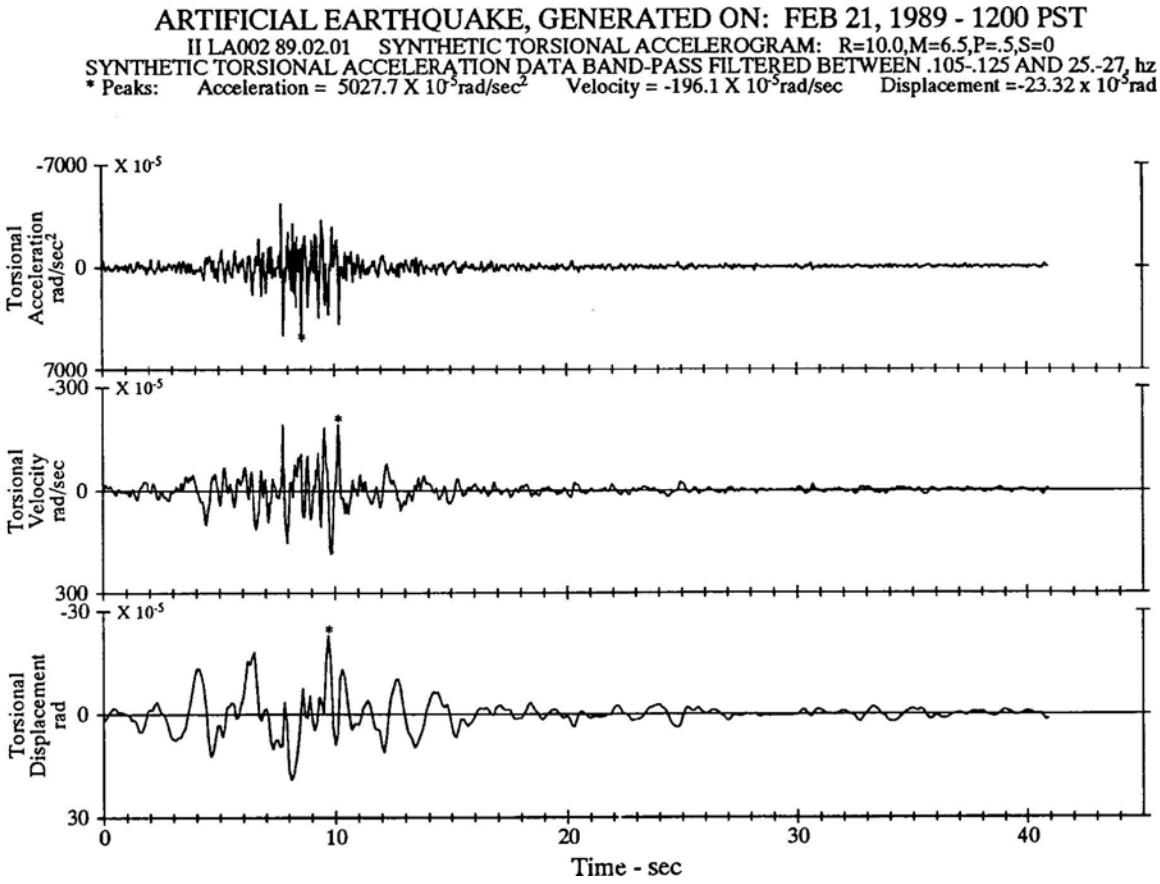

Fig.2 Artificial earthquake synthetic torsional accelerogram

$$\frac{\Phi_{nm}(\omega)}{V_{nm}(\omega)} = \frac{i\omega}{c_{nm}} \tag{2}$$

from which the rocking time histories can be constructed. **Figure 3** is a plot of the rocking acceleration, velocity and displacement at the same site as the corresponding translational motions in Figure 1.

Recently, Lee and Trifunac (2009) developed an alternate simple approximate algorithm for generating torsional and rocking Fourier spectral amplitudes from that of the corresponding translational accelerograms. Inverse Fourier transform can then be used to generate the rotational

torsion and rocking time histories. In short, algorithms exist for generating synthetic rotational torsion and rocking accelerograms from both synthetic or from actually recorded accelerograms.

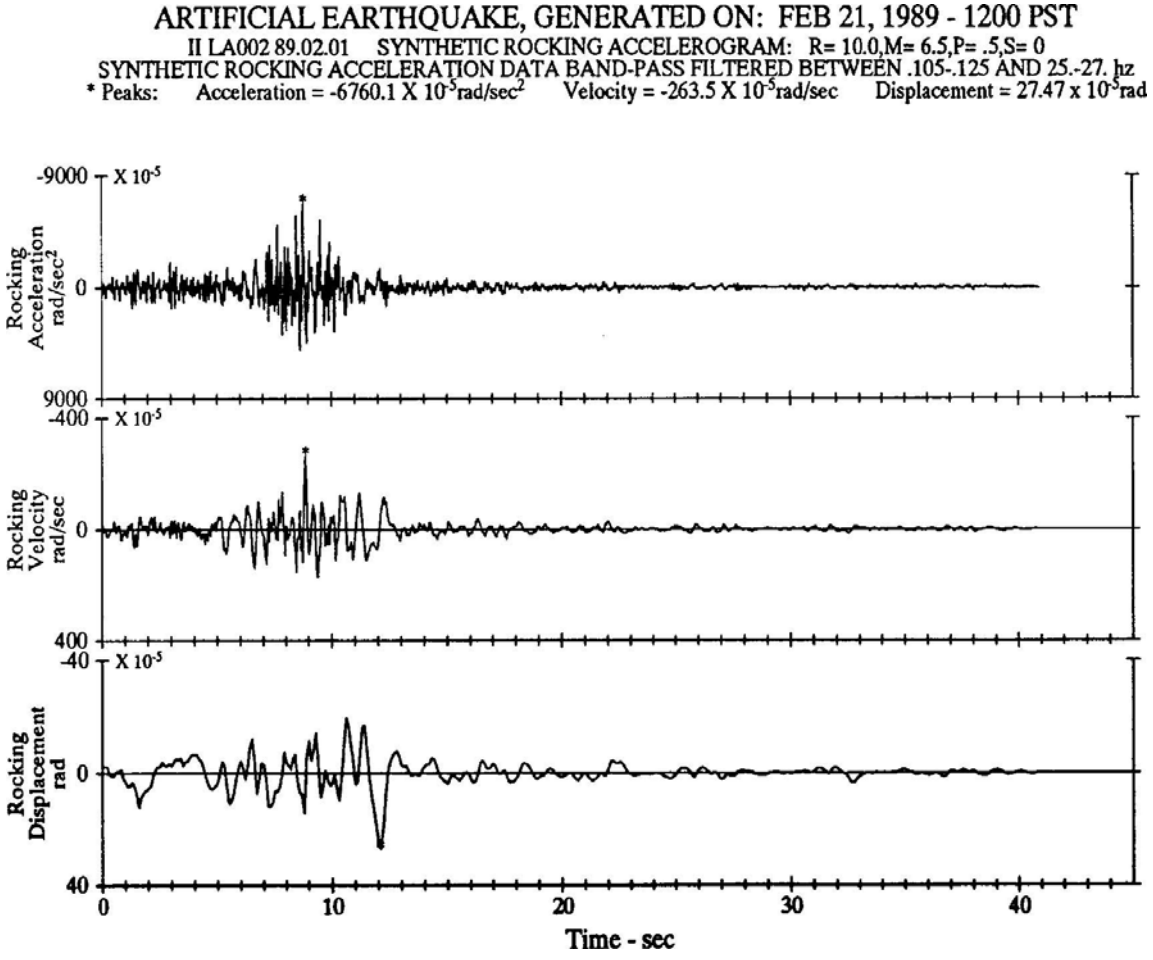

Fig.3 Artificial earthquake synthetic rocking accelerogram

I.4 The Synthetic Surface Strains

Next we consider the estimation of surface strains associated with strong earthquake motions related to the translational components of body and surface Rayleigh and Love waves at the half-space surface. Studies of earthquake-induced damage to engineered structures show that there are cases of damage, which result from the differential motions caused by large strains associated with ground shaking (Trifunac, 1979b, 1997). In some cases, these strains are

superimposed on the dynamic response, and only contribute to the resultant total response. In other cases, when the characteristic frequencies of the system differ from the principal frequency content of strong motion, these local strains may affect the structural systems in a quasi-static manner. Long underground pipelines and railroad tracks may buckle, and bridges may collapse because of the excessive differential support motions, due to excessive local strains associated with earthquake ground shaking (Trifunac and Todorovska, 1997a, 1997b; Trifunac et al., 1996). Studies of the responses of long structures excited by ground shaking (Kojić et al., 1988; Todorovska and Trifunac, 1989, 1990a, 1990b; Trifunac and Todorovska, 1997a) have demonstrated the need for detailed description of motions at various points of single (or multiple) foundation(s), with emphasis on the differential motions associated with large surface strains.

Expressions for surface strains were first described for incident ***P, SV*** and ***SH*** body waves (Trifunac, 1979b), and later extended to Rayleigh and Love surface waves (Lee, 1990). Again, the m-th mode of acceleration of horizontal (in-plane) motion, $\ddot{u}_1$ for Rayleigh waves has Fourier Transform within the frequency band $\omega_n \pm \Delta\omega_n$ given by $H_{nm}(\omega)$, and the corresponding Fourier transform of the m-th mode of surface strains, $\mathbf{E_{11,nm}(\omega)}$ and $\mathbf{E_{22,nm}(\omega)}$ in the same frequency band $\omega_n \pm \Delta\omega_n$ are given by (Lee, 1990):

$$\begin{aligned} \mathbf{E_{11,nm}(\omega)} &= = \frac{-i}{\omega c_{nm}} H_{nm}(\omega) \\ \mathbf{E_{22,nm}(\omega)} &= = \frac{-i}{\omega c_{nm}} \left(\frac{2}{(\alpha/\beta)^2} - 1 \right) H_{nm}(\omega) \end{aligned} \tag{3}$$

where $c_{nm} = c_m(\omega_n)$ is the Rayleigh-wave phase velocity of the m-th mode at frequency $\omega = \omega_n$. Similarly, with Fourier Transform of the m-th mode of acceleration of horizontal (anti-plane) motion, $\ddot{u}_3$ for Love waves within the frequency band $\omega_n \pm \Delta\omega_n$ given by $H_{nm}(\omega)$, the corresponding Fourier transform of the m-th mode of surface strains, $\mathbf{E_{13,nm}(\omega)}$ in the same frequency band $\omega_n \pm \Delta\omega_n$ is given by (Lee, 1990):

$$\mathbf{E_{13,nm}(\omega)} = = \frac{-i}{2\omega c_{nm}} H_{nm}(\omega) \tag{4}$$

where $c_{nm} = c_m(\omega_n)$ is the Love-wave phase velocity of the m-th mode at frequency $\omega = \omega_n$. Equations (3) and (4) enable the Fourier transform of all 3strain components and the corresponding time histories to be generated.

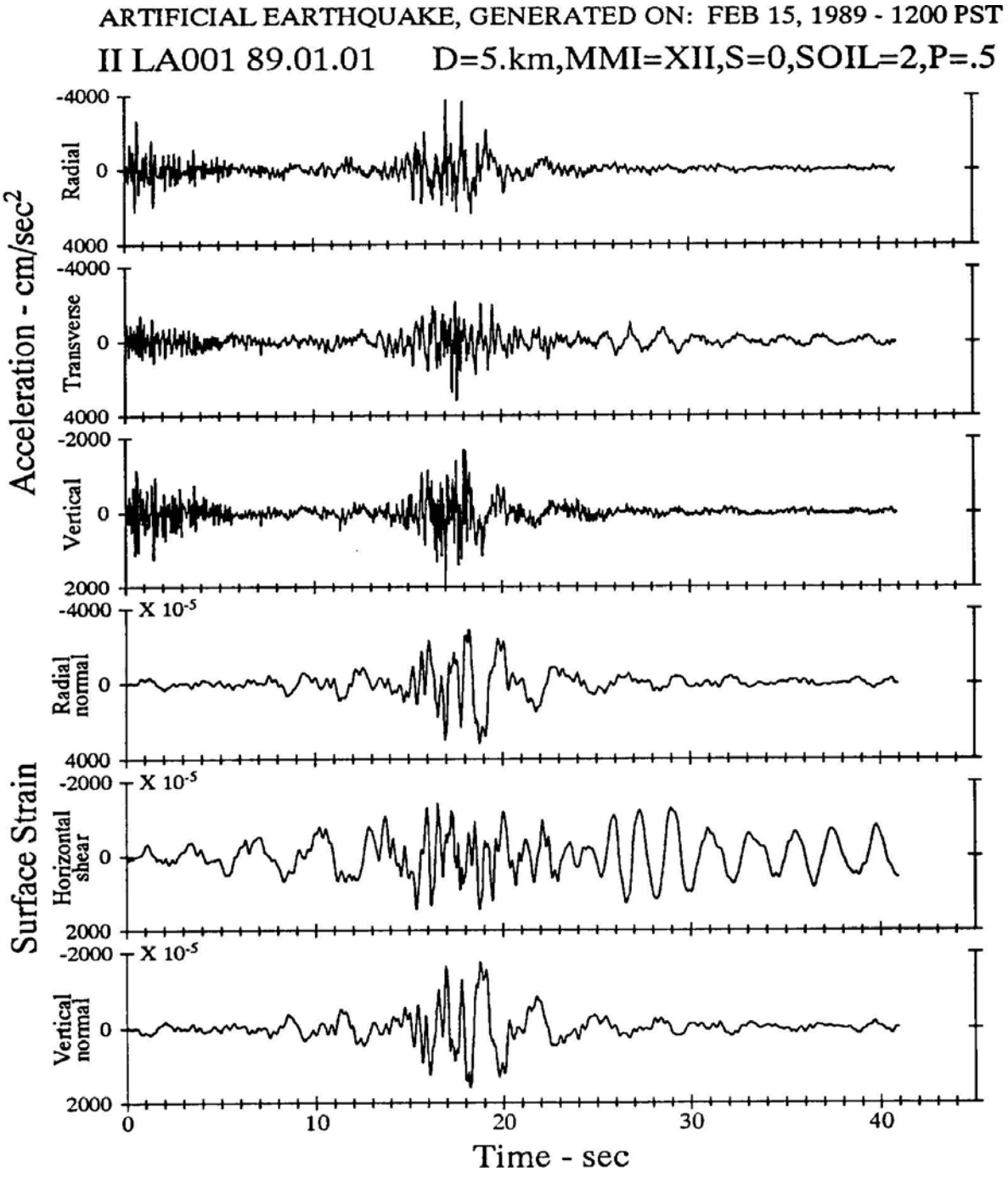

Fig.4 Artificial earthquake synthetic translation & surface strain accelerograms

To illustrate the effect of "large" strains, we modify the Westmoreland soil site model in Imperial Valley (Lee, 1990) to have a 50 m layer with shear wave velocity of 50 m/s (was 980m/s) at the top, and a second 130 m layer with shear wave velocity of 300 m/s. For depths greater than 180 m, we adopt the material properties as in the old Imperial Valley Site model, which was considered in many of our previous examples on synthetic motions. As a result, for short periods, the phase and group velocities would be reduced from 0.98 km/s to 0.05 km/s. Thus modified site will exemplify "soft" soil and geologic conditions in which the strains can be "large". We also consider large amplitudes of strong shaking, in the immediate vicinity of the epicenter.

Figure 4 presents an example computed for the site intensity, **MMI =XII**, source at epicentral distance of $R = 5\text{km}$ for s = 0 (site on alluvium) and $s_L = 2$ (deep soil site), and for p = 0.5, where p is the probability of exceedance for the empirically computed spectrum (Trifunac, 1989a, 1989b). These conditions result in peak accelerations (37.3 m/s^2 for radial, 31.9 m/s^2 for transverse, and 18.5 m/s^2 for vertical ground motions) larger than what has been recorded so far, and thus illustrate extreme response amplitudes and the associated strains. The resulting peak strains are, respectively, 0.03, 0.01 and 0.02. Because the strains are proportional to ku (=ωu/c), the overall appearance of strain versus time is similar to that of the ground motion velocity.

I.5 The Synthetic Curvograms

Next we will describe the synthetic curvograms of earthquake ground motions.

Analyses of the effects of strong earthquake shaking on engineered structures are typically only performed for dynamic forces that result from strong motion accelerations. However, pseudo-static deformations that result from wave passage under long structures may also contribute forces, which, in certain cases, may be larger than the dynamic forces (Kojić et al., 1988; Todorovska and Lee, 1989; Todorovska and Trifunac, 1989, 1990a, 1990b). Such loadings and the resulting response of structures depend on the nature of ground waves, inhomogeneities in the soil, sediments or rock under the foundation, the surface topography near

structure, and on the nature of the structure-foundation system.

For ground waves that are long relative to the plan dimensions of a structure, it is possible to describe the strong ground motion in terms of the translational and rotational components of ground motion (Gupta and Trifunac, 1987, 1988; Lee and Trifunac, 1985, 1987; Trifunac, 1982). For short ground waves with wavelengths comparable to or shorter than the structural dimensions, the details of the wave passage analysis must be worked out to obtain realistic response analyses (Kojić et al., 1988; Todorovska and Trifunac, 1990b).

This is illustrated in **Figure 5**, which shows the plane view of a rectangular foundation deformed into bending by the passing ground wave. Since the significance of such a deformation for structural response can be evaluated with sufficient accuracy, if the radius of curvature of ground deformation is known, in this section, we describe a method for evaluating the curvograms (plots of curvature versus time) on ground surface. Trifunac (1990) extended the method for generation of synthetic translational (Trifunac, 1971b; Wong and Trifunac, 1978, 1979), rocking (Lee and Trifunac, 1987), torsional (Lee and Trifunac, 1985) accelerograms, and strain (Lee, 1990) time histories, to obtain curvograms of strong motion.

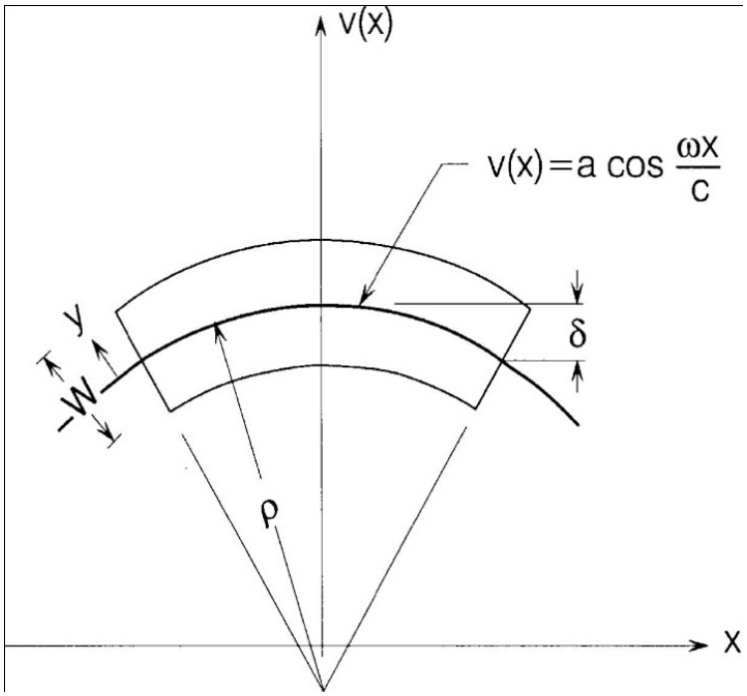

Fig.5 Curvature

Let x_1, x_2 and x_3 be the radial, vertical and transverse coordinates. Let c be the apparent phase velocity of wave motion in the radial x_1-direction. Let u_1, u_2 and u_3 be the displacements in the x_1, x_2 and $x_3$directions. It can be shown that the curvature in the vertical plane, $k_2(t)$, is (Trifunac, 1990):

$$k_2(t)=\frac{\partial^2 u_2/\partial x_1^2}{\left[1+\left(\partial u_2/\partial x_1\right)^2\right]^{3/2}} \approx \partial^2 u_2/\partial x_1^2 = \frac{\ddot{u}_2}{c^2} \quad \textbf{(vertical)} \tag{5a}$$

Likewise (Trifunac, 1990):

$$\begin{aligned} k_3(t) &\approx \partial^2 u_3/\partial x_1^2 = \frac{\ddot{u}_3}{c^2} && \textbf{(transverse)} \\ k_1(t) &\equiv 0 && \textbf{(radial)} \end{aligned} \tag{5b}$$

The above equations show that, with $A_{nm}(\omega)$ the translational components of m-th mode of surface (Rayleigh or Love) waves within the frequency band $\omega_n \pm \Delta\omega_n$, the corresponding Fourier component of curvature is

$$K_{nm}(\omega)=\frac{A_{nm}(\omega)}{C_{nm}^2} \tag{6}$$

where, as before, C_{nm} is the phase velocity of the m-th mode of surface waves within the frequency band $\omega_n \pm \Delta\omega_n$. Combining all modes and frequencies again gives the total Fourier transform, and hence the time histories of curvatures.

Figure 6 shows an example, considering a site with earthquake MMI intensity = *XII* from a source at distance of *R = 5 km*. The site again is assumed to be on sediments (s = 0) and $S_L = 2$ (stiff-soil site conditions). As in the strain case, we picked the West Moreland site in Imperial Valley by modifying the top layer to consist of two 'soft' layers of thickness 50m and 130m and with shear wave velocities of 50 and 300 m/s respectively. Figure 6 plots the resulting radial, transverse and vertical accelergrams, together with the associated transverse and vertical curvograms. The smallest radii of curvature corresponding to $k_{2,\max}=0.46\times10^{-4}cm^{-1}$ and $k_{3,\max}=0.68\times10^{-4}cm^{-1}$, with the corresponding radii of curvatures being $\rho_{2,\min}=217m$ and $\rho_{3,\min}=147m$.

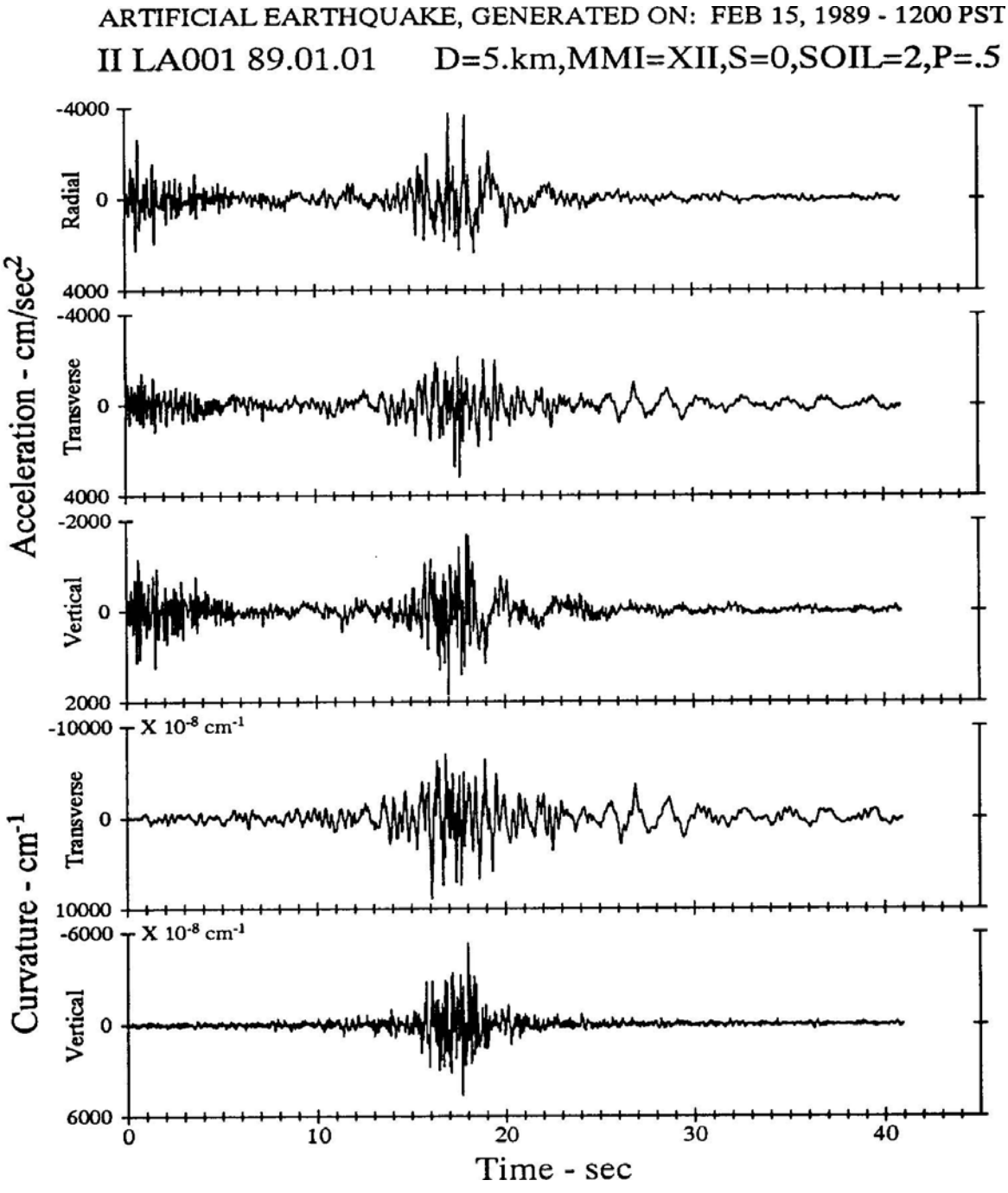

Fig.6 Artificial earthquake synthetic accelerogram and curvature accelerogram

With this, a comprehensive method for synthesizing realistic strong motion accelerograms

(translations and rotations), strains and curvatures at the surface of a layered half-space has been reviewed. The advantages of this method are that the results are consistent with all known characteristics of the recorded strong shaking. In particular, these accelerograms (translations and rotations, strains and curvatures) all have non-stationary characteristics in time, which are derived from the known dispersive properties of earthquake waves, guided through shallow low-velocity layers of the earth crust.

These dispersive characteristics can be introduced directly as an input into the computer program, and thus can portray directly the geologic environment of each specific site. Other scaling functionals, required for the synthesis of artificial accelerograms presented here, are: (i) the Fourier amplitude spectrum, and (ii) the frequency-dependent duration of strong shaking. These two functionals can be estimated via the empirical scaling relations developed either in terms of earthquake magnitude or in terms of Modified Mercalli Intensity.

It has been shown how the rocking and torsional accelerograms can be generated from the synthetic translational accelerograms, by applying the straightforward exact physical principles of elastic wave propagation. The rotational accelerograms obtained in this way have realistic physical properties, and should resemble actual rotational ground motions, as long as the synthetic translational accelerograms, from which those are derived, have such corresponding physical properties.

Using the linear theory of wave propagation, the strain amplitudes can be evaluated exactly in three-dimensions. When local geologic conditions are too complex to model near-surface motions by the equivalent parallel layer models, the method presented here can be modified to give realistic representation of near-surface translations, rotations, and strains (e.g., see Moeen-Vaziri and Trifunac (1988a, 1988b)).

The above example (Lee, 1990) in **Figure 4** illustrates the strain amplitudes implied by the linear theory of wave motion, and can be taken to represent “average” or “typical” estimates, for magnitudes, site intensities, or local conditions considered. In general, the strain amplitudes will increase with an overall increase in the strong motion amplitudes, and with a decrease in shear wave velocities of soil and sedimentary layers near the ground surface. Time- dependence

of strain components near the ground surface is roughly proportional to the corresponding components of ground velocity, and thus, peak strains will also increase with peak ground velocity.

Finally, the above example (Trifunac 1990) in Figure 7 shows that the radii of curvature in the range of one to several hundred meters may occur for very large accelerations (1-3 g), near epicenter, and when the local soil and geologic conditions are characterized by low wave velocities (e.g., 50 m/s). Such conditions correspond only to the instances of exciting very large amplitudes of waves with short wave lengths, and can be expected to occur for soft soil and geologic site conditions near epicenters of earthquakes with high stress drop.

II. Synthetic Rotational Motions of Surface and Body Waves in and Below a Layered Medium

With the Surface and Body waves defined on and below the surface of a layered medium in Report 2, in this chapter we extend the representations of those waves to include the rotational (torsion and rocking), strain and curvature components of motion. We begin with a brief review of the translational waves from Report 2.

II.1 Synthetic Translational Motions of Love and Body SH Waves On and Below a Layered Medium – a Brief Review

Let $c = c(\omega)$ be the wave speed of a mode of Love waves in the half-space with n elastic layers over half space. c is also the (horizontal) phase velocity of the waves in each layer of the elastic media above the half space (Figure **II.1**)

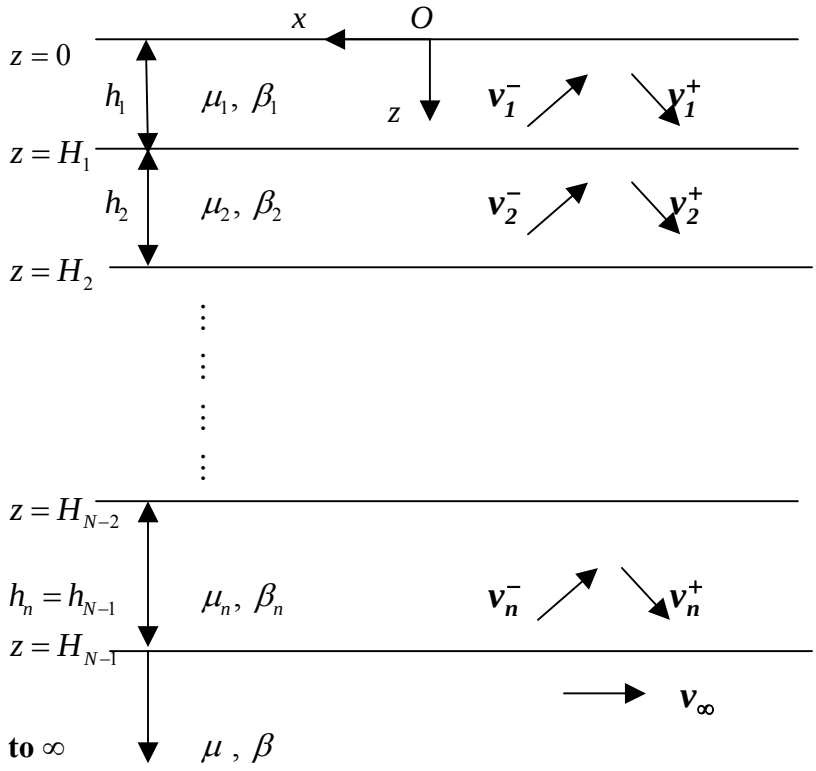

Figure II.1 *N*-layered half-space with Love waves

(From Figure II.1 of Report 2)

For each layer l, with $l = 1, \ldots, N$, the displacement of the Waves in the layer take the form (in the anti-plane, y-component direction):

v_1^-, v_1^+ :

$$v_l^- = C_l^- e^{ik(x-\gamma_l z)}$$
$$v_l^+ = C_l^+ e^{ik(x+\gamma_l z)} \qquad \textbf{Report 2 (2.1)}$$

Those are respectively the upward and downward Love waves present in the l^{th} layer. Here $k = k(\omega) = \omega / c(\omega)$ is the horizontal wave number of the waves at frequency ω and with phase velocity $c = c(\omega)$. The term e^{ikx}, which is also the same in each layer, is the horizontal component of the waves, which together with the time harmonic term $e^{i\omega t}$, corresponds to the waves propagating in the ***–ve*** x direction. The terms $e^{\mp ik\gamma_l y}$ are the vertical components of the waves with the ***negative*** term propagating upwards (***–ve*** y) and the ***positive*** term propagating downwards (y). Here $\gamma_l = \gamma_l(\beta_l)$ is given by

$$\gamma_l = \frac{\left(k_{\beta_l}^2 - k^2\right)^{1/2}}{k} = \left(\left(k_{\beta_l}/k\right)^2 - 1\right)^{1/2} = \left(\left(c/\beta_l\right)^2 - 1\right)^{1/2} \qquad \textbf{Report 2 (2.2)}$$

so that $k\gamma_l$ is the vertical wave number of the waves in the l^{th} layer of the medium with shear wave velocity β_l. In general, the wave velocities increase as one moves down through the layers, so that $\beta_1 < \beta_2 < \ldots < \beta_n < \beta$, with the semi-infinite half-space layer at the bottom having the highest shear wave speed β. With $c = c(\omega)$ the wave speed of the surface Love waves there, $c < \beta$, and the surface waves take the form:

$$v_\infty = C_\infty e^{ik(x-\gamma z)} = C_\infty e^{ikx - k\bar{\gamma} z} \qquad \textbf{Report 2 (2.3)}$$

where
$$\bar{\gamma} = \frac{\left(k^2 - k_\beta^2\right)^{1/2}}{k} = \left(1 - \left(k_\beta/k\right)^2\right)^{1/2} = \left(1 - \left(c/\beta\right)^2\right)^{1/2} \qquad \textbf{Report 2 (2.4)}$$

$\bar{\gamma}$ is the complement of γ and is real, so that the term $e^{ikx - k\bar{\gamma} y}$ in C_∞ corresponds to a surface wave term whose amplitude is exponentially decaying with depth (in y) below the surface.

The coefficients C_l^-, C_l^+, respectively of the waves, w_l^-, w_l^+, in each layer ***l***, for l = **1** to **n**, are all related by the stress and displacement boundary conditions, as given in Chapter II of Report 2 and will not be repeated here.

For the case of body ***SH*** waves incident from the semi-infinite medium, we will consider the model in Figure II.2. It is the same N-layered media model as in Figure II.1, for the case of Love surface waves, but now the waves in all layers are body waves.

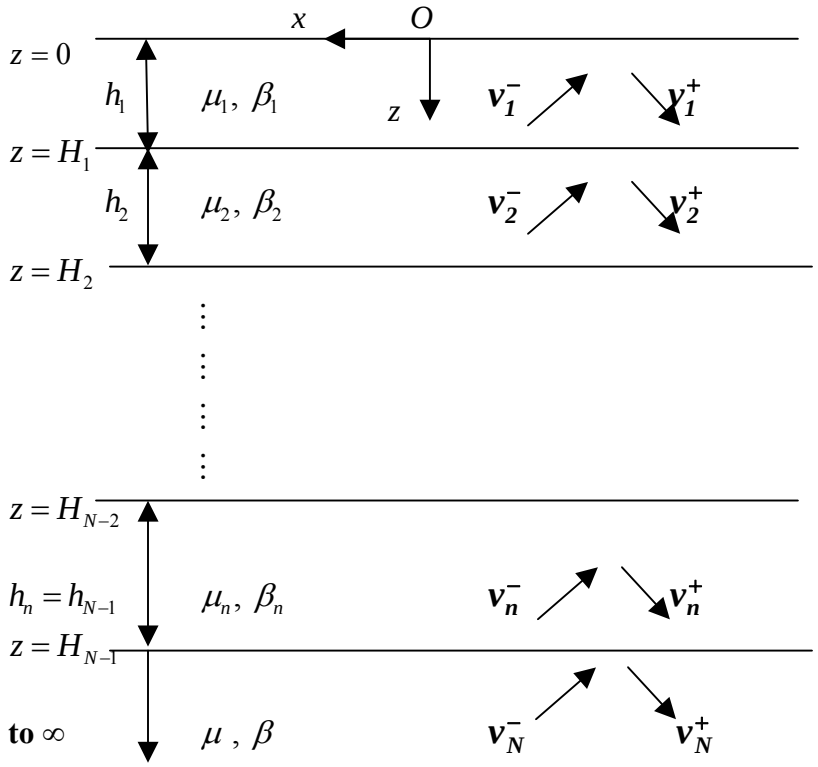

Figure II.2 n-layered half-space with incident body SH waves
(From Figure II.2 of Report 2)

The body ***SH*** waves in all layers have a common constant phase velocity c, now independent of frequency ω, and dependent only on the incident angle of the body SH waves. It is higher than $\beta_{max} = \beta_N$, the shear wave speed at the bottom semi-infinite N^{th} layer.

The wave $v_N = v_\infty$ in the bottom semi-infinite layer will also be replaced by the waves v_N^- and v_N^+, respectively the incident and reflected body SH waves:

$$v_N^-,\ v_N^+ : \qquad \begin{aligned} v_N^- &= C_N^- e^{ik(x-\gamma_N z)} = C_N^- e^{-ik\gamma_N z} e^{ikx} \\ v_N^+ &= C_N^+ e^{ik(x+\gamma_N z)} = C_N^+ e^{+ik\gamma_N z} e^{ikx} \end{aligned} \qquad \textbf{Report 2 (2.15)}$$

as in all the other layers $l = 1,\ 2,\ \ldots,\ N-1$ (Equation (2.1) above).

II.2 Synthetic Translational Motions of Rayleigh and Body P and SV Waves On and Below Surface of a Layered Medium – a Brief Review

We begin by a brief review from Chapter III of Report 2, and let $c = c(\omega)$ be the phase velocity of a mode of Rayleigh waves in the half-space with N elastic layers. c is also the (horizontal) phase velocity of both the P- and SV-waves in each layer of the elastic media above the half space such that $c < \beta_{\max} = \beta_N$, the shear wave speed at the bottom semi-infinite N^{th} layer (Figure II.3):

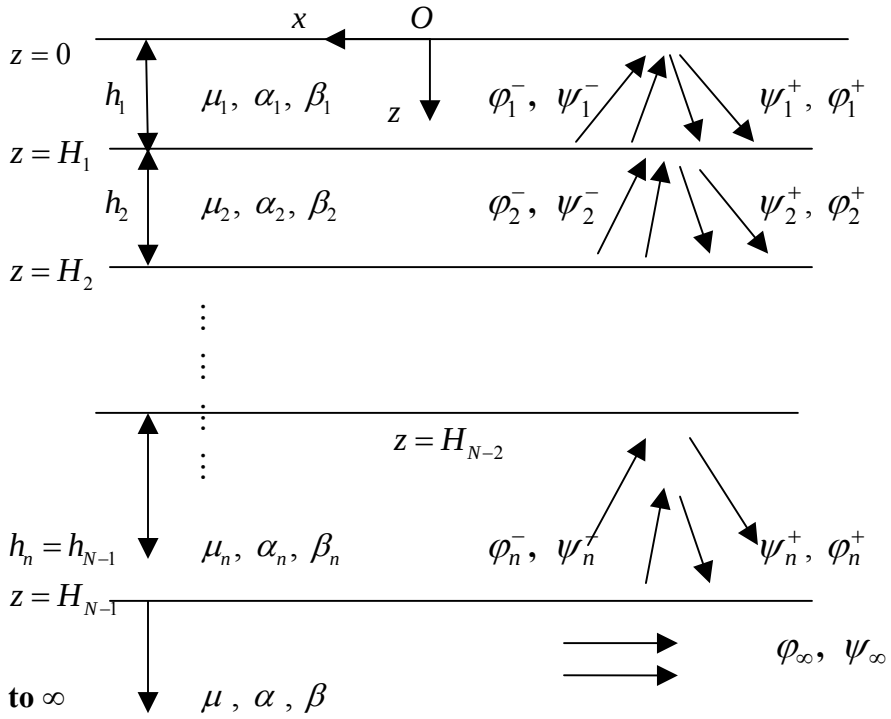

Figure II.3 N-layered half-space with Rayleigh waves

(From Figure III.1 of Report 2)

For each layer l, with $l = 1, \ldots, N$, the ***P***- and ***SV***-Waves in the layer respectively take the form:

$\varphi_l^-, \varphi_l^+, \psi_l^-, \psi_l^+$:

$$\begin{aligned} \varphi_l^- &= A_l^- e^{ik\left(x - a_l z\right)} \\ \varphi_l^+ &= A_l^+ e^{ik\left(x + a_l z\right)} \\ \psi_l^- &= B_l^- e^{ik\left(x - b_l z\right)} \\ \psi_l^+ &= B_l^+ e^{ik\left(x + b_l z\right)} \end{aligned} \qquad \textbf{Report 2 (3.1)}$$

They are the upward and downward propagating waves present in the l^{th} layer. $k = k(\omega) = \omega / c(\omega)$ is the horizontal wave number of the P- and SV-waves at frequency ω and phase velocity $c = c(\omega)$. The term e^{ikx}, which is also the same in each layer, is the horizontal component of the waves, which together with the time harmonic term $e^{i\omega t}$, corresponds to waves propagating in the *–ve x* direction. The terms $e^{\mp ika_l z}$ for the P-waves and $e^{\mp ikb_l z}$ for the SV-waves are respectively the vertical components of the waves. The ones with the ***–ve*** *exponent* are propagating upwards (***–ve*** *y*) and those with the ***+ve*** *exponent* are propagating downwards (***+ve*** *y*). Here $a_l = a_l(\alpha_l, c)$ and $b_l = b_l(\beta_l, c)$ are respectively given by

$$\begin{aligned} a_l &= \frac{\left(k_{\alpha_l}^2 - k^2\right)^{1/2}}{k} = \left(\left(k_{\alpha_l} / k\right)^2 - 1\right)^{1/2} = \left(\left(c / \alpha_l\right)^2 - 1\right)^{1/2} \\ b_l &= \frac{\left(k_{\beta_l}^2 - k^2\right)^{1/2}}{k} = \left(\left(k_{\beta_l} / k\right)^2 - 1\right)^{1/2} = \left(\left(c / \beta_l\right)^2 - 1\right)^{1/2} \end{aligned} \qquad \textbf{Report 2 (3.2)}$$

so that ka_l and kb_l are the vertical wave numbers of the ***P***- and ***SV***-waves in the l^{th} layer of the medium with longitudinal wave speed α_l and shear wave velocity β_l. In general, the wave speeds increase as one goes down into the layers, so that $\beta_1 < \beta_2 < \ldots < \beta_N < \beta$, with the semi-infinite half-space layer at the bottom having the highest shear wave speed β. The same can be said about the longitudinal wave speeds, so that $\alpha_1 < \alpha_2 < \ldots < \alpha_N < \alpha$, with is α the longitudinal

wave speed of the semi-infinite medium. With $c = c(\omega)$ the wave speed of the surface Rayleigh waves, $c < \beta < \alpha$, and the surface waves take the form:

$$\varphi_\infty = A_\infty e^{ik(x-az)} = A_\infty e^{ikx-k\bar{a}z}$$
$$\psi_\infty = B_\infty e^{ik(x-bz)} = B_\infty e^{ikx-k\bar{b}z} \qquad \textbf{Report 2 (3.3)}$$

where

$$\bar{a} = \frac{\left(k^2 - k_\alpha^2\right)^{1/2}}{k} = \left(1 - \left(k_\alpha / k\right)^2\right)^{1/2} = \left(1 - \left(c/\alpha\right)^2\right)^{1/2}$$
$$\bar{b} = \frac{\left(k^2 - k_\beta^2\right)^{1/2}}{k} = \left(1 - \left(k_\beta / k\right)^2\right)^{1/2} = \left(1 - \left(c/\beta\right)^2\right)^{1/2} \qquad \textbf{Report 2 (3.4)}$$

and $\bar{a}$, $\bar{b}$ are respectively the complements of a, b and both are real, so that the terms $e^{-k\bar{a}z}$ in φ_∞ and $e^{-k\bar{b}z}$ in ψ_∞ both correspond to surface wave terms with amplitudes that are exponentially decaying with depth below the surface.

Chapter III of Report 2 gave a detailed derivation of the equations relating the coefficients A_l^-, A_l^+, B_l^-, B_l^+ of the wave potentials φ_l^-, φ_l^+, ψ_l^-, ψ_l^+ in each of the l^{th} layer from $l = 1$ on top to the semi-infinite layer $l = N$ at the bottom. They are related by the stress and displacement continuity equations between the layers. Please refer to Chapter III of Report 2 for further details.

For the case of ***body P*** or ***SV*** waves incident from the semi-infinite medium, we will consider the model here in **Figure II.4**, same as in Report 2 Figure III.2. It is the same *N*-layered model as in **Figure II.3** above, for the case of Rayleigh surface waves, but now the ***P*** and ***SV*** waves in all layers are body waves. The body waves in all layers have a common constant phase velocity c, now independent of frequency ω, and dependent only on the incident angle of ***P*** or ***SV*** waves. For incident ***P*** waves, $\psi_N^- = 0$ at the bottom layer, and c is higher than $\alpha_{\max} = \alpha_N$, the longitudinal ***P*** wave speed at the bottom semi-infinite N^{th} layer. For incident ***SV*** waves, $\varphi_N^- = 0$, and the phase velocity c is higher than $\beta_{\max} = \beta_N$, the shear *SV* wave speed at the bottom semi-infinite N^{th} layer (Report 2 Figure III.2).

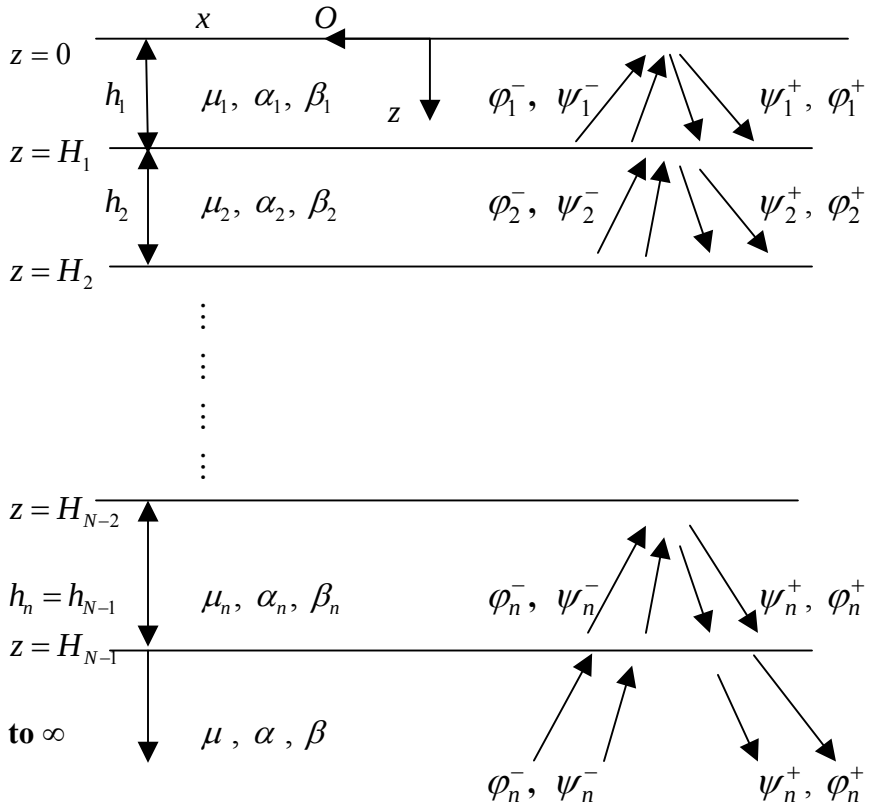

Figure II.4 n-layered half-space with Body P and SV waves (From Figure III.2 of Report 2)

The Rayleigh waves $\varphi_N = \varphi_\infty$ and $\psi_N = \psi_\infty$ at the bottom semi-infinite layer will now be replaced by the body *P* waves φ_N^- and φ_N^+, and *SV* waves ψ_N^- and ψ_N^+ respectively, the incident and reflected body *P* and *SV* waves:

$$\varphi_N^-,\ \varphi_N^+,\ \psi_N^-,\ \psi_N^+ : \qquad \begin{aligned} \varphi_N^- &= A_N^- e^{ik(x - a_N z)} \\ \varphi_N^+ &= A_N^+ e^{ik(x + a_N z)} \\ \psi_N^- &= B_N^- e^{ik(x - b_N z)} \\ \psi_N^+ &= B_N^+ e^{ik(x + b_N z)} \end{aligned} \qquad \textbf{Report 2 (3.15)}$$

as in all the other layers $l = 1,\ 2,\ \ldots,\ N-1$, in Equation (3.1) of Report 2.

With all the surface and body waves available at each layer, we are now ready to describe the associated rotational components of motions.

II.3 Synthetic Rotational Motions of Surface and Body Waves On and Below Surface of a Layered Medium

Starting with the translational components of motions, $\tilde{U} = (U, V, W)$, the rotational components of motion are defined by

$$\tilde{\Omega} = \tfrac{1}{2}\tilde{\nabla} \times \tilde{U} = \tfrac{1}{2}\begin{vmatrix} i & j & k \\ \partial/\partial x & \partial/\partial y & \partial/\partial z \\ U & V & W \end{vmatrix} = \tfrac{1}{2}\begin{vmatrix} i & j & k \\ \partial/\partial x & 0 & \partial/\partial z \\ U & V & W \end{vmatrix} \tag{2.1}$$

since $U = U(x,z)$, $V = V(x,z)$ and $W = W(x,z)$, and all components of motions are dependent only on *x* and, with $\partial/\partial y(\ ) = 0$. Thus

Rotational Motion:

$$\tilde{\Omega} = \begin{pmatrix} \Omega_x \\ \Omega_y \\ \Omega_z \end{pmatrix} = \tfrac{1}{2}\begin{pmatrix} -\partial V/\partial z \\ \partial U/\partial z - \partial W/\partial x \\ \partial V/\partial x \end{pmatrix} \tag{2.2}$$

with

$\Omega_x = -\tfrac{1}{2}\partial V/\partial z$ = **Anti-plane Rocking** component of the Love and body ***SH*** waves in the *x*-direction,

$\Omega_y = \tfrac{1}{2}\left(\partial U/\partial z - \partial W/\partial x\right)$ = **In-plane Rocking** component of the Rayleigh and body ***P, SV*** waves in the ***x-z*** plane, or the *y*- direction, and

$\Omega_z = \tfrac{1}{2}\partial V/\partial x$ = **Anti-plane Torsional** component of the Love and body ***SH*** waves in the vertical *z*-direction.

As in the cases of Torsional (Lee and Trifunac, 1985) and Rocking (Lee and Trifunac, 1987) accelerograms at the half-space surface, we can also compute the 1st and 2nd time derivatives of the **Torsional** and **Rocking** motions to obtain the Torsional and Rocking accelerogram time-histories at points below the half-space surface in the layered media. The three components can be called the **rotational** accelerogram time histories associated with the **translational** motions:

Torsional and **Rocking Velocities:**

$$\frac{\partial \Omega}{\partial t} = \begin{pmatrix} \dot{\Omega}_x \\ \dot{\Omega}_y \\ \dot{\Omega}_z \end{pmatrix} = \frac{1}{2} \begin{pmatrix} -\partial \dot{V} / \partial z \\ \partial \dot{U} / \partial z - \partial \dot{W} / \partial x \\ \partial \dot{V} / \partial x \end{pmatrix} \tag{2.3}$$

and

Torsional and **Rocking Accelerations:**

$$\frac{\partial^2 \Omega}{\partial t^2} = \begin{pmatrix} \ddot{\Omega}_x \\ \ddot{\Omega}_y \\ \ddot{\Omega}_z \end{pmatrix} = \frac{1}{2} \begin{pmatrix} -\partial \ddot{V} / \partial z \\ \partial \ddot{U} / \partial z - \partial \ddot{W} / \partial x \\ \partial \ddot{V} / \partial x \end{pmatrix} \tag{2.4}$$

The computation of the 1st and 2nd time derivatives of the torsional and rocking motions do not require much of additional work. This is because, as in the case of Torsional (Lee and Trifunac, 1985) and Rocking (Lee and Trifunac, 1987) accelerograms at the half-space surface, the Torsional and Rocking accelerations can be first computed, in the frequency domain, directly, as $\partial / \partial x$ and $\partial / \partial z$ derivatives, from the corresponding translational acceleration components, as given in Report 2, from which the Torsional and Rocking velocity, and Torsional and Rocking displacement motions can also be computed in the frequency domain.

Similarly the strain components of motions are given by the symmetric matrix:

$$[\varepsilon] = \begin{bmatrix} \varepsilon_x & \varepsilon_{xy} & \varepsilon_{xz} \\ \varepsilon_{yx} & \varepsilon_y & \varepsilon_{yz} \\ \varepsilon_{zx} & \varepsilon_{zy} & \varepsilon_z \end{bmatrix} = \begin{bmatrix} \partial U / \partial x & \frac{1}{2}\left(\cancel{\partial U / \partial y} + \partial V / \partial x \right) & \frac{1}{2}\left(\partial U / \partial z + \partial W / \partial x \right) \\ \varepsilon_{yx} & \cancel{\partial V / \partial y} & \frac{1}{2}\left(\partial V / \partial z + \cancel{\partial W / \partial y} \right) \\ \varepsilon_{zx} & \varepsilon_{zy} & \partial W / \partial z \end{bmatrix} \tag{2.5}$$

again with all components of motions being dependent only on *x* and, with $\partial / \partial y (\ ) = 0$. Thus

$$[\varepsilon]=\begin{bmatrix}\varepsilon_x & \varepsilon_{xy} & \varepsilon_{xz}\\ \varepsilon_{yx} & \varepsilon_y & \varepsilon_{yz}\\ \varepsilon_{zx} & \varepsilon_{zy} & \varepsilon_z\end{bmatrix}=\begin{bmatrix}\partial U/\partial x & \frac{1}{2}\partial V/\partial x & \frac{1}{2}\left(\partial U/\partial z+\partial W/\partial x\right)\\ \varepsilon_{yx} & 0 & \frac{1}{2}\partial V/\partial z\\ \varepsilon_{zx} & \varepsilon_{zy} & \partial W/\partial z\end{bmatrix} \tag{2.6}$$

Taking symmetry into account, five out of six components of the strain matrix exist, with the only component of strain that vanishes everywhere being ε_y, the normal strain in the anti-plane *y*- direction. Note that before, when strain is calculated at the half-space surface (Lee, 1990), the shear strain $\varepsilon_{xz}=0$, since the corresponding shear stress $\tau_{xz}=2\mu\varepsilon_{xz}=0$ at the half-space surface.

In the same way as in the computation of the Torsional and Rocking accelerograms in Equations (2.3) and (2.4) above, one can compute the first and second time derivatives of the strain matrix to obtain the strain accelerogram time histories at points below the half-space surface in the layered medium:

Strain velocities:

$$\frac{\partial}{\partial t}[\varepsilon]=[\dot{\varepsilon}]=\begin{bmatrix}\dot{\varepsilon}_x & \dot{\varepsilon}_{xy} & \dot{\varepsilon}_{xz}\\ \dot{\varepsilon}_{yx} & \dot{\varepsilon}_y & \dot{\varepsilon}_{yz}\\ \dot{\varepsilon}_{zx} & \dot{\varepsilon}_{zy} & \dot{\varepsilon}_z\end{bmatrix}=\begin{bmatrix}\partial \dot{U}/\partial x & \frac{1}{2}\partial \dot{V}/\partial x & \frac{1}{2}\left(\partial \dot{U}/\partial z+\partial \dot{W}/\partial x\right)\\ \dot{\varepsilon}_{yx} & 0 & \frac{1}{2}\partial \dot{V}/\partial z\\ \dot{\varepsilon}_{zx} & \dot{\varepsilon}_{zy} & \partial \dot{W}/\partial z\end{bmatrix} \tag{2.7}$$

and

Strain accelerations:

$$\frac{\partial^2}{\partial t^2}[\varepsilon]=[\ddot{\varepsilon}]=\begin{bmatrix}\ddot{\varepsilon}_x & \ddot{\varepsilon}_{xy} & \ddot{\varepsilon}_{xz}\\ \ddot{\varepsilon}_{yx} & \ddot{\varepsilon}_y & \ddot{\varepsilon}_{yz}\\ \ddot{\varepsilon}_{zx} & \ddot{\varepsilon}_{zy} & \ddot{\varepsilon}_z\end{bmatrix}=\begin{bmatrix}\partial \ddot{U}/\partial x & \frac{1}{2}\partial \ddot{V}/\partial x & \frac{1}{2}\left(\partial \ddot{U}/\partial z+\partial \ddot{W}/\partial x\right)\\ \ddot{\varepsilon}_{yx} & 0 & \frac{1}{2}\partial \ddot{V}/\partial z\\ \ddot{\varepsilon}_{zx} & \ddot{\varepsilon}_{zy} & \partial \ddot{W}/\partial z\end{bmatrix} \tag{2.8}$$

The computations of the 1st and 2nd time derivatives of the strain motions also do not require much extra work. This is because, as in the case of Torsional (Lee and Trifunac, 1985)

and Rocking (Lee and Trifunac, 1987) accelerograms and the strain computations (Lee 1990) at the half-space surface, the strain accelerations can be first computed, in the frequency domain, directly, as $\partial/\partial x$ and $\partial/\partial z$ derivatives, from the corresponding translational acceleration components, as given in Report 2, from which the strain velocity, and Torsional and Rocking displacement motions can then be computed in the frequency domain.

As in Trifunac (1990), the curvature in the radial, transverse and vertical directions are respectively given by:

Radial Curvature:
$$K_1(t) \approx \partial^2 U/\partial x^2 = \ddot{U}/c^2 \qquad (2.9)$$

Transverse Curvature:
$$K_2(t) \approx \partial^2 V/\partial x^2 = \ddot{V}/c^2 \qquad (2.10)$$

and

Vertical Curvature:
$$K_3(t) = \frac{\partial^2 W/\partial x^2}{\left[1+\left(\partial W/\partial x\right)^2\right]^{3/2}} \approx \partial^2 W/\partial x^2 = \ddot{W}/c^2 \qquad (2.11)$$

Those are all computed directly from the translational components, the numerical implementation of which is summarized in the next section. In fact, they each correspond to the ***2nd derivative of the translational motion*** with respect to ***x*** in the radial direction.

II.4 The Numerical Implementation of Translational Motions – a Brief Review

The following is derived from Section IV.1 of Report 2: "The Original Thomson-Haskell's Transfer Matrix Method" (Thomson, 1950 and Haskell, 1953). The results are summarized briefly as follows.

(1) Love Waves

In Section IV.1 of Report 2, we used the following equation for Love Waves in each layer l, for $l = 1, 2, \ldots, N$:

$$\begin{pmatrix} v_l(z) \\ \tau_l(z) \end{pmatrix} = \begin{bmatrix} 1 & 1 \\ i\mu_l k\gamma_l & -i\mu_l k\gamma_l \end{bmatrix} \begin{bmatrix} e^{i\mu_l k\gamma_l z} & 0 \\ 0 & e^{-i\mu_l k\gamma_l z} \end{bmatrix} \begin{bmatrix} 1 & 1 \\ i\mu_l k\gamma_l & -i\mu_l k\gamma_l \end{bmatrix}^{-1} \begin{pmatrix} v_l(0) \\ \tau_l(0) \end{pmatrix}$$

or $$\begin{pmatrix} v_l(z) \\ \tau_l(z) \end{pmatrix} = [T_l][E_l(z)][T_l]^{-1} \begin{pmatrix} v_l(0) \\ \tau_l(0) \end{pmatrix}$$ **Report 2 (4.4)**

for local coordinate $0 \le z \le h_l$, at any point in the l^{th} layer. In particular, at the bottom point of the l^{th} layer, where $z = h_l$, Report 2, Equation (4.4) becomes:

$$\begin{pmatrix} v_l(h_l) \\ \tau_l(h_l) \end{pmatrix} = [T_l][E_l(h_l)][T_l]^{-1} \begin{pmatrix} v_l(0) \\ \tau_l(0) \end{pmatrix}$$

$$\begin{pmatrix} v_l(h_l) \\ \tau_l(h_l) \end{pmatrix} = [\mathcal{H}_l] \begin{pmatrix} v_l(0) \\ \tau_l(0) \end{pmatrix}$$ **Report 2 (4.5)**

where $[\mathcal{H}_l] = [T_l][E_l(h_l)][T_l]^{-1}$ is the Haskell propagator matrix that expresses the displacement-stress state vector at the bottom of the l^{th} layer in terms of that at the top of the layer.

Next, define a set of displacement-stress state vectors, for $l = 1, 2, \ldots, N$:

$$\begin{pmatrix} V_l \\ \mathrm{T}_l \end{pmatrix} = \left. \begin{pmatrix} v_l(z) \\ \tau_l(z) \end{pmatrix} \right|_{z=0}$$ **Report 2 (4.6)**

which corresponds respectively to the state vector at the top of each layer. Since the stress-displacement state vectors are continuous across the interface from one medium to the one below, one can write Equation (4.5) as

$$l = 1,\ 2,\ \ldots,\ N-1 \quad \begin{pmatrix} V_{l+1} \\ \mathrm{T}_{l+1} \end{pmatrix} = [T_l][E_l(h_l)][T_l]^{-1} \begin{pmatrix} V_l \\ \mathrm{T}_l \end{pmatrix} = [\mathcal{H}_l] \begin{pmatrix} V_l \\ \mathrm{T}_l \end{pmatrix}$$ **Report 2 (4.7a)**

In the reverse order, we also have

$$\begin{pmatrix} V_l \\ \mathrm{T}_l \end{pmatrix} = [T_l][E_l(h_l)]^{-1}\ [T_l]^{-1} \begin{pmatrix} V_{l+1} \\ \mathrm{T}_{l+1} \end{pmatrix} = [\mathcal{H}_l]^{-1} \begin{pmatrix} V_{l+1} \\ \mathrm{T}_{l+1} \end{pmatrix}$$ **Report 2 (4.7b)**

The displacement-stress vector at the top of the last (semi-infinite) layer can then be expressed in terms of that at the top of the 1st surface layer:

$$\begin{pmatrix} V_N \\ T_N \end{pmatrix} = [\mathcal{H}_{N-1}][\mathcal{H}_{N-2}]\cdots[\mathcal{H}_1]\begin{pmatrix} V_1 \\ T_1 \end{pmatrix} \qquad \textbf{Report 2 (4.8a)}$$

or in the reverse order

$$\begin{pmatrix} V_1 \\ T_1 \end{pmatrix} = [\mathcal{H}_1]^{-1}\cdots[\mathcal{H}_{N-2}]^{-1}[\mathcal{H}_{N-1}]^{-1}\begin{pmatrix} V_N \\ T_N \end{pmatrix} \qquad \textbf{Report 2 (4.8b)}$$

Report 2 Equations (4.4) through (4.8) allow the displacement-stress vector to be calculated at every point of every layer in the layered half space.

(2) Rayleigh Waves

In Section IV.1 of Report 2, we derive the following equation for Love Waves at each layer l, for $l = 1, 2, \ldots, N$:

$$\begin{pmatrix} \tilde{u}_l(z) \\ \tilde{\sigma}_l(z) \end{pmatrix} = \begin{bmatrix} T_l^1 & T_l^2 \\ T_l^3 & T_l^4 \end{bmatrix}\begin{bmatrix} E_l^+(z) & 0 \\ 0 & E_l^-(z) \end{bmatrix}\begin{bmatrix} T_l^1 & T_l^2 \\ T_l^3 & T_l^4 \end{bmatrix}^{-1}\begin{pmatrix} \tilde{u}_l(0) \\ \tilde{\sigma}_l(0) \end{pmatrix}$$

or

$$\begin{pmatrix} \tilde{u}_l(z) \\ \tilde{\sigma}_l(z) \end{pmatrix} = [T_l][E_l(z)][T_l]^{-1}\begin{pmatrix} \tilde{u}_l(0) \\ \tilde{\sigma}_l(0) \end{pmatrix} \qquad \textbf{Report 2 (4.23)}$$

for local coordinate $0 \le z \le h_l$, at any point in the l^{th} layer below. In particular, at the bottom point of the l^{th} layer, where $z = h_l$, Report 2 Equation (4.23) becomes:

$$\begin{pmatrix} \tilde{u}_l(h_l) \\ \tilde{\sigma}_l(h_l) \end{pmatrix} = [T_l][E_l(h_l)][T_l]^{-1}\begin{pmatrix} \tilde{u}_l(0) \\ \tilde{\sigma}_l(0) \end{pmatrix}$$

$$\begin{pmatrix} \tilde{u}_l(h_l) \\ \tilde{\sigma}_l(h_l) \end{pmatrix} = [\mathcal{H}_l]\begin{pmatrix} \tilde{u}_l(0) \\ \tilde{\sigma}_l(0) \end{pmatrix} \qquad \textbf{Report 2 (4.24)}$$

where $[\mathcal{H}_l] = [T_l][E_l(h_l)][T_l]^{-1}$ is again the Haskell propagator matrix for Rayleigh waves, that expresses the displacement-stress state vector at the bottom of the l^{th} layer in terms of that at the top of the layer.

As for the case of Love waves, we define a set of displacement-stress state vectors, for $l = 1, 2, \ldots, N$, one for each layer, as:

$$\begin{pmatrix} \tilde{U}_l \\ \tilde{\Sigma}_l \end{pmatrix} = \begin{pmatrix} \tilde{u}_l(z) \\ \tilde{\sigma}_l(0) \end{pmatrix}\Bigg|_{z=0} = \begin{pmatrix} \tilde{u}_l(0) \\ \tilde{\sigma}_l(0) \end{pmatrix} \qquad \textbf{Report 2 (4.25)}$$

which corresponds to the state vector at the top of each layer. Since the stress-displacement state vectors are continuous across the interface from one layered medium to the one below, one can write Equation (4.24) as:

$$l = 1,\ 2,\ \ldots,\ N-1 \qquad \begin{pmatrix} \tilde{U}_{l+1} \\ \tilde{\Sigma}_{l+1} \end{pmatrix} = [T_l]\,[E_l(h_l)]\,[T_l]^{-1} = [\mathcal{H}_l] \begin{pmatrix} \tilde{U}_l \\ \tilde{\Sigma}_l \end{pmatrix} \qquad \textbf{Report 2 (4.26a)}$$

In the reverse order, we also have

$$\begin{pmatrix} \tilde{U}_l \\ \tilde{\Sigma}_l \end{pmatrix} = [T_l]\,[E_l(h_l)]^{-1}[T_l]^{-1} \begin{pmatrix} \tilde{U}_{l+1} \\ \tilde{\Sigma}_{l+1} \end{pmatrix} = [\mathcal{H}_l]^{-1} \begin{pmatrix} \tilde{U}_{l+1} \\ \tilde{\Sigma}_{l+1} \end{pmatrix} \qquad \textbf{Report 2 (4.26b)}$$

The displacement-stress vector at the top of the last (semi-infinite) layer can then be expressed in terms of that at the top of the 1st surface layer:

$$\begin{pmatrix} \tilde{U}_N \\ \tilde{\Sigma}_N \end{pmatrix} = [\mathcal{H}_{N-1}][\mathcal{H}_{N-2}]\cdots[\mathcal{H}_1] \begin{pmatrix} \tilde{U}_1 \\ \tilde{\Sigma}_1 \end{pmatrix} \qquad \textbf{Report 2 (4.27a)}$$

or in the reverse order $$\begin{pmatrix} V_1 \\ \tilde{\Sigma}_1 \end{pmatrix} = [\mathcal{H}_1]^{-1} \cdots [\mathcal{H}_{N-2}]^{-1}[\mathcal{H}_{N-1}]^{-1} \begin{pmatrix} V_N \\ \tilde{\Sigma}_N \end{pmatrix} \qquad \textbf{Report 2 (4.27b)}$$

Equations (4.24) through (4.28) allow the displacement-stress vector to be calculated at every point of every layer in the half space from top to bottom.

In Report 2, Section IV.2 on "The Improved Matrix Propagator Algorithm", the method of Liu (2010) was adopted to derive an improved Thomson-Haskell transfer matrix method. Instead of directly multiplying the Thomson-Haskell propagator matrix, this method defines for each layer an intermediate stiffness matrix and state vector and performs the propagation through an intermediate step at each layer. This modified scheme keeps the simplicity of the original propagator method with the intermediate step able to efficiently avoid and exclude the exponential growth terms. The following is a brief summary of the scheme for Rayleigh waves as in Liu (2010). It is also modified to cover the case of incident ***P, SV*** body waves (see Chapter III, Report 2).

The state vector in Report 2 Equations (4.26a) and (4.26b) above is written in terms of a layered stiffness matrix $\boldsymbol{S}_l$, namely, $\left(\tilde{\Sigma}_l\right)=\left[\boldsymbol{S}_l\right]\left(\tilde{\boldsymbol{U}}_l\right)$ expressing the stress vector in terms of the displacement vector, so that

$$\begin{pmatrix}\tilde{\boldsymbol{U}}_l\\ \tilde{\Sigma}_l\end{pmatrix}=\begin{bmatrix}\boldsymbol{I}\\ \boldsymbol{S}_l\end{bmatrix}\tilde{\boldsymbol{U}}_l \qquad \textbf{Report 2 (4.28)}$$

and the Thomson-Haskell Propagator matrix equation takes the form:

$$\begin{bmatrix}\boldsymbol{I}\\ \boldsymbol{S}_l\end{bmatrix}\tilde{\boldsymbol{U}}_l=\left[\boldsymbol{T}_l\right]\begin{bmatrix}\boldsymbol{\mathcal{E}}_l^{-} & \boldsymbol{0}\\ \boldsymbol{0} & \boldsymbol{\mathcal{E}}_l^{+}\end{bmatrix}\left[\boldsymbol{T}_l\right]^{-1}\begin{bmatrix}\boldsymbol{I}\\ \boldsymbol{S}_{l+1}\end{bmatrix}\tilde{\boldsymbol{U}}_{l+1} \qquad \textbf{Report 2 (4.31)}$$

Direct substitution in the calculation would involve adding and subtracting expressions involving the exponential terms in $\boldsymbol{\mathcal{E}}_l^{-}$ and $\boldsymbol{\mathcal{E}}_l^{+}$. As pointed out in Report 2, when $\boldsymbol{c}<\boldsymbol{\alpha}_l$ or $\boldsymbol{c}<\boldsymbol{\beta}_l$, these exponents are real, and so the additions and subtractions of these exponentially increasing and exponentially decreasing terms together makes the terms numerically unstable, with possible overflow and underflow, especially when the frequency is high and/or the layer is thick.

Liu (2010) proposed a step to avoid such numerical problem. From Equations (4.22), (4.25) and (4.28)

$$\begin{bmatrix}\boldsymbol{I}\\ \boldsymbol{S}_l\end{bmatrix}\tilde{\boldsymbol{U}}_l=\begin{pmatrix}\tilde{\boldsymbol{U}}_l\\ \tilde{\Sigma}_l\end{pmatrix}=\begin{pmatrix}\tilde{\boldsymbol{u}}_l(\boldsymbol{0})\\ \tilde{\boldsymbol{\sigma}}_l(\boldsymbol{0})\end{pmatrix}=\left[\boldsymbol{T}_l\right]\begin{pmatrix}\tilde{\boldsymbol{C}}_l^{+}\\ \tilde{\boldsymbol{C}}_l^{-}\end{pmatrix} \qquad \textbf{Report 2 (4.32a)}$$

Rewrite it in terms of an intermediate 'auxiliary' stiffness matrix $\left[\bar{\boldsymbol{S}}_l\right]$, and call $\bar{\boldsymbol{U}}_l=\tilde{\boldsymbol{C}}_l^{+}$:

$$\begin{bmatrix}\boldsymbol{I}\\ \boldsymbol{S}_l\end{bmatrix}\tilde{\boldsymbol{U}}_l=\left[\boldsymbol{T}_l\right]\begin{bmatrix}\boldsymbol{I}\\ \bar{\boldsymbol{S}}_l\end{bmatrix}\bar{\boldsymbol{U}}_l\ ,$$

where from (4.31) $\qquad \begin{bmatrix}\boldsymbol{I}\\ \bar{\boldsymbol{S}}_l\end{bmatrix}\bar{\boldsymbol{U}}_l=\begin{bmatrix}\boldsymbol{\mathcal{E}}_l^{-} & \boldsymbol{0}\\ \boldsymbol{0} & \boldsymbol{\mathcal{E}}_l^{+}\end{bmatrix}\left[\boldsymbol{T}_l\right]^{-1}\begin{bmatrix}\boldsymbol{I}\\ \boldsymbol{S}_{l+1}\end{bmatrix}\tilde{\boldsymbol{U}}_{l+1}$ $\qquad$ **Report 2 (4.32b)**

Define another intermediate $\left[\boldsymbol{P}_l\right]$ matrix for each layer $\boldsymbol{l}$:

$$\left[\boldsymbol{P}_l\right]=\begin{bmatrix}\boldsymbol{P}_l^{1}\\ \boldsymbol{P}_l^{2}\end{bmatrix}=\left[\boldsymbol{T}_l\right]^{-1}\begin{bmatrix}\boldsymbol{I}\\ \boldsymbol{S}_{l+1}\end{bmatrix} \qquad \textbf{Report 2 (4.33)}$$

and solving for $\bar{S}_l$ gives (Liu, 2010):

$$\bar{S}_l = \left[\mathcal{E}_l^+\right]\left[P_l^2\right]\left[P_l^1\right]^{-1}\left[\mathcal{E}_l^+\right] \qquad \textbf{Report 2 (4.35)}$$

This has the numerical advantage that should the waves in the layer be surface-wave type and non-harmonic $\left(c < \alpha \text{ or } c < \beta\right)$, the terms in $\left[\mathcal{E}_l^+\right]$ would be exponentially decaying, and hence would tend to zero, especially when the layer thickness or the wave frequency is large.

The case of Love surface waves proceeds the same way, except the matrices are half the size, namely 2 x 2 instead of 4 x 4, and scalar matrices.

Section IV.4 of Report 2: "The New Numerical Implementation for P, SV Body Waves" shows that the procedure for P, SV body waves follows the same concept but is applied in a different order. It is different from Rayleigh waves because, instead of surface waves at the bottom semi-infinite layer, we have incident P or SV body waves coming from below. The reader is referred to that section for a complete description.

The case of incident SH body waves also proceeds the same way, except the matrices are half the size, namely 2 x 2 instead of 4 x 4, and scalar matrices.

IV.5 Numerical Implementation of the derivatives of the Tanslational Motions

If is seen from the above equations (Equations (2.1) – (2.8)) that the computation of the Torsion, Rocking and Strain time histories all involve either or both of the d/dx and d/dz derivatives of the corresponding translational acceleration $\left(\ddot{U},\ddot{V},\ddot{W}\right)^T$, velocity $\left(\dot{U},\dot{V},\dot{W}\right)$ and displacement $\left(U,V,W\right)$ time histories.

The numerical procedure for computing the d/dx and d/dz derivatives of the corresponding translational motions follow along the same line as those of the corresponding translational motions as described in Chapter IV: "The Numerical Implementation" of Report 2.

For the case of Love and Body ***SH*** Waves, we consider Equation (4.4) of Report 2 above for each layer l, with $l = 1, 2, \ldots, N$, this time re-introducing the *x*-dependence term e^{ikx} into both sides of the equation:

$$\begin{pmatrix} v_l(z) \\ \tau_l(z) \end{pmatrix} e^{ikx} = \begin{bmatrix} 1 & 1 \\ i\mu_l k\gamma_l & -i\mu_l k\gamma_l \end{bmatrix} \begin{bmatrix} e^{i\mu_l k\gamma_l z} & 0 \\ 0 & e^{-i\mu_l k\gamma_l z} \end{bmatrix} \begin{bmatrix} 1 & 1 \\ i\mu_l k\gamma_l & -i\mu_l k\gamma_l \end{bmatrix}^{-1} \begin{pmatrix} v_l(0) \\ \tau_l(0) \end{pmatrix} e^{ikx}$$

or

$$\begin{pmatrix} v_l(z) \\ \tau_l(z) \end{pmatrix} e^{ikx} = [T_l][E_l(z)][T_l]^{-1} \begin{pmatrix} v_l(0) \\ \tau_l(0) \end{pmatrix} e^{ikx} \qquad \textbf{Report 2 (4.4)}$$

so that the *x*-derivative takes the simple form:

$$\frac{d}{dx}\begin{pmatrix} v_l(z) \\ \tau_l(z) \end{pmatrix} e^{ikx} = ik\begin{pmatrix} v_l(z) \\ \tau_l(z) \end{pmatrix} e^{ikx} = ik[T_l][E_l(z)][T_l]^{-1} \begin{pmatrix} v_l(0) \\ \tau_l(0) \end{pmatrix} e^{ikx} \qquad \textbf{(2.12)}$$

and the numerical implementation of the *x*-derivative of the Love waves and Body ***SH*** waves proceed in the same way as for the translational waves, with the additional factor ik multiplied at each frequency.

Similarly for the *z*-derivative:

$$\frac{d}{dz}\begin{pmatrix} v_l(z) \\ \tau_l(z) \end{pmatrix} e^{ikx} = \begin{pmatrix} v_l'(z) \\ \tau_l'(z) \end{pmatrix} e^{ikx} = [T_l][E_l'(z)][T_l]^{-1} \begin{pmatrix} v_l(0) \\ \tau_l(0) \end{pmatrix} e^{ikx} \qquad \textbf{(2.13)}$$

with

$$[E_l'(z)] = \frac{d}{dz}[E_l(z)] = \frac{d}{dz}\begin{bmatrix} e^{i\mu_l k\gamma_l z} & 0 \\ 0 & e^{-i\mu_l k\gamma_l z} \end{bmatrix} = i\mu_l k\gamma_l \begin{bmatrix} e^{i\mu_l k\gamma_l z} & 0 \\ 0 & -e^{-i\mu_l k\gamma_l z} \end{bmatrix} \qquad \textbf{(2.14)}$$

Again the numerical implementation of the *z*-derivative of the Love waves and Body ***SH*** waves proceed in the same way as for the translational waves, with the matrix $\left[\boldsymbol{E_l'(z)}\right]$ replacing $\left[\boldsymbol{E_l(z)}\right]$ at each frequency.

For the case of Rayleigh waves and ***P, SV*** body waves, we consider Report 2 Equation (4.23) above for each layer $\boldsymbol{l}$, with $\boldsymbol{l = 1,\ 2,\ \ldots,\ N}$, this time re-introducing the *x*-dependence term $\boldsymbol{e^{ikx}}$ into both sides of the equation:

$$\begin{pmatrix} \tilde{u}_l(z) \\ \tilde{\sigma}_l(z) \end{pmatrix} = \begin{bmatrix} T_l^1 & T_l^2 \\ T_l^3 & T_l^4 \end{bmatrix} \begin{bmatrix} E_l^+(z) & 0 \\ 0 & E_l^-(z) \end{bmatrix} \begin{bmatrix} T_l^1 & T_l^2 \\ T_l^3 & T_l^4 \end{bmatrix}^{-1} \begin{pmatrix} \tilde{u}_l(0) \\ \tilde{\sigma}_l(0) \end{pmatrix}$$

or

$$\begin{pmatrix} \tilde{u}_l(z) \\ \tilde{\sigma}_l(z) \end{pmatrix} e^{ikx} = \left[T_l\right]\left[E_l(z)\right]\left[T_l\right]^{-1} \begin{pmatrix} \tilde{u}_l(0) \\ \tilde{\sigma}_l(0) \end{pmatrix} e^{ikx} \qquad \textbf{Report 2 (4.23)}$$

so that the *x*-derivative takes the form:

$$\frac{d}{dx}\begin{pmatrix} \tilde{u}_l(z) \\ \tilde{\sigma}_l(z) \end{pmatrix} e^{ikx} = ik\begin{pmatrix} \tilde{u}_l(z) \\ \tilde{\sigma}_l(z) \end{pmatrix} e^{ikx} = ik\left[T_l\right]\left[E_l(z)\right]\left[T_l\right]^{-1} \begin{pmatrix} \tilde{u}_l(0) \\ \tilde{\sigma}_l(0) \end{pmatrix} e^{ikx} \qquad \textbf{(2.15)}$$

and the numerical implementation of the *x*-derivative of the Rayleigh waves and body ***P*** and ***SV*** waves proceed in the same way as for the translational waves, with the additional factor $\boldsymbol{ik}$ multiplied at frequency.

Similarly for the *z*-derivative, with $\left[\boldsymbol{E_l'(z)}\right] = \begin{bmatrix} E_l^{+\prime}(z) & 0 \\ 0 & E_l^{-\prime}(z) \end{bmatrix}$:

$$\frac{d}{dz}\begin{pmatrix} \tilde{u}_l(z) \\ \tilde{\sigma}_l(z) \end{pmatrix} e^{ikx} = \begin{pmatrix} \tilde{u}_l'(z) \\ \tilde{\sigma}_l'(z) \end{pmatrix} e^{ikx} = \left[T_l\right] \begin{bmatrix} E_l^{+\prime}(z) & 0 \\ 0 & E_l^{-\prime}(z) \end{bmatrix} \left[T_l\right]^{-1} \begin{pmatrix} \tilde{u}_l(0) \\ \tilde{\sigma}_l(0) \end{pmatrix} e^{ikx} \qquad \textbf{(2.16)}$$

and from Report 2, Equation (4.19):

$$\frac{d}{dz}E_l^+(z) = E_l^{+\prime}(z) = \begin{bmatrix} +ika_l e^{+ika_l z} & 0 \\ 0 & +ikb_l e^{+ikb_l z} \end{bmatrix}$$

and $$\frac{d}{dz}E_l^-(z) = E_l^{-\prime}(z) = \begin{bmatrix} -ika_l e^{-ika_l z} & 0 \\ 0 & -ikb_l e^{-ikb_l z} \end{bmatrix} \quad \textbf{(2.17)}$$

The numerical implementation of the *z*-derivative of the Rayleigh waves and body ***P*** and ***SV*** waves proceed in the same way as the translational waves, with the matrix $\left[E_l'(z)\right] = \begin{bmatrix} E_l^{+\prime}(z) & 0 \\ 0 & E_l^{-\prime}(z) \end{bmatrix}$ replacing $\left[E_l(z)\right]$ at each frequency.

In the next chapter we will use the above-modified Thomson-Haskell propagator matrix adopted from Section IV of Report 2 for the Rotational Motions defined above. Since all the Torsional, Rocking and Strain motions are linear combinations of these d/dx and d/dz derivatives of the corresponding translational motions, we will refer to these d/dx and d/dz derivatives in all subsequent chapters as "Rotational motions".

III. Surface and Body Waves Rotational Mode Shapes

III.1 Introduction

As in Report I, we will use the computed phase velocities for the 5 modes of Love waves and 5 modes of Rayleigh waves at the Imperial Valley El Centro 6-layered site model. Using the modified Thomson-Haskell propagator matrix adopted from Section IV of Report 2 for the Rotational Motions defined in the previous chapter, the relative rotation amplitudes can be computed for each mode of the Love waves for each frequency where the waves exist and in each layer of the half-space. We will assume the displacement amplitude to be one at the half-space surface.

Section III.2 will describe the ***Love*** Wave Rotational modes #1 to #5, the five modes for which the calculations were made to obtain the phase velocities $\boldsymbol{c = c(T)}$, for the range of periods starting from 15sec down to 0.04sec. The rotational motions will be the $\boldsymbol{d/dx}$ and $\boldsymbol{d/dz}$ motions. Those will be the motions computed by normalizing the transverse displacement amplitudes to be 'one' at the half-space surface. Those will be followed by Section III.3 of the mode shapes of body ***SH*** waves for a given incident angle. Those will be taken to be the "13th mode" of waves to be included in the generation of synthetic translational motions in the (anti-plane, SH) transverse direction. For brevity, the graphs of mode shapes for all the periods of all five modes of Love waves and body ***SH*** waves of a selected incident angle is not included here.

Next in Section III.4 we illustrate the mode shapes for the five modes of ***Rayleigh*** surface waves. As in the case of Love waves, the relative rotational amplitudes are now be computed for each mode of the Rayleigh waves for each frequency where the waves exist and in each layer of the half-space. There will be two components of in-plane rotational motions, the $\boldsymbol{d/dx}$ and $\boldsymbol{d/dz}$ (rotational) motions. We will normalize the displacement amplitude of both components with respect to the vertical z-component of motion at the half-space surface. They will be

rotational motions from Rayleigh waves of mode#1 and 2 for the phase velocities $\boldsymbol{c = c(T)}$, in the range of periods starting from 15sec down to 0.04sec. This is followed by Section III.5 on the mode shapes of body ***P*** and ***SV*** waves for a given incident angle. This will be taken to be the "11^{th} and 12^{th} modes" of waves to be included in the generation of synthetic translational motions in the (in-plane, P and SV) radial and vertical directions. Again, for brevity of this presentation, the graphs of mode shapes for all the periods of all five modes of ***Rayleigh*** waves and body ***P*** and ***SV*** waves of a selected incident angle will not be included here.

In summary, modes #1 to #5 are the Love wave rotational modes, modes #6 to #10 are the Rayleigh wave rotational modes. Modes #11 and #12 are the body in-plane rotational modes respectively for incident P- and SV-waves. Finally mode #13 is the body anti-plane rotational mode for incident SH-waves.

Note also that both the x- and z- distances are measured in ***km***, while the trnalsational modes ***U***, ***V*** and ***W*** are measured in ***cm***, the derivatives $\boldsymbol{d/dx}$ and $\boldsymbol{d/dz}$ of the mode shapes ***U***, ***V*** and ***W*** all thus have a built-in factor of $\boldsymbol{cm/km} = 10^{-2}\boldsymbol{m}/10^{3}\boldsymbol{m} = 10^{-5}$. This is why in all rotational plots; the modes are labeled as $\left(10^{5}\right)\boldsymbol{d/dx}, \boldsymbol{d/dz}$ to reflect the fact that amplitude of 4 (for example) actually means 4×10^{-5}.

III.2 Love Waves Rotational Modes

Mode #1 has phase velocities for all 91 periods in the range from 15 sec down to 0.04 sec. The Thomson-Haskell computation gives the mode shapes of the Mode#1 Love waves in the same wide period range. **Figure III.1** shows the plots of such Love wave $\boldsymbol{d/dx}$ and $\boldsymbol{d/dz}$ (rotational) mode shape amplitudes at four selected periods: $\boldsymbol{T = 5,\ 1.0,\ 0.5,\ and\ 0.1\ s}$.

As stated above, the displacement amplitude of the mode shape (Report 2) is normalized to be one ($=1\,\boldsymbol{cm}$) at the surface of the half-space, so that the translational mode shape in Report

2 and the rotational mode shape values here have the scaling factors or transfer function values of the waves amplitudes along the depth from the half-space surface. Each graph shows the dV/dx and dV/dz mode shapes versus the distance z, which is the depth in kilometers below the half-space surface.

Since $dV/dx = ikV$, the dV/dx (dashed line) mode shapes are just scaled versions of the displacement (V) mode shapes, scaled by the wave number k. Since $V = 1$ at $z = 0$, the half-space surface, the imaginary part of dV/dx starts equal to k at the half-space surface, and just like the translational mode, stays positive all the way, and finally decays to zero down below. The waves at long periods decay slower than the waves at short periods. Note that the amplitudes stay below the initial value of k all the way.

As an example, the dV/dx mode shape for the waves at $T = 5\text{sec}\ (0.2hz)$ period in the top-left graph starts at $k\left(\times 10^{-5}\right) = 0.6\left(\times 10^{-5}\right)$, at the surface, decays slowly and stays above zero all the way down to $z = 6km$, which is just inside the semi-infinite half-space medium, the 6th layer in the model, where $z > 5.58km$. The mode shape for the waves at $T = 1\text{sec}\ (1.0hz)$ period in the top-right graph decays a bit faster from initial value of $k\left(\times 10^{-5}\right) = 5.58\left(\times 10^{-5}\right)$ and stays above zero only down to $z \sim 1.5km$, which is just inside the 3rd layer in the model, where $0.73 \le z \le 1.71km$. The mode shape for the waves at $T = 0.5\text{sec}\ (2.0hz)$ period in the bottom-left graph decays much faster and stays above zero only down to $z \sim 0.7km$, which is close to the bottom of the 2nd layer in the model, where $0.18 \le z \le 0.73km$. Finally, the dV/dx mode shape for the waves at $T = 0.1\text{sec}\ (10.0hz)$ period, in the bottom-left graph, decays so fast that it stays above zero only down to $z \sim 0.2km$, which is inside the 2nd layer in the model, with the 1st layer in the range $0.0 \le z \le 0.18km$.

Figure III.1 Mode #1. Love Wave Rotational Mode Shapes at $T = 5, 1.0, 0.5, 0.1$ *s*

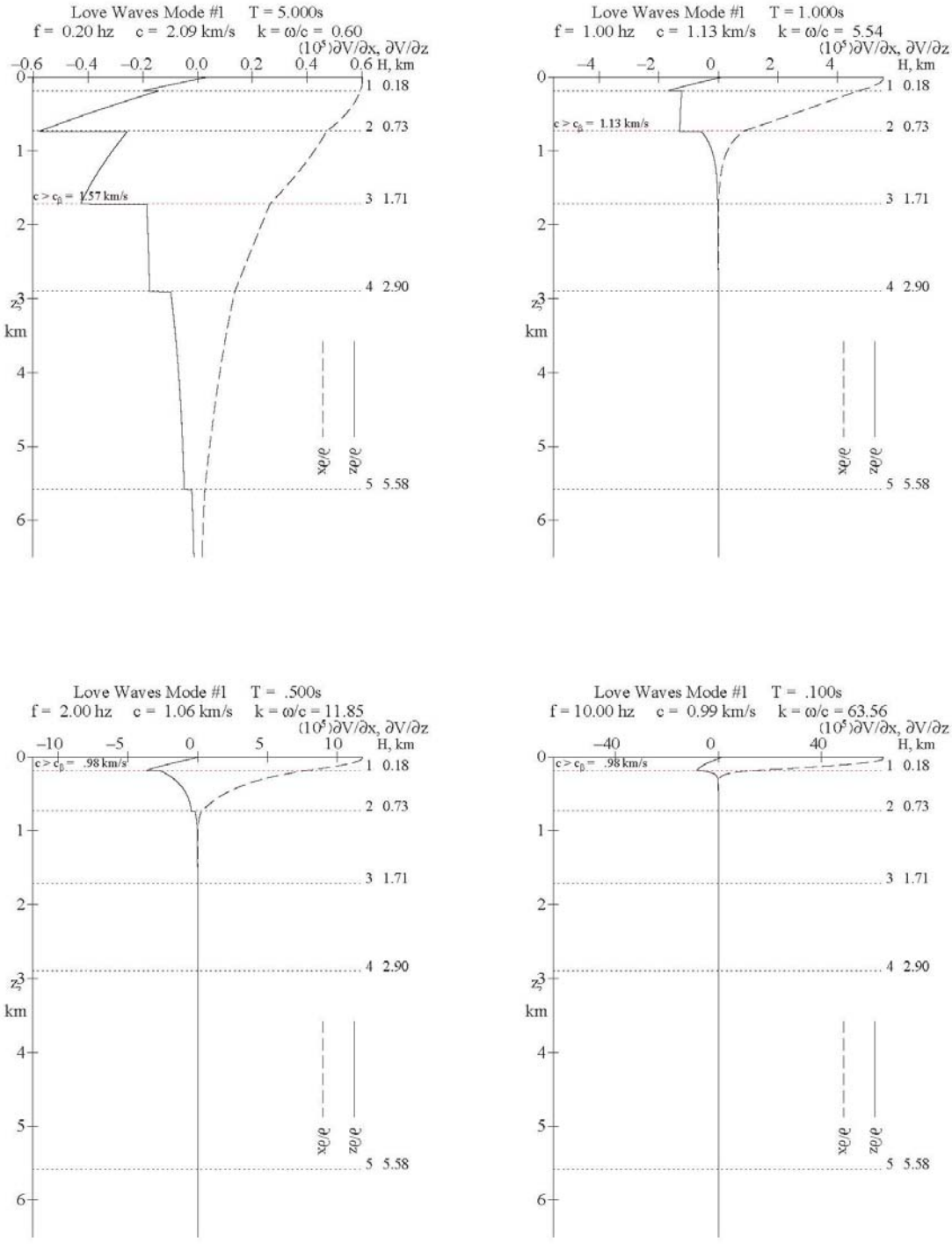

The solid lines in each graph are the dV/dz mode shapes. They represent the shear strain $\gamma_{yz} = 2\varepsilon_{yz} = \partial V/\partial z$ at each point on or below the half-space surface. Since the shear stress $\tau_{yz} = 2\mu\varepsilon_{yz} = 0$ at the half-space surface, so does the strain dV/dz. In going down from the surface along z, the strain goes from one layer to another and exhibits jumps at the layered interface. This is because the shear stresses are continuous at the interface, and because of the differences in the shear moduli from layer to layer, the strains are discontinuous at the interface. Far from the surface, just like the dV/dx mode shape amplitudes decay to zero.

Mode #2 has phase velocities for all 70 periods in the range from 3.8 sec down to 0.04 sec. The Thomson-Haskell computation gives the mode shapes of the Mode #2 Love waves in the same wide period range. **Figure III.2** shows the plots of such Love wave dV/dx and dV/dz mode shape amplitudes at four selected periods: $\boldsymbol{T = 3.0,\ 1.0,\ 0.3,\ \text{and}\ 0.1\ s}$. As for Mode #1, each graph shows the mode shape amplitudes versus the distance z, measured as depth in kilometers below the half-space surface.

The mode #2 dV/dx (dashed line) mode shapes, like the mode #1 mode shape, starts with mode number k at $z = 0$ on the surface. Unlike Mode #1, which started positive and stayed positive before decaying to zero, the dV/dx mode #2 will decay to negative values at some depth and stay negative before decaying to zero. The mode shape at long periods decays slower than the mode shape at short periods. As an example, the mode shape for the waves at $T = 3.6\,\text{sec}\ (0.28hz)$ period in the top-left graph decays slowly, turns negative in the 3rd layer, $0.73 \le z \le 1.71km$, at around $z \sim 1.5km$, reaching a negative minimum in the 4th layer around $z \sim 3km$. It stays negative all the way down beyond $z = 10km$, outside the range of the plots, way below the half-space medium, the 6th layer in the model, where $z > 5.58km$.

Figure III.2 Mode #2. Love Wave Mode Shapes at $T = 3.0,\ 1.0,\ 0.3,\ 0.1\ s$

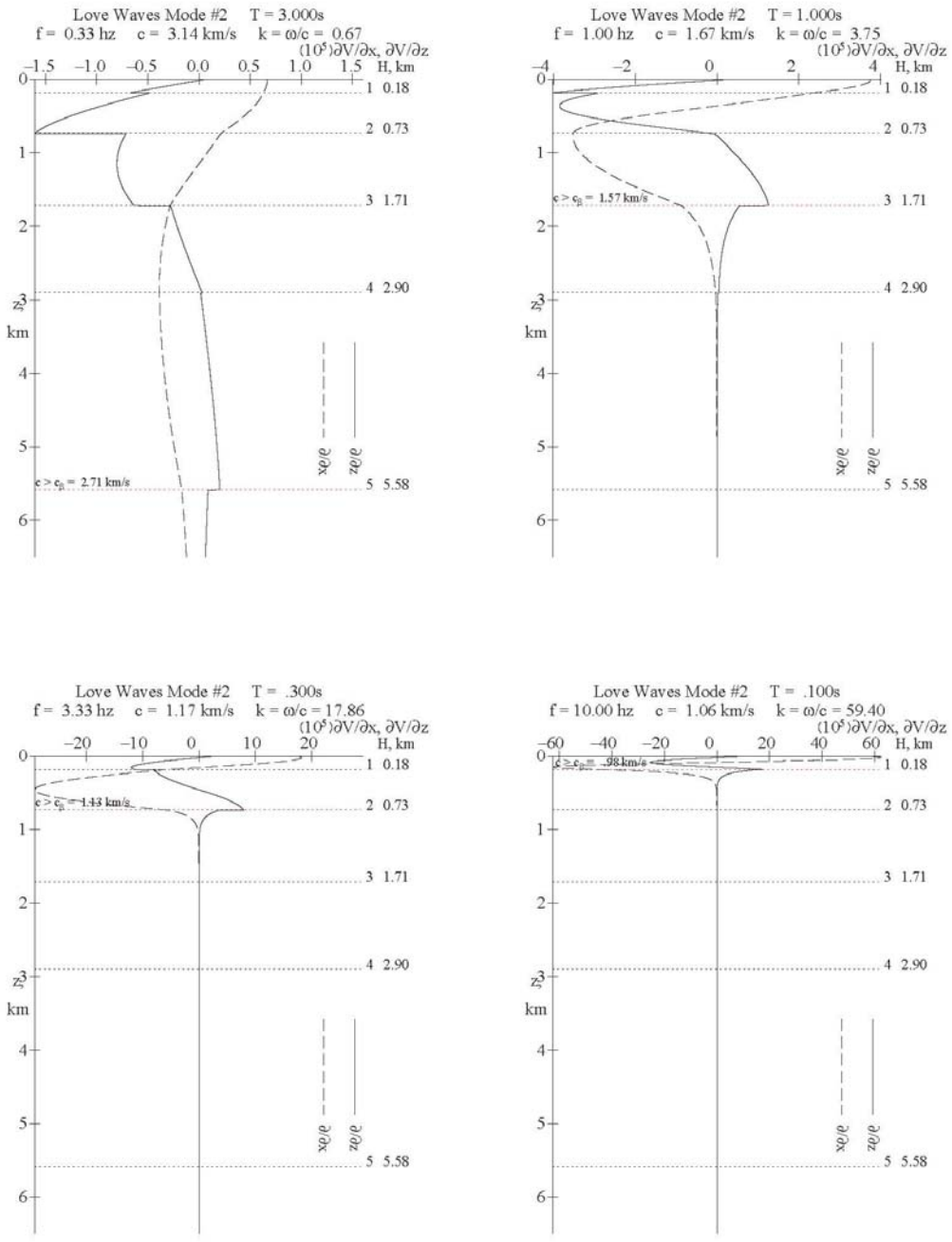

The dV/dx mode shape for the waves at $T = 1\text{sec}\ (1.0hz)$ period, in the top-right graph, decays a bit faster to negative values around $z \sim 0.5km$, in the 2nd layer, $0.18 \le z \le 0.73km$. It stays negative, with the negative minimum (close to but above $-k$) right at the start of the 3rd

layer at $z = 0.73km$, then decays to zero right at the interface of the 4th and 5th layer at $z = 2.90km$.

Figure III.3 Mode#3 Love Waves Mode Shapes at $T = 2.0,\ 0.75,\ 0.2,\ 0.075\ s$

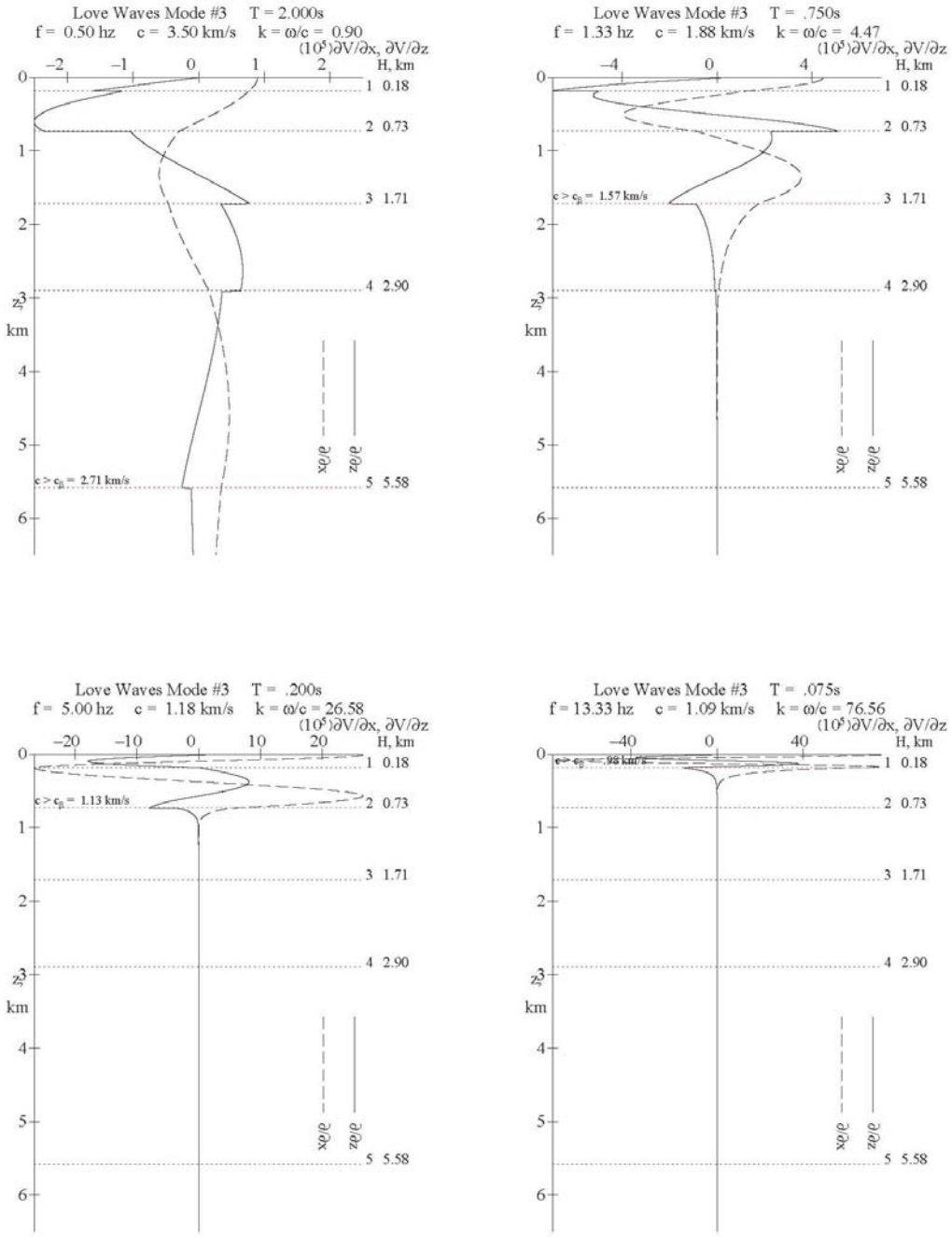

The dV/dx mode shape for the waves at $T = 0.3\,\text{sec}\ (3.33hz)$ period, shown in the bottom-left graph, starts at $k = 17.86$ and decays much faster to negative values around $z \sim 0.15km$ in the top 1st layer $0.0 \le z \le 0.18km$. It stays negative, reaching a negative minimum below $-1.5k$, around $z \sim 0.5km$ in the 2nd layer, $0.18 \le z \le 0.73km$. It then decays to zero right at the start of the 3rd layer, $0.73 \le z \le 1.71km$, before $z \sim 0.8km$.

Finally, the dV/dx mode shape for the waves at $T = 0.1\,\text{sec}\ (10.0hz)$ period in the bottom-right graph decays so fast that it goes negative right in the top 1st layer, $0.0 \le z \le 0.18km$, reaches its negative minimum close to the interface of the 1st and 2nd layers at $z = 0.8km$ and then, decays to zero in the same 2nd layer. The dV/dz (solid line) mode shapes for all graphs start small at the top, decaying to negative values and then to zero just like the dV/dx mode shapes.

Mode #3 has phase velocities for 61 periods in the range from 2.0 sec down to 0.04 sec. The Thomson-Haskell computation gives both dV/dx and dV/dz rotational mode shapes of the Mode #3 of Love waves in the same period range. **Figure III.3** shows the plots of these mode shape amplitudes at four selected periods: $T = 2.0,\ 0.75,\ 0.2,\ \text{and}\ 0.075\ s$. The rotational mode shapes, like those of translations, have the features expected for the 3rd mode, namely, each graph cross the zero line twice before decaying to zero at some depth below.

III.3 Body SH Rotational Waves with a Given Incident Angle

Figure III.4 shoes the plots of ***SH*** body wave mode shape amplitudes at four selected periods: $T = 5.0,\ 1.5,\ 0.50,\ \text{and}\ 0.15\ s$, assuming a given angle of incidence of body ***SH*** waves at $\gamma = 84^o$ with respect to the vertical direction from the bottom semi-infinite 6th layer. Such dV/dx and dV/dz mode shapes can be computed at all 91 periods in the range from $T = 15.0\ s$ down to $T = 0.04\ s$.

Figure III.4 SH Body Waves (Incidence at 84^o) at T = 5.0, 1.5, 0.50, 0.15 s

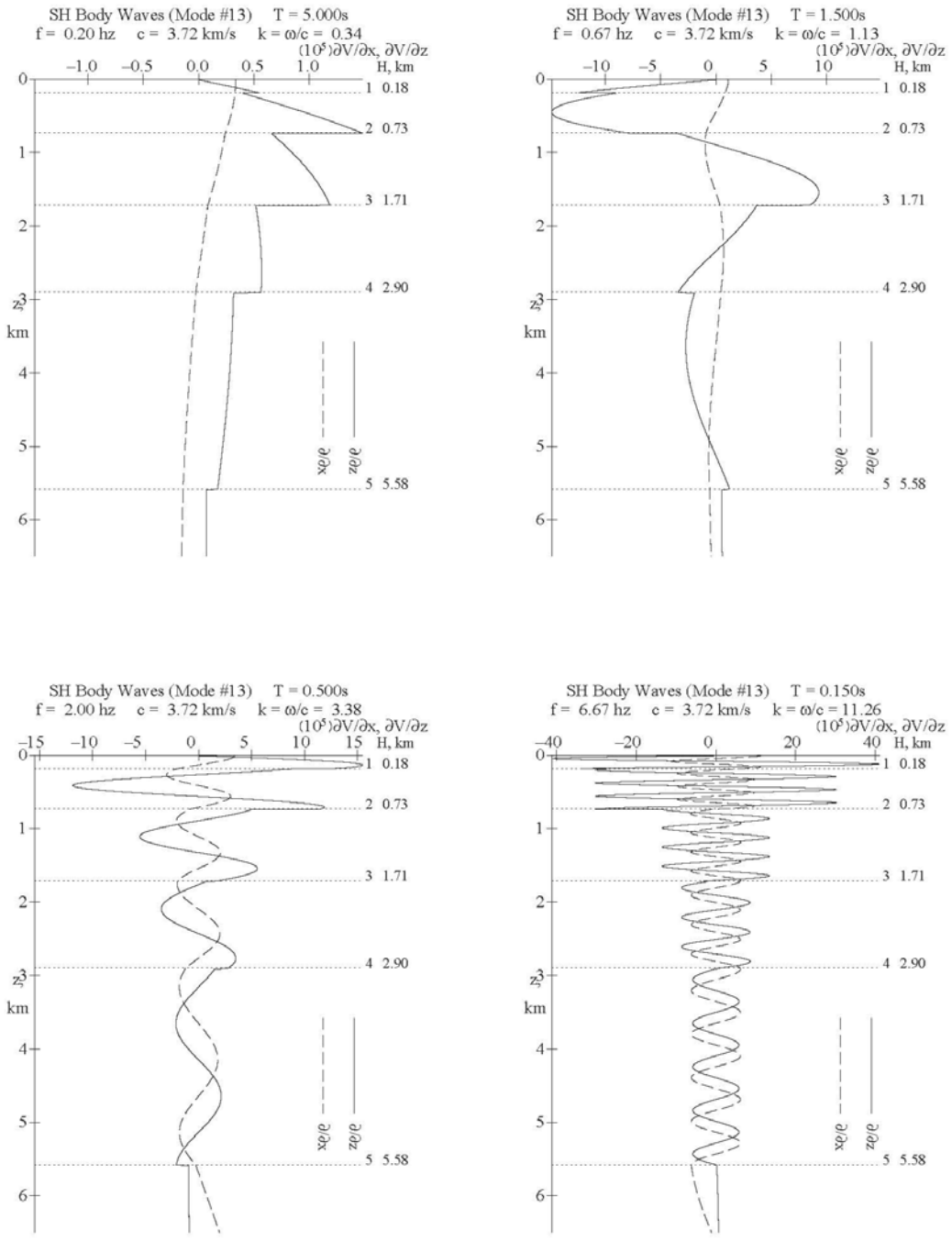

This corresponds to an almost horizontal angle of incidence. The actual angle of incidence used will be different in each case, dependent on

1) The location and focal depth of the earthquake source,
2) The location of the recording site and its epicentral distance from the source.

In each case, the mode shapes are normalized to have amplitude one at the half-space surface of $z = 0$. At depth, the body SH waves will then all have amplitudes that oscillate. Unlike the surface Love waves above, these are body waves and hence the mode shape amplitudes will not decay to zero as depth increase.

The next chapter will consider one case where the site is in the near field of an earthquake source, with hypocentral distance $D \approx 10km$. In such a case, a ray path is traced so that the ray will take the shortest time to travel from the source to the site, and as the next section shows, each ray will have a different angle of incidence.

III.4 Rayleigh Waves Rotation Mode Shapes

Next we illustrate the dV/dx and dV/dz (rotational) mode shapes for the first two modes of ***Rayleigh*** surface waves. As in the case of Love waves, with the modified Thomson-Haskell propagator matrix defined in Chapter II above, the relative rotation amplitudes can now be computed for each mode of the Rayleigh waves for each frequency where the waves exist and in each layer of the half-space. There will now be 2 components of in-plane motions, the horizontal *x*-component and the vertical *z*-component. As in Report 2, we will normalize the translational displacement amplitude of both components with respect to the vertical z-component of motion at the half-space surface (Report 2).

This section will describe the *Rayleigh* Waves dV/dx and dV/dz (rotational) mode #1 and mode #2, for the phase velocities $c = c(T)$, in the range of periods starting from 15sec down to 0.04sec. This is followed by Section III.5 with the rotation mode shapes of body ***P*** and ***SV*** waves for a given incident angle. This will be taken to be the "11^{th} and 12^{th} modes" of waves to be included in the generation of synthetic translational motions in the (in-plane, ***P*** and ***SV***) radial and vertical directions.

The mode #1 of Rayleigh waves has phase velocities for all 91 periods from 15 sec down to 0.04 sec. The modified Thomson-Haskell computation thus gives the $d(U,W)/dx$ and $d(U,W)/dz$ (rotational) mode shapes of the mode #1 of Rayleigh waves in the same wide period range at every specified point below the surface. **Figure III.5** shows the plots of two components (*x*- and *z*-) of such Rayleigh wave $d(U,W)/dx$ and $d(U,W)/dz$ mode shapes at the same four selected periods: $\boldsymbol{T = 5,\ 1.0,\ 0.5,\ \text{and } 0.1\ s}$.

The amplitudes of the mode shapes of both components are normalized with respect to the vertical component W of motion at the surface of the layered half-space, so that the mode shape values become the scaling factors for transfer function values of the waves at different depths starting with the amplitudes on the half-space surface. Each graph has two components of the mode shape amplitudes versus the distance *z*, measured in ***km*** below the half-space surface. Recall from Report 2, where it was noted that at the half-space surface, with the *z*-component motion $W(z)|_{z=0} = 1$ cm , the *x*-component of motion, $U(z)|_{z=0} = i\gamma\, W(z)|_{z=0} = i\gamma$, is an imaginary number, where γ is a ratio computed from the Haskell algorithm for estimating phase velocities of Rayleigh waves. With this normalization, $W(z)$ will stay real, while $U(z)$ will stay imaginary for all z. In Report 2, without loss of generality, only the imaginary part of $U(z)$ and the real part of $W(z)$ were plotted.

Consider the dU/dx and dW/dx mode shapes in **Figure III.5**. Since $dW/dx = ikW$, and the fact that $W(z)$ is taken to be real for all z, this makes dW/dx imaginary and so only the imaginary part of dW/dx is plotted and it is k times that of W. Similarly $dU/dx = ikU$, and the fact that $U(z)$ is imaginary, dU/dx is real and of opposite sign to the imaginary part of $U(z)$, and it is $-k$ times that of the imaginary part of U.

Figure III.6 Mode#1 of Rayleigh Waves. Rotation Mode Shapes at $T = 5, 1.0, 0.5, 0.1$ *s*

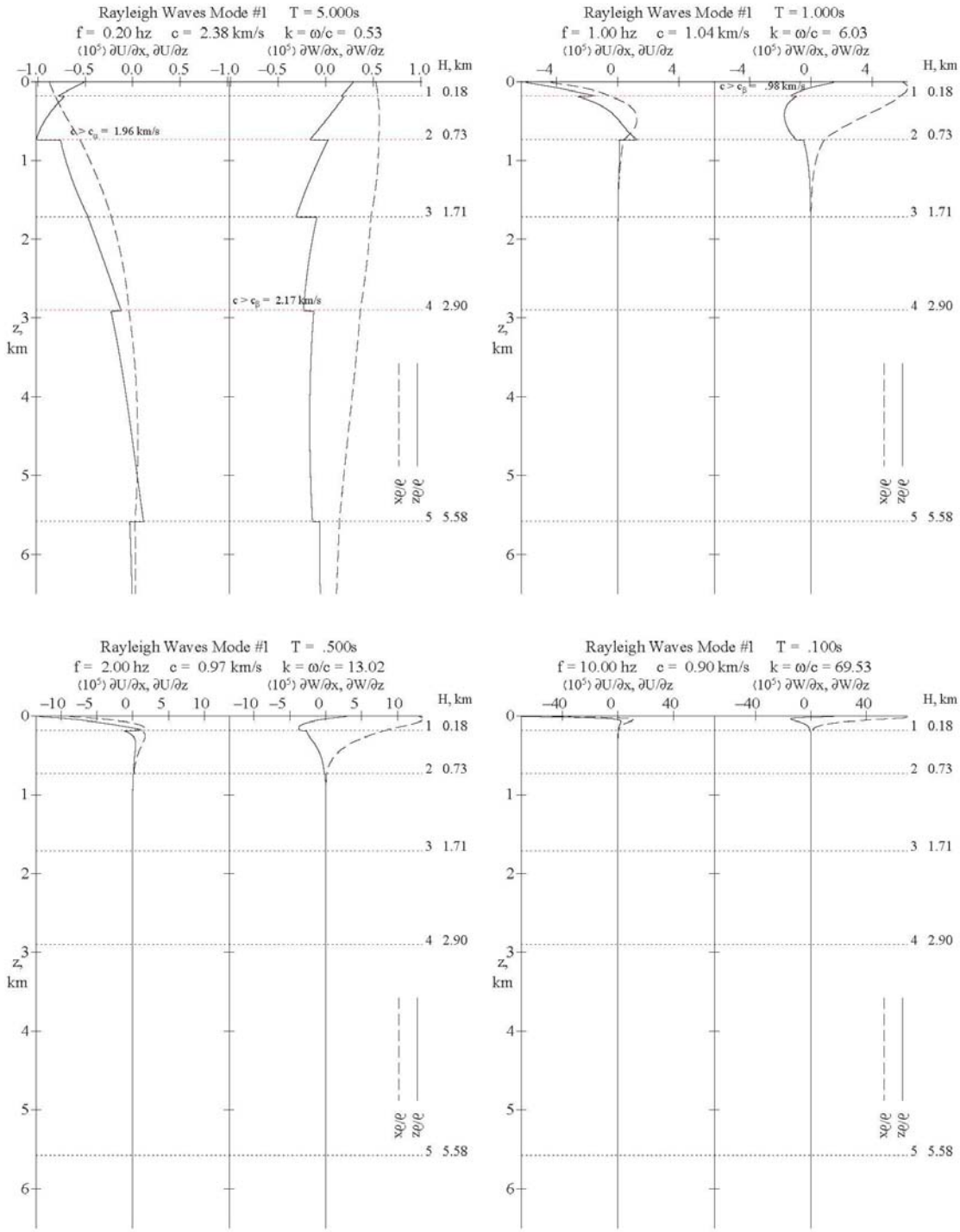

As expected for Mode #1 mode shape, all d/dx start at $z = 0$, on the surface, maintain the same sign without crossing the zero line, and decay to zero at some depth below the surface. The waves at long periods decay slower than the waves at short periods.

The (imaginary part of) dW/dx (dashed line) mode shape for the waves at $T = 5\,\text{sec}\ (0.2hz)$ period is shown in the right part of the top-left set of **Fig. III.5**. It starts with amplitude k on the surface, decays slowly and stays positive above zero all the way down to $z \sim 6km$, which is just inside the bottom, semi-infinite 6th layer. The (real) dU/dx the mode shape, on the other hand, starts at $\sim -1.6k \sim -0.85$, and stays negative before decaying to zero around $z \sim 5km$, near the bottom of the 5th layer.

The dU/dx and dW/dx mode shapes for both components at $T = 1\,\text{sec}$ period $(1.0hz)$ in the top-right graph decay a bit faster to zero around $z \sim 0.75km$, which is just inside the 3rdlayer in the model, where $0.73 \le z \le 1.71km$. The mode shapes for the waves at $T = 0.5\,\text{sec}\ (2.0hz)$ period in the bottom-left graph decay much faster and stay above zero only down to $z \sim 0.5km$, inside the 2nd layer, where $0.18 \le z \le 0.73km$. Finally, the mode shapes for the waves at $T = 0.1\,\text{sec}\ (10.0hz)$ period, in the bottom-right graph decay so fast that they both decay to zero before $z \sim 0.15km$, which is inside the 1st layer of the model, $0.0 \le z \le 0.18km$.

Both the dU/dz and dW/dz mode shapes exhibit the same decaying behavior as the d/dx mode shapes, with the additional property that they both have jumps at the layer interfaces, a property already observed for the anti-plane dV/dz mode shapes, because of the discontinuous shear moduli across the interfaces.

One interesting similarities between this and the Love wave mode shapes is that the amplification factor can be quite large compared with that of the translational components because the translational mode shapes can have large, steep slopes and hence these derivatives are large.

Figure III.6 Mode#2 of Rayleigh Waves. *x*- and *z*- Mode Shapes at ***T* = 3, 1, 0.3, 0.1 *s***

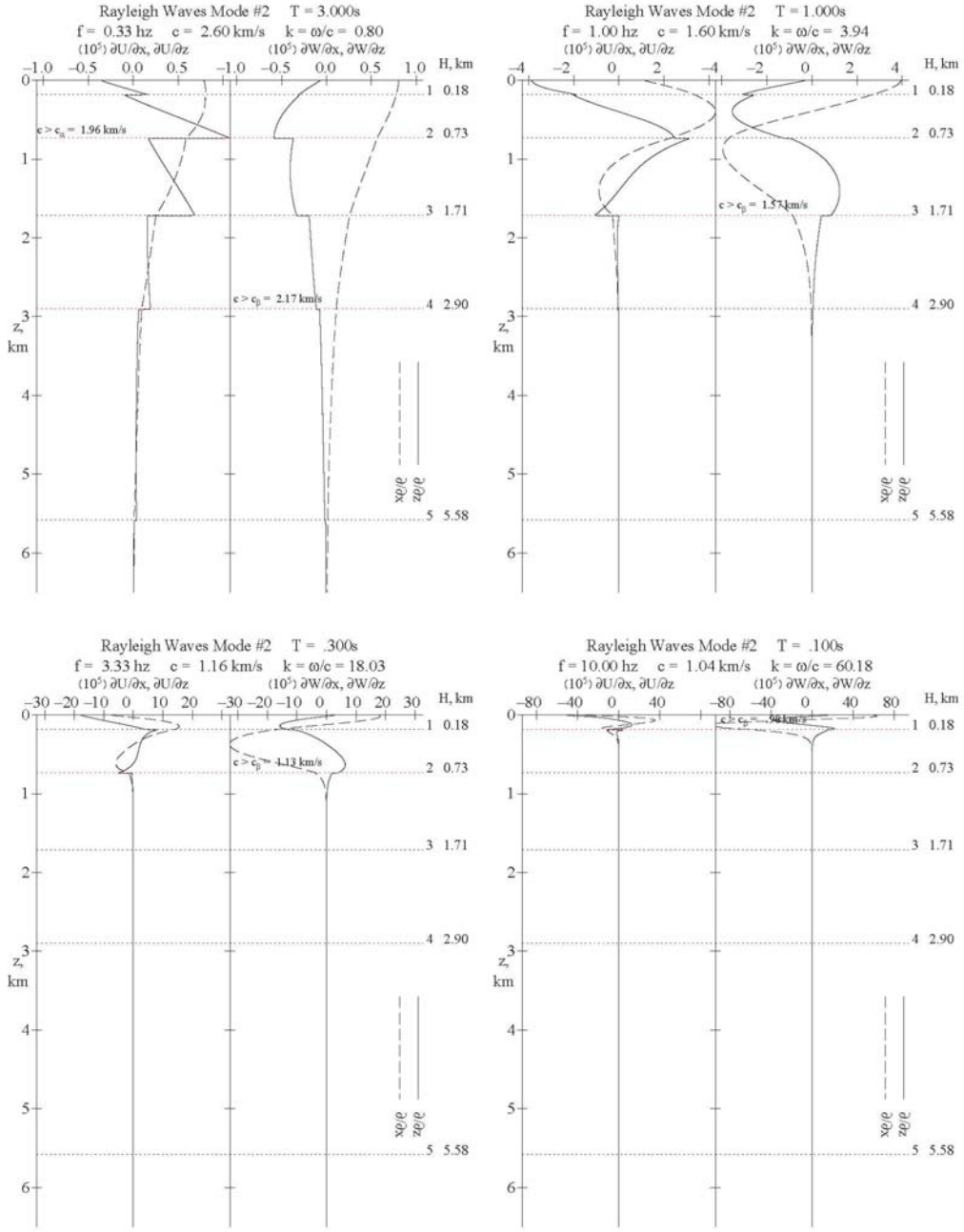

Mode #2 of Rayleigh waves has phase velocities at 74 periods in the range from 4.6 sec down to 0.04 sec. The Thomson-Haskell computation gives the mode shapes of the Mode #2 in

the same wide period range. **Figure III.6** illustrates the plots of d/dx and d/dz of both horizontal U and vertical W components of Rayleigh wave mode shape amplitudes at four selected periods: $T = 3.0,\ 1.0,\ 0.3,$ **and** $0.1\ s$. The translational *z*-component displacement amplitude is normalized to one at the surface of the half-space, so that the mode shape values again become the scaling factors or transfer function values of the waves along the depth for mode #2 waves. Each graph shows plots of the rotational mode shape amplitudes for both components versus depth in kilometers.

As in the case of translational motions, the mode #2 shapes will change sign and cross the zero line before decaying to zero at some depth below. Also, the waves at long periods decay slower than the waves at low periods.

Note that the jumps for the d/dz rotational motions across each layer interface are more pronounced for Mode #2 than for Mode #1, especially at longer periods. All the motions also die down beyond the 3rd layer from top. For shorter periods, or higher frequencies in the bottom two graphs, they are already negligible right after the 2nd layer. The rotational mode shapes for Mode #3 to Mode #5 all show the same similar trend.

III.5 Body P and SV Rotational Mode Shapes of a Given Incident Angle

Figure III.7 illustrates the plots of ***P*** and ***SV*** body wave rotational mode shapes at four selected periods: $T = 5.0,\ 1.5,\ 0.50,$ **and** $0.15\ s$, assuming a given angle of incidence for ***P***-waves at $\gamma = 84^o$ with respect to the vertical direction from the bottom semi-infinite 6th layer. Such mode shapes exist at all 91 periods in the range from $T = 15.0\ s$ down to $T = 0.04\ s$.

Figure III.8 is the corresponding plot of ***P*** and ***SV*** body rotational wave mode shapes at the same four selected periods: $T = 5.0,\ 1.5,\ 0.50,$ **and** $0.15\ s$, assuming the same given angle of incidence, this time for ***SV***- waves at $\gamma = 84^o$.

As for the body ***SH***- waves, this corresponds to an almost horizontal angle of incidence. The angle of incidence used will be different for each case, and will dependent on

Figure III.7 P and SV Body Wave modes for Incident P Waves at $\gamma = 84^o$ $T = 5.0,\ 1.5,\ 0.50,$ and $0.15\ s$

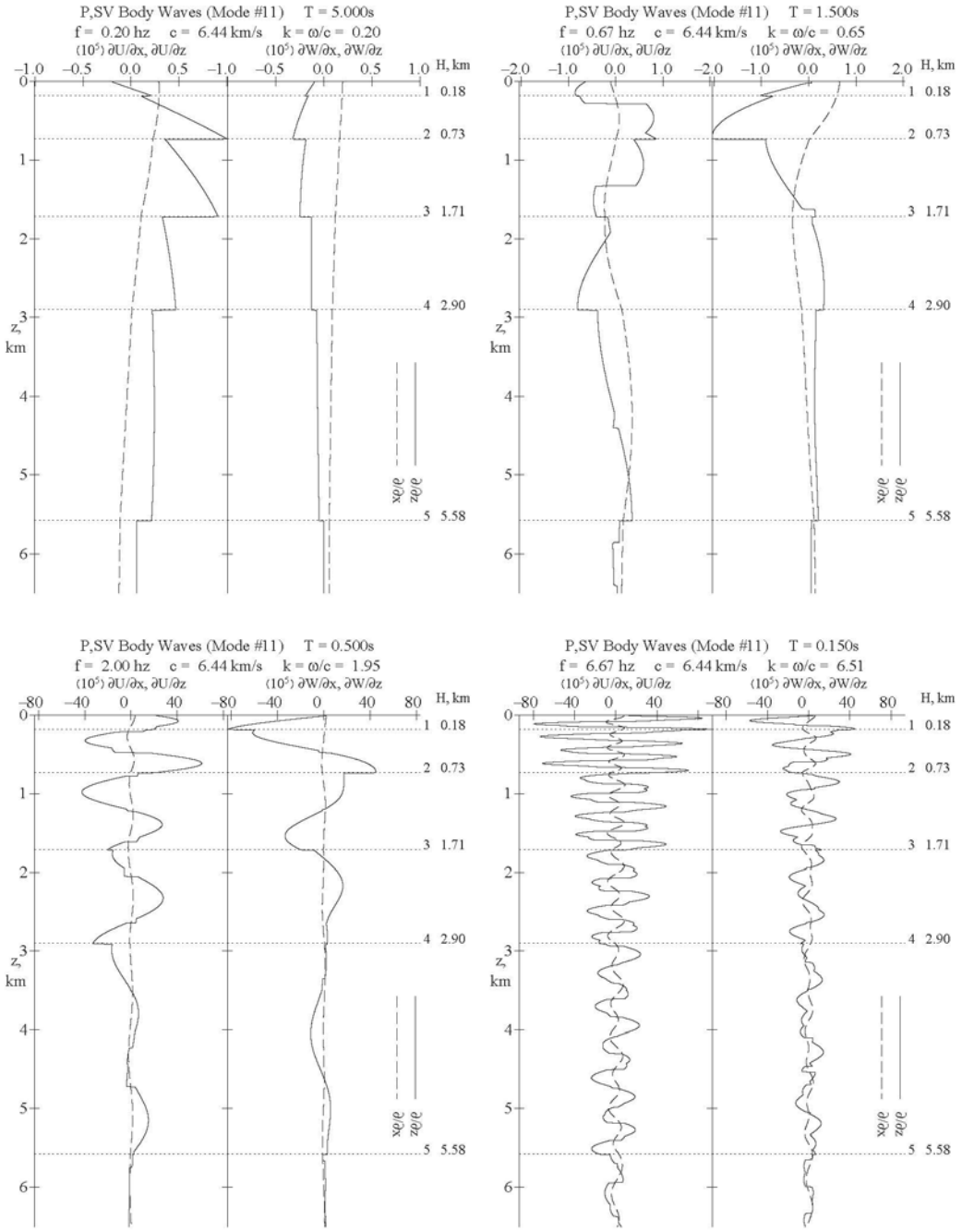

Figure III.8 P and SV Body Wave modes for Incident SV-Waves at $\gamma = 84^o$ $T = 5.0,\ 1.5,\ 0.50,$ and $0.15\ s$

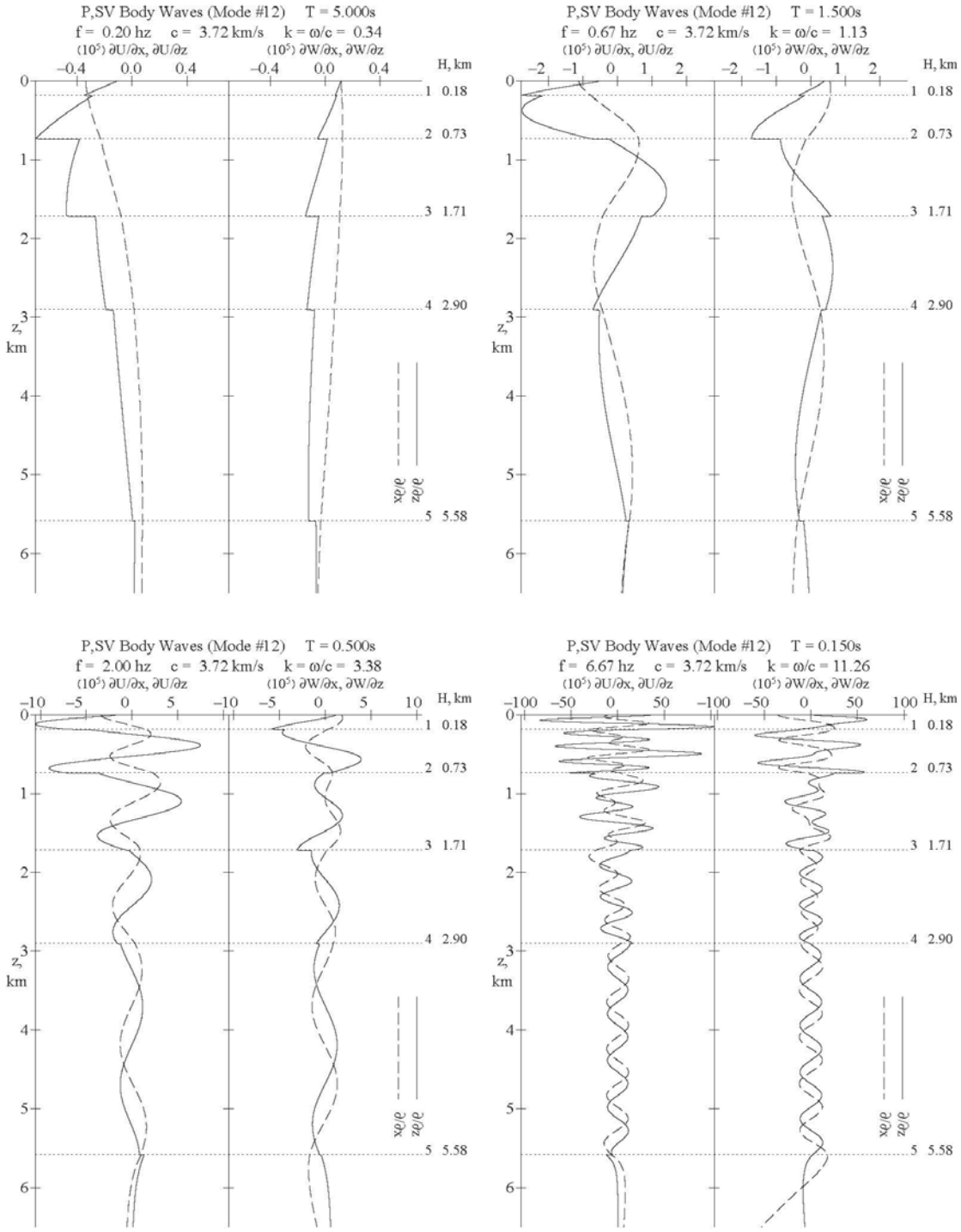

1) The location and focal depth of the earthquake source,
2) The location of the recording site and its epicentral distance from the source.

For example, the incident angles from the bottom semi-infinite media from very small to very large hypocentral distances, say from $D = 10km$ to $D = 70km$ for the El Centro layered model considered in this report, are between $\gamma = 83^o$ and $\gamma = 85^o$.

IV. The Synthetic Transverse Rotational Motions

IV.1 Introduction

With the rotational mode shapes and Transfer functions available for the 5 modes of Love waves and 1 "mode" of Body SH waves from the last chapter, the procedures of Report 2 for generating the synthetic transverse components of acceleration at all depths *z* below the surface can now be extended to the transverse components of rotational motions. We will pick the same El Centro 6-Layered elastic model and select the following two ***Case Studies*** for the earthquake source and site characteristics:

Case Studies:

1) ***Case Study 1:*** $M = 6.5,\ R = 8.0km,\ H = 6.0km,\ s = 0,\ s_L = 2$

2) ***Case Study 2:*** $M = 6.5,\ R = 40.0km,\ H = 9.0km,\ s = 0,\ s_L = 2$

where

M = earthquake magnitude

R = epicentral distance

H = focal depth of earthquake, corresponding to a hypocentral distance of

$$D = \left(R^2 + H^2\right)^{1/2} = \left(8.0^2 + 6.0^2\right)^{1/2} = 10.0km$$

s = geologic site condition of the recording site, with

s = 0, alluvial site, s = 1, intermediate site and s = 2, rock site

s_L = soil condition of the recording site, with

s_L = 0, rock soil, s_L =1, intermediate soil and s_L =2, soft soil type

The two cases are for the same site, with the same geological and soil site conditions, and are subjected to an earthquake of the same magnitude. They differ only in the epicentral distances and the earthquake focal depths. ***Case Study 1*** illustrates near-field motions with small epicentral distance and shallow focal depth. ***Case Study 2*** has larger epicentral distance and slightly deeper focal depth.

In both ***Case Studies 1 and 2***, we compute the *Translational motions* as in Report 2, and now the *Rotational motions* at points on and below the surface along a vertical line $(x = 0)$ from the surface $(z = 0)$ down to a depth of $z = 6$ km below. The revised computer program, SYNACCS, will be used to compute the Translational and Rotational motions at any point (x, z) on or below the surface. At a point (x, z) where $x \neq 0$ and further to the right, the Fourier Transform of the various acceleration components, here and in Report 2, all include the term e^{ikx} to account for the time shift resulting from the waves arriving at the point further and further away. However, the fact that digital Fast Foruier Transform (FFT) of the finite sequence of Fourier terms is used in the calculation, this will result in all time series at all points to have nonzero amplitudes starting at $t = 0$, although this beginning portion of the time series up to the arrival of the fastest waves is physically associated only with the processing noise. To account for the actual time arrival of time series at points to the right of the line $x = 0$, we use the following procedure to put zeros at points at the beginning of the record:

Suppose a component of the synthetic time series is defined at a horizontal distance of $x = H$ km to the right of the vertical line $x = 0$, and that the fastest waves of all modes that contribute to the component have a phase velocity of $c(T) = c$ km/s. The fastest waves would thus have to take a time of $T = H / c$ seconds to arrive at the point. This component of record is then assumed to have a time delay of T sec. We define a step function $H(T)$ as

$$H(t) = \begin{cases} 0 & t < T \\ 1 & t \geq T \end{cases} \tag{4.1}$$

and multiply the time series of the component by this step function, so that it is essentially zero before the fastest waves arrive. This elimination of small but negligible amplitudes in the time series is important for proper starting of calculations in the cases where SYNACCS is used to

define input motions into the finite element or finite difference "boxes" of soil surrounding the structures in soil-structure response analyses.

The Updated program SYNACCS can now generate time series from each mode of surface ***Rayleigh*** and ***Love*** waves, and each mode of body ***P, SV*** and **SH** waves. The above procedure can also be applied separately to the data from each mode of body or surface waves, since each mode has a slightly different phase velocity.

IV.2 *Case Study 1:* $M = 6.5,\ R = 8.0km\ \&\ H = 6.0km\ (D = 10.0km),\ s = 0,\ s_L = 2$

As described in Section VII.1, Report 2, the time history at the top surface $z = 0$ will be generated by the SYNACC method (**Trifunac, 1971b; Wong and Trifunac, 1978, 1979**; **Lee and Trifunac, 1985, 1987**), using the current SYNACCS algorithm, which includes a mode of ***SH*** body waves (Mode #13). **Figure IV.1** (Figure VII.1 of Report I) here is a plot of the ray path taken by the SH body waves from the earthquake source to the recording site.

Figure IV.1 (Figure VII.1of Report I) SH Body Waves Ray Path from Source

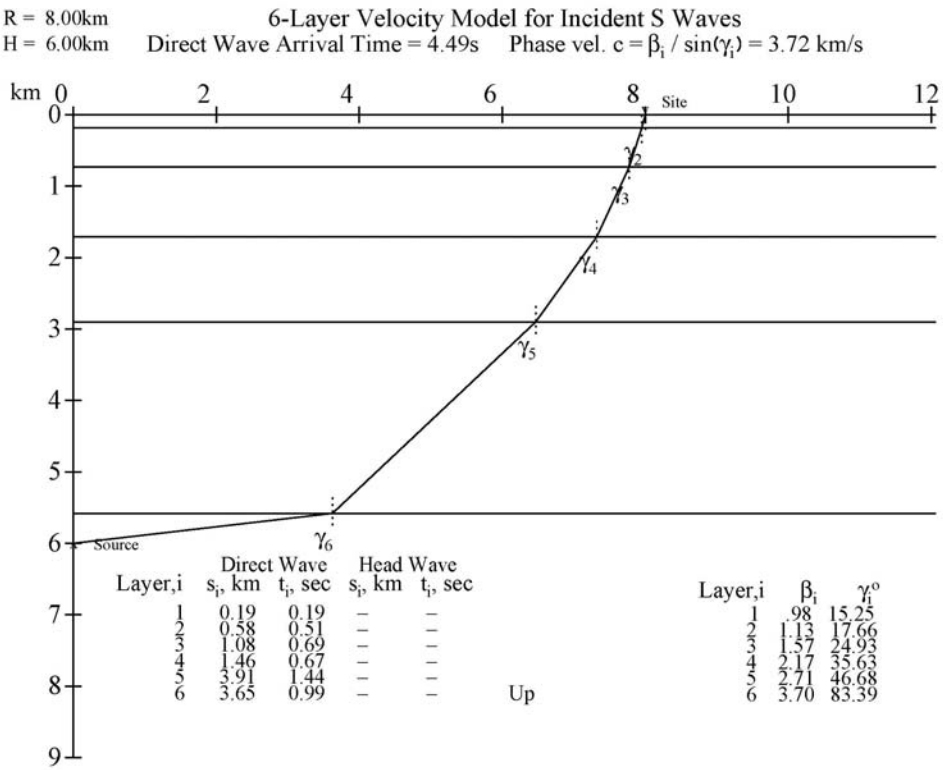

The ray path is chosen so that the phase velocities at each layer of the 6-layered media are the same, or that the angles of the ray travel are determined so that Snell's Law is satisfied at each interface, namely, for the layer $i = 1,\ 2,\ \ldots,\ 6$:

$$c = \beta_i \,/\sin(\gamma_i) = \ \textbf{3.72 km/s, a constant} \qquad \textbf{Report 2 (VII.1)}$$

where

β_i = shear wave speed, and

γ_i = angle the ray makes with respect to the vertical directional the i^{th} layer.

It shows that the ray will start at an angle of $\gamma_6 \sim \mathbf{83.4}^o$ with respect to vertical direction, with almost horizontal path, and bend up into the layered media so that it arrives at the site with $\gamma_1 \sim \mathbf{15.3}^o$, with respect to the vertical direction.

Figure IV.2 gives the synthetic $\partial\ddot{V}/\partial x$ and $\partial\ddot{V}/\partial z$ rotational acceleration time-histories calculated using the earthquake parameters of the Case Study 1 in Section IV.1 above. It corresponds to a hypocentral distance of $D = \left(R^2 + H^2\right)^{1/2} = \left(8.0^2 + 6.0^2\right)^{1/2} = 10.0km.$ the **SYNACCS** program determines that the appropriate duration of the accelerogram record should be just above 40 seconds. The depth of each accelerogram is labeled at intervals 0.5km apart. Of the 120 accelerogram time histories, five of them are plotted green, and labeled ***1*** to ***5***. The ones labeled ***1*** to ***5*** are those at depths, which are closest to the interfaces between adjacent layers in the site model. The corresponding acceleration time histories of the transverse translational component, **'$\ddot{V}(z)$'**, can be found in Figure VII.3 of Report 2.

Note that, as in Report 2, the actual time scale of the above time histories has been shifted to have a common time scale, where $T = 0$ **sec** is defined by SYNACCS to be the arrival time $R/c_{\max}$, where R is the epicentral distance and $c_{\max}$ is the maximum velocity of the waves.

This synthetic component of rotational motion, $\partial V/\partial x$ and its 1st and 2nd time derivatives, $\partial \dot{V}/\partial x$ and $\partial \ddot{V}/\partial x$, correspond to the time-histories of synthetic ***shear strain***, $\gamma_{yx} = 2\varepsilon_{yx}$. From equation (2.2) above, $\Omega_z = \frac{1}{2}\partial V/\partial x$, also represents the synthetic antiplane component of Torsional ***motion***, the ***z***-component of rotation.

Similarly, the synthetic component of rotational motion, $\partial V/\partial z$ and its 1st and 2nd time derivatives, $\partial \dot{V}/\partial z$ and $\partial \ddot{V}/\partial z$, correspond to the time-histories of synthetic ***shear strain***, $\gamma_{yz} = 2\varepsilon_{yz}$. From equation (2.2) above, $\Omega_x = -\frac{1}{2}\partial V/\partial z$, represent the synthetic antiplane component of ***Rocking motion***, the ***x***-component of rotation.

Perusal of Figure IV.2 here, together with Figure VII.3 of Report 2, shows that, at such short distance of $D = 10.0km$, both the Love waves and body waves arrive within a few seconds.

For the $\partial \ddot{V}/\partial x$ motions on the left, the SH body waves have the same phase velocity at all periods and the figure shows that the direct arrival time of the ***SH*** body waves is around $T \sim 4.49s$. The arrival times for Love waves will be different for different modes, and for waves at different periods, since the phase velocities $c = c(T)$, depend on the period of the waves. The rotation time histories show that the strong-motions arrive at about $T \sim 5.0s$, which follows right after the direct arrival time of body waves. They are thus not very distinguishable in the near-filed, due to short hypocentral distance.

The $\partial \ddot{V}/\partial z$ motions on the right do show the arrival of two sets of waves, namely the rotational component of body transverse ***SH***- waves and the surface Love waves. Here the body ***SH*** waves arrive first, with the surface waves arriving about 6 seconds later.

Figure IV.2 $\partial\ddot{V}/\partial x$ **Synthetic Acc.:** $M = 6.5,\ R = 8.0km,\ H = 6.0km,\ s = 0,$ **and** $s_L = 2$ $\partial\ddot{V}/\partial z$

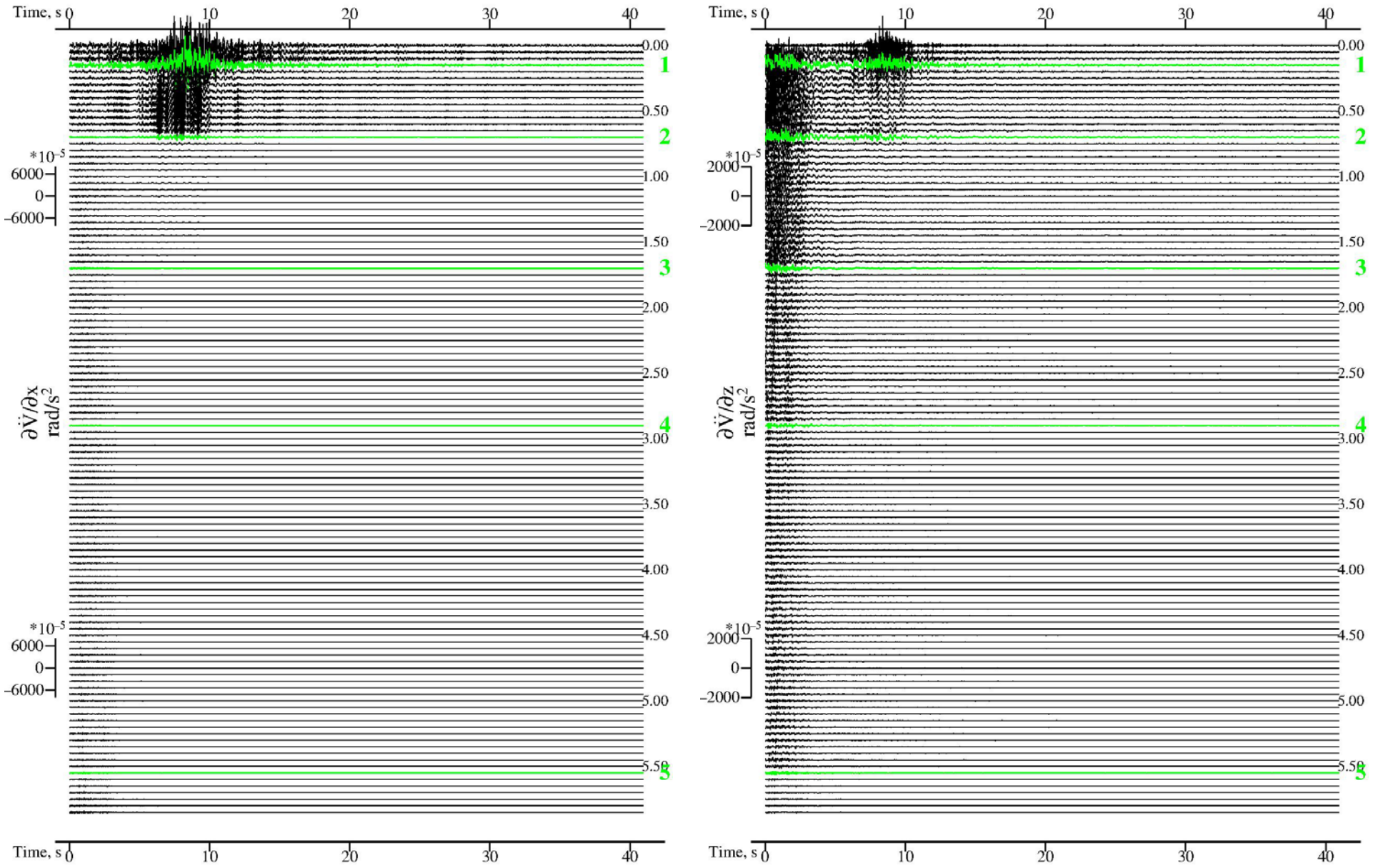

The strong motion of rotation $\partial\ddot{V}/\partial x$ is observed at depths in the first two top layers, up to $z \sim 0.7km$. Smaller motions are in the 3rd layer up to $z \sim 1.7km$, beyond which the motions become small and negligible. This is consistent with the mode shape amplitudes of Love waves (Section V Report 2), where it was found that, for all modes, at moderate periods, the motions stay close to, but are always less than, those at the top surface, in the first two layers, and then began to die down further below. The attenuation is faster for the waves at higher frequencies. The strong motion rotations $\partial\ddot{V}/\partial z$ decay even faster with depth, showing the strong motions only in the 1st layer and the beginning of the 2nd layer, around up to $z \sim 0.3km$. The body ***SH*** wave motions of $\partial\ddot{V}/\partial z$, on the other hand, are more noticeable down to, and beyond the 3rd layer at $z \sim 1.7km$.

Figure IV.3 shows the corresponding synthetic rotational motions $\partial\dot{V}/\partial x$ and $\partial\dot{V}/\partial z$ (velocity). The actual depth of each velocity time function is labeled at each 0.5 km apart. Of the 100 velocity time histories, six of them are plotted green, and labeled ***1*** to ***5***. They are those rotation time histories at depths on or closest to the interfaces between adjacent layers.

The new SYNACCS program computes the rotational velocity at all depths from the corresponding rotational acceleration time histories from the Fourier transform in the frequency domain, and then taking its inverse Fourier transform.

Figure IV.4 shows the corresponding synthetic rotational motions $\partial V/\partial x$ and $\partial V/\partial z$ (displacements) calculated for the same El Centro site. The consecutive depths of each plotted displacement are again 0.5km apart. Of the 120 displacement time histories, five are again plotted green, and labeled ***1*** to ***5***., and correspond to those at depths, which are closest to the interfaces between adjacent layers. The new SYNACCS computer program computes the rotational displacement at all depths from the corresponding rotational acceleration time histories in the frequency domain, and then takes its inverse Fourier transform.

Figure IV.3 $\partial\dot{V}/\partial x$ **Synthetic Vel.:** $M = 6.5,\ R = 8.0km,\ H = 6.0km,\ s = 0,$ **and** $s_L = 2$ $\partial\dot{V}/\partial z$

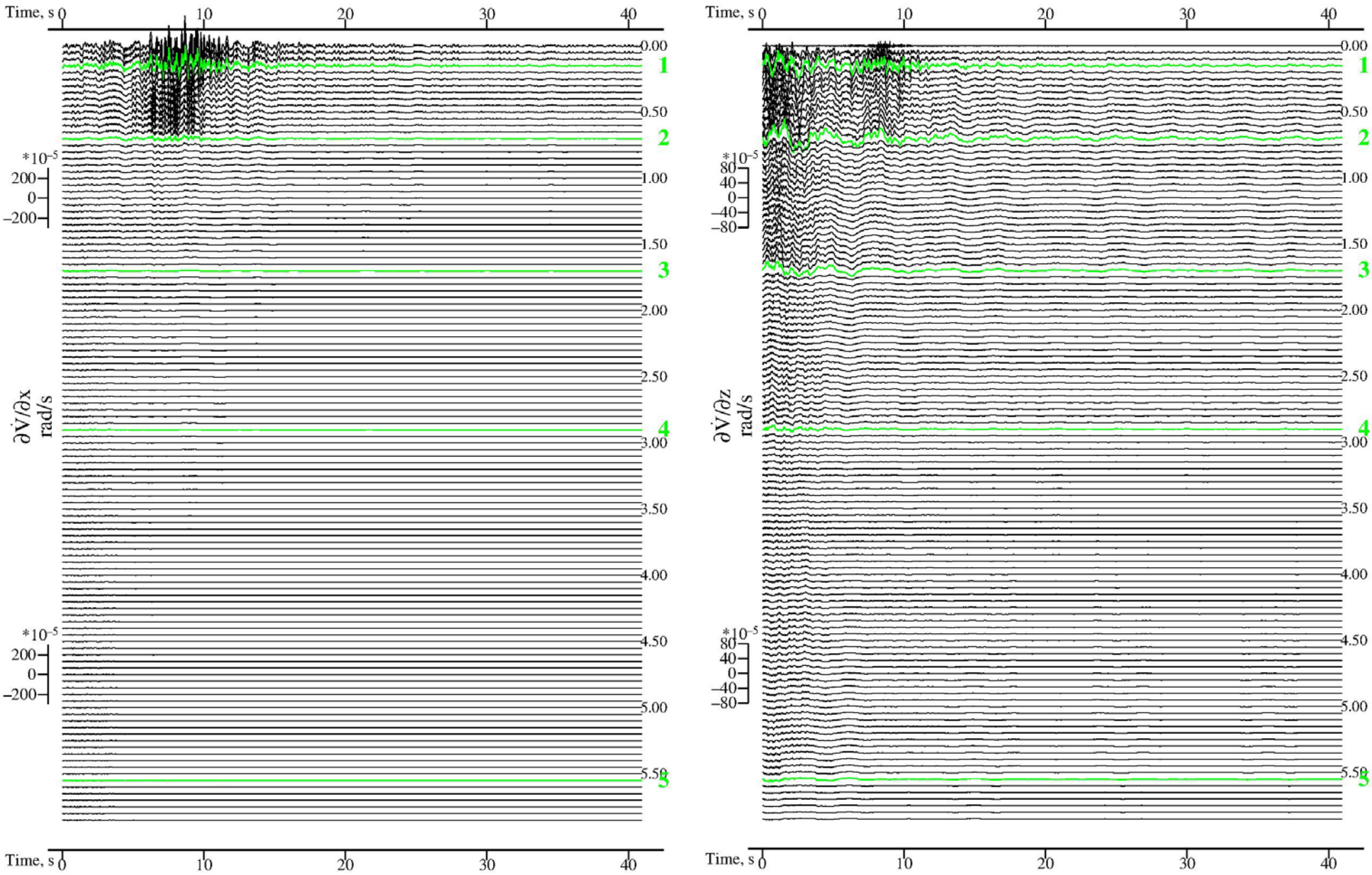

Figure IV.4 $\partial V/\partial x$ **Synthetic Disp.:** $M = 6.5$, $R = 8.0km$, $H = 6.0km$, $s = 0$, and $s_L = 2$ $\partial V/\partial z$

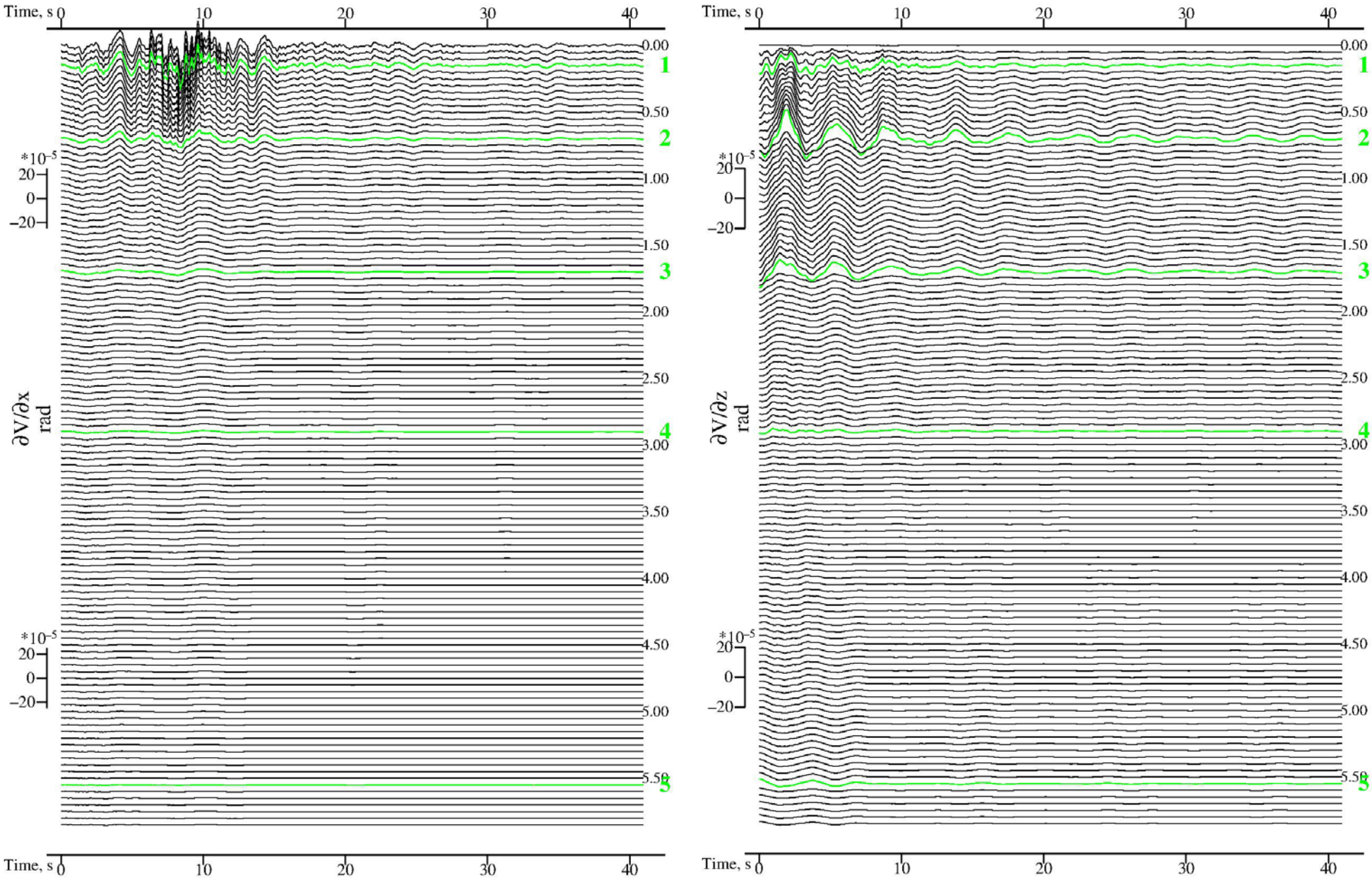

IV.3 The Three-Dimensional (3-D) Plots for *Case Study 1*

It is instructive also to plot the above two-dimensional ***(2-D)*** time histories of rotational acceleration $\partial\ddot{V}/\partial x$, $\partial\ddot{V}/\partial z$, velocity $\partial\dot{V}/\partial x$, $\partial\dot{V}/\partial z$ and displacements $\partial V/\partial x$, $\partial V/\partial z$, respectively in **Figures IV.2, 3 and 4**, as three-dimensional ***(3-D)*** time histories figures.

Figure IV.5 in the next page is the ***3-D*** plot of the translational motions of the same 120 accelerations corresponding to **Figure IV.2**. The two horizontal longitudinal and transverse coordinate axes are now correspondingly the **time** axis and the **depth** below surface. The vertical axis shows the amplitude of **acceleration** in cm/s^2. The five green lines, labeled 0 to 5, again correspond to the positions where the layers meet. **Figures IV.6 and IV.7,** which follow, show the ***3-D*** representation of rotational synthetic velocities and displacement, corresponding to the ***2-D*** plots of **Figures IV.3 and IV.4.**

IV.4 Separating the Body and Surface Waves Plots of *Case Study 1*

Since it is known that the body waves and surface waves arrive at different times, their contributions to the synthetic motions are thus best visualized by plotting them separately. The ***3-D*** plots in **Figure IV.8** represent the rotational acceleration time histories $\partial\ddot{V}/\partial x$ and $\partial\ddot{V}/\partial z$ of the body waves and of surface waves. The body wave time histories on the left show that the waves arrive at the beginning and dominate the motions at all depths within the first 5- seconds. The body wave rotational motions are also seen at all depths below the surface. The surface wave time histories on the right show that the motions which arrive later, at about 7 seconds after the first arrival time. In this example the body wave rotational peak acceleration has a much smaller maximum compared with that of the surface waves. This results from the fact that the weights assigned to the five modes of surface love waves are higher than the weight assigned to the mode of body waves. Combining the motions of the body waves and of surface waves results in the complete acceleration time histories, which are shown in **Figure IV.5** and repeated as the plot in the last row at the bottom.

Figure IV.5 Synthetic Rotational Acceleration at $M = 6.5$, $R = 8.0km$ & $H = 6.0km$, $s = 0$, $s_L = 2$

$\partial\ddot{V}/\partial x$

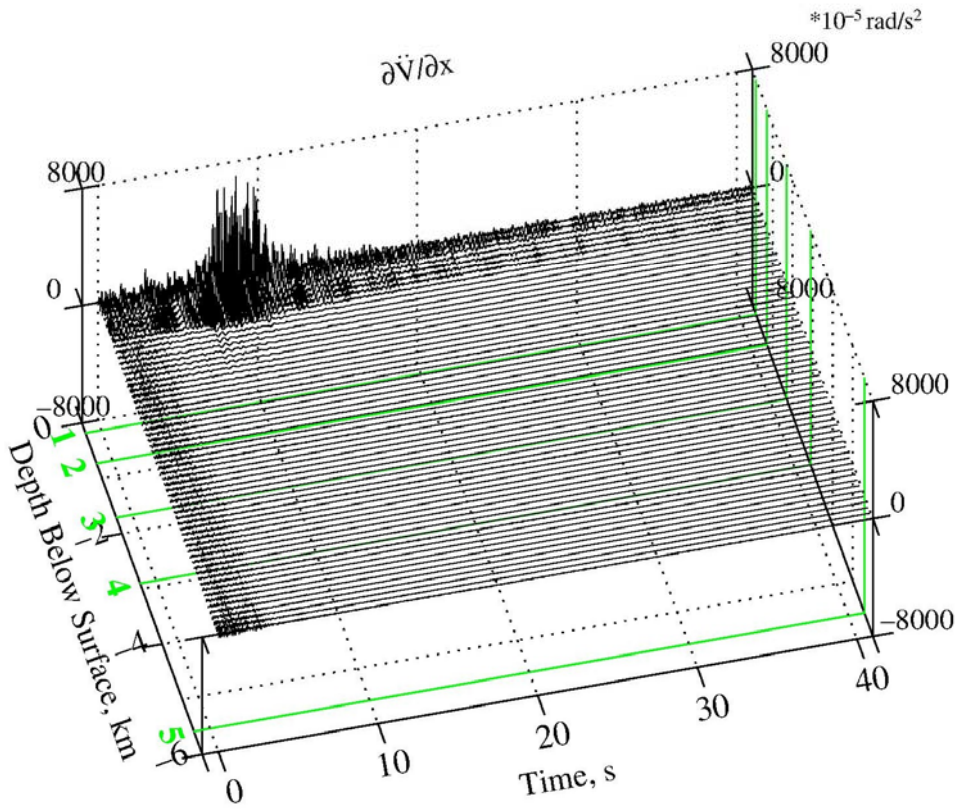

$\partial\ddot{V}/\partial z$

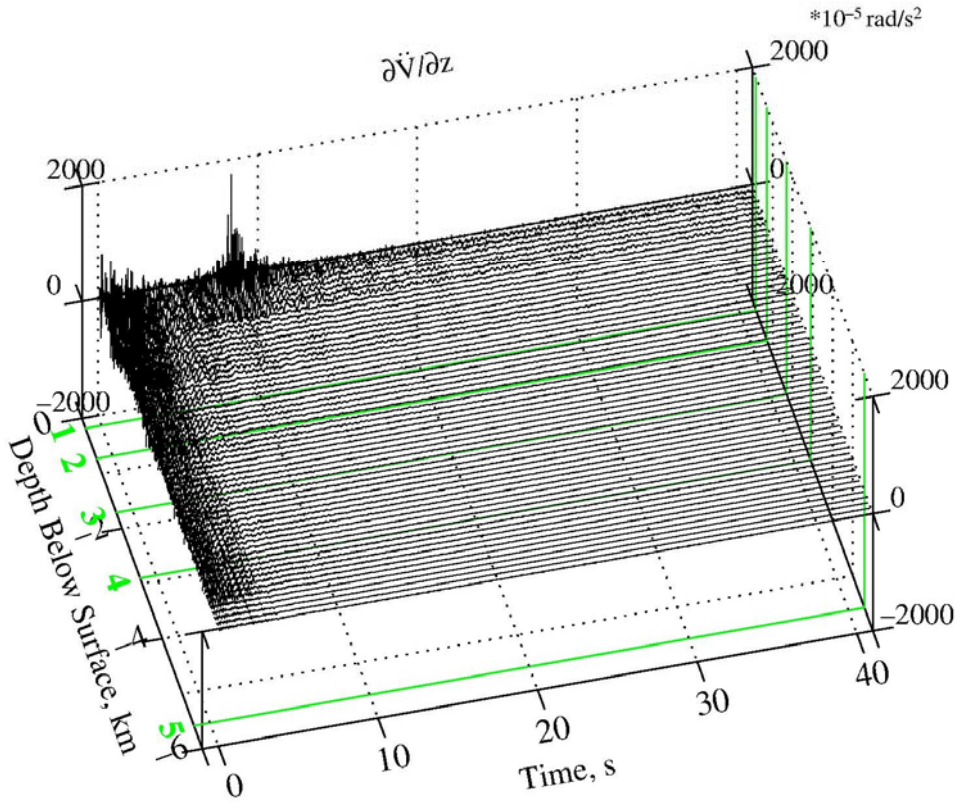

Figure IV.6	**Synthetic Rotational Velocity at $M = 6.5,\ R = 8.0km\ \&\ H = 6.0km,\ s = 0,\ s_L = 2$**
$\partial\dot{V}/\partial x$	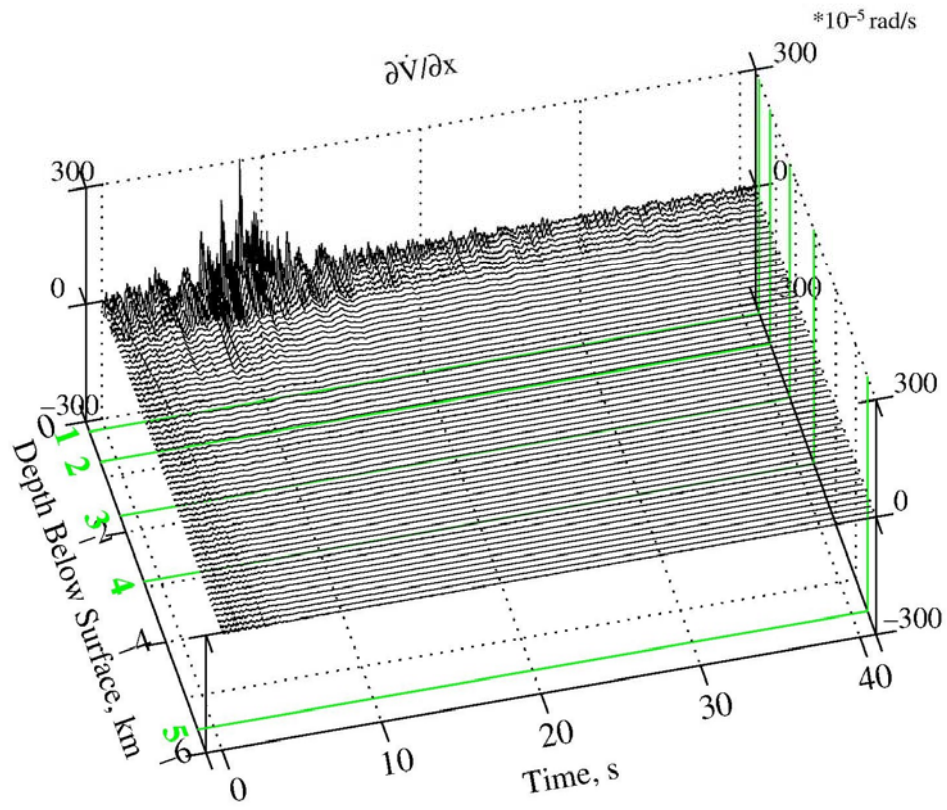
$\partial\dot{V}/\partial z$	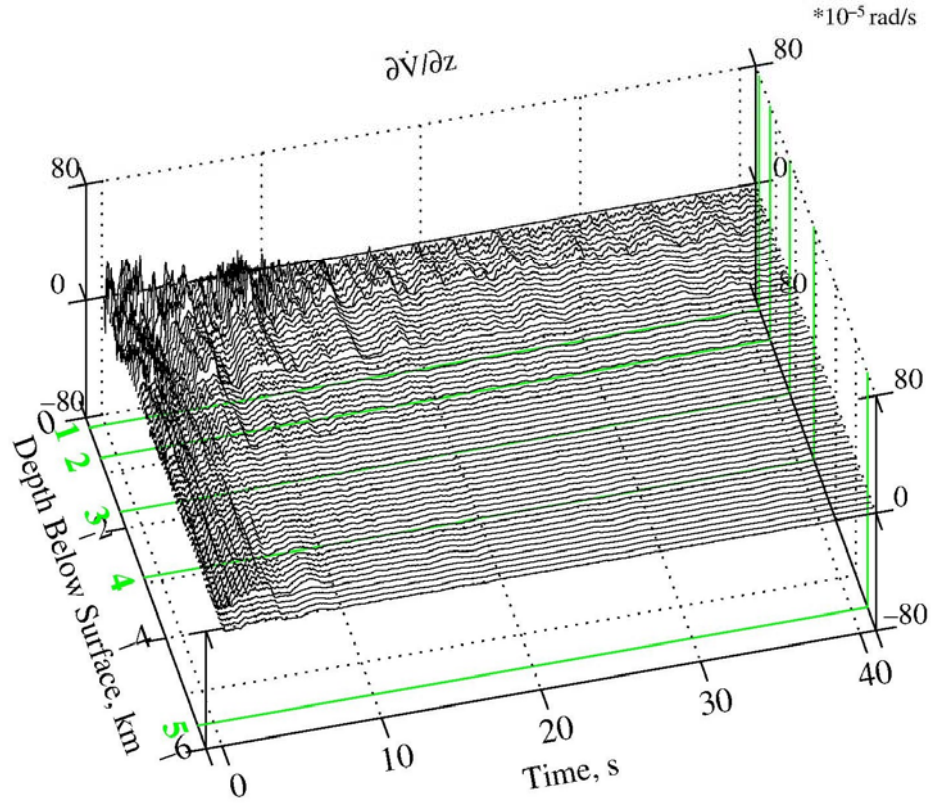

Figure IV.7 Synthetic Rotational Displacement at $M = 6.5$, $R = 8.0km$ & $H = 6.0km$, $s = 0$, $s_L = 2$

$\partial V/\partial x$

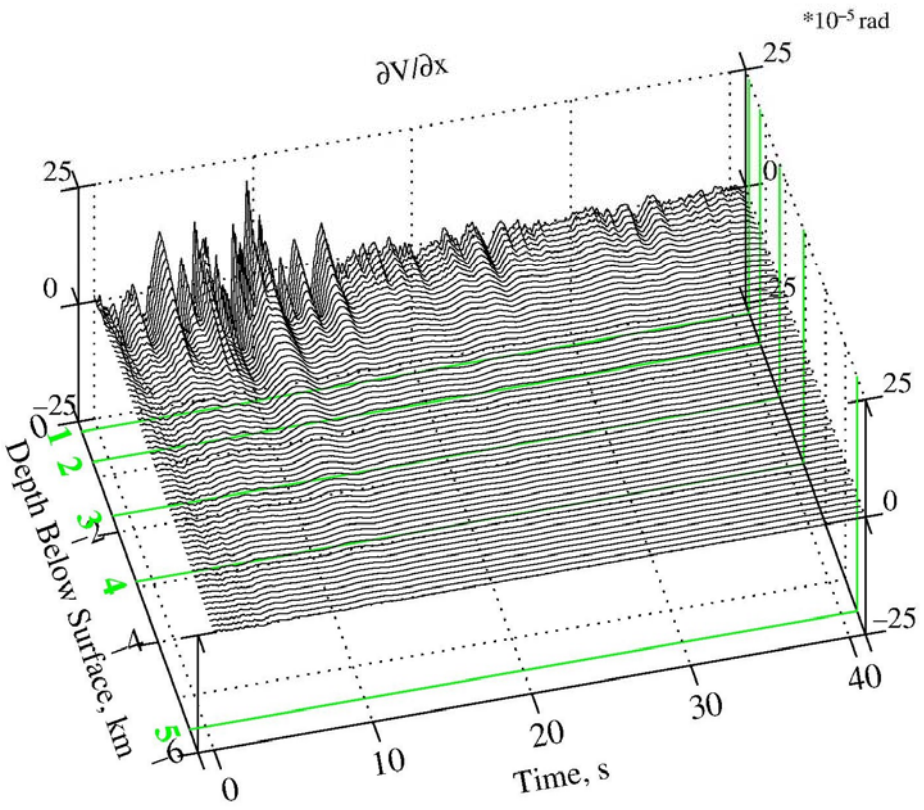

$\partial V/\partial z$

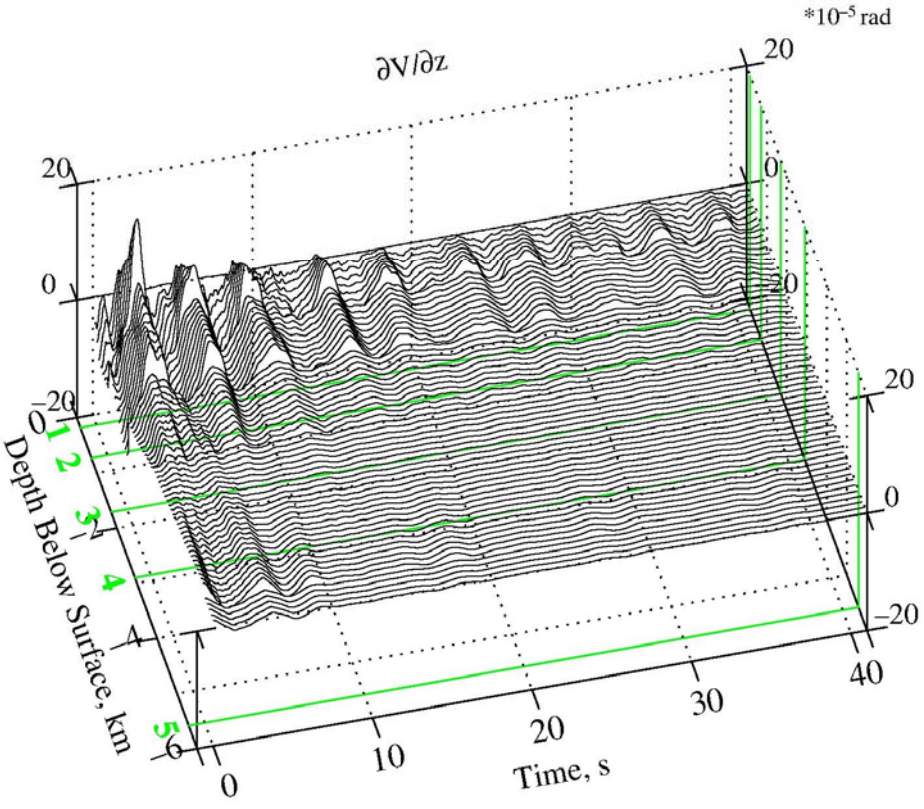

The two columns of 3-D graphs in **Figure IV.9** represent the velocity time histories $\partial\dot{V}/\partial x$ and $\partial\dot{V}/\partial z$ of the body waves and the surface waves. As for the acceleration time histories, the body wave velocity time histories in the top row, especially the $\partial\dot{V}/\partial z$ motions, display noticeable motions only during the first 8 seconds, after which the motions die out. These motions are also noticeable at all depths. The surface wave velocity time histories in the middle row show strong motions only in the top two layers and the maximum motions occur at around 10 seconds from the earthquake origin time. The last row again shows the total motions.

Figure VI.10 shows the rotational $\partial V/\partial x$ and $\partial V/\partial z$ displacement time histories of the body waves and of the surface waves. The $\partial V/\partial x$ component shows that the motions are completely dominated by the surface waves, with the body waves at all depths being very small. The $\partial V/\partial z$ component is different. It shows that the motions are completely dominated by the body waves at all depths.

IV.5 *Case Study 2:* $M = 6.5,\ R = 40.0km,\ H = 9.0km\ (D = 41.0km),\ s = 0,$ and $s_L = 2$

We now consider an example of far field motion, for epicentral distance $R = 40.0km$ and an earthquake source at a focal depth of $H = 9.0km$. This corresponds to a hypocentral distance of $D = \left(R^2 + H^2\right)^{1/2} = \left(40.0^2 + 9.0^2\right)^{1/2} = 41$ km. **Figure IV.11 (same as Report 2, Figure VII.9)** shows a plot of the path taken by the ***SH*** body waves from the earthquake source to the recording site. As before, the path is chosen so that the phase velocities in each layer are the same, or that the angles the ray travels are determined so that Snell's Law is satisfied at each interface.

Figure IV.8 Contributions of Body and Surface Waves to Total Synthetic Rotational Acceleration

$\partial\ddot{V}/\partial x$ **Body Waves** $\partial\ddot{V}/\partial z$ $10^{-5}\ rad/s^2$

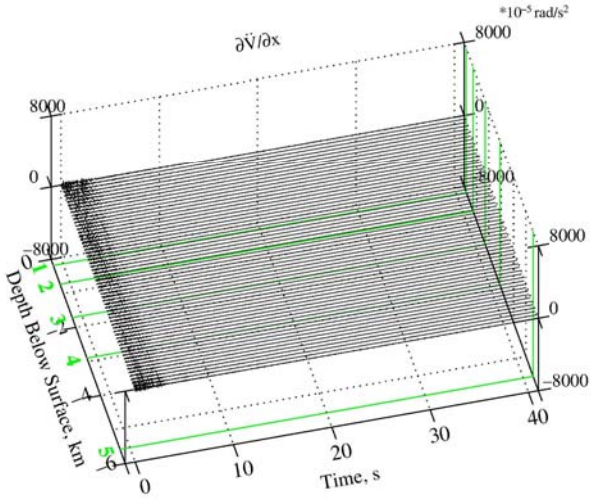

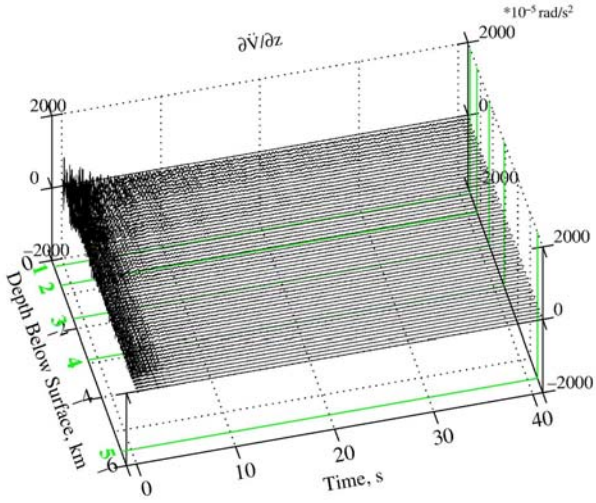

$\partial\ddot{V}/\partial x$ **Surface Waves** $\partial\ddot{V}/\partial z$ $10^{-5}\ rad/s^2$

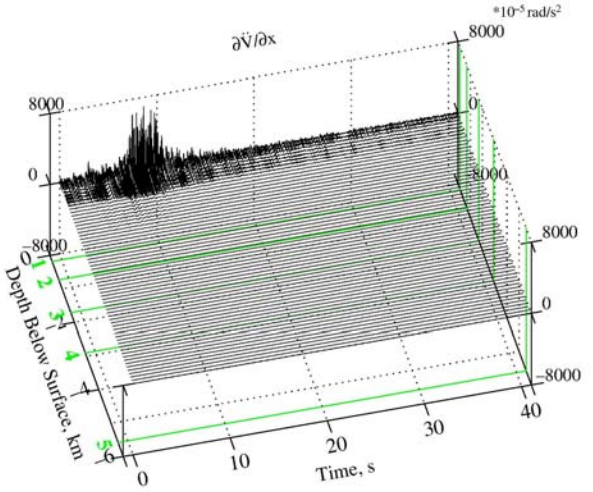

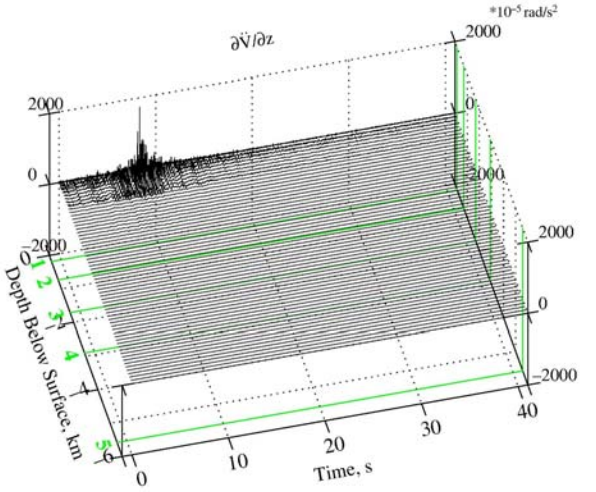

$\partial\ddot{V}/\partial x$ **All (Body + Surface) Waves** $\partial\ddot{V}/\partial z$ $10^{-5}\ rad/s^2$

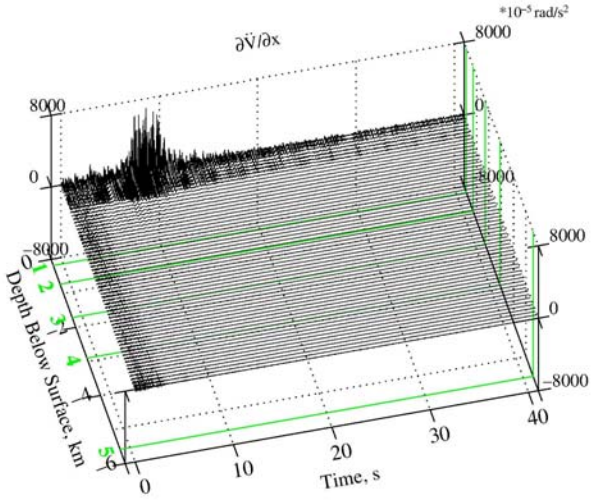

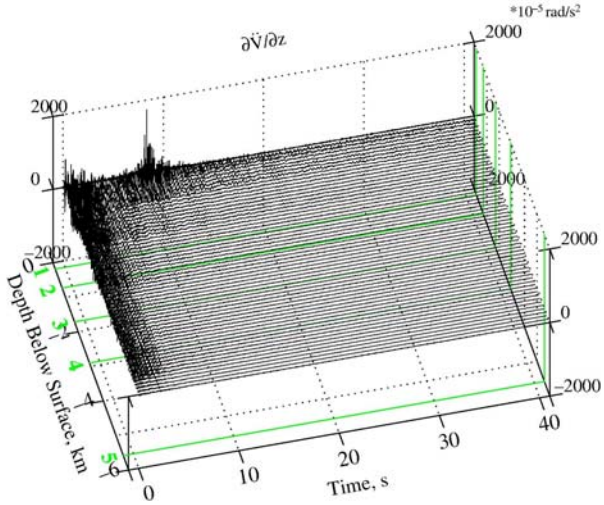

Figure IV.9 Contributions of Body and Surface Waves to Total Synthetic Rotational Velocity

$\partial\dot{V}/\partial x$ **Body Waves** $\partial\dot{V}/\partial z$ 10^{-5} rad/s

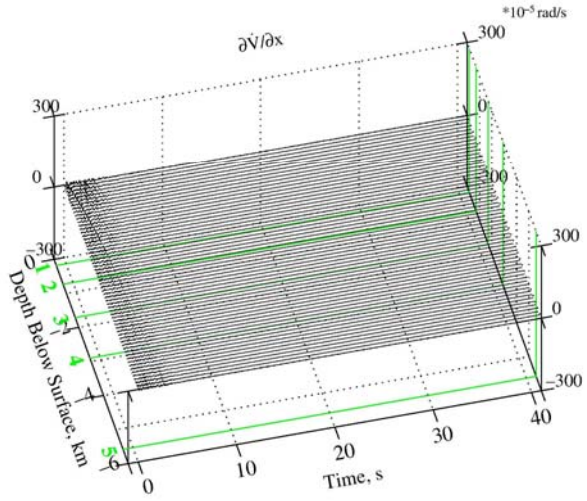

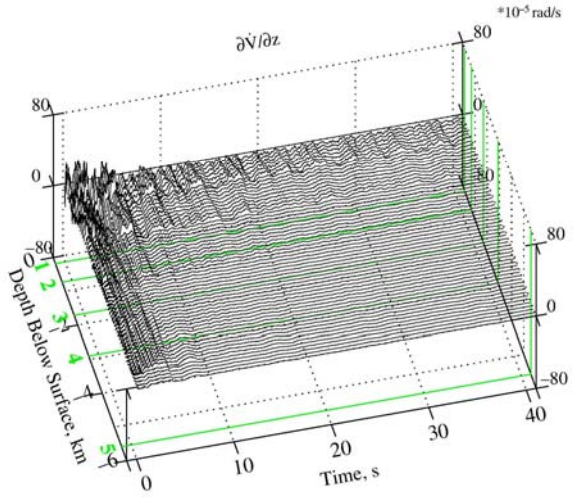

$\partial\dot{V}/\partial x$ **Surface Waves** $\partial\dot{V}/\partial z$ 10^{-5} rad/s

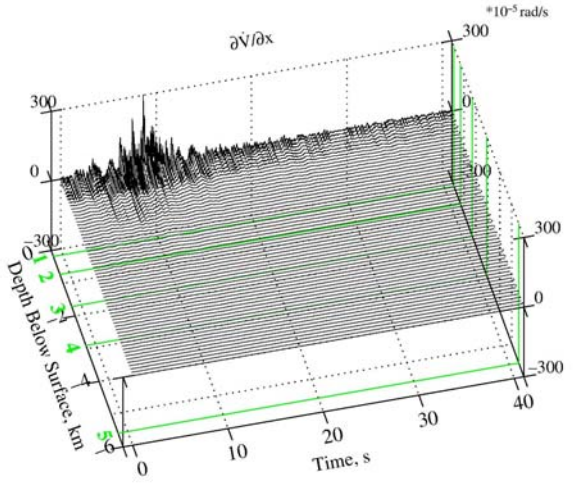

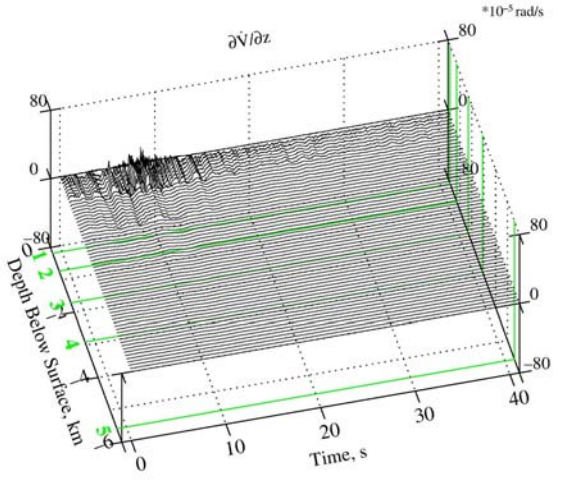

$d\dot{V}/dx$ **All (Body + Surface) Waves** $\partial\dot{V}/\partial z$ 10^{-5} rad/s

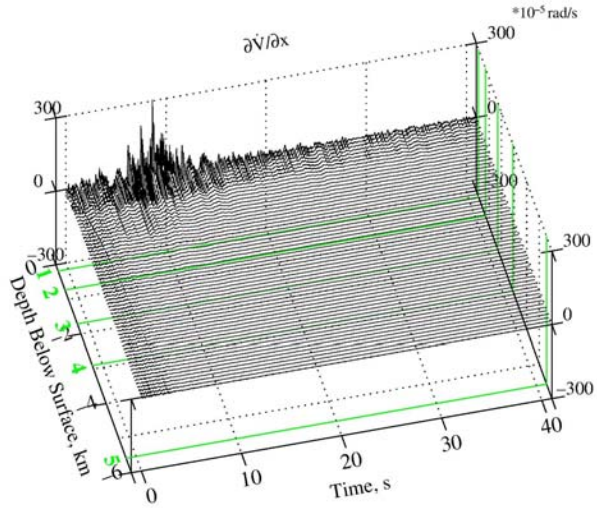

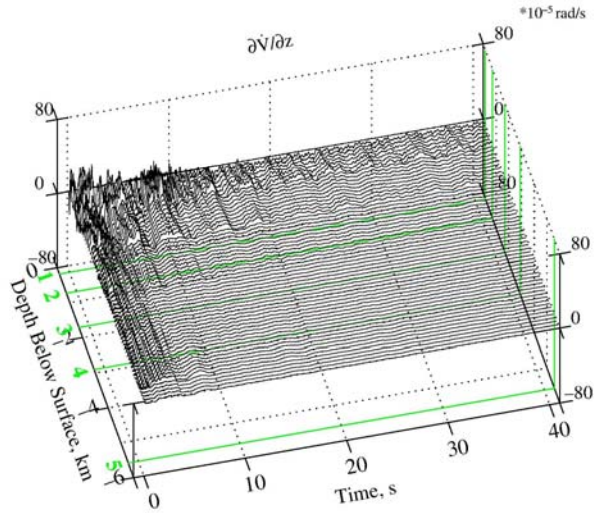

Figure IV.10 Contributions of Body and Surface Waves to Total Synthetic Rotational Displacement

$\partial V/\partial x$ **Body Waves** $\partial V/\partial z$ 10^{-5} ***rad***

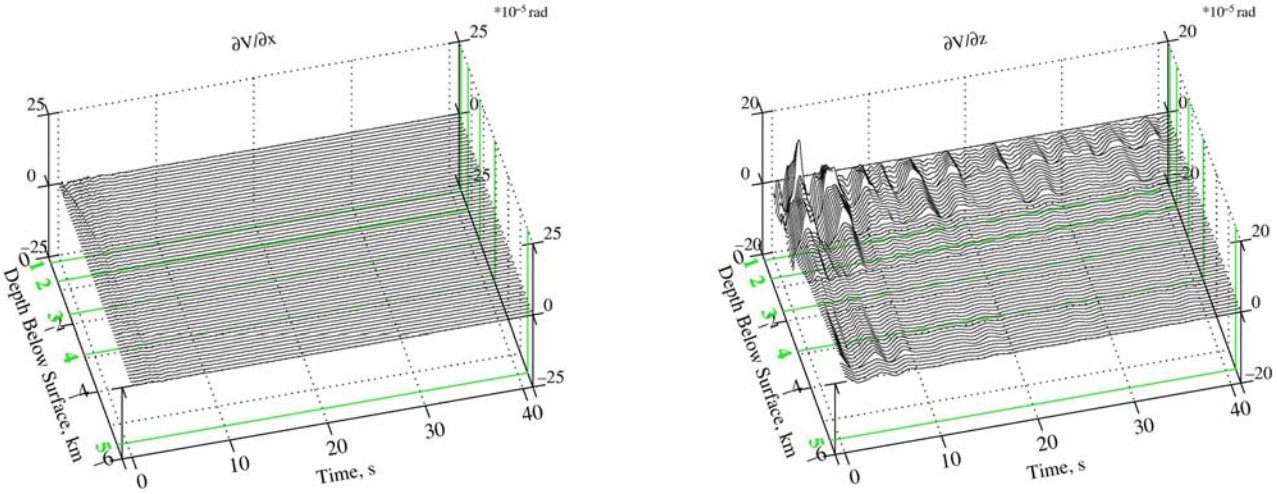

$\partial V/\partial x$ **Surface Waves** $\partial V/\partial z$ 10^{-5} ***rad***

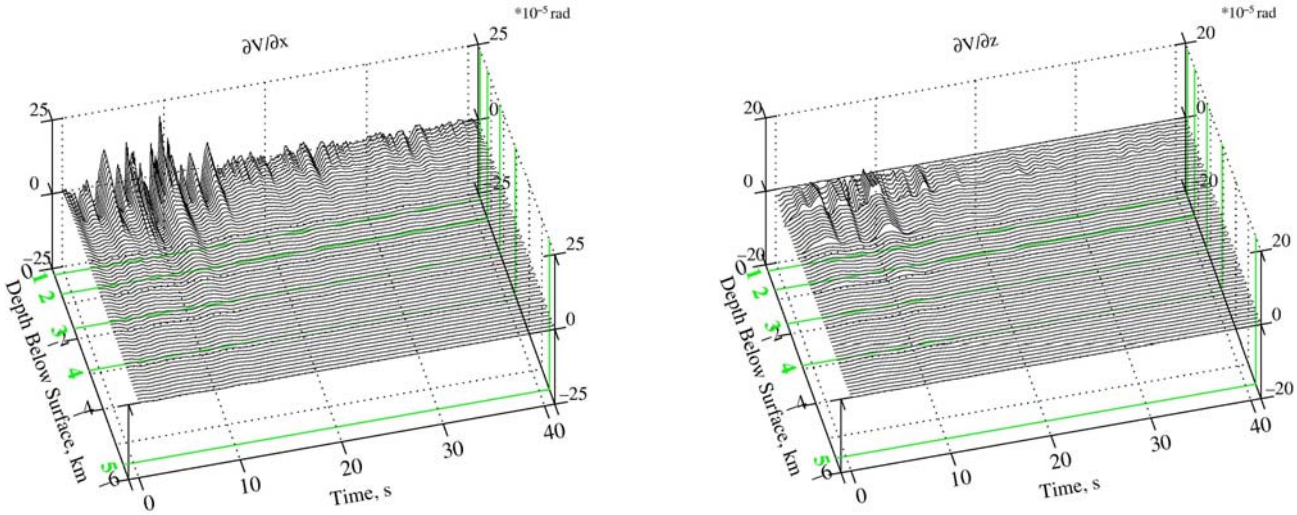

$\partial V/\partial x$ **All (Body + Surface) Waves** $\partial V/\partial z$ 10^{-5} ***rad***

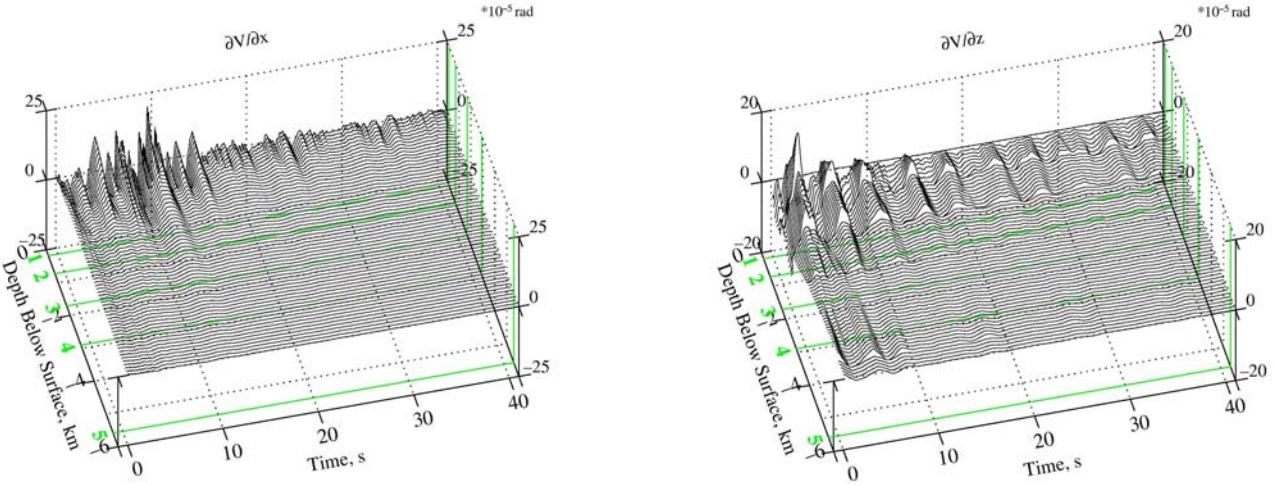

This results in the ray starting at an angle of $\gamma_6 \sim 84.5^o$ with respect to vertical, and propagating up the layered media so that it is incident at the site with $\gamma_1 \sim 15.3^o$ with respect to vertical, a case of near vertical incidence.

Figure IV.11 SH Body Waves Ray Path from Source to Site

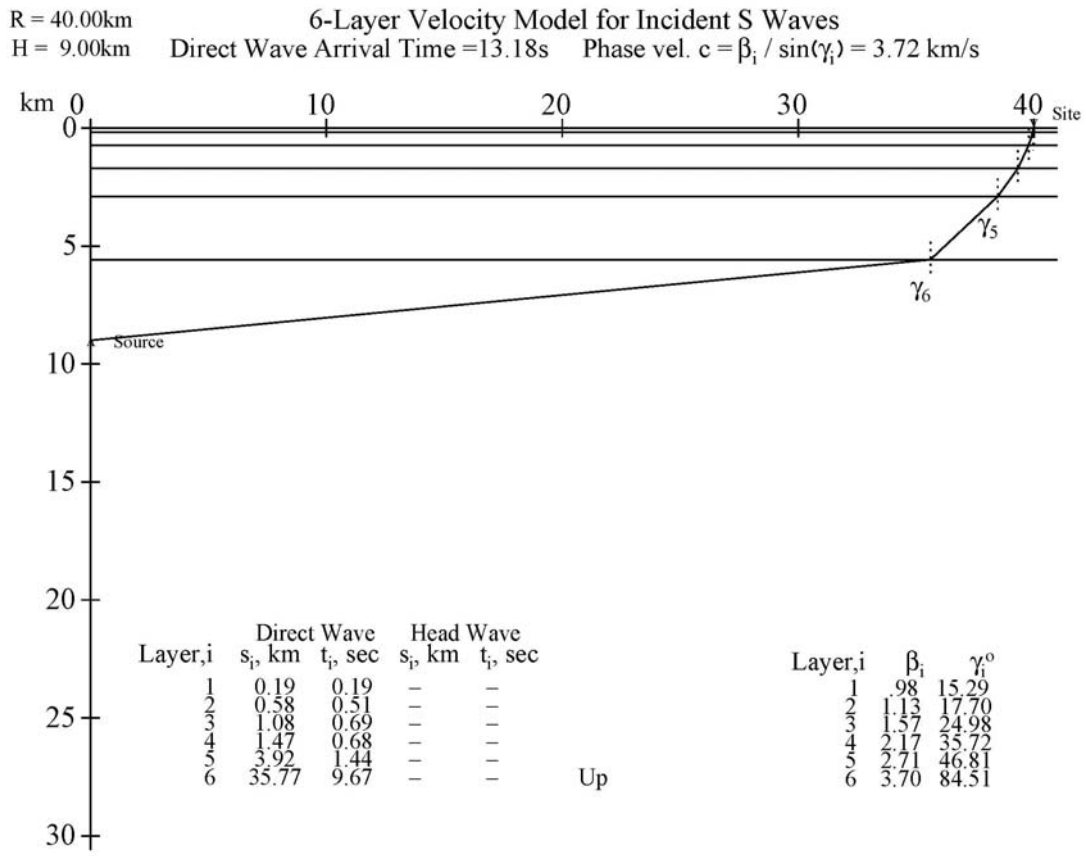

Layer,i	Direct Wave s_i, km	Direct Wave t_i, sec	Head Wave s_i, km	Head Wave t_i, sec
1	0.19	0.19	–	–
2	0.58	0.51	–	–
3	1.08	0.69	–	–
4	1.47	0.68	–	–
5	3.92	1.44	–	–
6	35.77	9.67	–	–

Layer,i	β_i	γ_i^o
1	.98	15.29
2	1.13	17.70
3	1.57	24.98
4	2.17	35.72
5	2.71	46.81
6	3.70	84.51

The surface waves, on the other hand, have a phase velocity at each frequency that is lower than the phase velocity of the body ***SH*** waves, which is ~ 3.7 ***km / s*** . Not traveling as fast as the body waves, they arrive at the site at a later time. For the case considered here of an epicentral distance $\boldsymbol{R = 40km}$, some of the modes of Love waves may have a phase velocity of 1.0 ***km / s*** or less at some dominant frequencies, and thus would take more than 40 **sec** to arrive at the site. Note that for the in-plane ***P*** and ***SV*** body waves, the first arrival time is faster (~ 7.6 ***s*** **ec** as described in

the next chapter). During many earthquakes, strong surface waves can arrive sooner than this, even at large epicentral distances. This can be attributed to the fact that the surface and body waves are often generated not just at the earthquake source, but also at the edge of an alluvial valley, which can be closer to the site.

To account for such modeling, **SYNACCS** is programmed to have two "hypocentral distances" to be defined by the user. The first hypocentral distance is the (actual) epicentral distance from the earthquake source to the site. The second "hypocentral distance" is a smaller distance from some representative edge of a valley where the site is located. The first hypocentral distance will be used as one of the parameters for the regression to estimate the Fourier amplitudes of the waves at the site. The second hypocentral distance can be used to estimate the arrival times of dominating surface waves. Since this second distance is closer, the travel time of thus modeled waves will be shorter and their duration shorter.

For our example in ***Case Study 2***, the first hypocentral distance is $\boldsymbol{D = D_1 = 41\ km}$, and the second "hypocentral distance" is assumed to be $\boldsymbol{D = D_2 = 25\ km}$. The body ***SH*** waves are assumed to be incident from the bottom layer at an angle of incidence of 84^o with respect to the vertical direction

Figure IV.12 shows the synthetic $\partial\ddot{V}/\partial x$ and $\partial\ddot{V}/\partial z$ ***3D*** rotational acceleration time-histories calculated using the earthquake parameters of the **Case Study 1**. It corresponds to a hypocentral distance of $\boldsymbol{D = \left(R^2 + H^2\right)^{1/2} = \left(40.0^2 + 9.0^2\right)^{1/2} = 41.0km.}$ for which the **SYNACCS** program determines that the appropriate duration of the accelerogram record should be above 40 seconds.

The two synthetic $\partial\ddot{V}/\partial x$ and $\partial\ddot{V}/\partial z$ ***3D*** rotational acceleration time-histories in the figure are plotted with the same scale. As in ***Case Study 1***, the ***SH*** body waves are present during the first 10 seconds of motions, while the surface waves, using the 2nd distance of $\boldsymbol{D_2 = 25\ km}$ to calculate the arrival times, have dominant motions between 10 and 30 seconds of the record. This is different from the corresponding acceleration time histories of the transverse translational

component, $\ddot{V}(z)$, in the ***3D*** plot in **Figure VII.11** of Report 2, where we considered only the hypocentral distance of $D = 41$ ***km*** to calculate arrival time, so that the dominant motions are between 20 and 40 seconds in the record, due to later arrival of surface waves. It also shows that for the $\partial\ddot{V}/\partial x$ motions, the ***SH*** body waves are small compared with the surface waves, whereas for the $\partial\ddot{V}/\partial z$ motions, the ***SH*** body waves are more dominant.

Figure IV.13 shows the corresponding synthetic $\partial\dot{V}/\partial x$ and $\partial\dot{V}/\partial z$ ***3D*** rotational velocity time-histories. Again both components are plotted with the same scale, showing that the $\partial\dot{V}/\partial x$ motions are more significant than the $\partial\dot{V}/\partial z$, as for the acceleration rotations.

Figure IV.14 shows the corresponding synthetic $\partial\dot{V}/\partial x$ and $\partial\dot{V}/\partial z$ ***3D*** rotational displacement time-histories, and shows a similar trend.

IV.6 The Curvatures for Transverse Motions

Recall from Equation (2.10) in Chapter 2, where the curvature in the transverse direction is defined as

Transverse Curvature: $$K_2(t) \approx \partial^2 V/\partial x^2 = \ddot{V}/c^2$$ **From (2.10)**

It is computed directly from the translational components, computed together with the rotational motions. In fact, they each correspond to the ***2nd derivative of the transverse translational motion*** with respect to ***x*** in the radial direction.

Figures IV.15 and 16 show the transverse curvatures at depths below the surface computed respectively for the ***two Case Studies: 1 and 2***.

Figure IV.12 **Synthetic Rotational Acceleration at $M = 6.5,\ R = 40km\ \&\ H = 9km,\ s = 0,\ s_L = 2$**

$\partial\ddot{V}/\partial x$

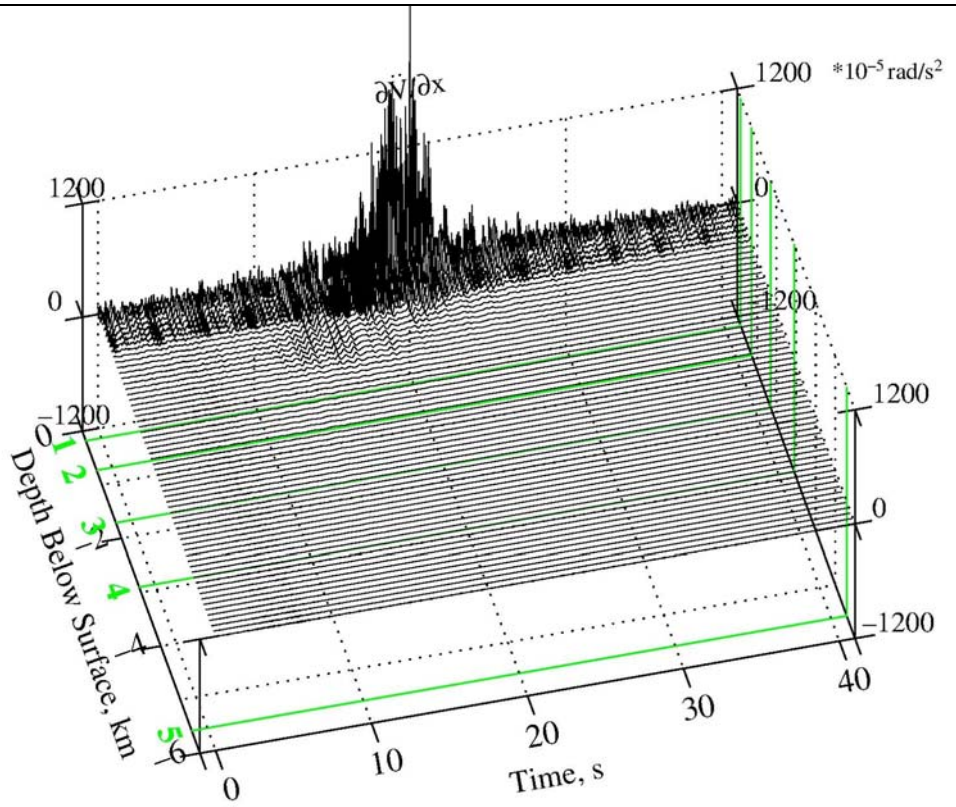

$\partial\ddot{V}/\partial z$

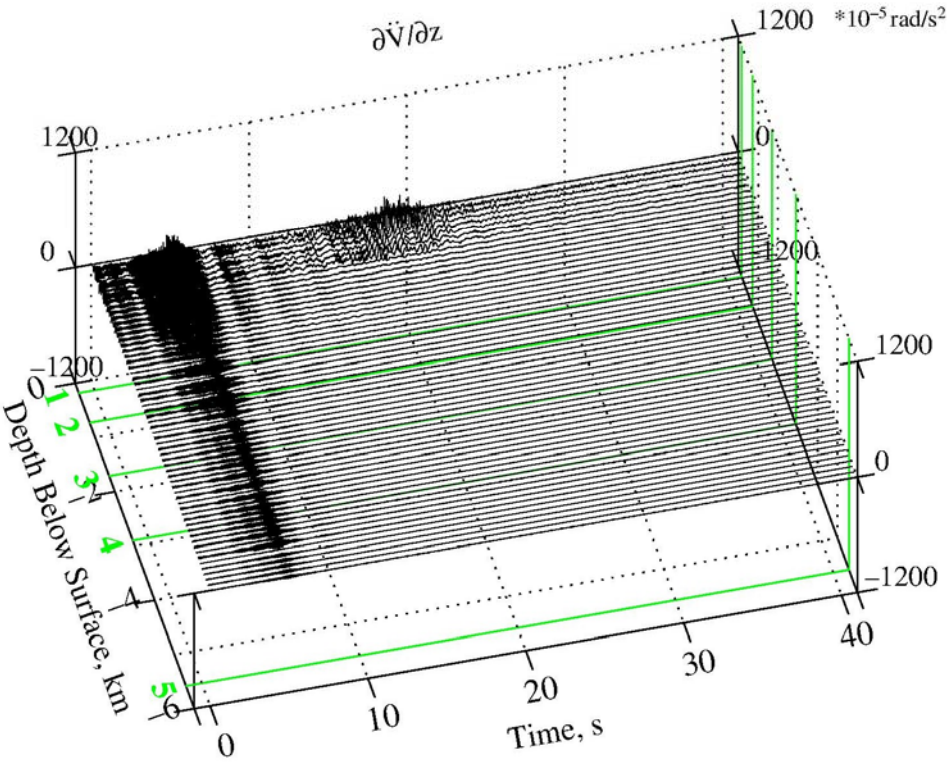

Figure IV.13 **Synthetic Rotational Velocity at $M = 6.5$, $R = 40km$ & $H = 9km$, $s = 0$, $s_L = 2$**

$\partial\dot{V}/\partial x$

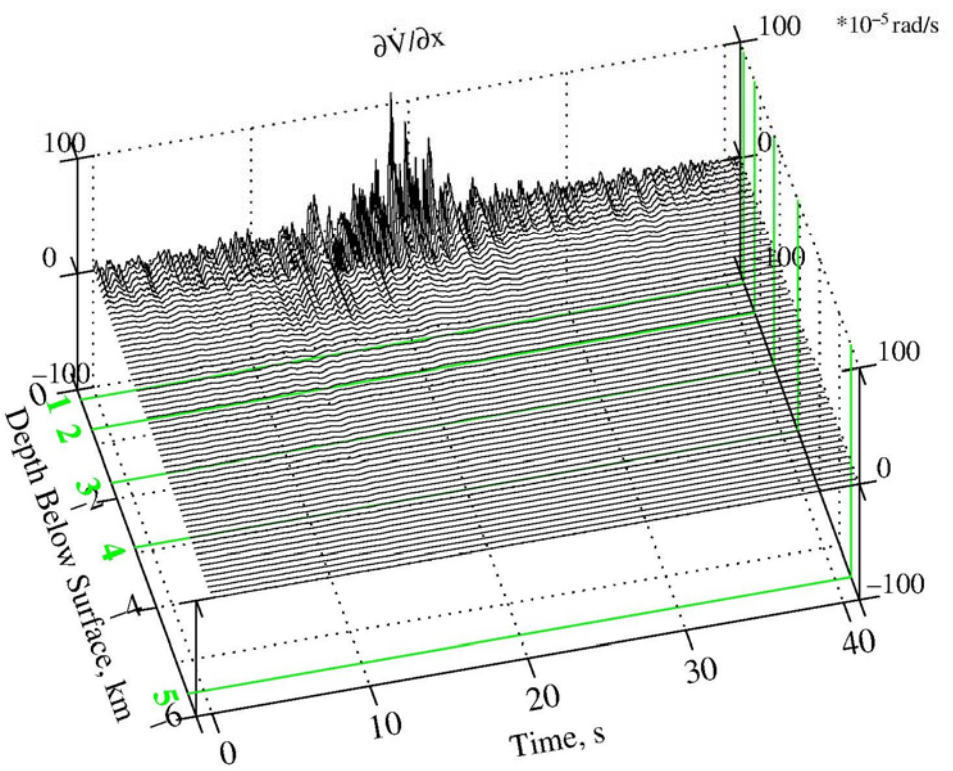

$\partial\dot{V}/\partial z$

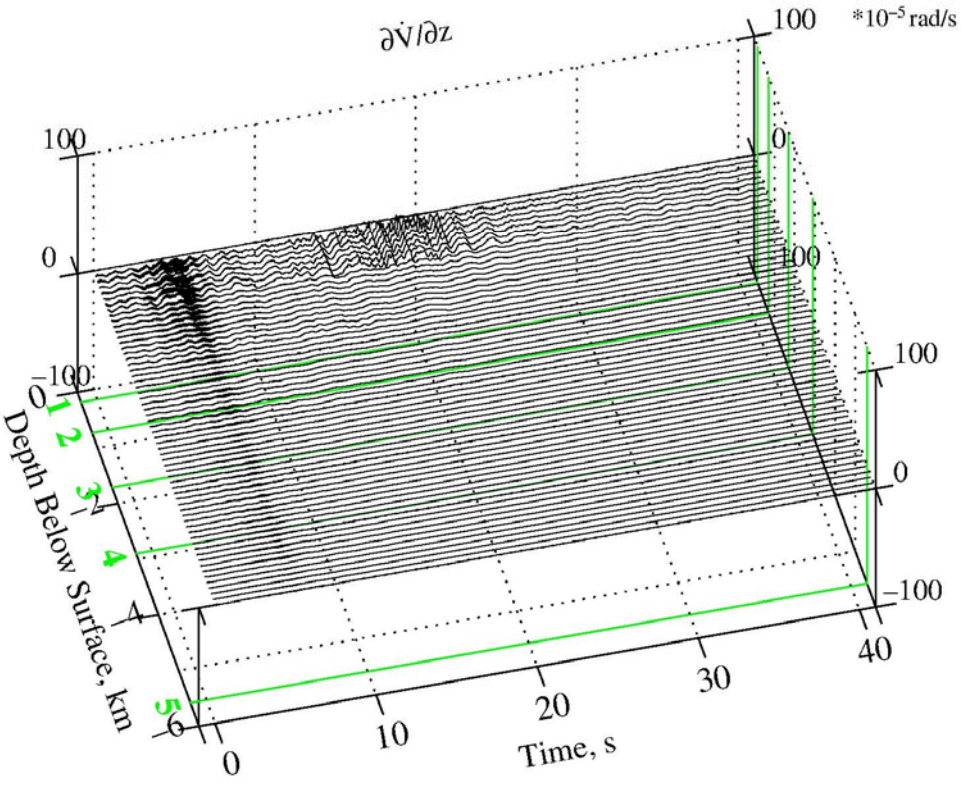

Figure IV.14 **Synthetic Rotational Displacement at $M = 6.5$, $R = 40km$ & $H = 9km$, $s = 0$, $s_L = 2$**

$\partial V/\partial x$

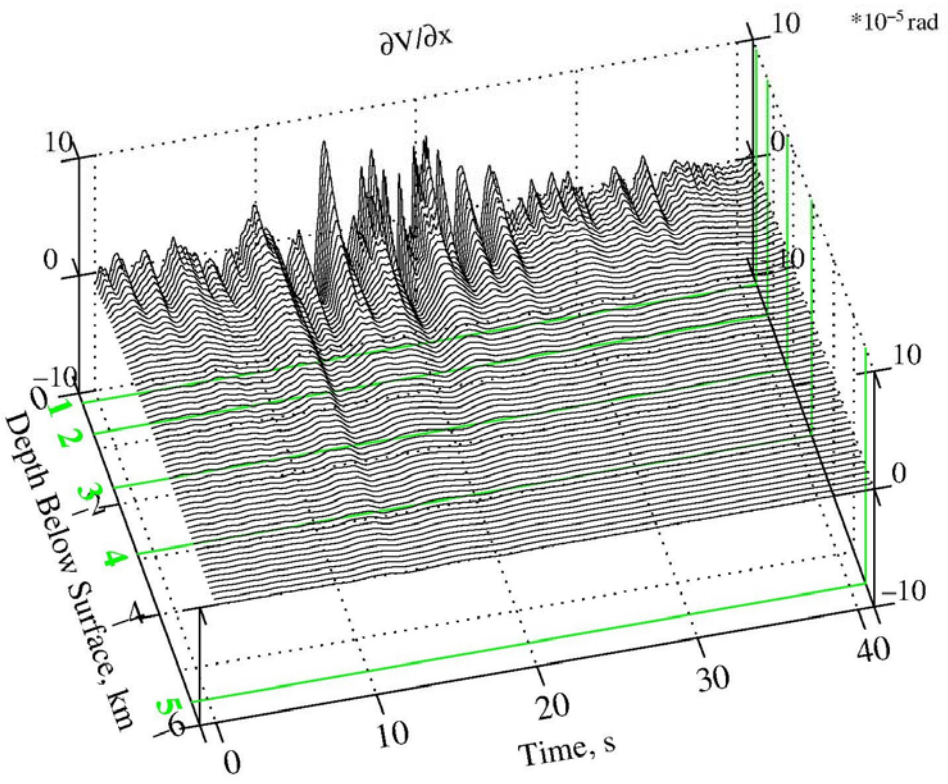

$\partial V/\partial z$

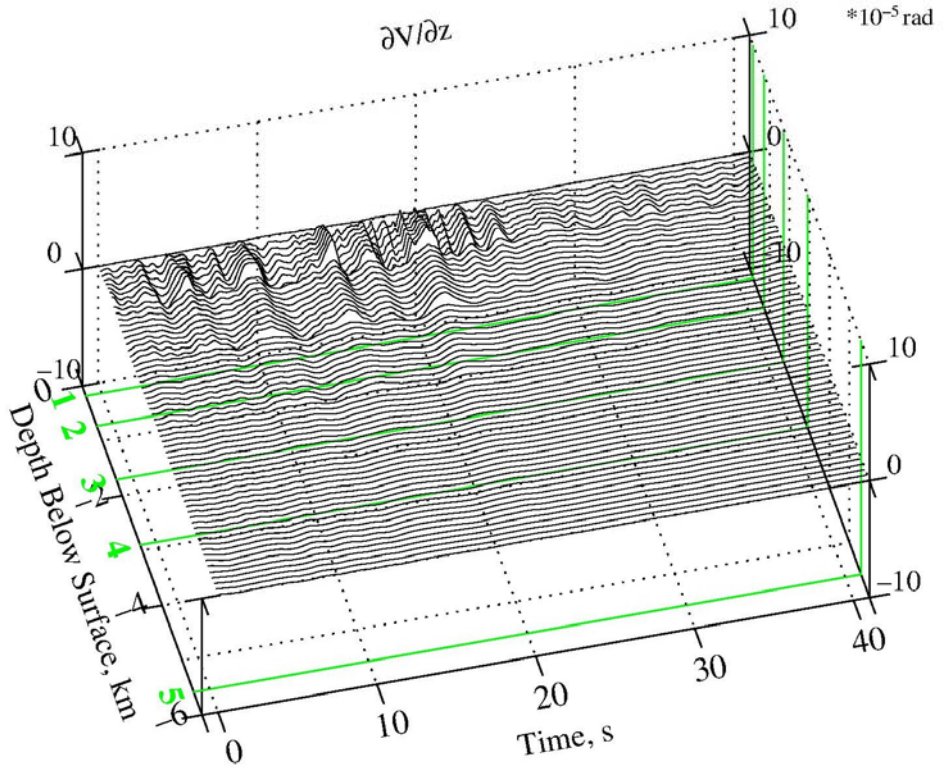

Note that the 2nd derivative of the transverse motions gives the curvature motions. Since the translational motions are in units of ***cm*** and the distances are measured in ***km***, they have the units of cm/km^2, or $cm/10^{10}cm^2$ or $10^{-10}\,rad/cm$.

For ***Case Study 1***, at near-field site ($D = 10km$), **Figure IV.15** shows that the curvature motions are of the order of $20\times10^{-9}\,rad/cm$, and the motions are again significant only on the two top layers of the media, or down to **0.7km**. Further, the strong motions occur around the 10-seconds mark of the record.

For ***Case Study 2***, at far-field site ($D = 41km$), **Figure IV.16** shows that the curvature motions are smaller, of the order less than $10\times10^{-9}\,rad/cm$, and the motions are significant only in the top layer of the media, or down to **0.18km**. The second layer, down to **0.7km** of depth, has smaller motion. Further, the strong motions occur later, around the 20-seconds mark of the record.

Finally, to be consistent with all other parts of this report, we will next plot the above two-dimensional ***(2-D)*** time histories of these transverse curvatures for Case Studies 1 and 2 respectively in **Figures IV.17 and IV.18**, as three-dimensional ***(3-D)*** time histories figures.

Figure IV.17 is the ***3-D*** plot of the transverse curvature motions of the same 120 accelerations corresponding to **Figure IV.15** for ***Case Study 1***. The two horizontal longitudinal and transverse coordinate axes are now correspondingly the **time** axis and the **depth** below surface. The vertical axis shows the amplitude of **curvatures, in unit of** $10^{-9}\,rad/cm$. The five green lines, labeled ***0*** to ***5***, again correspond to the positions where the layers meet.

Figure IV.15 **Synthetic Transverse Curvature at $M = 6.5$, $R = 8.0km$ & $H = 6.0km$, $s = 0$, $s_L = 2$**

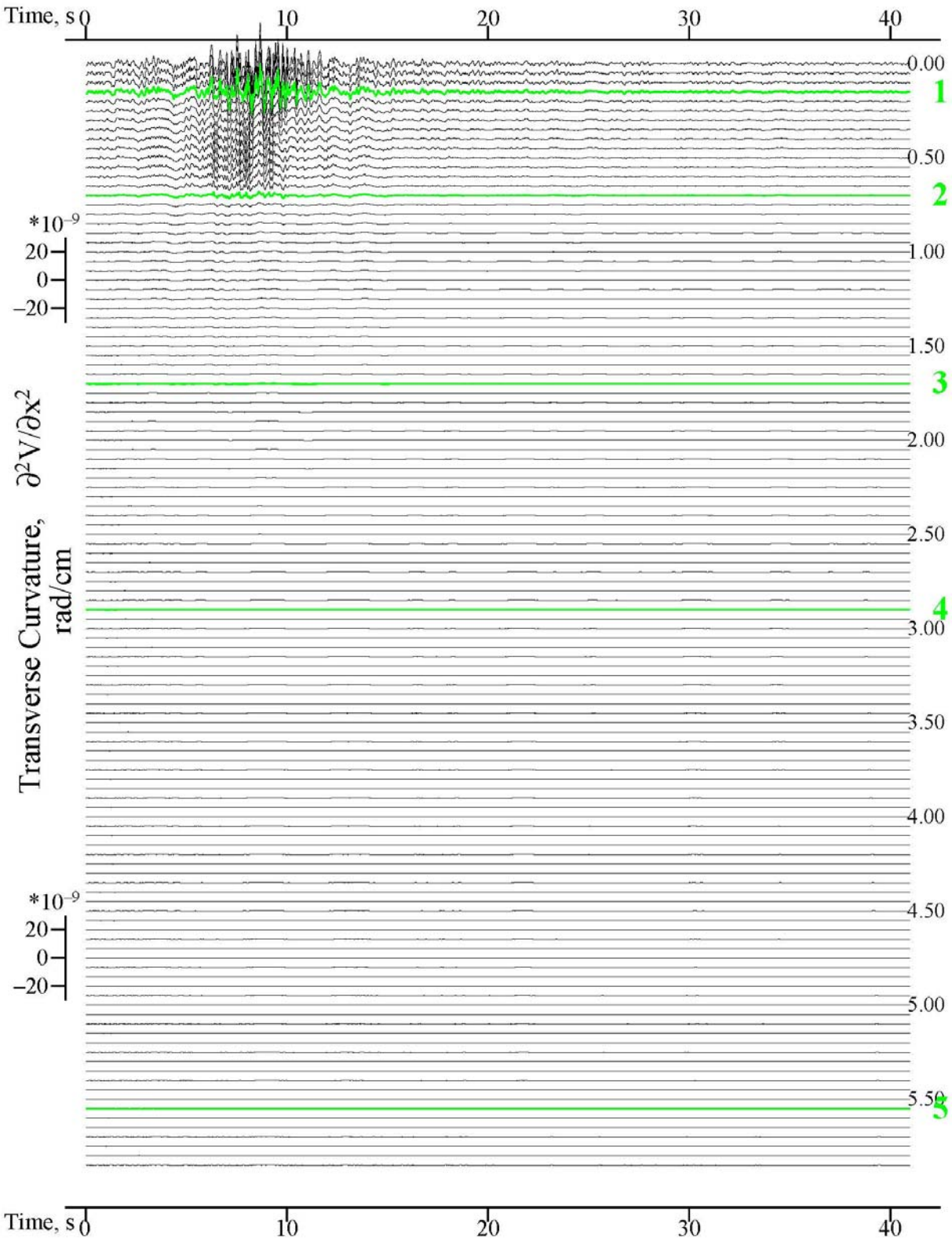

Figure IV.16 **Synthetic Transverse Curvature at $M = 6.5$, $R = 40km$ & $H = 9km$, $s = 0$, $s_L = 2$**

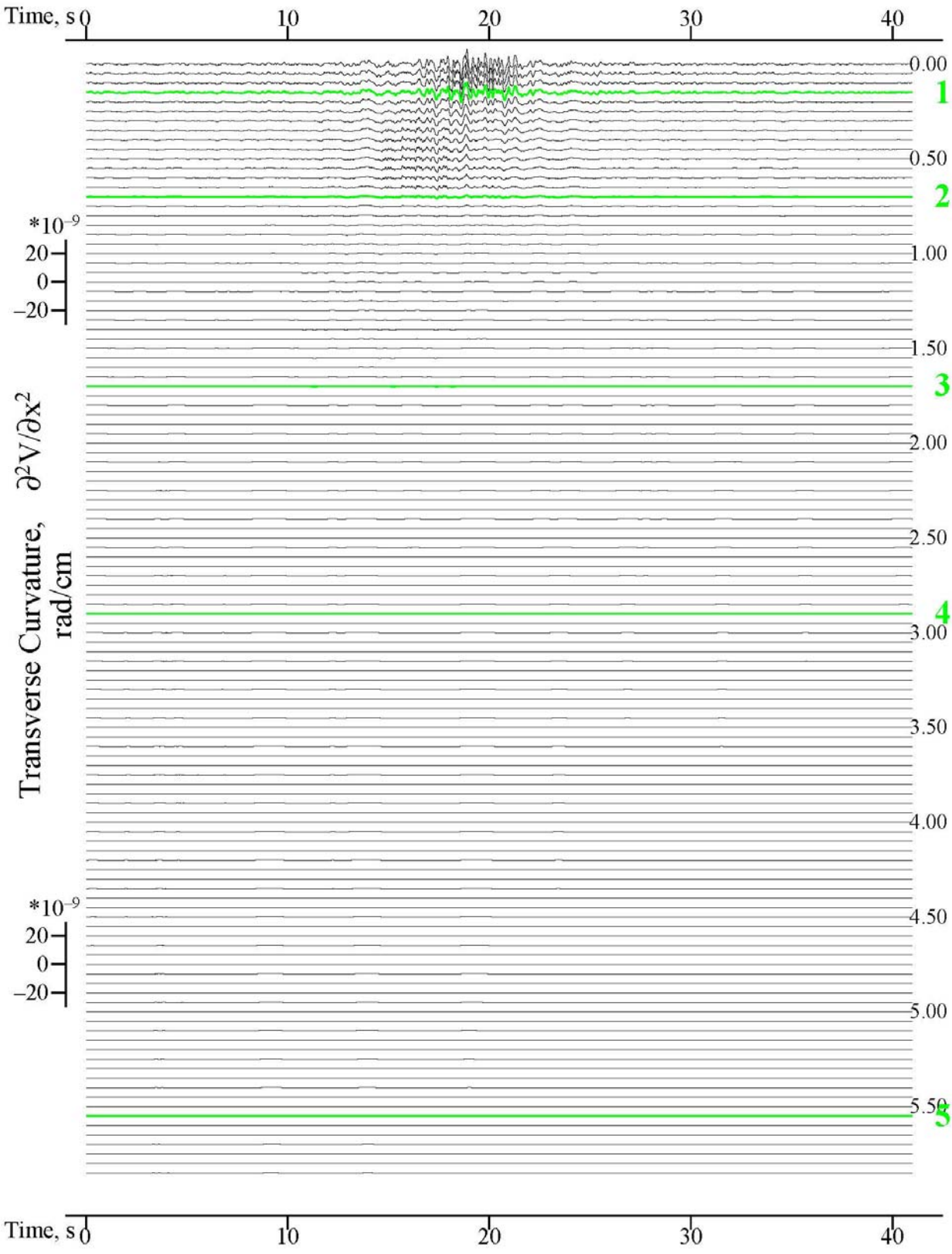

Figure IV.17 Synthetic Transverse Curvature at $M = 6.5,\ R = 8.0km\ \ \&\ \ H = 6.0km,\ s = 0,\ s_L = 2$

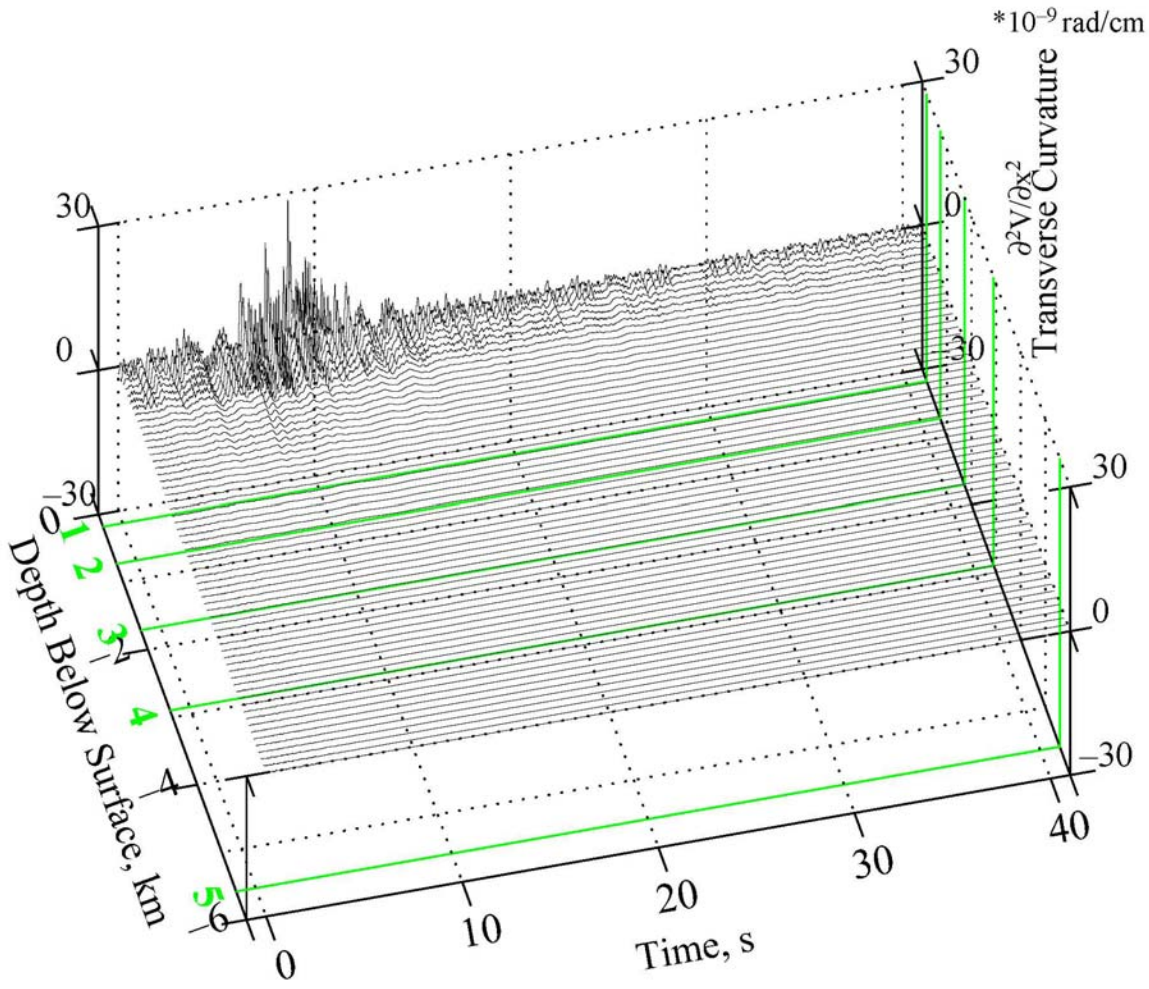

V. The Synthetic Radial and Vertical Rotational Motions

V.1 Introduction

We will again select the same El Centro 6-Layered elastic model and will consider the following two ***Case Studies*** of earthquake source and site characteristics:

Figure IV.18 **Synthetic Transverse Curvature at $M = 6.5,\ R = 40km\ \&\ H = 9km,\ s = 0,\ s_L = 2$**

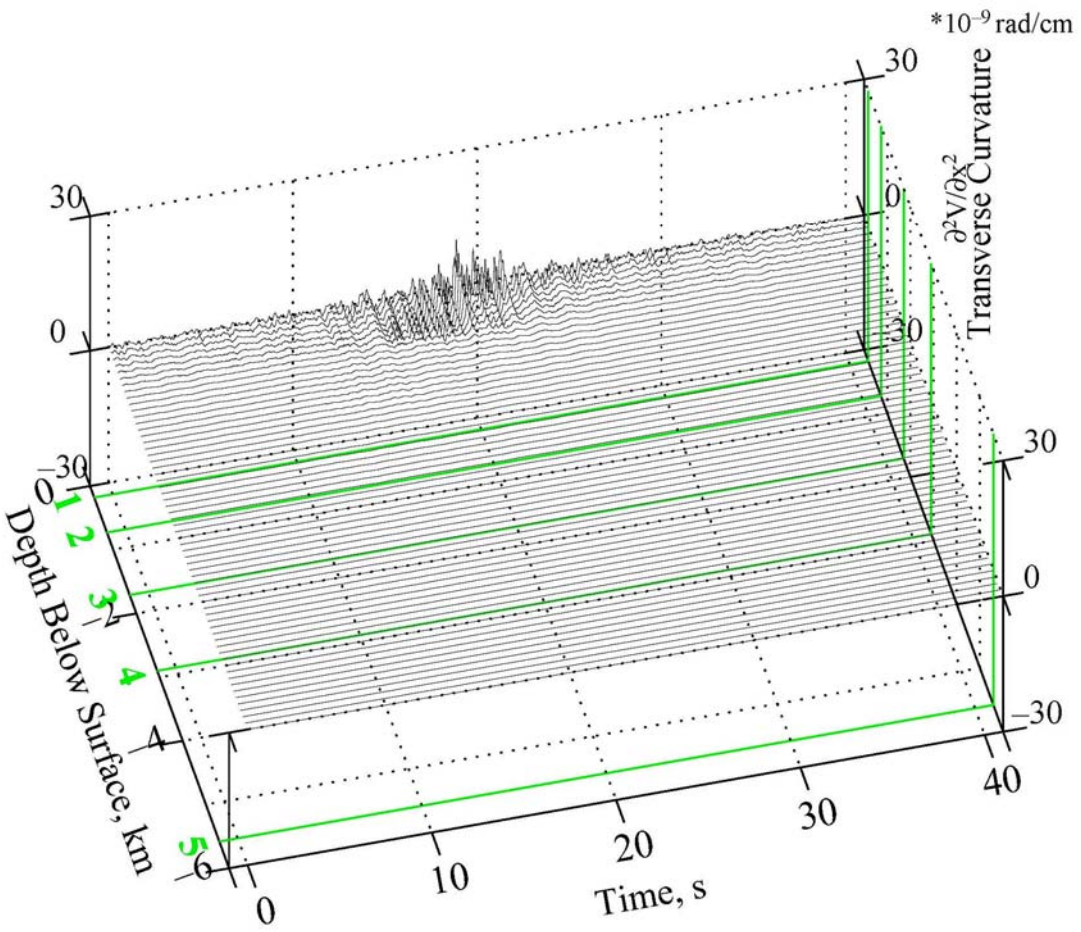

Case Studies:

3) ***Case Study 1:*** $M = 6.5,\ R = 8.0km,\ H = 6.0km,\ s = 0,\ s_L = 2$

4) ***Case Study 2:*** $M = 6.5,\ R = 40.0km,\ H = 9.0km,\ s = 0,\ s_L = 2$

where the earthquake parameters M, R, H, s, s_L are defined as in Chapter IV for the Synthetic Transverse Rotational motions. The two cases are again on the same site, with the same geological site and soil conditions, and are subjected to an earthquake of the same magnitude. They differ only in the epicentral distances and the earthquake focal depths. ***Case Study 1*** studies

near-field motions with small epicentral distance and shallow focal depth. ***Case Study 2*** has larger epicentral distance and slightly deeper focal depth.

V.2 *Case Study 1*: $M = 6.5,\ R = 8.0km\ \ \&\ \ H = 6.0km\ \left(D = 10.0km\right),\ s = 0,\ s_L = 2$

As before, the time histories at the top surface $z = 0$ are generated by the existing SYNACC method, and the current SYNACCS algorithm is used to include the five modes of ***Rayleigh*** surface waves (modes #1 to #5), and two modes of longitudinal, ***P*** waves (mode #11) and shear, ***SV*** waves (mode #12).

Figure V.1 (Report 2, Figure VIII.1a) shows the ray path taken by the P-waves from the earthquake source to the recording site. The ray path is chosen so that the phase velocities at each layer of the 6-layered media are the same, or that the angles the ray travels are determined so that Snell's Law is satisfied at each interface, for the layers $i = 1,\ 2,\ \ldots,\ 6$:

$$c = \alpha_i \,/\sin\left(\gamma_i\right) = \ \textbf{6.44 km/s, a constant} \qquad \textbf{Report 2 (8.1)}$$

where α_i = are the compressional wave speeds, and γ_i = angles the ray makes with respect to the vertical direction at the i^{th} layer. It shows the ray starting at an angle of $\gamma_6 \sim 83.4^o$ with respect to the vertical, and progressing up the layered media and arriving at the site with $\gamma_1 \sim 15.3^o$.

Figure V.2 (Report 2, Figure VIII.1b) shows the ray path taken by the (slower) SV body waves. The ray path is again chosen so that the phase velocities at each layer of the 6-layered media are the same (Equation 7.1 of Report 2, Chapter VII). It shows that the ray will start at an angle of $\gamma_6 \sim 83.4^o$ with respect to vertical, and then progress up the layered media arriving at the site with $\gamma_1 \sim 15.3^o$. Note that P-waves have almost the same starting angle at the source and ending angle at the site.

Figure V.1 (Report 2, Figure VIII.1a) P- Body Waves Ray Path from Source to Site

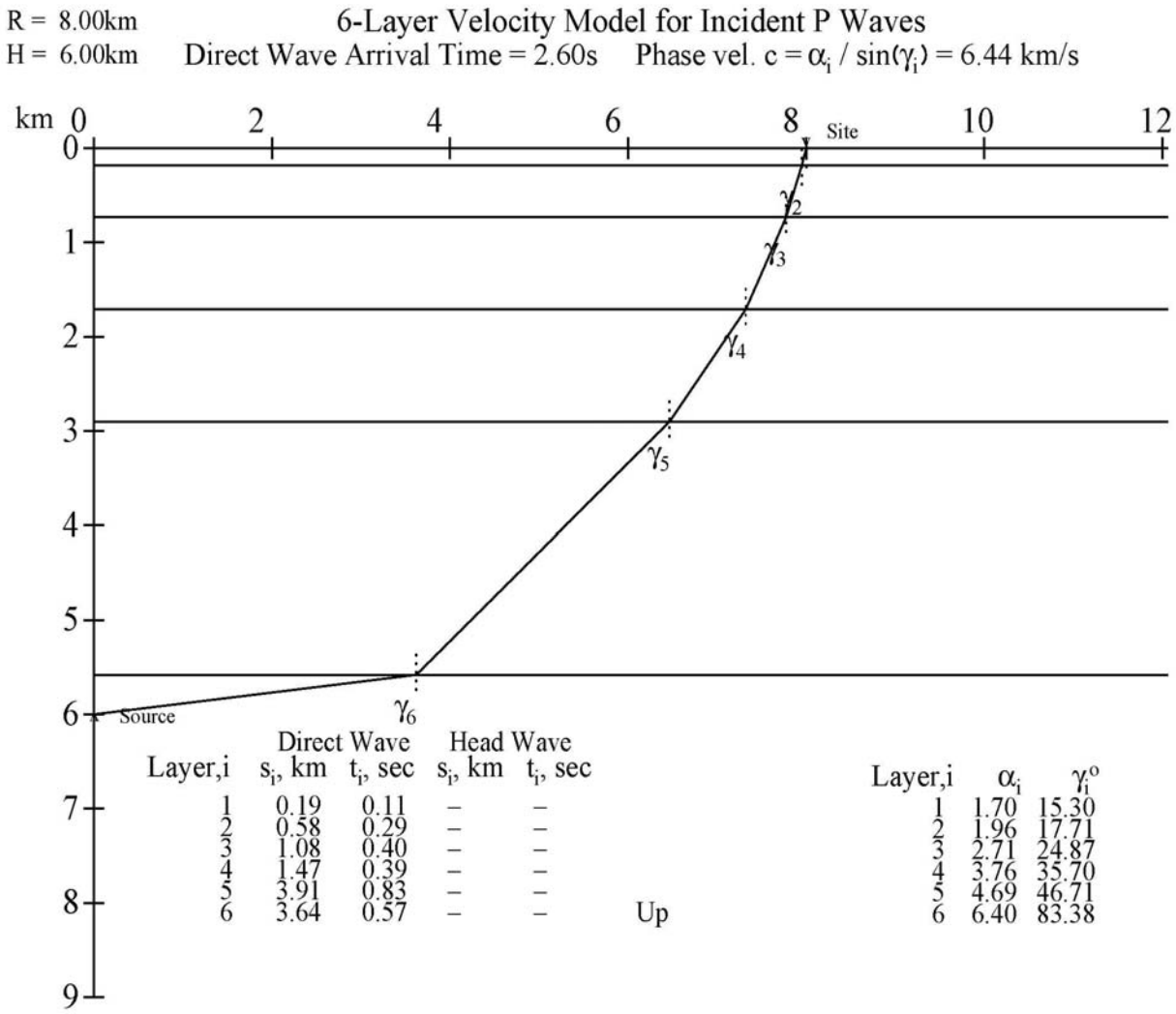

Layer,i	Direct Wave s_i, km	Direct Wave t_i, sec	Head Wave s_i, km	Head Wave t_i, sec
1	0.19	0.11	–	–
2	0.58	0.29	–	–
3	1.08	0.40	–	–
4	1.47	0.39	–	–
5	3.91	0.83	–	–
6	3.64	0.57	–	–

Up

Layer,i	α_i	γ_i^o
1	1.70	15.30
2	1.96	17.71
3	2.71	24.87
4	3.76	35.70
5	4.69	46.71
6	6.40	83.38

Figure V.2 (Report 2, Figure VIII, 1b) SV- Body Waves Ray Path from Source to Site

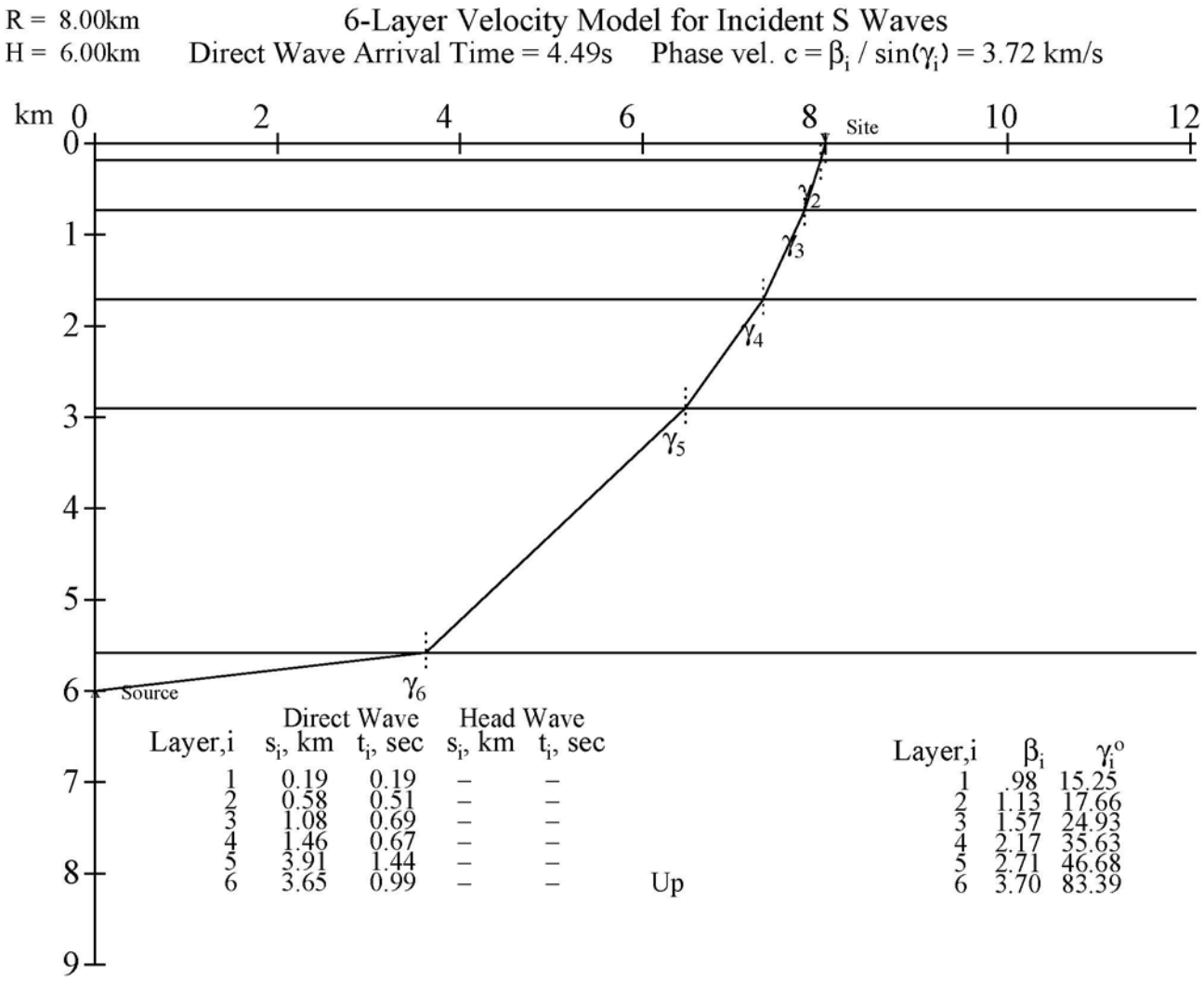

With both the ***P***- and ***SV***- body waves generating an extra mode in the layered media, together with the five modes of ***Rayleigh*** waves, they can now be used to generate the radial and vertical components of synthetic ***rotational*** as well as the synthetic ***translational*** motions at all depths on and below the surface.

Figure V.3a shows the synthetic $\partial\ddot{U}/\partial x$, $\partial\ddot{U}/\partial z$ rotational acceleration time histories derived from the horizontal $U(z)e^{i(kx+\omega t)}$ motions, calculated for the El Centro six-layered site model, at 120 depths equally spaced from the surface to almost 6km below the surface, for the present Case Study, at the hypocentral distance $D = 10.0km$. The **SYNACCS** computer program again determines that the appropriate duration of the accelerogram record should be just about 40 seconds. Similarly **Figure V.3b** shows the synthetic $\partial\ddot{W}/\partial x$, $\partial\ddot{W}/\partial z$ rotational acceleration time histories derived from the corresponding vertical $W(z)e^{i(kx+\omega t)}$ motions. As in the examples of the transverse (anti-plane) rotational components of motions in Chapter IV, the accelerograms are shown at 0.5km spacing. Of the 120 acceleration time histories, five are plotted **green**, and labeled ***1*** *to* ***5***, at depths closest to the interfaces between the adjacent layers.

The synthetic component of rotational motion, $\partial U/\partial x$ and its 1st and 2nd time derivatives, $\partial\dot{U}/\partial x$ and $\partial\ddot{U}/\partial x$, correspond to the time-histories of synthetic ***normal strain***, ε_x. Similarly, the synthetic component of rotational motion, $\partial W/\partial z$ and its 1st and 2nd time derivatives, $\partial\dot{W}/\partial z$ and $\partial\ddot{W}/\partial z$, correspond to the time-histories of synthetic ***normal strain***, ε_z.

As for the two derivative components $\partial U/\partial z$ and $\partial W/\partial x$, from equation (2.2) above, $\Omega_y = \frac{1}{2}\left(\partial U/\partial z - \partial W/\partial x\right)$ is the in-plane ***Rocking*** component of the Rayleigh and body ***P, SV*** waves in the ***x-z*** plane, or the y- component of rotation, while $\varepsilon_{xz} = \frac{1}{2}\left(\partial U/\partial z + \partial W/\partial x\right)$ is the ***Shear Strain*** the ***x-z*** plane. Combinations (sums and differences) of these two derivative components, together with their 1st and 2nd time derivatives, $\partial\dot{U}/\partial z$, $\partial\ddot{U}/\partial z$ and $\partial\dot{W}/\partial x$ $\partial\ddot{W}/\partial x$, give the time histories of synthetic ***Rocking*** and ***Shear Strain*** ε_{xz} accelerations.

Figure V.3a $\partial\ddot{U}/\partial x$ **Synthetic Rotational Acc.:** $M = 6.5,\ R = 8.0km,\ H = 6.0km,\ s = 0,$ **and** $s_L = 2$ $\partial\ddot{U}/\partial z$ $10^{-5}\ rad/s^2$

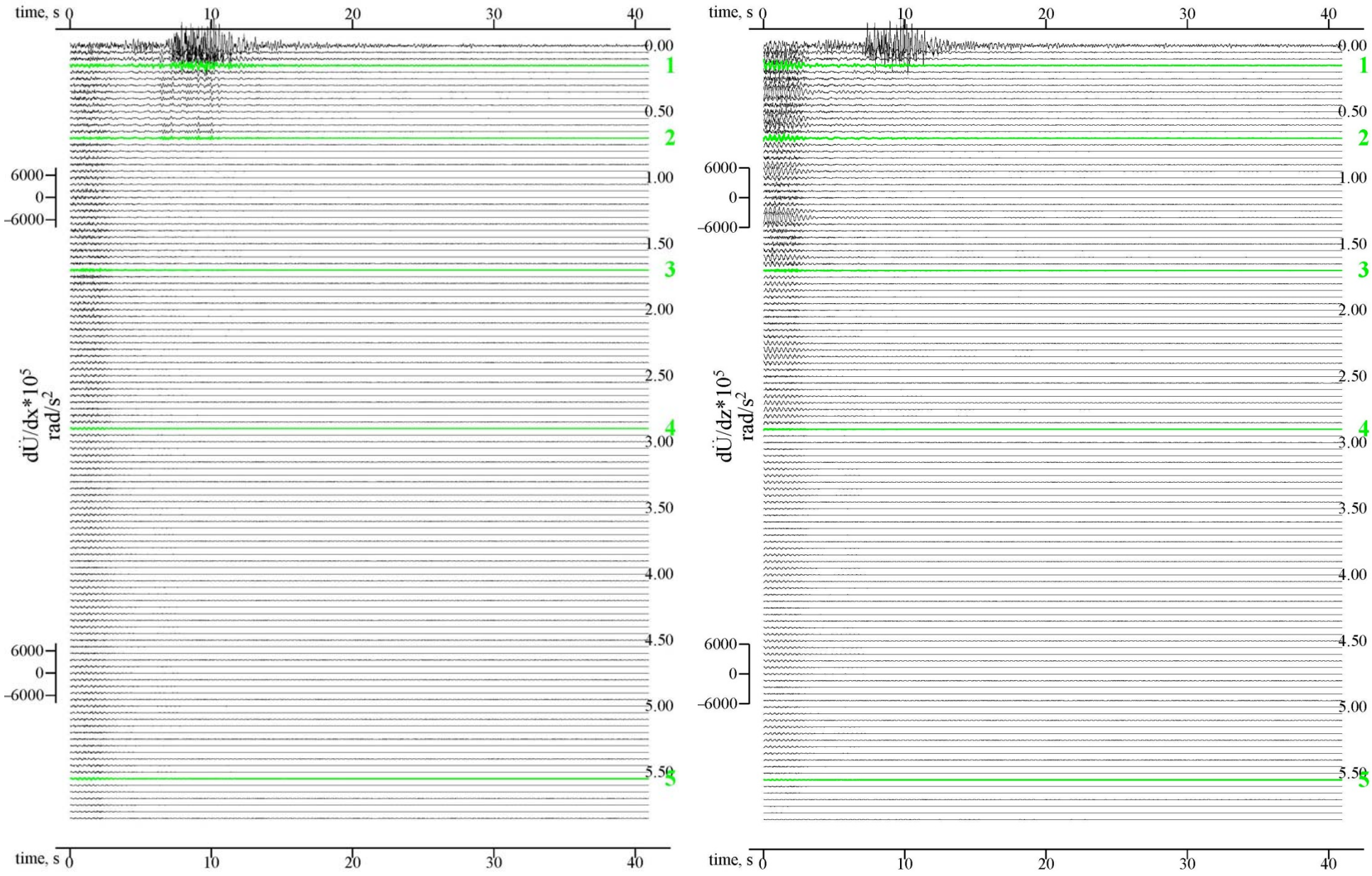

Figure V.3b $d\ddot{W}/dx$ **Synthetic Rotational Acc.:** $M = 6.5,\ R = 8.0km,\ H = 6.0km,\ s = 0,$ **and** $s_L = 2$ $d\ddot{W}/dz$

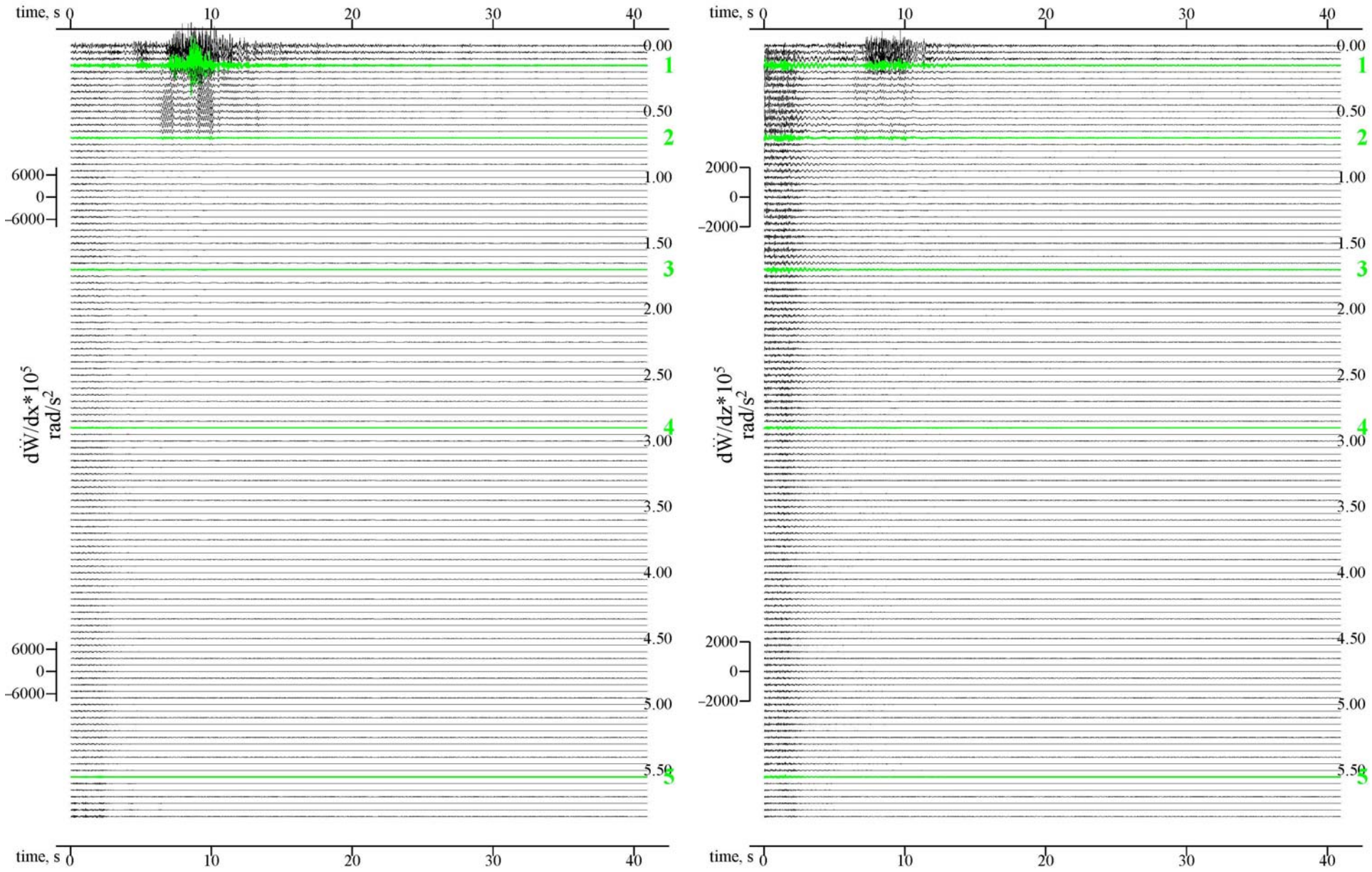

The corresponding acceleration time histories of the horizontal $U(z)$ and vertical $W(z)$ translational motions can be seen in **Figures VIII.3a, b o**f Report 2.

Recall that the time scale of the time histories has been shifted to have a common time origin, where $T = 0$ **sec** is defined by SYNACCS to be the time R/c_{max}, with R the epicentral distance and c_{max} the maximum phase velocity of the waves. In other words, $T = 0$ **sec** is the arrival time of the first (fastest) wave. Perusal of **Figure VIII.3a,b in Report 2** for the translational motions, together with the rotational motions here in **Figures V.3a, b,** will show that, for near filed distance with $D = 10.0km$, both the Rayleigh waves and ***P***- and ***SV***-body waves arrive within a few seconds after the start of the earthquake. The ***SH*** body waves have the same phase velocity at all periods and the direct arrival time of the ***P***-waves (**Figure V.1**) is $T = 2.60s$, while the arrival time for the ***SV***- waves (**Figure V.2**) is $T = 4.49s$. The arrival times for the Rayleigh waves will be different for different modes, and for different periods, since the phase velocities, $c = c(T)$, depend on the periods, as shown by the dispersion curves in **Report 2 Figure I.1**. The plots of acceleration curves show that the strong-motions are all within the first 10 seconds from the first arrivals.

Another point to note is that, for all rotational components, the strong-motion is seen at the depths of just below the top layer, down to $z \sim 0.3km$. Smaller rotational motions are observed in the 2rd layer up to $z \sim 0.7km$, beyond which these motions become small.

This is consistent with the mode shapes of Rayleigh waves in Chapter IV, where it is found that, for all modes of the ***x***- and ***z***- derivatives (rotational) of Rayleigh waves, at moderate periods, large motions occur practically in the first two top layers, and then began to die down at greater depths. The decay of amplitudes with depth is even faster for waves with higher frequencies. In the examples we considered for this writing the maximum of all components of rotational motions are observed in the first two layers from the top, for most periods.

Figure V.4a $d\dot{U}/dx$ **Synthetic Rotational Vel.:** $M = 6.5,\ R = 8.0km,\ H = 6.0km,\ s = 0,$ **and** $s_L = 2$ $d\dot{U}/dz$

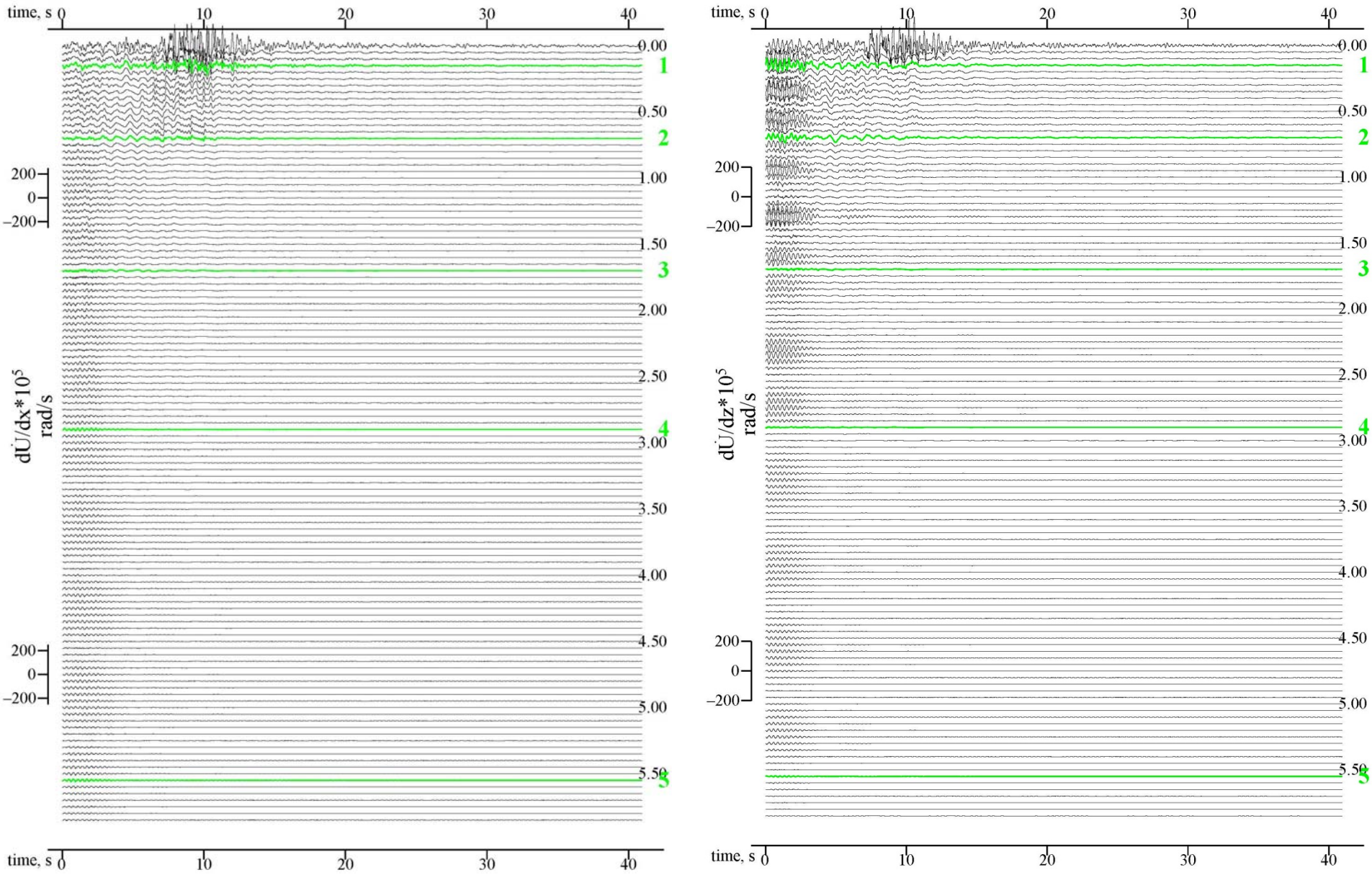

Figure V.4b $d\dot{W}/dx$ **Synthetic Rotational Vel.:** $M = 6.5,\ R = 8.0km,\ H = 6.0km,\ s = 0,$ **and** $s_L = 2$ $d\dot{W}/dz$

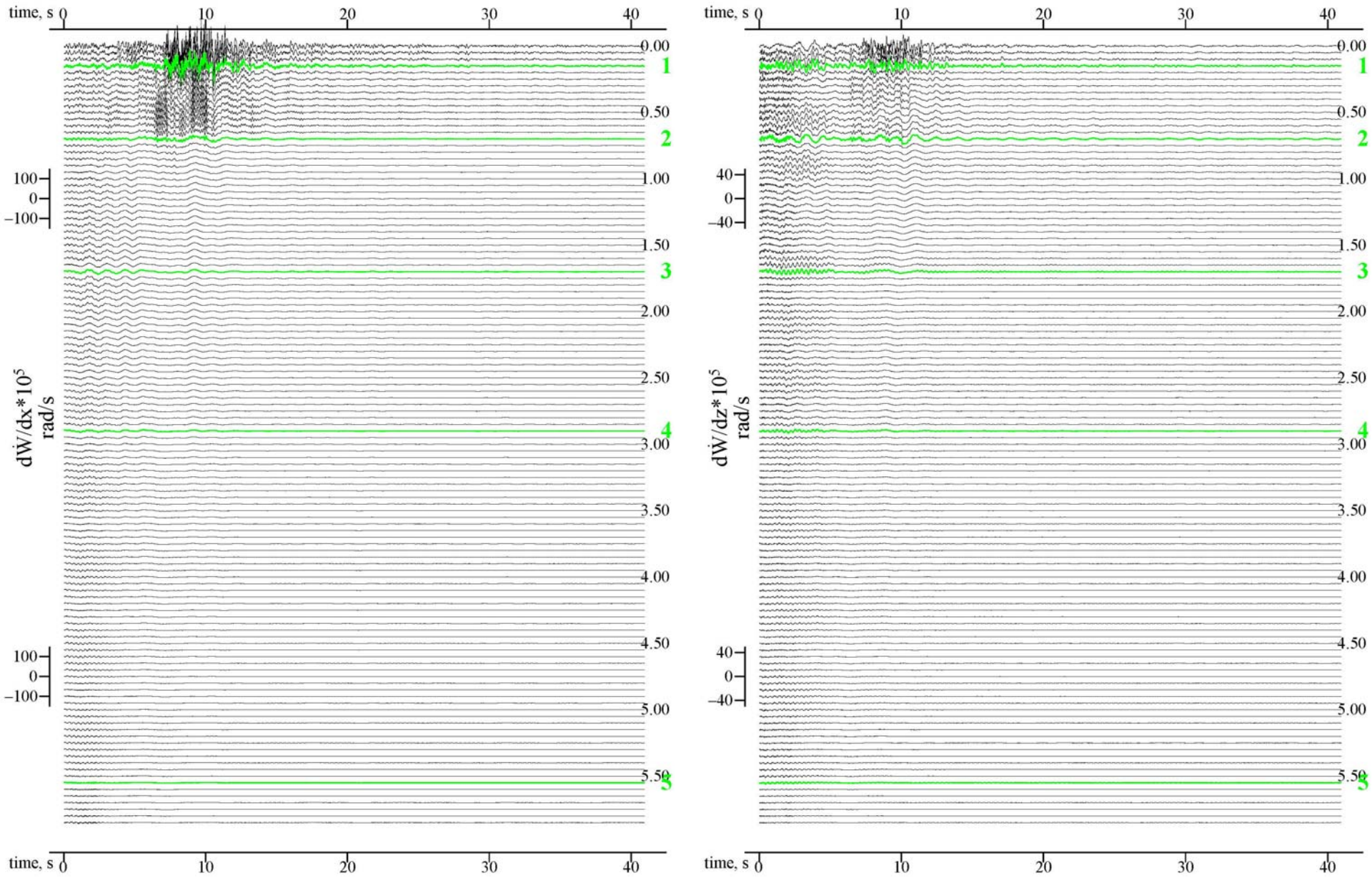

For the transverse and rotational components in Chapter IV and for the radial and vertical rotational components in the example considered here, it is observed that for the six-layered model in Imperial Valley, El Centro, ***large rotational motions occur mainly on or near the surface***. This is consistent with the rotational mode shapes of Rayleigh waves in the last chapter, where it was found that, for all modes of Rayleigh waves, at moderate periods, large motions occur in the first *two* top layers, and then began to die down at greater depths. The decay of amplitudes with depth becomes faster for waves with higher frequencies.

Figure V.4a, b shows the synthetic rotational velocity calculated for the El Centro six-layered site, respectively for the ***x***- and ***z***- derivatives of both the horizontal $\boldsymbol{U(z)}$ and vertical $\boldsymbol{W(z)}$ components of motion. The velocity traces are again shown at depths 0.5km apart. Of the 120 velocity time histories, five are plotted green, and labeled ***1*** to ***5***. Those are at depths, which are closest to the interfaces between adjacent layers. The new SYNACCS program computes the velocity at all depths from the corresponding rotational acceleration time histories using the Fourier transform in the frequency domain, to get the velocity spectra, and then taking its inverse Fourier transform.

These observations for velocity also apply to accelerations, namely, the strong-motion rotations are again observed in the top two layers of this cite, up to $\boldsymbol{z = 0.7km}$. However, unlike acceleration, all components of the velocity rotational motions do not completely die down even at larger depths.

Figures V.5a, b show the plots of the corresponding synthetic rotational displacement of the same components of motions. The new SYNACCS program computes the displacement at all depths from the corresponding acceleration time histories in the frequency domain to get the displacement spectra, and then taking its inverse Fourier transform. The same observations for displacement time histories can be made as for accelerations, namely, the strong-motions are observed in the first three layers of the example model, up to $\boldsymbol{z = 1.7km}$. Unlike accelerations, the displacements, especially for the vertical components, do not quickly die down even at large depths.

Figure V.5a dU/dx **Synthetic Rotational Disp.:** $M = 6.5,\ R = 8.0km,\ H = 6.0km,\ s = 0,$ and $s_L = 2$ dU/dz

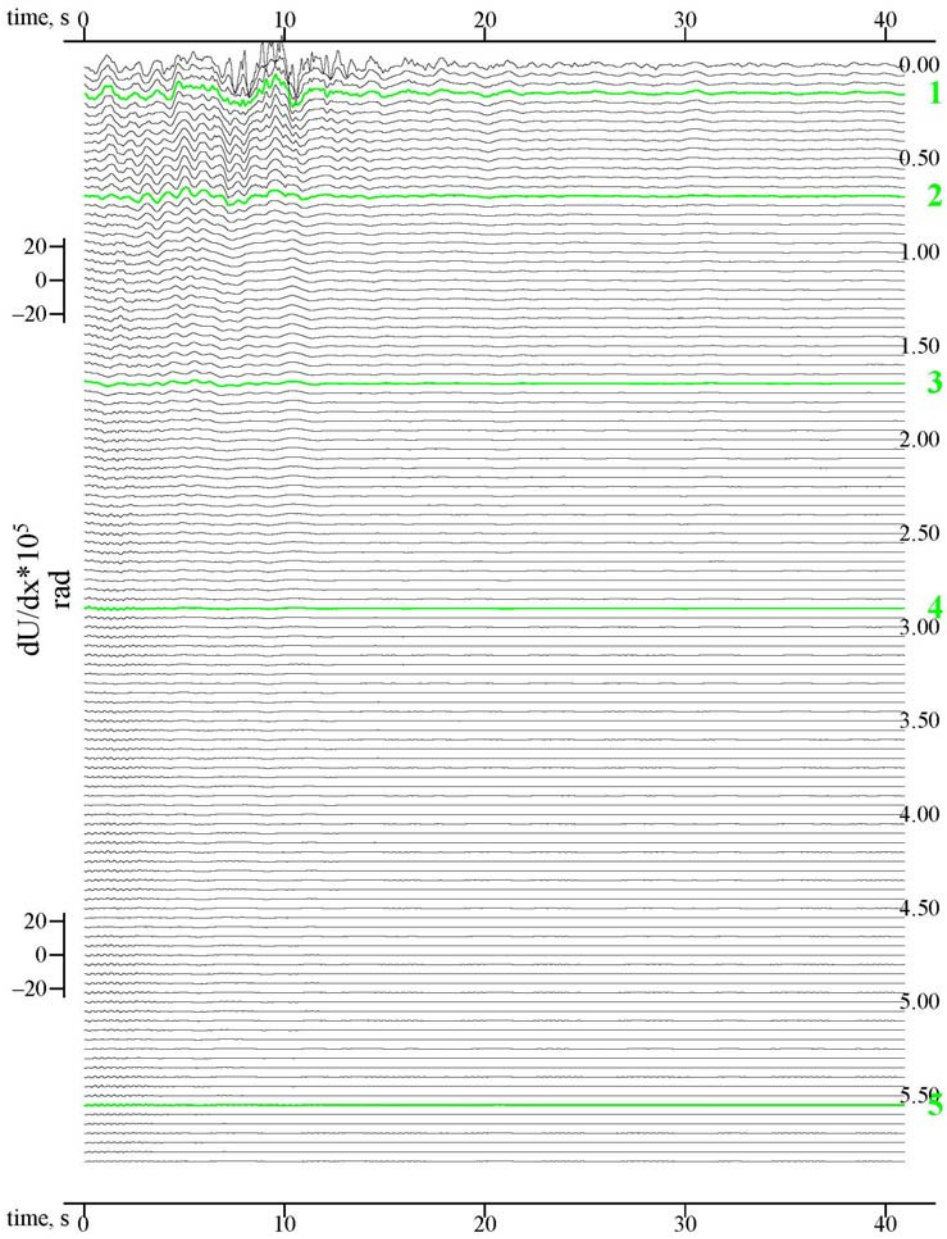

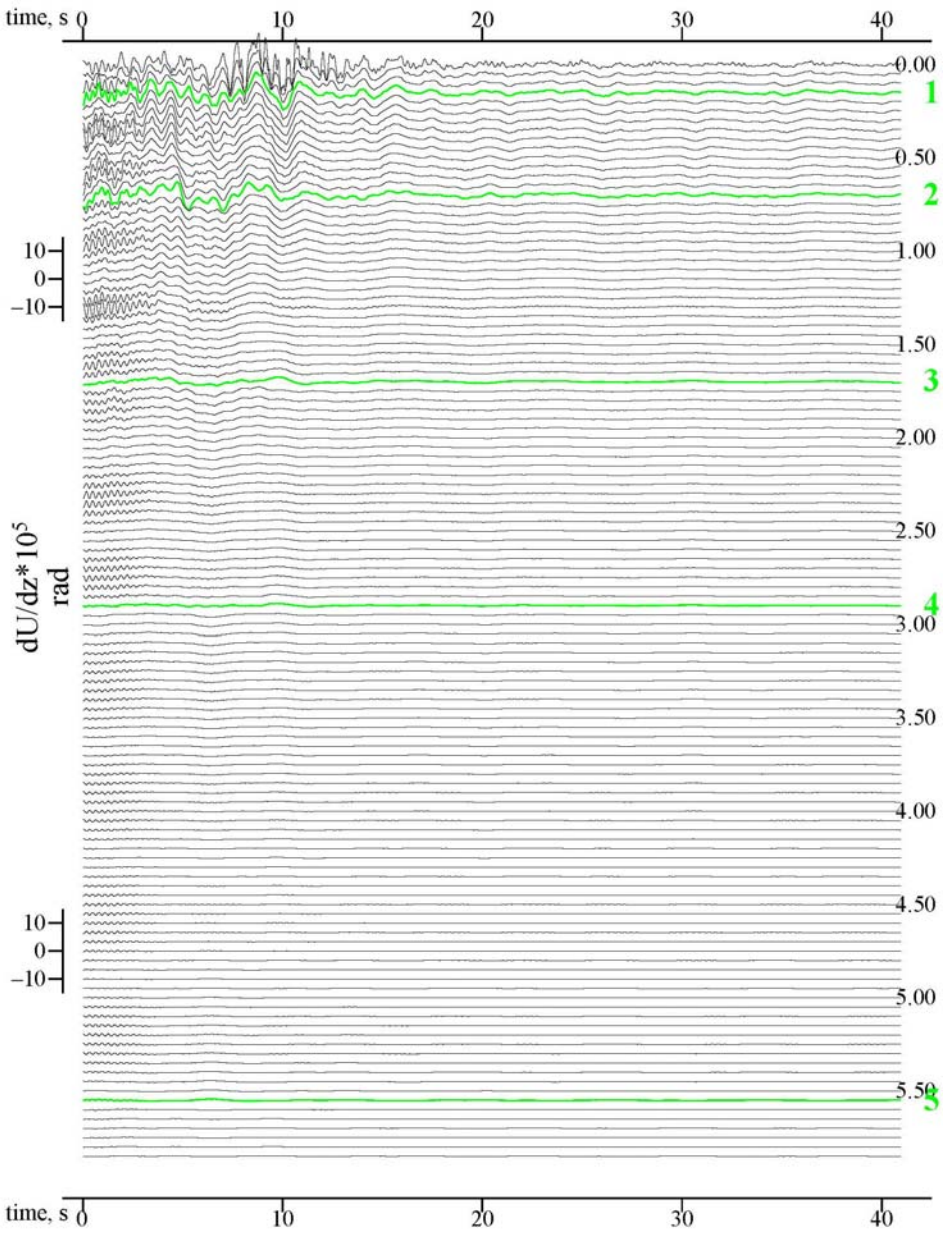

Figure V.5b dW/dx **Synthetic Rotational Disp.:** $M = 6.5,\ R = 8.0km,\ H = 6.0km,\ s = 0,$ **and** $s_L = 2$ dW/dz

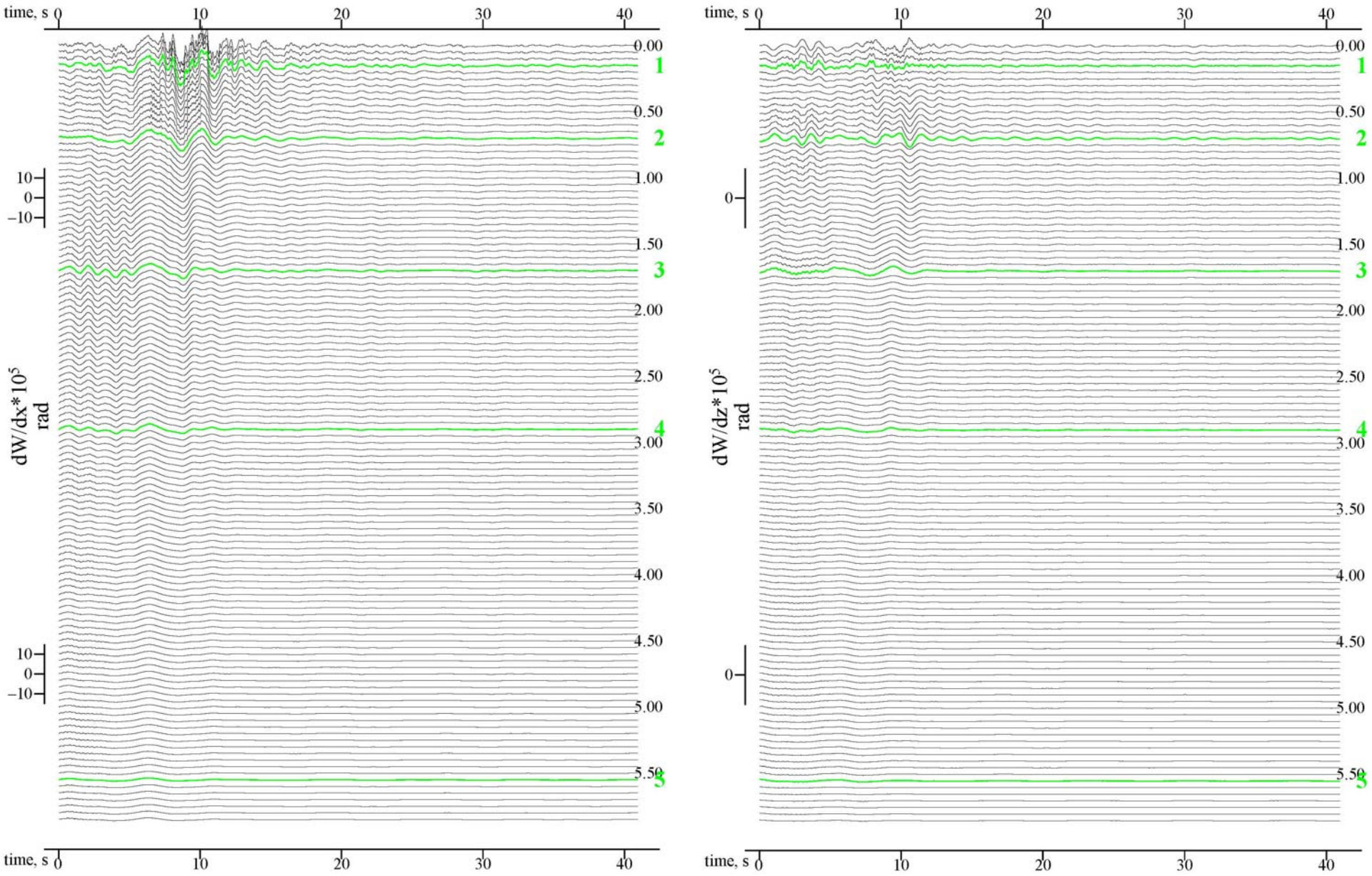

V.3 The Three-Dimensional (*3-D*) Plots for *Case Study 1*

As for the transverse rotational components in Chapter IV, the same time histories of synthetic rotational acceleration, velocity and displacements, from Figures V.3, 4 and 5, will now be presented as three-dimensional (3-D) figures.

The next six pages will be the portrait ***3-D*** figures corresponding to the six landscape ***2-D*** figures above.

Figure V.6a, b are the ***3-D*** plots of synthetic rotational accelerations of the horizontal radial and vertical components for the same 120 acceleration time histories corresponding to the ***2-D*** Figures V.3a, b.

Figures V.7a, b and **Figure V.8a, b** show the ***3-D*** views of the rotational velocity and displacement for the horizontal and vertical components corresponding to the ***2-D*** plots in Figures V.4a, b and V.5a, b.

V.4 Separating the Body and Surface Waves Plots for *Case Study 1*

In both the ***2-D*** plots (**Figures V.3a, b to Figures V.5a, b**) and the ***3-D*** plots (**Figures V.6a, b to Figures V.8a, b**), it is seen that in the synthetic accelartion, velocity and displacement rotation time histories, the body waves and surface waves arrive at different times, as in the case of the rotational transverse motions in Chapter IV and the tranlslational motions in Chapter VII and VIII of Report 2. As pointed out before, this is because the body waves have the highest phase velocities and hence much faster arrivals compared to all modes of surface waves at all periods. Further the body waves can be significant at all depths below surface, while the motions of all modes of surface waves decay from the surface towards increasing depth. For the translational motions studied in Report 2, the surface wave motions are noticeable only in the top three layers from the surface, up to $\boldsymbol{z = 1.7km}$. For the rotational surface waves here, they decay even faster, and the motions are noticeable only on the top two layers, up to about $\boldsymbol{z = 0.7km}$.

Figure V.6a **Synthetic Rotational Acceleration at $M = 6.5$, $R = 8.0km$ & $H = 6.0km$, $s = 0$, $s_L = 2$**

$d\ddot{U}/dx$

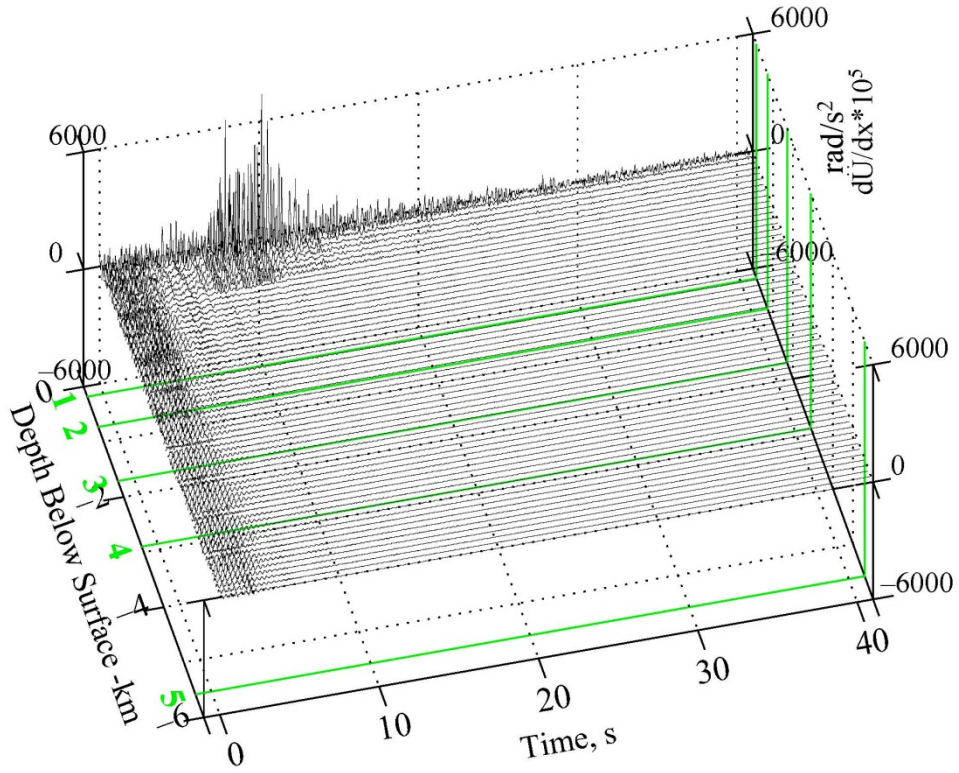

$d\ddot{U}/dz$

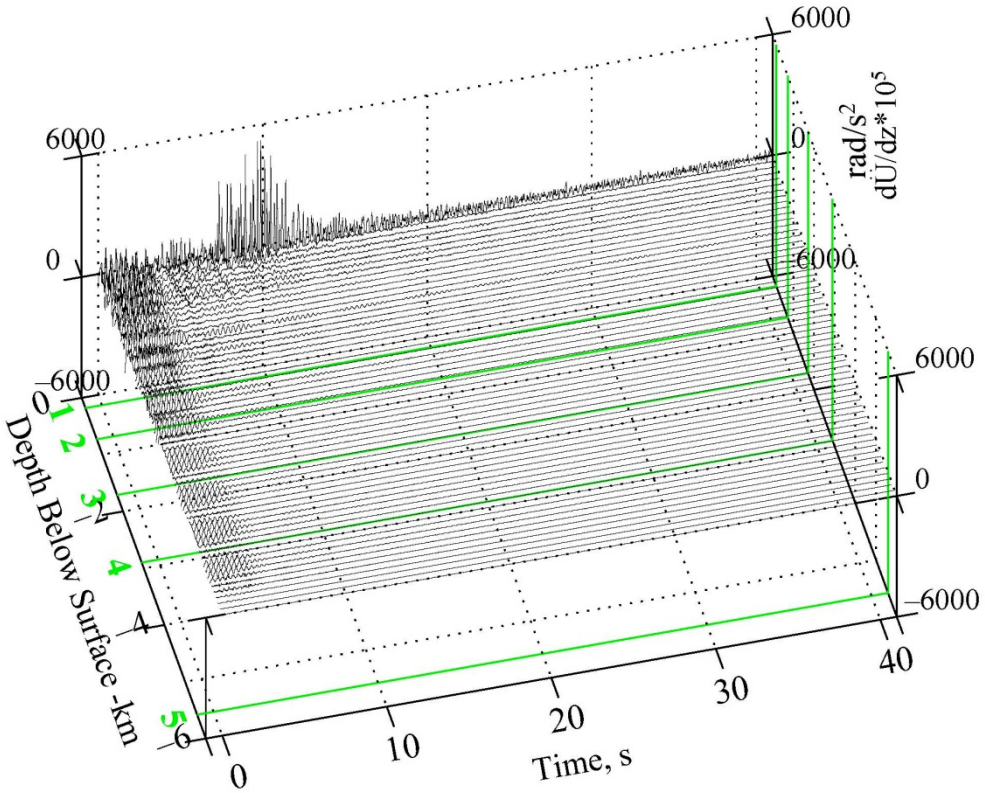

Figure V.6b **Synthetic Rotational Acceleration at $M = 6.5$, $R = 8.0km$ & $H = 6.0km$, $s = 0$, $s_L = 2$**

$d\ddot{W}/dx$

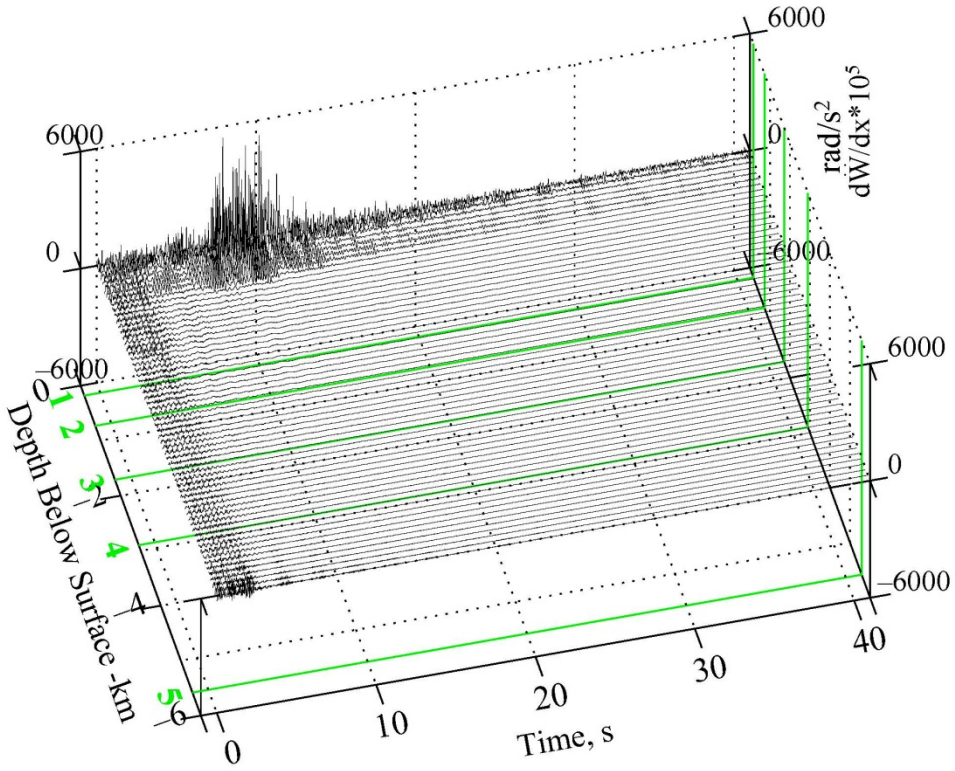

$d\ddot{W}/dz$

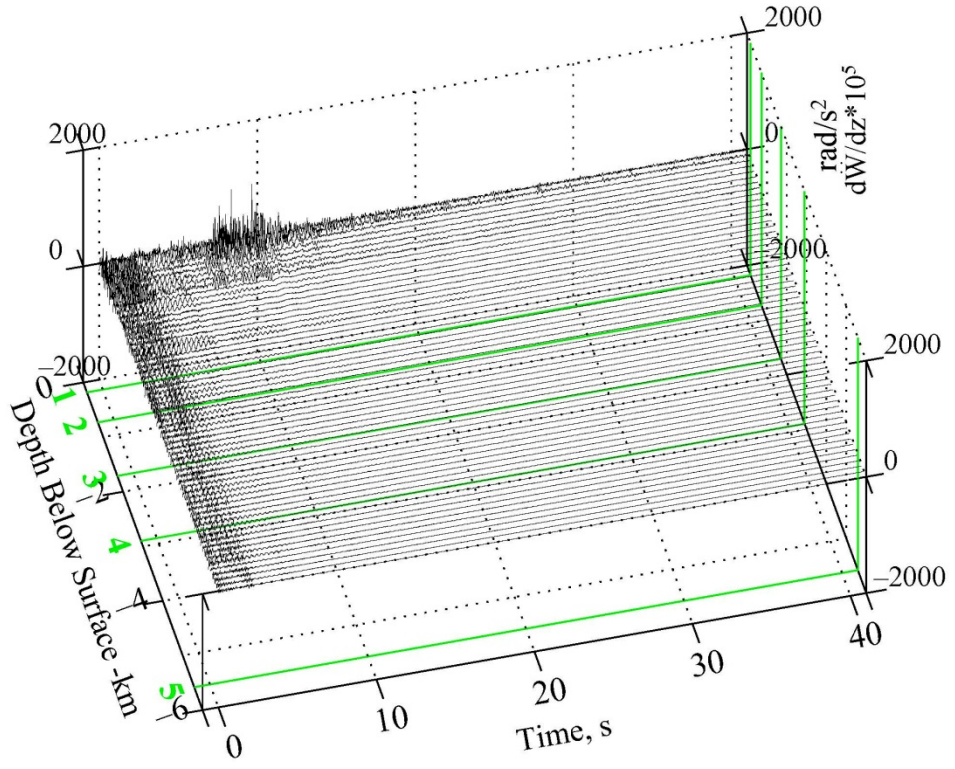

Figure V.7a **Synthetic Rotational Velocity at $M = 6.5$, $R = 8.0km$ & $H = 6.0km$, $s = 0$, $s_L = 2$**

$d\dot{U}/dx$

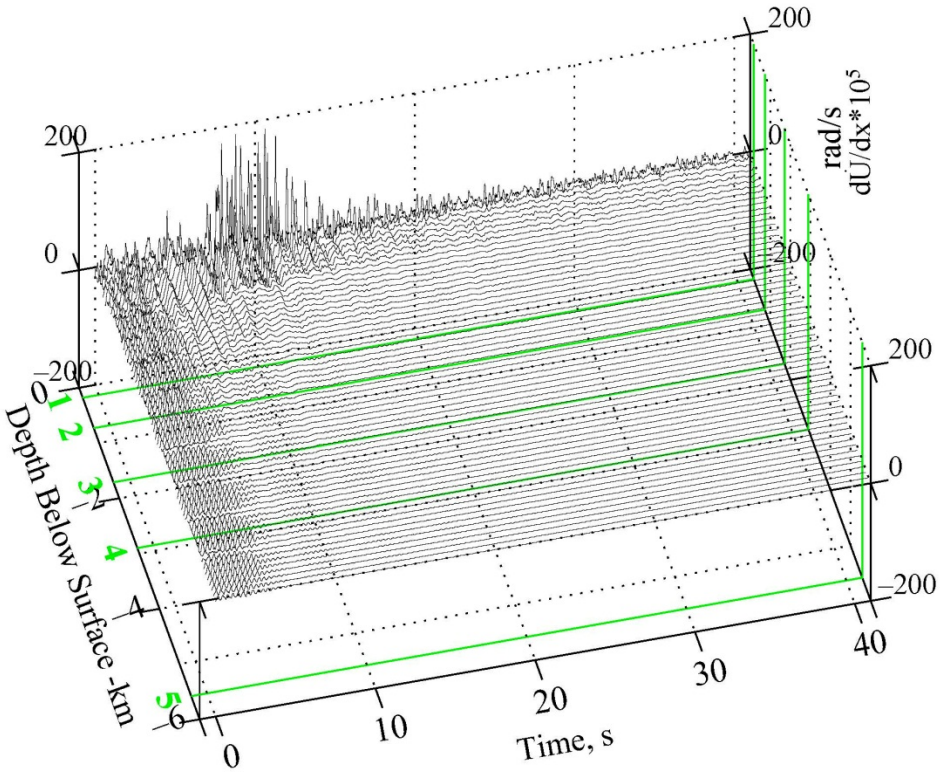

$d\dot{U}/dz$

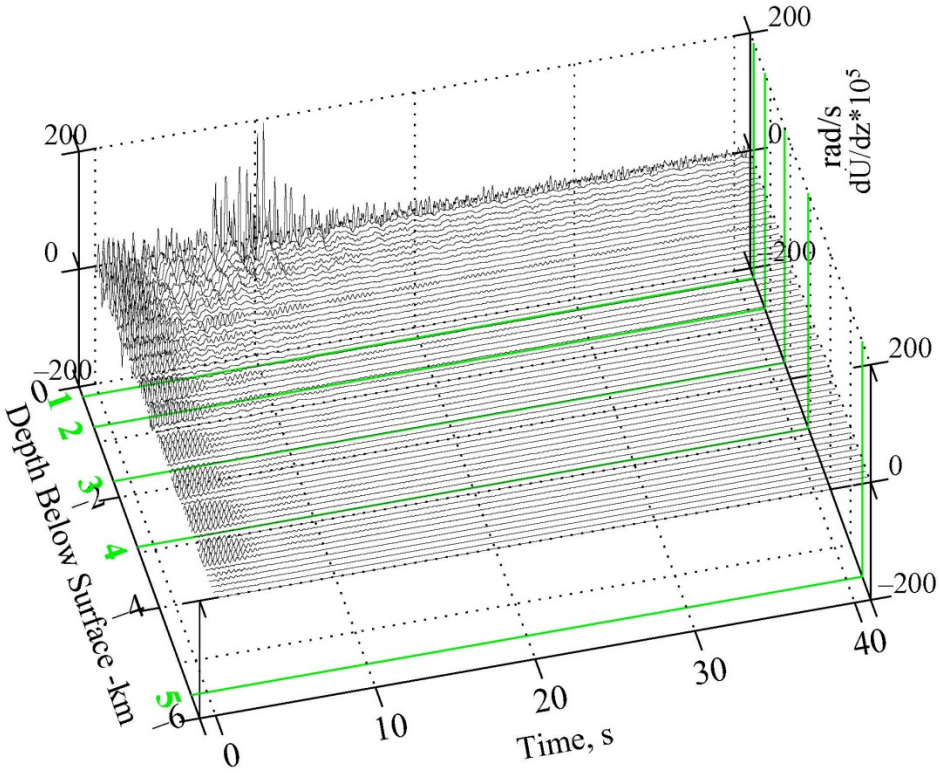

Figure V.7b **Synthetic Rotational Velocity at $M = 6.5$, $R = 8.0km$ & $H = 6.0km$, $s = 0$, $s_L = 2$**

$d\dot{W}/dx$

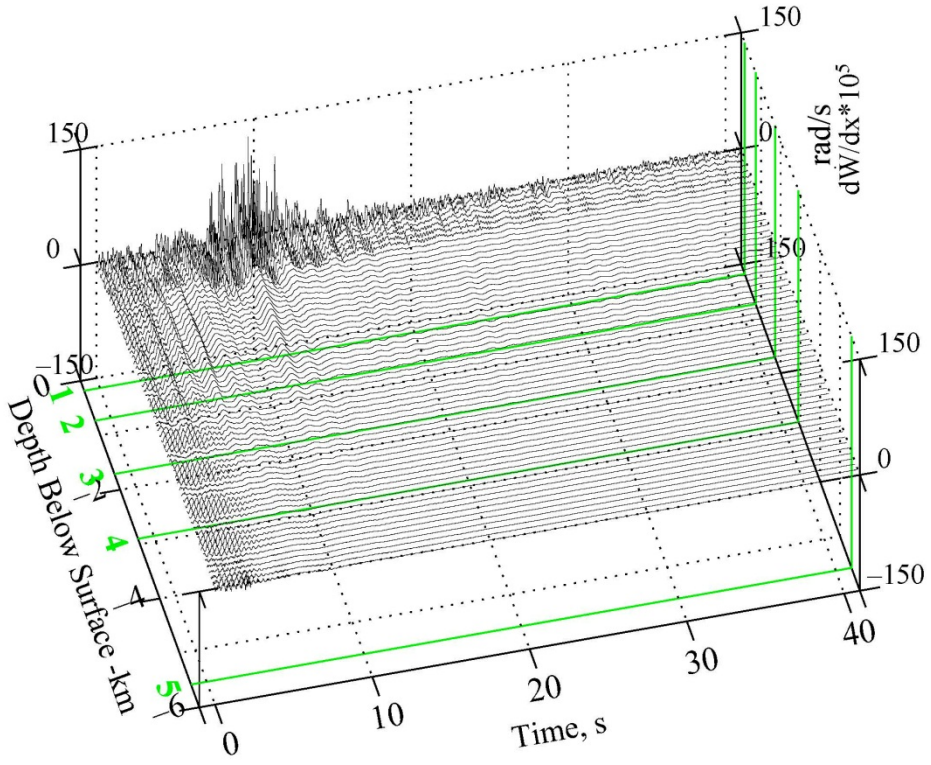

$d\dot{W}/dz$

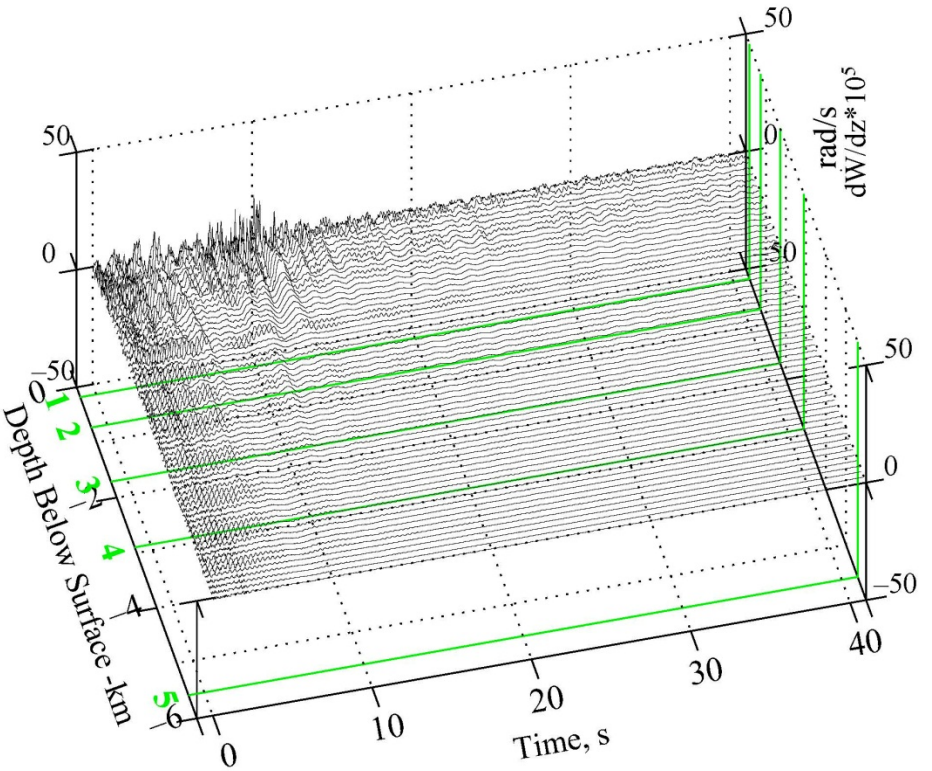

Figure V.8a **Synthetic Rotational Displacement at $M = 6.5,\ R = 8.0km$ & $H = 6.0km,\ s = 0,\ s_L = 2$**

dU/dx

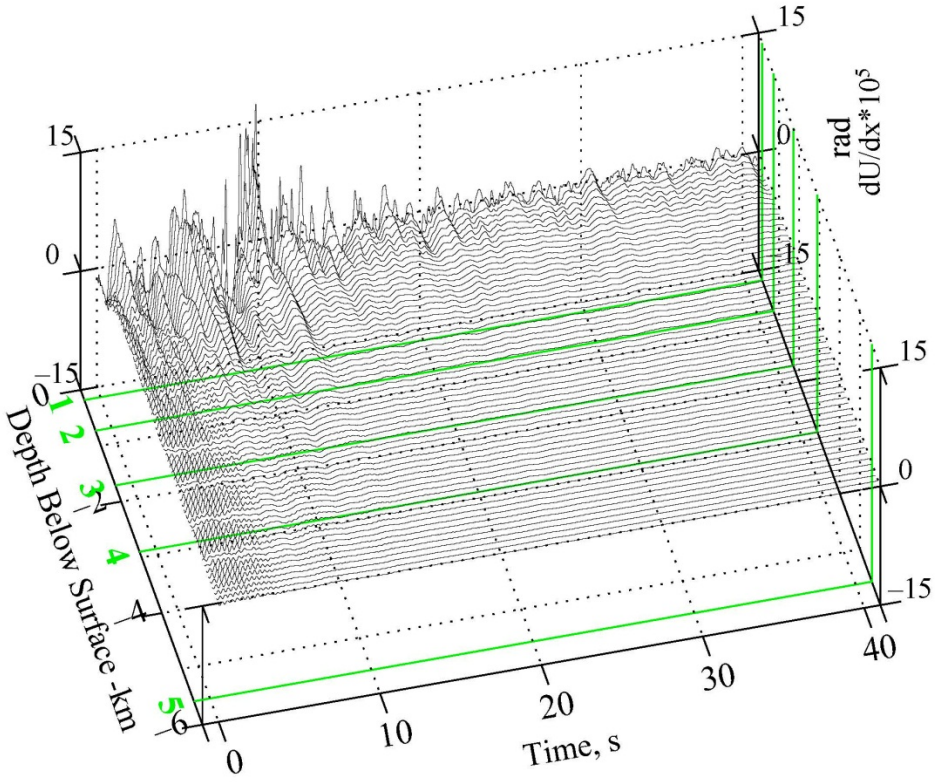

dU/dz

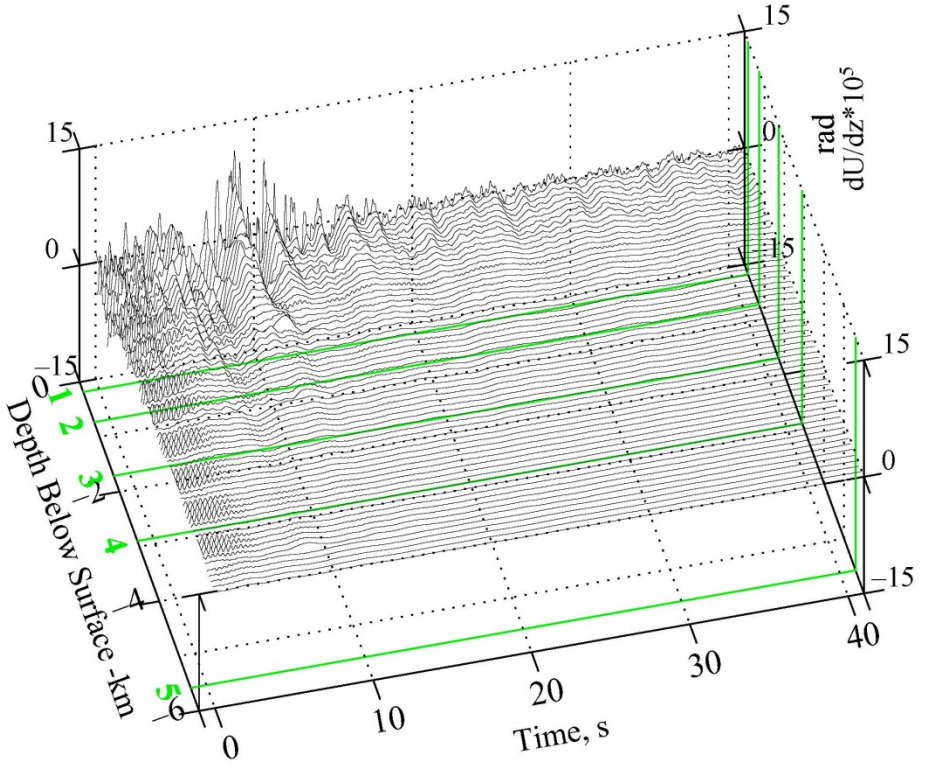

Figure V.8b **Synthetic Rotational Displacement at $M = 6.5,\ R = 8.0km$ & $H = 6.0km,\ s = 0,\ s_L = 2$**

dW/dx

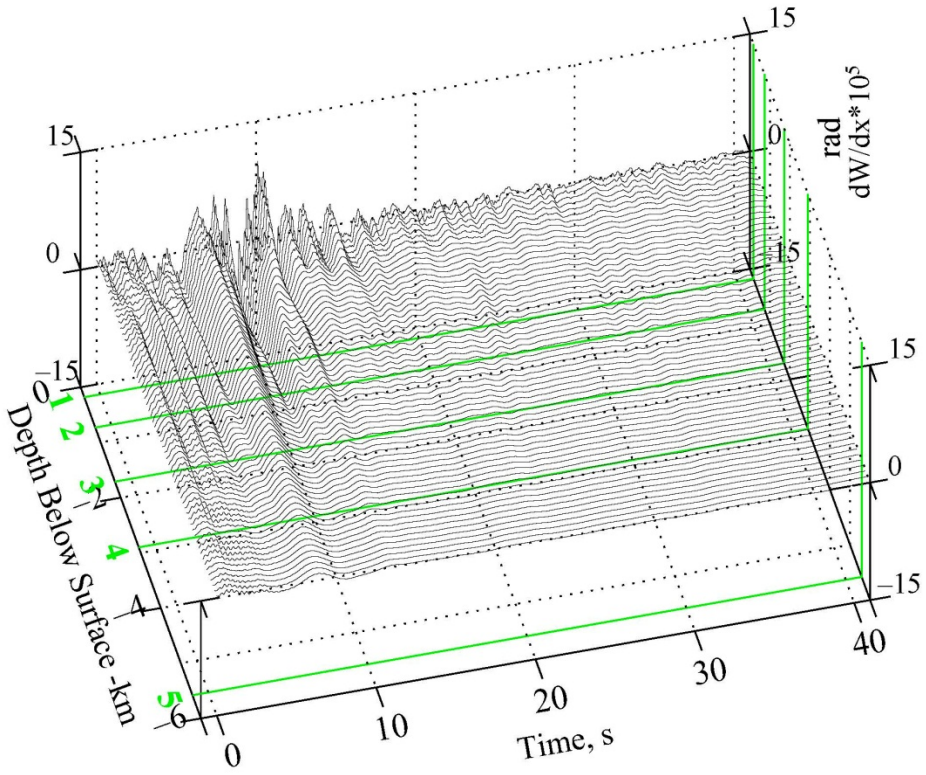

dW/dz

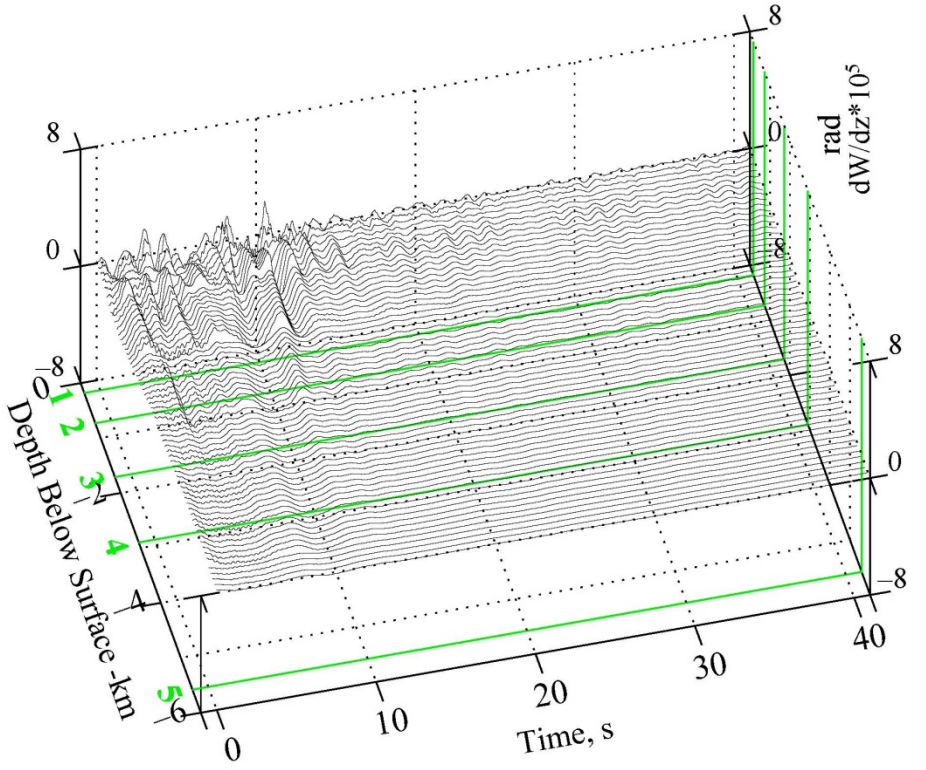

The separate contributions to the synthetic motions from body waves and surface waves can be better visualized by plotting them separately, as in **Figures V.9a, b, 10a, b and 11a, b** below.

Figure V.9a shows the derivatives, $d\ddot{U}/dx$ and $d\ddot{U}/dz$ of the horizontal, radial *x*-component acceleration time-histories of the body waves, the surface waves, and the total sum waves, plotted in separate graphs. **Figure V.9b** shows the corresponding plots for the derivatives, $d\ddot{W}/dx$ and $d\ddot{W}/dz$ of the vertical z- component of motion.

In both figures, Figures **V.9a** (x-comp) and **V.9b** (z-comp), the rotational body waves (in the top row) arrive at the very beginning and dominate the motions at all depths within the first 10+ seconds. The surface waves (in the middle row) arrive later, with the motions not significant until 5-10 seconds after the record starts. Combining the motions of the body waves and surface waves results in the acceleration time histories of the total synthetic motions as shown in **Figure V.6a, b**, replotted here in the bottom row, where the two types of motions are clearly distinguishable.

The graphs of **Figures V.10a, b** (x-comp) and (z-comp) represent the rotational velocity time histories of the body waves and of surface waves. The trend of the velocity time histories is the same as that of the accelerations. The surface wave velocity time histories (on the right) have strong motions only at the top two layers of the media and the maxima occur at around the 10 seconds mark after the motons start.

The two 3-D graphs of **Figures V.11a, b** (x-comp) and (z-comp) represent the rotational displacement time histories of the body waves and of surface waves. Unlike the acceleration time histories, the rotational displacement time histories of body wave (on the left) have smaller motions at all depths, even during the first 10 seconds, compared to that of the surface waves. The surface wave rotational displacement time histories (in the middle row) are more dominant, again only in the top two layers, and the maxima occur again at around the 10-seconds mark after the earthquake starts.

Figure V.9a Contributions of Body and Surface Waves to Total Synthetic Rotational Acceleration

$d\ddot{U}/dx$ **Body Waves** $d\ddot{U}/dz$

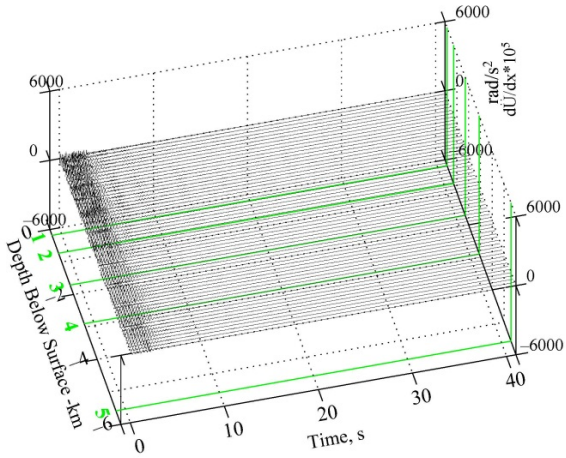

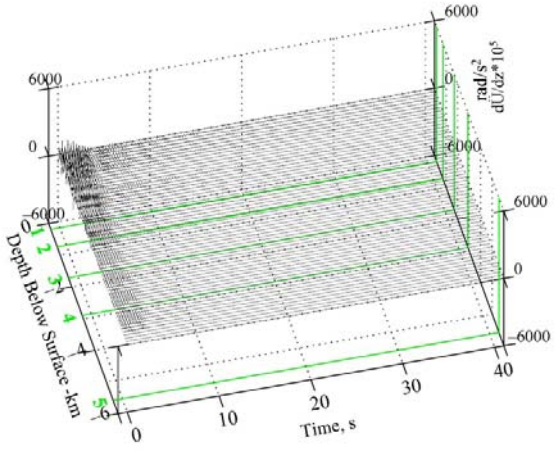

$d\ddot{U}/dx$ **Surface Waves** $d\ddot{U}/dz$

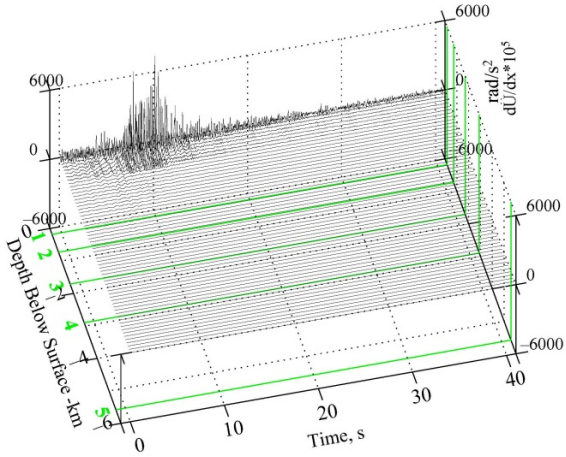

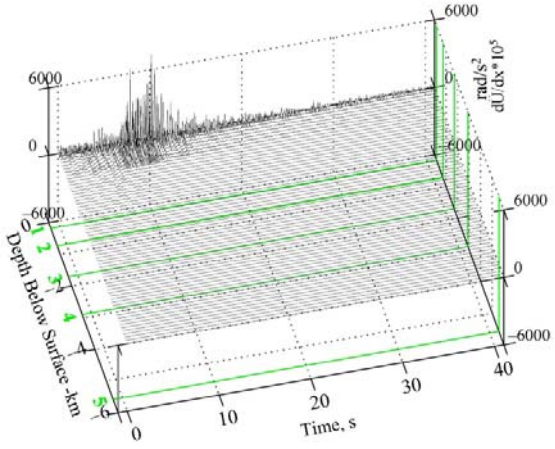

$d\ddot{U}/dx$ **All (Body + Surface) Waves** $d\ddot{U}/dz$

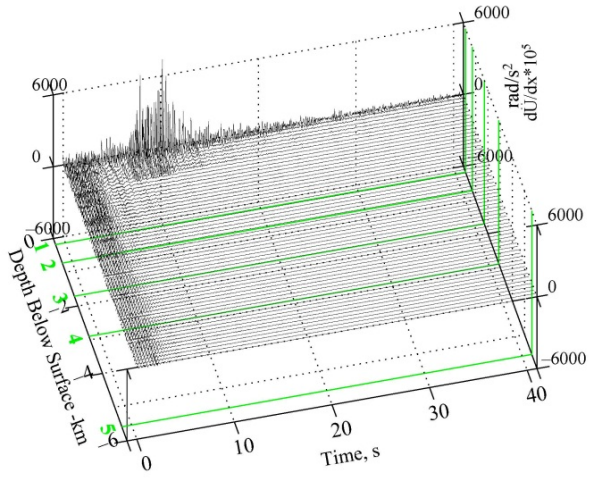

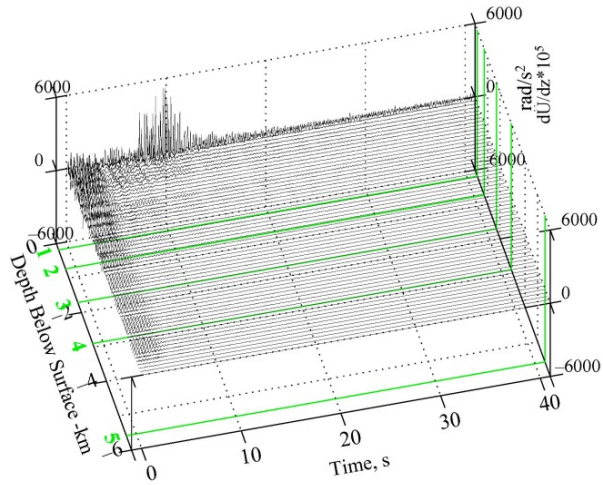

Figure V.9b Contributions of Body and Surface Waves to Total Synthetic Rotational Acceleration

$d\ddot{W}/dx$ **Body Waves** $d\ddot{W}/dz$

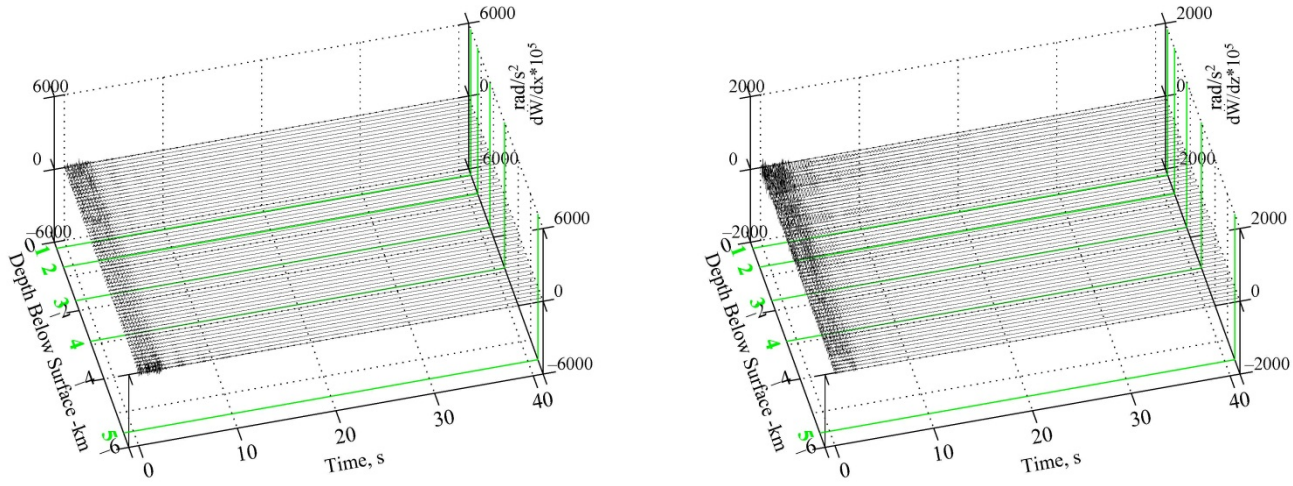

$d\ddot{W}/dx$ **Surface Waves** $d\ddot{W}/dz$

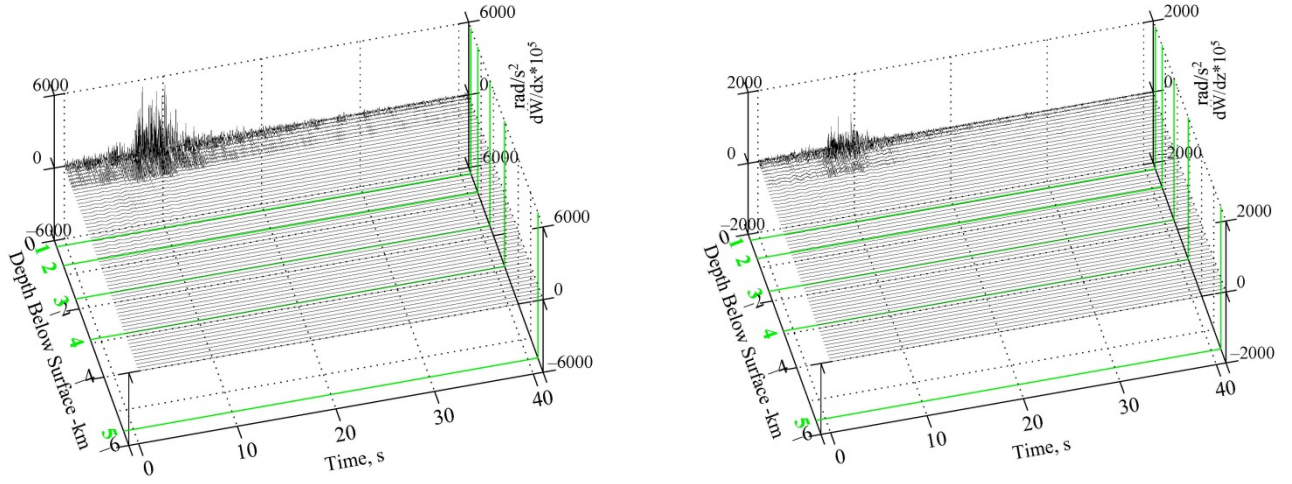

$d\ddot{W}/dx$ **All (Body + Surface) Waves** $d\ddot{W}/dz$

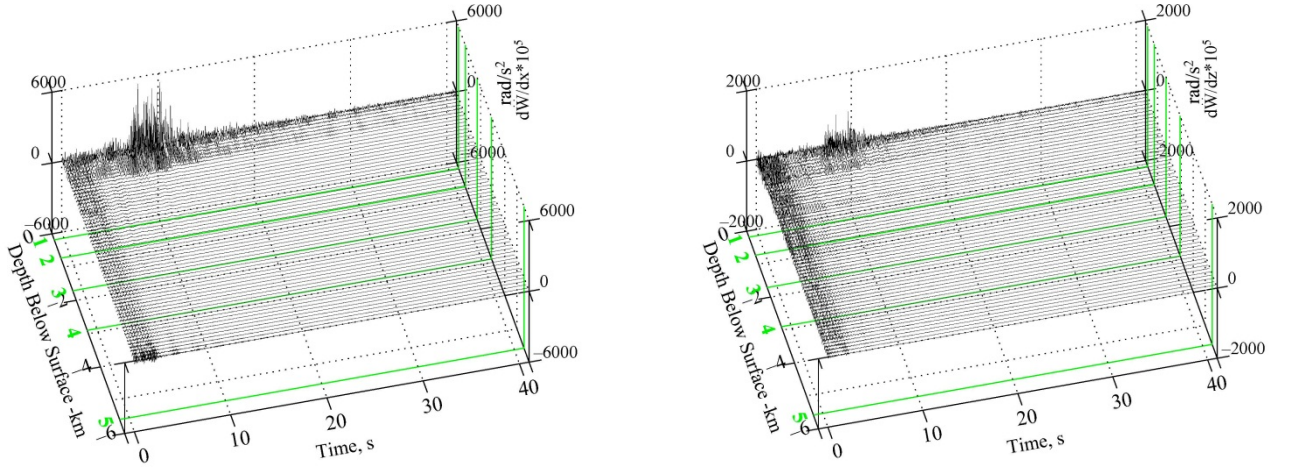

Figure V.10a Contributions of Body and Surface Waves to Total Synthetic Rotational Velocity

$d\dot{U}/dx$ **Body Waves** $d\dot{U}/dz$

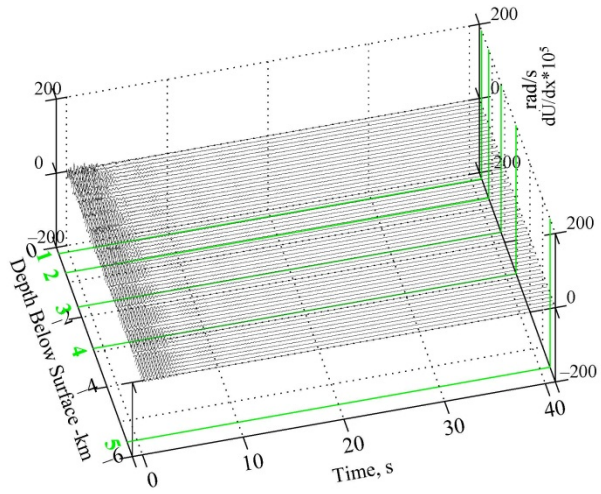

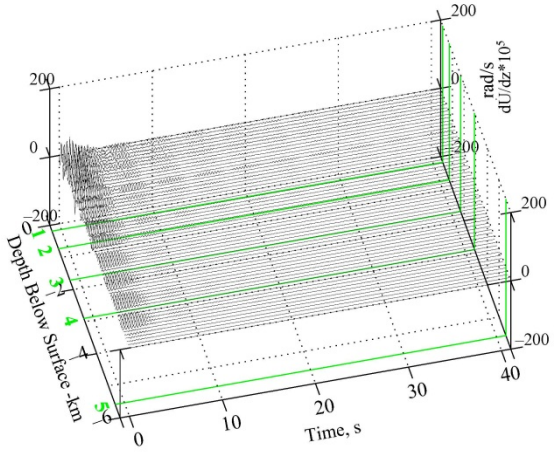

$d\dot{U}/dx$ **Surface Waves** $d\dot{U}/dz$

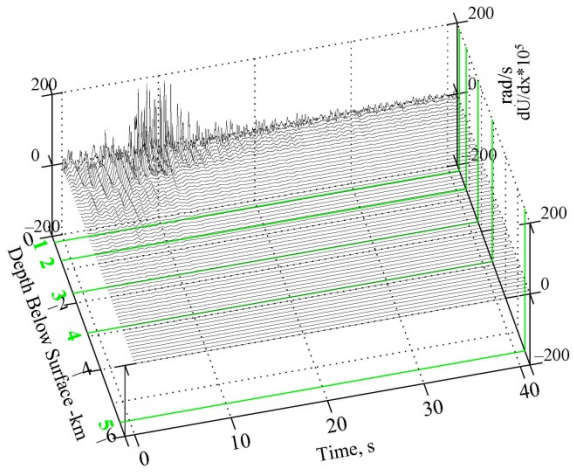

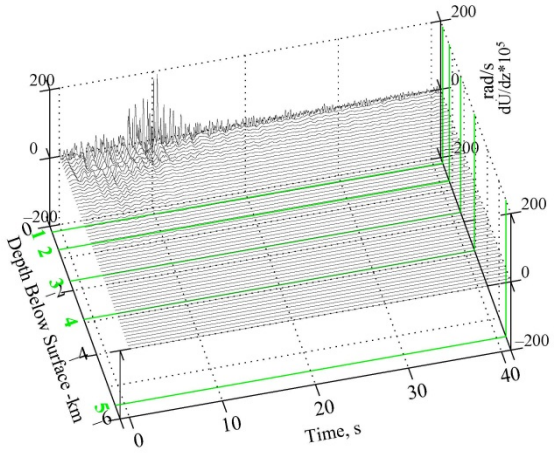

$d\dot{U}/dx$ **All (Body + Surface) Waves** $d\dot{U}/dz$

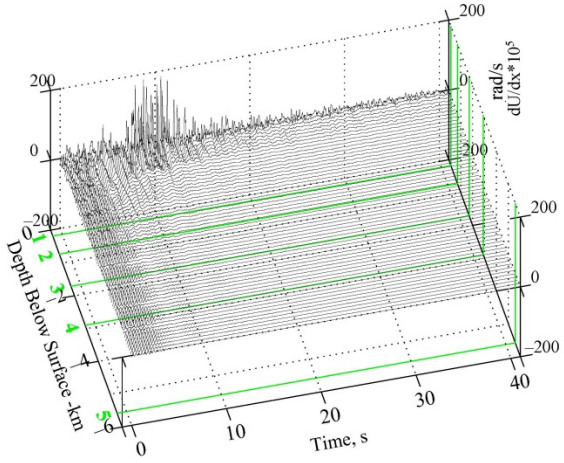

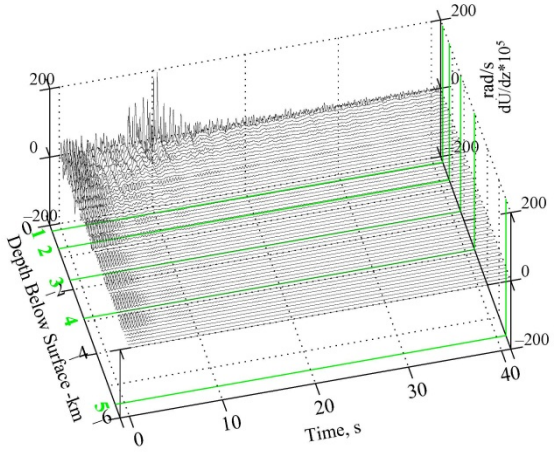

Figure V.10b Contributions of Body and Surface Waves to Total Synthetic Rotational Velocity

$d\dot{W}/dx$ **Body Waves** $d\dot{W}/dz$

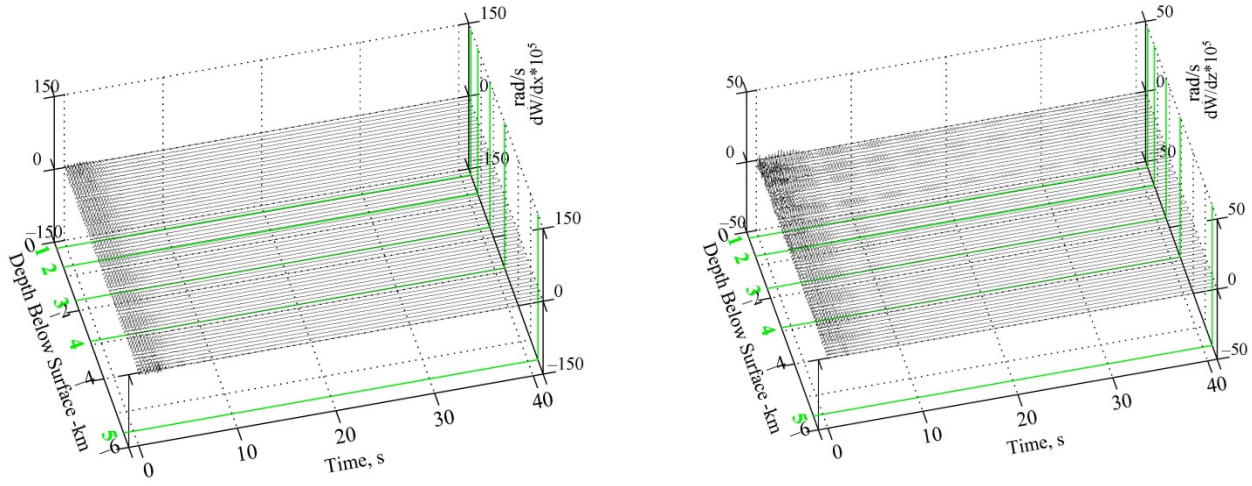

$d\dot{W}/dx$ **Surface Waves** $d\dot{W}/dz$

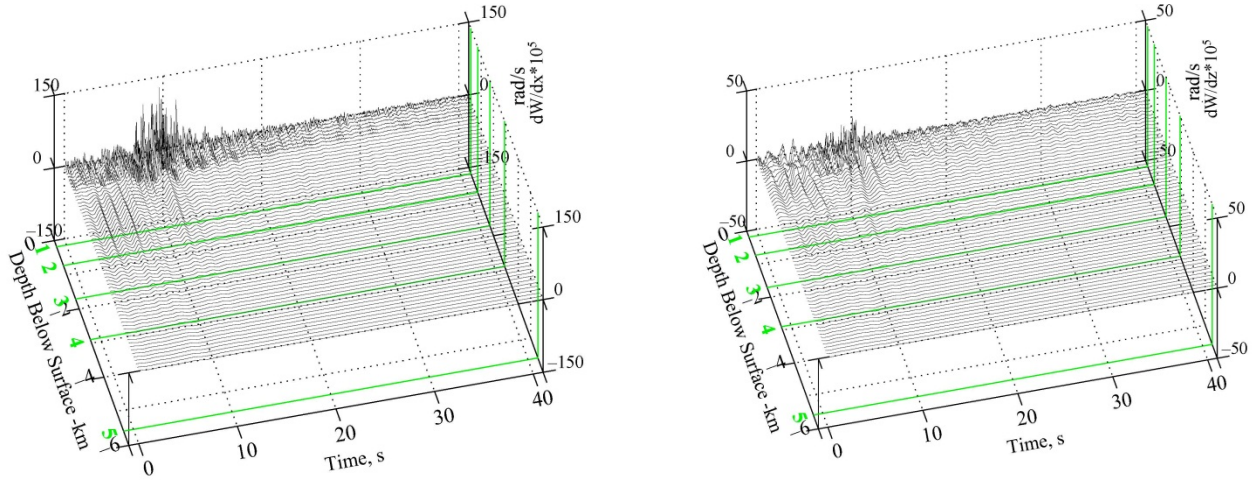

$d\dot{W}/dx$ **All (Body + Surface) Waves** $d\dot{W}/dz$

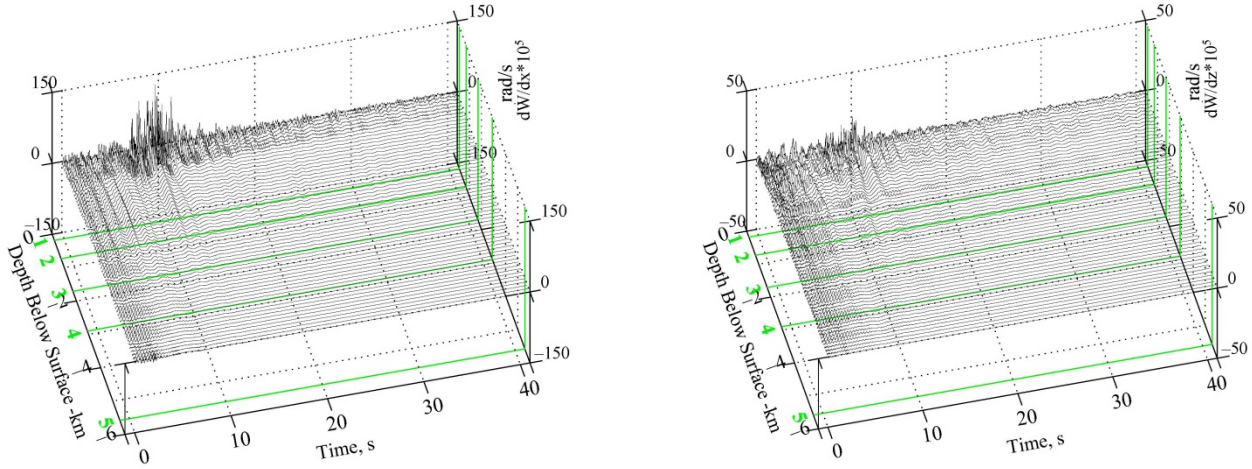

Figure V.11a Contributions of Body and Surface Waves to Total Synthetic Rotational Displacement

dU/dx **Body Waves** ***dU/dz***

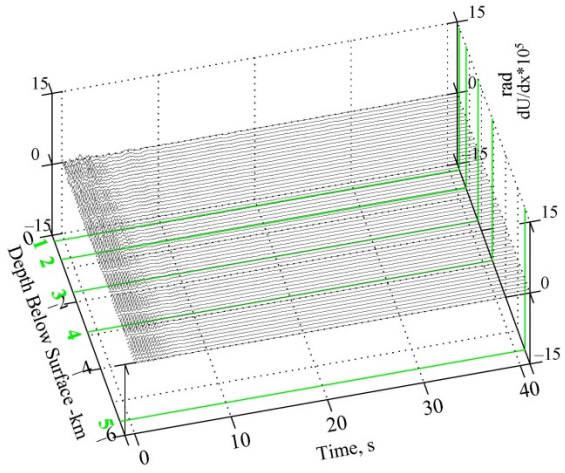

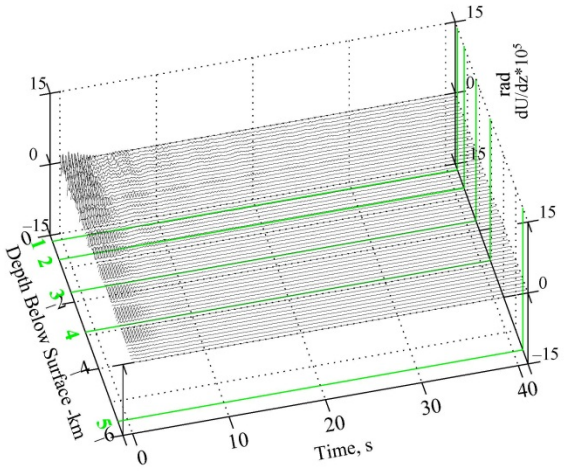

dU/dx **Surface Waves** ***dU/dz***

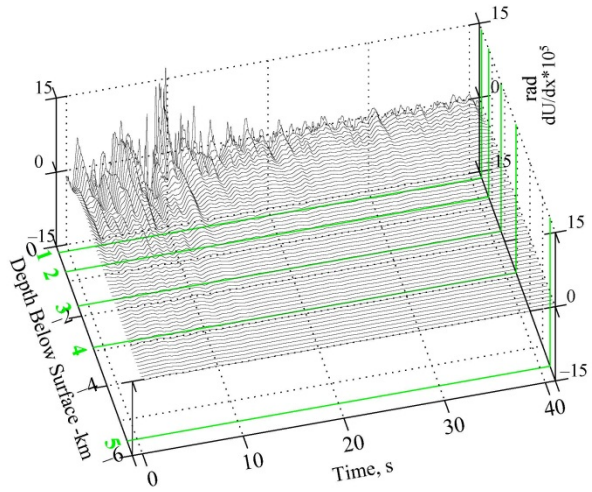

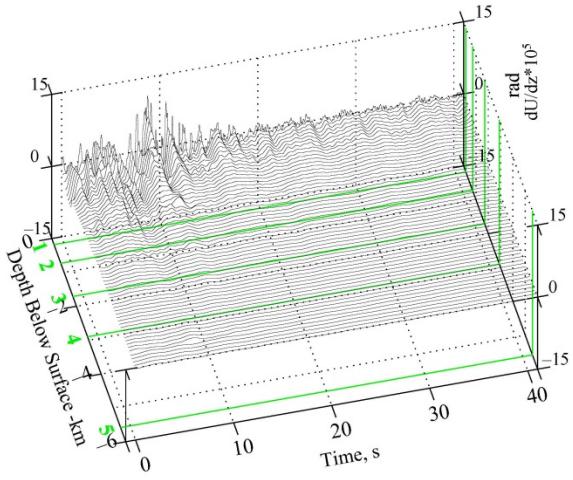

dU/dx **All (Body + Surface) Waves** ***dU/dz***

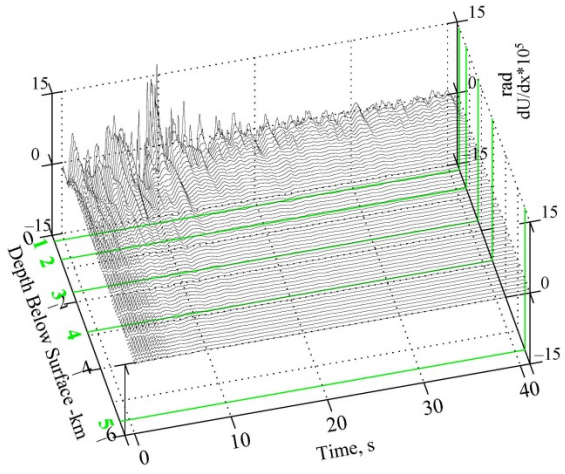

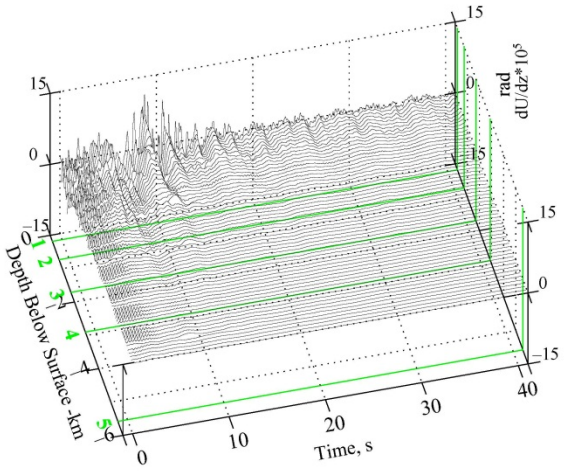

Figure V.11b Contributions of Body and Surface Waves to Total Synthetic Rotational Displacement

dW/dx **Body Waves** ***dW/dz***

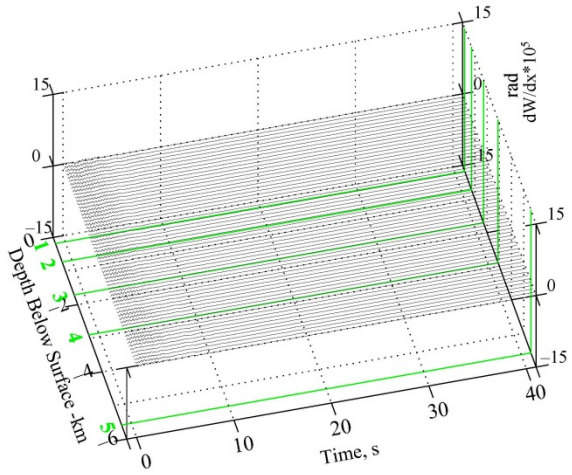

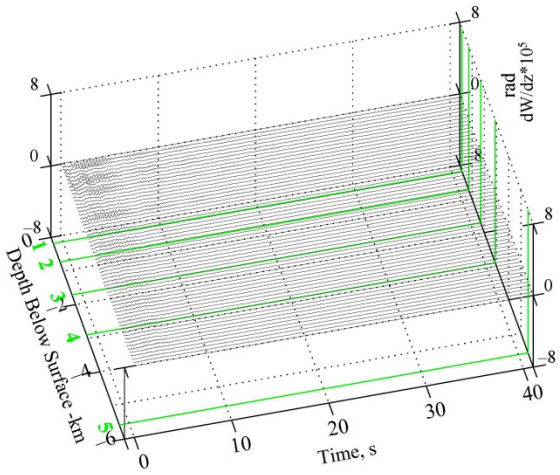

dW/dx **Surface Waves** ***dW/dz***

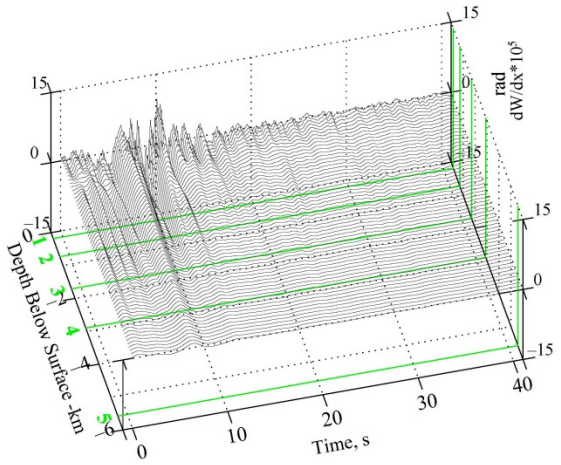

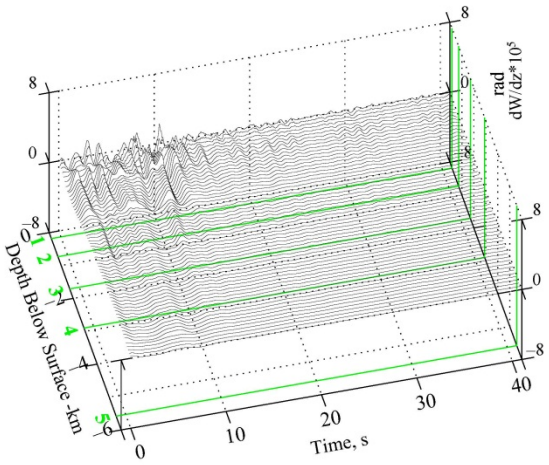

dW/dx **All (Body + Surface) Waves** ***dW/dz***

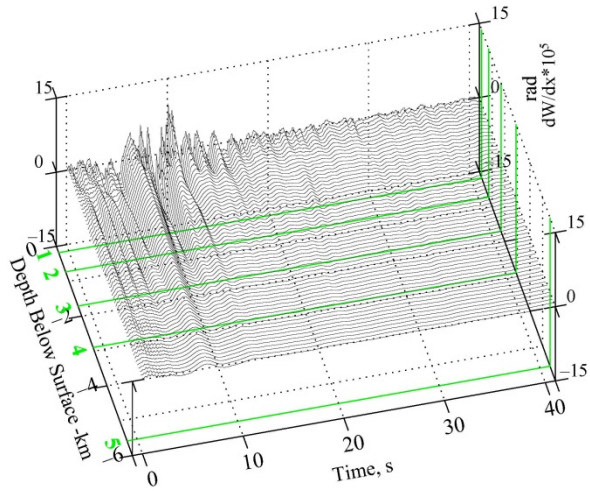

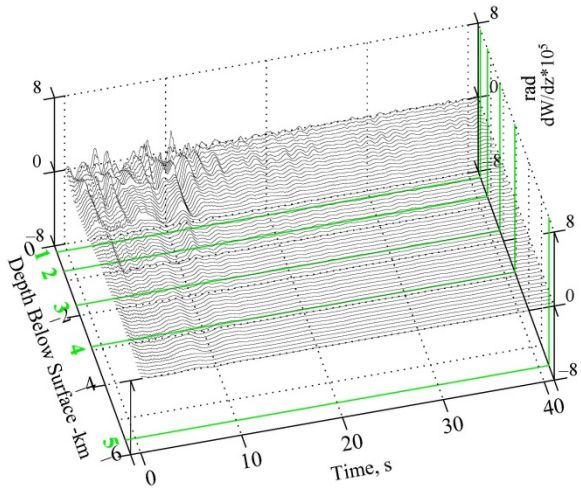

V.5 *Case Study 2:* $M = 6.5,\ R = 40.0km,\ H = 9.0km\ (D = 41.0km),\ s = 0,$ and $s_L = 2$

As in Chapter IV, We now consider an example of far field motion, for epicentral distance $R = 40.0km$ and an earthquake source at a focal depth of $H = 9.0km$. This corresponds to a hypocentral distance of $D = \left(R^2 + H^2\right)^{1/2} = \left(40.0^2 + 9.0^2\right)^{1/2} = 41\ \text{km}$.

Figure V.12a (same as Report 2, Fig. VIII.9a) shows a plot of the ray path taken by the (faster) P waves, from the earthquake source to the recording site. As before, the ray path is chosen so that the phase velocities at each layer of the 6-layered media are the same.

Figure V.12a (same as Report 2, Fig. VIII.9a) P Waves Ray Path from Source to Site

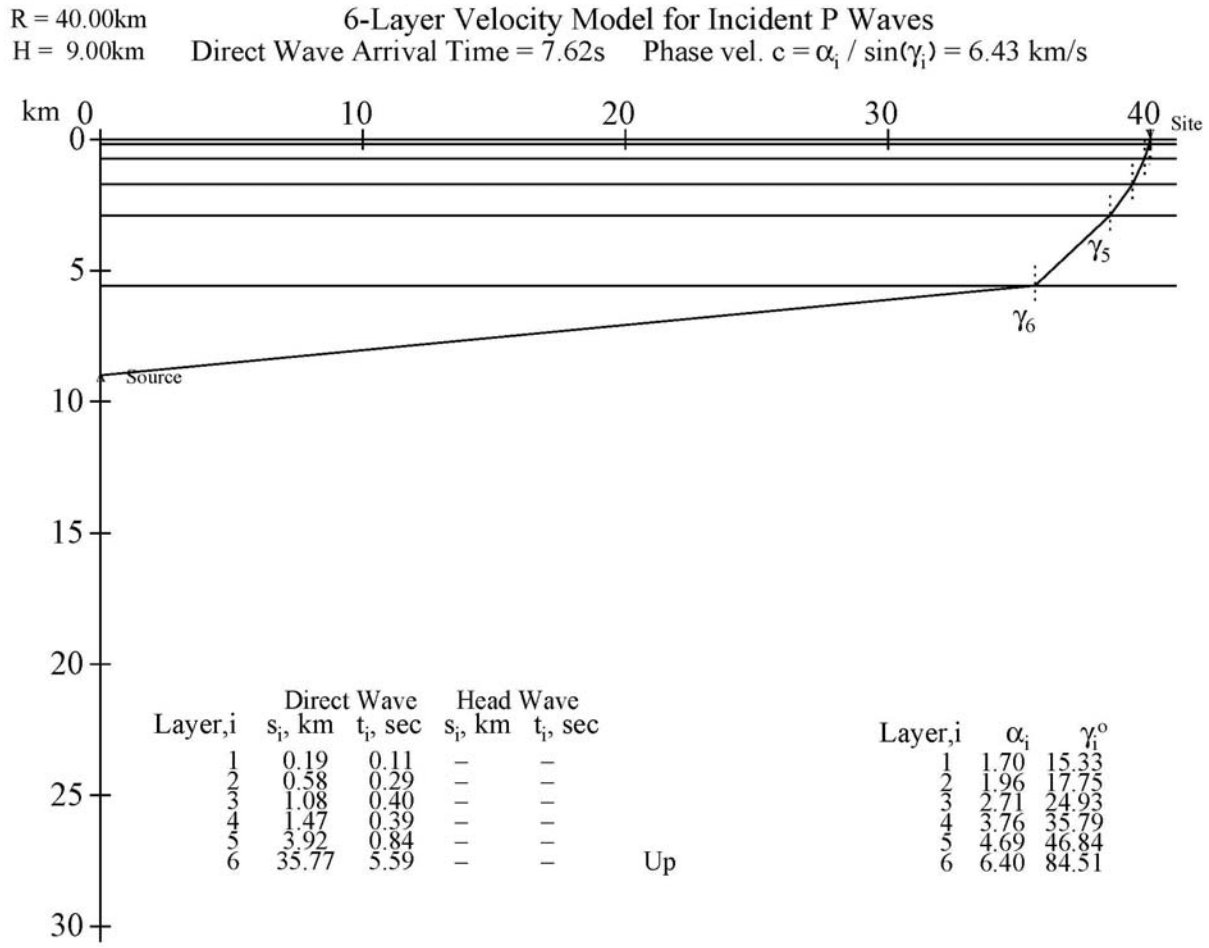

Layer,i	Direct Wave s_i, km	Direct Wave t_i, sec	Head Wave s_i, km	Head Wave t_i, sec
1	0.19	0.11	–	–
2	0.58	0.29	–	–
3	1.08	0.40	–	–
4	1.47	0.39	–	–
5	3.92	0.84	–	–
6	35.77	5.59	–	–

Layer,i	α_i	γ_i^o
1	1.70	15.33
2	1.96	17.75
3	2.71	24.93
4	3.76	35.79
5	4.69	46.84
6	6.40	84.51

The phase velocity at all layers is given by

$$c = \alpha_i \,/\sin(\gamma_i) = \textbf{ 6.43 km/s, a constant} \qquad \textbf{Report 2 (VIII.2)}$$

where α_i = P wave speed, and γ_i = angle the ray makes with respect to the vertical direction at the i^{th} layer. The ray will start at an angle $\gamma_6 \sim \mathbf{84.5}^o$ with respect to vertical direction, and progress up the layered media arriving at the site with $\gamma_1 \sim \mathbf{15.3}^o$. The phase velocity at all layers is the same.

Figure V.12b (same as Report 2, Fig. VIII.9b) shows the ray path taken by the (slower) SV waves from the earthquake source to the recording site.

Figure V.12b (same as Report 2, Fig. VIII.9b) Ray Path of SV Waves from Source to Site

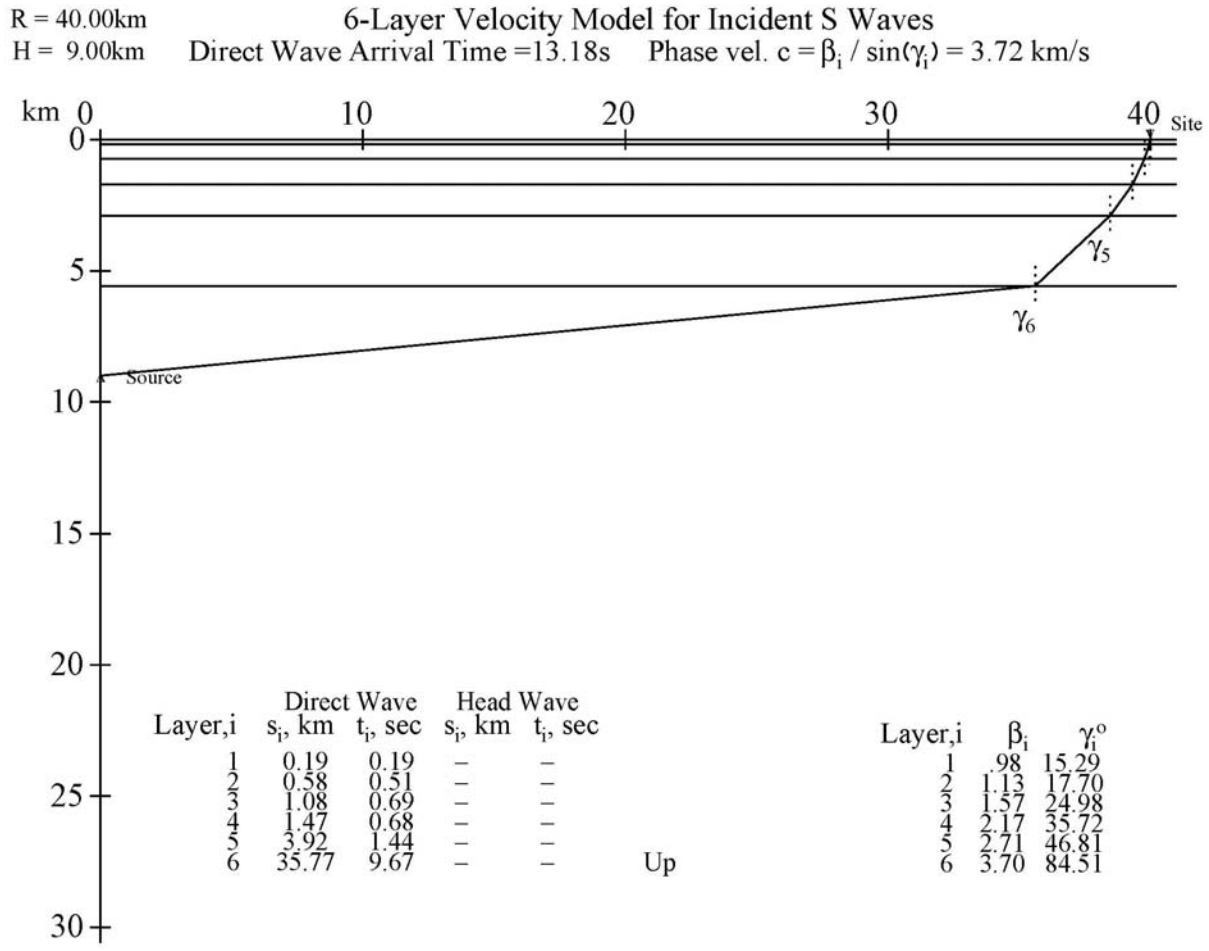

Layer,i	Direct Wave s_i, km	Direct Wave t_i, sec	Head Wave s_i, km	Head Wave t_i, sec
1	0.19	0.19	–	–
2	0.58	0.51	–	–
3	1.08	0.69	–	–
4	1.47	0.68	–	–
5	3.92	1.44	–	–
6	35.77	9.67	–	–

Layer,i	β_i	γ_i^o
1	.98	15.29
2	1.13	17.70
3	1.57	24.98
4	2.17	35.72
5	2.71	46.81
6	3.70	84.51

This results in the ray starting with an angle $\gamma_6 \sim \mathbf{84.5}^o$ with respect to vertical, and progressing up the layered media and arriving at the site with $\gamma_1 \sim \mathbf{15.3}^o$. These are practically the same angles as for the incident P-waves, even though the phase velocity is slower: $\boldsymbol{c = 3.72 km / s}$.

As in Chapter IV, we note that in many recordings, the surface waves do arrive sooner than what would be expected from the calculation of arrival times using actual hypocentral distance between source and site. This can be attributed to the fact that significant portion of surface and body waves can be generated at the edge of an alluvial valley which is closer to the site than the source. **SYNACCS** accounts for this by allowing two hypocentral distances to be selected (see Chapter IV, Section IV.5). The first hypocentral distance is the distance from the earthquake source to the site, and the second "hypocentral distance" is the smaller distance from some (closer) edge of valley to the site. The first hypocentral distance will still be used as one of the scaling parameters in the regression equation used to estimate the Fourier amplitudes of the waves at the site. The second hypocentral distance will be used to estimate the arrival times of the modes of surface waves at each frequency.

For ***Case Study 2*** here, the first hypocentral distance is now $\boldsymbol{D = D_1 = 41\ km}$, and the second (smaller) hypocentral distance is again assumed to be $\boldsymbol{D = D_2 = 25\ km}$. The body ***P, SV*** waves are assumed to be incident from the bottom layer at an angle of 84^o with respect to the vertical direction. Those will become almost vertical by the time they get to the site, at the surface.

As in **Figures V.3a, b** for ***Case Study 1*****, Figure V.13a** gives ***2D*** plots of the synthetic $\partial\ddot{U}/\partial x$, $\partial\ddot{U}/\partial z$ rotational acceleration time histories derived from the horizontal $\boldsymbol{U(z)e^{i(kx+\omega t)}}$ motions, calculated for the El Centro six-layered site model, at 120 depths equally spaced from the surface to almost 6km below the surface. The updated **SYNACCS** computer program again determines that the appropriate duration of the accelerogram record should be just about 40 seconds. Similarly **Figure V.13b** gives the corresponding plots of the synthetic $\partial\ddot{W}/\partial x$, $\partial\ddot{W}/\partial z$

rotational acceleration time histories derived from the corresponding vertical $W(z)e^{i(kx+\omega t)}$ motions.

Both figures show that the ***P*** and ***SV*** body waves, which are present in the first 10 seconds of the record, are small when compared with the surface Rayleigh waves portion of the record, which are dominant between 10 seconds to 30 seconds of the record. Further, the motions are only significant in the first layer of the media, up to ***0.18km*** below the surface, and may be still noticeable in the 2nd layer, down to about **0.70km** from the surface. Below that the rotational motions are smaller. The plots show that the $\partial\ddot{U}/\partial x$ and $\partial\ddot{U}/\partial z$ are comparable, but that the $\partial\ddot{W}/\partial x$ motions are slightly more significant than $\partial\ddot{W}/\partial z$.

Figures V.14a, b show the corresponding synthetic $\partial\dot{U}/\partial x$, $\partial\dot{U}/\partial z$ and $\partial\dot{W}/\partial x$, $\partial\dot{W}/\partial z$ ***2D*** rotational velocity time-histories. The plots show that the $\partial\dot{U}/\partial x$ and $\partial\dot{U}/\partial z$ are comparable, but that the $\partial\dot{W}/\partial x$ motions are again slightly more significant than $\partial\dot{W}/\partial z$, as for the acceleration rotations.

Figures V.15a, b show the corresponding synthetic $\partial U/\partial x$, $\partial U/\partial z$ and $\partial W/\partial x$, $\partial W/\partial z$ ***2D*** rotational displacement time-histories. They show similar trends as the corresponding rotational velocity and acceleration motions.

Figure V.13a	$\partial\ddot{U}/\partial x$ Synthetic Acc.: $M = 6.5,\ R = 40.0km,\ H = 9.0km,\ s = 0,$ and $s_L = 2$ $\partial\ddot{U}/\partial z$	

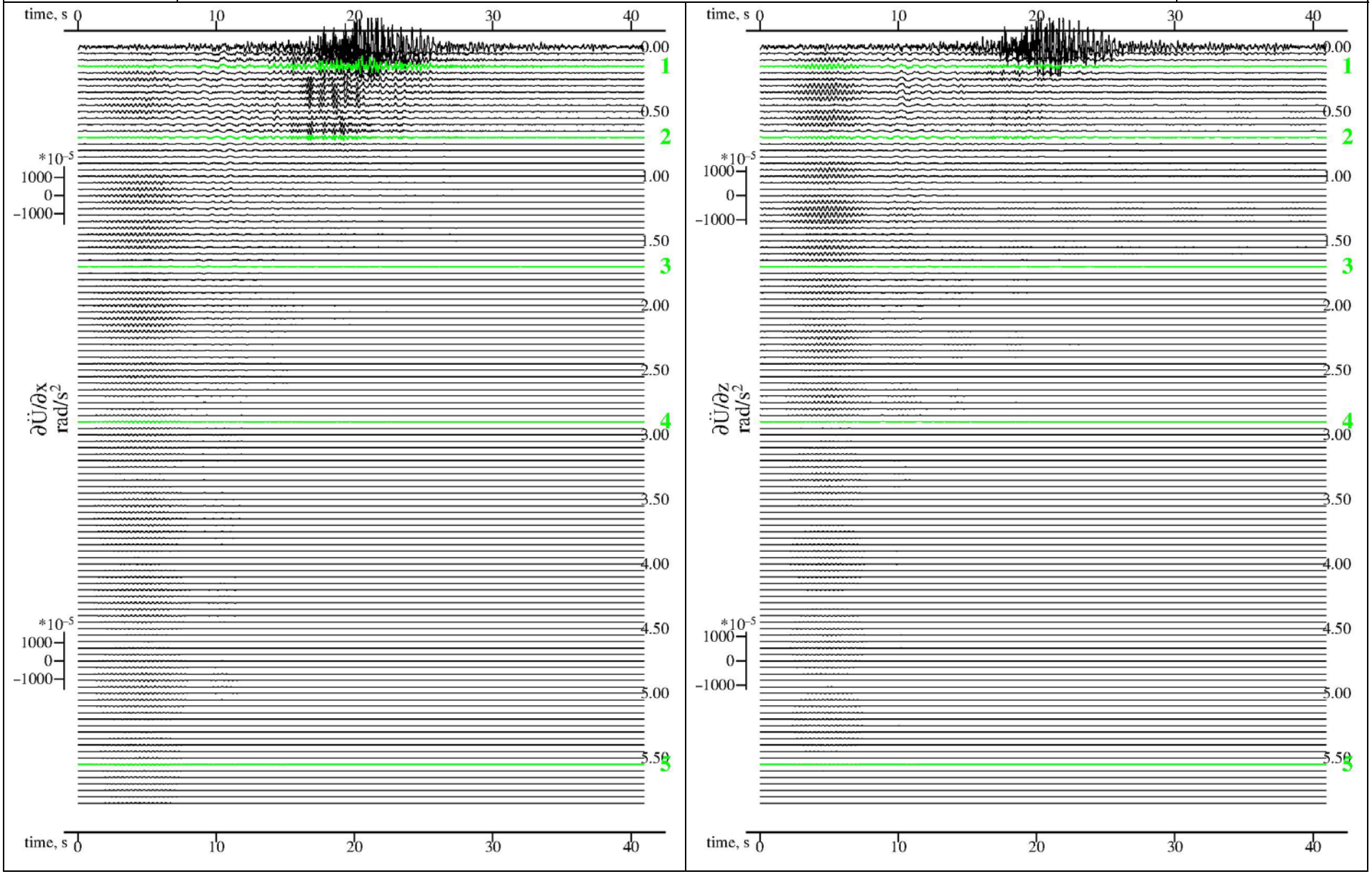

Figure V.13b	$\partial\ddot{W}/\partial x$ Synthetic Acc.: $M = 6.5,\ R = 40.0km,\ H = 9.0km,\ s = 0,$ and $s_L = 2$ $\partial\ddot{W}/\partial z$	

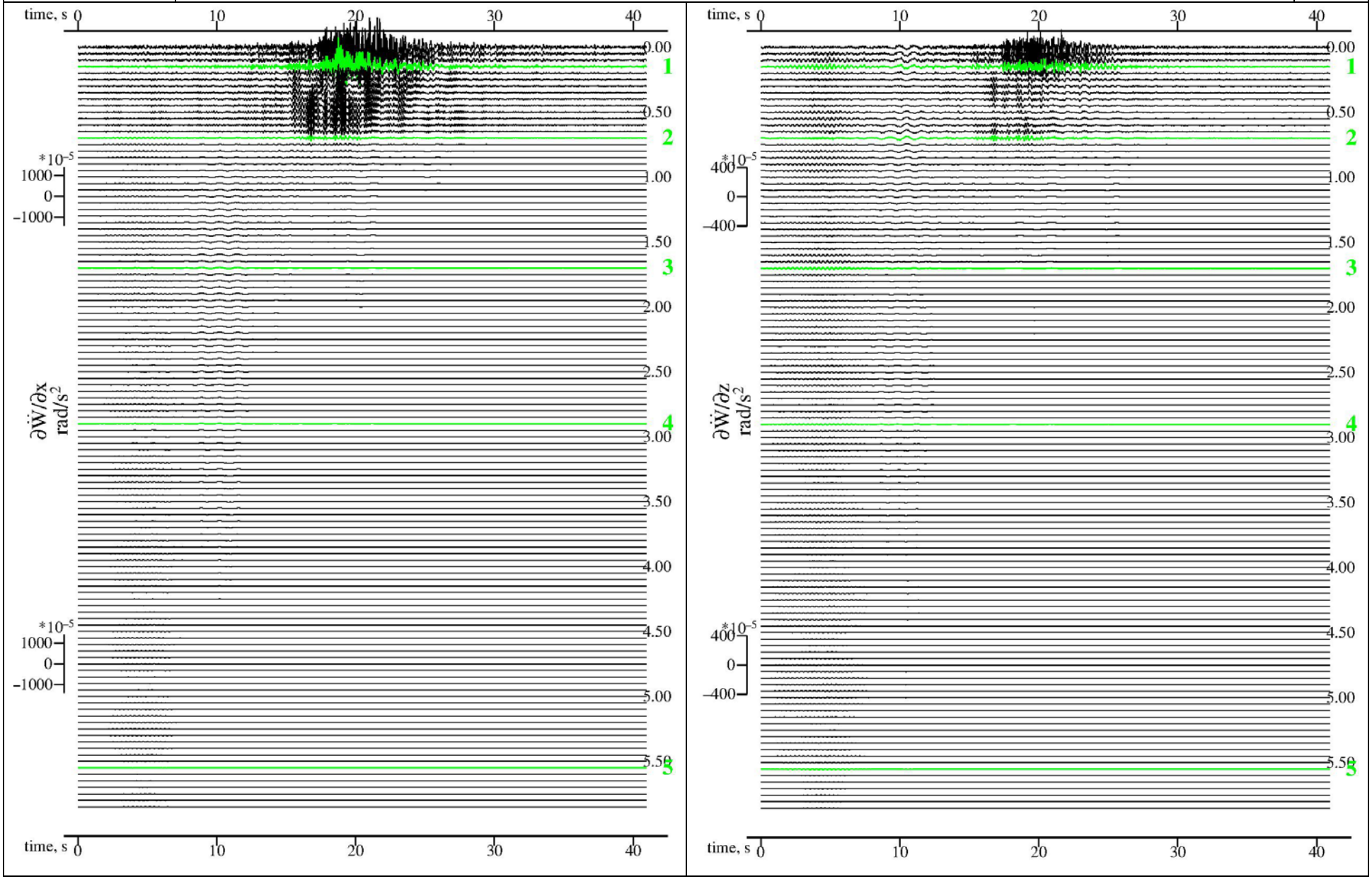

Figure V.14a $\partial\dot{U}/\partial x$ **Synthetic Velocity:** $M = 6.5,\ R = 40.0km,\ H = 9.0km,\ s = 0,$ **and** $s_L = 2$ $\partial\dot{U}/\partial z$

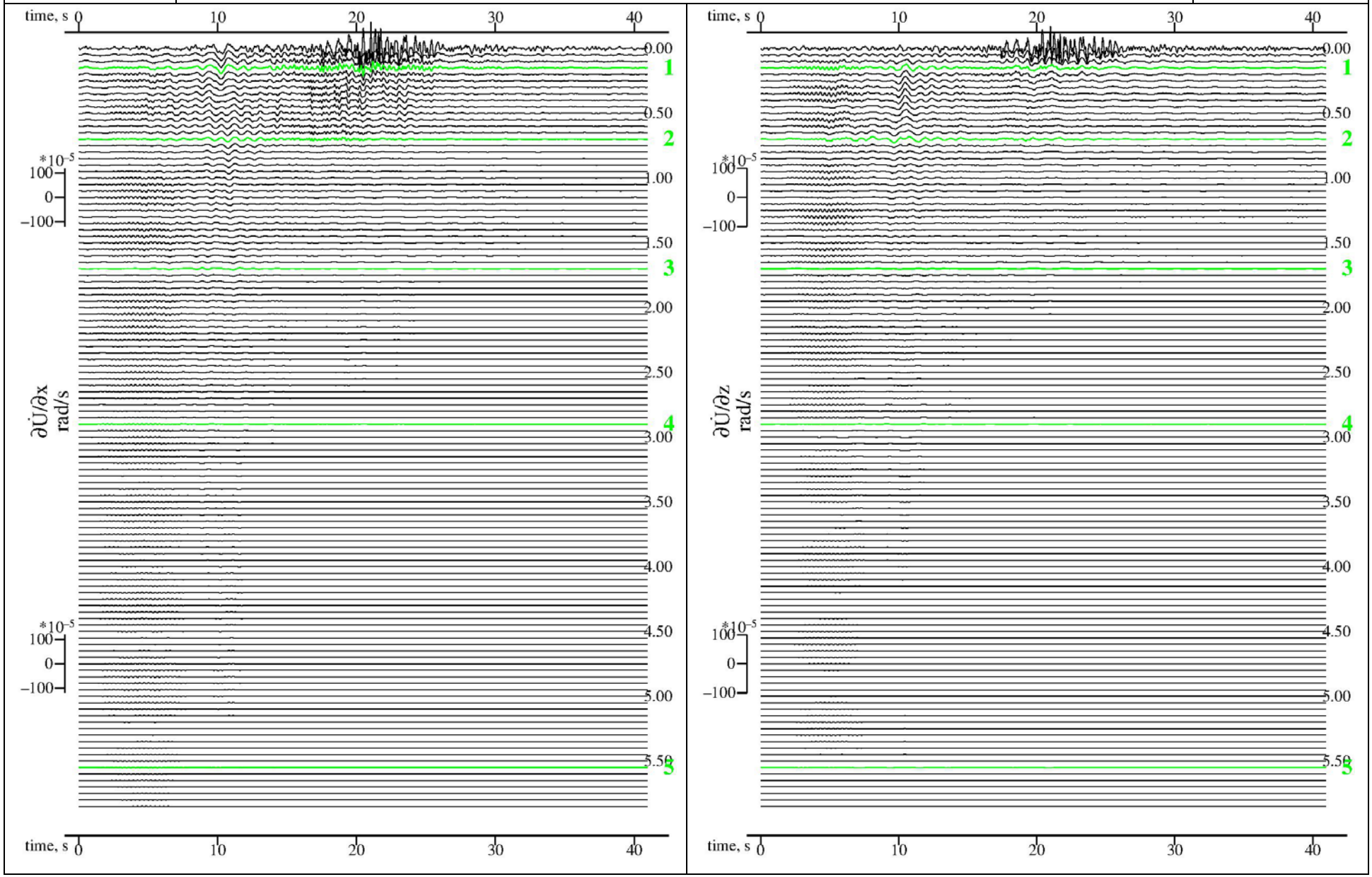

Figure V.14b $\partial\dot{W}/\partial x$ **Synthetic Velocity:** $M = 6.5,\ R = 40.0km,\ H = 9.0km,\ s = 0,$ **and** $s_L = 2$ $\partial\dot{W}/\partial z$

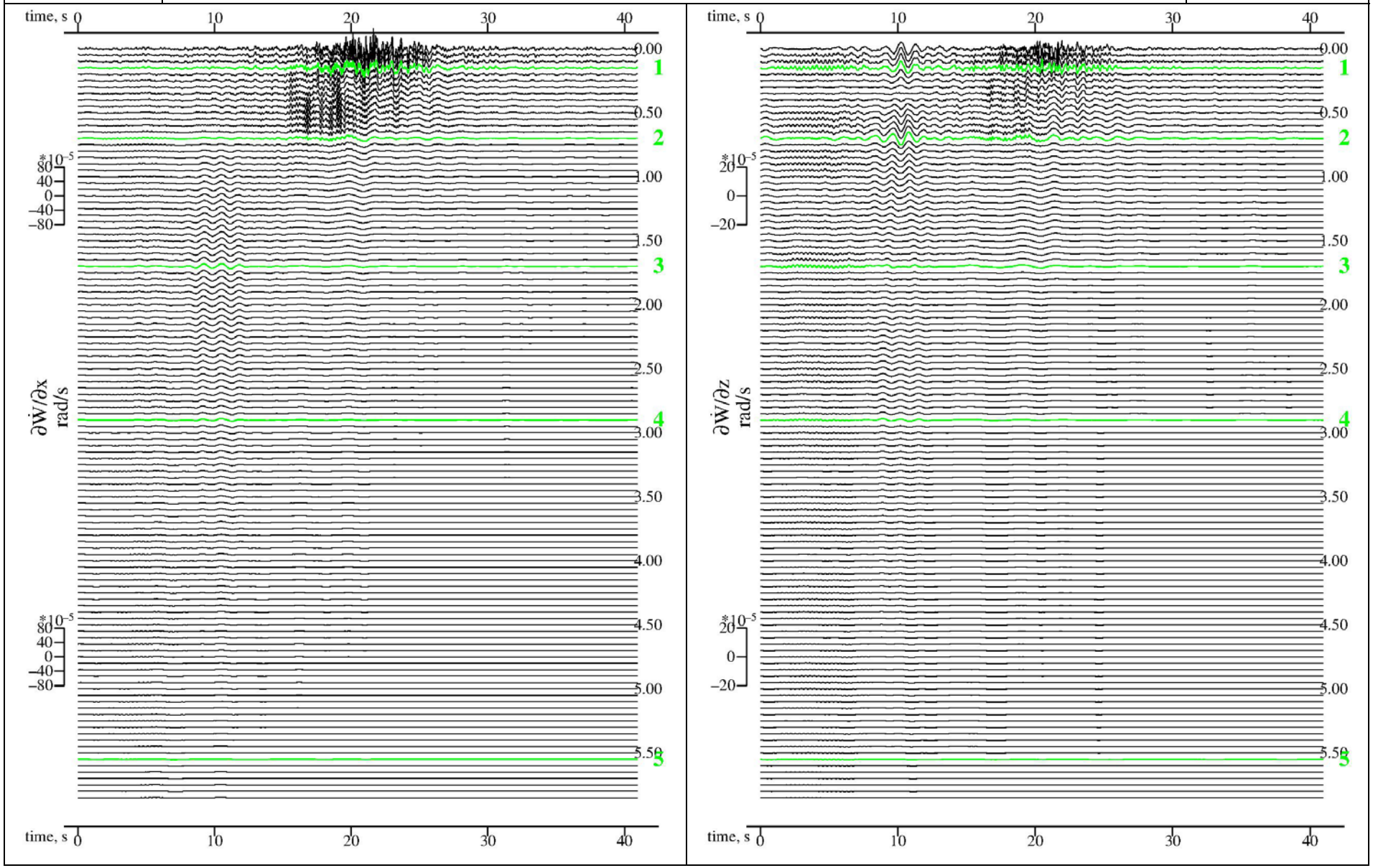

Figure V.15a	$\partial U/\partial x$	Synthetic Displacement: $M = 6.5$, $R = 40.0km$, $H = 9.0km$, $s = 0$, and $s_L = 2$	$\partial U/\partial z$	

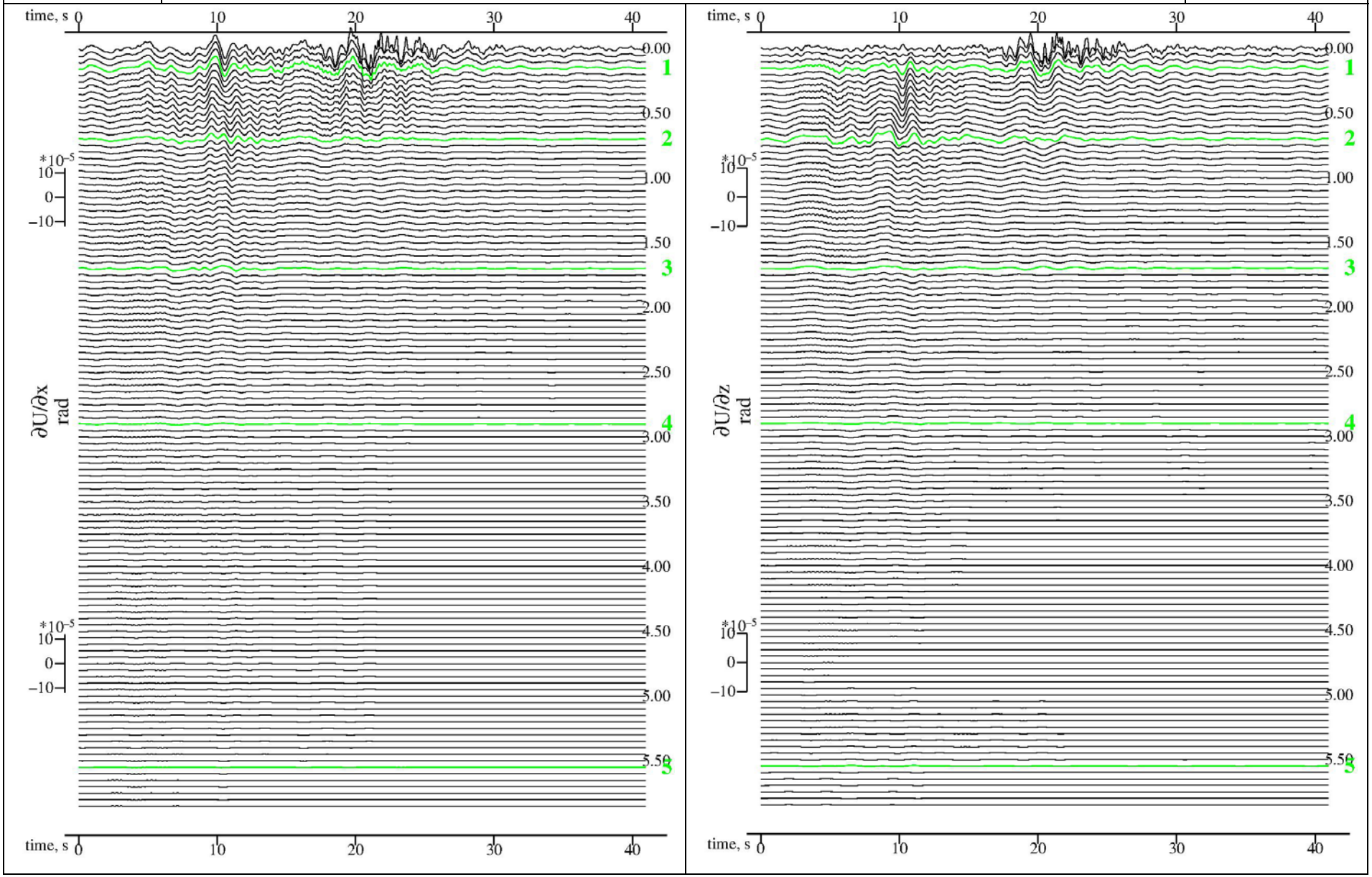

Figure V.15b	$\partial W/\partial x$	Synthetic Displacement: $M = 6.5$, $R = 40.0km$, $H = 9.0km$, $s = 0$, and $s_L = 2$	$\partial W/\partial z$	

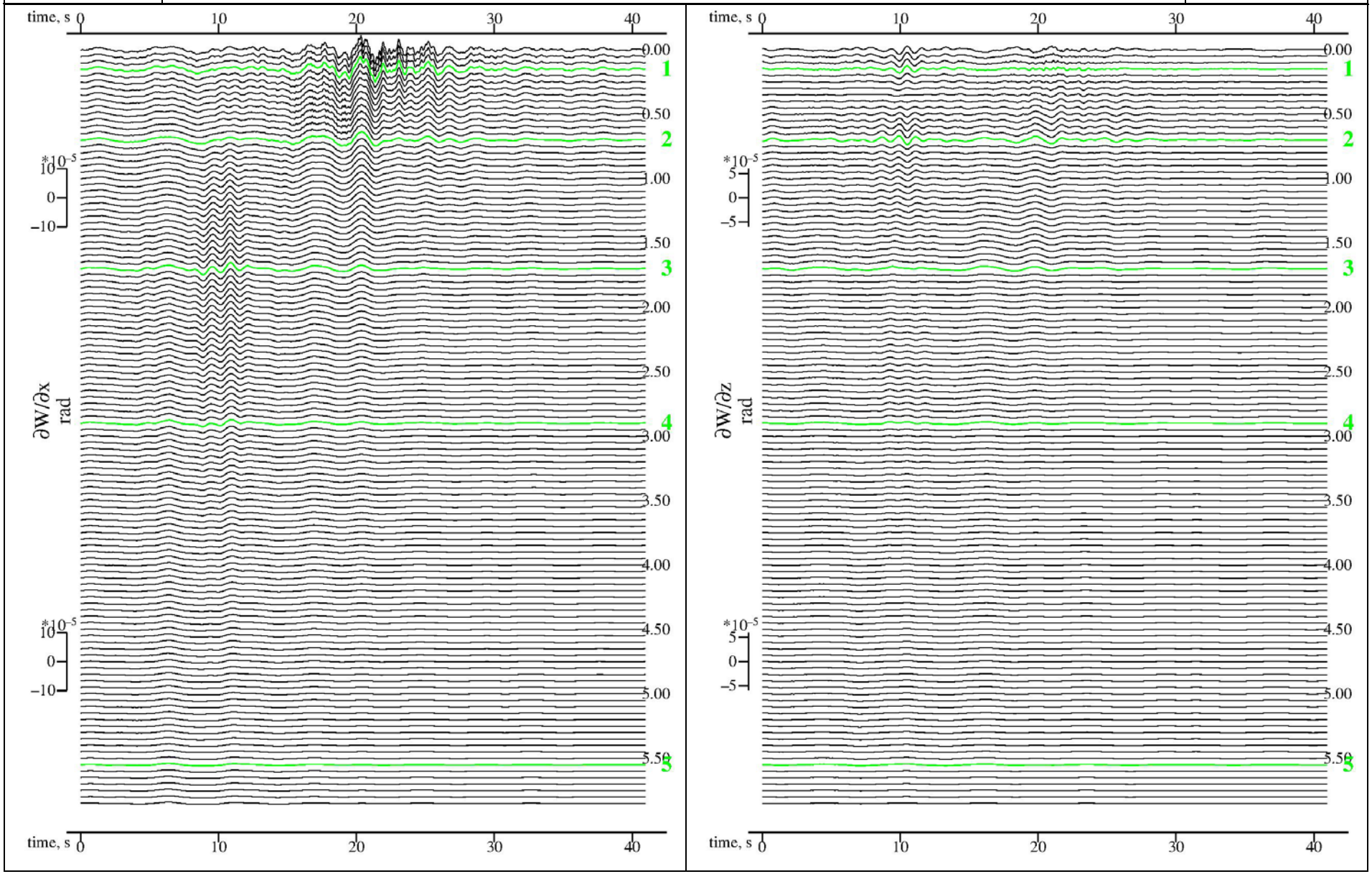

Figures V.16a, b, as in the previous sections, are the ***3D*** plots of the rotational acceleration motions, $\partial\ddot{U}/\partial x$, $\partial\ddot{U}/\partial z$ and $\partial\ddot{W}/\partial x$, $\partial\ddot{W}/\partial z$ corresponding to the ***2D*** rotational plots in **Figures V.13a, b**. Those are included here for completeness.

Figures V.17a, b, show the ***3D*** plots of the rotational velocity motions, $\partial\dot{U}/\partial x$, $\partial\dot{U}/\partial z$ and $\partial\dot{W}/\partial x$, $\partial\dot{W}/\partial z$ corresponding to the ***2D*** rotational plots in **Figures V.14a, b**. Finally, **Figures V.18a, b** show the ***3D*** plots of the rotational displacement motions, $\partial U/\partial x$, $\partial U/\partial z$ and $\partial W/\partial x$, $\partial W/\partial z$ which correspond to the ***2D*** rotational plots in **Figures V.15a, b**.

V.6 The Curvatures for Radial and Vertical Motions

Recall from Equations (2.9) and (2.11), in Chapter 2, where the curvature in the radial and vertical directions were defined as

Radial Curvature:
$$K_1(t) \approx \partial^2 U/\partial x^2 = \frac{\ddot{U}}{c^2} \qquad \textbf{(2.9)}$$

And

Vertical Curvature:
$$K_3(t) = \frac{\partial^2 W/\partial x^2}{\left[1+\left(\partial W/\partial x\right)^2\right]^{3/2}} \approx \partial^2 W/\partial x^2 = \frac{\ddot{W}}{c^2} \qquad \textbf{(2 .11)}$$

computed directly from the translational components, together with the rotational motions. In fact, those each correspond to the ***2nd derivative of the radial and vertical translational motions*** with respect to ***x*** in the radial direction.

Figures IV.19 and 20 show the radial and vertical curvatures at depths below the surface computed for the ***Case Study 1.***

Figure V.16a	$\partial\ddot{U}/\partial x$ **Synthetic Acc.: $M = 6.5$, $R = 40.0km$, $H = 9.0km$, $s = 0$, and $s_L = 2$** $\partial\ddot{U}/\partial z$	

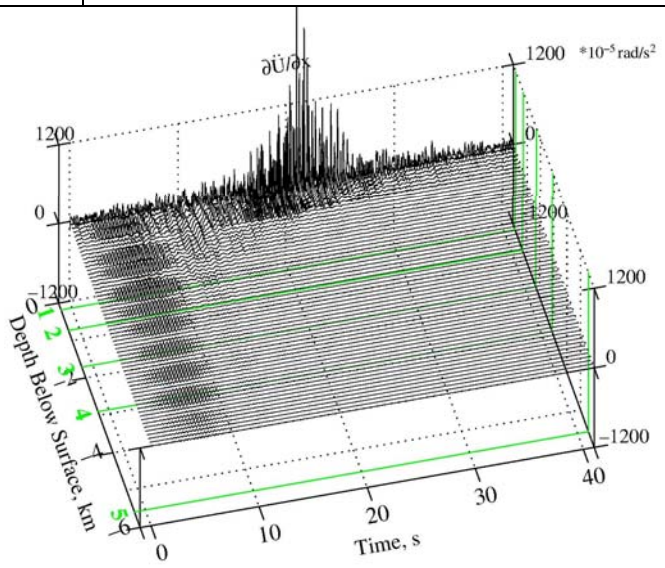

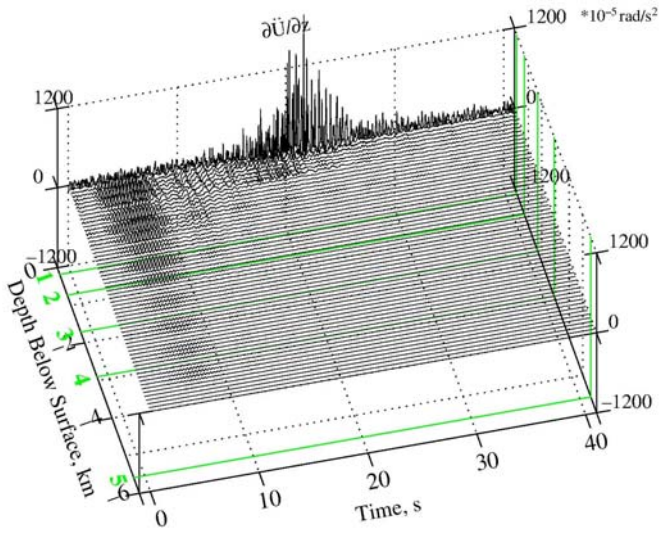

Figure V.16b	$\partial\ddot{W}/\partial x$ **Synthetic Acc.: $M = 6.5$, $R = 40.0km$, $H = 9.0km$, $s = 0$, and $s_L = 2$** $\partial\ddot{W}/\partial z$	

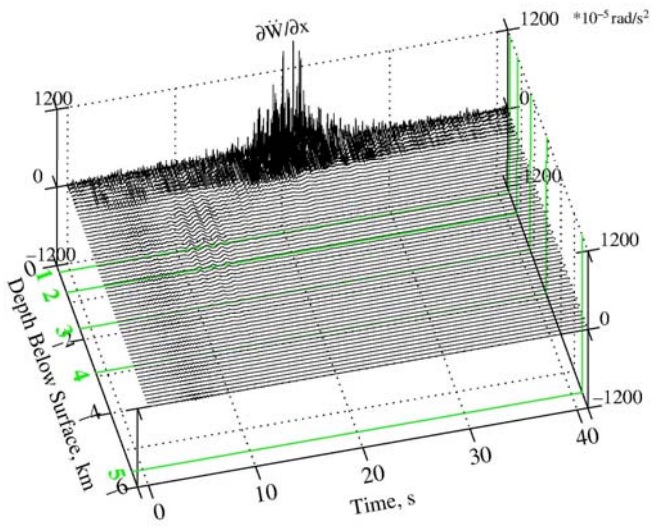

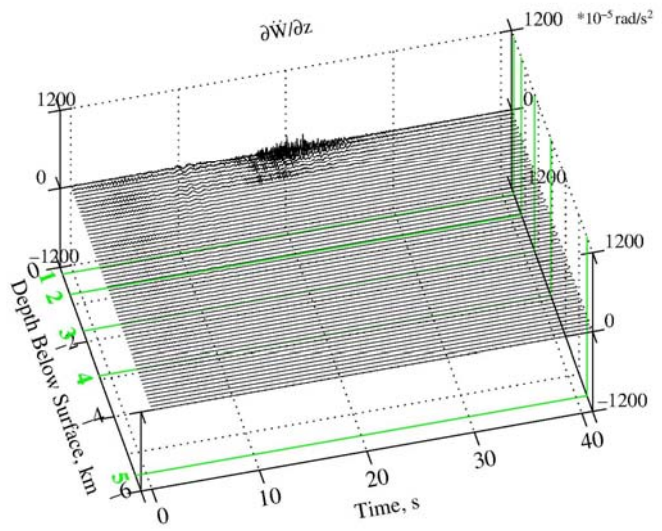

Figure V.17a $\partial\dot{U}/\partial x$ **Synthetic Velocity:** $M = 6.5,\ R = 40.0km,\ H = 9.0km,\ s = 0,$ **and** $s_L = 2$ $\partial\dot{U}/\partial z$

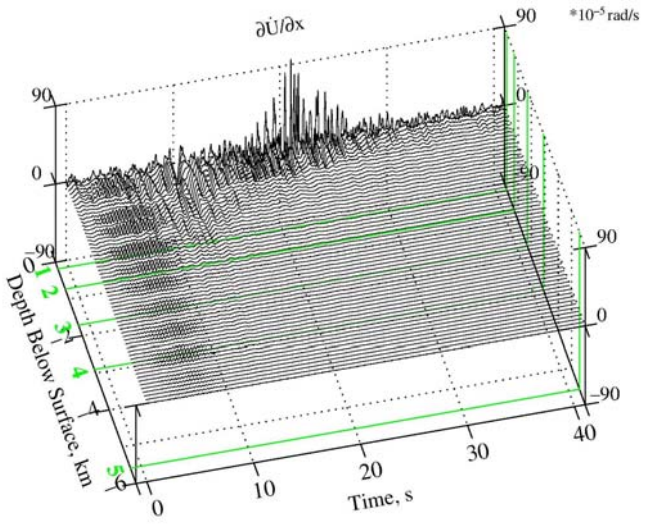

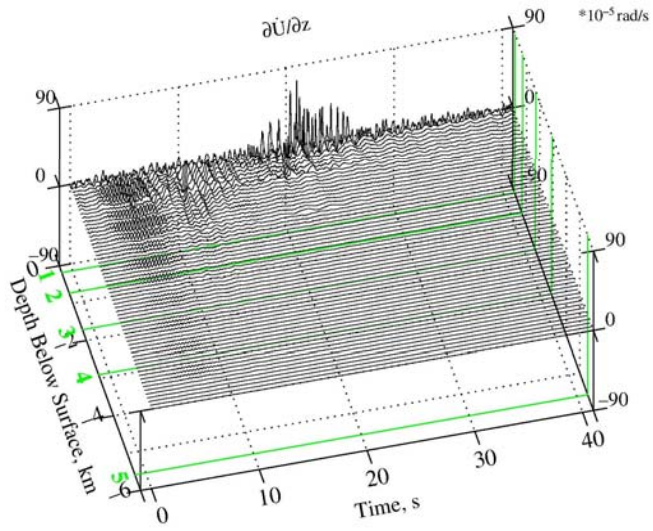

Figure V.17b $\partial\dot{W}/\partial x$ **Synthetic Velocity:** $M = 6.5,\ R = 40.0km,\ H = 9.0km,\ s = 0,$ **and** $s_L = 2$ $\partial\dot{W}/\partial z$

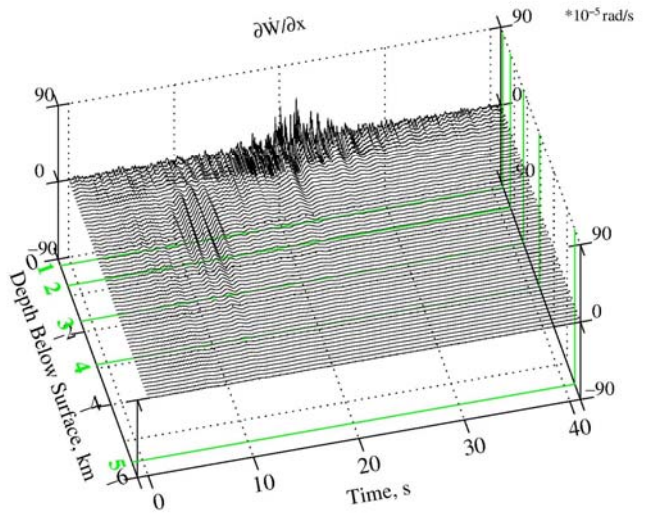

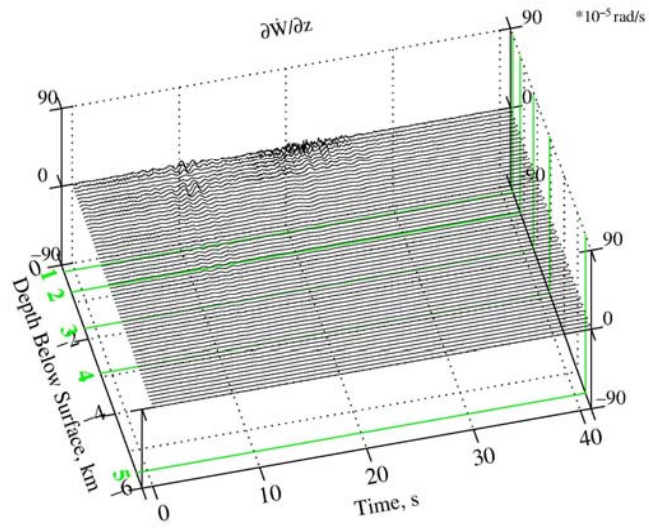

Figure V.18a $\partial U/\partial x$ **Synthetic Displacement:** $M = 6.5,\ R = 40.0km,\ H = 9.0km,\ s = 0,$ **and** $s_L = 2$ $\partial U/\partial z$

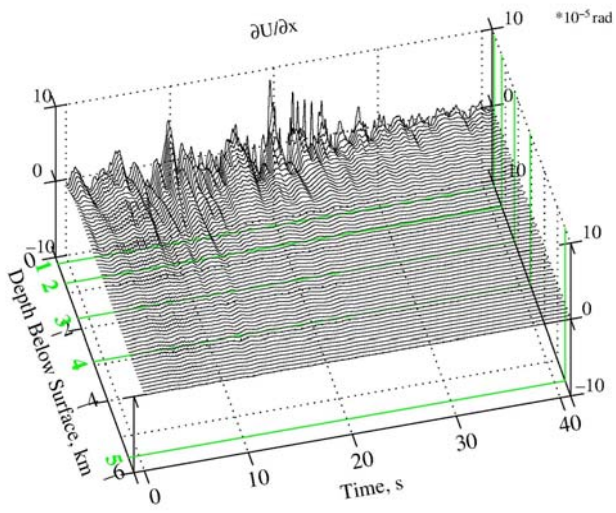

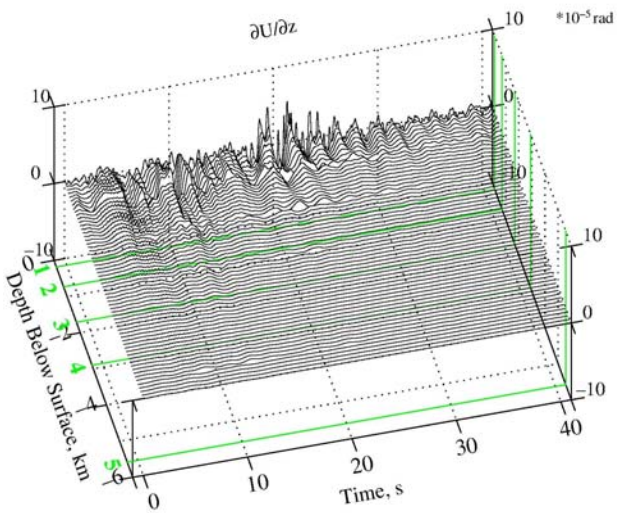

Figure V.18b $\partial W/\partial x$ **Synthetic Displacement:** $M = 6.5,\ R = 40.0km,\ H = 9.0km,\ s = 0,$ **and** $s_L = 2$ $\partial W/\partial z$

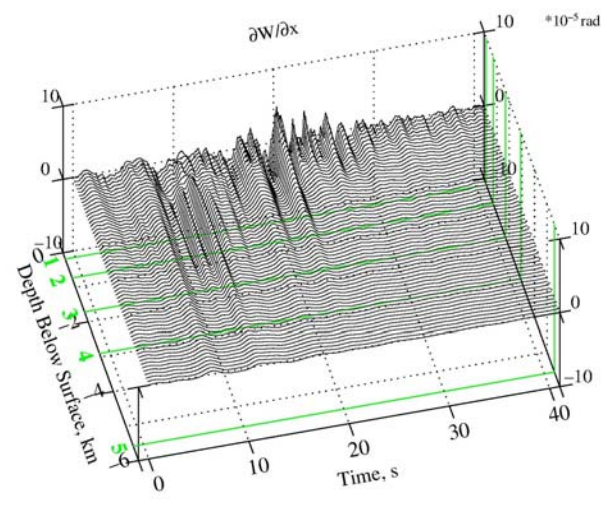

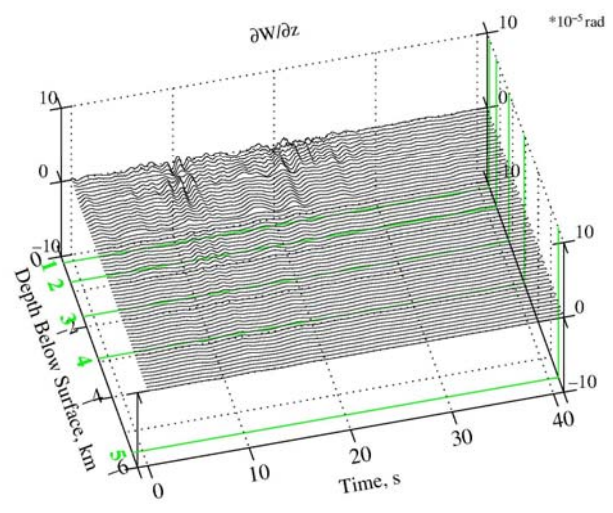

Figures IV.21 and 22 show the radial and vertical curvatures at depths below the surface computed for the ***Case Study 2.***

Note that, as for the transverse curvatures in Chapter IV, the 2nd derivative of the translational motions corresponds to the curvature motions. As before, since the translational motions are in units of ***cm*** and the distances are measured in ***km***, they have the units of $\boldsymbol{cm/km^2}$, or $\boldsymbol{cm/10^{10}cm^2}$ or $\boldsymbol{10^{-10}\,rad/cm}$.

For ***Case Study 1***, at a near-field site ($\boldsymbol{D = 10km}$), **Figures IV.19 and 20** show that both curvatures are of the order of $\boldsymbol{20\times10^{-9}\,rad/cm}$, with the radial curvature higher than the vertical curvature. The motions are again large only on the top layer of the media, or down to about **0.18km**. The strong motions occur around the 10-seconds mark of the record.

For ***Case Study 2***, at a far-field site ($\boldsymbol{D = 41km}$), **Figures IV.21 and 22** show that the curvatures are smaller. Being further away from the earthquake source, the radial curvature is of the order less than $\boldsymbol{10\times10^{-9}\,rad/cm}$, and smaller for the vertical curvatures. Also, the curvatures are significant only on the top layer of the media, or down to about **0.18km**. The strong motions occur around and beyond the 20-seconds mark of the record.

Figure V.19 **Synthetic Radial Curvature at $M = 6.5$, $R = 8.0km$ & $H = 6.0km$, $s = 0$, $s_L = 2$**

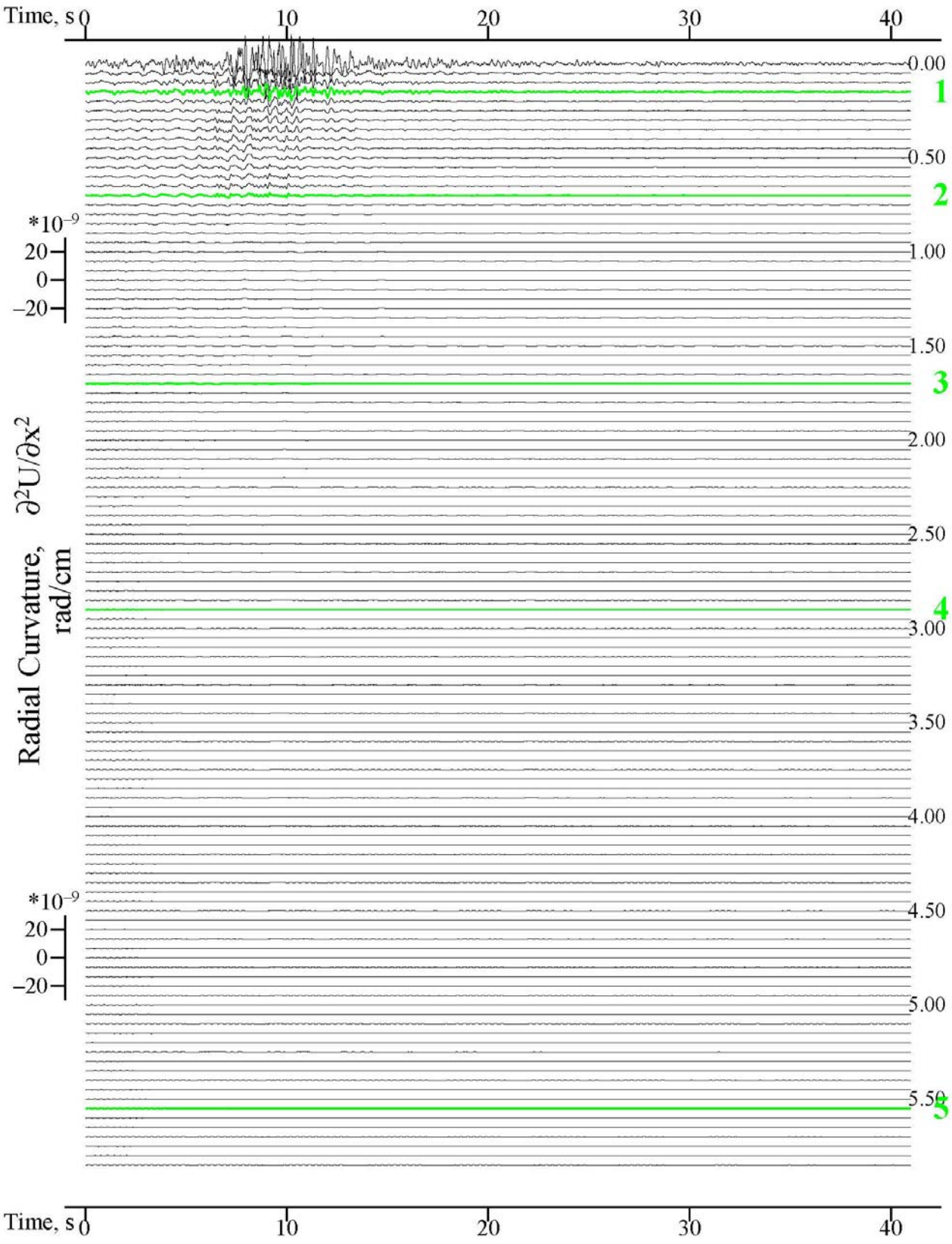

Figure V.20 Synthetic Vertical Curvature at $M = 6.5$, $R = 8.0km$ & $H = 6.0km$, $s = 0$, $s_L = 2$

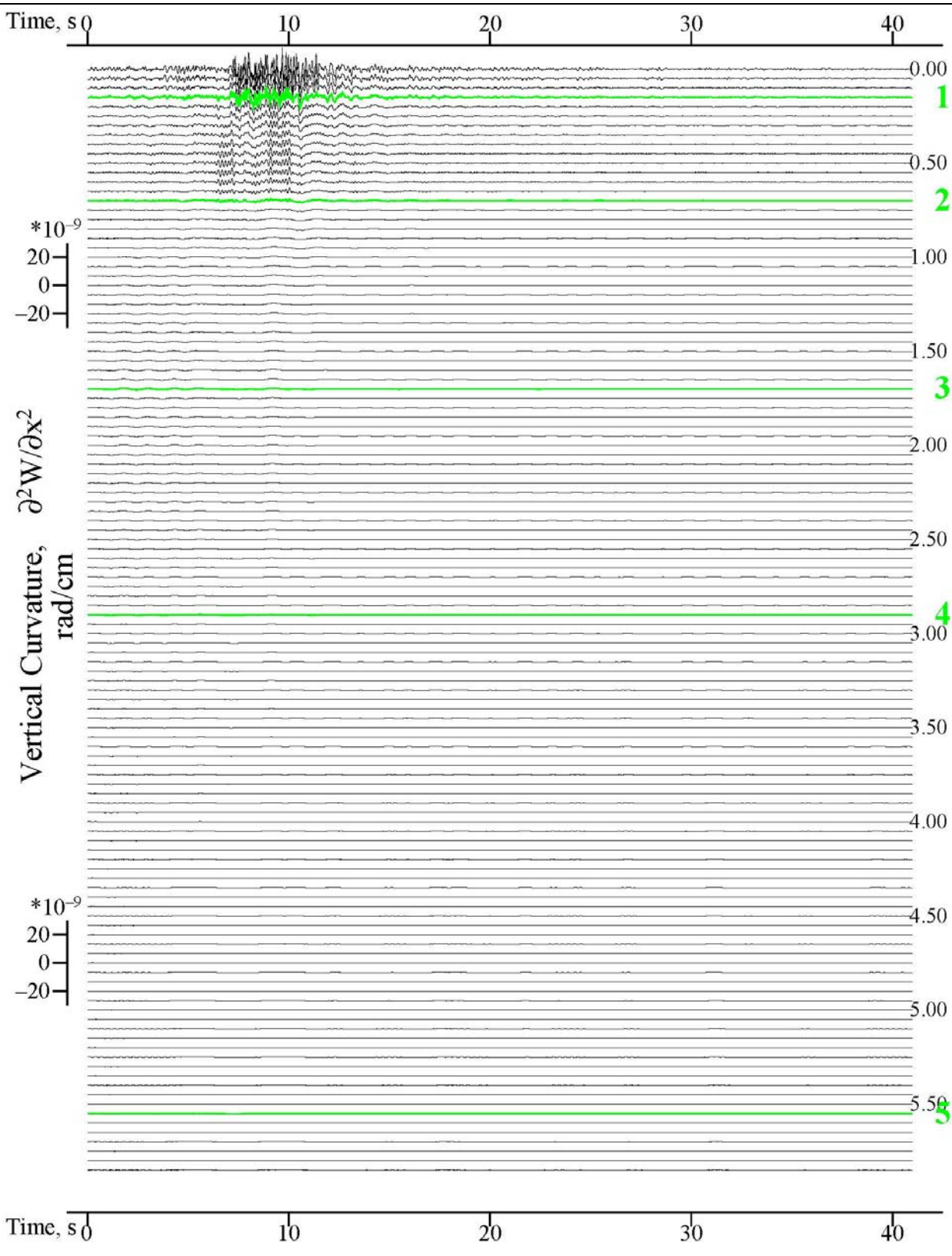

Figure V.21 Synthetic Radial Curvature: $M = 6.5$, $R = 40.0km$, $H = 9.0km$, $s = 0$, and $s_L = 2$

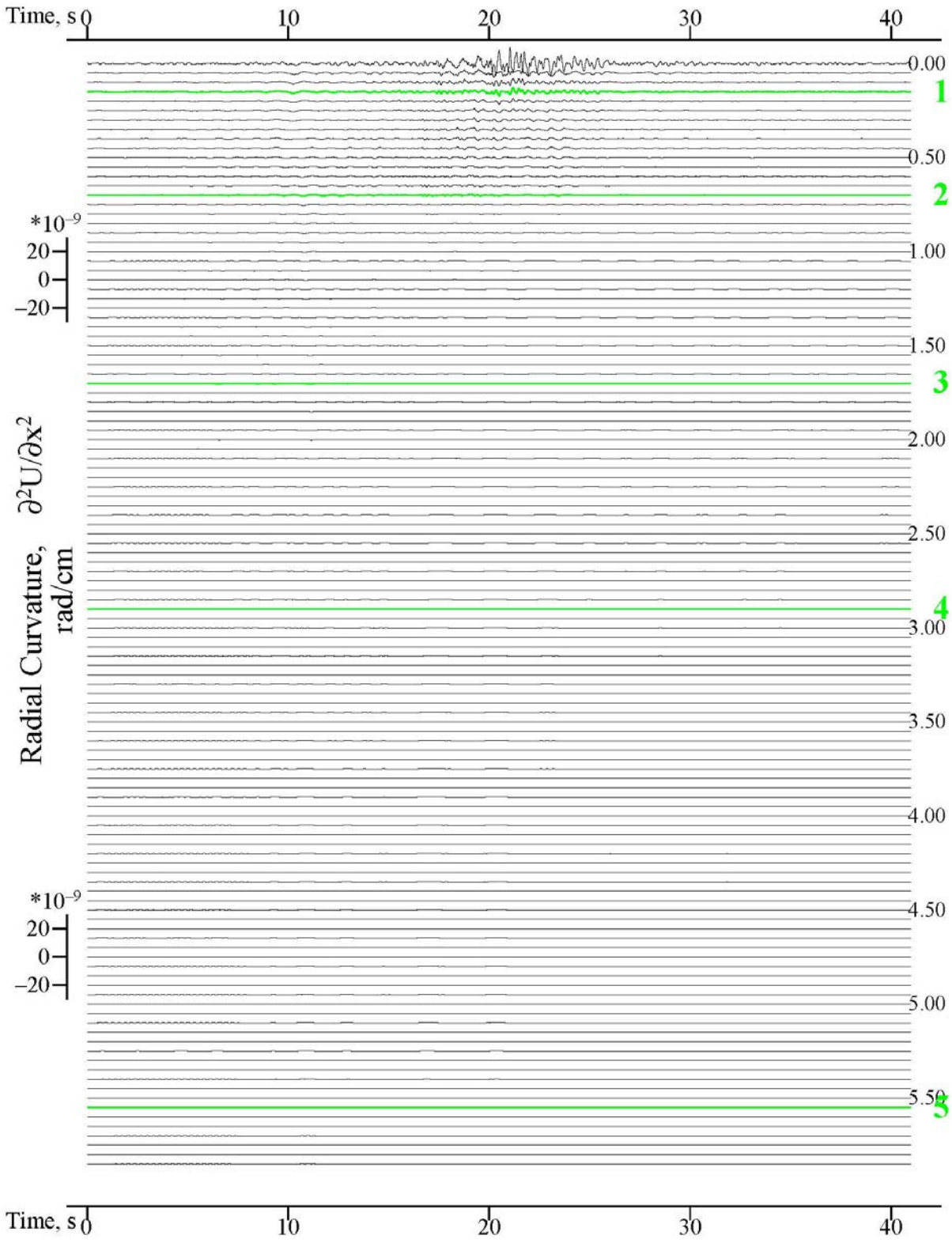

Figure V.22 Synthetic Vertical Curvature: $M = 6.5$, $R = 40.0km$, $H = 9.0km$, $s = 0$, and $s_L = 2$

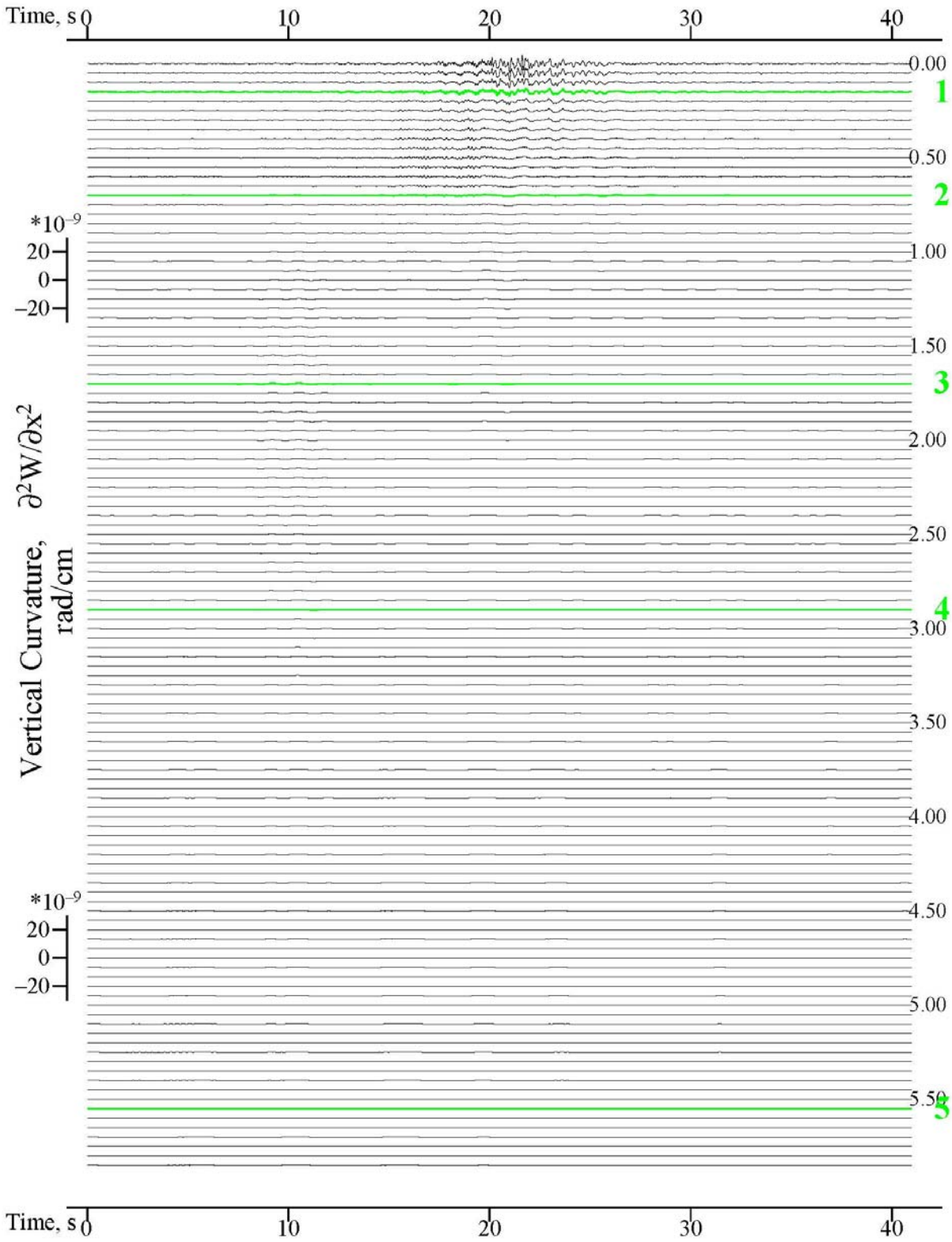

Summary – Engineering Applications

In this report we have described theory and numerical examples which use ***SYNACCS*** computer program, which for a given site and at a given epicentral distance from an earthquake, with given magnitude or seismic intensity, with known local site geology and soil characterization, can compute the in-plane *x*-, *z*- and out-of-plane *y*- components of translational strong motions, together with the d/dx and d/dz derivatives of those translational motions at any point (x, z) on the surface or below the surface.

For engineering applications, besides the translational $(\boldsymbol{U,V,W})$ motions and their $\boldsymbol{d/dx}$ and $\boldsymbol{d/dz}$ derivatives, one also needs to know the "rotations" (torsion, rocking, normal and shear strain and curvature components) of those motions. In the following is a summary of how these "rotations", as described in the above chapters, can be computed from the derivatives of translational motions:

Chapter IV:

Torsion: $\Omega_z = \frac{1}{2}\partial V/\partial x$

(Out-of-plane) Rocking: $\Omega_x = -\frac{1}{2}\partial V/\partial z$

and their corresponding 1st and 2nd time derivatives (see Equations (2.2), (2.3) & (2.4)).

Chapter V:

(In-plane) Rocking: $\Omega_y = \frac{1}{2}\left(\partial U/\partial z - \partial W/\partial x\right)$

and their corresponding 1st and 2nd time derivatives (see Equations (2.2), (2.3) & (2.4)).

Note that the out-of-plane normal strain $\varepsilon_y = \partial V/\partial y = 0$, as indicated in Equation (2.2).

The corresponding Strain components of motions are:

Chapter IV:

(Out-of-plane) Shear Strain: $\varepsilon_{xy} = \frac{1}{2}\partial V / \partial x$

$\varepsilon_{yz} = \frac{1}{2}\partial V / \partial z$

and their corresponding 1st and 2nd time derivatives (see Equations (2.6), (2.7) & (2.8)).

Chapter V:

(In-plane) Normal Strain: $\varepsilon_x = \partial U / \partial x$

$\varepsilon_z = \partial W / \partial z$

(In-plane) Shear Strain: $\varepsilon_{xz} = \frac{1}{2}\left(\partial U / \partial z + \partial W / \partial x\right)$

and their corresponding 1st and 2nd time derivatives (also see Equations (2.6), (2.7) & (2.8)).

Finally the **Curvatures of motion,** first given in Chapter II:

Transverse Curvature: $K_2(t) \approx \partial^2 V / \partial x^2 = \frac{\ddot{V}}{c^2}$ **(2.10)**

are computed and given in **Chapter IV.6**, and

Radial Curvature: $K_1(t) \approx \partial^2 U / \partial x^2 = \frac{\ddot{U}}{c^2}$ **(2.9)**

Vertical Curvature: $K_3(t) = \frac{\partial^2 W / \partial x^2}{\left[1 + \left(\partial W / \partial x\right)^2\right]^{3/2}} \approx \partial^2 W / \partial x^2 = \frac{\ddot{W}}{c^2}$ **(2 .11)**

are computed and given in **Chapter V.6**.

References

1. Bielak, J. (1978). Dynamic Response of Nonlinear Building-Foundation System, Earthqu. Engng. Struct. Dynam., Vol. 6, 17-30.

2. Buchen, P.W. and R. Ben-Hador (1996). Free mode surface-wave computations, *Geophys. J. Int.* ***124****, 869-887.*

3. Chapman , C.H. (2003). Yet another Elastic Plane- Wave Layer-Matrix algorithm, *Geophys. J. Int.* ***154****, 212-223.*

4. Chapman , C.H. and R.A. Phinney (1972). Diffracted Seismic Signals and their Numerical Solution, *Math. Comp .Phys.,* ***12****, 165-230.*

5. Dorman, J.M., M. Ewing and J. Oliver (1960). Study of Shear Velocity Distribution by Mantle Rayleigh Waves, *Bull Seismol. Soc. Am.,* ***50****, 87-115.*

6. Dravinski, M. and Trifunac, M.D. (1979). Static, Dynamic and Rotational Components of Strong Shaking near Faults, Report CE 79-06, Dept. of Civil Eng., Univ. of Southern California, Los Angeles, California, U.S.A.

7. Dravinski, M. and Trifunac, M.D. (1980). Response of Layer to Strike-Slip Vertical Fault, Proc. Engineering Mech. Div., ASCE, No. EM4, pp. 609-621.

8. Dunkin J.W. (1965). Computations of modal solutions in layered elastic media at high frequencies, *Bull. Seismol. Soc. Am.,* ***55(2)****, 335-358.*

9. Gupta, I.D. and Trifunac, M.D. (1987). A Note on Contribution of Torsional Excitation to Earthquake Response of Simple Symmetric Buildings, Earthqu. Engng and Engng Vibrat., Vol. 7, No. 3, 27-46.

10. Gupta, I.D. and Trifunac, M.D. (1988). A Note on Contribution of Rocking Excitation to Earthquake Response of Simple Buildings, Bull. Indian Soc. Earthquake Tech., Vol. 25, No. 2, 73-83.

11. Gupta, V.K. and Trifunac, M.D. (1990a). Response of Multistoried Buildings to Ground Translation and Rocking during Earthquakes, J. Prob. Engng Mech., Vol. 5, No. 3, 138-145.

12. Gupta, V.K. and Trifunac, M.D. (1990b). A Note on Contributions of Ground Torsion to Seismic Response of Symmetric Multistoried Buildings, Earthqu. Engng Engng Vib., Vol. 10, No. 3, 27-40.

13. Gupta, V.K. and Trifunac, M.D. (1990c). Response of Multistoried Buildings to Ground Translation and Torsion during Earthquakes, Europ. Earthqu. Engng, IV(1), 34-42.

14. Gupta, V.K. and Trifunac, M.D. (1991). Effects of Ground Rocking on Dynamic Response of Multistoried Buildings during Earthquakes, Struct. Engng/Earthqu. Engng,

JSCE, Vol. 8, No. 2, 43-50.

15. Haskell, N.A. (1953). The Disperson of Surface waves on Multilayered Media, *Bull Seismol. Soc. Am., **43**, 17-34.*

16. Hudson, D. E. (1983a). History of Accelerograph Development, Proc. of the Golden Anniversary Workshop on Strong Motion Seismology, U.S.C., 29-56.

17. Hudson, D. E. (1983b). Strong Motion Instrumentation Systems, Proc. of the Golden Anniversary Workshop on Strong Motion Seismology, U.S.C, 73-86.

18. Kennett , B.L.N. (1974). Reflection, Rays and Reverberations, *Geophys. J. Int. **64**, 1685-1696.*

19. Kennett , B.L.N. (1983). Seismic Wave Propagation in a stratified Media. *Cambridge University Press, New York.*

20. Kennett, B.L.N. (2001). The Seismic Wavefield Vol. I: Introduction and Theoretical Developement, *Cambridge University Press,*

21. Kennett, B. L. N. (2003). The Seismic Wavefield. Volume II: Interpretation of Seismograms on Regional and Global Scales,*Cambridge University Press,*

22. Kennett , B.L.N and N.J. Kerry (1979). Seismic Waves in a stratified Half-Space, *Geophys. J. R. Astr. Soc. **57**, 557-583.*

23. Knopoff, L. (1964). A Matrix Method for Elastic Wave Problems, *Bull Seismol. Soc. Am., **45**, 431-438.*

24. Kobori, T. and Shinozaki, I. (1973). Torsional Vibration of Structure due to Obliquely Incident SH Waves, Proc. 5th European Conf. Earthqu. Engng, Vol. 1, Paper No. 22, 1-5.

25. Lee, V.W. (1979). Investigation of Three-Dimensional Soil-Structure Interaction, Report CE 79-11, Dept. of Civil Eng., Univ. of Southern California, Los Angeles, California, U.S.A.

26. Lee, V.W. (1990). Surface Strains Associated with Strong Earthquake Shaking, Proc. JSCE, No. 422/I-14, pp. 187-194.

27. Lee, V.W. (2002). Empirical Scaling of Strong Earthquake Ground Motion: Part I: Attenuation and Scaling of Response Spectra, *ISET J. Earthquake Technology, **39(4)** ,219–254.*

28. Lee, V.W. (2006)**.** Empirical Scaling of Strong-Motion Response Spectral Amplitudes - a Review" *ISET J. Earthquake Technology, 44(1) Special Issue **#476,** 39-69,* **Mar 07.**

29. Lee, V.W. and Trifunac, M.D. (1985). Torsional Accelerograms, Int. J. Soil Dynam.Earthqu. Engng, Vol. 4, No. 3, 132-139.

30. Lee, V.W. and Trifunac, M.D. (1987). Rocking Strong Earthquake Accelerations, Int. J.

Soil Dynam. Earthqu. Engng, Vol. 6, No. 2, 75-89.

31. Lee, V.W. and Trifunac, M.D. (1989). A Note on Filtering Strong Motion Accelerograms to Produce Response Spectra of Specified Shape and Amplitude, *Europ. Earthqu. Engng, VIII(2), 38-45.*

32. V.W. Lee & M.D. Trifunac (2009) Empirical Scaling of Rotational Spectra of Strong Earthquake Ground Motion, BSSA Special Issue on "Rotational Seismology and Engineering Applications, *Bull. Seismo. Soc. America,* Rotational seismology and engineering applications, *99(2B) 1378-1390.* May 2009.

33. Lee, V.W. and Trifunac, M.D. (2012) Elastic and Surface Waves Propagating in Elastic Layered media, Personal communication.

34. Liu, T. (2010). Efficient Reformulation of the Thomson-Haskell Method for Computation of Surface Waves in Layered Half-Space, Short Note, *Bull. Seismol. Soc. Am., **100(5A)**, 2310-2316.*

35. Liu, T., C. Zhao and Y. Duan (2012). Generalized Transfer Matrix Method for Propagation of Surface Waves in Layered azimuthally Anisotropic Half-Space,*Geophys. J. Int. **190**, 1204-1212*

36. Luco, J.E. (1976). Torsional Response of Structures for SH Waves: The Case of Hemispherical Foundation, Bull. Seism. Soc. Amer., Vol. 66, 109-123.

37. Luco, J.E. and R.J. Apsel (1983). On the Green's function for a Layered Half-Space, Part I, *Bull Seismol. Soc. Am., **73**, 909-929.*

38. Ma, Y., R. Wang and H. Zhoul (2012). A Note on the equivalence of the Three Major Propagator Algorithms for Computational Stability and Efficiency, *Earthq. Sci., **25**, 55-64.*

39. Moeen-Vaziri, N. and Trifunac, M.D. (1988a). Scattering and Diffraction of Plane SH-Waves by Two-Dimensional Inhomogeneities, Soil Dynam. Earthqu. Engng, Vol. 7, No. 4, 179-188.

40. Moeen-Vaziri, N. and Trifunac, M.D. (1988b). Scattering and Diffraction of Plane P and SV Waves by Two-Dimensional Inhomogeneities, Soil Dynam. Earthqu. Engng, Vol. 7, No. 4, 189-200.

41. Nathan, N.D. and MacKenzie, J.R. (1975). Rotational Components of Earthquake Motions, Can. J. Civil Eng., Vol. 2, pp. 430-436.

42. Newmark, N.M. (1969). Torsion in Symmetrical Buildings, Proc. 4th World Conf. Earthqu. Engng, Santiago, Chile, A3.19-A3.32.

43. Pitteway, M.L.V. (1965). The Numerical Calculation of Wave-Fields, Reflection Coefficients and Polarization for Long Radio Waves in the Lower Ionosphere I, *Phil.*

*Trans. R. Soc. London, **A 257,** 219-241.*

44. Press, F., D. Harkrider and C.A. Seafeldt (1961). A Fast, Convenient Program for Computation of Surface Wave Dsipersion curves on multilayered media, *Bull. Seismol. Soc. Am., **51**,495-502.*

45. Randall, M.J. (1967). Fast Programs for Layered Half-Space Problems, *Bull Seismol. Soc. Am., **57**, 1299-1316.*

46. Thomson, W.T. (1950). Transmission of Elastic Waves Through a Stratified Solid Media, *J. Appl. Phys. 21, 89-93.*

47. Thrower, E.N. (1965). The Computation of Dispersion of Elastic Waves in Layered Media, *J. Sound Vib., **2**, 210-226.*

48. Todorovska, M.I. and Lee, V.W. (1989). Seismic Waves in Buildings with Shear Walls or Central Core, ASCE J. Eng. Mech., Vol. 115, No. 12, 2659-2686.

49. Todorovska, M.I. and Trifunac, M.D. (1989). Antiplane Earthquake Waves in Long Structures, ASCE J. Eng. Mech., Vol. 115, No. 2, 2687-2708.

50. Todorovska, M.I. and Trifunac, M.D. (1990a). Propagation of Earthquake Waves in Buildings with Soft First Floor, ASCE J. Eng. Mech., Vol. 116, No. 4, 892-900.

51. Todorovska, M.I. and Trifunac, M.D. (1990b). A Note on Excitation of Long Structures by Ground Waves, ASCE J. Eng. Mech., Vol. 116, No. 4, 952-964.

52. Todorovska, M.I. and Trifunac, M.D. (1992). Effect of Input Base Rocking on the Relative Response of Long Buildings on Embedded Foundations, Europ. Earthqu. Engng, Vol. VI, No. 1, 36-46.

53. Trifunac, M.D. (1971a). Response Envelope Spectrum and Interpretation of Strong Earthquake Ground Motion, *Bull. Seism. Soc. Amer., **61**, 343-356.*

54. Trifunac, M.D. (1971b). A Method for Synthesizing Realistic Strong Ground Motion, *Bull. Seism. Soc. Amer., **61**, 1755-1770.*

55. Trifunac, M.D. (1972a). Stress Estimates for San Fernando, California, Earthquake of 9 February 1971: Main Event and Thirteen Aftershocks", *Bull. Seism. Soc. Amer., **62**, 721-750.*

56. Trifunac, M.D. (1972b). Tectonic Stress and Source Mechanism of the Imperial Valley, California, Earthquake of 1940, *Bull. Seism. Soc. Amer., **62**, 1283-1302.*

57. Trifunac, M.D. (1973). Analysis of Strong Earthquake Ground Motion for Prediction of Response Spectra, *Earthqu. Engng Struct. Dynam., **2(1)**, 59-69.*

58. Trifunac, M.D. (1976). Preliminary Empirical Model for Scaling Fourier Amplitude

Spectra of Strong Ground Acceleration in Terms of Earthquake Magnitude, Source to Station Distance and Recording Site Conditions, *Bull. Seism. Soc. Amer.*, ***66**, 1343-1373.*

59. Trifunac, M.D. (1979a). Preliminary Empirical Model for Scaling Fourier Amplitude Spectra of Strong Motion Acceleration in Terms of Modified Mercalli Intensity and Geologic Site Conditions, *Earthqu. Engng Struct. Dynam.*, ***7**, 63-74*.

60. Trifunac, M.D. (1979b). A Note on Surface Strains Associated with Incident Body Waves, *Bull. EAEE*, ***5**, 5-95*.

61. Trifunac, M.D. (1989a). Dependence of Fourier Spectrum Amplitudes of Recorded Strong Earthquake Accelerations on Magnitude, Local Soil Conditions and on Depth of Sediments, Earthqu. Engng Struct. Dynam., Vol. 18, No. 7, 999-1016.

62. Trifunac, M.D. (1989b). Empirical Scaling of Fourier Spectrum Amplitudes of Recorded Strong Earthquake Accelerations in Terms of Magnitude and Local Soil and Geologic Conditions, Earthqu. Engng Engng Vib., Vol. 9, No. 2, 23-44.

63. Trifunac, M.D. (1990). Curvograms of Strong Ground Motion, ASCE J. Eng. Mech., Vol. 116, No. 6, 1426-1432.

64. Trifunac, M.D. (1993). Long Period Fourier Amplitude Spectra of Strong Motion Acceleration, *Soil Dynam. Earthqu. Engng*, ***12(6)**, 363-382*.

65. Trifunac, M.D. (1994). Q and High Frequency Strong Motion Spectra, *Soil Dynam. Earthqu. Engng*, ***13(3)**, 149-161*.

66. Trifunac, M.D. (1995a). Pseudo Relative Velocity Spectra of Earthquake Ground Motion at Long Periods, *Soil Dynam. Earthqu. Engng*, ***14(5)**, 331-346.*

67. Trifunac, M.D. (1995b). Pseudo Relative Velocity Spectra of Earthquake Ground Motion at High Frequencies, *Earthqu. Engng Struct. Dynam.*, ***24(8)**, 1113-1130.*

68. Trifunac, M.D. (1997). Differential Earthquake Motion of Building Foundations, J. Structural Eng., ASCE, Vol. 123, No. 4, pp. 414-422.

69. Trifunac, M.D. and Anderson, J.G. (1977). Preliminary Empirical Models for Scaling Absolute Acceleration Spectra, *Report **CE 76-03**, Dept. of Civil Eng., Univ. of Southern California, Los Angeles, California, U.S.A.*

70. Trifunac, M.D. and Brady, A.G. (1975). A Study on the Duration of Strong Earthquake Ground Motion, *Bull. Seism. Soc. Amer.*, ***65**, 581-626*.

71. Trifunac, M.D. and Lee, V.W. (1978). Dependence of the Fourier Amplitude Spectra of Strong Motion Acceleration on the Depth of Sedimentary Deposits, *Report **CE 78-14**, Dept. of Civil Eng., Univ. of Southern California, Los Angeles, California, U.S.A.*

72. Trifunac, M.D. and Lee, V.W. (1985). Preliminary Empirical Model for Scaling Fourier

Amplitude Spectra of Strong Ground Acceleration in Terms of Earthquake Magnitude, Source to Station Distance, Site Intensity and Recording Site Conditions, *Report **CE 85-03**, Dept. of Civil Eng., Univ. of Southern California, Los Angeles, California, U.S.A.*

73. Trifunac, M.D. and Todorovska, M.I. (1997a). Response Spectra and Differential Motion of Columns, Earthquake Eng. Structural Dyn., Vol. 26, No. 2, 251-268.

74. Trifunac, M.D. and Todorovska, M.I. (1997b). Northridge, California, Earthquake of 17 January 1994: Density of Pipe Breaks and Surface Strains, Soil Dynamics Earthquake Eng., Vol. 16, No. 3, 193-207.

75. Trifunac, M.D. and Todorovska, M.I. (2001). A Note on Useable Dynamic Range in Accelerographs Recording Translation, Soil Dynamics Earthquake Eng., Vol. 21, No. 4, 275-286.

76. Trifunac, M.D., Todorovska, M.I. and Ivanovic, S.S. (1996). Peak Velocities, and Peak Surface Strains during Northridge, California, Earthquake of 17 January 1994, Soil Dynamics Earthquake Eng., Vol. 15, No. 5, 301-310.

77. Trifunac, M.D. and Westermo, B.D. (1976a). Dependence of Duration of Strong Earthquake Ground Motion on Magnitude, Epicentral Distance, Geologic Conditions at the Recording Station and Frequency of Motion, *Report **CE 76-02**, Dept. of Civil Eng., Univ. of Southern California, Los Angeles, California, U.S.A.*

78. Trifunac, M.D. and Westermo, B.D. (1976b). Correlations of Frequency Dependent Duration of Strong Earthquake Ground Motion with the Modified Mercalli Intensity and the Geologic Conditions at the Recording Stations, *Report **CE 77-03**, Dept. of Civil Eng., Univ. of Southern California, Los Angeles, California, U.S.A.*

79. Trifunac, M.D. and Novikova, E.I. (1994). State of the Art Review on Strong Motion Duration, *10th Europ. Conf. Earthqu. Engng, Vienna, Austria. **1**, 131-140.*

80. Trifunac, M.D. and Novikova, E.I. (1995). Duration of Earthquake Fault Motion in California, *Earthqu. Engng Struct. Dynam., **24(6)**, 781-799.*

81. Tso, W.K. and Hsu, T.I. (1978). Torsional Spectrum for Earthquake Motions, Earthqu. Engng Struct. Dynam., Vol. 6, 375-382.

82. Wang, R.(1999). A Simple Orthonormalization Method for Stable and Efficient Computation of Green's Functions, *Bull Seismol. Soc. Am., **89**,733-741.*

83. Watson, T.H. (1970). A Note on Fast Computation of Rayleigh Wave Dsipersion in the Multi-Layered Half-Space, *Bull Seismol. Soc. Am., **60**,161-166.*

84. Wong, H.L. and Trifunac, M.D. (1978). Synthesizing Realistic Strong Motion Accelerograms, *Report **CE 78-07**, Dept. of Civil Eng., Univ. of Southern California, Los Angeles, California, U.S.A.*

85. Wong, H.L. and Trifunac, M.D. (1979). Generation of Artificial Strong Motion Accelerograms, *Earthquake Engineering Structural Dynamics, **7**, 509-527.*

APPENDIX R4-1
(Reporting Date 1 August 2013)

REPORT No. IV – Part I
Contract No.: 87055-11-0562
RSP Project ID (R525.1)

REPORTING DATE – 1 August 2013

PROJECT TITLE: Interfacing Seismological Description of Strong Ground Motion with Engineering Analysis of Soil Structure Interaction for Nuclear Power Plants

REPORT SUBMITTED BY: Structural and Earthquake Engineering Consultants (SEEC) Inc.
855 Arcadia Ave. #E, Arcadia, CA 91007 USA
Contact name: M. D. Trifunac
Phone: (626) 447-9382
Email: trifunac@usc.edu, misha.trifunac@gmail.com

to

Canadian Nuclear Safety Commission

ATTENTION: Nanci Laroche, Nebojsa Orbovic
280 Slater St., Ottawa, Ontario, Canada, K1P 5S9
E-mail: research-recherche@cnsc-ccsn.gc.ca
Nebojsa.Orbovic@cnsc-ccsn.gc.ca

Scattering and Diffraction by Irregular Layered Elastic Media - Part I: Love and Body SH Waves

I. Introduction

There are many studies reported in literature, which consider the seismic body and surface wave motions in the regions of sudden change in the thickness of surface layers (as in transition from oceanic to continental crust, for example) or more generally in the vicinity of irregular layers which depart significantly from the classical parallel representation of shallow earth crust. However, the excitations considered in these studies (incident wave motions) cannot easily be modified to work with the body and surface wave trains specified by SYNACC methodology, which is conveniently compatible with engineering specification of design earthquake motions, deterministically or via seismic hazard analysis. To this, in the following we outline a method for describing the motions in irregular shaped layers for input motions arriving from the parallel-layered half space, as specified by SYNACC method. In this Part – I, we consider only the out of plane motions, in two-dimensional representation of irregular layers for SH and Love wave excitation. We will address the in plane motions associated with P, SV and Rayleigh waves in the future reports.

II. Love Surface and Body SH Waves On and Below the Surface of an Elastic Layered Media

Recall that in Report I we considered an *N*-Layered half-space with Love waves or Body SH waves incident from the left (Report I, Figure **II.1**):

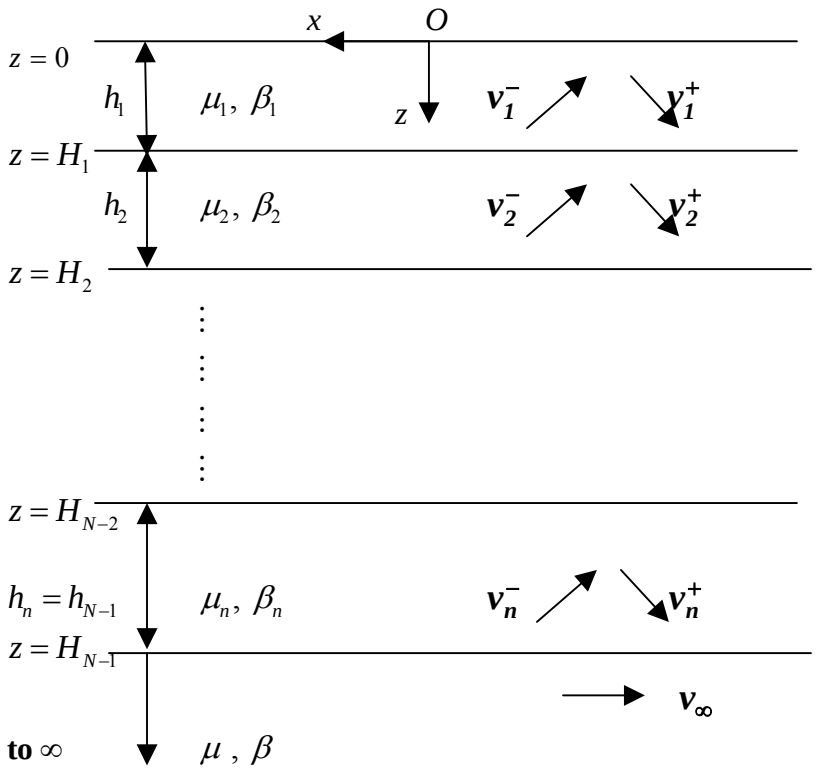

(Report I: Figure II.1 N-layered half-space with Love waves)

For *each of these regular layers* $\boldsymbol{l}$, with $\boldsymbol{l = 1, \ldots, N}$, the displacement of the Love surface Waves in the layer take the form (in the anti-plane, y-component):

$\boldsymbol{v_1^-, v_1^+}$ **:**

$$\boldsymbol{v_l^- = C_l^- e^{ik(x-\gamma_l z)}}$$
$$\boldsymbol{v_l^+ = C_l^+ e^{ik(x+\gamma_l z)}} \qquad \text{Report I (2.1)}$$

They are respectively the upward and downward propagating waves present in the $\boldsymbol{l^{th}}$ layer. Here $\boldsymbol{k = k(\omega) = \omega / c(\omega)}$ is the horizontal wave number of the waves at frequency $\boldsymbol{\omega}$ and having phase velocity $\boldsymbol{c = c(\omega)}$. The term $\boldsymbol{e^{ikx}}$, which is the same in

each layer, is the horizontal component of the waves, which together with the time harmonic term $e^{i\omega t}$, corresponds to the waves propagating in the ***–ve*** *x* direction. The terms $e^{\mp ik\gamma_l y}$ are the vertical components of the waves with the ***negative*** term propagating upwards (***–ve*** *y*) and the ***positive*** term propagating downwards (*y*). Here $\gamma_l = \gamma_l(\beta_l)$ is given by

$$\gamma_l = \frac{\left(k_{\beta_l}^2 - k^2\right)^{1/2}}{k} = \left(\left(k_{\beta_l}/k\right)^2 - 1\right)^{1/2} = \left(\left(c/\beta_l\right)^2 - 1\right)^{1/2} \qquad \text{Report I (2.2)}$$

so that $k\gamma_l$ is the vertical wave number of the waves in the l^{th} layer of the medium with shear wave velocity β_l. In general, the wave velocities increase as one moves down through the layers, so that $\beta_1 < \beta_2 < \ldots < \beta_n < \beta$, with the semi-infinite half-space layer at the bottom having the highest shear wave speed β. With $c = c(\omega)$ the wave speed of the surface Love waves there, $c < \beta$, and the surface waves take the form:

$$v_\infty = C_\infty e^{ik(x - \gamma z)} = C_\infty e^{ikx - k\bar{\gamma} z} \qquad \text{Report I (2.3)}$$

where $$\bar{\gamma} = \frac{\left(k^2 - k_\beta^2\right)^{1/2}}{k} = \left(1 - \left(k_\beta/k\right)^2\right)^{1/2} = \left(1 - \left(c/\beta\right)^2\right)^{1/2} \qquad \text{Report I (2.4)}$$

$\bar{\gamma}$ is the complement of γ and is real, so that the term $e^{ikx - k\bar{\gamma} y}$ in v_∞ corresponds to a surface wave term whose amplitude is exponentially decaying with depth (in y) below the surface. With β_l the shear wave speed in the l^{th} layer of the medium, and $c = c(\omega)$, the Love wave speed and also the (horizontal) phase velocity of the waves in each layer of the elastic media above the half space (Fig.1), we can have $c \geq \beta_l$ or $c < \beta_l$. If $c \geq \beta_l$, the term $\gamma_l = \gamma_l(\beta_l)$ in Equation (2.2) is real and both waves v_l^+ and v_l^- in Equation (1) will correspond to harmonic plane waves. If, however, $c < \beta_l$ then, as from Equation (2.2):

$\gamma_l = \left(\left(c/\beta_l\right)^2 - 1\right)^{1/2}$ is imaginary and $\bar{\gamma}_l = \left(1 - \left(c/\beta_l\right)^2\right)^{1/2}$ is real Report I (2.5)

III. Love and Body SH Waves incident on an Irregular Layered Elastic Media

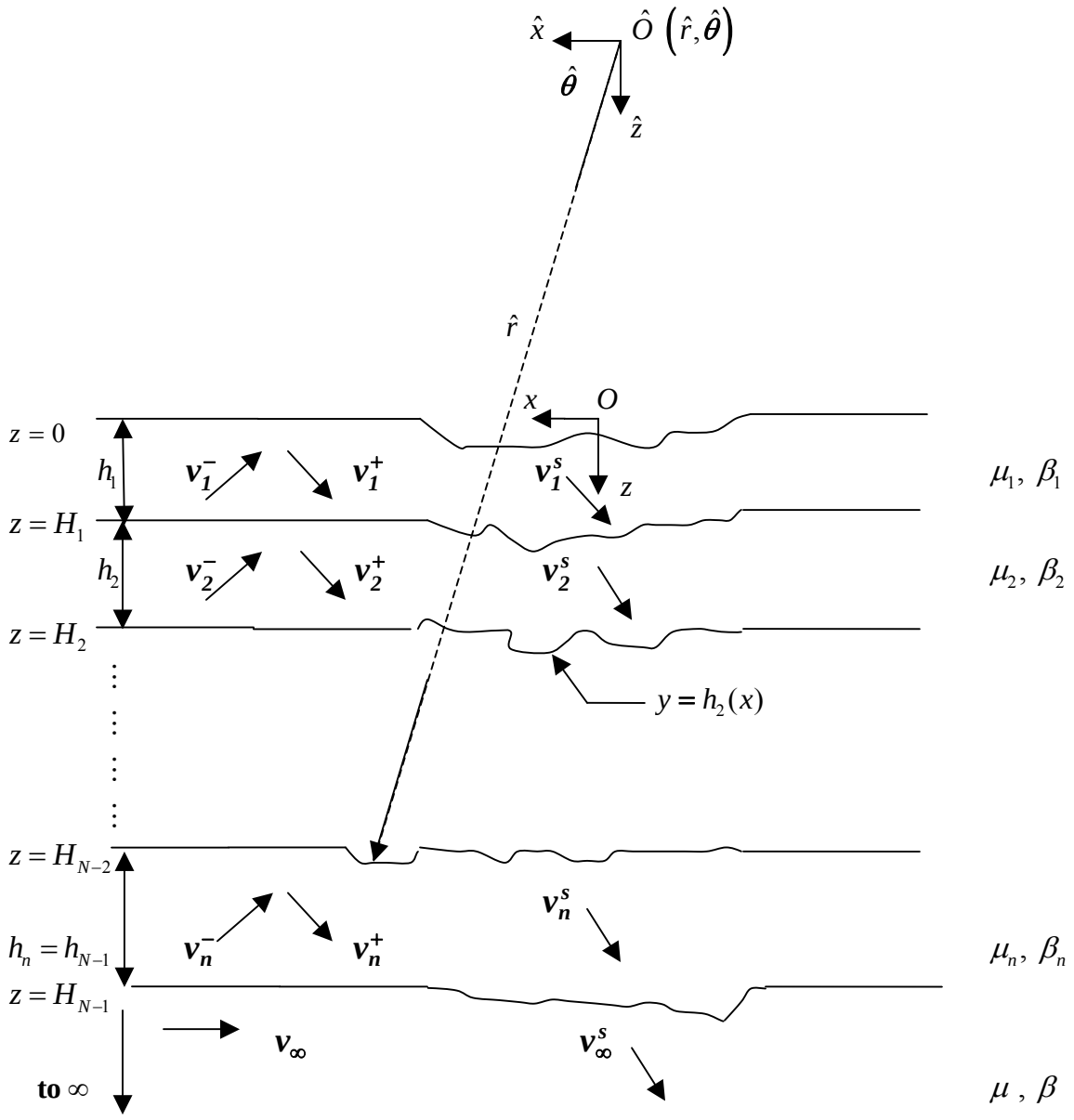

Figure 1 Irregular-Shaped N-layered half-space with Love waves

The left part of the above figure shows Love waves propagating along an *N*-layered half-space where the layers are perfectly flat. Next we consider the right segment

of the same figure, when this is not the case. **Figure 1** shows a model where the parallel layers begin to depart from perfectly flat configuration. Without loss of generality, we will assume that each of the irregular surfaces, at each interface between the l^{th} and $(l+1)^{th}$ layer, which extends from $x=-\infty$ to $x=+\infty$ can be represented by a curve $z=h_l(x)$. We assume that this curve will be the flat surface $z=H_l$ almost everywhere, but will deviate from the flat surface within some finite region where it is defined numerically by a set of points (x_i, z_i). This curve can also be represented by polar coordinates $(\hat{r}, \hat{\theta})$, with $\hat{r}=\hat{r}(\hat{\theta})$ in a common coordinate system $(\hat{x}, \hat{z})$, with origin at some point $\hat{O}$ above the half space, as shown in Figure 1.

With the surface Love waves v_l^-, v_l^+ or body SH waves at each layer l incident upon these irregular surfaces, additional scattered waves are generated, which can be represented by

$$v_l^s = \sum_{n=0}^{\infty} \left(A_{l,n}^{(1)} H_n^{(1)}(k_l \hat{r}) + A_{l,n}^{(2)} H_n^{(2)}(k_l \hat{r}) \right) \cos n\theta \tag{1}$$

with both outgoing and incoming waves, for each layer $l=1,2,\ldots,N-1$, all except the last semi-infinite layer. For the last semi-infinite layer, $l=N$, the scattered wave, $v_\infty^s = v_N^s$, takes the form

$$v_\infty^s = v_N^s = \sum_{n=0}^{\infty} A_{\infty,n} H_n^{(1)}(k\hat{r}) \cos n\theta \tag{2}$$

with only outgoing waves, satisfying Somerfield's radiation condition at infinity.

The scattered waves, together with the free-field surface Love Waves, form the resultant waves in the layered media. Writing $v_l^{ff} = v_l^+ + v_l^-$ as the free-field surface Love or Body SH waves in the l^{th} media, the resultant wave in the same media is $v_l = v_l^{ff} + v_l^s$, which, together must satisfy the following set of boundary conditions below (Lee and Wu, 1994a).

1) On the half-space surface, $y = h_0(x)$, the resultant waves in the top layer $(l = 1)$ must together satisfy the half-space surface free-field stress condition:

$$\tau_{nt} = \mu_1 \frac{\partial v_1}{\partial \hat{n}} = \mu_1 \frac{\partial \left(v_1^{ff} + v_1^s \right)}{\partial \hat{n}} = 0, \tag{3a}$$

$$\text{or} \qquad \frac{\partial v_1^s}{\partial \hat{n}} = -\frac{\partial v_1^{ff}}{\partial \hat{n}} \tag{3b}$$

2) For $l = 1, 2, \ldots, N-1$, at the interface between the l^{th} layer and the $(l+1)^{th}$ layer below, $y = h_l(x)$, the resultant waves in these two layers must satisfy the continuity of displacement and stress at the interface:

$$\boldsymbol{v}_l = \boldsymbol{v}_l^{ff} + \boldsymbol{v}_l^s = \boldsymbol{v}_{l+1}^{ff} + \boldsymbol{v}_{l+1}^s = \boldsymbol{v}_{l+1} \tag{4a}$$

or $$\boldsymbol{v}_l^s - \boldsymbol{v}_{l+1}^s = -\left(\boldsymbol{v}_l^{ff} - \boldsymbol{v}_{l+1}^{ff} \right) \tag{4b}$$

$$\mu_l \frac{\partial v_l}{\partial \hat{n}} = \mu_{l+1} \frac{\partial v_{l+1}}{\partial \hat{n}} \tag{5a}$$

$$\mu_l \frac{\partial \left(v_l^{ff} + v_l^s \right)}{\partial \hat{n}} = \mu_{l+1} \frac{\partial \left(v_{l+1}^{ff} + v_{l+1}^s \right)}{\partial \hat{n}}$$

$$\text{or} \quad \mu_l \frac{\partial v_l^s}{\partial \hat{n}} - \mu_{l+1} \frac{\partial v_{l+1}^s}{\partial \hat{n}} = -\left(\mu_l \frac{\partial v_l^{ff}}{\partial \hat{n}} - \mu_{l+1} \frac{\partial v_{l+1}^{ff}}{\partial \hat{n}} \right) \tag{5b}$$

with the unknown wave functions on the left-hand side, and the known functions on the right-hand side. Here, in equations (3) and (5), $\hat{n}$ is the normal at a boundary point (x, y) where $y = h_l(x)$, and $\frac{\partial}{\partial \hat{n}}(\ )$ is the corresponding normal derivative of the wave functions given by:

$$\frac{\partial}{\partial \hat{n}}(\ ) = \tilde{\nabla}(\ ) \cdot \hat{n} = \cos\alpha \frac{\partial}{\partial r}(\ ) + \frac{\sin\alpha}{r} \frac{\partial}{\partial \theta}(\ ) \tag{6a}$$

where α is the angle that the normal $\hat{n}$ makes with the radial vector, as shown in **Figure 2** (Lee and Wu, 1994a,b). For the free-field waves, which are given in rectangular coordinates, Eqn. (6) can also be expressed as

$$\frac{\partial}{\partial \hat{n}}(\ ) = \tilde{\nabla}(\ ) \cdot \hat{n} = n_x \frac{\partial}{\partial x}(\ ) + n_y \frac{\partial}{\partial y}(\ ) \tag{6b}$$

where the normal $\hat{n}$ is expressed in rectangular coordinates as $\hat{n} = n_x \hat{e}_x + n_y \hat{e}_y$, and $\hat{e}_x$, $\hat{e}_y$ are respectively the unit vectors in the *x*- and *y*- directions.

On the flat part of the interface between the l^{th} and $(l+1)^{th}$ layer, on the curve $y = h_l(x)$, where $y = H_l$, since the Love waves already satisfy the continuity of displacement and stress conditions, only the scattered waves will appear in the continuity equations at those points.

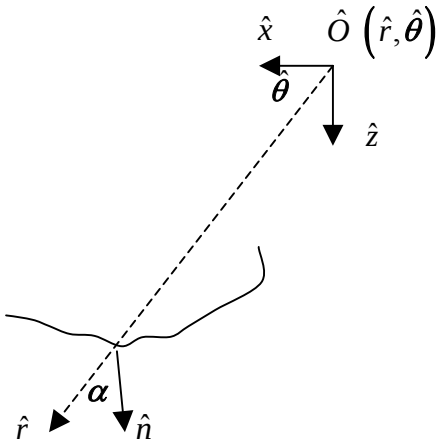

Figure 2 Angle α between radial vector and normal at a point

Then, Equations (3b), (4b) and (5b) can be written as:

$$\frac{\partial v_1^s}{\partial \hat{n}} = -\tau_1^{ff} = \begin{cases} -\dfrac{\partial v_1^{ff}}{\partial \hat{n}} & \text{on an irregular surface point of } y = h_0(x), \\ 0 & \text{on a flat surface point of } y = h_0(x) = 0 \end{cases} \tag{7}$$

$$v_l^s - v_{l+1}^s = -\delta v_l^{ff} = \begin{cases} -\left(v_l^{ff} - v_{l+1}^{ff}\right) & \text{on an irregular surface point of } y = h_l(x), \\ 0 & \text{on a flat surface point of } y = h_l(x) = H_l \end{cases} \tag{8a}$$

and $$\mu_l \frac{\partial v_l^s}{\partial n} - \mu_{l+1} \frac{\partial v_{l+1}^s}{\partial n} = -\delta\tau_l^{ff}$$

$$= \begin{cases} -\left(\mu_l \dfrac{\partial v_l^{ff}}{\partial n} - \mu_{l+1} \dfrac{\partial v_{l+1}^{ff}}{\partial n} \right) & \text{on an irregular surface point of } y = h_l(x), \\ 0 & \text{on a flat surface point of } y = h_l(x) = H_l \end{cases} \tag{8b}$$

To solve this boundary-valued problem, one would have to find a wave function, v_l, as given in Equation (1) for each layer $l = 1, 2 \ldots, N-1$, and as in Equation (2) for the bottom semi-infinite layer $l = N$.

IV. The Method of Weighted Residues (Moment) Method

This section will follow the approach previously described in Lee and Wu (1994a,b). It is included and summarized here for completeness of this presentation. It is seen from the above sections that the wave functions at each layer together have to satisfy the set of boundary conditions numerically at every point of the interface given in Equations (7), (8) and (9). Since the surfaces are now irregular, a numerical procedure has to be applied.

Harrington (1967) in his classical paper: "Matrix Methods for field Problems", presented a well-defined unified treatment of most of the existing numerical methods for the above boundary-valued problems, which he called the "Moment Methods". He applied the method to Electromagnetic waves problems. Following Fenlon (1969), with applications to acoustic wave problems, Lee and Wu (1994a,b) applied the method to elastic wave problems with arbitrary-shaped canyons in elastic half-space. Another common name for the "Moment Method" is the "Method of Weighted Residues". Here is a brief summary of the method, following Lee and Wu (1994a,b).

Assume that a general equation to be satisfied is of the form

$$\mathcal{L} f = g \tag{9}$$

where $\mathcal{L}$ is a linear operator, f is an unknown function to be solved, and g is a given known function. The boundary conditions in equations (7), (8) and (9) above are all of this form, with $\mathcal{L}$ a linear combination of the identity and the derivative operators, f a sum or difference of the unknown wave functions and their derivatives in adjacent media, and g the corresponding sum or difference of the known free-filed Love wave functions and their derivatives in adjacent media. Each of the unknown wave functions f is here represented as a series of basis functions $\ldots, f_0, f_1, \ldots, f_n, \ldots$

$$f = \sum_n c_n f_n \tag{10}$$

with c_n a sequence of unknown coefficients to be determined. The range of the indices of the functions can either be infinite ($-\infty$ to ∞) or semi-infinite (0 to ∞). Since $\mathcal{L}$ is a linear operator, Equation (10) takes the form, in terms of residues, ε, to be set to zero:

$$\varepsilon = \sum_n c_n \mathcal{L} f_n - g = 0 \tag{11}$$

Next, we choose a scalar inner product $\langle f, g \rangle$ to be defined on any pair of functions in the domain of $\mathcal{L}$, and a set of weight functions $\ldots, w_0, w_1, \ldots, w_n, \ldots$ in the domain. We take the inner product of the residues with each weight function and equate it to zero:

$$\begin{aligned} \langle \varepsilon, w_m \rangle &= \left\langle \sum_n c_n \mathcal{L} f_n - g, w_m \right\rangle \\ &= \sum_n c_n \langle \mathcal{L} f_n, w_m \rangle - \langle g, w_m \rangle = 0 \\ \textbf{so} \quad & \sum_n \langle \mathcal{L} f_n, w_m \rangle \, c_n = \langle g, w_m \rangle \end{aligned} \tag{12a}$$

or in matrix form:

$$\left[A_{mn}\right] \{c_n\} = \{g_m\} \tag{12b}$$

with $\left[A_{mn}\right] = \langle \mathcal{L} f_n, w_m \rangle$ a matrix of infinite order, and $\{g_m\} = \langle g, w_m \rangle$ a known vector computed from the free-field surface Love waves or Body SH waves. The matrix is composed of ***(2N-1)*** set of boundary conditions in Equations (7), (8) and (9) for the set of ***(2N-1)*** coefficients from the ***(2N-1)*** wave functions in Equations (1) and (2) for the ***N***-Layered media.

Depending on the choice of the weight functions, these weight functions can also be considered as a set of basis functions, orthogonal with respect to the inner product, and with the residues expanded in terms of these basis functions, using the inner product, we set each term of the expansion to be zero.

Using the weighted residue method, the boundary conditions at each layer take the form:

1) Starting at the top layer, the half space surface, from Eqn. (3b):

$$\sum_{n=0}^{\infty} \sum_{j=1,2} \left\langle \frac{\partial}{\partial \hat{n}} \left(H_n^{(j)}(k_1 \hat{r}) \cos n\theta \right), w_m \right\rangle A_{1,n}^{(j)} = -\left\langle \frac{\partial v_1^{ff}}{\partial \hat{n}}, w_m \right\rangle \tag{13a}$$

or in matrix form, at the top surface of the 1st layer (surface of the half-space):

$$\sum_{n=0}^{\infty}\left[\left\langle\frac{\partial}{\partial\hat{\boldsymbol{n}}}\left(H_n^{(1)}(k_1\hat{r})\cos n\theta\right),w_m\right\rangle\quad\left\langle\frac{\partial}{\partial\hat{\boldsymbol{n}}}\left(H_n^{(2)}(k_1\hat{r})\cos n\theta\right),w_m\right\rangle\right]\begin{Bmatrix}A_{1,n}^{(1)}\\A_{1,n}^{(2)}\end{Bmatrix}=-\left\langle\frac{\partial v_1^{ff}}{\partial\hat{\boldsymbol{n}}},w_m\right\rangle \tag{13b}$$

2) For the interface between the l^{th} and $(l+1)^{th}$ layer, for $l=1,2,3\ldots$ from Eqns. (8a), and (8b):

$$\sum_{n=0}^{\infty}\sum_{j=1,2}\left\langle H_n^{(j)}(k_l\hat{r})\cos n\theta,w_m\right\rangle A_{l,n}^{(j)}-\left\langle H_n^{(j)}(k_{l+1}\hat{r})\cos n\theta,w_m\right\rangle A_{l+1,n}^{(j)}$$
$$=-\left\langle v_l^{ff}-v_{l+1}^{ff}\ ,\ w_m\right\rangle \tag{14a}$$

$$\sum_{n=0}^{\infty}\sum_{j=1,2}\mu_l\left\langle\frac{\partial}{\partial\hat{\boldsymbol{n}}}\left(H_n^{(j)}(k_l\hat{r})\cos n\theta\right),w_m\right\rangle A_{l,n}^{(j)}-\mu_{l+1}\left\langle\frac{\partial}{\partial\hat{\boldsymbol{n}}}\left(H_n^{(j)}(k_{l+1}\hat{r})\cos n\theta\right),w_m\right\rangle A_{l+1,n}^{(j)}$$
$$=-\left\langle\mu_l\frac{\partial v_l^{ff}}{\partial\hat{\boldsymbol{n}}}-\mu_{l+1}\frac{\partial v_{l+1}^{ff}}{\partial\hat{\boldsymbol{n}}}\ ,\ w_m\right\rangle \tag{14b}$$

or in matrix form, at each interface between the l^{th} and $(l+1)^{th}$ layer, for $l=1,2,3\ldots$:

$$\sum_{n=0}^{\infty}\sum_{j=1,2}\begin{bmatrix}\left\langle H_n^{(j)}(k_l\hat{r})\cos n\theta,w_m\right\rangle & -\left\langle H_n^{(j)}(k_{l+1}\hat{r})\cos n\theta,w_m\right\rangle\\ \mu_l\left\langle\frac{\partial}{\partial\hat{\boldsymbol{n}}}\left(H_n^{(j)}(k_l\hat{r})\cos n\theta\right),w_m\right\rangle & -\mu_{l+1}\left\langle\frac{\partial}{\partial\hat{\boldsymbol{n}}}\left(H_n^{(j)}(k_{l+1}\hat{r})\cos n\theta\right),w_m\right\rangle\end{bmatrix}\begin{Bmatrix}A_{l,n}^{(j)}\\A_{l+1,n}^{(j)}\end{Bmatrix}$$
$$=-\begin{Bmatrix}\left\langle v_l^{ff}-v_{l+1}^{ff}\ ,\ w_m\right\rangle\\ \left\langle\mu_l\frac{\partial v_l^{ff}}{\partial\hat{\boldsymbol{n}}}-\mu_{l+1}\frac{\partial v_{l+1}^{ff}}{\partial\hat{\boldsymbol{n}}}\ ,\ w_m\right\rangle\end{Bmatrix} \tag{14c}$$

Note that for the interface between layer $N-1$ and the (bottom, last) semi-infinite layer N, Eqns. (14a) and (14b) will have only the outgoing wave terms $A_{N,n}^{(1)},\ n=0,1,2\ldots$ and without the incoming wave terms $A_{N,n}^{(2)},\ n=0,1,2\ldots$

V. Numerical Implementation

In this section will demonstrate the numerical procedure used to apply to the system of complex equations derived in the last section, which uses the method of weighted residues. In studying the set of equations, it is observed that for an elastic half-space with $N\ (\geq 1)$ layers, there are $(N-1)$ interfaces in-between the layers, plus the topmost half-space with no elastic medium above.

At this topmost half-space surface, there is one set of zero-stress equations (at $z=0$) (Eqn. (3)) involving the wave coefficients in the topmost 1^{st} layer. At each of the $(N-1)$ interfaces in-between the layers, there are 2 sets of the stress and displacement continuity equations (Eqns. (4) and (5)). There is thus a total of $2(N-1)+1=2N-1$ equations. Each of the top $(N-1)$ layers has two sets of waves, the upward and downward going, or the outgoing and incoming waves (Eqn. (1)). They are represented by Hankel functions of the 1st and 2nd kind, the outgoing and incoming waves, respectively. On the other hand, the bottom-most semi-infinite layer has only one set of waves, the downward going or outgoing waves (Eqn. (2)). They are represented by Hankel functions of the 1st kind. This gives a total of $2(N-1)+1=2N-1$ set of waves from all the layers.

In summary, we have $(2N-1)$ set of equations for $(2N-1)$ set of waves. If each of such $(2N-1)$ set of waves has *M* terms, with *M* unknown coefficients, we will have a total of $M\times(2N-1)$ unknowns we need to solve. Ideally each set of waves has, $M=\infty$, or infinite number of terms and there are $\infty\times(2N-1)$ number of equations. In reality, we have to truncate those to finitely many *M* terms for each set of waves, with the number *M* often dependent on the frequency of the waves and the complexity of the equations. With *M* finite, we have a task of solving the $M\times(2N-1)$ set of complex equations for the $M\times(2N-1)$ set of unknowns.

Numerically, we know that the Hankel functions of both the 1st and 2nd kinds are both complex, and increase in magnitudes with increasing order. Thus if all the $\boldsymbol{M\times(2N-1)}$ unknowns are put together in the $\boldsymbol{M\times(2N-1)}$ complex equations, one would have a very large set of complex equations to solve, whose terms often have increasing magnitudes with increasing *M*. It would be very difficult to solve them all at once.

Since each set of equations at each interface involves only waves at each side of the interface, a simple, elegant numerical algorithm can be derived to allow each set of wave coefficients at each media to be solved separately, making the problem more simple numerically. In other words, we are solving *M* complex equation in *M* unknowns at each step. The following is a comprehensive description of this numerical procedure.

The idea is very simple. Starting from the top surface, where $\boldsymbol{z=0}$, we have the matrix equation for the zero-stress boundary condition along the whole (regular and irregular) surface of the half-space, in the form:

$$\left[\boldsymbol{E}_1\right]\left\{\tilde{\boldsymbol{A}}_1^{(1)}\right\} + \left[\boldsymbol{E}_1^*\right]\left\{\tilde{\boldsymbol{A}}_1^{(2)}\right\} + \left\{\tilde{\boldsymbol{e}}_1\right\}\Big|_{z=0} = \boldsymbol{0} \tag{15a}$$

where from Eqn. (13b):

$\left[\boldsymbol{E}_1\right]$ is the matrix with elements $\left\langle \dfrac{\partial}{\partial \hat{\boldsymbol{n}}}\left(\boldsymbol{H}_n^{(1)}(\boldsymbol{k}_1\hat{\boldsymbol{r}})\cos n\theta\right), \boldsymbol{w}_m \right\rangle$,

$\left[\boldsymbol{E}_1^*\right]$ is similarly the matrix with elements $\left\langle \dfrac{\partial}{\partial \hat{\boldsymbol{n}}}\left(\boldsymbol{H}_n^{(2)}(\boldsymbol{k}_1\hat{\boldsymbol{r}})\cos n\theta\right), \boldsymbol{w}_m \right\rangle$

$\left\{\tilde{\boldsymbol{A}}_1^{(1)}\right\}$, $\left\{\tilde{\boldsymbol{A}}_1^{(2)}\right\}$ are respectively the vectors $\left\{\boldsymbol{A}_{10}^{(1)}, \boldsymbol{A}_{11}^{(1)}, \boldsymbol{A}_{12}^{(1)}, \ldots\right\}$, $\left\{\boldsymbol{A}_{10}^{(2)}, \boldsymbol{A}_{11}^{(2)}, \boldsymbol{A}_{12}^{(2)}, \ldots\right\}$ and (15b)

$\left\{\tilde{\boldsymbol{e}}_1\right\}$ is the vector $\left\langle \dfrac{\partial \boldsymbol{v}_1^{ff}}{\partial \hat{\boldsymbol{n}}}, \boldsymbol{w}_m \right\rangle$

Eliminating $\left\{\tilde{\boldsymbol{A}}_1^{(2)}\right\}$, one has, at $\boldsymbol{z=0}$:

$$\begin{aligned} \left\{\tilde{\boldsymbol{A}}_1^{(2)}\right\} &= -\left[\boldsymbol{E}_1^*\right]^{-1}\left(\left[\boldsymbol{E}_1\right]\left\{\tilde{\boldsymbol{A}}_1^{(1)}\right\} + \left\{\tilde{\boldsymbol{e}}_1\right\}\right)\Big|_{z=0} \\ &= -\left[\boldsymbol{E}_1^*(0)\right]^{-1}\left(\left[\boldsymbol{E}_1(0)\right]\left\{\tilde{\boldsymbol{A}}_1^{(1)}\right\} + \left\{\tilde{\boldsymbol{e}}_1(0)\right\}\right) \end{aligned} \tag{16}$$

In the interface between the 1st and 2nd layer, the continuity equations take the form:

$$\left[E_1\right]\left\{\tilde{A}_1^{(1)}\right\} + \left[E_1^*\right]\left\{\tilde{A}_1^{(2)}\right\} + \left\{\tilde{e}_1\right\}\Big|_{z=h_1} = \left[E_2\right]\left\{\tilde{A}_2^{(1)}\right\} + \left[E_2^*\right]\left\{\tilde{A}_2^{(2)}\right\} + \left\{\tilde{e}_2\right\}\Big|_{z=h_1}, \text{ or}$$

$$\begin{aligned}&\left[E_1(h_1)\right]\left\{\tilde{A}_1^{(1)}\right\} + \left[E_1^*(h_1)\right]\left\{\tilde{A}_1^{(2)}\right\} + \left\{\tilde{e}_1(h_1)\right\} \\ &= \left[E_2(h_1)\right]\left\{\tilde{A}_2^{(1)}\right\} + \left[E_2^*(h_1)\right]\left\{\tilde{A}_2^{(2)}\right\} + \left\{\tilde{e}_2(h_1)\right\}\end{aligned} \tag{17}$$

for stress continuity. Similarly, for the displacement continuity equations:

$$\begin{aligned}&\left[D_1(h_1)\right]\left\{\tilde{A}_1^{(1)}\right\} + \left[D_1^*(h_1)\right]\left\{\tilde{A}_1^{(2)}\right\} + \left\{\tilde{d}_1(h_1)\right\} \\ &= \left[D_2(h_1)\right]\left\{\tilde{A}_2^{(1)}\right\} + \left[D_2^*(h_1)\right]\left\{\tilde{A}_2^{(2)}\right\} + \left\{\tilde{d}_2(h_1)\right\}\end{aligned} \tag{18}$$

Using Eqn. (16), $\left\{\tilde{A}_1^{(2)}\right\}$ can be eliminated from the L.H.S. of the stress Eqn. (17):

$$\begin{aligned}&\left[E_1(h_1)\right]\left\{\tilde{A}_1^{(1)}\right\} + \left[E_1^*(h_1)\right]\left\{\tilde{A}_1^{(2)}\right\} + \left\{\tilde{e}_1(h_1)\right\} \\ &\left[E_1(h_1)\right]\left\{\tilde{A}_1^{(1)}\right\} + \left[E_1^*(h_1)\right]\left(-\left[E_1^*(0)\right]^{-1}\left(\left[E_1(0)\right]\left\{\tilde{A}_1^{(1)}\right\} + \left\{\tilde{e}_1(0)\right\}\right)\right) + \left\{\tilde{e}_1(h_1)\right\} \\ &= \left[\mathcal{E}_1(h_1)\right]\left\{\tilde{A}_1^{(1)}\right\} + \left\{\tilde{e}_1(h_1)\right\}\end{aligned} \tag{19a}$$

where

$$\begin{aligned}\left[\mathcal{E}_1(h_1)\right] &= \left[E_1(h_1)\right] - \left[E_1^*(h_1)\right]\left[E_1^*(0)\right]^{-1}\left[E_1(0)\right] \\ \left\{\tilde{e}_1(h_1)\right\} &= \left\{\tilde{e}_1(h_1)\right\} - \left[E_1^*(h_1)\right]\left[E_1^*(0)\right]^{-1}\left\{\tilde{e}_1(0)\right\}\end{aligned} \tag{19b}$$

In exactly the same way, $\left\{\tilde{A}_1^{(2)}\right\}$ can be eliminated from the L.H.S. of the displacement Eqn. (18), resulting in:

$$\begin{aligned}&\left[D_1(h_1)\right]\left\{\tilde{A}_1^{(1)}\right\} + \left[D_1^*(h_1)\right]\left\{\tilde{A}_1^{(2)}\right\} + \left\{\tilde{d}_1(h_1)\right\} \\ &\left[D_1(h_1)\right]\left\{\tilde{A}_1^{(1)}\right\} + \left[D_1^*(h_1)\right]\left(-\left[E_1^*(0)\right]^{-1}\left(\left[E_1(0)\right]\left\{\tilde{A}_1^{(1)}\right\} + \left\{\tilde{e}_1(0)\right\}\right)\right) + \left\{\tilde{d}_1(h_1)\right\} \\ &= \left[\mathcal{D}_1(h_1)\right]\left\{\tilde{A}_1^{(1)}\right\} + \left\{\tilde{d}_1(h_1)\right\}\end{aligned} \tag{20a}$$

where

$$\begin{aligned}\left[\mathcal{D}_1(h_1)\right] &= \left[D_1(h_1)\right] - \left[D_1^*(h_1)\right]\left[E_1^*(0)\right]^{-1}\left[E_1(0)\right] \\ \left\{\tilde{d}_1(h_1)\right\} &= \left\{\tilde{d}_1(h_1)\right\} - \left[D_1^*(h_1)\right]\left[E_1^*(0)\right]^{-1}\left\{\tilde{e}_1(0)\right\}\end{aligned} \tag{20b}$$

The continuity matrix equations at the interface of the 1st and 2nd layer now take the form, without the $\left\{\tilde{A}_1^{(2)}\right\}$ terms:

$$\begin{aligned}&\left[\mathcal{E}_1(h_1)\right]\left\{\tilde{A}_1^{(1)}\right\} + \left\{\tilde{e}_1(h_1)\right\} \\ &\quad = \left[E_2(h_1)\right]\left\{\tilde{A}_2^{(1)}\right\} + \left[E_2^*(h_1)\right]\left\{\tilde{A}_2^{(2)}\right\} + \left\{\tilde{e}_2(h_1)\right\}\end{aligned} \tag{21a}$$

$$\begin{aligned}&\left[\mathcal{D}_1(h_1)\right]\left\{\tilde{A}_1^{(1)}\right\} + \left\{\tilde{d}_1(h_1)\right\} \\ &\quad = \left[D_2(h_1)\right]\left\{\tilde{A}_2^{(1)}\right\} + \left[D_2^*(h_1)\right]\left\{\tilde{A}_2^{(2)}\right\} + \left\{\tilde{d}_2(h_1)\right\}\end{aligned} \tag{21b}$$

In matrix form, Eqns. (21a) and (21b) become:

$$\begin{bmatrix} E_2(h_1) & E_2^*(h_1) \\ D_2(h_1) & D_2^*(h_1) \end{bmatrix}\begin{Bmatrix} \tilde{A}_2^{(1)} \\ \tilde{A}_2^{(2)} \end{Bmatrix} = \begin{bmatrix} \mathcal{E}_1(h_1) \\ \mathcal{D}_1(h_1) \end{bmatrix}\left\{\tilde{A}_1^{(1)}\right\} + \begin{Bmatrix} \tilde{e}_1(h_1) - \tilde{e}_2(h_1) \\ \tilde{d}_1(h_1) - \tilde{d}_2(h_1) \end{Bmatrix} \tag{22}$$

which shows that both $\left\{\tilde{A}_2^{(1)}\right\}$ and $\left\{\tilde{A}_2^{(2)}\right\}$ of the coefficients of the waves in the 2nd layer can be expressed in terms of the single set of $\left\{\tilde{A}_1^{(1)}\right\}$ coefficients of waves in the top layer. One can thus write:

$$\begin{Bmatrix} \tilde{A}_2^{(1)} \\ \tilde{A}_2^{(2)} \end{Bmatrix} = \begin{bmatrix} E_2(h_1) & E_2^*(h_1) \\ D_2(h_1) & D_2^*(h_1) \end{bmatrix}^{-1}\left(\begin{bmatrix} \mathcal{E}_1(h_1) \\ \mathcal{D}_1(h_1) \end{bmatrix}\left\{\tilde{A}_1^{(1)}\right\} + \begin{Bmatrix} \tilde{e}_1(h_1) - \tilde{e}_2(h_1) \\ \tilde{d}_1(h_1) - \tilde{d}_2(h_1) \end{Bmatrix}\right) \tag{23a}$$

so that such a transformation is obtained:

$$\begin{Bmatrix} \tilde{A}_2^{(1)} \\ \tilde{A}_2^{(2)} \end{Bmatrix} = \left(\begin{bmatrix} \mathcal{T}_{21}(h_1) \\ \mathcal{T}_{22}(h_1) \end{bmatrix}\left\{\tilde{A}_1^{(1)}\right\} + \begin{Bmatrix} \tilde{t}_{21}(h_1) \\ \tilde{t}_{22}(h_1) \end{Bmatrix}\right) \tag{23b}$$

Repeating this iteration at each interface of layers proceeding downwards one can start with the continuity equations at interface between layer *l* and *l+1*, as in Eqns. (18a,b), at the interface $z = h_l$:

$$\begin{aligned}&\left[E_l(h_l)\right]\left\{\tilde{A}_l^{(1)}\right\} + \left[E_l^*(h_l)\right]\left\{\tilde{A}_l^{(2)}\right\} + \left\{\tilde{e}_l(h_l)\right\} \\ &\quad = \left[E_{l+1}(h_l)\right]\left\{\tilde{A}_{l+1}^{(1)}\right\} + \left[E_{l+1}^*(h_{l+1})\right]\left\{\tilde{A}_{l+1}^{(2)}\right\} + \left\{\tilde{e}_{l+1}(h_l)\right\}\end{aligned} \tag{24a}$$

$$\begin{aligned}&\left[D_l(h_l)\right]\left\{\tilde{A}_l^{(1)}\right\} + \left[D_l^*(h_l)\right]\left\{\tilde{A}_l^{(2)}\right\} + \left\{\tilde{d}_l(h_l)\right\}\\ &\quad = \left[D_{l+1}(h_l)\right]\left\{\tilde{A}_{l+1}^{(1)}\right\} + \left[D_{l+1}^*(h_l)\right]\left\{\tilde{A}_{l+1}^{(2)}\right\} + \left\{\tilde{d}_{l+1}(h_l)\right\}\end{aligned} \tag{24b}$$

As in Eqn. (23b), $\left\{\tilde{A}_l^{(1)}\right\}$ and $\left\{\tilde{A}_l^{(2)}\right\}$ are to be expressed in terms of $\left\{\tilde{A}_1^{(1)}\right\}$:

$$\begin{Bmatrix}\tilde{A}_l^{(1)}\\ \tilde{A}_l^{(2)}\end{Bmatrix} = \left(\begin{bmatrix}T_{l1}(h_l)\\ T_{l2}(h_l)\end{bmatrix}\left\{\tilde{A}_1^{(1)}\right\} + \begin{Bmatrix}\tilde{t}_{l1}(h_l)\\ \tilde{t}_{l2}(h_l)\end{Bmatrix}\right) \tag{25}$$

from which Eqns. (24a,b) can be expressed as, with the coefficients $\left\{\tilde{A}_1^{(1)}\right\}$ of waves in the top layer on the R.H.S.:

$$\begin{aligned}&\left[E_l(h_l)\right]\left\{\tilde{A}_1^{(1)}\right\} + \left\{\tilde{e}_l(h_l)\right\}\\ &\quad = \left[E_{l+1}(h_l)\right]\left\{\tilde{A}_{l+1}^{(1)}\right\} + \left[E_{l+1}^*(h_l)\right]\left\{\tilde{A}_{l+1}^{(2)}\right\} + \left\{\tilde{e}_{l+1}(h_l)\right\}\end{aligned} \tag{26a}$$

$$\begin{aligned}&\left[D_l(h_l)\right]\left\{\tilde{A}_1^{(1)}\right\} + \left\{\tilde{d}_l(h_l)\right\}\\ &\quad = \left[D_{l+1}(h_l)\right]\left\{\tilde{A}_{l+1}^{(1)}\right\} + \left[D_{l+1}(h_l)\right]\left\{\tilde{A}_{l+1}^{(2)}\right\} + \left\{\tilde{d}_{l+1}(h_1)\right\}\end{aligned} \tag{26b}$$

or again in matrix form, as in Eqn. (23a):

$$\begin{bmatrix}E_{l+1}(h_l) & E_{l+1}^*(h_l)\\ D_{l+1}(h_l) & D_{L+1}^*(h_l)\end{bmatrix}\begin{Bmatrix}\tilde{A}_{l+1}^{(1)}\\ \tilde{A}_{l+1}^{(2)}\end{Bmatrix} = \begin{bmatrix}E_l(h_l)\\ D_l(h_l)\end{bmatrix}\left\{\tilde{A}_1^{(1)}\right\} + \begin{Bmatrix}\tilde{e}_l(h_l) - \tilde{e}_{l+1}(h_l)\\ \tilde{d}_l(h_l) - \tilde{d}_{l+1}(h_l)\end{Bmatrix} \tag{27a}$$

resulting in a transformation, as in Equation (23b), expressing the coefficients $\left\{\tilde{A}_{l+1}^{(1)}\right\}$ and $\left\{\tilde{A}_{l+1}^{(2)}\right\}$ for layer *(l+1)* to be expressed in terms of $\left\{\tilde{A}_1^{(1)}\right\}$ from waves of the top layer.

$$\begin{Bmatrix}\tilde{A}_{l+1}^{(1)}\\ \tilde{A}_{l+1}^{(2)}\end{Bmatrix} = \left(\begin{bmatrix}T_{l+1,1}(h_l)\\ T_{l+1,2}(h_l)\end{bmatrix}\left\{\tilde{A}_1^{(1)}\right\} + \begin{Bmatrix}\tilde{t}_{l+1,1}(h_l)\\ \tilde{t}_{l+1,2}(h_l)\end{Bmatrix}\right) \tag{27b}$$

The reason why we select to have the coefficients of all waves in each layer expressed in terms of (one of the two) a set of coefficients of waves n the top layer is because, we know, for surface waves, that the top layer waves are dominant.

The above described procedure will continue until the interface with the bottom semi-infinite layer $l = N$ is reached, namely at $z = h_{N-1}$. There the continuity equations will be different from those in the previous interfaces, since the bottom semi-infinite layer will now have only one set of waves, namely, the downward, outgoing waves. The stress and displacement continuity equations now take the form, as in Eqn. (24a,b), with $l = N-1,\ l+1 = N$:

$$\begin{aligned}\left[E_{N-1}(h_{N-1})\right]\left\{\tilde{A}_{N-1}^{(1)}\right\} + \left[E_{N-1}^{*}(h_{N-1})\right]\left\{\tilde{A}_{N-1}^{(2)}\right\} + \left\{\tilde{e}_{N-1}(h_{N-1})\right\} \\ = \left[E_{N}(h_{N-1})\right]\left\{\tilde{A}_{N}^{(1)}\right\} + \left\{\tilde{e}_{N}(h_{N-1})\right\}\end{aligned} \tag{26a}$$

$$\begin{aligned}\left[D_{N-1}(h_{N-1})\right]\left\{\tilde{A}_{N-1}^{(1)}\right\} + \left[D_{N-1}^{*}(h_{N-1})\right]\left\{\tilde{A}_{N-1}^{(2)}\right\} + \left\{\tilde{d}_{N-1}(h_{N-1})\right\} \\ = \left[D_{N}(h_{N-1})\right]\left\{\tilde{A}_{N}^{(1)}\right\} + \left\{\tilde{d}_{N}(h_{N-1})\right\}\end{aligned} \tag{26b}$$

As before, the coefficients $\left\{\tilde{A}_{N-1}^{(1)}\right\}$ and $\left\{\tilde{A}_{N-1}^{(2)}\right\}$ of the waves in the $(N-1)^{th}$ layer can be expressed in terms of $\left\{\tilde{A}_{1}^{(1)}\right\}$, that of the waves in the top layer

$$\begin{aligned}\left[\mathcal{E}_{N-1}(h_{N-1})\right]\left\{\tilde{A}_{1}^{(1)}\right\} + \left\{\tilde{e}_{N-1}(h_{N-1})\right\} \\ = \left[E_{N}(h_{N-1})\right]\left\{\tilde{A}_{N}^{(1)}\right\} + \left\{\tilde{e}_{N}(h_{N-1})\right\}\end{aligned} \tag{27a}$$

$$\begin{aligned}\left[\mathcal{D}_{N-1}(h_{N-1})\right]\left\{\tilde{A}_{1}^{(1)}\right\} + \left\{\tilde{d}_{N-1}(h_{N-1})\right\} \\ = \left[D_{N}(h_{N-1})\right]\left\{\tilde{A}_{N}^{(1)}\right\} + \left\{\tilde{d}_{N}(h_{N-1})\right\}\end{aligned} \tag{27b}$$

with new matrices $\left[\mathcal{E}_{N-1}(h_{N-1})\right]$, $\left[\mathcal{D}_{N-1}(h_{N-1})\right]$ and vectors $\left\{\tilde{e}_{N-1}(h_{N-1})\right\}$, $\left\{\tilde{d}_{N-1}(h_{N-1})\right\}$ in terms of $\left\{\tilde{A}_{1}^{(1)}\right\}$, the wave coefficients of the top layer, on the L.H.S. of the equations.

Equations (27a) and (27b) are the final form of the matrix equations, from which the wave coefficients $\left\{\tilde{A}_{1}^{(1)}\right\}$ of the top layer and $\left\{\tilde{A}_{N}^{(1)}\right\}$ in the bottom semi-infinite layer

are to be related. Normally, one will rewrite Eqns. (27a), expressing $\left\{\tilde{\boldsymbol{A}}_{\mathrm{N}}^{(\mathrm{l})}\right\}$ in terms of $\left\{\tilde{\boldsymbol{A}}_{1}^{(1)}\right\}$, as:

$$\left\{\tilde{\boldsymbol{A}}_{N}^{(1)}\right\} = \left[\boldsymbol{E}_{N}\left(\boldsymbol{h}_{N-1}\right)\right]^{-1}\left(\left[\boldsymbol{\mathcal{E}}_{N-1}(\boldsymbol{h}_{N-1})\right]\left\{\tilde{\boldsymbol{A}}_{1}^{(1)}\right\} + \left\{\tilde{\boldsymbol{e}}_{N-1}(\boldsymbol{h}_{N-1})\right\} - \left\{\tilde{\boldsymbol{e}}_{N}\left(\boldsymbol{h}_{N-1}\right)\right\}\right) \quad (28a)$$

And substituting it into Eqn. (27b), which becomes a matrix equation with $\left\{\tilde{\boldsymbol{A}}_{1}^{(1)}\right\}$ of the top layer as the only set of unknowns:

$$\begin{aligned}&\left(\left[\boldsymbol{\mathcal{D}}_{N-1}(\boldsymbol{h}_{N-1})\right]-\left[\boldsymbol{D}_{N}\left(\boldsymbol{h}_{N-1}\right)\right]\left[\boldsymbol{E}_{N}\left(\boldsymbol{h}_{N-1}\right)\right]^{-1}\left[\boldsymbol{\mathcal{E}}_{N-1}(\boldsymbol{h}_{N-1})\right]\right)\left\{\tilde{\boldsymbol{A}}_{1}^{(1)}\right\}\\ &= \left[\boldsymbol{D}_{N}\left(\boldsymbol{h}_{N-1}\right)\right]\left[\boldsymbol{E}_{N}\left(\boldsymbol{h}_{N-1}\right)\right]^{-1}\left\{\tilde{\boldsymbol{e}}_{N-1}(\boldsymbol{h}_{N-1})\right\}+\left\{\tilde{\boldsymbol{d}}_{N}\left(\boldsymbol{h}_{N-1}\right)\right\} - \left\{\tilde{\boldsymbol{d}}_{N-1}(\boldsymbol{h}_{N-1})\right\}\end{aligned} \quad (28b)$$

from which the coefficients $\left\{\tilde{\boldsymbol{A}}_{1}^{(1)}\right\}$ can now be evaluated, after which the coefficients of the waves in all layers can be found.

VI. The Diffracted Mode Shapes of Love and SH Body Waves

VI.1 The input free-field Waves

Recall Report I, where we considered an *N*-Layered half-space with Love waves or Body SH waves incident from the left into a regular parallel layered media (Report I, Figure **II.1**). In a sub-section of Chapter **V** in Report I we plotted the displacement mode shapes of Mode#1 to Mode#5 Love surface waves for a selected range of periods starting from 15 sec down to 0.04 sec (0.07Hz to 25Hz) This was followed by another sub-section of the mode shapes resulting from body SH waves for a given incident angle. For convenience in programming we take the body SH waves as the "6^{th} mode" of waves in the parallel layered media.

Each of these 6 mode shapes at each period (frequency) will be used as the free-field input waves into the irregular parallel layered media to be studies here. In what follows, we will take a rather simple 2-layered media to illustrate the process. The following parameters are used for the 2-layered media:

Table 1

2 Layer Velocity Model				
Layer	Thickness, km	P-wave Speed, α, km/s	S-wave Speed, β, km/s	Density, ρ gm/cc
1	1.38000	1.70000	.98000	1.28000
2	∞	6.40000	3.70000	2.71000

They are the same 1^{st} and last layers of the 6-layered model considered in Report I, except that the top layer is now 1.38 km thick. The computer Program, "Haskel.exe", is again used to calculate the phase velocities of each mode of Love waves, as in Report I, in the period range of periods from 14.0 sec down to 0.04 sec for a total of 91 discrete period values.

Figure VI.1 shows the input free-field Mode Shape for Mode#1 Love Waves at four selected periods, T = 5.0, 1.5, 0.5 and 0.01 sec, or at frequency, f = 0.20, 0.67, 2.0 and 10.0 Hz. As before, for Mode#1 waves, the Mode shapes are constructed at all 91 pre-selected period values. It is noted from the figures that, at all the periods shown, the wave amplitudes of the mode shapes are scaled to have a maximum amplitude of 1 at the half-space surface, and that the amplitudes are practically zero at and below the interface of the two layers, which is at 1.38km depth.

Figure VI.2 shows the input free-field Mode Shapes for the corresponding Mode#2 Love Waves at four selected period, T = 2.0, 1.0, 0.3 and 0.08 sec. For Mode#2 Love Waves, the modes do not exist at all 91 periods, but instead from T = 2.2 sec (Period#30). So the four periods plotted here are selected from a narrower range. As before, the mode shapes are scaled to have a maximum amplitude of 1 starting from the surface at $\boldsymbol{z = 0}$. A characteristic of the Mode#2 Love waves is that the Mode shape at each period now decreases to negative values, reaching a negative minimum before asymptotically approaching zero. Again, as for Mode#1, the amplitudes are practically zero at and below the interface of the two layers $\boldsymbol{(z = 1.38 km)}$.

Figure VI.3 illustrates the input free-field Mode Shapes for the corresponding Mode#3 Love Waves at four selected period, T = 1.0, 0.8, 0.4 and 0.08 sec. For Mode#3 Love Waves, the modes do not exist at all 91 periods, starting at T = 1.1 sec (Period#40). As before, the mode shapes are scaled to have a maximum amplitude of 1 starting from the surface $\boldsymbol{z = 0}$. A characteristic of the Mode#3 Love waves is that the Mode shape at each period decreases to negative values, reaches a negative minimum, and then crosses the zero axis back to positive amplitudes, before asymptotically approaching zero. Again, as for Mode#1 and Mode#2, the amplitudes are practically zero at and below the interface of the two layers $\boldsymbol{(z = 1.38 km)}$.

Figure VI.1 Mode#1 Mode Shapes at f = 0.20, 0.67, 2.0 and 10.0 Hz

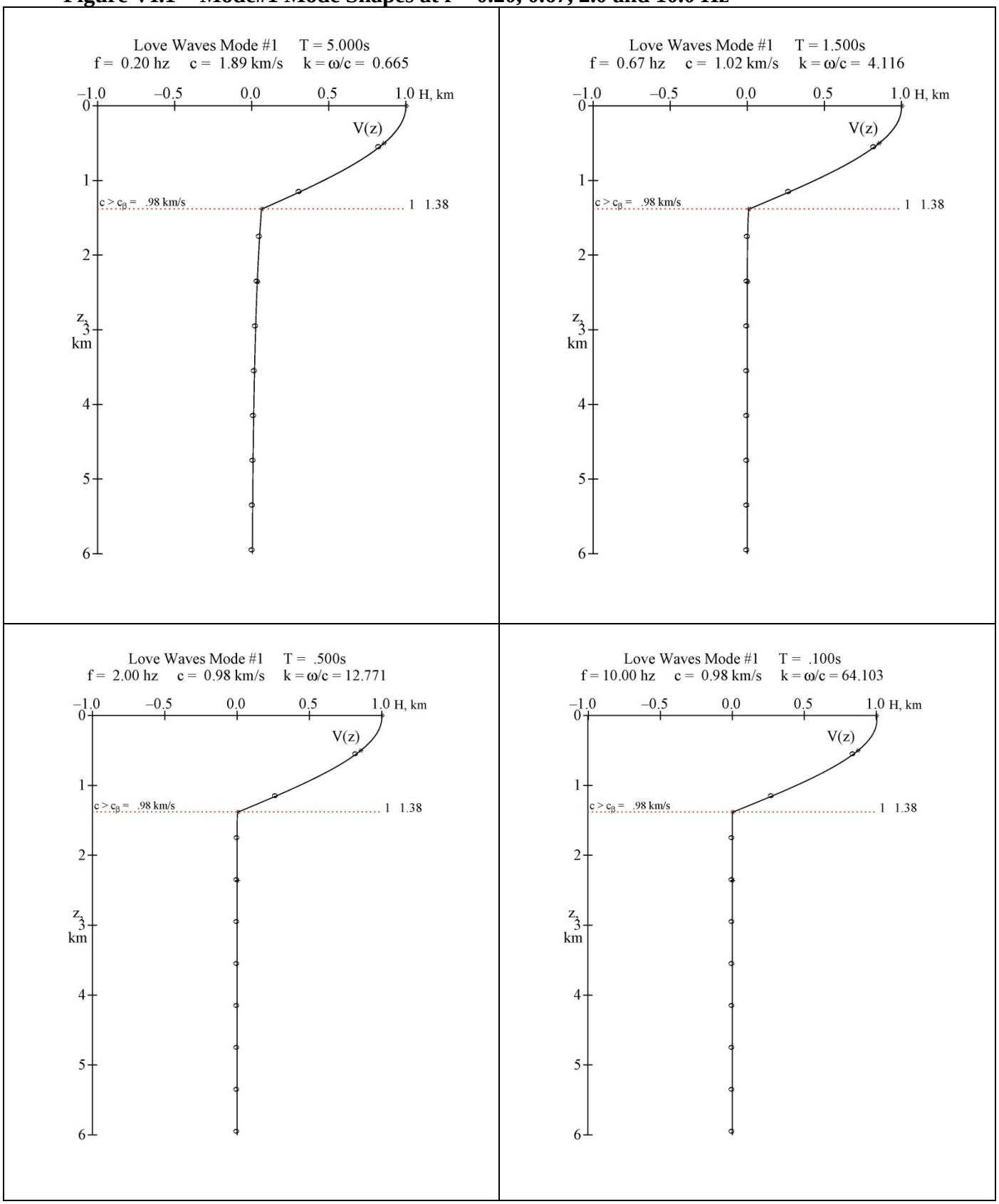

Figure VI.2 Mode#2 Mode Shapes at f = 0.50, 1.0, 3.33 and 12.5 Hz

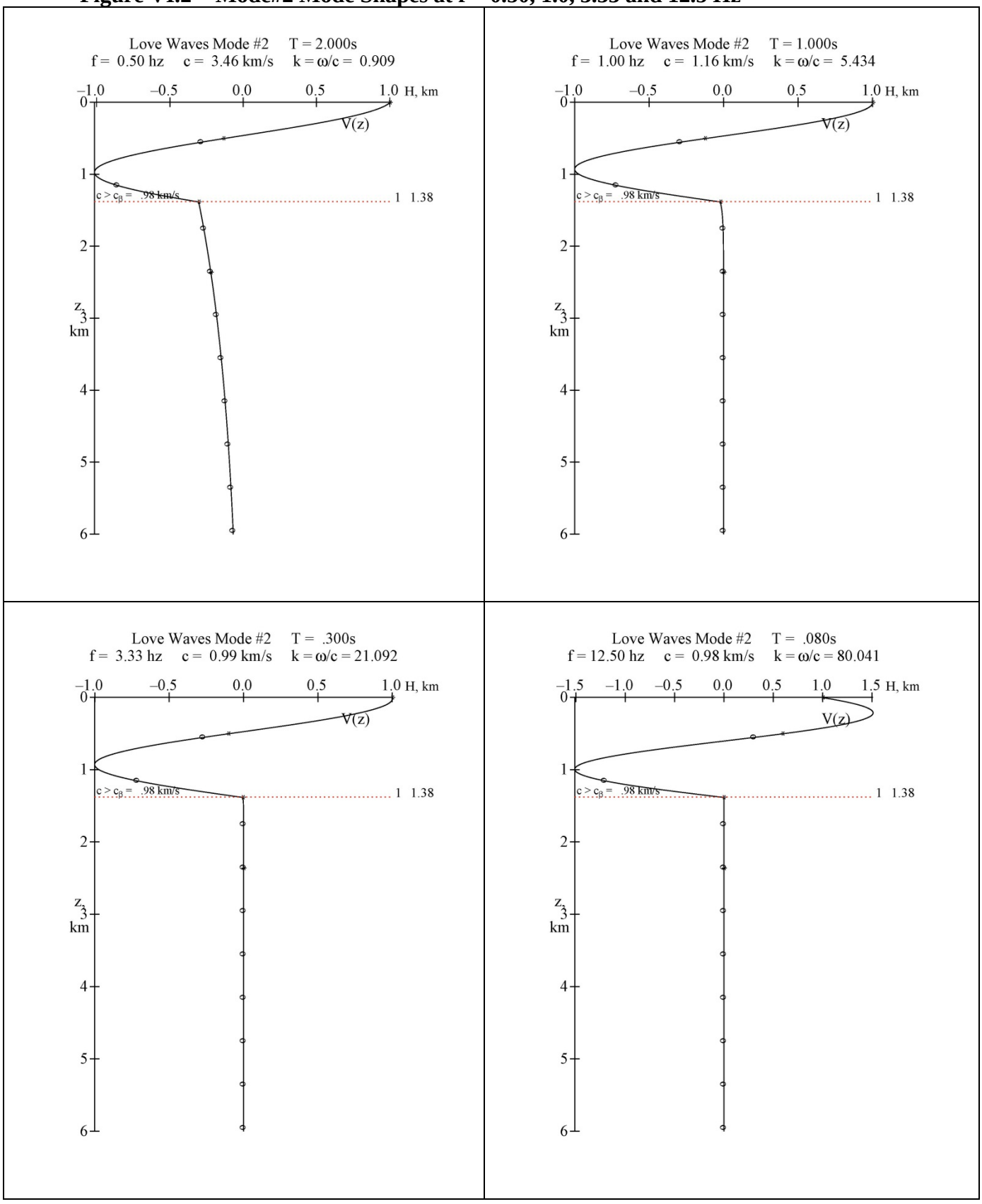

Figure VI.3 Mode#3 Mode Shapes at f = 1.0, 1.25, 2.50 and 12.50 Hz

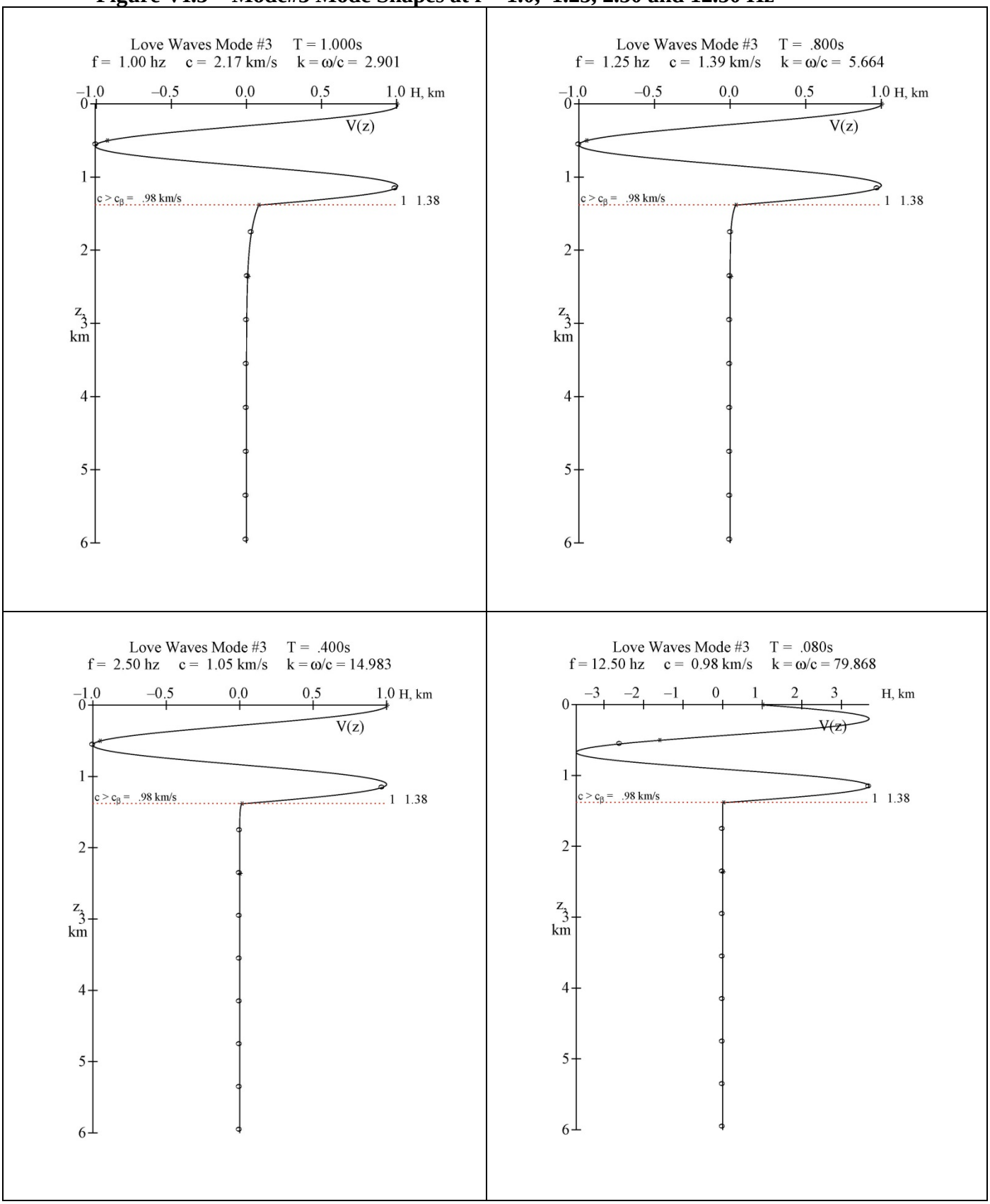

The same observations can be made for Modes #4 and #5 free-field Love waves. Their plots have been omitted here.

Finally, the free-field mode shapes for incident SH body waves are considered next. Figure VI.4 shows the input free-field Mode Shapes for the corresponding SH Body Waves with angle of incidence of $\gamma = 60^o$ with respect to the horizontal direction at four selected periods, T = 4.0, 1.0, 0.4 and 0.10 sec., or at frequency, f = 0.25, 1.0, 2.5 and 10.0 Hz. As in the case of Mode#1 Love waves, the Mode shapes exist at all 91 pre-selected period values. It is seen from the figures that, at all the periods shown, the wave amplitudes of the mode shapes are again scaled to have maximum amplitude of 1 at the half-space surface. Unlike the Love waves, depending on the period of the body waves, the waves do not decrease to zero deeper down from the surface. The waves in the first layer are harmonic, oscillating at the given period of the waves between the scaled maximum amplitude of ± 1, and the oscillation increases with decreasing period, or increasing frequency, as the figure shows.

Below the first layer, on the semi-infinite layer, it continues to oscillate, though at a higher period and lower amplitude, but they are not depreciating to zero, since the body waves are harmonic waves, harmonic in both the horizontal *x*- and vertical *z*- directions.

We thus will expect in the next sub-section that the diffracted waves from SH Body waves will behave differently from those from the Love surface waves.

Figure VI.4 SH Body Waves Mode Shapes at f=0.25, 1.0, 2.5 and 10.0 Hz

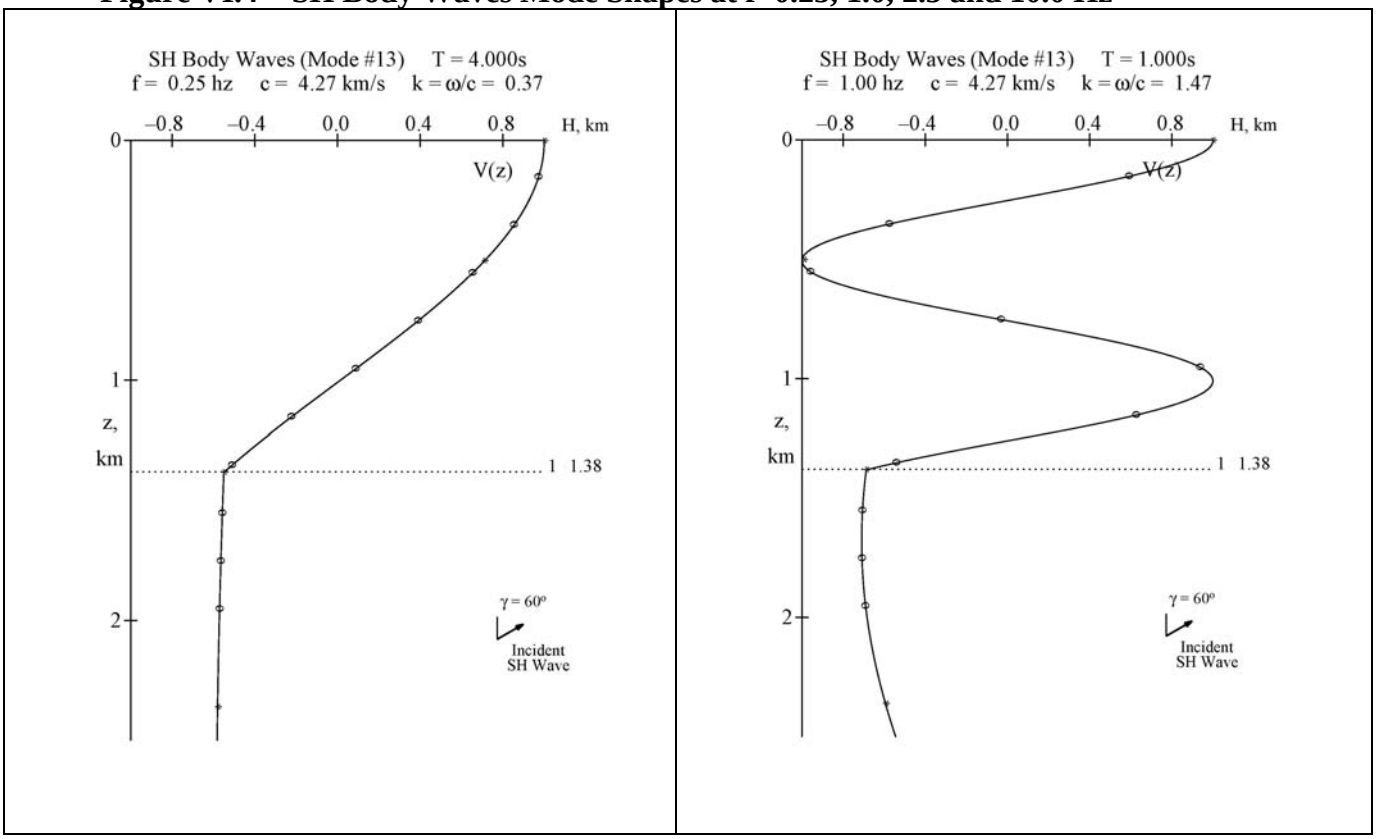

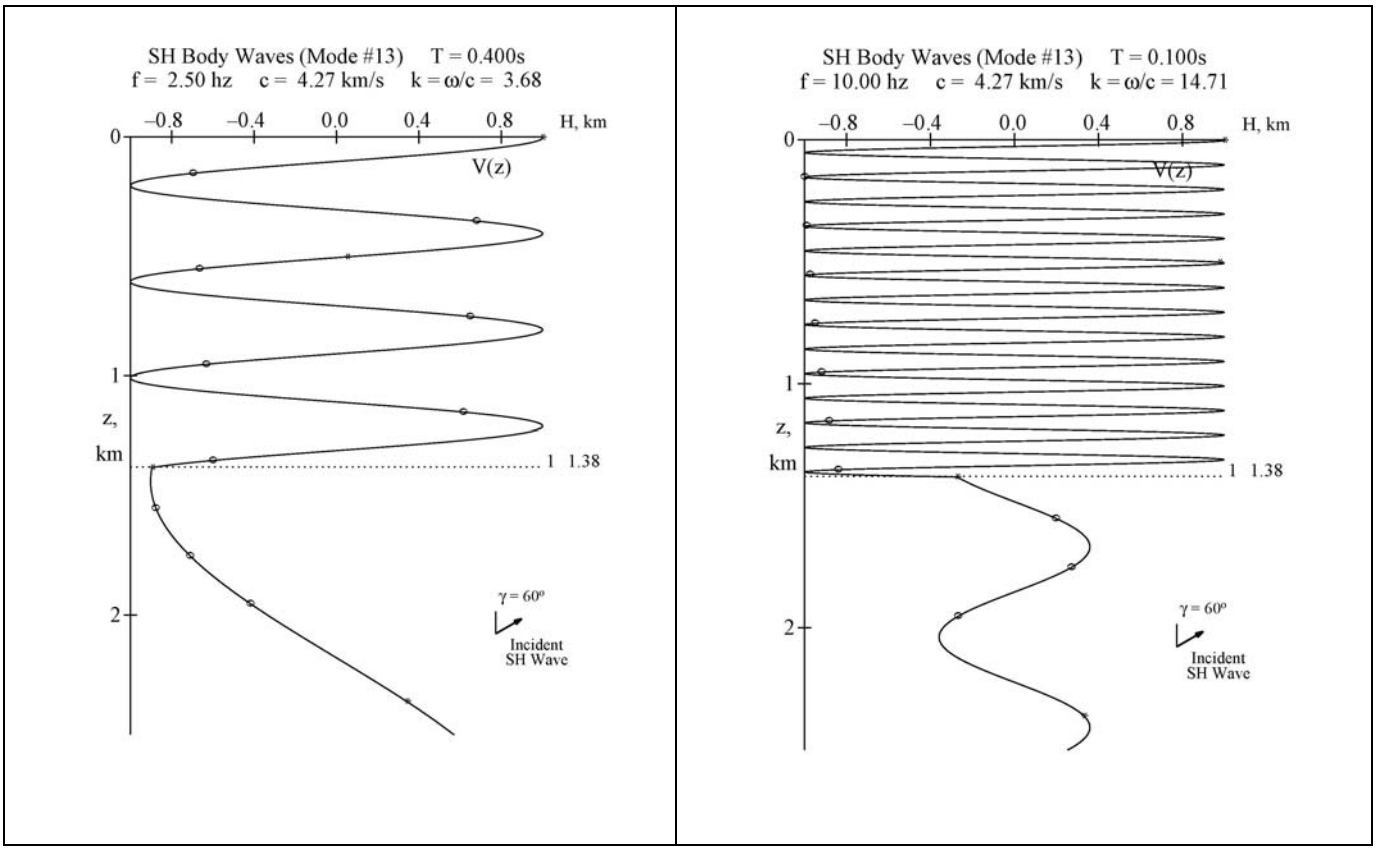

VI.2 The Diffracted Mode Shapes

We next consider the case of irregularly shaped layered media superimposed onto the parallel two-layered media. We select a shallow, "almost-flat" ellipse with a ratio of "Vertical minor axis / Horizontal major axis = 0.1" at both the half-space surface and at the interface of the two layers. The half-width or radius of the horizontal major axis is taken to be 1.0 km long for both, or a major diameter is 2.0 km long. Thus the half-width or radius of the minor axis is 0.1 km deep, the case of a very shallow ellipse. Figure VI.5 is a sketch of such a 2-Layered elastic media. We then consider:

i) Incident Love Surface waves, and

ii) Incident Body SH waves

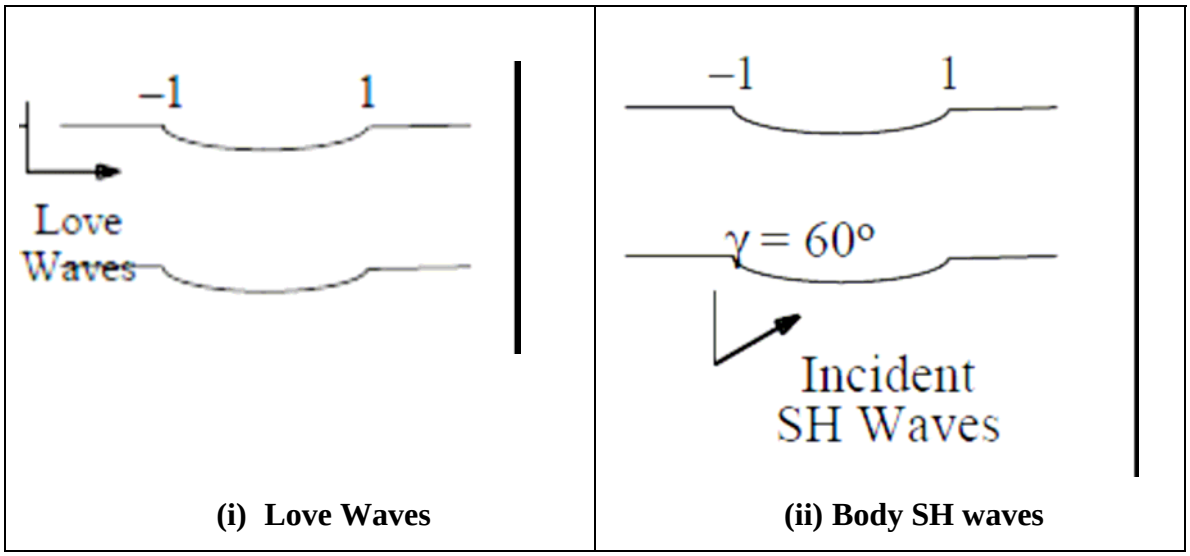

(i) Love Waves **(ii) Body SH waves**

Figure VI.5 The Irregular 2-Lyered Media with Incident SH Body Waves

The next five figures, Figure VI.6 to VI.10 show the diffracted mode shapes for Mode #1 to Mode#5 of Love Waves. Each Mode is plotted at four selected frequencies, f = 13.33, 18.18, 20.0 & 25.0 Hz. These are frequencies below the period of 0.1 sec (or frequency beyond 10Hz) as it was found that since the irregular part of the layer is small, the long period waves "do not see" the irregularities and the diffracted waves are small to insignificant.

Figure **IV.6** shows the Diffracted Mode Shapes for Mode#1 Love Waves at the above stated four selected frequencies. With the irregular almost-flat elliptic surfaces from $x = -1.0$ km to $x = +1.0$ km on both the half-space surface $(z = 0\,\text{km})$ and the surface of interface of the 2 media $(z = 1.38\,\text{km})$, the diffracted mode shapes are plotted at equally spaced intervals along x from $x = -2.0$ km to $x = +2.0$ km at 0.1 km apart. The dashed line on the left side of each graph represents the input free-field Mode shapes propagating along the parallel-layered media from the left, arriving at the irregular surfaces. For all frequencies up to almost 15.0 Hz, the waves are unaffected by the almost-flat irregular surfaces. At the irregular interfaces between the 2 media, as pointed out in the previous section, and as can also be seen from the dashed line on the left, the mode shape amplitudes are almost zero. That is, not much scattering and diffraction can be expected in this case.

As the frequencies of incident waves increase from 15.0 to 25.0 Hz, as in the next 3 graphs shown, where the frequencies are respectively, f = 18.18, 20.0 and 25.0 Hz, it is seen that the incident Love Waves experience some scattering and diffraction in the top layer. This is most noticeable for the 25 Hz mode shape in the lower right corner of this figure.

Figures **IV.7** through **IV.10** show the scattered and diffracted shapes for Mode#2 to Mode#5 Love Waves at the same four frequencies. The scattered and diffracted motions are more complex as the Mode Number increases.

In the future we will analyze the multi-layered media with the layers having more complex and larger irregularities. It is expected that for those the scattered and diffracted patterns will become more complicated, especially as the number of layers increase, and as the layers get closer and closer together. We will also use the complete synthetic motions in SYNACC, which will include all mode shapes simultaneously. The above elementary examples nevertheless illustrate the essence of the phenomena, which is easier to decipher in the presence of only one mode excitation.

Figure VI.6 Mode#1 Diffracted Mode Shapes at f = 13.33, 18.18, 20.0 & 25.0 Hz

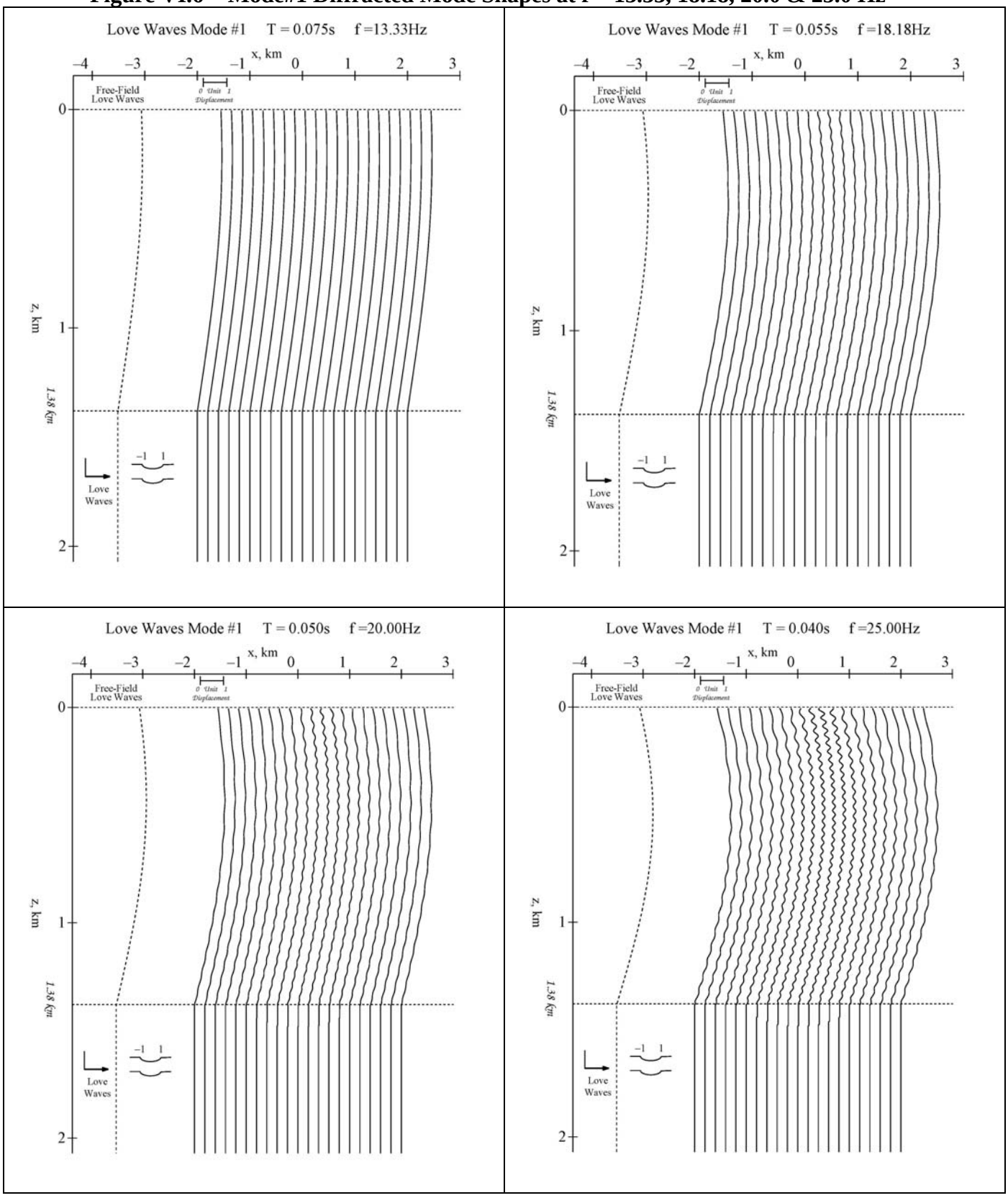

Figure VI.7 Mode#2 Diffracted Mode Shapes at f = 13.33, 18.18, 20.0 & 25.0 Hz

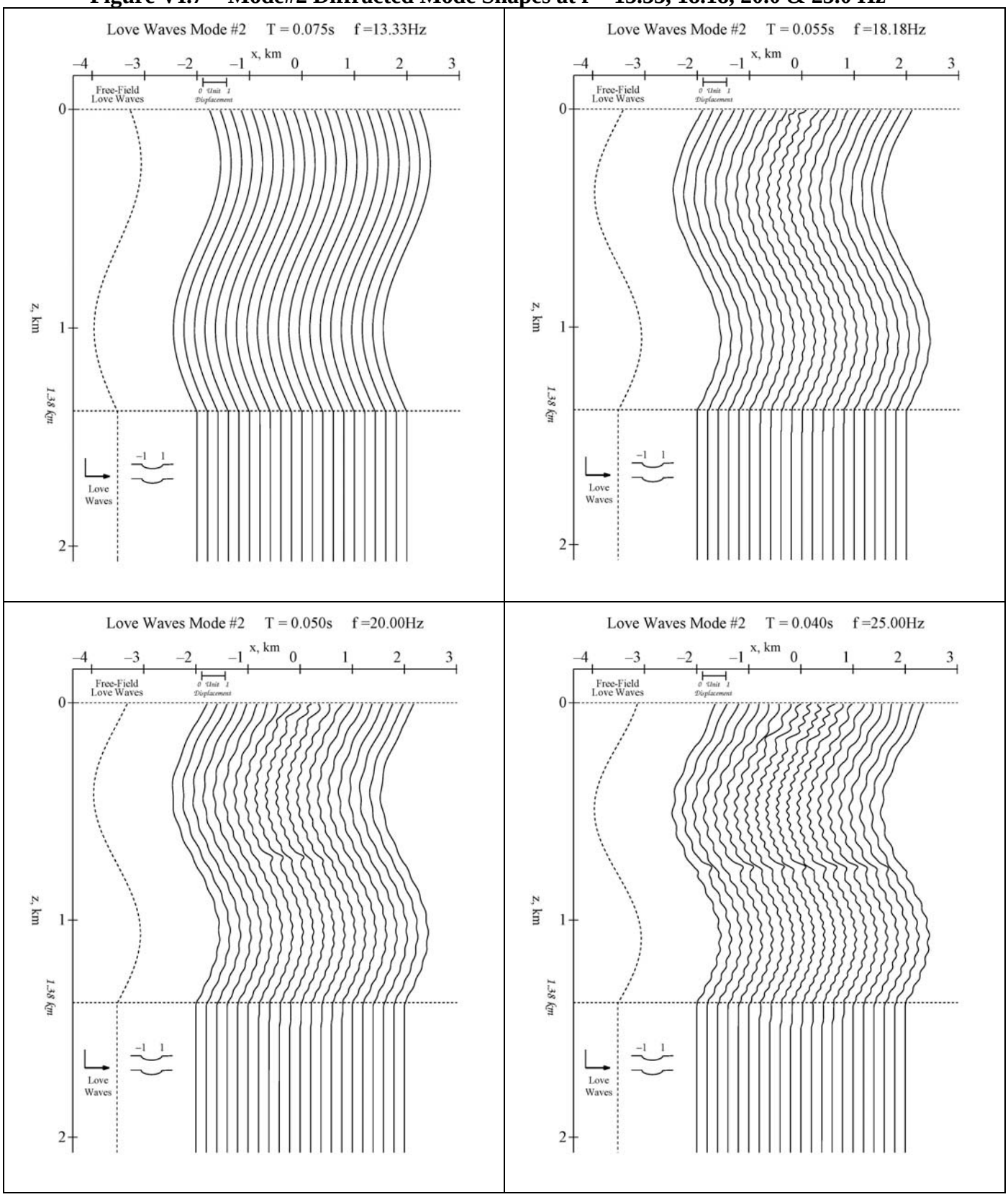

Figure VI.8 Mode#3 Diffracted Mode Shapes at f = 13.33, 18.18, 20.0 & 25.0 Hz

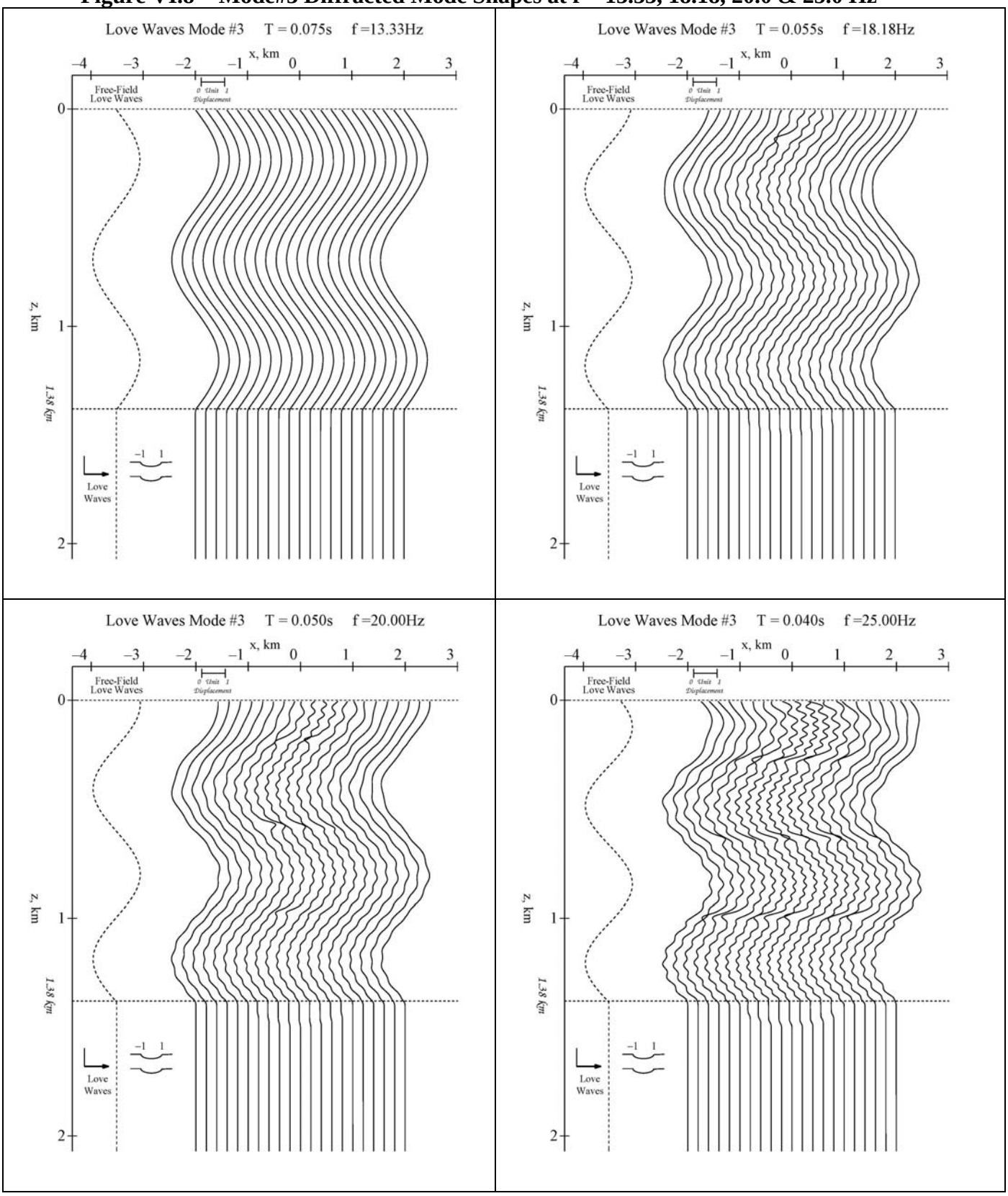

Figure VI.9 Mode#4 Diffracted Mode Shapes at f = 13.33, 18.18, 20.0 & 25.0 Hz

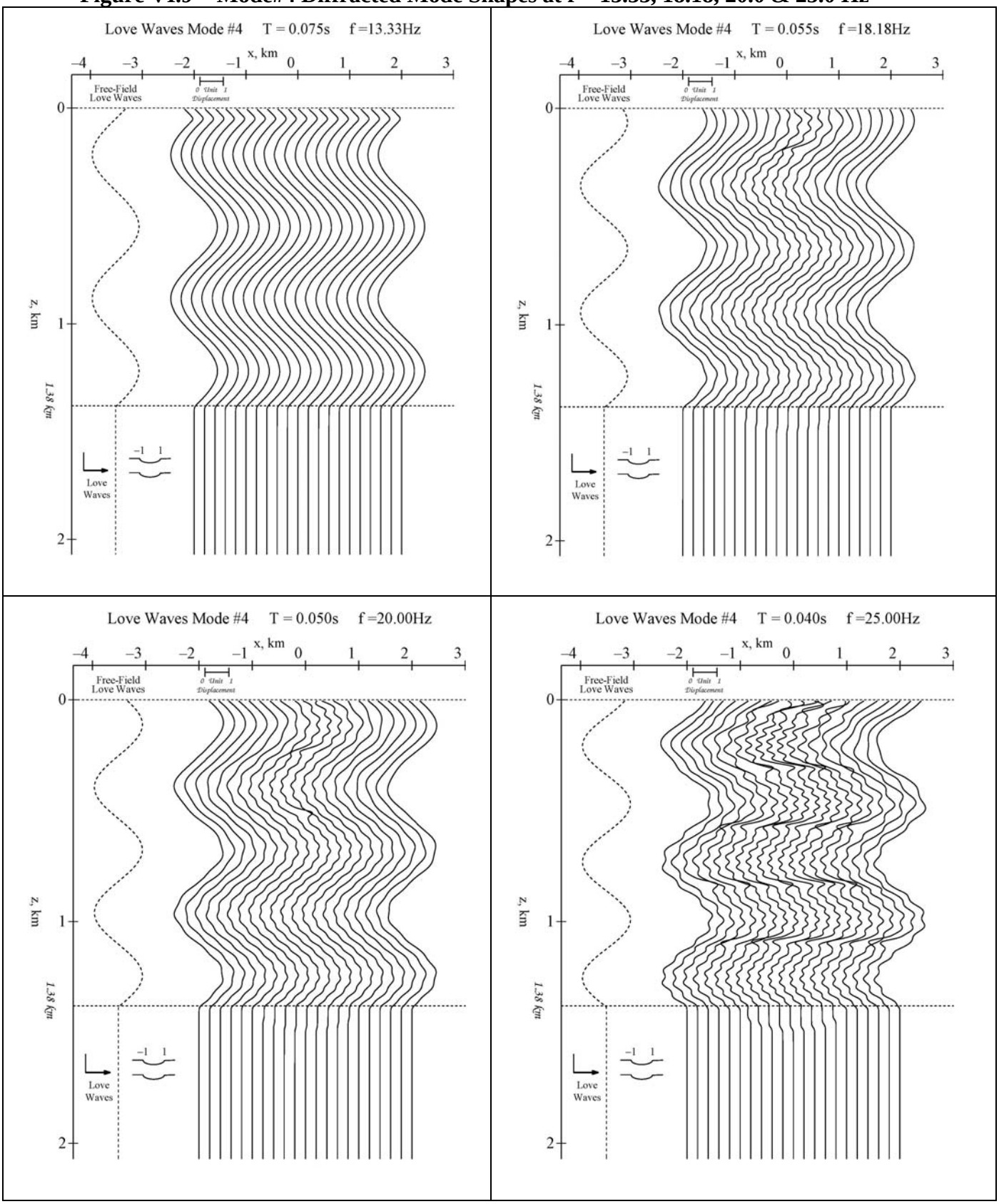

Figure VI.10 Mode#5 Diffracted Mode Shapes at f = 13.33, 18.18, 20.0 & 25.0 Hz

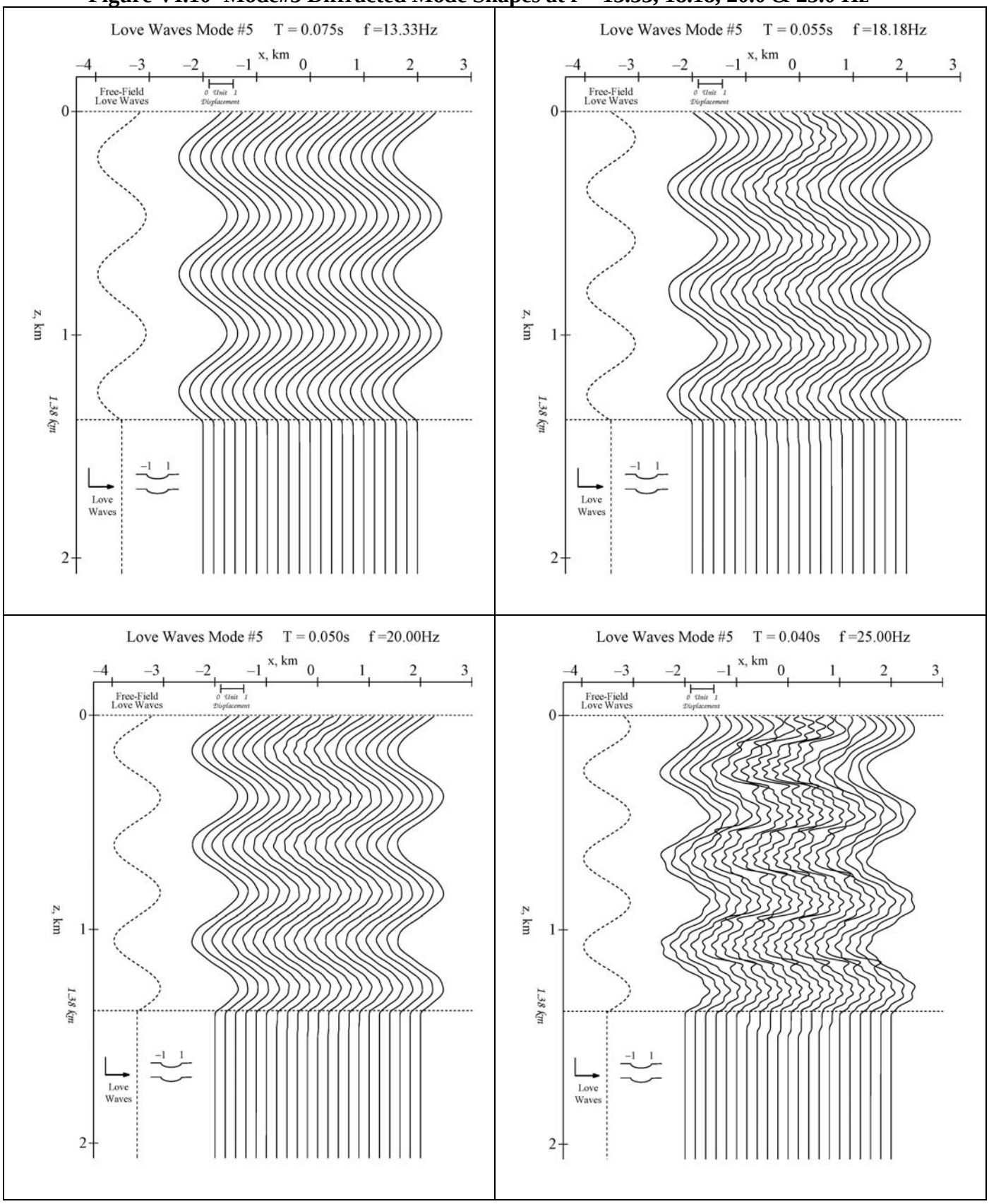

Figure **VI.11** shows the scattered and diffracted Mode Shapes corresponding to incident plane SH Body Waves. As seen from Figure **VI.4** above, the input free-field Body SH waves, unlike the Love waves, are oscillatory in both layers, and do not decrease to zero bellow the interface.

As with the examples for Love waves, the irregular almost-flat elliptic surfaces are from $x = -1.0$ km to $x = +1.0$ km on both the half-space surface $(z = 0\,\text{km})$ and the surface of interface of the 2 media $(z = 1.38\,\text{km})$. The scattered and diffracted mode shapes are again plotted at equally spaced intervals along x from $x = -2.0$ km to $x = +2.0$ km at 0.1 km apart. Again, the dashed line on the left side of each graph represents the input free-field mode shapes of body SH waves propagating through the parallel-layered media from below and arriving at the irregular surfaces. The angle of incidence of the body waves is assumed to be $\gamma = 60^o$ with respect to the horizontal. At all frequencies, the mode shapes of the scattered and diffracted waves are oscillatory and have different amplitudes.

As the frequencies of the waves increase from 15.0 to 25.0 Hz, as the next 3 graphs show, where the frequencies are respectively, f = 18.18, 20.0 and 25.0 Hz, it is seen that the body SH waves experience large scattering and diffraction in both the top layer and in the semi-infinite media. The amplification of the mode amplitudes for the examples shown gets greater than two. Table 2 illustrates the amplification factors at selected frequencies

Table 2

Frequency, Hz	16.67	18.18	20.00	20.83	21.74	22.73	23.81	25.00
Amplification	2.61	2.56	2.58	2.61	2.63	2.57	2.70	2.57

In the future work we will analyze the multi-layered media with more layers and with the layers being closer together. It is expected that the scattered and diffracted patterns will be much more complicated as the number of layers increase, as the irregularity of the layer geometries increases and as the layers get closer together.

Figure VI.11 SH Body Waves Diffracted Mode Shapes at f = 13.33, 18.18, 20.0 & 25.0 Hz

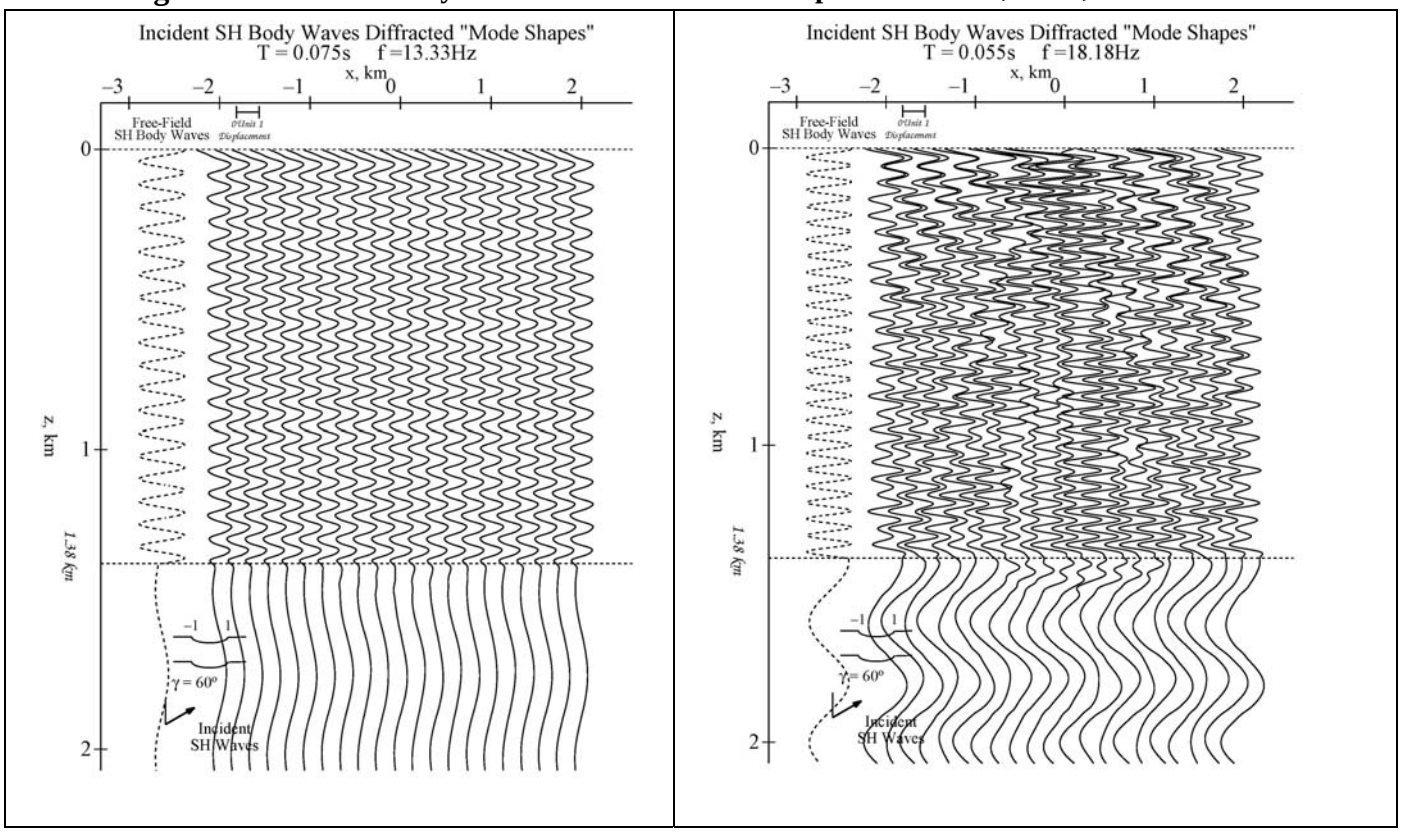

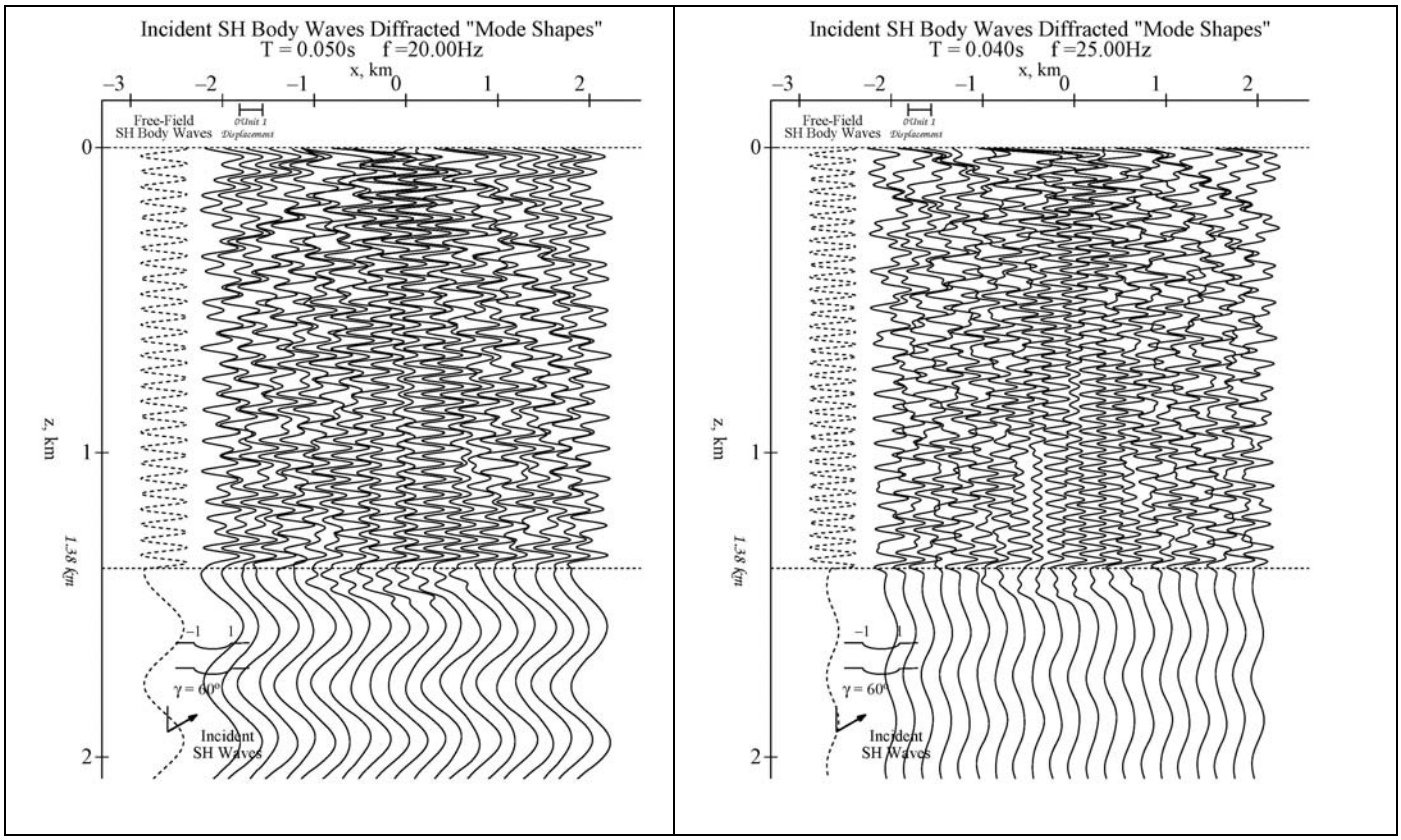

References

1. **V. W. Lee & X.Y. Wu** Application of the Weighted Residual Method to Diffraction by 2-D Canyons of Arbitrary Shape, I: Incident SH Waves, *Int. J. Soil Dynamics & Earthquake Eng., 13(5),* 1994, 355-364, *10 Pages, 17 Refs.*, **Oct, 1994a.**

2. **V. W. Lee & X.Y. Wu** Application of the Weighted Residual Method to Diffraction by 2-D Canyons of Arbitrary Shape, II: Incident P, SV & Rayleigh Waves, *Int. J. Soil Dynamics & Earthquake Eng., 13(5),* 1994, 365-373, *9 Pages, 24 Refs.*, **Oct, 1994b.**

3. **Mow, Chao-Chow and Pao, Yih-Hsing** (1973). "The Diffraction of Elastic Waves and Dynamic Stress Concentrations", Institute of Physics Publishing, 617

4. **SEEC**. Synthetic Translational Motions of Surface Waves On or Below a Layered Media**, Report I, 2013.**

APPENDIX R4-2

(Reporting Date 20 October 2013)

REPORT No. IV – Part II

Contract No.: 87055-11-0562

RSP Project ID (R525.1)

REPORTING DATE – 20 October 2013

PROJECT TITLE: Interfacing Seismological Description of Strong Ground Motion with Engineering Analysis of Soil Structure Interaction for Nuclear Power Plants

REPORT SUBMITTED BY: Structural and Earthquake Engineering Consultants (SEEC) Inc.

855 Arcadia Ave. #E, Arcadia, CA 91007 USA

Contact name: M. D. Trifunac

Phone: (626) 447-9382

Email: trifunac@usc.edu, misha.trifunac@gmail.com

to

Canadian Nuclear Safety Commission

ATTENTION: Nanci Laroche, Nebojsa Orbovic

280 Slater St., Ottawa, Ontario, Canada, K1P 5S9

E-mail: research-recherche@cnsc-ccsn.gc.ca

Nebojsa.Orbovic@cnsc-ccsn.gc.ca

Scattering and Diffraction by Irregular Layered Elastic Media - Part II: Rayleigh and Body P, SV Waves

I. Introduction

This report is a continuation of our sequence of reports to CNSC on waves in elastic layered media:

1. Interfacing Seismological Description of Strong Ground Motion with Engineering Analysis of Soil Structure Interaction for Nuclear Power Plants, **Report I, 2013**

2. Synthetic Translational Motions of Surface Waves On or Below a Layered Media**, Report II, 2013.**

3. Synthetic Rotational Motions of Surface Waves On or Below a Layered Media**, Report III, 2013.**

4. **Part 1** - Diffraction Around An Irregular Layered Elastic Media, I: Love and Body SH Waves, **Report IV-1, 2013.**

This is a continuation of Report IV, Part I for the case of Love and Body SH waves in irregular layered elastic media. In this report, we will consider the case of Rayleigh and Body P, SV waves for the same irregular layered elastic media. The method of weighted residues, or the Moment method, is again used in the analysis.

II. Rayleigh and Body P, SV Waves incident on an Irregular Layered Media

We consider again the case of an ***N***-layered half space with Rayleigh and/or body P, SV waves incident from the left. For each regular flat layer ***l,*** with ***l = 1,*** …, ***N*** , the ***P***- and ***SV***-Wave Potentials in the layer respectively take the form:

$\varphi_l^-,\ \varphi_l^+,\ \psi_l^-,\ \psi_l^+$:

$$\begin{aligned} \varphi_l^- &= A_l^- e^{ik(x-a_l z)} \\ \varphi_l^+ &= A_l^+ e^{ik(x+a_l z)} \\ \psi_l^- &= B_l^- e^{ik(x-b_l z)} \\ \psi_l^+ &= B_l^+ e^{ik(x+b_l z)} \end{aligned}$$

Report II (3.1)

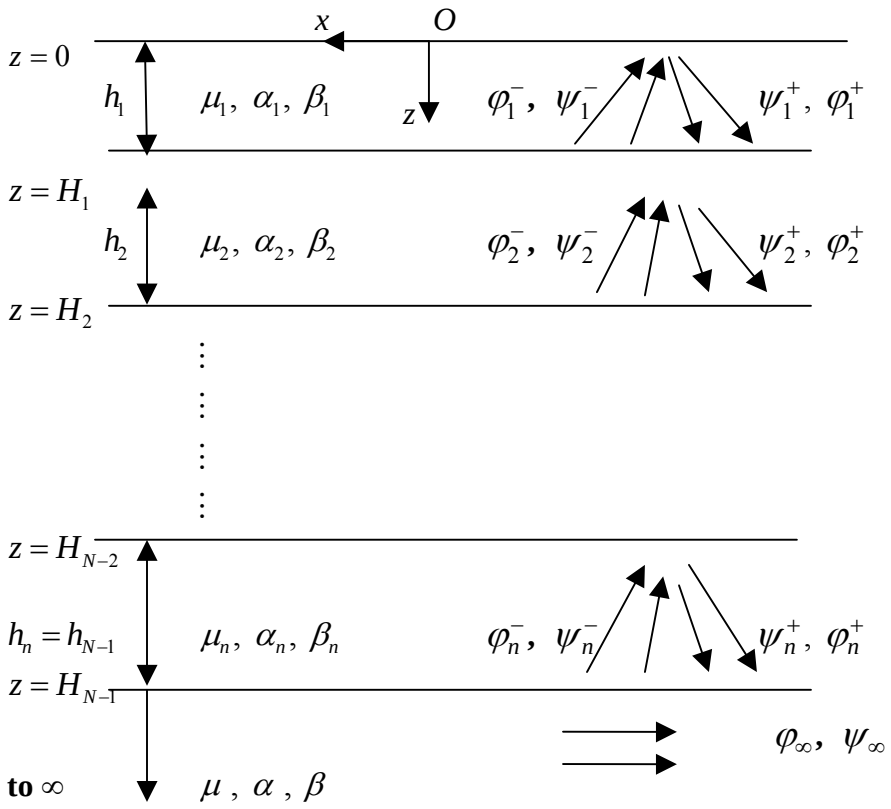

Figure 1: From Report II Figure III.1 N-layered half-space with Rayleigh waves

As before, theose are respectively the upward and downward propagating waves present in i^{th} layer, and $\boldsymbol{k = k(\omega) = \omega / c(\omega)}$ is the horizontal wave number of the ***P***- and ***SV***-waves at frequency ω and phase velocity $\boldsymbol{c = c(\omega)}$. The term $\boldsymbol{e^{ikx}}$, which is also the same in each layer, is the horizontal component of the waves, which together with the time harmonic term $\boldsymbol{e^{i\omega t}}$, corresponds to waves propagating in the *–ve x* direction. The terms $\boldsymbol{e^{\mp ika_l z}}$ for the ***P***-waves and $\boldsymbol{e^{\mp ikb_l z}}$ for the ***SV***-waves are respectively the vertical components of the waves. The ones with the ***–ve*** *exponent* are propagating upwards (***–ve*** *y*) and those with the ***+ve*** *exponent* are propagating downwards (***+ve*** *y*). Here $\boldsymbol{a_l = a_l(\alpha_l, c)}$ and $\boldsymbol{b_l = b_l(\beta_l, c)}$ are respectively given by

$$\boldsymbol{a_l = \frac{\left(k_{\alpha_l}^2 - k^2\right)^{1/2}}{k} = \left(\left(k_{\alpha_l}/k\right)^2 - 1\right)^{1/2} = \left(\left(c/\alpha_l\right)^2 - 1\right)^{1/2}}$$

$$\boldsymbol{b_l = \frac{\left(k_{\beta_l}^2 - k^2\right)^{1/2}}{k} = \left(\left(k_{\beta_l}/k\right)^2 - 1\right)^{1/2} = \left(\left(c/\beta_l\right)^2 - 1\right)^{1/2}}$$

Report II (3.2)

so that $\boldsymbol{ka_l}$ and $\boldsymbol{kb_l}$ are the vertical wave numbers of the ***P***- and ***SV***-waves in the $\boldsymbol{l^{th}}$ layer of the medium with longitudinal wave speed α_l and shear wave velocity $\boldsymbol{\beta_l}$. In general, the wave speeds increase as one goes down into the layers, so that $\boldsymbol{\beta_1 < \beta_2 < \ldots < \beta_N < \beta}$, with the semi-infinite half-space layer at the bottom having the highest shear wave speed β. The same can be said about the longitudinal wave speeds, so that $\boldsymbol{\alpha_1 < \alpha_2 < \ldots < \alpha_N < \alpha}$, with $\boldsymbol{\alpha}$ the longitudinal wave speed of the semi-infinite medium furthest below being the highest. With $\boldsymbol{c = c(\omega)}$ the wave speed of the surface Rayleigh waves, $\boldsymbol{c < \beta < \alpha}$, and the surface waves take the form:

$$\boldsymbol{\varphi_\infty = A_\infty e^{ik(x - az)} = A_\infty e^{ikx - k\bar{a}z}}$$

$$\boldsymbol{\psi_\infty = B_\infty e^{ik(x - bz)} = B_\infty e^{ikx - k\bar{b}z}}$$

Report II(3.3)

where

$$\bar{a} = \frac{\left(k^2 - k_\alpha^2\right)^{1/2}}{k} = \left(1 - \left(k_\alpha / k\right)^2\right)^{1/2} = \left(1 - \left(c/\alpha\right)^2\right)^{1/2}$$

$$\bar{b} = \frac{\left(k^2 - k_\beta^2\right)^{1/2}}{k} = \left(1 - \left(k_\beta / k\right)^2\right)^{1/2} = \left(1 - \left(c/\beta\right)^2\right)^{1/2}$$

Report II (3.4)

and $\bar{a}$, $\bar{b}$ are respectively the complements of a, b and both are real, so that the terms $e^{-k\bar{a}z}$ in φ_∞ and $e^{-k\bar{b}z}$ in ψ_∞ both correspond to surface wave terms with amplitudes that are exponentially decaying with depth below the surface.

With β_l the shear wave speed in the l^{th} layer of the medium, and $c = c(\omega)$, the Rayleigh wave speed and also the (horizontal) phase velocity of the waves in each layer of the elastic media above the half space (Report II Figure **III.1**), we can have $c \geq \beta_l$ or $c < \beta_l$.

We will next consider the case when the layers are not perfectly flat.

III. Rayleigh and Body P, SV Waves incident on an Irregular Layered Media

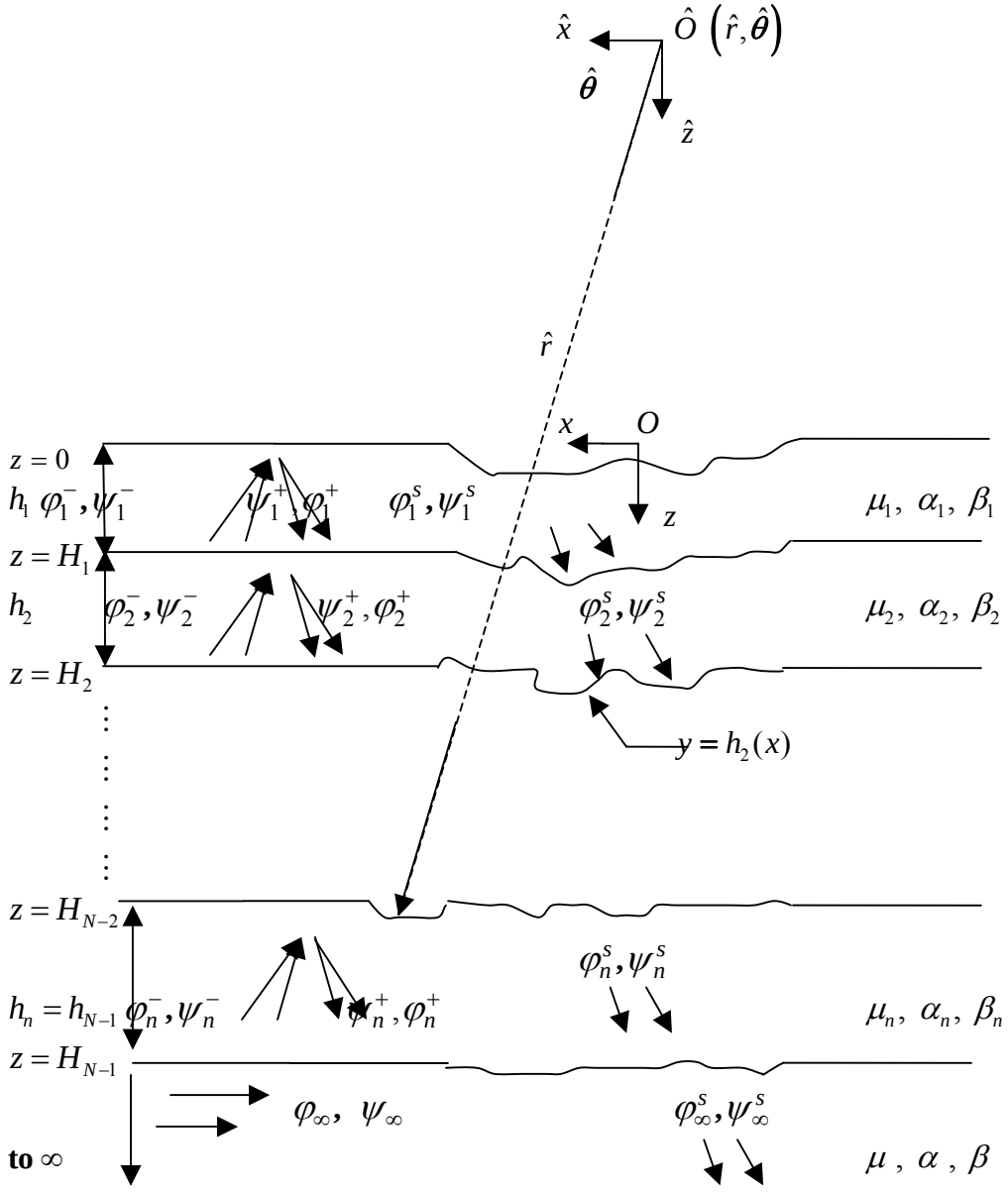

Figure 2 Irregular-Shaped N-layered half-space with Rayleigh waves

Figure 2 here is a model where the parallel layers are not perfectly flat in some finite region, but are flat elsewhere. Without loss of generality, we will assume that each of these irregular surfaces at each interface between the l^{th} and $(l+1)^{th}$ layer, which

extends from $x=-\infty$ to $x=+\infty$ can be represented by a curve $z=h_l(x)$ at the interface. We assume that this curve will be the flat surface $z=H_l$ almost everywhere, but will deviate from the flat surface within some finite region where it can be defined numerically by a set of points (x_i, z_i). The same curve can also be represented in polar coordinates $(\hat{r},\hat{\theta})$, with $\hat{r}=\hat{r}(\hat{\theta})$ in a common coordinate system $(\hat{x},\hat{z})$ with origin at some point $\hat{O}$ above the half space as shown.

As in the case of surface Love waves, with the surface Rayleigh waves potentials or body P, SV wave potentials φ_l^-, φ_l^+ for P waves, and ψ_l^-, ψ_l^+ for SV waves at each layer l incident on these irregular surfaces, additional scattered wave potentials are generated, which can be represented by

$$\begin{aligned}\varphi_l^s &= \sum_{n=0}^{\infty}\left(A_{l,n}^{(1)}H_n^{(1)}(k_{\alpha_l}\hat{r})+A_{l,n}^{(2)}H_n^{(2)}(k_{\alpha_l}\hat{r})\right)\cos n\theta \\ \psi_l^s &= \sum_{n=0}^{\infty}\left(B_{l,n}^{(1)}H_n^{(1)}(k_{\beta_l}\hat{r})+B_{l,n}^{(2)}H_n^{(2)}(k_{\beta_l}\hat{r})\right)\cos n\theta\end{aligned} \tag{1}$$

with both outgoing and incoming waves, for each layer $l=1,2,\ldots,N-1$, all except the last semi-infinite layer. For the last semi-infinite layer, $l=N$, the scattered wave, $\varphi_\infty^s=\varphi_N^s$ and $\psi_\infty^s=\psi_N^s$ respectively the P- and SV- potentials, take the form

$$\begin{aligned}\varphi_\infty^s &= \varphi_N^s = \sum_{n=0}^{\infty}A_{\infty,n}H_n^{(1)}(k_{\alpha_l}\hat{r})\cos n\theta \\ \psi_\infty^s &= \psi_N^s = \sum_{n=0}^{\infty}B_{\infty,n}H_n^{(1)}(k_{\beta_l}\hat{r})\cos n\theta\end{aligned} \tag{2}$$

with only outgoing waves satisfying Somerfield's radiation condition at infinity.

The scattered waves, together with the free-filed surface Rayleigh or body P, SV Waves, form the resultant waves in the layered media. Writing $\varphi_l^{ff}=\varphi_l^+ + \varphi_l^-$ and $\psi_l^{ff}=\psi_l^+ + \psi_l^-$ respectively as the free-field surface Rayleigh or Body P, SV waves in the l^{th} media, the resultant waves in the same media are $\varphi_l=\varphi_l^{ff}+\varphi_l^s$, and $\psi_l=\psi_l^{ff}+\psi_l^s$, respectively for the P and SV wave potentials, which, together, must satisfy the following set of boundary conditions (Lee and Wu, 1994b).

1) On the half-space surface, $\boldsymbol{y = h_0(x)}$, the resultant waves in the top layer ($l = 1$) must together satisfy the half-space surface traction (stress) free boundary condition:

$$\tilde{\boldsymbol{T}} = T_r \hat{\boldsymbol{e}}_r + T_\theta \hat{\boldsymbol{e}}_\theta = 0 \quad \text{at} \quad \boldsymbol{y = h_0(x)} \tag{3}$$

or separating the contribution of Traction due to the free-field and scattered waves:

$$\tilde{\boldsymbol{T}} = \tilde{\boldsymbol{T}}^{ff} + \tilde{\boldsymbol{T}}^{s} \tag{4a}$$

gives, at $\boldsymbol{y = h_0(x)}$:

$$\begin{aligned} \boldsymbol{T_r^s} &= \boldsymbol{-T_r^{ff}} \\ \boldsymbol{T_\theta^s} &= \boldsymbol{-T_\theta^{ff}} \end{aligned} \tag{4b}$$

2) For $l = 1, 2, \ldots, N-1$, at the interface between the l^{th} layer and the $(l+1)^{th}$ layer below, $y = h_l(x)$, the resultant waves in these two layers must satisfy the continuity of displacement and stress at the interface, at $\boldsymbol{y = h_l(x)}$:

$$\begin{aligned} \tilde{\boldsymbol{U}}_l &= \tilde{\boldsymbol{U}}_{l+1} \\ \tilde{\boldsymbol{T}}_l &= \tilde{\boldsymbol{T}}_{l+1} \end{aligned} \tag{5}$$

with $\boldsymbol{U_l}$, $\tilde{\boldsymbol{T}}_l$ respectively the displacement and Traction vectors in layer $\boldsymbol{l}$, and $\boldsymbol{U_{l+1}}$, $\tilde{\boldsymbol{T}}_{l+1}$ the corresponding ones in layer $\boldsymbol{l+1}$. Separating the contribution of the displacement and Traction due to the free-field and scattered waves:

$$\begin{aligned} \tilde{\boldsymbol{U}}_l &= \tilde{\boldsymbol{U}}_l^{ff} + \tilde{\boldsymbol{U}}_l^{s} \\ \tilde{\boldsymbol{T}}_l &= \tilde{\boldsymbol{T}}_l^{ff} + \tilde{\boldsymbol{T}}_l^{s} \end{aligned} \tag{6a}$$

gives, at $\boldsymbol{y = h_l(x)}$:

$$\begin{aligned} \tilde{\boldsymbol{U}}_l^s - \tilde{\boldsymbol{U}}_{l+1}^s &= -\left(\tilde{\boldsymbol{U}}_l^{ff} - \tilde{\boldsymbol{U}}_{l+1}^{ff}\right) \\ \tilde{\boldsymbol{T}}_l^s - \tilde{\boldsymbol{T}}_{l+1}^s &= -\left(\tilde{\boldsymbol{T}}_l^{ff} - \tilde{\boldsymbol{T}}_{l+1}^{ff}\right) \end{aligned} \tag{6b}$$

with the unknown wave functions on the left-hand side, the known functions on the right-hand side. As in equation (3) above, both the displacement and Traction vectors can at each layer be expressed in the radial and angular components:

$$\tilde{\boldsymbol{U}}_l = \left(\boldsymbol{U}_l\right)_r \ \hat{\boldsymbol{e}}_r + \left(\boldsymbol{U}_l\right)_\theta \ \hat{\boldsymbol{e}}_\theta$$
$$\tilde{\boldsymbol{T}}_l = \left(\boldsymbol{T}_l\right)_r \ \hat{\boldsymbol{e}}_r + \left(\boldsymbol{T}_l\right)_\theta \ \hat{\boldsymbol{e}}_\theta \tag{7}$$

so that the displacement and Traction vectors in Equation (20b) can be separated into component forms, **at** $\boldsymbol{y = h_l(x)}$:

$$\left(\boldsymbol{U}^s_{l+1}\right)_r - \left(\boldsymbol{U}^s_l\right)_r = -\left(\left(\boldsymbol{U}^{ff}_{l+1}\right)_r - \left(\boldsymbol{U}^{ff}_l\right)_r\right)$$
$$\left(\boldsymbol{U}^s_{l+1}\right)_\theta - \left(\boldsymbol{U}^s_l\right)_\theta = -\left(\left(\boldsymbol{U}^{ff}_{l+1}\right)_\theta - \left(\boldsymbol{U}^{ff}_l\right)_\theta\right) \tag{8a}$$

and

$$\left(\boldsymbol{T}^s_{l+1}\right)_r - \left(\boldsymbol{T}^s_l\right)_r = -\left(\left(\boldsymbol{T}^{ff}_{l+1}\right)_r - \left(\boldsymbol{T}^{ff}_l\right)_r\right)$$
$$\left(\boldsymbol{T}^s_{l+1}\right)_\theta - \left(\boldsymbol{T}^s_l\right)_\theta = -\left(\left(\boldsymbol{T}^{ff}_{l+1}\right)_\theta - \left(\boldsymbol{T}^{ff}_l\right)_\theta\right) \tag{8b}$$

Here the radial and angular components of Traction, $\boldsymbol{T_r}$ and $\boldsymbol{T_\theta}$, can be expressed in terms of the various components of stresses in cylindrical coordinates (Lee and Wu, 1994b):

$$\boldsymbol{T_r} = \sigma_r \cos\alpha + \tau_{r\theta} \sin\alpha$$
$$\boldsymbol{T_\theta} = \sigma_\theta \sin\alpha + \tau_{r\theta} \cos\alpha \tag{9}$$

where α is the angle that the normal $\hat{\boldsymbol{n}} = \boldsymbol{n_r}\hat{\boldsymbol{e}}_r + \boldsymbol{n_\theta}\hat{\boldsymbol{e}}_\theta = \cos\alpha\ \hat{\boldsymbol{e}}_r + \sin\alpha\ \hat{\boldsymbol{e}}_\theta$ makes with the radial vector, as shown in **Figure 3** (Lee and Wu, 1994a,b)

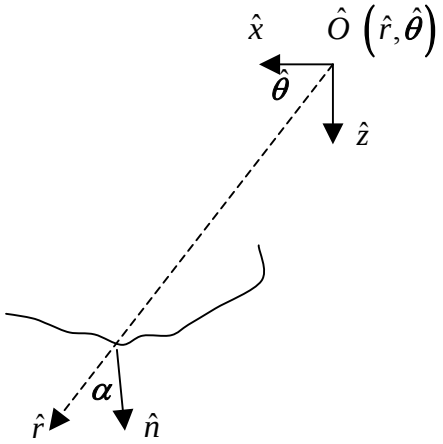

Figure 3 Angle α between radial vector and normal at a point

Expressions for the radial and angular components of the displacement vectors and stresses can be expressed in terms of the corresponding wave potentials (Mow and Pao, 1973). They will take the form, for the scattered wave potentials, at a point $(r,\theta)=(\hat{r}(\theta),\theta)$ on the irregular surface (or at any point anywhere):

$$\begin{aligned}\left(U_l^s\right)_r &= \sum_n \sum_{j=1,2} A_{l,n}^{(j)} D_{r1}^{(j)}(n,k_{\alpha_l}\hat{r},\theta) + B_{l,n}^{(j)} D_{r2}^{(j)}(n,k_{\beta_l}\hat{r},\theta)\\ \left(U_l^s\right)_\theta &= \sum_n \sum_{j=1,2} A_{l,n}^{(j)} D_{\theta 1}^{(j)}(n,k_{\alpha_l}\hat{r},\theta) + B_{l,n}^{(j)} D_{\theta 2}^{(j)}(n,k_{\beta_l}\hat{r},\theta)\end{aligned} \tag{10}$$

where $D_{r1}^{(j)}(n,k_{\alpha_l}\hat{r},\theta)$, $D_{r2}^{(j)}(n,k_{\beta_l}\hat{r},\theta)$ are the corresponding radial displacements from the ***P***- and ***SV***- scattered wave potentials, and $D_{\theta 1}^{(j)}(n,k_{\alpha_l}\hat{r},\theta)$, $D_{\theta 2}^{(j)}(n,k_{\beta_l}\hat{r},\theta)$ are their corresponding angular displacements.

Similarly, the Traction components at a point on the irregular surface $(r,\theta)=(\hat{r}(\theta),\theta)$ with normal $\hat{n}=n_r\hat{e}_r+n_\theta\hat{e}_\theta=\cos\alpha\,\hat{e}_r+\sin\alpha\,\hat{e}_\theta$ take the form:

$$\begin{aligned}\left(T_l^s\right)_r &= \sum_n \sum_{j=1,2} A_{l,n}^{(j)} \mathcal{T}_{r1}^{(j)}(n,k_{\alpha_l}\hat{r},\theta,\hat{n}) + B_{l,n}^{(j)} \mathcal{T}_{r2}^{(j)}(n,k_{\beta_l}\hat{r},\theta,\hat{n})\\ \left(T_l^s\right)_\theta &= \sum_n \sum_{j=1,2} A_{l,n}^{(j)} \mathcal{T}_{\theta 1}^{(j)}(n,k_{\alpha_l}\hat{r},\theta,\hat{n}) + B_{l,n}^{(j)} \mathcal{T}_{\theta 2}^{(j)}(n,k_{\beta_l}\hat{r},\theta,\hat{n})\end{aligned} \tag{11}$$

where, $\mathcal{T}_{r1}^{(j)}=\mathcal{T}_{r1}^{(j)}(n,k_{\alpha_l}\hat{r},\theta,\hat{n})$, $\mathcal{T}_{r2}^{(j)}=\mathcal{T}_{r2}^{(j)}(n,k_{\beta_l}\hat{r},\theta,\hat{n})$ are the corresponding radial components of Traction from the ***P***- and ***SV***- scattered wave potentials. Similarly $\mathcal{T}_{\theta 1}^{(j)}=\mathcal{T}_{\theta 1}^{(j)}(n,k_{\alpha_l}\hat{r},\theta,\hat{n})$, $\mathcal{T}_{\theta 2}^{(j)}=\mathcal{T}_{\theta 2}^{(j)}(n,k_{\alpha_l}\hat{r},\theta,\hat{n})$ are their corresponding angular stresses.

Using the weighted residue method, as in the case of Love waves, the boundary conditions at each layer take the form:

1) Starting in the top layer, the half space surface, from Eqns. (18b) and (25):

$$\sum_{n=0}^{\infty} \sum_{j=1,2} \left\langle \mathcal{T}_{r1}^{(j)}(n,k_{\alpha_1}\hat{r},\theta,\hat{n})\ ,w_m\right\rangle A_{1,n}^{(j)} + \left\langle \mathcal{T}_{r2}^{(j)}(n,k_{\beta_1}\hat{r},\theta,\hat{n})\ ,w_m\right\rangle B_{1,n}^{(j)} = -\left\langle \left(T_1^{ff}\right)_r, w_m\right\rangle$$

$$\sum_{n=0}^{\infty}\sum_{j=1,2}\left\langle T_{\theta 1}^{(j)}(n,k_{\alpha_1}\hat{r},\theta,\hat{n})\ ,w_m\right\rangle A_{1,n}^{(j)}\ +\ \left\langle T_{\theta 2}^{(j)}(n,k_{\beta_1}\hat{r},\theta,\hat{n})\ ,w_m\right\rangle B_{1,n}^{(j)}\ =\ -\left\langle \left(T_1^{ff}\right)_\theta ,w_m\right\rangle \tag{12}$$

2) For the interface between the l^{th} and $(l+1)^{th}$ layer, for $l=1,2,3\ldots$ from Eqns. (22a), and (24) for displacements:

$$\begin{aligned}&\sum_{n=0}^{\infty}\sum_{j=1,2}\Big[\left\langle D_{r1}^{(j)}(n,k_{\alpha_l}\hat{r},\theta),w_m\right\rangle A_{l,n}^{(j)}\ +\left\langle D_{r2}^{(j)}(n,k_{\beta_l}\hat{r},\theta),w_m\right\rangle B_{l,n}^{(j)}\\ &-\left\langle D_{r1}^{(j)}(n,k_{\alpha_{l+1}}\hat{r},\theta),w_m\right\rangle A_{l+1,n}^{(j)}\ -\left\langle D_{r2}^{(j)}(n,k_{\beta_{l+1}}\hat{r},\theta),w_m\right\rangle B_{l+1,n}^{(j)}\ \Big]\ =\ -\left\langle \left(U_l^{ff}\right)_r-\left(U_{l+1}^{ff}\right)_r\ ,\ w_m\right\rangle\end{aligned} \tag{13a}$$

$$\begin{aligned}&\sum_{n=0}^{\infty}\sum_{j=1,2}\Big[\left\langle D_{\theta 1}^{(j)}(n,k_{\alpha_l}\hat{r},\theta),w_m\right\rangle A_{l,n}^{(j)}\ +\left\langle D_{\theta 2}^{(j)}(n,k_{\beta_l}\hat{r},\theta),w_m\right\rangle B_{l,n}^{(j)}\\ &-\left\langle D_{\theta 1}^{(j)}(n,k_{\alpha_{l+1}}\hat{r},\theta),w_m\right\rangle A_{l+1,n}^{(j)}\ -\left\langle D_{\theta 2}^{(j)}(n,k_{\beta_{l+1}}\hat{r},\theta),w_m\right\rangle B_{l+1,n}^{(j)}\ \Big]\ =\ -\left\langle \left(U_l^{ff}\right)_\theta-\left(U_{l+1}^{ff}\right)_\theta\ ,\ w_m\right\rangle\end{aligned} \tag{13b}$$

and from Eqns. (22b) and (25) for stresses:

$$\begin{aligned}&\sum_{n=0}^{\infty}\sum_{j=1,2}\Big[\left\langle T_{r1}^{(j)}(n,k_{\alpha_l}\hat{r},\theta,\hat{n})\ ,w_m\right\rangle A_{l,n}^{(j)}\ +\ \left\langle T_{r2}^{(j)}(n,k_{\beta_l}\hat{r},\theta,\hat{n})\ ,w_m\right\rangle B_{l,n}^{(j)}\\ &-\left\langle T_{r1}^{(j)}(n,k_{\alpha_{l+1}}\hat{r},\theta,\hat{n})\ ,w_m\right\rangle A_{l+1,n}-\left\langle T_{r2}^{(j)}(n,k_{\beta_{l+1}}\hat{r},\theta,\hat{n})\ ,w_m\right\rangle B_{l+1,n}^{(j)}\Big]\ =\ -\left\langle \left(T_l^{ff}\right)_r-\left(T_{l+1}^{ff}\right)_r,w_m\right\rangle\end{aligned} \tag{14a}$$

$$\begin{aligned}&\sum_{n=0}^{\infty}\sum_{j=1,2}\Big[\left\langle T_{\theta 1}^{(j)}(n,k_{\alpha_l}\hat{r},\theta,\hat{n})\ ,w_m\right\rangle A_{l,n}^{(j)}\ +\ \left\langle T_{\theta 2}^{(j)}(n,k_{\beta_l}\hat{r},\theta,\hat{n})\ ,w_m\right\rangle B_{l,n}^{(j)}\\ &-\left\langle T_{\theta 1}^{(j)}(n,k_{\alpha_{l+1}}\hat{r},\theta,\hat{n})\ ,w_m\right\rangle\ A_{l+1,n}^{(j)}-\left\langle T_{\theta 2}^{(j)}(n,k_{\beta_{l+1}}\hat{r},\theta,\hat{n})\ ,w_m\right\rangle\ B_{l+1,n}^{(j)}\Big]\ =\ -\left\langle \left(T_l^{ff}\right)_\theta-\left(T_{l+1}^{ff}\right)_\theta,w_m\right\rangle\end{aligned} \tag{14b}$$

In matrix form, Eqns. (13a,b) and (14a,b) take the form:

$$\sum_{n=0}^{\infty}\sum_{j=1,2}\begin{bmatrix} D_{r1}^{(j)}(l,m,n) & D_{r2}^{(j)}(l,m,n) & -D_{r1}^{(j)}(l+1,m,n) & -D_{r2}^{(j)}(l+1,m,n) \\ D_{\theta 1}^{(j)}(l,m,n) & D_{\theta 2}^{(j)}(l,m,n) & -D_{\theta 2}^{(j)}(l+1,m,n) & -D_{\theta 2}^{(j)}(l+1,m,n) \\ T_{r1}^{(j)}(l,m,n) & T_{r2}^{(j)}(l,m,n) & -T_{r1}^{(j)}(l+1,m,n) & -T_{r2}^{(j)}(l+1,m,n) \\ T_{\theta 1}^{(j)}(l,m,n) & T_{\theta 2}^{(j)}(l,m,n) & -T_{\theta 1}^{(j)}(l+1,m,n) & -T_{\theta 2}^{(j)}(l+1,m,n) \end{bmatrix}\begin{Bmatrix} A_{l,n}^{(j)} \\ B_{l,n}^{(j)} \\ A_{l+1,n}^{(j)} \\ B_{l+1,n}^{(j)} \end{Bmatrix}$$

$$= -\begin{Bmatrix} \left\langle \left(U_l^{ff}\right)_r - \left(U_{l+1}^{ff}\right)_r \ , \ w_m \right\rangle \\ \left\langle \left(U_l^{ff}\right)_\theta - \left(U_{l+1}^{ff}\right)_\theta \ , \ w_m \right\rangle \\ \left\langle \left(T_l^{ff}\right)_r - \left(T_{l+1}^{ff}\right)_r \ , w_m \right\rangle \\ \left\langle \left(T_l^{ff}\right)_\theta - \left(T_{l+1}^{ff}\right)_\theta \ , w_m \right\rangle \end{Bmatrix} \qquad \text{(14c)}$$

with properly defined matrix elements $D_{r1}^{(j)}(l,m,n)$,… and $T_{r1}^{(j)}(l,m,n)$,… etc.

The traction components of motions at each interface are computed from the corresponding strain components of motions, which are available form Report III: "Synthetic Rotational Motions of Surface Waves On or Below a Layered Media**".**

Note that for the interface between layer $N-1$ and the (last) semi-infinite layer N , Eqns. (27a,b) and (28a,b) will have only the outgoing wave terms $A_{N,n}^{(1)}$, $B_{N,n}^{(1)}$, $n=0,1,2\ldots$ and without the incoming wave terms $A_{N,n}^{(2)}$, $B_{N,n}^{(2)}$, $n=0,1,2\ldots$

IV. Numerical Implementation

This section will illustrate the numerical procedure that can be used to solve the system of complex equations, which were derived in the last section, by using the method of weighted residues. In studying the set of equations, it is observed that for an elastic half-space with N (≥ 1) layers, there are $(N-1)$ interfaces in-between the layers, plus the topmost half-space with no elastic medium above.

At this topmost half-space surface, there is one set of zero-stress equations (at $z=0$) (Eqn. (3)) involving the wave coefficients in the topmost *1st* layer. At each of the $(N-1)$ interfaces in-between the layers, there are 2 sets of the stress and displacement continuity equations (Eqns. (4) and (5)). There is thus a total of $2(N-1)+1=2N-1$ set of equations. Each of the top $(N-1)$ layers has two sets of waves, the upward and downward going, or the outgoing and incoming waves (Eqn. (1)). Those are represented by Hankel functions of the 1st and 2nd kind, the outgoing and incoming waves, respectively. On the other hand, the bottom-most semi-infinite layer has only one set of waves, the downward going or outgoing waves (Eqn. (2)). Those are represented by Hankel functions of the 1st kind. This gives a total of $2(N-1)+1=2N-1$ set of waves from all the layers.

In summary, we have a set of $(2N-1)$ equations for $(2N-1)$ waves. If each of such $(2N-1)$ sets of waves has *M* terms, with *M* unknown coefficients, we will have a total of $M\times(2N-1)$ unknowns we need to solve. Ideally each set of waves should have, $M=\infty$, or infinite number of terms and there are $\infty\times(2N-1)$ corresponding equations. In reality, we have to truncate to finite number with M terms for each set of waves, with the number *M* often dependent on the frequency of the waves and the complexity of the equations. With *M* finite, we have a task of solving the $M\times(2N-1)$ complex equations for the $M\times(2N-1)$ unknowns.

Numerically, we know that the Hankel functions of both the 1st and 2nd kind are both complex, and increase in magnitudes with increasing order. Thus if all the $\boldsymbol{M \times (2N-1)}$ unknowns are put together in the $\boldsymbol{M \times (2N-1)}$ complex equations, one would have a very large set of complex equations to solve, whose terms often have increasing magnitudes with increasing *M*. It would be a numerical nightmare to solve them all at once.

Since each set of equations at each interface involves only waves at each side of the interface, a simple, elegant numerical algorithm can be derived to allow each set of wave coefficients in each medium to be solved separately, making the problem simpler numerically. In other words, we are solving *M* complex equation in *M* unknowns at each step. The following is a detailed description of the numerical procedure.

The idea is very simple. Starting from the top surface, where $\boldsymbol{z = 0}$, we have the matrix equation for the zero-stress boundary condition along the whole (regular and irregular) surface of the half-space, in the form:

$$\left[\boldsymbol{E}_1\right]\left\{\tilde{\boldsymbol{C}}_1^{(1)}\right\} + \left[\boldsymbol{E}_1^*\right]\left\{\tilde{\boldsymbol{C}}_1^{(2)}\right\} + \left\{\tilde{\boldsymbol{e}}_1\right\}\Big|_{z=0} = \boldsymbol{0} \qquad (15a)$$

where from Eqn. (13b):

$\left[\boldsymbol{E}_1\right]=\left[\boldsymbol{E}_1^{(1)}\right]$ is the matrix with elements defining the stress terms from the P- and SV scattered waves in the top layer with the Hankel functions $\boldsymbol{H_n^{(1)}\left(k_{\alpha 1} r\right)}$ and $\boldsymbol{H_n^{(1)}\left(k_{\beta 1} r\right)}$,

$\left[\boldsymbol{E}_1^*\right]=\left[\boldsymbol{E}_1^{(2)}\right]=\boldsymbol{conjug}\left[\boldsymbol{E}_1^{(1)}\right]$ is the matrix corresponding to the stress terms in the top layer with the Hankel functions $\boldsymbol{H_n^{(2)}\left(k_{\alpha 1} r\right)}$ and $\boldsymbol{H_n^{(2)}\left(k_{\beta 1} r\right)}$,

$\left\{\tilde{\boldsymbol{C}}_1^{(1)}\right\}$, $\left\{\tilde{\boldsymbol{C}}_1^{(2)}\right\}$ are respectively the two vectors $\left\{\boldsymbol{A}_{10}^{(1)}, \boldsymbol{B}_{10}^{(1)}, \boldsymbol{A}_{11}^{(1)}, \boldsymbol{B}_{11}^{(1)}, \boldsymbol{A}_{12}^{(1)}, \boldsymbol{B}_{12}^{(1)}, \ldots\right\}^T$ and $\left\{\boldsymbol{A}_{10}^{(2)}, \boldsymbol{B}_{10}^{(2)}, \boldsymbol{A}_{11}^{(2)}, \boldsymbol{B}_{11}^{(2)}, \boldsymbol{A}_{12}^{(2)}, \boldsymbol{B}_{12}^{(2)}, \ldots\right\}^T$ in the top layer, and

(15b)

$\left\{\tilde{\boldsymbol{e}}_1\right\}$ is the vector of the free-field stresses in the top layer.

As in the case of Love and SH body waves, eliminating $\left\{\tilde{\boldsymbol{C}}_1^{(2)}\right\}$, one has, at $\boldsymbol{z = 0}$**:**

$$\begin{aligned}\left\{\tilde{C}_1^{(2)}\right\} &= -\left[E_1^*\right]^{-1}\left(\left[E_1\right]\left\{\tilde{C}_1^{(1)}\right\} + \left\{\tilde{e}_1\right\}\right)\Big|_{z=0} \\ &= -\left[E_1^*(0)\right]^{-1}\left(\left[E_1(0)\right]\left\{\tilde{C}_1^{(1)}\right\} + \left\{\tilde{e}_1(0)\right\}\right)\end{aligned} \tag{16}$$

In the interface between the 1st and 2nd layer, the continuity equations take the form:

$\left[E_1\right]\left\{\tilde{C}_1^{(1)}\right\} + \left[E_1^*\right]\left\{\tilde{C}_1^{(2)}\right\} + \left\{\tilde{e}_1\right\}\Big|_{z=h_1} = \left[E_2\right]\left\{\tilde{C}_2^{(1)}\right\} + \left[E_2^*\right]\left\{\tilde{C}_2^{(2)}\right\} + \left\{\tilde{e}_2\right\}\Big|_{z=h_1}$, or

$$\begin{aligned}&\left[E_1(h_1)\right]\left\{\tilde{C}_1^{(1)}\right\} + \left[E_1^*(h_1)\right]\left\{\tilde{C}_1^{(2)}\right\} + \left\{\tilde{e}_1(h_1)\right\} \\ &= \left[E_2(h_1)\right]\left\{\tilde{C}_2^{(1)}\right\} + \left[E_2^*(h_1)\right]\left\{\tilde{C}_2^{(2)}\right\} + \left\{\tilde{e}_2(h_1)\right\}\end{aligned} \tag{17}$$

for stress continuity. Here $\left\{\tilde{C}_2^{(1)}\right\}$, $\left\{\tilde{C}_2^{(2)}\right\}$ are respectively the two corresponding vectors $\left\{A_{20}^{(1)}, B_{20}^{(1)}, A_{21}^{(1)}, B_{21}^{(1)}, A_{22}^{(1)}, B_{22}^{(1)}, \ldots\right\}^T$ and $\left\{A_{20}^{(2)}, B_{20}^{(2)}, A_{21}^{(2)}, B_{21}^{(2)}, A_{22}^{(2)}, B_{22}^{(2)}, \ldots\right\}^T$ in the second layer, and $\left[E_2\right]\left(=\left[E_2^{(1)}\right]\right), \left[E_2^*\right]\left(=\left[E_2^{(2)}\right]\right)$ are respectively the matrices with elements defining the stress terms from the P- and SV scattered waves in the 2nd layer with the Hankel functions of the 1st and 2nd kinds, corresponding to the coefficients $\left\{\tilde{C}_2^{(1)}\right\}$, $\left\{\tilde{C}_2^{(2)}\right\}$ just as how they are defined in the top 1st layer

Similarly, for the displacement continuity equations between the 1st and 2nd layer:

$$\begin{aligned}&\left[D_1(h_1)\right]\left\{\tilde{C}_1^{(1)}\right\} + \left[D_1^*(h_1)\right]\left\{\tilde{C}_1^{(2)}\right\} + \left\{\tilde{d}_1(h_1)\right\} \\ &= \left[D_2(h_1)\right]\left\{\tilde{C}_2^{(1)}\right\} + \left[D_2^*(h_1)\right]\left\{\tilde{C}_2^{(2)}\right\} + \left\{\tilde{d}_2(h_1)\right\}\end{aligned} \tag{18}$$

Using Eqn. (16), $\left\{\tilde{C}_1^{(2)}\right\}$ can be eliminated from the L.H.S. of the stress Eqn. (17):

$$\begin{aligned}&\left[E_1(h_1)\right]\left\{\tilde{C}_1^{(1)}\right\} + \left[E_1^*(h_1)\right]\left\{\tilde{C}_1^{(2)}\right\} + \left\{\tilde{e}_1(h_1)\right\} \\ &\left[E_1(h_1)\right]\left\{\tilde{C}_1^{(1)}\right\} - \left[E_1^*(h_1)\right]\left[E_1^*(0)\right]^{-1}\left(\left[E_1(0)\right]\left\{\tilde{C}_1^{(1)}\right\} + \left\{\tilde{e}_1(0)\right\}\right) + \left\{\tilde{e}_1(h_1)\right\} \quad (19a) \\ &= \left[\tilde{E}_1(h_1)\right]\left\{\tilde{C}_1^{(1)}\right\} + \left\{\tilde{e}_1(h_1)\right\}\end{aligned}$$

where

$$\begin{aligned}\left[\tilde{E}_1(h_1)\right] &= \left[E_1(h_1)\right] - \left[E_1^*(h_1)\right]\left[E_1^*(0)\right]^{-1}\left[E_1(0)\right] \\ \left\{\tilde{e}_1(h_1)\right\} &= \left\{\tilde{e}_1(h_1)\right\} - \left[E_1^*(h_1)\right]\left[E_1^*(0)\right]^{-1}\left\{\tilde{e}_1(0)\right\}\end{aligned} \tag{19b}$$

In exactly the same way, $\{\tilde{C}_1^{(2)}\}$ can be eliminated from the L.H.S. of the displacement Eqn. (18), resulting in:

$$\begin{aligned}
&[D_1(h_1)]\{\tilde{C}_1^{(1)}\} + [D_1^*(h_1)]\{\tilde{C}_1^{(2)}\} + \{\tilde{d}_1(h_1)\} \\
&[D_1(h_1)]\{\tilde{C}_1^{(1)}\} - [D_1^*(h_1)][E_1^*(0)]^{-1}\left([E_1(0)]\{\tilde{C}_1^{(1)}\} + \{\tilde{e}_1(0)\}\right) + \{\tilde{d}_1(h_1)\} \qquad (20a) \\
&\quad = \quad [\mathcal{D}_1(h_1)]\{\tilde{A}_1^{(1)}\} + \{\tilde{d}_1(h_1)\}
\end{aligned}$$

where

$$\begin{aligned}
[\mathcal{D}_1(h_1)] &= [D_1(h_1)] - [D_1^*(h_1)][E_1^*(0)]^{-1}[E_1(0)] \\
\{\tilde{d}_1(h_1)\} &= \{\tilde{d}_1(h_1)\} - [D_1^*(h_1)][E_1^*(0)]^{-1}\{\tilde{e}_1(0)\}
\end{aligned} \qquad (20b)$$

The continuity matrix equations at the interface of the 1st and 2nd layer now take the simplified form, without the $\{\tilde{C}_1^{(2)}\}$ terms:

$$\begin{aligned}
&[\mathcal{E}_1(h_1)]\{\tilde{C}_1^{(1)}\} + \{\tilde{e}_1(h_1)\} \\
&\quad = \quad [E_2(h_1)]\{\tilde{C}_2^{(1)}\} + [E_2^*(h_1)]\{\tilde{C}_2^{(2)}\} + \{\tilde{e}_2(h_1)\} \qquad (21a)
\end{aligned}$$

$$\begin{aligned}
&[\mathcal{D}_1(h_1)]\{\tilde{C}_1^{(1)}\} + \{\tilde{d}_1(h_1)\} \\
&\quad = \quad [D_2(h_1)]\{\tilde{C}_2^{(1)}\} + [D_2^*(h_1)]\{\tilde{C}_2^{(2)}\} + \{\tilde{d}_2(h_1)\} \qquad (21b)
\end{aligned}$$

In matrix form, Eqns. (21a) and (21b) become:

$$\begin{bmatrix} E_2(h_1) & E_2^*(h_1) \\ D_2(h_1) & D_2^*(h_1) \end{bmatrix}\begin{Bmatrix} \tilde{C}_2^{(1)} \\ \tilde{C}_2^{(2)} \end{Bmatrix} = \begin{bmatrix} \mathcal{E}_1(h_1) \\ \mathcal{D}_1(h_1) \end{bmatrix}\{\tilde{C}_1^{(1)}\} + \begin{Bmatrix} \tilde{e}_1(h_1) - \tilde{e}_2(h_1) \\ \tilde{d}_1(h_1) - \tilde{d}_2(h_1) \end{Bmatrix} \qquad (22)$$

which shows that both $\{\tilde{C}_2^{(1)}\}$ and $\{\tilde{C}_2^{(2)}\}$ of the coefficients of the waves in the 2nd layer can be expressed in terms of the single set of $\{\tilde{C}_1^{(1)}\}$ coefficients of waves in the top layer. One can thus write:

$$\begin{Bmatrix} \tilde{C}_2^{(1)} \\ \tilde{C}_2^{(2)} \end{Bmatrix} = \begin{bmatrix} E_2(h_1) & E_2^*(h_1) \\ D_2(h_1) & D_2^*(h_1) \end{bmatrix}^{-1}\left(\begin{bmatrix} \mathcal{E}_1(h_1) \\ \mathcal{D}_1(h_1) \end{bmatrix}\{\tilde{C}_1^{(1)}\} + \begin{Bmatrix} \tilde{e}_1(h_1) - \tilde{e}_2(h_1) \\ \tilde{d}_1(h_1) - \tilde{d}_2(h_1) \end{Bmatrix}\right) \qquad (23a)$$

so that such a transformation is obtained:

$$\begin{Bmatrix}\tilde{C}_2^{(1)}\\ \tilde{C}_2^{(2)}\end{Bmatrix}=\left(\begin{bmatrix}T_{21}(h_1)\\ T_{22}(h_1)\end{bmatrix}\left\{\tilde{C}_1^{(1)}\right\}+\begin{Bmatrix}\tilde{t}_{21}(h_1)\\ \tilde{t}_{22}(h_1)\end{Bmatrix}\right) \tag{23b}$$

Repeating this iteration at each interface of layers proceeding downwards one can start with the continuity equations at interface between layer *l* and *l+1*, as in Eqns. (18a,b), at the interface $z=h_l$:

$$\begin{aligned}&\left[E_l(h_l)\right]\left\{\tilde{C}_l^{(1)}\right\}+\left[E_l^*(h_l)\right]\left\{\tilde{C}_l^{(2)}\right\}+\left\{\tilde{e}_l(h_l)\right\}\\ &\quad=\left[E_{l+1}(h_l)\right]\left\{\tilde{C}_{l+1}^{(1)}\right\}+\left[E_{l+1}^*(h_{l+1})\right]\left\{\tilde{C}_{l+1}^{(2)}\right\}+\left\{\tilde{e}_{l+1}(h_l)\right\}\end{aligned} \tag{24a}$$

$$\begin{aligned}&\left[D_l(h_l)\right]\left\{\tilde{C}_l^{(1)}\right\}+\left[D_l^*(h_l)\right]\left\{\tilde{C}_l^{(2)}\right\}+\left\{\tilde{d}_l(h_l)\right\}\\ &\quad=\left[D_{l+1}(h_l)\right]\left\{\tilde{C}_{l+1}^{(1)}\right\}+\left[D_{l+1}^*(h_l)\right]\left\{\tilde{C}_{l+1}^{(2)}\right\}+\left\{\tilde{d}_{l+1}(h_l)\right\}\end{aligned} \tag{24b}$$

As in Eqn. (23b), suppose by induction, $\left\{\tilde{C}_l^{(1)}\right\}$ and $\left\{\tilde{C}_l^{(2)}\right\}$ are to be expressed in terms of $\left\{\tilde{C}_1^{(1)}\right\}$:

$$\begin{Bmatrix}\tilde{C}_l^{(1)}\\ \tilde{C}_l^{(2)}\end{Bmatrix}=\left(\begin{bmatrix}T_{l1}(h_l)\\ T_{l2}(h_l)\end{bmatrix}\left\{\tilde{C}_1^{(1)}\right\}+\begin{Bmatrix}\tilde{t}_{l1}(h_l)\\ \tilde{t}_{l2}(h_l)\end{Bmatrix}\right) \tag{25}$$

from which Eqns. (24a,b) can be expressed as:

$$\begin{aligned}&\left[\mathcal{E}_l(h_l)\right]\left\{\tilde{C}_1^{(1)}\right\}+\left\{\tilde{e}_l(h_l)\right\}\\ &\quad=\left[E_{l+1}(h_l)\right]\left\{\tilde{C}_{l+1}^{(1)}\right\}+\left[E_{l+1}^*(h_l)\right]\left\{\tilde{C}_{l+1}^{(2)}\right\}+\left\{\tilde{e}_{l+1}(h_l)\right\}\end{aligned} \tag{26a}$$

$$\begin{aligned}&\left[\mathcal{D}_l(h_l)\right]\left\{\tilde{C}_1^{(1)}\right\}+\left\{\tilde{d}_l(h_l)\right\}\\ &\quad=\left[D_{l+1}(h_l)\right]\left\{\tilde{C}_{l+1}^{(1)}\right\}+\left[D_{l+1}(h_l)\right]\left\{\tilde{C}_{l+1}^{(2)}\right\}+\left\{\tilde{d}_{l+1}(h_l)\right\}\end{aligned} \tag{26b}$$

or again in matrix form, as in Eqn.(23a):

$$\begin{bmatrix}E_{l+1}(h_l) & E_{l+1}^*(h_l)\\ D_{l+1}(h_l) & D_{L+1}^*(h_l)\end{bmatrix}\begin{Bmatrix}\tilde{C}_{l+1}^{(1)}\\ \tilde{C}_{l+1}^{(2)}\end{Bmatrix}=\begin{bmatrix}\mathcal{E}_l(h_l)\\ \mathcal{D}_l(h_l)\end{bmatrix}\left\{\tilde{C}_1^{(1)}\right\}+\begin{Bmatrix}\tilde{e}_l(h_l)-\tilde{e}_{l+1}(h_l)\\ \tilde{d}_l(h_l)-\tilde{d}_{l+1}(h_l)\end{Bmatrix} \tag{27a}$$

resulting in a transformation, as in Equation (23b), expressing the coefficients $\left\{\tilde{C}_{l+1}^{(1)}\right\}$ and $\left\{\tilde{C}_{l+1}^{(2)}\right\}$ for layer *(l+1)* in terms of $\left\{\tilde{C}_1^{(1)}\right\}$ from waves of the top layer.

$$\begin{Bmatrix} \tilde{C}_{l+1}^{(1)} \\ \tilde{C}_{l+1}^{(2)} \end{Bmatrix} = \left(\begin{bmatrix} T_{l+1,1}(h_l) \\ T_{l+1,2}(h_l) \end{bmatrix} \{ \tilde{C}_1^{(1)} \} + \begin{Bmatrix} \tilde{t}_{l+1,1}(h_l) \\ \tilde{t}_{l+1,2}(h_l) \end{Bmatrix} \right) \tag{27b}$$

The reason why we select to have the coefficients of all waves in each layer expressed in terms of (one of the two) a set of coefficients of waves in the top layer is because, we know, for surface waves, and possibly body waves, the top layer waves are more dominant.

The above described procedure will continue until the interface with the bottom semi-infinite layer $l = N$ is reached, namely at $z = h_{N-1}$. There the continuity equations will be different from those in the previous interfaces, since the bottom semi-infinite layer will now have only one set of waves, namely, the downward, outgoing waves. The stress and displacement continuity equations now take the form, as in Eqn. (24a,b), with $l = N-1,\ l+1 = N$:

$$\begin{aligned} &\left[E_{N-1}(h_{N-1}) \right] \{ \tilde{C}_{N-1}^{(1)} \} + \left[E_{N-1}^{*}(h_{N-1}) \right] \{ \tilde{C}_{N-1}^{(2)} \} + \{ \tilde{e}_{N-1}(h_{N-1}) \} \\ &\quad = \left[E_N(h_{N-1}) \right] \{ \tilde{C}_N^{(1)} \} + \{ \tilde{e}_N(h_{N-1}) \} \end{aligned} \tag{26a}$$

$$\begin{aligned} &\left[D_{N-1}(h_{N-1}) \right] \{ \tilde{C}_{N-1}^{(1)} \} + \left[D_{N-1}^{*}(h_{N-1}) \right] \{ \tilde{C}_{N-1}^{(2)} \} + \{ \tilde{d}_{N-1}(h_{N-1}) \} \\ &\quad = \left[D_N(h_{N-1}) \right] \{ \tilde{C}_N^{(1)} \} + \{ \tilde{d}_N(h_{N-1}) \} \end{aligned} \tag{26b}$$

As before, the coefficients $\{ \tilde{A}_{N-1}^{(1)} \}$ and $\{ \tilde{A}_{N-1}^{(2)} \}$ of the waves in the $(N-1)^{th}$ layer can be expressed in terms of $\{ \tilde{A}_1^{(1)} \}$, that of the waves in the top layer

$$\begin{aligned} &\left[\mathcal{E}_{N-1}(h_{N-1}) \right] \{ \tilde{C}_1^{(1)} \} + \{ \tilde{e}_{N-1}(h_{N-1}) \} \\ &\quad = \left[E_N(h_{N-1}) \right] \{ \tilde{C}_N^{(1)} \} + \{ \tilde{e}_N(h_{N-1}) \} \end{aligned} \tag{27a}$$

$$\begin{aligned} &\left[\mathcal{D}_{N-1}(h_{N-1}) \right] \{ \tilde{C}_1^{(1)} \} + \{ \tilde{d}_{N-1}(h_{N-1}) \} \\ &\quad = \left[D_N(h_{N-1}) \right] \{ \tilde{C}_N^{(1)} \} + \{ \tilde{d}_N(h_{N-1}) \} \end{aligned} \tag{27b}$$

with new matrices $\left[\mathcal{E}_{N-1}(h_{N-1})\right]$, $\left[\mathcal{D}_{N-1}(h_{N-1})\right]$ and vectors $\left\{\tilde{e}_{N-1}(h_{N-1})\right\}$, $\left\{\tilde{d}_{N-1}(h_{N-1})\right\}$ in terms of $\left\{\tilde{C}_1^{(1)}\right\}$, the wave coefficients of the top layer, on the L.H.S. of the equations.

Equations (27a) and (27b) are the final form of the matrix equations, from which the wave coefficients $\left\{\tilde{C}_1^{(1)}\right\}$ of the top layer and $\left\{\tilde{C}_N^{(1)}\right\}$ in the bottom semi-infinite layer are to be related. Normally, one will rewrite Eqns. (27a), expressing $\left\{\tilde{C}_N^{(1)}\right\}$ in terms of $\left\{\tilde{C}_1^{(1)}\right\}$, as:

$$\left\{\tilde{C}_N^{(1)}\right\} = \left[E_N(h_{N-1})\right]^{-1}\left(\left[\mathcal{E}_{N-1}(h_{N-1})\right]\left\{\tilde{C}_1^{(1)}\right\} + \left\{\tilde{e}_{N-1}(h_{N-1})\right\} - \left\{\tilde{e}_N(h_{N-1})\right\}\right) \quad (28a)$$

And substituting it into Eqn. (27b), which becomes a matrix equation with $\left\{\tilde{C}_1^{(1)}\right\}$ of the top layer as the only set of unknowns:

$$\begin{aligned}&\left(\left[\mathcal{D}_{N-1}(h_{N-1})\right]-\left[D_N(h_{N-1})\right]\left[E_N(h_{N-1})\right]^{-1}\left[\mathcal{E}_{N-1}(h_{N-1})\right]\right)\left\{\tilde{C}_1^{(1)}\right\}\\ &= \left[D_N(h_{N-1})\right]\left[E_N(h_{N-1})\right]^{-1}\left\{\tilde{e}_{N-1}(h_{N-1})\right\} + \left\{\tilde{d}_N(h_{N-1})\right\} - \left\{\tilde{d}_{N-1}(h_{N-1})\right\}\end{aligned} \quad (28b)$$

from which the coefficients $\left\{\tilde{C}_1^{(1)}\right\}$ can now be evaluated, after which the coefficients of the waves in all layers can be found.

V. The Diffracted Mode Shapes of Rayleigh and P, SV Body Waves

V.1 The input free-field Waves

Recall from Report II where we considered an *N*-Layered half-space with Rayleigh waves or Body P, SV waves incident from the left over a regular parallel layered media (Report II, Figure **II.1**). In a sub-section of Chapter **V** in Report II we plotted the displacement mode shapes of Mode#1 to Mode#5 Rayleigh surface waves for a selected range of periods starting from 15 sec down to 0.04 sec (0.07Hz to 25Hz) This is followed by another sub-section of the mode shapes resulting from body P, SV waves for a given incident angle. We actually take the body P and SV waves as the 11^{th} and 12^{th} "modes" of waves in the parallel-layered media.

Each of these mode shapes at each period (frequency) will be used as the free-field input wave into the irregular layered media to be studies here. In what follows, we will take a rather simple 2-layered medium to illustrate the process, as in the case of Love and body SH waves. The following parameters are used for the 2-layered media:

Table 1

2 Layer Velocity Model				
Layer	Thickness, km	P-wave Speed, α, km/s	S-wave Speed, β, km/s	Density, ρ gm/cc
1	1.38	1.70	.98	1.28
2	∞	6.40	3.70	2.71

They are the same 1^{st} and last layers of the 6-layered model given in Report II, except the top layer is now 1.38 km thick. The computer Program, "Haskel.exe", is again used to calculate the phase velocities of each mode of Rayligh waves, as in Report II, in the period range from 14.0 sec down to 0.04 sec for a total of 91 discrete period values.

Figure V.1 shows the input free-field Mode Shapes for **Mode#1** of Rayleigh waves for both the horizontal (x-) and vertical (z-) components of motions at four selected periods, **T = 5.0, 1.5, 0.5 and 0.15 sec**, or at frequencies, **f = 0.20, 0.67, 2.0** and

6.67 Hz. As before, for Mode#1 waves, the Mode shapes are again available at all 91 pre-selected period values. It is noted from the figures that, at all the periods shown, the wave amplitudes of the mode shapes are scaled to have a maximum amplitude of 1 at the half-space surface, and that the amplitudes are practically zero at and below the interface of the two layers, which is at 1.38km depth.

Figure V.2 is the input free-field Mode Shapes for the corresponding **Mode#2** of **Rayleigh waves** for both the horizontal (x-) and vertical (z-) components of motions at four selected periods, **T = 3.0, 1.5, 0.3 and 0.15 sec** or at frequencies, **f = 0.33, 0.67, 3.33** and **6.67 Hz**. For Mode#2 of Rayleigh waves, the modes are available not at all 91 periods, but from **T = 4.6 sec** (Period#18, down from T=14.0 sec for Mode#1). So the four periods plotted here are selected from a narrower range. As before, the mode shapes are scaled to have the maximum amplitude of 1 starting from the surface $z = 0$. A characteristic of the Mode#2 is that the Mode shape at each period now decreases to negative values, reaches a negative minimum and then asymptotically approach zero. Again, as for Mode#1, the amplitudes are practically zero at and below the interface of the two layers $(z = 1.38 km)$.

Figure V.3 shows the input free-field mode shape for the corresponding **Mode#3** of **Rayleigh waves** for both the horizontal (x-) and vertical (z-) components of motion at four selected period, **T = 2.4, 1.2, 0.24** and **0.15 sec** or at frequencies, **f = 0.42, 0.83, 4.17** and **6.67 Hz**. For Mode#3 of Rayleigh wave, the modes do not exist at all 91 periods, but start from **T = 2.6 sec** (Period#28, down from T=14.0 sec for Mode#1). So the four periods plotted here are again selected from a narrower range. As before, the mode shapes are scaled to have the maximum amplitude of 1 starting from the surface $z = 0$.

Figure V.1 Mode#1 Rayleigh Mode Shapes at f = 0.20, 0.67, 2.0 and 6.67 Hz

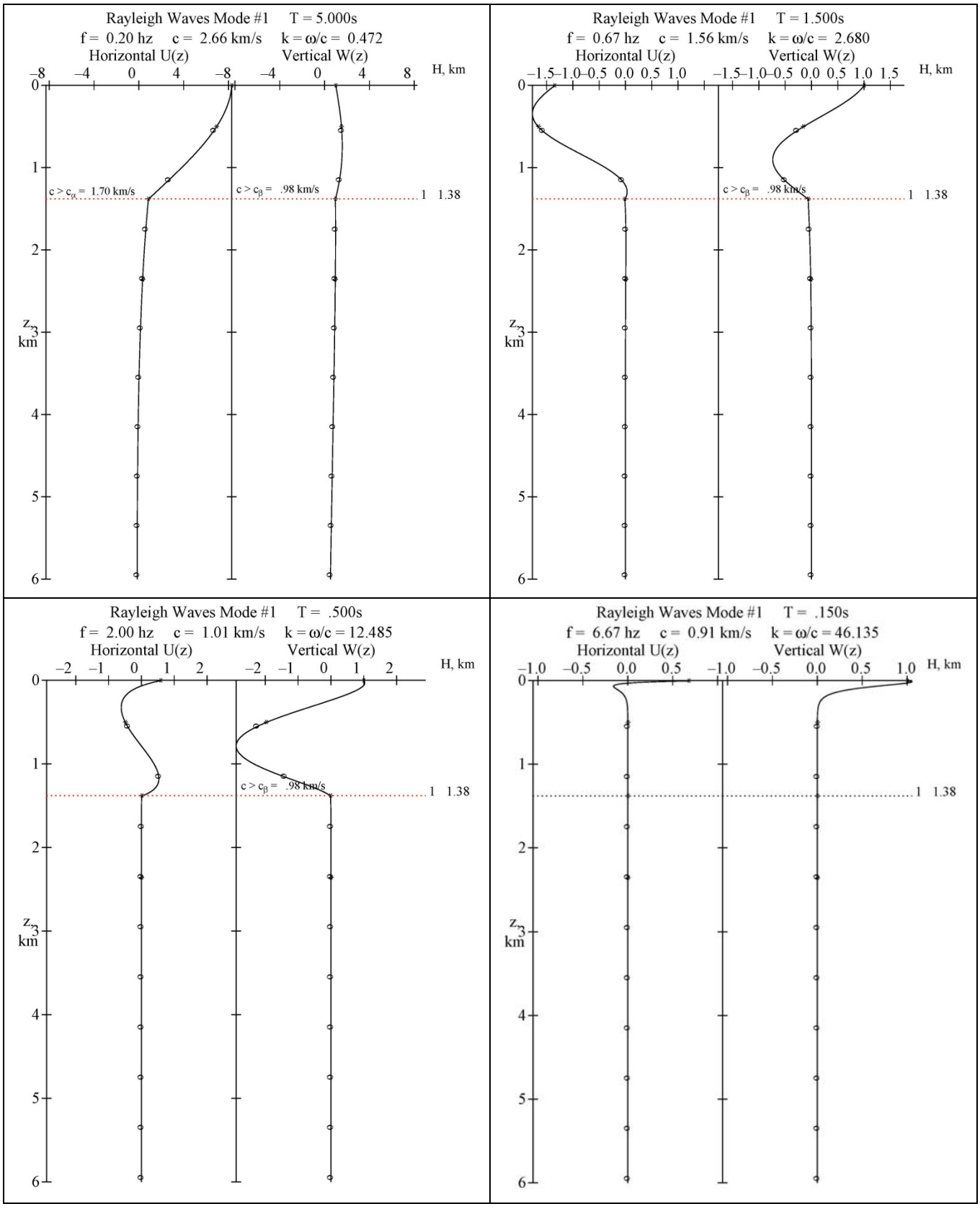

Figure V.2 Mode#2 Rayleigh Mode Shapes at f = 0.33, 0.67, 3.33 and 6.67 Hz

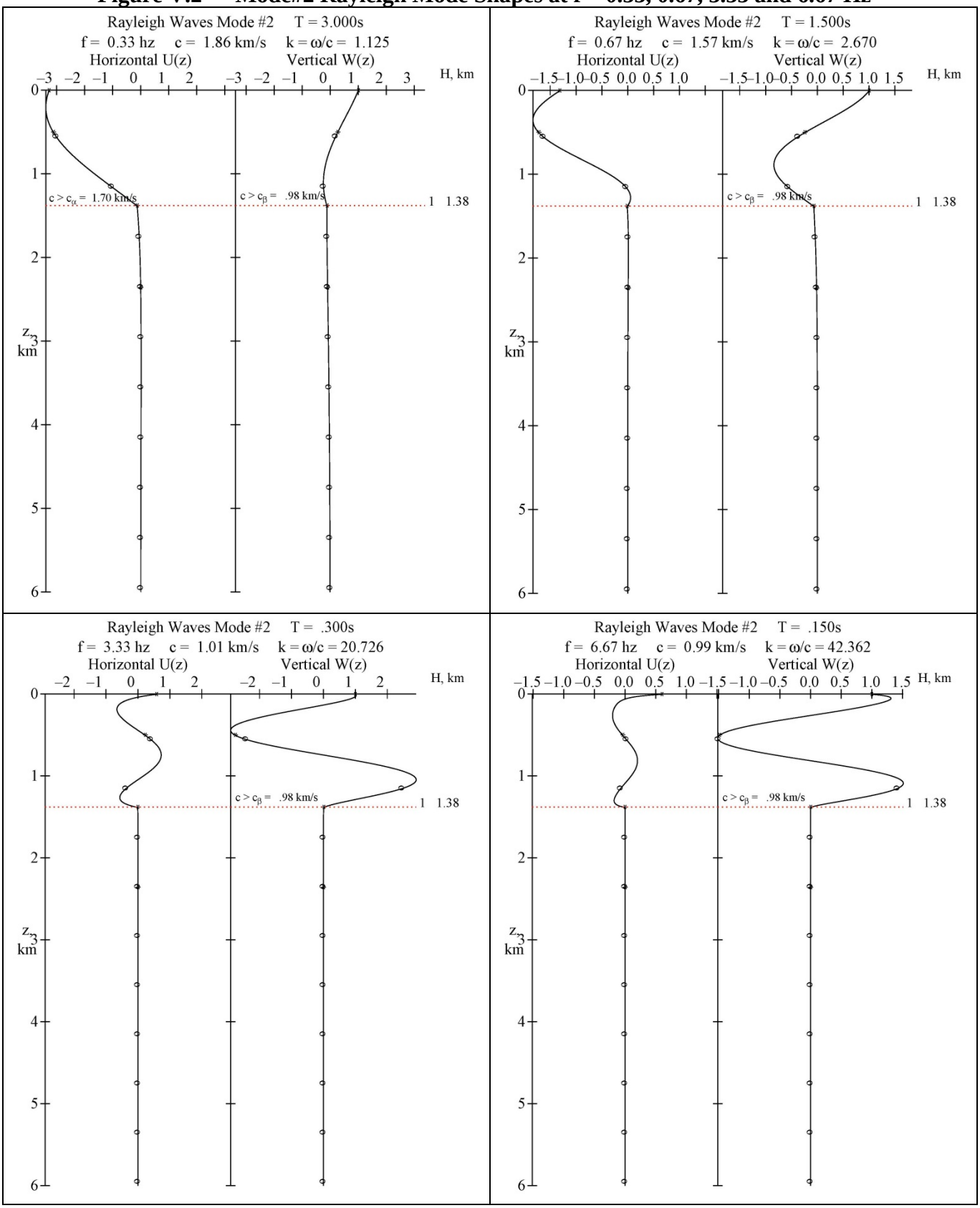

Figure V.3 Mode#3 Rayleigh Mode Shapes at f = 0.42, 0.83, 4.17 and 6.67 Hz

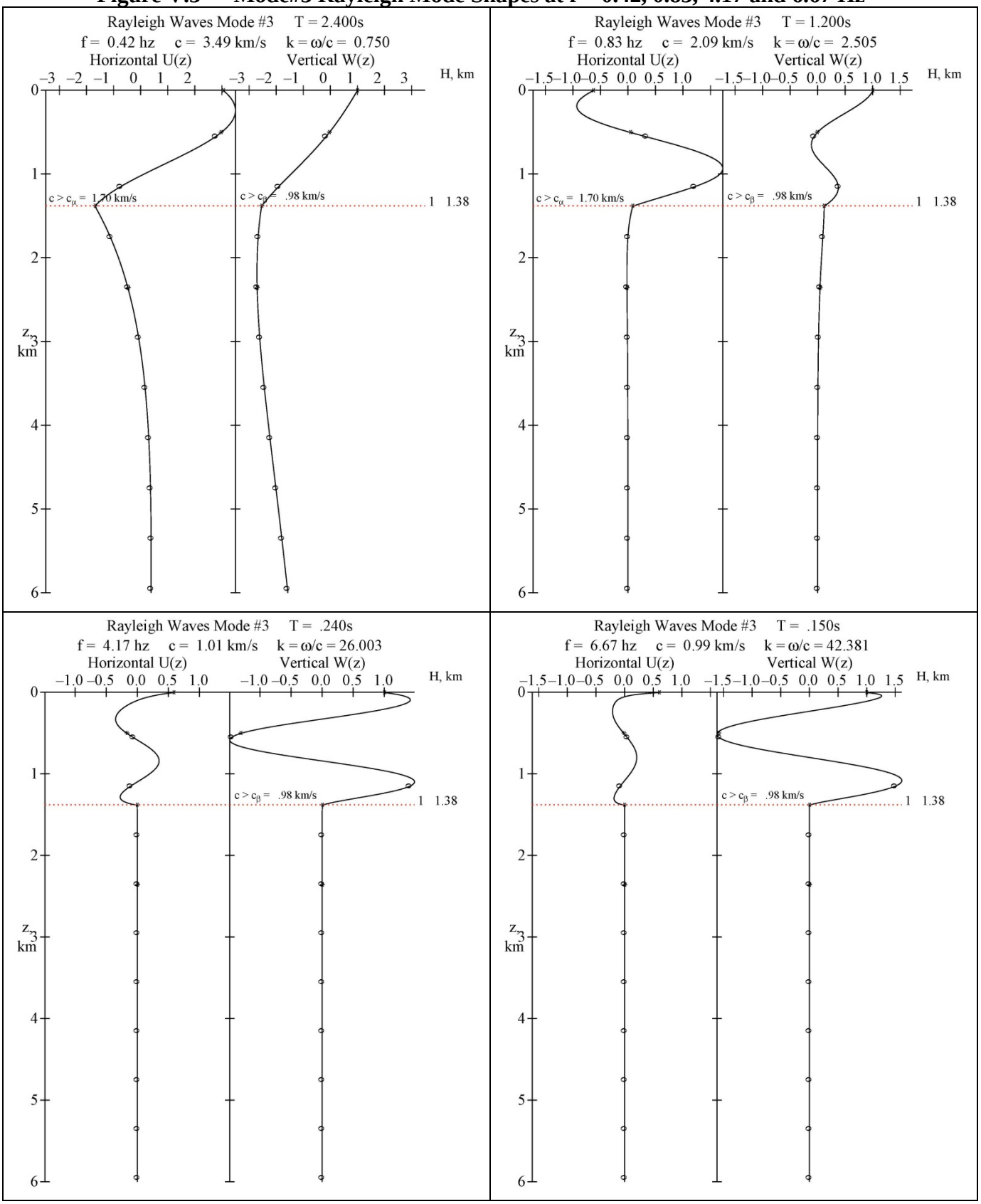

A characteristic of the Modes #2 and #3 of Rayleigh waves is that the Mode shapes for both the horizontal and vertical components of motion at each period now decrease to have negative values, reach a negative minimum, then cross the zero axis back to have positive amplitudes, and reach a positive maximum, before asymptotically approaching zero. Again, as in Modes #1 and #2, the amplitudes are practically zero at and below the interface of the two layers $(z = 1.38 km)$.

We expect the scattered and diffracted waves to be small at the interface. The same observations and conclusions can be made for Mode #4 and #5 free-field Rayleigh waves. Their plots have been omitted here.

Finally, the free-field mode shapes for incident P and SV body waves are plotted next. **Figure V.4** shows the input free-field Mode Shapes for the corresponding P- and SV- Body waves with angle of incidence of $\gamma = 60^o$ with respect to the horizontal, at two selected periods, T = 1.0, 0.3 sec., or at frequencies, f = 1.0, 3.33 Hz. The top two graphs are for incident P-waves, while the bottom two graphs are for incident SV- waves. As in the case of Mode#1 of Rayleigh waves, the Mode shapes are available at all 91 pre-selected period values for both incident P- and SV- body waves. It is noted from the figures that, at the periods shown, the wave amplitudes of the mode shapes are again scaled to have maximum amplitude of 1 at the half-space surface. Unlike the Rayleigh surface waves, depending on the period of the body waves, the waves do not decrease with depth. The waves in the first layer are harmonic, oscillating at the given wave length between the scaled maximum amplitude of ± 1, and the oscillation increases with decreasing period.

Below the first layer, in the semi-infinite medium, the mode shapes continue to oscillate, and do not decrease towards zero, since the body waves are harmonic waves, harmonic in both the horizontal *x*- and vertical *z*- directions.

We thus expect (in the next sub-section) that the diffracted waves from P and SV body waves will behave differently from Rayleigh surface waves.

Figure V.4 Mode#11,12 Incident P, SV Body Waves Mode Shapes at f = 1.0, 3.33 Hz

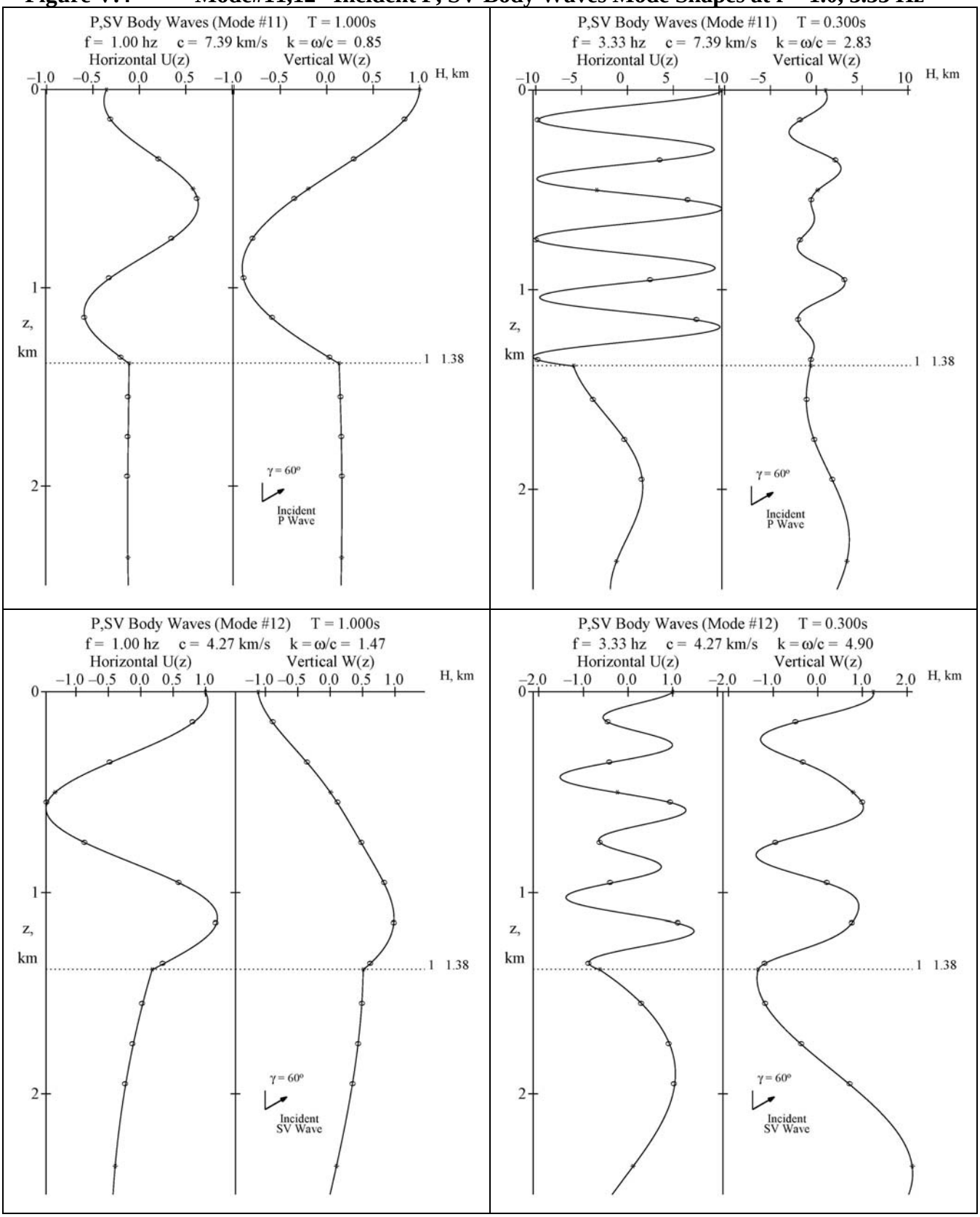

V.2 The Diffracted Mode Shapes

We next consider the case of irregularly shaped layered media inserted into the parallel two-layers. We select here the same irregular layered medium model as that for Love surface waves and Body SH waves. It is a shallow, "almost-flat" ellipse with a ratio of vertical minor axis / horizontal major axis = 0.1 at both the half-space surface and at the interface of the two layers. The half-width radius of the horizontal major axis is taken to be 0.1 km long for both, and the major diameter is 2.0 km long. Thus the half-width or radius of the minor axis is 0.1 km deep, and this corresponds to a very shallow ellipse. **Figure V.5** shows a sketch of such 2-Layered elastic medium for cases of

i) Incident Rayleigh Surface waves, and

ii) Incident Body P or SV waves

(i) Rayleigh Waves **(ii) Body P, SV waves**

Figure V.5 The Irregular 2-Lyered Medium with Incident Waves

The next five figures, **Figure V.6 to V.10** show the scattered and diffracted mode shapes for Modes #1 to #5 of Rayleigh Waves. Each Mode has the shapes plotted at four selected frequencies, **f = 13.33, 18.18, 20.0 & 25.0 Hz.** These are frequencies below period of 0.1 sec (or frequencies beyond 10Hz) as it was found that the long period waves do "not see" the irregularities and the diffracted waves are insignificant.

Figure V.6a and **V.6b** show the scattered and diffracted mode shapes respectively for the horizontal x-component and vertical z-component motions of Mode#1 of Rayleigh waves at four selected periods **T=4.0, 1.0, 0.5 and 0.30 sec,** or at frequencies of **f = 0.25, 1.0, 2.0 & 3.33 Hz**. With the irregular almost-flat elliptic surfaces from $x = -1.0$ km to $x = +1.0$ km on both the half-space surface $(z = 0\,\text{km})$ and at the interface of the 2

media $(z = 1.38\,\text{km})$, the diffracted mode shapes are plotted at equally spaced intervals along x from $x = -2.0\,\text{km}$ to $x = +2.0\,\text{km}$ at $0.1\,\text{km}$ apart. The dashed line on the left side of each graph represents the input free-field Mode shapes propagating along the parallel-layered media from the left and arriving towards the irregular surfaces. The shapes of the elliptic canyon on top and at the interface are also plotted with dashed lines, showing how they have deformed due to the elliptic inhomogeneity.

For all periods above 1 sec the waves are unaffected by almost-flat irregular surfaces, as illustrated by the case for **T=4.0s** in the two figures (**V.6a & b**). At the irregular interfaces between the 2 media, as pointed out in the previous section, as can also be seen by the dashed line on the left, the free-filed incoming mode shape amplitudes are already very small. Clearly not much diffraction is to be expected in this case.

For periods below **T=0.3s**, the amplitudes of x-component of Mode 1 Rayleigh waves decrease so fast that the waves are practically zero not far below the half-space surface, and hence there are hardly any scattered and diffracted waves.

Figure V.6a Mode#1 x-comp. Diffracted Mode Shapes at f = 0.25, 1.0, 2.0 & 3.33Hz

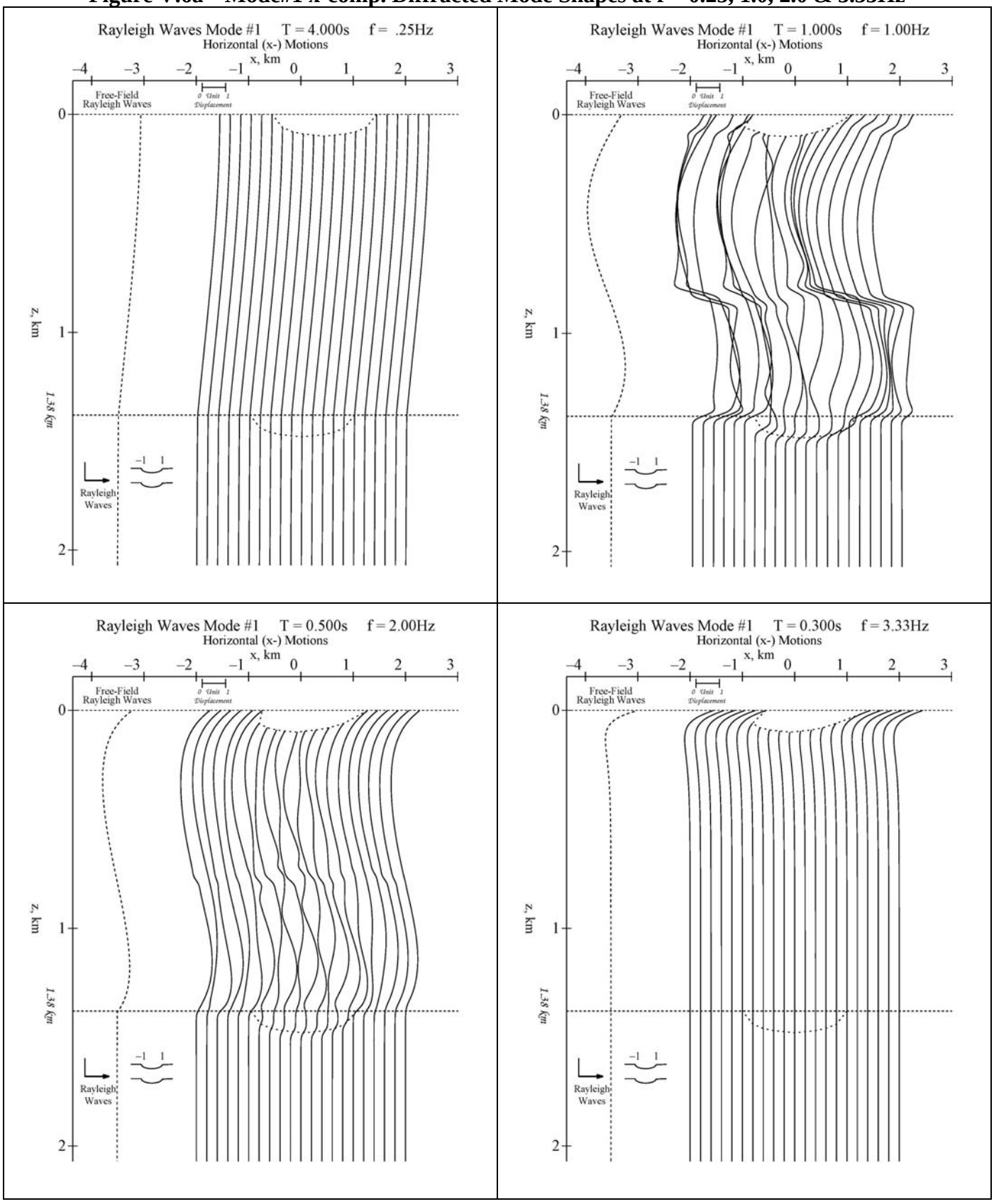

Figure V.6b Mode#1 z-comp. Diffracted Mode Shapes at f = 0.25, 1.0, 2.0 & 3.33Hz

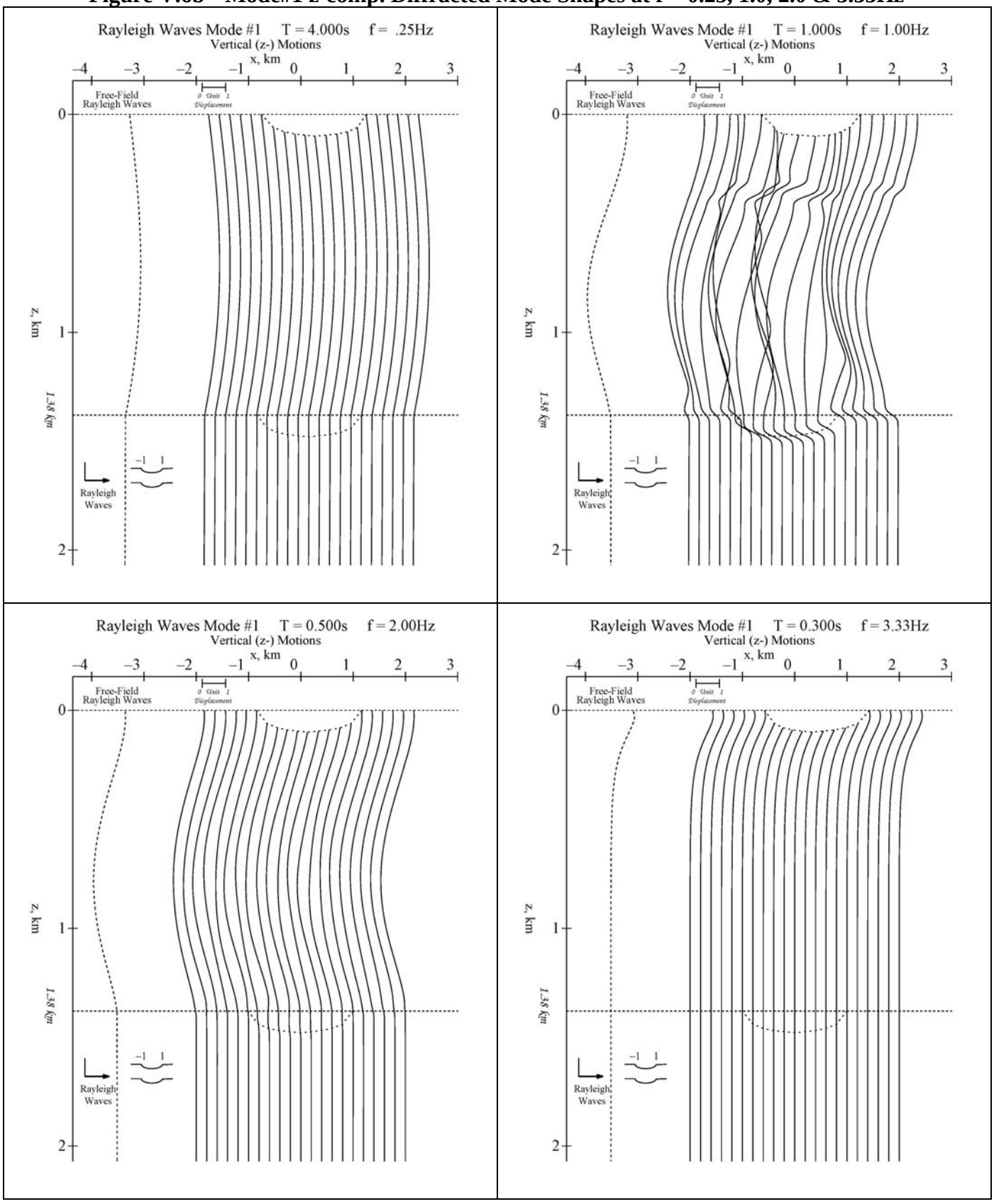

The cases for the higher modes of Rayleigh waves are much different, however. Figures **IV.7a, b** through **IV.10a, b** show the corresponding diffracted Mode Shapes for Modes #2 to #5 of Rayleigh waves.

As stated above, the higher mode Rayleigh waves, unlike the Mode#1 waves, are more oscillatory in the top layer before decaying to almost zero at the interface with the 2nd layer. As the Mode number increases, both the mode shapes of the input free-field and those of the diffracted Rayleigh waves here go through the *(M-1)* sign changes going down vertically from the top surface, where *"M"* is the mode number. Thus the diffracted mode shapes are also more oscillatory at the top layer. This behavior increases with increasing frequency. Further, the scattered and diffracted motions become more complex, for both the horizontal x- and vertical z-component motions, as the mode number increases (Figure **IV.6a,b** through **IV.10a,b).**

At present, we are able to do the calculations of the diffracted waves for the Rayleigh waves mode#2 to 5 up to ***f = 6.67Hz*** *(period# 61,* ***T = 0.15s****). Calculations for frequencies beyond this and up to the highest frequency of* ***f = 25.0Hz*** *(period# 91,* ***T = 0.04s****) will require more work on the numerical procedures to ensure convergence and accurate computational results. This is what we are currently working on.*

We will then also examine multi-layered media with the layers being closer together. It is expected that those diffracted patterns will become more complicated as the number of layers increase, and as the layers get closer together.

Figure V.7a Mode#2 x-comp. Diffracted Mode Shapes at f = 1.0, 2.0, 3.33 & 6.67Hz

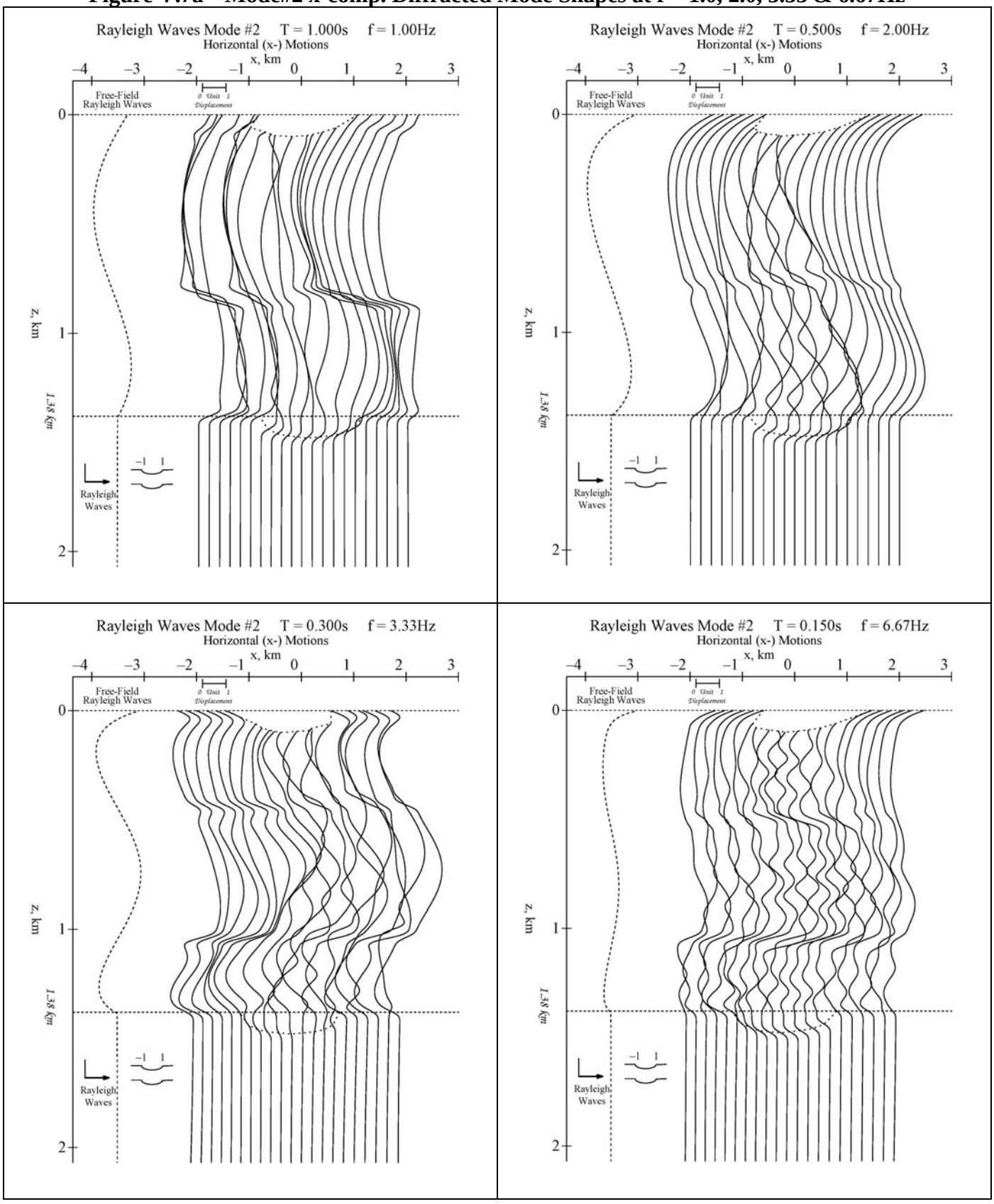

Figure V.7b Mode#2 z-comp. Diffracted Mode Shapes at f = 1.0, 2.0, 3.33 & 6.67Hz

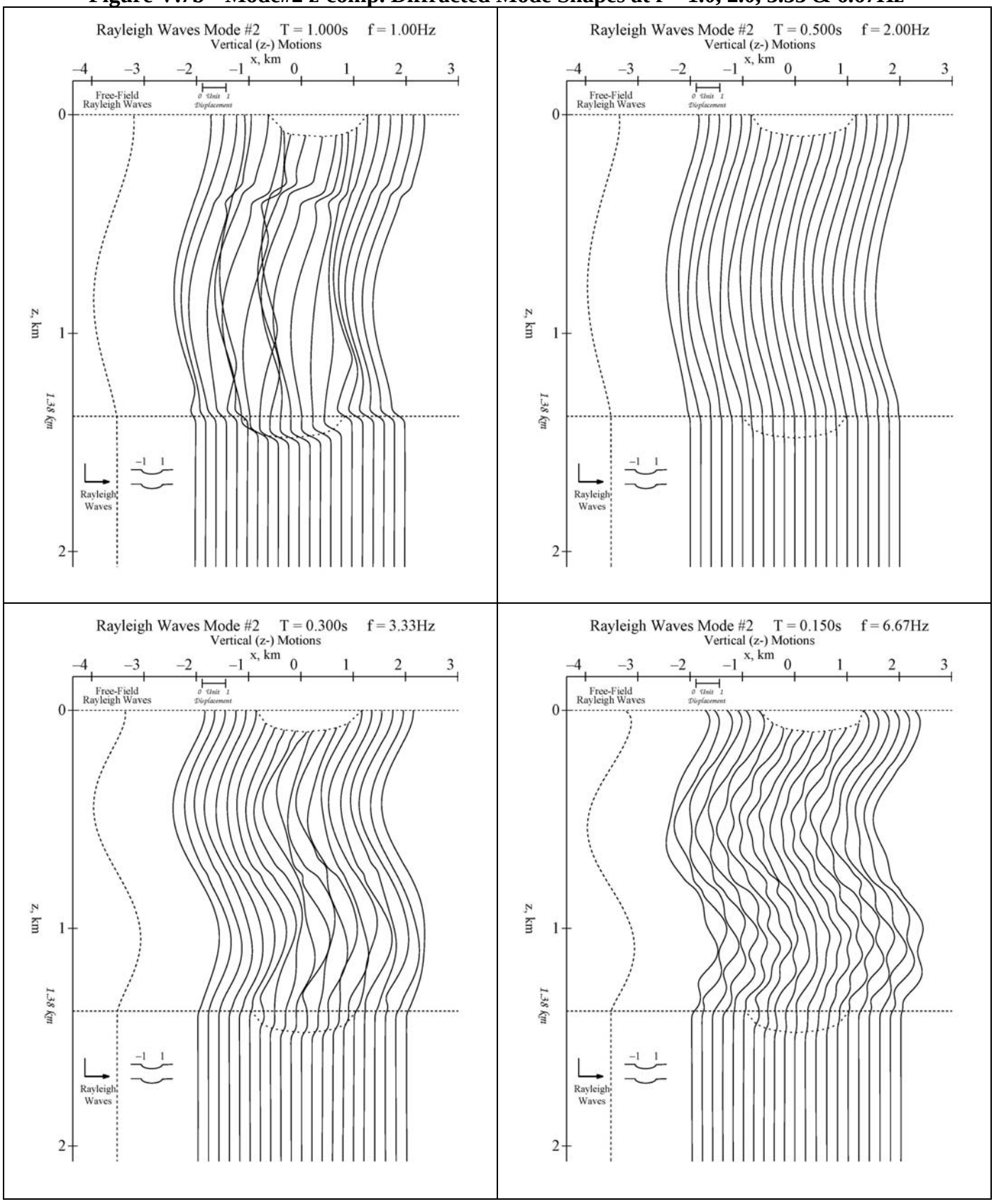

Figure V.8a Mode#3 x-comp. Diffracted Mode Shapes at f = 1.0, 2.0, 3.33 & 6.67Hz

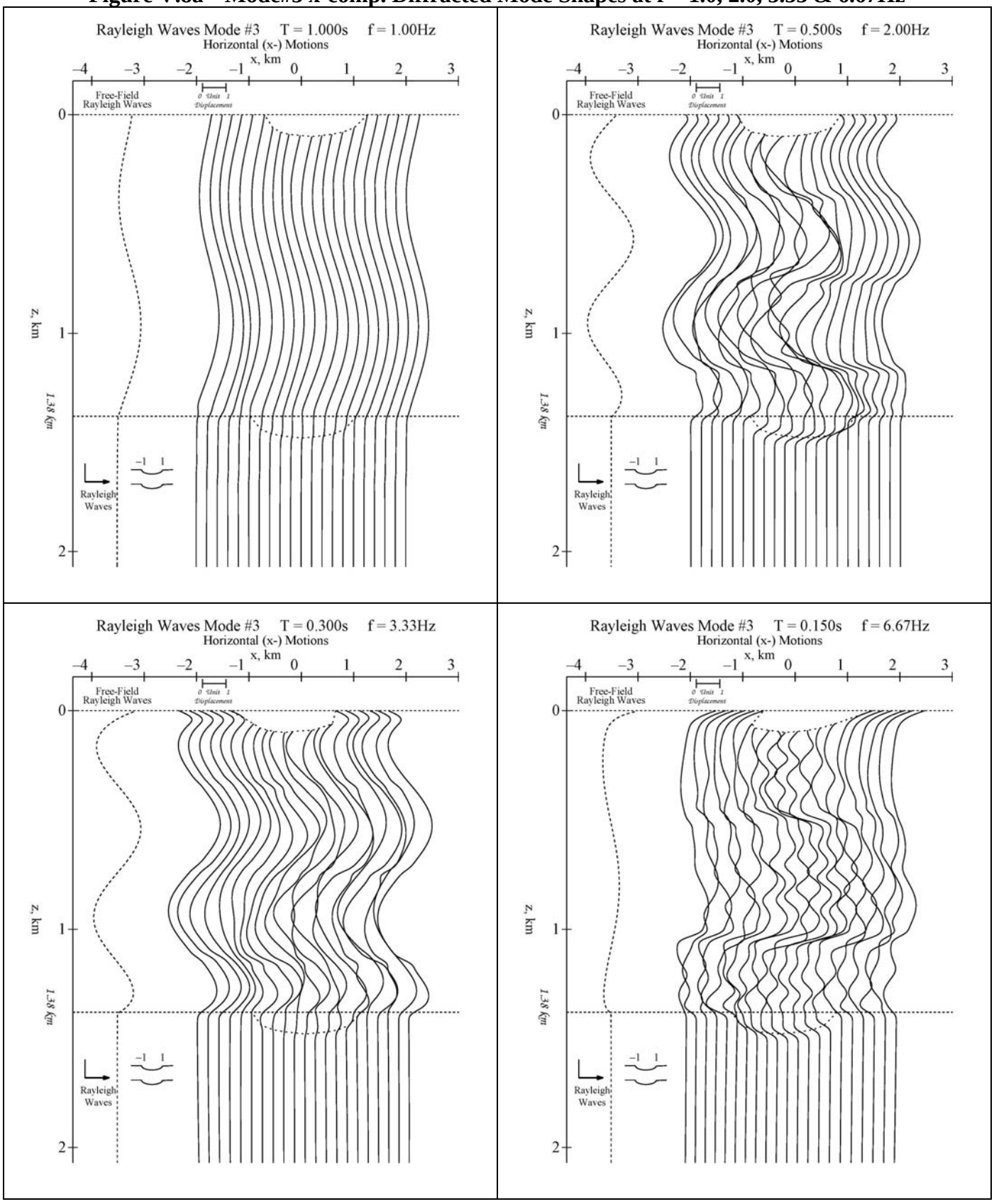

Figure V.8b Mode#3 z-comp. Diffracted Mode Shapes at f = 1.0, 2.0, 3.33 & 6.67Hz

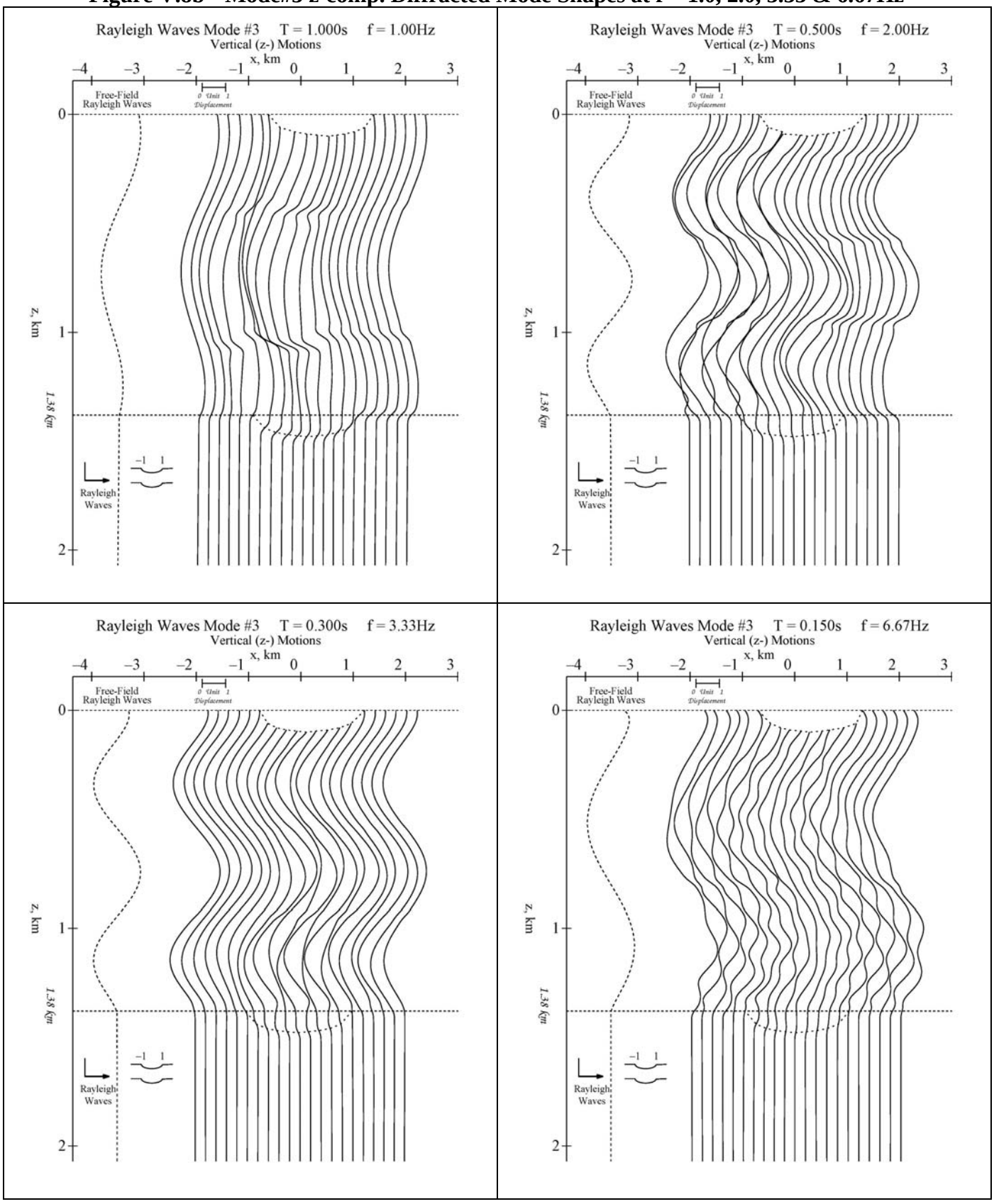

Figure V.9a Mode#4 x-comp. Diffracted Mode Shapes at f = 1.0, 2.0, 3.33 & 6.67Hz

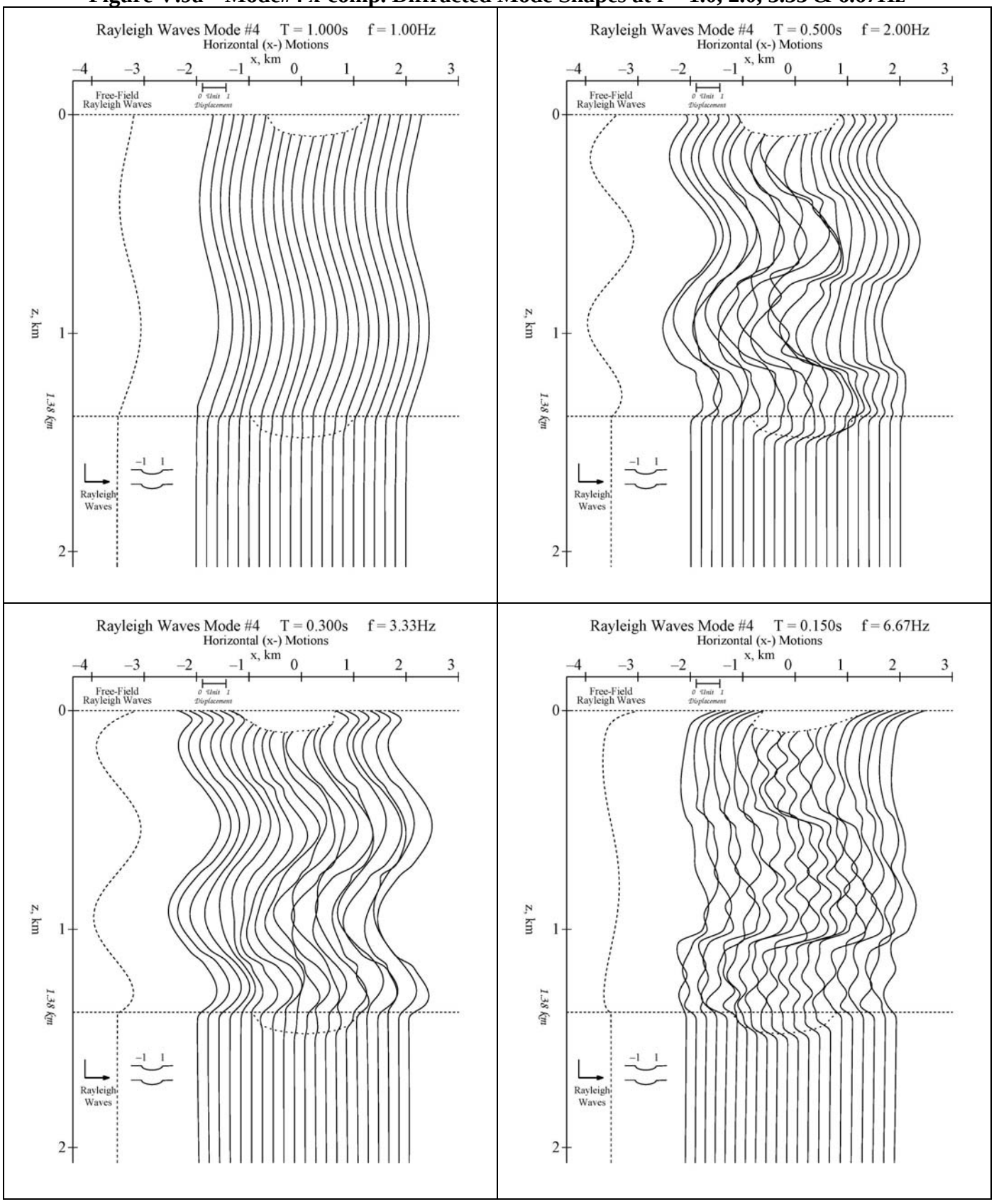

Figure V.9b Mode#4 z-comp. Diffracted Mode Shapes at f = 1.0, 2.0, 3.33 & 6.67Hz

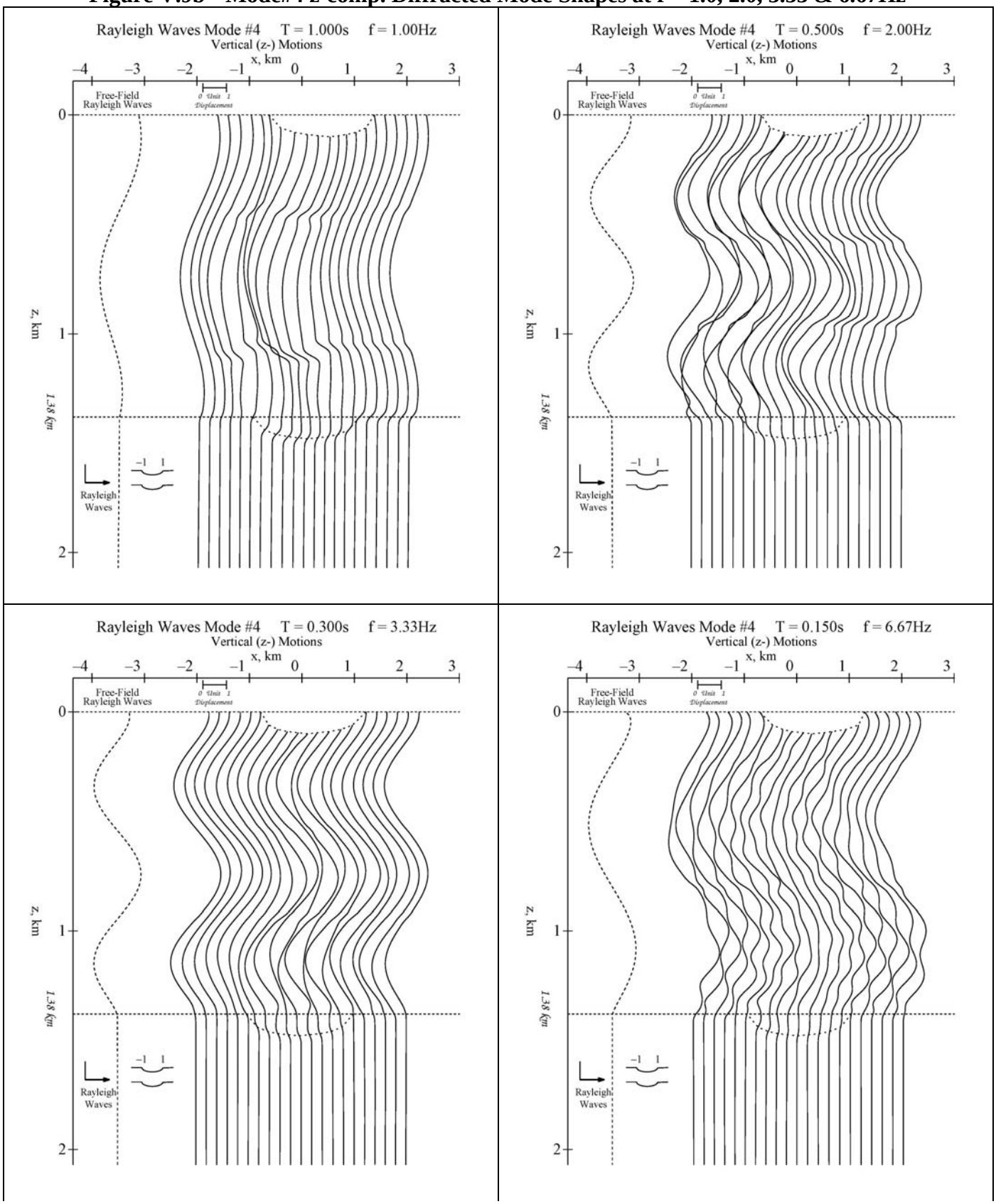

Figure V.10a Mode#5 x-comp. Diffracted Mode Shapes at f = 1.0, 2.0, 3.33 & 6.67Hz

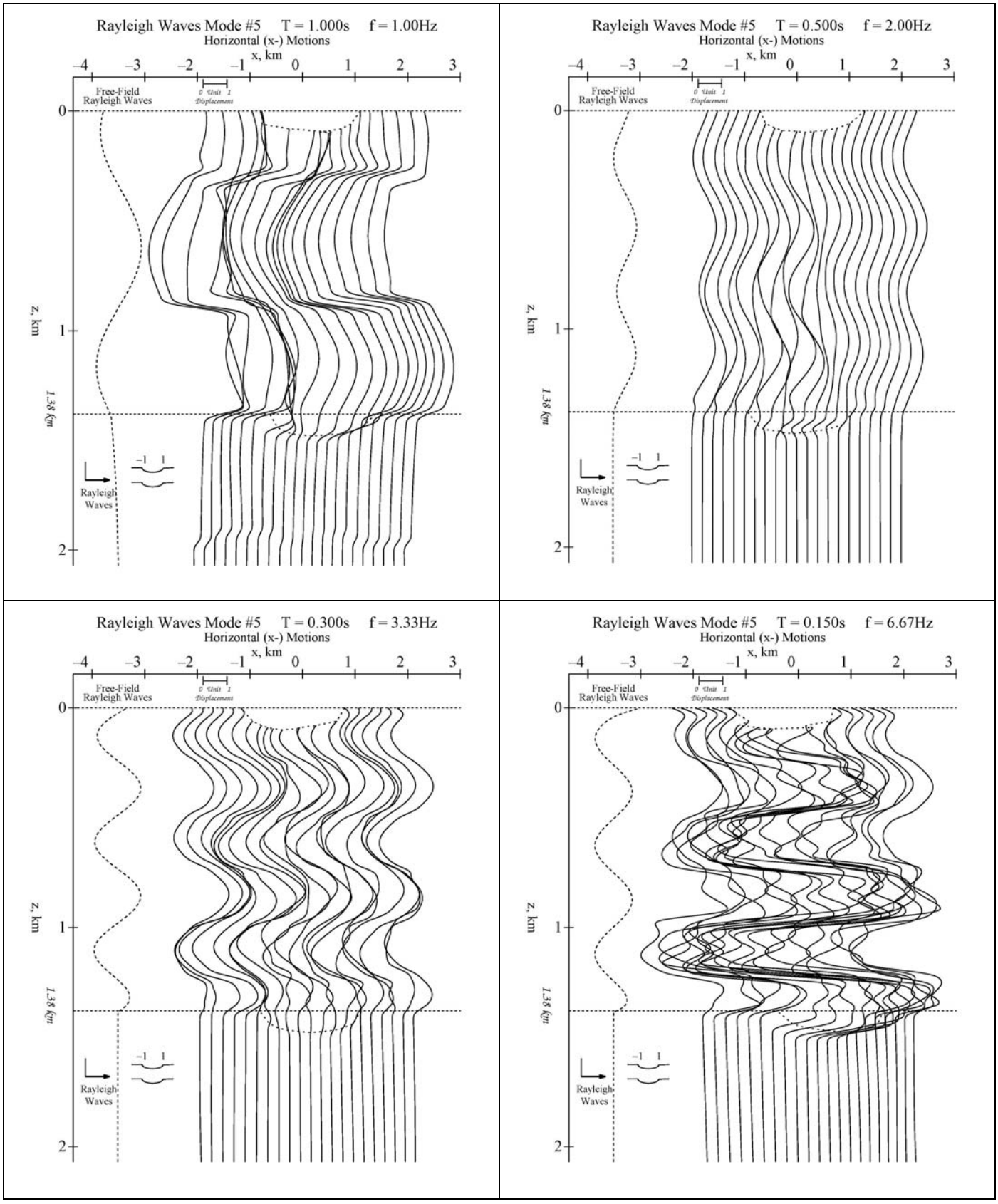

Figure V.10b Mode#5 z-comp. Diffracted Mode Shapes at f = 1.0, 2.0, 3.33 & 6.67Hz

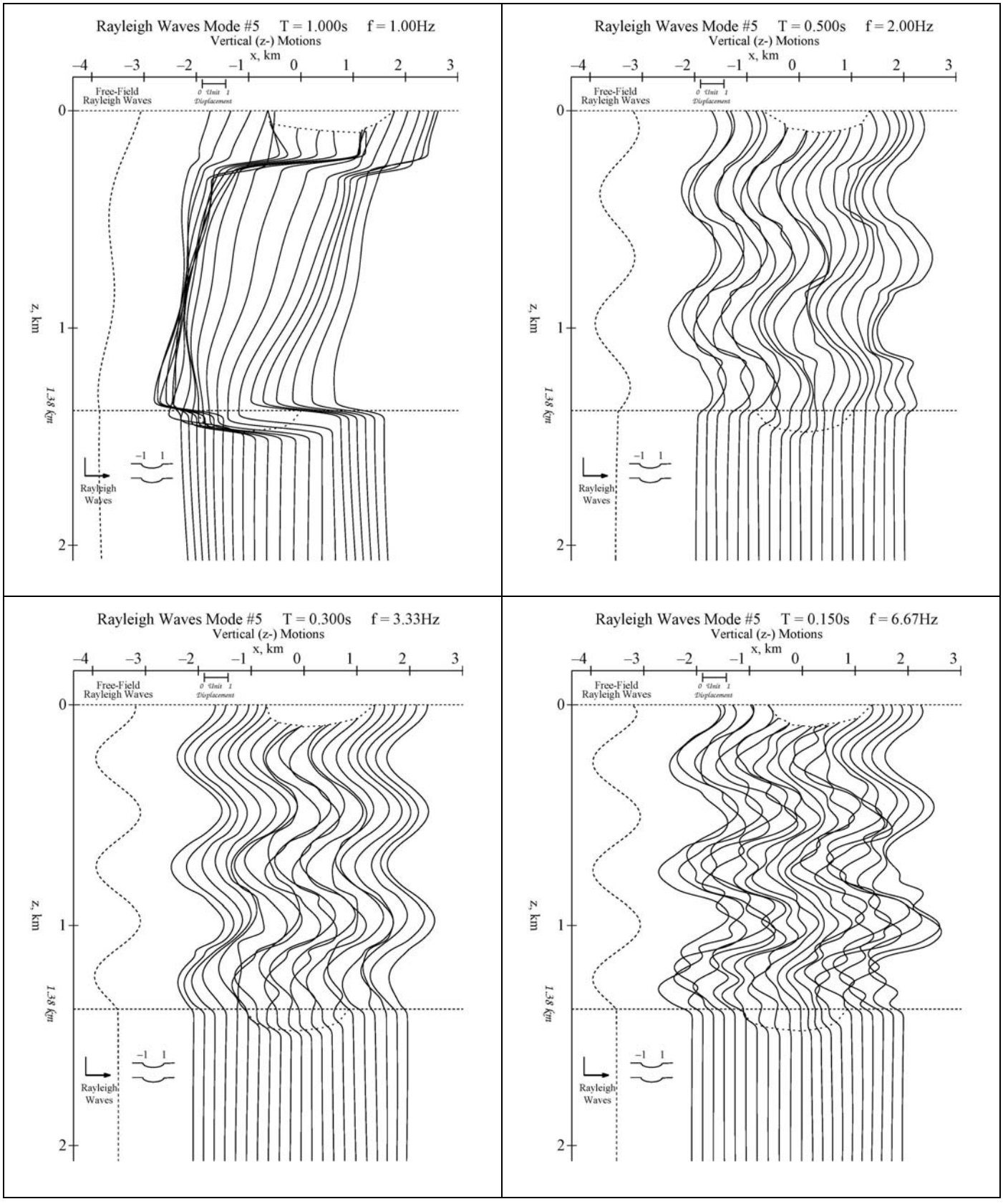

Finally, Figures **V.11a, b** show the horizontal x- and vertical z-component motions of diffracted mode shapes corresponding to incident plane P- and SV- body waves. In each figure, the top two graphs are respectively for incident P- and incident SV-waves at period of **T=1sec**. The bottom two graphs are respectively for incident P- and incident SV-waves at period of **T=0.3sec**. As seen from Figure **V.4** above, the input free-field mode shapes of the Body P- and SV- waves, unlike the Rayleigh waves, are more oscillatory in both layers, without decreasing to zero bellow the interface. Their oscillatory nature also increases significantly with frequencies.

In **Figures V.11a, b** the irregular almost-flat elliptic surfaces are between $x = -1.0\,\text{km}$ and $x = +1.0\,\text{km}$, on both the half-space surface $(z = 0\,\text{km})$ and at the interface of the 2 layers $(z = 1.38\,\text{km})$, and the diffracted mode shapes are plotted at equally spaced intervals along x from $x = -2.0\,\text{km}$ to $x = +2.0\,\text{km}$, at $0.1\,\text{km}$ apart. As before, the dashed line on the left side of each graph represents the input free-field mode shapes of body P- or SV- Waves propagating through the parallel-layered medium from below and arriving at the irregular surfaces. The angle of incidence of the body waves is $\gamma = 60^o$ with respect to the horizontal. At all frequencies, the mode shapes of the diffracted waves are very oscillatory and are of very different amplitudes than those of the incident free-field waves.

At the frequency of **f=3.33Hz**, the diffracted waves are already very oscillatory and of large amplification relative to the free-field mode shapes. The amplification is indeed much greater than two, as previously observed for body SH-waves.

At present, as for the case of Rayleigh waves, we are able to do the calculations of the diffracted waves for the incident P- and SV-body waves up to ***f = 6.67Hz*** *(period # 61,* ***T = 0.15s****). Calculations for frequencies beyond this, and up to the highest frequency of* ***f = 25.0Hz*** *(period # 91,* ***T = 0.04s****), will require more work on the numerical procedures to ensure convergence and meaningful, computational results. This is what we are currently working on.*

We will next work on multi-layered media with the layers closer together. It is expected that these diffracted patterns will be far more complicated as the number of layers increase, and as the layers get closer and closer together.

Figure V.11a P-,SV-Body Waves x-comp. Diffracted Mode Shapes at f = 1.0 & 3.33 Hz

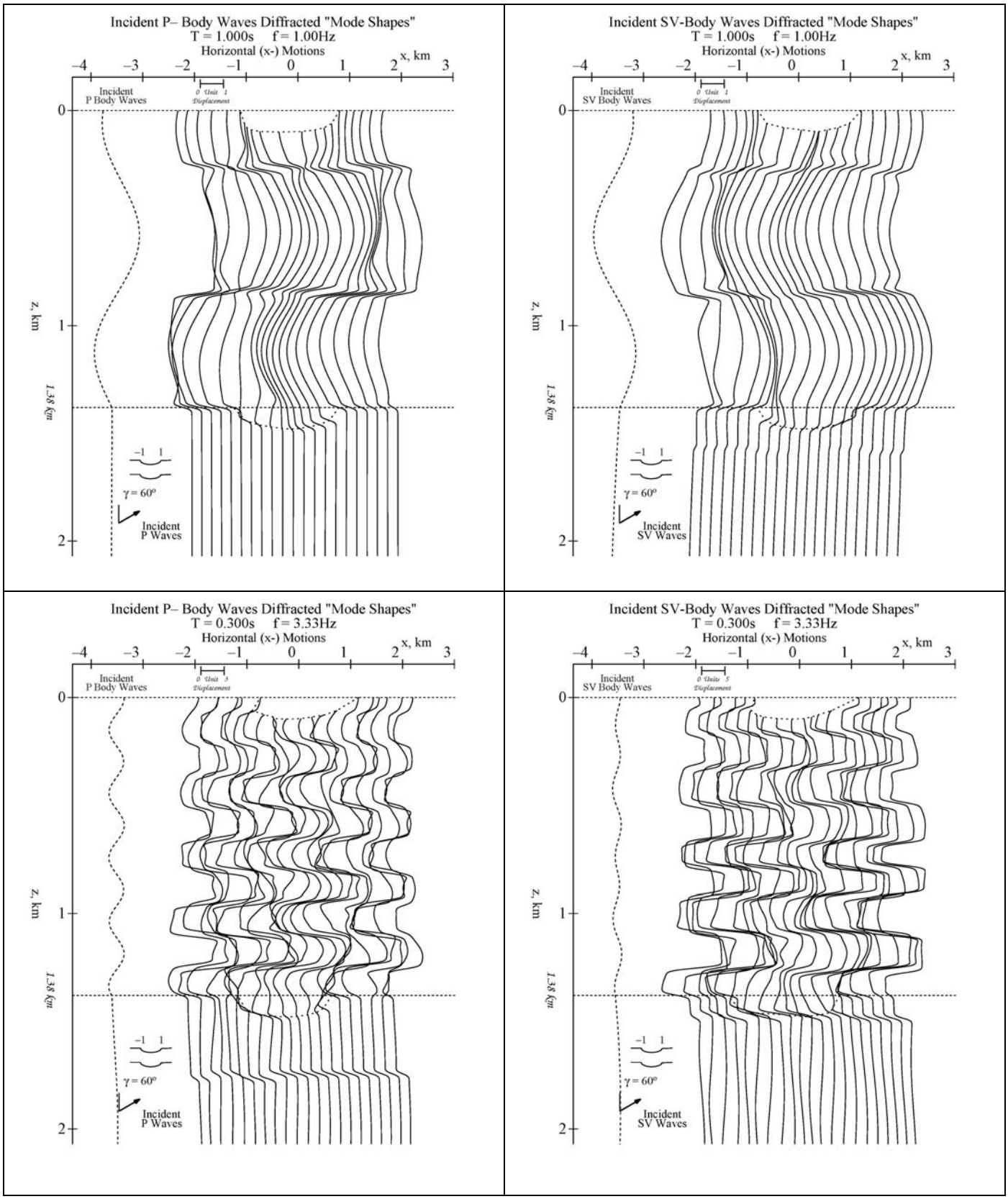

Figure V.11b P-,SV-Body Waves z-comp. Diffracted Mode Shapes at f = 1.0 & 3.33 Hz

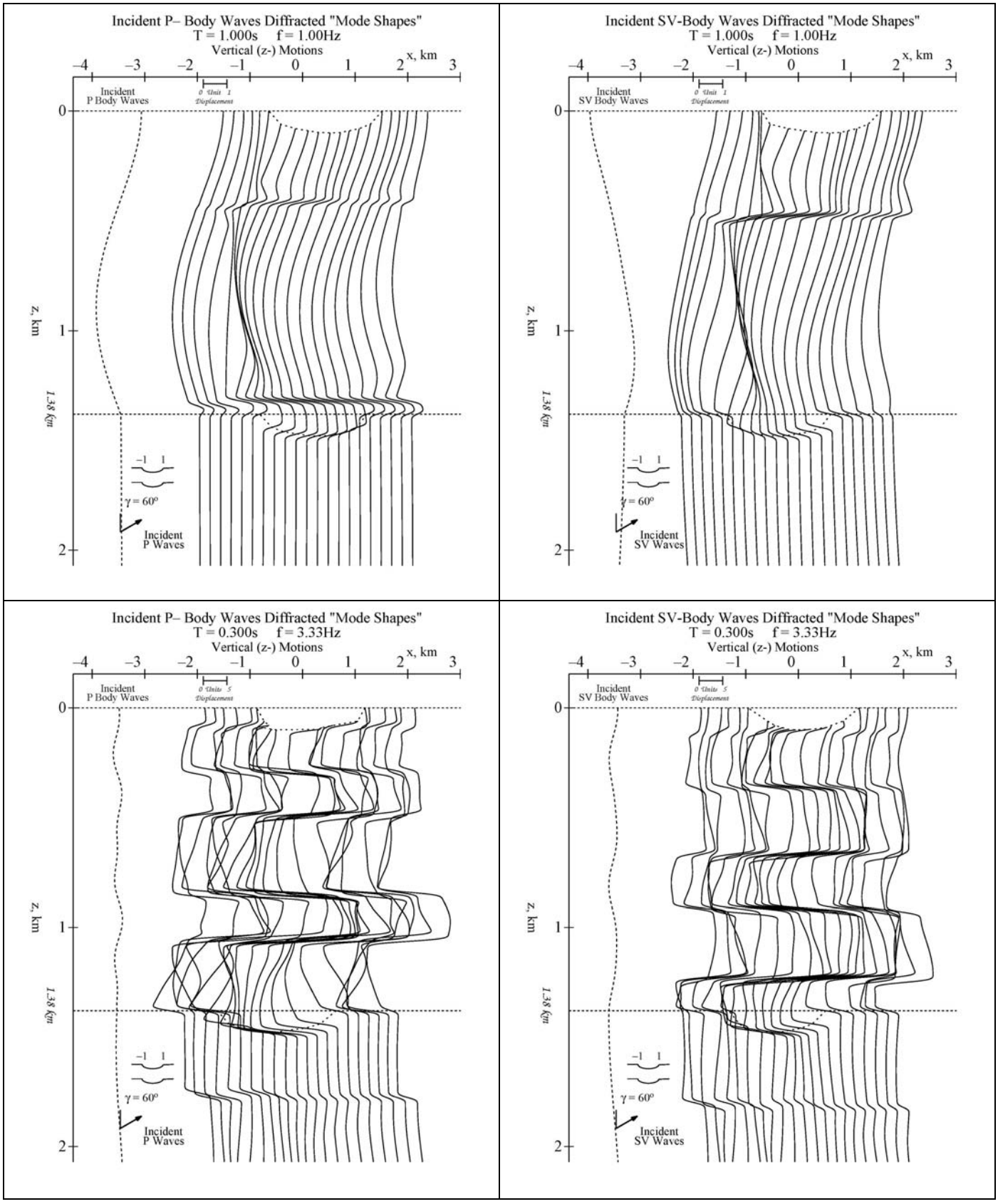

References

1. **V. W. Lee & X.Y. Wu.** Application of the Weighted Residual Method to Diffraction by 2-D Canyons of Arbitrary Shape, I: Incident SH Waves, *Int. J. Soil Dynamics & Earthquake Eng., 13(5),* 355-364, **Oct, 1994a.**

2. **V. W. Lee & X.Y. Wu.** Application of the Weighted Residual Method to Diffraction by 2-D Canyons of Arbitrary Shape, II: Incident P, SV & Rayleigh Waves, *Int. J. Soil Dynamics & Earthquake Eng., 13(5),* 365-373, **Oct, 1994b.**

3. **Mow, Chao-Chow & Pao, Yih-Hsing** (1973). The Diffraction of Elastic Waves and Dynamic Stress Concentrations, Institute of Physics Publishing, 617

4. **M.D. Trifunac & V. W. Lee:** Interfacing Seismological Description of Strong Ground Motion with Engineering Analysis of Soil Structure Interaction for Nuclear Power Plants, **Report I, 2013**

5. **M.D. Trifunac & V. W. Lee:** Synthetic Translational Motions of Surface Waves on or Below a Layered Media**, Report II, 2013.**

6. **M.D. Trifunac & V. W. Lee:** Synthetic Rotational Motions of Surface Waves On or Below a Layered Media**, Report III, 2013.**

7. **M.D. Trifunac & V. W. Lee:** Diffraction Around An Irregular Layered Elastic Media, I: Love and Body SH Waves, **Report IV-Part 1, 2013.**

APPENDIX R5

(Date Submitted 2 February 2014)

Manual on how to use and execute EQSYNACC - to generate Synthetic Accelerograms for Points on or Below the Half-space

I. The Original Synthetic Accelerogram Program for Points on Half-space: SYNACC

The synthetic translational and rotational components of acceleration are constructed to have a required Fourier amplitude spectrum, $FS(\omega)$, and a given duration, $D(\omega)$, at the half-space surface of a given site. A complete review of the method first proposed by **Trifunac (1971b)**, and later refined by **Wong and Trifunac (1978, 1979)**, for the generation of synthetic accelerograms, can also be found in the review paper by **Lee (2002).** In short, the following files and information are needed to construct synthetic motions:

1. **Period.dat**: the Data file of the Periods of waves
2. **HskWav.dat**: Wave Dispersion Data at a Site
3. **InSyn.dat: Input data file for SYNACC.EXE**
4. **Option** to be used for constructing the Fourier Amplitudes in the given Frequency Band

I.1 Period.dat

The data file is listed as follows, to be read in by the program:

0.040	0.042	0.044	0.046	0.048	0.050
0.055	0.060	0.065	0.070	0.075	0.080
0.085	0.090	0.095	0.10	0.11	0.12
0.13	0.14	0.15	0.16	0.17	0.18
0.19	0.20	0.22	0.24	0.26	0.28
0.30	0.32	0.34	0.36	0.38	0.40
0.42	0.44	0.46	0.48	0.50	0.55
0.60	0.65	0.70	0.75	0.80	0.85
0.90	0.95	1.00	1.10	1.20	1.30
1.40	1.50	1.60	1.70	1.80	1.90
2.00	2.20	2.40	2.60	2.80	3.00
3.20	3.40	3.60	3.80	4.00	4.20
4.40	4.60	4.80	5.00	5.50	6.00
6.50	7.00	7.50	8.00	8.50	9.00
9.50	10.00	11.00	12.00	13.00	14.00
15.00					

There is a total of 91 periods from **0.040 sec to 15.00 sec**. In terms of frequency this corresponds to the frequency range of **0.07 Hz to 25 Hz**. The reason for using 91 periods is only traditional, and we continue to use it to maintain consistency with many of our older papers, which deal with empirical scaling of spectral amplitudes and also use the 91 periods.

I.2 Hskwav.dat: The Original Haskell Program - HASKEL.EXE

This section will describe the input needed to generate the wave dispersion data at a site: Hskwav.dat

I.2.1 Input: The Layered Media Elastic Properties

Following Trifunac (1971), Wong and Trifunac (1978), at a given site, we first select an approximate geological profile to be represented by the equivalent parallel-layered media. A model can have N layers. For each layer l with l=1 to N the parameters h_l, α_l, β_l and ρ_l must be specified, where

h_l = layer thickness,

α_l = P −wave velocity,

β_l = S −wave velocity, and

ρ_l = density of the l^{th} layer,

of the medium, with the bottom $l = N$ medium of infinite thickness.

The file HskLin.dat here is an example of one such file used in Report I:

Hsklin.dat:

6 LAYER Imperial Valley VELOCITY MODEL			
0.18	1.70	0.98	1.28
0.55	1.96	1.13	1.36
0.98	2.71	1.57	1.59
1.19	3.76	2.17	1.91
2.68	4.69	2.71	2.19
.00	6.40	3.70	2.71
15, 0.1,1.0,10,0			

The 1st line is the number of elastic layers, *N*, in the medium, followed by a name identifying the medium. N lines and four columns then follow it with elastic properties in each layer. The first column is the thickness of each layer in km. The second column is the P-wave speed in the layer in km/s. The third column is the shear wave speed in the layer in km/s. The fourth and last column is the mass density of the layer in gm/cc. This it is followed by a line with 5 numbers: 15., 0.1, 1.0, 10, 0, which respectively are:

i) TST = 15 sec = Starting maximum Period,
ii) TMIN = 0.1 sec = Down to minimum Period,
iii) DTS = 1.0 sec = Spacing of Periods to start,
iv) Nsmx = 10 = Recommended number of iterations for search of the roots.
v) NMCL = 0, Number of Modes of Rayleigh and Love waves (set to default of 5)

I.2.2 Output: Wave Dispersion Data at the Half-Space Surface of the Site

With the input file **Hsklin.dat**, the original program **Haskel.exe** is first executed. It will compute, for both the Rayleigh and Love surface waves their group and phase velocities, each at a starting period from $\boldsymbol{T = 15\,sec}$ down to $\boldsymbol{T \sim 0.1\,sec}$ or in a frequency range from $\boldsymbol{f = 0.07\,Hz}$ to $\boldsymbol{f \sim 10\,Hz}$. This will give, for each $\boldsymbol{m = 1}$ to $\boldsymbol{5}$ modes of Rayleigh waves and Love waves, $\boldsymbol{C_m(\omega_n)}$ and $\boldsymbol{U_m(\omega_n)}$, respectively, their phase and group velocities, at a set of discrete frequencies $\boldsymbol{\omega_n}$. For Rayleigh waves, **HASKEL.EXE** also gives the ratios of the vertical to horizontal displacement amplitudes at the half-space surface. The output data will be in the file **Hskout.dat**. The set of discrete frequencies $\boldsymbol{\omega_n}$ is usually a set of non-uniform frequencies within the selected frequency range. The program then interpolate to the frequencies corresponding to the 91 discrete periods of the data file **Period.dat** above, and outputs the data in **Hskwav.dat**, which will be the input file for **SYNACC.EXE**.

Along with the calculations of group and phase velocities of each mode of surface waves completed in the late 1970's, no data were generated for the corresponding body P, SV and SH waves. An "empirical mode" of body wave was created for both the longitudinal P- and shear S-

waves. The P-wave mode was created using an empirical curve that ranged from α_{min} to α_{max} from short period to long period, where α_{min} and α_{max} are respectively the minimum and the maximum P-wave velocities is the layered media. Similarly, the S-wave mode was created using an empirical curve that ranged from β_{min} to β_{max} from short period to long period, where β_{min} and β_{max} are respectively the minimum and maximum S-wave velocity is the layered media. Such approximate representation of body wave modes will be replaced here by the real P, SV and SH body wave modes calculated analytically from body waves incident from below. This will be described in subsequent sections of this report.

Figure 1 is a plot of the phase velocities for five modes of Rayleigh waves and five modes of Love waves for the 6-layered El Centro Imperial Valley site whose layered media properties are those given in the file **Hsklin.dat** above. The Rayleigh waves are plotted as solid lines and the Love waves as dashed lines. The horizontal axis for period is plotted in logarithmic scale from around $T = 0.04\,\mathbf{sec}$ to $T = 15\,\mathbf{sec}$.

On the left side of the figure, between $T = 0.10\,\mathbf{sec}$ and $T = 0.40\,\mathbf{sec}$ are two lines, one solid and one dashed. The solid line shows a smooth step function going from α_{min} to α_{max}, representing the empirical body P-wave, while the dashed graph is the corresponding step function from β_{min} to β_{max} representing the body S-wave. These curves were used in the previous generations of this program. As will be shown in later sections, calculations are now included for P, SV and SH Body waves incident onto the layered half-space.

Figure 1 Phase Velocities for Love & Surface Waves

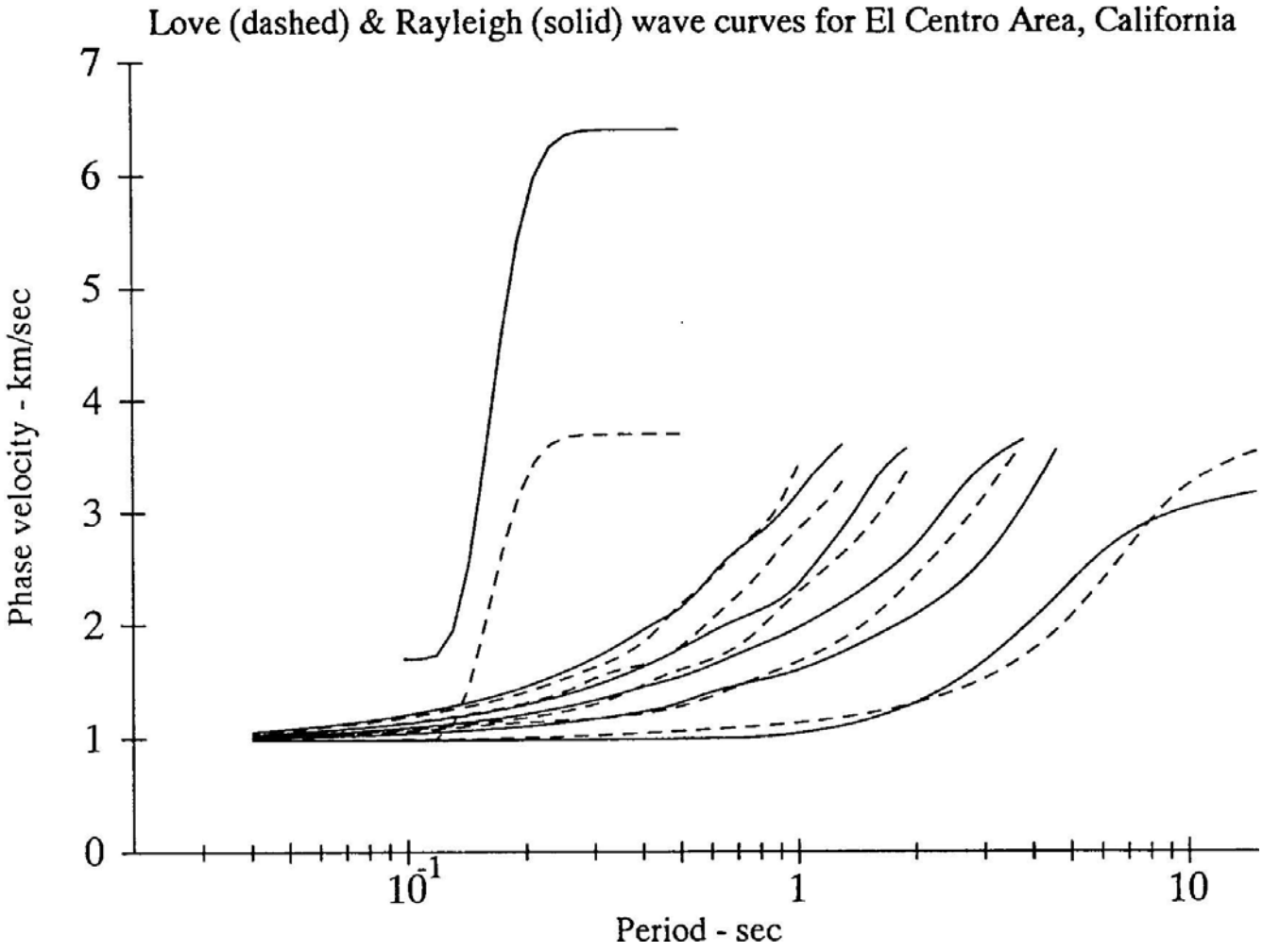

I.3 Insyn.dat: Input data for SYNACC.EXE

SYNACC will next open the file **InSyn.dat** in unit NU1 and read in a sequence of input info:

```
OPEN(NU1,FILE='InsynS.dat',STATUS='OLD')
```

1) **Input 1:** IWRT: Output Mode

   IWRT =0: Output ALL input read in
   =1: Simplified Output

```
      Write(*,1111)
1111   FORMAT(' INPUT IWRT = ')
      READ(NU1,*)IWRT
```

2) **Input 2:** Date and Time of the Synthetic Earthquake

```
      Write(*,*)' INPUT MONTH,DAY,YEAR,HOUR,MIN& SEC.:'
      READ(NU1,*)IMON,IDAY,IYEAR,IHOUR,IMIN,ISEC
```

3) **Input 3:** ICHOIC - Options to be used for constructing the Fourier Amplitudes in the given Frequency Band

```
      Write(*,*)' OPTIONS: (0)QUIT,'
      Write(*,*)' (1)MAG-SITE,(2)MMI-SITE,(3)MAG-DEPTH,(4)MMI-DEPTH,'
      Write(*,*)' (5)INPUT FS,(6)MAG-DEPTH-SOIL,(7)MAG-SITE-SOIL,'
      Write(*,*)' (8)MMI-DEPTH-SOIL, OR (9)MMI-SITE-SOIL MODEL?'
      Write(*,1)
      READ(NU1,*)ICHOIC
```

This part of the input will be described in full detail in (the next) Section I.4

4) **Input 4:** INMAX, PDURN

INMAX= number of times allowed to double the duration to allow for late arrival waves

```
      Write(*,*) ' INMAX (2,4,8,16...),PDURN = '
      READ(NU1,*)INMAX,PDURN
```

5) **Input 5: IGYZBE**

IGYZBE= Initial random number to be used to generate the synthetic accelorgram

```
      Write(*,3)
      READ(NU1,*)IGYZBE
```

6) **Input 6:** Synthetic Record Reference name

It is of the form XXNNN, where 'XX' are alphabetic characters and 'NNN' are numeric digits.

```
      Write(*,21)' INPUT SYNTHETIC RECORD REFERENCE # (XXNNN): ')
      READ(NU1,22)(IREF(I),I=1,3)
22    FORMAT(40A2)
```

7) **Input 7:** Synthetic Record log number

```
Write(*,*)' INPUT SYNTHETIC RECORD LOG # (80.01.12): '
READ(NU1,22)(IREF(I),I=4,7)
```

8) **Input 8:** IFDUR, duration parameter

IFDUR	=0	do not impose the empirical scaling to get duration. Instead, duration is computed from the epicentral distance and dispersion curves,
	=1	Impose the empirical scaling to calculate duration

```
Write(*,2)' INPUT DURATION PARAMETER(0/1): '
READ(NU1,*)IFDUR
```

9) **Input 9:** IPR, probability level

IPR is a number between 1 and 9 corresponding to the probability level of 0.1 to 0.9

```
Write(*,*)' INPUT PROBABILITY LEVEL #, (1 TO 9, FOR .1 TO .9): '
READ(NU1,*)IPR
```

10) **Input 10:** Earthquake parameters depending on ICHOIC of Input 3

Depending of the option ICHOIC, earthquake parameters like magnitude or intensity, epicentral distance, …. are input here. This part of the input will be described in more detail in (the next) Section I.4

11) **Input 11:** NWAVE, total number of dispersion waves

```
Write(*,*)' INPUT THE TOTAL # OF DISPERSION MODES, NWAVE(10)
= '
READ(NU1,*) NWAVE
```

12) **Input 12:** Output Haskel velocity data Filename

```
Write(*,*)' THIS PROGRAM READS IN RAYLEIGH & LOVE WAVE
DATA,'
Write(*,*)' FROM OUTPUT OF HASKEL & HSKFIX PROGRAMS,'
Write(*,*)' HASKEL VEL. DATA Filename(A20)
Read(nu1,9001)INFILE                    !12/2/12 char*30 infile
```

13) **Input 13:** Yes/No for 1st arrival time at T=0

```
Write(*,6201)' MIN. ARRIVAL TIME AS T=0? (0)Y(1)N (0/1): '
READ(NU1,*)ITMIN
```

14) Input 14: Mode participation factor

```
MPFCTR=1
Write(*,*)'  MODE PARTICIPATING METHOD? (1/2): ')
READ(NU1,*)MPFCTR
```

I.4 Options to be used for constructing the Fourier Amplitudes in the given Frequency Band

Currently **SYNACC** has a total of ***nine*** options to construct the Fourier amplitudes in the given frequency band. All except one are constructed from empirical regression equations.

I.4.1 The Original and Current Regression Equations

Programmed into the original synthetic accelerogram program **SYNACC.EXE** currently has the ***nine*** options by which the Fourier amplitudes for the synthetic acceleorgrams at the half-space surface can be generated. All except the 5^{th} option are regression equations developed from the 1970s, through the 1980s and 1990s for the generation of Fourier and Response spectral amplitudes and the duration of strong-motion records.

The first 4 options are the original set of regression equations developed in the 1970's and 1980's for the *Magnitude* or *MMI* models with local site geology specified by site conditions *(s = 0,1,2 respectively for geological rock, intermediate and sites on sediments)* or depth of alluvium, *h in km*. The 5^{th} option allows the users to input their own Fourier amplitudes. The 6^{th} to 9^{th} options were added in the early 90's for respectively the *Mag-Site-Soil, MMI-Site-Soil, Mag-Depth-Soil* and *MMI-Depth-Soil* models where the soil condition, s_L is added as an additional scaling parameter in the regression, an upgrade of the corresponding first four options.

These are the format statements in **SYNACC.EXE** used to inform the user what to input, depending on the options described in what follows:

```
CC-----------------------------------------------------------------------
1       FORMAT(' INPUT CHOICE PARAMETER(0 TO 9): ')
2       FORMAT(' INPUT DURATION PARAMETER(0/1): ')
3       FORMAT(' INITIAL RANDOM INTEGER <OR 0 FOR SAME AS LAST RUN>: ')
4       FORMAT(' INPUT EPICENTRAL DISTANCE (KM): ')
5       FORMAT(' INPUT MAGNITUDE SCALE: ')
6       FORMAT(' INPUT PROBABILITY LEVEL #, (1 TO 9, FOR .1 TO .9): ')
7       FORMAT(' INPUT SITE CONDITION (0/1/2): ')
8       FORMAT(' INPUT COMPONENT SPECIFICATION (0:HORZ,1:VERT): ')
9       FORMAT(' INPUT M.M.I. SCALE: ')
10      FORMAT(' INPUT DEPTH OF ALLUVIUM (KM): ')
11      FORMAT(' CHOICE OPTION NUMBER = ',I2)
12      FORMAT(' DURATION PARAMETER = ',I2)
13      FORMAT(' INITIAL RANDOM # [=0 IF READ FROM SYNRAN.DAT]: ',I9)
14      FORMAT(' EPICENTRAL DISTANCE (KM) = ',F10.3)
15      FORMAT(' MAGNITUDE SCALE = ',F5.2)
16      FORMAT(' PROBABILITY LEVEL, P(.1<P<.9): ',F3.1)
17      FORMAT(' SITE CONDITION = ',I1)
18      FORMAT
    1(' COMPONENT(0:RAD,1:TRAN,2:VERT,3:TORSION,4:ROCKING) = ',I1)
19      FORMAT(' M.M.I. SCALE = ',I2)
20      FORMAT(' DEPTH OF ALLUVIUM (KM) = ',F10.1)
```

SYNACC will first request from the user the option (ICHOIC) to be used:

```
      WRITE(*,*)' OPTIONS: (0)QUIT,'
      WRITE(*,*)' (1)MAG-SITE,(2)MMI-SITE,(3)MAG-DEPTH,(4)MMI-DEPTH,'
      WRITE(*,*)' (5)INPUT FS,(6)MAG-DEPTH-SOIL,(7)MAG-SITE-SOIL,'
      WRITE(*,*)' (8)MAG-DEPTH-SOIL, OR (9)MMI-SITE-SOIL MODEL?'
      WRITE(*,1)
      READ(NU1,*)ICHOIC
```

1) Option 1: Magnitude-Site Model (Trifunac, 1976, Trifunac and Lee, 1985)

```
      CC-----------------------------------------------------------------
      CC    ICHOIC=1: INPUT DISTANCE, MAGNITUDE,
      CC              SITE CONDITIONS:       MAG-SITE MODEL
      CC-----------------------------------------------------------------
            WRITE(*,4)
            READ(NU1,*)DIST
            WRITE(*,5)
            READ(NU1,*)AM
            WRITE(*,7)
            READ(NU1,*)IS
```

2) Option 2: Intensity-Site Model (Trifunac, 1979, Trifunac and Lee, 1985-04)

```
      CC-----------------------------------------------------------------
      CC    ICHOIC=2: INPUT DISTANCE, MM INTENSITY, CONFIDENCE LEVEL,
      CC    SITE CONDITION:   MMI-SITE MODEL
      CC-----------------------------------------------------------------
            WRITE(*,4)
            READ(NU1,*)DIST
            WRITE(*,9)
            READ(NU1,*)MMI
```

```
            WRITE(*,7)
            READ(NU1,*)IS
```

3) Option 3: Magnitude-Depth Model (Trifunac and Lee, 1978, 1989, Westermo and Trifunac, 1978))

```
      CC-----------------------------------------------------------------------
      CC    ICHOIC=3: INPUT DISTANCE, MAGNITUDE, CONFIDENCE LEVEL,
      CC     DEPTH:         MAG-DEPTH MODEL
      CC-------------------------------------------------------------
            WRITE(*,4)
            READ(NU1,*)DIST
            WRITE(*,5)
            READ(NU1,*)AM
            WRITE(*,10)
            READ(NU1,*)DEPTH
      CC              ALLLUV. DEPTH NOW READ IN UNITS OF KM
```

4) Option 4: Intensity-Depth Model (Trifunac and Lee, 1985)

```
      CC-----------------------------------------------------------------------
      CC    ICHOIC=4: INPUT DISTANCE, MM INTENSITY, CONFIDENCE LEVEL,
      CC       DEPTH:       MMI-DEPTH MODEL
      CC-------------------------------------------------------------
            WRITE(*,4)
            READ(NU1,*)DIST
            WRITE(*,9)
            READ(NU1,*)MMI
            WRITE(*,10)
            READ(NU1,*)DEPTH
      CC              ALLLUV. DEPTH NOW READ IN UNITS OF KM
```

5) Option 5: Use Input FS data

```
      CC-----------------------------------------------------------------------
      CC    ICHOIC=5: INPUT USER'S FOURIER SPECTRUM, TOTAL OF NTAB
POINTS.
      CC-------------------------------------------------------------
                        NTAB=91
            WRITE(*,4)
            READ(NU1,*)DIST
            WRITE(*,321)DIST
      321           FORMAT('20D=',F5.1,',USER INPUT FS AMPS AT 91 PERIODS.')
            WRITE(*,*)' FOR THE 91 PERIODS:'
            WRITE(*,'(1X,13F6.2)')(PRD(I),I=1,91)
            WRITE(*,*)' INPUT 91 HORZ RADIAL FS AMP IN UNITS OF IN/SEC:'
            READ(NU1,*) (AU(IJ,1),IJ=1,NTAB)
            WRITE(*,*)' INPUT 91 HORZ TRANSVERSE FS AMP IN UNITS OF
      IN/SEC:'
            READ(NU1,*) (AU(IJ,3),IJ=1,NTAB)
            WRITE(*,*)' INPUT 91 VERT FS AMP IN UNITS OF IN/SEC:'
            READ(NU1,*) (AU(IJ,2),IJ=1,NTAB)
```

6) Option 6: Magnitude-Site-Soil Model

```
      CC-----------------------------------------------------------------------
      CC     ICHOIC=6       MAG-SITE-SOIL MODEL
```

```
CC-----------------------------------------------------------------------
WRITE(*,*)' INPUT HYPO DIST(KM),MAG,SITE(0/1/2),SOIL(0/1/2):'
READ(NU1,*) Disti, AM,IS,ISOIL
```

7) Option 7: Intensity-Site-Soil Model (Trifunac, 1991)

```
CC-----------------------------------------------------------------------
CC     ICHOIC=7       MMI-SITE-SOIL MODEL
CC-----------------------------------------------------------------------
WRITE(*,*)' INPUT HYPO DIST(KM),MMI,SITE(0/1/2),SOIL(0/1/2):'
READ(NU1,*)DIST,MMI,IS,ISOIL
```

8) Option 8: Magnitude-Depth-Soil Model (Trifunac and Lee, 1987, 1989)

```
CC-----------------------------------------------------------------------
CC     ICHOIC=8       MAG-DEPTH-SOIL MODEL
CC-----------------------------------------------------------------------
WRITE(*,*)' INPUT HYPO DIST(KM),MAG,DEPTH(km),SOIL(0/1/2):'
READ(NU1,*) Disti, AM,DEPTH,ISOIL
```

9) Option 9: Intensity-Depth-Soil Model (Lee, 1990)

```
CC-----------------------------------------------------------------------
CC     ICHOIC=9       MMI-DEPTH-SOIL MODEL
CC-----------------------------------------------------------------------
WRITE(*,*)' INPUT HYPO DIST(KM),MMI,DEPTH(km),,SOIL(0/1/2):'
READ(NU1,*)DIST,MMI,DEPTH,ISOIL
```

Example 1:

Here is an example of the **SYNACC** input file **InSyn.DAT** for **option#6, ICHOIC=6**:

InSynDat:

1	IWRT
01,01,13,12,00,00	CURRENTDATE (Mo-Da-Yr) &TIME (00:00:00)
6	ICHOIC,MODEL#
2, .875	INMAX, PDURN
12345	INITIALRANDOM # between <-32767,32767>
LA003	RECORDREFERENCE NAME
89.03.01	RECORDLOG #
1	DURNATION PARAMETER (0/1)
5	PROB LEVEL (1 TO 9)
1.5, 6.5, 0, 2	HYPOCENTRAL DIST,MAG/MMI,SITE/DEPTH,SOIL
10	# OF WAVE MODES
HSKWAV.DAT	
0	T=0 At Dist/Cmax
2	MODE PARTICIPATION FACTOR

Example 2:

Here is another example of the **SYNACC** input file **InSyn.DAT** for **option#5, ICHOIC=5**, where the user inputs for the **3 components, Radial Transvers and Vertical Fourier amplitude data:**

InSyn.dat:

```
1                       IWRT
01,01,13,12,00,00       CURRENTDATE (Mo-Da-Yr) &TIME (00:00:00)
5                       ICHOIC,MODEL#
2,.875                  INMAX, PDURN
12345                   INITIALRANDOM # between <-32767,32767>
LA003                   RECORDREFERENCE NAME
89.03.01                RECORDLOG #
1                       DURNATION PARAMETER (0/1)
5                       PROB LEVEL (1 TO 9)
 1.00000E-10  1.00000E-10  3.94577E-01  3.94800E-01
 2.05194E-01  3.25239E-01  3.93269E-01  3.76363E-01
 2.49990E-01  2.54802E-01  6.85321E-01  3.63371E-01
 6.42797E-01  7.00448E-01  5.24887E-01  1.02113E+00
1.34502E+00  1.65811E+00  3.05650E+00  2.81909E+00
4.49047E+00  3.65102E+00  6.02187E+00  5.33620E+00
3.33898E+00  6.96100E+00  1.03893E+01  1.24187E+01
1.43819E+01  1.90009E+01  6.81712E+00  2.48083E+01
2.16060E+01  1.89132E+01  2.10551E+01  2.55125E+01
1.66354E+01  9.61588E+00  1.30416E+01  9.97679E+00
1.78276E+01  2.11354E+01  1.93958E+01  1.22380E+01
2.02096E+01  1.35959E+01  9.66726E+00  1.38484E+01
2.19153E+01  1.98801E+01  2.78279E+01  3.55078E+01
2.10803E+01  2.55126E+01  2.44259E+01  1.99576E+01
1.21552E+01  1.59339E+01  1.06934E+01  1.20950E+01
1.27204E+01  1.34753E+01  1.44391E+01  2.07096E+01
3.57730E+01  4.53028E+01  4.99574E+01  4.13284E+01
3.36581E+01  2.80684E+01  2.30985E+01  1.86020E+01
1.67221E+01  1.51307E+01  1.36718E+01  1.23297E+01
1.07276E+01  9.53787E+00  8.96607E+00  9.17404E+00
9.35428E+00  9.51199E+00  9.40564E+00  8.05007E+00
6.83720E+00  5.74562E+00  3.86015E+00  2.28893E+00
1.52479E+00  1.77728E+00  1.99610E+00                End of FS Radial Comp.
 1.00000E-10  1.00000E-10  2.31009E-01  1.94537E-01
 3.19194E-01  3.83051E-01  3.76469E-01  3.32717E-01
```

4.43216E-01	5.09405E-01	4.04593E-01	5.44001E-01
4.89834E-01	3.01687E-01	7.09059E-01	1.37829E+00
1.27044E+00	2.21121E+00	2.04364E+00	4.62448E+00
4.79836E+00	2.79309E+00	5.69368E+00	6.53701E+00
8.06265E+00	3.63794E+00	1.13821E+01	1.01337E+01
5.93430E+00	2.41781E+01	1.72239E+01	1.99994E+01
1.20149E+01	2.22880E+01	1.37573E+01	1.24219E+01
1.64474E+01	1.27367E+01	1.83200E+01	2.73839E+01
2.88879E+01	2.37006E+01	2.61794E+01	2.06856E+01
2.95908E+01	1.02047E+01	1.51625E+01	1.86747E+01
2.17198E+01	2.72379E+01	3.20074E+01	1.73098E+01
1.86640E+01	1.29285E+01	2.74345E+01	2.43018E+01
1.83995E+01	1.11270E+01	1.50910E+01	1.54509E+01
1.50808E+01	1.37118E+01	1.86422E+01	2.99603E+01
4.27058E+01	4.49779E+01	4.38568E+01	3.28721E+01
2.31079E+01	2.08690E+01	1.91644E+01	1.76222E+01
1.57691E+01	1.40516E+01	1.24772E+01	1.10288E+01
1.14860E+01	1.22635E+01	1.24978E+01	1.20185E+01
1.16030E+01	1.12395E+01	1.07896E+01	9.72566E+00
8.77375E+00	7.91703E+00	6.43724E+00	5.20409E+00
4.39439E+00	4.07555E+00	3.79923E+00	End of FS Transverse Comp.
1.00000E-10	1.00000E-10	4.59384E-01	3.17400E-01
4.38541E-01	3.33765E-01	3.86963E-01	1.17292E+00
6.97446E-01	1.03180E+00	9.03084E-01	1.78482E+00
5.54601E-01	9.67074E-01	1.27816E+00	1.41444E+00
3.90060E+00	4.10452E+00	3.13484E+00	1.95386E+00
4.53177E+00	1.18723E+00	5.14047E+00	5.65238E+00
6.60988E+00	2.85910E+00	3.17751E+00	3.52807E+00
8.17153E+00	9.91231E+00	1.27238E+01	4.76816E+00
7.27592E+00	2.97489E+00	5.21361E+00	5.07673E+00
4.32826E+00	9.07128E+00	2.04633E+00	1.24525E+01
1.01732E+01	5.53326E+00	6.02687E+00	1.14904E+01
9.38652E+00	9.88448E+00	1.13447E+01	6.72983E+00
1.17014E+01	7.19098E+00	6.32351E+00	9.26453E+00
8.32524E+00	5.78888E+00	6.38161E+00	8.23842E+00
8.39110E+00	1.05250E+01	1.17266E+01	1.08374E+01
8.69151E+00	5.03464E+00	6.84980E+00	1.09076E+01
1.42376E+01	1.04890E+01	7.56431E+00	7.11810E+00
6.72146E+00	6.49314E+00	6.29370E+00	6.11326E+00
5.35652E+00	4.63204E+00	3.96794E+00	3.35696E+00
4.28392E+00	5.30411E+00	5.57428E+00	4.85386E+00
4.22950E+00	3.68318E+00	3.26290E+00	3.20659E+00
3.15620E+00	3.11086E+00	3.03253E+00	2.96726E+00

```
2.82022E+00     2.54681E+00   2.30987E+00                End of FS Vertical Comp.
10                            # OF WAVE MODES
HSKWAV.DAT
0                             T=0 At Dist/Cmax
2                             MODE PARTICIPATION FACTOR
```

I.5 The SYNACC Output Files

With the input files of SYNACC all read in, SYNACC will

1) Use each mode of the Wave Dispersion Data at the site and their arrival times at each frequency band of waves to assemble the contribution of each mode of surface and Body waves at each frequency band.

2) Determine the Relative Amplitudes and Phrases of all body and surface wave modes, sum up all the modes of waves in the frequency domain and by inverse Fourier Transform, create the (Volume 2, Corrected) time-histories of Total Accelerogram.

3) The above process was performed for the following components of motions:

   i) The **Radial**, **Transverse** and **Vertical** (Trifunac, 1971; Wong and Trifunac, 1978, 1979) components of **Translational** motions, with respective output files: **V2X01.DAT, V2Y01.DAT and V2Z01.DAT**.

   ii) The **Torsion** (Lee and Trifunac, 1985) and **Rocking** (Lee and Trifunac, 1987) components of **Rotational** Motions, with respective output files: **V2T01.DAT** and **V2R01.DAT**.

   iii) The **Radial Normal, Horizontal Shear** and **Vertical Normal** components of **Strain** (Lee, 1990) Time History, all in one output file**: V2E01.DAT**.

   iv) The **Radial, Transverse** and **Vertical** components of **Curvature** (Trifunac, 1990) Time Histories (**Curvograms**), all in one output file**: V2E01.DAT**.

Figure 2 is an example of one such translational accelerogram time history at the el Centro Imperial Valley site generated by an earthquake of magnitude $\boldsymbol{M = 6.5}$ at an hypocentral distance of $\mathbf{10}\boldsymbol{km}$. This is generated from the original synthetic accelerogram program

SYNACC.EXE and represents one component of the translational motions at the half-space surface at the site. The input option for **Option 1** above**: Magnitude-Site Model (Trifunac, 1976, Trifunac and Lee, 1985)** for a site condition of $\boldsymbol{s = 0}$, which is the site condition for an alluvial site. A peak ground acceleration of $\left|\boldsymbol{a}_{\max}\right| \sim \boldsymbol{450\, cm/s^2}$ or almost "***half a g"*** is attained, which is consistent and similar to the data recorded during the **1940 Imperial Valley Earthquake** in California.

Figure 2 Synthetic Translational Accelerogram Time Histories

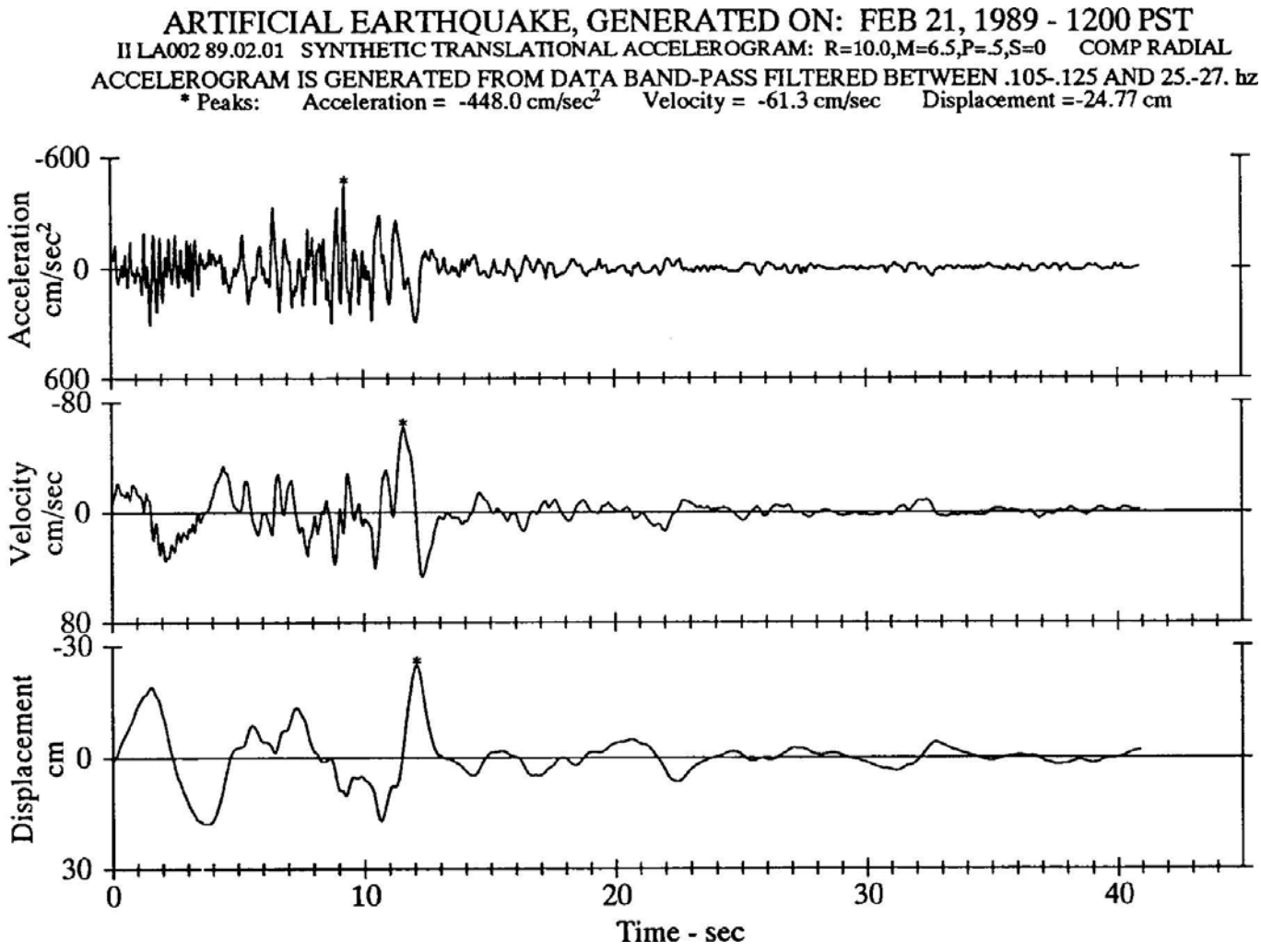

II. The Updated Synthetic Accelerogram Program for Points on or Below Half-space Surface: EQSYNACC

The updated Synthetic Accelerogram Program here is created as a result of the work described in the following two reports:

1. Synthetic Translational Motions of Surface Waves On or Below a Layered Media**, Report II, 2013.**

2. Synthetic Rotational Motions of Surface Waves On or Below a Layered Media**, Report III, 2013.**

II.1 The Updated Haskel Program for Points on or Below Half-space Surface

In Section II of **Report II: Synthetic Translational Motions of Surface and Body Waves On or Below a Layered Media, 2013,** starting with the Wave Dispersion File **Hskwav.dat** on the Half-space surface at a site, we were able to construct the Synthetic Translational Motions of Love and Body SH Waves for points on or Below a Half-space Layered Medium. In Section III of the same Report, we were next able to construct the Synthetic Translational Motions of Rayleigh and Body P and SV Waves for those same points on or below the Half-space Layered Medium. Here the Translational components are the **Radial, Transverse and Vertical components of motion**, namely translational acceleration $\left(\ddot{U},\ddot{V},\ddot{W}\right)^T$, velocity $\left(\dot{U},\dot{V},\dot{W}\right)$ and displacement $\left(U,V,W\right)$ time histories. The numerical calculations for each mode at each frequency of waves are described in Section IV of Report I, 2013.

Figure 3 here is **Figure V.1 of Report II,** which gives the plots of the transverse (***y***-) component of Love wave mode shape amplitudes at four selected periods: $\boldsymbol{T = 5,\ 1.0,\ 0.5,\ \text{and}\ 0.1\ s}$. The amplitude of the mode shape is normalized to be one at the surface of the half-space, so that they are the scaling factors or transfer function values of the waves along the depth from the half-

space surface for mode #1 waves. Each graph shows the mode shape amplitudes versus the distance *z*, which is the depth in kilometers below the half-space surface.

Figure 3: Report II Fig. V.1 Love Waves Mode#1 at $T = 5,\ 1.0,\ 0.5,\ 0.1\ s$

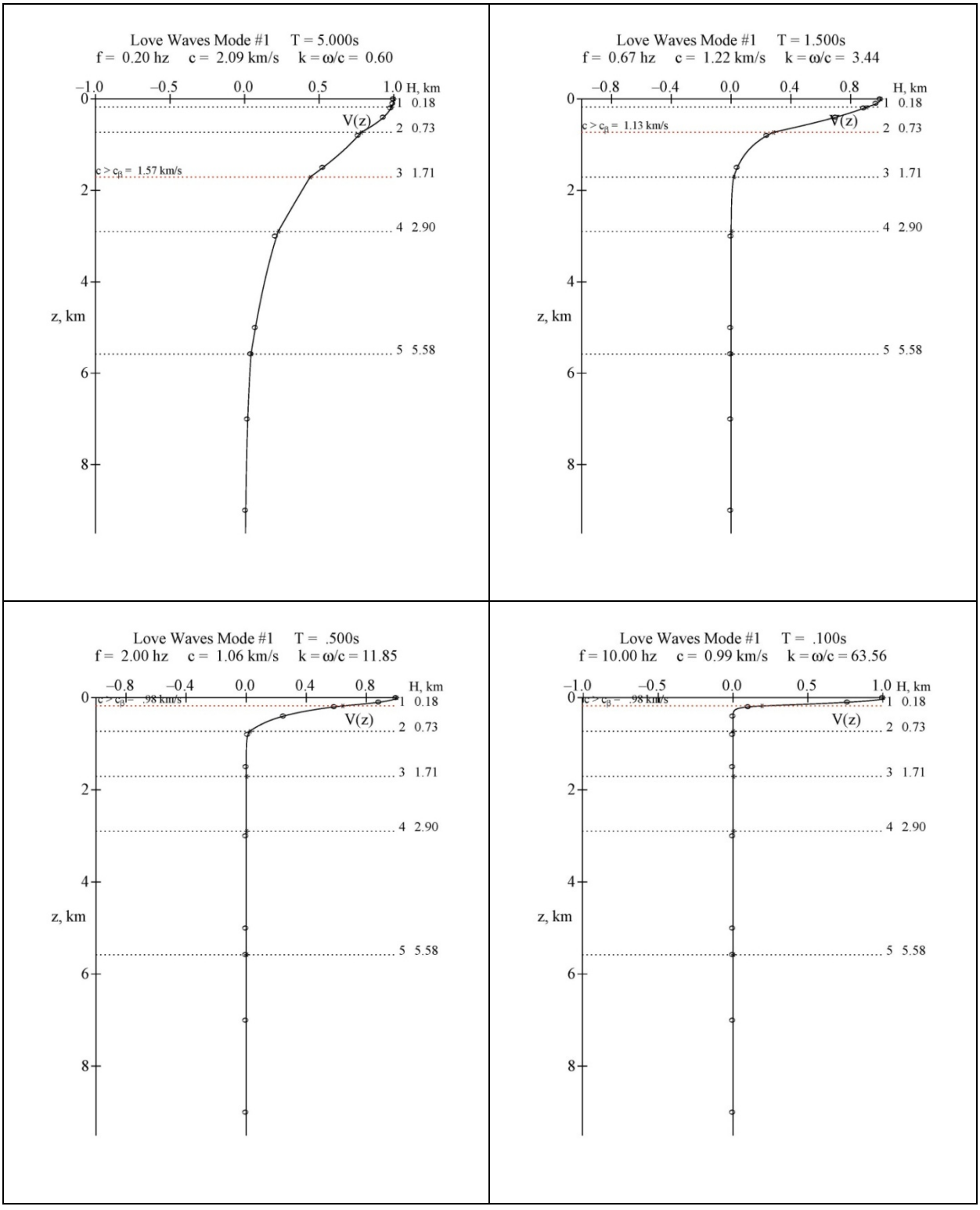

Figure 4 is **Report II Figure VI.1**, Rayleigh wave mode#1 amp. at 4 periods.

Figure 4: Report II Fig. VI.1 Rayleigh Mode#1 *x*- and *z-comp.* at $T = 5,\ 1.0,\ 0.5,\ 0.1\ s$

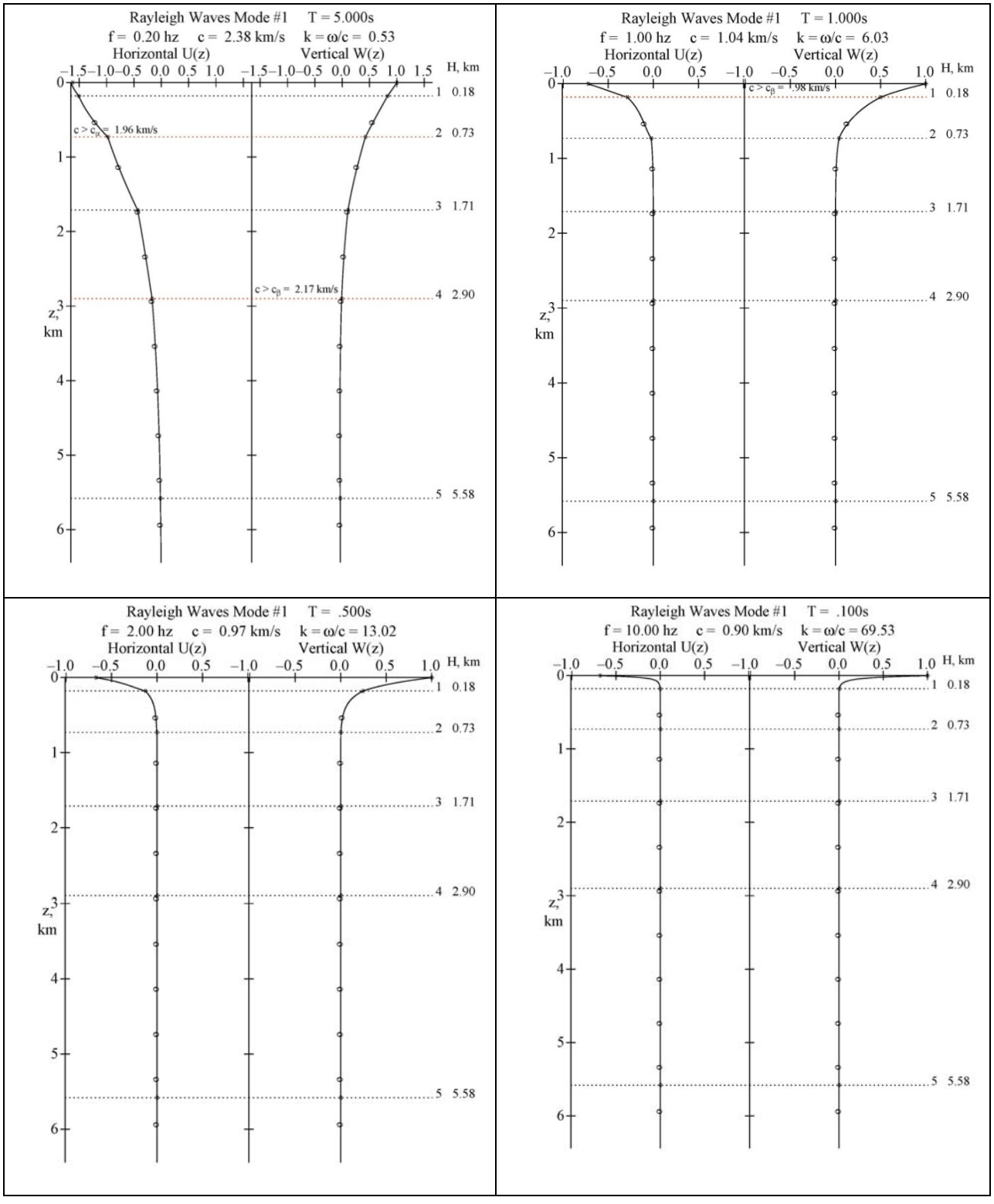

Later, in the Section II of **Report III: Synthetic Rotational Motions of Surface and Body Waves On or Below a Layered Media, 2013,** we were able to extend the analysis and results of the Report I to construct the Synthetic Rotational Motions of Love and Body SH waves for points on or Below a Half-space Layered Medium. In Section III of the same Report, we next constructed the Synthetic Rotational Motions of Rayleigh and Body P, SV waves for those same points on or Below the Half-space Layered Medium. The computation of the Rotational components of motions: Torsion, Rocking and Strain time histories all involve either or both of the d/dx and d/dz derivatives of the corresponding translational acceleration $\left(\ddot{U},\ddot{V},\ddot{W}\right)^T$, velocity $\left(\dot{U},\dot{V},\dot{W}\right)$ and displacement $\left(U,V,W\right)$ time histories. The numerical calculations for each mode at each frequency of waves are described in Section IV.5 of Report II, 2013.

Figure 5 is **Figure III.1 of Report III**, which shows the plots of Love wave mode #1 d/dx and d/dz (rotational) mode shape amplitudes at four selected periods: $T = 5,\ 1.0,\ 0.5,$ **and** $0.1\ s$. This corresponds to the translational component (**Figure 3** here) of **Figure V.1 of Report II,** where the displacement amplitudes are normalized to be one ($=1\ cm$) at the half-space surface, so that the rotational mode shape values here are the transfer function values of the waves along the depth from the half-space surface for this mode of Love waves. Each graph shows the dV/dx and dV/dz mode shapes versus the distance *z*, which is the depth in kilometers below the half-space surface.

Figure 6 is **Figure III.6 of Report III,** which shows the plots of ***x***- and ***z***-components of the Rayleigh wave $d(U,W)/dx$ and $d(U,W)/dz$ mode#1 mode shapes at the same four periods. The amplitudes of the mode shapes of both components are normalized with respect to the vertical component W of motion at the surface of the layered half-space, so that the mode shape values are again the transfer function values of the waves at different depths from the half-space surface.

Figure 5: Report III Fig.III.1 Love Waves Rotational Mode#1 at $T = 5,\ 1.0,\ 0.5,\ 0.1\ s$

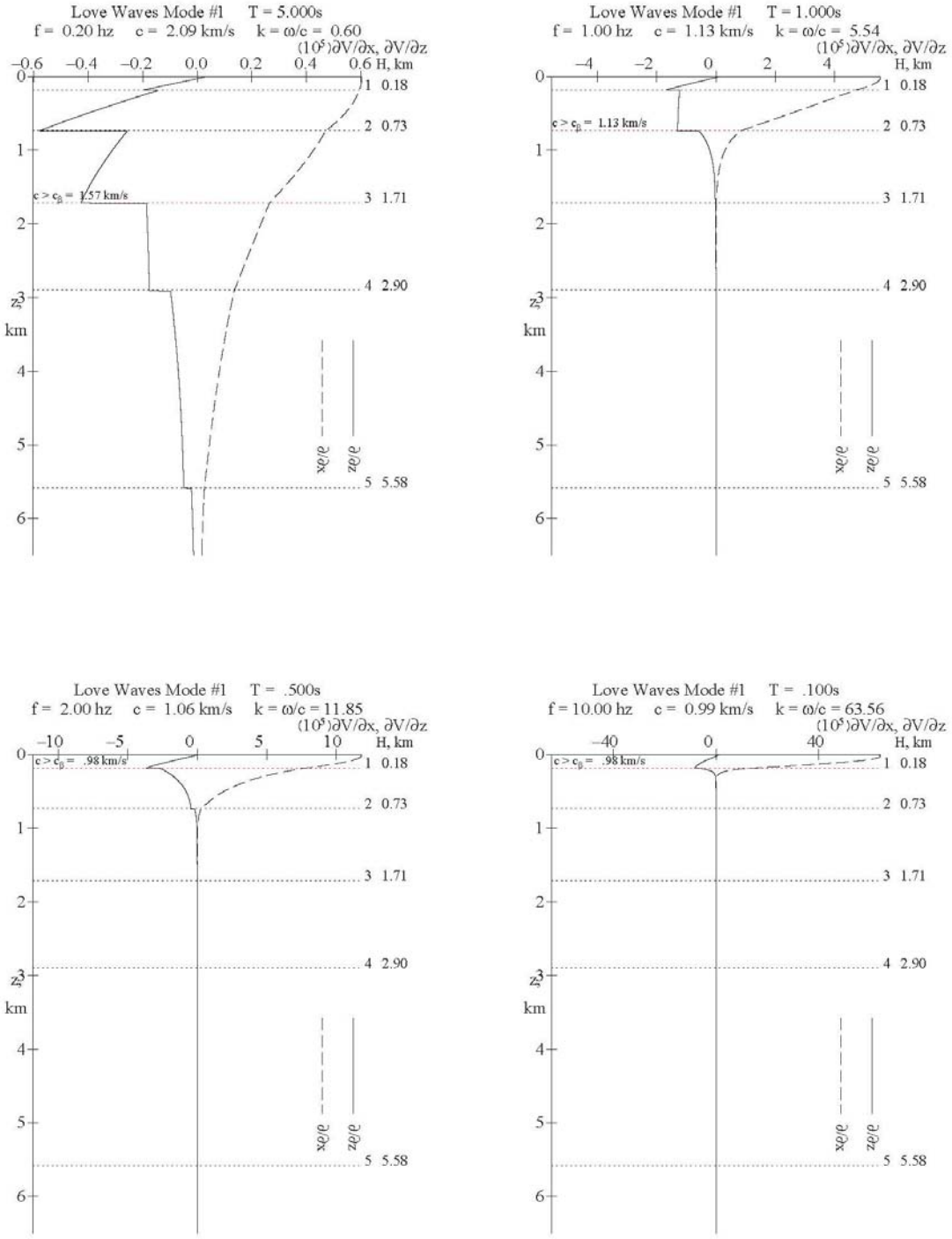

Figure 6: Report III Fig.III.6 Rayleigh Waves Rotational Mode#1 at $T = 5,\ 1.0,\ 0.5,\ 0.1\ s$

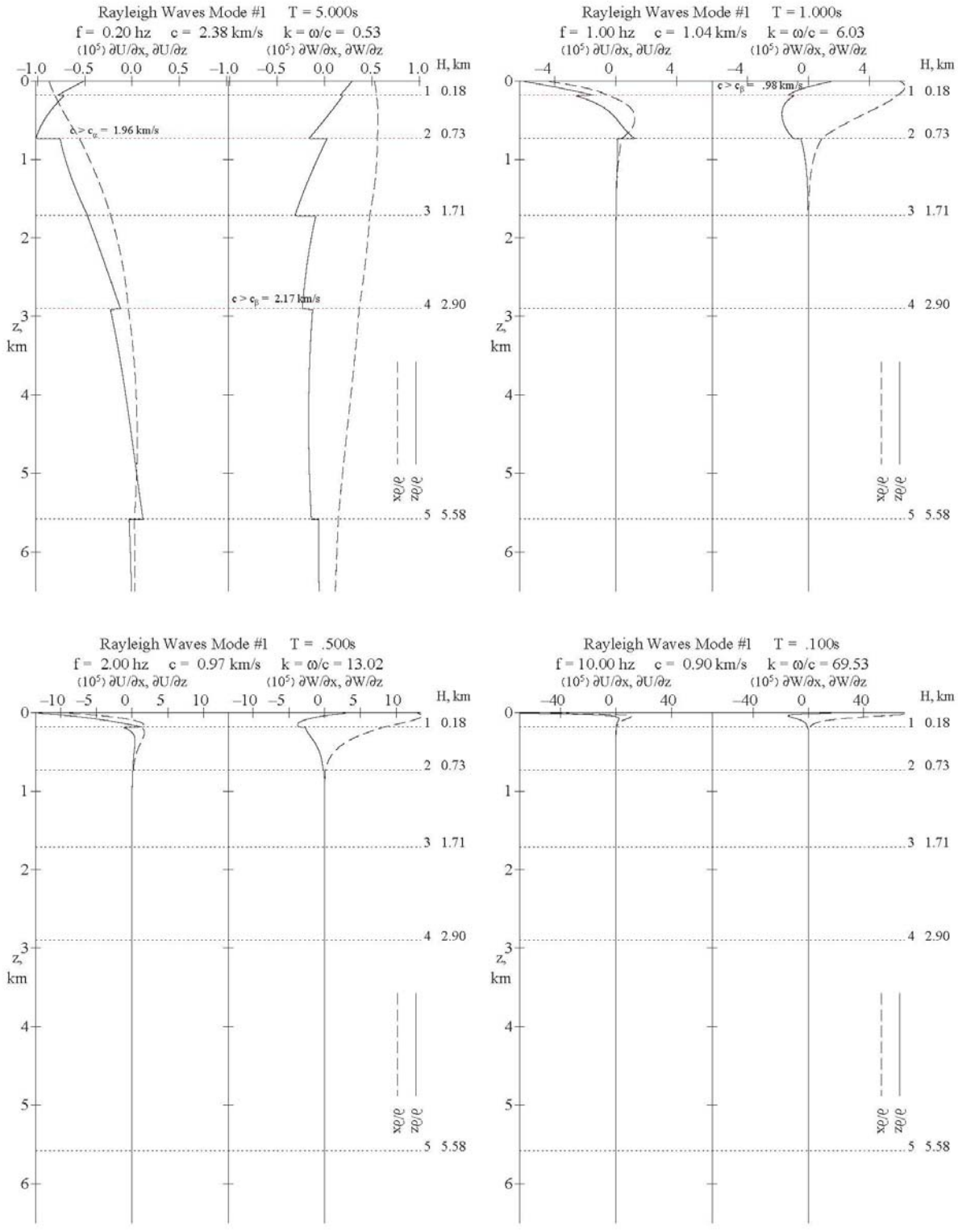

II.2 The Input and Output Files for New HskzdzModes.EXE

With the available data at each frequency of each mode of surface Rayleigh and Love waves, and body P, SV and SH waves, an identical file as Hskwav.dat for the wave dispersion data at the half-space surface at the site can now be constructed at any given point on or below the half-space surface. The procedure is as follows:

1) A data file Zxcoord.dat is created, which consists of the specified *z*- and *x*-coordinates of the points on or below the site. The lines below show an example of a part of such a file consisting of 120 points vertically below the site. The first line specifies the number of points and the exponent factor used to make the data in units of km. The '0' here means the data are in units of km. If the data are given in meters, then it would be '-3' meaning $\mathbf{10^{-3}}$ km. Starting from the 2nd line, the 1st column contains the z-coordinates and the 2nd column the x-coordinates, which are all 0's here. This 2nd column is of no use here, but will be needed later to generate the synthetic accelerogram data at a specified point with ***(z, x)*** coordinates from the site.

Example 1: Zxcoord.dat for points vertically below a given site:

```
 120        0    # of points, 10^exponent of km
0.05     0.00
0.10     0.00
0.15     0.00
0.20     0.00
0.25     0.00
0.30     0.00
0.35     0.00
0.40     0.00
0.45     0.00
0.50     0.00
0.55     0.00
0.60     0.00
   :        :    (Lines from z=0.65down to z=5.60 skipped…)
5.65     0.00
5.70     0.00
5.75     0.00
5.80     0.00
```

```
5.80      0.00
5.85      0.00
5.90      0.00
5.95      0.00
6.00      0.00
```

The ***z***-coordinates specified here from $z = 0.05$ (below the surface) to $z = 6.0\ km$ (down) are equally spaced at $0.05\ km$ apart. The point $z = 0.0\ km$ on the half-space surface will by default be included.

Example 2: Zxcoord.dat for points at a fixed depth varying in the horizontal direction (left to right):

```
                                  # of points, 10^exponent of
      140          -3             km
   192.97         1.5
   192.97         3.0
   192.97         4.5
   192.97         6.0
   192.97         7.5
   192.97         9.0
   192.97        10.5
   192.97        12.0
   192.97        13.5
   192.97        15.0
   192.97        16.5
   192.97        18.0
   192.97        19.5
:             :              (Lines from x=21.0 to x=196.5 skipped…)
   192.97       198.0
   192.97       199.5
   192.97       201.0
   192.97       202.5
   192.97       204.0
   192.97       205.5
   192.97       207.0
   192.97       208.5
   192.97       210.0
```

Here the 140 points of ***(z,x)***coordinates are input in units of $10^{-3}\ km$ or in units of

meters. They are all at a depth $z = 192.97 \times 10^{-3} km$ or $192.97m$ with the x-coordinates ranging from $x = 1.5m$ to $x = 210m$ in steps of $1.5m$. The point $x = 0.0\ km$ at the same depth of $z = 192.97m$ will be included by default.

2) This and the dispersion file **Hskwav.dat,** output from **HASKEL.EXE** in the previous section, now become the input for **NewHSKzDzModes.EXE** program. The file **Hskwav.dat** contains the phase and group velocities for each mode of surface Rayleigh and Love waves at each period at the point $z = 0.0$ on the half-space surface.

This program reads the data in the file Hskwav.dat, and using the modified Haskel-Thompson propagator matrices created in Section IV.3 of Reports II and Section IV.3 of Report III, produces the internal propagator matrix files, **RYLGMTRX.DAT** and **LOVEMTRX.DAT**,for both the translational and rotational component of motions respectively for the Rayleigh and Love surface wave modes and also the (newly developed) body P, SV and SH wave modes for given angles of incidence from the bottom semi-infinite media. As an example, for the 6 layered media, we use angles of incidence of 83^o and 84.5^o (with respect to horizontal) for the purpose of creating synthetic accelerograms at hypocentral distances of 10 and $40\ km$.

3) This program will at each z-coordinate in the file Zxcoord.dat (starting at $z = 0.0\ km$ on the half-space surface), produce an updated Wave dispersion file, **HSKwav.___,** where **'.___'** in the file extension is the index number of the z-coordinate in the file **Zxcoord.dat**. For the example file **Zxcoord.dat** above, this would range from ***'000'*** ($z = 0.0\ km$) at the surface to ***'120'*** ($z = 6.0\ km$) at the very bottom of the layered medium. The program will produce, for each of the files **Hskwav.___,** 5 modes of Rayleigh and 5 modes of Love surface waves. For each mode, at each period, **NewHSKzDzModes.EXE,** as the name suggests, will write the following at each period of each mode of Rayleigh waves:

T, Period of the Rayleigh wave in seconds,

i) ***c,*** Phase velocity of the Rayleigh wave in km/s,

ii) ***u,*** Group velocity of the Rayleigh wave in km/s,

iii) $\boldsymbol{W/U}$ Ratio of vertical to horizontal wave displacement amplitudes,

iv) $\boldsymbol{U}$, the relative ***x***-component of Rayleigh wave translational motion, which is

v) available as an imaginary number (See Report II),

vi) $\boldsymbol{W}$, the ***z***-component of Rayleigh wave translational motion, which is a real number (See Report II), and normalized to be =1 at the half-spaced surface,

vii) $\boldsymbol{dU/dz\left(\times 10^{-5}\right)}$, the ***z***-derivative of the ***x***-component of Rayleigh wave motion,

viii) $\boldsymbol{dW/dz\left(\times 10^{-5}\right)}$, the ***z***-derivative of the ***z***-component of Rayleigh wave motion,

ix) $\boldsymbol{dU/dx\left(\times 10^{-5}\right)}$, the ***x***-derivative of the ***x***-component of Rayleigh wave motion,

$\boldsymbol{dW/dx\left(\times 10^{-5}\right)}$, the ***x***-derivative of the ***z***-component of Rayleigh wave motion,

And similarly at each period of each mode of Love waves (Transverse direction):

i) ***T,*** Period of the Love wave in seconds,

ii) ***c,*** Phase velocity of the Love wave in km/s,

iii) ***u,*** Group velocity of the Love wave in km/s,

iv) Ratio =0.0 since this doesn't apply to Love waves

v) $\boldsymbol{V}$, the ***y***-component of wave translational motion, which is available as a real number (See Report II), and normalized to be =1 at the half-spaced surface

vi) $\boldsymbol{dV/dz\left(\times 10^{-5}\right)}$, the ***z***-derivative of the ***y***-component of Love wave motion,

vii) $\boldsymbol{dV/dz\left(\times 10^{-5}\right)}$, the ***z***-derivative of the ***y***-component Love wave motion,

4) In exactly the same way as for the five modes of Rayleigh waves and five modes of Love waves, additional modes corresponding to the waves from incident body P-, SV and SH- waves, respectively modes # 11, 12 and 13 for a specified angle of incidence are created, and written in files **BodyW___.___,** where **'W___'**in the file name specifies the angle of incidence of the Body waves. For example, **'W845'**would correspond to body waves with incident angle of **84.5**^{o} . **'.___'** in the file extension is again the index number of the ***z***-coordinate.

Appendix A-1 shows the **Mode 1 of Rayleigh waves** of the output file **Hskwav.000** of the Program **"NewHSKzDzModes.EXE"**

Appendix A-2 shows the **Mode 1 of Love waves** of the same output file **Hskwav.000.**

Appendix A-3 shows the **Mode 11 of body P- Wave** in the file **BodyW845.000**

II.3 The Updated Synthetic Accelerogram Program for Points On or Below the Half-Space Surface: EQSYNACC.EXE

With the dispersion data of the Rayleigh and Love surface waves and the body P, SV and SH waves computed at points on and below the half-space surface, the synthetic translational and rotational components of the acceleration, velocity and displacement time histories at every point on or below the half-space surface will next be constructed. Each such point will have a designated Fourier amplitude spectra and a designated duration.

Here is the structure of he Working Folder:

Working

1) **Batch files**: **SynAnnn.BAT**

Example of **SynAnnn.BAT, with 'nnn' = '025'**:

SynA025.BAT

```
MD z025
CD z025
COPY ..\1ZFolder\*.* *.*
COPY ..\InsynS\InSynS.025 InSynS.dat
CALLAccSynS
CD ..\
```

2) **Data files:** **Period.dat, Zxcoord.dat**

3) **Subfolders:** **Working\Programs**
Working\1ZFolder
Working\InSynS
Working\HskWav
Working\BodyW__ (Example: **Working\BodyW830\)**

The following set of files and information are needed to construct the synthetic motions at all the points:

1 **Period.dat**: the Data file of the Periods of waves. This is the same data file given in **Section I.1** above for the original SYNACC program.

2. **Zxcoord.dat:** the same data file of the ***z*-** and ***x*-** coordinates of the points as given in Section II.2 above.

3. **..\HskWav\HskWav.___:** Wave Dispersion Data of the Rayleigh and Love surface waves at every point on or below the half-space surface at the given Site. Here the file extension **"._____"** is again the index number of the (***z, x)*-**coordinate in the file **Zxcoord.dat.** Since there are now many such files, one for each point in the file **Zxcoord.dat,** they are all placed in the subfolder..**HskWav**\inside the working directory (folder).

4. **..\BodyW___\BodyW___.___:**the file of additional modes corresponding to waves from incident **P-, SV- and SH- body waves**, respectively modes # 11, 12 and 13 for the specified angle of incidence, as described in **Section II.2** above. As in the case of the Haskell wave files, there is one file for each point in the file **Zxcoord.dat,** and they are also all placed in the subfolder..**BodyW___**\inside the working directory (folder), where **'W___'** in the name of the folder specifying the angle of incidence of the body waves, as for all the body wave files in the subfolder.

5. **..\InSynS\InSyn.___:** These are the input files for the updated program **EQSYNACC.EXE.** They are the same input file as **InSyn.dat**for the original **SYNACC.EXE** program as described in **Section I.3** above. The difference now is that there are many such files, one for each point in the file **Zxcoord.dat.** Those are all placed in the subfolder **..\InSynS**\inside the working directory (folder). There are also now additional lines of input, to identify the coordinates

of the point on or below the site where the synthetic accelerogram data are to be generated. Here is a brief description of the file, with emphasis on where the additional inputs are, in addition to those for **InSyn.dat** described in **Section I.3** above:

1) **Input 1:** IWRT: Output Mode
2) **Input 2:** Date and Time of the Synthetic Earthquake
3) **Input 3:** ICHOIC–

   Options to be used for constructing the Fourier Amplitudes in the given frequency band
4) **Input 4:** INMAX, PDURN
5) **Input 5: IGYZBE**
6) **Input 6:** Synthetic Record Reference name of
7) **Input 7:** Synthetic Record log number
8) **Input 8:** IFDUR, duration parameter
9) **Input 9:**IPR, probability level
10) **Input 10:**Earthquake parameters depending on ICHOIC of Input 3

Inputs #1 to #10 here are identical to that used in the original 'SYNACC.EXE" program. As described in Section I.3 above. The following ***(NEW) inputs*** are modified for the **Updated 'EQSYNACC.EXE' Program:**

11) **Input 11:** NWAVE, total number of dispersion waves
12) **Input 12:**Output Haskell Surface wave Velocity data Filename

Here there's one Haskell velocity data file for each **(z, x)** coordinates given in the file **Zxcoord.dat**, and those are of the form **..\Hskwav\Hskwav.___**, where the file extension **'.___'** is the index number of the (***z, x)*** coordinate in the file **Zxcoord.dat.** The files are all in a separate subfolder **HskWav** inside the EQSYNACC working folder **Working\.**

13) **Input 13:*(z, x)*** coordinate Location on or below the site, 10^exp in km

This is the same input as used in the file **Zxcoord.dat**.

```
write(*,*)' at (z,x)E__ (+/-exp) ='                    !!!New
read(NU1,*,err=6101)zLoc,xLoc,kexp                     !!!New
```

14) **Input 14:** Output Body wave Velocity data Filename

```
!8/4    add Bodywave file          !!!New
        write(*,*)' Body Wave Mode Shape Filename(a20): '
        read(nu1,9001)BodyFile          !12/2/12 now 30 chars long
        write(*,9001)' ',BodyFile
```

Here there's one Body wave velocity data file for each **(z, x)** coordinates given in the file **Zxcoord.dat**, and those are of the form **..\Bodywave\BodyW___.___**, where the file extension **'.___'** is the index number of the (***z, x)*** coordinate in the file **Zxcoord.dat.** The files are all in a separate subfolder **BodyW___** inside the EQSYNACC working folder **Working\ .**

15) **Input 15:** Yes/No for 1st arrival time at T=0

16) **Input 16:** Mode participation factor

Input #15 and 16 are identical to **Input #13 and 14** of the input file for the **Original "SYNACC.EXE' program.**

The following file **InSyn.025** is an example of such an input file:

InSyn.025:

```
1                           IWRT
01,01,13,12,00,00           CURRENT DATE (Mo-Da-Yr) & TIME (00:00:00)
6                           ICHOIC, MODEL#
2,.875                      INMAX, PDURN
12345                       INITIAL RANDOM # <-32767,32767>
LA003                       RECORD REF NAME
1208.025                    RECORD LOG #
1                           DURNATION PARAMETER (0/1)
5                           PROB LEVEL (1 TO 9)
4125, 6.5, 0, 2             HYPO. DIST, MAG/MMI,SITE/DEPTH,SOIL
10                          # OF WAVE MODES
..\HSKWAV\HSKWAV.025
```

1.250, .000 0	**z, x Location, 10^exp km**
..\BodyW840\BodyW840.025	
0	**T=0 At Dist/Cmax**
2	**MODE PARTICIPATION FACTOR**

II.4 The EQSYNACC Output Files

With the input files of **EQSYNACC** all read in, execution of **EQSYNACC** will

1) Create, for each point of ***(z, x)*** coordinate in the file Zxcoord.dat, a subfolder inside the working folder **\Working** of some generic name **\Working\zx___,** where '___' in the subfolder name is index number of the (***z, x)*** coordinate in the file **Zxcoord.dat.**

2) At each such subfolder, the program **EQSYNACC.EXE** will use the same algorithm and procedure as the original program **SYNACC.EXE** to generate each mode of synthetic acceleration data, as described in **Section I.5** above, namely, to use each mode of the Wave Dispersion Data at the site and their arrival times at each frequency band of waves to assemble the contribution of each mode of surface and Body waves at each frequency band. Currently, there are five modes of Rayleigh waves (Mode#1 to 5), five modes of Love waves (Mode#6 to 10), one mode for each of the Incident Body P, SV and SH waves (Mode#11 to 13)

3) At each point ***(z, x)*** on or below the half-space surface at the site, the Relative Amplitudes and Phrases of each mode of Rayleigh and Love Surface Waves were determined relative to that at the surface point where $z = 0$ using the mode shape data files in the folder**..** **\Hskwav**. Similarly, the Relative Amplitudes and Phases of each mode of Body P, SV and SH waves were determined relative to that at the surface, using the mode shape data files in the folder**..** **\BodyW___,** where **'W___'** in the name of the folder specifies the angle of incidence of the Body waves used. All modes of the waves at each point are then summed up in the frequency domain.

4) At the surface point ***(z, x) = (0, 0),*** the translational components of the Fourier

amplitudes of acceleration are scaled to be the same as those calculated by the regression equations specified by the parameter **'ICHOIC'** in **Input#3**. The Fourier amplitudes of all points of ***(z, x)*** below are then scaled relatively as in previous step 3). By Inverse Fourier Transform, using FFT, the (Volume 2, Corrected) time-histories of Total Accelerogram are created.

5) The above process was performed for the following components of translational motions:

The **Radial**, **Transverse** and **Vertical** (Trifunac, 1971; Wong and Trifunac, 1978, 1979) components of **Translational** motions (the **U-, V-, W-** components), respectively

The Translational files:

V2X01.DAT

V2Y01.DAT

V2Z01.DAT.

These are the same output files as in the original SYNACC, which are now extended for all defined points on or below the half-space surface.

Figures 7a and 7b are examples of plots of the output files for points on and below the half-space surface at a site. They are the Figures VIII.3a and b from Report II, plots of such synthetic accelerations respectively for both the horizontal $\boldsymbol{U(z)}$ and vertical $\boldsymbol{W(z)}$ components, calculated for the El Centro six-layered site model, at 100 depths equally spaced from the surface to almost 6km below the surface, and hypocentral distance of $\boldsymbol{D = 10.0km}$, The EQSYNACC.EXE program determines that the appropriate duration of the time histories should be around 40 seconds. As described in Report II, the acceleration time histories are at depths 0.6m apart. Of the 100 acceleration time histories, six are plotted **green**, and labeled **0** to **5**. The one labeled **0** is the accelerogram at the top surface $\boldsymbol{z = 0}$, while the ones labeled **1** to **5** are at depths at or closest to the interfaces between adjacent layers.

Figure 7a: Report II- Fig.VIII.3a Synthetic Acceleration for **M**=6.5, **R**=8.0km, **H**=6.0km, **s**=0, **soil**=2

Horizontal, Radial Motions

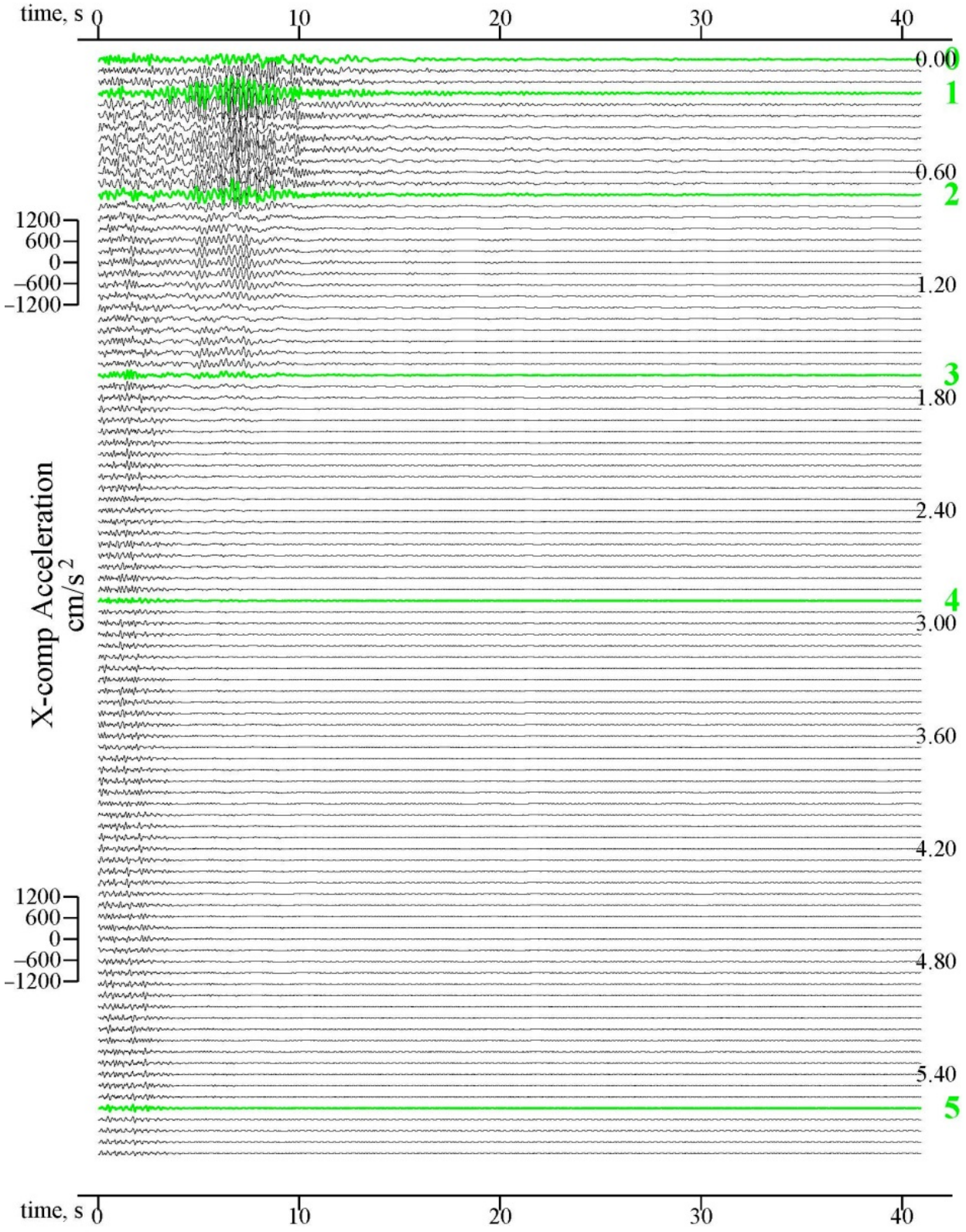

Figure 7b: Report II-Fig.VIII.3b Synthetic Acceleration for **M**=6.5, **R**=8.0km, **H**=6.0km, **s**=0, s**oil**=2

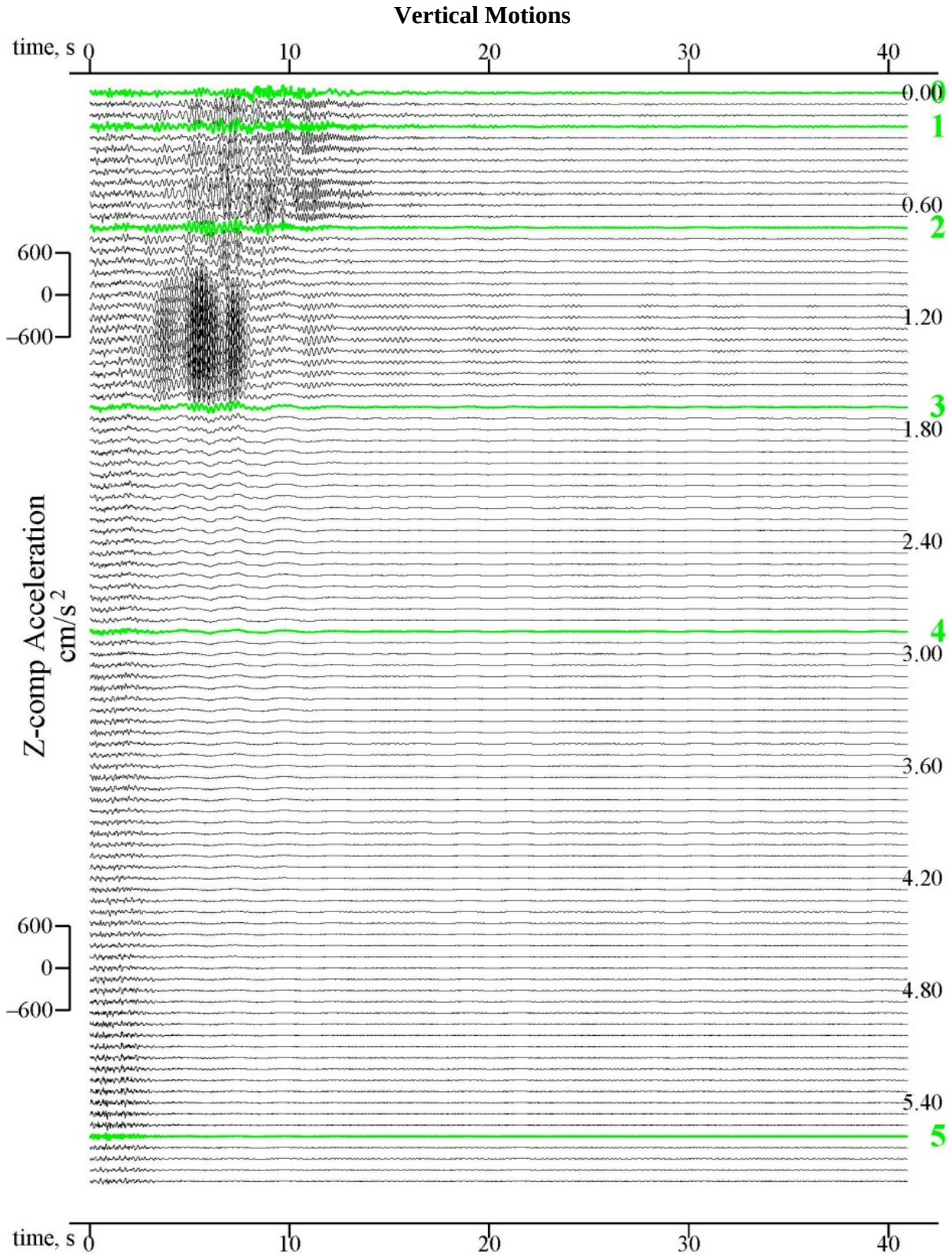

6) Unlike the Original **SYNACC.EXE** program, which will output the **Torsion** and **Rocking** components of **Rotational** Motions, and the **Strains**, the **NEW EQSYNACC.EXE** program will output the **d/dx-** and **d/dz-** derivatives of the **U-(Radial), V-(Transverse) and W-(Vertical)** translational components, or respectively

The **d/dx- derivative files:**

V2DUDX.DAT

V2DVDX.DAT

V2DWDX.DAT

and **the d/dz- derivative files:**

V2DUDZ.DAT

V2DVDZ.DAT

V2DWDZ.DAT

from which the **Rocking, Torsion** and **Strain** component time histories can be computed. For example, The synthetic motion, $\partial U/\partial x$ is the synthetic ***normal strain***, ε_x Similarly, $\partial W/\partial z$ is the synthetic ***normal strain***, ε_z . As for the two derivative components $\partial U/\partial z$ and $\partial W/\partial x$, those are used to compute, $\Omega_y = \frac{1}{2}\left(\partial U/\partial z - \partial W/\partial x\right)$, the in-plane ***Rocking*** component of the Rayleigh and body ***P, SV*** waves in the ***x-z*** plane, or the y- direction rotation, while $\varepsilon_{xz} = \frac{1}{2}\left(\partial U/\partial z + \partial W/\partial x\right)$ is the ***Shear Strain*** in the ***x-z*** plane.

Figures 8a and 8b are from **Report III Figures V.3a and V.3b. Figure 8a** shows plots of the synthetic $\partial \ddot{U}/\partial x$, $\partial \ddot{U}/\partial z$ rotational acceleration time histories again calculated for the El Centro six-layered site model, at depths equally spaced from the surface to almost 6km below the surface, for hypocentral distance of $D = 10.0km$, as in Figures 7a and 7b. Similarly **Figure 8b** gives plots of the synthetic $\partial \ddot{W}/\partial x$, $\partial \ddot{W}/\partial z$ rotational acceleration time histories derived from the corresponding vertical translational motions.

Figure 8a: Report III Fig. V.3a $\partial\ddot{U}/\partial x$ **Synthetic Rotational Acc.:** $M = 6.5,\ R = 8.0km,\ H = 6.0km,\ s = 0,\ s_L = 2$ $\partial\ddot{U}/\partial z$ $10^{-5}\ rad/s^2$

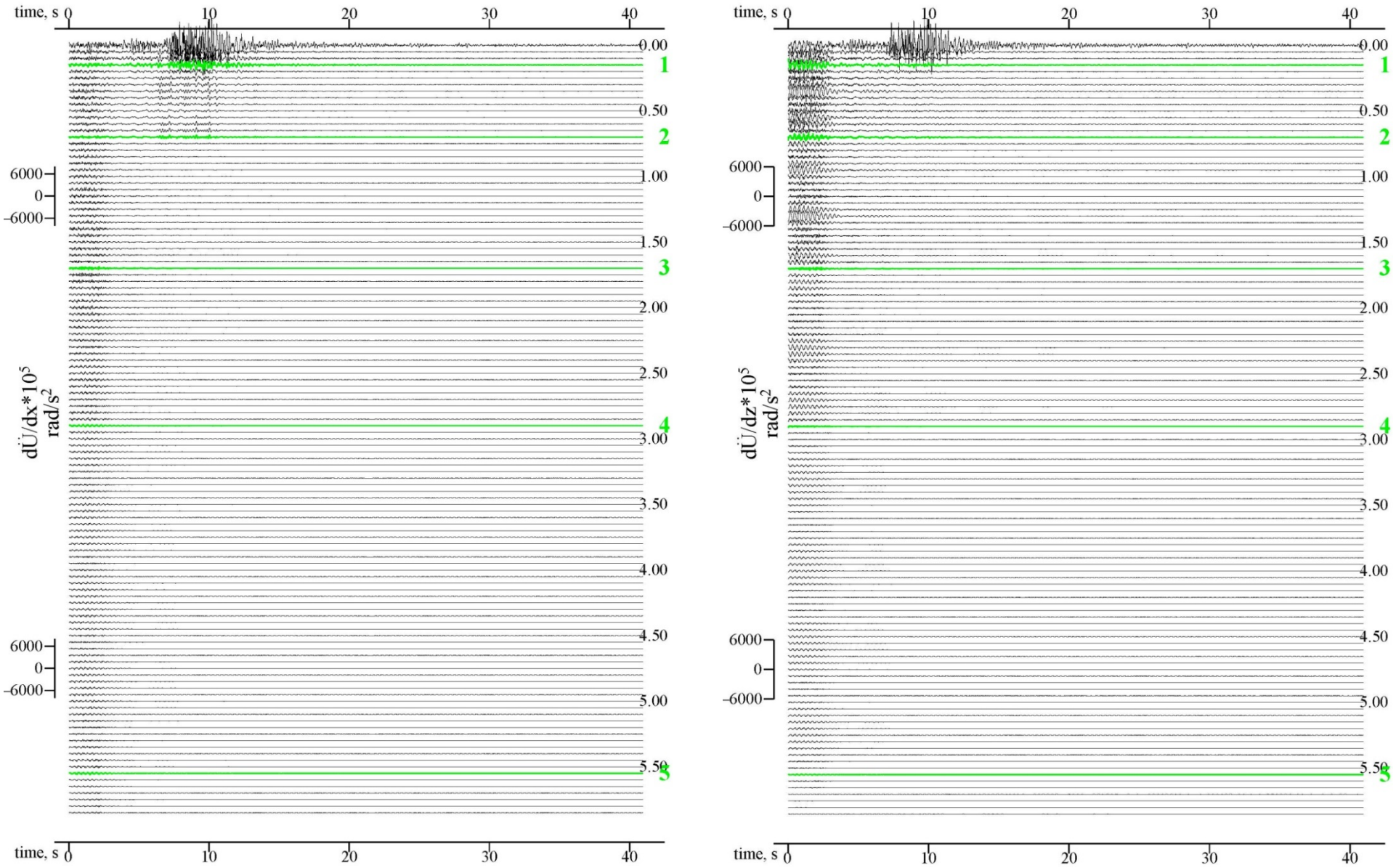

Figure 8b: Report III Fig. V.3b $d\ddot{W}/dx$ **Synthetic Rotational Acc.:** $M = 6.5,\ R = 8.0km,\ H = 6.0km,\ s = 0,\ s_L = 2$ $\partial\ddot{W}/\partial z$ $10^{-5}\ rad/s^2$

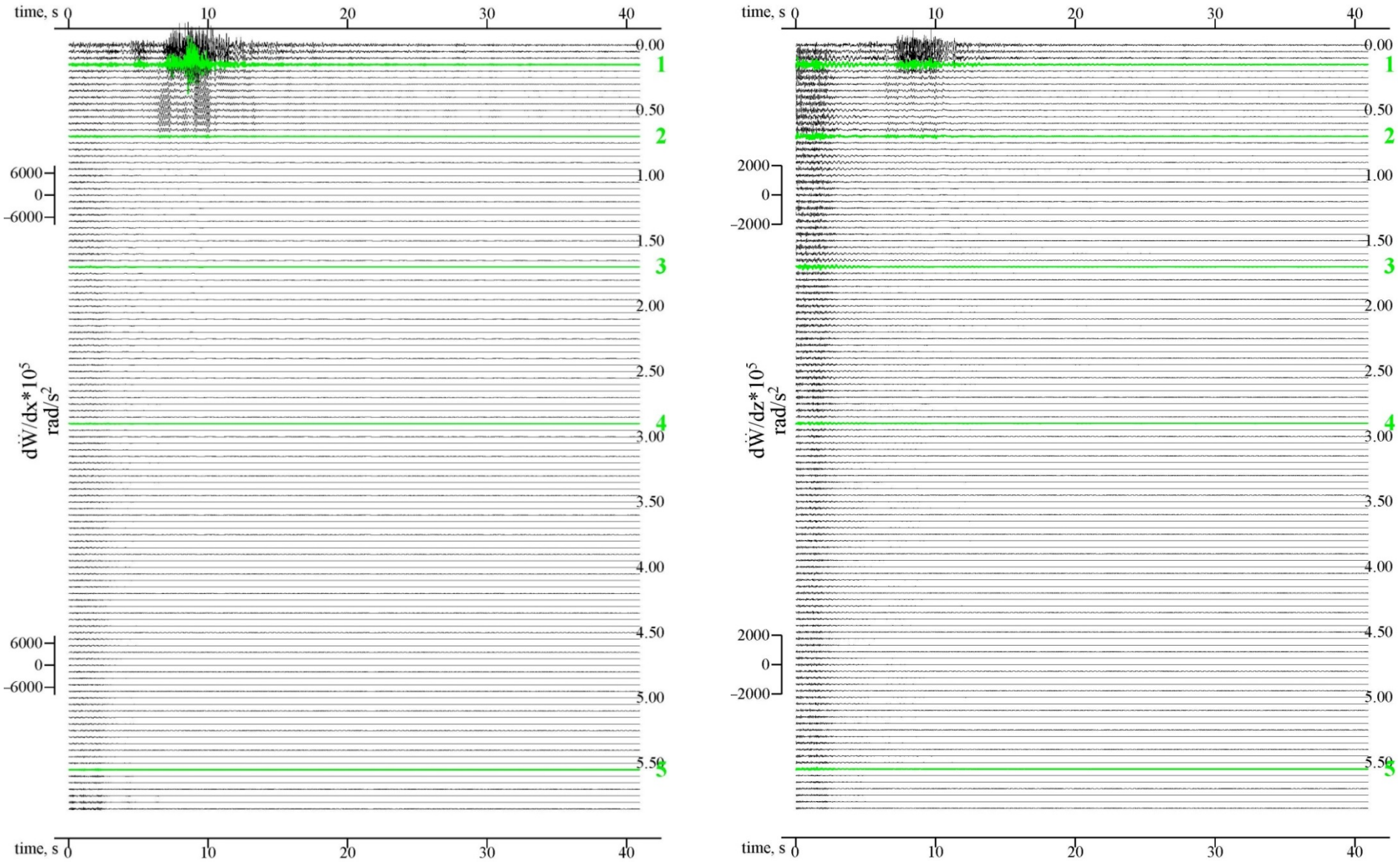

7) The **Radial, Tranverse** and **Vertical** components of **Curvature** (Trifunac, 1990) Time Histories (**Curvograms**), are all in one output file**: V2K01.DAT**. This is the same as in the original **SYNACC.EXE** program.

8) The New **EQSYNACC.EXE** program currently has an updated version which, at the request of the user, outputs the above files separately for each mode of motions. These files are named as follows:

	The Translational files:		
Mode#	**Radial**	**Transverse**	**Vertical**
1	**V2X01.M01**	**V2Y01.M01**	**V2Z01.M01**
2	**V2X01.M02**	**V2Y01.M02**	**V2Z01.M02**
3	**V2X01.M03**	**V2Y01.M03**	**V2Z01.M03**
⋮	⋮	⋮	⋮
11	**V2X01.M11**	**V2Y01.M11**	**V2Z01.M11**
12	**V2X01.M12**	**V2Y01.M12**	**V2Z01.M12**
13	**V2X01.M13**	**V2Y01.M13**	**V2Z01.M13**

where the extension **'.M__'** indicates the **Mode#** of the data in the file. Here **M01** through **M05** are the 5 modes of **Rayleigh** waves, M06 through M10 are the 5 modes of Love waves. **M11** through **M13** are respectively the incident **Body P-, SV- and SH-** waves. Similarly for the **d/dx** and **d/dz** derivatives files:

	The d/dx and d/dz derivatives files:		
Mode#	**Radial d/d/x, d/dz**	**Trans. d/d/x, d/dz**	**Vertical d/d/x, d/dz**
1	**V2DUD(X,Z).M01**	**V2DVD(X,Z).M01**	**V2DWD(X,Z).M01**
2	**V2DUD(X,Z).M02**	**V2DVD(X,Z).M02**	**V2DWD(X,Z).M02**
3	**V2DUD(X,Z).M03**	**V2DVD(X,Z).M03**	**V2DWD(X,Z).M03**
⋮	⋮	⋮	⋮
11	**V2DUD(X,Z).M11**	**V2DVD(X,Z).M11**	**V2DWD(X,Z).M11**
12	**V2DUD(X,Z).M12**	**V2DVD(X,Z).M12**	**V2DWD(X,Z).M12**
13	**V2DUD(X,Z).M13**	**V2DVD(X,Z).M13**	**V2DWD(X,Z).M13**

References

1. **V. W. Lee (1990)** Surface Strains Associated with Strong Earthquake Shaking, *Proc. J.S. C.E., 422(n* I-14), 187-194**.**

2. **V.W. Lee (2002).** Empirical Scaling of Strong Earthquake Ground Motion: Part III: Synthetic Strong Motion, *ISET J.Earthquake Technology, 39(4), 273-310.*

3. **V. W. Lee & M.D. Trifunac (1985)** Torsional Accelerograms, *Int. J. Soil Dynamics & Earth quake Eng., 4(3), 132-139,8 Pages,* **Aug, 85**

4. **V. W. Lee & M.D. Trifunac (1987)** Rocking Strong Earthquake Accelerations, *Int. J. Soil Dynamics & Earthquake Eng., 6(2),* 75-89.

5. **M. D. Trifunac (1971**) A Method for Synthesizing Realistic Strong Ground Motion, *Bull. Seism. Soc. Amer.,* 61(6), 1739-1753.

6. **M. D. Trifunac (1976)** Preliminary Empirical Model for Scaling Fourier Amplitude Spectra of Strong Ground Acceleration in Terms of Earthquake Magnitude, Source to Station Distance and Recording Site Conditions, *Bull. Seism. Soc. Amer*., 66(4), 1343-1373.

7. **M. D. Trifunac (1990)** Curvograms of Strong Ground Motion, ASCE, EMD, 116(6), 1426-1432.

8. **M. D. Trifunac (1991)** Empirical Scaling of Fourier Spectrum Amplitudes of Recorded Strong Earthquake Accelerations in Terms of Modified Mercalli Intensity, Local Soil Conditions and Depth of Sediments, *Int. J. Soil Dynamics and Earthquake Eng.*, 10(1), 65-72.

9. **M.D. Trifunac & V. W. Lee (1978)** Dependence of the Fourier Amplitude Spectra of Strong-Motion Accelerograms on Depths of Sedimentary Deposits, *Civil Eng. Report CE 78-14,* Univ. of Southern Cal., Los Angeles**.**

10. **M.D. Trifunac & V. W. Lee (1985)** Preliminary Empirical Model for Scaling Fourier Amplitude Spectra of Strong Ground Acceleration in Terms of Earthquake Magnitude, Source to Station Distance, Site Intensity and Recording Site Conditions, *Civil Eng. Report CE 85-03*, Univ. of Southern Cal., Los Angeles**.**

11. **M.D. Trifunac &V. W. Lee (1989)** Empirical Model for Scaling Fourier

Amplitude Spectra of Strong Earthquake Ground Acceleration in Terms of Earthquake Magnitude, Source to Station Distance, Site Intensity and Recording Site Conditions, *Int. J. Soil Dynamics & Earthquake Eng.,8(3),* 110-125.

12. **M.D. Trifunac &V. W. Lee (2013a)** Synthetic Translational Motions of Surface Waves On or Below a Layered Media**, S.E.E.C. Report II, 2013.**

13. **M.D. Trifunac &V. W. Lee (2013b)** Synthetic Rotational Motions of Surface Waves On or Below a Layered Media**, S.E.E.C. Report III, 2013.**

14. **B.D. Westermo & M.D. Trifunac (1978)** Correlations of the Frequency Dependent Duration of Strong Earthquake Ground Motion with the Magnitude, Epicentral Distance and the Depth of Sediments at the Recording Site, *Department of Civil Engineering, Report CE 78-12*, University of Southern Calif., Los Angeles, California.

15. **H.L. Wong & M.D. Trifunac (1978)** Synthesizing Realistic Strong Motion Accelerograms, *Department of Civil Engineering, Report CE 78-07*, University of Southern Calif., Los Angeles, California.

16. **H.L. Wong & M.D. Trifunac (1979)** Generation of Artificial Strong Motion Accelerograms, *Int. J. Earthquake Engineering Struct. Dynamics,* 7(6), 509-527.

Appendix A.1

Mode 1 Rayleigh Waves in Hskwav.000:

6 LAYER Velocity Model				
Imperial Valley VELOCITY MODEL				
Thickness, km	alpha, km/s	beta, km/s	density	Depth from top, km
0.18	1.70	0.98	1.28	0.18
0.55	1.96	1.13	1.36	0.73
0.98	2.71	1.57	1.59	1.71
1.19	3.76	2.17	1.91	2.90
2.68	4.69	2.71	2.19	5.58
.00	6.40	3.70	2.71	5.58

RAYLEIGH WAVE DISPERSION
LAYER VELOCITY MODEL FOR

PERIOD	C	U	RATIO	Imag[U(z)]	Real[W(z)]	dU/dz(^-5)	dW/dz(^-5)	dU/dx(^-5)	dW/dx(^-5)
Rayleigh Wave Mode# 1 U,W(z) at z= .000E-3 km									
15.00	3.17131	2.96209	1.32144	1.32144E+00	1.00000E+00	-1.32084E-01	5.85346E-02	-1.74541E-01	1.32084E-01
14.00	3.15297	2.89729	1.36955	1.37000E+00	1.00000E+00	-1.42342E-01	6.53771E-02	-1.94944E-01	1.42342E-01
13.00	3.13177	2.85438	1.42305	1.42000E+00	1.00000E+00	-1.54329E-01	7.36517E-02	-2.19618E-01	1.54329E-01
12.00	3.10639	2.79749	1.483	1.48000E+00	1.00000E+00	-1.68555E-01	8.38300E-02	-2.49968E-01	1.68555E-01
11.00	3.07499	2.72319	1.54973	1.55000E+00	1.00000E+00	-1.85756E-01	9.65417E-02	-2.87872E-01	1.85756E-01
10.00	3.03486	2.62693	1.62225	1.62000E+00	1.00000E+00	-2.07034E-	1.12635E-01	-3.35861E-	2.07034E-01

						01		01	
9.50	3.00841	2.56712	1.65985	1.66000E+00	1.00000E+00	-2.19846E-01	1.22378E-01	-3.64912E-01	2.19846E-01
9.00	2.98196	2.50730	1.69744	1.70000E+00	1.00000E+00	-2.34118E-01	1.33274E-01	-3.97402E-01	2.34118E-01
8.50	2.94606	2.42245	1.73263	1.73000E+00	1.00000E+00	-2.50911E-01	1.45794E-01	-4.34736E-01	2.50911E-01
8.00	2.90741	2.33224	1.76601	1.77000E+00	1.00000E+00	-2.70137E-01	1.59990E-01	-4.77064E-01	2.70137E-01
7.50	2.85779	2.22061	1.79214	1.79000E+00	1.00000E+00	-2.93149E-01	1.76188E-01	-5.25364E-01	2.93149E-01
7.00	2.79710	2.09476	1.80778	1.81000E+00	1.00000E+00	-3.20903E-01	1.94552E-01	-5.80122E-01	3.20903E-01
6.50	2.72535	1.95668	1.81232	1.81000E+00	1.00000E+00	-3.54686E-01	2.15573E-01	-6.42805E-01	3.54686E-01
6.00	2.63182	1.80471	1.79182	1.79000E+00	1.00000E+00	-3.97899E-01	2.39102E-01	-7.12963E-01	3.97899E-01
5.50	2.51546	1.64997	1.74071	1.74000E+00	1.00000E+00	-4.54151E-01	2.65120E-01	-7.90544E-01	4.54151E-01
5.00	2.37800	1.49917	1.65672	1.66000E+00	1.00000E+00	-5.28443E-01	2.93605E-01	-8.75482E-01	5.28443E-01
4.80	2.31929	1.43994	1.61705	1.62000E+00	1.00000E+00	-5.64396E-01	3.06071E-01	-9.12656E-01	5.64396E-01
4.60	2.25468	1.38552	1.56468	1.56000E+00	1.00000E+00	-6.05811E-01	3.17891E-01	-9.47900E-01	6.05811E-01
4.40	2.18951	1.33155	1.51113	1.51000E+00	1.00000E+00	-6.52199E-01	3.30520E-01	-9.85557E-01	6.52199E-01
4.20	2.12237	1.28024	1.45259	1.45000E+00	1.00000E+00	-7.04871E-01	3.43375E-01	-1.02389E+00	7.04871E-01
4.00	2.05344	1.23135	1.38951	1.39000E+00	1.00000E+00	-7.64958E-01	3.56464E-01	-1.06292E+00	7.64958E-01
3.80	1.98326	1.18361	1.3245	1.32000E+00	1.00000E+00	-8.33713E-01	3.70326E-01	-1.10425E+00	8.33713E-01

3.60	1.91099	1.13780	1.25623	1.26000E+00	1.00000E+00	-9.13312E-01	3.84772E-01	-1.14733E+00	9.13312E-01
3.40	1.83720	1.09297	1.18768	1.19000E+00	1.00000E+00	-1.00588E+00	4.00645E-01	-1.19466E+00	1.00588E+00
3.20	1.76143	1.04942	1.11876	1.12000E+00	1.00000E+00	-1.11472E+00	4.18232E-01	-1.24710E+00	1.11472E+00
3.00	1.68433	1.00883	1.05289	1.05000E+00	1.00000E+00	-1.24346E+00	4.39066E-01	-1.30923E+00	1.24346E+00
2.80	1.60677	0.97045	0.98941	9.89000E-01	1.00000E+00	-1.39659E+00	4.63404E-01	-1.38180E+00	1.39659E+00
2.60	1.53024	0.93858	0.93324	9.33000E-01	1.00000E+00	-1.57924E+00	4.94261E-01	-1.47381E+00	1.57924E+00
2.40	1.45624	0.91263	0.88377	8.84000E-01	1.00000E+00	-1.79778E+00	5.32832E-01	-1.58882E+00	1.79778E+00
2.20	1.38512	0.89147	0.8408	8.41000E-01	1.00000E+00	-2.06191E+00	5.81404E-01	-1.73365E+00	2.06191E+00
2.00	1.31735	0.87300	0.80482	8.05000E-01	1.00000E+00	-2.38478E+00	6.43670E-01	-1.91932E+00	2.38478E+00
1.90	1.28465	0.86338	0.7894	7.89000E-01	1.00000E+00	-2.57420E+00	6.81482E-01	-2.03207E+00	2.57420E+00
1.80	1.25236	0.85104	0.77549	7.75000E-01	1.00000E+00	-2.78727E+00	7.24886E-01	-2.16150E+00	2.78727E+00
1.70	1.22044	0.83627	0.76291	7.63000E-01	1.00000E+00	-3.02841E+00	7.74825E-01	-2.31040E+00	3.02841E+00
1.60	1.18814	0.82400	0.75132	7.51000E-01	1.00000E+00	-3.30516E+00	8.32785E-01	-2.48323E+00	3.30516E+00
1.50	1.15573	0.86507	0.74028	7.40000E-01	1.00000E+00	-3.62437E+00	8.99796E-01	-2.68305E+00	3.62437E+00
1.40	1.12973	0.85971	0.73718	7.37000E-01	1.00000E+00	-3.97262E+00	9.82124E-01	-2.92854E+00	3.97262E+00
1.30	1.10444	0.85923	0.73439	7.34000E-01	1.00000E+00	-4.37617E+00	1.07780E+00	-3.21382E+00	4.37617E+00
1.20	1.08090	0.86756	0.73182	7.32000E-01	1.00000E+00	-4.84410E+00	1.18887E+00	-3.54501E+00	4.84410E+00

1.10	1.06005	0.87857	0.72876	7.29000E-01	1.00000E+00	-5.38841E+00	-1.31693E+00	-3.92686E+00	-5.38841E+00
1.00	1.04122	0.88427	0.7247	7.25000E-01	1.00000E+00	-6.03445E+00	-1.46660E+00	-4.37316E+00	-6.03445E+00
0.95	1.03223	0.88435	0.72223	7.22000E-01	1.00000E+00	-6.40737E+00	-1.55193E+00	-4.62759E+00	-6.40737E+00
0.90	1.02334	0.91565	0.71956	7.20000E-01	1.00000E+00	-6.82209E+00	-1.64627E+00	-4.90890E+00	-6.82209E+00
0.85	1.01663	0.91437	0.71505	7.15000E-01	1.00000E+00	-7.27107E+00	-1.74361E+00	-5.19917E+00	-7.27107E+00
0.80	1.00994	0.91369	0.71007	7.10000E-01	1.00000E+00	-7.77668E+00	-1.85187E+00	-5.52199E+00	-7.77668E+00
0.75	1.00334	0.91325	0.7045	7.05000E-01	1.00000E+00	-8.34969E+00	-1.97273E+00	-5.88236E+00	-8.34969E+00
0.70	0.99671	0.91058	0.69829	6.98000E-01	1.00000E+00	-9.00561E+00	-2.10894E+00	-6.28853E+00	-9.00561E+00
0.65	0.98985	0.90540	0.69171	6.92000E-01	1.00000E+00	-9.76556E+00	-2.26536E+00	-6.75494E+00	-9.76556E+00
0.60	0.98254	0.89800	0.68498	6.85000E-01	1.00000E+00	-1.06581E+01	-2.44834E+00	-7.30056E+00	-1.06581E+01
0.55	0.97440	0.89036	0.67817	6.78000E-01	1.00000E+00	-1.17241E+01	-2.66645E+00	-7.95094E+00	-1.17241E+01
0.50	0.96526	0.87532	0.67237	6.72000E-01	1.00000E+00	-1.30186E+01	-2.93555E+00	-8.75334E+00	-1.30186E+01
0.48	0.9612	0.87101	0.67066	6.71000E-01	1.00000E+00	-1.36184E+01	-3.06297E+00	-9.13328E+00	-1.36184E+01
0.46	0.95696	0.86681	0.66921	6.69000E-01	1.00000E+00	-1.42734E+01	-3.20337E+00	-9.55193E+00	-1.42734E+01
0.44	0.95254	0.86303	0.66811	6.68000E-01	1.00000E+00	-1.49915E+01	-3.35898E+00	-1.00160E+01	-1.49915E+01
0.42	0.94797	0.85995	0.66738	6.67000E-01	1.00000E+00	-1.57811E+01	-3.53203E+00	-1.05320E+01	-1.57811E+01
0.40	0.94328	0.85777	0.66706	6.67000E-01	1.00000E+00	-1.66525E+01	-3.72529E+00	-1.11082E+01	-1.66525E+01

0.38	0.93855	0.85663	0.66713	6.67000E-01	1.00000E+00	-1.76173E+01	-3.94153E+00	-1.17530E+01	-1.76173E+01
0.36	0.93382	0.85662	0.66758	6.68000E-01	1.00000E+00	-1.86902E+01	-4.18440E+00	-1.24772E+01	-1.86902E+01
0.34	0.92918	0.85779	0.66837	6.68000E-01	1.00000E+00	-1.98885E+01	-4.45793E+00	-1.32929E+01	-1.98885E+01
0.32	0.92470	0.86004	0.66946	6.69000E-01	1.00000E+00	-2.12339E+01	-4.76727E+00	-1.42152E+01	-2.12339E+01
0.30	0.92047	0.86303	0.67078	6.71000E-01	1.00000E+00	-2.27536E+01	-5.11852E+00	-1.52626E+01	-2.27536E+01
0.28	0.91653	0.86572	0.67225	6.72000E-01	1.00000E+00	-2.44836E+01	-5.51978E+00	-1.64591E+01	-2.44836E+01
0.26	0.9128	0.86674	0.67384	6.74000E-01	1.00000E+00	-2.64747E+01	-5.98278E+00	-1.78397E+01	-2.64747E+01
0.24	0.90933	0.88049	0.67547	6.75000E-01	1.00000E+00	-2.87904E+01	-6.52182E+00	-1.94470E+01	-2.87904E+01
0.22	0.90692	0.88286	0.67687	6.77000E-01	1.00000E+00	-3.14911E+01	-7.14840E+00	-2.13154E+01	-3.14911E+01
0.20	0.9049	0.88761	0.67811	6.78000E-01	9.99999E-01	-3.47175E+01	-7.89524E+00	-2.35424E+01	-3.47175E+01
0.19	0.90409	0.88996	0.67864	6.79000E-01	1.00000E+00	-3.65775E+01	-8.32472E+00	-2.48230E+01	-3.65775E+01
0.18	0.90339	0.89213	0.6791	6.79000E-01	1.00000E+00	-3.86395E+01	-8.79997E+00	-2.62401E+01	-3.86395E+01
0.17	0.90282	0.89409	0.6795	6.79000E-01	1.00000E+00	-4.09383E+01	-9.32899E+00	-2.78176E+01	-4.09383E+01
0.16	0.90235	0.89581	0.67983	6.80000E-01	1.00000E+00	-4.35196E+01	-9.92203E+00	-2.95859E+01	-4.35196E+01
0.15	0.90199	0.89727	0.68009	6.80000E-01	1.00000E+00	-4.64394E+01	-1.05918E+01	-3.15830E+01	-4.64394E+01
0.14	0.90172	0.89853	0.68029	6.80000E-01	1.00000E+00	-4.97714E+01	-1.13551E+01	-3.38590E+01	-4.97714E+01
0.13	0.90154	0.90017	0.68044	6.80000E-01	1.00000E+00	-5.36107E+01	-1.22337E+01	-3.64789E+01	-5.36107E+01

0.12	0.90153	0.90405	0.68054	6.81000E-01	1.00000E+00	-5.80789E+01	1.32552E+01	-3.95250E+01	5.80789E+01
0.11	0.90201	0.91301	0.68061	6.81000E-01	9.99999E-01	-6.33250E+01	1.44541E+01	-4.30997E+01	6.33250E+01
0.10	0.90363	0.94321	0.68064	6.81000E-01	1.00000E+00	-6.95327E+01	1.58717E+01	-4.73268E+01	6.95327E+01
0.095	0.90496	0.97596	0.68065	6.81000E-01	1.00000E+00	-7.30848E+01	1.66827E+01	-4.97452E+01	7.30848E+01
0.090	0.90868	0.98358	0.68065	6.81000E-01	1.00000E+00	-7.68292E+01	1.75374E+01	-5.22938E+01	7.68292E+01
0.085	0.91313	0.98336	0.68065	6.81000E-01	1.00000E+00	-8.09521E+01	1.84785E+01	-5.51001E+01	8.09521E+01
0.080	0.91759	0.98313	0.68066	6.81000E-01	1.00000E+00	-8.55935E+01	1.95383E+01	-5.82602E+01	8.55935E+01
0.075	0.92205	0.98291	0.68066	6.81000E-01	1.00000E+00	-9.08582E+01	2.07401E+01	-6.18435E+01	9.08582E+01
0.070	0.92651	0.98269	0.68066	6.81000E-01	1.00000E+00	-9.68795E+01	2.21145E+01	-6.59420E+01	9.68795E+01
0.065	0.93097	0.98246	0.68066	6.81000E-01	1.00000E+00	-1.03832E+02	2.37016E+01	-7.06743E+01	1.03832E+02
0.060	0.93542	0.98224	0.68066	6.81000E-01	1.00000E+00	-1.11949E+02	2.55545E+01	-7.61995E+01	1.11949E+02
0.055	0.93988	0.98202	0.68066	6.81000E-01	1.00000E+00	-1.21547E+02	2.77454E+01	-8.27323E+01	1.21547E+02
0.050	0.94434	0.98179	0.68067	6.81000E-01	9.99999E-01	-1.33070E+02	3.03762E+01	-9.05771E+01	1.33070E+02
0.048	0.94612	0.9817	0.68067	6.81000E-01	1.00000E+00	-1.38354E+02	3.15824E+01	-9.41736E+01	1.38354E+02
0.046	0.94790	0.98161	0.68067	6.81000E-01	1.00000E+00	-1.44099E+02	3.28936E+01	-9.80835E+01	1.44099E+02
0.044	0.94969	0.98152	0.68067	6.81000E-01	1.00000E+00	-1.50365E+02	3.43239E+01	-1.02349E+02	1.50365E+02
0.042	0.95147	0.98143	0.68067	6.81000E-01	1.00000E+00	-1.57230E+02	3.58912E+01	-1.07022E+02	1.57230E+02

0.040	0.95325	0.97955	0.68067	6.81000E-01	1.00000E+00	1.64783E+02	-3.76154E+01	1.12163E+02	-1.64783E+02

Appendix A.2

Mode 1 Love waves in Hskwav.000:

LOVE WAVE DISPERSION
LAYER VELOCITY MODELFOR

PERIOD	c, km/s	u, km/s	n/a	Real[V(z)]	dV/dz(^-5)	dV/dx(^-5)
Love WaveMode# 1V(z) atz= .000E-3 km						
15.00	3.53897	3.21717	0	1.00000E+00	0.00000E+00	1.18362E-01
14.00	3.50616	3.04785	0	1.00000E+00	0.00000E+00	1.28003E-01
13.00	3.46498	2.93077	0	1.00000E+00	0.00000E+00	1.39488E-01
12.00	3.41070	2.77435	0	1.00000E+00	0.00000E+00	1.53517E-01
11.00	3.33717	2.58106	0	1.00000E+00	0.00000E+00	1.71163E-01
10.00	3.23653	2.35901	0	1.00000E+00	0.00000E+00	1.94133E-01
9.50	3.16800	2.24421	0	1.00000E+00	0.00000E+00	2.08771E-01
9.00	3.09946	2.12942	0	1.00000E+00	0.00000E+00	2.25243E-01
8.50	3.00846	2.00112	0	1.00000E+00	0.00000E+00	2.45707E-01
8.00	2.91278	1.87267	0	1.00000E+00	0.00000E+00	2.69639E-01
7.50	2.79834	1.74359	0	1.00000E+00	0.00000E+00	2.99377E-01
7.00	2.67256	1.61918	0	1.00000E+00	0.00000E+00	3.35857E-01
6.50	2.53706	1.49991	0	1.00000E+00	0.00000E+00	3.81010E-01
6.00	2.39071	1.39319	0	1.00000E+00	0.00000E+00	4.38028E-01
5.50	2.24004	1.30007	0	1.00000E+00	0.00000E+00	5.09990E-01
5.00	2.08823	1.22022	0	1.00000E+00	0.00000E+00	6.01771E-01

4.80	2.02748	1.19065	0	1.00000E+00	0.00000E+00	6.45628E-01
4.60	1.96792	1.16619	0	1.00000E+00	0.00000E+00	6.94088E-01
4.40	1.90847	1.14221	0	1.00000E+00	0.00000E+00	7.48242E-01
4.20	1.85022	1.12080	0	1.00000E+00	0.00000E+00	8.08551E-01
4.00	1.79305	1.10172	0	1.00000E+00	0.00000E+00	8.76047E-01
3.80	1.73695	1.08425	0	1.00000E+00	0.00000E+00	9.51939E-01
3.60	1.68268	1.06951	0	1.00000E+00	0.00000E+00	1.03723E+00
3.40	1.62975	1.05634	0	1.00000E+00	0.00000E+00	1.13391E+00
3.20	1.57859	1.04521	0	1.00000E+00	0.00000E+00	1.24383E+00
3.00	1.52953	1.03594	0	1.00000E+00	0.00000E+00	1.36931E+00
2.80	1.48174	1.02771	0	1.00000E+00	0.00000E+00	1.51443E+00
2.60	1.43635	1.02101	0	1.00000E+00	0.00000E+00	1.68247E+00
2.40	1.39266	1.01508	0	1.00000E+00	0.00000E+00	1.87985E+00
2.20	1.35054	1.00983	0	1.00000E+00	0.00000E+00	2.11471E+00
2.00	1.31009	1.00528	0	1.00000E+00	0.00000E+00	2.39800E+00
1.90	1.29049	1.00331	0	1.00000E+00	0.00000E+00	2.56255E+00
1.80	1.27131	1.00163	0	1.00000E+00	0.00000E+00	2.74572E+00
1.70	1.25252	1.00021	0	1.00000E+00	0.00000E+00	2.95084E+00
1.60	1.23424	0.99925	0	1.00000E+00	0.00000E+00	3.18171E+00
1.50	1.21622	0.99851	0	1.00000E+00	0.00000E+00	3.44411E+00
1.40	1.19894	0.99845	0	1.00000E+00	0.00000E+00	3.74330E+00
1.30	1.18203	0.99869	0	1.00000E+00	0.00000E+00	4.08891E+00
1.20	1.16559	0.99925	0	1.00000E+00	0.00000E+00	4.49214E+00
1.10	1.14972	1.00008	0	1.00000E+00	0.00000E+00	4.96815E+00
1.00	1.13442	1.00081	0	1.00000E+00	0.00000E+00	5.53868E+00
0.95	1.12696	1.00098	0	1.00000E+00	0.00000E+00	5.86878E+00
0.90	1.11957	1.00106	0	1.00000E+00	0.00000E+00	6.23571E+00
0.85	1.11229	1.00074	0	1.00000E+00	0.00000E+00	6.64573E+00

0.80	1.10505	1.00027	0	1.00000E+00	0.00000E+00	7.10735E+00
0.75	1.09785	0.99908	0	1.00000E+00	0.00000E+00	7.63090E+00
0.70	1.09063	0.99753	0	1.00000E+00	0.00000E+00	8.23009E+00
0.65	1.08337	0.99539	0	1.00000E+00	0.00000E+00	8.92257E+00
0.60	1.07591	0.99237	0	1.00000E+00	0.00000E+00	9.73313E+00
0.55	1.06824	0.98873	0	1.00000E+00	0.00000E+00	1.06942E+01
0.50	1.06026	0.98450	0	1.00000E+00	0.00000E+00	1.18522E+01
0.48	1.05699	0.98268	0	1.00000E+00	0.00000E+00	1.23842E+01
0.46	1.05361	0.98081	0	1.00000E+00	0.00000E+00	1.29641E+01
0.44	1.05015	0.97890	0	1.00000E+00	0.00000E+00	1.35980E+01
0.42	1.04666	0.97701	0	1.00000E+00	0.00000E+00	1.42931E+01
0.40	1.04302	0.97518	0	1.00000E+00	0.00000E+00	1.50601E+01
0.38	1.03937	0.97337	0	1.00000E+00	0.00000E+00	1.59084E+01
0.36	1.03558	0.97178	0	1.00000E+00	0.00000E+00	1.68536E+01
0.34	1.03177	0.97026	0	1.00000E+00	0.00000E+00	1.79109E+01
0.32	1.02787	0.96905	0	1.00000E+00	0.00000E+00	1.91026E+01
0.30	1.02393	0.96804	0	1.00000E+00	0.00000E+00	2.04545E+01
0.28	1.01996	0.96727	0	1.00000E+00	0.00000E+00	2.20008E+01
0.26	1.01598	0.96692	0	1.00000E+00	0.00000E+00	2.37860E+01
0.24	1.01202	0.96684	0	1.00000E+00	0.00000E+00	2.58690E+01
0.22	1.00809	0.96708	0	1.00000E+00	0.00000E+00	2.83307E+01
0.20	1.00424	0.96766	0	1.00000E+00	0.00000E+00	3.12833E+01
0.19	1.00237	0.96809	0	1.00000E+00	0.00000E+00	3.29912E+01
0.18	1.00051	0.96855	0	1.00000E+00	0.00000E+00	3.48888E+01
0.17	0.99870	0.96912	0	1.00000E+00	0.00000E+00	3.70080E+01
0.16	0.99693	0.96976	0	1.00000E+00	0.00000E+00	3.93908E+01
0.15	0.99520	0.97048	0	1.00000E+00	0.00000E+00	4.20899E+01
0.14	0.99356	0.97147	0	1.00000E+00	0.00000E+00	4.51708E+01

0.13	0.99198	0.97281	0	1.00000E+00	0.00000E+00	4.87230E+01
0.12	0.99051	0.97473	0	1.00000E+00	0.00000E+00	5.28615E+01
0.11	0.98932	0.97814	0	1.00000E+00	0.00000E+00	5.77365E+01
0.10	0.98851	0.97922	0	1.00000E+00	0.00000E+00	6.35622E+01
0.095	0.98811	0.97935	0	1.00000E+00	0.00000E+00	6.69347E+01
0.090	0.98763	0.97939	0	1.00000E+00	0.00000E+00	7.06876E+01
0.085	0.98716	0.97943	0	1.00000E+00	0.00000E+00	7.48813E+01
0.080	0.98668	0.97947	0	1.00000E+00	0.00000E+00	7.96001E+01
0.075	0.98620	0.97950	0	1.00000E+00	0.00000E+00	8.49481E+01
0.070	0.98572	0.97954	0	1.00000E+00	0.00000E+00	9.10601E+01
0.065	0.98525	0.97958	0	1.00000E+00	0.00000E+00	9.81115E+01
0.060	0.98477	0.97962	0	1.00000E+00	0.00000E+00	1.06339E+02
0.055	0.98429	0.97966	0	1.00000E+00	0.00000E+00	1.16063E+02
0.050	0.98382	0.97969	0	1.00000E+00	0.00000E+00	1.27730E+02
0.048	0.98363	0.97971	0	1.00000E+00	0.00000E+00	1.33078E+02
0.046	0.98343	0.97973	0	1.00000E+00	0.00000E+00	1.38892E+02
0.044	0.98324	0.97974	0	1.00000E+00	0.00000E+00	1.45234E+02
0.042	0.98305	0.97976	0	1.00000E+00	0.00000E+00	1.52179E+02
0.040	0.98286	0.98008	0	1.00000E+00	0.00000E+00	1.59819E+02

Appendix A.3

Mode 11 Body P- Waves in BodyW845.000:

6 LAYER Velocity Model				
Imperial Valley VELOCITY MODEL				
Thickness, km	alpha, km/s	beta, km/s	density	Depth from top, km
0.18	1.70	0.98	1.28	0.18
0.55	1.96	1.13	1.36	0.73
0.98	2.71	1.57	1.59	1.71
1.19	3.76	2.17	1.91	2.90
2.68	4.69	2.71	2.19	5.58
.00	6.40	3.70	2.71	5.58

BODY WAVE DISPERSION
LAYER VELOCITY MODEL FOR

PERIOD	c, km/s	(n/a)	(n/a)	Imag[U(z)]	Real[W(z)]	dU/dz(^-5)	dW/dz(^-5)	dU/dx(^-5)	dW/dx(^-5)
Body P- Wave Mode# 11 U,W(z) at z= .000E-3 km									
15.00	6.45000	0	0	-1.80906E+00	1.00000E+00	-6.49620E-02	-3.94119E-02	1.17520E-01	6.49620E-02
14.00	6.45000	0	0	-1.85095E+00	1.00000E+00	-6.96021E-02	-4.32049E-02	1.28830E-01	6.96022E-02
13.00	6.45000	0	0	-1.89027E+00	1.00000E+00	-7.49561E-02	-4.75168E-02	1.41688E-01	7.49562E-02
12.00	6.45000	0	0	-1.92613E+00	1.00000E+00	-8.12025E-02	-5.24530E-02	1.56407E-01	8.12026E-02
11.00	6.45000	0	0	-1.95777E+00	1.00000E+00	-8.85845E-02	-5.81615E-02	1.73429E-01	8.85846E-02

10.00	6.45000	0	0	-1.98495E+00	1.00000E+00	-9.74430E-02	-6.48658E-02	1.93420E-01	9.74431E-02
9.50	6.45000	0	0	-1.99703E+00	1.00000E+00	-1.02572E-01	-6.86954E-02	2.04839E-01	1.02572E-01
9.00	6.45000	0	0	-2.00834E+00	1.00000E+00	-1.08270E-01	-7.29224E-02	2.17443E-01	1.08270E-01
8.50	6.45000	0	0	-2.01907E+00	1.00000E+00	-1.14639E-01	-7.76244E-02	2.31464E-01	1.14639E-01
8.00	6.45000	0	0	-2.02915E+00	1.00000E+00	-1.21804E-01	-8.28879E-02	2.47159E-01	1.21804E-01
7.50	6.45000	0	0	-2.03753E+00	1.00000E+00	-1.29924E-01	-8.87788E-02	2.64725E-01	1.29924E-01
7.00	6.45000	0	0	-2.04009E+00	1.00000E+00	-1.39204E-01	-9.52396E-02	2.83989E-01	1.39204E-01
6.50	6.45000	0	0	-2.02453E+00	1.00000E+00	-1.49912E-01	-1.01783E-01	3.03502E-01	1.49912E-01
6.00	6.45000	0	0	-1.96026E+00	1.00000E+00	-1.62405E-01	-1.06765E-01	3.18356E-01	1.62405E-01
5.50	6.45000	0	0	-1.79231E+00	1.00000E+00	-1.77169E-01	-1.06492E-01	3.17542E-01	1.77169E-01
5.00	6.45000	0	0	-1.48654E+00	1.00000E+00	-1.94886E-01	-9.71564E-02	2.89705E-01	1.94886E-01
4.80	6.45000	0	0	-1.34018E+00	1.00000E+00	-2.03006E-01	-9.12409E-02	2.72066E-01	2.03006E-01
4.60	6.45000	0	0	-1.19448E+00	1.00000E+00	-2.11833E-01	-8.48570E-02	2.53030E-01	2.11833E-01
4.40	6.45000	0	0	-1.05752E+00	1.00000E+00	-2.21461E-01	-7.85423E-02	2.34201E-01	2.21462E-01
4.20	6.45000	0	0	-9.31259E-01	1.00000E+00	-2.32007E-01	-7.24582E-02	2.16059E-01	2.32007E-01
4.00	6.45000	0	0	-8.03692E-01	1.00000E+00	2.51353E-01	-8.49203E-02	1.95786E-01	2.43608E-01
3.80	6.45000	0	0	-5.73926E-01	1.00000E+00	6.49222E-01	-1.90320E-01	1.47171E-01	2.56429E-01
3.60	6.45000	0	0	-1.21849E+00	1.00000E+00	-	2.74417E-01	3.29814E-01	2.70675E-01

						1.10328E+00			
3.40	6.45000	0	0	-8.37301E-01	1.00000E+00	-2.86597E-01	-8.04764E-02	2.39968E-01	2.86597E-01
3.20	6.45000	0	0	-7.20895E-01	1.00000E+00	-3.04509E-01	-7.36187E-02	2.19519E-01	3.04509E-01
3.00	6.45000	0	0	-5.93310E-01	1.00000E+00	-3.24810E-01	-6.46289E-02	1.92713E-01	3.24810E-01
2.80	6.45000	0	0	-4.04105E-01	1.00000E+00	-3.48011E-01	-4.71631E-02	1.40633E-01	3.48011E-01
2.60	6.45000	0	0	-1.96669E-01	1.00000E+00	-3.74781E-01	-2.47189E-02	7.37079E-02	3.74781E-01
2.40	6.45000	0	0	-7.44285E-02	1.00000E+00	-4.06012E-01	-1.01343E-02	3.02189E-02	4.06013E-01
2.20	6.45000	0	0	-4.72817E-02	1.00000E+00	-4.42923E-01	8.67461E-03	2.09421E-02	4.42923E-01
2.00	6.45000	0	0	-1.28314E-01	1.00000E+00	-4.87215E-01	2.83372E-02	6.25166E-02	4.87215E-01
1.90	6.45000	0	0	-2.62172E-01	1.00000E+00	-5.12858E-01	-4.50919E-02	1.34457E-01	5.12858E-01
1.80	6.45000	0	0	-4.62670E-01	1.00000E+00	8.88796E-01	-8.39972E-02	2.50466E-01	5.41350E-01
1.70	6.45000	0	0	1.08812E-01	1.00000E+00	-1.29557E+00	5.99271E-02	-6.23703E-02	5.73194E-01
1.60	6.45000	0	0	8.61284E-02	1.00000E+00	-6.09019E-01	1.80184E-02	-5.24538E-02	6.09019E-01
1.50	6.45000	0	0	1.75171E-01	1.00000E+00	-6.49620E-01	5.11451E-02	-1.13794E-01	6.49620E-01
1.40	6.45000	0	0	9.34311E-03	1.00000E+00	-6.96021E-01	1.20801E-01	-6.50301E-03	6.96022E-01
1.30	6.45000	0	0	-3.76042E-01	1.00000E+00	-7.49561E-01	-9.45278E-02	2.81867E-01	7.49562E-01
1.20	6.45000	0	0	-2.11961E-01	1.00000E+00	-8.12025E-01	-5.77219E-02	1.72118E-01	8.12025E-01
1.10	6.45000	0	0	2.11456E+00	1.00000E+00	-	-6.30851E-01	-	8.85846E-01

						8.50732E+00		1.87317E+00	
1.00	6.45000	0	0	-1.07758E-01	1.00000E+00	-9.74430E-01	2.31645E-01	1.05003E-01	9.74431E-01
0.95	6.45000	0	0	-4.06482E-01	1.00000E+00	-1.02572E+00	1.51760E-01	4.16935E-01	1.02572E+00
0.90	6.45000	0	0	-5.00290E-01	1.00000E+00	-1.08270E+00	-1.81654E-01	5.41664E-01	1.08270E+00
0.85	6.45000	0	0	-2.12769E-01	1.00000E+00	-1.14639E+00	-8.18005E-02	2.43916E-01	1.14639E+00
0.80	6.45000	0	0	2.03166E-01	1.00000E+00	-1.51744E+00	-8.56182E-02	-2.47463E-01	1.21804E+00
0.75	6.45000	0	0	6.25002E-01	1.00000E+00	-1.29924E+00	2.72324E-01	-8.12028E-01	1.29924E+00
0.70	6.45000	0	0	5.26729E-01	1.00000E+00	-1.39204E+00	5.62471E-01	-7.33230E-01	1.39204E+00
0.65	6.45000	0	0	-1.54140E+00	1.00000E+00	-1.49912E+00	-7.74941E-01	2.31075E+00	1.49912E+00
0.60	6.45000	0	0	-2.89206E-01	1.00000E+00	-1.62405E+00	-4.59319E-01	4.69685E-01	1.62405E+00
0.55	6.45000	0	0	9.70465E-03	1.00000E+00	-1.77169E+00	-2.83281E-02	-1.71937E-02	1.77169E+00
0.50	6.45000	0	0	2.55393E+00	1.00000E+00	-2.59862E+01	-2.28896E+00	-4.97726E+00	1.94886E+00
0.48	6.45000	0	0	3.82539E-01	1.00000E+00	-2.03006E+00	2.60436E-01	-7.76577E-01	2.03006E+00
0.46	6.45000	0	0	5.26907E-03	1.00000E+00	-2.11833E+00	6.37821E-01	-1.11616E-02	2.11833E+00
0.44	6.45000	0	0	-6.62124E-01	1.00000E+00	-2.21461E+00	-4.91759E-01	1.46635E+00	2.21462E+00
0.42	6.45000	0	0	3.15404E-01	1.00000E+00	-1.51427E+02	-1.00947E+00	-7.31761E-01	2.32007E+00
0.40	6.45000	0	0	-5.09269E-01	1.00000E+00	-2.43608E+00	-4.16057E-01	1.24062E+00	2.43608E+00

0.38	6.45000	0	0	1.36556E-01	1.00000E+00	2.56429E+00	-5.39895E-01	-3.50168E-01	2.56429E+00
0.36	6.45000	0	0	8.34954E-02	1.00000E+00	3.47495E+00	-7.77881E-01	-2.26001E-01	2.70675E+00
0.34	6.45000	0	0	1.61742E-01	1.00000E+00	2.86597E+00	1.59213E+00	-4.63548E-01	2.86597E+00
0.32	6.45000	0	0	-7.83054E-01	1.00000E+00	9.90475E+00	-7.99664E-01	2.38447E+00	3.04510E+00
0.30	6.45000	0	0	3.57629E-02	1.00000E+00	3.58843E+00	2.52771E-01	-1.16162E-01	3.24810E+00
0.28	6.45000	0	0	3.46575E-01	1.00000E+00	3.48011E+00	1.34672E+00	-1.20612E+00	3.48011E+00
0.26	6.45000	0	0	-2.46652E+00	1.00000E+00	1.53945E+01	5.48702E+00	-9.24403E+00	3.74781E+00
0.24	6.45000	0	0	1.75647E+00	1.00000E+00	1.21399E+01	3.69668E+00	-7.13148E+00	4.06013E+00
0.22	6.45000	0	0	-1.00638E+00	1.00000E+00	1.35494E+01	1.49488E+00	-4.45749E+00	4.42923E+00
0.20	6.45000	0	0	1.71676E-01	1.00000E+00	4.87215E+00	1.00635E+00	-8.36430E-01	4.87215E+00
0.19	6.45000	0	0	-1.42609E+00	1.00000E+00	2.84408E+01	6.57357E+00	-7.31384E+00	5.12858E+00
0.18	6.45000	0	0	5.53923E-01	1.00000E+00	1.88426E+01	2.05407E+00	-2.99866E+00	5.41350E+00
0.17	6.45000	0	0	-4.42545E-01	1.00000E+00	1.01859E+01	2.08252E+00	-2.53664E+00	5.73194E+00
0.16	6.45000	0	0	-1.10177E+00	1.00000E+00	2.80501E+01	4.94037E+00	-6.71000E+00	6.09019E+00
0.15	6.45000	0	0	-3.65427E+00	1.00000E+00	2.87556E+01	8.17365E+00	-2.37389E+01	6.49620E+00
0.14	6.45000	0	0	9.48046E-01	1.00000E+00	1.38859E+01	2.21293E+00	-6.59861E+00	6.96022E+00
0.13	6.45000	0	0	-3.64750E+00	1.00000E+00	3.03608E+01	1.00898E+01	-2.73403E+01	7.49562E+00
0.12	6.45000	0	0	1.24707E-01	1.00000E+00	8.12025E+00	3.39607E-01	-1.01266E+00	8.12026E+00

0.11	6.45000	0	0	-7.95266E+00	1.00000E+00	1.37413E+02	-2.36257E+01	7.04483E+01	8.85845E+00
0.10	6.45000	0	0	-5.27639E-01	1.00000E+00	-1.04044E+01	1.93421E+00	5.14147E+00	9.74430E+00
0.095	6.45000	0	0	-1.63671E+00	1.00000E+00	1.69910E+01	-5.63007E+00	1.67880E+01	1.02572E+01
0.090	6.45000	0	0	-4.02834E-03	1.00000E+00	-1.08270E+01	7.97454E-01	4.36148E-02	1.08270E+01
0.085	6.45000	0	0	3.95053E-01	1.00000E+00	-1.15267E+01	1.51881E+00	-4.52884E+00	1.14639E+01
0.080	6.45000	0	0	2.26467E-01	1.00000E+00	-1.22488E+01	1.19878E+00	-2.75845E+00	1.21804E+01
0.075	6.45000	0	0	6.69894E-01	1.00000E+00	-1.29924E+01	2.91885E+00	-8.70354E+00	1.29924E+01
0.070	6.45000	0	0	3.30943E+00	1.00000E+00	-4.18887E+01	1.54497E+01	-4.60687E+01	1.39204E+01
0.065	6.45000	0	0	1.41389E-01	1.00000E+00	2.56898E+01	-4.61849E+00	2.11959E+00	1.49912E+01
0.060	6.45000	0	0	-1.28346E-01	1.00000E+00	-1.62405E+01	7.75379E-01	2.08440E+00	1.62405E+01
0.055	6.45000	0	0	-9.08622E-01	1.00000E+00	5.69378E+01	-6.55676E+00	1.60980E+01	1.77169E+01
0.050	6.45000	0	0	3.95032E+01	1.00000E+00	5.63086E+02	2.58183E+02	-7.69862E+02	1.94886E+01
0.048	6.45000	0	0	2.49486E+00	1.00000E+00	-3.07547E+01	1.69852E+01	-5.06472E+01	2.03006E+01
0.046	6.45000	0	0	-4.14021E-01	1.00000E+00	2.11833E+01	-2.94124E+00	8.77032E+00	2.11833E+01
0.044	6.45000	0	0	6.90904E-02	1.00000E+00	-2.21461E+01	1.08889E+00	-1.53009E+00	2.21462E+01
0.042	6.45000	0	0	1.21869E+00	1.00000E+00	2.32007E+01	-9.48222E+00	2.82745E+01	2.32007E+01
0.040	6.45000	0	0	-2.84811E-01	1.00000E+00	-2.43608E+01	2.32682E+00	-6.93822E+00	2.43608E+01